OpenCourseWare

Lagrangian and Eulerian Representations of Fluid Flow

by Prof. James F. Price

Lagrangian and Eulerian representations of fluid flow

Part 1: Kinematics and the equations of motion

James F. Price

Woods Hole Oceanographic Institution,
Woods Hole, Massachusetts, 02543
https://www2.whoi.edu/staff/jprice/ jprice@whoi.edu

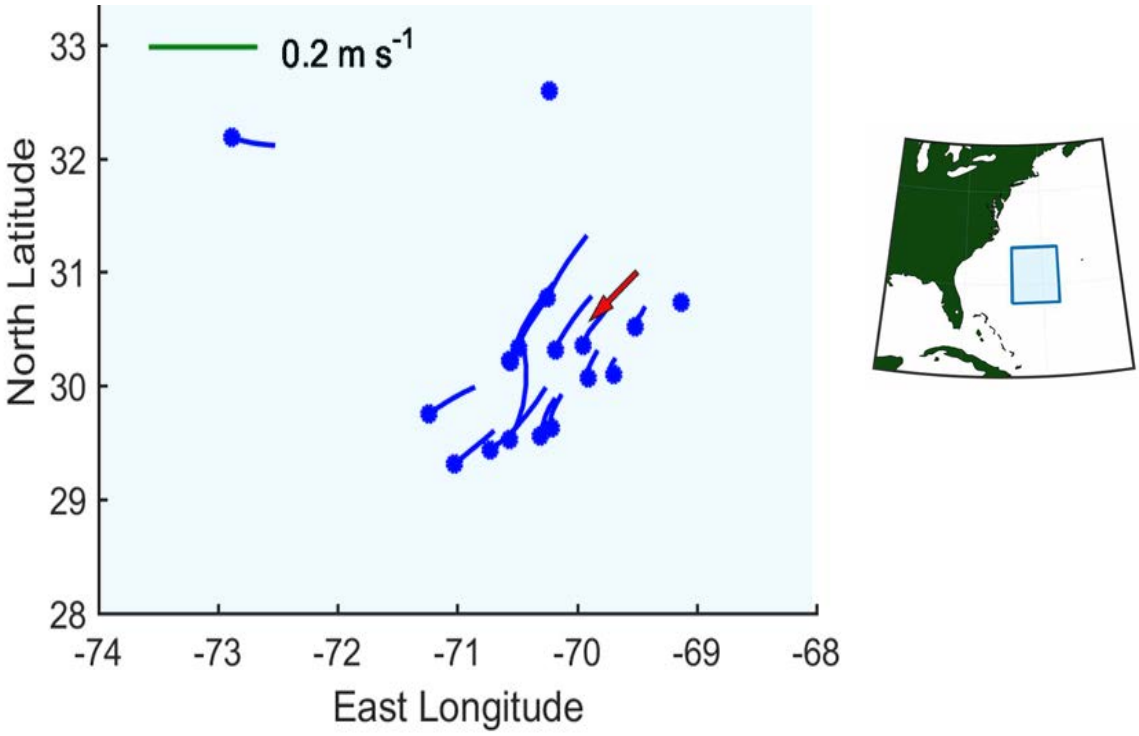

Figure 1: Lagrangian and Eulerian measurements of ocean currents at a depth of 1300 m in the subtropical western North Atlantic. The blue comets are five day-long (Lagrangian) trajectories of neutrally buoyant floats, and the red vector is the (Eulerian) current measured by a fixed current meter and scaled similarly. To see these data in motion visit https://www2.whoi.edu/staff/jprice/wp-content/uploads/sites/199/2022/06/LDE1300.mp4 The goal of this essay is to help you develop an understanding of both the Lagrangian and the Eulerian systems, and especially to appreciate how they may be used side-by-side in the analysis of a fluid flow.

Abstract: This essay introduces the two systems that are widely used to observe and analyze fluid flows. The first system, termed Lagrangian, seeks to observe or calculate the trajectories of specific fluid parcels. Lagrangian methods will sometimes be the most efficient way to sample a fluid flow, and, the physical conservation laws are inherently Lagrangian since they apply to specific fluid volumes. However, the Lagrangian equations of motion applied to a three-dimensional continuum are awkward for many applications, and thus the majority of theory in fluid mechanics has been developed within the second system, termed Eulerian, which seeks to observe or calculate the fluid velocity at fixed positions. The premise of this essay is that an improved understanding and appreciation of both systems will help you build the framework for your continued study of fluid mechanics.

The transformation of the conservation laws from a Lagrangian to an Eulerian system can be envisaged in three steps. (1) The first is dubbed the Fundamental Principle of Kinematics: the fluid velocity at a given time and fixed position (the Eulerian velocity) is equal to the velocity of the fluid parcel (the Lagrangian velocity) that is present at that position at that instant. Thus while we often speak of Lagrangian velocity or Eulerian velocity, it is important to keep in mind that these are merely (but significantly) different ways to represent a given fluid flow. (2) A similar relation holds for time derivatives of fluid properties, say a passive tracer, c: the time rate of change observed on a specific fluid parcel, $Dc/Dt = \partial c/\partial t$ in the Lagrangian system, has a counterpart in the Eulerian system, $Dc/Dt = \partial c/\partial t + \mathbf{V} \cdot \nabla c$, called the material derivative. The material derivative at a given position is equal to the Lagrangian time rate of change of the parcel that is present instantaneously at that position. And lastly, (3) The physical conservation laws apply to extensive quantities, i.e., the mass or the momentum of a specific fluid volume. The time derivative of the integral of a tracer over a moving fluid volume (a Lagrangian quantity) can be transformed into the equivalent Eulerian time derivative for the corresponding intensive quantity (the tracer concentration) by means of the Reynolds Transport Theorem.

In an Eulerian system, transport by the fluid flow is represented by the advection term of the material derivative, $\mathbf{V} \cdot \nabla c$, the vector product of the fluid velocity and the gradient of the tracer. In general, both of these vectors will be unknowns, and the nonlinearity of advection leads to many of the challenging phenomena of fluid dynamics. There are some bounds upon what advection alone can do. For variables that can be written in conservation form, e.g., mass and momentum, advection can not be a net source or sink when integrated over a closed domain.

The Lagrangian solution for a tracer comes in two parts, the parcel trajectory and the tracer value of the parcel. The tracer balance of a parcel will include the effects of a local source and of the change in volume, but crucially, the motion of a parcel does not in and of itself cause a change in tracer amplitude. An Eulerian solution comes in one piece that includes the effects of advection, $\mathbf{V} \cdot \nabla(\ )$, and so is likely to be more complex than is the corresponding, two-piece Lagrangian solution.

The method of characteristics seeks to develop an Eulerian solution of first order partial differential equations (PDEs), such as the advection equation, by defining an equivalent system of (usually simpler) ordinary differential equations (ODEs). The first step is to solve for the characteristics of the PDE, which are the parcel trajectories if the PDE is an advection equation. The second step applies the initial data to the characteristics, and the third step solves for the effects of a source acting along the characteristics. If the source vanishes, then the initial data are transported unchanged (adiabatically) along the characteristics.

More on Fig. (1). The subsurface SOFAR floats that made these trajectories were tracked acoustically. They transmit low frequency (250 Hz) pulses that are partially trapped within a sound speed minimum at about 1 km depth below the sea surface called the SOFAR channel. Trapped, low frequency sound can propagate thousands of kilometers without intersecting the surface or the sea floor. Sound pulse arrivals observed at two or more locations enable float tracking over ocean basin scales. These floats endure for up to several years, providing a long term and large space scale Lagrangian view of ocean currents. The potential vorticity balance of the wave-like motion seen here will be discussed in Part 2. These data are a small part of the subsurface float archive available online from https://www.aoml.noaa.gov/phod/ , and then search for 'float trajectories'. A Matlab script that will read and plot these data: https://www2.whoi.edu/staff/jprice/wp-content/uploads/sites/199/2023/07/Subsurffloats.txt

Author's Preface

Topics in Fluid Dynamics:

i) Lagrangian and Eulerian representations of fluid flow
ii) Dimensional analysis of models and data sets
iii) a Coriolis tutorial

This collection of three essays grew out of my experience teaching the graduate-level introduction to fluid mechanics in the MIT/WHOI Joint Program in Oceanography. Students enter the Joint Program with widely varying experience in mathematics and physics and the goal of this introductory course is to help each student learn the fundamental concepts and tools of fluid mechanics that will be an essential foundation for their research in oceanic and atmospheric sciences.

There are a number of modern, comprehensive textbooks that can serve most of the objectives of this kind of course very well. However, it seemed to me that there were three specific topics that could benefit from a greater depth of treatment than a comprehensive text can afford; these were (i) Lagrangian and Eulerian representations of fluid flow, (ii) Dimensional analysis, and (iii) the Coriolis force. The first topic is either omitted or barely mentioned in introductory texts, and a cursory treatment of the second and third topics leaves many students in a state of mystery. Of course, what is clear and sufficient for one student (or instructor) may be inadequate or unsatisfying for another student (or instructor) having a different background or level of interest. There is no doubt that the Coriolis force is described rigorously in many classical mechanics texts. However, for most physics and engineering students, the consequences of the Coriolis force are not compelling: slightly deflected rockets and very slowly precessing pendulums. But for a student of the atmosphere or ocean, the Coriolis force is vital — it shapes the structure of most large scale, low frequency flows, and so its consequences will be

encountered nearly every working day. A few additional hours devoted to a thorough-going understanding of the origin and properties of the Coriolis force will be, for them, time well spent.

With that as the backdrop, I set out to write three essays dealing with each topic in turn and with the goal of making a clear and accessible written source combined with numerical problems and software, where possible. Compared with the necessarily brief treatment of these topics found in most introductory texts, these essays go into somewhat greater depth, and at least occasionally make explicit mention of the relevant contrast class, i.e., a useful explanation must show what *is*, and it can be very helpful to consider at least a part of what *is not*, and to understand what alternatives may exist.

The second and third of these essays, 'Dimensional analysis' and 'a Coriolis tutorial', have a clearly defined scope. Examples treated in these essays are often geophysical or fluid mechanical, but the scope of dimensional analysis goes far beyond geophysics. The goal of this first essay, 'Lagrangian and Eulerian representations', is in some respects more ambitious. The overt goal is to introduce the kinematics of fluid flow by studying the transformation of observations and conservation laws between Lagrangian and Eulerian systems. An implicit, deeper goal is to address a question that lurks in the minds of many first-year students: what is it that makes fluid mechanics different from the rest of classical mechanics, and, while we are at it, why is fluid mechanics so challenging?

These essays are in the public domain for all personal, educational purposes consistent with the Creative Commons license, BY-NC-SA, and they may be freely copied and distributed for educational purposes. I will be grateful to hear your comments and questions, and especially for suggestions that will help make these essays more accessible or more useful for your purpose.

Jim Price
June 2006; revised August 2023
Woods Hole Oceanographic Institution
jprice@whoi.edu

Contents

1 The kinematics of fluid flow. 6

1.1 What is the issue? Complex kinematics, mainly . . . 7
1.2 Two ways to observe and describe a fluid flow . . . 9
1.2.1 Lagrangian coordinates are the positions and the properties of fluid parcels . . . 9
1.2.2 Eulerian coordinates are the fluid properties at fixed positions . . . 11
1.3 The goal and the plan — Lagrangian to Eulerian . . . 12
1.4 The key ideas of this section . . . 13
1.5 Homework problems and projects . . . 16
1.6 About this essay . . . 16

2 The Lagrangian (or material) coordinate system. 17

2.1 A simple Lagrangian flow . . . 18
2.2 Mass and momentum conservation in a Lagrangian system . . . 19
2.3 An exact wave equation in one dimension . . . 23
2.4 The agony of the three-dimensional Lagrangian equations . . . 25
2.5 The joys of Lagrangian measurement . . . 27
2.5.1 An economy of scale . . . 27
2.5.2 Diagnosing source terms . . . 30
2.6 Key ideas . . . 32
2.7 Problems . . . 33

3 The Eulerian (or field) coordinate system. 33

3.1 The formal transformation of Lagrangian to Eulerian velocity . . . 34
3.2 Transforming time derivatives; the material derivative . . . 36
3.3 Transforming integrals and their time derivatives via the Reynolds Transport Theorem . . . 37
3.4 The Eulerian equations of motion . . . 40
3.4.1 Mass conservation represented in field coordinates . . . 40
3.4.2 The flux form of the Eulerian equations. . . . 42
3.4.3 Momentum conservation represented in field coordinates . . . 45
3.4.4 Fluid mechanics requires a stress tensor . . . 46
3.4.5 The flux form of the momentum equation; Reynolds number . . . 51
3.4.6 Energy conservation; the First Law of Thermodynamics applied to a fluid . . . 53
3.4.7 Vorticity balance . . . 54
3.5 Remarks on the Eulerian equations . . . 55
3.6 Key ideas . . . 56
3.7 Problems . . . 56

4 An advection problem, two ways **57**
4.1 The Lagrangian solution . . . 58
4.2 The Eulerian solution via the method of characteristics . . . 59
4.3 Comments on these Lagrangian and Eulerian solutions . . . 62
4.4 More advanced problems via the method of characteristics . . . 62
4.4.1 With a source . . . 63
4.4.2 Variable coefficient and non-conservation . . . 65
4.4.3 When the current is advected . . . 66
4.5 Key ideas . . . 68
4.6 Problems . . . 69

5 Coming up in Part 2 **71**

6 Appendices **71**
6.1 Physical properties of fluids and solids . . . 71
6.1.1 In response to a normal stress, liquids and solids are not very different . . . 72
6.1.2 In response to shear stress, solids deform and fluids will *flow*, often in very complex ways . . . 74
6.2 Composite functions and inverse functions . . . 78
6.2.1 Functions of functions . . . 78
6.2.2 Inverse functions and their derivatives . . . 80
6.2.3 Rules for differentiation and change of variables in integrals . . . 81

7 Index **82**

1 The kinematics of fluid flow.

This essay introduces some of the key concepts and mathematical tools that make up the foundation of fluid mechanics, a vast subject that encompasses widely diverse materials and phenomena. The emphasis here is upon the flow of non-exotic fluids — air and water — that make up the Earth's fluid environment.[1,2] The intermediate spatial scales and comparatively slow speeds of the atmosphere and

[1] Footnotes provide references, extensions or qualifications of material discussed in the main text. Appendices are used to include material that is relevant but probably not essential for most readers. Footnotes and appendices may be skipped on first reading.

[2] An invaluable web source for fluid dynamics generally is the collection of films by Ascher Shapiro and colleagues and specifically, 'Eulerian Lagrangian Description': https://video.odl.mit.edu/videos/591abfae9b1d432f9f9cdd05e40261da/

ocean are well within the realm of classical mechanics: conservation of mass, conservation of momentum and angular momentum and conservation of energy. The theme of this essay follows from the question — How can these conservation laws be codified in a way that is suitable for the analysis of a fluid flow?

In principle the answer is straightforward; erect a coordinate system that is suitable for describing a fluid flow, and then derive the mathematical form of the conservation laws that correspond to that coordinate system. The definition of a coordinate system is a matter of choice, and the issues are mainly in the realm of kinematics, i.e., the description of motion rather than physical properties.

1.1 What is the issue? Complex kinematics, mainly

Some day soon you will have the opportunity to study the fluid dynamics of a domain that is grand in scale and vitally important to humankind, the circulation of an ocean basin or the Earth's atmosphere. But for now you can make useful qualitative observations in a domain that is small and accessible: even the flow in a teacup will reveal some of the essential kinematic aspects of fluid flow that are common to many fluid phenomena. To initiate flow in a tea cup you need only apply a gentle, linear push on the fluid with a spoon, say, and then observe the result. The motion of the fluid bears no obvious resemblance to this simple forcing. The fluid that is pushed directly by the spoon can not simply plow straight ahead, both because water is effectively incompressible for such gentle motion and because the inertia of the fluid that would have to be displaced is appreciable. Instead, the fluid piles up in front of the spoon and then flows around both edges from front to back. The result is a pair of swirling, coherent features called vortices, or eddies, that spin in opposite directions (Fig. 2).[3] These vortices are clearly two-dimensional, despite that the forcing was a one-dimensional push. This vortex pair moves slowly through the fluid, consistent with the notion that the vortices are mutually advected by one another. Careful observation will reveal that most of the linear (one-dimensional) momentum imparted by the push is contained within their collective, translational motion. Momentum is certainly conserved, but the qualitative structure of the resulting fluid flow would be very hard to anticipate from intuition derived from solid mechanics. Still greater complexity will result if the initial push is made more vigorous; the fluid motion will spontaneously become three-dimensional and irregular, or turbulent. Thus the qualitative structure of the flow depends not only upon the geometry of the forcing, which is expected, but also upon its amplitude.

After a short time, a few tens of seconds, the smallest spatial scales of the motion will be damped by viscosity leaving larger and larger scales of motion. This damping process is in the realm of physics since it depends upon a physical property of the fluid, the viscosity, and also upon the physical scale (i.e., the size) of the flow features. Thus even though our intent in this essay is to emphasize kinematics, we can not go far with observation of real fluids before acknowledging physical phenomena. The last surviving flow feature in a tea cup forced by an impulse is likely to be a slowly revolving vortex that fills the entire domain.

What do these observations portend for a theory or description of a fluid flow? For one, every parcel[4]

[3] This and similar figures were made by the author using AI and DALL.E 2.

[4] Fluid material is variously referred to as a particle, a parcel or a patch. A fluid particle is equivalent to a solid particle in that it denotes a specific piece of the material that has a vanishing extent. If the interest is position only, then a fluid particle would suffice. A fluid parcel is a particle with a small but finite area and volume and hence can be pushed around by normal and

Figure 2: To make and observe a fluid flow you need only:

Push gently then watch,
eddies swirling left and right,
move ahead as one.

that participates in fluid flow is literally pushed and pulled by all of the surrounding fluid parcels via shear stress and normal stress (reviewed in Sec. 6.1). Thus the motion of a given fluid parcel can not be predicted in isolation from its surroundings, rather we have to predict the motion of all of the surrounding fluid parcels as well. How extensive are these so-called surroundings? It depends upon how far backward or forward in time the analysis must extend, and also upon how rapidly signals including waves are propagated within the fluid. If a parcel is followed long enough, then every parcel will have a dependence upon the entire domain occupied by the fluid. In other words, even if the goal was limited to calculating the motion of just one parcel or the flow at just one site, it will often be necessary to solve for the fluid motion over the entire domain at all times of interest. As remarked already and as you have observed (if you have studied your teacup) fluid flows will often develop motion on all accessible spatial scales, from the scale of the domain down to a scale set by viscous or diffusive properties of the fluid, typically a few millimeters in water. What was intended to be a small and simple (but unconstrained) fluid flow will thus spontaneously transform into an irregular, three-dimensional phenomenon that fills the entire, available domain and that has spatial scales much smaller and much larger than that imposed by the forcing. The tea cup and its fluid flow are well within the domain of classical physics and so everything observed is consistent with the familiar conservation laws for mass, momentum, angular momentum and energy.

It is this complex kinematics of fluid flow that most distinguishes fluid flows from the motion of otherwise comparable solid materials. The physical origin of this complex kinematics is the ease with which fluids undergo shear deformation combined with the generally small effect of viscosity on medium to large scale motions. The practical consequence is that an appropriate description and theory of fluid flow must be able to define motion and acceleration on arbitrarily small spatial scales, and that the coordinates of a fluid theory or model must, in principle, vary continuously. (Though in practice, the coordinates of numerical models are defined as finite grids, having a grid interval that then becomes an important aspect of the solution.)

---

shear stresses. Parcels are the fare of the dynamical equations. A tracer patch is a macro-scale parcel that is big enough to become significantly deformed in time. The spot of cream that you may have used as the tracer in your teacup experiments is such a patch. When ‘point’ is used as a noun it will always mean a point in space, i.e., a position, rather than a fluid particle or parcel.

1.2 Two ways to observe and describe a fluid flow

Let's suppose that your task is to make a quantitative description of a fluid flow, first by observation, and then by constructing a theory or model. There are two ways to accomplish the observations, either by tracking specific, identifiable fluid material volumes that are carried about with the flow, the Lagrangian method, or by observing the fluid velocity at locations that are fixed in space, the Eulerian method (Fig. 3). Both methods are used widely in the analysis of the atmosphere and oceans, and in fluid mechanics generally. This essay aims to investigate both systems, and emphasizes the transformation of data and conservation laws from one system to the other.

1.2.1 Lagrangian coordinates are the positions and the properties of fluid parcels

The most natural way to observe a fluid flow is to observe the trajectories of small, recognizable parcels of a passive tracer that are carried along by the flow (almost certainly your observation method in the tea cup experiment). For the purpose of a continuum theory, it is essential to identify specific parcels. One possibility is to use the position of the parcels at some specified time, say the initial time, $t = 0$. Denote the initial position by $\mathbf{A}$, with Cartesian components, $(a,\ b,\ c)$. Let $\tilde{X}$ denote the position vector of a parcel whose Cartesian components are the lowercase $(\tilde{x},\ \tilde{y},\ \tilde{z})$, i.e, $\tilde{x}$ is the x-coordinate of a parcel, $\tilde{y}$ is the y-coordinate and so on. Notice that a tilde $\tilde{(\ )}$ is appended to the symbols that represent Lagrangian position to distinguish from the Eulerian position (just plain $\mathbf{X}$) coming soon. (There is no tilde with the initial position $\mathbf{A}$ since it will be reserved for the Lagrangian system.) It will be assumed that the position of parcels or floats at all later times can be observed to form a parcel trajectory,

$$\tilde{\mathbf{X}} \ = \ \tilde{\mathbf{X}}(\mathbf{A},t) \tag{1}$$

The trajectory $\tilde{\mathbf{X}}$ of specific fluid parcels is a dependent variable in a Lagrangian description (along with pressure and density) and the initial position $\mathbf{A}$ and time, t, are the independent variables. The velocity of a parcel is the time rate change of the parcel position (1) holding $\mathbf{A}$ fixed, and called the

$$\text{Lagrangian velocity:} \qquad \boxed{\tilde{\mathbf{V}}(\mathbf{A},t) \ = \ \frac{d\tilde{\mathbf{X}}(\mathbf{A},t)}{dt}\,|_{\mathbf{A}\,=\,constant} \ = \ \frac{\partial\tilde{\mathbf{X}}(\mathbf{A},t)}{\partial t}} \tag{2}$$

If instead of a parcel trajectory from a theory we have an observed float trajectory (a float is any artificial, trackable surrogate for a fluid parcel) then holding $\mathbf{A}$ constant would be replaced by holding the float identity fixed.

Eq.(2) is the first instance of the important idea of a time-derivative made while holding the parcel (or float) identity fixed, denoted by a capital D and called the

$$\text{material derivative generally:} \qquad \boxed{\frac{D(\ )}{Dt} \ \equiv \ \frac{d(\ )}{dt}\,|_{\mathbf{A}\,=\,constant}} \tag{3}$$

A material derivative D/Dt applied to a Lagrangian variable is equivalent to a partial derivative with respect to time, as in Eq. (2), since $\mathbf{A}$ is held constant. The equivalent material derivative in an Eulerian

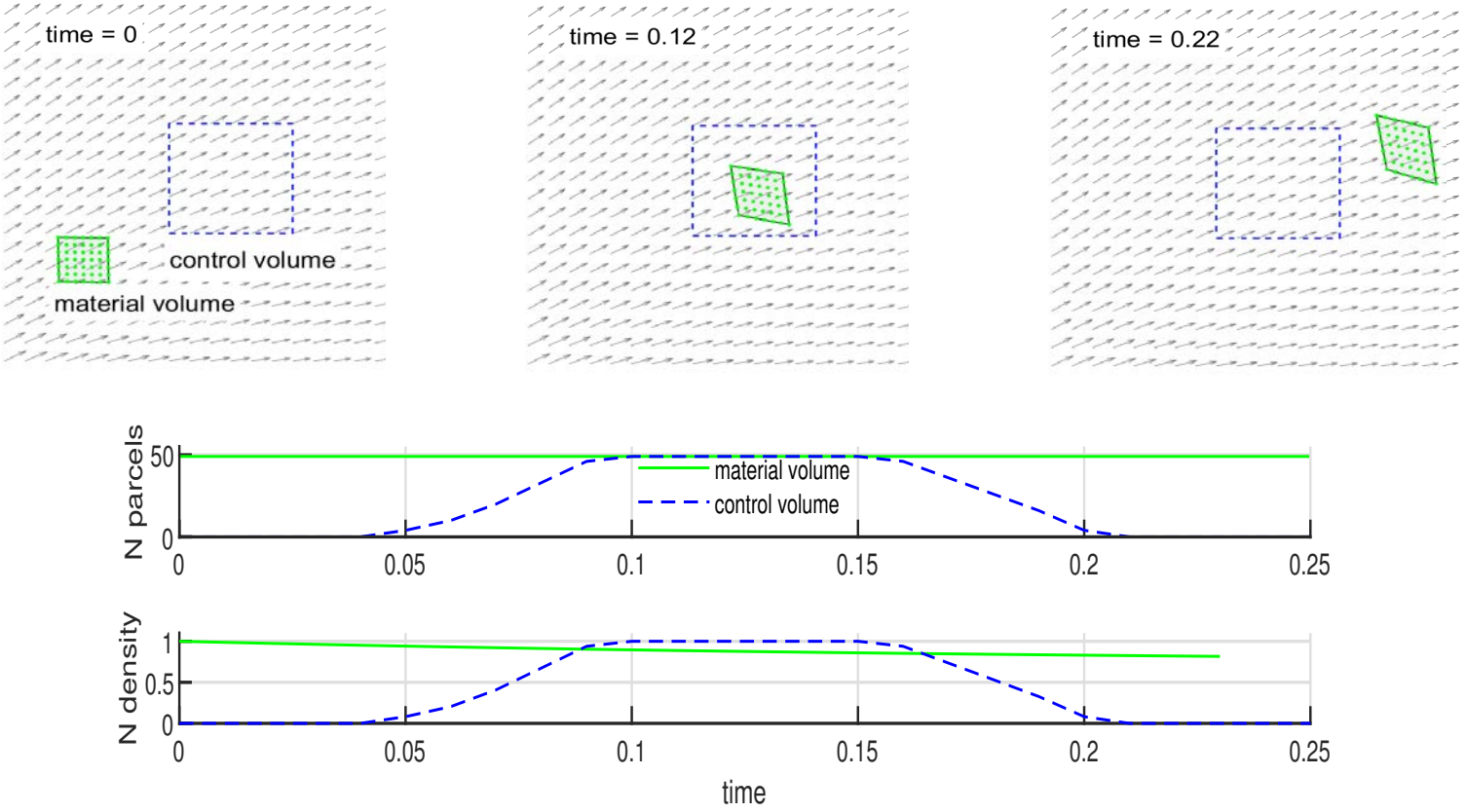

Figure 3: **(upper)** Three snapshots from a numerical tracer advection experiment that illustrate Lagrangian and Eulerian representations. A passive tracer was inserted into a velocity field given by the regular array of vectors that are directed mainly to the right and upward. This velocity field is steady, and has some divergence. It is an ideal fluid flow in that there is no diffusion. The initial condition at left includes a patch of tracer that is shaded gray with a green boundary and includes 49 passive, green parcels. This is a material volume in that it is defined by these marked fluid parcels and it moves exactly with the fluid. A control volume is defined by the dotted blue box that is fixed in space and is completely invisible to the flow. The fluid material inside the control volume is changed continually by the flow: tracer begins to enter the control volume at time = 0.05, and is flushed out by time = 0.22. **(middle panel)** Some tracer statistics. The number of parcels, N, (the 49 green dots) within the material volume (the solid green line) and within the control volume (the dashed blue line) as a function of time. The parcel count within the material volume is constant in time, since parcels do not cross the boundary of a material volume in ideal fluid flow. On the other hand, the parcel count within the control volume is strongly time-dependent due to advection of parcels through the boundaries. **(lower panel)** The parcel number density (per area) normalized by the maximum value. The parcel density within the material volume (green line) decreases with time on account of the divergence, which increases the area of the material volume, but does not change the parcel count, constant at $N = 49$. Compare this with the parcel density in the control volume (the blue dashed line) which is strongly time-dependent as parcels were advected into and then out of the control volume. A Lagrangian representation seeks to observe and predict the position, pressure and tracer properties of material volumes that move with the flow; an Eulerian representation seeks to observe and predict these fluid properties within fixed control volumes. This example illustrates that Lagrangian and Eulerian representations may be qualitatively different, even while describing the same flow.

system has a significantly different form that will be developed in Sec. 3.[5]

1.2.2 Eulerian coordinates are the fluid properties at fixed positions

If tracking fluid parcels is impractical, then the fluid velocity could be observed by means of current meters that are implanted at fixed positions, $\mathbf{X}$, the usual field coordinate (and notice there is no tilde). The essential component of every current meter is a transducer that converts fluid motion into a readily measured signal, e.g., the rotary motion of a propeller or the Doppler shift of a sound pulse. Regardless of the mechanical details, the velocity sampled in this way, termed the 'Eulerian' velocity, $\mathbf{V}$, is intended to be the velocity (2) of the fluid parcel that is present, instantaneously, within the fixed and suitably small volume of space that is sampled by the transducer. A formal definition, here said to be the Fundamental Principle of Kinematics or FPK,

$$\text{Eulerian velocity via the FPK:} \qquad \boxed{\mathbf{V}(\mathbf{X},t)\,|_{\mathbf{X}=\tilde{\mathbf{X}}(\mathbf{A},t)} \;=\; \frac{\partial \tilde{\mathbf{X}}(\mathbf{A},t)}{\partial t}} \tag{4}$$

This equation contains both Eulerian and Lagrangian variables, $\mathbf{X}$ and $\tilde{\mathbf{X}}$, and the entire content of (4) hinges upon the distinction between them. The plain (no tilde) $\mathbf{X}$ is a fixed, field coordinate. With a tilde appended, $\tilde{\mathbf{X}}$ is the position of a specific fluid parcel, here identified by the starting position, $\mathbf{A}$. No doubt the FPK Eq. (4) looks a bit abstract, but it codifies a clear and concrete meaning: the (Eulerian) fluid velocity at a given time and at a fixed position $\mathbf{X}$ is the (Lagrangian) velocity of the fluid parcel that happens to be present at that position, at that instant in time. The velocity $\mathbf{V}$ is a dependent variable in an Eulerian description, as are pressure and density (and possibly other thermodynamic properties) and the independent variables are the position, $\mathbf{X}$, and time, t. The Eulerian velocity defined by the FPK may be seen as a composite function constructed from the Lagrangian velocity and position (composite functions are reviewed in an appendix, Sec. 6.2).[6]

One way to appreciate the difference between the Lagrangian velocity $\tilde{\mathbf{V}}$ and the Eulerian velocity $\mathbf{V}$ is to note that $\tilde{\mathbf{X}}$ in the Lagrangian velocity of Eq. (2) is the position of a moving parcel, while $\mathbf{X}$ in Eq. (4) is the arbitrary and fixed position of a current meter. Parcel position is a result of the fluid flow rather than our choice, aside from the initial position. As time runs, the position of any specific parcel will change, barring that the flow is static. The velocity observed at the current meter position will be the velocity of the sequence of parcels (each having a different $\mathbf{A}$) that move through that position as time runs. In general, the Lagrangian and Eulerian velocities are different, and in many cases they will be qualitatively different, as illustrated by the tracer advection experiment of Fig. (3).[7] However, there are specific, related times and places — given by the FPK — where the Lagrangian and Eulerian velocities and other fluid properties are equal.

[5] There are about twenty boxed equations in this essay, beginning with Eq. (2), that you are likely to encounter over and over again in a study of fluid mechanics.

[6] The present usage FPK is idiosyncratic, and you might never see it elsewhere. The claim that the FPK is 'fundamental' is sustainable if, as presumed here in Part 1, the starting point of an analysis is a (Lagrangian) trajectory.

[7] In some fields it is common to refer to transport by fluid motion as 'convection'. Convection is also used to refer to fluid motion caused specifically by density differences. In the end, the terms 'advection' and 'convection' are synonymous.

The float and current meter data of Fig. (1) afford an opportunity to check the FPK in practice: when the flow is smoothly varying on the horizontal scale of the float cluster, and when the floats surround the current meter mooring, the Lagrangian velocity (the blue comets are five-day long trajectories) and the Eulerian velocity (the single red vector) appear to be very similar. But at other times, and especially when the velocity is changing direction rapidly in time or in space, the equality expected from the FPK is not obvious.[8]

The present use of Lagrangian and Eulerian is standard. If no such label is appended, then Eulerian is almost always understood to be the default.[9] This Lagrangian/Eulerian usage should not be construed to mean that there are two physical fluid velocities. Rather, a given fluid flow can be sampled in two quite different ways, by tracking specific parcels or foats (Lagrangian), or by observing the velocity of the sequence of fluid parcels that flow through a fixed site (Eulerian). The formal statement of the relationship between these systems is the FPK, Eq. (4). Much of what follows in this essay amounts to variants or extensions of the FPK combined with the familiar conservation laws of classical physics.

1.3 The goal and the plan — Lagrangian to Eulerian

Now that we have learned (or imagined) how to observe a fluid flow at one or a few parcels or sites, we can begin to think about surveying the entire domain. This will require an important decision regarding the sampling method; should these observations come from tracking a large number of fluid parcels (or floats) as they wander throughout the domain, or, by deployment of current meters at many additional sites? In principle, either approach could suffice to define the flow if done in exhaustive detail (an example being the solution from the ocean circulation model of Fig. 5). Nevertheless, the observations themselves and the analysis needed to understand these observations would be quite different, as will be discussed in examples below.

In practice, the choice of a sampling method will probably be decided more by the availability of floats or current meters, then by any Lagrangian or Eulerian preference that you may happen to hold. Thus it commonly happens that observations are made in one system, and then diagnostic analysis is performed in the other system. A similar kind of duality arises in the development of models and theories; the (Lagrangian) parcels of a fluid flow follow conservation laws that are identical with those followed by the solid particles of classical dynamics. Nevertheless, the theory applied to a continuum model of fluid flow is almost always Eulerian. The goal of this essay is to help you develop some

[8] If a model seems to be consistent with relevant observations, then there may not be much more to say. Potentially much more interesting would be an outright failure of a plausible theory. What would we do here if the float and current meter velocities did *not* appear to be similar? We would not lay the blame on Eq. (4), which is, in effect, an identity, i.e., it defines what we mean by the Eulerian velocity. Instead, we would start to question, in roughly this order: 1) If $\tilde{\mathbf{X}} = \mathbf{X}$ as required by the FPK, since this would imply a collision between float and current meter (none was reported). 2) If some time-averaging had been applied. It was, inevitably, and time-averaging can have a surprising effect that will be taken up in Part 2. 3) Whether the float tracking accuracy was sufficient, and whether the current meter had been improperly calibrated or had malfunctioned.

[9] This usage is not the least bit descriptive of the two systems in the way that 'material' and 'field' are, somewhat. It is also inaccurate as historical attribution; Lamb, *Hydrodynamics*, 6th ed., (Cambridge Univ. Press, 1937) credits Leonard Euler with developing both representations. Whether good history or not, this essay propagates the Lagrangian and Eulerian usage because it is so thoroughly ingrained into the topic that any attempt to make a change would cause more confusion than benefit.

understanding of both systems, and to appreciate how Lagrangian and Eulerian data, models and concepts may be woven together to implement the analysis of fluid flow.

The point of view and the plan taken by this essay is that Lagrangian observation and conservation properties are the starting point, Sec. 2. However, this felicity does not extend all the way to the three-dimensional Lagrangian equations of motion, which are awkward for most applications. The object of Sec. 3 is then to derive the Eulerian equations of motion starting from a Lagrangian perspective. The powerful method of characteristics, taken up in Sec. 4, uses the properties of advection to construct a system of ordinary differential equations that are the equivalent of a first order, partial differential equation. This can lead to an insightful analysis of advection phenomenon, e.g., shock waves. Sec. 5 is a very brief preview of the topics considered in Part 2. Sec. 6 is made up of two appendices. Sec. 6.1 reviews the physical properties of fluids, and the response to normal and tangential stress. Sec. 6.2 reviews the mathematical properties of composite functions. Each section is concluded with a list of key ideas and a few homework problems or projects. An overall summary is provided by the Abstract.

1.4 The key ideas of this section

1) The distinctive property of a fluid is that it will *flow* when subjected to a shear stress or an unconstrained normal stress (reviewed in the appendix of Sec. 6.1).

2) Even when the physics is purely classical, the kinematics of even a simple (but unconstrained) fluid flow can be daunting, and requires coordinate systems that are adequate to a continuous medium.

3) The motion of fluid parcels is entangled in the sense that the motion of any one fluid parcel is determined by the pressure and shear stress exerted by all of the neighboring parcels. Given sufficient time, the relevent neighborhood will extend all the way to the domain boundary.

4) A given fluid flow may be described and modelled in one of two ways. A Lagrangian description follows the motion of specific, moving fluid volumes called parcels. An Eulerian description is of velocity and other fluid properties at fixed points in space.

5) The Eulerian velocity at a given $(\mathbf{X}, t)$ is the (Lagrangian) velocity of the parcel moving through that $\mathbf{X}$ and at that time, i.e., instantaneously in space and time. The formal relation between Eulerian and Lagrangian velocity is here said to be the Fundamental Principal of Kinematics, or FPK, and which amounts to a composite function constructed from Lagrangian trajectories.

6) A fluid flow may be defined fully by a sufficient number of either Lagrangian or Eulerian measurements. In many investigations it will be helpful or necessary to transform data from one system to the other, e.g., Lagrangian observations may be mapped into an Eulerian field via the FPK. The reverse transformation, Eulerian velocity field to Lagrangian trajectories, is an essential diagnostic of material (tracer) transport and requires an integration (taken up in Part 2).

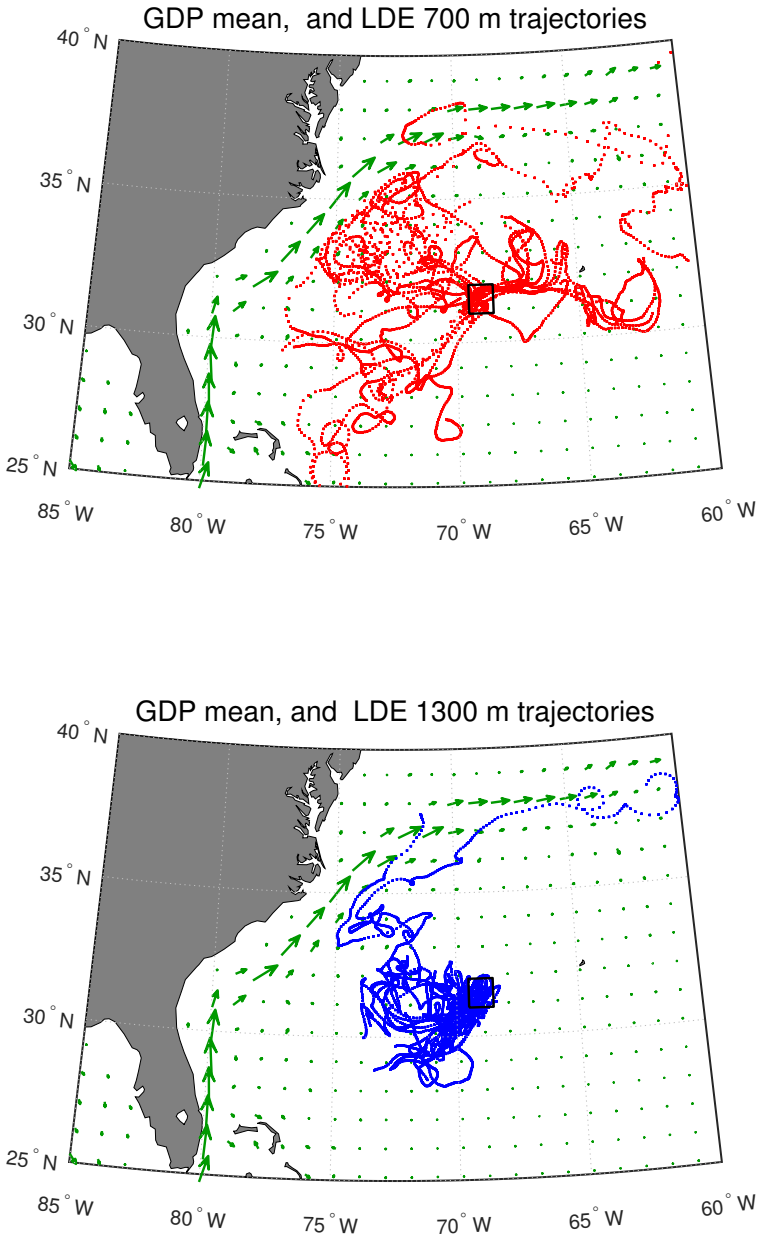

Figure 4: Trajectories of acoustically-tracked SOFAR floats from a depth of 700 m **(upper)** and 1300 m **(lower)** that were deployed as part of the Local Dynamics Experiment (LDE). (A subset of this data is in Fig. 1.) Floats were launched in the small rectangular region near 32 N, 69 W, which is the central Sargasso Sea. The dots are at one day intervals, and the trajectories are of variable duration, nominally one year. The regularly-spaced array of green vectors is the time-mean near-surface velocity estimated over roughly three decades by the Global Drifter Program (GDP, Sec. 2.4). There is some, limited qualitative similarity between these two very different data sets, but also striking differences. Both reveal a comparatively swift, generally northeastward flow along the northern and western edge of the Sargasso Sea, the Gulf Stream. In the GDP long-term mean, the Gulf Stream looks to be laminar. However, the instantaneous Gulf Stream that is evident in several of these SOFAR float tracks meanders vigorously, sometimes forming complete loops called Gulf Stream rings. Within the central Sargasso Sea, the time-mean flow is westward and very small compared to the time-dependent currents associated with mesoscale eddy variability, which has a time scale (period) of several months. The complex and entangled trajectories of the mid-ocean flow have been characterized as spaghetti diagrams (Prof. Tom Rossby, personal communication).

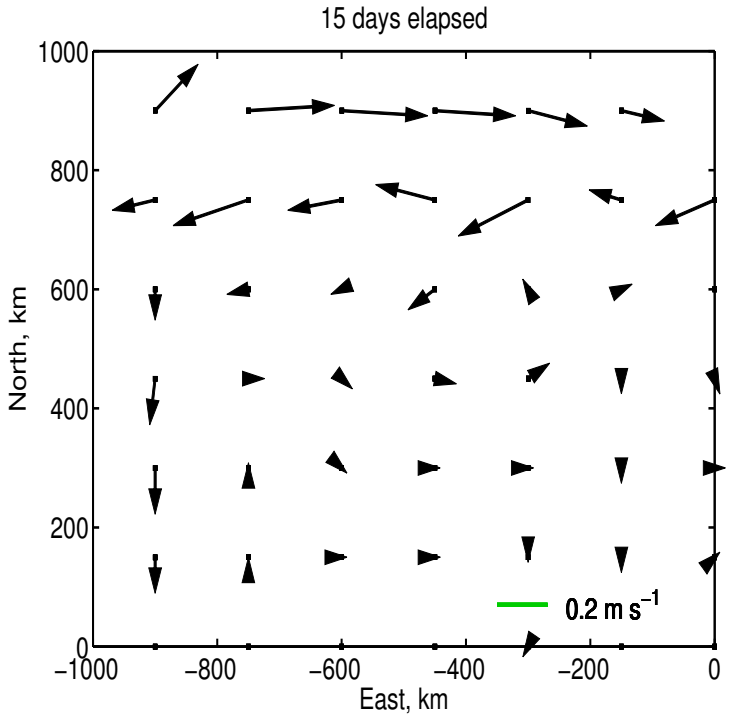

Figure 5: An ocean circulation model solved by an Eulerian system, and then sampled for the Eulerian velocity (the regularly spaced black vectors) and for a comparable number of parcel trajectories (green comets that will appear in the animation linked below). The domain is a square basin 2000 km by 2000 km driven by a basin-scale wind having negative curl, as if a subtropical gyre. Only the northwestern quadrant of the model domain and only the upper most layer of the model are shown here. The main circulation feature is a rather thin western and northern boundary current that flows clockwise. There is also a well-developed westward recirculation just to the south of the northern boundary current. This westward flow is (baroclinically) unstable and oscillates with a period of about 60 days, comparable to the period of the north-south oscillation of the float cluster seen in the cover graphic. This particular model solution suffers from poor horizontal resolution, the grid interval being one fourth the interval between velocity vectors plotted here. As one consequence, the simulated fluid must be assigned an unrealistically large viscosity, more like cold molasses than water (viscosity is reviewed in Sec. 6.1). A result is less variance in small scale features than is realistic for the ocean, but as much as this model grid can resolve. This ocean model is available from the author's web page. To see these data animated, visit https://www2.whoi.edu/staff/jprice/wp-content/uploads/sites/199/2022/06/basinmovie.mp4

1.5 Homework problems and projects

1) How many observation points do you estimate would be required to define completely the fluid flow in a teacup? In particular, what is the smallest spatial scale on which there is a significant variation of the fluid velocity? Does the number depend upon the state of the flow, i.e., whether it is weakly or strongly stirred? Does it depend upon time in any way? The viscosity of water varies by a factor of about four as the temperature varies from 0 to 100 Centigrade. Can you infer the sense of this viscosity variation from your observations? To achieve a much larger range of viscosity, consider a mixture of water and honey. What fundamental physical principles, e.g., conservation of momentum, second law of thermodynamics, can you infer from purely qualitative observations?

2) The fluid motion in a teacup may also include waves: capillary waves have short wavelengths, only a few centimeters, while gravity waves can have any larger wavelength, and may appear mainly as a sloshing back and forth over the entire tea cup. Waves can propagate momentum and energy much more rapidly than can the vortices of Fig. 2. Capillary and gravity waves owe their entire existence to the free surface, and may not appear at all if the speed at which the spoon is pushed through the fluid does not exceed a certain threshold. Can you estimate roughly what that speed is? It may be helpful to investigate this within a somewhat larger container.

3) To verify that air and water *are* Newtonian (stress proportional to deformation rate; viscosity and stress are reviewed in Sec. 6.1) requires rather precise laboratory measurements that are not likely to be accessible. But, it is very helpful to understand what a Newtonian fluid *is not,* and there are many non-Newtonian fluids that are encountered routinely. High molecular weight polymers such as paint and mayonnaise are said to be 'shear-thinning'. Under a small stress these materials may behave like very weak solids, i.e., they will deform but not quite flow until subjected to a shear stress that exceeds some threshold that is often an important characteristic of the material. 'Shear-thickening' fluids are less common, and can appear to be quite bizarre. Here's one you can make at home: a solution of about three parts cold water and two parts of corn starch powder will make a fluid that flows under a gentle stress like a very viscous fluid. But when the corn starch solution is pushed too vigorously, it will suddenly seize up, forming what seems to be a (weak) solid. Try adding a drop of food coloring to the cold water, and observe how or whether the dyed material can be stirred and mixed into the remainder. Sketch the qualitative stress/deformation (or rate of deformation) relationship for these non-Newtonian fluids, as in Figs. (21) and (22). From the vantage of a small water bug: does the water appear to be more or less viscous than it does to a human-sized swimmer?

1.6 About this essay

Readers are presumed to be familiar with basic concepts of classical mechanics and with multivariable calculus. Some prior exposure to fluid mechanics will be very helpful as well, but less for the technical details than for the all-important motivation — if a passing mention of Lagrangian observations or Lagrangian models has piqued your interest, then this essay might be for you.

The intent for this essay is educational. This essay is not a research monograph, nor is it a research review, but there are links to selected research articles. It is best used as a supplement (rather than as a substitute) to a comprehensive fluid mechanics text. The primary reason is that the plan (outlined in Sec. 1.3) is to start with a Lagrangian perspective, and then transform step by step to the Eulerian system most

often used for theory. The shortest and easiest path to useful results is instead an Eulerian treatment from the outset, and which is the plan of most introductory textbooks.[10]

Financial support during the first preparation of this essay in 2006 was provided by the Academic Programs Office of the Woods Hole Oceanographic Institution. Additional salary support was provided by the U.S. Office of Naval Research. Administrative support during the revision of 2023 was provided by Woods Hole Oceanographic Institution.

These essays and associated materials may be cited by the MIT OpenCourseWare address: Price, James F., 12.808 Supplemental Material, Topics in Fluid Dynamics: Dimensional Analysis, a Coriolis tutorial, and Lagrangian and Eulerian Representations (Spring 2022), https://ocw.mit.edu/courses/res-12-001-topics-in-fluid-dynamics-fall-2023 (date accessed). Future, major revisions will be archived on the MIT/OCW site, while minor, interim revisions will be posted to the author's web page, https://www2.whoi.edu/staff/jprice/ Copying and distribution for educational purposes is specifically allowed consistent with the license: Creative Commons, CC BY-NC-SA. For further rights and obligations see https://creativecommons.org/licenses/

This essay is dedicated to Prof. Peter Niiler, 1937 - 2010, Scripps Institution of Oceanography, whose enthusiasm, creativity and dedication to ocean science made possible the Global Drifter Program discussed in Sec. 2.4.1.

2 The Lagrangian (or material) coordinate system.

One helpful way to envision a fluid flow is as an ongoing coordinate transformation that maps parcels from a starting position, $\mathbf{A}$, into the positions $\tilde{\mathbf{X}}$ at later times. A sequence of positions $\tilde{\mathbf{X}}(\mathbf{A}, t_1)$, $\tilde{\mathbf{X}}(\mathbf{A}, t_2)$ ... $\tilde{\mathbf{X}}(\mathbf{A}, t_n)$ is a trajectory, Eq. (1). Each trajectory must be tagged with a unique $\mathbf{A}$, which is thus a constant on that trajectory, and serves to identify the parcel. It is assumed that the mapping from $\mathbf{A}$ to $\tilde{\mathbf{X}}$ is continuous in that adjacent parcels will never be split apart, and neither will one parcel occupy the same position as another parcel. The formal statement of this is that the determinant of the Jacobian of the transformation $\mathbf{A}$ to $\tilde{\mathbf{X}}$ does not vanish.[11] A physical interpretation is that the fluid density does not vanish or become infinite (Sec. 2.4). With these conventional assumptions in place, the mapping of parcels from initial to subsequent positions, Eq. (1), can be inverted so that a Lagrangian representation

[10] Excellent, modern examples include P. K. Kundu and I. C. Cohen, *Fluid Mechanics* (Academic Press, 2001), by B. R. Munson, D. F. Young, and T. H. Okiishi, *Fundamentals of Fluid Mechanics, 3rd ed.* (John Wiley and Sons, NY, 1998), by D. C. Wilcox, *Basic Fluid Mechanics* (DCW Industries, La Canada, CA, 2000) and by D. J. Acheson, *Elementary Fluid Dynamics* (Clarendon Press, Oxford, 1990). A superb text that emphasizes experiment and fluid phenomenon is by D. J. Tritton, *Physical Fluid Dynamics* (Oxford Science Pub., 1988). Two other classic references, comparable to Lamb but more modern are by Landau, L. D. and E. M. Lifshitz, 'Fluid Mechanics', (Pergamon Press, 1959) and G. K. Batchelor, 'An Introduction to Fluid Dynamics', (Cambridge U. Press, 1967). An especially good discussion of the physical properties of fluids is Ch. 1 of Batchelor's classic text. A rather advanced source for fluid kinematics is Chapter 4 of Aris, R., *Vectors, Tensors and the Basic Equations of Fluid Mechanics*, (Dover Pub., New York, 1962). A superb monograph that goes far beyond the present discussion of Lagrangian models is by A. Bennett, *Lagrangian Fluid Dynamics*, Cambridge Univ. Press, 2006.

[11] The important Jacobian operator arises on several occasions. An excellent introduction to and interpretation of the Jacobian is available online thanks to the Khan Academy, https://youtu.be/p46QWyHQE6M

can be transformed to an Eulerian representation,

$$\underbrace{\tilde{\mathbf{X}} = \tilde{\mathbf{X}}(\mathbf{A},t)}_{\text{Lagrangian representation}} \quad \Longleftrightarrow \quad \underbrace{\mathbf{A} = \mathbf{A}(\tilde{\mathbf{X}},t)}_{\text{(part way to) Eulerian representation}} \tag{5}$$

at least in principle. In a Lagrangian representation, the starting position, $\mathbf{A}$, is the independent spatial variable, and is presumed known, and the subsequent positions $\tilde{\mathbf{X}}$ is the dependent variable.

The essence of (5) is that a given $\mathbf{A}$ and time map to a unique $\tilde{\mathbf{X}}$. When that holds, then the mapping can be reversed by changing the sign of the velocity. Transport by a fluid velocity is deterministic and time-reversible. A fluid model that considers advection alone is an idealization that is often and aptly called an 'ideal fluid', or sometimes an Euler fluid. A more realistic fluid model will acknowledge also diffusion, either by molecular processes (the viscosity of Sec. 6.1), or by fast time scale, unresolved motions (discussed in Part 2, Sec. 4). In the presence of diffusion, a given parcel does not map into a unique position, but rather into a cloud whose radius grows as the square root of the elapsed time. Diffusion is stochastic and is not time-reversible.; diffusion is thus not consistent with Eq. (5). This essay emphasizes fluid flow, and omits diffusion unless specifically noted.

2.1 A simple Lagrangian flow

All this talk of coordinate transformations is rather abstract — it is time for an example of an ideal Lagrangian flow. For the present purpose it is appropriate to consider a one-dimensional domain denoted by R^1. Compared with a three-dimensional domain, R^3, this minimizes algebra greatly and so helps to highlight the important features of a Lagrangian description. However, there are important aspects of a three-dimensional flow that are not contained in one space dimension, and so this will have to be extended to three dimensions in Sec. 2.4. But for now, assume to know the trajectories of all the parcels in a one-dimensional domain with spatial coordinate x, and non-dimensional time, $t \geq 0$, by way of the explicit formula

$$\tilde{x}(a,t) = U_o\, t + a(1+2t)^{1/2}, \tag{6}$$

where U_o is a spatially-uniform velocity and a is the initial position. Once we identify a parcel by specifying the starting position, $\tilde{x}(t=0) = a$, this handy little formula gives the position, $x = \tilde{x}$, of that specific parcel at any later time. It is most unusual to have so much information presented in such a convenient way, and in fact, this particular flow has been concocted to have just enough complexity to be interesting for the present purpose, but has no physical significance. Notice that there are no parameters in Eq. (6) that give any sense of a physical length scale or time scale, i.e., whether this is meant to describe the flow in a capillary or an ocean basin.

The (Lagrangian) velocity of a parcel is readily calculated as the time derivative of the position holding a constant,

$$\tilde{u}(a,t) = \frac{\partial \tilde{x}}{\partial t} = U_o + a(1+2t)^{-1/2}, \tag{7}$$

and the acceleration is just

$$\frac{\partial^2 \tilde{x}}{\partial t^2} \;=\; \frac{\partial \tilde{u}}{\partial t} \;=\; -a(1+2t)^{-3/2}. \tag{8}$$

These are the same thing as the velocity and the acceleration of a solid particle, which is part of the appeal of the Lagrangian system.

Given the initial positions of four parcels, say a = (0.1, 0.3, 0.5, 0.7), the trajectories and velocities follow from Eqs. (6) and (7) (Figs. 6 upper and middle). Note that the velocity depends upon the initial position, a. If $\tilde{u}$ did not depend upon a, then the flow would necessarily be spatially uniform, i.e., all the fluid parcels in the domain would have exactly the same velocity, U_o. The flow shown here has the following form: all parcels shown (and all of the fluid in $a > 0$) are moving in the direction of positive x; parcels that started at larger a move a little faster, Eq. (7). All of the parcels having $a > 0$ are also decelerating and the magnitude of the deceleration increases with a, Eq. (8). If the density remained nearly constant, which it does in most geophysical flows but does not in the one-dimensional flow defined by Eq. (6), then it would be appropriate to infer a force directed in the negative x direction (more on this below).

The Lagrangian representation Eq. (6) shows, in the most straightforward way possible, where fluid parcels released into a flow at the initial time and position $x = a$ will be found at some later time. If the need was to observe how a fluid flow carried a pollutant from a source (the initial position) into the rest of the domain, then this Lagrangian representation would be ideal; we could simply release or tag parcels over and over again at the source position, and then observe or calculate where the parcels were carried by the flow.

2.2 Mass and momentum conservation in a Lagrangian system

This section will develop the Lagrangian forms of mass and momentum conservation that are required for a forward calculation in the Lagrangian system, i.e., to predict rather than to analyze or observe a fluid flow. This will continue with a one-dimensional geometry until Sec. 2.4. As above, this assumes an ideal fluid so that all effects of diffusion are omitted, including the effects of viscosity (momentum diffusion).

In the simple flow defined by (6) the velocity is solely in the x-direction, and all variations of the pressure, fluid density, etc., are in the x-direction only (Fig. 7). Let's follow a material (linear) volume of fluid that occupies the interval $a_1 < x < a_2$ in the initial state. The cross-sectional area of this material volume is denoted by H and is presumed constant, as if a pipe flow. At some later time, this volume will be displaced to a new position where its endpoints will be at $x = \tilde{x}_1$ and $x = \tilde{x}_2$.

Mass conservation. The mass of the volume in its initial state is just

$$M_o \;=\; H\bar{\rho}_0(a)(a_2 - a_1), \tag{9}$$

where the overbar indicates mean value. After the material volume is displaced, the end points will be at $\tilde{x}_1(a_1,t)$, etc., but the mass in the displaced position will be unchanged,

$$M \;=\; H\bar{\rho}(a,t)(\tilde{x}_2 - \tilde{x}_1) \;=\; M_o. \tag{10}$$

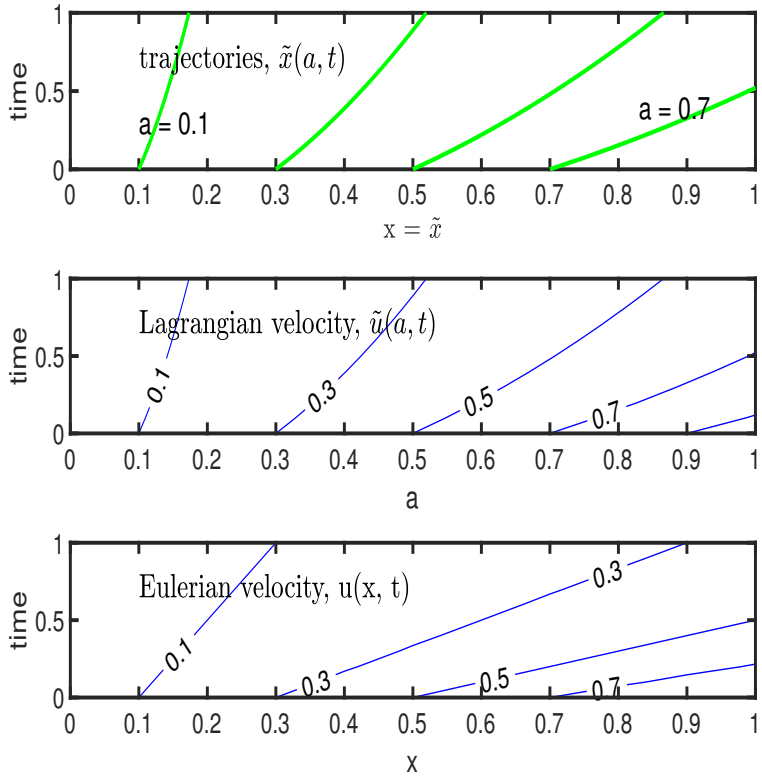

Figure 6: Lagrangian and Eulerian representations of the one-dimensional, time-dependent flow defined by the trajectories of Eq. (6). **(upper)** The solid green lines are the trajectories $\tilde{x}(a,t)$ of four parcels whose initial positions were $a = 0.1$, 0.3, 0.5 and 0.7 (left to right). **(middle)** The Lagrangian velocity, $\tilde{u}(a,t) = \partial\tilde{x}/\partial t$, as a function of initial position, a, and time. The solid blue lines are contours of constant velocity, not trajectories as above. **(lower)** The corresponding Eulerian velocity field $u(x,t)$ dicussed in Sec. 3.1, and again the lines are contours of constant velocity. These three graphs look similar because of the very simple geometry of the trajectories, Eq. (6), but they are three quite different things.

How can we be so sure? Because in this presumed ideal fluid, the parcels that make up the volume can not move through one another or through the parcels on the end points that mark the boundaries. Thus the material contained within this volume remains the same under fluid flow and hence the name 'material volume'; a two-dimensional example was sketched in Fig. (3). Equating the masses in the initial and subsequent states,

$$\bar{\rho}_0(a)(a_2 - a_1) \;=\; \bar{\rho}(a,t)(\tilde{x}_2 - \tilde{x}_1),$$

shows that the density of the parcel at later times is related to the initial density by

$$\bar{\rho}(a,t) \;=\; \bar{\rho}_0(a)\frac{a_2 - a_1}{\tilde{x}_2 - \tilde{x}_1}.$$

If the interval of Eqs. (9) and (10) is small, and assuming that ρ is smoothly varying, then the ratio of the

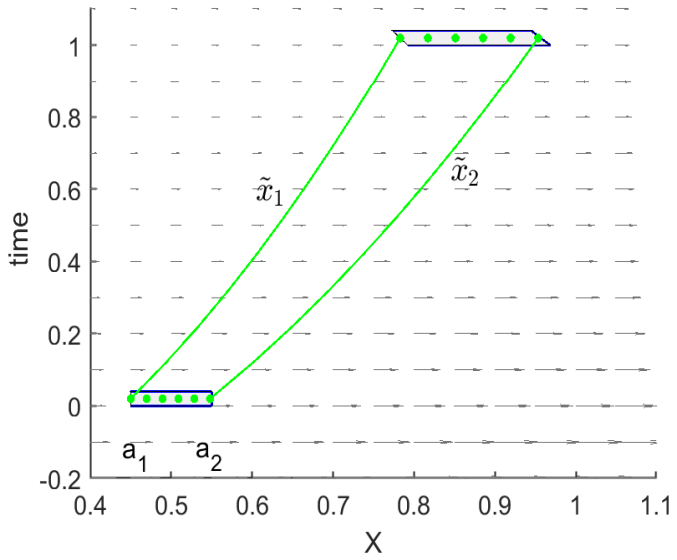

Figure 7: The one-dimensional velocity field $u(x,t)$ of Eq. (26) is plotted as the array of velocity vectors. The grey bar represents a material line whose end points are the parcels at $\tilde{x}_1$ and $\tilde{x}_2$ and whose trajectories $\tilde{x}(a,t)$ are the green lines. This velocity field is divergent and hence the length of the material line increases in time; the mass density decreases in inverse proportion. The parcels that make up this one-dimensional material volume maintain their relative order.

lengths becomes the partial $\tilde{x}$ derivative, and

$$\text{Lagrangian mass conservation in 1-d:} \quad \boxed{\tilde{\rho}(a,t) \;=\; \rho_0(a)\left(\frac{\partial \tilde{x}}{\partial a}\right)^{-1}} \tag{11}$$

which holds for an ideal fluid (no diffusion and no exchange with the exterior). This is exact, since no terms involving products of small changes have been dropped. The important term here is $\partial\tilde{x}/\partial a$, called the linear deformation. In the case sketched in Fig. (7), the displacement increases in the direction of increasing a, and hence $\partial\tilde{x}/\partial a > 1$ and this fluid flow is accompanied by an increase in the volume (here just length) of a parcel, compared with the initial state.

A convenient, normalized measure of the linear deformation is the condensation,

$$C(a,t) \;=\; \left(\frac{\partial \tilde{x}}{\partial a}\right)^{-1} - 1 \;=\; \frac{\rho-\rho_o}{\rho_o}. \tag{12}$$

If $\frac{\partial\tilde{x}}{\partial a} > 1$ so that the parcel has been stretched, then $C < 0$ and the associated fractional density change will be negative. For small amplitude motions, e.g., most acoustic waves, the condensation hovers around zero. The condensation that accompanies the simple Lagrangian flow Eq. (6) is

$$C(a,t) \;=\; \frac{1}{(1+2t)^{1/2}} - 1 \;\leq\; 0$$

and is not small for $t \;=\; O(1)$. This is an artifact of a one-dimensional flow: if a one-dimensional flow has some spatial variation then it will have a comparably large condensation; a two- or three-dimensional flow is not so constrained. As noted in Sec. 2.4, the three-dimensional version of the linear deformation is the change in volume of a unit volume, which is estimated by the determinant of the Jacobian of the transformation $\mathbf{A} \;\rightarrow\; \tilde{\mathbf{X}}$.

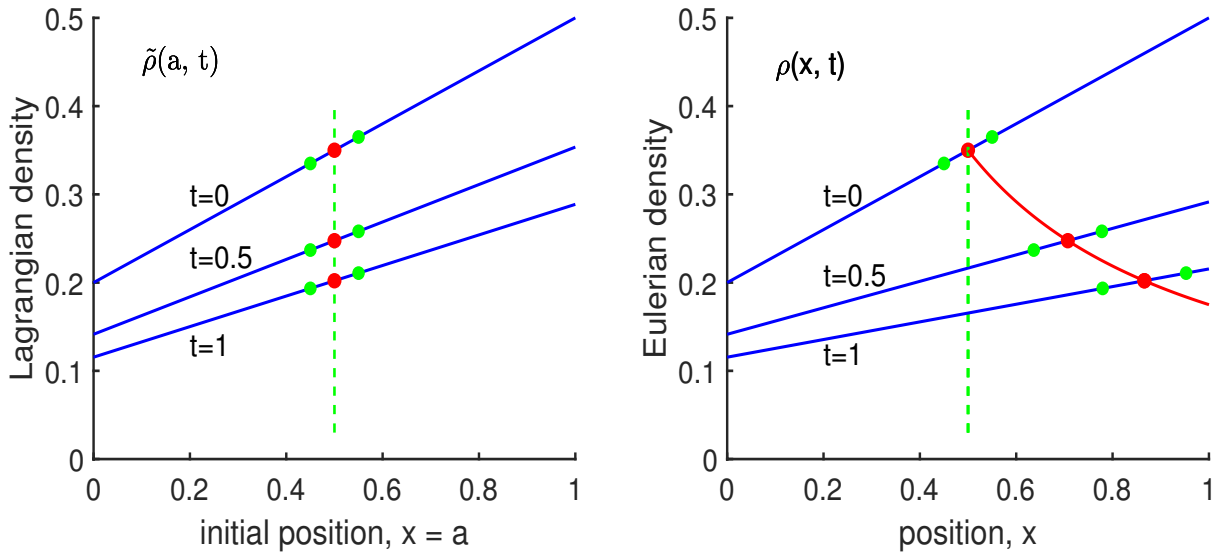

Figure 8: **(left)** A Lagrangian representation of density $\tilde{\rho}(a,t)$ given by Eq. (14) and evaluated at three times, $t = 0, 0.5, 1$. The red and green dots represent three parcels, $a = 0.45, 0.5, 0.55$. These parcels do not move in these Lagrangian coordinates (a,t), but the density decreases in time due to the linear deformation (stretching) shown in the previous figure. **(right)**. The Eulerian representation of this density (Eulerian conservation equations are discussed in detail in Sec. 3). The same three parcels are shown here too, and they move in this coordinate space; the red curve is the trajectory in (x, ρ) of the center parcel. The Eulerian density $\rho(x,t)$ decreases with time due to stretching (the distance between the three parcels increases with time), and due to advection of the density profile toward larger x (the parcels shift rightward with increasing time).

This one-dimensional Lagrangian statement of mass conservation shows that density changes of a material volume are inversely related to the linear deformation. Thus when a material volume is stretched (expanded) compared with the initial state, the case shown schematically in Fig. (7), the density of the fluid within that volume will necessarily be decreased compared with ρ_0. Indeed, in this one-dimensional ideal fluid model, the only way that the density of a material volume can change is by linear deformation. It is important to understand that motion alone — that is, a spatially-uniform motion without deformation, e.g., the U_o of Eq. (7) — will not cause a change in the density.

As an example of density represented in a Lagrangian system, assume an initial density distribution

$$\rho_0(a) \;=\; \rho_c + \Gamma a, \tag{13}$$

with ρ_c and Γ positive constants, that is embedded in the Lagrangian flow, Eq. (6), that produces trajectories $\tilde{x} \;=\; U_o\, t \;+\; a(1+2t)^{1/2}$ and linear deformation $\partial\tilde{x}/\partial a \;=\; (1+2t)^{1/2}$. By Eqs. (11) and (13) the Lagrangian density of this flow evolves as

$$\tilde{\rho}(a,t) \;=\; \frac{\rho_c + \Gamma a}{(1+2t)^{1/2}}, \quad \text{and} \quad \tilde{x}(a,t) \;=\; U_o\, t \;+\; a(1+2t)^{1/2}. \tag{14}$$

This density is evaluated for $\rho_c = 0.2$, $\Gamma = 0.3$, $U_o = 0$ and at three times in Fig. (8), left, the blue lines.

The density at constant a, i.e., the density of a given parcel, decreases with time on account of the linear deformation of this flow, as in Fig. (7).

Fig. (8) also includes three parcels identified by their initial positions and corresponding densities. In the Lagrangian coordinates, $\tilde{\rho}(a,t)$, these parcels are stationary, despite that they move in physical space, (x,t). If there was no deformation, then the density would be constant in time on each parcel: as noted above, motion alone (absent deformation) does not change the mass density of a parcel (and omitting diffusion). However, knowing only the density of a parcel but not its position, would be incomplete for most purposes. A useful Lagrangian solution will be the density $\tilde{\rho}(a,t)$, and the trajectory, $\tilde{x}(a,t)$, written alongside as in Eq. (14). Thus the Lagrangian solution comes in two parts: the tracer property on moving parcels (mass density in this case), as well as the trajectory of those parcels.

Momentum conservation. As noted in Sec. 2.1, a fluid parcel is presumed to follow Newton's laws of classical mechanics. For the present purpose, pressure is presumed to be the only force acting upon a material volume, i.e., there is no viscosity and no other external force. Pressure is important in almost every flow, but small scale flows may also be effected significantly by viscous effects. A fluid model that makes use of these idealizations (no diffusion and pressure forces only) is variously referred to as a perfect fluid, an ideal fluid, or sometimes an Euler fluid.

Consider the (linear) volume of Fig. (7). The pressure force on the right side of this volume will be $-P(\tilde{x_2})H$ and the pressure force on the left side $P(\tilde{x_1})H$ (the sign changes with the unit normal). The net pressure force on the volume is then the sum, $F = -(P(\tilde{x}_2) - P(\tilde{x}_1))H$. The acceleration is $\frac{\partial^2 \tilde{x}}{\partial t^2}$ and the mass of the material volume is just $M = \rho H(\tilde{x}_2 - \tilde{x}_1)$. Classical momentum conservation (mass $\times$ acceleration = force) applied to this material volume is then

$$\rho H(\tilde{x}_2 - \tilde{x}_1)\frac{\partial^2 \tilde{x}}{\partial t^2} \;=\; -(P(\tilde{x}_2) - P(\tilde{x}_1))H.$$

Dividing by the $\tilde{x}$ interval $\tilde{x}_2 - \tilde{x}_1$, and taking the limit procedure above gives

$$\text{Lagrangian momentum conservation in 1-d:} \quad \boxed{\frac{\partial^2 \tilde{x}}{\partial t^2} \;=\; -\frac{1}{\rho}\frac{\partial P}{\partial \tilde{x}}} \tag{15}$$

This may look familiar on first sight (just like the pressure gradient you may know from basic fluid mechanics, and that will arise in the Eulerian system, Sec. 3.4.3), but notice that this gradient of pressure is with respect to $\tilde{x}$, which is a dependent variable in a Lagrangian system. This becomes awkward in two or three space dimensions (more on this in Sec. 2.4).

2.3 An exact wave equation in one dimension

An equation of state, $P = P(\rho)$, or, $\rho = \rho(P)$ (Eq. (126) of the appendix, Sec. 6.1), provides a third and crucial piece of information by linking pressure with density, and we already know that the density is related inversely to the linear deformation. Thus the system of equations, Eqs. (126), (11) and (15) are in principle a complete set for the three unknown variables $\tilde{x}$, ρ and P. It is often useful to reduce such a system of equations to a single equation in one variable, if possible, and in this one-dimensional system it

is straightforward. The pressure term may be eliminated from the momentum equation (15) by substituting the derivative of pressure from an equation of state,

$$\frac{\partial P(\rho)}{\partial a} = \frac{dP(\rho)}{d\rho}\frac{\partial \rho}{\partial a}.$$

The derivative of density may in turn be eliminated by using the mass conservation relation, Eq. (11),

$$\frac{\partial \rho}{\partial a} = -\rho_o \frac{\partial^2 \tilde{x}}{\partial a^2}/(\frac{\partial \tilde{x}}{\partial a})^2.$$

Substitution into the momentum equation then yields an exact, nonlinear wave equation in one dimension:

$$\frac{\partial^2 \tilde{x}}{\partial t^2} = \frac{\frac{dP}{d\rho}(\rho_0 \frac{\partial \tilde{x}}{\partial a})}{(\frac{\partial \tilde{x}}{\partial a})^2}\frac{\partial^2 \tilde{x}}{\partial a^2}. \tag{16}$$

It is nonlinear because the term $(\frac{\partial \tilde{x}}{\partial a})^2$ is nonlinear; the term $\frac{dP}{d\rho}(\rho_0 \frac{\partial \tilde{x}}{\partial a})$ is also likely to be nonlinear, depending upon the appropriate equation of state. For some purposes, e.g., modeling the very intense acoustic waves that are produced by an explosion, this kind of nonlinear equation is necessary. But for many, everyday phenomena the nonlinear equation is not warranted and is an unnecessary encumbrance. For example, the condensation accompanying a mid-audio range sound having a frequency of 1000 Hz, and an amplitude that would be considered appreciable to the ear is very small, C is O(10^{-6}).[12] Thus the derivative $\partial \tilde{x}/\partial a$ is very, very close to 1 and the density that appears in $dP/d\rho$ can be taken to be the nominal density, ρ_0, with very little error. These approximations of small amplitude motion are often called the acoustic approximations, and with these in place the resulting governing equation is the linear, elementary wave equation,

$$\frac{\partial^2 \tilde{x}}{\partial t^2} = c^2 \frac{\partial^2 \tilde{x}}{\partial a^2}. \tag{17}$$

where the constant coefficient $c_0^2 = \frac{dP}{d\rho}(\rho_0)$ is the nondispersive wave speed squared. In this small amplitude (linear) limit there is nothing remaining that is characteristic of the Lagrangian system, and we might just as well have started with a simpler Eulerian representation.

The one-dimensional form of the Lagrangian equations (11), (15) and (16) are very handy, and if fluid dynamics was one-dimensional, then these equations would be our touchstone; we might never need anything more. However, one-dimensional phenomenon are exceedingly rare, and these one-dimensional equations do not admit, e.g., shear deformation, which two and three-dimensional fluids do with aplomb. Thus, in a one-dimensional flow the parcels maintain their relative order, while in a two- or three-dimensional flow, the trajectories are liable to become entangled[13] with no apparent order. This is evident even in the flow in a teacup, but not in the one-dimensional figures plotted here. Very commonly, a fluid flow will be fully three-dimensional and time-dependent, and a useful analysis will require the three-dimensional equations of motion. The three-dimensional Lagrangian equations are awkward

[12] D. H. Towne, *Wave Phenomenon*, Dover Pub., 1967, is highly recommended for more on acoustic phenomena.

[13] 'Entangled' is used here in the geometric and homey sense of a bowl of spaghetti (Fig. 4), and not in the quantum physics sense of entangled photons.

(difficult) for most purposes, and are not often used in their full form. If you are curious to see how or why this awkwardness arises, then read on. Otherwise you can skip ahead to Sec. 2.5 with little practical loss.

2.4 The agony of the three-dimensional Lagrangian equations

To see how the complication arises in three-dimension, begin with the component equations,

$$\frac{\partial^2 \tilde{x}}{\partial t^2} = -\frac{1}{\rho}\frac{\partial P}{\partial \tilde{x}}, \qquad \frac{\partial^2 \tilde{y}}{\partial t^2} = -\frac{1}{\rho}\frac{\partial P}{\partial \tilde{y}}, \qquad \frac{\partial^2 \tilde{z}}{\partial t^2} = -\frac{1}{\rho}\frac{\partial P}{\partial \tilde{z}} - g. \tag{18}$$

These are hopeful on first sight. But on second sight there is a significant problem with the pressure gradient, in that the spatial derivative is taken with respect to the material coordinates $(\tilde{x}, \tilde{y}, \tilde{z})$, which in the Lagrangian system are *dependent* variables. In this form, the pressure gradient is the derivative of one unknown with respect to another unknown, which is extraordinarily difficult. The spatial derivative we would much prefer is with respect to an independent variable, which in the Lagrangian system is the initial position, the (a, b, c). Assuming that the transformation $\mathbf{A} \rightarrow \tilde{\mathbf{X}}$ exists, then the gradient may be written in terms of the (a, b, c). In general, the present position of a parcel will be dependent upon all three components of the initial position, i.e., $\tilde{x} = \tilde{x}(a, b, c)$, and vice versa, $a = a(\tilde{x}, \tilde{y}, \tilde{z})$. By the chain rule applied to composite functions, the $\tilde{x}-$component of the pressure gradient may be rewritten as

$$\frac{\partial P}{\partial \tilde{x}} = \frac{\partial P}{\partial a}\left(\frac{\partial \tilde{x}}{\partial a}\right)^{-1} + \frac{\partial P}{\partial b}\left(\frac{\partial \tilde{x}}{\partial b}\right)^{-1} + \frac{\partial P}{\partial c}\left(\frac{\partial \tilde{x}}{\partial c}\right)^{-1}, \tag{19}$$

and of course similarly for the $\tilde{y}$ and $\tilde{z}$ components (not written out). Using this form of the pressure gradient, the momentum equations are

$$\frac{\partial^2 \tilde{x}}{\partial t^2} = \frac{\partial P}{\partial a}\left(\frac{\partial \tilde{x}}{\partial a}\right)^{-1} + \frac{\partial P}{\partial b}\left(\frac{\partial \tilde{x}}{\partial b}\right)^{-1} + \frac{\partial P}{\partial c}\left(\frac{\partial \tilde{x}}{\partial c}\right)^{-1},$$

$$\frac{\partial^2 \tilde{y}}{\partial t^2} = \frac{\partial P}{\partial a}\left(\frac{\partial \tilde{y}}{\partial a}\right)^{-1} + \frac{\partial P}{\partial b}\left(\frac{\partial \tilde{y}}{\partial b}\right)^{-1} + \frac{\partial P}{\partial c}\left(\frac{\partial \tilde{y}}{\partial c}\right)^{-1},$$

and

$$\frac{\partial^2 \tilde{z}}{\partial t^2} = \frac{\partial P}{\partial a}\left(\frac{\partial \tilde{z}}{\partial a}\right)^{-1} + \frac{\partial P}{\partial b}\left(\frac{\partial \tilde{z}}{\partial b}\right)^{-1} + \frac{\partial P}{\partial c}\left(\frac{\partial \tilde{z}}{\partial c}\right)^{-1} - g. \tag{20}$$

The spatial derivatives of pressure are all with respect to the independent variables, the (a, b, c), which is progress, but the pressure gradient written in the material coordinates is quite formidable. It is possible to simplify the momentum equations somewhat by rearranging in a way that leaves only a single presure gradient term in each component equation, see Lamb,[9] Article 1.13.

$$\frac{\partial^2 \tilde{x}}{\partial t^2}\frac{\partial \tilde{x}}{\partial a} + \frac{\partial^2 \tilde{y}}{\partial t^2}\frac{\partial \tilde{y}}{\partial a} + \left(\frac{\partial^2 \tilde{z}}{\partial t^2} + g\right)\frac{\partial \tilde{z}}{\partial a} = -\frac{1}{\rho}\frac{\partial P}{\partial a},$$

$$\frac{\partial^2\tilde{x}}{\partial t^2}\frac{\partial\tilde{x}}{\partial b}+\frac{\partial^2\tilde{y}}{\partial t^2}\frac{\partial\tilde{y}}{\partial b}+(\frac{\partial^2\tilde{z}}{\partial t^2}+g)\frac{\partial\tilde{z}}{\partial b} \;=\; -\frac{1}{\rho}\frac{\partial P}{\partial b},$$

$$\frac{\partial^2\tilde{x}}{\partial t^2}\frac{\partial\tilde{x}}{\partial c}+\frac{\partial^2\tilde{y}}{\partial t^2}\frac{\partial\tilde{y}}{\partial c}+(\frac{\partial^2\tilde{z}}{\partial t^2}+g)\frac{\partial\tilde{z}}{\partial c} \;=\; -\frac{1}{\rho}\frac{\partial P}{\partial c}. \tag{21}$$

But now the accelertion terms are very difficult, and so this has evidently traded one problem, seen in (20), for another one that is no better. The bottom line is that we are not going to make direct use of these equations. Nevertheless there is value in knowing that the difficulty came from the pressure gradient, Eq. (19), and the dependence of parcel position upon the three-dimensional initial position, i.e., that $\tilde{x}=\tilde{x}(a,b,c)$. This suggests that a possible work-around could be to evaluate the pressure in field coordinates, i.e., the usual (x,y,z), and then apply the pressure gradient, computed in field coordinates at the position of the parcels, to each parcel. Thus, Lagrangian parcels can be tracked as they move and accelerate through an Eulerian grid. This is the strategy of the Particle in Cell model architecture discussed in Part 2.

The three-dimensional mass conservation equation is also complex but has a very clear interpretation,

$$\rho \;=\; \rho_0 \begin{vmatrix} \frac{\partial\tilde{x}}{\partial a} & \frac{\partial\tilde{x}}{\partial b} & \frac{\partial\tilde{x}}{\partial c} \\ \frac{\partial\tilde{y}}{\partial a} & \frac{\partial\tilde{y}}{\partial b} & \frac{\partial\tilde{y}}{\partial c} \\ \frac{\partial\tilde{z}}{\partial a} & \frac{\partial\tilde{z}}{\partial b} & \frac{\partial\tilde{z}}{\partial c} \end{vmatrix}^{-1} \;=\; \rho_0/J\left(\frac{\partial(\tilde{x},\tilde{y},\tilde{z})}{\partial(a,b,c)}\right), \tag{22}$$

where J is the determinant of the Jacobian of the transformation $\mathbf{A}\rightarrow\tilde{\mathbf{X}}$ (to be concise, often just the Jacobian, J). The Jacobian is the change in the unit volume when going from (a,b,c) to $(\tilde{x},\tilde{y},\tilde{z})$ (footnote 11). Notice that this density equation is diagnostic (no time derivative) rather than prognostic as are most budget equations. The density of this presumed Euler fluid may be calculated knowing the three-dimensional condensation (Sec. 2.3.1) given by the Jacobian above (which is asking quite a lot). If the fluid is incompressible, then $\rho=\rho_o$ and the Jacobian is unity and the mapping from $\mathbf{A}$ to $\tilde{\mathbf{X}}$ is volume conserving,

$$\frac{\rho}{\rho_o} \;=\; J\left(\frac{\partial(\tilde{x},\tilde{y},\tilde{z})}{\partial(a,b,c)}\right)^{-1}=1 \tag{23}$$

(cf. the flow of Fig. 3 which has a small divergence and thus a small decrease in the number density of the material volume).

At the outset of this essay the question was posed: How can the conservation laws of classical physics be applied to the calculation of a fluid flow? Here in Eqs.(126), (21) and (22) is one possible answer for an ideal fluid; five equations in five unknowns, density ρ, the pressure p, and the parcel position, $(\tilde{x},\tilde{y},\tilde{z})$.[14] However, evaluating the pressure gradient terms is, not to put too fine a point on it, very difficult in a two- or three-dimensional Lagrangian system. With no intent to make this seem

[14] An insightful history of the Lagrangian equations and links to recent research is available from https://www.researchgate.net/profile/Uriel-Frisch/publication/260295078

hopeless, there are two hurdles presented by the Lagrangian system. (1) Some form of nonlinearity is inevitable in a theory of fluid mechanics, but the Lagrangian form of it, in which each term of the pressure gradient is multiplied by two or three deformation terms, is difficult to evaluate and to interpret. In some applications it would be appropriate to linearize these equations, but the result is (usually) the same linear equations that arise also from the Eulerian equations (Sec. 3). (2) The Lagrangian equations involve a second derivative with respect to time, where even one integration can be challenging. The (analytic) solution of the Lagrangian equations requires solving for parcel trajectories in one fell swoop. In contrast, within an Eulerian system we can solve for the velocity (one integration in time), and then integrate the velocity solution in a separate, offline step to find parcel trajectories (a theme of Part 2), if they are required. In many cases we may have no interest in knowing the trajectories of specific parcels and if so then a Lagrangian solution may tell us much more than we want to know. That would not be grounds for complaint, except that this additional information has to be provided, which is some part of the challenge for Lagrangian solutions. To summarize this subsection — it is a fair generalization[15] that the three-dimensional Lagrangian momentum equations, Eq. (21), are not as handy for most theoretical purposes as are the three-dimensional Eulerian equations that will be taken up in Sec. 3.

2.5 The joys of Lagrangian measurement

Lagrangian measurements come in many different forms, but all have in common that they seek to follow the position of a proxy of a fluid parcel, e.g., a neutrally buoyant float (Fig. 1) that moves more or less faithfully with the surrounding fluid. The identity of a specific float can be represented by a superscript index appended to the position vector, ${}^{j}\tilde{\mathbf{X}}(t)$. In practice, floats can be identified in the way they are tracked; the acoustically-tracked SOFAR floats of Fig. 1 transmitted within a twice-daily time window that was unique to each float. Satellite-tracked sea-surface drifters have an identifier that is transmitted via satellite link along with the drifter's position and the time. The basic, raw data of a Lagrangian float observation is thus a float identifier, a parameter that varies from one trajectory to another, the time, the independent variable, and the float position, the dependent variable. There will often be other measurements, including temperature, pressure and more, that may be encoded with the position reports.

2.5.1 An economy of scale

Lagrangian measurements can be advantageous for some purposes, and sometimes Lagrangian measurements are simply expedient, i.e., they may be the most practicle way to obtain extensive measurements. Lagrangian measurement methods may enjoy an economy of scale because it often

[15] To which there are many important exceptions, including adiabatic tracer advection problems considered here in Sec. 4. Just a few somewhat exotic examples: To the approximation of potential flow theory, a finite number of interacting, free vortices advect one another about in ways that can be remarkably intricate. Fig. 2 is the simplest example with just two vortices; imagine a collection of dozens of such vortices. There are also continuum problems wherein Lagrangian theory is tractable and even advantageous: in surface gravity wave problems, where the free surface is a constant in Lagrangian coordinates, and nonlinear acoustic waves where the full nonlinear equations may be reduced to a single governing equation, at least in one space dimension, Eq. (16). This list could go on and on, but for further examples in detail see instead the monograph by Bennett noted in footnote 10.

happens that the major cost of a float-tracking experiment lies in the tracking infrastructure, while additional floats or trackable particles are comparatively inexpensive and sometimes almost free.

Particle Imaging Velocimetry, PIV. A widely-used and rapidly developing observational technique involves the generation of the Eulerian velocity field by observing large numbers of (Lagrangian) floats or trackable particles. The basic idea is an application of the FPK: the trajectory of a given float, ${}^j\tilde{\mathbf{x}}(t)$, is time-differenced over a short time interval to give an estimate of the Eulerian velocity at the centered place and time of the Lagrangian data,

$$\mathbf{V}(\mathbf{X} = {}^j\tilde{\mathbf{X}}, t) \;=\; \frac{\partial\, {}^j\tilde{\mathbf{X}}(t)}{\partial t}. \tag{24}$$

This is a discretized version of the FPK Eq. (4) in that the tag ${}^j(\;)$ replaces the initial position $\mathbf{A}$ required in a continuum theory. The tag ${}^j(\;)$ may or may not be retained with the Eulerian velocity.

An implementation of this method on laboratory scale, known as Particle Imaging Velocimetry (PIV), was developed starting in the mid-1980s and is rapidly evolving and expanding today.[16] The PIV technique makes use of what can be very small and inexpensive particles that can be seeded into a laboratory flow in almost unlimited numbers, e.g., neutrally buoyant plastic beads in water. Assuming that the fluid is not opaque, the particles may be illuminated by a pulsed laser source and imaged with high speed cameras. Provided that the individual particles or the pattern that they form can be recognized from one image frame to the next, then it is fairly straightforward to differentiate particle or cluster position with respect to time, and so form a map, sometimes in three-dimensions and in great detail, of the Lagrangian fluid velocity throughout an experimental domain. If the temporal sampling interval is small enough that the particle's Lagrangian velocity is quasi-constant, then the estimated velocity makes a good estimate of the Eulerian velocity at the central time and position of the differentiation, and without the encumberance of a mechanical transducer. Tracers used in the PIV technique may be naturally occurring fluid properties, e.g., density or thermal anomalies[17]

The Global Drifter Program, GDP. The GDP is a world-wide consortium of oceanic, atmospheric and climate scientists that has deployed almost 30,000 instrumented buoys that drift freely on the ocean surface (Fig. 9).[18] The data stream includes the drifter identification, GPS-derived position, and sea

[16] A link to an extensive consortium of PIV investigators and applications is https://velocimetry.net/index.htm

[17] See http://www.irisa.fr/vista/Themes/Demos/MouvementFluide/infra.html The value of such detailed and comprehensive measurements is made especially clear by Crowley, C. J., J. L. Pughe-Sanford, W. Toler, M. C. Krygier, R. O. Grigoriev and M. F. Schatz, 2022, Turbulence tracks recurrent solutions, Proceedings of the National Academy of Sciences. DOI: 10.1073/pnas.2120665119 An application to biophysical problems in a natural environment is discussed by https://www.quantamagazine.org/what-can-jellyfish-teach-us-about-fluid-dynamics-20230628/

[18] These drifters consist of a positively buoyant surface float about 40 cm in diameter that holds batteries, sensors and satellite receivers and transmitters. A cable connects to a very large, slightly negatively buoyant drogue at 15 m depth that serves to tag the current at that near-surface depth. Drifters that lose their drogue display a spurious downwind motion that can be corrected. The basic drifter costs about $2000 and has a nominal life span of about one and a half years. To learn much more about drifters visit the GDP website, https://www.aoml.noaa.gov/phod/gdp. The vision of a collaborative, world-wide GDP is by Niiler, P. P., 2001: The world ocean surface circulation. In Ocean Circulation and Climate, G. Siedler, J. Church and J. Gould, eds., Academic Press, Volume 77 of International Geophysics Series, 193-204. For an insightful analysis and interpretation of surface drifter data see Laurindo, L. C., A. Mariano, and R. Lumpkin, 2017: An improved near-surface velocity climatology for the global ocean from drifter observations. Deep-Sea Res. I, 124, 73-92. The North Atlantic part of this analysis

Figure 9: The Global Drifter Program has observed the world ocean since the 1990s.

You could do this gig:
Drift freely on wind and waves,
tell us what you see.

surface temperature. Many drifters also measure barometric pressure and some also measure wind speed and direction. These data are transmitted in near-real time via satellite link to operational data centers and disseminated worldwide on the Global Telecommunication System (GTS). These near-realtime drifter data have considerable utility, including that they make a significant, cost-effective contribution to the body of marine observations available on the GTS network for the support of weather and marine forecasting.

A long-standing goal of the GDP is to make and report measurements over virtually the entire world ocean at roughly 500 km intervals. To this end, there are now (mid-November, 2022) roughly 1300 operational surface drifters contributed by twenty five partner nations. Drifters may be launched from almost any ship, and thereafter the sampling by these freely drifting instruments is inherently uncontrolled and so is liable to be nonuniform. The estimation of an Eulerian velocity field requires a mapping of the irregularly sampled drifter velocity estimates onto a preferred, regular grid, say via a kriging interpolation. Some form of time-averaging is usually applied at this stage in order to supress high frequency motions, such as tides. Thus the raw estimates from (24) are fairly heavily analyzed, which entails some risk of introducing artifacts.

Sampling may be correlated with the properties of the surface current. In the month June 2021 (Fig. (10) there were many drifters in the central subtropics, where there is a convergence of wind-diven, near-surface currents, (aka, the Sargasso Sea, after the floating macro-algae that also accumulates in this region) and there were very few drifters near the equator, which is a region of surface current divergence associated with easterly trade winds and a diverging near-surface current. If the winds vary seasonally, then there is the potential for a correlation between sampling density and the current, leading to a contribution to the estimated mean velocity sometimes called Stokes drift, about which more in Part 2, Sec. 2. The interpolated, time-averaged and wind-corrected near-surface velocity, Fig. (10), right, is said to be the pseudo-Eulerian mean velocity to acknowledge its considerable distance from the direct and simple FPK.

The large and growing GDP data base has been used to make detailed maps of the long term mean,

is shown in Fig. (10).

Eulerian near-surface velocity.[19] The North Atlantic basin is shown in Fig. (10), and since all currents are to the same scale, this emphasizes the largest velocities found near the western boundary of the basin and in the near-equatorial zone. The time-mean currents of the mid-ocean are very small by comparison, $O(10^{-2})$ of a western boundary current, and are not easy to discern here.[20] The western boundary current is generally northward from the equator to Labrador, and southward from the Denmark Strait to a confluence east of Labrador. Zonal near-equatorial currents occur in three bands, from north to south: eastward flow around 8 N, westward flow very near the equator, and westward flow also at about 8 S. The averaging into a (very) long-term mean as done here obscures that there is a substantial seasonal variation of the near-equatorial currents and the western boundary current within the Gulf of Mexico. The western boundary current otherwise shows little seasonal variation, i.e, the average summer looks a lot like the average winter.[21] The western boundary current is highly variable instantaneously (time scales of days to months), evident in the subsurface float tracks of Fig. (4).

2.5.2 Diagnosing source terms

If the goal of an experiment is to measure the force applied to a fluid, then by tracking parcels in time it is straightforward to estimate the acceleration, and go on to assert Newton's laws of classical dynamics in exactly the form used in classical (solid particle) dynamics, i.e.,

$$\frac{\partial^2 {}^{\mathbf{j}}\tilde{\mathbf{X}}}{\partial t^2} = \frac{1}{{}^{j}M}\mathbf{F}, \tag{25}$$

where $\mathbf{F}$ is the net force imposed upon that parcel by the environment, and M is the parcel mass. What that force may have been, i.e., whether a pressure gradient or frictional force, can not be told without supporting information.

The possible advantages of following the fluid (and thus a material volume) and directly observing fluid properties is illustrated by the tracer advection experiment of Fig. (3). When following the fluid, the tracer density changed only by virtue of divergence, there being no external source in that case. In many flows, the divergence is very small and may be taken as zero to a good approximation. In that event, the tracer is constant on moving parcels. Of course, to know where the resulting density applies will require observing the trajectory, but that is usually an integral part of any Lagrangian measurement. If observing in a fixed Eulerian frame, the tracer density changed by the same divergence plus a very large effect of advection of the tracer field through a control volume (advection in the sense $\mathbf{V}\cdot\nabla(\text{tracer})$ will be discussed in detail Sec. 3). Generally, the ocurrence of advection is expected, and is not necessarily interesting. On the other hand the possible source terms may require complex and uncertain parameterizations that need to be observed and checked. The comparative size of the source term and the advection term will vary greatly from one case to the next, and so no broad conclusions can be told. Nevertheless, if estimating a source term is an experimental goal, then Lagrangian measurements may offer some inherent advantage insofar as they account for the motion of the fluid via the directly observed

[19] https://www.aoml.noaa.gov/phod/gdp/ then search for 'mean velocity'.

[20] High resolution maps: https://www2.whoi.edu/staff/jprice/wp-content/uploads/sites/199/2022/12/NA-GDPmean-1.pdf

[21] Monthly maps: https://www2.whoi.edu/staff/jprice/wp-content/uploads/sites/199/2022/12/NA-monthly.mp4

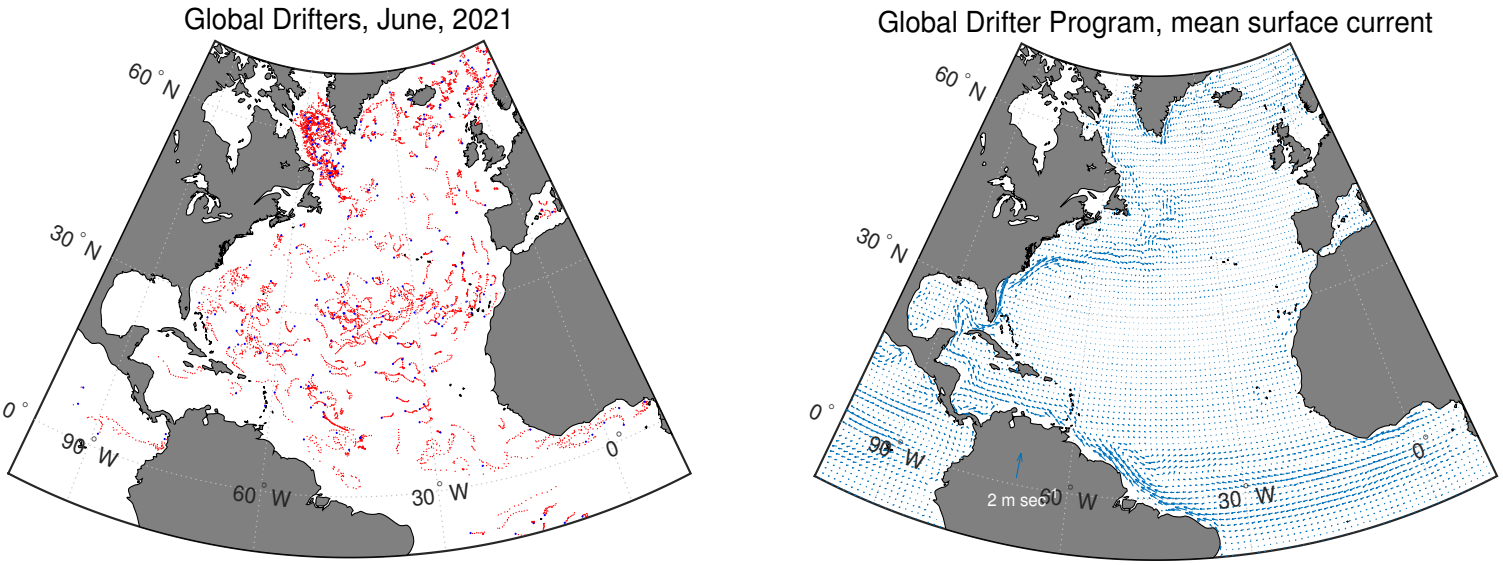

Figure 10: Surface drifter data acquired by the Global Drifter Program, GDP, and analyzed and archived by the Drifter Data Assembly Center, Atlantic Oceanographic and Meteorological Laboratory, National Oceanic and Atmospheric Administration.[18] (These figures are by the author.) **(left)** Drifter trajectories during June 2021. Red dots are at two day intervals; the last day is a blue dot. This is less than one percent of the total surface drifter data. During this month, the active drifters were distributed widely over the North Atlantic basin, but not uniformly. There were many drifters in the Labrador Sea following a recent, *ad hoc* deployment, and very few drifters in the Gulf of Mexico, which is somewhat blocked by the Windward Islands. **(right)** The time-mean velocity over three decades analyzed by Laurindo, Mariano and Lumpkin (2017).[18] The direct effect of the local wind was removed by an empirical fit. Notwithstanding the several analysis challenges, this is probably the best extant view of the time-mean, near-surface circulation of the oceans.

trajectory. An example of this is in Sec. 6, Part 2, where the float data of Fig. 1 will be analyzed for vorticity balance.

What's gone missing? This essay plus Part 2 emphasize two aspects of Lagrangian data analysis that are especially apropos the Lagrangian and Eulerian theme, *viz.*, large numbers of Lagrangian data facilitate mapping of velocity fields, Sec. 2.5.1, and, the inherently simpler tracer balance on observed trajectories can facilitate dynamical inferences, noted just above. This is very far from a complete account of the possible applications of Lagrangian data. Other important uses include inference of diffusion evident in the seemingly random dispersion of floats (as in Fig. 4)[22] and, the study of coherent Lagrangian structures, i.e., distinct flow features, typically large amplitude eddies, that retain their tracer content even while the surrounding fluid disperses tracer rapidly.[23]

[22] A highly recommended review of analysis methods for Lagrangian data is by LaCase, J. H., 2008: Statistics from Lagrangian observations, Prog. in Oceanogr., 77, 1-29. A discussion of the dispersion seen in Fig. (4) is https://www2.whoi.edu/staff/jprice/wp-content/uploads/sites/199/2024/01/Pdispers-WNA.pdf

[23] For these aspects of Lagrangian analysis, see Fredj, E., D. F. Carslon, Y. Amitai, A. Gozolchiani and H. Geldor, 2016, The particle tracking and analysis toolbox (PaTATO) for Matlab. Limnology and Oceanography Methds, 14, 586 - 599. doi:

2.6 Key ideas

1) A fluid flow can be viewed as an ongoing transformation of parcel positions from an initial position, $\mathbf{A}$, to a subsequent position $\tilde{\mathbf{X}}$. A sequence of positions of a given parcel (or float) is called a trajectory.

2) Under the plausible assumption that the determinant of the Jacobian of the transformation from $\mathbf{A}$ to $\tilde{\mathbf{X}}$ does not vanish, then trajectories $\tilde{\mathbf{X}}(\mathbf{A},t)$ may be inverted for $\mathbf{A}$.

3) The material time derivative $D/Dt = \partial/\partial t$ of parcel position is the Lagrangian velocity, and the second time derivative is the acceleration. These are the same as the solid particle velocity and acceleration.

4) The conservation laws (mass and momentum) apply to specific material volumes, and so in that important sense the conservation laws are what we would call Lagrangian. The equation of motion of a fluid parcel is the same as that of a solid particle. The issue for fluid mechanics is to know what the force is, since it comes from the interaction of a parcel with its complete surroundsings via normal and tangential stresses. (The ideal fluid model used to here considers only the former.)

5) In an ideal fluid, the density of a fluid parcel will be inversely proportional to the linear deformation (in one space dimension) or more generally to the Jacobian of the transformation $\mathbf{A} \rightarrow \tilde{\mathbf{X}}$ in two or three dimensions. A spatially uniform velocity will not cause a change in the volume or density of fluid parcels.

6) The Lagrangian representation of density comes in two parts: the density itself, $\tilde{\rho}(a,t)$, and the position (trajectory), $\tilde{x}(a,t)$. This is the basis for several useful soultion methods that will be discussed in Part 2.

7) The one dimensional Lagrangian conservation equations for mass and momentum may be reduced to an exact, nonlinear wave equation. One-dimensional flows are, however, a very limited and special case.

8) The three dimensional Lagrangian equations are quite complex, generally, and are not often used in their full form. The Lagrangian acceleration is not the problem; the pressure gradient is at issue, because the spatial gradient of pressure in a three-dimensonal flow will depend (in general) upon the three-dimensional initial position.

9) Lagrangian observation methods have the potential of two useful properties:

   i) Economy of scale. Lagrangian mesaurements may be feasible for very large numbers of floats or trackable particles, and so permit detailed mapping in space. Particle Imaging Velocimtery and the Global Drifter Program are examples on the laboratory and ocean basin scale.

   ii) Simpler dynamical inferences. The time rate change of a fluid property, say a tracer concentration, may be more readily attributed to a source, without having to estimate the often very

10.1002/lom3.10114. Also, Sebille, E., and colleagues, 2016, Lagrangian ocean analysis: Fundamentals and practices. Ocean Modelling: https://doi.org/10.1016/j.ocemod.2017.11.008

large effects of advection due to fluid motion (as is neccesary in an Eulerian system, Sec. 3). In effect, Lagrangian observations account for advection by observing directly the trajectory (a corollary of 6) above).

2.7 Problems

1) The discussion of fluid flow in this section omitted mention of diffusion in favor of an ideal fluid model that recognizes only resolved, larger-scale flow. Of course, diffusion actually happens, and is especially evident in smaller (tea cup-size) domains. In practice, how long can you follow a parcel (a small patch of dye) around in a stirred tea cup before it effectively disappears by diffusion into its surroundings? Does this depend upon the vigor or the details of the stirring?

2) The trajectories of Eq. (6) include the possibility of a spatially-uniform velocity, U_o. When evaluated in Fig. (8), U_o was set to zero. How would the solutions for density change if $U_o > 0$, say? Suppose instead that U_o is non-zero, but the a-dependent component = 0, i.e., that there is no linear deformation. How would the solutions for density change in that case?

3) Refer to the density solutions of Fig. (8). Can you use the Lagrangian solution to find the Eulerian solution, i.e., can you relate the left and right sides of Fig. (8)? This anticipates the Eulerian solutions of Sec. 3 and the method of characteristics in Sec. 4.

4) Can you show that the linear wave speed in the case of an adiabatic ideal gas is just $c_0^2 = \tilde{z}P_0/\rho_0$, and for the exact nonlinear wave equation, $c^2 = c_0^2 \frac{\partial \tilde{x}}{\partial a}^{-(\tilde{z}+1)}$. Thus the wave speed is greater in regions of condensation, $C > 1$, i.e., where the density is increased compared to ρ_0.

5) Can you spot the one-dimensional momentum equation (15) in the thicket of terms shown in Eqs. (21)? And, for bonus points, where is our friendly one-dimensional density equation (11) in the three-dimensional Jacobian?

6) Some fun with composite functions (reviewed in Sec. 6.2). Explain the difference between $\mathbf{V_L}(\mathbf{A},t)$ and $\mathbf{V_L}(\mathbf{A}(\tilde{\mathbf{x}},t),t)$.

3 The Eulerian (or field) coordinate system.

The goal of this section is to develop the Eulerian statements of mass and momentum conservation. The approach will be a start with the Lagrangian form of the kinematic relations and conservation laws, and then transform step by step to their Eulerian equivalent — velocity is in Sec. 3.1, time derivatives in Sec. 3.2, and volume integrals in Sec. 3.3.

3.1 The formal transformation of Lagrangian to Eulerian velocity

Let's start by using the FPK formalism to calculate the Eulerian velocity that corresponds to the (one-dimensional) Lagrangian trajectory and velocity of Eqs. (6) and (7). The parcel trajectories may be readily inverted to yield

$$a(\tilde{x},t) \;=\; \frac{\tilde{x} \;-\; U_o\, t}{(1 \;+\; 2t)^{-1/2}}.$$

Now eliminate a from $\tilde{u}$ of Eq. (7) in favor of the position, $\tilde{x}$, to find

$$\tilde{u}(a(\tilde{x},t),t) \;=\; U_o \;+\; \tilde{x}(1+2t)^{-1}.$$

This is the velocity at the position $x = \tilde{x}$ and time = t, which is just what we mean by Eulerian velocity, and so it is appropriate to relabel this function and the position $\tilde{x}$ to arrive at

$$u(x,t) \;=\; U_o \;+\; x(1+2t)^{-1}, \tag{26}$$

which is sampled in Fig. (6), lower. This procedure amounts to forming a composite function from the Lagrangian trajectory and velocity (composite functions are reviewed in Sec. 6.2). Notice that the spatially-uniform velocity, U_o, carries over directly.

The velocity field defined by Eq. (26) happens to look a lot like the Lagrangian velocity when plotted over the same range of a and x, cf. Figs. (6), middle and lower; u and $\tilde{u}$ are both positive and increase in the positive x direction. They both decrease with time. But while there are obvious similarities in this case, there are fundamental differences. The independent coordinates of u and $\tilde{u}$ are different things - the Lagrangian data depends upon a, the initial x-coordinate of a parcel, while the Eulerian data is a function of the field coordinate, x. To compare the Eulerian and the Lagrangian velocities is thus a bit like comparing apples and oranges; they are not the same kind of thing despite that they have the same dimensions, they describe the same flow, and in this very simple example, they do look a lot alike.

Though different generally, there are specific times and places where the Lagrangian and Eulerian velocities *are* equal, consistent with the FPK. To see this, let's follow the parcel tagged by $a = 0.5$, and choose an Eulerian observation site at (arbitrarily) $x = 0.7$. This parcel crosses the observation site at $t = 0.48$, Fig. (11) upper. At that time, and only at that time, the Lagrangian and Eulerian velocities are equal, cf., Fig. (11) middle. This is an exact equality, since there has been no need for approximation in this very simple transformation Lagrangian $\rightarrow$ Eulerian.

This transformation from the Lagrangian trajectories to the Eulerian velocity field required a time derivative of the trajectories, and the initial position was eliminated. Given only (26), we wouldn't know which parcel was present at a given x and time. In many cases this will not be of concern. But if the need was to know the origin of pollutants carried on the wind and observed at a field site, then it would be of first importance. To recover that Lagrangian information, and thus to go from an Eulerian velocity field to Lagrangian trajectories, requires an integration, taken up in Part 2.

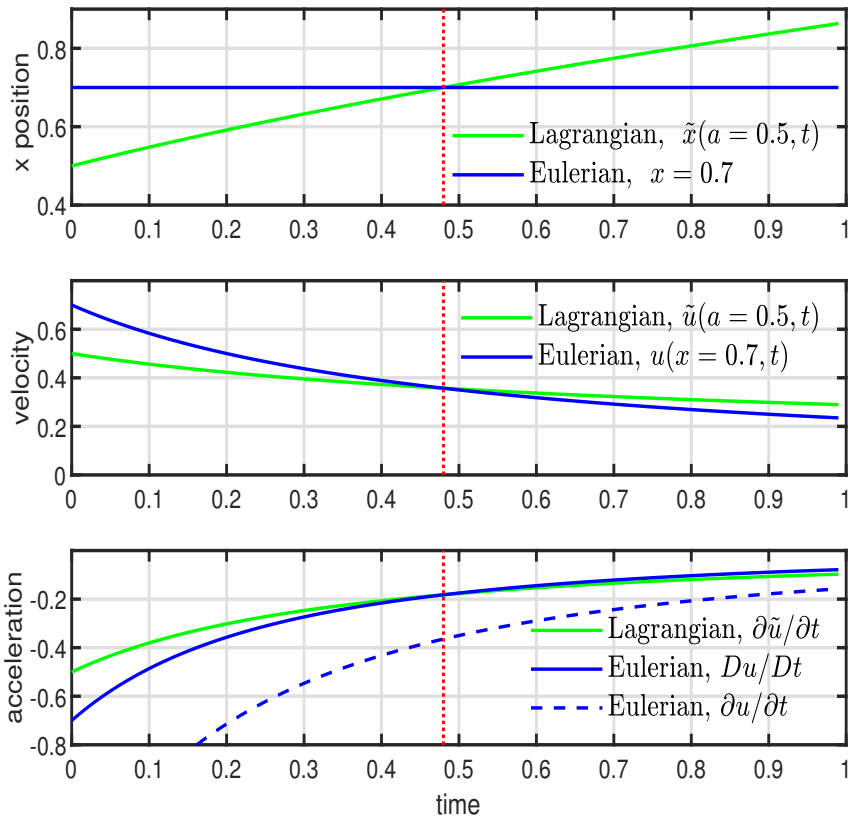

Figure 11: Lagrangian and Eulerian representations of the one-dimensional, time-dependent flow defined by the trajectories of Eq. (6) with $U_o = 0$. **(upper)** Positions. The trajectory of the parcel having $a = 0.5$ is the green, solid line. A fixed observation site, $x = 0.7$ is also shown (blue line). Note that this particular trajectory crosses $x = 0.7$ at time $t = 0.48$, computed from Eq. (6) and marked with a red dotted line in each panel. **(middle)** Velocities. The Lagrangian velocity of the parcel defined by $a = 0.5$ (green line) and the Eulerian velocity at the fixed position, $x = 0.7$ (blue line). Notice that the Lagrangian velocity of this specific parcel (green line) and the Eulerian velocity at the fixed position (blue line) are equal at $t = 0.48$, but not otherwise. This is illustrative of the FPK that was used to calculate the Eulerian velocity. **(lower)** Accelerations. The Lagrangian acceleration of the parcel $a = 0.5$ (green, solid line) and the Eulerian acceleration evaluated at the fixed position $x = 0.7$ (two blue lines). As will be discussed in Sec. 3.2, there are two ways to compute a time rate change of velocity in the Eulerian system; the partial time derivative holding x constant is shown as a blue dashed line, and the material time derivative, $Du/Dt = \partial u/\partial t + u\partial u/\partial x$, is a blue solid line. The latter is the counterpart of the Lagrangian acceleration $\partial\tilde{u}/\partial t$ in the sense that at the time the parcel crosses the Eulerian observation site, $Du/Dt = \partial\tilde{u}/\partial t$. Thus the Eulerian material derivative of velocity (the acceleration) at a fixed point and given time is equal to the Lagrangian acceleration of the parcel moving through that point at that time (but not otherwsie). This is the basis of the Eulerian equations of motion.

3.2 Transforming time derivatives; the material derivative

Transforming the acceleration, or time derivatives generally, is taken up next. Consider a scalar variable s in the Lagrangian system and so $\tilde{s}(a,t)$. The time rate of change holding a fixed is just

$$\frac{D\tilde{s}}{Dt} = \frac{\partial \tilde{s}}{\partial t}, \tag{27}$$

the partial time derivative, as noted before. In the case that $\tilde{s}$ is the fluid velocity given by Eq. (7), then

$$\frac{D\tilde{u}}{Dt} \;=\; \frac{\partial \tilde{u}}{\partial t} \;=\; -a(1+2t)^{-3/2}, \tag{28}$$

which is Eq. (8).

Now presume that the trajectory can be inverted so that $a = a(\tilde{x},t)$ is known, and hence so is $\tilde{s}(a(\tilde{x},t),t)$. The function of the inner variables alone is then $s(x,t)$, which is the Eulerian representation of s, or,

$$s(x,t) \;=\; \tilde{s}(a(\tilde{x},t),t). \tag{29}$$

Take the time derivative of the right hand side while holding a constant. By application of the chain rule for composite functions,

$$\frac{Ds(x,t)}{Dt} \;=\; \frac{\partial s}{\partial \tilde{x}}\frac{\partial \tilde{x}}{\partial t} \;+\; \frac{\partial s}{\partial t}. \tag{30}$$

The time derivative $\partial\tilde{x}/\partial t$ holding a constant is just the velocity of a fluid parcel, $\tilde{u}$, and writing $\tilde{x}$ as x, then with minor rearrangement and relabelling, we arrive at

Eulerian material time derivative in 1-d: $$\boxed{\frac{Ds}{Dt} \;=\; \frac{\partial s}{\partial t} \;+\; u\frac{\partial s}{\partial x}} \tag{31}$$

This may be exercised and checked by transforming the material derivative of the Eulerian velocity field $u(x,t)$ of Eq. (26) into the corresponding Lagrangian form to compare with the Lagrangian acceleration given by Eq. 28. The material time derivative of this velocity field is just

$$\frac{Du}{Dt} \;=\; (\frac{\partial}{\partial t} \;+\; u\frac{\partial}{\partial x})x(1+2t)^{-1} \;=\; -2x(1+2t)^{-2} \;+\; x(1+2t)^{-2} \;=\; -x(1+2t)^{-2}.$$

To find the corresponding Lagrangian acceleration, eliminate this x in favor of a using the known trajectory for this flow, Eq. (6), to find

$$\frac{Du}{Dt}(\tilde{x}(a,t),t) \;=\; -a(1 \;+\; 2t)^{-3/2},$$

which is the same as the Lagrangian acceleration, Eq. (28). Thus, the Du/Dt given by Eq. (31) is indeed the Eulerian equivalent of $D\tilde{u}/Dt$, as intended.

In a three-dimensional Cartesian system with coordinates (x,y,z) and velocity (u,v,w), the material

time derivative represented in an Eulerian system is

$$\frac{D}{Dt} = \frac{\partial}{\partial t} + u\frac{\partial}{\partial x} + v\frac{\partial}{\partial y} + w\frac{\partial}{\partial z}, \tag{32}$$

or using more compact vector notation,[24]

$$\text{Eulerian material derivative in 3-d:} \qquad \boxed{\frac{D(\ )}{Dt} = \frac{\partial(\ )}{\partial t} + V\cdot\nabla(\ )} \tag{33}$$

The importance of the D/Dt operator can by gauged from the veritable boatload of names that it has acquired in the literature — D/Dt is called the convective derivative, the substantive or substantial derivative, the Stokes derivative and the material derivative (the choice here). D/Dt is also said to be the time derivative 'following the flow'. This is appropriate insofar as $\partial\tilde{x}/\partial t$ in Eq. (30) is with a held constant. However, this could be misleading if it was interpreted to mean parcel tracking in the Lagrangian sense, i.e., for an extended time. Rather, the operator D/Dt gives, entirely in field coordinates (just x in the one-dimensional case), the time rate of change that would be observed by a parcel moving through the point x at the time t; thus D/Dt follows the flow only instantaneously in both x and t. An example is in Fig. 11, lower; the Lagrangian acceleration and the material time derivative of velocity (evaluated in their respective systems) are equal when they are evaluated at a common position and time, in Fig. (11) at $a = 0.5$, $x = 0.7$ and t= 0.48, in the same way that the corresponding Lagrangian and Eulerian velocities are equal at this common position and time, Fig. (11), middle.

3.3 Transforming integrals and their time derivatives via the Reynolds Transport Theorem

The conservation laws of classical physics apply to material volumes, e.g., the moving gray volume of Fig.(3), and not to control volumes that are fixed in space. The Eulerian equivalent of a moving, material fluid volume will be the third key piece of the transformation of kinematics and dynamics from Lagrangian to Eulerian form. This relation is called the Reynolds Transport Theorem, or RTT (and yes, this is the same Reynolds of Reynolds number fame in Sec. 6.1.2).

[24] The gradient operator expanded in Cartesian coordinates is

$$\nabla = e_x\frac{\partial}{\partial x} + e_y\frac{\partial}{\partial y} + e_z\frac{\partial}{\partial z},$$

with **e** the unit vector. The advective derivative term $V\cdot\nabla$ of (33) is, in effect, a scalar that is multiplied onto the variable being differentiated, and it is sometimes written $(V\cdot\nabla)$ to emphasize this property. In a Cartesian coordinate system the D/Dt operator produces four terms for each component of a vector being differentiated, one term being the partial with respect to time, and three terms arising from the advective rate of change. However, when D/Dt is expanded in cylindrical polar coordinates it becomes five terms, the additional advective term arising from the θ dependence of the r and θ unit vectors (in the Cartesian system the unit vectors are constant). In spherical polar coordinates the D/Dt operator expands to six terms. It is sometimes helpful to represent the advective derivative of velocity by the following vector identity $(\mathbf{V}\cdot\nabla)\mathbf{V} = \frac{1}{2}\nabla(\mathbf{V}^2) + (\nabla\times\mathbf{V})\times\mathbf{V}$, which is less likely to be misinterpreted. This form is especially useful when treating an ideal fluid, wherein frictional effects vanish and so too may the curl of the velocity, also called the vorticity (Sec. 4).

The essential content of the RTT can be understood by considering the integral in R^1 of an intensive fluid property, say, $\tilde{s}$, over a moving material volume of fluid (Fig. 7) (this is, of course, a linear volume, the results being easily extended to R^3),

$$\tilde{S}(t) \;=\; \int_{\tilde{x}_1}^{\tilde{x}_2} \tilde{s}(\tilde{x},t)d\tilde{x}. \tag{34}$$

The volume integral $\tilde{S}(t)$ is an extensive property, which may be subject to a physical conservation law,[25] say $\frac{DS}{Dt} = 0$, or if there is a source Q then, $\frac{DS}{Dt} = Q$, (examples will follow). To make the best use of such a conservation law we need to write the integral Eq. (34) in terms of the field variables, just x in one dimension.

To proceed, represent the integral by a sum over some large number K of infinitesimal segments, $\delta\tilde{x}_k$,

$$\tilde{x}_2 - \tilde{x}_1 \;=\; \sum_K \delta\tilde{x}_k,$$

$$\tilde{S}(t) \;=\; \int_{\tilde{x}_1}^{\tilde{x}_2} s(\tilde{x},t)d\tilde{x} \;\approx\; \sum_K s(\tilde{x}_k,t)\delta\tilde{x}_k. \tag{35}$$

The number K is fixed while the length of the total interval, $\tilde{x}_2 - \tilde{x}_1$, may change with time and thus we have to allow that the material segments $\delta\tilde{x}_k$ will vary with time. With that understood, the time derivative can be taken through the summation operator,

$$\frac{D\tilde{S}}{Dt} \;\approx\; \sum_K \left(\frac{D\tilde{s}(\tilde{x}_k)}{Dt}\delta\tilde{x}_k \;+\; \tilde{s}(\tilde{x}_k)\frac{D\delta\tilde{x}_k}{Dt}\right). \tag{36}$$

The first term on the right hand side is expected, and the second term accounts for a possible change in the material length, $D\delta\tilde{x}_k/Dt$. The time derivative of this length is just the velocity difference at the location of the two parcels that mark its endpoints,

$$\frac{D\delta\tilde{x}_k}{Dt} \;=\; \frac{D\delta x_k}{Dt} \;=\; \frac{D}{Dt}(x_{k+1} \;-\; x_k) \;=\; u_{k+1} - u_k,$$

where $u_k \;=\; \frac{Dx_k}{Dt}$ is the fluid velocity at $x_k = \tilde{x}_k$, etc. When the length δx is infinitesimal the velocity difference may be written

$$(u_{k+1} - u_k) \;=\; \frac{\partial u}{\partial x}\delta x$$

[25] It is sometimes helpful to make clear whether a given fluid property is 'intensive' or 'extensive'. (1) An intensive property of a fluid is measurable at a point, e.g., density, while an extensive property of a fluid is an integral over a finite volume, e.g., the volume itself or the mass of the fluid volume. An extensive property is thus probably not directly measurable. (2) Imagine two volumes of fluid, V_1 and V_2, having densities ρ_1 and ρ_2. Now suppose that the volumes are added together to make a new volume, V_3. Aside from from nonlinear effects in the equation of state, the new volume will be $V_3 = V_1 + V_2$, while the new density will be $\rho_3 = (\rho_1 V_1 + \rho_2 V_2)/V_3$. Thus the extensive property, the masses, add up when volumes are combined, while the corresponding intensive property, the densities, are a volume-weighted average. (3) Extensive properties such as mass, and internal energy, may be subject to a conservation law, while the corresponding intensive properties, density and temperature, will generally not be. Nevertheless, as we will see in this section, conservation laws for extensive properties will lead to useful differential balance equations for the intensive properties.

and hence

$$\frac{D\delta x}{Dt} = \frac{\partial u}{\partial x}\delta x.$$

Collecting these results into Eq. (36) gives

$$\frac{D\tilde{S}}{Dt} = \approx \int_{x_1}^{x_2}(\frac{Ds}{Dt} + s\frac{\partial u}{\partial x})dx. \tag{37}$$

In one dimension, the time derivative over a material volume is related to the equivalent field quantities via the important

Reynolds Transport Theorem in 1-d:
$$\boxed{\frac{D\tilde{S}}{Dt} = \frac{D}{Dt}\int_{\tilde{x}_1}^{\tilde{x}_2}\tilde{s}(\tilde{x},t)\,d\tilde{x} = \int_{x_1}^{x_2}(\frac{Ds}{Dt} + s\frac{\partial u}{\partial x})\,dx} \tag{38}$$

where $x_1 = \tilde{x}_1$, etc. at the time the transformation is made. Thus to transform the time derivative of a material volume into field coordinates requires accounting for the time rate of change of volume. (We will demonstrate the RTT in an application to mass conservation discussed below.)

Generalization of the RTT to three-dimensions: If instead of a one-dimensional 'volume' used in the examples above, suppose that the issue is a three-dimensional volume, $dVol = dx\,dy\,dz$ in Cartesian coordinates. It is straightforward to show that the time derivative of the differential volume is

$$\frac{D\ dVol}{Dt} = (\frac{\partial u}{\partial x} + \frac{\partial v}{\partial y} + \frac{\partial w}{\partial z})dVol = \nabla\cdot V\ dVol \tag{39}$$

$\nabla\cdot V$ is the divergence of the fluid velocity in three dimensions and is the volumetric (or normalized) time rate change of the differential volume, i.e., $\nabla\cdot V = dVol^{-1}(d/dt)(dVol)$. The RTT in three dimensions is then a straightforward generalization of the one-dimensional form, Eq. (38),

RTT in 3-d:
$$\boxed{\frac{D}{Dt}\iiint_{material}\tilde{s}\,dVol = \iiint_{field}(\frac{Ds}{Dt} + s\nabla\cdot V)\,dVol} \tag{40}$$

The RTT is an exact, kinematic relationship that holds for an intensive fluid property, e.g., s could be the mass density, ρ, or the momentum density, $\rho\mathbf{V}$. The RTT serves a crucial purpose — to show how fluid flow effects the time rate change of the corresponding extensive quantity, i.e., the S in our notation, and moreover, to show this crucial result in field coordinates. The RTT is thus the last piece needed to give a practical (widely useful) answer to the question posed in the opening paragraph of Section 1, *viz.*, how can we apply the conservation principles of classical physics to a fluid flow? The statement of mass and momentum are discussed below. Physics, as opposed to kinematics, enters the development when the corresponding extensive quantity, e.g., mass or momentum, is asserted to be conserved under fluid flow, and including external sources, if any.[26]

[26] A superb reference on the Reynolds Transport Theorem and much else that is relevant to fluid dynamics is by C. C. Lin and L. A. Segel, *Mathematics Applied to Deterministic Problems in the Natural Sciences* (MacMillan Pub., 1974).

3.4 The Eulerian equations of motion

3.4.1 Mass conservation represented in field coordinates

An important application of the RTT is to the mass of a moving, three-dimensional volume of fluid, which is thus an extensive property defined on a specific material volume. There is no source or sink for mass in the classical physics that is presumed to hold, and thus the physics of mass conservation is that the mass $\tilde{M}$ of a specific material volume (and thus the tilde) must remain exactly constant,

$$\frac{D\tilde{M}}{Dt} = 0, \tag{41}$$

for all flow conditions. We can make no such assertion for the corresponding intensive property, the mass density, ρ, nor for the mass inside of a control volume that is fixed in space.

The mass conservation Eq. (41) has a clear and precise physical meaning, but it is not in and of itself directly useful as a means to predict mass or density in most models of fluid flow. A form that will be useful follows from application of the Reynolds Transport Theorem,

$$\frac{D\tilde{M}}{Dt} = \frac{D}{Dt}\iiint_{material} \tilde{\rho}\, dVol = \iiint_{field} \left(\frac{D\rho}{Dt} + \rho\nabla\cdot V\right) dVol = 0. \tag{42}$$

If this integral relation holds at all times and for all positions within a domain, and if the integrand is smooth (no discontinuities), then the integrand must vanish at all times and positions in that domain[27] and so yielding the differential form of

$$\text{Eulerian mass conservation:} \quad \boxed{\frac{D\rho}{Dt} + \rho\nabla\cdot V = 0} \tag{43}$$

The meaning of Eq. (43) is as follows: say the material derivative of density is negative, $\frac{D\rho}{Dt} < 0$ at a point in space, then given that $\rho > 0$, there must be a divergence of the fluid velocity, $\nabla\cdot\mathbf{V} > 0$, at that point. Thus the fluid parcel that is instantaneously at that point will have decreasing density and an inversely proportional increasing volume. This is a kinematic relationship that holds regardless of what the cause of the density change might be, i.e., whether due to a pressure variation or heat exchange with the surroundings, or even a phase change of the fluid material. Thus Eq. (43) is not by itself sufficient to predict or understand *why* density might change, which comes instead from a thermodynamic state equation, as discussed further below. However, it is worth noting that Eq. (43) does *not* hold if the fluid volume exchanges material with its surroundings by diffusion, e.g., say of salt in the case of sea water or water vapor if air. In that (very common) case we would have to allow a source term appropriate to the

[27] The Dubois-Reymond lemma: it is given that an integral of the sort Eq. (42) but here in R^1, $\int_{x_1}^{x_2}\sigma(x)dx = 0$, vanishes for any x_1, x_2 and that σ is smooth. If we now suppose that $\sigma(x_a) > 0$ this leads to a contradiction. Given that σ is smooth, then there will be some neighborhood around x_a where $\sigma(x) > 0$. Choose x_1 and x_2 to lie within this neighborhood, and apply the mean value theorem to the integral to find that $\sigma(\bar{x})(x_2 - x_1) \geq 0$. This contradicts what is known about this integral, and hence the conclusion is that $\sigma(x)$ must be zero at every point. In other words, the only smooth function whose integral is zero on every interval is the zero function.

specific conditions.

The mass conservation relation may be written in a form that shows the separate effects of advection and of velocity divergence; in one dimension,

$$\frac{\partial \rho}{\partial t} \;=\; -\,(\,u\frac{\partial \rho}{\partial x} \;+\rho\frac{\partial u}{\partial x}), \tag{44}$$

and for two or three-d,

$$\frac{\partial \rho}{\partial t} \;=\; -\,(\mathbf{V}\cdot\nabla\rho \;+\; \rho\nabla\cdot\mathbf{V}). \tag{45}$$

The one-dimensional density and velocity of Sec. 2.2 provide an example; recall that the Lagrangian density and the trajectory were, repeating Eqs. (6) and (14),

$$\tilde{\rho}(a,t) \;=\; \frac{\rho_c+\Gamma a}{(1+2t)^{1/2}} \quad \text{and} \quad \tilde{x}(a,t) \;=\; U_o t \;+\; a(1+2t)^{1/2}, \tag{46}$$

from which the Eulerian density may be calculated by algebra; eliminate a in favor of $x \;=\; \tilde{x}$ to find,

$$\rho(x,t) \;=\; \frac{\rho_c}{(1+2t)^{1/2}} \;+\; \frac{\Gamma(x-U_o t)}{(1+2t)}, \tag{47}$$

(Fig. (8), right) and recall the Eulerian velocity,

$$u(x,t) \;=\; U_o + \frac{x}{(1+2t)}. \tag{48}$$

To exercise the Eulerian density equation (44), compute the local rate of change of this density

$$\frac{\partial \rho}{\partial t} \;=\; -\,(\frac{\rho_c}{(1+2t)^{3/2}} \;+\; \frac{2\Gamma(x-U_o t)}{(1+2t)^2} \;+\; \frac{\Gamma U_o}{1+2t}), \tag{49}$$

and verify that it is the sum of an advection term, evaluated from (47) and (48),

$$u\frac{\partial \rho}{\partial x} \;=\; \frac{\Gamma(x-U_o t)}{(1+2t)^2} \;+\; \frac{\Gamma U_o}{(1+2t)}, \tag{50}$$

and a divergence term,

$$\rho\frac{\partial u}{\partial x} \;=\; \frac{\rho_c}{(1+2t)^{3/2}} \;+\; \frac{\Gamma(x-U_o t)}{(1+2t)^2}. \tag{51}$$

The divergence term (51) is negative (when on the right hand side of Eq. 44) since this flow is divergent, $\frac{\partial u}{\partial x} > 0$, and fluid volumes are stretched by the flow. This divergence process is in common with the Lagrangian density equation, (11), where it appears as the linear deformation, effectively the time-integrated divergence. The advection term is also negative, because $u > 0$, and the density increases toward positive x. The effect of translating or 'advecting' this density profile toward positive x is thus to cause the density observed at a fixed point to decrease with time.

It is important appreciate that the density observed at a fixed point can change due solely to an

advection process even while the density observed on moving parcels may remain constant. The only thing required in one dimension is a spatial variation of density combined with a nonzero velocity, and that can include the spatially-uniform velocity, U_o. In a more realistic multi-dimensional space, the condition is that $\mathbf{V}\cdot\nabla\rho$ is nonzero. A 'frozen field' balance is said to hold when the local rate of change is due mainly to advection, and is not uncommon.

Now that we have a Lagrangian and Eulerian solution side by side in (46) and (47) it is interesting and worthwhile to consider how they are different, despite that they describe the same 'flow'. The Eulerian solution (47) is complete in one piece, $\rho(x,t)$ (assuming the x-coordinates are known, of course). The Eulerian solution contains within it the effects of divergence of the fluid motion, as well as the effects of the fluid motion, the advection process. Compare this with the Lagrangian solution (46) that comes in two pieces, the density on moving parcels $\tilde{\rho}(a,t)$, which in this presumed ideal fluid model changes only by divergence (linear deformation), and the time-dependent position of those parcels, $\tilde{x}(a,t)$. The latter is the fluid motion. The two-part Lagrangian solution thus simplifies the density equation considerably, an idea that can be exploited to real advantage in the method of characteristics and in various numerical schemes, e.g., semi-Lagrangian advection, both taken up in Part 2. But, you have to know the trajectory.

3.4.2 The flux form of the Eulerian equations.

Another way to write the Eulerian mass conservation equation (43) is to collect terms under the gradient operator,

$$\text{mass conservation, flux form:} \quad \boxed{\frac{\partial\rho}{\partial t} + \nabla\cdot(\rho\mathbf{V}) = 0} \tag{52}$$

An Eulerian budget equation in this form is said to be in 'flux' or 'conservation' form and has two important properties. To make it clear that these properties follow from the conservation form of the equation rather than the physical properties of the intensive property mass density, ρ, it is helpful to consider the same equation for an arbitrary, intensive scalar s,

$$\frac{\partial s}{\partial t} + \nabla\cdot\mathbf{s} = 0 \tag{53}$$

which could be mass per unit volume, ρ, or momentum per unit volume, $\rho\mathbf{V}$. Thus $s\times Volume = S$ is an extensive property, e.g., mass or momentum. The vector $\mathbf{s}$ is the flux of s and could be due to transport by the moving fluid, e.g., $\mathbf{s} = s\mathbf{V}$ obtains for any fluid property. The flux could also arise from molecular diffusion, $\mathbf{s} = -K\nabla s$, if a Fickian diffusion law is appropriate. In either event, $\mathbf{s}$ is a vector with dimensions $s \doteq s\ length\ \ time^{-1}$ so that $s\times area \doteq S\,time^{-1}$. For the moment it will be assumed that $\mathbf{s}$ depends linearly upon s, so that $s = 0$ over some neighborhood implies that the flux $\mathbf{s} = 0$ as well.

A volume integral of s taken over a fixed portion of a domain, i.e., a control volume (Fig. 13), gives the total amount of s within the control volume,

$$S = \int_{x1}^{x2}\int_{y1}^{y2}\int_{z1}^{z2} s\,dxdydz = \iiint_{field} s\,dVol.$$

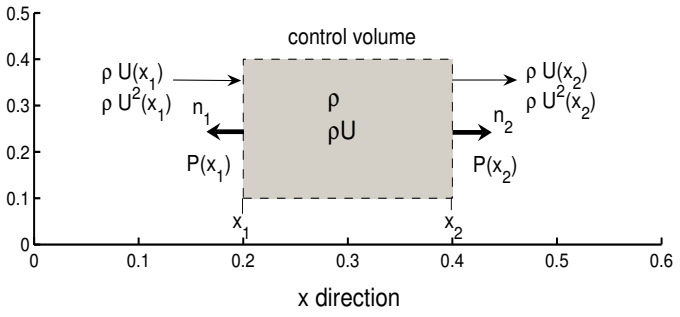

Figure 12: A schematic of a control volume (fixed in space) set in an ideal fluid in order to evaluate the Eulerian budgets of mass and momentum. The face of the control volume that is normal to the x-direction has an area A (not shown). In this one-dimensional Eulerian system the independent coordinates are the x-position, and the time, t. The dependent variables are the fluid density, $\rho(x,t)$, the momentum, $\rho u(x,t)$, and the pressure, $P(x,t)$. The one-dimensional fluxes of mass, ρu, and momentum, ρu^2, are implied by the arrows coming into or leaving the control volume.

This volume integral taken over the left and right sides of Eq. (53) gives

$$\iiint\limits_{field} \frac{\partial s}{\partial t}\, dVol \;=\; -\iiint\limits_{field} \nabla\cdot\mathbf{s}\, dVol \tag{54}$$

The time derivative can be moved outside the volume integral over the fixed limits, x_1, x_2, etc., of the control volume and Gauss' divergence theorem used on the right side to find that

$$\frac{\partial}{\partial t}\iiint\limits_{field} s\, dVol \;=\; \frac{\partial S}{\partial t} \;=\; -\iint\limits_{field} \mathbf{s}\cdot\mathbf{n}\, da. \tag{55}$$

Thus S can change only because of a flux across the surface of the control volume, Figs. (12) and (13). If it happens that the flux is uniform in space and so is non-divergent, $\nabla\cdot\mathbf{s} = 0$, Eq. (54), then S will remain constant in time. The first key point is that the quantity of interest for Eulerian budgets is the *flux divergence*, rather than the flux itself.

Now imagine that the boundaries of the control volume expand to infinity. It may be assumed without loss of generality that the variable b and the flux $\mathbf{s}$ will be vanishing at infinity, i.e., that the flow is bounded in space, and hence the flux on the surfaces vanishes as well. Over this control volume it follws that

$$\iint \mathbf{s}\cdot\mathbf{n}\, da \;=\; 0 \;=\; \frac{\partial S}{\partial t}$$

and S is constant in time. The second key point is that, given the present boundary conditions, the total amount of s can not change due to the flux $\mathbf{s}$, even though the flux $\mathbf{s}$ may act to redistribute b within the domain so that at a given point in space, s could be highly time-dependent. The same thing would result if the flux $\mathbf{s}$ vanished on the boundary of a finite domain, e.g., if the flux was due to fluid motion and the domain boundary was an impermeable surface.

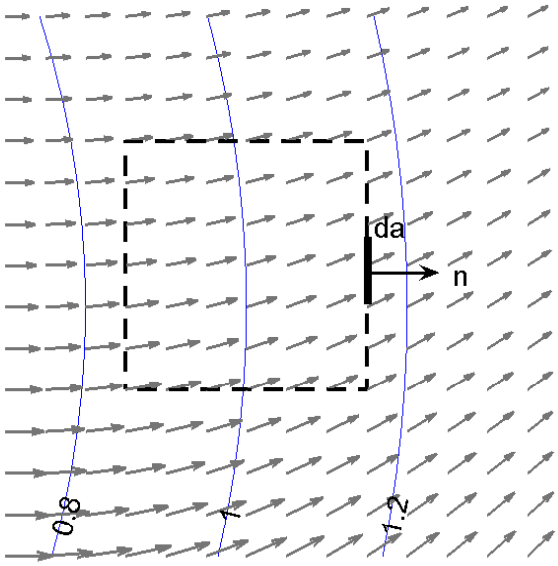

Figure 13: A control volume is fixed in space and has imaginary sides (dashed lines) and a two-dimensional slice through a velocity field, $\mathbf{V}$, and isolines of a fluid intensive property, s. The flux of b due to transport by the fluid velocity is $\mathbf{s} = s\mathbf{V}$; the flux of s through a differential surface element of the control volume is then $\mathbf{s} \cdot \mathbf{n} da$, where $\mathbf{n}$ is the outward unit vector normal to the surface. A question for you: given what may be seen from this figure, how will the total amount of s in this control volume, S, change with time?

Incompressible flow: for many purposes, fluids may appear to be infinitely stiff. The velocity divergence term is clearly necessary in the mass conservation equation, and plays a prominent role in the one-dimensional example. Nevertheless, for most phenomenon of the atmosphere or ocean and for many engineering flows, the fluid velocity that is associated with the velocity divergence is very, very small compared to the (actual) fluid velocities and may often be ignored with no appreciable error. Under this incompressibility assumption, the velocity is assumed to follow

$$\text{incompressible flow:} \quad \boxed{\nabla \cdot \mathbf{V} = 0} \tag{56}$$

which in effect says that the volume (rather than the mass) of fluid parcels is constant in time. In one-dimension this requires the velocity to be spatially uniform, which is not an interesting case (and so our one-dimensional flow is highly and unrealistically divergent). In two dimensions or three dimensions this need not be the case. For example, in two dimensions, a gentle linear deformation in say the x-direction may be almost exactly compensated by a linear deformation of the opposite sign in the y-direction, with the result that the area of a two-dimensional material volume will remain nearly constant and so the fluid will appear to be very nearly incompressible, even while the shape of the material volume may change greatly.

Even with the incompressibility assumption in place, it is not inconsistent to have a model in which density may nevertheless change, and indeed density changes may be of primary importance in causing the flow of an incompressible fluid. Under the incompressibility assumption, density may be computed from an equation of state given the pressure, temperature, salinity, etc., with no reference made to the divergence of the fluid velocity. That the divergence may be ignored is a useful mathematical

approximation that is contingent upon the physical phenomenon under consideration. One important class of phenomena, acoustic waves, owe their entire existence to velocity divergence and associated pressure changes. The incompressibility assumption is valid provided that the fluid velocity is much less than the speed of sound, which holds well for most natural flows of the atmosphere and ocean.

3.4.3 Momentum conservation represented in field coordinates

A second and very important application of the Reynolds Transport Theorem arises on consideration of momentum balance. The momentum of a moving, three-dimensional volume of fluid can be written

$$\tilde{N} = \iiint\limits_{material} \tilde{\rho}\tilde{V}\, dVol. \tag{57}$$

Because this is a material volume we can assert Newton's Second Law, that the momentum of this specific volume of fluid can change only if there is a net force, F,

$$\frac{D\tilde{N}}{Dt} = \iiint\limits_{material} F\, dVol, \tag{58}$$

acting on the fluid. This $\tilde{\mathbf{F}}$ could include inertial forces, such as gravitational mass attraction or the Coriolis force that act throughout the volume, and normal or tangential stresses (Section 6.1) that act on the surface of the volume. By means of the Reynolds Transport Theorem and the mass conservation relation, the left side of Eq. (58) may be written in field coordinates as

$$\frac{D\tilde{N}}{Dt} = \frac{D}{Dt}\iiint\limits_{material} \tilde{\rho}\tilde{\mathbf{V}}\, dVol \;=\; \iiint\limits_{field} \rho\frac{DV}{Dt}\, dVol. \tag{59}$$

A term that might have been expected,

$$\frac{D\rho}{Dt}V, \tag{60}$$

has dropped out by application of the mass conservation requirement. Thus the momentum of a fluid parcel (or marked fluid volume) can change only because of a change of the velocity. The right side of Eq. (58) is a volume integral over field coordinates that is evaluated over the volume occupied instantaneously by the moving fluid,

$$\iiint\limits_{material} \tilde{F}\, dVol \;=\; \iiint\limits_{field} F\, dVol, \tag{61}$$

and thus from Eqs. (59) and (61),

$$\iiint\limits_{field} \rho\frac{DV}{Dt}\, dVol \;=\; \iiint\limits_{field} F\, dVol. \tag{62}$$

The volume considered here is arbitrary, and so the integral relation holds for every volume. The differential form of the momentum balance for a fluid continuum is

$$\text{Eulerian momentum balance:} \quad \boxed{\frac{DV}{Dt} = \frac{\partial V}{\partial t} + (V\cdot\nabla)V = F/\rho} \tag{63}$$

The volume of the integrals in Eq. (62) is the volume that is instantaneously coincident with the material volume indicated in Eq. (57). For the purpose of finding F, this may be regarded as a fixed control volume, and the stress acts upon the fluid that is instantaneously contained within the control volume.

3.4.4 Fluid mechanics requires a stress tensor

Now to specify the force, F, which will proceed in two steps. The first step amounts to mathematical bookkeeping on the stress tensor, essentially a 3x3 matrix of stress components that may be used to evaluate the stress vector acting on any face of a control volume. The second step is to specify what those stress components are. Stresses within a fluid depend upon the physical properties of the fluid and the flow itself, and so this involves something more than kinematics and bookkeeping.

The specification of the stress on a given surface requires a 3x3 object because the surface and the stress vector are both 3-dimensional (Fig. 19). That is, the stress vector is defined by three components, and the surface upon which the stress acts is defined by the unit normal vector, and thus another three components. A full representation of the stress within a fluid generally requires nine components at each point in space. It can be very helpful to think of these grouped into a single entity, a 3x3 object called the stress tensor, $\mathbb{S}$,

$$\mathbb{S} = \begin{pmatrix} S_{xx} & S_{xy} & S_{xz} \\ S_{yx} & S_{yy} & S_{yz} \\ S_{zx} & S_{zy} & S_{zz} \end{pmatrix}, \tag{64}$$

that can be added and multiplied with the same rules that apply to matrices. (Note this reuse of S to represent a stress, vs. a scalar tracer in Sec. 3.2 and 3.3., and the subscripts identify the element of the tensor, and not partial derivatives.) By convention, the first subscript on a stress component indicates the direction of the stress (the projection of the stress vector on to the unit vectors), and the second subscript indicates the orientation of the surface via the direction of the outward unit normal of the surface. [28]

A handy property of the stress tensor is that the matrix product $\mathbb{S}\cdot\mathbf{n}$ picks out the components of the stress vector acting on the face whose unit normal vector is $\mathbf{n}$. For example, let the unit normal for the upper face of the cube in Fig. (19) be $\mathbf{n_u}$, which thus has components (0; 0; 1) (the semicolon delimiters indicate that these elements are arranged in a column vector), and so $\mathbb{S}\cdot\mathbf{n_u} = (S_{xz};\ S_{yz};\ S_{zz})$, is a three element (column vector) of the components of the stress vector acting upon the upper face of the parcel. The force associated with this stress acting upon a differential area of the surface, da, is then

$$d\mathbf{F} = \mathbb{S}\cdot\mathbf{n}\, da, \tag{65}$$

[28] It can be argued that three pairs of the stress tensor components are equal, $S_{yx} = S_{xy}, S_{xz} = S_{zx}$ and $S_{zy} = S_{yz}$, at least for ordinary fluids such as air and water. This leaves six unique components and a stress tensor that is symmetric, $\mathbb{S} = \mathbb{S}'$. A little more on this below.

where the stress tensor is evaluated at the position of the differential area. The unit normal of the lower (downward looking) face of the control volume of Fig. (1) has components (0; 0; -1) and so the stress vector on that face has components $\mathbb{S}\cdot\mathbf{n_l} = -(S_{xz};\ S_{yz};\ S_{zz})$, where these components are evaluated at the position of the lower face. If it happened that the stress components were the same on the upper and lower faces, then the stress exerted by the overlying fluid on the upper face of the volume would be equal in direction and magnitude to the stress exerted by the fluid within the volume on the underlying fluid, in which case the net stress on the control volume, $\mathbb{S}\cdot\mathbf{n_u} + \mathbb{S}\cdot\mathbf{n_l} = \mathbb{S}\cdot(\mathbf{n_u}+\mathbf{n_l}) = 0$, would vanish.

Given Eq. (65) for the differential force, the net force on the fluid within the control volume may be computed by summing over the entire surface,

$$\mathbf{F} = \iint \mathbb{S}\cdot\mathbf{n}\, da, \tag{66}$$

where da is the differential area associated with the unit normal $\mathbf{n}$. Both $\mathbf{S}$ and $\mathbf{n}$ will, in general, vary over the surface. It is often desirable to express the net force as an integral over the volume of the object, rather than its surface, and this transformation is made by application of the tensor form of the divergence theorem,[29]

$$\mathbf{F} = \iint \mathbb{S}\cdot\mathbf{n}\, da = \iiint \nabla\cdot\mathbb{S}^{\mathbf{t}}\, dv. \tag{67}$$

Stress tensor in an ideal fluid, pressure only: The stress tensor has to be defined at every point in space and thus a tensor stress field is coincident with the velocity field. At first this seems a bit daunting; we had the goal of solving for the pressure and the velocity fields, and now it seems that we have to solve for a tensor field as well. However, as will see shortly, the stress tensor depends upon the velocity and the pressure in a straightforward way, so that nothing beyond the velocity and pressure fields will be required.

The stress vector due to pressure is just $-P\mathbf{n}$. Hence the stress tensor for a fluid that sustains only pressure forces, an ideal fluid, is simply

$$\mathbb{S}_{ideal} = \mathbb{P} = \begin{pmatrix} -P & 0 & 0 \\ 0 & -P & 0 \\ 0 & 0 & -P \end{pmatrix}, \tag{68}$$

an isotropic tensor (the same in all directions). The net pressure force is then

$$\boxed{\mathbf{F_{pressure}} = \iint \mathbb{P}\cdot\mathbf{n}\, da = \iiint \nabla\mathbb{P}\, dv = -\iiint \nabla P\, dv} \tag{69}$$

where the divergence theorem was applied to convert the surface integral into a volume integral and the

[29] This is probably not familiar, so I'll try to make it plausible. Each row of the stress tensor may be considered to be a vector, S_{1j}, S_{2j}, S_{3j}, so that there are three vectors whose components are numbered by the index j. Each of these vectors can be treated by way of the familiar divergence theorem for vectors, $\oint S_{ij} n_j da = \oint \frac{\partial S_{ij}}{\partial x_j} dv$ with i = 1, 2 or 3. Thus each row (or vector) of the tensor goes through separately. When we represent the divergence operator using symbolic notation, with ∇ a row vector operator that will be multiplied on the left of $\mathbf{S}$, then to operate on rows (each vector separately) we must operate on the transpose of $\mathbf{S}$, and thus $\mathbf{S^t}$ arises in Eq. (67). Later it will turn out that $\mathbf{S^t} = \mathbf{S}$.

last step holds only for isotropic tensors. The pressure force per unit volume is then

$$\mathbf{F}_{\mathbf{pressure}}/Vol \;=\; -\nabla P \;=\; -(\frac{\partial P}{\partial x}\mathbf{e_x} + \frac{\partial P}{\partial y}\mathbf{e_y} + \frac{\partial P}{\partial z}\mathbf{e_z}). \tag{70}$$

Stress tensor in a Newtonian, viscous fluid: In Sec. 6.1 it was claimed that the viscous shear stress in a simple shear flow in which the u component of velocity varied in the z-direction only (Figure 22) was $\tau_{xz} = \nu\frac{\partial u}{\partial z}$. There is nothing special about the z direction and if the u component of velocity varied in the y-direction, then there should arise a viscous stress in the x-direction that is exerted on the y-face of the parcel in exactly the same way. That viscous shear stress component would then be labelled

$$\tau_{xy} = \nu\frac{\partial u}{\partial y},$$

with a switch from S, indicating a stress generally, to τ to indicate a viscous stress in particular (you should make a sketch that shows this kind of shear flow and check whether the sense of the stress is given correctly by this equation).

An x-directed stress acting upon the x-face might be different, however, since this would involve a linear deformation rate rather than a shear deformation rate. For some fluids it is found experimentally that the viscosity for a linear deformation rate is not equal to the viscosity associated with shearing deformation, in much the same way that the bulk modulus of a solid is generally not equal to the shear modulus (Table 1, Sec. 6.1). While acknowledging that this is plausible for fluids as well, it will nevertheless be presumed here that there is only one viscosity, ν. Thus a linear deformation rate will produce or require a normal viscous stress,

$$\tau_{xx} = \nu\frac{\partial u}{\partial x}.$$

In most cases this normal viscous stress will be very much less than the normal stress associated with pressure.[30] With these three examples in hand, we can write the viscous stress tensor for Newtonian fluids in which the stress and rate of deformation are related linearly (Fig. 22),

$$\text{stress tensor for a Newtonian fluid:} \quad \boxed{\mathbb{T} \;=\; \nu\mathbb{G}} \tag{71}$$

[30] A viscous normal stress is somewhat harder to envision than is a viscous shear stress. But imagine a fluid column that is falling under the influence of gravity while restrained by a normal viscous (tensile) stress associated with the linear deformation rate of the elongating fluid column, e.g., the pitchdrop experiment (see footnote 38).

where the

velocity gradient tensor:
$$\mathbb{G} = \begin{pmatrix} \frac{\partial u}{\partial x} & \frac{\partial u}{\partial y} & \frac{\partial u}{\partial z} \\ \frac{\partial v}{\partial x} & \frac{\partial v}{\partial y} & \frac{\partial v}{\partial z} \\ \frac{\partial w}{\partial x} & \frac{\partial w}{\partial y} & \frac{\partial w}{\partial z} \end{pmatrix} \tag{72}$$

The tensor $\mathbb{G}$, called the velocity gradient tensor in this context, is very useful in that it contains all of the first partial derivatives of the velocity field in a single, readily manipulated object. It will appear again on several occasions in Part 2.

To find the viscous force per unit volume, apply the tensor equivalent of the divergence theorem, Eq. (67),

$$\mathbf{F}_{\mathbf{viscous}} = \iint \mathbb{T} \cdot \mathbf{n}\, da = \iiint \nabla \cdot \mathbb{T}\, dv. \tag{73}$$

The force per unit volume, written in vector and component form is then

$$\mathbf{F}_{\mathbf{viscous}}/Vol = \nu \nabla^2 \mathbf{V} = \nu \begin{pmatrix} \frac{\partial^2 u}{\partial x^2} + \frac{\partial^2 u}{\partial y^2} + \frac{\partial^2 u}{\partial z^2} \\ \frac{\partial^2 v}{\partial x^2} + \frac{\partial^2 v}{\partial y^2} + \frac{\partial^2 v}{\partial z^2} \\ \frac{\partial^2 w}{\partial x^2} + \frac{\partial^2 w}{\partial y^2} + \frac{\partial^2 w}{\partial z^2} \end{pmatrix}. \tag{74}$$

(Note that ∇^2 operating on a vector yields another vector, whose components are the Laplacian of the components of the original vector.) In all of the above it has been assumed that the viscosity is a constant.

The expression (74) for the viscous force per unit volume may at first look formidable because of the second derivatives and the large number of terms involved. But notice that it is linear and does not couple the components together, i.e., in the x-component equation there appears only the x-component of velocity, albeit differentiated with respect to all three spatial coordinates. The viscous force per unit volume may be familiar to you as the diffusion term of the elementary heat diffusion equation, and indeed, the momentum components are diffused through a fluid in laminar flow just the way that thermal energy is diffused through a solid.[31] Diffusion, or viscosity in the case of fluid momentum, acts to smooth out lumps and bumps in the velocity profile (in any direction) with the rate given by the viscosity times the Laplacian.[32]

[31] It bears emphasis that this is valid for molecular diffusion in a laminar flow in which Eq. (130) applies. Turbulent motion may cause mixing in a fluid that is often parameterized as a diffusion process, Fig. (22), in which case the equivalent viscosity (stress/shear) is likely to be a complex function of the flow, and not just a physical property of the fluid.

[32] Even a spatially homogeneous but asymmetric stress tensor would a induce very large (infinite) angular acceleration locally

Navier-Stokes equations: Given this specification of pressure and viscous forces,

$$\mathbf{F} \;=\; \mathbf{F}_{pressure} + \mathbf{F}_{viscous} \;=\; -\nabla P \;+\; \nu\nabla^2\mathbf{V},$$

the Eulerian form of the momentum balance equation is then, including the body force due to gravity,

$$\text{Navier-Stokes equation:} \qquad \boxed{\frac{\partial \mathbf{V}}{\partial t} \;+\; (\mathbf{V}\cdot\nabla)\mathbf{V} \;=\; \frac{-1}{\rho}\nabla\mathbf{P} \;+\; \frac{\nu}{\rho}\nabla^2\mathbf{V} \;-\; g\mathbf{e_z}} \tag{75}$$

If the density is regarded as variable, then we can not write the velocity of the Euler fluid in flux form directly, but use instead the momentum density, i.e., $\rho\mathbf{V}$. By adding the mass conservation equation to the momentum equation and with minor rearrangement (that you should verify),

$$0 \;=\; \frac{\partial}{\partial t}\begin{pmatrix} \rho u \\ \rho v \\ \rho w \end{pmatrix} + \frac{\partial}{\partial x}\begin{pmatrix} \rho u^2 \;+\; p \;-\; \nu\dfrac{\partial u}{\partial x} \\ \rho uv \;-\; \nu\dfrac{\partial v}{\partial x} \\ \rho uw \;-\; \nu\dfrac{\partial w}{\partial x} \end{pmatrix} + \frac{\partial}{\partial y}\begin{pmatrix} \rho vu \;-\; \nu\dfrac{\partial u}{\partial y} \\ \rho v^2 \;+\; p \;-\; \nu\dfrac{\partial v}{\partial y} \\ \rho vw \;-\; \nu\dfrac{\partial w}{\partial y} \end{pmatrix} + \frac{\partial}{\partial z}\begin{pmatrix} \rho wu \;-\; \nu\dfrac{\partial u}{\partial z} \\ \rho wv \;-\; \nu\dfrac{\partial v}{\partial z} \\ \rho w^2 \;+\; p \;-\; \nu\dfrac{\partial w}{\partial z} \;+\; \Phi \end{pmatrix} \tag{76}$$

where the gravitational potential $\Phi = \rho gz$. [33]

There is a lot of symmetry in the momentum equations, and they can be written in a much more compact (though abstruse) form by introducing a momentum flux tensors for the advection terms and gravity, added to the viscous stress and pressure stress tensors, $\mathbb{T}$ and $\mathbb{P}$ (Section 2.3). The momentum flux tensor

$$\mathbb{A} = \rho\begin{pmatrix} uu & uv & uw \\ vu & vv & vw \\ wu & wv & ww \end{pmatrix},$$

can be written as the direct vector product

$$\mathbb{A} \;=\; \mathbf{V}\mathbf{V}^t \tag{77}$$

within a fluid, unless balanced by some other (exotic) external force that exerts a torque. The inference is that for non-exotic fluids such as air and water, the stress tensor must be symmetric. To insure this, $\mathbb{S}$ is often evaluated in a form that enforces symmetry, $\mathbb{S} = 1/2\nu(\mathbb{G}+\mathbb{G}')$ so that $\mathbb{S}_{ij} = \mathbb{S}_{ji}$. The first form shown here in Eq. (71) isn't wrong, but it may be impractical for calculations.

[33] Most arbitrary quantities are *not* subject to a strict conservation law. For example, in a two particle collision, the kinetic energy will be conserved only in the special case that the collision is 'elastic', so that no energy is lost to deformation, acoustic waves, etc. On the other hand, if the particles stick together after the collision, then the kinetic energy will decrease by an amount that depends upon the particular conditions of mass and initial velocity. Thus the kinetic energy and higher moments of the velocity are not conserved in most collisions or during mixing events in a fluid. More often a conservation law will not obtain because of the presence some external source, e.g., gravity, that does not vanish with the fluid velocity and hence the global integral need not be conserved. In that case we should probably call the governing equation the momentum 'balance' or 'budget' rather than 'conservation ', though this distinction is often ignored.

where $\mathbf{V}$ is a 3x1 column vector and the transpose $\mathbf{V}^t$ is a 1x3 row vector; hence $\mathbb{A}$ is 3x3. The gravitational tensor is just

$$\mathbb{Y} = \rho g z \begin{pmatrix} 0 & 0 & 0 \\ 0 & 0 & 0 \\ 0 & 0 & 1 \end{pmatrix}$$

Define the total momentum flux tensor

$$\mathbb{M} = \mathbb{A} + \mathbb{P} - \mathbb{T} + \mathbb{Y}.$$

The tensor form of the Eulerian momentum balance is then

$$\text{momentum balance, conservation form:} \quad \boxed{\frac{\partial(\rho \mathbf{V})}{\partial t} + \nabla \cdot \mathbb{M} = 0} \tag{78}$$

where this ∇ is a three element row vector, $\nabla = (\frac{\partial}{\partial x}, \frac{\partial}{\partial y}, \frac{\partial}{\partial z})$. There is little gain in this for the pressure and gravitational terms. But having written the momentum balance equation in tensor form we now can assert two important properties: 1) The tensor equation (78) is valid in any (Cartesian) coordinate system, assuming that it is correct in one coordinate system, and 2) The components of the tensors transform under a rotation of the coordinate axes as

$$\mathbb{A}' = \mathbf{V}'(\mathbf{V}')^{\mathbf{t}} = \mathbb{R}\,\mathbb{A}\,\mathbb{R}^t, \tag{79}$$

where $\mathbb{R}$ is the rotation tensor.[34]

3.4.5 The flux form of the momentum equation; Reynolds number

Consider a very simple example; suppose that the aim is to account for the $x-$component of momentum within a control volume of $x-$length l, and width and height w and h, and suppose too that the y and z variations of the fluxes can be ignored (Fig. 12). The $x-$component of the total momentum flux is $\mathbb{M}_{(1,1)}$,

$$\mathbb{M}_{(1,1)} = \rho u^2 + p - \nu(\partial u/\partial x). \tag{80}$$

The integral momentum budget for this fixed control volume is then

$$\begin{aligned} lwh\frac{\partial \rho u}{\partial t} &= wh(\,\mathbb{M}_{(1,1)}(x=l) - \mathbb{M}_{(1,1)}(x=0)\,) \\ &= wh(-\rho u^2 - p + \nu\frac{\partial u}{\partial x})\,|_{x=l} - (-\rho u^2 - p + \nu\frac{\partial u}{\partial x})\,|_{x=0}). \end{aligned} \tag{81}$$

[34] We can readily infer this last result from the form of the momentum flux tensor, Eq. (77). If the velocity vector (components) transform under rotation of coordinate axes as $\mathbf{V}' = R\mathbf{V}$, and given that $(\mathbf{V}')^t = (R\mathbf{V})^t = \mathbf{V}^{\mathbf{t}}R^t$, then by substitution into the middle term of Eq. (79) and using the associative property of matrix multiplication we verify the transformation rule for Cartesian tensors. (A good review of tensor algebra is Ch. 2 of Kundu and Cohen (2001) noted in footnote 10.)

Dividing through by the volume, lwh, taking the limit that l becomes small, application of mass conservation (Eq. (60) and *voila*, out pops the differential form of the momentum balance,

$$\frac{\partial u}{\partial t} = -u\frac{\partial u}{\partial x} - \frac{1}{\rho}\frac{\partial p}{\partial x} + \frac{\nu}{\rho}\frac{\partial^2 u}{\partial x^2}. \tag{82}$$

The only slightly disagreeable part of this procedure is that the forcing terms were applied to points, a control volume, rather than to a material fluid volumes, but the RTT leads to the same thing.

The value of this derivation is that it may be most natural to make assertions about the physical properties of a flow at the first stage of this procedure, Eq. (80), where the flux is prescribed. Here we have included all three of the terms that might contribute to momentum flux, but often this is not necessary or appropriate. In most flows the pressure gradient is of leading importance, and the interesting question is likely to be how the advective and diffusive terms compare to one another. To make a rough estimate of these terms requires an estimate of the length scale, L, over which the current component varies by about 100%. That is, what value of L is appropriate to the relations,

$$\frac{\partial u}{\partial x} \text{ is } O(\frac{U}{L}) \quad \text{and} \quad \frac{\partial^2 u}{\partial x^2} \text{ is } O(\frac{U}{L^2}),$$

where the big O notation means the order of magnitude without regard to the sign. For example, if $u = A\,sin(kx)$, then $\partial u/\partial x = A\,k\,cos(kx)$ is $O(Ak)$ and so $U = A$ and $L = k^{-1} = \lambda/2\pi$. If the aim is a rough estimate, we might ignore the factor 2π and just say that L is $O(\lambda)$. Of course, when factors of 2π or 2 cascade, as they do for the second derivative, then this could eventually lead to trouble. But with that in mind, let's proceed to estimate the ratio of the advective term to the diffusive term as

$$\frac{\text{advection}}{\text{viscous drag}} = \frac{u\frac{\partial u}{\partial x}}{\nu\frac{\partial^2 u}{\partial x^2}} \text{ is } O(\frac{u^2/L}{\nu u/L^2}) = O(\frac{UL}{\nu}) = O(Re), \tag{83}$$

where Re is the important nondimensional,

Reynolds number: $$Re = \frac{\text{advection}}{\text{viscous drag}} = \frac{UL}{\nu}$$

The Reynolds number is liable to be important whenever viscosity is at issue. The most uncertain aspect of Re will often be the length scale, L. For the wave-like motion shown in the cover graphic, we can estimate that $U \approx 0.1$ m s^{-1}, and that $L \approx 100$ km, roughly. Using the known kinematic viscosity of water, $\nu = 10^{-4}$ m^2 s^{-1}, then $Re \approx 10^8$. No matter how crude the estimate of L, it is unmistakable that the viscous drag term is much, much, much smaller than the advection term in this instance. After making a few such estimates, you will be entirely justified in dropping (without even mentioning) the viscous, diffusive contribution to the momentum flux in the case that the momentum budget is evaluated for such large scale motions.

You might well wonder if the viscosity term is ever important. Yes, but the viscous term is of leading importance only for scales of motion that are very, very small compared to the basin scale of oceanic or

atmospheric motions. Recall the flow in a tea cup; the smallest scales of motion are vortices having $L = 0.005$ m, roughly, and a typical speed $U = 0.05$ m s^{-1}, and hence $Re \approx 1/2$. You may have noticed that these small scales of motion are damped rather quickly, within a few seconds. Can this be attributed to viscosity? The time scale required for diffusion to propagate a signal over a distance L is roughly $t_{diff} = L^2/\nu$, deduced from dimensional analysis or from a solution of the diffusion equation, while the rotation time for a vortical motion is $t_{adv} = L/U$. The ratio of these time scales is $t_{diff}/t_{adv} = Re$, once again the Reynolds number, and so yes, viscous diffusion of momentum is evidently sufficient to damp the smallest vortical motions in a few seconds, or the order of several vortex rotations. What we can go on to infer from this, and verify by observation, is that larger vortices last longer, all else equal.

3.4.6 Energy conservation; the First Law of Thermodynamics applied to a fluid

As a final application we will consider the balance of thermal energy in a compressible fluid. The First Law of Thermodynamics keeps track of several kinds of energy storage and energy exchange that may occur between a given fluid volume and the environment, schematically,

$$\frac{dE}{dt} \;=\; WorkRate \;+\; HeatSource \tag{84}$$

where $E \;=\; \rho C_v T$, is the internal energy, and C_v is the heat capacity of the fluid in an isovolume process, taken to be a known physical property of the fluid, and a constant for this purpose. *WorkRate* is the rate at which mechanical work is done by the environment on the fluid volume. In the case of an Euler fluid, this can be due only to the rate of work by pressure, $-P\mathbf{n}\cdot\mathbf{V}$, evaluated over the surface of the volume. *HeatSource* is the divergence of heat fluxes due to radiation, $-\nabla\cdot\mathbf{Q}$, and conduction, $-\kappa\nabla T$, where κ is the thermal conductivity of the fluid, and to a body source due to the dissipation of kinetic energy to internal energy, ε. In most cases ε is negligibly small compared to the heat fluxes or *WorkRate* and will be omitted from here on. Our final result will be appropriate for geophysical flows but not completely general. The approximate balance of thermal energy is then:

$$\frac{DE}{Dt} \;=\; C_v \frac{D}{Dt} \iiint\limits_{material} \rho T \; dVol \;=\; -\oint P\mathbf{n}\cdot\mathbf{V}\; da \;-\; \oint \kappa\nabla T\cdot\mathbf{n}\; da \;+\; \iiint\limits_{material} -\nabla\cdot\mathbf{Q}\; dVol. \tag{85}$$

Applying the divergence theorem to the surface integrals and the RTT and then collecting terms under the volume integral yields the differential form of the thermal energy balance in field coordinates:

$$\rho C_v \frac{DT}{Dt} \;=\; -P\nabla\cdot\mathbf{V} \;+\; \kappa\nabla^2 T \;-\; \nabla\cdot\mathbf{Q}. \tag{86}$$

To simplify this a little further, the fluid will be presumed to be an ideal gas described the equation of state $P = \rho RT$, where $R = C_p - C_v$ is the universal gas constant and C_p is the heat capacity at constant pressure (Table 1). The divergence of fluid velocity may be eliminated by use of the mass conservation equation (43) and then the equation of state,

$$-P\nabla\cdot\mathbf{V} \;=\; -\frac{P}{\rho}\frac{D\rho}{Dt} \;=\; \frac{P}{\rho}\frac{\partial\rho}{\partial T}\Big|_P \frac{DT}{Dt} \;=\; -\frac{P}{\rho}\frac{P}{RT^2}\frac{DT}{Dt} \;=\; -\rho R\frac{DT}{Dt}.$$

When this is substituted into Eq. (86) the result is the

$$\text{first law of thermodynamics for an ideal gas:} \quad \boxed{\rho C_p \frac{DT}{Dt} \;=\; \kappa \nabla^2 T \;-\nabla\cdot\mathbf{Q}} \tag{87}$$

where notice the heat capacity is now C_p in place of C_v, which is significant for a gas. For many liquids and solids the distinction between C_p and C_v is not large.

3.4.7 Vorticity balance

The curl of the three-dimensional velocity gives the

$$\text{three-dimensional vorticity:} \quad \boxed{\xi \;=\; \nabla\times\mathbf{V}} \tag{88}$$

The curl of the momentum equation gives the corresponding

$$\text{three-dimensional vorticity balance:} \quad \boxed{\frac{D\xi}{Dt} \;=\; (\xi\cdot\nabla)\mathbf{V} \;-\; (\nabla\cdot\mathbf{V})\xi \;+\; \frac{\nabla\rho\times\nabla P}{\rho^2} \;+\; \nu\nabla^2\xi} \tag{89}$$

This requires rearranging terms only, with no new approximations or additions, and hence this is not a new equation independent of the momentum balance. It takes some experience to appreciate that vorticity balance can be a very useful guide to the evolution of an important subset of the flows governed by the momentum balance. Vorticity is present in some but not all of the phenomonenon contained within the former. Specifically, the curl operator gives zero when operating on any vector that is derivable from a scalar potential, and most importantly the pressure gradient, ∇P, and thus

$$\nabla\times\nabla P \;=\; 0.$$

The curl operator thus eliminates the often very signifcant effects of a pressure gradient (though with an important exception noted below) and also of gravity. Fluid flows that are due mainly to these two important forces, e.g., gravity waves, are thus invisible to (filtered out of) the vorticity equation, while most ocean currents and winds (and many, many other phenomenon) go through unscathed.

The terms of the vorticity equation are

$(\xi\cdot\nabla)\mathbf{V}$, which represents the tipping (or turning) and stretching of the vorticity vector that arises when there is velocity shear in the direction of the vorticity vector. This is a mechanism for turning horizontal vorticity into the vertical (as occurs in tornadogenesis) and important for distributing vorticity within small-scale, three-dimensional flows. Not considered further here.

$-(\nabla\cdot\mathbf{V})\xi$, which accounts for the amplifiction of vorticity when the fluid is stretched or compressed. This is very important in the vorticity balance of the oceanic flow of Fig. 1, and discussed further in Sec. 4.

$(\nabla\rho\times\nabla P)/\rho^2$, is the vorticity expression for flows that are generated by density differences, e.g., a

diurnal sea breeze circulation. This is sometimes caled a solenoial term, after the crossing isolines of density and pressure that are present when this term is nonzero. Not pursued here.

$\nu\nabla^2\xi$ is the diffusion of vorticity that follows directly from the assumption of Newtonian diffusion of momentum. To this approximation, vorticity diffuses through a fluid just like heat (temperature differences). In Part 2 we will see a model of vorticity diffusion that accounts for the evolution of the irrotational vortices generated in the tea cup experiment.

Notice that the first, second, and fourth terms are proportional to vorticity. They represent processes that can change vorticity, but can not generate vorticity from an irrotational flow (boundary conditions aside). That is not the case with the solenoidal term.

3.5 Remarks on the Eulerian equations

The momentum equations (75) have two terms that are characteristic of fluid flows, the pressure gradient term and the advection terms. Pressure is a scalar, and the gradient of the pressure appears in each of the component equations. A localized pressure perturbation in a three-dimensional flow is thus likely to induce motion in all three components. The pressure gradient thus acts to couple the component equations, and is generally the physical process that allows for (or enforces) mass conservation; as fluid converges into a given volume the pressure will rise and so produce a compensating pressure-driven divergence, e.g., acoustic and gravity waves if high or low frequency. The pressure gradient term is linear, and does not, in and of itself, present any special mathematical difficulty.

Advection endows many fluid flows with rich spatial structure and complexity, and advection is the process that most distinguishes a fluid flow from solid mechanics. The advection terms are nonlinear, in general, and hence the advective terms stymie most of the familiar PDE solution techniques that require superposition of solutions. There are many cases in which the advection terms are demonstrably much, much smaller than the pressure gradient term, and so they may be omitted to leave a linear momentum balance equation. A linearized system of that sort omits some of the distinctive character of fluid flow but may nevertheless be entirely appropriate for the analysis of small amplitude, wave-like motions, especially.

The (Eulerian) momentum, mass and energy equations are impressive, and it might seem that writing them out in full would be a significant step towards the solution of a fluid mechanics problem. Well, yes and no. An understanding of the origin and the meaning of these equations is a vital first step toward understanding fluid mechanics. But it is essential to appreciate that these equations are extremely general, and their content is as their name implies — that momentum, mass and energy are conserved consistent with classical physics. And here's the punch line, there is *nothing more implied than that*. Momentum conservation may occur by virtue of wave motions or swirling vortices or seemingly random turbulence. It is not unusual that a flow (even in a tea cup) may include all three phenomena at once.

3.6 Key ideas

1) The vast majority of theory and modelling of fluid mechanics is carried out within an Eulerian framework.

2) The independent variables of an Eulerian model are fixed spatial coordinates (field coordinates) and time. The dependent variables are the fluid velocity, pressure, density, etc. defined on the fixed coordinates.

3) The central elements of an Eulerian model or theory include the Eulerian velocity, the material time rate of change operator, and the conservation laws. These are derivable from a Lagrangian origin via the FPK, the material time derivative holding parcel identity fixed, and the Reynolds Transport Theorem.

4) The material time derivative includes an advection term, the dot product of the fluid velocity and a tracer gradient, that represents the effects of fluid flow in an Eulerian conservation equation. In general, the velocity and the tracer gradient are unknowns, which makes the advection term nonlinear (more precisely, bilinear).

5) The advection term may be written in flux form by combining with the mass conservation relation. This helps make clear that for most purposes it is the divergence of the flux that is the relevant quantity, rather than the flux itself.

6) An Eulerian solution for density, say, comes in one complete piece, $\rho(x,t)$, that includes the effects of stretching and advection (ideal fluid). This may be compared with the Lagrangian solution that comes in two pieces, the density itself which includes the effects of stretching, and the trajectory.

7) The normal and tangential stresses on a fluid parcel in R^3 may be written as a 3x3 tensor. The diagonal elements include an isotropic pressure, and the off-diagonal elements are tangential stresses, e.g., viscous stress.

8) Many fluids, including air and water, are Newtonian in the sense that viscous stress in laminar flows is found to be approximately proportional to the velocity shear times the fluid viscosity, a thermodynamic property of the fluid.

9) Turbulent flow is far more common than is laminar flow. Under controlled circumstances (e.g., unperturbed, smooth boundary) the transition from laminar to turbulent flow for a given geometry may occur at a critical Reynolds number. In a turbulent flow, the stress depends upon flow properties other than just the local shear.

3.7 Problems

1) Here's another simple Lagrangian solution $\tilde{x} = a(e^t + 1)$ with a a constant. Compute and interpret the Lagrangian velocity $\tilde{(u)}(a,t)$ and the Eulerian velocity field $u(x,t)$. Suppose that two parcels have initial positions $a = 2a$ and $2a(1+\delta)$ with $\delta \ll 1$; how will the distance between these parcels change with

time? How is the rate of change of this distance related to $u(x,t)$? (Hint: consider the divergence of the velocity field, $\partial u/\partial x$.) Suppose the trajectories are instead $\tilde{x} = a(e^t - 1)$.

2) A couple of questions for you. (1) Can you show that the material derivative of parcel position is just the velocity? In this respect, the material derivative could also be said to be more fundamental than is the FPK. (2) Suppose a one-dimensional domain as above, and a fluid variable that has an initial, Lagrangian distribution $b = ca$, with trajectories $\tilde{x} = a + Vt$, and V a constant. Given that b is conserved in every material volume, find the equivalent material derivative in the Eulerian system. Interpret the local rate of change of b. (3) Suppose instead that $Db/Dt = a$, with a a constant; how does $b(x,t)$ evolve?

3) The Eulerian conservation equation for mass in an ideal fluid flow includes an advection term and a divergence term, Eqs. (44). Assume that the flow includes a spatially-uniform component, U_o. Compare the effects of this U_o within the advection process, (50) and the divergence process (51). The solutions of Fig. (8) were evaluated assuming $U_o = 0$. How would the solutions change if instead $U_o = 0.2$, say.

4) You should fill in the steps leading up to Eq. (59) to verify that this is true whenever the extensive property, say H, is the volume integral of ρh, where ρ is mass density and h is the corresponding intensive property.

5) After deriving the vector form of the pressure gradient force per unit volume we went back and derived the z-component of the pressure force without the use of vector or tensor notation. You should do the same for the viscous force per unit volume in the case shown in Fig. 22, a flow in the x-direction only, and with shear in the z-direction only. Find the viscous force on the upper and lower faces of a parcel, then the sum, and allow the dimensions to shrink to infinitesimal. Locate the resulting term in the full 3-dimensional equation, (74). Suppose that the flow has reached a steady state, as in Fig. 22. What is the profile of viscous stress throughout the fluid? Now imagine that the stress has just been imposed at the surface and the flow is developing. Qualitatively, what is the stress profile in this transient case? The lower boundary condition in Fig. (22) is presumed to be no-slip, so that $u(z = 0) = 0$, which is appropriate for real fluids having a finite viscosity. What is the equivalent boundary condition for a heat diffusion problem? What are the corresponding, plausible surface boundary conditions?

4 An advection problem, two ways

This section will develop the Lagrangian and Eulerian perspectives on an elementary advection problem. To keep the focus on the concepts and methods, this problem will be kept simple: a passive tracer, c, in a prescribed, ideal fluid flow in R^1, with space and time field coordinates (x,t). There will be no diffusion, and to start, no source for the tracer, and so the tracer dynamics will be termed adiabatic. There will be no requirement for mass or volume conservation, and no pressure gradient, and hence the fluid parcels of this model do not interact with one another as they do in a real fluid flow. With these restrictive assumptions in place, the governing equation for the tracer c is

$$\frac{Dc}{Dt} = 0, \tag{90}$$

where D/Dt is the material derivative, and could be evaluated in Lagrangian or Eulerian coordinates. For the first version of this problem, take the current to be

$$U = constant, \tag{91}$$

a steady, uniform translation toward positive x. The initial condition data (IC) will be given at $t = 0$ along the x axis,

$$c(x, t = 0) \;=\; \exp(-x^2/2), \tag{92}$$

a Gaussian hump with amplitude and width of 1. The set of three equations (90) - (92) define an advection/initial value problem for the tracer c in which advection is the only active process.

4.1 The Lagrangian solution

The Lagrangian version of this problem is very straightforward. The tracer in material coordinates is $\tilde{c}(a,t)$, with a the initial position, and Eqs. (90) and (92) are

$$\frac{D\tilde{c}(a,t)}{Dt} \;=\; \frac{\partial \tilde{c}(a,t)}{\partial t} \;=\; 0, \quad \text{with an IC} \quad \tilde{c}(a, t = 0) \;=\; \exp(-a^2/2). \tag{93}$$

The governing equation states that $\tilde{c}$ does not depend upon time, and so

$$\tilde{c}(a,t) \;=\; \tilde{c}(a),$$

and given the IC (93), the Lagrangian solution for tracer concentration is just

$$\tilde{c}(a) \;=\; \exp(-a^2/2). \tag{94}$$

Each parcel (each a) has a tracer value assigned at the beginning, $t = 0$, and then keeps that value for all time, no matter how fast or how far it travels.

To make any use of this requires knowing also the parcel positions. Because the velocity U is spatially uniform, U may be treated as a Lagrangian velocity, and so from (91),

$$\frac{\partial \tilde{x}(a,t)}{\partial t} \;= U \quad \text{with IC} \quad \tilde{x}(a, t = 0) \;=\; a,$$

and hence

$$\tilde{x}(a,t) \;=\; a \;+\; Ut. \tag{95}$$

Eqs. (94) and (95) define the tracer concentration and the parcel positions, and thus make a complete Lagrangian solution. This solution may be readily interpreted in field coordinates, (Fig. 14) when the tracer concentration is envisioned to be a third (vertical) coordinate. The solution (Fig. 14) shows that the Gaussian hump in tracer concentration is translated to the right at the steady speed U, and without change in amplitude or width.

Toward the end of Sec. 2.4, a (soft) conclusion was that the Lagrangian momentum equations are

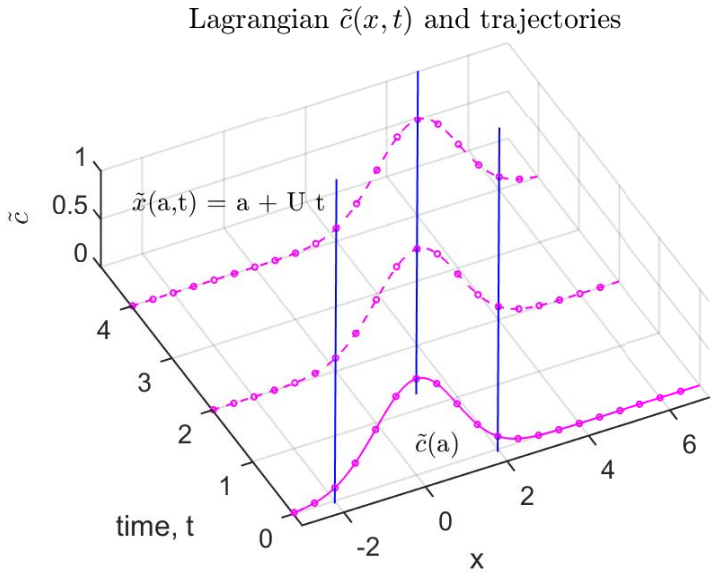

Figure 14: An Eulerian (field coordinate) interpretation of the Lagrangian solution Eqs. (94) and (95) of a tracer, $\tilde{c}(x,t)$, in a uniform flow $U = 1$ that translates fluid parcels toward positive x. The magenta dots are parcels at discrete values of a. The vertical coordinate represents the tracer concentration, which has no geometric significance. The blue lines are parcel trajectories, $\tilde{x}(a,t)$, evaluated at several discrete a, and which have a uniform slope $dt/dx = 1/U$. According to the governing equation, (93), the tracer value on parcels, $\tilde{c}(a)$, is constant in time as parcels move along their respective trajectories, $\tilde{x}(a,t)$.

often difficult to apply. This Lagrangian tracer solution might seem to contradict that conclusion, but notice that the current was here prescribed, and not computed from a momentum equation that would usually include a pressure gradient and diffusion. In this somewhat exceptional circumstance, the Lagrangian system is advantageous.

4.2 The Eulerian solution via the method of characteristics

In an Eulerian system, the tracer distribution is defined on a field, $c(x,t)$, with x and t the usual space and time coordinates. The governing equation corresponding to (90) is then

$$\frac{D\,c(x,t)}{Dt} \;=\; \frac{\partial c}{\partial t} + U\frac{\partial c}{\partial x} \;=\; 0. \tag{96}$$

This PDE is linear in the first partial derivatives (there is no occurrence of nonlinear terms such as $(\partial c/\partial x)^2$, or of $(\partial c/\partial x)(\partial c/\partial y)$), it has constant coefficients (the uniform velocity, U), and it is homogeneous (each term contains c or a derivative of c). An appropriate initial condition is

$$c(x,\, t=0) \;=\; exp(-x^2/2). \tag{97}$$

The solution of a first order PDE like (96) can be sought via the method of characteristics (MoC). The MoC seeks an Eulerian solution by taking account of the (in some ways) simpler tracer balance of a Lagrangian perspective. The concepts developed within the MoC are thus highly germane to the present discussion of Lagrangian/Eulerian methods, and they are frequently referenced in many fields of applied mathematics.

The basis of the MoC is a geometric interpretation of first order PDEs like (96). A generalized gradient

vector of the field $c(x,t)$ is

$$\nabla c \;=\; (\frac{\partial c}{\partial x},\; \frac{\partial c}{\partial t}). \tag{98}$$

The directional derivative of $c(x,t)$ in the direction of a vector $\Lambda \;=\; (\lambda_1,\; \lambda_2)$ (usually normalized) is just the vector product of Λ and this ∇c,

$$\Lambda \cdot \nabla c \;=\; \lambda_1 \frac{\partial c}{\partial x} \;+\; \lambda_2 \frac{\partial c}{\partial t}. \tag{99}$$

If it is given that

$$\Lambda \cdot \nabla c \;=\; 0, \tag{100}$$

then it may be inferred that Λ is perpendicular to the gradient of c, or just as well, that Λ is parallel to curves of constant c. Comparing (99) with (96) and identifying the components of the vector Λ with the coefficients of the PDE, in this case $\lambda_1 \;\propto\; U$ and $\lambda_2 \;\propto\; 1$, it is evident that c is constant along curves that are parallel to the vector field $(U,1)$. This is a key result, and the basis of the MoC. These curves are said to be the 'characteristic' curves of the PDE (96). In the case of an advection equation like (96), the coefficients are the velocity components, and the characteristic curves are parcel trajectories. However, the notion of characteristic curves is not dependent upon this interpretation, and the MoC applies to many first order PDE.

The MoC can be envisaged in three steps.

Step 1, calculate the family of characteristics curves that are parallel to the coefficient vector, here just $(U,\; 1)$. One way to do this, though it may seem a little indirect on first sight, is to seek a parametric form of the characteristic curves, $(x_\gamma(s),\; t_\gamma(s))$, where s is the parameter that will trace out the curve. (If the notion of a parameterized curve is unfamiliar, then you should take a quick detour to Problem 1) that starts with a refresher.) The important thing to note is the relationship between $x_\gamma(s)$ and $y_\gamma(s)$, and that s is the common link between them. The tangent vector to a parameterized curve is just

$$\Gamma \;=\; (\frac{dx_\gamma}{ds},\; \frac{dt_\gamma}{ds}),$$

and the condition that makes this tangent vector parallel to the coefficient vector $(U,\; 1)$ is that

$$\frac{dx_\gamma}{ds} \;=\; U, \quad \text{and,} \quad \frac{dt_\gamma}{ds} \;=\; 1. \tag{101}$$

The two ordinary differential equations (101) thus serve to define the family of characteristic curves of Eq. (96). Appropriate ICs are

$$x_\gamma \;=\; x_o \quad \text{when} \;\; s \;=\; 0, \;\; \text{and} \;\; t_\gamma \;=\; 0 \quad \text{when} \;\; s \;=\; 0. \tag{102}$$

These ordinary differential equations (ODEs) can be readily integrated to yield

$$x_\gamma \;=\; x_o \;+\; Us, \quad \text{and,} \quad t_\gamma \;=\; s. \tag{103}$$

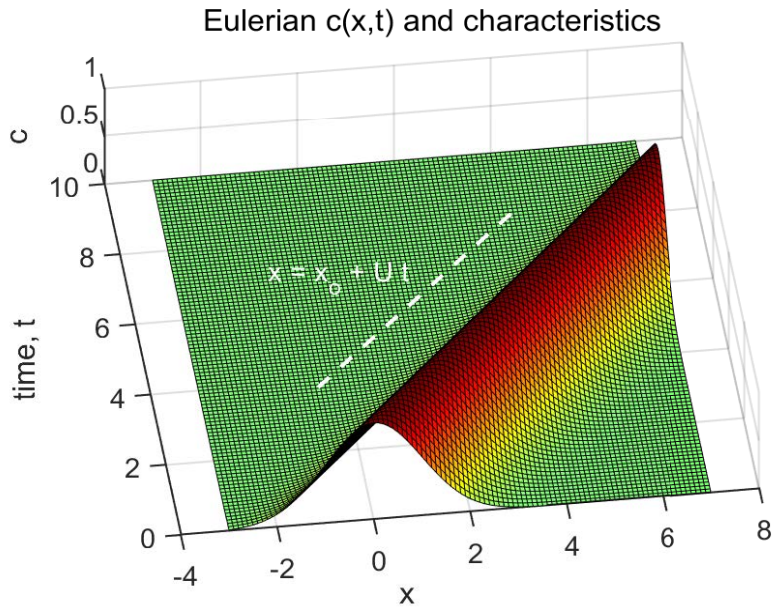

Figure 15: The Eulerian representation of a tracer field, $c(x,t)$, that is embedded in a uniform flow $U = 1$ that translates c to the right. The dashed white line $x = x_o + Ut$ is one characteristic curve of the flow; all other characteristics (different x_o) are parallel. Notice that $c(x,t)$ is constant in the direction parallel to a characteristic curve.

Eliminating s from (103) gives

$$x_\gamma = x_o + Ut_\gamma. \tag{104}$$

The family of characteristic curves along which $c =$ constant in this problem is given parametrically by Eqs. (103), or explicitly by Eq. (104). In the special case of a uniform velocity, U, considered here, the characteristics curves are straight lines having slope $dt_\gamma/dx_\gamma = 1/U$ (the slope is $\propto 1/U$ because the ordinate is time rather than x). The characteristic curves will not be parallel in the much more common circumstance that the current varies in space, Sec. 4.4. Notice that these characteristics are the same as the trajectories of the fluid parcels in the Lagrangian solution, cf. Fig. (15). The MoC follows from the expectation that the tracer balance will be simplest when sought along these characteristic curves. Indeed, in this adiabatic problem, the tracer values are simply advected (propagated or transported) along the characteristics without change.

Step 2, apply the boundary/initial data at some point along each of the characteristic curves: if we know the tracer at any point on a characteristic, then we know it at all points on that characteristic. Here that information is given by initial data, Eq. (97), that specifies $c(x,\ t = 0)$. Eliminate x_o from (92) using Eqs. (104) to find the explicit solution,

$$c(x,t) \ = \ \exp\left(-(x-Ut)^2/2\right). \tag{105}$$

Since the tracer balance was presumed to be adiabatic, the Gaussian distribution of $c(x,t)$ that was prescribed in the IC is shifted steadily to the right at the rate U, and with no change in amplitude or width of the initial hump, Fig. (15). This is equivalent to the Lagrangian solution of Sec. 4.1, as it should be.

Step 3 is to account for a source, postponed to a later example in Sec. 4.4.1.

4.3 Comments on these Lagrangian and Eulerian solutions

As emphasized on several occasions, Lagrangian and Eulerian solutions are quite different conceptually, even when they describe the same 'flow'. The Eulerian solution for the tracer is complete in one piece, Eq. (105). The Eulerian solution contains within it the effects of the fluid motion, the advection process, which is all that happens in the present problem. Compare this with the Lagrangian solution that comes in two pieces: the tracer value on moving parcels Eq. (94), and the position of those parcels, Eq. (95). The latter is the fluid motion. This two-part Lagrangian approach simplifies the tracer equation, but, you have to know the trajectories.

As we worked through the two solutions above, the intent was to be consistent within the Lagrangian system while in Sec. 4.1 — all about parcels with no fields — or the Eulerian system in Sec. 4.2 — all about fields but no parcels. When it is time to interpret or display a solution, there is no bar to mixing concepts; we can say c is constant along characteristics in an ideal fluid flow, or, equivalently, parcels conserve their tracer value as they move along trajectories in adiabatic flow. And, we can usually interpret a Lagrangian solution in field coordinates, as in Fig. (14). However, it is good practice to be conscious of mixing Lagrangian and Eulerian concepts when working toward a solution.

If you have been comparing these two solutions methods, then you are probably thinking that the MoC is somewhat abstract (formal and mathematical as opposed to physical reasoning), and more trouble than it was worth. In the present elementary problem, probably so. However there are some important phenomena that are best treated or interpreted via the MoC, an example being shock waves in Sec. 4.4.2. And, the notion of characteristics comes up fairly often in applied mathematics. You may also be harboring some doubt that the elementary advection problem examined to here could have anything to do with a genuine fluid mechanics problem; there was no reference to mass and momentum conservation, there was no accounting for a pressure gradient, and the fluid velocity was simply prescribed. True again, but there is more practical value in this very idealized problem than may be apparent on first sight. In every numerical integration that solves complex fluid systems, there comes the crucial task of advecting the fluid property fields, momentum, density, tracers, etc., with a velocity field that will be known. That very important piece of the numerical integration process — advection *per se* — is what we have considered in the problems above, and the ideas developed here will be put to good, practical use in Part 2, Sec. 4.

4.4 More advanced problems via the method of characteristics

The MoC can give useful insight into a variety of interesting phenomenon, including flows in higher dimensions and in cases with external forcing. The method is applicable to model equations that are first order and linear in the partial derivatives, e.g.,

$$\frac{\partial c}{\partial t} + u(c,x,y)\frac{\partial c}{\partial x} + v(c,x,y)\frac{\partial c}{\partial y} = Q(c,x,y), \tag{106}$$

but that may contain non-constant and nonlinear coefficients as well as a source or sink, Q.[35] Notice that the coefficients of the first order terms in (106) are here said to be u and v, as if velocity components in an advection equation, however that is not necessary. The governing equation (106) can be reduced to a set of ODEs beginning with the characteristics, which are just as seen in Sec. 4.2, one per independent variable,

$$\frac{dt_\gamma}{ds} = 1, \qquad \frac{dx_\gamma}{ds} = u(c,x,y), \quad \text{and} \quad \frac{dy_\gamma}{ds} = v(c,x,y), \tag{107}$$

and when a source is present, one additional ODE

$$\frac{dc}{ds} = Q(c,x,y), \tag{108}$$

that is discussed next. The solution of the characteristic equations (107) may not be trivial as they were in Sec. 4.2 where the current was uniform.[36]

4.4.1 With a source

To see the effect of a source (or if negative, a sink), Q, consider the one-dimensional version of Eq. (106) with IC as in Sec. 4.2, and now with an external source that causes a linear decay, say

$$\frac{Dc}{Dt} = Q = -\alpha c \tag{109}$$

where α is a positive constant. This non-adiabatic model could represent heat transfer from the fluid to the environment when the temperature difference is proportional to c, i.e., c is a temperature anomaly with respect to an infinite sink. In that case, c should relax back to the environmental temperature at long times, $t >> \alpha^{-1}$.

Step 3 is to evaluate the effect of the source. Consider that x and t are functions of s and so $c(x(s),t(s)) = c(s)$ is a composite function of the inner independent variable, s. The total derivative of c with respect to s is, by the chain rule,

$$\frac{dc}{ds} = \frac{\partial c}{\partial x}\frac{dx}{ds} + \frac{\partial c}{\partial t}\frac{dt}{ds}. \tag{110}$$

[35] There is no pressure gradient! As a consequence, fluid parcels can pile up, one on top of another, with no consequences (although a shock may form, Sec. 4.4.3). This is very different from the dynamics of what in Sec. 1.1 was dubbed 'ordinary fluids', water and air, which would develop a localized, high pressure anomaly that would sooner or later inhibit the further pile up of fluid. How fast this pressure anomaly develops and how fast the flow responds determines the speed of gravity waves and acoustic waves supported by the fluid. Is there any real fluid system that might be treatable by the very reduced dynamics (essentially advection only) considered in this discusion of the method of characteristics? The very high speed flow of a dilute gas as occurs in a rocket nozzle.

[36] The limitation to first order PDEs may seem severe, but first order equations are very common and important in physics and engineering, well beyond the (extensive) realm of fluid mechanics. Many kinds of second order wave equations can be factored into a pair of first order PDEs and then treated by the MoC (but not here). Where the MoC comes up wanting is cases when the governing equation has both first and second order partial differentials, as occurs when diffusion is acknowledged. Such parabolic systems do not entail a well-defined propagation speed, rather the entire domain is affected instantaneously by the diffusion process, and so not described well by characteristics.

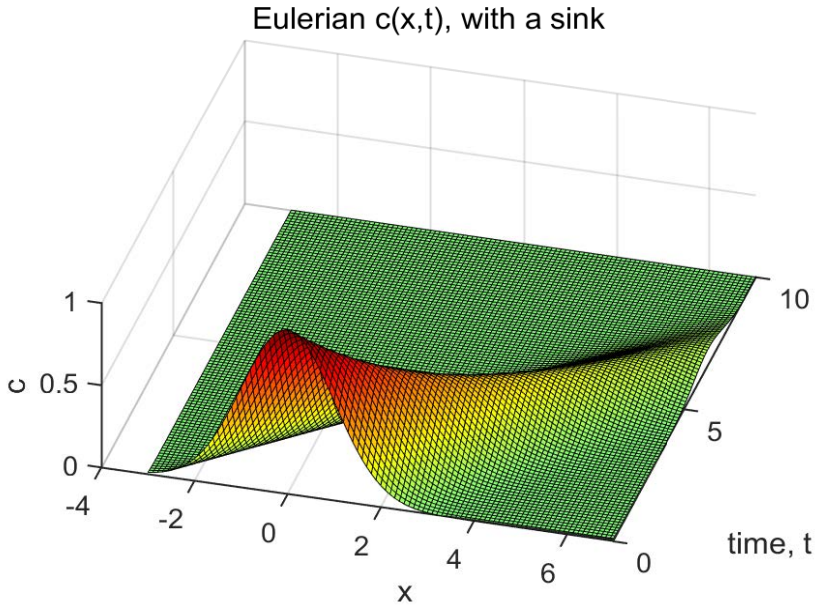

Figure 16: The Eulerian representation of a tracer field, $c(x,t)$, in a uniform flow $U = 1$ that has characteristics that are straight lines with slope $1/U$ as in the previous figure. There is a sink $Q = -\alpha c$ that causes an exponential decay of the tracer along the charactersitics curves. Here the coefficient $\alpha = 1/3$.

If $dx/ds = U$, and $dt/ds = 1$, then (110) is the directional derivative of c in the direction of the characteristic curves. In the previous, adaiabtic problem (Sec. 4.2) the tracer was constant along characteristic cuves. In this case, c is not constant, but instead decreases because of the sink, Q. Rewriting (110) using (109) gives

$$\frac{dc}{ds} = -\alpha c, \tag{111}$$

for which a suitable IC is $c(s = 0) = \exp(-x_o^2/2)$. This may be readily integrated to find c along the characteristics,

$$c(s) = \exp(-\alpha s)\exp(-x_o^2/2).$$

The characteristics are unchanged, since c is a passive tracer that has no effect on the velocity. Combining this with the previous, adiabatic solution (105), noting that $s = t$, and eliminating x_o yields

$$c(x,t) = \exp(-\alpha t)\exp(-(x-Ut)^2/2).$$

Thus the tracer concentration decreases exponentially in time along the characteristics on account of the sink (Fig. 16).

The MoC made this solution process seem easy since it broke up the PDE into two ODEs, one describing the effects of advection, which propagates c along characteristic curves without change, and the second describing the effects of the sink, Q, which in this case causes an exponential decrease in time along a characteristic. It is no accident that this looks and feels a lot like the Lagrangian perspective and solution of Sec. 4.1, however, the MoC does not rely upon the transport process being the motion of fluid parcels.

4.4.2 Variable coefficient and non-conservation

The two problems considered above could have been solved without invoking the MoC since they have a clear and simple physical interpretation. Now consider an equally simple problem where a physical interpretation is not so obvious. Suppose the governing equation is

$$\frac{\partial c}{\partial t} + x\,\frac{\partial c}{\partial x} = 0, \tag{112}$$

which is linear, but with a variable coefficient, x. The IC is presumed to be

$$c(x, t=0) = f(x_o), \tag{113}$$

where the function f can be left unspecified. The characteristic equations of (112) are

$$\frac{dt_\gamma}{ds} = 1, \quad \text{and} \quad \frac{dx_\gamma}{ds} = x. \tag{114}$$

Assuming IC

$$t_\gamma(s=0) = 0 \quad \text{and} \quad x_\gamma(s=0) = x_o,$$

then the characteristic curves are

$$t_\gamma = s, \quad \text{and} \quad x_\gamma = x_o \exp(s) = x_o \exp(t_\gamma). \tag{115}$$

These characteristics make a fan shape centered on $x = 0$ that widens exponentially with time. The solution comes from eliminating x_o between (113) and (114), to find

$$c(x,\, t) = f(x \exp(t)), \tag{116}$$

which you should check by substitution into the governing equation (112).

If the initial tracer distribution is a Gaussian, then

$$c(x,\, t) = \exp(-(x \exp(t))^2/2), \tag{117}$$

which is not so easy to intuit. However, if the fan-shaped characteristics of Fig. (17), left, made sense, and if you can imagine propagating $c(x_o) = \exp(-x_o^2/2)$ along those characterstics, then it is pretty clear that the eolsution will be (117) and Fig. (17), right. This is an example, and there are many others, wherein the characteristics of the MoC are a very effective aid to visualizing (intuiting) a solution.

A surprising property of this solution is that the amount of tracer increases exponentially in time, evident in Fig. (18). To understand how this happens, it is helpful to rewrite (112) in conservation form,

$$\frac{\partial c}{\partial t} + \frac{\partial(\text{flux of c})}{\partial x} = 0,$$

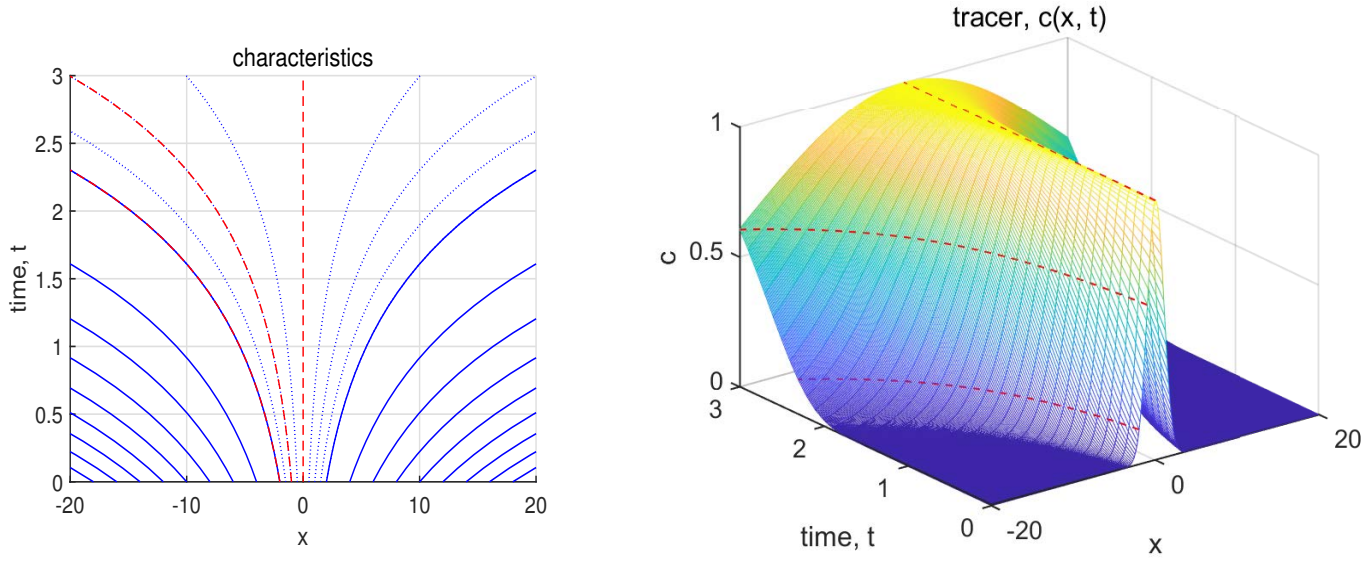

Figure 17: **(left)** Characteristic curves of the governing equation (112). The red dashed curves are for $x_o = 0, -1, -2$. **(right)**. The tracer $c(x,t)$ from (112) and (113) asuming that $f(x_o) = exp(-x_o^2/2)$. The tracer is constant along the characteristics at left, including the three red, dashed lines which correspond to those at left. Notice that the area under the curve $c(x)$ increases with time, and thus the total amount of tracer is not conserved.

as far as possible. Consider that

$$\frac{\partial(xc)}{\partial x} = c + x\frac{\partial c}{\partial x},$$

and so if c is added to both sides of the governing equation (112) and then

$$\frac{\partial c}{\partial t} + \frac{\partial(xc)}{\partial x} = c. \tag{118}$$

The lefthand side is in conservation form, but now there is a source term c on the righthand side. It might not have been obvious looking at the original PDE (112), but from its equivalent (118), it is apparent that the net amount of tracer should increase with time, as indeed it does. Moreover, the rate of increase is proportional to c, i.e., exponential.

4.4.3 When the current is advected

Now consider a problem in which the tracer is the current u,

$$\frac{Du}{Dt} = \frac{\partial u}{\partial t} + u\frac{\partial u}{\partial x} = 0. \tag{119}$$

The initial condition is presumed to be a Gaussian hump,

$$u(x, t = 0) = U\exp(-x_o^2/2), \tag{120}$$

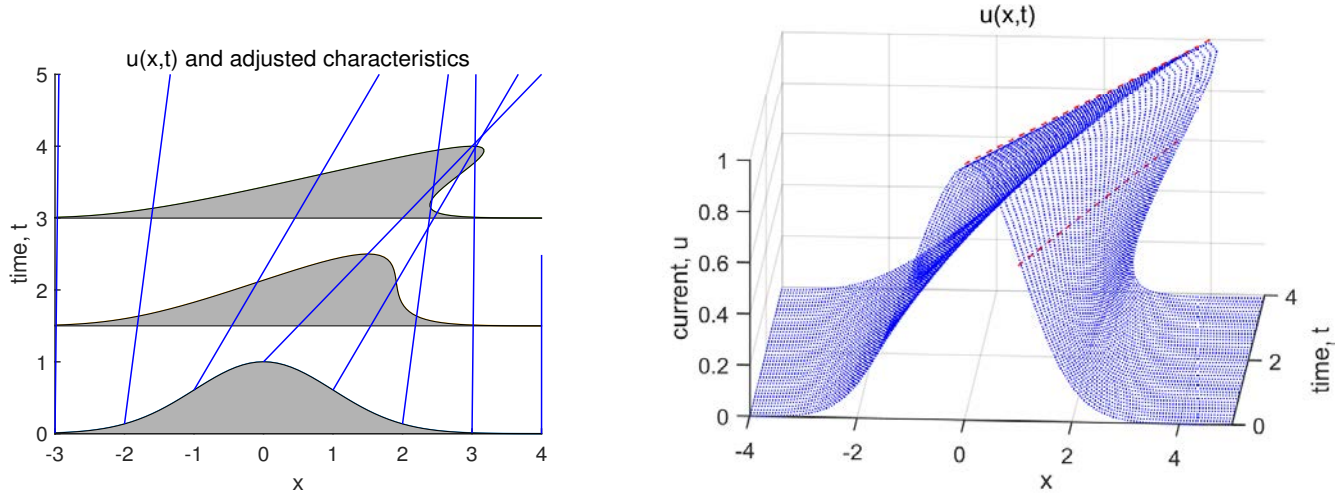

Figure 18: **(left)** The characteristics of the flow governed by Eqs. (119) and (120). Because the initial current profile varies with x (a Gaussian) the characteristics do not have a uniform slope. **(right)**. The current profile, $u(x,t)$ as a surface in three-dimensions. The Gaussian hump propagates to the right, and the peak of u moves the fastest. Consequently the slope on the rightward side of the peak increases until $t = \exp(1/2) \approx 1.7$ when this $u(x,t)$ becomes multivalued, which is unphysical. The elementary MoC solution (122) no longer applies, and the subsequent evolution has to account for the formation of a shock across which the current may be discontinuous but still momentum-conserving.

with U the amplitude (not the uniform value, as in Sec. 4.2). This governing equation may be rewritten in a conservation form

$$\frac{Du}{Dt} = \frac{\partial u}{\partial t} + \frac{\partial u^2/2}{\partial x} = 0.$$

The governing equation (119), often called the inviscid Burgers equation, is not linear because the advection term is the product of two unknowns, u and $\partial u/\partial x$, and so the wide array of methods that are available to solve linear PDEs will not be applicable. This governing equation is linear in its first order, partial derivatives, however, and well-suited for treatment via the MoC.

The current u is constant along characteristics,

$$\frac{du}{ds} = \frac{\partial u}{\partial t}\frac{dt}{ds} + \frac{\partial u}{\partial x}\frac{dx}{ds} = 0$$

that are the solutions of

$$\frac{dt_\gamma}{ds} = 1, \quad \text{and} \quad \frac{dx_\gamma}{ds} = u(x_o).$$

The characteristics are then

$$t_\gamma = s, \quad \text{and} \quad x_\gamma = x_o + U exp(-x_o^2/2)\, s,$$

with an explicit solution (eliminate s)

$$x_\gamma = x_o + U exp(-x_o^2/2)\, t_\gamma. \tag{121}$$

These characteristics are straight lines, Fig. (18), left, since the speed u is constant along characteristics. But a significant difference from the elementary problem of Sec. 4.2 is that the slope of the characteristics will vary with x_o. Far from the origin, the characteristic lines are nearly vertical in the x,t plane, while close to the origin the characteristics have a minimum slope and thus a maximum dx/dt and u.

The solution may be found by eliminating x_o from (120) and (121),

$$u(x,t) \;=\; U\exp\left(-(x-u(x,t)t)^2/2\right), \tag{122}$$

which is not separable into an explicit solution (u isolated on one side of the equation). This is typical of quasi-linear problems such as Burgers equation. Because the governing inviscid Burgers equation can be written in conservation form, and because the distribution of u is bounded, the domain-wide integral of u is conserved.

The solution (122) is not easy to see until it is graphed, Fig. (18), right, and even then the interpretation is aided considerably by reference to the characteristics. The most rapidly moving part of the hump that begins near the origin ($a = 0$) will sooner or later overtake the slower moving part that began at larger x (this coarse description is refined in Problem 5) below). After some elapsed time, the charactersistics will cross, and u at that point will have an infinite derivative, $\partial u/\partial x$, Fig. (18), right. If the method of characteristics is continued, the solution for u will then appear to be triple-valued at that (x,t) and beyond. In the case that u is the current, a multi-valued solution makes no physical sense and has to be rejected. Evidently the governing equation (119) has omitted some physical process(es), e.g., diffusion or viscosity, that will become important when the derivative $\partial/\partial x$ becomes large. Even with diffusion present, the derivative may, nevertheless, become very large and the flow said to form a shock wave, across which the current is nearly discontinuous. The conservation of momentum should hold regardless of the details of the field, and the subsequent motion of a shock wave can be determined from fundamental principles.

4.5 Key ideas

1. An elementary initial value problem for a passive tracer in an ideal fluid flow may be solved in either a Lagrangian or an Eulerian system. The Lagrangian solution comes in two parts, tracer concentration on moving parcels (conserved at the initial value if the flow is adiabatic) and the position of those parcels. The Eulerian solution is complete in one piece, a tracer field that depends upon the field coordinates, space and time.

2. The two-part Lagrangian solution may be readily transformed into the Eulerian solution by eliminating reference to the initial position. The Eulerian solution for tracer concentration alone is not so readily transformed to the Lagrangian solution.

3. The method of characteristics (MoC) is applicable to the solution of first order PDEs, which arise in many contexts besides fluid mechanics. The tracer is represented on a field, and hence the MoC is an Eulerian method. The starting point is the recognition that the tracer balance will be simplest when evaluated along the characteristic curves of the governing PDE. The characteristics may be

computed from the coefficients of the partial derivative terms, and if the PDE is an advection equation, the characteristics are parcel trajectories.

4. If the flow is adiabatic (no source or diffusion) then the tracer will be constant along a characteristic. If a source is present, then it may be accounted by another ODE that solves for the tracer along the characteristics, i.e., along parcel trajectories.

5. The interpretation of an Eulerian solution can borrow Lagrangian concepts, even when the governing PDE is not an advection equation.

4.6 Problems

1) The method of characteristics makes important use of the idea of parameterized curves. The independent variable of these curves is often represented by s, which can seem a little mysterious because it need not be defined precisely. This problem includes a brief background on parameterized curves, and then offers a short quiz that should help refresh your memory of this occasionally very useful device.

The points $(x,\ y)$ that lie on a circle of radius r are related by the familiar

$$x^2 + y^2 = r^2. \tag{123}$$

Suppose that you need to write y as an explicit function of x for use in some later calculation. The algebra is trivial, $y = \pm\sqrt{r^2 - x^2}$, and the meaning is clear. However, this has not given us a function because one value of x maps into two values of y and vice-versa (which is, of course, a fundamental property of a circle). One work-around is to define two functions, say $y_+ = +\sqrt{r^2 - x^2}$ and $y_- = -\sqrt{r^2 - x^2}$, and then check each time to insure the correct choice. That is inelegant and can be inefficient.

Alternatively, consider a parameterized version of (123), say

$$x_\gamma = r\cos(s) \quad \text{and} \quad y_\gamma = r\sin(s), \tag{124}$$

where s is the independent variable, and in this context often said to be the 'parameter' of this new version of a circle. This parameterized circle is defined via explicit functions, although two of them, and now with this interloper, s. Are there advantages to this? Here are some questions that will help you decide.

(i) Over what range should s be varied in (124) in order to fill out a complete circle?

(ii) Show that the slope of the tangent to the curve is $(dy_\gamma/ds)/(dx_\gamma/ds)$.

(iii) Suppose the same range of s as in 1), but now take the parameterization to be $x_\gamma = r\cos(2s)$ and $y_\gamma = r\sin(2s)$. What changed? Does the slope formula still work? Suppose that s is proportional to time; how about the rate, $\partial x_\gamma/\partial t$?

(iv) Now try $x_\gamma = r\cos(s^2)$ and $y_\gamma = r\sin(s^2)$. Same questions.

(v) It is beginning to seem as if s can be almost anything, so let's try an experiment with the relationship between s, x_γ and y_γ, say $x_\gamma = r\cos(s)$ and $y_\gamma = r\sin(2s)$ and then $x_\gamma = r\cos(s)$ and $y_\gamma = r\sin(s^2)$. Do these parameterize a circle?

(vi) We didn't say what kind of numbers s was meant to be, so you probably assumed the reals. Suppose instead that s is the integers, or how about the Fibonacci sequence?

(vii) So, after all of this ..... what is s ?

2) Given the Lagrangian solution Eqs. (94) and (95), compute the corresponding Eulerian solution. Could you do this absent either (94) or (95)?

3) Compute the Lagrangian solution for the case of a source or sink, Eq. (109) in Sec. 4.4.1.

4) An initial value problem for a tracer $c(x,t)$ that you can solve via the method of characteristcs:

$$\frac{\partial c}{\partial t} + U\frac{\partial u}{\partial x} = 1, \quad \text{and} \quad c(x,t=0) = cos(x),$$

where U is a constant. (Major hint: $c(x,t) = t + cos(x-Ut)$). For an excellent web-based resource that will help you with this problem, see https://www.youtube.com/watch?v=tNP286WZw3o A Matlab script that implements the method of charcteristics in symbolic math is https://www2.whoi.edu/staff/jprice/wp-content/uploads/sites/199/2023/10/MoCsymbolic.txt

5) Crossing characteristics. We saw in Sec. 4.4.3 that characteristic curves will eventually cross when (as usually occurs) the current varies in space. Let's find out when that will happen for the problem considered there. It is helpful to think of the motion along characteristics as the motion of fluid parcels whose x positions are given by $x = x_o + \exp(-x_o^2/2)$. A 'collision' will occur when $\partial x(x_o,t)/\partial x_o = 0$, and the separation between parcels vanishes. Can you show that the first time of such a collision is $t_{coll} = \exp(1/2)$ and the location is $x_{coll} = 2$, cf. Fig. (18). Collisions are especially noteworthy, but not the only phenomena illuminated by the characterstics; e.g., what happens on the left side of the current maximum?

6) Given a first order, nonlinear PDE

$$\frac{\partial u}{\partial t} + h(u)\frac{\partial u}{\partial x} = 0$$

with IC

$$u(x,\, t=0) = \Psi(x).$$

Verify by direct substitution that an implicit solution is

$$u(x,\, t) = \Psi(x - h(u)\, t).$$

5 Coming up in Part 2

A complete model of a fluid flow will likely require the Eulerian mass and momentum equations derived in Sec. 3, together with a state equation. The definition of a specific problem requires a number of additional steps including simplification where appropriate, and careful consideration of the boundary and initial conditions. Finding and exploring the solutions of such a system will often require a great deal of time and effort, and frequently an appeal to numerical and experimental methods. Most of your research of fluid mechanics will be devoted to just that kind of task.

The scope and goals of the Part 2 essay start with the (generous) assumption that you have generated an analytic or a numerical solution of the velocity field. The question addressed in Part 2 is how to analyze these solutions for properties of interest, especially parcel trajectories. Thus the direction of Part 2 is Eulerian to Lagrangian.

6 Appendices

6.1 Physical properties of fluids and solids

Classical fluid mechanics, like classical thermodynamics, is concerned with macroscopic phenomena (bulk properties) rather than microscopic (molecular-scale) phenomena. In fact, the molecular makeup of a fluid will be studiously ignored in all that follows, and the crucially important physical properties of a fluid, e.g., its mass density, ρ, heat capacity, Cp, among others, must be provided from outside of this theory, Table (1). It will be assumed that these physical properties, along with flow properties, e.g., the pressure, P, velocity, $\mathbf{V}$, temperature, T, etc., are in principle definable at every point in space, as if the fluid was a smoothly varying continuum, rather than a swarm of very fine, discrete particles (molecules).

The space occupied by the material will be called the domain. Solids are materials that have a more or less intrinsic configuration or shape and do not conform to their domain under nominal conditions. Fluids do not have an intrinsic shape; gases are fluids that will completely fill their domain (or container) and liquids are fluids that form a free surface in the presence of gravity.

An important property of any material is its response to an applied force, Fig. (19). If the force on the face of a cube, say, is proportional to the area of the face, as will often be the case, then it is appropriate to consider the force per unit area, called the stress, and represented by the symbol S if a scalar, by $\mathbf{S}$ if a three component stress vector, and by $\mathbb{S}$ when considering a nine component stress tensor. The latter is introduced here briefly and in more detail in Sec. 3.4. The SI units of stress are Newtons per meter squared, which is commonly represented by a derived unit, the Pascal, or Pa. Why there is a stress and how the stress is related to the physical properties and the motion of the material are questions of first importance in many investigations, but for now the stress is presumed given.

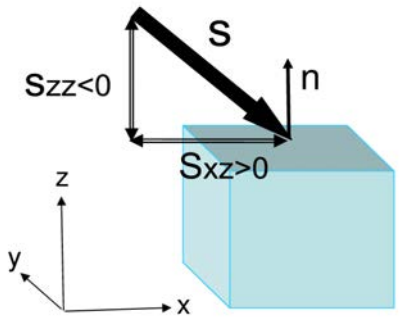

Figure 19: An orthogonal triad of Cartesian unit vectors and a small cube of material. The surrounding material is presumed to exert a stress, **S**, upon the face of the cube that is normal to the z axis. The outward-directed unit normal of this face is $\mathbf{n} = \mathbf{e_z}$. To manipulate the stress vector it will usually be necessary to resolve it into components: Szz is the projection of **S** onto the $\mathbf{e_z}$ unit vector and is negative, and S_{xz} is the projection of **S** onto the $\mathbf{e_x}$ unit vector and is positive. Thus the first subscript on S indicates the direction of the stress component and the second subscript indicates the orientation of the face upon which it acts. This ordering of the subscripts is a convention, and it is not uncommon to see this reversed.

The component of stress that is normal to the upper surface of the material in Fig. (19) is denoted S_{zz}. A normal stress can be either a compression, if $S_{zz} \leq 0$, as implied in Fig. (20), or a tension, if $S_{zz} \geq 0$. The most important compressive normal stress is almost always due to pressure rather than to viscous effects, and when the discussion is limited to compressive normal stress only, S_{zz} is identified as the pressure.

6.1.1 In response to a normal stress, liquids and solids are not very different

Every material will undergo some volume change as the ambient pressure is increased or decreased, though the amount varies quite widely from gases to liquids and solids. To make a quantitative measure of the volume change, let P_0 be the nominal pressure and h_0 the initial thickness of the fluid sample; denote the pressure change by δP and the resulting thickness change by δh. The normalized change in thickness, $\delta h/h_0$, is called the linear deformation (linear in this case meaning that the displacement is in line with the stress). The linear deformation is of special significance in this one-dimensional configuration because the volume change is equal to the linear deformation, $\delta V = V_0 \delta h/h_0$ (in a two- or three-dimensional fluid this need not be the case, Section 6.3). The mass of material, $M = \rho V$, is not affected by pressure changes and hence the mass density, $\rho = M/V$, will change inversely with the linear deformation;

$$\frac{\delta\rho}{\rho_0} = -\frac{\delta V}{V_0} = -\frac{\delta h}{h_0}, \tag{125}$$

where δ is a small change, $\delta \ll 1$. Assuming that the dependence of thickness change upon pressure can be observed in the laboratory, then $\delta h = \delta h(P_0, \delta P)$ together with Eq. (125) are the rudiments of an equation of state, the functional relationship between density, pressure and temperature, $\rho = \rho(P,T)$ or equivalently, $P = P(\rho,T)$, with T the absolute temperature in Kelvin. The archetype of an equation of state is that of an ideal gas, $PV = nRT$ where n is the number of moles of the gas and $R = 8.31$ Joule moles^{-1} K^{-1} is the universal gas constant.

Some physical properties of air, sea and land (granite)

	density ρ, kg m^{-3}	heat capacity Cp, J kg^{-1} C^{-1}	bulk modulus B, Pa	sound speed c, m s^{-1}	shear modulus K, Pa	viscosity ν, Pa s
air	1.2	1000	1.3×10^5	330	na	18×10^{-6}
sea water	1025	4000	2.2×10^9	1500	na	1×10^{-3}
granite	2800	2800	4×10^{10}	5950	2×10^{10}	$\geq 10^{22}$

Table 1: Approximate, nominal values of some thermodynamic variables that are required to characterize materials to be described by a continuum theory. These important data must be derived from laboratory studies. For air, the values are at standard temperature, 0 C, and nominal atmospheric pressure, 10^5 Pa. The bulk modulus shown here is for adiabatic compression; under an isothermal compression the value for air is about 30% smaller; the values are nearly identical for liquids and solids. na is not applicable. The viscosity of granite is temperature-dependent; granite is brittle at low temperatures, but appears to flow as a highly viscous material at temperatures above a few hundred C.

An important class of phenomenon may be described by a reduced equation of state having state variables density and pressure alone,

$$\rho = \rho(P), \quad \text{or equivalently,} \quad P = P(\rho). \tag{126}$$

It can be presumed that ρ is a monotonic function of P and hence that $P(\rho)$ should be a well-defined function of the density. A fluid described by Eq. (126) is said to be 'barotropic' in that the gradient of density will be everywhere parallel to the gradient of pressure, $\nabla\rho = (\partial\rho/\partial P)\nabla P$, and hence surfaces of constant density will be parallel to surfaces of constant pressure.

The stiffness or inverse compressibility of the material is

$$B = \frac{S_{zz}}{\delta h/h} = -V_0\frac{\delta P}{\delta V} = \rho_0\frac{\delta P}{\delta\rho}, \tag{127}$$

called the bulk modulus. Notice that B has the units of stress or pressure, Pa, and is much like a normalized spring constant; B times the normalized linear strain (or volume change or density change) gives the resulting pressure change. The numerical value of B is the pressure increase required to compress the volume by 100% of V_0. Of course, a complete compression of that sort does not happen outside of black holes, and the bulk modulus should be regarded as the first derivative of the state equation, accurate for small changes around the ambient pressure, P_0. Gases are readily compressed; a pressure increase $\delta P = 10^4$ Pa, which is 10% above nominal atmospheric pressure, will cause an air sample to compress by about $B^{-1}10^4 Pa = \delta V/V_o = 7\%$ under adiabatic conditions. Most liquids are quite resistant to compressive stress, e.g., for water, $B = 2.2\times10^9$ Pa, which is less than but comparable to the bulk modulus of a very stiff solid, granite (Table 1). Thus the otherwise crushing pressure in the abyssal ocean, up to about 1000 times atmospheric pressure in the deepest trench, has a rather small effect upon sea water, compressing it and raising the density by only about five percent above sea level values. Water is stiff enough and pressure changes associated with geophysical flows small enough that

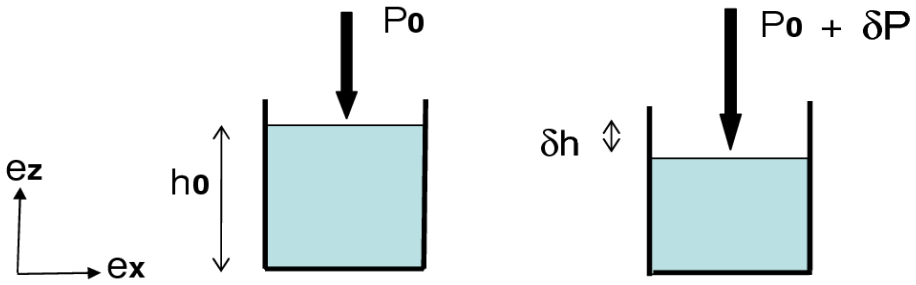

Figure 20: A solid or fluid sample confined within a piston has a thickness h_0 at the ambient pressure P_0. If the pressure is increased by an amount δP, the material will be compressed by the amount δh and the volume decreased in proportion. The work done during this compression will raise the temperature of the sample, perhaps quite a lot if the material is a gas, and it becomes important to define whether the sidewalls allow heat flux into the surroundings (isothermal compression) or not (adiabatic compression); the B in Table 1 is the latter.

for many purposes water may be idealized as an incompressible fluid, as if B was infinite. Surprisingly, in many circumstances the same is true for air.

The first several physical properties listed in Table 1 suggest that water has more in common with granite than with air, our other fluid. The character of fluids becomes evident in their response to anything besides a compressive normal stress. Fluids are qualitatively different from solids in their response to a tensile normal stress, i.e., $S_{zz} \geq 0$, which is resisted by many solid materials, especially metals, with almost the same strength that they exhibit to compression. In contrast, gases do not resist tensile stress at all, while liquids do so only very, very weakly when compared with their resistance to compression. Thus if a fluid volume is compressed along one dimension but is free to expand in a second, orthogonal, direction (which the one-dimensional fluid confined in a piston, Fig. (20), can not, of course) then the volume may remain nearly constant though the fluid may undergo significant linear deformation, i.e., a compression and a nearly compensating expansion in an orthogonal direction.

6.1.2 In response to shear stress, solids deform and fluids will *flow*, often in very complex ways

A stress that is parallel to (in the plane of) the surface that receives the stress is called a 'shear' stress.[37] A shear stress that is in the x direction and applied to the upward face of the cube in Fig. (19) would be labeled S_{xz} and a shear stress in the y-direction, S_{yz}. A measure of a material's response to a steady shear stress is the shear deformation, r/h, where r is the steady (equilibrium) sideways displacement of the face that receives the shear stress and h is the column thickness (Fig. 21, and note that the cube of material is presumed to be stuck to the lower surface). The corresponding stiffness for shear stress, or shear

[37] The word *shear* has an origin in the Middle English *scheren*, which means to cut with a pair of sliding blades. A velocity shear is a spatial variation of the velocity in a direction that is perpendicular to the velocity vector.

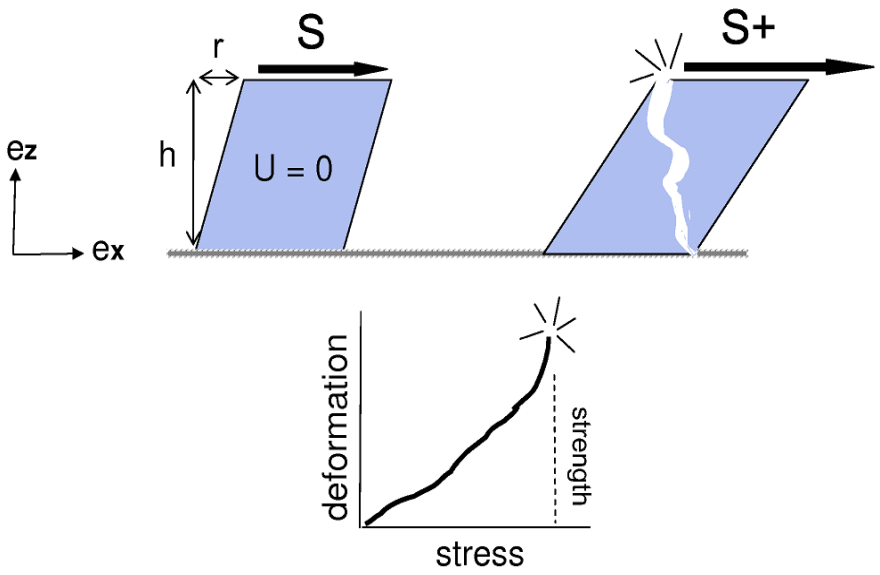

Figure 21: A vector stress, **S**, is imposed upon the upper face of a cube of solid material that is attached to a lower surface. Given the orientation of this face with respect to the unit vectors, this stress can also be represented by a single component, S_{xz}, of the stress tensor (Section 2.2.1). For small values of the stress, a solid will come to a static equilibrium in which an elastic restoring force balances the shear stress. The shear deformation (also called the shear 'strain') may be measured as r/h for small angles. It is fairly common that homogeneous materials exhibit a roughly linear stress/deformation relationship for small deformations. But if the stress exceeds the strength of the material, a solid may break, an irreversible transition. Just before that stage is reached the stress/deformation ratio is likely to decrease.

modulus, is then defined as

$$K = \frac{S_{xz}}{r/h}, \tag{128}$$

which has units of pressure. The magnitude of K is the shear stress required to achieve a shear deformation of $r/h = 1$, which is past the breaking point of most solid materials. For many solids the shear modulus is comparable to the bulk modulus (Table 1).[38]

Fluids are qualitatively different from solids in their response to a shear stress. Ordinary fluids such as air and water have no intrinsic configuration, and hence fluids do not develop a restoring force that can provide a static balance to a shear stress.[39] There is no volume change associated with a pure shear

[38] The distinction between solid and fluid seems clear enough when considering ordinary times and forces. But materials that may appear unequivocally solid when observed for a few minutes may be observed to flow, perhaps only very, very slowly, when observed over many days or millenia. Glaciers are a very important natural example, and see also the pitch drop experiment: https://smp.uq.edu.au/pitch-drop-experiment.

[39] There is no volume change associated with a pure shear deformation and thus no coupling to the bulk modulus. There does occur a significant linear deformation, compression and expansion, in certain directions examined in a later section, 6.3. While fluids have no *intrinsic* restoring forces or equilibrium configuration, nevertheless, there are important restoring forces set up within fluids in the presence of an acceleration field. Most notably, gravity will tend to restore a displaced free surface back towards level. Earth's rotation also endows the atmosphere and oceans with something closely akin to angular momen-

deformation and thus no coupling to the bulk modulus. Hence, there is no meaningful shear modulus for a fluid since r/h will not be steady. Rather, the distinguishing physical property of a fluid is that it will move or 'flow'[40] in response to a shear stress, and moreover, a fluid will continue to flow so long as a shear stress is present.

When the shear stress is held steady, and assuming that the geometry does not interfere, the shear deformation rate, $h^{-1}(dr/dt)$, may also be steady or have a meaningful time-average. In analogy with the shear modulus, a generalized viscosity, Υ, may be defined as the ratio of the measured shear stress to the shear deformation rate,

$$\Upsilon = \frac{S_{xz}}{h^{-1}dr/dt}. \tag{129}$$

This ratio of shear stress to shear deformation rate will depend upon the kind of fluid material and also upon the flow itself, i.e., the speed, $U = dr/dt$ of the upper moving surface and the column thickness, h. This generalized viscosity times a unit, overall velocity shear $U(z=h)/h = h^{-1}(dr/dt) = 1\ \mathrm{s}^{-1}$ is the shear stress required to produce the unit velocity shear.

Laminar flow at small Reynolds number: If the flow depicted in Fig. 22 is set up carefully, it may happen that the fluid velocity U will be steady, with velocity vectors lying smoothly, one on top of another, in layers or 'laminar' flow (the upper left of Fig. 22). The ratio of stress to shear then defines a fluid property

$$\text{viscosity:} \qquad \boxed{\nu = \frac{S_{xz}}{\partial U/\partial z}} \tag{130}$$

or sometimes dynamic viscosity.

Newtonian fluids, air and water: Fluids for which the viscosity in laminar flow is a thermodynamic property of the fluid alone and not dependent upon the shear stress magnitude are dubbed 'Newtonian' fluids, in recognition of Isaac Newton's insightful analysis of frictional effects in fluid flow. Air and water are found to be Newtonian fluids to an excellent approximation.

If the fluid is Newtonian, then it is found empirically that the conditions for laminar flow include that a nondimensional parameter called the

$$\text{Reynolds number:} \qquad \boxed{Re = \frac{\rho U h}{\nu}} \tag{131}$$

will satisfy the inequality $Re \leq 400$, where U is the speed of the upper (moving) surface relative to the lower, fixed, no-slip surface. The Reynolds number arises several times in this essay, and will be discussed in more detail in a later section, 3.5.4. If water, then in practice this means that the speed must be very low or the column thickness very small. The laminar flow velocity $U(z)$ of a Newtonian fluid will vary linearly with z and the velocity shear at each point in z will then be equal to the overall shear deformation rate, $\partial U/\partial z = h^{-1}(dr/dt)$, the particular laminar flow sketched in Fig. 22 upper left.

---

tum that provides a restoring tendency for horizontal displacements; the oscillatory wave motion seen in the cover graphic is an example.

[40] Fluid and flow have a nearly common eytemology in the Latin *fluidus* and *fluere*.

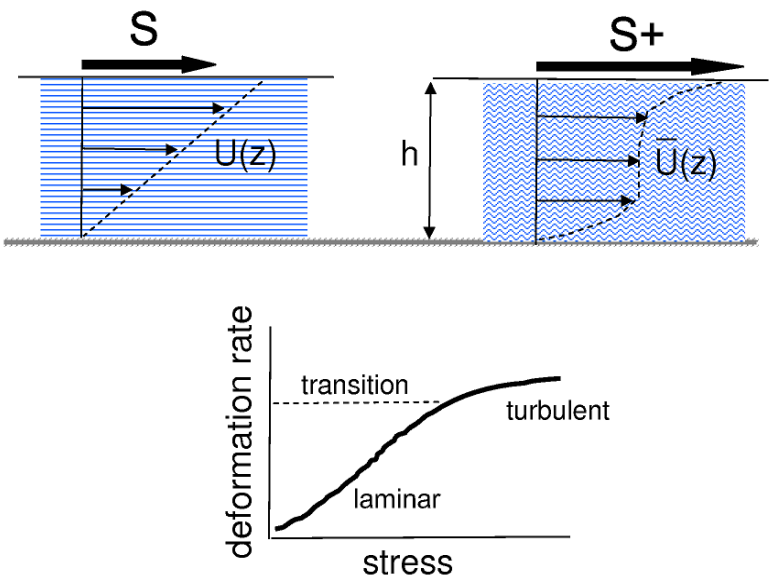

Figure 22: A vector stress, **S**, is imposed upon the upper face of a cube of fluid material that is sitting on a no-slip lower surface. Since we are considering only the z-dependence of the flow, it is implicit that the fluid and the stress are uniform in the horizontal. The response of a fluid to a shear stress is quite different from that of a solid in as much as a fluid has no intrinsic shape and so develops no elastic restoring force in response to a deformation. Instead, an ordinary fluid will move or flow so long as a shear stress is imposed and so the relevant kinematic variable is the shear deformation rate. For small values of the stress and assuming a Newtonian fluid, the fluid velocity, $U(z)$, may come into a laminar and steady state with a uniform vertical shear, $\partial U/\partial z = U(h)/h = constant = S_{xz}/\nu$, that can be readily observed and used to infer the fluid viscosity, ν, given the measured stress. For larger values of stress (right side) the flow may undergo a reversible transition to a turbulent state in which the fluid velocity is two or three-dimensional and unsteady despite that the stress is steady. The time average velocity $\overline{U(z)}$ is likely to be well-defined provided the external conditions are held constant. In this turbulent flow state, the time-averaged shear $\partial\overline{U}/\partial z$ will vary with z, being larger near the boundaries. The shear stress and the time-averaged overall deformation rate, $\overline{U(h)}/h$, are not related by a constant viscosity as obtains in the laminar flow regime, and across the turbulent transition the stress/deformation rate ratio will increase.

Assuming that the fluid viscosity and its dependence upon temperature, density, etc. are known, then the relationship Eq. (130) between viscosity, stress and velocity shear may just as well be turned around and used to estimate the viscous shear stress from a given velocity shear. This is the way that viscous shear stress will be incorporated into the momentum balance of a fluid parcel (Section 3.4.3). It is important to keep in mind that Eq. (130) is not an identity or a universal, physical law, but rather a contingent experimental law that applies only for laminar, steady flow. If instead the fluid velocity is unsteady and two- or three dimensional, i.e., turbulent and which is much more common, then for a given upper surface speed $U(h)$, the shear stress will be larger, and sometimes quite a lot larger, than the laminar value predicted by Eq. (130) (Figure 22).[41] Evidently then, Eq. (130) has to be accompanied by

[41] Viscosity and turbulence can in some limited respects mimic one another; a given stress and velocity shear can be consistent with either a large viscosity in laminar flow, or, a smaller viscosity (and thus higher Reynolds number) in tur-

Eq. (131) along with a description of the geometry of the flow, i.e., that h is the distance between parallel planes (and not the distance from one plate or the diameter of a pipe, for example). In most geophysical flows the equivalent Reynolds number is enormously larger than the upper limit for laminar flow indicated by Eq. (131) and consequently geophysical flows are seldom laminar and steady, but are much more likely to be turbulent and unsteady. Thus, for a given velocity shear, it very commonly happens that properties of the flow, rather than the physical properties of the fluid alone, determine the stress.

6.2 Composite functions and inverse functions

6.2.1 Functions of functions

Composite functions are, essentially, functions of functions. The formalism of composite functions is relevant on several occasions, including that the transformation of velocity from a Lagrangian to an Eulerian system amounts to the construction of a composite function, the velocity as a function of position.

This appendix aims to review some of the salient features of composite and inverse functions using simple examples. Let f by a function of a single variable, say

$$f(y) = 1 + y/3, \tag{132}$$

in which case the notation $f(y)$ means — take the variable found in the argument, multiply by $1/3$ and then add 1 (simple indeed). An equation of the sort Eq. (132) does not by itself make it clear whether we mean to define the function f, or whether we intend to evaluate $f(y)$ by assigning a value to y. In this context it is clear that this defines f, since y serves only to hold a place, i.e., it is a dummy variable that could just as well have be written x or z.

Now suppose that y can be or must be regarded as a function of an independent variable x,

$$y = g(x),$$

and for example,

$$g(x) \;=\; x^2, \tag{133}$$

with x real and $x > 0$. Restricting the domain of x and y insures that the inverse of g, written g^I, exists and will be used below.

A composite function, h, may be constructed from f and g by taking g to be the argument for f, i.e.,

$$h \;=\; f(g). \tag{134}$$

bulent flow. The pioneering investigators of liquid helium assumed that the flow in the very small laboratory apparatus used to estimate viscosity must be laminar, when in fact it was turbulent. This delayed the recognition that superfluid helium has a nearly vanishing viscosity (A. Griffin, Superfluidity: a new state of matter. In *A Century of Nature*. Ed. by L. Garwin and T. Lincoln. The Univ. of Chicago Press, 2003.) An excellent introduction to modern experimental research on turbulence including some Lagrangian aspects is by R. Ecke, The turbulence problem, available online at http://library.lanl.gov/cgi-bin/getfile?01057083.pdf

The function g inside the parentheses is termed the inner function, and f is termed the outer function. Given the present example (132) and (133), the composite function is

$$h(x) \;=\; f(g(x)) = f(x^2) = 1 + x^2/3, \tag{135}$$

plotted as the blue line of (Fig. 138). Thus when we discuss a composite function it is implicit that there are three functions in play: an outer function f, an inner function g, and the composite function, $h = f(g)$. Notice that the composite function depends upon the dummy variable x, i.e., the independent variable of a composite function is the independent variable of the inner function.

In general,

$$h(x) \neq f(y),$$

where the intent here is that h is to be evaluated at x and f is to be evaluated at y, with as yet no restriction placed upon x or y. However, it is true that

$$h(x) = f(y)\;|_{y=g(x)}, \tag{136}$$

where $(\;)\;|_{y=y(x)}$ means that the argument of f is equal to the inner function evaluated at the x that appears as the argument on the left hand side. In other words, it is true that $h(x) = f(y)$ just in case the values of x and y are related by the inner function. With a little reflection this seems fairly obvious, but an equivalent way to state this is not quite so transparent, namely

$$h(x)\;|_{x=g^I(y)} \;\; = f(y), \tag{137}$$

where g^I indicates the inverse of the inner function, g. In the example noted above,

$$g^I(y) = y^{1/2},$$

the positive square root of y, and sure enough,

$$h(y^{1/2}) \;=\; 1 \;+\; y/3 \;=\; f(y).$$

The relation (137) is exactly the form used to state the FPK, Eq. (4), the definition of Eulerian velocity:

the Eulerian velocity $\mathbf{V} \rightarrow h$, the composite function,
the field coordinate, $\mathbf{X} \rightarrow x$, the argument of the composite function
the Lagrangian velocity $\tilde{\mathbf{V}} \rightarrow f$, the outer function,
the trajectory inverse, $\mathbf{A}(\tilde{\mathbf{X}}) \rightarrow g(x)$, the inner function, and
the material coordinate, $\tilde{\mathbf{X}} \rightarrow y$, the argument of the outer function.

Thus when we start with a Lagrangian perspective, presuming to know the Lagrangian trajectories, their inverse and the Lagrangian velocity, then the Eulerian velocity field can be constructed as a composite function made up from these Lagrangian data — no derivatives or integrations required.

6.2.2 Inverse functions and their derivatives

A somewhat general definition of an inverse function g^I is

$$g^I(g(x)) \;=\; g(g^I(x)) \;=\; x. \tag{138}$$

Thus the inverse function undoes the function (nothing surprising in that). The relation (138) is especially easy to apply to the example $g(x) = x^2$ suggested here. Since the domain of x was restricted to the positive, real numbers, the inverse function in this case is just

$$g^I(x) \;=\; x^{1/2},$$

the positive square root.

The inverse of the slightly more complex composite function (135) is best found with a more systematic procedure.[42] Let $w \;=\; h(x) = 1 + x^2/3$. Now solve this for $x \;=\; \sqrt{(3w-3)}$. Switch the places (labels) of x and w, and take this new x to be the argument of the putative inverse function,

$$h^I(x) \;=\; \sqrt{(3x \;-\; 3)}, \tag{139}$$

the red line of Fig. (138). You can check that (139) is indeed the inverse function of (135) by verifying

$$h^I(h(x)) \;=\; x. \tag{140}$$

The derivative of an inverse function bares a simple and useful relationship to the derivative of the function itself. Let's show this for the composite function, h and it's inverse h^I noted just above. Take the derivative of the left and right sides of (140) using the chain rule to find

$$\frac{dh^I(h)}{dh}\,\frac{dh}{dx} \;=\; \frac{dx}{dx} \;=\; 1,$$

and so

$$\frac{dh^I(h)}{dh} \;=\; 1/\frac{dh}{dx}. \tag{141}$$

The left side derivative d/dh might look a little unusual but is easy to evaluate; take the derivative of $h^I(w)$ with respect to a dummy argument, w, i.e., $dh^I/dw \;=\; (3/2)/\sqrt{3w \;-\; 3}$, and then evaluate this at $w \;=\; h(x) \;=\; 1 \;+\; x^2/3$, to find $dh^I(h)/dh \;=\; (3/2)\,x^{-1}$, the reciprocal of dh/dx of (135). Thus the derivative of the inverse of a function is the reciprocal of the derivative of the function (this is easier to see in the example of Fig. (23) than it is to say). Eq. (141) is a very useful result when it comes time to convert derivatives from one coordinate system to another in Sec. 2.2, and on.

[42] An excellent refresher on the procedure for finding the inverse of a function may be found online by a search for 'How to find the inverse of a function (NancyPi)'.

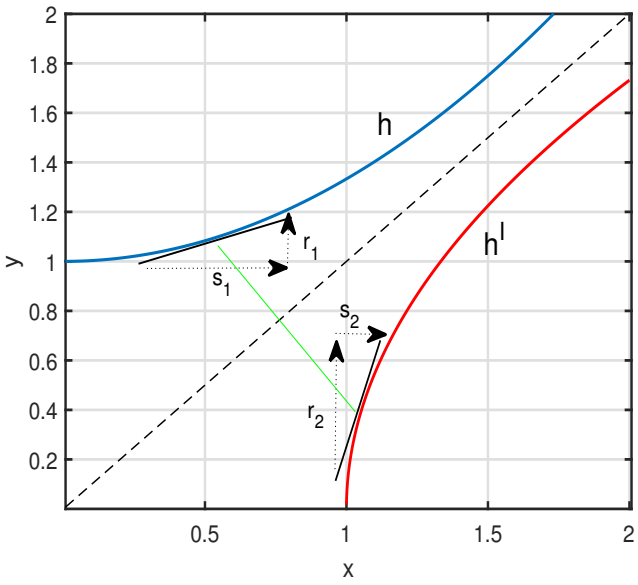

Figure 23: The function $h(x) = 1 + x^2/3$ is the blue line, and its inverse, $h^I(x) = (3x-3)^{1/2}$, is the red line. The inverse, h^I, is the reflection of h across $y = x$, the dashed, black line. Notice that the slopes of h and h^I are reciprocals when they are evaluated at points that are reflections across $x = y$, e.g., the thin green line connects the point $(x,\ y) = (0.5,\ h(0.5))$ with its reflection, $(x,\ y) = (h(0.5),\ h^I(h(0.5))$. By inspection, $r_1/s_1 \approx 1/(r_2/s_2)$, as expected from Eq. (141).

6.2.3 Rules for differentiation and change of variables in integrals

Given a composite function $h(x) = f(g(x))$ and its derivative

$$\frac{dh}{dx} = \frac{d}{dx}f(g) = \frac{df}{dg}\frac{dg}{dx} \tag{142}$$

via the chain rule. Now let F be the antiderivative of f, i.e.,

$$F(y) = \int f(y)dy \tag{143}$$

and so

$$F(y)' = \frac{dF}{dy} = f(y).$$

If it is the case that $y = g(x)$ then $F(g(x))$ is a composite function and by the chain rule,

$$\frac{d\,F(g)}{dx} = F'\frac{dg}{dx} = f\frac{dg}{dx}.$$

Upon integrating the left and right sides,

$$F(g(x)) = \int f(g)\frac{dg}{dx}dx. \tag{144}$$

If F is the antiderivative of $\int f(y)dy$, then $F(g)$ is the antiderivative of $\int f(g(x))\frac{dg}{dx}dx$.

We can also transform the independent variable of an integral by direct substitution of $y = g(x)$, and

so

$$\int_{y_1}^{y_2} f(y)dy = \int_{x_1=g^I(y_1)}^{x_2=g^I(y_2)} f(g(x))\frac{dg}{dx}dx. \tag{145}$$

The most interesting part of this is $dy \rightarrow \frac{dg}{dx}dx$, which accounts for the stretching or compression of the differential length. (In a two- or three-dimensional geometry this will be the determinant of the Jacobian of the transformation, examples below.) Thus we can change the independent variable y of the integral of Eq. (143) to x in Eq. (145), provided that $y = g(x)$ and x can be thought of as the inner function and independent variable of a composite function. This result will be invoked in Sec. 3.3 to change an integral over $\tilde{x}$, which is time-dependent when tracking a moving material volume, to the equivalent integral over x, the field coordinate and which is time-independent (the Reynolds Transport Theorem).

Index

adiabatic, 57

Burgers equation, 67

characteristic curve, 60
characteristics, 61
composite functions, 78
compressibility, 73
condensation, 21
conservation form, 42
control volume, 10
convection, 11

domain, 71

entangled, 24
equation of motion; Lagrangian, 1 -d, 23
equation of motion; Lagrangian, 1-d, 23
Eulerian
    measurement, 9
extensive variable, 38

flux form, 42
FPK, 11
frozen field, 42
Fundamental Principle of Kinematics, FPK, 11

incompressible, 44
inner function, 79
intensive variable, 38

kinematics, 8

Lagrangian
    measurement, 9
laminar flow, 76
linear deformation, 21

mass conservation, 40
material derivative, 37
material volume, 10
method of characteristics, 59

Newtonian fluids, 76
normal stress, 72

outer function, 79

PIV, 28

Reynolds number, 53
Reynolds Transport Theorem, RTT, 37

shear modulus, 75
shear stress, 75
shock, 68
stress
    shear , 74
stress
    normal, 72
substantive derivative, 37

tangent vector, 60
tensor
    stress, 46
turbulence, 77

velocity
    Eulerian, 11

wave equation; nonlinear, Lagrangian, 24

Lagrangian and Eulerian representations of fluid flow
Part 2: Advection of parcels and fields

James F. Price

Woods Hole Oceanographic Institution,
Woods Hole, Massachusetts, 02543
https://www2.whoi.edu/staff/jprice/ jprice@whoi.edu

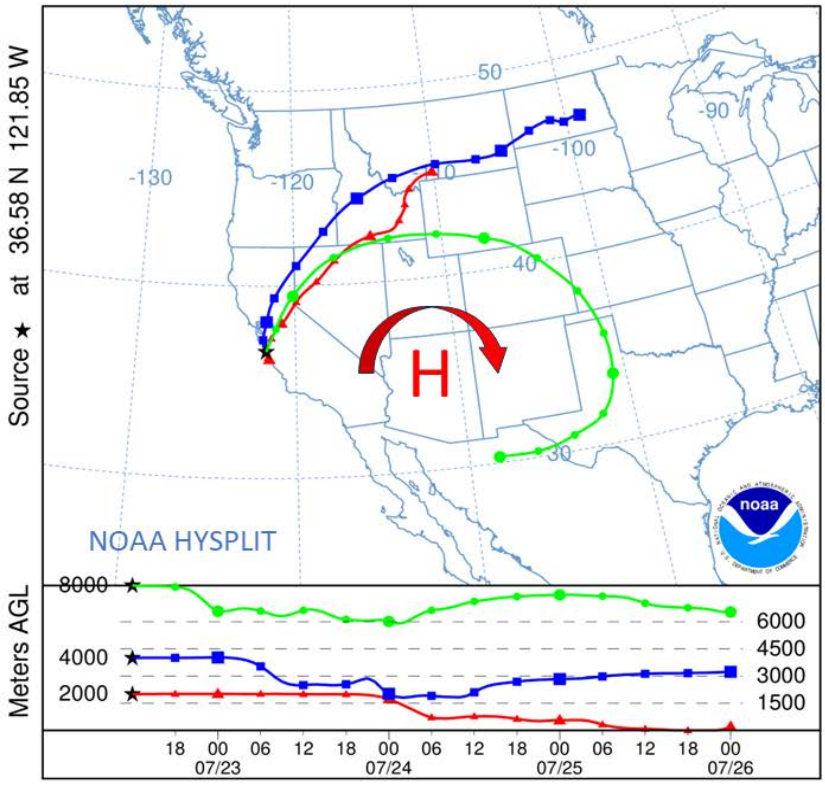

Figure 1: Tracer transport by fluid flow may be represented by parcel trajectories, the Lagrangian perspective of these simulated balloon trajectories, or by advection of tracer fields, the Eulerian perspective. The goal of this essay is to learn how Lagrangian and Eulerian methods and data may be used side-by-side. These trajectories were computed by the NOAA HYSPLIT system with essential wind data in the form of gridded (Eulerian) velocity fields computed by a weather forecast model. This kind of Eulerian to Lagrangian transformation is a central theme of this essay.

Abstract: This essay continues an introduction to Lagrangian and Eulerian methods of fluid mechanics. Part 1 argued that Lagrangian observations and conservation laws are the natural starting point for an analysis of fluid flows, though the resulting Lagrangian equations of motion are generally very difficult. The majority of theory is developed within Eulerian systems, and so this Part 2 flips the script: the starting point is presumed to be a known velocity field (Eulerian), and the theme is transformation to several kinds of Lagrangian diagnostic quantities, especially trajectories.

If what we know is a velocity field, then to know where a parcel is going, we have to know where it is. This amounts to inverting the fundamental principle of kinematics (FPK) of Part 1. Computation of a trajectory is an integration in time of the velocity at the moving position of the parcel. The fidelity of the trajectory will depend in a straightforward way upon the spatial resolution of the velocity field and upon the temporal resolution of the integration. There are a number of useful variants on the notion of a trajectory, including streaklines, which show the location of parcels that have a common source but different starting times, and backwards trajectories, that show where parcels present at a given position and time have come from. These are important tools for air quality forecasts, for example.

If the Eulerian velocity has been time-averaged or otherwise undersamples the velocity, then the FPK (or its inverse) does not apply, strictly. The difference between the time-averaged Lagrangian and Eulerian velocities may be attributed to Stokes drift, a material (Lagrangian) velocity that arises from correlation between parcel displacement and the spatial gradient of the Eulerian velocity. Stokes drift is especially important when this correlation is high, as it is in wind-driven gravity wave motion on the ocean surface. In that case the Stokes drift is downwind and surface intensified, and can be fairly large amplitude.

Advection represents the transport of fluid properties at a definite rate and direction, that of the fluid velocity. Some Eulerian numerical models treat advection as an adiabatic process that translates parcels along the characteristics defined by the velocity field. These so-called semi-Lagrangian methods often provide a significant improvement in efficiency or accuracy compared to strictly Eulerian methods that advect the tracer field.

Advection does more than simply transport fluid. A velocity field that is spatially-varying (the norm) may cause linear and shear deformation of a fluid parcel. Deformation may cause an initially compact patch of a tracer to be strained into long, thin filaments that have a greatly increased perimeter. A nonuniform velocity may also cause a fluid parcel to rotate. The rotation rate, called the vorticity, is analogous to angular momentum and follows a particularly useful conservation law. The Cauchy-Stokes decomposition theorem relates the eigenvectors of the velocity gradient tensor to these deformations and to the rotation rate.

Most real fluid flows are made up of a range of time and space scales, spanning anything from one to eight decades (tea cup to the atmosphere). Most all analyses begin with the definition of the scales that will be resolved, and so by exclusion define the smaller space and faster time scales that will be unresolved, but whose effects may be treated statistically or by a parameterization. In the case that the fast time scale motion is a random walk, a suitable (Eulerian) parameterization may be an effective diffusivity. Deformation by a resolved flow plus effective diffusivity can lead to significantly enhanced mixing of a tracer.

More on Fig. (1). The emphasis here is on methods, mainly, but these simulated balloon trajectories reveal some of the inner workings of an important weather phenomenon that you might have experienced — a heat dome. The balloons were launched from the coast of central California in July 2023, and their trajectory was forecast ahead for 3.5 days. They were ballasted for initial altitudes of 2000, 4000 and 8000 m above ground level (AGL, lower panel) and thereafter maintained constant pressure. The ground rose beneath the balloons as they drifted toward mid-continent. The balloon at the highest altitude (the blue line) made a sweeping, clockwise-turning trajectory consistent with the free, geostrophic wind around a large, slowly evolving high pressure system. By comparison, the lower-level balloon trajectories showed evidence of the frictional effects expected within the atmospheric boundary layer (the lowest several kilometers of the atmosphere) *viz.*, reduced speed compared to the geostrophic wind at altitude, and trajectories that turned toward lower pressure (to the left looking downwind). Other trajectories that were started on the periphery of the high pressure system did the same. This pattern implies a horizontally divergent wind within the boundary layer that is largely compensated by descending air at mid-levels. The descending air is warmed by adiabatic compression, resulting in dry, clear skies and consequent high solar insolation at ground level. The high pressure weather pattern may persist for days or even a few weeks, as it did on this occasion, leading to prolonged high surface temperature, drought, and wildfires. This heat dome phenomenon was widespread during summer, 2023.

These trajectories are thanks to NOAA HYSPLIT, https://www.ready.noaa.gov/HYSPLIT.php a comprehensive Lagrangian analysis system for the atmosphere that offers excellent tutorials for new users. For much more on HYSPLIT, see A. F. Stein, R. R. Draxler, G. D. Rolph, B. J. B. Stunder and M. D. Cohen (2015), NOAAs HYSPLIT Atmospheric Transport and Dispersion Modeling System. Bull. of the American Met. Soc., Volume 96, Issue 12, pp. 2059 - 2077, DOI: https://doi.org/10.1175/BAMS-D-14-00110.1

Contents

1 Eulerian solutions ⇒ Lagrangian diagnostics **5**

1.1 Goal and plan 5

1.2 Acknowledgments 7

2 Tracking parcels in a velocity field **7**

2.1 Parcel trajectories 7

2.2 Backward trajectories 9

2.3 Streaklines are a snapshot of parcels having a common origin 10

2.4 Streamlines are parallel to an instantaneous flow field 11

2.5 Tracking parcels around a steady vortex given limited Eulerian data 12

2.5.1 The zeroth-order approximation, or PVD . . . 13
2.5.2 The first order approximation . . . 14
2.6 Tracking parcels in water waves . . . 16
2.6.1 The zeroth order approximation, closed loops . . . 17
2.6.2 The first order approximation, Lagrange = Euler + Stokes . . . 17
2.7 Key ideas . . . 20
2.8 Problems . . . 21

3 Rotation and deformation of fluid parcels 22
3.1 The simplest shear flow . . . 24
3.2 Physical rotation rate and vorticity . . . 26
3.3 Deformation rate . . . 28
3.4 Rotation rate and deformation rate tensors . . . 29
3.5 The Cauchy-Stokes Decomposition Theorem brings this all together . . . 32
3.6 Application to the vortex flows . . . 32
3.7 Key ideas . . . 34
3.8 Problems . . . 35

4 Advection by resolved and unresolved motions 36
4.1 Reynolds averaging of advection terms leads to eddy fluxes . . . 37
4.2 A random walk as a first model of unresolved advection . . . 38
4.3 An Eulerian description of dispersion by a random walk; effective diffusivity . . . 40
4.4 Stirring and mixing: when advection and diffusion act at once, Peclet number . . . 43
4.4.1 Following the particle cloud, the Lagrangian view . . . 45
4.4.2 Watching a control volume, the Eulerian view . . . 46
4.5 Appendix: The Lamb-Oseen vortex . . . 49
4.5.1 How to make a starting vortex . . . 49
4.5.2 Diffusion of vorticity . . . 50
4.5.3 The inner core, solid body rotation . . . 51
4.6 Key ideas . . . 52
4.7 Problems . . . 53

5 Models that combine Lagrangian and Eulerian concepts 54
5.1 Numerical treatments of advection . . . 54
5.1.1 Discretized data and numerical solution . . . 55
5.1.2 Lagrangian advection of parcels . . . 56
5.1.3 Eulerian advection of a tracer field . . . 57
5.1.4 Semi-Lagrangian advection . . . 59

5.2 Layered models of the stratified ocean interior 60
5.3 Particle in Cell models utilize hybrid dynamics 61
5.4 Key ideas 64
5.5 Problems 64

6 Lagrangian analysis of an oceanic flow. 65
6.1 Estimating the potential vorticity 66
6.2 Potential vorticity as a tracer 68
6.2.1 Potential vorticity and changing latitude 70
6.2.2 Potential vorticity and changing layer thickness 70
6.3 Wave properties of the observed motion 72
6.4 Key ideas 72
6.5 Problems 72

7 Index 73

1 Eulerian solutions ⇒ Lagrangian diagnostics

This is the second of a two part introduction to Lagrangian and Eulerian representations of fluid flow. Part 1 emphasized the kinematics of fluid flow, and the application of the conservation laws of classical physics to modelling a fluid flow. The point of view taken in Part 1 is that the Lagrangian perspective is fundamental in two respects: what we mean by fluid flow is generally the motion of specific fluid volumes or parcels, and, the conservation laws apply to such specific fluid volumes. It seems like the Lagrangian perspective is off to a strong start. However, the equations of motion written in Lagrangian coordinates are quite difficult for most complex problems, and so the vast majority of theory and modelling is carried out within Eulerian systems that represent fluid properties as fields rather than material volumes. The weather forecast model that generated the wind field required to calculate the balloon trajectories of Fig. 1 is an example. All such models calculate their solutions for wind and other air properties on four dimensional fields (grids), three space dimensions and time. These models are thus fundamentally Eulerian, though many of them make good use of Lagrangian submodels at key junctures, especially when accounting for advection.

1.1 Goal and plan

The broad goal of this essay is an improved understanding of advection, i.e., the transport of parcels and fields by a fluid flow. 'Parcels and fields' implies Lagrangian and Eulerian representations, and this essay

considers both. The aim is to understand how these representations are related, and why and how we may transform data from one to the other.

Sec. 2 begins with the most important and widely used version of this transformation, calculation of Lagrangian trajectories from an Eulerian velocity field, as in Fig. (1). In principle this is straightforward; the Lagrangian velocity is evaluated using the fundamental principle of kinematics (the FPK of Part 1) in reverse, and integrated over time. There can be interesting complications when time-averaging occurs either by virtue of the observation method, or via the analysis. The FPK (or its inverse) applies to the instantaneous velocity, and may not apply when time averages enter. A new kind of velocity, sometimes called Stokes drift, arises when parcel displacement and the fluid velocity are correlated as in surface gravity waves.

Advection by a spatially-varying flow also deforms fluid volumes, which is considered in Sec. 3. The Cauchy-Stokes Decomposition Theorem provides a concise accounting of the rotation and deformation of fluid parcels in terms of the eigenvalues and eigenvectors of the velocity gradient tensor. The rotation rate is proportional to the curl of the velocity, the vorticity, which is an analog of angular momentum. Vorticity follows a somewhat simpler governing equation than does momentum, and can be a valuable diagnostic (Sec. 6).

Sec. 4 acknowledges that most real fluid flows are comprised of a wide range of time and space scales, some of which are resolved and treated explicitly, and some of which may be on such small scale (time or space) that they simply have to be treated in aggregate, that is, statistically. Reynolds averaging shows that one consequence of the small scale motion is likely to be a flux of tracer that may sometimes be modelled as a diffusion process. In most real flows, advection and diffusion act concurrently, and deformation by the resolved scale of motion will often cause tracers to be drawn into thin streaks that have much greater surface area than would occur absent the deformtion. This stirring process can accelerate the homogenization of a tracer.

Numerical models have considerable freedom to choose how specific terms and processes are evaluated, and an understanding of Lagrangian-Eulerian representations can be very helpful in understanding the design of efficient numerical methods, Sec. 5. Advection of tracer fields can be represented by a straightforward evaluation of the Eulerian advection terms, $\mathbf{V} \cdot \nabla(\text{tracer})$, or, it can be treated by following the predicted or hindcast motion of parcels that conserve their tracer values. This latter approach, often called semi-Lagrangian advection, can yield efficient and accurate numerical solutions of advection processes. Particle in Cell models are the semi-Eulerian complement; they follow particles for long times and so are Lagrangian, but evaluate pressure gradients or gravitational attraction by mapping particle masses to a grid.

Finally, Sec. 6 returns to the Lagrangian observations of Part 1 Fig. 1 for an analysis of the vorticity balance of the mesoscale motion (space scales $O(10^5)$ m). The vorticity is estimated from a velocity gradient tensor fitted to a cluster of floats that are followed for several months. The vorticity of the float cluster is observed to change in a way that is consistent with approximate conservation of the potential vorticty, the sum of planetary and relative vorticity divided by the water depth.

1.2 Acknowledgments

Financial support during preparation was provided by the Academic Programs Office of the Woods Hole Oceanographic Institution and by the U.S. Office of Naval Research. Administrative support was provided by the Department of Physical Oceanography, Woods Hole Oceanographic Institution.

This essay is dedicated to Prof. Tom Rossby, Graduate School of Oceanography, University of Rhode Island, whose generosity and enthusiasm for Lagrangian measurements of the ocean made a lasting impression.

These essays and associated materials may be cited by their Massachuetts Institute of Technology OpenCourseWare address: Price, James F., 12.808 Supplemental Material, Topics in Fluid Dynamics: Dimensional Analysis, a Coriolis tutorial, and Lagrangian and Eulerian Representations, https://ocw.mit.edu/courses/res-12-001-topics-in-fluid-dynamics-fall-2023 (date accessed). Future, major revisions will be archived on the MIT/OCW site, while minor, interim revisions will be posted to the author's web page, https://www2.whoi.edu/staff/jprice/ Copying and distribution for educational purposes is specifically allowed consistent with the license: Creative Commons, CC BY-NC-SA.

2 Tracking parcels in a velocity field

2.1 Parcel trajectories

Let the position of a specific parcel be denoted by $\tilde{\mathbf{X}}(t)$, where the tilde denotes a Lagrangian variable as in Part 1. The trajectory of a parcel is the history of the integrated Lagrangian velocity,

$$\tilde{\mathbf{X}}(\mathbf{A},t) \;=\; \int_0^t \tilde{\mathbf{V}}(\mathbf{A},t) \;+\; \mathbf{A}, \tag{1}$$

where the parcel is identified by the initial position, $\mathbf{A}$. The presumption made here in Part 2 is that we know the Eulerian velocity field, $\mathbf{V}(\mathbf{X},t)$, which may be evaluated for the necessary Lagrangian velocity by reversing the fundamental principal of kinematics (FPK) of Part 1,

$$\boxed{\tilde{\mathbf{V}}(\mathbf{A},t) \;=\; \mathbf{V}(\mathbf{X}=\tilde{\mathbf{X}}(\mathbf{A},\,t),t)} \tag{2}$$

The entire content of this important equation rests on the presence (or not) of the tildes. A literal translation of (2) is that the Lagrangian velocity of a parcel that is at the position $\tilde{\mathbf{X}}(\mathbf{A},t)$ is the Eulerian velocity at that position $\mathbf{X} \;=\; \tilde{\mathbf{X}}(\mathbf{A},t)$. In words — to know where you are going, you have to know where you are (Fig. 2).[1]

Given (1) and (2), we have the prescription for a

parcel trajectory from Eulerian velocity: $$\boxed{\tilde{\mathbf{X}}(\mathbf{A},t) \;=\; \int_0^t \mathbf{V}(\mathbf{X}=\tilde{\mathbf{X}}(\mathbf{A},t),t) \;+\; \mathbf{A}} \tag{3}$$

[1]This and similar figures were made by the author using AI and DALL.E 2.

Figure 2: Have you ever had a day that left you wondering...

Swirling and chaotic,
Where will life carry me next?
Well, where am I now?

The trajectory equations (3) are typically implicit, in that the integrand will usually depend upon $\tilde{\mathbf{X}}$. If the x component of velocity u depends upon y or v, or if v depends upon x or u, then these are coupled equations that have to be solved simultaneously. In either case, the integration of (3) will generally have to be sought with numerical methods. The trajectory will certainly have to be solved numerically when $\mathbf{V}$ is the product of a numerical model and comes in the form of gridded, four-dimensional fields (x, y, z and t), as in Fig. (1). The procedure is straightforward in principle. Given a present position and time, find the present velocity by four-dimensional interpolation of the gridded Eulerian fields. Using this velocity, step the position forward in time. At the new position, again interpolate the Eulerian fields to obtain the new velocity, and step forward in time once more, repeating to the end. The accuracy and efficiency of the trajectory calculation will often be improved by employing somewhat sophisticated interpolation schemes, and by time-stepping with predictor-corrector or Runga-Kutta schemes.

Granted that most applications will require numerical methods, it is nevertheless useful to consider a very simple two-dimensional velocity field that will permit analytic solutions,

$$\mathbf{V}(x,y,t) \;=\; x\mathbf{e}_x \;+\; \frac{y}{1+2t}\mathbf{e}_y, \tag{4}$$

which is plotted for two times in Fig. 3. The component equations of a trajectory are then

$$\frac{d\tilde{x}}{dt} \;=\; \tilde{x}, \quad \text{and} \quad \frac{d\tilde{y}}{dt} \;=\; \frac{\tilde{y}}{1+2t}. \tag{5}$$

Since the tilde appears on all of the x and y, we can just as well drop them, with the understanding that x and y are the coordinates of a specific, moving parcel, and, the x and y on the right hand sides of (5) are the same thing as the x and y on the left hand sides. Suitable initial conditions are

$$x \;=\; a, \quad \text{and} \quad y \;=\; b \quad \text{at} \quad t \;=\; t_o.$$

Within each component equation the independent variables can be readily separated,

$$\frac{dx}{x} \;=\; dt \quad \text{and} \quad \frac{dy}{y} \;=\; \frac{dt}{(1+2t)},$$

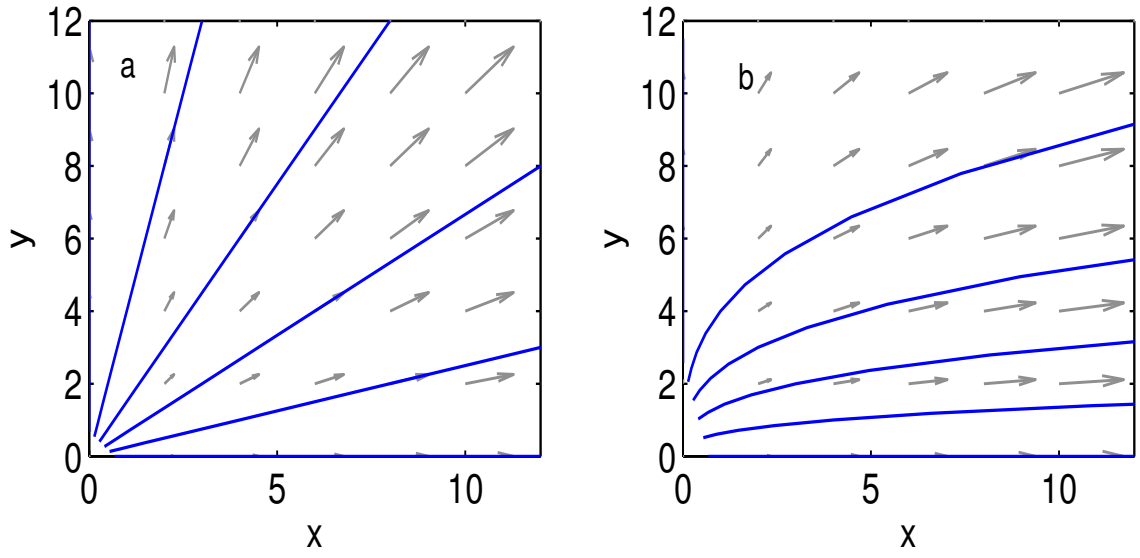

Figure 3: **(left)** Velocity field and streamlines (the family of blue, solid lines) for Eq. (5) at $t = 0$, and at $t = 1$ **(right)**. The velocity at a given point turns clockwise with time as the y-component of the velocity decreases with time.

and then integrated over the limits a to x, b to y, and t_o to t to yield the trajectory components,

$$x(a,t_o,t) \;=\; a\; exp(t-t_o) \qquad \text{and} \qquad y(b,t_o,t) \;=\; b\frac{(1+2t)^{1/2}}{(1+2t_o)^{1/2}}. \tag{6}$$

The y-component was seen also in Part 1, but here the initial time has been retained for use below.

Trajectories starting from a few different a and b are in Fig. 4. The Eulerian velocity is everywhere upward and to the right, and so it is no surprise that the trajectories do about the same thing, Fig. 3. The trajectories bend downward in time, consistent with the temporally-decreasing y-component of the velocity field. In a later section 2.5 we will see a case where the Eulerian and the Lagrangian mean flows are qualitatively different, and the trajectories could not have been anticipated in advance of an integration.

2.2 Backward trajectories

Trajectories are forward in time in that they show where a parcel released at a given point and time will be found at some later time due to transport by the velocity field. However, if we know the history of the velocity field, then this parcel tracking can be reversed to determine where a parcel observed at a given time and place came from. Let t_o be the present time, t_b be the time going backward, then $t' = t_o - t_b$ is the time in the past, and the origin of the parcel may be evaluated from

$$\tilde{\mathbf{x}}(t') \;=\; -\int_0^{t'} \mathbf{V}\left(\tilde{\mathbf{x}}(t'),t'\right) dt', \tag{7}$$

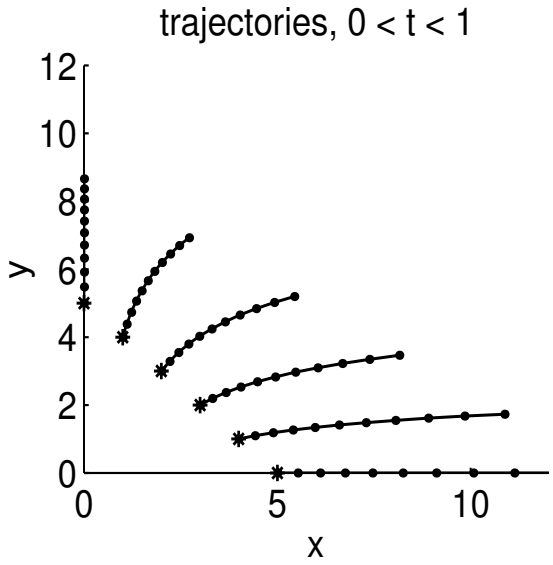

Figure 4: Trajectories of six parcels that were released into the flow given by Eq. (5). The sources are shown by asterisks. They were released at the same time, $t_o = 0$, and tracked until $t = 1$. Dots along the trajectories are at time intervals of 0.1. In this very simple flow, the trajectories are as you would expect from the Eulerian velocity field seen above. That will not always be the case with flows that have more complex time and space dependence.

and similarly for the $\tilde{y}$-component. This kind of backward trajectory calculation is the backbone of air quality studies that seek to determine the source of pollutants observed at a given site.[2]

The essential idea of a backward trajectory is that a given parcel position can be associated with a unique position at any previous time. This is plausible for advection by a resolved velocity field, but not when diffusion is also present. Diffusion effectively spreads the future position of a parcel over a domain that grows as the square root of time. Indeed, the notion of a discrete, trackable parcel and diffusion are somewhat incompatible, and better to think instead of the tracer value. In the presence of diffusion, the tracer value at a given time and place will depend upon some average of the tracer field over a domain that size of which increases with the elapsed time.

2.3 Streaklines are a snapshot of parcels having a common origin

Another useful characterization of the history of parcel positions is called a streakline, which shows the positions, at a fixed time, of all of the parcels which at some earlier time passed through a given point. A natural example of this is the plume of smoke coming from a point source located at $\mathbf{x}_p$ and recorded, say by a photograph taken at a time, t_p. The information needed to construct a streakline is contained within the trajectory, Eq. (6). To construct a streakline, release parcels one after the other from a fixed source. The first parcel is released at time $t_0 = 0$, and let the trajectory run until $t = t_p$, and then take a

[2]Examples are at https://www.arl.noaa.gov/hysplit/ and a very thorough tutorial on methods used to estimate backward trajectories from meteorolgical data is online at https://www.ready.noaa.gov/documents/Tutorial/html/index.html See also https://diginole.lib.fsu.edu/islandora/object/fsu:389481/datastream/PDF/view

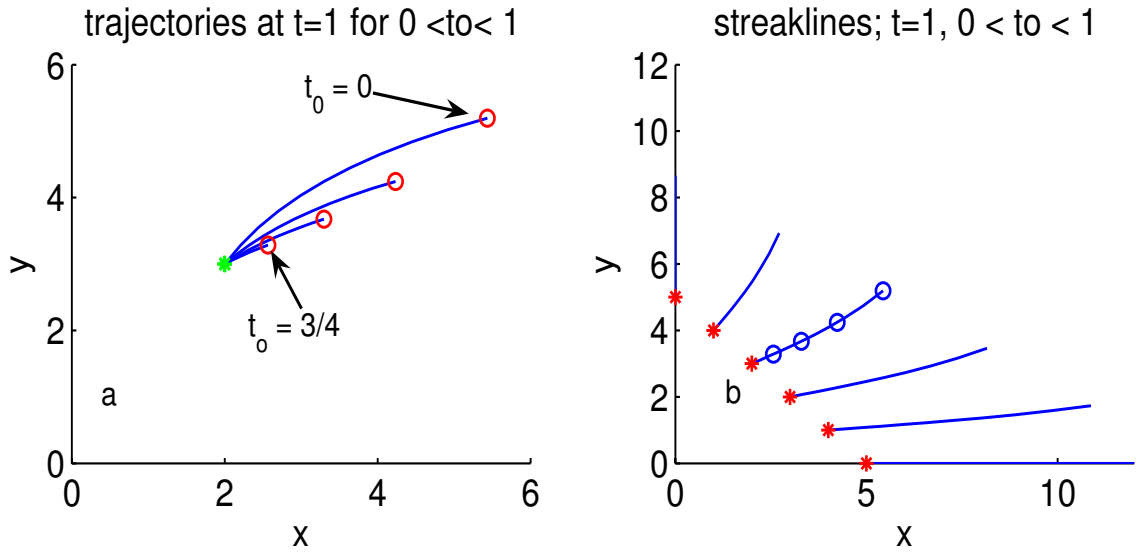

Figure 5: **(left)** Trajectories of five parcels that were released from a common source, (x,y) = (2,3), and tracked until $t = 1$. The parcels were released at different initial times, $t_0 = 0,\ 1/4,\ 2/4,\ 3/4$, and 1. The latter trajectory has zero length. The end points of the trajectories are the open circles, the locus of which forms a streakline. **(right)** Streaklines from several different sources. These streaklines start at $t_0 = 0$ and the 'photograph' was taken at $t_p = 1$. Notice that these streaklines end at the endpoint of the trajectories of Fig. 4 (they have that one point in common) but that streaklines generally have a different shape (different curvature) from the trajectories made over the same time range. In this figure and in previous ones (Fig. 2b) the two quantities being compared are only slightly different, and you might well wonder if, for example, streaklines are some kind of approximation to trajectories. The answer is no, in general, they are qualitatively different things.

photograph. The only data retained from this trajectory is the position at time $t = t_p$, i.e., record $\mathbf{x}(t_p, \mathbf{x}_p, t_0 = 0)$. A second parcel is released a little later, say at $t_0 = \frac{1}{4}$, and again let the trajectory run until $t = t_p$, keeping only the last position, $\mathbf{x}(t_p, \mathbf{x}_p, t_0 = \frac{1}{4})$. A third parcel is released at $t_0 = \frac{2}{4}$, and so on. It appears, then, that a recipe for making a streakline from a trajectory is to treat the initial time, t_0, as a variable, while holding t constant at t_p, and also the initial position at $\mathbf{x} = \mathbf{x_p}$. Several streaklines are in Fig. 5. Notice that in this time-dependent flow, trajectories and streaklines are not parallel.

2.4 Streamlines are parallel to an instantaneous flow field

Still another and widely useful method for depicting a velocity field is to draw the streamlines, a family of lines that are everywhere parallel to the velocity. Time is fixed, say at $t = t_f$, and thus streamlines portray the direction field of a velocity field, with no reference to parcels or trajectories or time-dependence of any sort. There is more than one way to construct a set of streamlines, but a method that lends itself to generalization is to solve for the parametric representation of a curve, $\mathbf{x}(s)$ that is everywhere parallel to the velocity;

$$\boxed{\frac{d\mathbf{x}}{ds} = \mathbf{v}(t_f, x, y)} \tag{8}$$

or in components;

$$\frac{dx}{ds} = u(t_f,x,y); \quad \frac{dy}{ds} = v(t_f,x,y). \tag{9}$$

A suitable initial condition is $x(s_0) = x_0$, etc. Notice that s is here a dummy variable; any other symbol could be used, but s is conventional.[3] $\mathbf{x}$ is the position of a point on a line, where just above $\mathbf{x}$ meant the position of a parcel. This reuse of symbols is risky practice, but it is also almost unavoidable. Given the velocity components Eq. (5), these equations are also readily integrated to yield a family of streamlines:

$$x = x_0\, exp(s-s_0); \quad y = y_0\, exp\left(\frac{s-s_0}{1+2t_f}\right), \tag{10}$$

and recall that t_f is the fixed time chosen to draw the streamlines. The integration constants may be chosen so that a given streamline will pass through an arbitrary position. There is no rule for choosing these positions; in Fig. 3 there were five positions chosen arbitrarily, and then s was varied over sufficient range to sweep through the domain. Other streamlines could be added if needed to help fill out the picture. No particular value is attached to a given streamline. The streamline's sophisticated cousin, the streamfunction, has isolines that are also parallel to velocity, and which are assigned values that are directly related to the speed of the flow and the distance between streamlines.

2.5 Tracking parcels around a steady vortex given limited Eulerian data

The previous sections developed the formal methods needed to transform Eulerian velocity (Lagrangian) trajectories and other variables that help depict properties of a fluid flow. An understanding of the formal steps is important, of course, but the ease with which those transformations were made resulted from the assumption of a very simple closed solution for the Eulerian velocity — not something you are likely to encounter outside of a homework problem. In practice, partial and incomplete information is the norm, and so this section will consider an approximate analysis method based upon an expansion of the velocity field in Taylor series. This yields results that are interesting and important of themselves, especially the notion of Stokes drift that will come up in Sec. 2.6.

The power and the limitations of the Taylor series method can be appreciated by analysis of parcel motion in a steady, irrotational vortex in R^2. The radial and azimuthal velocity components of such a vortex are

$$\mathbf{V} = \begin{pmatrix} u_r \\ u_\theta \end{pmatrix} = \begin{pmatrix} 0 \\ \frac{C}{2\pi r} \end{pmatrix} \tag{11}$$

where r is the distance from the vortex center. The $1/r$ dependence of the azimuthal speed is the distinguishing feature of an irrotational vortex. C is a constant, termed the circulation,

$$C = \oint \mathbf{V}\cdot d\mathbf{s},$$

[3]The notion of a parameterized curve is central to the method of characteristics discussed in Part 1, Sec. 4. The parameter s could be regarded as time, with care not to confuse this use of time with the time-dependence of the velocity field (which is suppressed while drawing a map of streamlines). This helps make clear that streamlines are parallel to parcel trajectories in steady flows, and, are also the characteristics of the advection equation.

where $d\mathbf{s}$ is the vector line segment along a path that encloses the vortex center and that is traversed in an anti-clockwise direction. C measures the vortex strength, and without loss of generality we can set $C = -2\pi$ to define a vortex that rotates clockwise, Fig. (6). Parcel trajectories in this steady vortex will be circular, and a parcel will make a complete orbit in a time $T = (2\pi r)^2/C$. The Cartesian velocity components of the vortex are

$$\begin{pmatrix} u \\ v \end{pmatrix} = \frac{C}{2\pi r}\begin{pmatrix} \sin\theta \\ \cos\theta \end{pmatrix} \tag{12}$$

where $r = (x^2 + y^2)^{1/2}$ and the angle $\theta = \text{atan}(y/x)$ is measured counter-clockwise from the x-axis.

An irrotational vortex is an idealization of the vortex flow produced by the convergent flow into a drain or the starting vortex left behind an accelerating airfoil. These vortices have several interesting properties that will be considered in later sections (including why they are said to be irrotational). For now, (12) makes a convenient flow into which floats and current meters may be inserted in order to investigate kinematics.

2.5.1 The zeroth-order approximation, or PVD

For the sake of this development, imagine that the only thing known about this vortex is the velocity observed at one fixed site, say $(x,\ y) = (0,\ 1)$. The velocity observed at this fixed site, $\mathbf{V}_0 = \mathbf{V}(x,\ y)$ is, of course, an Eulerian velocity, and is a steady, uni-directional flow having Cartesian components $(U_0,\ V_0) = -(C/2\pi r,\ 0) = (1,\ 0)$. What, if anything, can be inferred about parcel trajectories from this very limited data?

If no other information was available, then out of desperation one might estimate a pseudo-trajectory, called a progressive vector diagram, or PVD, by integrating this Eulerian velocity in time as if it were the Lagrangian velocity of a moving parcel,

$$\delta\mathbf{x}_0 \ = \ \int \mathbf{V}(x_o,t)\, dt \ = \ \begin{pmatrix} U_0\, t \\ 0 \end{pmatrix}. \tag{13}$$

It is essential to understand that (13) is wrong, formally, as it completely misses the distinction between Lagrangian and Eulerian velocity (you would never do that, would you?).

It is fruitful to think of the PVD estimate as a zeroth-order approximation of a true trajectory. The PVD in this case indicates a linear, pseudo-trajectory, consistent with the velocity observed at the fixed site, Fig. (6), dotted line. A PVD is a useful way to visualize a current meter record or a wind record insofar as it gives a direct measure of how much fluid has gone past an observation site. Is there any flow condition under which a PVD could be interpreted as if it were a true, parcel trajectory? Yes, a PVD would represent a true trajectory if the Eulerian velocity field was spatially uniform. Observations made at any position would then be equal to observations made anywhere else, including at the moving position of a parcel. A spatially uniform flow is a degenerate case of little practical interest, but this helps to show that the issue is the spatial variation of the flow.

From the example of a steady vortex flow of Fig. (6), it would appear that the PVD is a reasonable estimate provided that the inferred displacement is considerbly less than the horizontal scale, L, over

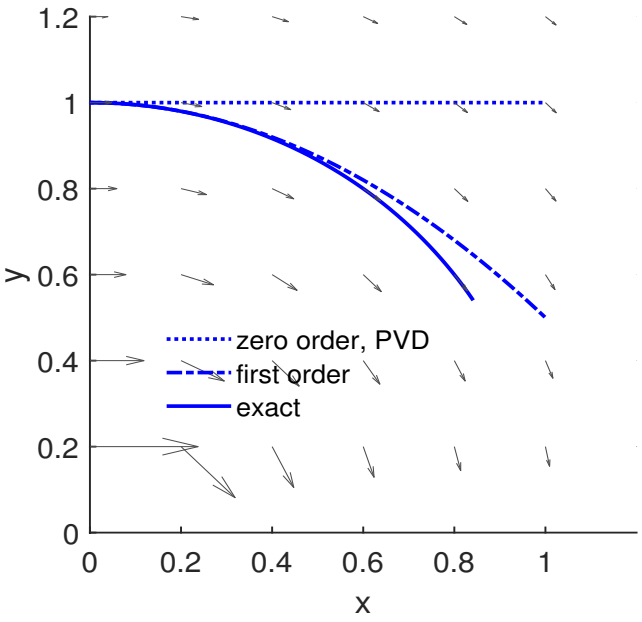

Figure 6: Parcel tracking around an irrotational vortex. A parcel was launched at $(x,y) = (0,1)$ and tracked up to $\delta t = 1$. The exact trajectory (solid line) is easily computed in cylindrical coordinates. The zeroth order approximation, or PVD, in which the Eulerian velocity measured at the fixed observation site (where $U_\theta = 1$) has been integrated as if it were the Lagrangian velocity, is the dotted line and has a net displacement $\delta x_o = 1$. The PVD starts off well enough, but begins to diverge noticably from the exact trajectory after the displacement exceeds about 0.1. The first order trajectory (dash dot line) accounts approximately for the spatial variation of the velocity and is somewhat better than the PVD, but it too becomes rather inaccurate as the displacement becomes comparable to the length scale of the flow, L, in this case the distance to the vortex center, $L = 1$.

which the flow changes significantly. This condition could be written

$$\delta x_0 \approx U\, t_a << L,$$

with U the speed and t_a the advection time, or

$$\frac{t_a\, U}{L} << 1.$$

An advection time that satisfies this condition will be called the short time advection approximation, since time (rather that U or L) is likely to be the independent variable. By inspection, the horizontal scale of this vortex flow is estimated to be the radial distance to the vortex center, $L = 1$ at the site chosen, and $U = 1$, as well. Hence the PVD pseudo-trajectory makes a reasonable estimate of the actual trajectory for times $t_a \leq 0.1$, which is 1/10 of the elapsed time shown in the trajectories of Fig. (6). In problem 4) below, the error of the PVD (defined as distance to the trajectory) will be estimated as $\delta t^2/2$ and so $\delta t \leq 0.1$ should be acceptable for many purposes.

2.5.2 The first order approximation

Evidently we can not get far from the starting point knowing only the velocity at that one point, so let's give ourselves another piece of information, the velocity gradients, but only at the starting point. With

this new piece of data we can take some account of the spatial variation of the velocity. The plan is to represent the velocity field in the vicinity of the stating point by expanding in a Taylor series, here for each component separately,

$$\begin{aligned} u(x,y) &= u_0 + \frac{\partial u}{\partial x}\delta x + \frac{\partial u}{\partial y}\delta y + HOT, \\ v(x,y) &= v_0 + \frac{\partial v}{\partial x}\delta x + \frac{\partial v}{\partial y}\delta y + HOT, \end{aligned} \tag{14}$$

where (u_0, v_0) is the velocity observed at the starting point, the partial derivatives are evaluated at the same point, and HOT is the sum of all the higher order terms that are proportional to $\delta x^2, \delta x^3$, etc. In effect, this presumes knowing not only the velocity but also the (spatial) partial derivatives of velocity, though at one position only. It is convenient to use a vector and tensor notation to write equations like these in a form

$$\mathbf{V}(x,y) = \mathbf{V}_0 + \mathbb{G}\cdot\delta\mathbf{x} + HOT, \tag{15}$$

where $\mathbb{G}$ is the velocity gradient tensor encountered in Sec. 3, Part 1, and repeated here for the two-dimensional case at hand,

$$\mathbb{G} = \begin{pmatrix} \dfrac{\partial u}{\partial x} & \dfrac{\partial u}{\partial y} \\ \\ \dfrac{\partial v}{\partial x} & \dfrac{\partial v}{\partial y} \end{pmatrix}$$

$\mathbb{G}$ is a device to streamline notation; when we (matrix) multiply $\mathbb{G}$ into a displacement vector (written as a column vector), the result is the velocity difference that corresponds to that displacement vector.[4] It is easy to see that if the displacement vector was doubled or halved, then the result would be twice or half the velocity difference. Thus, multiplication by a velocity gradient tensor serves to make a linear transformation on a displacement vector. In general, the result will be a velocity difference vector having a different direction from that of the displacement vector, and of course it has a different amplitude and different physical dimensions as well. The velocity gradient tensor evaluated at the observation site

[4] **G** is a Cartesian tensor for which the multiplication rules are the same as that of matrices. This raises the question — is there a difference between a matrix and a tensor? A matrix is more general in that the elements can be pretty much anything. A matrix is usually an array of numbers that have a relationship to some other matrix (or vector) so that the rules of matrix multiplication, addition, etc., yield the desired form. There are no restrictions on what the matrix elements represent: there could be elements representing temperature and savings account balance in the same matrix. There is no implied rule that specifies how the matrix elements should change if the scale or system of units should change, say Farenheit to Centigrade and dollars to euros. On the other hand, a tensor is intended to represent a physical quantity having a geometric significance and thus a magnitude and a direction. The elements of a velocity gradient tensor have a crucially important dependence upon a coordinate system. For example, if rectangular coordinate axes are rotated 45 degrees clockwise, then the elements of the velocity gradient tensor must rotate 45 degrees anti-clockwise so that the velocity shear, which has a physical meaning, is invariant to the arbitrary orientation of the coordinate system. The elements of a velocity gradient tensor are thus said to be contravariant with respect to the unit vectors of the coordinate system. No such transformation rule is implied for the elements of a matrix.

$(x_s,\, y_s) = (1,\, 0)$ has a simple form

$$\mathbb{G} \;=\; \frac{C}{2\pi}\begin{pmatrix} 0 & 1 \\ 1 & 0 \end{pmatrix} \;=\; \begin{pmatrix} 0 & -1 \\ -1 & 0 \end{pmatrix},$$

where recall we have taken $C = -2\pi$.

The PVD approximation amounts to an integration of the first term only of the Taylor series, while ignoring the spatial variation of the velocity altogther. Since this approximation omits all terms that are first and higher power in the displacement, the PVD is termed the zeroth order, pseudo-trajectory. The first order trajectory, i.e., the first correction to the trajectory, can then be computed by dropping the HOT from Eq. (15), and approximating

$$\delta\mathbf{x}_0 \;=\; \int \mathbf{V}_0\, dt$$

and integrating in time,

$$\delta\mathbf{x}_1 \;=\; \delta\mathbf{x}_0 \;+\; \mathbb{G}\cdot\mathbf{V}_0 t^2/2. \tag{16}$$

This gives a considerable improvement upon the zeroth-order PVD (Fig. 6), the dot-dash line. If our interest was limited to short times only, then this might make a useful approximate solution for a trajectory. However, after sufficient time has passed and the displacement becomes comparable to the length scale of the flow, the radius of the vortex, then this first order pseudo-trajectory also accumulates a noticeable error. Adding an evaluation of the next term of the HOT would delay the failure, in general, but in any steady vortex flow the displacement will eventually carry a parcel a long distances from its origin. One way to describe this shortcoming is that approximation methods built around a Taylor series expansion are not uniformly valid in time when applied to a steady vortex flow.

2.6 Tracking parcels in water waves

The notion of such a pseudo-trajectory may be applied fruitfully to a wavelike motion in which the parcel displacements during a wave passage are small compared to the wavelength. Consider a surface gravity (water) wave having a surface displacement

$$\eta(x,t) \;=\; a\cos(kx-\omega t), \tag{17}$$

where a is the amplitude of the surface displacement, $k = 2\pi/\lambda$ is the wavenumber given the wavelength λ and ω is the wave angular frequency (it is assumed that ω and $k > 0$). The argument of the trigonometric function shows that this surface displacement moves rightward as a progressive wave having a phase speed $c = \omega/k$. The two-dimensional and time-dependent velocity field associated with this wave

$$\mathbf{V}(x,z,t) \;=\; Ue^{kz}\begin{pmatrix} \cos(kx-\omega t) \\ \sin(kx-\omega t) \end{pmatrix}, \tag{18}$$

where z is the depth, positive upwards from the surface. The amplitude or speed at the surface is $U = a\omega$ and decays with depth on an e-folding scale $1/k$. This exponential decay with depth is appropriate for a wave whose wavelength is less than the water depth, a so-called deep water wave. If the wavelength is

much greater than the water depth, in which case a shallow water wave, the x component of the velocity is approximately independent of depth and the z component is linear with depth and vanishes at the (flat) bottom.[5]

2.6.1 The zeroth order approximation, closed loops

The (Eulerian) velocity observed at a fixed point is a rotary current, often called the wave's orbital velocity, of amplitude $a\omega e^{kz}$ that turns clockwise with time at the angular frequency ω (assuming that x increases to the right). Given the known velocity the PVD-like parcel displacements are estimated by integrating $\mathbf{V}(x,z,t)$ with respect to time while holding x and z constant,

$$\delta\mathbf{x}_0 \;=\; ae^{kz}\begin{pmatrix} -\sin(kx-\omega t) \\ \cos(kx-\omega t) \end{pmatrix}. \tag{19}$$

The PVD indicates that parcels move in a closed rotary motion with each wave passage and that the net motion is zero, consistent with the wave-average of the Eulerian velocity.

The analysis of motion around a vortex suggests that this PVD for a gravity wave would probably give a fairly accurate prediction for the actual parcel displacements provided that the parcel displacements were much, much less than the scale over which the wave orbital velocity varies. In this case the scale is k^{-1} in either direction, so that this condition is equivalent to requiring that the wave steepness, $ak = 2\pi a/\lambda$ must be much less than 1. This is also the condition under which the linear solution gives an accurate waveform of the surface displacement, a pure sinusoid, which we have assumed with Eq. (17).

2.6.2 The first order approximation, Lagrange = Euler + Stokes

However, it is dubious that this zeroth order approximation of the trajectories can tell us anything reliable about the actual trajectories, and so let's proceed to calculate the first order velocity via Eq. (15). The velocity gradient tensor for this wave is just

$$\mathbb{G} \;=\; a\omega k e^{kz}\begin{pmatrix} -\sin(kx-\omega t) & \cos(kx-\omega t) \\ \cos(kx-\omega t) & \sin(kx-\omega t) \end{pmatrix}$$

[5] An excellent introduction to surface gravity waves is 'Water Wave Mechanics for Engineers and Scientists', by R. G. Dean and R. A. Dalrymple, World Scientific Pub. Co., 1991. For Stokes drift in particular see also Longuet-Higgins, M. S., 1969. 'On the transport of mass by time-varying ocean currents'. *Deep-Sea Res.*, **16**, 431-447 and Longuet-Higgins, M. S., 1986. 'Eulerian and Lagrangian aspects of surface waves', *J. Fluid Mech.*, **173**, 683-707.

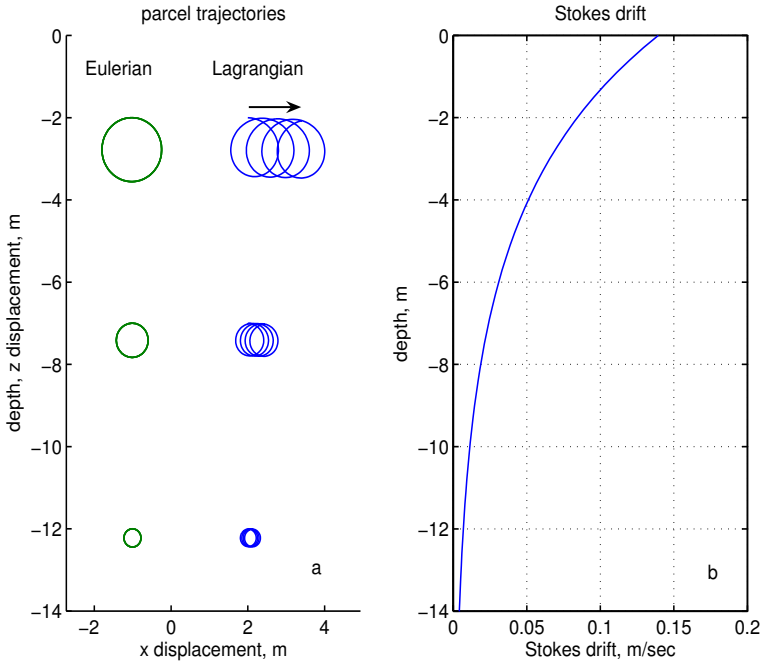

Figure 7: **(left)** Parcel trajectories underneath a deep-water, surface gravity wave that is presumed to be propagating from left to right. The amplitude of the surface displacement was taken to be $a = 1$ m and the wavelength $\lambda = 50$ m. The Eulerian trajectories (or PVDs) are closed circular orbits around which the parcels move clockwise. The Lagrangian trajectories were computed by integrating numerically for four periods (= 22.6 sec) and are open loops indicating there is a net drift of fluid parcels from left to right (shown as an arrow). **(right)** Stokes drift for this wave computed from Eq. (20). An animation of a gravity wave and parcel trajectories is linked in the next figure.

and matrix-multiplying into the zeroth order displacement given by Eq. (19) gives the first order velocity (insofar as the HOT have been dropped),

$$\begin{aligned} \mathbf{V}_1(z) &= a^2\omega k e^{2kz}\begin{pmatrix} \sin^2(kx-\omega t)+\cos^2(kx-\omega t) \\ 0 \end{pmatrix} \\ &= Uake^{2kz}\begin{pmatrix} 1 \\ 0 \end{pmatrix}, \end{aligned} \tag{20}$$

where recall $U = a\omega$ is the amplitude of the orbital velocity at the surface. The coefficient $Uak = a^2k^2c$ is the wave steepness squared times the phase speed. This velocity is independent of time and x, and so the first order displacement is easily computed,

$$\delta\mathbf{x}_1(z) = \mathbf{V}_1(z)t, \tag{21}$$

where there is no particular initial position. Notice that this formula relates the displacement of a parcel to a depth, i.e., a field coordinate, so that it gives a field representation of a Lagrangian property.

Quite unlike the PVD, Eq. (21) indicates that fluid parcels have a substantial net motion in the

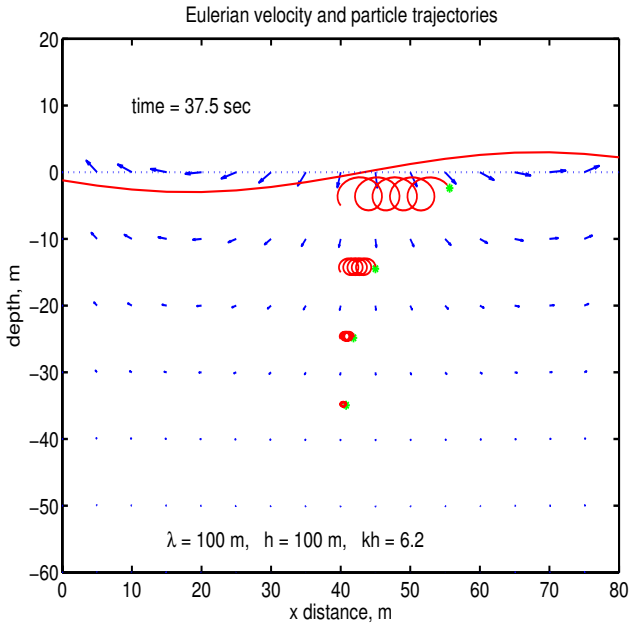

Figure 8: A surface gravity wave propagating from left to right as computed on linear theory. The wave orbital velocity is the array of vectors and the sinusoidal red line is the free surface. This is a rather steep wave: the wave angular frequency ≈ 1 s^{-1}, the surface displacement is 3 m, the wavelength is 100 m in a water depth of 100 m. The spiralling red lines are the trajectories of parcels computed numerically. Notice that parcels have a mean motion to the right, in the direction of the wave propagation, Stokes drift. An animation is available at https://www2.whoi.edu/staff/jprice/wp-content/uploads/sites/199/2022/06/gwavemovie.mp4

direction of the wave propagation, often called Stokes drift or mass transport velocity, that is a fraction $2\pi\frac{a}{\lambda}e^{kz}$ of the orbital motion amplitude. For example, for a wave having an amplitude of $a = 1$ m and wavelength of $\lambda = 50$ m, the orbital motion at the surface is about 1.11 m s^{-1} where the Stokes drift is about 0.14 m s^{-1}. The Stokes drift decreases rapidly with depth, about twice as fast as does the wave orbital velocity.

The vertically integrated Stokes drift is the mass transport per unit length,

$$M = \rho \int_{-\infty}^{0} \mathbf{V}_1(z)dz = \begin{pmatrix} \rho U a/2 \\ 0 \end{pmatrix},$$

and also the momentum per unit area associated with the wave. The kinetic energy per unit area of the wave motion is

$$K = \rho \int_{-\infty}^{0} \mathbf{V}(z)^2 dz = \rho U c a/4.$$

Thus the momentum in the direction of gravity wave propagation and the kinetic energy of gravity waves are related by the particle-like relation

$$M = \frac{2K}{c},$$

which holds for other kinds of waves, e.g., electromagnetic waves, that have genuine momentum.[6] Thus, the Stokes drift turns out to be much more than a residual effect of switching from an Eulerian to a Lagrangian coordinate system and indeed it is one of the most important means by which surface gravity waves interact with other scales of motion.[7] It is notable that all of the information needed to calculate the Stokes drift was present in the Eulerian velocity field, Eq. (18). However, to reveal this important phenomenon required an analysis that was explicitly Lagrangian, i.e., that tracked parcels over a significant duration.

Two comments regarding the Stokes drift. First, it has been estimated as the product of two terms that are derived from a linear solution, the velocity gradient tensor and the PVD displacement, and is thus 'bilinear'. The amplitude of the Stokes drift is proportional to the wave amplitude squared. This seems to imply that the Stokes drift estimated from a nonlinear wave might be rather different from that calculated here. We don't intend to carry this calculation any further, but will simply note that this is not the case, assuming only that the nonlinear wave is not grossly distorted from the linear solution. A nonlinear correction to the linear solution gives only a nonlinear correction squared (and probably very small) to the Stokes drift. Second, the Stokes drift can be envisaged as the difference between the time-integral of the Eulerian and Lagrangian velocities in the sense that, averaged over a wave, the various fluid velocities can be imagined related by Euler + Stokes = Lagrange (see Longuet-Higgins of footnote 5, and in the surface wave case, Euler = 0). This stands in marked contrast to the FPK which, recall, applies to the *instantaneous* velocity. Thus Stokes drift arises from time-averaging or integrating, which most observation techniques necessarily do, of course, if only to yield data sets of a manageable size. In other cases, averaging may arise as an inevitable byproduct of the sampling procedure. In either event, the formal FPK may not apply.

2.7 Key ideas

1) Most models in fluid mechanics are Eulerian, and their solutions are defined on a finite grid of spatial coordinates (numerical models) or a continuous field (analytic models). Given complete Eulerian data of this kind it is more or less routine to compute the trajectories of fluid parcels.

2) Calculation of a trajectory from Eulerian data will almost always involve solving an implicit equation or integral: To know where you are going, you have to know where you are.

[6] Waves that exist on a physical medium need *not* have a genuine momentum of this sort, though they will have a momentum flux, see M. E. McIntyre, 'On the wave momentum myth', *J. Fluid Mech.*, **106**, 331-347, 1981. An excellent recent reference on the topic of wave momentum is by D. Rowland, 'Comments on "What happens to energy and momentum when two oppositely-moving wave pulses overlap?"', *Am. J. Phys.*, **72**(11), 1425-1429, 2004. Surface gravity waves have momentum by virtue of the displaced free surface. Here's a small problem for you: show that the Eulerian mean momentum over the water column is equal to the mass transport associated with Stokes drift by making the same kind of (bilinear) approximation for transport that we made for Stokes drift, i.e., assume that the wave velocity $\mathbf{V}$ under the displaced surface is given by Eq. (26) evaluated at $z = 0$, and compute the wave mean of $\eta\mathbf{V}$.

[7] Stokes drift will transport fluid properties as well as any material, e.g., plankton, that are suspended in the fluid. The role of Stokes drift in ocean circulation and ocean ecology is an active topic in ocean science, see McWilliams, J.C. and J.M Restrepo, 'The wave-driven ocean circulation.' *J. Phys. Oceanogr.* **29**, 2523-2540, 1999.

3) Advection alone (without diffusion) is reversible in time. Given the history of the Eulerian velocity, it is possible to compute backwards trajectories that show where fluid came from.

4) Streaklines are the locus of the trajectories that started at a given point but at different times (as in a smoke plume from a fixed, ongoing source).

5) If only limited information is available to define a velocity field, then the estimation of a trajectory will be compromised to some degree. The most extreme example, known as a progressive vector diagram, integrates the velocity observed at a fixed site to compute a pseudo-trajectory, or PVD. A PVD may be a useful approximation to the true Lagrangian trajectory originating from a given point, for short times, $t_a U/L << 1$.

6) The next approximation, utilizing the partial derivatives of velocity, does somewhat better than a PVD, but also fails once the integration time yields a displacement that is comparable to the dominant spatial scale of the velocity field.

7) There is no general relation between the pseudo-trajectories noted above and genuine Lagrangian trajectories observed for long times/large displacements. This is a corollary of 2) above: To know where you will be in the medium- or long-term future, you will have to know where you are at each step of the journey.

8) Parcel trajectories in the presence of wave motion may show a significant mean flow that results from a correlation of parcel displacement and the wave propagation. In the case of surface water waves, there can be a significant Lagrangian mean flow in the direction of the wave propagation, Stokes drift.

2.8 Problems

1) There is an important family anniversary event coming up, and your big idea is a balloon flight for the entire family. You had better get this right. Start with a visit to the HYSPLIT web site, https://www.ready.noaa.gov/HYSPLIT.php and under the READY menu banner select Balloon flight forecasting tools. As you will soon discover, HYSPLIT is not a homework toy model, but rather a comprehensive and sophisticated forecasting tool that will require a little effort on your part. You will be queried for the parameters of a simulated balloon flight that can be forecast ahead for a few days. Define the launch site to be your present position, and choose a height 2000 meters above the ground. Compute the forecast for a flight of, say 48 hours. Did the balloon carry you some place you might want to go? If not, try varying the altitude of the balloon, and the launch time/date, and see if you can come closer to a desirable or at least a safe, dry termination. How sensitive is the trajectory to the launch position?

2) Given the irrotational vortex flow of Sec. 2.5.1, show that the PVD approximation has an error (defined as the distance to the corresponding point on the actual trajectory) that is due almost entirely to the y component of the displacement. Show too that for short integration times, the error increases as δt^2, and hence that $t_a U/L << 1$ makes a plausible bound on the acceptable error of a PVD. Suppose that the launch site for the PVD is taken to be $(x,\ y) = (0,\ 0.2)$, which is much closer the vortex center than the site chosen in Sec. 2.5.1. How does the time t_a change in that case?

3) Stokes drift is a very robust phenomenon that can be produced and observed with quite modest means: fill a flat container with water to a depth of about 2-4 cm. A bath tub works well, but even a large cake pan will suffice. To make gravity waves use a cylinder having a diameter of roughly the water depth and a length that is about half the width of the tank. Oscillate the wave maker up and down with a frequency that makes gravity waves and observe the motion of more or less neutrally buoyant particles; some that float and others that sink to the bottom. You can easily vary three things, the amplitude of the waves, the depth of the water, and the width of the wave maker. Are the waves in your tank shallow water or deep water waves? Describe the mean flow (if any) set up by the oscillating wave maker, and how or whether it varies with the configuration of the tank and wave maker.

4) Suppose that the one-dimensional velocity in a progressive wave is given as $Ucos(kx-\omega t)$. Calculate the Stokes drift approximation of the mean parcel motion in this wave, and compare the result to the numerical integration of the full trajectory equation, i.e., $dx/dt = Ucos(kx(t)-\omega t)$. This requires a small program or script and can be accomplished with a rather crude numerical method. For what range of wave steepness does the Stokes drift estimate give an accurate estimate of the mean flow? Why do parcels have a Stokes drift in this wave?, i.e., explain why parcels in this wave velocity field have a net motion. What happens at large steepness? How does this compare with your observations from the bath tub? How does this compare with the Stokes drift of a deep water gravity wave?

5) Suppose that you can make perfect Lagrangian measurements at arbitrarily fine temporal resolution. How would you use these data to construct the corresponding Eulerian velocity field? Now suppose, more realistically, that your Lagrangian measurements are averages over some finite time interval, say many wave periods in a case where surface gravity waves are present. How would you (or could you) construct the corresponding Eulerian velocity field from those data?

3 Rotation and deformation of fluid parcels

You have likely noticed that advection by a real fluid flow does much more than simply translate parcels from place to place; the swirling flow in a teacup will cause a tracer patch (a macroscale parcel) to rotate, and will draw out a tracer patch into a long, thin streak. This rotation, and the change in shape, called a deformation, can have significant consequences.

To pose a definite problem, consider the motion of a tracer patch that is released into a steady, clockwise rotating, vortical flow; first a solid body rotation, in which the azimuthal speed increases with radius as r

$$\textbf{solid body vortex}, \quad \mathbf{V} = (u_r, \ u_\theta) = (0, \ \Omega_o \, r), \tag{22}$$

where Ω_o is the rotation rate, and then an

$$\textbf{irrotational vortex}, \quad \mathbf{V} = (u_r, \ u_\theta) = (0, \ \frac{\Omega_o \, r_o^2}{r}), \tag{23}$$

in which the azimuthal velocity decreases with r as is $1/r$. There is no radial velocity in either vortex. The rotation rate at $r = 1$ was taken to be $\Omega_o = -1$, which is clockwise, and $r_o = 1$.

These vortex flows are idealizations, and yet with a little effort (imagination?) something akin to both kinds of vortices can be observed in the flow in a teacup: more or less irrotational vortices are

observed to spill off the edges of a spoon that is pushed through the fluid, and at longer times the azimuthal motion that fills the teacup may approximate a solid body rotation (except near the edges).[8]

The first task is advect the tracer with these velocity fields. Given the azimuthal symmetry of these vortex flows, it is desirable to calculate the tracer advection in polar coordinates $(r,\ \theta)$. The polar coordinates of the points $(x_b,\ y_b)$ that define the boundary of the tracer patch were computed from the usual,

$$r_b \ = \ \sqrt{(x_b^2 + y_b^2)} \ \text{ and } \ \theta_b \ = \ \text{atan}(y_b, x_b).$$

The radius is unchanged by the purely azimuthal vortex flows, while the angle θ changes at the rate $\Omega(r)$ appropriate to the r and vortex model,

$$r_b^{i+1} \ = \ r_b^i \quad \text{and} \quad \theta_{\rm b}^{\rm i+1} \ = \ \theta_{\rm b}^{\rm i} \ + \ \delta {\rm t}\, \Omega({\rm r}), \tag{24}$$

with $(\ \ )^i$ the i-th time, and δt is a small time step. The solution for $r(t)_b$ and $\theta(t)_b$ is, in effect, a characteristic for the parcel b, and can be computed as far out in time as needed. Since there is no diffusion or source (the flow is adiabatic), the tracer is constant in time along the charateristics (Sec. 4, Part 1).

The tracer is transported clockwise in both vortices (Fig. 9) as expected from the sign of Ω; there is nothing quite as surprising as Stokes drift (Sec. 2.5) that can make the Lagrangian mean flow (the long term displacement of a parcel) qualitatively different from the Eulerian mean flow (what you would guess given the velocity field). Aside from that, the effects of advection are remarkably different. The solid body rotation (Fig. 9, left) leaves the shape of the tracer patch unchanged, while the orientation changes at the rate $-\Omega$ that characterizes the rotation rate of the entire vortex. The irrotational vortex (Fig. 9, right) produces a strong deformation of the tracer patch, but leaves the average orientation of the tracer patch unchanged (hard to see this given the large deformation) The area of the tracer patch is unchanged in either case.

These changes in the orientation and shape of the tracer patch are due solely to advection by the velocity *field*, Eqs. (22) and (23). The goal of this section is to find out what specific properties of a velocity field are relevant. Here again we are asking for an explanation of Lagrangian properties — the size, rotation rate and shape of a fluid material volume — in terms of the Eulerian velocity field, $\mathbf{V}(x,y)$.

[8]These vortex models are very useful, despite that they each have unphysical properties in the limit of small or large r. The irrotational vortex has a singularity in u_θ at $r = 0$, while the u_θ of a solid body rotation grows linearly and without bound with r. A hybrid made from these two idealizations — solid body rotation near the center of a vortex, Eq. (22), matched to an irrotational profile $u_\theta(r)$ from Eq. (23) at some larger r — avoids both problems. This is called a Rankine vortex, and can make a convenient, first approximation to some real vortices, e.g., a hurricane. A time-dependent, viscous model of an irrotational, point vortex, called the Lamb-Oseen vortex, shows the evolution into a Rankine vortex, Sec. (4.5).

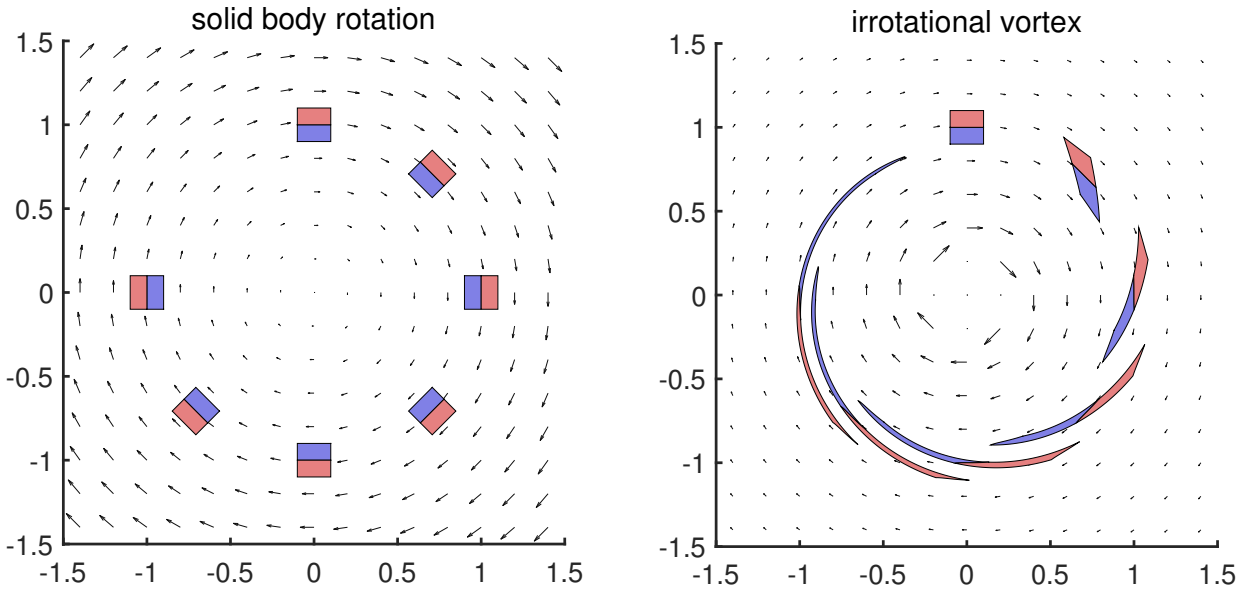

Figure 9: A small, square patch of a bi-colored, passive tracer (length 0.2 on each side) was released into a steady, clockwise rotating vortex and advected through 3/4 of a full revolution. The tracer patch is plotted at sucessive time intervals $\pi/4$. **(left)** This vortex is a solid body rotation. The patch rotated, but the area and shape were unchanged. **(right)** In this experiment, the vortex was irrotational. Advection carried the tracer patch clockwise around the vortex center just as before, and it also deformed the tracer patch into a long, thin filament. Nevertheless, this tracer patch did not rotate. Area was conserved as before.

3.1 The simplest shear flow

The specific goal of this section is to understand the tracer evolution seen in Fig. (9). To develop the tools needed for this, it will be helpful to start with the simplest possible shear flow,

$$\mathbf{V}(x,y) = \begin{pmatrix} u \\ v \end{pmatrix} = \begin{pmatrix} V_0 + \beta y \\ 0 \end{pmatrix} \tag{25}$$

This flow is homogeneous in that the shear is $\partial u/\partial y = \beta = 0.7$ and constant in time and space (the units of shear are time^{-1}, which may be left unspecified for the present). The mean velocity, $V_0 = 0.5$. An initially square tracer patch embedded in this flow evolves as shown in Fig. (10); the tracer patch is translated to the right, rotated clockwise, and deformed into a parallelogram. The translation is, of course, due to V_0, and the rotation and deformation are evidently related to the velocity shear.

For short times (small displacements) the Eulerian velocity field around a given point, $(x_0,\ y_0)$ may be approximated by the first terms of a Taylor expansion (as in Sec. 2.5 and repeated here),

$$\mathbf{V}(x,y) = \mathbf{V}_0(x_0,y_0) \ + \ \mathbb{G}\cdot\delta\mathbf{x} \ + \ HOT, \tag{26}$$

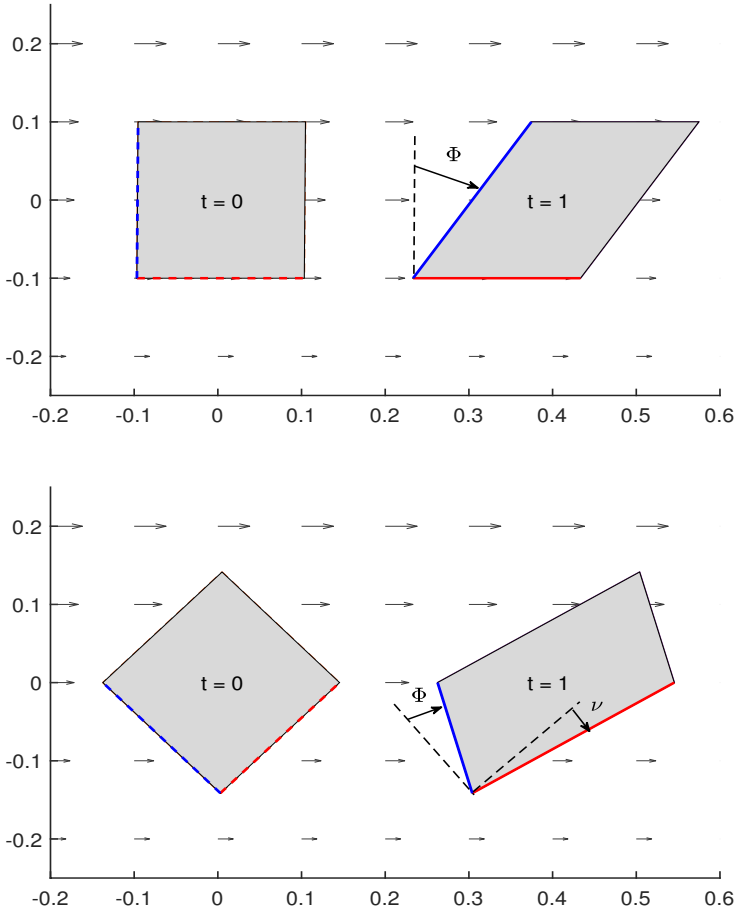

Figure 10: **(upper)** A square patch of a passive tracer was released into a homogeneous shear flow, Eq. (25), and advected for an elapsed time = 1. Advection caused this tracer patch to be translated to the right, rotated clockwise through about 20 deg, and deformed. **(lower)** The same velocity field, but here the initial tracer patch was rotated 45 deg. The rigthward translation and the rotation (suitably defined) apear to be the same as before, but the deformation was quite different.

where $\delta\mathbf{x}$ is a small displacement away from (x_0, y_0) and

$$\mathbb{G} = \begin{pmatrix} \dfrac{\partial u}{\partial x} & \dfrac{\partial u}{\partial y} \\ \\ \dfrac{\partial v}{\partial x} & \dfrac{\partial v}{\partial y} \end{pmatrix}$$

is the velocity gradient tensor (Sec. 2.5.2) evaluated at (x_0, y_0). The velocity gradient tensor evaluated at any point in the homegeneous shear flow (25) is just

$$\mathbb{G} = \begin{pmatrix} 0 & \beta \\ 0 & 0 \end{pmatrix} = \begin{pmatrix} 0 & 0.7 \\ 0 & 0 \end{pmatrix}. \tag{27}$$

There is no simple, single figure that suffices to illustrate even a 2x2 tensor, but it is possible to show what a tensor *does* when it multiplies a vector. A general account is that tensor multiplication on a vector makes a linear transformation of the vector. And thus, multiplication of a velocity gradient tensor on to a displacement vector yields a velocity (difference) vector that will in general have a magnitude, physical

dimensions and direction that are all different than that of the displacement vector. To see this, multiply $\mathbb{G}$ onto a set of unit (displacement) vectors, **e**, that span 360 deg, and plot the resulting velocity difference, $\delta\mathbf{V} = \mathbb{G}\mathbf{e}$, at the end of each unit vector, Fig. (11), upper left. For example, $\mathbb{G}$ times a unit displacement to the 'north' (positive y) produces a velocity difference to the 'east', $\mathbb{G}$ times a unit vector to the 'east' gives zero. The velocity differences plotted in this way happen to look a lot like the velocity field itself, since the shear is spatially uniform (homogeneous). However, this diagram applies at the specific point (x_o, y_o) where $\mathbb{G}$ has been evaluated, and are not a map of the velocity field *per se*.

For short times, this velocity field advects the tracer patch as if it was the Lagrangian velocity, cf. the first approximation of a trajectory computed in Fig. (6). Ths shears of the velocity field thus have important consequences for the displacement, rotation and deformation of a tracer patch. [9]

3.2 Physical rotation rate and vorticity

This shear flow changes the orientation of the tracer patch. Consider the case of a tracer patch that is initially aligned with the coordinate axes, Fig. (10, upper, and denote the angle of the blue axis with respect to the vertical (dashed line) by ϕ. By simple geometry (developed in Problem 1) below),

$$\frac{d\phi}{dt} = -\frac{\partial u}{\partial y}$$

for short times. Similarly, denote the angle between the red axis (orthogonal to the blue axis and thus initially horizontal) and the horizontal by υ, and a short calculation shows that

$$\frac{d\upsilon}{dt} = \frac{\partial v}{\partial x}.$$

In this specific example, the angle $\upsilon = 0$ initially, and stays that way since $\partial v/\partial x = 0$. The same sort of analysis can be done with a different set axes rotated at $\pi/4$ (Fig. 10, lower). It is evident that ϕ and ν change in the same sense (rotated clockwise) and in this specific case these angles change at about the same rate, which is about half (by inspection) of the previous $d\phi/dt$ computed on the blue axis in the case above. Clearly, the rate of change of the orientation (direction) of the sides of the tracer patch depends upon their orientation.

A plausible measure of the rotation rate of the patch as a whole is the average of the angular rates computed on orthogonal axes,

$$\omega = \frac{1}{2}(\frac{d\upsilon}{dt} + \frac{d\phi}{dt}) = \frac{1}{2}(\frac{\partial v}{\partial x} - \frac{\partial u}{\partial y}). \tag{28}$$

For this specific shear flow, $\omega = \partial u/\partial y = \alpha = -0.7$. This ω is called the physical rotation rate in the

[9] As you look at Fig. (11) and consider that it derived from the very simple shear flow of Eq. (25), you are probably wondering how this could possibly be progress — something very simple has been turned into a small blizzard of velocity diagrams that, you are cautioned, really aren't velocity maps at all. True enough, but hang on a little longer; once you have become familiar with these tensors and the Cauchy-Stokes Theorem, you will have the means to calculate useful, intelligible results for any velocity field.

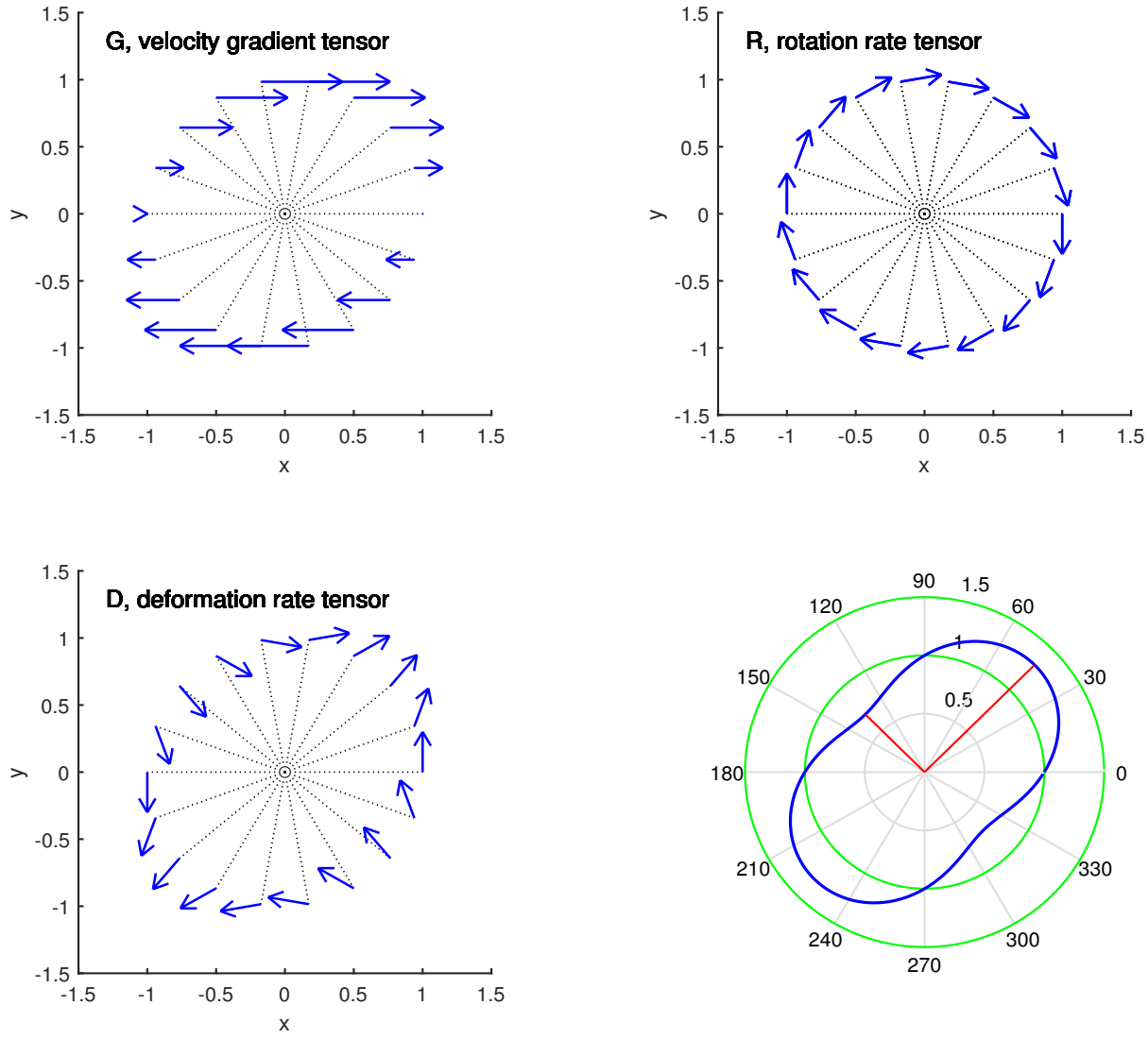

Figure 11: **(upper left)** The velocity gradient tensor $\mathbb{G}$ of the homogeneous shear flow, Eq. (27), has been multiplied into a sequence of unit vectors with varying directions (the dotted lines) and the resulting velocity plotted at the end of the unit vectors. This gives the impression of a map, but all of this should be envisioned to hold at a single point. **(upper right)** The rotation rate tensor $\mathbb{R}$ has been multiplied into a sequence of unit vectors. **(lower left)** The deformation rate tensor $\mathbb{D}$ multiplied into the unit vectors. Note that $\mathbb{G} = \mathbb{R} + \mathbb{D}$. **(lower right)** The blue, peanut-shaped ellipse is the linear deformation rate plus 1. The eigenvectors of the deformation rate tensor $\mathbb{E}$ are the red lines. Notice that the maximum and minimum values of the linear deformation rate are aligned with the eigenvectors.

sense that a neutrally buoyant paddle wheel embedded in this flow should rotate at this rate.[10] By inspection this appears to be a good estimate also for the case where the initial tracer patch was rotated, but a more convincing demonstration of the general applicability of (28) will come from the rotation tensor defined just below.

Despite that ω is the rotation rate of a physical object, ω is very seldom used in the practical analyses of fluid motion (solid mechanics is different in this regard). It is generally more useful to characterize the rotation of a fluid by a closely related measure called vorticity, χ, and which is $\chi = 2\omega$,

$$\text{vorticity in } \mathrm{R}^2\text{:} \qquad \boxed{\qquad - \qquad - \qquad} \tag{29}$$

The vorticity and the vorticity balance equation, which is the curl of the momentum balance, are ubiquitous. For that reason it makes sense to leave the factor 2 with ω rather than χ. The factor 2 will not come up again until Sec. 6, when the vorticity of wind or ocean currents is added to 2 times the physical rotation rate of the Earth to form the absolute vorticity observed from an inertial reference frame.

In two-dimensions, the vorticity is effectively a scalar, i.e, a single number. In R^3 the vorticity $\nabla \times \mathbf{V}$ is a vector with three components. Vorticity is invariant to the orientation of the tracer patch with respect to the coordinate system. The vorticity of a fluid is analogous in many respects to the angular momentum of a rotating solid. It differs in being defined point-wise, and has no moment arm or center. The appeal and utility of vorticity comes from its somewhat simpler conservation law compared with that of momentum (Sec. 3.4, Part 1), and partly for that reason the vorticity balance can often be used to real advantage in the diagnosis (and prediction) of fluid flows (an example is in Sec. 6).

3.3 Deformation rate

In the common case that the angles ϕ and ν change at different rates, then the tracer patch will necessarily change shape or deform. One possible measure of the shape of a parcel is the interior angle between, say the upper and right limbs of the orthogonal axes, Γ, and evidently $\Gamma = \pi/2 + \phi - \upsilon$, Fig. (10). If it happens that ϕ and υ change by the same amount, then Γ =constant, and the parcel will simply rotate without deforming, i.e., a solid body rotation. But if the angles change at a different rate, as they do in Fig. (10), upper, then the shape of the parcel will necessarily change, and

$$\frac{d\Gamma}{dt} = \frac{d\upsilon}{dt} - \frac{d\phi}{dt} = \frac{\partial v}{\partial x} + \frac{\partial u}{\partial y}. \tag{30}$$

If the angle ϕ changes while the lengths of the parcel sides remain constant, then this kind of time-varying deformation is called a *shear* deformation or strain rate. This is the case in Fig. (10), upper, when the angle ϕ is small. This particular shear deformation rate is in the plane parallel to the x-axis.

But suppose that the same square tracer patch is rotated by 45 degrees before being released into the

[10] An especially good illustration of this is found in the Shapiro fluid mechanics video 'Vorticity', https://video.odl.mit.edu/videos/2e75fb6283de4b54a09ee0da1c8e78e9/

flow. The effect of advection then appears to be quite different (Fig. 10, lower); the sides of the parcel remain (almost) orthogonal, but now the lengths of the sides are compressed or stretched (lower right side. A deformation rate that causes a change in the length of a material line is termed a *linear* deformation rate.

Unlike the vorticity, the deformation rate can not be written as a vector operator on the velocity, and from Fig.(10) it seems that when the deformation rate that is diagnosed with a given orthogonal axes pair (the sides of the parcel), the result is entirely dependent upon the orientation of these axes with respect to the flow. This is a hint that there is more to say about the deformation rate than the special case Eq. (30) can inform.

3.4 Rotation rate and deformation rate tensors

The deformation rate may change the shape and the size (area) of a parcel, while rotation alone can not. This suggests that it may be useful to separate the rotational part of the velocity gradient tensor from all the rest. This is straightforward because the rotation is associated with the anti-symmetric part of the velocity gradient tensor, and any (N x N) tensor can be factored into symmetric and anti-symmetric component tensors in the following steps. Let $\mathbb{G}'$ be the transpose of $\mathbb{G}$,

$$\mathbb{G}' = \begin{pmatrix} \frac{\partial u}{\partial x} & \frac{\partial v}{\partial x} \\ \\ \frac{\partial u}{\partial y} & \frac{\partial v}{\partial y} \end{pmatrix}$$

and now subtract and add $\mathbb{G}'$ to $\mathbb{G}$ as

$$\begin{aligned} \mathbb{G} &= \frac{1}{2}(\mathbb{G}-\mathbb{G}') + \frac{1}{2}(\mathbb{G}+\mathbb{G}') \\ &= \mathbb{R} + \mathbb{D}. \end{aligned} \tag{31}$$

The effect is to decompose $\mathbb{G}$ into two new tensors

$$\mathbb{R} = \frac{1}{2}\begin{pmatrix} 0 & -(\frac{\partial v}{\partial x}-\frac{\partial u}{\partial y}) \\ \\ \frac{\partial v}{\partial x}-\frac{\partial u}{\partial y} & 0 \end{pmatrix} \tag{32}$$

and

$$\mathbb{D} = \begin{pmatrix} \frac{\partial u}{\partial x} & \frac{1}{2}(\frac{\partial u}{\partial y}+\frac{\partial v}{\partial x}) \\ \\ \frac{1}{2}(\frac{\partial u}{\partial y}+\frac{\partial v}{\partial x}) & \frac{\partial v}{\partial y} \end{pmatrix} \tag{33}$$

$\mathbb{R}$ is the **rotation rate tensor** and by its construction is anti-symmetric, $R_{12} = -R_{21}$, and $R_{11} = R_{22} = 0$. In R^2, $\mathbb{R}$ has only one unique component that is equal to the physical rotation rate, in this case ω, Eq. (28). When $\mathbb{R}$ is multiplied onto a set of unit vectors the result is a velocity difference $\delta\mathbf{V} = \mathbb{R}\mathbf{e}$ that is normal to the unit vector and has the same amplitude (same speed) for all directions of the unit vector. The rotation associated with $\mathbb{R}\,\mathbf{e}$ is readily apparent, Fig. (11, upper right) and Fig. (10), upper row, and for the simple shear flow of Eq. (27), the physical rotation rate is just $\omega = -\frac{1}{2}\partial u/\partial y = -0.35$, and thus 0.35 radians $\approx$ 20 degrees over a time interval = 1 (Fig. 10, upper row). The vorticity of this shear flow is then 2ω = -0.7. The vorticity is a physical property of the flow, and hence its value should be (and is) independent of the arbitrary choice of a coordinate system, whether cartesion and rotated (Fig. 10 upper row, left and right) or cylindrical, or any other.

$\mathbb{D}$ is the **deformation rate tensor,** and is symmetric, $D_{12} = D_{21}$. In general, the diagonal elements are non-zero and are not equal. Thus the deformation rate tensor $\mathbb{D}$ in R^2 has three independent components (in general). The resulting velocity difference, $\delta\mathbf{V} = \mathbb{D}\ \mathbf{e}$, where $\mathbf{e}$ is the unit vector, varies in direction and amplitude depending upon the direction of $\mathbf{e}$ the (in the specific case shown in Fig. (11d) the amplitude happens to be constant). The linear deformation rate in a given direction is given by the component of $\delta\mathbf{V}$ that is parallel (or anti-parallel) to the unit vector in that specific direction. There are two special directions in which the linear deformation rate is either a minimum or a maximum. Given the specific $\mathbb{G}$ of Eq. (27), the minimum linear deformation rate is -0.35 and is found when the unit vector makes an angle of 135 (or 315) degrees with respect to the x axis (Fig. 11b); the maximum linear deformation rate is 0.35 and is at 45 (or 225) degrees. Thus a parcel will be compressed along a line that is oriented 135 (or 315) degrees (with respect to the x axis) and will be stretched along a line normal to this, 45 (or 225) degrees. Notice too that when the unit vector is pointing in these special directions, the velocity difference and the unit vector are either anti-parallel or parallel, and the relationship among $\mathbb{D}, \mathbf{e}$, and $\delta\mathbf{V}$ may then be written

$$\mathbb{D}\,\mathbf{e} = \delta\mathbf{V} = \lambda\,\mathbf{e},$$

where λ is a real number. These special directions are thus the directions of the *eigenvectors* of the symmetric tensor $\mathbb{D}$, and the amplitude of the linear deformation rate in those directions is given by the corresponding *eigenvalues*, λ = -0.35 and +0.35 for this particular $\mathbb{D}$.[11]

The deformation rate is proportional to the rate at which adjacent fluid parcels slide past one another, which, in the presence of viscosity, leads to a viscous stress. Since the solid body-rotational part of the velocity gradient tensor does not contribute to linear or shear deformation, it may as well be subtracted from the velocity gradient tensor before computing the viscous stress (Sec. 3, Part 1). Thus the viscous stress tensor is often written $\mathbb{T} = \nu\mathbb{D}$, which insures that the stress tensor will be symmetric.

Divergence. Another important quantity that was encountered in Part 1, Sec. 3.5, is the divergence, the sum of the linear deformation rates measured in any two orthogonal directions. Let L_x be an

[11] Eigenvectors and eigenvalues are a central theme of linear algebra and will not be reviewed here. Excellent references are by J. Pettofrezzo *Matrices and Transformations* (Dover Pub., New York, 1966) and for undergraduate-level applied mathematics generally, M. L. Boas, *Mathematical Methods in the Physical Sciences, 2nd edition* (John Wiley and Sons, 1983). If you have access to Matlab, https://www.mathworks.com/academia/courseware/matrix-methods.html is a very useful tutorial, including eigenvectors and values.

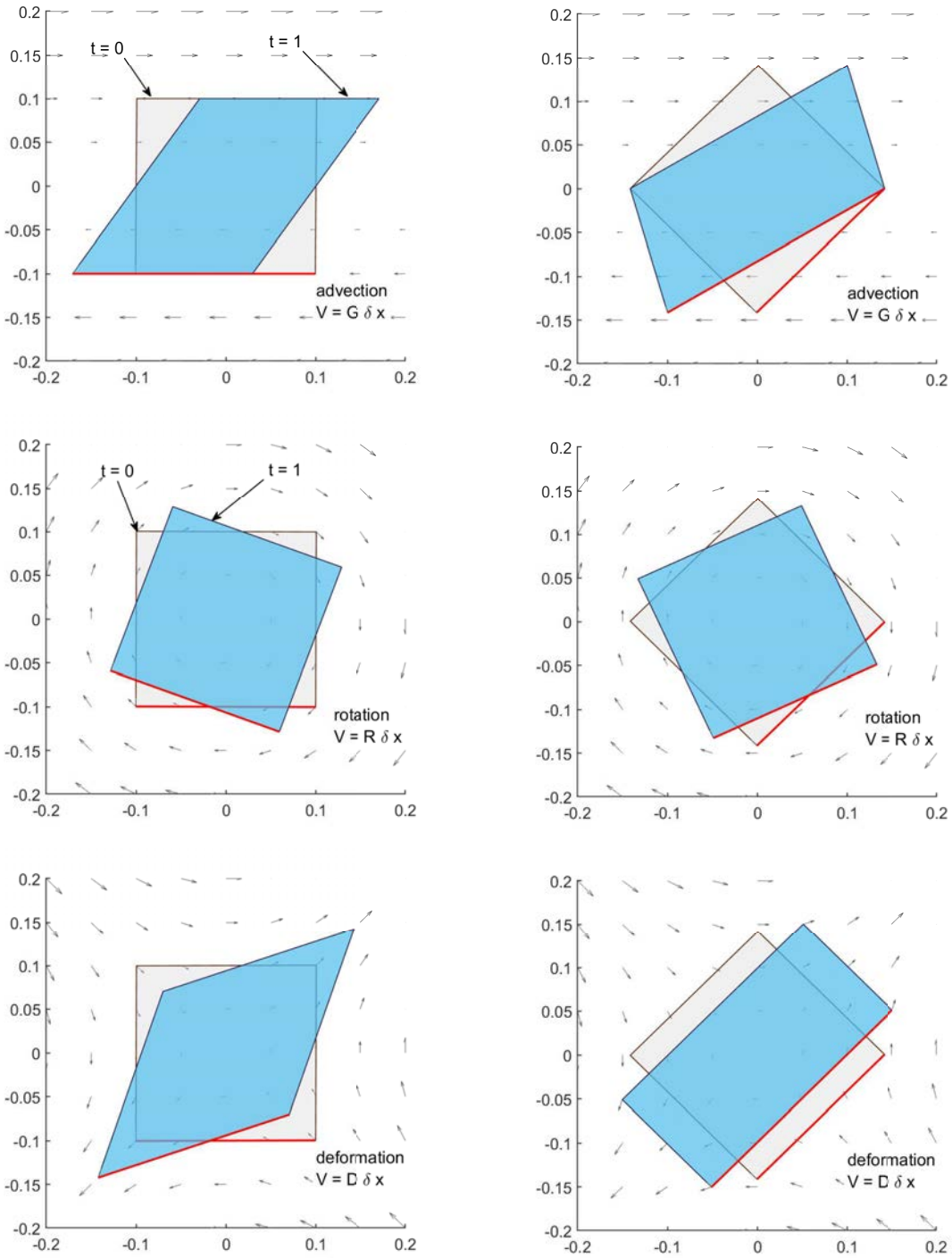

Figure 12: A square patch of passive tracer was released into a prescribed velocity field and advected for an elapsed time = 1. The initial patch is light gray; after advection the patch is blue. The tracer patch in the right column was first rotated 45 deg. **(upper row)** The velocity was computed from the velocity gradient tensor, $\mathbf{V} = \mathbb{G}\boldsymbol{\delta}\mathbf{x}$, Eq. (25), with no mean flow. This is otherwise a repeat of Fig. (10). **(middle row)** This velocity was computed from the rotation tensor, $\mathbf{V} = \mathbb{R}\boldsymbol{\delta}\mathbf{x}$, with no mean flow and no deformation. These tracer patches both rotate clockwise without deformation. The amount of rotation is independent of the orientation of the patch. **(lower row)** This velocity field was $\mathbf{V} = \mathbb{D}\boldsymbol{\delta}\mathbf{x}$. The tracer patch at left illustrates shear deformation, while the tracer patch at right was elongated and compressed in orthogonal directions, illustrating linear deformation. The effect of a deformation velocity field depends upon the orientation of the tracer patch with respect to the eigenvectors of the deformation tensor. In all six cases the area of the patch was conserved, indicating zero divergence.

(infinitesimal) line segment parallel to the x-direction, then

$$\frac{dL_x}{dt} = L_x \frac{\partial u}{\partial x}, \tag{34}$$

and similarly for L_y. Thus if a tracer patch has an area $A = L_x L_y$, then the normalized rate of change of the area is just

$$\text{divergence in 2-d:} \quad \boxed{\frac{1}{A}\frac{d}{dt}A = \frac{\partial u}{\partial x} + \frac{\partial v}{\partial y} = \nabla \cdot V}$$

The divergence is the sum of the eigenvalues of the deformation tensor, and also the trace of $\mathbb{D}$, $\mathbb{D}_{11} + \mathbb{D}_{22}$. In the specific case of the shear flow Eq.(25), the divergence happens to be zero, though the linear deformation rate in most directions is not zero. The divergence is a scalar, and is the same for any orientation of the parcel or of the coordinate axes. Thus, like the 2-d vorticity, the divergence is invariant to coordinate rotation.

3.5 The Cauchy-Stokes Decomposition Theorem brings this all together

The discussion above is summarized by the Cauchy-Stokes Theorem — the fluid motion at a given place and time may be resolved into three components:

Translation — advection by the spatial mean velocity $\mathbf{V}_o$.

Rotation — induced by advection in a sheared velocity field. The physical rotation rate is 1/2 $\nabla \times \mathbf{V}$ and is the off- diagonal elements of the rotation rate tensor, $\mathbb{R}$. The rotation rate is invariant to coordinate rotation.

Deformation — a change in shape and area (in 2-d) of a material volume caused by advection in a sheared velocity. The maximum and minimum linear deformation rate are given by the eigenvectors and eigenvalues of the deformation rate tensor, $\mathbb{D}$. The sum of the eigenvalues is the divergence, $\nabla \cdot \mathbf{V}$, which gives the rate of change of area. Divergence is an invariant to coordinate rotation.

3.6 Application to the vortex flows

Solid body rotation. Let's now try this formalism on the vortex flows of Fig. (9). A good case could be made for doing these calculations in polar coordinates, but for now the more familiar rectangular coordinate representation of the solid body rotation is

$$u = \Omega\, y, \quad \text{and} \quad v = -\Omega\, x,$$

where the rotation rate Ω is a constant. The appropriate tensors are

$$\mathbb{G} = \begin{pmatrix} 0 & \Omega \\ -\Omega & 0 \end{pmatrix} \qquad \mathbb{R} = \begin{pmatrix} 0 & \Omega \\ -\Omega & 0 \end{pmatrix} \qquad \mathbb{E} = \begin{pmatrix} 0 & 0 \\ 0 & 0 \end{pmatrix}$$

Note that these $\mathbb{G}$, $\mathbb{R}$, $\mathbb{E}$ happen to hold throughout the vortex, which is unusual. Given all of the zeros, this case looks to be somewhat degenerate, however, the formalism works as intended; $\mathbb{R}$ indicates (physical) rotation at the rate Ω everywhere in the vortex, and $\mathbb{D}$ indicates zero deformation, and of course zero divergence throughout the vortex. Thus, advection by a solid body rotation does not change the area or the shape of a tracer patch in any way (which we knew already from Fig. 9), though it does cause a rotation.

Irrotational vortex. Now consider an irrotational vortex, which makes better use of this formalism. In cartesian coordinates,

$$u = \Omega\, r_o^2\, \frac{y}{r^2} \quad \text{and} \quad v = -\Omega\, r_o^2\, \frac{x}{r^2},$$

where $r^2 = x^2 + y^2$, r_o is a constant, and Ω is as before. The difference between this vortex and the solid body rotation is the $1/r^2$ dependence of the azimuthal speed. By choosing $r_o = 1$, and the Ω used above, the azimuthal speed, $u_\theta = \Omega r$, is equal to that of the solid body rotation at $r = 1$, but not otherwise. The velocity gradient tensor of this flow is

$$\mathbb{G} = \frac{\Omega r_o^2}{r^4} \begin{pmatrix} -2xy & x^2 - y^2 \\ x^2 - y^2 & 2xy \end{pmatrix}$$

The rotation rate tensor vanishes throughout,

$$\mathbb{R} = \frac{\Omega r_o^2}{r^4} \begin{pmatrix} 0 & 0 \\ 0 & 0 \end{pmatrix}$$

and so the deformation rate tensor is just

$$\mathbb{E} = \mathbb{G}.$$

The two eigenvectors of this tensor are

$$\frac{\Omega r_o^2}{r^4} \begin{pmatrix} f(x,y) \\ 1 \end{pmatrix} \quad \text{and} \quad \frac{\Omega r_o^2}{r^4} \begin{pmatrix} -f(x,y) \\ 1 \end{pmatrix}$$

where

$$f(x,y) = \frac{\sqrt{4x^2y^2 + (x^2 - y^2)^2}}{x^2 - y^2} - \frac{2xy}{x^2 - y^2}$$

and the two corresponding eigenvalues are

$$\sqrt{4x^2y^2 + (x^2 - y^2)^2} \quad \text{and} \quad -\sqrt{4x^2y^2 + (x^2 - y^2)^2}.$$

At the initial position of the tracer patch, $(x,y) = (0,1)$,

$$\mathbb{E} = \frac{\Omega r_o^2}{r^4}\begin{pmatrix} 0 & -1 \\ -1 & 0 \end{pmatrix} \qquad \mathbb{D}_{vector} = \frac{1}{\sqrt{2}}\begin{pmatrix} -1 & -1 \\ -1 & 1 \end{pmatrix} \qquad \mathbb{D}_{value} = \frac{\Omega r_o^2}{r^4}\begin{pmatrix} -1 & 1 \end{pmatrix}$$

where the eigenvectors are the column vectors of $\mathbb{D}_{vector}$ and the eigenvalues are the first and second elements of $\mathbb{D}_{value}$. The first eigenvalue is negative, and hence the tracer patch will be compressed in the direction of the first eigenvector, 225 and 45 degrees anticlockwise from positive x. The second eigenvalue is positive, and hence the tracer patch will be stretched along the directio of the second eigenvector, 135 and 315 degrees. The eigenvectors and values will vary in space; after the tracer patch had been advected clockwise, and centered on $(x,y) = (1,0)$, the values at that site are

$$\mathbb{E} = \frac{\Omega r_o^2}{r^4}\begin{pmatrix} 0 & 1 \\ 1 & 0 \end{pmatrix} \qquad \mathbb{D}_{vector} = \frac{1}{\sqrt{2}}\begin{pmatrix} -1 & 1 \\ 1 & 1 \end{pmatrix} \qquad \mathbb{D}_{value} = \frac{\Omega r_o^2}{r^4}\begin{pmatrix} -1 & 1 \end{pmatrix}$$

The eigenvalues are unchanged, but the eigenvectors are rotated clockwise through 90 degrees, and hence the deformation relative to the tracer patch continued. The normalized rate of stretching is

$$\frac{1}{L}\frac{dL}{dt} = \frac{\Omega r_o^2}{r^4} = 1,$$

and persists as the tracer patch is advected clockwise by the vortical flow. By the time $t = \frac{3}{2}\pi$, the patch had been stretched by a factor $\frac{3}{2}\pi$, and compressed by the reciprocal. The initially square tracer patch was thus drawn into a long, thin filament, all the while conserving its area and thus the net content of the tracer. This kind of filamentation process is a common property of most real flows, and is often called 'stirring', especially when it is generated deliberately to enhance mixing (more on this in the next section).

3.7 Key ideas

1) A fluid flow having some spatial variability (which is to say all real flows) may cause a tracer patch to rotate, change shape (deform) and possibly change volume. Along with the transport, these are often crucial effects of advection.

2) The instantaneous rotation and deformation of a tracer patch (Lagrangian properties) may be related to the velocity gradient tensor defined on the Eulerian velocity field via the Cauchy-Stokes Theorem.

3) Physical rotation rate is the average at which orthogonal axes rotate. Vorticity is defined to be twice the physical rotation rate and has properties analogous to angular momentum, though defined point-wise in a fluid.

4) Deformation rate may be characterizd as the strectching (or compression) of fluid lines along orthogonal directions. The eigenvectors of the deformation tensor indicate the directions in which the linear deformation is the maximum and minimum. The values are gien by the eigenvalues.

5) The trace of the deformation tensor is an invariant called the divergence, which is the rate of change of the normalized area (in R^2).

6) The estimation of finite amplitude rotation or deformation requires an integration in time of the advection equation, that, in effect, continually updates the rotation and deformation tensors.

3.8 Problems

1) Go back and take another look at the (stirred) fluid flow in a teacup. Do you see evidence of divergence, rotation or deformation?

2) Refer to Fig. (10), upper. Let the initial vertical side of the tracer patch be h, and let the relative displacement of the upper left corner be d. Show that the included angle ϕ changes with time as $d\phi/dt = (1/h)\partial d/\partial t = \partial u/\partial y$ provided that ϕ is small, in effect, at short times. How does this estimate at long times? In a similar vein, what is the short and long time dependence of the hypotenuse, $\sqrt{h^2+d^2}$?

3) It was noted that the average rotation rate of a tracer patch defined by Eqs. (28) or (29) is independent of the orientation of the axes with respect to the tracer patch. Can you verify this by inspection of Fig. (10), or by Fig. (12), middle?

4) Refer to Fig. (12), lower right. Compare (quantitatively) the linear deformation rate in the directions 45 degrees and 135 degrees with the observed change of the tracer patch length and width in Fig. (12), lower right. Compare also with the distance between opposite vertices of the square (and then parallelogram) of Fig. (12), lower left.

5) The decomposition of the velocity gradient tensor as $\mathbb{G} = \mathbb{R} + \mathbb{D}$ is linear, as is the operation of tensor multiplication. Can you verify from Fig. (12) (by inspection at several points) that that the sum of the rotation velocity field and the deformation velocity field (middle and lower rows) does indeed add up to the 'advection' velocity of the upper row? Specifcally, what happens to the y-component fo the velocity?

6) A good example of a simple flow in which to examine stirring and mixing is a confluent flow, $u(x,y) = b*x$ and $v(x,y) = -b*y$. What are the rotation and deformation tensors for this flow? Suppose the start is a square tracer patch offset from the $x-$axis. What is the long-time tracer distribution? An animation of this case (including some random particle motion that is discussed in Sec. 4) is available from https://www2.whoi.edu/staff/jprice/wp-content/uploads/sites/199/2022/08/confluence.mp4

4 Advection by resolved and unresolved motions

Every real fluid flow will be made up of motions that have a more or less extensive range of time and space scales. In the case of flow in a tea cup, the largest scale of motion will usually be a vortex that will fill the entire domain and then slowly decay (tens of seconds) due to viscous drag with the bottom and sides of the cup. Small scale motions, including irrotational vortices generated by the initial stirring, will be present at the beginning of an experiment, and viscous boundary layers a few millimeters thick will show the direct effect of boundary friction. The range of spatial scales in a teacup is quite limited, only about one order of magnitude, because viscosity sets the lower bound to be not much less than the domain size. The scales of motion of the atmosphere span at least eight orders of magnitude, from thousands of kilometers in the westerly wind belts, down to centimeters in viscous boundary layers that are in contact with a smooth surface and the equivalent of viscous boundary layers in the tea cup. It is quite possible to model explicitly (numerically) the entire range of motion in a tea cup,[12] but it is certainly not possible to do so for the atmosphere.

The first step in every practical analysis will be to decide what range of the scales of motion will be resolved, either by observations or modelled explicitly, and an acknowledgment of the scales that will have to be left unresolved, whether for practical or conceptual reasons. If the spatial or temporal scales of the unresolved motions are larger than the scales of interest, then the issue may be as simple as observing or defining the average velocity, the $\mathbf{V_o}$ of the Cauchy Stokes Theorem. But very often the unresolved scales will include smaller space scales and faster time scales. In that case the scale separation is often written as

$$\mathbf{v} \;=\; \mathbf{V} \;+\; \mathbf{v}', \tag{35}$$

where $\mathbf{v}$ is the total, or actual velocity, and $\mathbf{V}$ is the resolved velocity estimated by a linear averaging applied to $\mathbf{v}$ over some suitable space or time scale, say a time T,

$$\mathbf{V}(\mathbf{x},\mathbf{t}) \;=\; \overline{\mathbf{v}} \;=\; \frac{1}{T}\int_t^{t+T} \mathbf{v}(\mathbf{x},\mathbf{t})dt. \tag{36}$$

The unresolved velocity, $\mathbf{v}' = \mathbf{v} - \mathbf{V}$, is often termed the 'eddy' velocity, though without implying a closed circulation. The average of the eddy velocity

$$\overline{\mathbf{v}'} \;=\; \frac{1}{T}\int_t^{t+T} \mathbf{v}'dt \;=\; 0.$$

The significance of (35) lies in the kind and the extent of the averaging that is applied to the total velocity to define the resolved velocity. Temporal averaging is most common (36), but spatial averaging and ensemble averaging are possible and quite useful as well.[13] There is no inconsistency in allowing that the resolved velocity $\mathbf{V}$ can be varying in time. But, for this averaging to be most useful, there should

[12] Ok, but why would you? See Luo G, Hou TY. 2014, Potentially singular solutions of the 3D axisymmetric Euler equations. Proc. Natl Acad. Sci. USA 111, 12 96812 973. (doi:10.1073/pnas.1405238111), and https://www.bbc.com/news/av/uk-england-london-54195597

[13] For more on Reynolds averaging, see https://www2.whoi.edu/staff/jprice/wp-content/uploads/sites/199/2023/11/Randall-RA.pdf

be a time scale T over which $\mathbf{V}$ varies only a little, and yet is long enough that averages of the eddy velocity and its moments (example below) will be reasonably well-converged to meaningful averages. For this to hold rigorously, there will have to be a separation of time scales between the resolved and the eddy velocities, sometimes referred to as a spectral gap, though in practice there is likely to be a continuum of time (or space) scales.

4.1 Reynolds averaging of advection terms leads to eddy fluxes

Having defined the resolved velocity, the issue then turns to accounting for the effects of the smaller/faster scale eddy motions, even though not observing or modelling the eddy motion in detail. This problem — accounting for the effects of unresolved motions — is a significant part of the research effort in fluid dynamics; Reynolds averaging gives us a place to start.

Presume an advection/diffusion equation for a scalar variable, c, having no special properties, i.e., a passive tracer,

$$\frac{\partial c}{\partial t} \;=\; -\nabla\cdot(\mathbf{v}c) + K_c\nabla^2 c, \tag{37}$$

with K_c the molecular diffusivity of c. As noted above, it is almost always necessary to distinguish resolved from unresolved motions as in (36), and the same holds for tracer distribution, and so let

$$c \;=\; C \;+\; c'.$$

Substitute these into the advection equation (37) and average again to find the governing equation for the resolved tracer field, C,

$$\frac{\partial C}{\partial t} \;=\; -\nabla\cdot(\mathbf{V}C) \;-\; \nabla\cdot\overline{(\mathbf{v}'c')} \;+\; K_c\nabla^2 C. \tag{38}$$

Rather than the four advection terms that might have been expected, there are only two advection terms since the cross-products of resolved and unresolved variables vanish under the presumed linear averaging operation, e.g.,

$$\overline{\nabla\cdot(\mathbf{V}c')} \;=\; \nabla\cdot\overline{\mathbf{V}c'} \;=\; \nabla\cdot\mathbf{V}\,\overline{c'} \;=0.$$

The key finding from this Reynolds averaging procedure is that the net effect of the eddy motion acting upon the resolved-scale tracer distribution is the cross-correlation, $\overline{\mathbf{v}'c'}$, that appears in (38). This term is variously called an eddy flux or an eddy-covariance. Reynolds averaging alone doesn't tell us anything regards the physical process that makes up the eddy flux.

As an example of an eddy flux, consider the vertical flux of water vapor (evapotranspiration), F $[mass\ length^{-2}\ time^{-1}]$, at a height of a few tens of meters in the atmospheric boundary layer above a horizontally homogeneous, open field. The total vertical flux will be, in general,

$$F \;=\; \rho_{air}(WQ \;+\; \overline{w'q'} \;-\; K_q\frac{\partial q}{\partial z}). \tag{39}$$

The species being transported is q, the water vapor mixing ratio (closely proportional to humidity). The first term on the right is transport by the mean vertical velocity, W, which may be assumed negligible if

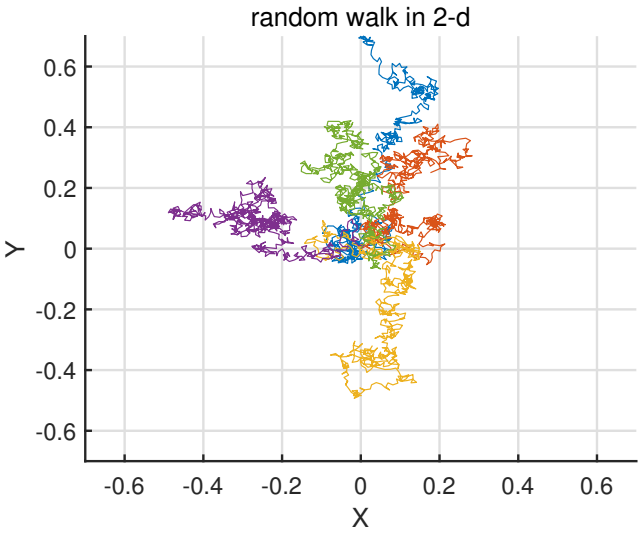

Figure 13: Five particle trajectories from the random walk, Eq. (40), up to time $t = 2\pi$. In each trajectory there are 628 steps of distance $s = 0.01$, which give an appearance much like Brownian motion. The next five trajectories will have similar overall amplitude, but likely to be completely different in detail.

there are no significant horizontal variations of topography. The third term represents the flux of water vapor due to molecular diffusion, and is completely negligible if the boundary layer is well-mixed and turbulent, which is nearly always the case. The second term on right is the vertical eddy flux, with w' the vertical component of the eddy (wind) velocity, and q' the comparable eddy component of the water vapor mixing ratio. From observations we know that this eddy flux is almost always the dominant process of water vapor vertical transport within the atmospheric boundary layer. To estimate an observed eddy flux requires rather precise measurements of w and q, since q' is typically O(10^{-2}) Q, and at a temporal resolution of O(0.1 sec). A stable average of this eddy flux requires about ten minutes of high frequency sampling.[14]

4.2 A random walk as a first model of unresolved advection

The discussion above is fairly abstract, and so it will be helpful to consider a concrete example in which the resolved velocity is a vortex of the kind considered in Sec. 3, and eddy velocity will be associated with a random walk of discrete particles. The statistics of the random walk are presumed to be known, but not its detailed motion. In the upcoming Sec. 4.4 these two 'flows' will be added together to make a flow with two distinct scales, and thus advection by resolved and unresolved motions at once. But for now, consider just the eddy velocity $\mathbf{v}'$ and the resulting eddy flux.

In place of the continuous, passive tracer c noted above, the flow will be observed by computing the trajectories of discrete, freely drifting material particles executing a random walk. The calculation is as follows: particles were launched at $t = 0$ at the origin, $(x, y) = (0, 0)$. At each time, $t_i = i\delta t$, the position of the jth particle was advanced through a small, random vector displacement

$$ {}^{j}\mathbf{x}'_{i+1} \;=\; {}^{j}\mathbf{x}'_{i} \;+\; {}^{j}\delta\mathbf{x}_{i}, $$

[14] Measuring and interpreting eddy fluxes is an object in meteorology and many other fields. An excellent primer on the topic of eddy flux measurement in the atmosphere's land boundry layer is by https://www.licor.com/env/support/Eddy-Covariance/videos/ec-method-02.html

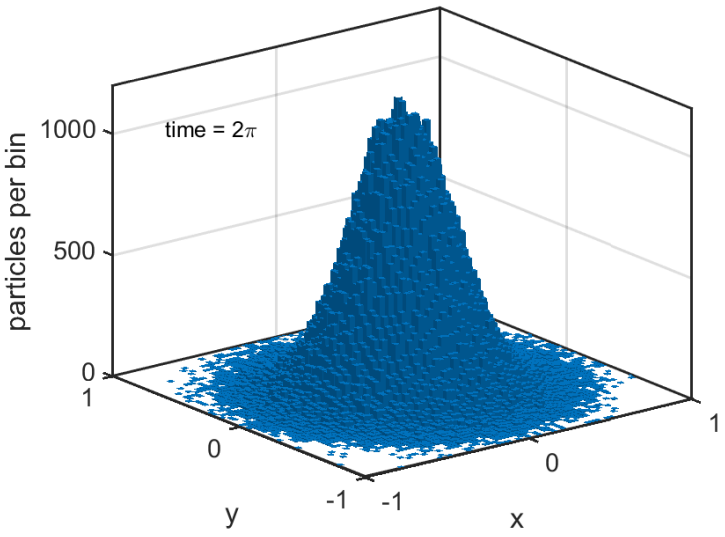

Figure 14: A histogram of the particle count per (arbitrary) bin width, from an ensemble of 500,000 random walk trajectories like those of Fig. (25). This data is from time $t = 2\pi$. At later times, the distribution spreads laterally as $\sqrt{t}$ and the peak amplitude decreases as $1/t$.

where

$$ {}^{j}\delta\mathbf{x}_i \;=\; \begin{pmatrix} {}^{j}\delta x_i \\ {}^{j}\delta y_i \end{pmatrix} \;=\; \frac{s}{\sqrt{2}} \begin{pmatrix} \cos({}^{j}\mu_i) \\ \sin({}^{j}\mu_i) \end{pmatrix}, \tag{40} $$

and s is a small, fixed step size that we are free to choose, $s = 0.01$. There is no need to assign units at this point, but the dimensions will be kept consistent and noted on occasion. Random comes from the angle μ, which is uniformly distributed on the interval $0 \le \mu < 2\pi$. Each realization of δx is unique; there is no memory from one step to the next, and so there is zero lagged correlation in time for a given particle. There is zero cross-correlation between any two particles on ensemble average. The time step is taken to be $\delta t = 0.01$ and hence the speed of the random walk is $|\mathbf{w}| = s/\delta t = 1.0$. The experiments were run for a duration, T, up to 10π and thus there will be $n = T/\delta t = 3141$ steps in each trajectory during a full experiment. Five typical trajectories are shown in Fig. (25). The number of particles in the ensemble, N, is almost unconstrained by the minimal computational demand of the random walk calculation. N may be chosen to give either legible graphics when every particle is shown, N = 10,000, or much larger, up to 500,000, to give well-converged ensemble averages denoted by angle brackets,

$$ < \tilde{y} > \;=\; \frac{1}{N} \sum_{j=1}^{N} {}^{j}\tilde{y}. $$

Such a large N is excessive for many purposes. Notice that the ensemble averaging is over discrete, not continuous variables. The identity of each particle is retained throughout an experiment, characteristic of Lagrangian method. Whether such a random walk is a faithful model of a turbulent flux of the sort referenced in Eq. (39) is a (very) good question that will be visited in Sec. 4.4.

The eddy motion prescribed via Eq. (40) is a classical random walk in two dimensions, and has well-known statistical properties.[15] First, while any one particle might end up anywhere within a radius

[15] A random walk is interesting and important in its own right as it can make a useful model of the stochastic processes that arise in a very wide range of contexts, from economics to astrophysics. The basics of random walk are described well in

wT of its launch position, the ensemble average of x' and y' will vanish for all times, e.g.,

$$< x'_n > \;=\; < \sum_{i=1}^{n} {}^j\delta x_i > \;=\; n\, s < \cos({}^j\mu_i) > \;=\; 0,$$

which is consistent with the intent that this is the eddy component of particle displacement. However, the ensemble average of the *squared* displacement in x or y, e.g.,

$$< x'^2_n > \;=\; < \sum_{k=1}^{n} {}^j\delta x_k \times \sum_{l=1}^{n} {}^j\delta x_l > \tag{41}$$

does not vanish, in general. The product of sums on the right may be written

$$< \sum_{k=1}^{n} {}^j\delta x_k \times \sum_{l=1}^{n} {}^j\delta x_l > \;=\; < \sum_{i=1}^{n} {}^j\delta x_i^2 > \;+\; < 2 \sum_{k>l}^{n} \sum_{l=1}^{n} {}^j\delta x_k \, {}^j\delta x_l > . \tag{42}$$

The second term at right is the product of the δxs at different times, $k > l$. This vanishes on ensemble average, since the angle μ at each step is independent of the μ at the previous (or any other) time step. Thus the ensemble average of the mean square of x' increases with the elapsed time, t, as

$$< x'^2_n > \;=\; < \sum_{i=1}^{n} {}^j\delta x_i^2 > \;=\; n\, s^2 < \cos\left({}^j\mu_i\right)^2 > \;=\; \frac{1}{2} n\, s^2 \;=\; \frac{1}{2} s\, |\mathbf{w}|\, t. \tag{43}$$

It is often preferable to consider the root mean square of x' or r', and these grow as the square root of the elapsed time, Fig. (15), left,

$$\boxed{\sqrt{< x'^2_n >} \;\propto\; \sqrt{n} \;\propto\; \sqrt{t}}$$

This square root time dependence of the rms displacement is perhaps the most characteristic and important property of a random walk.

4.3 An Eulerian description of dispersion by a random walk; effective diffusivity

The particle trajectories discussed above are Lagrangian, in that they record the motion of (simulated) material particles. This seems natural for the definition of a random walk and the description of an evolving tracer patch or particle cloud. However, to make contact with most theory and modelling, this Lagrangian description is best translated into its Eulerian equivalent.

When particle trajectories are available in large numbers, as they are here, the particle concentration (particles per unit area) is analogous to the continuous passive tracer, c. The two-dimensional, Reynolds averaged advection equation for this tracer is just, repeating (38),

$$\frac{\partial C}{\partial t} \;=\; -\,\mathbf{V}\cdot\nabla C - \nabla\cdot\overline{\mathbf{v}'c'} \;+\; K_c \nabla^2 C.$$

https://mathworld.wolfram.com/RandomWalk2-Dimensional.html

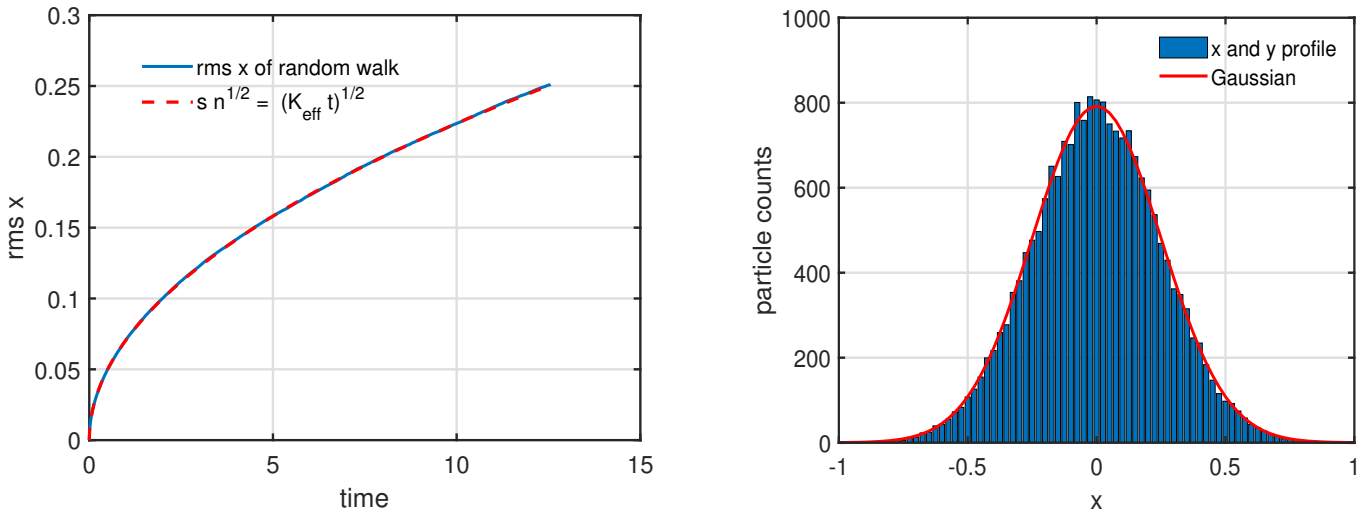

Figure 15: Statistical properties of the random walk, Eq. (40). **(left)** Root mean square x displacement as a function of time from an experiment that tracked a very large number of particles (blue line). The expected rms for this process is $\sigma = s\sqrt{n/2}$, where s is the step size and n the number of steps up to the time = $n\delta t$ (red dashed line, which is directly on top of the blue line). **(right)** Particle concentration at the time $t = 2\pi$ as a function of x or y made by cutting across the distribution of Fig. (26) along $y = 0$ and $x = 0$ and averaged (blue bars). The red line is the concentration from the solution (46) of the classical diffusion equation which uses the known σ of the random walk at left. This favorable comparison supports the use of classical diffusion concepts, e.g., effective diffusivity, to describe the dispersion of particles by a random walk.

To solve this for C requires knowing the resolved velocity, $\mathbf{V}$, here taken to be a prescribed vortex flow of the kind seen in Sec. 3, and the eddy flux, $\overline{\mathbf{v}'c'}$. Evaluating this latter term will require several assumptions, some bordering on guesses, that can be checked against known the random walk. The path taken here is to apply the classical mixing length theory to estimate an effective diffusivity, K_{eff}, of the random walk. The speed of the eddy velocity $\mathbf{v}'$ is estimated to be the speed of the random walk, w, which is homogeneous, isotropic and known,

$$|\mathbf{v}'| \approx w = \frac{s}{\delta t}.$$

The eddy anomaly of the tracer concentration, c', is less obvious, but as a guess, try

$$c' = s\,|\nabla C|,$$

which presumes that the step size, s, of the random walk is a mixing length acting on the resolved tracer field. There is no direction associated with the random walk step, and so this too is a relation for magnitude only. To here this gives

$$|\overline{\mathbf{v}'c'}| \approx w\,s|\nabla C|.$$

The right hand side has the form of a Fickian diffusion, $-K\,\nabla C$, provided that $K_{eff} \approx w\,s$ is an effective

diffusivity associated with the random walk. Eq. (43) indicates a factor 1/2 coming from the ensemble averaging of the random direction, μ, and so, provisionally,

$$K_{eff} \approx \frac{1}{2} s\, w. \tag{44}$$

This K_{eff} is a constant (homogeneous and steady) that may be taken outside of the gradient operator, and the eddy flux term may be estimated as

$$\overline{\mathbf{v}' c'} = -K_{eff}\, \nabla C.$$

The direction of the eddy flux comes from the assumption that it will be anti-parallel to the gradient of C, i.e., the usual sense of a heat flux from hot to cold. The Reynolds-averaged advection equation (38) can then be written as an advection/diffusion balance for the resolved tracer C,

$$\frac{\partial C}{\partial t} = -\mathbf{V} \cdot \nabla C + K_{eff} \nabla^2 C + K_c\, \nabla^2 C. \tag{45}$$

The process of the eddy flux — a fast time and short space scale random advection — has thus been parameterized as an effective diffusivity, $K_{eff} = \frac{1}{2} sw$, acting upon the resolved tracer field.[16]

To check that this parameterization of eddy flux is indeed appropriate for this case, the statistics of the random walk may be compared with the solution for suitably calibrated two-dimensional, Fickian (classical) diffusion,

$$\frac{\partial C}{\partial t} = K_c\, \frac{1}{r}\, \frac{\partial}{\partial r} \left(\frac{r\, \partial C}{\partial r} \right)$$

Assume an initial condition that corresponds to the experiment of Fig. (14), a radially symmetric and highly localized delta function of tracer C centered over the origin, and a boundary condition that tracer concentration vanishes at infinity,

$$C(r,\, t=0) \propto \Delta(r), \quad \text{and} \quad C(r,\, t) \to 0 \ \text{ as } \ r \to \infty.$$

The solution for C is then a Gaussian

$$C(r,t) = \frac{1}{2\pi\, \sigma^2} \exp\left(\frac{-r^2}{2\sigma^2} \right), \tag{46}$$

with a time-dependent standard deviation σ,

$$\sigma(t) = \sqrt{2\, K_c\, t}.$$

[16] A parameterization provides an estimate of something that would otherwise remain unknown, in this case an eddy flux, in terms of something that is known at least in principle, here the statistics of a random walk and the gradient of the resolved tracer field. It is important to keep in mind that a parameterization is not an identity, and will not be valid universally. Rather, parameterizations are likely to be more or less *ad hoc* and useful over a limited range, which may be very difficult to define fully and precisely. Most parameterizations should be treated with some skepticism, and subjected to testing whenever possible. This is especially important when the parameterization exerts a significant influence upon the end result of a model or an analysis, as it does here.

This is often said to be the 'fundamental solution' for 2-d diffusion. To compare this solution with the random walk, choose $K_c = K_{eff} = w\,s/2 = 0.01$ (dimensional units of K are $[length^2\ time^{-1}]$). The solution (46) and the particle count histogram shown in Fig. (15), right, have been normalized to give a net particle count of $N = 500,000$, consistent with the random walk ensemble.

The time-dependent standard deviation and the instantaneous distribution particle density of the random walk are, superficially, indistinguishable from this solution for Fickian (classical) diffusion (46), Fig. (15). This is a well known result, and yet it is still a little bit surprising, considering that advection and diffusion are quite different processes.[17] A conclusion drawn from this comparison is that the familiar usage 'diffusion' and the parameterized advection/diffusion equation (45) are useful terms and concpets in an Eulerian theory that seeks to describe the dispersal of particles that occurs in a (Lagrangian) random walk.[18]

Figure 16: Stirring and mixing:

Spinning, shearing flows
wrapping tracer filaments
that embrace and merge.

4.4 Stirring and mixing: when advection and diffusion act at once, Peclet number

The random walk and the vortex flows of Sec. 3 have been combined on the assumption that the two flows are independent. As we will see, their joint effect may not be a linear addition, however.

The initial condition for these experiments had the particles (N = 10,000) uniformly distributed over a circular area of radius 0.1 and centered on $(x,\ y) = (0,\ 1)$. The perimeter of this circle was advected by

[17] There are limits in which random walk and diffusion do indeed give quite different results. Consider that classical diffusion follows a parabolic partial differential equation that requires all boundary data at all times up to the present. Even the most distant boundary will thus have an some effect, even if infinitesimal, on every point in the domain of a classical diffusion problem. By contrast, the maximum speed at which a random walk can propagate a signal is just $|w|$, which is finite, as it should be, physically. In that regard, a random walk would appears to be a more plausible representation of a physical process than is classical diffusion. For more on this see Keller, J., 2004, Diffusion at finite speed and random walks, Proc Natl Acad Sci U S A. 101(5): 11201122. Published online 2004 Jan 20. doi: 10.1073/pnas.0307052101

[18] The success of the mixing length parameterization in this case is so compelling that you might be led to expect similar success in other cases, and in other problems. Probably not! More likely is that the eddy velocity will be inhomogeneous, anisotropic and dependent upon the resolved velocity shear, among others. In that event, a constant and isotropic effective diffusivity will not obtain the way it did in this especially simple case of a random walk that was independent of the resolved flow. A good strategy might be to regard the mixing length hypothesis as a null model, and then see if you can devise a better model by taking account of the specific eddy process(es) in your problem.

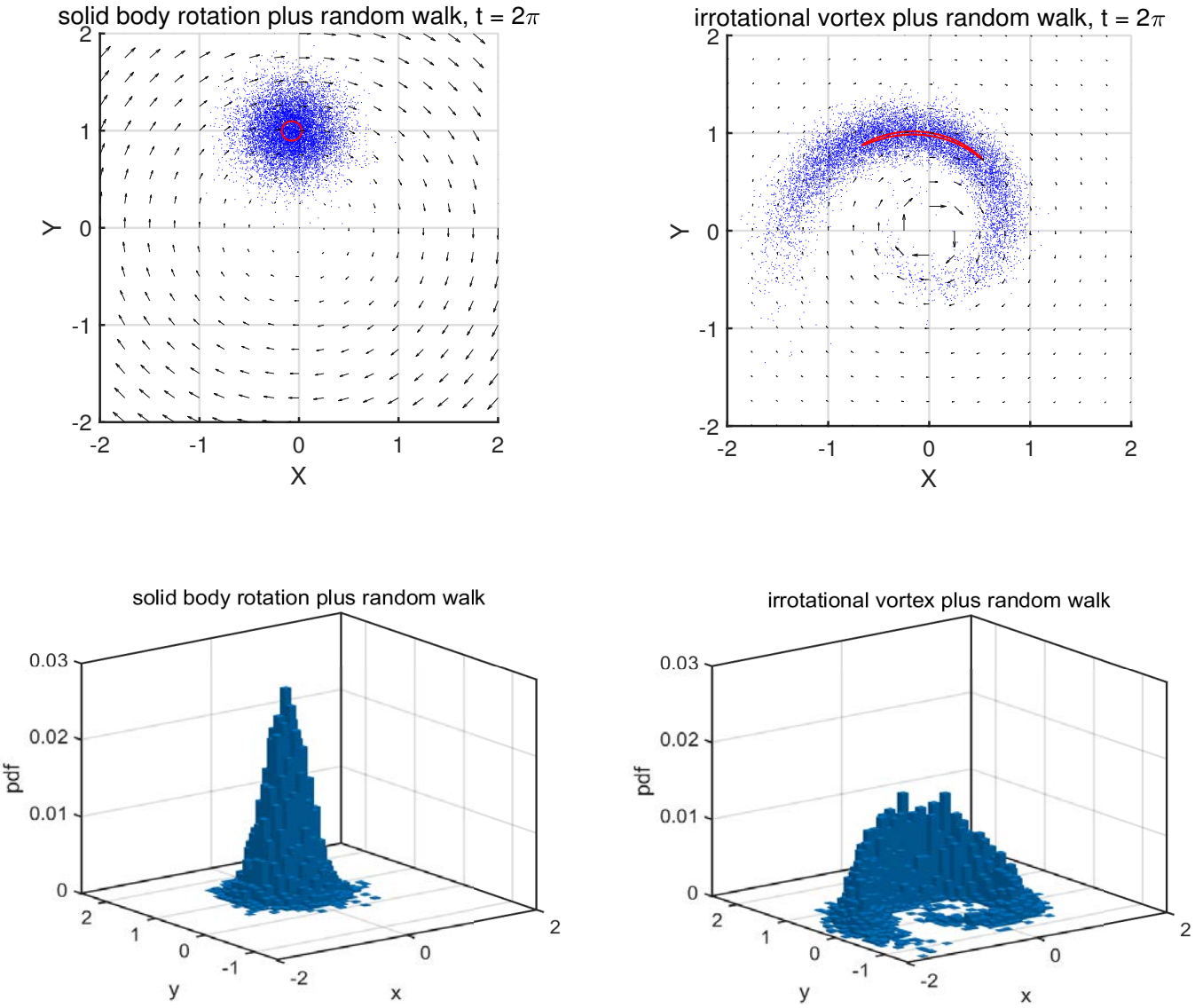

Figure 17: Advection plus random walk of freely drifting particles placed into a solid body rotation **(left)** and into an irrotational vortex **(right)**. The initial perimeter of the particle cloud is in red outline at upper left, and was advected by the vortex flow, but not subject to the random walk. This is intended to show deformation, which occurs in the irrotational vortex at right, but not in the solid body rotation at left. The upper panels are snapshots at $t = 2\pi$ and one complete revolution, and the lower panels are the corresponding probability density distributions (10,000 particles and 900 bins). The solid body rotation leaves the cluster perimeter unchanged, while the random walk diffused particles into the surrounding fluid. The irrotational vortex caused the cloud to be deformed into a thin filament which consequently had a significantly increased perimeter. As a result, there was enhanced diffusion of the particles out of the initial cloud, as evidenced by the much reduced peak in the histogram. Animations of these experiments are available at https://www2.whoi.edu/staff/jprice/wp-content/uploads/sites/199/2022/07/sm-solid.mp4 and https://www2.whoi.edu/staff/jprice/wp-content/uploads/sites/199/2022/07/sm-irrot.mp4

the prescribed vortex flow (solid body or irrotational), but not diffused, and shown by the red outline (Fig. 17) to give an indication of deformation. The distribution of particles after a time $t = 2\pi$ and one full revolution of either vortex at $r = 1$ is in Fig. (17). The solid body rotation and irrotational vortices gave remarkably different particle distributions.

How to describe and interpret what we see here? If our interest is what happens within the fluid itself, then a description that follows the particle cloud is appropriate and is discussed in the next section. If the goal is to describe the particle density at a fixed location, then diagnosing the particle budget over a control volume is appropriate, Sec. 4.4.2.

4.4.1 Following the particle cloud, the Lagrangian view

One straightforward and useful diagnostic is the area of the cloud. This may be estimated from a histogram of particle positions (Fig. 14) by summing the area of the bins that have at least one particle. This gives an upper bound on the cloud size. These statistics have been estimated over four experiments. The first two of these serve mainly to calibrate our view of diffusion and advection taken separately, and then the third and fourth experiments reveal the phenomenon of interest, stirring and mixing.

No diffusion. First, consider that there is no diffusion, and that advection is by the solid body rotation (the red line, no random walk, of Fig. 18, left). In that case the cloud size remains constant at the initial value, $\pi r_0^2 = 0.03$. The same holds for advection by the irrotational vortex.

No advection. Second, consider that there is a random walk, but with no advection (the magenta line of Fig. 18), left. The particle cloud expands, isotropically, as in Figs. (14) and (15), and the area grows linearly in time as $\text{area} \propto \sigma(t)^2 = K_{eff}\, t$. To make an equality of this relation requires a factor of about 9 multiplying the right side to account for the difference between the standard deviation of the particle distribution σ, and the leading edge of the particle cloud, which is about a factor of 3 greater.

Solid body rotation plus diffusion. Third, suppose that there is diffusion as well as advection by a solid body rotation, the solution of Fig. (17), upper left. The area of the expanding cloud in this experiment (the blue line of Fig. 18, left) is virtually identical to that found with diffusion alone. The clear conclusion from this is that advection (absent deformation) and rotation, as occurs in a solid body rotation, have no effect on the diffusive growth of the particle cloud.

Irrotational vortex plus diffusion. Fourth, and most interesting, is the case of diffusion plus advection by the irrotational vortex (Fig. 17, upper right). The irrotational vortex causes a strong deformation of the particle cloud as seen before, which does not by itself change the area of the particle cloud. But, when deformation is combined with diffusion, the result can be a fairly dramatic increase of cloud size, here about a factor 3 (cf. the blue and green lines of Fig. 18, left). The large increase in cloud area follows from the deformation of the cloud into a long filament, which would be very thin absent diffusion. The initial particle cluster was a circular area having radius $r_o = 0.1$ and an initial circumference of $0.2\pi \approx 0.63$. The deformation of the irrotational vortex extended (stretched) the sides of the initial cluster at a rate $2r_o\Omega$, which caused the circumference to grew almost linearly with time, from 0.6 to about $0.4\Omega T \approx 13$ by the end of the experiment, five revolutions, $t/2\pi = 5$. Diffusion acting across the greatly increased perimeter of the particle cloud was much more effective at mixing particles into the

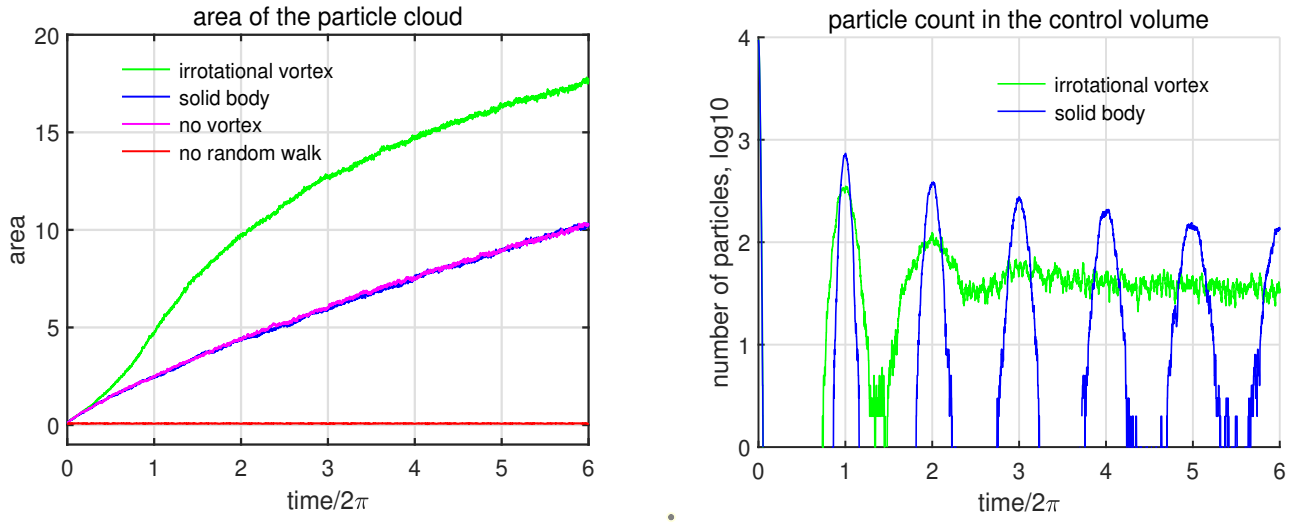

Figure 18: Lagrangian and Eulerian views of the evolving particle distribution. **(left)** The area of the cloud estimated as the sum of the area of every histogram bin (Fig. 17, lower) having at least one particle. Other possible measures of the area, e.g., the e-folding width squared, will give smaller estimates of the area, but similar time-dependence and comparison of one case to another. There are four experiments shown here. The red line is for a case having no random walk, and advection by either kind of vortex; area is conserved. The magenta line has the random walk with no vortex flow. The blue line is random walk plus a solid body rotation, and is indistinguishable from the random walk only case. Lastly, the green line is the random walk plus advection by an irrotational vortex. **(right)** The particle count in a control volume that at $t = 0$ coincided with the initial particle positions (the red circle at 12 o'clock in Fig. 17, upper left). The vortex flows were either an irrotational vortex (green line) or the solid body rotation (blue line). There was a large pulse of particle count at time intervals of 2π as the particle cloud was carried into and then out of the CV by the vortex flow. This advection signal was much more persistent in the solid body vortex case than in the irrotational vortex case. In the latter case, the particle concentration was nearly isotropic after about three revolutions, and so the signal of azimuthal advection was nearly extinguished thereafter.

surrounding fluid than was diffusion acting on a symmetric particle cloud, cf. the green and blue lines of Fig. (18), left.

A closer look at this last solution shows that the rate of increase of the area had three fairly well-defined stages. For very short times, $t/2\pi \leq 0.2$, the increase in area was the same for the solid body rotation case and the irrotational vortex case. Deformation was not significant for very short times while the particle cloud was still fairly compact and isotropic (round). During an intermediate time, $0.5 < t/2\pi < 4$, deformation caused a significant increase in the growth rate as described above. At still longer times, $t/1\pi > 5$, the particle cloud had been wrapped completely around the vortex center, and the particle distribution was almost isotropic thereafter. Further deformation was of little or no consequence. The area of the cloud continued to grow slowly as particles were diffused outward to larger radius.

4.4.2 Watching a control volume, the Eulerian view

If the need was to characterize the particle density field, that is, particle density at fixed points in space, then a different approach is required. One way is to take the particle count within a control volume (CV) (in this 2-d domain, actually a control area) that can be any size and shape. Here the CV was taken to be coincident with the initial particle launch region, a circular area with radius 0.1 centered on $(x,y) = (1,0)$ and fixed in space.

Solid body rotation. The solution for the case of solid body rotation plus diffusion is in Fig. (18), right, the blue line. This is very different from the prvious (Lagrangian) characteriztion of cloud size. The particle count shows a very pronounced, periodic pulse at time intervals of 2π as the particle cloud is advected into and then out of the CV (this is fairly obvious, but is easier to see in the animation linked in the caption of Fig. 17). Advection by the resolved vortex velocity thus has a dominant effect on the particle count in a fixed CV.

The full advection/diffusion equation, Eq. (45) is relevant to the particle field in this Eulerian frame. Advection and diffusion are distinct processes, and the Peclet number,

$$Pe \propto \frac{\text{advection tendency}}{\text{diffusion tendency}} \propto \frac{|\mathbf{V}\cdot\nabla C|}{|K_{eff}\nabla^2 C|} \propto \frac{UC/L}{K_{eff}C/L^2} \propto \frac{UL}{K_{eff}},$$

provides a framework that will help us think in quantitative ways about their comparative magnitude. U is the scale of the resolved vortex velocity that does the advection; $U = U_\theta = 1$ at $r = 1$ is appropriate. $K_{eff} = 0.01$ is the effective diffusivity in these experiments. In this problem (and often) the interesting thing turns out to be the length scale, L, that characterizes the tracer distribution in the sense that $\partial C/\partial x$ is O(C/L) and $\partial^2 C/\partial x^2$ is O(C/L^2). C is the spatially-varying part of the C field, which divides out of this Pe. The L is taken to be the initial radius of the particle cloud and so $L = 0.1$. Given these parameters, $Pe = 10$, and the inference is that the evolution of the particle density at a fixed site will be due mainly to advection. In the case of the solid body rotation and the fixed CV (Fig. 18, right, blue line), it clearly is, at least during the first few revolutions of the vortex flow.

The effect of diffusion by the random walk was to broaden the particle cloud over time, resulting in a reduced peak amplitude of the particle count on each successive pass through the CV. Nevertheless, the local rate of change of C (or particle number) within the fixed CV was still due mainly to advection, since larger L (even though caused by diffusion) favors advection compared with diffusion. If U is made smaller or K_{eff} is made larger, then the expected qualitative changes implied by a smaller Pe are realized, i.e., a greater effect of diffusion than in the nominal case. However, for $Pe > 1$, advection dominates the instantaneous balance at intermediate and long times unless the relationship of $\mathbf{V}$ and ∇C changes significantly, which it may (discussed further below).

Another form of Peclet number, a displacement Peclet number, illustrates explicit dependence upon elapsed time,

$$Pe_d = \frac{\text{advection distance}}{\text{diffusion distance}} = \frac{U\,t}{\sqrt{K\,t}} = \frac{Un}{w\sqrt{n}},$$

the ratio of advection distance to the diffusion distance at time, t (and note that n is a pure number with no physical dimension). At very short times, say one step of the random walk, $n = 1$, and given that $U = w$, the motion of a single particle is due equally to the resolved flow and the eddy velocity. At long

times, after many random steps, the displacement of a particle will be due mainly to the advection distance, which grows as $t \propto n$, vs. the diffusion distance which grows as $\sqrt{t} \propto \sqrt{n}$.

Irrotational vortex During the first several revolutions, time$/2\pi < 2$, the azimuthal advection was much as it was in the previous experiment, but after about $t/(2\pi) > 3$, the signal of advection was nearly extinguished.

What happened to *Pe*? The Peclet number makes use of one length scale to characterize the first and second derivatives of the tracer field (the particle cloud) that are relevant to advection and diffusion. The dependence upon one length scale is plausible at the start of an experiments when the particle cloud was isotropic. However, this may fail dramatically when the particle cloud has evolved far from the initial condition, in this case into a long and very thin filament. The appropriate length scale for the advection term should represent the component of the gradient that is parallel (or anti-parallel) to the advecting velocity. After about three revolutions of the irrotational vortex, the particles were smeared out over a cloud that was nearly azimuthally symmetric, and hence the advection effect due to the azimuthal velocity was greatly diminished compared with the advection of the initial condition. The appropriate length scale for diffusion is the smaller of the width and the length of the particle cloud, which can be very different when deformation stretches the particle cloud into a thin filament, as it has here. Thus the Pe estimate made from the length scale $L = r_o$ appropriate to the initial condition was not relevant once the particle cloud had evolved far away from the isotropic initial condition. Indeed at long times, further evolution of the particle cloud was due mainly to diffusion, just as it is in the Lagrangian description of the previous subsection.

The important result of this last calculation is that the combined effect of deformation and diffusion produced a near-homogeneous equilibrium much more rapidly than would occur in the absence of deformation, i.e., by diffusion acting alone. At this level of detail, there is a significant difference between diffusion by a small scale random walk (or molecular diffusion) which acts to reduce tracer gradients by mixing, and a deformation rate by the resolved flow, often called 'stirring' when it is quasi-random, which acts to increase mean square gradients.[19]

Reversible stirring. The deformation caused by the irrotational vortex after one revolution may be undone by simply reversing the direction of the vortex (Fig. 31) while omitting the random walk. After another 2π elapsed time, the initial particle cloud (the red outline) returned to its starting position; the resolved scale deformation, even though quite large, is reversible. The dispersal of particles by the random walk does not reverse, however, unless we were to store each step for each particle, about 6,000,000 in total, and played that tape backwards.[20]

[19] An excellent introduction to stirring and mixing is by Thiffeault, J-L., 2010, Lecture 1: Stirring and mixing. Notes by S. Pegler and A. O'Rourke. https://www2.whoi.edu/staff/jprice/wp-content/uploads/sites/199/2023/11/Thiffeault-SM.pdf. A very interesting discussion of the Peclet number as a measure of deterministic vs. random process is by Gommes, C., and J. Tharakan, 2020, The Peclet number of a casino: Diffusion and convection in a gambling context. A. J. Phys., 88(6), 439-447. https://ui.adsabs.harvard.edu/abs/2020AmJPh..88..439G/abstract A simple Matlab script you can use to integrate this case and the other vortex flows discussed in Sec. 5.4 is https://www2.whoi.edu/staff/jprice/wp-content/uploads/sites/199/2023/12/stirandmix.txt

[20] An animation of this case is https://www2.whoi.edu/staff/jprice/wp-content/uploads/sites/199/2022/08/sm-unwind.mp4

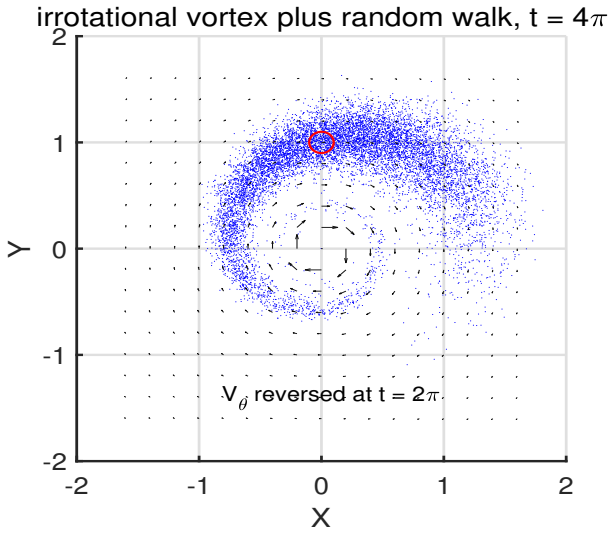

Figure 19: Can the stirring and mixing be reversed? The end state of the irrotational vortex/random walk experiment, Fig. (17), lower left, was used as the initial state of a follow-on experiment in which the direction of rotation was reversed and the integration continued until $t = 4\pi$. The perimeter of the initial particle cluster (red circle) was restored exactly, but the diffusion of particles was not.

4.5 Appendix: The Lamb-Oseen vortex

We now have most of the pieces in place to understand a phenomenon called the Lamb-Oseen (LO) vortex. This has only a tangential connection with the Lagrangian-Eulerian theme of this essay and so is included as an appendix. The LO vortex is nonetheless interesting in that it bridges the apparently huge divide between an irrotational vortex and solid body rotation. The solution of the LO vortex is also one of the few simple, time-dependent solutions of the Navier-Stokes equations.

4.5.1 How to make a starting vortex

The LO vortex can be thought of as an idealization of the starting vortex that forms behind an airplane wing, or, a teaspoon pushed through a tea cup. High pressure (relative high free surface height) builds up in front of the accelerated spoon and low pressure occurs behind. A starting vortex forms as fluid flows around the edge of the spoon from higher to lower pressure. Since the fluid that makes up most of the vortex is driven mainly by this pressure gradient, most of the fluid within the vortex is free of vorticity. A comparatively small volume of fluid makes contact with the spoon through a thin viscous boundary layer that imparts vorticity having a sense that is consistent with the swirling motion of the larger vortex (negative if clockwise). Most of this vorticity is concentrated in a compact, central core. The core is surrounded by fluid that is in vortical motion, but is nevertheless vorticity-free.[21]

The strength of the vortex may be measured by the circulation, C,

$$C = \oint \mathbf{V}\cdot\mathbf{ds} = \iint (\nabla\times\mathbf{V})\cdot\mathbf{n}\, da = \iint \chi\, da, \tag{47}$$

[21] An isolated vortex having one sign of vorticity is oftentimes referred to as a monopole and described as if two-dimensional, as here. In practice, the vortex formed by a spoon pushed through a tea cup will be three-dimensional, with a continuation along the bottom edge and connecting to a mirror image vortex on the opposite side (e.g., Fig. 2, Part 1). That there is a vortex pair, rather than an isolated monopole, is of considerable importance in the evolution of the flow.

the line integral of velocity around a closed loop. By Stokes' Theorem,[22] this line integral is equal to the total flux of vorticity, $\nabla \times \mathbf{V} \cdot \mathbf{n}$ through any surface that is bounded by the loop. In the two-dimensional case of interest here, C is also equal to the areal integral of the (scalar) vorticity, χ, over the surface that is bound by the loop. If the loop does not surround the vortex core, then $\chi = 0$ everywhere over the surface, and so $C = 0$. If the loop does enclose the vortex core, then $C = \tilde{z}$, which can be termed the vortex strength.

4.5.2 Diffusion of vorticity

If the vorticity is highly localized, then the initial distribution $\chi_o(r)$ may be idealized as a delta function of r,

$$\chi_o \;=\; \tilde{z}\,\delta(r)\;. \tag{48}$$

Assuming an integration path that is a circle of radius r centered on this core, then Stokes' Theorem shows that

$$V_\theta(r) \;=\; \frac{\tilde{z}}{2\pi r}, \tag{49}$$

the velocity profile that we have been calling an irrotational vortex. This V_θ has a singularity at the origin which is unphysical; vorticity may be highly localized, but in a real fluid it can not be a literal delta function on account of viscosity, if nothing else. To allow that the initial vortex core will have a finite width, σ_o, the delta function of Eq. (48) may be represented by a normalized Gaussian,

$$\tilde{z}\,\delta(r) \;\approx\; \frac{\tilde{z}}{2\pi\sigma_o^2}\,\exp\left(\frac{-r^2}{2\sigma_o^2}\right), \tag{50}$$

that may be made arbitrarily narrow, $\sigma_o \to 0$, to give a strongly peaked distribution having the integral properties of a delta function. In the example below of an LO vortex in water, $\sigma_o \;\approx\; 0.1$ cm (by inspection).

We have seen that an irrotational vortex will have significant deformation near the core that will enhance the mixing of particles and presumably vorticity into the outlying fluid. On the reasonable assumptions that the vortex is azimuthally symmetric and that the radial velocity is negligible, then the vorticity of the vortex will evolve according to the linear diffusion equation,

$$\frac{\partial \chi}{\partial t} \;=\; \nu\nabla^2\chi \;=\; \nu\,\frac{1}{r}\,\frac{\partial}{\partial r}\left(r\,\frac{\partial \chi}{\partial r}\right), \tag{51}$$

where ν is the kinematic viscosity of the fluid. If water at room temperature, $\nu \approx 0.01$ cm^2 sec^{-1} (note the CGS units). The initial condition is Eq. (48) plus (50) and the boundary condition is $\chi \to 0$ as $r \to \infty$. The solution for the vorticity distribution is then the fundamental solution of the two-dimensional heat equation, Eq. (46) and (Fig. 20, upper),

$$\chi(r,t) \;=\; \frac{\tilde{z}}{4\pi\nu(t+t_o)}\,\exp\left(\frac{-r^2}{4\nu(t+\pi t_o)}\right) \tag{52}$$

[22] https://www.byjus.com/maths/stokes-theorem

modified with a time offset $t_o = \sigma_o^2/(2\pi\nu) \approx 0.15$ sec to allow for a finite core of radius σ_o and the χ_o of Eq. (48). As time runs, vorticity diffuses into the surrounding fluid, and the associated azimuthal velocity is (Fig. 20, center),

$$V_\theta(r\,t) \;=\; \frac{1}{r}\int_0^r r\,\chi\;dr \;=\; \frac{\tilde{z}}{2\pi r}(1 \;-\; \exp(\frac{-r^2}{4\nu(t+\pi t_o)})). \tag{53}$$

4.5.3 The inner core, solid body rotation

This solution has two familiar limits. In the inner core of the vortex, $r << \sqrt{4\nu t}$ (small r or large t), the vorticity is quasi-uniform with r and decaying in time. The velocity of the inner core increases linearly with r and decreases in time,

$$V_\theta \;\approx\; \frac{\tilde{z}r}{8\pi\nu t}, \quad \text{a decaying, solid body rotation.}$$

At large radius or small time, $r >> \sqrt{4\nu t}$, the vorticity is very small and steady, and the azimuthal velocity decreases as $1/r$,

$$V_\theta \;\approx\; \frac{\tilde{z}}{2\pi r}, \;\text{the initial, irrotational vortex, not yet affected appreciably by viscosity.}$$

This solution for a time-dependent diffusive vortex, known as a Lamb-Oseen vortex, shows how an irrotational vortex, which has significant deformation and viscous stress, will evolve in time into a solid body rotation which has vorticity but no deformation or viscous stress. A solid body rotation could thus be steady, except that the velocity profile $V_\theta \propto r$ insures that a solid body will sooner or later interact with surrounding fluid or boundary.

The pressure anomaly associated with the displaced free surface, $P = \rho g z$, has no dynamical role in the vorticity balance (51). However, a pressure anomaly has an essential role in the momentum balance, insofar as it provides the radially-inward, centripetal force required to provide a quasi-static balance to the centrifugal force of the azimuthal velocity. The free surface displacement may be computed from a steady, radial force balance

$$\frac{V_\theta^2}{r} \;=\; g\frac{\partial z}{\partial r}$$

integrated from the far field inwards (Fig. 20, lower),

$$z(r) \;=\; -\int_\infty^r \frac{V_\theta^2}{gr}\,dr \;+\; z(\infty).$$

Notice that the free surface in the vortex center is a relative low, regardless of the sense of the azimuthal flow. This is not the case for much larger, geophysical vortices that are significantly influenced by the Coriolis force (next Sec. 7). The free surface displacement is especially easy to observe and so is a useful diagnostic (for more on the free surface see Problem 4 below).

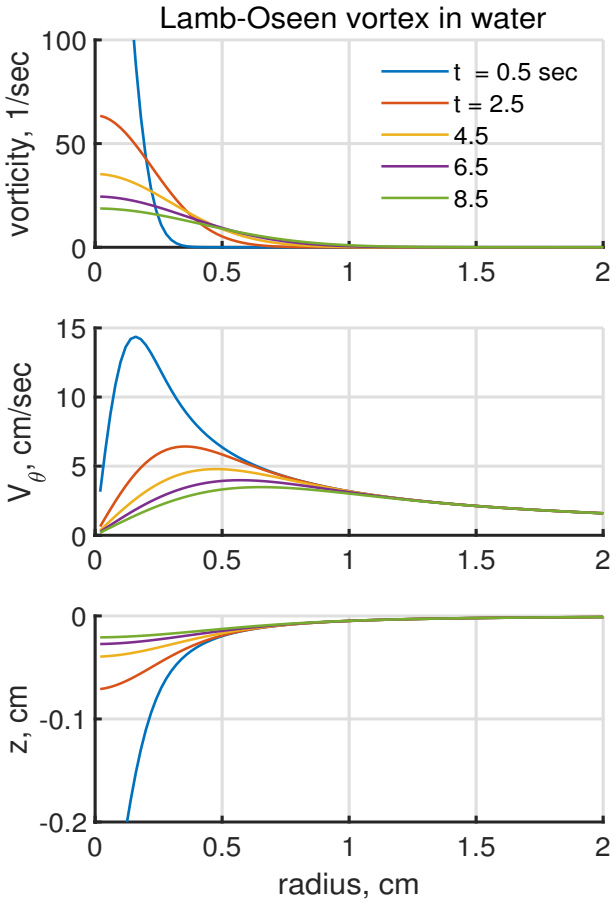

Figure 20: Some properties of a Lamb-Oseen vortex in water having $\tilde{z} = 20$ cm^2 sec^{-1} and $\nu = 0.01$ cm^2 sec^{-1}. The vorticity **(upper)** was initially concentrated very near the origin, and then diffused outward with time. The azimuthal velocity **(middle)** and the free surface displacement **(lower)**. The dimensional scales are those of a small irrotational vortex in water. Profiles are shown at 2 sec intervals, beginning at $t = 0.5$ sec. Even at very short times, 0.5 sec, there was a discernible core of the vortex that was in solid body rotation. Outlying regions, $r > 1$ cm, were irrotational (velocity decreasing as $1/r$) for the duration shown here.

4.6 Key ideas

1 The basis for some improved algorithms for estimating advection is the notion that parcel trajectories are the characteristics of an advection equation.

2 All real fluid flows have a more or less wide range of time and space scales: for a tea cup, about one order of magnitude; for the atmosphere, about ten orders of magnitude. The first step of an analysis will be the definition of the scale(s) that will be resolved, and those that will have to be left unresolved, frequently smaller time and space scales.

3 Linear (Reynolds) averaging may be used to define the resolved scale, and implicitly the unresolved or eddy scales. The net effect of the eddy motion on the resolved scale may often be accounted as an eddy flux, the cross-correlation of the eddy velocity and an intensive fluid property.

4 The classical mixing length theory yields a parameterization of the eddy flux as an effective diffusivity, K, acting on the resolved tracer field. This may work well when the eddy velocity is a random walk, isotropic, homogeneous and independent of the larger scale. It should not be taken as a general solution/parameterization of eddy fluxes.

5 The Peclet number UL/K can make a useful estimate of the magnitude of advection by the resolved scale compared with diffusion $\propto K$ provided that a single length scale L is appropriate for both the gradient and the Laplacian operators. This is likely to be violated as the tracer field evolves with time.

6 A very important consequence of advection is that it may (usually will) be accompanied by deformation that changes the shape of fluid parcels. If sustained, deformation will tend to produce long and thin streaks of tracer that have a greatly increased perimeter and thus much more readily diffused into the surrounding fluid compared with tracer in a zero deformation flow. Random deformation is often described as stirring, and the combined effect of stirring and mixing (diffusion) leads to comparatively rapid homogenization.

4.7 Problems

1) Given that the actual velocity **v** is nondivergent, apply a Reynolds averaging procedure to show that the resolved velocity and the eddy velocity are also nondivergent.

2) Arguably the most important characteristic of a random walk is that the long term, ensemble mean displacement measured by the root mean square of x, y or r grows as the square root of time. Can you explain how this comes about in a few sentences? Can you use the formalism of Eqs. (41) and (42) to describe the growth of correlated motion, i.e., a mean flow (as opposed to a random walk)?

3) A good example of a resolved flow in which to examine stirring and mixing is a confluent flow, $u(x,y) = b\,x$ and $v(x,y) = -b\,y$ (Problem 6 of the previous section). Consider a random walk in this flow. At long times, the tracer will be confined to an increasingly narrow filament that is parallel to the $x-$axis. At some long time, the dispersion of particles away from the ever-lengthening and thinning filament will be balanced by the ongoing linear deformation, a compression, yielding an equilibrated filament width, albeit with ever-diminishing particle concentration. Can you test that the balanced width of this filament is closely proportional to the Batchelor scale, $L_B = \sqrt{K/b}$? What causes the particle concentration to decrease? An animation of this case is available from
https://www2.whoi.edu/staff/jprice/wp-content/uploads/sites/199/2022/08/confluence.mp4

4) Given the solution of a Lamb-Oseen vortex, Eq. (53), show that the free surface in the core of the initial vortex is $z \propto 1/r^2$, while the core is in irrotational motion (only a very short time, tenths of seconds). The free surface at the center of the vortex then appears to have a noticeable dimple. But after viscosity has diffused vorticity away from the center, and an appreciable central region is in solid body rotation, show that the free surface is then $z \propto r^2$and the free surface at the center of the vortex appears to be flat. Look for this rapid (less than a second) transition in the shape of the free surface in the vortices you can make by pushing a paddle (or any flat object) through still water. (Were you surprised by how viscous water appears to be in this context? I was.)

5 Models that combine Lagrangian and Eulerian concepts

A wide variety of numerical models have developed around the idea of combining the most advantageous aspects of Lagrangian and Eulerian methods and concepts. Hybrid models are feasible because numerical models have the option to treat the different terms and processes of an equation of motion or tracer balance by wholly different methods. Thus, advection may be treated by a Lagrangian (parcel-tracking) method, Sec. 5.1, while the pressure field might be better evaluted by mapping fluid properties (e.g., mass density) on to a fixed, Eulerian grid, Sec. 5.3.

5.1 Numerical treatments of advection

This subsection 5.1 will consider finite difference methods for solving a one-dimensional tracer advection problem, first by a purely Lagrangian method, then a purely Eulerian method, and then finally by a hybrid method called semi-Lagrangian. This latter method is called semi-Lagrangian because parcel identity is retained only for short times. Such semi-Lagrangian treatments of advection are very widely used, and are a significant motivation for understanding both Lagrangian and Eulerian systems.

The test problem will be the one-dimensional, time-dependent balance of a passive tracer, $c(x,\ t)$,

$$\frac{D\ c(x,t)}{D\ t}\ =\ Q(x,t). \tag{54}$$

The initial tracer distribution is a two-level, top-hat pulse of half width 1,

$$c(x,t=0)\ =\ c_o(x),$$

which has sharp edges (Fig. 21, left, the blue line). The boundary condition is that tracer goes to zero at very large $\pm x$. A current is specified as

$$u(t) = U_0\ sin(10\pi\ t/t_M), \tag{55}$$

where t_M is the duration of the experiment, 10,000, and t/t_M is the normalized time. The current amplitude $U_0 = 0.01$ is sufficient to carry (advect) the tracer pulse back and forth across the model domain ten times, and with a displacement that is several times the initial pulse width. The external source Q is also presumed to be a known function of time,

$$Q\ =\ Q_o sin(J\pi\ t/t_M),$$

with J the number of half-cycles, and could be, e.g., heating by solar insolation. There is no diffusion and so this is otherwise an ideal fluid. The one-dimensional geometry assumed here minimizes algebra and eases the presentation, but it is not general: important complications can arise in two or three space dimensions that will be noted toward the end of Sec. 5.1.

This problem has an exact solution that may be found by the method of characteristics (see Problem 2) at the end of this section). In the exact solution, and assuming $Q = 0$, the tracer profile will overlay the

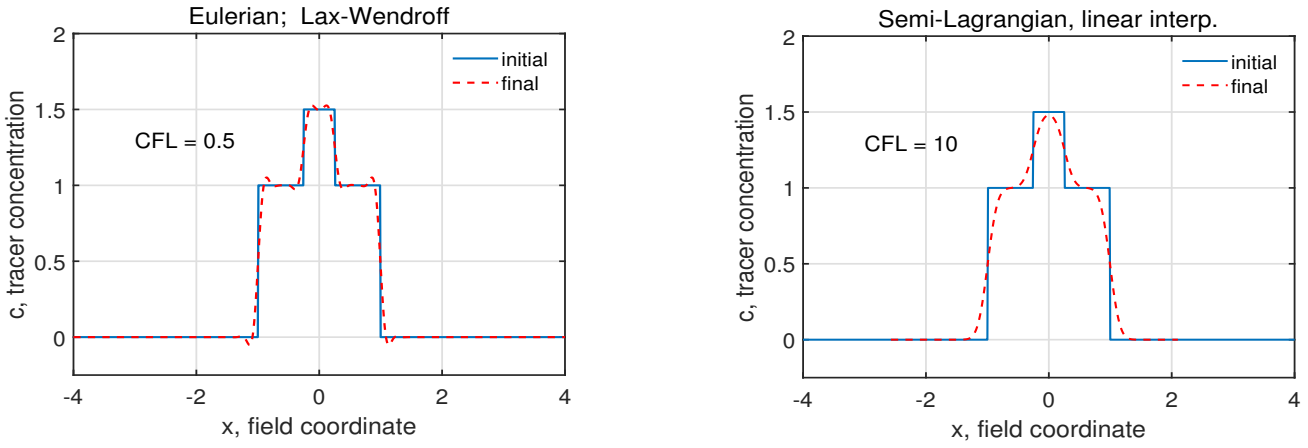

Figure 21: Tracer advection experiments solved by numerical methods on a one-dimensional domain. The initial tracer distribution was a two-level top-hat (solid blue line) that was advected back and forth across the center of the domain through ten complete cycles. An exact solution will have the end time solution (red dashed line) overlay the initial distribution. The left panel is the solution computed with an Eulerian second order Lax-Wendroff scheme with a time step $\delta t = 0.5$, and CFL = 0.5. The right panel shows the solution computed with a semi-Lagrangian scheme (Sec. 5.1.3) using a linear interpolation to evaluate the tracer at the estimated parcel departure positions. This solution was computed with a considerably larger time step, $\delta t = 10$ and so CFL = 10. These solutions display roughly comparable though quite different errors: high frequency noise in the Lax-Wendroff solution, and diffusive-like broadening of the pulse in the semi-Lagrangian solution. A significant practical difference is that the semi-Lagrangian solution required far fewer steps.

initial profile at every half cycle of the current, Fig. (21).

5.1.1 Discretized data and numerical solution

One-dimensional models and exact solutions are *not* the usual fare of fluid mechanics. Rather, most real problems and certainly most research problems require solution by numerical methods that can treat multi-dimensional and nonlinear systems. (Of course, exact solutions to highly simplified problems can be essential as a means to check and to interpret numerical solutions.)

To represent a tracer distribution within a one-dimensional numerical calculation requires at least two discrete arrays, one that represent the tracer,

$$c = [c_1 \;\; c_2 \;\; \ldots \, c_N],$$

with N the number of elements, or nodes, and a second array that represents space,

$$x = [x_1 \;\; x_2 \;\; \ldots \;\; x_N],$$

and that is in a one-to-one correspondence with c. We could also include an array of times, but this is peripheral to the main point. The same comment applies to the source term, Q, and to the current, u.

The space coordinates could be interpreted in one of two ways depending upon whether the calculation will take a Lagrangian or an Eulerian prespective. The x_n could be regarded as the time-dependent $\tilde{x}$-coordinates of moving parcels; the $\tilde{x}_n$ is then the position of the $n-$th parcel having tracer c_n. A superscript time index on $\tilde{x}$ is essential, i.e., $\tilde{x}_n^i$, while the corresponding $\tilde{c}_n$ are constant, and so do not require a superscript to denote the time. There is generally no need to keep all of the time levels, $t = [t_1\ t_2\ \ldots\ t_M]$, but notice that $t^i = i\,\delta t$ with δt the time step. If we let $(\ )^i$ be the present time level, then $(\ )^{i+1}$ is the next time level. This is, of course, Lagrangian view of (54), and the tilde is our notational convention that distinguishes Lagrangian from Eulerian variables when they are being considered side-by-side as here.

Alternatively, the x_n could be field coordinates, i.e., the fixed positions in space where we seek the solution for the time-dependent tracer. In that case the x nodes could be spaced equally at grid interval δx and so $x_n = n\delta x$ and $L = N\,\delta x$ is the width of the domain. The tracer is then time dependent, and so requires a time superscript, c_n^i is the i-th time (the present time) value of c at the n-th node.

To summarize, a discretized view of the tracer balance (54) can be either

Lagrangian: the time-varying position of parcels, $\tilde{x}_n^i$, each of which have a fixed tracer, $\tilde{c}_n$, or,

Eulerian: a time-varying tracer, c_n^i, defined on fixed field coordinates, x_n.

In several key respects the discussion that follows is in parallel with the method of characteristics (Part 1, Sec. 4). And specifically, the source term may often be dealt with separately from the advection term. If, the source term is external, e.g., solar insolation, then the only restriction on the time step is that it must be small enough to resolve the temporal variation of the source. If solar insolation, tens of minutes or hourly will probably suffice. Solving for the advection process is more challenging.

5.1.2 Lagrangian advection of parcels

This problem is very simple when viewed from a Lagrangian perspective. The adiabatic tracer balance is just

$$\frac{D\,\tilde{c}_n}{Dt} = \frac{\partial \tilde{c}_n}{\partial t} = 0, \tag{56}$$

or in other words,

$$\tilde{c}_n = c_{on},$$

and the tracer value on each moving parcel is fixed in time at the initial value. The entire phenomenon is contained in the motion of the parcels given by the trajectory equation,

$$\frac{\partial\,\tilde{x}_n}{\partial\,t} = \tilde{u}. \tag{57}$$

In the problem defined here, the velocity is a known function of time only, and so a sufficient, if elementary, finite difference form of the trajectory equation is just

$$\tilde{x}_n^{i+1} = \tilde{x}_n^i + \delta t\,u^i. \tag{58}$$

Notice that (58) is first order, and forward in time, and there are no space derivatives required. This is trivial to integrate in the present test problem, the only constraint on the time step is that it should be small enough to resolve the time dependence of the current. With that satisfied, the solution is almost exact (as in the method of characteristics) and so there is no reason to show it here. You can see this solution in the script noted in footnote 24 below, and experiment with different time steps.

In two or three dimensions there can be a significant practical shortcoming inherent to a purely Lagrangian model that does not arise in this one-dimensional test problem. Namely, the parcel trajectories are likely to become entangled, and the parcels distributed very unevenly across the model domain.[23] If the model required solving for the velocity and thus the pressure gradient and the laplacian needed for momentum diffusion, then this uneven and uncontrolled distribution of parcel positions (which are the positions where we know the solution) could become a significant issue. This is akin to the problem of evaluating a pressure gradient in the three-dimensional Lagrangian equations noted in Sec. 2.5 of Part 1. A viable solution is to map the Lagrangian data onto a grid, and then evaluate the pressure or gravitational mass attraction at the position of the parcels; this is the hybrid, Particle in Cell approach that will be discussed in Sec. 5.3.

5.1.3 Eulerian advection of a tracer field

Now consider the purely Eulerian version of (54) in which c is a function of the field coordinates x and time, t,

$$\frac{D\,c(x,t)}{Dt} \;=\; \frac{\partial c(x,t)}{\partial t} \;+\; u(x,t)\frac{\partial c}{\partial x} \;=\; 0. \tag{59}$$

In the Eulerian frame, the task is to calculate how the advection of the tracer field $c(x,t)$ changes c at the discrete, fixed grid point(s), x_n, of an Eulerian model grid. To evaluate the advection term requires the velocity, u, that is either specified or may be presumed known by the same method used to solve for the tracer.

A plausible, simple finite difference estimate of the gradient of c at x_n is the centered, first difference around x_n,

$$\frac{\partial c}{\partial x} \;\approx\; \frac{c_{n+1} \;-\; c_{n-1}}{x_{n+1} \;-\; x_{n-1}} \;=\; \frac{c_{n+1} \;-\; c_{n-1}}{2\delta x}, \tag{60}$$

and as a first guess for the time derivative,

$$\frac{\partial c}{\partial t} \;\approx\; \frac{c^{i+1} - c^{i}}{t^{i+1} \;-\; t^{i}} \;=\; \frac{(c^{i+1} - c^{i})}{\delta t}.$$

Forward in time, centered in space: Putting these two finite difference estimates together with (59) gives a very concise prescription, or 'scheme', for stepping the tracer ahead in time,

$$c_n^{i+1} \;=\; c_n^{i} \;-\; \delta t\; u_n^{i}\; \frac{(c_{n+1}^{i} - c_{n-1}^{i})}{2\delta x}. \tag{61}$$

[23] See Welander, P., 1955, Studies on the General Development of Motion in a Two-Dimensional, Ideal Fluid, Tellus, May, 1955, 141-156. Online at https://onlinelibrary.wiley.com/doi/abs/10.1111/j.2153-3490.1955.tb01147.x

Thus, given c^i and the current, u^i_n, (61) provides an explicit estimate of the next time level, c^{i+1}. This is an explicit estimate in that the right hand side involves previous time levels only. An implicit estimate would include c^{i+1} on the right hand side. This scheme is called 'forward in time, centered in space', or FTCS.

The Eulerian numerical solutions to follow have been evaluated with a grid interval $\delta x = 0.01$, and with a nominal time step $\delta t = 1.0$, but varied from case-to-case. The end time is $t_M = 10000$ and hence there are $M = 10000$ time steps for the nominal δt.

The simple and intuitive FTCS integration scheme (61) seems hopeful, but it turns out to be wildly unstable; the tracer values quickly diverge and the calculation blows up, figuratively.[24] How and why the FTCS method is unstable can be anticipated from a von Neuman stability analysis, which is outside the present scope.[25] the finte difference advection terms tends to generate spurious high frequency (space scale $2\delta x$) variability, that can quickly swamp the physical process of advection that was intended by (59). In some cases these numerical errors can be minimized by choosing using a sufficiently small time step, δt. A very important parameter that characterizes the size of the time step is the nondimensional CFL number

$$CFL = \frac{U\ \delta t}{\delta x},$$

where U is the maximum amplitude of the advecting flow. For most explicit finite difference schemes, stability requires that the time step gives a CFL number less than 1, otherwise a time step will amount to an extrapolation that will be unstable. Accuracy may require that the CFL be considerably less than 1.

Second-order, Lax-Wendroff: Much better results come from the widely used Lax-Wendroff method, which is a second order, explicit scheme,

$$c^{i+1}_n = c^i_n - \delta t\ u^i\ \frac{c^i_{n+1} - c^i_{n-1}}{2\ \delta x} + \delta t^2\ u^{i2}\ \frac{c^i_{n+1} + c^i_{n-1} - 2c^i_n}{2\ \delta x^2}. \tag{62}$$

Compared with the unfortunate FTCS, there is a new term on the right hand side that can be interpreted as a diffusion process — a finite difference second space derivative multiplied by a coefficient that looks like an effective diffusivity, $\propto\ \delta t\ u^2$. Though not intentionally built into this scheme, this term acts to damp the growth of high frequency spatial variability coming from the first order advection term. The solution for tracer distribution computed via the Lax-Wendroff method with $\delta t = 0.5$ and CFL = 0.5 (Fig. 21, left, the red dashed line) shows some high spatial frequency noise on the edges of the tracer pulse, but otherwise looks good (but what can be considered good or bad will depend very much upon intended use of the solution). [26]

[24] The time-dependent solution for this and other schemes is displayed by the Matlab script LandEadvection.m available at https://www2.whoi.edu/staff/jprice/wp-content/uploads/sites/199/2023/04/LandEadvection.txt This script was written to be readily modified to your own experiments.

[25] A concise article on stability generally is https://www.flow3d.com/resources/cfd-101/numerical-issues/computational-stability/

[26] There is no denying that a comparison of numerical solutions as in Fig. (21) is deadly-dull. Considerbly better is to see how these and other solutions develop in time.[24] Some solutions start off with high frequency noise that slowly dissipates (or not, FTCS), and others show a secular trend in the peak amplitude, e.g., a persistent decay of the pulse amplitude that may mimic diffusion. This is very pronounced with a scheme called upwind differencing (shown in the script noted above, but not here) that seems well-conceived in as much as it recognizes that advection has an inherent direction, from upwind to downwind.

5.1.4 Semi-Lagrangian advection

There are hybrid numerical schemes that adhere to the spirit of (56) while keeping an Eulerian core and avoiding the problems associated with entangled trajectories. The solution is sought on a fixed spatial grid, while tracking parcels for only short times that do not generate complex, entangled trajectories. There are several plausible ways to do this in detail, but the central idea is that advection alone should be adiabatic.

Suppose that the model equations have been stepped forward to yield the tracer at a grid point x_n at a time t^i. From the Lagrangian perspective, and considering only advection, then the tracer at that grid point should be the tracer of the parcel that departed an upstream position at the previous time t^{i-1}, and then arrived at the grid node x_n at time t^i. (This is assuming that the present parcel position has a one-to-one mapping with previous times, and that there is no diffusion.) Given the known velocity field and its short-term history, the upstream departure point for this x_n, say x_{n-dp} may be calculated by a backwards-in-time integration of the trajectory equations,

$$x^i_{n-dp} \;=\; x^i_n \;-\; \delta t\; u^i$$

(57). It is very likely that the estimated departure point, x_{n-dp}, will not coincide with a node of the Eulerian grid, and so an estimate of the tracer value at the departure point will require an interpolation of the tracer field at the departure time. For example, suppose x_{n-dp} falls between the grid nodes x_m and x_{m+1}, and that the distance (no sign) to $x_m$is a. A linear interpolation to find the tracer at the departure point would then be

$$c^{i-1}_{n-dp} \;=\; c^{i-1}_m \;+\; \frac{a}{\delta x}(c^{i-1}_m \;-\; c^{i-1}_{m+1}),$$

and so

$$c^i_n \;=\; c^{i-1}_{n-dp}.$$

Most importantly, no CFL-like criteria arises here, and the time step need only resolve the time-dependence of the advecting current. Since the parcel identity is retained during only a single time step, a method of this kind is often referred to as semi-Lagrangian.

In the semi-Lagrangian solution shown in Fig. (21) right, the time step was taken to be $\delta t = 10$ and hence $CFL \;=\; 10$. Despite this comparatively large CFL, the end time solution isn't bad. There is some fairly pronounced smearing of the sharp edges of the tracer pulse caused by the repeated (10,000 times) linear interpolation. This smearing can be significantly reduced by use of a spline interpolation, (see Problem 2) below).

The practical difference between this semi-Lagrangian scheme compared with an explicit Eulerian scheme (Lax-Wendroff) is a significantly increased permissible time step. This has considerable value in applications where computational efficiency is a premium, say in weather forecasting or climate forecasting over long times.[27] On first sight it may seem as if the semi-Lagrangian method has given us a greatly reduced computational burden for nothing more than a modest complication of the model code.

[27] Staniforth, A. and J. Cote, 1991. Semi-Lagrangian integration methods for atmospheric numerical models - A review. Mon. Wea. Rev., 119, 2206 - 2224. A recent and very comprehensive discussion is by Fletcher, S., 2019, Semi-Lagrangian Advection Methods and Their Applications in Geoscience, Elsevier, ISBN: 9780128172223

But with a little reflection, it seems that this gain in efficiency comes from appeciating and exploiting the (fundamental) Lagrangian perspective that advection alone is an adiabatic process.

5.2 Layered models of the stratified ocean interior

An important example of a numerical model that is Lagrangian in one specific way while being Eulerian otherwise is the use of a layered representation of the vertical stratification of the ocean. The ocean interior has weak but important stratification that can be presumed to be stable (denser fluid always lying below less dense fluid, except in special circumstances that can be accounted explicitly when necessary). Important terms of the Eulerian density balance include the local rate of change of density and vertical advection,

$$\frac{\partial \rho}{\partial t} = -w\frac{\partial \rho}{\partial z} + ... \tag{63}$$

which is enough to discuss the issue. Numerical implementation of the vertical advection term does not present any exceptional difficulty but the result will generally include some spurious vertical diffusion that will eventually smear out the ocean's thermocline after the density profile has been advected up and down, perhaps thousands of times, by internal waves, which if modelled exactly would be adiabatic. The smearing effect may be likened to vertical mixing, and will occur to some degree even if no real (physical) vertical mixing was intended. Over the course of a long integration, such spurious (numerical) vertical mixing may lead to unrealistic density stratification.[28]

One antidote to this kind of spurious vertical mixing is to implement a Lagrangian representation of the vertical structure and advection process (63). In place of a vertical grid, the density profile is represented by discrete layers of thickness h within which the density and horizontal velocity are presumed to be uniform in the vertical.[29] Density changes from one layer to the next by a specified jump, $\delta\rho$, that is generally presumed to be constant in time (though that can be realxed, if required). The layers are thus defined by the upper and lower depths of material surfaces, coincident with the density jumps, $\delta\rho$, that move with the fluid according to the continuity relation,

$$\frac{\partial h}{\partial t} = -\nabla\cdot(h\mathbf{V}),$$

with $\mathbf{V}$ the uniform horizontal velocity within the layer. The vertical coordinates, the surfaces that define the h, are thus Lagrangian insofar as they are embedded within the fluid. The horizontal velocity is evaluated and stepped forward using an Eulerian system, and the vertical density profile and pressure readily calculated from the known layer thicknesses and density jumps. The density profile can change with time as the layer thicknesses change, but by holding the density jumps constant, the resulting vertical advection is assured of being adiabatic, i.e., without mixing. Layers defined by density tend to remain well behaved in that they are not likely to overturn and become entangled the way that horizontal

[28] Griffies, S. M., Pacanowski, R. C., and R. W. Hallberg. (2000) Spurious diapycnal mixing associated with advection in a z-coordinate model. Mon. Wea. Rev., 28, 538-564.

[29] Bleck, R. (2002) An oceanic general circulation model framed in hybrid isopycnic-Cartesian coordinates. Ocean Model., 4, 55-88.

surfaces would be in a vortex, for example. Such layered models are widely used in ocean modelling.

No scheme is without problems, and e.g., sustained divergence (as may occur in the ocean surface layer due wind stress) can cause the layer to become very thin and even vanish. Vanishing, or even very thin layers are troublesome for momentum balance (an example occurs in the wind-driven flow of the Indian Ocean noted in 'a Coriolis tutorial', Part 5). At the other extreme, e.g., in regions where there is significant heat loss to the atmosphere, the density may become homogeneous and so without vertical structure, or at least none that can be represented by such a layered model.

The same sort of spurious mixing is associated also with horizontal advection, but likely to be smaller than the genuine or intended horizontal mixing and so less onerous. However, if the goal of a model study is to investigate long range or long time tracer transport in the horizontal, then the same basic idea, that tracer transport may be modeled by the movement of discrete material surfaces, can be extended to three dimensions.[30] The fluid is represented by discrete, three-dimensional volumes of fluid that are bounded by material surfaces. These are, in effect, macroscale parcels, sometimes called 'sacks' since their bounding surfaces move with the fluid. The tracer concentration within a given sack is presumed constant in time unless an external source or some horizontal or vertical mixing process is explicitly implemented. The main task then becomes to solve for the three-dimensional motion of the bounding surfaces, where the necessary three-dimensional velocity is evaluated from what may be a highly deformed assemblage of three-dimensional sacks, e.g., imagine following macroscale parcels in the tea cup vortices of Fig. 2.

5.3 Particle in Cell models utilize hybrid dynamics

The considerable appeal of the Lagrangian system derives from the straightforward representation of the equation(s) of motion, written here as coupled first order PDEs,

$$\frac{\partial \tilde{\mathbf{X}}_\mathbf{i}}{\partial t} = \tilde{\mathbf{V}}_\mathbf{i}, \quad \text{and} \quad \frac{\partial \tilde{\mathbf{V}}_\mathbf{i}}{\partial t} = \frac{\tilde{\mathbf{F}}_\mathbf{i}}{M_i} \tag{64}$$

and from the tracking of identifiable particles (or parcels), the $\tilde{\mathbf{X}}_\mathbf{i}$. The awkwardness of the Lagrangian system arises when evaluating the $\tilde{\mathbf{F}}_\mathbf{i}$, often a pressure gradient (Sec. 2.4) and in a more general model, diffusion terms as well, in part because of the uncontrolled spatial distribution of Lagrangian particles. A variety of numerical modelling strategies have evolved from the goal of making use of (64) while mitigating the problems associated with evaluating the $\tilde{\mathbf{F}}$.

One major branch of this hybrid model family is called Particle in Cell (PIC) models. These combine the equations of motion (64) and particle tracking while representing the force $\tilde{\mathbf{F}}$ by way of a field formulation, i.e., on a fixed (Eulerian) grid. The particles of a PIC model thus move about within a regular grid or cells. PIC models are very widely used to simulate the dynamics of fluids that may be idealized as a dilute gas: on the small scale, the flow of laboratory-scale plasmas, in which case the particles are charged, elementary particles or ions, and on the large scale, the evolution of galaxies and even the entire universe, in which case the particles are stars or star clusters.

[30] Haertel, P. (2019) A Lagrangian ocean model for climate studies. Climate, 7, 41. DOI: 10.3390/cli7030041

To introduce the essential motive behind and the structure of a PIC model we will consider a maximally simplified model from numerical cosmology in which the fluid is a dilute ensemble of point-like masses, i.e., stars, that interact solely by gravitational mass attraction. A central goal of numerical cosmology is to understand how the markedly inhomogeneous mass distribution observed in the present universe could have evolved from what must have been very small mass/energy anomalies in the newly-born universe.[31] The starting point is the hypothesis that the motion of the stars (and mass generally) is governed by the initial condition, the big bang, and therafter modified mainly by gravitational interaction between each star pair. The Newtonian gravitational force on a star i due to another star, j, is just

$$\tilde{\mathbf{F}}_{i,j} \;=\; G\frac{M_i\,M_j}{|\tilde{\mathbf{X}}_j-\tilde{\mathbf{X}}_i|^3}(\tilde{\mathbf{X}}_j-\tilde{\mathbf{X}}_\mathbf{i}), \tag{65}$$

where G is the gravitational constant, $6.6743\times10^{-11}\ \ \mathrm{m}^3\ \ \mathrm{kg}^{-1}\ \ \mathrm{s}^{-2}$, M_i is the mass of star i, and $\tilde{\mathbf{X}}_i-\tilde{\mathbf{X}}_j$ is the vector displacment between pairs of stars. The gravitational force on star i is an attaction toward star j and vice versa. Our interest is in cases where there are many stars interacting gravitationally, and the net gravitational attraction on star i is then the linear sum of the gravitational attraction to all of the other stars in the ensemble. For an ensemble of N stars, the net force on star i is then

$$\sum_{i\neq j,j=1}^{N}\mathbf{F}_{i,j} \;=\; G\sum_{i\neq j,j=1}^{N}\frac{M_i\,M_j}{|\tilde{\mathbf{X}}_j-\tilde{\mathbf{X}}_i|^3}(\tilde{\mathbf{X}}_j-\tilde{\mathbf{X}}_i). \tag{66}$$

Particle-Particle models. If the ensemble is a small star cluster, then N is O(10^4) and the force on each member may be computed by the straighforward evaluation of the mutual interactions (66). Such systems are termed Particle - Particle (P-P) models, and are purely Lagrangian.[32]

The number of calculations required to evaluate the mutual gravitational force within a P-P ensemble increases as N^2, N stars each affected by N ensemble members. This N^2 computational burden may become intractable if the simulated particles are intended to represent physical stars one to one. For example, the number of stars in a typical galaxy like our Milky Way is O(10^{11}) (100 billion), which can not be calculated via (66). The same holds for the charged particles of even a very small plasma. A

[31] This subsection follows an excellent introduction to the PIC methods of numerical cosmology by Knebe, A., How to simulate the universe in a computer. https://astronomy.swin.edu.au/sao/guest/knebe/ . For a discussion of recent research see https://www.quantamagazine.org/coder-physicists-are-simulating-the-universe-to-unlock-its-secrets-20180612/ and for greater technical detail, Bertschinger, E. 1998, Simulations of structure formation in the universe. Annu. Rev. Astron. Astrophys., 36:599-654. An interesting discussion of the differences in a fluid continuum simulation vs. particle simulation is https://www.quantamagazine.org/the-tiny-physics-behind-immense-cosmic-eruptions-20230515/

[32] Notice that gravitational attraction goes as 1/separation^2, which becomes singular when point-like stars are nearing a collision. As the separation becomes very small the acceleration becomes very large and the consequent change in velocity is not likely to be resolved adequately by a time step that would be appropriate for the generally slow motions of the vast majority of well-separated stars. The numerical solution would then likely show the nearly colliding stars shooting away from one another at very high speed in a (spurious) phenomenon called two-particle collision. This may be mitigated by adding an ad hoc 'softening' factor to the distance between star pairs, i.e., in place of the actual distance, use instead distance + ε, with ε a relatively small positive constant. This is in most respects a detail compared with other important phenomenon that have been neglected here: 1) the all-important initial condition of mass distribution includes small anomalies inferred from the infrared background, 2) that the universe is expanding, 3) most of gravity is associated with dark matter (apparently) and not just visible stars as implied here, and 4) radiation pressure is a significant counter to gravitational mass attraction.

curative for this N^2 problem comes in stages which first give up some spatial resolution, and then the give up the simplicity of Eq. (66) in favor of a field perspective on the mass distibution.

Spatial averaging and Tree models. First, consider the gravitational attraction due to a comparatively small cluster of stars that is very far away from the point of interest (cluster radius $\ll$ distance to the cluster). The net gravitational attraction due to the cluster will then be approximated well by representing the cluster by a single massive particle that is located at the center of mass of the cluster. In that way, a great many individual stars may be replaced by one massive particle that gives very similar gravitational attraction at distant points. This kind of approximation is most appropriate when the region of particular interest is a small subset of the entire domain, in which case the outlying regions may be represented economically by this sptial averaging with no appreciable loss of fidelity. Models that make use of this approximation are sometimes termed 'Tree' models, since the scale of the spatial averaging increases with distance away from the region of interest. Like the P-P models, these are purely Lagrangian.

Particle in Cell models are semi-Eulerian. A second modelling approximation, and the one of particular interest here, is to retain the Lagrangian equations of motion and long-term particle tracking, while taking an Eulerian perspective when estimating the gravitational interactions. Thus, in place of evaluating the N^2 discrete particle-particle interactions of (66) directly, evaluate instead the gravitational potential *field* associated with a spatially smoothed mass distribution. The mass density at the fixed spatial coordinate $\mathbf{X}$, i.e., a grid point (and a field varible and so no tilde) is estimated as the local, spatially-averaged mass density

$$\rho(\mathbf{X}) \;=\; \sum_j M_j W(\mathbf{X}-\mathbf{h},\tilde{\mathbf{X}}_\mathbf{i}), \tag{67}$$

with W a window function (e.g., uniform or triangular) and h a length scale that sets the effective width of W, usually a small fraction of the domain width. The grid interval of the $\mathbf{X}$ array determines the spatial resolution of the gravitational potential field estimated from solution of the Poisson equation,

$$\nabla^2\Phi \;=\; 4\pi G\,\rho(\mathbf{X}), \tag{68}$$

where $\rho(\mathbf{X})$ is the spatially-averaged mass field evaulated from (67). The solution for Φ requires solving the elliptic equation (68) with suitable boundary conditions; if the domain is the entire universe, reentrant; if the domain encompasses only a single galaxy, then vanishing at infinity. Given the solution for $\Phi(x,y,z)$, the gravitational force on a given star is then readily evaluated as

$$\mathbf{F}_\mathbf{i} \;=\; -M_i\,\nabla\Phi(\tilde{\mathbf{X}}_\mathbf{i}). \tag{69}$$

The position of a given star $\tilde{\mathbf{X}}_i$ will generally not coincide with a gridpoint of the $\nabla\Phi$ field, and hence the evaluation of (69) will require an interpolation of the $\nabla\Phi$ field to each $\tilde{\mathbf{X}}_\mathbf{i}$. This interpolation plus the spatial smoothing of (68) and (67) obscures the fine spatial-scale variation of gravitational attraction associated with the actual spatial distribution of discrete particles in favor of the smoothed (spatially) field contributed by the neighboring particles and more distant clusters. This sets the smallest resolvable feature in the evolving mass density field to be not less than several grid intervals of the Φ field, but in return the computational load is greatly reduced compared with attempting the corresponding Particle-Particle model, from N^2 down to $Nlog(N) \ll N^2$, which is characteristic of sorting algorithms.

PIC models executed on cloud-based resources can simulate truly enormous ensembles, recently 10^9 particles, and over an elapsed time that is a significant fraction of the lifetime of the universe. The solutions of the most sophisticated PIC model simulations can be mass distributions that look, qualitatively and quantitatively, much like the observed distribution of galaxies and mass in our universe.[33]

5.4 Key ideas

1) Models that are meant to represent real fluid phenomenon generally have to be solved using numerical methods. Numerical models have the opportunity to treat different physical processes (and thus different terms) in a tracer balance by methods that are appropriate to the process, e.g., advection by a Lagrangian particle-tracking method, and evaluation of the mutual forces between particles by mapping to an Eulerian grid.

2) A semi-Lagrangian integration scheme treats advection as an adiabatic transport of discrete parcels that are followed for only a short time, and so do not develop complex, entangled trajectories. A semi-Lagrangian scheme may yield good accuracy and stability, and with a time step considerably greater than is permitted by the CFL criterion appropriate to a comparable, explicit, Eulerian advection scheme.

3) Some fluid systems are inherently anisotropic, e.g., because they have a marked aspect ratio, e.g., very large width to depth, as obtains for the basin scale oceans and global scale atmosphere. In that case, vertical advection may be viewed as the rise and fall of impermeable material surfaces across which the density diffrences remain constant (adiabatic).

4) An inherent difficulty with a pure Lagrangian scheme is that spatial gradients of the pressure or of gravitational mass attraction between particles are very likely to become ill-sampled as trajectories become entangled. A cure for this is to compute the quantities that require spatial gradients by mapping the mass distribution onto an (Eulerian) grid which allows straighforward estimation of pressure or gravitational mass attraction. Lagrangian parcels can then move through the grid, subject to the local pressure field or mass attraction of the surrounding parcels. This kind of Particle in Cell model architecture is widely used in studies of cosmology and plasma physics. PIC models could be dubbed semi-Eulerian, since their core is Lagrangian, but with a very important (Eulerian) mapping step required to evaluate the mutual forces between particles.

5.5 Problems

1) Use the Method of Characteristics to solve the tracer balance of Eqs. (54) and (55). You can do this informally, with no need to introduce parameterized trajectory equations.

[33] See the recent, remarkable application of PIC modelling to the evolution of the universe reported by https://academic.oup.com/mnras/article/512/4/5823/6524208

2) A Matlab project following on Sec. 5.1; experiments that you can carry out using the script LandEadvection linked in footnote 24.

(i) The pure Lagrangian scheme gives nearly exact solution for the nominal time step, $\delta t = 1.0$. What sensitivity (what change in accuracy) is there to larger or smaller δt?

(ii) It was noted in Sec. 5.1.3 that the FTCS scheme is unstable for the nominal CFL, 0.5. Can you discern a small enough time step that the FTCS is reasonably accurate?

(iii) You will notice that trouble for the FTCS starts on the sharp edges of the tracer square pulse. Suppose the IC is made to be Gaussian and smooth instead of a square pluse. Does that relieve the instability or merely delay it?

(iv) How does the accuracy of the semi-Lagrangian scheme depend upon the time step? Compare this to i) above.

6 Lagrangian analysis of an oceanic flow.

This final section will return to an analysis of the ocean currents observed by SOFAR floats and shown in the cover image of Part 1, and in Fig. (22).[34] These data show a coherent oscillation from northeast to southwest over a distance of several hundred kilometers, and on a time scale (period) of about two months. The change in direction of the motion appears to propagate across the float cluster from southeast to northwest, more or less perpendicular to the motion itself, suggestive of a plane wave. There are striking changes in the relative vorticity, e.g., anti-cyclonic when the floats are furthest poleward, that leads to the present analysis.

The phenomenon revealed by these data is interesting in itself, and, the analysis of these data makes good use of one of the fundamental properties of Lagrangian method, *viz.*, that a Lagrangian tracer balance comes in two pieces, the tracer value on moving parcels, and the trajectory of those parcels. The trajectory is observed directly, and so the issue is reduced to the tracer alone, one of the notional joys of Lagrangian observation discussed in Sec. 2.4.2 of Part 1. The tracers in this case are the vorticity and potential vorticity.

Many fluid phenomenon are illuminated by analysis of their vorticity balance, and perhaps nowhere is this more true than in the analysis of low frequency geophysical fluids (low frequency compared to gravity waves). Indeed, most understanding of low frequency geophysical flows comes by understanding

[34] To see these data in motion, visit https://www2.whoi.edu/staff/jprice/wp-content/uploads/sites/199/2022/06/LDE1300.mp4 This analysis and several of the figures in this section were abstracted from from Price, J. F., and H. T. Rossby, 1982, Observations of a barotropic planetary wave in the western North Atlantic. *J. Mar. Res.*, Vol 40 Supp., 543 - 558. https://www2.whoi.edu/staff/jprice/wp-content/uploads/sites/199/2023/11/PriceRossby-82.pdf

the distribution and the balance of q,

$$\text{the potential vorticity of a layer} \qquad \boxed{q \;=\; \frac{\chi \;+\; f}{h}} \tag{70}$$

The terms of the potential vorticity are:

the relative vorticity, $\chi \;=\; \nabla \times \mathbf{V}$,

the planetary vorticity, $\boxed{f \;=\; \Omega \cdot \mathbf{n} \;=\; 2\,\Omega\,\sin(latitude)}$

the layer thickness, h, taken to be the entire water column thickness, about which more below.

6.1 Estimating the potential vorticity

There were 18 floats in total, but this analysis will be carried out on only 12 of these that formed a coherent cluster on a horizontal scale of several hundred kilometers and for a period of several months. This excludes several floats that were farthest to the northwest, and seemed to meander randomly with low speeds, and three floats that were farthest to the southeast and that were caught up in a smaller, sub-mesoscale anti-cyclonic eddy that was advected by the larger, mesoscale motion emphasized here. This decision to analyze 12 of the 18 available floats amounts to a scale separation (Sec. 4.1) that is based on the observed phenomenon, mainly, but also on horizontal scale.[35]

Vorticity. The analysis begins with an estimation of the velocity gradient tensor (Sec. 3). The east and north gradients of the east and north velocity components were estimated by fitting a 2-dimensional plane to each velocity component, at daily intervals. The floats provide measurements of say the east or u-component of velocity at $n = 12$ float locations, (x_i, y_i), where i denotes a specific float. Let the cluster average of u, x, and y be $\bar{u} = \frac{1}{n}\Sigma u_i$ and similarly for $\bar{x}$ and $\bar{y}$. Now make a fit of a linear function of x and y to the measured $u(x_i, y_i)$ by minimizing the mean square difference,
$\Sigma_n \left(u(x_i, y_i) - (u_0 + a(x_i - \bar{x}) + b(y_i - \bar{y})\right)^2$ to find the best fit values of the coefficients that are interpreted as first partial derivatives, i.e., $a \;=\; \partial u/\partial x$ and $b \;=\; \partial u/\partial y$. The same is done for the v component of the velocity. The goodness of the fit may be diagnosed by the fraction of the velocity variance accounted for (labeled FIT in Fig 26).

Given an estimate of the velocity gradient tensor on each day, the vorticity and the divergence may then be readily formed by sums and differences of the horizontal shears, as in the Cauchy-Stokes Theorem of Sec. 3.5. These estimates are Lagrangian in that they were made on a material volume that was tagged by float cluster and followed for an extended period of time. (The Lagrangian variables in this section omit the tilde ($\tilde{}$), which should be understood.)

[35] The unresolved (unanalyzed) motion is more characteristic (more typical) of the open, mid-ocean than is the rather energetic, polarized motion emphasized here.

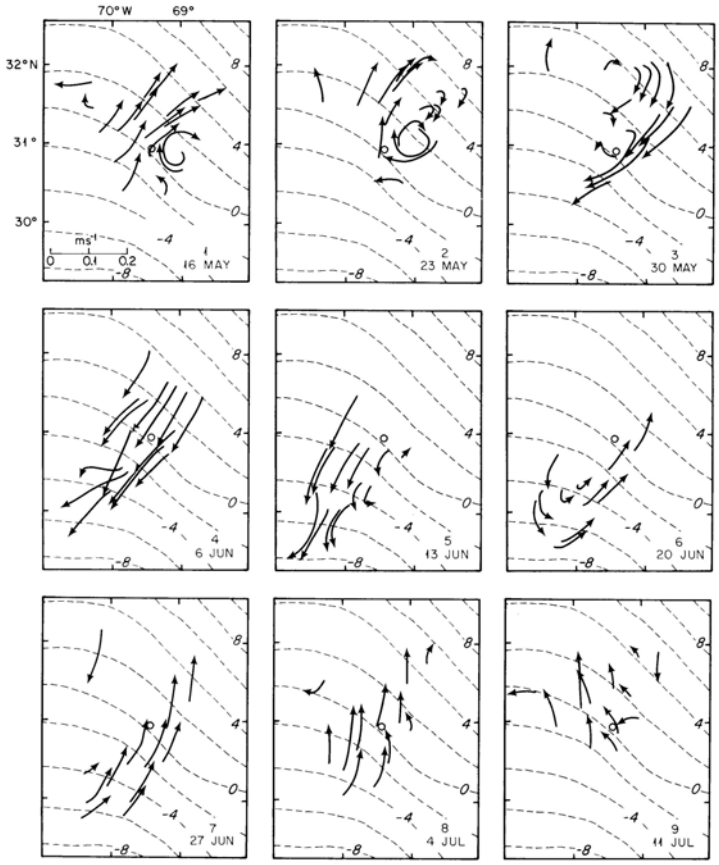

Figure 22: Maps of SOFAR float trajectories at weekly intervals. The region is the central Sargasso Sea, about 700 km west-southwest of Bermuda, and these floats were at a depth of 1300 m. A speed scale is in the upper left panel. The dashed contour lines in the background are lines of constant f/h in units of percent of f. The center of this figure just happened to be the location where the relative vorticity of the motion was approximately zero, and the zero of f/H is assigned there as well. There are two obvious kinds of motion evident here, the dominant motion is a northeast to southwest oscillation, the potential vorticity aspects of which are described in the main text. There was also a comparatively small, anticyclonic eddy centered on 31 N 69 W (on 16 May) that is not dealt with here. For an animation of these data, see the link in footnote 34.

Planetary vorticity. In the context of potential vorticity balance, the important variable f is often called the 'planetary vorticity' (while in the context of the momentum balance it is usually called the 'Coriolis parameter'). This name is apt because even when a fluid column is at rest with respect to Earth-bound observers, i.e., there is no horizontal wind or ocean current and so the relative vorticity $\chi = 0$, the column will nevertheless be rotating with respect to an inertial observer by virtue of riding along on the surface of a rotating, spherical Earth. The magnitude of this Earth's rotation-induced vorticity is given by the projection of Earth's (physical) rotation vector, Ω, onto the unit normal of the horizontal face of the column, $\mathbf{n}$, as $f = \Omega \cdot \mathbf{n} = 2\,\Omega\,\sin(latitude)$, where $\Omega = 2.729 \times 10^{-5}$ rad s^{-1} is Earth's (physical) rotation rate (one revolution per 23 hours, 56 minutes, 4 seconds). Earth's rotation vector (the spin axis) is closely aligned toward the north star, or pole star, Polaris, Fig. (23)[36], which is a very important direction that is defined with respect to the distant stars. The planetary vorticity thus has a direct dependence upon latitude, which is trivial to evaluate given the central latitude of the float cluster. A fluid column sitting directly over the north pole has a planetary vorticity that is two times the Earth's physical rotation rate, $f = 2\Omega$; if the column is at 30 N, the planetary vorticity is $f = \Omega$ and for a column on the equator, $f = 0$ and the planetary vorticity vanishes (Fig. 24). A column sitting over the south pole would

[36]The starscape image of Fig. (23) is thanks to Gavin Heffernan and the SkyGlow Project, https://vimeo.com/693011167, and modified slightly by the author.

Figure 23: Earth can claim no special place in the universe, but

Pole star, Polaris,
marks Earth's special direction
in isotropic space.

have a planetary vorticity $f = -2\Omega$.

If f is dubbed the planetary vorticity, then it is appropriate to call $\chi = \nabla \times \mathbf{V}$ the 'relative vorticity', since $\mathbf{V}$ is the fluid velocity relative to the rotating Earth and is the wind or current that we can observe directly. An inertial observer will see that the vorticity of a column is the sum of the planetary and relative vorticity, called the

$$\text{absolute vorticity,} \qquad \boxed{\xi \;=\; f \,+\, \chi}$$

An Earth-bound observer will observe directly only the relative vorticity.

Thickness. The thickness of a column is defined by material surfaces, i.e., density surfaces in the interior of the ocean (baroclinic motions) or by the sea floor and sea surface (barotropic motions). The thickness will be evaluated from the latter, provisionally, a choice that can be tested with the data.

6.2 Potential vorticity as a tracer

The balance of potential vorticity for a layer (70) may be derived from the adiabatic momentum and mass conservation equations for a rotating fluid layer in just a few steps: the curl of the momentum balance forms the vorticity, and eliminates the pressure gradient; the resulting horizontal divergence is eliminated in favor of the layer thickness (as in the Lagrangian treatment of vertical advection discussed in Sec. 5.2). For somewhat greater detail see e.g., a Coriolis tutorial, Part 2, Sec. 2. Aside from what are usually small effects of diabatic processes — bottom drag, wind stress curl, or diffusion — the q of a given fluid column in the open ocean is expected to be conserved approximately,

$$\frac{Dq}{Dt} \;=\; \frac{\partial q}{\partial t} \;=\; \frac{\partial (\frac{\chi + f}{h})}{\partial t} \;=\; 0, \tag{71}$$

at least for short times, a few months. Our interest is in the balance of the changes in relative vorticity and planetary or stretching vorticity (described below) and so it is useful to consider the linear, difference form of (71),

$$\delta\chi \;+\; \delta f \;-\; (\chi \,+\, f)\frac{\delta h}{h} \;=\; 0, \tag{72}$$

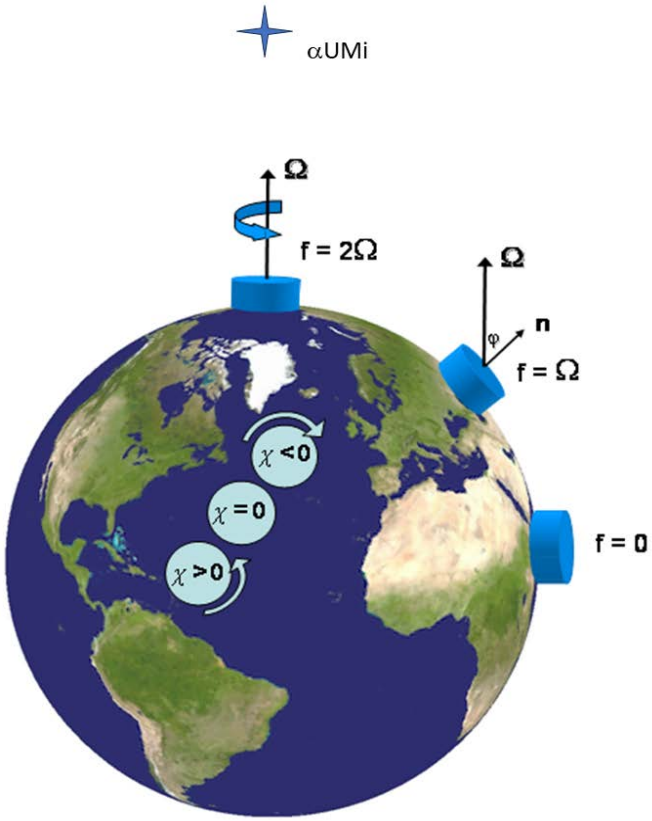

Figure 24: The spin axis Ω of our rotating Earth maintains a nearly steady direction toward a distant star, Polaris, α UMi, which is thus Earth's pole star (Fig. (23). The darker blue columns at right show that the horizontal rotation of a column due to Earth's rotation is $f = 2\Omega$ sin(latitude); the angle ϕ between the unit normal and Earth's rotation vector Ω is the co-latitude. The three lighter blue columns show the sense of relative vorticity acquired by a column that is displaced to the north or south while maintaining constant thickness. It is natural to show a column spinning about its center when it acquries relative vorticity, as here. However, the float cluster of Fig. (22) indicates that the relative vorticity was due mainly to horizontal shear rather than curvature, as implied by these spinning, vortical columns.

or when evaluated from observations,

$$R \quad + \quad P \quad + \quad \quad T \quad \quad = \quad \varepsilon \tag{73}$$

where

$$\delta(\,) \;=\; \int_{t_0}^{t} \frac{d}{dt}(\,)\, dt$$

is the change in time following a given float cluster and presumably a material volume. Note that no one part of the expanded potential vorticity is conserved, but only the sum of the three terms.

The potential vorticity q is an intensive, scalar property of a (rotating) fluid, and has three properties that make it useful for the analysis of low frequency, geophysical flows: (1) The potential vorticity is transported with the fluid as a tracer, rather than with gravity wave phase speeds, as applies for momentum. Thus, q serves to tag the fluid, much like a passive tracer. (2) However, q is obviously closely related to the vorticity and the horizonal velocity, and in many cases knowledge of the distribution of q is sufficient to recover the horizontal velocity (though not when gravity waves are important). (3) The curl operation needed to form the vorticity equation from the momentum equation eliminates the pressure gradient (or any force derivable from a potential) which in low frequency flows is closely balanced with the Coriolis force. These two large nearly balancing terms make it difficult to analyze an observed momentum balance for the comparatively small terms/processes that allow the velocity to change. The

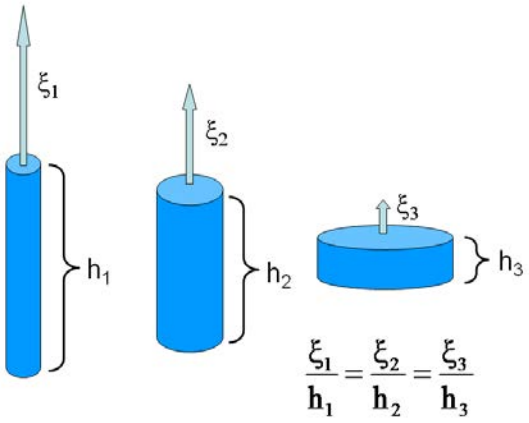

Figure 25: A schematic showing a spinning, deformable fluid cylinder that conserves its volume as thickness changes. Absent diabatic processes, it should also conserve angular momentum, ξ/h, as it undergoes changes in thickness, i.e., more positive ξ as the column lengthens (or stretched). If the vorticity is relative vorticity only, then this is directly analogous to the increased spin rate of an ice skater who pulls in her arms.

potential vorticity balance brings these processes (at least the adiabatic processes) to the fore.

6.2.1 Potential vorticity and changing latitude

Assuming for the moment that the thickness is constant, then the absolute vorticity of a column will be conserved, $d\xi/dt = 0$, or $\xi = \chi + f = constant$, including when a column changes latitude. For example, suppose that a fluid column is at rest at a mid-latitude so that it has a planetary vorticity f_0 and zero relative vorticity. Thus its absolute vorticity is just $\chi = f_0$. If this column is displaced toward the pole, as happened to the float cluster starting on ca. 16 May (Figure 22), then the planetary vorticity of the column will certainly increase. If the column maintains a constant absolute vorticity, $\xi = \chi + f = f_0$, it will acquire negative or anticyclonic relative vorticity,[37] $\delta\chi = f_0 - \delta f$, the amount given by the change in the planetary vorticity. After a couple of weeks of northeastward motion, the entire cluster reversed direction and moved back toward the southwest. As the float cluster moved equatorward, it acquired positive or cyclonic relative vorticity, which in this case served to erase the negative relative vorticity acquired during the poleward displacement. An observer who witnessed this motion from an inertial reference frame (outside the rotating Earth) would note that the absolute vorticity of the cluster remained constant (aside from thickness changes, discussed next). An Earth-bound observer, i.e., what we can see in Fig. (22), will see that the cluster lost and gained relative vorticity as it oscillated north to south.

6.2.2 Potential vorticity and changing layer thickness

Another and often very important aspect of vorticity balance is that changes in column thickness will have an effect upon the relative vorticity much like the effect of changing planetary vorticity. For a given

[37] Relative vorticity or rotation that is in the same direction as Earth's rotation is said to *cyclonic*, which comes from the Greek *kyklon* for circular motion. Cyclonic rotation is thus counterclockwise in the northern hemisphere and clockwise in the southern hemisphere. *Anticyclonic* is the reverse.

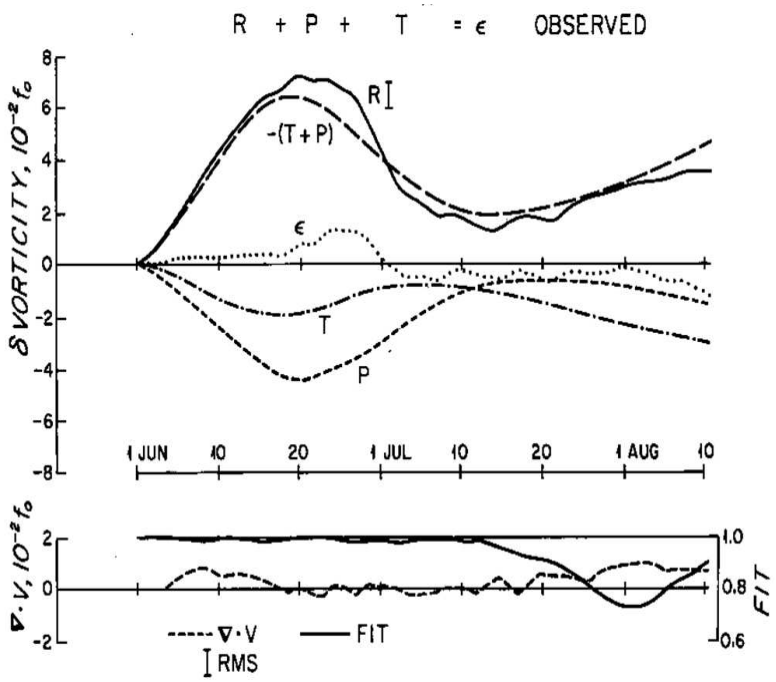

Figure 26: The balance of potential vorticity estimated from the float data of Fig. (22). The estimates begin on 1 June, as the float cluster moved southwestward through the center of the oscillation. The lower panel shows the divergence of the horizontal velocity along with FIT, the fraction of the velocity variance accounted for by the fitted plane; so long as FIT exceeds about 0.9, the velocity field is described well by a mean and the cluster-averaged horizontal shears in x and y. The sum $-(T+P)$, the topographic and planetary vorticity terms of Eq. (72), is consistent with the relative vorticity term, R, and thus with the conservation of potential vorticity by this motion.

column, the moment of inertia is $\propto 1/h$, and the absolute angular momentum is thus $\propto \xi/h$, which is just the potential vorticity noted above. If the thickness changes, then so too does the moment of inertia and the absolute vorticity, exactly as would be expected from angular momentum conservation. Thus when a fluid column is squashed, the result will be a slowed rotation rate (aside from changes in latitude and thus a change in planetary vorticity), and the reverse will happen if a column is stretched. In the example of the float cluster described here, the water depth shoaled gently toward the east and thus when the column moved northeast, it was apparently squashed by about 100 m out of a nominal thickness of 5000 m, or by roughly 2 percent, while at the same time f increased by about 3 percent. The changes in thickness and planetary vorticity were roughly comparable and in phase for this particular motion, and, are consistent with the change in relative vorticity that we can see directly in the float data (Fig. 26). Thus, the potential vorticity of this motion appears to be conserved approximately when the column thickness is identified with the water column thickness (i.e., the water depth). This implies that the motion was barotropic, with no appreciable effect of tilted density surfaces.[38]

It is noteworthy that a change in f/h of only about 5 percent is sufficient to account for the rather impressive change in the relative vorticity, about 5 percent of f_0, and by extension, of the current, which had an amplitude of roughly 0.15 m s^{-1}. Thus what would seem to be comparatively small changes in latitude or column thickness result in significant changes in the relative vorticity and the current itself. The reason, hinted at above, is that the planetary vorticity f is generally much larger then the relative vorticity of most ocean currents (and most winds) and hence the planetary vorticity represents a large 'potential' of the relative vorticity, which can be realized by changing either the latitude, and thus the

[38] Barotropic motions are quite common in the ocean, i.e., astronomical tides. However, low frequency, mesoscale eddy motions are likely to be significantly baroclinic. In that case, the column thickness would be defined better by density surfaces, and the phase of the motion quite different at different depths in the water column.

Coriolis parameter, f, or the column thickness.

6.3 Wave properties of the observed motion

You likely noticed that the floats oscillated in a specific direction, roughly northeast to southwest, and if you look closely you can see that the change in direction appears to propagate from southeast to northwest across the float array. In other words, the motion appears to be that of a polarized, or plane wave. The period and the wavelength may be readily estimated from an autocorrelation lagged in space and time, and were about 60 days and 340 km. The wave vector was toward 300 deg True, and the phase speed was about 0.06 m $\sec^{-1}$. These time and space scales are consistent with a short, barotropic Rossby wave, for which the planetary beta effect and the topographic effect discussed above are comparable, i.e., a planetary/topographic wave. Group speed inferred from the relevant dispersion relation was eastward and about 0.05 m $\sec^{-1}$, i.e., very slow.

6.4 Key ideas

1. Vorticity is proportional to the fluid rotation rate, and is an analogous to the angular momentum of a rotating solid. Important differences are that vorticity is defind locally (at every point) and does not refer to a moment arm.

2. Vorticity follows a conservation law that is more like that of a passive tracer than of momentum, since it is not propagated with gravity waves. The balance of vorticity can thus be the basis of an insightful analysis of many (not all) fluid flows.

3. The vorticity of large scale geophysical flows includes a very important contribution from the planetary rotation. The planetary voricity, f, is considerably larger than the relative vorticity of most large scale winds and ocean currents.

4. Planetary rotation is not apparent to Earth-bound observers, but becomes evident as relative vorticity when fluid columns change latitude; if toward larger f, then the induced relative vorticity is negative.

5. Similarly, planetary rotation is converted to relative vorticity when a fluid column is squashed or stretched in the direction parallel to Earth's rotation vector, analogous to a change in the moment of inertia.

6.5 Problems

1) An intertial-frame observer making observations of the velocity of a fluid column on Earth's surface will be able to observe (calculate) the absolute vorticity. We Earth-bound observers will be able to observe directly only the relative vorticity, χ, from observations of wind or ocean currents. Can you think of a way to infer the planetary vorticity, f from observations of the stars that are overhead? Refer to Fig.

(23), which is not looking directly 'up', and consider the special cases of a polar observation site and then an equatorial site.

2) How does the absolute vorticity change during the motion analyzed here?

3) This analysis was carried out in a Lagrangian coordinate or reference frame, in that the floats followed a material volume of fluid. The Eulerian statement of potential vorticity conservation (that we would be much more likely to use for a complete, predictive model) is just $\frac{D\tilde{q}}{Dt} = \frac{\partial \tilde{q}}{\partial t} + \mathbf{V} \cdot \nabla \tilde{q} = 0$. How would the northeast to southwest oscillation appear if it was observed at a fixed site, i.e., from an Eulerian reference frame? Consider three cases: (1) the idealized case that only variations of planetary vorticity are present, and assume that f can be expanded in a Taylor series, $f = f_0 + by$. (2) that only variations of water depth are important, and finally, (3) consider the actual, observed current field of Fig (22) and whether 'frozen field' advection of relative vorticity would have been observed (Sec. 6.1).

Index

absolute vorticity, 68
advection, 5
advection time, 14
anticyclonic, 70

backward trajectory, 10

Cauchy-Stokes theorem, 22
CFL number, 58
circulation, 12, 50
confluence, 35
control volume, 47
cosmology, numerical, 62
cyclonic, 70

deformation rate tensor, 30
divergence, 30

eddy flux, 37
eddy velocity, 36
effective diffusivity, 42
eigenvectors, eigenvalues, 30
entangled, 57

FPK, 6
FTCS, 58
fundamental solution, 43
f , 66

heat dome, 3
hybrid models, 54
HYSPLIT, 3

inner core, 51
irrotational vortex, 12, 22

Lamb-Oseen vortex, 23
Lax-Wendroff, 58
layered models, 61

matrices and tensors, 15

parameterization, 42
particle-particle model, 62
pathline, 7
Peclet number, 47
Peclet number, displacement, 47
physical rotation rate, 26
PIC, particle in cell, 61
planetary vorticity, 67
planetary wave, 72
potential vorticity, 66
PVD, 16

random walk, 39
Rankine vortex, 23
relative vorticity, 68
Reynolds averaging, 37
Rossby wave, 72
rotation rate , 26
rotation rate tensor, 30

scale separation, 36
semi-Lagrangian advection, 59
solid body rotation, 22
stirring, 34, 48
Stokes drift , 17
streakline, 10
streamline, 11

tensor
    velocity gradient, 15
trajectory, 7
tree model, 63

vorticity, 28

wave momentum, 19

Dimensional Analysis of Models and Data Sets,
Similarity Solutions and Scaling Analysis

James F. Price
Dept. of Physical Oceanography, Woods Hole Oceanographic Institution
Woods Hole, Massachusetts, 02543
http:// www.whoi.edu/science/PO/people/jprice jprice@whoi.edu

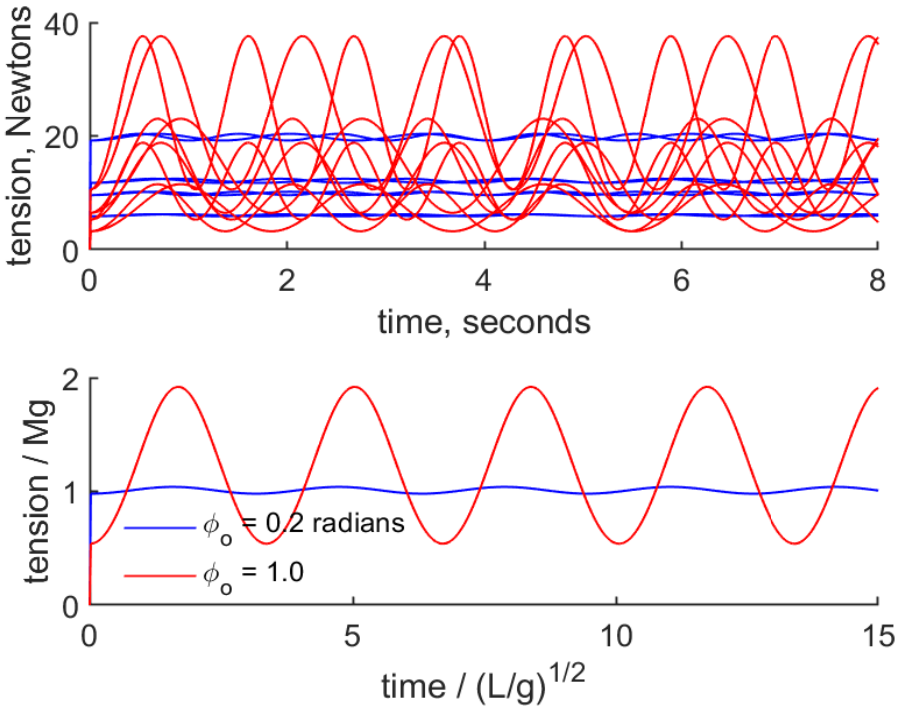

Figure 1: This essay is an introduction to dimensional analysis, one of the most valuable tools of applied mathematics. The essential idea is a change of variables from the usual dimensional variables to nondimensional variables that are formed from scales natural to the phenomenon. An immediate benefit, illustrated here, is that the nondimensional variables will be fewer in number than the dimensional variables. These data are tension in the line of a simple pendulum computed during 16 numerical experiments. In the upper panel, these data are shown in dimensional coordinates, time in seconds and tension in Newtons. In the lower panel, the same data are shown in nondimensional coordinates defined from natural scales of a pendulum: time is scaled by (nondimensionalized by) the reduced period of small amplitude oscillation, $\sqrt{L/g}$, and tension is scaled by the weight of the bob, Mg. With these choices, the 16 distinct dimensional solutions collapse into two solutions that differ only by their initial angular displacement, ϕ_o, large or small amplitude (red or blue lines). These graphs present the same data, but the nondimensional version is far more legible. Better still, it applies to all similar simple pendulums (similar in this case means the same ϕ_o).

Summary. Dimensional analysis may be applied with advantage to virtually every quantitative model and data set. In rare but important cases the result of a dimensional analysis will be a nearly complete solution. More often the result will be a partial solution, an efficient way to display a large data set, or reliable guidance for simplifying model equations.

A method for performing a dimensional analysis proceeds in three steps. The first step is to list the dependent variable and all of the independent variables and parameters that are thought to be significant. The premise of dimensional analysis is that a complete equation made from this list of variables and parameters, dubbed a VPlist, is best written in nondimensional variables that are independent of the choice of units, i.e., whether SI or Imperial. The outcome of a dimensional analysis will be most useful when the VPlist is concise, while also including the most important variables that define the phenomenon. This requires a compromise that can best be achieved with reference to observations or numerical solutions.

The second step is calculation of a null space basis of the corresponding dimensional matrix. Each vector of the null space basis corresponds to a nondimensional variable, the number of which is less than the number of dimensional variables. This reduction in the number of variables is a key result of dimensional analysis. The nondimensional variables may themselves be viewed as a basis set, and in most cases their form will not be determined fully by dimensional analysis alone.

The third and artful step is to choose a form of the nondimensional variables that will maximize utility and insight. The properties of a null space basis facilitate this process. The most important choice is the scale used to nondimensionalize the dependent variable. A good strategy is to compute this scale from a physically motivated even if highly simplified, zero order model for the dependent variable. The remaining nondimensional variables can then be formed in ways that define the geometry of the problem or that correspond to the ratios of terms in a model equation, e.g., the Reynolds number that arises often in models of fluid dynamics.

When applied to data sets, dimensional analysis can help find efficient ways to display a large data set and thus help find correlations. Aerodynamic drag on a moving object is an important example. For a given object, i.e. a sphere or a cylinder, a zero order solution for drag can represent inertial or viscous processes. Either way, the resulting nondimensional drag, often called the drag coefficient, will depend upon a Reynolds number, Re, alone. The choice of the zero order solution (inertial or viscous) can be made to minimize the Re-dependence within a subrange of Re.

When applied to model equations, dimensional analysis can help simplify equations by reducing the number of parameters. If, in addition, the choice of the scales considers magnitude, then the comparative magnitude of terms in an equation will be evidenced by their nondimensional coefficients. This scaling analysis sets the stage for simplifications and further analysis.

Contents

1 Learning dimensional analysis **5**

1.1 The goal and the plan for this essay . . . 5
1.2 A method of dimensional analysis . . . 6
1.3 About this essay . . . 7

2 An informal dimensional analysis of a simple pendulum **8**

2.1 Mathematical models of a simple, inviscid pendulum . . . 8
2.1.1 Analytic solutions . . . 11
2.1.2 Numerical solutions. . . . 11
2.2 A VPlist of the most important Variables and Parameters . . . 12
2.3 The premise of dimensional analysis — invariance to a change of units . . . 13
2.3.1 How many nondimensional variables? . . . 15
2.3.2 Nondimensional variables formed with the natural scales of a VPlist . . . 15
2.4 Other dependent variables of a simple pendulum . . . 18
2.4.1 Period of the oscillation . . . 18
2.4.2 Tension in the line . . . 20
2.5 Parameters . . . 21
2.6 Summary: Why use nondimensional variables? . . . 23
2.7 Pendulum problems . . . 23

3 A basis set of nondimensional variables **25**

3.1 The mathematical problem . . . 25
3.2 Computing the null space . . . 26
3.2.1 A basis set of nondimensional variables of the angular displacement . . . 27
3.2.2 A basis set for tension in the line . . . 28
3.3 Properties of a null space basis . . . 29
3.4 Automated calculation . . . 31
3.5 Null space problems . . . 32

4 Damping a simple pendulum **34**

4.1 Observations of the decaying amplitude . . . 34
4.2 A preliminary VPlist for the decay rate of a simple pendulum . . . 34
4.3 Aerodynamic drag on a moving sphere and cylinder . . . 37
4.3.1 A zero order solution as a scale for the dependent variable . . . 39
4.3.2 Nondimensional parameters; the Reynolds number . . . 41
4.3.3 Three-dimensional flow effects upon drag . . . 42
4.4 Evaluating models of a damped pendulum . . . 43
4.4.1 A numerical solution . . . 43
4.4.2 An approximate model of the decay rate . . . 44

4.5 Damped pendulum problems 46

5 A similarity solution for diffusion in one dimension **48**
5.1 Dimensional analysis to simplify or reduce a model system 48
5.2 Tuning the VPlist 50
5.3 When there is only one independent, nondimensional variable 51
5.4 An oscillating upper boundary; Stokes second problem 53
5.5 Diffusion problems 54

6 Choosing scales with a purpose **57**
6.1 A nonlinear projectile problem 57
6.2 Small parameter → small term? 59
6.3 Scaling the dependent variable 62
6.4 Approximate and iterated solutions 63

7 Applications / Homework projects **66**
7.1 The Planck program, natural units for the universe 66
7.1.1 A new fundamental constant with dimension mass 66
7.1.2 Planck problems 67
7.2 Open channel flow through a weir 69
7.3 How fast did dinosaurs run? 72
7.4 The expanding blast wave of an intense explosion 74
7.5 Planetary orbits 76
7.5.1 Discovering a harmony in the heavens 77
7.5.2 An orbital mechanism 79

8 Index **79**

1 Learning dimensional analysis

This is an introduction to dimensional analysis, one of the most widely useful and rewarding methods of applied mathematics. It may be applied fruitfully to almost any quantitative model or data set on topics ranging from dinosaurs[1] to donuts[2]
and the most fundamental theories of physics.[3]
Dimensional analysis is most useful, sometimes indispensable, for problems that have no solvable theory. Dimensional analysis can always make a little progress towards a solution, and some of these, e.g., the universal spectrum of inertial-range turbulence and the log-layer profile of a turbulent boundary layer, are landmarks in fluid mechanics. More often, the result of dimensional analysis will be a broad hint at the form of a solution or a more efficient way to display a large data set. The pendulum data of Fig. (1) are an example: the nondimensional version of the data is far more legible than is the dimensional version, and it is far more useful in that it applies to all similar, simple pendulums.

"A dinosaur and a donut," image generated by OpenAI's DALL·E 2, 2024.

Dimensional analysis can lead to insights that would have been hard to discover in a mass of dimensional data. The maximum tension in the line of a simple pendulum is found to be proportional to the mass of the bob, M (not surprising) and independent of the line length, L, which is not so obvious, Fig. (1), lower. The maximum tension increases significantly with the amplitude of the motion, set by ϕ_o. These results are typical of those coming from dimensional analysis — seldom complete if taken alone, but nevertheless an important step toward improved understanding in many investigations.

1.1 The goal and the plan for this essay

The goal is to help you learn a systematic and partially automated method of dimensional analysis that you will be able to apply to your own research. The key to learning is motivation — why should you devote your time and energy to this task? With that question in mind, the concepts and advantages of dimensional analysis are developed in Sec. 2 by treating a familiar problem, the oscillations of a simple pendulum, using an informal method of dimensional analysis. A more rigorous and partially automated method of dimensional analysis is described in Sec. 3. This method is applied to more advanced applications and topics including a damped, viscous pendulum in Sec. 4, a similarity solution for diffusion in one dimension in Sec. 5, and scaling analysis of

[1] Dinosaurs: J. R. Hutchinson and M. Garcia, 2002, 'Tyrannosaurus was not a fast runner', Nature **415**, 1018–1022.

[2] Donuts: Delaplace, G., K. Loubire, F. Ducept and R. Jeantet, 2015, *Dimensional Analysis of Food Processes,* Elsevier, ISBN : 9781785480409, http://www.iste.co.uk/book.php?id=876.

[3] Physics: Wilczek, F., 1999, 'Getting its from bits,' Nature **397**, 303–306 and https://cds.cern.ch/record/403150/

projectile motion in variable gravity in Sec. 6. Additional applications and homework projects are in Sec. 7.

1.2 A method of dimensional analysis

The method of dimensional analysis espoused here can be envisioned in three steps, previewed below and described in detail in Sec. 3.

1. Definition of a problem. The first step is to define a problem by making a list of the relevant variables. The list starts with one dependent variable, and continues with the independent variables and parameters that are thought to be important for determining that dependent variable. This list of Variables and Parameters is dubbed the VPlist (Sec. 2). That something useful could follow from such a minimal specification is at the heart of what makes dimensional analysis so widely applicable,[4] and also a bit mysterious. The premise of dimensional analysis is that a complete equation is best written in a form that is invariant to the arbitrary choice of units, i.e., whether SI or Imperial, or any other. When that constraint is implemented by a dimensional analysis, the dimensional variables that make up the VPlist will appear in combinations that are nondimensionalized (normalized or divided) by scales that are natural to the problem.

2. Calculating a basis set of nondimensional variables. The usual method of finding the nondimensional variables relies upon the long-running Buckingham Pi theorem to define the number of required nondimensional variables, followed by inspection.[5] That works well for small problems such as the simple pendulum of Sec. 2. For larger problems, e.g., the damped pendulum of Sec. 4, it can be helpful to compute the nondimensional variables from the null space basis set of the dimensional matrix that characterizes the VPlist.[6] This calculation (Sec. 3) leads immediately to a complete, orthogonal set (a basis set) of nondimensional variables.

[4] E. S. Taylor said this regarding dimensional analysis: 'For the amount of time and effort required to understand it and use it, dimensional analysis offers unusually great rewards and it therefore should become a part of the tool kit of every engineer...'. I agree wholeheartedly, and would include physical scientists, data scientists and applied mathematicians among those who will benefit. Taylor, E. S. , 1974, *Dimensional analysis for engineers*, Clarendon Press.

[5] An introduction to dimensional analysis can be found in most comprehensive fluid mechanics textbooks. Recent examples include P. K. Kundu and I. C. Cohen, 2001, *Fluid Mechanics*, Academic Press, and B. R. Munson, D. F. Young, and T. H. Okiishi, 1998, *Fundamentals of Fluid Mechanics*, John Wiley and Sons, 3rd ed. An older but still very useful reference is by H. Rouse, 1946, *Elementary Mechanics of Fluids*, Dover Publications, NY. A particularly good discussion of the relationship between dimensional analysis and other analysis methods is by C. C. Lin and L. A. Segel, 1974, *Mathematics Applied to Deterministic Problems in the Natural Sciences* MacMillan Pub. Also Bender, E. A., 1977, 'An Introduction to Mathematical Modelling', Dover Publications. A very appealing source available online is https://ocw.mit.edu/courses/6-055j-the-art-of-approximation-in-science-and-engineering-spring-2008/

[6] Price, J. F., 2006, 'Dimensional analysis of models and data sets', *Am. J. Phys.*, **71**(5), 437-447.

3. Constructing a preferred basis set. More important than the calculation *per se* is that the properties of a null space basis provide very useful guidance for the third, and artful step of an analysis — the reordering, as necessary, of the initial basis set of nondimensional variables into a form that maximizes utility and insight. This is emphasized in the examples of Secs. 4, 6 and 7. The most important choice is the scale[7] used to nondimensionalize the dependent variable. A good choice for this scale is likely to come from a highly simplified, zero order model of the dependent variable. From that perspective, dimensional analysis develops into scaling analysis discussed in Sec. 6.

1.3 About this essay

This essay has been written for students who are at the level of a first or second course in classical physics or applied mathematics, e.g., fluid dynamics or partial differential equations. The intent is to provide a resource that is suitable for self-study. A first edition was published online in 2006. The present 2024 edition aims for improved clarity and offers a wider range of homework projects.

Copying and distribution for educational purposes is encouraged, consistent with the Creative Commons license CC BY-NC-SA. It may be cited by the web address on the Massachusetts Institute of Technology OpenCourseWare — Price, James F., 12.808 Supplemental Material, Topics in Fluid Dynamics: Lagrangian and Eulerian Representations, a Coriolis tutorial, and Dimensional Analysis of Models and Data Sets,
https://ocw.mit.edu/courses/res-12-001-topics-in-fluid-dynamics-fall-2023 (date accessed).

The author was supported by the Seward Johnson Chair in Physical Oceanography, MIT/WHOI Joint Program in Oceanography, and by the U.S. Office of Naval Research. My thanks to Sidney Batchelder of WHOI for the Python scripts linked in Sec. 3.4, and to Jack Whitehead of WHOI for his thoughtful comments on a draft manuscript.

[7] The word 'scale' is used here as a noun and a verb, and alongside 'normalize' and 'nondimensionalize'. The present usage is standard, but merits a brief explanation. When used as a noun, scale refers to a quantity used to measure a variable via normalization, i.e., division. For example, a standard meter is a length scale that may be divided into some variable length, L. The result is nondimensional, a length/length, but typically reported in the units of the normalization, 'L = xx meters'. In place of a standard length, a length scale may also be formed from variables that are intrinsic to a problem, and then the scale is said to be a 'natural scale'. This is an important aspect of dimensional analysis. In that case, the result of a normalization is again nondimensional, but the units are generally not attached directly and so must be explained elsewhere. When 'scale' is used as a verb or an adjective, as in 'scaling analysis', it usually means to perform a normalization in a way that considers also the magnitude of the scale.

2 An informal dimensional analysis of a simple pendulum

The first problem taken up in some depth involves the oscillatory motion of a tabletop-size, simple pendulum, Fig. (2).[8] A significant appeal of a simple pendulum is that it can be made and observed with very inexpensive materials. The bob position is defined by the angular displacement away from vertical, ϕ. The amplitude of the displacement, Φ, may be readily estimated from the measured cord, c, at the endpoint of the arc as $\Phi = \sin^{-1}(c/L)$, and the period of an oscillation easily measured with a stopwatch, uncertain to about 0.3%. These data will be referred to as 'observed' in later Fig. (4). What was not measured was the time-dependent displacement, $\phi(t)$, and the tension in the line. These observations are primitive compared to those made in some other studies[9] but they nevertheless serve an imporrant purpose, *viz.,* to help ensure that the analysis methods discussed here — theoretical, numerical, and dimensional analysis — are relevant to a real, physical system.

The motion of such a pendulum is only lightly damped by drag with the surrounding air and can be characterized by two distinct time scales – a very regular, fast time-scale oscillation having a period, P, of a few seconds, and a slow, more-or-less exponential decay of the amplitude having a time-scale, $\Gamma^{-1} \gg P$, of tens of minutes. This Sec. 2 will study the fast, oscillatory motion, idealized as if energy conserving. The aim is to show how dimensional analysis can help us understand how the oscillatory motion depends upon the properties of the pendulum, e.g., the length of the line, mass of the bob, etc. Sec. 4 will take up the more complex dynamics associated with damping.

2.1 Mathematical models of a simple, inviscid pendulum

Dimensional analysis is especially valuable when dealing with problems that do not admit a known or solvable mathematical model. That is not the case for a simple pendulum, for which mathematical models are well-known and very useful for generating data sets including the tension in the line, Fig. (1), and angular displacement, Fig. (3).

[8] A simple pendulum is a common starting point for discussion of dimensional analysis including the classic text by P. W. Bridgman, 1937, *Dimensional Analysis*, 2nd ed., Yale Univ. Press, New Haven, CT, which will always be an excellent introduction to this topic. More advanced is Sedov, L. I., 1959, *Similarity and Dimensional Methods in Mechanics*, Academic Press, NY.

[9] Mathevet, R. N. Lamrani, P Ferrand, J.P. Castro, P. Marchou and C. M. Fabre, 2022, 'Quantitative analysis of a smartphone pendulum beyond linear approximation: A lockdown practical homework', Am. J. Phys., 90, 344 - 350. https://doi.org/10.1119/10.0010073

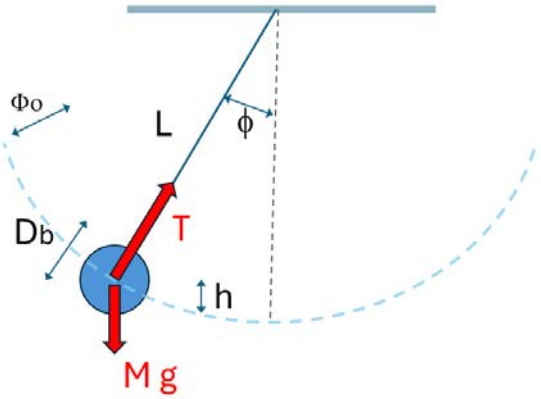

Figure 2: A simple (one bob) pendulum. In the example of the real pendulum observed here, the line is a thin monofilament of length $L = 1$ m. In models, the line is idealized as a rigid, massless rod. The bob is a small, spherical lead fishing weight having a mass of 20 grams. The distance of the bob above the lowest point of the arc is h. Not indicated here are the diameter of the line, D_l, and the density and viscosity of the air through which the pendulum swings.

The mathematical models considered here in Sec. 2 are appropriate to an undamped, energy-conserving simple pendulum. The basis is conservation of angular momentum: the angular momentum of the swinging bob, $M V_\phi L = M L^2 \, d\phi/dt$, is presumed to change only by virtue of the torque associated with the downward force of gravity acting on the bob,[10]

$$ML^2 \frac{d^2\phi}{dt^2} = -MLg \sin\phi, \tag{1}$$

and after minor rearrangement,

$$\frac{d^2\phi}{dt^2} = -\frac{g}{L} \sin\phi. \tag{2}$$

This will be referred to as the equation of motion. For comparison with the available observations, it is preferable to release the bob from a state of rest at a known displacement, ϕ_o, and so the initial conditions are

$$\phi = \phi_0 \quad \text{and} \quad \frac{d\phi}{dt} = 0 \quad \text{at} \quad t = 0. \tag{3}$$

Energy in this system is the sum of gravitational potential energy and kinetic energy

$$E = E_p + E_k. \tag{4}$$

The potential energy referenced to the lowest point in the arc, $\phi = 0$, is

$$E_p = Mgh = MgL(1 - \cos\phi), \tag{5}$$

[10] https://en.wikipedia.org/wiki/Pendulum and follow the link to mechanics.

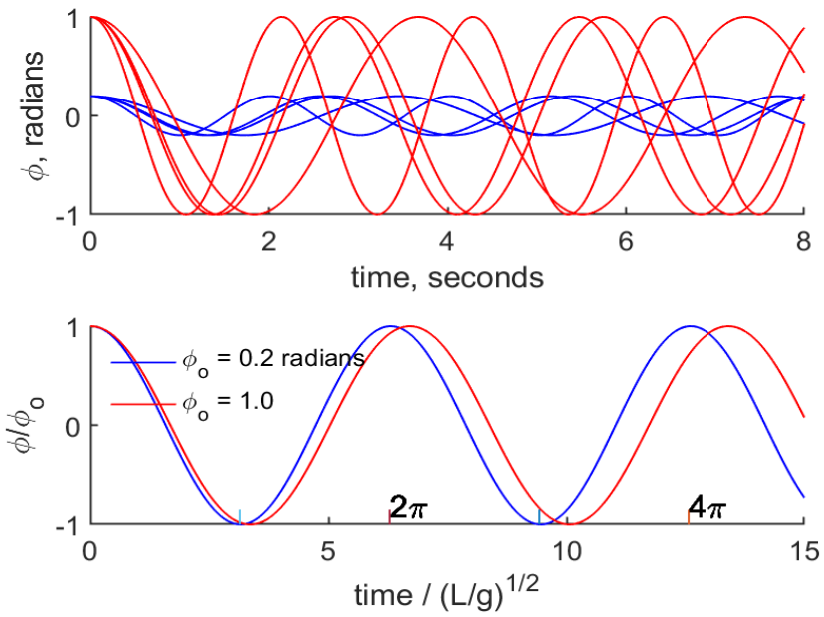

Figure 3: Numerical solutions for the angular displacement $\phi(t)$ of a simple pendulum. These are the same 16 solutions used to calculate the tension in the line of Fig. (1). **(upper)** Displacement plotted in dimensional units. The mathematical model of ϕ, Eqs. (2) and (3), does not depend upon M, and so there are eight distinct solutions here. **(lower)** The displacement data plotted in nondimensional units that will be discussed in Sec. 2.3. The eight distinct solutions shown above collapse to just two solutions that vary by the initial displacement, ϕ_o, a considerable simplification.

and the kinetic energy is

$$E_k \ = \frac{1}{2} M (L \frac{d\phi}{dt})^2. \tag{6}$$

When the bob is released from rest it has zero kinetic energy, and the total energy is then the initial potential energy,

$$E_o \ = \ MgL(1 - \cos\phi_o) \ = \ \text{constant} \ = \ E_p \ + \ E_k, \tag{7}$$

which is conserved (ignoring damping), and so from Eqs. (4) - (7),

$$MgL(1 - \cos\phi) \ + \ \frac{1}{2} M (L \frac{d\phi}{dt})^2 \ = \ MgL(1 - \cos\phi_o) \tag{8}$$

or

$$\frac{1}{2} (L \frac{d\phi}{dt})^2 \ = \ gL(\cos\phi - \cos\phi_o), \tag{9}$$

a useful relation for $\frac{d\phi}{dt}(\phi)$.

Tension in the line, T, appears in the radial equation of motion,

$$M \frac{d^2 L}{dt^2} \ = \ -T \ + \ M g \cos\phi \ + \ ML(\frac{d\phi}{dt})^2.$$

The line is presumed to be inextensible, $dL/dt = 0$, and so the tension may be diagnosed from a known $\phi(t)$ and

$$T = M\,g\,\cos\phi + ML(\frac{d\phi}{dt})^2. \tag{10}$$

2.1.1 Analytic solutions

The solution method for Eqs. (2) and (3) depends upon the initial angle, ϕ_0. If ϕ_0 is restricted to small amplitude, values less than about 0.1 radian, then $\sin\phi$ in Eq. (2) can be approximated well enough for many purposes by ϕ. The resulting linear model is that of a simple harmonic oscillator having the well-known solution

$$\phi(t) = \phi_0\cos(\frac{t}{\sqrt{L/g}}), \tag{11}$$

and hence the period of small amplitude oscillation is

$$P = 2\pi\sqrt{L/g}. \tag{12}$$

It is convenient to refer to the reduced period, $P/2\pi$, which is $\sqrt{L/g}$.

In the general case that ϕ_0 may take any value from $-\pi$ to π, a solution for the period cannot be written in elementary functions. However, the period can be calculated using the first integral provided by energy conservation (9) to find $d\phi/dt$ as a function of $\phi(t)$. Then, separate the variables ϕ and t, and integrate over one quarter of an oscillation, ϕ from ϕ_o to 0, and t from 0 to $P/4$, to arrive at an elliptic integral called 'theory' in Fig. (4),

$$P = 4\sqrt{\frac{L}{2g}}\int_0^{\phi_0}\frac{d\phi}{\sqrt{\cos\phi-\cos\phi_o}}. \tag{13}$$

2.1.2 Numerical solutions.

The equations of motion (2) and (3) are straightforward ODEs that may be solved by elementary finite difference methods for any value of ϕ_o. An ensemble of 16 numerical solutions was generated for two values each of line length, $L = (1, 1.8)$, mass of the bob, $M = (1, 2)$ kg, the acceleration of gravity, $g = (9.8, 6)$ m^2 s^{-1}, and the initial angle, $\phi_0 = (0.2, 1.0)$ radians, Figs. (1) and (3).

These numerical solutions occupy an important middle ground between the observations made on a real pendulum and the solutions of a solvable theory. The mathematical model that underlies the numerical solutions is known, and the numerical solutions for this problem can be very precise. However, all that we get from a numerical solution is the answer, the $\phi(t)$, for one specific case.

Developing insight for the parameter dependence and for the dynamics of a system will usually require an ensemble of solutions and further (dimensional?) analysis.

2.2 A VPlist of the most important Variables and Parameters

The starting point of a dimensional analysis is the assertion that there exists a solution for the angular displacement, $\phi(t)$,

$$\phi \;=\; F(t,\, g,\, M,\, L,\, \phi_o), \tag{14}$$

where F is for now an unknown function (and F will be used repeatedly in that role). A solution is a relation between the dependent variable, ϕ, and the independent variables, here just the time, t, and the pendulum properties, or parameters, that we expect will define the displacement.[11] Several properties of a simple pendulum would seem to be important and so are listed as parameters in the argument of F — the acceleration of gravity, g, the mass of the bob, M, and the length of the supporting line, L. To account for why there is motion at all, the initial displacement, ϕ_0, is also necessary. Parameters are variables that are constant during a particular realization — g, M, L and ϕ_0 in this list — but that vary over some range that defines the family of pendulums and environments that are of interest.

The Variables and Parameters that enter (14) will be compiled into a list, dubbed the VPlist, that defines a problem. A VPlist[12] includes the physical dimensions of each variable; the acceleration of gravity, g, has physical dimensions length time^{-2}, that is written here as a row vector whose components are the powers on $[\,\text{mass}\quad\text{length}\quad\text{time}\,]$, and hence $g \doteq [\,0\;1\;-2\,]$. Following (14), the VPlist for $\phi(t)$ is

(15)

- A preliminary VPlist for the oscillatory motion of a simple pendulum:

1. the angular displacement, $\phi \doteq [\,0\;\;0\;\;0\,]$, the one and only dependent variable,
2. time, $t \doteq [\,0\;\;0\;\;1\,]$, an independent variable,
3. acceleration of gravity, $g \doteq [\,0\;\;1\;\;\text{-}2\,]$, a parameter,
4. mass of the bob, $M \doteq [\,1\;\;0\;\;0\,]$, a parameter,
5. length of the line, $L \doteq [\,0\;\;1\;\;0\,]$, a parameter,
6. the initial angle, $\phi_0 \doteq [\,0\;\;0\;\;0\,]$, a parameter.

[11] The (putative) solution (14) is written as an explicit function for ϕ. This has been done to keep some focus on the dependent variable, but is not essential in what follows; we could just as well presume $F(\phi,\, t,\, g,\, M,\, L,\, \phi_o) \;=\; 0$.

[12] Why this made-up word? In most of the literature, including my previous work, this list of variables is referred to as a 'physical model'. A list of variables is some sort of model, but to call it a 'physical' model began to seem like an overuse of the term physical.

A VPlist of this kind is the entire specification required for the dimensional analysis of a simple pendulum. This can be turned around: in effect, this VPlist defines what is meant by 'simple pendulum'. Notice that there isn't much here: the meaningful, quantitative part of a VPlist is the collection of physical dimension vectors, in this case six vectors having three components, the powers of [mass length time]. Of the 18 components, 13 are zero, and the rest are small integers. The variable names that we associate with these vectors carry an important meaning for us, but play no part in the analysis.

What is most important is the assertion that the VPlist is complete, meaning that it includes all of the variables required to construct a mathematical model that could in principle yield a solution (14). If the corresponding mathematical model is not known, then an assertion of completeness can only be a hypothesis. It is highly desirable that the VPlist be as concise as possible, i.e., that it includes only those variables that have a significant effect upon the dependent variable. The selection of variables for a VPlist thus requires considerable judgment and will often entail trial and error that is best guided by reference to experimental or numerical data.

The VPlist (15) makes no mention of the viscosity or density of air, as if the pendulum was swinging in a vacuum. The same is true of the mathematical models of Sec. 2.1, and thus the numerical integrations that are made with those equations. We can be confident that this airless, energy conserving VPlist is consistent with those models and solutions. Whether these omissions are acceptable as a model of the real, observed pendulum of Fig. (2) is a different matter that will be decided by comparison to observations.

2.3 The premise of dimensional analysis — invariance to a change of units

It is taken for granted that every valid equation must be dimensionally consistent, or homogeneous: if the left side of an equation defines a length, then the right side had better be a length as well, or otherwise there has been an error.[13] This is the most basic application of dimensional analysis and is of considerable utility when checking complex expressions.

[13] A thoughtful, in-depth discussion of measurement and dimensional analysis is by A. A. Sonin, 2001, *The physical basis of dimensional analysis*, MIT. https://www2.whoi.edu/staff/jprice/wp-content/uploads/sites/199/2024/04/AASonin.pdf and Sonin, A. A., 2004, 'A generalization of the Π-theorem and dimensional analysis'. Proc. Nat. Acad. Sci., 101, No. 23, 8525 - 8526.

Now consider the units used to measure mass, length and time. Shall we measure a length by comparison to the standard meter, or by comparison to the standard foot?[14] If this seems to you to be a rather empty question, then you will be sympathetic to

> *The premise of dimensional analysis: The relationship expressed by a complete equation is best written in nondimensional variables that are invariant to the arbitrary choice of units.*

The key word here is 'best', and an important goal for this section is to show what that means.

Dimensional analysis is a systematic procedure for learning the form that the variables can take in an equation that satisfies units invariance. Angles are relevant here, and a good example. An angle is the ratio of two lengths, an arc length divided by the radius, and is thus inherently nondimensional. If the arc length and the radius are measured in units of meters, we will get a certain number. If units of feet are used to measure the same lengths, we will get precisely the same number for their ratio, that is, the same angle. Thus the left side of Eq. (14) is invariant to a change in the units of length. Consider the right hand side, which has two variables with fundamental dimension length, L and g. For the same invariance to the choice of units to hold also on the right hand side, the length and the acceleration of gravity must appear in the ratio L/g, or any power of the ratio, for example, $(L/g)^{1/2}$ or $(L/g)^2$ or $(L/g)^{-1}$. Otherwise a change in the units of length would almost certainly change the argument and hence the value of the (unknown) function F on the right hand side of Eq. (14). From these simple considerations we already know something useful about the units-invariant form of Eq. (14).

Consider the mass, M. A change in the units of mass should also leave F unchanged, and yet it is impossible to see how that could hold since M is the only variable in the VPlist having dimensions of mass. This informal dimensional analysis leads to the conclusion that a solution for ϕ that is invariant to a change of units cannot depend upon the mass of the bob only. Either there must be another parameter having a dimension mass that was omitted from the VPlist, or, the mass should be excluded from the list of relevant parameters. This is an immediate result also in the mathematical models (Eqs. (2) and (3)) where it follows from the equivalence of gravitational mass and inertial mass. The same result can be deduced by dimensional analysis in the absence of a mathematical model (provided that there is just one mass in the VPlist, and not distinct inertial and gravitational masses).

A similar consideration of the units used to measure time indicates that t, L, and g must also appear together in a nondimensional variable, say $t/\sqrt{L/g}$, or just as well $t^2/(L/g)$, since any power of this ratio is equally suitable. Absent some reason otherwise, we may as well leave the independent variable t to the first power and so choose the former, $t/\sqrt{L/g}$.

[14] The standard meter was first defined in terms of Earth's circumference, which was exceedingly cumbersome and not precise. The meter is now defined in terms of universal constants, the speed of light divided by the transition frequency between two hyperfine ground states of cesium. The standard foot was once defined by an average of actual human feet, convenient but not precise. It is now defined as a fixed fraction of a meter.

The upshot of this informal dimensional analysis is that the variables and parameters that appear in a units-invariant form of Eq. (14) will appear in combinations that are nondimensional, i.e., nondimensional variables. The simplest, but not the only possible version is

$$\text{the nondimensional form,} \qquad \phi \;=\; F(\frac{t}{\sqrt{L/g}}, \phi_0). \tag{16}$$

This may be compared to the starting point, Eq. (14), repeated here,

$$\text{the dimensional form,} \qquad \phi \;=\; F(t, g, M, L, \phi_o). \tag{17}$$

2.3.1 How many nondimensional variables?

The nondimensional version (16) represents significant progress. In place of a dependence upon one independent dimensional variable and four parameters as in (17), the nondimensional version (16) has a dependence upon one nondimensional independent variable, $t/\sqrt{L/g}$, and just one nondimensional parameter, ϕ_o. This is the kind of result that can be expected generally, and is important enough to state as a corollary to the premise,

Corollary 1: The number of nondimensional variables will be fewer than the number of corresponding dimensional variables.

The significance of this becomes evident when the data from an ensemble of numerical solutions is plotted using a nondimensional format in Figs. (1) and (3). The 16 (or 8) distinct dimensional solutions collapse into two nondimensional solutions that depend upon a nondimensional time and just one parameter, the initial displacement, ϕ_o, consistent with (16).

It is important to be able to anticipate the number of nondimensional variables, K, that is required to have a complete nondimensional form like (16). A useful rule of thumb: K is generally equal to the number of variables in the VPlist minus the number of fundamental dimensions in those variables. In the case of (15), there are six dimensional variables having three fundamental dimensions, mass, length and time, and so we can expect $K = 3$ nondimensional variables: ϕ, $t/\sqrt{L/g}$, and ϕ_o. Be cautioned, though, that while this informal estimate of K is correct in most practical problems, it is not fool proof. A better, rigorous calculation of K will be coming in Sec. 3.2.

2.3.2 Nondimensional variables formed with the natural scales of a VPlist

Nondimensional variables have a second inherent advantage over their dimensional cousins when, as here, they are formed with scales that are natural (or intrinsic) to the problem at hand. For

example, the natural time scale of a simple pendulum is, as you might guess, the reduced period of small amplitude oscillation, which has been used as the scale to form a nondimensional time,

$$t^* \;=\; \frac{t}{P/2\pi} \;=\; \frac{t}{\sqrt{L/g}}. \tag{18}$$

The variable t^* is a pure number that has the same numerical value regardless of the units used to measure t, g, and L, a hint that there might be something useful in this.

Nondimensional time may sound a bit esoteric, but amounts to nothing more than measuring time in units of the reduced, linear period while taking explicit account of the $\sqrt{L/g}$ dependence of the period. If the analysis was to consider one pendulum only, then the whole exercise would amount to dividing the time by a constant. But if the scope of the investigation is all possible pendulums, i.e., all possible L and g, then there is considerable merit to measuring time in these natural units, including that the linear (small amplitude) period of the oscillation is 2π for all simple pendulums, Sec. 2.4.1 and Fig. (4).

This second and in some ways deeper benefit of nondimensional variables may be stated as

> *Corollary 2: Nondimensional variables that are formed with natural scales will often have a physical significance that the dimensional variables, scaled in the arbitrary units of kilograms, meters and seconds, do not.*

The advantage extends to model equations: a time derivative transforms as $dt = dt^*\sqrt{(L/g)}$, and the equation of motion, Eq. (2), becomes

$$\frac{d^2\phi}{dt^{*2}} \;=\; -\sin\phi\,, \tag{19}$$

with the initial conditions (ICs) as before, Eq. (3). The solution will be of the form

$$\phi \;=\; F(t^*, \phi_0)\,, \tag{20}$$

which is just like Eq. (16). If the amplitude of the motion is small in the sense that $\sin\phi \approx \phi$ in Eq. (19), then the solution to the linearized Eq. (19) with (3) is

$$\phi \;=\; \phi_0 \cos t^*. \tag{21}$$

The dependence upon L and g has not been omitted, but rather has been subsumed into the nondimensional time, t^*, so that Eq. (21) suffices for all L and g. This new equation (19) has the small advantage that it is simpler notationally, and it may be easier to recognize a canonical form. However, a switch to nondimensional units will preclude the prospect of catching algebraic errors that could be detected easily in a dimensional equation as a dimensional *in*homogeneity.

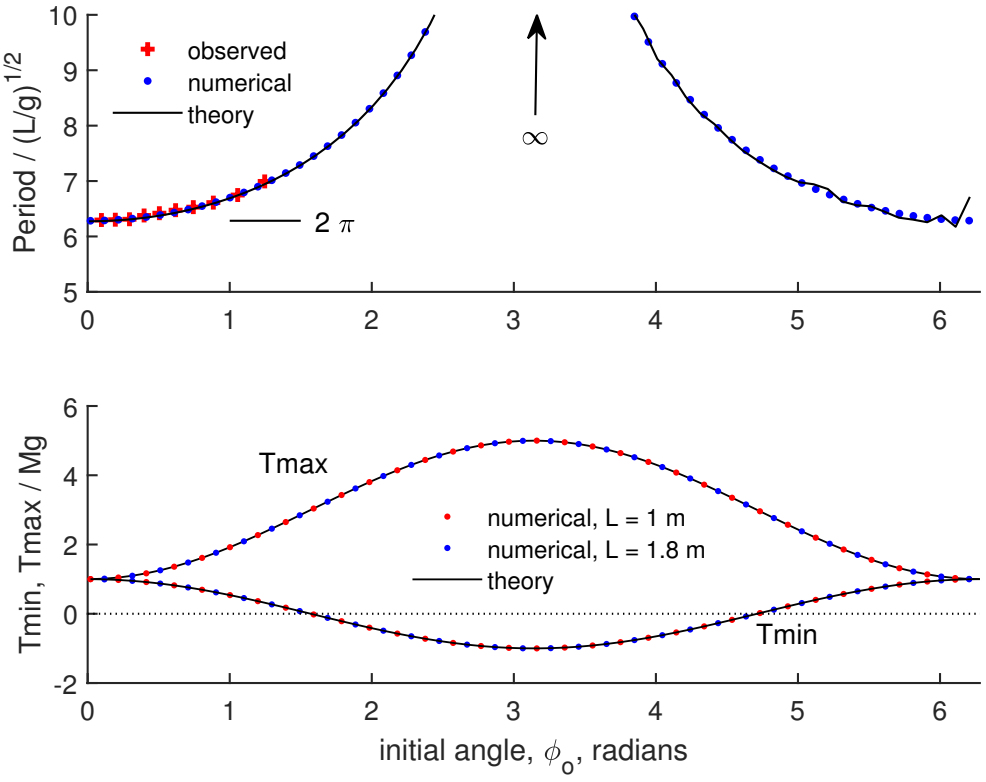

Figure 4: Observations and solutions for the period and the tension in the line of a simple pendulum as a function of the initial angle, ϕ_o. The flexible line of the real, observed pendulum and the initial condition $d\phi/dt = 0$ limit the initial angle to the range $\phi_0 < \pi/2$. In the mathematical models of Sec. 2.1, the line was idealized as a rigid, massless rod, and so all initial angles were possible, including $\phi_0 \rightarrow \pi$. **(upper)** The period in nondimensional coordinates. The data are from three sources: observations (red crosses), the period diagnosed from an ensemble of numerical solutions (blue dots), and as computed from theory, Eq. (13) (the black line). From dimensional analysis it is expected that the similarity function $F(\phi_0)$ evident here will hold for all simple pendulums that are consistent with the VPlist (15). **(lower)** The nondimensional minimum and maximum tension in the line. Data are from an ensemble of numerical solutions (the alternating red and blue dots are length $L = 1$ m or $L = 1.8$ m, and are indistinguishable), and from theory (the black line). Negative values of tension indicate that the line (massless rod) is in compression. There are no observations of tension.

Recall that the linear pendulum has the solution $\phi = \phi_0 \cos(t/\sqrt{L/g})$, Eq. (12), and note that the argument of the cosine is the same nondimensional time — it was there all along.[15] Evidently the difference between Eqs. (11) and (21) is in how you look at them: do you see the dimensional time, t, as the independent variable, or do you see instead the nondimensional time, $t^* = t/\sqrt{L/g}$? The answer will probably depend on both the stage of an investigation and upon your familiarity with dimensional analysis. Experimental data will generally be recorded in dimensional units (or the native units of the instruments), and it may also be preferable to carry out a numerical integration in dimensional units, if the magnitude of intermediate results is more familiar in those units. But when it comes time to report and interpret a collection of data from an ensemble of experiments, there can be a significant advantage to the use of nondimensional variables, evidenced in Figs. (1) and (3).[16]

2.4 Other dependent variables of a simple pendulum

2.4.1 Period of the oscillation

The most characteristic property of a pendulum is its period of oscillation, P. To observe the period, we simply measure the time interval between two extremes of the displacement. What can dimensional analysis tell us? The period does not vary with the dependent variable time, t, which should therefore be omitted from

- A VPlist for the period of oscillation of a simple pendulum: (22)

1. the period, $P \doteq$ [0 0 1], the dependent variable,
2. acceleration of gravity, $g \doteq$ [0 1 -2], a parameter,
3. length of the line, $L \doteq$ [0 1 0], a parameter,
4. the initial angle, $\phi_0 \doteq$ [0 0 0], a parameter.

Compared with Eq. (14), this VPlist also omits the mass of the bob, which we learned just above. Following the same reasoning that led to (16), and expecting that there will be $K = 4 - 2 = 2$ nondimensional variables,

$$\frac{P}{\sqrt{L/g}} = F(\phi_0). \tag{23}$$

For a given ϕ_o, the (dimensional) period of a simple pendulum is expected to increase in proportion to the square root of the length of the supporting line and is independent of the mass. These are among the truly fundamental results of mechanics, deduced from observations and experiments by Galileo Galilei, Fig. (5), near the beginning of the Scientific Revolution, ca., 1600.

[15] The arguments of trigonometric, exponential and logarithmic functions are always nondimensional.

[16] A far more profound example of natural units comes in Sec. 7.1 which considers Planck units that are thought to be universal — literally the same throughout the universe. However, for all of their considerable appeal, Planck units are remarkably awkward size-wise for the day-to-day phenomena encountered here on Earth.

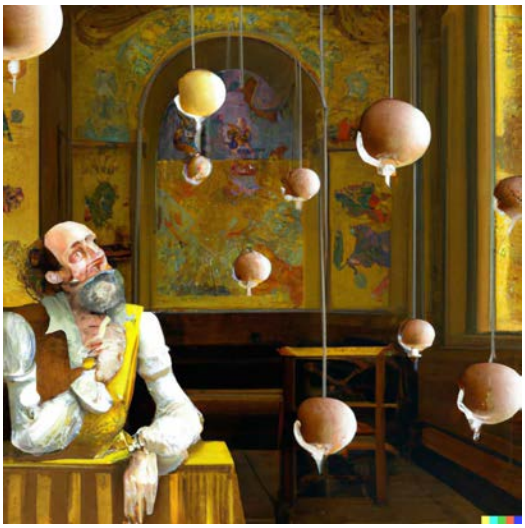

"Galileo Galilei observing chandeliers,"
image generated by OpenAI's DALL·E 2, 2024.

Figure 5: Galileo Galilei began a lifelong study of kinematics as a medical student observing chandeliers swinging in the breeze of a Pisa cathedral, ca. 1580. Clocks were then very primitive and Galileo timed their oscillations by counting his pulse. He reached several important conclusions: 1) every simple pendulum has a characteristic period of oscillation that is proportional to the square root of the length of the supporting line, 2) the period is independent of the mass of the bob, and, 3) the period of the oscillation is independent of the amplitude of the oscillation (now known to hold only for small amplitude motion.) These properties of a simple pendulum must have been noticed by many other cathedral-goers, but it was Galileo who quantified and reported the isochronicity property 3) of simple pendulums, a key concept that led to the later development of practical, accurate clocks.

Dimensional analysis has taken us part of the way to a solution in the form of Eq. (23), but not to the finish; the function $F(\phi_o)$ remains undefined and is not accessible to the methods of dimensional analysis alone. A function of the sort $F(\phi_o)$ will be referred to as a 'similarity function', in the sense that two simple pendulums having the same ϕ_o will have the same *non*dimensional period; the dimensional period will depend upon L and g as $P \propto \sqrt{L/g}$. The similarity function $F(\phi_o)$ might be determined by observations, the red crosses of Fig. (4), upper. A key contribution of dimensional analysis is that we can expect that the $F(\phi_o)$ inferred from observations made on our little table-top size pendulum will apply for all simple pendulums that are described by the VPlist (25). In this case we also have numerical and theoretical solutions that are consistent with the observations, and which are able to access the full range of ϕ_o.

The similarity function $F(\phi_o)$ of a simple pendulum has an important limit as the amplitude approaches zero; the similarity function approaches a constant value, $F(\phi_o \to 0) \ \to \ 2\pi$. From dimensional analysis, we can expect that this will hold for all simple pendulums that are described by the VPlist (22).

2.4.2 Tension in the line

For the tension, T, a force, we could write

$$T \;=\; F(t,\, M,\, L,\, g,\, \phi_0)\;, \tag{24}$$

which at this stage is not different from (14) (aside from the dependent variable).

- A VPlist for the tension in the line of a simple pendulum: (25)

1. the tension, $T \doteq$ [1 1 -2], the one and only dependent variable,
2. time, $t \doteq$ [0 0 1], the independent variable,
3. mass of the bob, $M \doteq$ [1 0 0], a parameter,
4. length of the line, $L \doteq$ [0 1 0], a parameter,
5. acceleration of gravity, $g \doteq$ [0 1 -2], a parameter,
6. the initial angle, $\phi_0 \doteq$ [0 0 0], a parameter.

The mathematical model for tension, Eq. (10), includes the angular velocity squared, $(d\phi/dt)^2$, which is proportional to the centrifugal acceleration. Even if we knew that, $d\phi/dt$ should be omitted from Eq. (25), since including $d\phi/dt$ would amount to having a second dependent variable that must itself depend upon t, M, L, g, and ϕ_0.

An informal analysis of this VPlist is much the same as that for $\phi(t)$ and leads quickly to $K = 6 - 3 = 3$ nondimensional variables,

$$\frac{T}{Mg} \;=\; F(\frac{t}{\sqrt{L/g}}, \phi_o), \tag{26}$$

the form used in Fig. (1), lower. The mass of the bob, M, *does* make an appearance in the nondimensional tension, since the dependent variable, T, is a force that has a dimension of mass. That the mass must appear is evident since the tension in the line will equal the weight of the bob, Mg, in the absence of motion, which is an important, limiting case. The maximum tension in the line of a swinging bob will exceed the weight of the bob by a factor that increases with the amplitude of the motion defined by ϕ_o.

The tension may also be characterized by a time-independent value, say $\hat{T}$, for example the minimum or maximum value during an oscillation, T_{min} and T_{max}, and so

- A VPlist for a time-independent tension: (27)

1. a time-independent tension, $\hat{T} \doteq$ [1 1 -2], the dependent variable,
2. the mass of the bob, $M \doteq$ [1 0 0], a parameter,
3. length of the line, $L \doteq$ [0 1 0], a parameter,
4. acceleration of gravity, $g \doteq$ [0 1 -2], a parameter,
5. the initial angle, $\phi_0 \doteq$ [0 0 0], a parameter.

The rule of thumb estimate of the number of nondimensional variables is $K = 5 - 3 = 2$, or one less than required for the time-dependent tension, and they are related by

$$\frac{\hat{T}}{Mg} = F(\phi_o). \tag{28}$$

This leads to a legible format of the numerical solutions, Fig. (4), lower. Notice that the length, L, has dropped out going from (26) to (28).

But which $\hat{T}$ is this, T_{min} or T_{max}? Evidently (27) and (28) are adequate for either, though of course there is a different similarity function $F(\phi_o)$ for T_{min} and T_{max}. This illustrates an important and perhaps unexpected property of VPlists generally: VPlists are likely to encompass a greater range of phenomena i.e., they are likely to be much less specific, than the phenomenon you intend to describe and analyze. And thus the VPlist (27) will suffice just as well for the time-averaged tension as it does for the minimum and maximum values. This is consistent with the comment made following Eq. (15) that a VPlist generally makes a rather spare description of a problem.

2.5 Parameters

One of the interesting aspects of dimensional analysis is that it treats parameters on an equal footing with dependent and independent variables. (The algorithms implemented here in Sec. 3 put the dependent and independent variables in a special place, just for convenience.)

Unnecessary parameters. Dimensional analysis has revealed that the period of a simple, inviscid pendulum does not depend upon the mass of the bob, M. This result might seem to suggest that the inclusion of extra or superfluous variables in a VPlist will not spoil the result. However, in most cases an extra variable will not be detected by a dimensional analysis, and will lead to an extra or at least an unnecessary nondimensional variable. For example, if we had included the bob diameter, D_b, in the VPlist (15), it would have been carried through to a nondimensional variable, D_b/L. Access to experimental data would soon show that D_b/L was of

no great significance in determining the period of a nearly conservative pendulum, and so it would have been dropped from the final result.

Omitted parameters. Will the omission of a relevant variable be detected? Yes, but rarely, and only if the omission makes it impossible to nondimensionalize the dependent variable. For example, if we analyzed tension under the assumption that the mass of the bob M would be irrelevant (as it was for the oscillation period) then it would be impossible to construct a nondimensional tension. That would be a clear signal that something important had been left out of the VPlist. However, if the dependent variable can be nondimensionalized with the variables that are included, and in practice that is much more likely, then the purely formal procedure of dimensional analysis will not be able to identify an incomplete VPlist.

Locally and globally constant parameters. In the discussion of a simple pendulum, it was implicit that our interest included all possible values of the initial displacement, $-\pi \leq \phi_o \leq \pi$. In that event, the parameter ϕ_o would be deemed a 'locally constant' parameter, meaning that it is constant for a given experiment or realization, but that it may vary from one realization to the next. This is the default meaning of 'parameter'.

Suppose instead that the scope of a study is limited to a single value of the initial displacement, say $\phi_o =$, and no other values are relevant. In that case, ϕ_o will be termed a 'globally constant' parameter, meaning that it is the same for every realization. The similarity function $F(\phi_o)$ would then be a constant specific to that , say $F(\phi_o =) = C$. The dependence of $\phi(t/\sqrt{L/g})$ upon nondimensional parameters that are made up solely from parameters that are constants (common examples could be heat capacity, fluid density and other thermodynamic parameters) may thus be ascribed to the similarity constant, and so

$$\phi(t/\sqrt{L/g}) = C$$

would suffice in this case. The globally constant nondimensional parameter ϕ_o may then be dropped from the list of nondimensional variables, though it leaves a mark on the similarity constant. If there are two such globally constant nondimensional parameters, say $\phi_o =$ and $\phi_1 =$, then this may be extended,

$$\phi(t/\sqrt{L/g}) = , C$$

and ϕ_o and ϕ_1 both dropped. The happy result[13] is that the number of relevant (or active) nondimensional parameters may be less than the number of nondimensional parameters that first appears.

2.6 Summary: Why use nondimensional variables?

The informal dimensional analysis of this section has shown two significant benefits that you can expect to follow from the use of nondimensional variables.

More efficient representation. There will be a reduced number of nondimensional variables compared with dimensional variables. This will often lead to a more legible presentation of complex data sets, as in Figs. (1) and (3). It will also streamline model equations.

Physical interpretation. When dimensional variables are scaled (nondimensionalized) with the natural scales of a phenomenon, as they will be during a dimensional analysis, they are likely to have a significant physical interpretation. For example, the nondimensional reduced period of a simple pendulum oscillation is found to be $\sqrt{L/g}$ for *all* simple pendulums in small amplitude motion. This kind of result could come from a mathematical model, if it is available, or from dimensional analysis, even if not.

A different and wider perspective. There is a third possible benefit of dimensional analysis that is not as immediate, but that you may come to appreciate with time and experience. The method and the goals of dimensional analysis are quite different from the intensely focussed analysis methods that characterize most research, e.g., solving an equation of motion as in Sec. 2.1. The change in perspective that comes with dimensional analysis, e.g., thinking about the range of the relevant parameters of a problem, may help you develop insights on your problem that wouldn't necessarily come as readily from a more focussed approach to problem solving.

2.7 Pendulum problems

1) Compare the tension and the angular displacement of Figs. (1) and (3). Why is the frequency of oscillation different for these two variables? Notice that the range of the (nondimensional) maximum tension seen in Fig. 4, lower, is 1 to 5, while the minimum tension has a range -1 to 1. Can you explain these values using energy conservation and the radial equation of motion, Eqs. (9) and (10) of Sec. 2.1?

2) The approximate isochronism of simple pendulums in small amplitude motion is an important result going all the way back to Galileo's systematic investigations. It is not immediately obvious why this should hold for simple pendulums, and indeed, it does not hold at large amplitudes. From what you can see in Fig. (4), how would you characterize the limit $P(\phi_o \rightarrow 0)$? Can you explain the approximate isochronicity at low amplitudes? Why is the departure at larger amplitude towards longer period oscillations? (Hint: What does this imply about the restoring force?) What is the similarity constant for ϕ_o = 0.01, 0.1, 1.0 and π radians?

3) The simple-minded observational methods used here did not include a means to measure the angular velocity, $\omega = d\phi/dt$, and so the initial ω was taken to be zero. The effect of this is to exclude an entire family of simple pendulums. What new phenomenon and nondimensional variables would appear if the scope of the study had included an initial ω?

4) It is amusing to think of making pendulum measurements on Mars or the Moon where gravity is different from Earth's, but it is likely that our pendulum experiments will remain Earthbound. If that is so, then is it really necessary to carry along a constant parameter g in the dimensional analysis, as in Eq. (23)? Whether g is viewed as a locally or globally constant parameter must depend upon the application and the required precision. Can you envision exploiting the g-dependence of the pendulum period to measure the rather small, O(10^{-3}), variations of g along Earth's surface? [17]

5) Lead is an appropriate material for the bob of a pendulum[18] since its comparatively high density results in less drag with the air. However, lead can be toxic if handled carelessly, and so instead of a lead bob, consider a wooden bob or perhaps a foam rubber bob. Should the density of such a bob appear in the VPlist? Why did we ever leave it out? Would the similarity constant 2π of the small amplitude period then change?

6) In the analysis of tension in the line, Sec. 2.4.2, it was noticed that the line length L dropped out when going from the time-dependent tension to the time-independent tension, Eqs. (26) to (28). Can you explain why or how this happened?

7) Free fall in constant gravity is closely related to the (constrained) motion of a simple pendulum. Suppose the dependent variable is the vertical coordinate, z, and that the equation of motion is just

$$\frac{d^2z}{dt^2} \;=\; -\,g. \tag{29}$$

The ICs are

$$z = z_o(t=0) \;\text{ and }\; \frac{dz}{dt} = 0 \;\text{ at }\; t = 0. \tag{30}$$

What is the dimensional analysis version of this problem? How does your dimensional analysis result for $z(t)$ compare to the result from integrating (29) and (30)?

---

[17] An interesting discussion of applications is by https://microglacoste.com/product/fg5-x-absolute-gravimeter/

[18] Lead's chemical symbol is Pb, from the Latin *plumbum*, from which is derived 'plumb bob', a lead ball suspended on a string and used to observe the direction of gravitational acceleration, i.e., the vertical. If the bob is set into motion, the plum bob is a simple pendulum that may be used to infer the magnitude of the gravitational acceleration.

3 A basis set of nondimensional variables

Once a VPlist has been defined, the second and mathematical step of a dimensional analysis is to find a complete set of nondimensional variables for that VPlist. With a little experience and for small problems such as the simple pendulum of Sec. 2, the nondimensional variables can be constructed by inspection. For larger problems it may be helpful to use a computational method described in Sec. 3.2 that has its roots in linear algebra.[6] This method differs from most others[5] in that it does not rely on the Buckingham Pi theorem, although it comes to the same result, and instead computes the null space basis of the dimensional matrix (defined below) to find a basis set of nondimensional variables. The value of this method lies less in the calculation, which is straightforward, but in the perspective it provides on the result.

3.1 The mathematical problem

How to calculate a set of nondimensional variables from a VPlist? The nondimensional variables, called Pi variables, Π, are presumed to be the products of the dimensional variables, say X_1, X_2 and X_3 that are raised to some power,

$$\Pi \;=\; X_1^{S_1} \times X_2^{S_2} \times X_3^{S_3}, \tag{31}$$

where the exponents S_1, S_2, S_3 are unknowns. This is consistent with the nondimensional variables found by the informal analyses of Sec. 2. For a very abbreviated example consider

- A VPlist for the period of a simple pendulum in small amplitude motion: (32)

1. period, $P \doteq [\,0 \;\; 0 \;\; 1\,]$, the dependent variable,
2. length of the line, $L \doteq [\,0 \;\; 1 \;\; 0\,]$, a parameter,
3. acceleration of gravity, $g \doteq [\,0 \;\; 1 \;\; -2\,]$, a parameter.

A Π variable formed as the product Eq. (31) will then have physical dimensions

$$\Pi \doteq S_1\,[0\;0\;1\,] \;+\; S_2[0\;1\;0\,] \;+\; S_3[0\;1\;-2\,] \tag{33}$$

and will be nondimensional

$$\Pi \doteq [\,0 \;\; 0 \;\; 0\,]$$

if the exponents satisfy

$$S_2 \;+\; S_3 \;=\; 0, \qquad \text{and} \qquad S_1 \;-2S_3 \;=\; 0. \tag{34}$$

This is two independent equations in three unknowns, and so this system is underdetermined. We may as well choose $S_1 = 1$ so that P will appear to the first power, and then $S_3 = 1/2$ and

$S_2 = -1/2$. Since this system is linear and homogeneous, $S_1 =$ and then $S_2 = - \ / \ 2$ and $S_3 = \ / \ 2$ with real is also a solution. In this case (and assuming $= 1$) there is just one nondimensional variable,

$$\Pi_1 \ = \ P^{S_1} \times L^{S_2} \times g^{S_3} \ = \ P^1 \times L^{-1/2} \times g^{1/2} \ = \ P/\sqrt{L/g}, \ = constant.$$

From experimental or theoretical analysis (Fig. 4) we know that this $constant \ = \ 2\pi$ provided that the amplitude of the motion is not relevant (and not included in the VPlist (32)).

3.2 Computing the null space

These are the kind of solutions we are looking for. However, we need *all* of the possible solutions and for systems that may be much larger (more variables). These complete solutions will come from solving

$$\mathbb{D}\mathbb{S} \ = \ 0, \tag{35}$$

where $\mathbb{D}$ is the dimension matrix, and $\mathbb{S}$ is the matrix of solution vectors that constitute the null space of $\mathbb{D}$. This is the matrix equivalent of Eqs. (31) - (33) (Problem 1 below).

$\mathbb{D}$ may be read directly from the VPlist. For the VPlist of the simple pendulum, Eq. (15), the dimension matrix is

$$\mathbb{D} \ = \ \begin{array}{c} \\ m \\ l \\ t \end{array} \begin{array}{c} \begin{array}{cccccc} \phi & t & M & L & g & \phi_0 \end{array} \\ \left[\begin{array}{cccccc} 0 & 0 & 1 & 0 & 0 & 0 \\ 0 & 0 & 0 & 1 & 1 & 0 \\ 0 & 1 & 0 & 0 & -2 & 0 \end{array} \right] \end{array}. \tag{36}$$

The columns of $\mathbb{D}$ correspond to the dimensional variables. The order of including the dimensional variables is noteworthy only insofar as the algorithm will seek to make the first few dimensional variables appear in the nondimensional variables with an exponent = 1. Hence it is helpful to have the dependent variable ϕ come first, the independent variable t come next, and after that there is no obvious, preferred ordering. The rows of $\mathbb{D}$ correspond to the physical dimension of those variables: row 1 is mass, row 2 is length and row 3 is time. This order is arbitrary, but has to be maintained once chosen.[19] Thus for the acceleration of gravity, which is the fifth dimensional variable in the VPlist, $g \doteq [0 \ 1 \ -2]$ and so the 5th column of $\mathbb{D}$ is $D_{15} \ = \ 0, \ \ D_{25} \ = \ 1,$ and $D_{35} = -2$.

The matrix $\mathbb{S}$ contains the unknown exponents. It is convenient to think of the columns of $\mathbb{S}$ as

[19] Within the main text the physical dimensions on a variable are written as a row vector to save space. These data are the column vectors of the matrix $\mathbb{D}$.

vectors, $\mathbf{S}$,

$$\mathbf{S_1} = \begin{bmatrix} S_{11} \\ S_{21} \\ S_{31} \\ S_{41} \\ S_{51} \\ S_{61} \end{bmatrix}, \quad \mathbf{S_2} = \begin{bmatrix} S_{12} \\ S_{22} \\ S_{32} \\ S_{42} \\ S_{52} \\ S_{62} \end{bmatrix} \quad \text{and} \quad \ldots\ldots \quad \mathbf{S_K} = \begin{bmatrix} S_{1K} \\ S_{2K} \\ S_{3K} \\ S_{4K} \\ S_{5K} \\ S_{6K} \end{bmatrix},$$

to which nondimensional variables will correspond one-to-one.

The system of equations (35) is underdetermined in the usual case that there are more unknown exponents (the number of dimensional variables) than there are independent equations (usually the number of physical dimensions and also the number of rows of $\mathbb{D}$). However, it can be less (see Problem 4 of Sec. 3.5). The number of columns in $\mathbb{S}$, and thus the number of vectors, $\mathbf{S}$, is K, and is found as a part of the calculation of the null space. To represent or span the null space requires a basis set of K vectors, from which any solution vector can be constructed (more on this below). This K has the same important interpretation as the K of Sec. 2.3.1; *viz.*, K is the number of nondimensional variables in a basis set.

The calculation of a null space basis proceeds along the lines of Eqs. (31) to (34); not difficult, but tedious if done by hand. The calculation of a null space basis is readily automated, as will be assumed from here on. Links to relevant scripts are in Sec. 3.4.

3.2.1 A basis set of nondimensional variables of the angular displacement

The null space basis for the time-dependent and finite amplitude angular displacement defined by the $\mathbb{D}$ of Eq. (36) has $K = 3$ solution vectors,

$$\mathbf{S_1} = \begin{bmatrix} 1 \\ 0 \\ 0 \\ 0 \\ 0 \\ 0 \end{bmatrix}, \quad \mathbf{S_2} = \begin{bmatrix} 0 \\ 1 \\ 0 \\ -1/2 \\ 1/2 \\ 0 \end{bmatrix}, \quad \text{and} \quad \mathbf{S_3} = \begin{bmatrix} 0 \\ 0 \\ 0 \\ 0 \\ 0 \\ 1 \end{bmatrix}.$$

The elements of $\mathbf{S}$ are required to be rational numbers. Here and typically, they are small rational numbers.

The corresponding basis set of K nondimensional variables is constructed from the solution

vectors as

$$\Pi_1 \;=\; \mathbf{X}^{\mathbf{S_1}} \;=\; \phi^1\, t^0\, M^0\, L^0\, g^0\, \phi_0^0, \;=\; \phi \tag{37}$$

$$\Pi_2 \;=\; \mathbf{X}^{\mathbf{S_2}} \;=\; \phi^0\, t^1\, M^0\, L^{-1/2}\, g^{1/2}\, \phi_0^0 \;=\; t/\sqrt{L/g}, \tag{38}$$

$$\Pi_3 \;=\; \mathbf{X}^{\mathbf{S_3}} \;=\; \phi^0\, t^0\, M^0\, L^0\, g^0\, \phi_0^1 \;=\; \phi_0, \tag{39}$$

where notice that the elements of the $\mathbf{S}$ vectors are exponents on the elements of the $\mathbf{X}$ vectors. The dependent variable ϕ appears in the first nondimensional variable only, and to the first power, a convenient property built in to the algorithm.

The functional relationship among the nondimensional Πs may be written as

$$\Pi_1 \;=\; F(\Pi_2,\, \Pi_3),$$

or, once again,

$$\phi(t) \;=\; F(\frac{t}{\sqrt{L/g}},\, \phi_0)\,. \tag{40}$$

Since the maximum of $\phi(t)$ will be equal to ϕ_o, it makes sense to normalize ϕ as

$$\frac{\phi(t)}{\phi_o} \;=\; F(\frac{t}{\sqrt{L/g}},\, \phi_0).$$

This amounts to dividing Π_1 by Π_3, which is allowed by properties of the null space (discussed in Sec. 3.3). But we can not then omit ϕ_o from the righthand side of (40) as that would reduce the basis set of nondimensional variables.

The mass M has an exponent of zero in all of the solution vectors, Eqs. (37) to (39), consistent with the informal analysis of Sec. 2 which showed that there was no way to construct a nondimensional variable from a single parameter having physical dimensions of mass. To say it a little differently, for the mass of the bob to be retained, there would have to be another parameter with dimension mass in the VPlist (as there will be in the more comprehensive models of Sec. 4). Notice that the angles ϕ and ϕ_0 sailed into the basis set of nondimensional variables untouched, since they were already nondimensional.

3.2.2 A basis set for tension in the line

Tension can be analyzed in the same manner, starting with the dimensional matrix read from the VPlist, (25),

$$\mathbb{D} \;=\; \begin{array}{c} \\ m \\ l \\ t \end{array} \begin{array}{c} \begin{array}{cccccc} T & t & M & L & g & \phi_0 \end{array} \\ \left[\begin{array}{cccccc} 1 & 0 & 1 & 0 & 0 & 0 \\ 1 & 0 & 0 & 1 & 1 & 0 \\ -2 & 1 & 0 & 0 & -2 & 0 \end{array}\right] \end{array}. \tag{41}$$

The null space basis vectors are

$$\mathbf{S_1} = \begin{bmatrix} 1 \\ 0 \\ -1 \\ 0 \\ -1 \\ 0 \end{bmatrix}, \quad \mathbf{S_2} = \begin{bmatrix} 0 \\ 1 \\ 0 \\ -1/2 \\ 1/2 \\ 0 \end{bmatrix}, \text{ and } \quad \mathbf{S_3} = \begin{bmatrix} 0 \\ 0 \\ 0 \\ 0 \\ 0 \\ 1 \end{bmatrix}.$$

A basis set of nondimensional variables is thus

$$\Pi_1 = \mathbf{X}^{\mathbf{S_1}} = T^1\, t^0\, M^{-1}\, L^0\, g^{-1}\, \phi_0^0 = T/Mg \tag{42}$$

$$\Pi_2 = \mathbf{X}^{\mathbf{S_2}} = T^0\, t^1\, M^0\, L^{-1/2}\, g^{1/2}\, \phi_0^0 = t/\sqrt{L/g}, \tag{43}$$

$$\Pi_3 = \mathbf{X}^{\mathbf{S_3}} = T^0\, t^0\, M^0\, L^0\, g^0\, \phi_0^1 = \phi_0. \tag{44}$$

The second and third of these are identical to Π_2 and Π_3 of the displacement noted above. The functional relationship for the time-dependent tension can then be written

$$\frac{T}{Mg} = F(\frac{t}{\sqrt{L/g}}, \phi_0). \tag{45}$$

Notice that the dependent variable T has been scaled by the weight of the bob, Mg, a fairly obvious natural scale in this problem.

A time-independent tension, say the minimum or the maximum during a complete oscillation, can be analyzed by omitting the time, t, to find

$$\frac{T_{min}}{Mg} = F(\phi_0), \quad \text{and} \quad \frac{T_{max}}{Mg} = F(\phi_0), \tag{46}$$

the forms used in Fig. (4), lower. Notice that the line length, L, has disappeared going from (45) to (46). It is a little jarring to see $F(\phi_o)$ on the right side of two different equations in (46), but keep in mind that this F is merely holding a place for a similarity function that has to be determined by some method beyond dimensional analysis.

3.3 Properties of a null space basis

It is important to understand the properties of a null space basis, and especially that a given null space basis is generally *not* a unique solution to the underdetermined problem of the sort Eq. (35) encountered in dimensional analysis. There are usually many possible solutions, and just as many null space bases. In fact, the specific null space basis that comes from a solution algorithm will

depend upon the order in which the dimensional variables are listed in the dimensional matrix. The construction of the best (most useful, most insightful) basis set of nondimensional variables is facilitated by the following three properties of a null space basis.

Property 1, P1: The number of solution vectors in a null space basis is $K = I - R$, where I is the number of dimensional variables and R is the rank of the dimensional matrix, $\mathbb{D}$.

It is highly desirable to have the smallest possible K. However, the rank, R, is determined strictly by the dimension matrix $\mathbb{D}$ and thus by the VPlist; there is nothing that can be done to change K, except to amend the VPlist.[20]

P2: Nondimensional variables correspond one-to-one with solution vectors of the null space, and are K in number. These nondimensional variables are themselves a basis set for the problem defined by the VPlist.

The K is the same for all basis sets and in that important regard, all basis sets are equally efficient, i.e., they all achieve the same reduction in the number of variables. Nevertheless, one particular basis set may be more useful than the others. A transformation from one basis set to another is readily accomplished because

P3: The vectors of a null space basis are linearly independent and they span the null space. Any vector that is a solution of the homogeneous system can thus be formed as a linear combination of the vectors that make up any basis set.

For example, if $\mathbf{S_1}$ and $\mathbf{S_2}$ are vectors in a null space basis, then their linear combination, say $\mathbf{S_3} = a_1\mathbf{S_1} + a_2\mathbf{S_2}$, with a_1 and a_2 any real number, is also a vector in the null space, and hence $\mathbf{S_3}$ is also a solution. Let the nondimensional variable corresponding to this new vector be Π_3. If Π_3 and Π_1 are preferred over the initial Π_1 and Π_2, then a revised basis set can be taken as Π_1 and Π_3, while omitting Π_2. The revised basis set has the same number of vectors and nondimensional variables as the initial basis set, and will also span the null space.

[20] The rank, R, of the dimension matrix is computed and reported as part of the automated calculation. It is useful to know how R may change. In brief, the rank of a matrix is the number of linearly independent rows or columns (the same for either). Suppose that a VPlist and thus the corresponding $\mathbb{D}$ includes a time scale, ω_1, and now add another time scale, ω_2. The number of dimensional variables increases by 1, but the rank of $\mathbb{D}$ does not increase because the new column associated with ω_2 is identical to the column that represents ω_1 and already present. The number K of nondimensional variables in the null space basis thus goes up by 1 with the inclusion of ω_2 in the VPlist. A special case considered in Problem 4) below is $\mathbb{D} = 0$, the zero matrix, which has rank of zero. For much more on the rank of a matrix and on the null space generally, see https://ocw.mit.edu/courses/18-06-linear-algebra-spring-2010/ and G. Strang, 1998, *Introduction to Linear Algebra*, Wellesley-Cambridge Press, Wellesley, MA.

Given these three properties of a null space basis, the initial basis set of nondimensional variables that comes directly from a calculation may be transformed to some other preferred basis set by multiplying or dividing the Πs in any order. Defining a preferred basis set of nondimensional variables by this kind of transformation is the third step of a dimensional analysis that will be emphasized in Secs. 4, 6 and 7.

3.4 Automated calculation

The calculation of a null space basis is best done by machine, say with Matlab

https://www2.whoi.edu/staff/jprice/wp-content/uploads/sites/199/2024/06/DanalysisA2.zip

or Python,

https://www2.whoi.edu/staff/jprice/wp-content/uploads/sites/199/2024/10/DA2Python.zip

To use the Matlab, unpack a script, DanalysisA2.m, and three functions, Dclear.m, Din.m and Dnullspace.m. Enter the red text below into a command window; the blue text is returned by Matlab.

DanalysisA2 starts a script that will run several cases automatically. You will be asked to reply to two questions that may be defaulted with n. To define a new problem, either edit this script, or, call the functions that make up the algorithm.

To use the functions, first declare the following variables to be global:

global D VPname nVP S Pi, where

D is the dimension matrix,
VPname is the name of a variable in the VPlist (character data),
nVP is the number of variables and parameters in the VPlist,
S is the null space vectors that we seek, and
Pi is a symbolic math representation of the nondimensional variables.

Dclear should be called at the start of a problem to reset these global variables.

Then enter the data that define the VPlist by a sequence of calls to Din('text', [mass length time]), once for each variable in the VPlist. The 'text' is the name of the variable, and the row vector defines the physical dimensions of 'text' as [mass length time]. Enter the single dependent variable first, then the independent variables, then the parameters, e.g., for the VPlist Eq. (15),

Din('phi', [0 0 0])	angular displacement, the single dependent variable
Din('t', [0 0 1])	time, an independent variable

```
Din('M', [ 1 0 0 ])      mass of the bob
Din('L', [ 0 1 0 ])      length of the line
Din('g', [ 0 1 -2 ])     acceleration of gravity
Din('phio', [ 0 0 0 ])   the initial angle.
```

That completes the VPlist for the oscillations of a simple pendulum. Now do the calculation,

```
Dnullspace
```

and Matlab will return the following:

```
The number of dimensional variables, I = 6
The rank of the dimension matrix, D, is R = 3
The number of non-d variables is K = I - R = 3
 The dimensional variables and solution vectors (exponents) that
        make one possible basis set of non-d variables are:

phi     t     M     L      g      phio
1       0     0     0      0      0
0       1     0    -0.5    0.5    0
0       0     0     0      0      1

A basis set of non-dimensional variables is thus:

(  phi,   t * sqrt(g) / sqrt(L),    phio )
```

This is consistent with Eq. (40), though written in an implicit form.[11]

3.5 Null space problems

1) Use the null space basis method to analyze the period of a simple pendulum given the VPlist (32). How many nondimensional variables are there? What does this imply for the similarity function, or is it a similarity constant? Given that there is only solution vector, verify by direct substitution that the matrix relation Eq. (35) is equivalent to Eqs. (31) - (33). What if an angle, say ϕ_o, is included in the analysis above? To add a new variable to an existing VPlist you need only call Din('phio', [0 0 0]), and then call Dnullspace to see the new result. What happens if a second length, L_2 is also included?

2) Suppose that you scramble the order of the VPlist of Eq. (15)? How about changing the order of the physical dimensions, i.e., in place of [mass length time] used here, how about [length mass time]?

3) In most problems the number of nondimensional variables, K, can be estimated by the rule of thumb noted in Sec. 2.3.1, K = the number of variables in the VPlist minus the number of fundamental units. But that doesn't always work, as the following example, which is contrived but not impossible, shows. Suppose that a VPlist consists of four velocities. The simple rule of thumb: there are two fundamental units, length and time, and so the expectation is $K = 4 - 2 = 2$ nondimensional variables. However, an application of the null space method indicates 3 nondimensional variables because the dimension matrix has rank $R = 1$ (the minimum, aside from the special case of a zero matrix; discussed below) since the variables all have the same dimensionality. Some questions for you: What are the nondimensional variables in this case, and which estimate of their number is correct? Suppose a fifth variable having dimension length, $L \doteq [\,0\;1\;0\,]$ is added into the VPlist; what changes? Suppose a sixth variable having dimension time is added?

4) A good test on a model or algorithm is that it behaves appropriately at the limits of its domain. In this context, an interesting limit is a case in which all of the variables of a VPlist are nondimensional, as if the output of a null space calculation was used as the input of a second calculation. The corresponding dimension matrix is then the zero matrix, $\mathbb{D} = 0$, i.e., all entries are zero, and which has a rank $R = 0$.[20] What do you expect from a null space calculation? Form a hypothesis, and then run such a calculation beginning with a VPlist comprising three angles, say.

5) The dimensional analysis of tension in the line, Sec. 2.4.2, and Eq. (46), concluded that the time-independent tension, i.e., the minimum or maximum over an oscillation, is independent of the line length, L. This was suggested by a handful of numerical experiments seen in Fig. (1), and dimensional analysis assures that this holds rigorously for the VPlist that describes the most important properties of a simple pendulum. Something for you to think about: does dimensional analysis provide a satisfactory *explanation* of this (small and singular) fact?

4 Damping a simple pendulum

The motion of a free-running pendulum will decay in time as energy is dissipated into the surrounding air.[21] This section will analyze the mechanisms that cause this damping.

4.1 Observations of the decaying amplitude

The amplitude of the oscillation, $\Phi(t)$, was observed by measuring the maximum of the cord length at intervals of 30 seconds to 2 minutes. To minimize the measurement noise associated with the rather coarse least count on the measured cord, 10^{-3} m, it was found helpful to study a longer pendulum, $L = 3.70$ m, than used before. The line was smooth monofilament having a diameter $D_l = 0.40 \times 10^{-3}$ m, and the bob was a nearly spherical, smooth lead fishing sinker with a diameter $D_b = 0.0211$ m and mass $M = 0.055$ kg. The line was supported on a needle bearing (a fishhook with the point impinging on a hard, metal surface) to minimize interactions between the swinging pendulum and its support.

The observed amplitude, $\Phi(t)$, (the red crosses of Fig. (6), upper) was found to be highly repeatable, and can be characterized roughly as an e-folding in about 10 minutes. During this time the pendulum made hundreds of oscillations, and hence the damping of this pendulum is weak in comparison to gravity; more on this below.

The decay rate of the oscillation amplitude is defined by

$$\Gamma \;=\; \frac{1}{\Phi}\frac{d\Phi}{dt}, \tag{47}$$

where Φ is the amplitude of the angular displacement (and $\phi(t)$ is the time-dependent, instantaneous angle). This Γ is an inverse time. It is expected that Γ will itself be amplitude-dependent and thus time-dependent.

4.2 A preliminary VPlist for the decay rate of a simple pendulum

The primary damping process is presumed to be aerodynamic drag between the swinging pendulum and the surrounding, viscous air.[22] If that is the case, then the diameter of the bob, D_b, and of the

[21] A pendulum-based clock requires an escapement mechanism to couple the pendulum into the clock mechanism, and, to do a very small positive work on each swing of the pendulum to offset frictional losses. One of the first successful mechanisms for a pendulum clock was designed by Galileo Galilei, late in life and after he had lost his sight. Pendulum-based clocks were later developed into the most precise means of time-keeping available for almost three centuries. https://en.wikipedia.org/wiki/Galileo_escapement

[22] An excellent introduction to viscosity in fluid flow is by http://galileo.phys.virginia.edu/classes/152.mf1i.spring02/ and see the chapter on Fluids. The pioneering work on this topic (and much else) is the remarkable study by Stokes, G. G.,

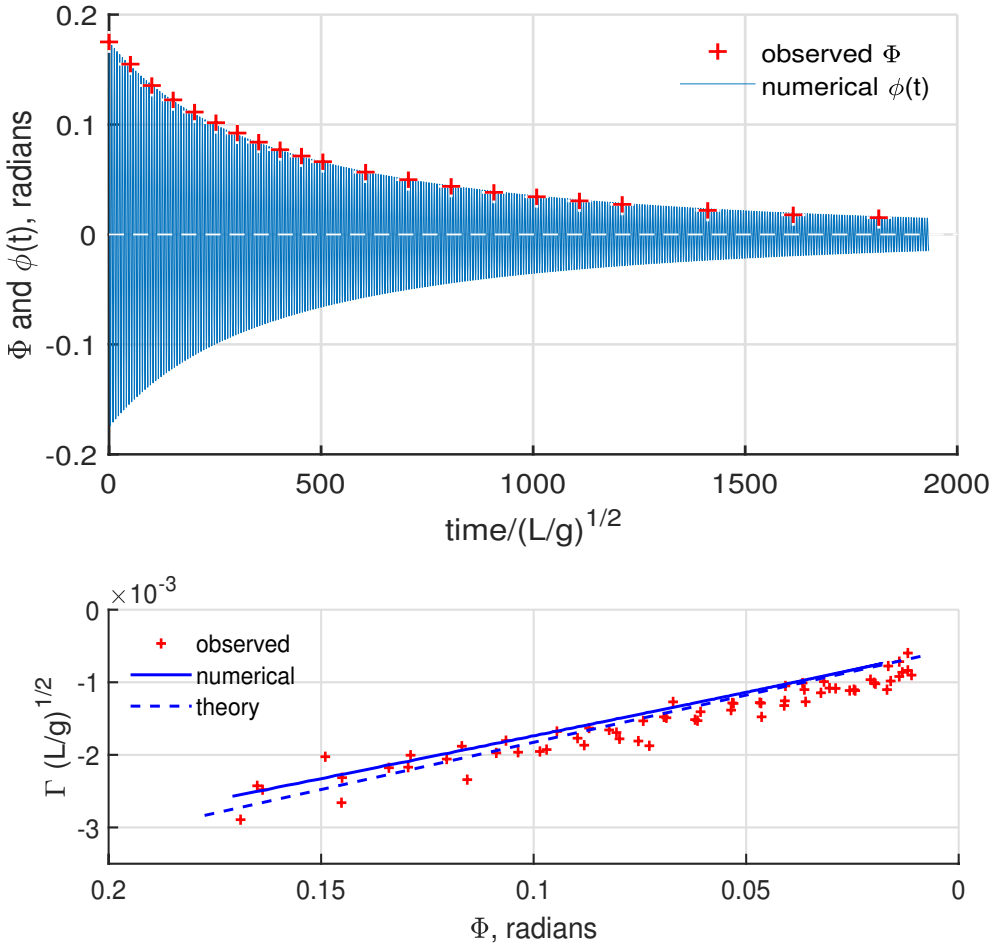

Figure 6: **(upper)** Observations of the amplitude, Φ, of a simple pendulum at intervals of 30 seconds to 2 minutes (the red crosses). Also shown here is a numerical solution for $\phi(t)$ (the thin, solid blue line), described in Sec. 4.4.1. **(lower)** The decay rate computed directly from Eq. (47) with data from three repetitions of the experiment (the red crosses), and from a numerical solution (blue, solid line). An approximate analytic solution, Eq. (70), is the blue, dashed line. Drag that is linear in the angular velocity produces exponential decay of the amplitude in time and thus a constant nondimensional decay rate. Drag that is quadratic in the angular velocity produces a nondimensional decay rate that decreases with decreasing amplitude, Φ. Most of what can be seen here is the latter.

line, D_l, would seem to be relevant, along with the density and kinematic viscosity of air, ρ and ν.

- A preliminary VPlist for the decay rate of a simple pendulum with viscosity: (48)

1. the decay rate, $\Gamma \doteq$ [0 0 -1], the dependent variable;
2. mass of the bob, $M \doteq$ [1 0 0], a parameter,
3. length of the line, $L \doteq$ [0 1 0], a parameter,
4. acceleration of gravity, $g \doteq$ [0 1 -2], a parameter,
5. the amplitude of the motion, $\phi_o \doteq$ [0 0 0], a parameter,
6. diameter of the line, $D_l \doteq$ [0 1 0], a parameter,
7. diameter of the bob, $D_b \doteq$ [0 1 0], a parameter,
8. density of air, $\rho \doteq$ [1 -3 0], a parameter (1.2 kg m^{-3}, nominal),
9. kinematic viscosity of air, $\nu \doteq$ [0 2 -1], a parameter (1.5×10^{-5} m^2 s^{-1}, nominal).

Dimensional analysis via the method of Sec. 3.2 (from here on omitting all of the intermediate steps) indicates a basis set of $K = 9 - 3 = 6$ nondimensional variables,

$$\Gamma\sqrt{L/g} = F(\phi_o, \frac{D_b}{L}, \frac{D_l}{L}, \frac{\rho D_b^3}{M}, \frac{g^{1/2}L^{3/2}}{\nu}). \tag{49}$$

The dependent variable, Γ is scaled with the fast, oscillatory time scale, $\propto \sqrt{L/g}$, the natural time scale of a simple pendulum, and is O(10^{-3}) for the nearly conservative pendulum observed here, Fig. (6). This is the sense in which this pendulum is weakly damped. The first nondimensional parameter, ϕ_o, is familiar as the amplitude of the motion. The next two nondimensional parameters have straightforward geometric interpretations, the third parameter is proportional to the buoyancy force on the bob (not significant since the density of lead is much greater than the density of air). The last nondimensional parameter involving the viscosity can be recast as a Reynolds number, which has an important physical interpretation discussed below. While the nondimensional variables and parameters are interpretable individually, we are not ready to make use of such a comprehensive model.[23] We may still be thinking of the nearly conservative pendulum of Sec. 2.1, but this nine-variable VPlist includes all simple pendulums and fluid mediums, including bobs that float and fluid that is sufficiently viscous that there is no oscillation. Before we can expect a useful result from dimensional analysis we will have to first identify the most relevant parameters for the kind of nearly conservative (weakly damped) pendulum described in Sec. 4.1.

1851, 'On the effect of the internal friction of fluids on the motion of pendulums'. Trans. of the Cambridge Philosophical Soc., Ninth Vol., No. 10, pp. 8 - 106. Bibcode: 1851TCaPS...9....8S More recent is P. T. Squire, 1986, 'Pendulum damping', Am. J. Phys. **54**, 984–991, and R. A. Nelson, and M. G. Olsson, 1985, 'The pendulum: Rich physics from a simple system', Am. J. Phys. **54**, 112–121.

[23] This looks like a big problem compared to those encountered up to here. However, it is small compared to the problems that arise in some real-world applications, e.g., food processing.[2]

4.3 Aerodynamic drag on a moving sphere and cylinder

A piecewise approach is tried next. Consider in isolation the aerodynamic drag on a smooth sphere (the bob) that is in steady motion through a viscous fluid (air) that is at rest. Despite the idealized configuration of this problem, it is challenging to compute the drag from first principles in the common case that the flow around the sphere is turbulent. However, dimensional analysis combined with laboratory measurement leads to a useful result.

- A VPlist for drag on a sphere moving steadily through viscous fluid: (50)

1. drag (a force), $H \doteq$ [1 1 -2], the dependent variable,
2. speed of the sphere, $U \doteq$ [0 1 -1], a parameter,
3. diameter of the sphere, $D_b \doteq$ [0 1 0], a parameter,
4. density of the fluid, $\rho \doteq$ [1 -3 0], a parameter,
5. kinematic viscosity of the fluid, $\nu \doteq$ [0 2 -1], a parameter.

There are five variables and parameters having three physical dimensions and hence there are two nondimensional variables in the preliminary basis set,

$$\Pi_1 \;=\; \frac{H}{\rho\, D_b^2\, U^2} \quad \text{and} \quad \Pi_2 \;=\; \frac{\nu}{U\, D_b}. \tag{51}$$

This Π_2 is the inverse of a very widely occurring nondimensional variable called the Reynolds number,

$$Re \;=\; \frac{U\, D_b}{\nu}, \tag{52}$$

which is preferred. From P2 of the null space (Sec. 3.3) we know that the Π_1 and Π_2 of Eq. (51) are not uniquely determined by dimensional analysis, and that we are free to reform the initial basis set by adding or subtracting the solution vectors to one another in any order, which amounts to multiplying or dividing the Πs in any order. The first change will be to simply invert the initial Π_2 of Eq. (51), and use instead the conventional Reynolds number,

$$\Pi_2 \;=\; \frac{U\, D_b}{\nu}.$$

Thus to here we have the slightly revised basis set,

$$\Pi_1 \;=\; \frac{H}{\rho\, D_b^2\, U^2}, \quad \Pi_2 \;=\; R_e \;=\; \frac{U\, D_b}{\nu}, \tag{53}$$

and so

$$\frac{H}{\rho\, D_b^2\, U^2} \;=\; C(Re), \tag{54}$$

which is close to a useful result. Notice that in place of the F used to indicate an unknown similarity function in Secs. 2 and 3, this Eq. (54) and the rest of this section will use instead C, which is said to be a 'drag coefficient'.

The drag coefficient on an immersed object is generally defined to be

$$C_d \;=\; \frac{H}{\frac{1}{2}\,\rho\,A\,U^2}, \tag{55}$$

with A the frontal area, $A \;=\; \pi D^2/4$ for a sphere. The factor $1/2$ in the denominator of (55) is almost always included. With these numerical factors acknowledged, the basis set (54) becomes[24]

$$\Pi_1 \;=\; \frac{H}{(\pi/8)\,\rho\,D_b^2\,U^2} \quad \text{and} \quad \Pi_2 \;=\; Re \;=\; \frac{U D_b}{\nu}. \tag{56}$$

Before accepting (56) as final, we should consider other possibilities, and specifically that Π_1 may also be multiplied by some power of the Reynolds number, Π_2. A somewhat general basis set is then

$$\frac{H}{(\pi/8)\,\rho\,D_b^2\,U^2}\,{R_e}^n \;=\; C_n(Re), \tag{57}$$

where n is any real number. This assumes that H and $\Pi_2 \;=\; Re$ may as well remain to the first power. The subscript n on C_n is to acknowledge that the drag coefficient (the similarity function in this problem), will be dependent upon n. In this case, the criterion for deciding the best n will be the n that yields the least variable drag coefficient, $C_n(Re)$.

Regardless of the n finally chosen, an essential result from Eq. (57) is that the nondimensional drag, the left side of (57), is expected to be a function of Re alone. Laboratory measurements of drag, speed, etc., can thus be used to define a similarity function $C_n(Re)$ that should hold for all steadily moving spheres or cylinders, just the way that the function $F(\phi_0)$ (Sec. 2.4) sufficed to define the period for all inviscid, simple pendulums. What is most important is that drag coefficients estimated from experiments conducted over a very wide range of speeds and through different Newtonian viscous fluids do indeed collapse to a well-defined, though not necessarily simple function of the Reynolds number alone, just as dimensional analysis had lead us to expect. Experimental estimates for spheres are in Fig. (7), left, and the result for cylinders is Fig. (7), right.

This is a result, characteristic of dimensional analysis, that is at once profound and trivial. One might say trivial because, after all, dimensional analysis told us that the drag coefficient

[24] The inclusion of these two numerical factors doesn't change anything fundamental about the drag coefficient (54). However, if we want to make contact with the huge body of historical studies on aerodynamic drag, then we should account for them. The factor 1/2 that multiplies ρU^2 can be viewed as the dynamic pressure of the Bernoulli equation, $P_d \;=\; \frac{1}{2}\rho U^2$, where U is the free stream velocity brought to zero on the surface of an object that is immersed in the flow. Dynamic pressure is the immediate mechanism of inertial drag, and can be measured directly.

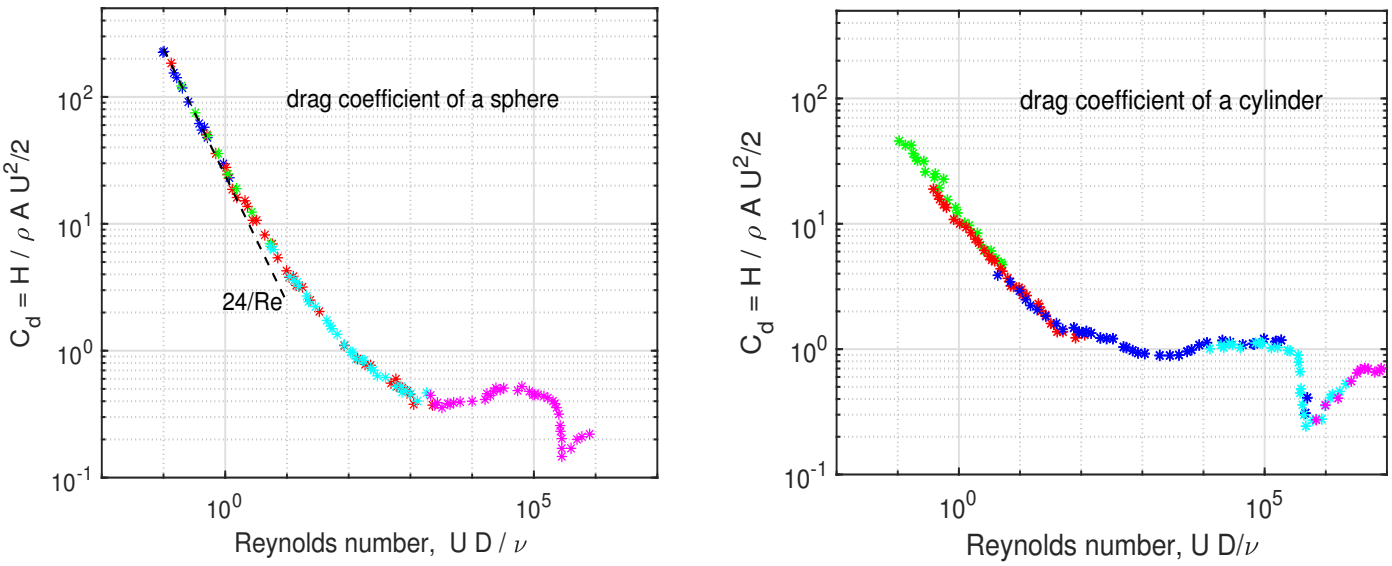

Figure 7: Experimental estimates of the conventional drag coefficient, $C_d = H/\frac{1}{2}\rho A U^2$, of a smooth sphere **(left)** and a cylinder **(right)** moving steadily through a viscous, Newtonian fluid, air, water and various oils. This is a representative subset of experimental data extracted from Rouse (1946) Sec. 4.[5]

should depend upon Re alone. From that perspective, an effective collapse of the experimental data to a single curve $C(Re)$ merely verifies that carefully controlled laboratory conditions can approximate the idealized VPlist (50). But it is also profound in that dimensional analysis has shown the way to a portable, useful result, the $C(Re)$ of Fig. (8), where there would otherwise have been be an unwieldy mass of highly specific data, as in going from Fig. (1), upper to lower.

4.3.1 A zero order solution as a scale for the dependent variable

The most important (and in this case the only) choice is how to nondimensionalize, or scale, the dependent variable, H, which then defines Π_1. The null space basis method has framed the issue in a convenient way, but the next step requires that something be added. One strategy is to choose a scale that reflects a physically meaningful 'zero order' solution for the dependent variable. A zero order solution is a highly simplified, approximate solution that has a physically plausible behavior in an appropriate limit (examples coming just below). If such a zero order solution can be found, then the corresponding nondimensional variable, Π_1, should have a magnitude of O(1) in that limit.

Constructing a zero order solution requires some sense of the physics of the problem. Visual observations of the flow around a steadily moving sphere suggest that drag can arise from two distinct processes.

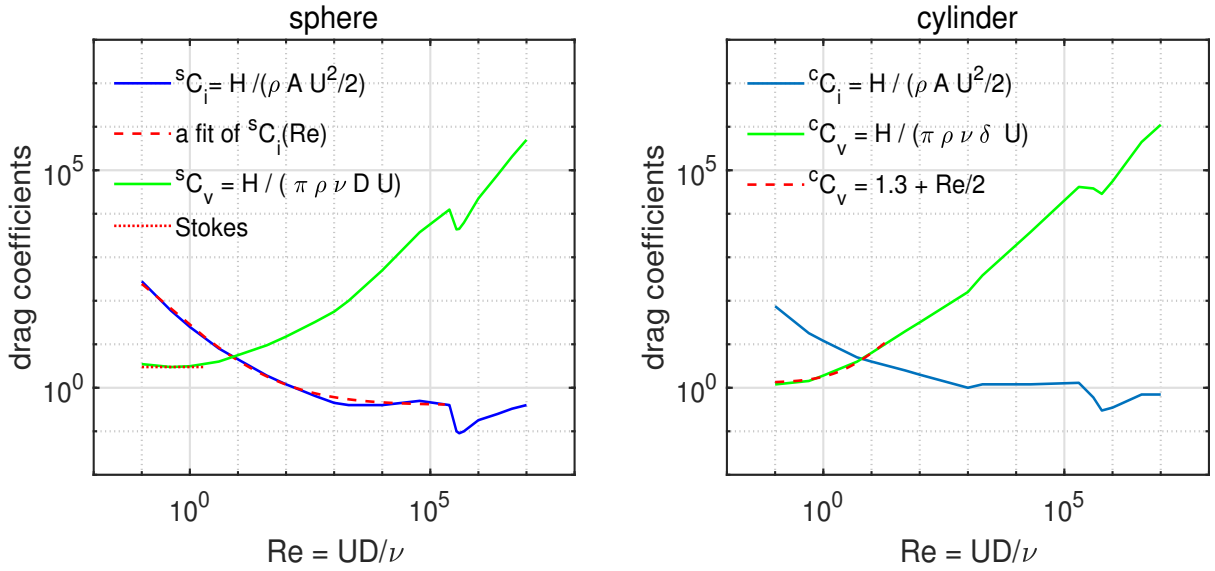

Figure 8: Empirical drag coefficients for a sphere, **(left)**, and a cylinder, **(right)**, moving at a steady speed U through a Newtonian viscous fluid. Two forms of a drag coefficient are shown here, the inertial drag coefficient denoted by C_i (the blue lines), and the so-called viscous drag coefficient denoted by C_v (the green lines). The inertial drag coefficients were read from Munson et al. (1998)[5], Fig. (7.7) and Rouse (1946),[5] Figs. (125) and (126) and the viscous drag coefficients were then computed by Eq. (57) with $n = 1$. Note that ${}^sC_v$ and ${}^cC_v$ are O(1) if Re is small, $Re \leq 1$, and that ${}^sC_i$ and ${}^cC_i$ are O(1) if the Reynolds number is much larger, $Re \geq 1000$. The dashed red lines are approximate fits to the drag coefficients in the Re range appropriate to the bob, Eq. (62), at left, or the line, Eq. (60), at right. The dotted red line at left and very small Re is Stokes' solution for creeping flow discussed in Sec. 4.5, Problem 1.

Viscous drag. If the sphere is moving very slowly so that the flow around the sphere is laminar and symmetric fore and aft with little or no wake, then the drag will be mainly viscous stress acting on the surface of the sphere. In the common case of a Newtonian fluid, the viscous, surface drag is proportional to the dynamic viscosity of the fluid, $\rho\,\nu$, times the shear of the flow around the sphere, $\rho\nu U/D_b$. Assuming that this viscous stress acts over a surface area proportional to D_b^2, then a zero order solution for drag on the sphere is $H \propto \rho\nu D_b U$. If this viscous, surface drag is the dominant drag-producing process, then it would be appropriate to nondimensionalize (scale) the aerodynamic drag as

$$\underline{\text{v}}\text{iscous drag coefficient for a }\underline{\text{s}}\text{phere:} \quad \frac{H}{\rho\nu D_b U} \;=\; {}^sC_v(Re), \tag{58}$$

on the expectation that the Re-dependence of ${}^sC_v$ would then be minimized compared to other choices. This is the $n = 1$ version of Eq. (57). This form of a drag coefficient will be used to estimate drag on the line of the pendulum in Sec. 4.4.

Inertial drag. Even if the fluid was nearly inviscid,[25] there would still be drag on a moving sphere because the fluid that is displaced by a moving object must be accelerated up to a speed $\propto U$. If the displaced fluid forms a turbulent wake, as is observed behind a rapidly moving sphere, then the drag would be expected to be roughly proportional to the rate of change of the momentum of the displaced fluid, $\propto \rho U$, times the rate of change of the volume of the wake, frontal area $A = \pi D_b^2/4$ times the speed, U. Thus the drag would be estimated as $H \propto \rho A U^2$. The drag coefficient that corresponds to this inertial drag process, often called 'form drag', is

$$\underline{\text{i}}\text{nertial drag coefficient for a } \underline{\text{s}}\text{phere:} \quad \frac{H}{\frac{1}{2}\rho A U^2} \;=\; {}^sC_i(Re), \tag{59}$$

which is the $n = 0$ version of Eq. (57). This is the form of the drag coefficient that is almost always encountered, as in Fig. (7), and is usually written C_d and said to be the 'drag coefficient' without mentioning inertial. The Re-dependence of ${}^sC_i$ shows the departures from inertial drag due to viscous effects, presumably. Either form of the drag coefficient effectively conveys the laboratory data and in that respect they are equally useful (consistent with P1 and P2 of a basis set, Sec. 3.2). However, if the range of the relevant Re is restricted, then it would be appropriate to use the form of the drag coefficient – inertial or viscous, $n = 0$ or $n = 1$ – that has the least variation over that subrange of Re. In this case, the inertial drag coefficient for a sphere will be used to estimate the aerodynamic drag on the bob.

4.3.2 Nondimensional parameters; the Reynolds number

Once the form of the dependent nondimensional variable, Π_1, has been set, the remaining nondimensional variables can be formed in ways that define the geometry of the problem, or that reflect a balance of terms in a governing equation, or that follow the established norms of your field. This is necessarily vague because the possibilities are almost limitless. However the task is eased by the null space basis method which ensures that you start with a complete basis set of nondimensional variables. All that you have to do (!) is rearrange the basis set to make the most useful basis set for your purpose.

In the example of aerodynamic drag on a moving sphere, there is only one remaining nondimensional variable, the Reynolds number, $Re = \frac{UD}{\nu}$ (or any power of the Reynolds number), where U is the speed of the current, usually in a free-stream or undisturbed region, D is the spatial scale over which U changes by O(1), and ν is the kinematic viscosity of the fluid. The Reynolds number is the ratio of advective to viscous terms in the Navier-Stokes momentum balance and arises very often in problems of fluid mechanics.

Recall that for the purpose of modeling drag, a slowly moving sphere has a nearly

[25] If the fluid is a superfluid having literally zero viscosity, then the viscous drag will vanish. Such superfluids are in effect a new state of matter for which quantum physics supplants classical physics.

undisturbed, laminar wake. Observational evidence shows that laminar flow occurs when Re is small, $Re \leq 1$, regardless of speed *per se*; a small diameter or large viscosity are equally important to Re. Dimensional analysis tells us as much in that the drag coefficient of a given class of object (e.g., spheres or cylinders) depends only upon Re. The small Re range is that of a small bug swimming through water, or the thin line of a pendulum swinging slowly through air. In the small Re range, the viscous drag coefficient ${}^sC_v$ is O(1), both numerically and in the sense that ${}^sC_v$ is nearly independent of Re for $Re \leq 1$ (Fig. 8).

For creatures and objects anywhere near our size, e.g., golf balls, bikers or automobiles, Reynolds numbers of $O(10^4)$ and greater are the norm, and inertial drag (form drag) is generally more important than is viscous drag. Notice that for moderately large Re, $Re \geq 10^3$, the inertial drag coefficient C_i is O(1) in magnitude and very roughly constant within subranges of Re (Fig. 8).[26]

The pendulum studied here has Reynolds numbers for the line and the bob that fall in an intermediate range in which both viscous and inertial drag are likely to be important, discussed further in the next section, 4.4.

4.3.3 Three-dimensional flow effects upon drag

Before leaving the subject of aerodynamic drag, it should be noted explicitly that the drag on an immersed object depends very sensitively upon the three-dimensional flow from front to back around the object, and not just the frontal area, which is the only geometric property accounted for in the drag coefficients (58) and (59). For example, a flat disk of a given area that is face-on to a flow will have a drag coefficient of about 2 at large Re. A tear-drop-shaped, streamlined object having the same frontal area may have a drag coefficient as low as 0.04, or a factor 50 less at the same Re.[27] As a consequence of this sensitive dependence of drag upon the three-dimensional flow around an object, each distinct shape will require its own drag coefficient denoted by a superscript, here a sphere or a cylinder, ${}^sC$ or ${}^cC$ in Fig. (8), left and right. (For a more ambitious approach to this, see Problem 6 in Sec. 4.5 below.)

[26] However, even at a very large Re it does not follow that viscosity is entirely irrelevant. Significant changes in the drag coefficient of a sphere or a cylinder occur in the vicinity $Re \approx 4 \times 10^5$ due to changes in the boundary layer flow around the object and the width of the turbulent wake (sometimes referred to as the 'drag crisis'). This is the Re range of a well-hit golf ball or tennis ball, and is consistent with the observation that aerodynamic drag on these objects has a surprising sensitivity to small scale surface roughness and to spin. For more on these phenomena see S. Vogel, 1994, *Life in Moving Fluids*, Princeton Univ. Press, and P. Timmerman, and J. P van der Weele, 1999, 'On the rise and fall of a ball with linear and quadratic drag', *Am. J. Phys.*, **67**, 538–546.

[27] An especially clear illustration of the flow around such objects is Plate XVIII of Rouse (1946)[5]

4.4 Evaluating models of a damped pendulum

4.4.1 A numerical solution

To model the decay process requires including the aerodynamic drag on the line and bob in the angular momentum balance (1). Drag will be estimated by means of the steady drag laws discussed above, and so it is assumed implicitly that the instantaneous speed of the bob or line gives the same drag as would a steady motion of the same speed. Whether this assumption is appropriate remains to be seen.

The main task is to account for the Re-dependence of the drag coefficients. Because the line is comparatively thin, $D_l = 0.4 \times 10^{-3}$m, the Reynolds numbers of the line $Re_l = UD_l/\nu$ are comparatively small, $Re_l \leq 20$, where $U = rd\phi/dt$, r is the distance from the pivot and an *a priori* estimate of $d\phi/dt$ is $\phi_o/\sqrt{L/g}$. In that small Re range the viscous drag coefficient on a cylinder may be approximated by

$$ {}^cC_v(Re_l) = 1.3 + \frac{Re_l}{2}, \tag{60}$$

(the short red dashed line of Fig. 7, right). The drag per unit length of the line, $\delta = dr$, can then be computed by the drag law corresponding to Eq. (58) as

$$ H = \pi \rho \nu \, {}^cC_v(Re_l) \, U \, dr$$

and the (dimensional) torque due to drag over the length of the line is

$$ \tau_l = \int_0^L r \, H \, dr = \rho \left(1.3 \frac{\pi}{2} \nu L^3 + \frac{1}{12} D_l L^4 \mid \frac{d\phi}{dt} \mid \right) \frac{d\phi}{dt}. \tag{61}$$

The absolute value operator ensures that the drag opposes the motion.

The bob has a comparatively large diameter, $D_b = 0.021$ m, and thus a much larger Reynolds number; $Re_b = L\frac{d\phi}{dt} D_b/\nu$ is O(1000). In this range of Re, a convenient fit to the inertial drag coefficient of a sphere is[26]

$$ {}^sC_i(Re_b) = \frac{24}{Re_b} + \frac{6}{1 + \sqrt{Re_b}} + 0.4, \tag{62}$$

the dashed red line of Fig. 7, left. The drag-induced torque on the bob is then estimated as

$$ \tau_b = \frac{\pi \rho}{8} \, {}^sC_i(Re_b) \, D_b^2 \, L^3 \mid \frac{d\phi}{dt} \mid \frac{d\phi}{dt}, \tag{63}$$

where Re_b and ${}^sC_i$ are evaluated at each time step of the numerical integration (with care to avoid division by zero when evaluating (62)).

The revised angular momentum balance is (in dimensional variables),

$$\frac{d^2\phi}{dt^2} \;=\; -\left(\frac{g}{L}\sin(\phi) \;+\; \frac{\tau_l \;+\; \tau_b}{L^2 M}\right). \tag{64}$$

Together with Eqs. (60) - (63) and the initial condition Eq. (3), this makes a complete if inelegant model that can be integrated numerically. With these drag terms included, the period of the oscillation is nearly unchanged, but the amplitude decays with an e-folding in about 10 minutes (Fig. 6, upper, the envelope of the thin blue line). The amplitude simulated by the numerical model looks plausible when compared with the observations, suggesting that this application of the steady drag laws for a sphere and cylinder is appropriate.

4.4.2 An approximate model of the decay rate

Numerical solutions are not revealing of parameter dependence, but given two modest approximations we can go on to deduce a model of the viscous pendulum that has transparent solutions. First, the angle ϕ is small enough in the case shown in Fig. (6), upper, that sinϕ of Eq. (55) can be approximated as ϕ. Second, the torque is due mostly, $\approx 80\%$, to the line, and so it should be acceptable to make the approximation that the inertial drag coefficient for the bob is a constant, $C_i = 0.7$, an average for the high Re_b range of the bob where most of the drag occurs. With these approximations, a solvable model for the simple, viscous pendulum (now in nondimensional variables)

$$\frac{d^2\phi}{dt^{*2}} \;=\; -\left(\phi \;+\; a\frac{d\phi}{dt^*} \;+\; b\,|\frac{d\phi}{dt^*}|\,\frac{d\phi}{dt^*}\right), \tag{65}$$

where the coefficient in the linear drag term is

$$a \;=\; \frac{\pi}{2}\frac{\rho\,\nu\,L^{3/2}}{M\,g^{1/2}} \tag{66}$$

and the coefficient in the quadratic term is

$$b \;=\; \frac{\rho}{8M}(0.7D_b^2\,L \;+\; \frac{2\pi}{3}D_l\,L^2). \tag{67}$$

The linear term $\propto a$ comes from the low Re limit of viscous drag on the line, and the quadratic term $\propto b$ comes from the higher Re approximations of inertial drag on the line and the bob.

Approximate solutions for small damping are given by Timmerman and van der Weele.[26] Linear drag causes the amplitude to decay at a nondimensional rate

$$\frac{1}{\Phi}\frac{d\Phi}{dt^*} \;=\; -\frac{a}{2} \tag{68}$$

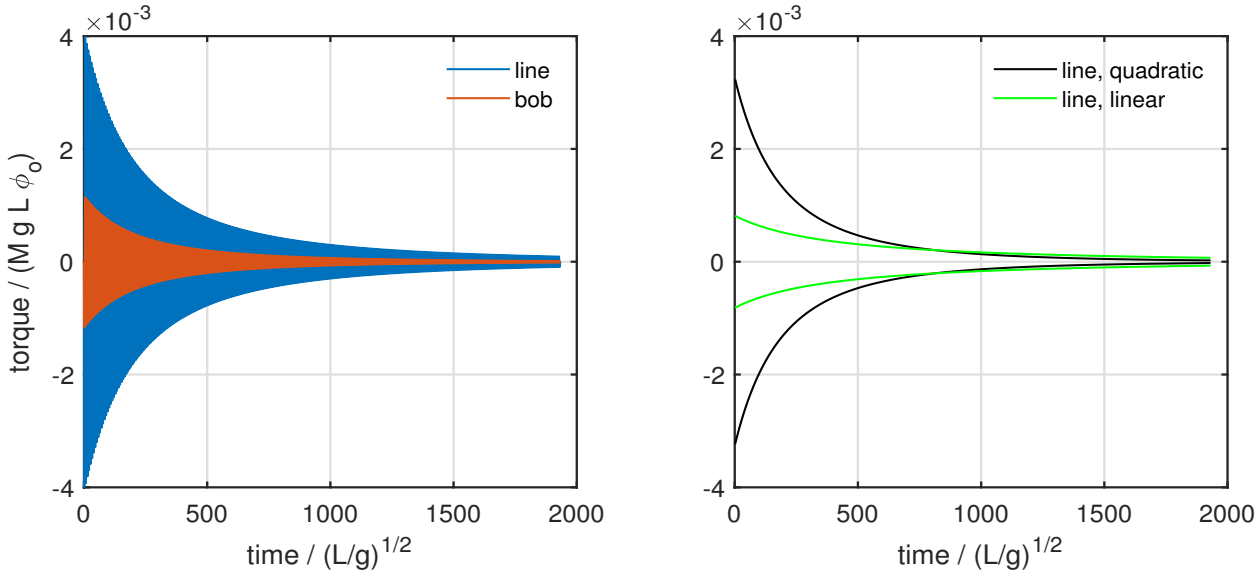

Figure 9: **(left)** The drag-induced torque on the line and the bob (blue and red lines) nondimensionalized with the gravitational-induced torque on the bob (which is much larger). The drag-induced torque on the line contributes about 80% of the total drag-induced torque. **(right)** The torque on the line due to quadratic and linear terms of Eqs. (65) - (67) (black and green lines; the envelope only is shown here). The sum is equal to the total shown as the blue line at left. For short times, when the amplitude of the displacement is largest, the torque on the line is due mainly to the quadratic term, and thus the inertial drag process. For longer time and smaller amplitude, the torque on the line is due about equally to the quadratic and linear terms, and thus about equally to inertial and viscous drag.

and the quadratic term causes decay at a rate

$$\frac{1}{\Phi}\frac{d\Phi}{dt^*} \;=\; -\frac{8}{6\pi}\frac{b}{}\Phi\,. \tag{69}$$

For small damping, these two may be added together, and when evaluated for the specific pendulum observed here (Sec. 4.1),

$$\Gamma\sqrt{L/g} \;=\; \frac{1}{\Phi}\frac{d\Phi}{dt^*} \;\approx\; -\;\left(5.2\times10^{-4} \;+\; 1.6\times10^{-2}\Phi\right) \tag{70}$$

shown as the blue, dashed line (theory) of Fig. (6), lower. This approximate solution gives a good account of the damping found in numerical simulations even for much stronger damping, e.g., by imposing a larger viscosity. It also shows clearly how the decay rate is expected to vary with the parameters that characterize the pendulum and the surrounding fluid. All of the pieces of this model were present in the first attempt at dimensional analysis of a damped, viscous pendulum, Eq. (49), though we were not prepared to interpret them at that time.

The decay rate, $\Gamma \;=\; \Phi^{-1}d\Phi/dt$, can be estimated from the observations and from the numerical solution by first differencing the observed and model-simulated amplitudes, Fig. (6),

lower. This makes a much more sensitive test of the drag formulations than does a comparison of the amplitude cf., Fig. (6), upper. The first thing to note is that the decay is not a simple exponential in time as it first appears on inspection of $\Phi(t)$. Instead, there is a significant dependence of the decay rate upon amplitude, with a greater decay at the beginning of an experiment when the amplitude was largest, $\Phi \geq 0.1$ radians, than at long times when the amplitude was small, ≤ 0.05 radians.

Within the numerical solution, the drag-induced torque on the pendulum was due mainly to drag on the line rather than drag on the bob. The drag on the line was due mainly to inertial drag at short times, when the amplitude of the motion was larger, and then due mainly to viscous drag at long times, when the amplitude was small, $\Phi \leq 0.05$ radians, cf. Figs. (6) and (9).

4.5 Damped pendulum problems

1) Stokes' landmark 1851 study of viscous fluid flow[22] included the detailed calculation of drag on a smooth sphere moving at a steady speed, U, through a viscous fluid. The speed was presumed to be slow enough that the flow remained laminar (no turbulence and no inertial effects). Such a slow flow is sometimes called 'creeping flow', and in practice requires that the Reynolds number must be very small, $Re = UR/\nu \leq O(1)$. Stokes found that the viscous drag on a sphere of radius R is then

$$H = 6\,\pi\,\nu\,R\,U. \tag{71}$$

How does this compare with the inferred (empirical) viscous drag coefficient of Fig. (8), left, at very low Re? And how about the inertial drag coefficient of Fig. (7), left, the dashed black line, $24/Re$?

2) Under the plausible assumption that the terminal (steady) velocity, U, of a dense sphere falling through viscous fluid reflects a balance of the viscous drag from (71) and buoyancy force, $\propto R^3\,g\delta\rho$, show that the Stokes settling velocity, U_{set}, is

$$U_{set} = \frac{2}{9}\,\frac{g\,\delta\rho}{\nu}\,R^2, \tag{72}$$

where $\delta\rho$ is the density difference $\rho_{sphere} - \rho_{fluid}$. This has proven to be an accurate and widely useful estimate of the settling velocity of small particles in air and water (dust and sediment). When the velocity may be observed and the density and radius of the particle are known, then (72) is a handy means for estimating the viscosity of the surrounding fluid. Now suppose that you do not know (72), but that you do know the VPlist for the corresponding dimensional analysis of velocity. What can you infer about the dependence of settling velocity U_{set} upon $\delta\rho$ and particle radius?

3) The decay rate (Fig. 6, lower) decreases significantly as the amplitude of the pendulum's motion dies away. At very small amplitude, $\Phi \leq 0.05$ radians, the visual observations of cord length made here were rather noisy (poor resolution). However, an extrapolation of the observed and modeled decay rates to $\Phi \rightarrow 0$ looks plausible. How does the inferred decay rate compare with the analytic solution for linear drag, Eq. (68)? It is surprising that (68) does not depend upon the line diameter, D_l. Can you explain why this model of linear, viscous drag-induced torque does not depend upon D_l, while the (generally more important) quadratic, inertial drag and torque do?

4) The empirical formula for the inertial drag coefficient $C_i(Re)$ Eq. (62) has terms that are proportional to Re^{-1}, $Re^{-1/2}$, and Re^0, and that are important at low, medium and high Re. We have considered the low Re limit in Problem 1 above, and now consider the high(er) Re limit. What does dimensional analysis tell us about the drag coefficient in the limit that Re is very large, say because $\nu \to 0$? (We won't know the value of C_i in that limit without help from laboratory data or sophisticated and intensive numerical computations, but we might expect it to be O(1), as indeed it is.)

5) Looking back at the first try at dimensional analysis for a damped pendulum, Sec. 4.1, it seems that the scope of the initial VPlist (48) was too broad. Let's try the opposite: narrow the scope to the one specific pendulum that was observed. Thus while L, D_l, D_b, and M are all relevant to the damping rate, they can also be declared 'globally constant' parameters (Sec. 2.7), if we choose to narrow the scope to just one specific pendulum. The same holds for g and the viscosity of air, ν. What are we left with? How does the new, greatly pared-down analysis compare with Fig. (6), lower?

6) Aerodynamic drag on an object is a property of the three-dimensional flow around the object, and not just its frontal area as the usual drag coefficient allows (7). Consider objects that are azimuthally symmetric in the direction parallel to the flow, e.g., a disk or a sphere or an ellipse, and suppose that we allow in just one length to define the object's geometry: the length from front to back, B. The ratio of this length compared to the diameter of the object is sometimes called fineness; $B/D \to 0$ for a thin disk, $B/D = 1$ for a sphere, and so on. Would you prefer a drag coefficient that varies with both Re and B/D, and so encompasses the entire family of azimuthally symmetric objects, or, would you prefer a separate drag coefficient for each shape, i.e., a Cd for each specific B/D. Discuss this in terms of locally and globally constant parameters, Sec. 2.7. Qualitatively, how would you expect the viscous drag coefficient to vary with B/D? How about the inertial drag coefficient?

7) It is surprising that the formulations for steady state flow and drag give accurate estimates of the aerodynamic drag on the bob and line of an oscillating, time-dependent pendulum. A possible rationalization: presume that the line interacts with the surrounding air on the scale of the line width, D_l. Can you show that the velocity change on this space scale is $O(D_l/L) \propto 10^{-3}$, i.e., very small? Hence, the flow around the line is quasi-steady. Where is this in the first try at dimensional analysis of a viscous pendulum, Eq. (48)?

5 A similarity solution for diffusion in one dimension

Dimensional analysis can help simplify and reduce a model system and help find solutions that might otherwise have been missed. A good example is afforded by Stokes' first problem (also called the Rayleigh boundary layer problem) in which a fluid column of uniform density is driven from rest by a speed, V_o, imposed on a boundary, here the upper boundary, $z = 0$, Fig. (10). The problem is to find the resulting current, $U(z,t)$. A key physical assumption is that the momentum supplied at the boundary will diffuse into the fluid at a rate set by the kinematic viscosity of the fluid, ν, times the velocity shear,

$$\tau \;=\; \nu \frac{\partial U}{\partial z}, \tag{73}$$

which is characteristic of Newtonian fluids (air and water). The quantity τ is proportional to the diffusive flux of momentum, and, it may also be interpreted as a shear stress, a horizontal force per unit area exerted by the fluid on a boundary or an adjacent fluid parcel. The kinematic viscosity is presumed to be a given constant, and not dependent upon the flow. In that case the governing equation for the current, $U(z,t)$, is the elementary one-dimensional diffusion equation,

$$\frac{\partial U}{\partial t} \;= \frac{\partial \tau}{\partial z} \;=\; \nu \frac{\partial^2 U}{\partial z^2}, \tag{74}$$

a partial differential equation (PDE) in z and t. The initial condition is a state of rest,

$$U(z, t = 0) \;=\; 0. \tag{75}$$

The boundary conditions are that the fluid sticks to an upper surface that is set into motion with the speed Vo at $t = 0$, and the fluid also sticks to a lower boundary at $z = -L$ that remains at rest. (Stokes first problem presumes that $L \to \infty$, discussed more below.) The two required boundary conditions on U are then

$$U(z = 0, t \geq 0) \;=\; Vo, \quad \text{and} \quad U(z = -L, t) = 0. \tag{76}$$

This linear PDE system is not difficult to solve; Fourier transform leads to an infinite sine series that can be summed to high accuracy, and numerical integration is straightforward (Fig. 10, left).[28]

5.1 Dimensional analysis to simplify or reduce a model system

Dimensional analysis can help point the way to yet another possibility, a similarity solution, that may yield more insight than is likely to come from an infinite series or from numerical data. As usual, a start can be made with a straightforward list of the important variables and parameters,

[28] Matlab code: https://www2.whoi.edu/staff/jprice/wp-content/uploads/sites/199/2024/08/Stokes1.txt

(77)

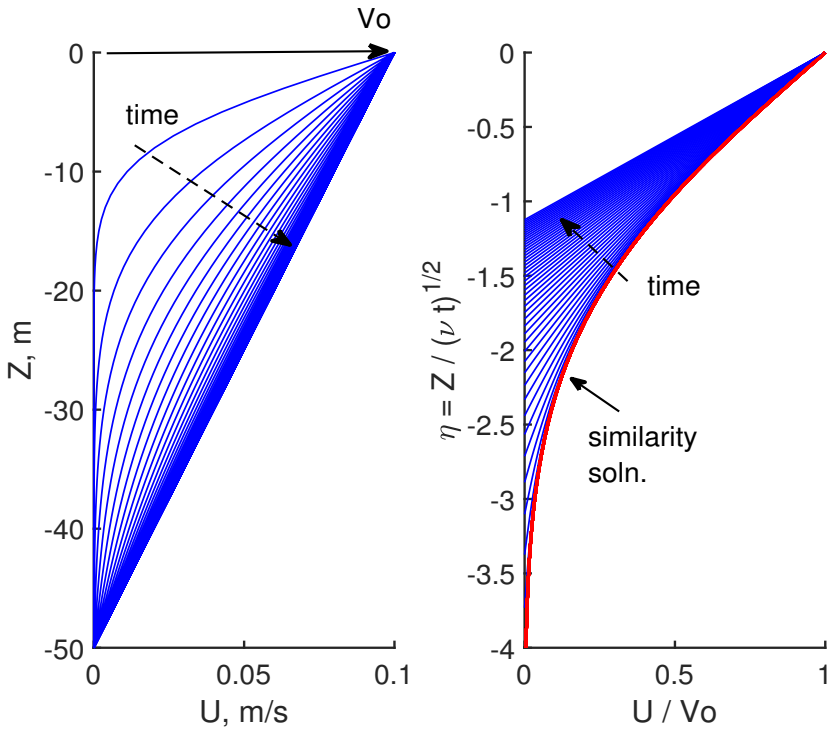

Figure 10: Numerical solution of the elementary diffusion model, Eqs. (74) - (76). **(left)** The solution in dimensional coordinates. The parameters are those of an upper ocean boundary layer over shallow water, $\nu = 10^{-2}$ m^2 s^{-1} and $L = 50$ m. Current profiles are plotted at intervals of 10^4 seconds. **(right)** The solution in nondimensional coordinates (blue lines) and the similarity solution, Eq. (86), (red line). The similarity solution presumes an infinitely deep fluid and does not recognize the no-slip boundary condition at $z = -L = -50$ m imposed here. For small time, only about the first three profiles, the numerical solutions are coincident with the similarity solution. At longer times the effect of finite depth and the no-slip lower boundary condition becomes appreciable, and the numerical solution departs from the similarity form.

- A VPlist for one-dimensional diffusion:

1. current, $U \doteq [\,0 \quad 1 \quad -1\,]$, the dependent variable,
2. time, $t \doteq [\,0 \quad 0 \quad 1\,]$, an independent variable,
3. depth, $z \doteq [\,0 \quad 1 \quad 0\,]$, a second independent variable,
4. surface boundary value, $Vo \doteq [\,0 \quad 1 \quad -1\,]$, a parameter,
5. the kinematic viscosity, $\nu \doteq [\,0 \quad 2 \quad -1\,]$, a parameter,
6. the depth of the fluid column, $L \doteq [\,0 \quad 1 \quad 0\,]$, a parameter.

Given this VPlist, a basis set of nondimensional variables has four members, and a relation among them may be written

$$\frac{U}{Vo} = F(\frac{zVo}{\nu}, \frac{tVo^2}{\nu}, \frac{z}{L}), \tag{78}$$

as one possibility.

5.2 Tuning the VPlist

The model equations, (74) - (76), are linear. In consequence, the numerical solutions show that the current at a given depth and time is directly proportional to the boundary value, Vo. Thus, the sole effect of changing Vo is to change the current in direct proportion. This important property has not been built into the VPlist, nor is it reflected in the initial basis set of nondimensional variables, Eq. (65). Instead, this VPlist includes a much more general problem in which Vo appears in the nondimensional variables combined with z and t as if Vo affected the diffusion process. In general, it does! On physical grounds, this can be expected to hold when the diffusion process results from turbulence generated by the boundary forcing rather than by (the implicitly laminar) diffusion process represented by ν. Whether the flow is turbulent or laminar depends upon the distance from the boundary, the current speed, and the fluid viscosity, i.e., a Reynolds number, zVo/ν.

If we insist that the diffusion process must be represented by a constant viscosity (what is meant by elementary diffusion) then we are implicitly limiting the analysis to small Reynolds number flows that are laminar, and the dynamics are identical to the diffusion of heat in a solid. To assert this idealization in the VPlist requires a small but significant change — retain the dependent variable U/Vo, but remove Vo from the list of parameters. A basis set for this revised VPlist is found to be

$$\frac{U}{Vo} \;=\; F(\frac{z}{\sqrt{t\nu}}, \frac{z}{L}), \tag{79}$$

which has one fewer variables than the initial basis set, Eq. (78), a significant change.

One step further — suppose that L is very large compared to the depth that diffusion has reached up to the time, t. This will be plausible if the fluid is very deep, or, the time very short. In that case the depth L will be irrelevant, and the current at a given depth ($z << L$) will depend only upon time, depth, and the kinematic viscosity that are combined into the single independent, nondimensional variable, η,

$$\eta = \frac{z}{\sqrt{t\nu}}, \tag{80}$$

and thus (79) may be written

$$\frac{U}{Vo} \;=\; F(\eta). \tag{81}$$

The variable η is said to be a 'similarity' variable, and the function $F(\eta)$ is a similarity function, something we have encountered before in Sec. 4 as the Reynolds number and drag coefficients. If Eq. (81) is relevant, then the current profiles at various times will have a similar shape, being more or less stretched out in z depending upon $\eta = z/\sqrt{t\nu}$, Fig. (6), right.

It has been noted on other occasions that the power of nondimensional analysis comes in large part from a reduction in the number of variables that is required to define a solution. Often the variables that are compacted are parameters, but on this occasion they are the independent variables, z and t. Dimensional analysis *per se* doesn't recognize the difference between a

parameter and an independent variable or even the dependent variable. The implementation of the null space method suggested here (Sec. 3.3) strives to keep the dependent variable to the first power, but beyond that, independent variables and parameters are treated as equal.

5.3 When there is only one independent, nondimensional variable

The analysis above suggests that the original governing equation (a partial differential equation in z and t) might be transformable into an ordinary differential equation in the single independent variable η. To see if this holds, substitute $U = V_o F(\eta)$ into the governing equation (74). The partial time derivative becomes

$$\frac{\partial U}{\partial t} = Vo\frac{\partial F}{\partial \eta}\frac{\partial \eta}{\partial t} = -VoF'\frac{\eta}{2t}, \tag{82}$$

where $F' = dF/d\eta$, and the second derivative with respect to z becomes

$$\frac{\partial^2 U}{\partial z^2} = VoF''\frac{1}{t\nu}. \tag{83}$$

Substitution into the governing equation and noting that z and t appear only in the combination $z/\sqrt{t}$ shows that the second order, linear partial differential equation (74) may indeed be transformed into the second order, linear ordinary differential equation (ODE),

$$F'' + \frac{1}{2}\eta F' = 0. \tag{84}$$

Substitution of η into the upper and lower boundary conditions gives

$$F(\eta = 0) = 1, \quad \text{and} \quad F(\eta = -\infty) = 0. \tag{85}$$

So far as the current is concerned, small time and large z are equivalent, and the initial condition is identical to the lower boundary condition. The ODE model equations (84) and (85) may be integrated by an approach much like that used with the finite amplitude pendulum, Eq. (13). First, let $G(\eta) = F'$ and substitute into (84). Separate variables, G and η, and integrate to find $F'(\eta)$. Then separate F and η, and integrate using (85) to find the similarity solution

$$\frac{U(\eta)}{Vo} = 1 - \frac{2}{\sqrt{\pi}}\int_0^{\eta/2} exp(-y^2)dy. \tag{86}$$

The integral at right is the error function, and this can be considered a closed solution.

A similarity solution (86) is valuable in at least two ways. Because it is exact, it can serve as a precise test of numerical or numerically evaluated solutions whose accuracy might be hard to assess *a priori*. Because it is more or less transparent, there are qualitative features evident in this

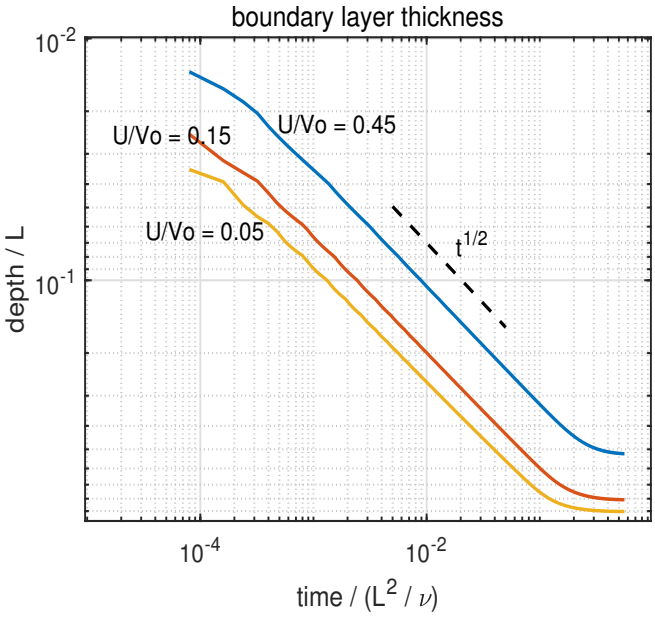

Figure 11: Boundary layer thickness, defined as the depth at which the current was 0.45, 0.15 or 0.05 of the imposed, surface value (three separate curves) diagnosed from the numerical solution of Fig. 10. Notice that there was an intermediate (nondimensional) time, $5 \times 10^{-4} \leq t/(L^2/\nu) \leq 10^{-1}$ during which the boundary layer thickness grew as $t^{1/2}$. The similarity solution Eq. (86) holds during this intermediate time, but not otherwise.

similarity solution that might have been missed in a mass of numerical data. In particular, note from (81) and (80) that a given value of η, say η_g, and thus a given value of $U/Vo = F(\eta_g)$, moves downward with time as

$$z_g \;=\; \eta_g \sqrt{t\,\nu}. \tag{87}$$

Thus the thickness of the layer that is directly affected by the boundary condition, i.e., the boundary layer, grows like the square root of time, Fig. (11), a characteristic of 1-dimensional elementary diffusion and random processes alike. This result can be turned around; the time t_g needed to diffuse a distance z_g away from the boundary is

$$t_g \;=\; \frac{z_g^2}{\nu\,\eta_g^2},$$

which forms a natural time scale for a one-dimensional diffusion problem.[29]

If the model domain includes a lower boundary at say $z = -L$ as here, then the similarity solution has the built-in limitation that it holds only for a limited, intermediate time interval. The elapsed time has to be long enough that the growing boundary layer does not retain the detailed imprint of the startup, which could never be a literal step function in time as is assumed. In a numerical model, the boundary layer must be thick enough that the current profile is not too strongly dependent upon the finite grid resolution. Judging from the curves of Fig. (10), this requires a time of about $t/(L^2/\nu) \geq 5 \times 10^{-4}$, in this numerical solution. However, the time can

[29] When we say that diffusion reaches a certain distance we mean that a given fraction of the boundary value amplitude is found at that distance from the boundary. The continuous diffusion equation has the unphysical property that every point in the domain is affected by the boundary condition instantaneously. If the point is very far away from the boundary in the sense that η is large, then the boundary effect will be correspondingly very small, though not zero.

not be too long either, or else diffusion will have caused an appreciable current near the lower boundary at $z = -L$. Once the current becomes appreciable near the lower boundary, judging from Fig. (10), $t/(L^2/\nu) \geq 10^{-1}$, the similarity solution will no longer hold accurately, and a more general solution of the form (79) will be required.

5.4 An oscillating upper boundary; Stokes second problem

Now consider another important diffusion problem that is in some respects the complement to the start-up problem discussed above. Suppose that the fluid is infinitely deep, so that there is no L to contend with, and that the upper boundary oscillates in time as $V_o cos(\omega t)$. If this has been going on for a very long time, the flow will become statistically steady though time-dependent, oscillating with the frequency ω imposed by the boundary. In this problem there is an important external time scale, ω, (an inverse time) that we cannot dispose of. Hence, there is no similarity solution, as in the case when the depth of the lower boundary was relevant, an imposed, external length scale.

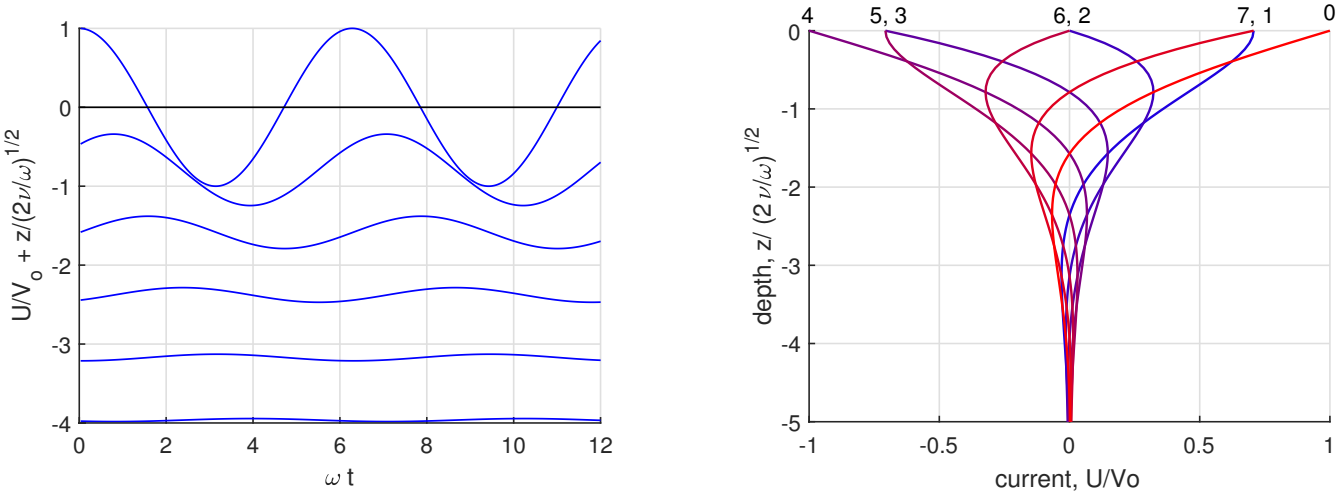

Figure 12: A solution for the time-dependent current under an imposed, oscillating surface current. **(left)** Time series of the current at six depths. **(right)** Eight profiles over one period of the surface current oscillation. The first profile is red, and successive profiles trend toward blue.

What to do? How about analyzing

- A VPlist for one-dimensional diffusion driven by an oscillating boundary: (88)

1. current, $U/Vo \doteq [\,0 \quad 0 \quad 0\,]$, the dependent variable,
2. depth, $z \doteq [\,0 \quad 1 \quad 0\,]$, an independent variable,
3. time, $t \doteq [\,0 \quad 0 \quad 1\,]$, an independent variable,
4. kinematic viscosity, $\nu \doteq [\,0 \quad 2 \quad -1\,]$, a parameter,
5. oscillation frequency of the boundary, $\omega \doteq [\,0 \quad 0 \quad -1\,]$, a parameter.

A basis set of nondimensional variables for this problem is then

$$\frac{U}{V_o} \;=\; F(\frac{z}{\sqrt{\nu/\omega}},\; \omega t). \tag{89}$$

This problem has a natural time scale, $\propto \omega^{-1}$, as well as a natural length scale, $\propto \sqrt{(}\nu/\omega)$, which depends upon the viscosity and the frequency, ω.

The solution can be presumed to be separable in depth and time,

$$U(z,t) \;=\; Real\left[A(z)\exp i\omega t\right].$$

The depth dependence has to be a decay with increasing depth, and the time dependence will be an oscillation at the frequency ω. Substitution into the governing PDE (74) and minding the boundary conditions gives[30]

$$\frac{U}{V_o} \;=\; \exp(z/\sqrt{2\nu/\omega})\; cos(\omega t - z/\sqrt{2\nu/\omega}), \tag{90}$$

which we might have guessed, or certainly can recognize, up to the factor $\sqrt{2}$ that appears in the length scale of (90). The solution reveals that the boundary effect diffuses into the fluid, producing a sinusoidal current at depth, Fig. (12). The current at depth lags the surface current, and the amplitude decays over a comparable depth scale.

5.5 Diffusion problems

1) Consider the steady solution of Sec. 5.3. Suppose that the (water) column has a finite depth, L, and that the experiment is run out to a time that is long enough that the current becomes essentially steady. As before, assume that the boundary value of the current, V_o has the sole effect of changing the amplitude of the current. A VPlist for steady diffusion is then

[30] A thorough description of this solution method is by https://youtu.be/Jtg3WOTZfSw

- A VPlist for a steady state, one-dimensional diffusion:

(91)

1. current, $U/Vo \doteq [\,0 \;\; 0 \;\; 0\,]$, the dependent variable,
2. depth, $z \doteq [\,0 \;\; 1 \;\; 0\,]$, the independent variable,
3. the kinematic viscosity, $\nu \doteq [\,0 \;\; 2 \;\; -1\,]$, a parameter,
4. the depth of the fluid column, $L \doteq [\,0 \;\; 1 \;\; 0\,]$, a parameter.

What do you find for U/V_o? What happened to the kinematic viscosity, ν? Where is the steady state solution evident in Fig. (10)? Can you interpret the steady solution in terms of the stress profile, $\tau(z)$, Eq. (74)? And specifically, how does the stress on the lower boundary (which is at rest) compare to the stress at the surface? Now suppose that the lower boundary is free-slip, which in practice means that there is no gradient normal to the surface, $\partial U/\partial z = 0$. What is the steady state $U(z/L)$ in that case?

2) The ocean surface layer. A classical boundary layer grows in thickness like $t^{1/2}$ or until the boundary layer reaches a lower boundary. On the other hand, we know that wind has been exerting a stress on the ocean surface for a very long time, and yet the surface boundary layer of the ocean, often called the Ekman layer, has a finite depth, very roughly, 50 m. The ocean surface layer is evidently not a classical boundary layer of the type considered here.

One important reason for this difference is that the ocean is rotating with respect to the distant stars at a rate $f = 2 \;\; \sin(\text{latitude})$, where is Earth's rotation rate, 7.272×10^{-5} s^{-1}. At mid-latitudes, $f \approx 10^{-4}$ s^{-1}. The rotation rate f should thus appear in a VPlist of the ocean surface boundary layer. Under the assumption that the fluid thickness L is not relevant, can you use dimensional analysis to show that a steady boundary layer thickness could be possible (dimensionally)? Assuming that the diffusivity is roughly $\nu = 10^{-2}$ m^2 sec^{-1}, can you make a correspondingly rough estimate of the (rotating) upper ocean boundary layer thickness? (Hint: O(100 m).) This is often called the Ekman layer depth.[31]

3) A seasonal cycle of subsurface land temperature. The diurnal and seasonal variation of solar radiation warms the Earth's surface periodically. Heat loss from the surface occurs via infrared radiation and by sensible and evaporative heat fluxes so that over a day or a year there may be a more or less closed diurnal or annual cycle of the surface temperature. The periodic (but not necessarily sinusoidal or regular) variation of surface temperature diffuses downwards into the ground at a rate that depends upon the properties of the subsurface soil and rock; solid rock and water-saturated soil have a thermal diffusivity (reusing ν) $\nu \approx 1.2 \times 10^{-11}$ m^2 s^{-1}, while loose, dry soil is a comparative insulator, $\nu \approx 0.5 \times 10^{-11}$ m^2 s^{-1}. The amplitude, depth of penetration and phase of the resulting subsurface temperature response is of considerable importance for the design and operation of geothermal energy projects.[32]

---

[31] On the equator, $f = 0$, and so the rotation effect that produces a finite-depth Ekman layer vanishes. Is a classical (very thick) boundary layer observed on the equator? No. The notion of an Ekman layer depth discussed above is not applicable very near the equator, where instead a basin-scale, hydrostatic pressure gradient caused by a tilted sea surface and oceanic thermocline (subsurface density variation in the vertical) largely balances the mean wind stress. This basin-scale asymmetry is the background for the El Nino - Southern Oscillation phenomenon.

[32] Cuhac, C., A. Makiranta, P. Valisuo, E. Hiltunen and M. Elmusrati, 2020, 'Temperature measurements on a solar and low enthalpy geothermal open-air asphalt surface platform in a cold climate region', Energies, 13, 979 - 998. doi:10.3390/en13040979.

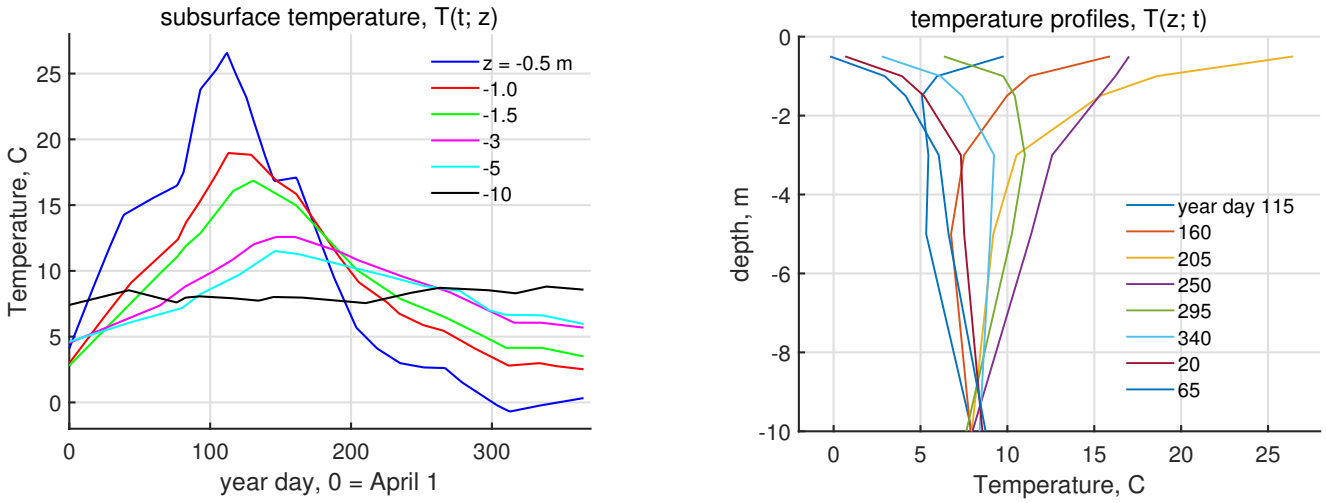

Figure 13: Subsurface (land) temperature observations made over a year as part of a geothermal energy study conducted in Finland by Cuhac et al. (2020).[32] These data were extracted from their Fig. (12). The data start in early April 2014 and continue until the following April. Notice that the beginning and ending temperatures do not coincide; evidently the following April was cooler than the first. Nevertheless, there is a clear signal of downward diffusing, summer warming.

A typical annual cycle of subsurface land temperature is in Fig. (13). Some questions for you: How would you characterize these data, e.g., what is the depth of penetration of the summer warming? In terms of the idealized (perfectly sinusoidal) model solution (90), what is a plausible value for the thermal diffusivity at this site? What departures do you discern between these observations and the idealized model solution? What depth of penetration would you expect for an otherwise comparable diurnal cycle?

6 Choosing scales with a purpose

Dimensional analysis amounts to normalizing (or dividing) dependent and independent variables by an appropriate scale. Appropriate has two parts. First, the scale must have the same physical dimensions (e.g., mass, length, time) as the dependent variable, say. Second, if the scale is chosen thoughtfully, then normalizing will yield a nondimensional dependent variable that has a meaningful magnitude. This second aspect of choosing a scale is often called 'scaling analysis'. A dimensional analysis can be performed with no thought given to a scaling analysis. However, the results of a dimensional analysis will often be considerably more useful if aspects of a scaling analysis are considered either from the outset, or at the third, interpretive step of a dimensional analysis.

6.1 A nonlinear projectile problem

To illustrate the role of a scaling analysis, consider the following projectile problem (after Lin and Segel (1974)[5]). The problem is to calculate the height of a projectile of mass m that is launched upwards with speed V from the surface of a planet having a radius R and mass M. To make the problem interesting, the variation of the gravitational acceleration with height will be acknowledged. To keep the problem simple, the likely important effect of aerodynamic drag on the projectile will be ignored. With this simplification, the vertical component of the equation of motion for the projectile is

$$m\frac{d^2z}{dt^2} \;=\; \frac{-mMG}{(R+z)^2},$$

where G is the universal gravitational constant. The acceleration of gravity on the planet's surface $z \;=\; 0$ can be defined as $g \;=\; MG/R^2$, a parameter, and the equation of motion rewritten

$$\frac{d^2z}{dt^2} \;=\; \frac{-g}{(1+z/R)^2}. \tag{92}$$

Suitable initial conditions are

$$z(t=0) \;=\; 0 \quad \text{and} \quad \frac{dz}{dt}(t=0) \;=\; V. \tag{93}$$

The projectile has an initial positive upward velocity, V, a parameter, and thereafter is subject only to a downward acceleration due to gravitational attraction to the planet. As the height of the projectile increases, the gravitational acceleration decreases, and at some large z the projectile could escape the gravitational tug of the planet altogether and continue into deep space. Clearly this is going to have something to do with the parameters g, R and V. To see just how, let's analyze a nondimensional form of the model equations (77) and (78), beginning with

(94)

- A VPlist of vertical motion in variable gravity:

1. height of the projectile above the planet surface, $z \doteq [\,0 \quad 1 \quad 0\,]$, the dependent variable,
2. time, $t \doteq [\,0 \quad 0 \quad 1\,]$, an independent variable,
3. the acceleration of gravity on the planet surface, $g \doteq [\,0 \quad 1 \quad -2\,]$, a parameter,
4. radius of the planet, $R \doteq [\,0 \quad 1 \quad 0\,]$, a parameter,
5. initial (vertical) speed, $V \doteq [\,0 \quad 1 \quad -1\,]$, a parameter.

The initial basis set of nondimensional variables for this VPlist is

$$\Pi_1 \;=\; \frac{z}{R}, \quad \Pi_2 \;=\; \frac{t}{R/V} \quad \text{and} \quad \Pi_3 \;=\; \frac{V^2}{gR}, \tag{95}$$

and the relation between these three nondimensional variables may be written

$$\frac{z}{R} \;=\; F(\frac{t}{R/V}, \frac{V^2}{gR}). \tag{96}$$

It will be helpful to denote these particular nondimensional variables with a prime,

$$z' \;=\; \frac{z}{R}, \quad \text{and} \quad t' \;=\; \frac{t}{R/V}$$

and the combination

$$\epsilon \;=\; \frac{V^2}{gR}.$$

With this notation, Eq. (96) is

$$z' \;=\; z'(t',\; \epsilon).$$

The maximum height that the projectile will reach, Z, is of particular interest, and the nondimensional form of Z corresponding to this initial basis set is

$$\frac{Z}{R} \;=\; F(\frac{V^2}{gR}),$$

or with the prime notation,

$$Z' \;=\; Z'(\epsilon). \tag{97}$$

Notice that $\epsilon \;=\; V^2/g\,R$ is the only nondimensional parameter in the relation for maximum height, i.e., g, R and V appear only in this combination. The parameter ϵ has a physical interpretation as the ratio of twice the initial kinetic energy of the projectile compared to the depth of the potential energy well of the planet evaluated on the planet's surface. A larger ϵ leads to a larger maximum height, and when $\epsilon \geq 2$, the kinetic energy exceeds the work required to climb out of the potential energy well. V is then said to be the escape velocity, approx. 12 km s^{-1} for Earth (ignoring drag

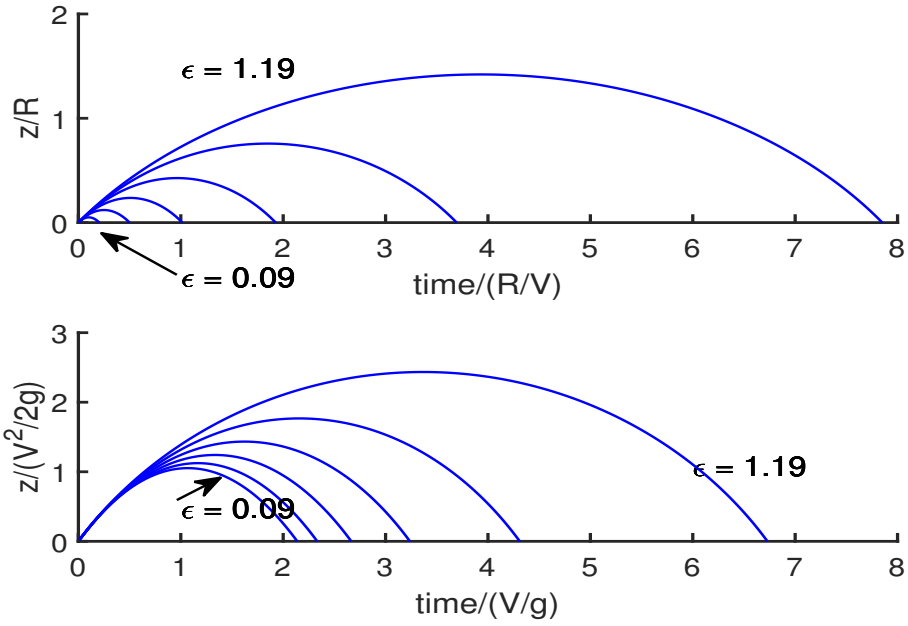

Figure 14: Projectile height computed numerically for several ϵ varying from 0.09 to 1.19. The solutions have been nondimensionalized in one of two ways; in the **(upper)** panel, using the initial basis set, Eqs. (96) and in the **(lower)** panel, using a second basis set built around a zero order solution described in Sec. 6.3. Notice that for small values of ϵ the set of curves in the lower panel appear to collapse toward one curve, while the set of curves in the upper panel do not.

with the atmosphere). Thus, in the usual (partial) way of dimensional analysis, we have already learned something useful about this problem.

Numerical solutions of Eqs. (92) and (93) nondimensionalized by this basis set look reasonable, Figs. (14), upper and (15), upper, in as much as Z' is a well-defined function of the nondimensional parameter ϵ. This is a mathematical certainty since these data are solutions of a numerical model whose parameters are known exactly and hence the VPlist and dimensional analysis should be consistent with the numerical solutions. This first basis set thus meets one of the main goals of dimensional analysis - to make a clear, concise presentation of what would otherwise be an unwieldy mass of data (imagine plotting the maximum height as a function of the three relevant dimensional variables).

6.2 Small parameter → small term?

An aspect of nondimensionalization that goes beyond previous discussions is the question of how or whether a nondimensional model equation can be used to develop an approximate solution. The

solution method considered here is that one or more of the most difficult terms of an equation might be dropped to yield a solvable problem. Once an approximate solution is at hand, the model equations can be amended to take account of the term dropped on the first pass, and solved again. Often the first such iteration will provide useful information regarding the consequences of the difficult term.

The initial basis set Eq. (97) amounts to scaling (and nondimensionalizing) the projectile height by the radius of the planet, R, and scaling time by the time interval required to move the distance R at a speed V. For the purpose of writing the model equation in nondimensional form, use that $z' = z/R$ and $t' = t/(R/V)$ and hence the nondimensional velocity of the projectile is

$$\frac{dz'}{dt'} = \frac{dz/R}{dt/(R/V)} = \frac{1}{V}\frac{dz}{dt}, \tag{98}$$

and the acceleration is

$$\frac{d^2z'}{dt'^2} = \frac{d^2z/R}{d(t/(R/V))^2} = \frac{R}{V^2}\frac{d^2z}{dt^2}. \tag{99}$$

When the equation of motion, Eq. (92), is written using these nondimensional variables the result is

$$\epsilon\frac{d^2z'}{dt'^2} = -\frac{1}{(1+z')^2} \tag{100}$$

and the ICs are just

$$z'(t=0) = 0 \quad \text{and} \quad \frac{dz'}{dt}(t=0) = 1. \tag{101}$$

The nondimensional equation of motion contains the single parameter, ϵ. For Earth-like values of R and g, and for V = 2000 m s^{-1} or less, say, ϵ is a small parameter, roughly 10^{-2}.

In this problem, the difficult, nonlinear, term is the z-dependent, gravitational acceleration term of Eq. (92). It is plausible that the z-dependence could be ignored if $z \ll R$, and by extension, if $\epsilon \ll 1$. Thus, it should be possible to solve the problem in the limit that $\epsilon \to 0$ and then go on to find a better solution by iteration. On that basis, it might seem plausible that a first approximation to Eq. (100) could be obtained by dropping the term multiplied by the small parameter ϵ, the acceleration term. However, the solution to the reduced equation, $0 = 1/(1+z')^2$, is $z' = \infty$, which is contrary to the assumption of small z', and is nonsensical, generally. Either the idea that we could find a useful approximation by starting from small ϵ is wrong, or, we erred in dropping the acceleration term. In fact, it was the latter step that failed; there was no justification for concluding that the acceleration term could be dropped simply because it is multiplied by the small parameter ϵ because we have no idea how big the nondimensional acceleration $\frac{d^2z'}{dt'^2}$ is compared with the terms kept, i.e., compared with 1. It turns out that $\frac{d^2z'}{dt'^2} \gg 1$ for $\epsilon \to 0$. As a result, when the acceleration term is dropped, it will not be possible to proceed toward an improved solution. It is important to understand that the nondimensional Eq. (100) is not at fault here; the terms of Eq. (100) still have the ratio one to another of the dimensional Eq. (92) since all that has been done is

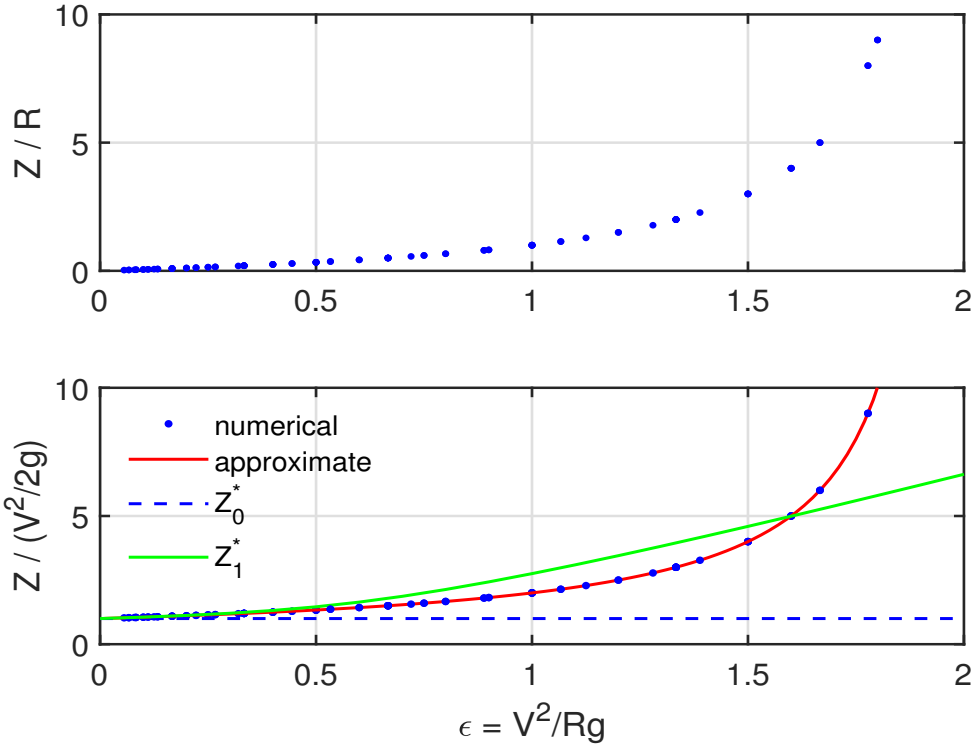

Figure 15: The maximum height of a projectile launched upwards at speed V from planets with a wide range of V, R and g. Each point is the maximum height diagnosed from a numerical solution. **(upper)** The maximum height nondimensionalized by R, consistent with the initial basis set of nondimensional variables, Eq. (96). **(lower)** Here the maximum height is nondimensionalized with a second basis set deduced from a scaling analysis (Sec. 6.3). Both basis sets show a clear-cut dependence of maximum height upon the single nondimensional parameter $\epsilon = V^2/gR$. Notice that as ϵ approaches 2 the nondimen sional height goes to infinity, indicating that the projectile has escaped the tug of gravity. In the lower panel, the dashed blue line is the maximum height from the zero order solution, Z_0^*, and the green line is the first order solution Z_1^* that takes some account of the reduced gravitational acceleration with height. The solid red line is an approximate solution Eq. (119) in which the effective gravitational acceleration is estimated as $g(1 - \epsilon/2)$.

to divide by parameters. However, the inferences that might be drawn from Eq. (100) could be in error.

If the intent is to estimate the relative size of terms that are multiplied by nondimensional parameters, then the nondimensional dependent variables, in Eq.(100) z' and $\frac{d^2z'}{dt'^2}$, will have to be O(1) in the limit that the small parameter, ϵ, goes to zero, the relevant limit here. [33] In the first nondimensional basis set considered for this problem, the planet radius R was used as the length scale for the height of the projectile. While R is certainly an important length scale, it nevertheless has no direct relation to the maximum size of z, i.e., there is no basis for supposing that Z/R is O(1), generally. The imposition of this additional requirement on the choice of the scales is often said to comprise a 'scaling' analysis, implying a purposeful and thoughtful choice of the basis set of nondimensional variables.

6.3 Scaling the dependent variable

To ensure that the nondimensional z is O(1) as $\epsilon \rightarrow 0$ we have to choose a scale that is consistent with a physically motivated, even if highly simplified, model solution in that limit; in Sec. 4 this was said to be a 'zero order' solution. In this problem, a zero order model for the dimensional height z follows from ignoring the height dependence of the gravitational acceleration in Eq. (92),

$$\frac{d^2z_0}{dt^2} \;=\; -\,g, \tag{102}$$

where $(\;)_0$ refers to the order, which will be formalized shortly. The ICs are exactly as before

$$z_0(t=0) \;=\; 0 \quad \text{and} \quad \frac{dz_0}{dt}(t=0) \;=\; V, \tag{103}$$

and the solution is

$$z_0 \;=\; Vt \;-\; gt^2/2. \tag{104}$$

The zero order maximum height is then

$$Z_0 \;=\; V^2/2g.$$

[33] In Sec. 5 the 'big O' notation was used to indicate the numerical order of magnitude, e.g., O(1) or O(10^2), say. Here the meaning is extended to indicate the asymptotic behavior of a function. If a function $f(\epsilon)$ is O(1) in the limit $\epsilon \rightarrow 0$, then the function $f(\epsilon) \rightarrow constant$ in that limit. The constant need not be 1, though we have taken care that it will be here. If $f(\epsilon)/\epsilon^n \rightarrow C$, then $f(\epsilon)$ is said to be O(ϵ^n) in that limit. There are other possible gauges against which to measure asymptotic behavior besides the simple power law dependence that will suffice here. For more detail on the big O notation see http://encyclopedia.thefreedictionary.com/Big%20O%20notation A few questions: Based upon what you can see in Fig. 15, how would you characterize the order of the functions $Z'(\epsilon)$ and $Z^*(\epsilon)$, i.e., are they order ϵ^{-1}, ϵ^0 or ϵ? What is the order of d^2z'/dt'^2, and how does this impact the inferences we might draw from Eq. (100)?

When this is used as the scale for vertical distance, we can be sure that the maximum of the nondimensional height ≈ 1 in the range of small ϵ. An appropriate time scale is the time it takes the acceleration g to erase the initial velocity V, and is V/g. This new choice of scales amounts to a new basis set of nondimensional variables that is derivable from Eq. (96) when Π_1 and Π_2 are multiplied by Π_3^{-1}, or, reusing the Πs,

$$\Pi_1 \;=\; \frac{z}{V^2/2g}, \quad \Pi_2 \;=\; \frac{t}{V/g} \quad \text{and} \quad \Pi_3 \;=\; \frac{V^2}{gR}. \tag{105}$$

The relation between these three nondimensional variables can be written

$$\frac{z}{V^2/2g} \;=\; F(\frac{t}{V/g},\; \frac{V^2}{gR}), \tag{106}$$

or using a $(\;)^*$ to denote these nondimensional variables,

$$z^* \;=\; F(t^*, \epsilon).$$

The nondimensional maximum height is then

$$\frac{Z}{V^2/2g} \quad = \quad F(\frac{V^2}{gR}), \qquad \text{or,} \tag{107}$$

$$\tag{108}$$

$$Z^* \quad = \quad Z^*(\epsilon), \tag{109}$$

with ϵ as before. This second basis set leads to a new interpretation, that $\epsilon \;\propto\; Z_0/R$, is the ratio of the zero order maximum height to the radius of the planet.

This new basis set also leads to a clearly defined functional dependence of maximum height upon the single parameter ϵ, Fig. (15), lower. This new form $Z^*(\epsilon)$ looks something like the initial form, $Z'(\epsilon)$, though with one significant difference. At small values of ϵ the new $Z^*(\epsilon)$ goes to a constant, 1, where the initial $Z'(\epsilon)$ decreased to zero as $\epsilon \to 0$. Thus, the new basis set is consistent with an underlying zero order solution in the limit of vanishing ϵ, where the initial basis set was not. This new basis set of nondimensional variables seems an obvious choice now that we have it in front of us, but then the first basis set seemed sensible as well (and was the form that happened to come from the computational algorithm).

6.4 Approximate and iterated solutions

We have now identified length and time scales that are appropriate specifically to the vertical motion of a free projectile in a constant gravitational field, as opposed to just any length and time

scales that may happen to be present in the VPlist. Using this new basis set, and that

$$z^* \;=\; \frac{z}{V^2/2g}, \quad \text{and} \quad t' \;=\; \frac{t}{V/g}$$

are the nondimensional height and time, the nondimensional velocity of the projectile is

$$\frac{dz*}{dt*} \;=\; \frac{dz/(V^2/2g)}{dt/(V/g)} \;=\; \frac{2}{V}\frac{dz}{dt}, \tag{110}$$

and the acceleration is

$$\frac{d^2z^*}{dt^{*2}} \;=\; \frac{d^2z/(V^2/2g)}{d(t/(V/g))^2} \;=\; \frac{2}{g}\frac{d^2z}{dt^2}. \tag{111}$$

When ϵ is small, the dimensional acceleration is approximately equal to g, and this $\frac{d^2z^*}{dt^{*2}}$ is thus O(1). The same is true for the nondimensional velocity. Despite that the velocity goes to zero at the top of the trajectory we still say that dz^*/dt^* is O(1), because our concern is with the largest magnitude of a term, rather than its average or smallest value. The equation of motion Eq. (100) in these nondimensional variables is

$$\frac{d^2z^*}{dt^{*2}} \;=\; \frac{-2}{(1+\epsilon z^*/2)^2} \tag{112}$$

and the initial condition is

$$z^*(t=0) \;=\; 0 \quad \text{and} \quad \frac{dz^*}{dt}(t=0) \;=\; 2. \tag{113}$$

It is helpful to expand the right hand side of Eq. (112) using a binomial expansion,

$$\frac{d^2z^*}{dt^{*2}} \;=\; -2 + 2\epsilon z^* - \frac{3}{2}\epsilon^2 z^{*2} + \epsilon^3 z^{*3} + HOT, \tag{114}$$

that will converge for $\epsilon z^*/2 \leq 1$. Because we have taken care to nondimensionalize the height and time with appropriate scales, the size of each of the terms can be told by the exponent on the parameter ϵ. The acceleration term and the first term on the right hand side are independent of ϵ or O(ϵ^0), which is to say O(1) (a factor 2 notwithstanding). The second term on the right hand side is O(ϵ), the third term is O(ϵ^2), and so on, and the HOT is the sum of all the terms that are higher order in ϵ. The order of a model is said to be the highest exponent of ϵ in the terms retained in the expansion.

When the terms multiplied by ϵ are dropped, there follows a useful first approximation to the projectile problem,

$$\frac{d^2z_0^*}{dt^{*2}} \;=\; -2,$$

which is the so-called zero order model Eq. (104) written in nondimensional form. The ICs are

exactly as Eq. (113) and the solution is

$$z_0^* \;=\; 2t^* - t^{*2}. \tag{115}$$

It seems that we have gone in a circle, but with Eq. (114) in hand we know how to proceed toward an improved solution; use this zero order solution as an estimate of z^* in the first order model, in which all terms higher order than ϵ^2 are omitted, to find,

$$\frac{d^2 z_1^*}{dt^{*2}} \;=\; -2 + 2\epsilon z^* \;\approx\; -2 + 2\epsilon z_0^* \tag{116}$$

$$\;=\; -2 + 2\epsilon(2t^* - t^{*2}), \tag{117}$$

which is easily integrable. The ICs do not involve ϵ, and the ICs of the first order model are Eq. (113) (the initial velocity is satisfied by the zero order solution alone). The first order solution is

$$z_1^* \;=\; 2t^* - t^{*2} \;+\; \epsilon(\frac{2}{3}t^{*3} \;-\; \frac{1}{6}t^{*4}). \tag{118}$$

Compared to the zero order solution, which appears here as the first and second terms on the right hand side, the new term is O(ϵ) and may be regarded as a correction to the zero order solution. The consequence of this new term for Z is that, for small ϵ so that t^* is O(1), there is an increased height compared to the zero order solution. Hence, this model and solution takes account (approximately) of the decrease in g with height. The maximum nondimensional height evaluated from Eq. (118), Z_1^*, shown as the green line in Fig. (15), lower, compares well with Z^* diagnosed from numerical solutions in the range $0 \leq \epsilon \leq 1/2$, and then begins to diverge from the numerical solution for larger ϵ, first above then below. Thus the first order solution represents approximately the effect of decreasing gravitational attraction with height above the planet's surface.[34]

An improved solution can be guessed by noting that the average value of z_0^* is $\approx 1/2$, and from Eq. (112) we might go on to guess that the height-dependent gravitational term in Eq. (117) could be estimated as the nominal gravity reduced by the factor $1 - \epsilon\frac{1}{2}$. This has the correct asymptotic behavior, i.e., it goes to 1 as ϵ vanishes, and it has the right qualitative behavior at $\epsilon = 2$ when the projectile should escape into deep space. The solution for the nondimensional maximum height is then

$$Z^\dagger = 1/(1 - \epsilon/2), \tag{119}$$

the solid red line of Fig. 15, lower, which compares well to Z^* diagnosed from the numerical solutions from the full model up to $\epsilon = 2$. Here and frequently, it happens that the first order model gives valuable insight into the parameter dependence (and one might say the physics) of a phenomenon in a way that numerical solutions, no matter how extensive and precise, may not.

[34] This iteration procedure is a simple and intuitive kind of perturbation analysis known as 'successive approximations' combined with an expansion in the small variable ϵ. Perturbation methods are powerful and very important techniques. Excellent references are Ch. 7 of Lin and Segel (1974),[3] and a very clear and concise text by J. G. Simmonds and J. E. Mann, 1986, *A First Look at Perturbation Theory*, Dover Publishing.

7 Applications / Homework projects

7.1 The Planck program, natural units for the universe

In Sec. 2 it was noted that the natural time scale of a simple pendulum is the reduced period, $P/2\pi = \sqrt{L/g}$, of small amplitude oscillation. When time is measured or normalized with this time scale, the parameters L and g disappear from the governing equation for a pendulum, a small convenience for calculations. This change of scale also points the way to a much more effective way to display a mass of data (Figs. (1) and (3)), and to think about pendulums generally. In 1899, Max Planck proposed something similar, but on a far, far grander scale — natural units for the universe.

Fundamental Physical Constants

constant	symbol	dimensions mass, length, time	SI value
speed of light	c	[0 1 -1]	299 792 458 m s^{-1}
Gravitational	G	[-1 3 -2]	6.674×10^{-11} kg^{-1} m^3 s^{-2}
Plancks const., reduced	$\hbar$	[1 2 -2]	1.054×10^{-34} kg m^2 s^{-2}

Table 1: Three of the Fundamental Physical Constants and their SI values. These important constants are known to considerably higher precision than implied here. To this short list could be added the charge of an electron and the Boltzmann constant, which would extend the scope to electro and thermodynamics.

7.1.1 A new fundamental constant with dimension mass

Even before the turn of the twentieth century it had been established that there were two fundamental physical constants that could be presumed to hold throughout virtually all of space and time, the speed of light in vacuum, c, and Newton's universal, gravitational constant, G (values in Table 1). Planck discovered a third fundamental constant, $\hbar \doteq [1 \quad 2 \quad -2]$, that represented the quantum of action appropriate to atomic scales, and it too could be presumed to be universal. Crucially, $\hbar$ includes the dimension mass. Given just these three universal constants, Planck recognized that one could construct the dimensions of any variable of mechanics.

In an address to the Prussian Academy of Sciences, he noted that units formed in this way would

> *necessarily retain their meaning for all times and for all civilizations, even extraterrestrial and non-human ones, and can therefore be designated as 'natural units.'*
>
> Max Planck, 1899

These natural units for the universe are called Planck units or Planck scales, Table 2.

Consider the Planck length, L_p to be the dependent variable of a VPlist; there are then four variables in the VPlist, L_p, plus the constants of Table (1), and the dimension matrix has rank $R = 3$. The inference from dimensional analysis is that there is one nondimensional variable,

$$\frac{L_p}{G\,h\,/\,c^4} \;=\; constant, \tag{120}$$

and that it is a constant. In other cases where the dimensional analysis came down to just one nondimensional variable, e.g., the period of a simple pendulum, the constant was found to be O(1) by comparison to observations or theory. Thus the nondimensional period, $P/\sqrt{L/g}$, is an appropriate representation of the period of a simple pendulum with respect to both the dependence upon L and g and the magnitude. Could that be the case also for the Planck length?

If the constant of Eq. (120) is O(1), then L_p is unimaginably small, $L_p \;=\; 1.616 \times 10^{-35}$ m, which is roughly 10^{-20} times the diameter of a proton. However, we do not know whether the Planck length has a direct physical interpretation, i.e., whether there is anything in nature having a length scale that is $\propto\; L_p$. This is a length scale that is well outside the reach of present experimental or observational methods, and so the suggestions for a physical interpretation are many and untestable: that it is the length scale of the nascent universe, that it is the smallest possible scale of a black hole, that it is the smallest possible, meaningful length, and so on. The physical interpretation of Planck length is an open question for physics and cosmology.

7.1.2 Planck problems

1) Use dimensional analysis to form a Planck time and mass from the fundamental constants c, G, and $\hbar$ of Table 1. How many nondimensional variables do you expect in the null space? You can check your method by computing the Planck length in SI units and comparing against Table 2.

Planck units

unit	symbol	construction	SI value
Planck mass	M_p	$\sqrt{\hbar G \,/\, c^3}$	2.176×10^{-8} kg
Planck length	L_p	$G\hbar/c^4$	1.616×10^{-35} m
Planck time	T_p	?	5.396×10^{-44} s
velocity		L_p/T_p = c	299 792 458 m s^{-1}
momentum		?	6.524 kg m s^{-1}
energy		$M_p c^2$	1.956×10^{9} kg m^2 s^{-2}

Table 2: Planck units for mass, length and time formed from the Fundamental Constants of Table 1. The entries ? are left for you to fill in.

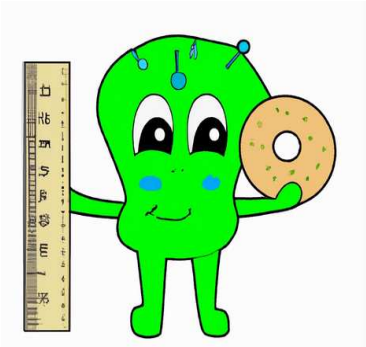

Come visit, Earthlings,
We have donuts, huge and tasty,
and well worth the trip.

"Interstellar ambassador offering a donut,"
image generated by OpenAI's DALL·E 2, 2024.

2) Interstellar (mis)understandings. SETI[35] has at last detected and deciphered a radio signal coming from the neighborhood of Alpha Centauri that has been repeated over and over again for what may have been a very long time. The message is a short piece of text (see above), and then a long string of 1s and 0s, evidently a large binary number, $N \approx 10^{34}$. This appears to be a generous peace offering from a very advanced civilization. Their donuts may be good, but could they possibly be good enough and big enough to be worth such a lengthy trip — four years for a photon and much, much longer for mere Earthlings. The number N presumably defines the donut size in Planck units, the most likely system for interstellar communication. However, the clever ambassador neglected to indicate whether it was Planck volume or mass or energy or length. Assuming that their donuts are comparable to ours in terms of density, consistency, etc., and that their planet has a gravitational acceleration comparable to Earth's, what is a plausible interpretation of the number N, i.e., just how big are these donuts?

[35] Search for ExtraTerrestrial Intelligence: https://www.seti.org/

3) The dimensional form of gravitational mass attraction between two masses M_1 and M_2 is calculated by Newton's law to be

$$F = \frac{GM_1M_2}{r^2}. \tag{121}$$

Show that when the variables in this equation are written in terms of the Planck units for force, mass and length (Table 2), e.g., $r' = r/L_P \doteq nond$, (121) is simplified somewhat to

$$F' = \frac{M_1'M_2'}{r'^2}.$$

Since every variable has a prime, the prime may as well be dropped to arrive at

$$F = \frac{M_1M_2}{r^2}. \tag{122}$$

The interpretation of (122) could be unclear if not accompanied by a brief explanation, and specifically, what happened to the important gravitational constant, G, of (121)?

7.2 Open channel flow through a weir

Figure 16: **(left)** An adjustable weir that controls the flow of fresh water from Shawme Pond at left into Cape Cod Bay and the North Atlantic to the right. **(right)** A fish ladder that facilitates the upstream journey of river herring to their spawning grounds in Shawme Pond. Photos by the author in Sandwich, Massachusetts.

The transport of water within rivers and canals is of great practical interest, and difficult to monitor by direct measurements of the velocity. An indirect but simple and reasonably accurate method for monitoring the transport of open channel flows is to measure the height of the water surface at a location upstream of a weir, a barrier erected across the flow.[36] A weir has a well-defined notch, often rectangular, through which the water may flow and then fall freely into a lower pool, Fig. (16), left. The volume transport through the notch, Q, is expected to have a

[36] A very clear and appealing discussion of the physics and practice of open channel flows is by Caspar Hewett, https://www.youtube.com/channel/UCv2u6bFc7SSFsPHf98M50Mg

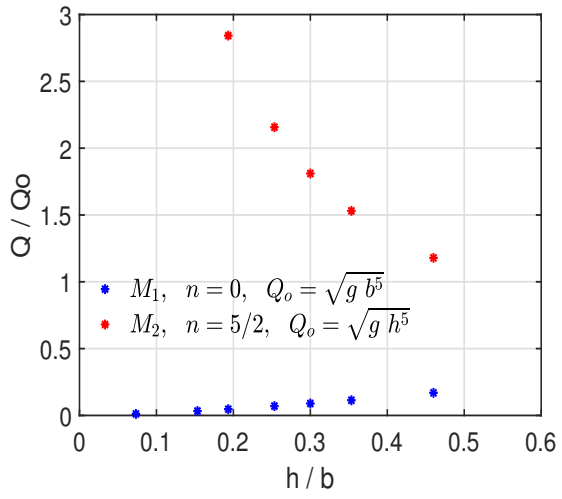

Figure 17: Two possible models of transport through a rectangular-notch weir evaluated using the transport data listed in the main text. Neither of these models indicates a satisfactory result insofar as the similarity functions have a very pronounced dependence upon h/b. These two models may be seen as end members of a family of models inferred from dimensional analysis (Eq. 125).

systematic dependence upon the width of the notch, here $b = 1.5$ m, and the upstream, still water surface height, h, measured with respect to the lower edge of the notch. The energy source in such a flow is gravitational potential energy released as the water falls through the notch, and hence the acceleration of gravity must be an important parameter. Water density would be relevant if the dependent variable was mass transport, but if the dependent variable is volume transport, then the water density may be omitted. That leaves a very concise VPlist for

- Volume transport through a rectangular-notch weir:

1. volume transport, $Q \doteq$ [0 3 -1], the dependent variable,
2. upstream water height, $h \doteq$ [0 1 0], the independent variable,
3. notch width, $b \doteq$ [0 1 0], a parameter,
4. acceleration of gravity, $g \doteq$ [0 1 -2], a parameter.

having only four variables and parameters and two physical dimensions, length and time. If attention is restricted to one specific weir, then two of these parameters, g and b, are 'globally' constant (Sec. 2.6).

The relationship $Q(h, b, g)$ may be inferred with help from dimensional analysis and the following data:[37]

upstream water level, h, m = [0.11 0.23 0.29 0.38 0.45 0.53 0.69]

volume transport, Q, m^3 s^{-1} = [0.097 0.286 0.403 0.601 0.773 0.982 1.46]

[37] Computed by a fairly comprehensive model that attempts to account for nominal friction at the weir as well as the finite size of the upstream basin: https://calcdevice.com/weir-spillway-id239.html

This VPlist is small enough that it can be analyzed by inspection, but let's use the null space basis method to illustrate an important point. If the variables and parameters of the VPlist are entered in the order above, then the nondimensional relationship among the variables comes out to be

$$M_1: \quad \frac{Q}{Q_o} \;=\; \frac{Q}{\sqrt{g\ b^5}} \;=\; F_1(\frac{h}{b}), \tag{123}$$

dubbed model M_1. This model is correct, (non)dimensionally, but notice the important term that scales the dependent variable, $Q_o \;=\; \sqrt{g\ b^5}$. If Q_o had come from a simplified model, then it could be a zero order solution with some physical significance. But in this case, Q_o is merely the first thing that came from the algorithm; it might be a good choice, or it might not be.

To find out, evaluate (123) using the data above, which gives the blue dots of Fig. (17). The result is not encouraging for $M1$ insofar as the h-dependence of the similarity function $F_1(h/b)$ is very substantial. Notice that this Q_o omits the upstream height, h, which we know is important. In fact, this Q_o is a constant for any one weir, and the crucially important dependence of Q upon h has to be relegated entirely to the similarity function of M_1. That isn't wrong, mathematically, but neither does this M_1 represent any real progress toward a useful model of weir transport.

Let's try the calculation again, but this time reversing the input order of h and b, to find a second model, M_2,

$$M_2: \quad \frac{Q}{\sqrt{g\ h^5}} \;=\; F_2(\frac{h}{b}), \tag{124}$$

This simply interchanges h with b, and now the zero order solution, $Q_o = \sqrt{g\ h^5}$, neglects b, the notch width, which is bound to be relevant. The argument h/b was retained in the similarity function F_2 so that M_1 and M_2 may be compared directly in Fig. (17). Model M_2 (the red dots of Fig. 17) seems no better than M_1 in that the similarity function varies significantly with h/b.

What can be learned from this? The calculation of a null space basis is a formal, logical (mathematical) procedure that takes no account of the physical meaning of the input variables. In this case, the calculation makes no distinction between two lengths, h and b, even while we know that they are quite different things.

You can improve on either of these first two models by combining the formal methods of dimensional analysis with physical insight, i.e., common sense plus a little experience. To start, show that a generalized relationship can be written

$$\frac{Q}{(g\ b^5)^{1/2} \times \left(\frac{h}{b}\right)^n} \;=\; {}^nF(\frac{h}{b}), \quad \text{where} \quad 0 \;\leq\; n \;\leq\; 5/2. \tag{125}$$

The first model M_1 is the case $n = 0$, and the second model M_2 is the case $n = 5/2$. Thus, dimensional analysis leads us to a family of models, depending upon the parameter, n, of which M_1 and M_2 are end members. The task is then to find the best n, the best member of the model family that has a physically sensible zero order solution, Q_o. A hint: Suppose a given h; what

would you then expect for the dependence of Q upon b? You can test your new model by evaluating the similarity function as in Fig. (17) using the data listed above. If the result looks promising, i.e., if your new model yields a quasi-constant (or at least a much less variable) similarity function, then it could be plausible to represent the similarity function by a similarity constant.

A weir transport formula generally has to be calibrated for each specific weir to account for a variety of secondary effects including friction, that depends upon whether the weir is broad-crested, as here in Fig. (16), or sharp-crested, as well as the configuration and size of the upstream basin, i.e., its depth, width and length. For any specific weir these are globally constant parameters (Sec. 2.6) and hence their consequences may be lumped into (ascribed to) a similarity constant. What do you find for this weir?[38]

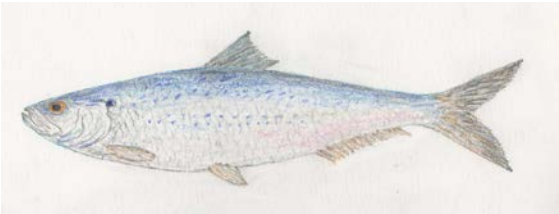

Figure 18: Blueback herring and the very similar alewife are known as river herring. An adult has a length up to 0.3 m and a mass of about 0.25 kg. The adult fish live at sea for four to five years, and then return to freshwater ponds to spawn in the spring. Drawing by the author.

The weir of Fig. (16) presents a formidable obstacle to the small river herring that migrate upstream from the North Atlantic to their spawning grounds in Shawme Pond. A springtime herring run was once an important food source for people and marine predators alike, but since the 1960s herring numbers have been greatly reduced by the damming of rivers and habitat degradation generally. The return of river herring to Shawme Pond is made much easier by a fish ladder, a bypass channel, Fig. (16), right, having a sequence of 12 identical small weirs and ponds. What would you expect for the variation of h from one weir to the next?

7.3 How fast did dinosaurs run?

The most tangible evidence of dinosaur locomotion comes from fossilized trackway data that shows the stride length, λ, the distance between successive prints of the same foot, as well as the foot length, f (Fig. 19).[39] It is often possible to estimate these parameters for a specific, distinguishable animal on a trackway, and it is easy to tell Theropods and Ornithopods (bipedal dinosaurs with bird-like feet) from Sauropods (quadrupedal, with elephant-like feet) though the species can not be told. Correlations made with fossil skeletons show that the hip height, h, is roughly proportional to the foot length, $h \approx 4f$. There is nothing directly evident regarding time or speed. However, an empirical relationship between these features of gross anatomy and the

[38] A typical similarity constant for weirs of the sort considered here is $\approx 1/2$.

[39] A remarkable example: https://www.fs.usda.gov/detail/gmug/news-events/?cid=FSEPRD1171521

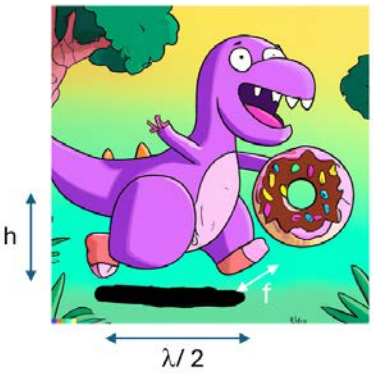

Figure 19: Evidence from fossil trackway data interpreted via dimensional analysis suggests that mighty Tyrannosaurus Rex was not a fast runner, typically. While the physical evidence and its analysis are fairly compelling, what do we know about her motivation and intention?

T Rex did not hurry,
Until, on a warm breeze, came the scent
Of sweet donut.

"T Rex running after a donut," image generated by OpenAI's DALL·E 2, 2024.

walking/running speeds for a very wide range of animals was developed by Alexander, 1976, A76,[40] on which this problem builds. How to infer dinosaur speed from trackway data?

- A VPlist for estimating running/walking speed from trackway observations:

1. speed, $V \doteq$ [0 1 -1], the dependent variable,
2. stride length, $\lambda \doteq$ [0 1 0], a parameter,
3. height of the hip joint, $h \doteq$ [0 1 0], a parameter,
4. acceleration of gravity, $g \doteq$ [0 1 -2], a parameter.

Gravity is highly likely to be relevant for any form of terrestrial locomotion, dinosaurs or not, and would seem to be the only plausible parameter that can provide the dimension time. There are four parameters having two dimensions, length and time, and so there are two nondimensional variables related by, as the first basis set,

$$\frac{V}{\sqrt{gh}} \;=\; F(\lambda/h). \tag{126}$$

where $F(\lambda/h)$ is an unknown similarity function. The dependent variable has been scaled with $\sqrt{gh}$, which is the phase speed of shallow water gravity waves on the sea surface. This is a natural scale from this VPlist, but is not the only possibility. The dependent nondimensional variable of (126) is the square root of an important nondimensional variable called the Froude number,

$$Fr \;= \frac{V^2}{gh},$$

[40] The pioneering study by Alexander, R. M., 1976, 'Estimates of speeds of dinosuars', Nature, Vol. 261, May 13. 129 - 130. See also R.. Alexander, 1991, 'How dinosaurs run', Sci. Am., 264, No. 4, 130 - 137. The first papers on this topic aimed to find correlations of the sort considered here, and discovered widespread, systematic relations that describe what would seem to be a very complex phenomenon — animal locomotion. Later papers have delved into the detailed structure of bones and muscles, e.g., W. I. Sellers and Manning, P. L., 2007, 'Estimating dinosaur maximum running speeds using evolutionary robotics'. Proc. Royal Soc. B, 274, 2711 - 2716. doi:10.1098/rsbp.2007.0846.

which often arises in contexts in which inertial forces $\propto V^2$ and gravitational forces $\propto g$ are at issue.

A76 used observations on the walking and running speed of living animals (including humans) to determine the similarity function $F(\lambda/h)$ of (126) and found that walking and running speed by a surprisingly wide variety of creatures — bipeds and quadrupeds, birds and mammals, creatures small and large — is consistent with

$$Fr \;=\; \frac{V^2}{gh} \;=\; .062\left(\frac{\lambda}{h}\right)^{3.33} \tag{127}$$

where the coefficient and the exponent were determined by fitting (126) to observations of U, λ and h.[41]

Given the following dinosaur trackway data of eight individual animals from A76,

stride, λ, m = [3.0 3.0 2.4 1.3 2.1 1.6 2.5 1.6]

hip height, h, m = [2.1 2.0 1.0 1.1 1.2 0.7 3.0 1.5]

estimate the speed of the responsible dinosaurs on the plausible assumption that (126) applies to these astounding creatures. The first six entries were made by bipedal dinosaurs, Theropods or Ornithopods, and the last two were made by quadrupedal Sauropods. Is there a systematic difference? An adult T Rex was a very large animal having a hip height up to $h = 4$ m. From what you can see in Fig. (19), how fast do you estimate T Rex was running on that occasion?

As we have seen in other problems, the detailed form of a solution is often not determined solely by dimensional analysis. Given λ and h, a speed requires a fourth parameter with dimension of time, and g is the obvious candidate. However, the way g enters does not have to follow (126), which uses $\sqrt{gh}$ as the velocity scale. Suppose instead that the dynamics of a swinging dinosaur leg is similar to a swinging pendulum; what do you get if the velocity scale is taken to be stride length / stride period $\propto \lambda/\sqrt{h/g}$? How can this be realized from the original form, Eq. (126)?

7.4 The expanding blast wave of an intense explosion

An interesting (although very grim) problem that yields to dimensional analysis is the analysis of the expanding blast wave that follows from the energy released into the atmosphere by an intense, localized explosion. The Trinity test of the first atomic bomb is an example of enormous historical

[41] Excluded from this analysis are animals that have a sprawled posture and support their weight mainly on their bellies, e.g., crocodilians and lizards. Recent and more comprehensive data collections reveal that there is, not unexpectedly, some systematic species dependence in the function (127). You may be pleased to know that humans are a little faster than the grand average reflected by (127).

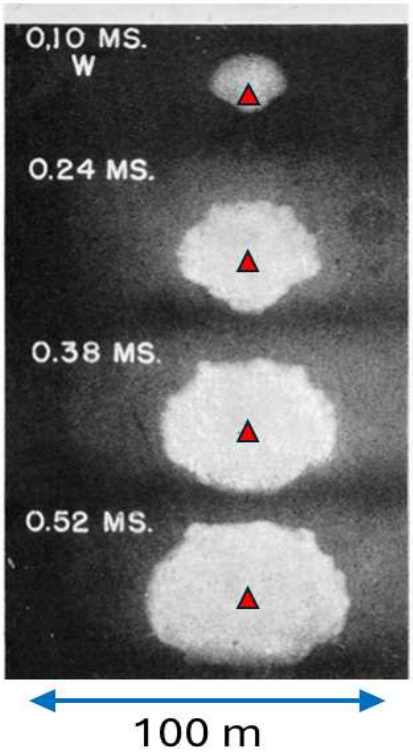

Figure 20: The 1945 Trinity test of the first atomic bomb as captured by very high-speed photography. Of this occasion, the project scientific director J. Robert Oppenheimer later recalled: '*W*e knew the world would not be the same. A few people laughed, a few people cried. Most people were silent.'

© 2024 The Royal Society. All rights reserved. This content is excluded from our Creative Commons license. For more information, see https://ocw.mit.edu/help/faq-fair-use.

import, Fig. (20), documented in high-speed photographs from Taylor (1950).[42] These rather coarse images allow estimates of the radius, $r(t)$, of the rapidly expanding blast wave (for short times, coincident with the fireball visible in the available photographs):

time, t, 10^{-3} s, = [0.1 0.24 0.38 0.80 1.36 1.93 15.0 127.0]

radius, r, m, = [12 18 25 34 40 45 110 170]

Taylor's in-depth analysis of the phenomenon calculated the increase in pressure caused by a point-like release of thermal energy, and the subsequent expansion of the heated, high pressure air against the much smaller pressure of the ambient atmosphere. He started with the equations for momentum, mass and energy balance and boiled the problem down to a similarity solution for the expanding radius, r,

$$r(t) \;=\; F(\kappa)\left(\frac{E_0\; t^2}{\rho_a}\right)^{1/5} \tag{128}$$

where $\rho_a = 1.25$ kg m^{-3} is the nominal density of air. The parameter κ is the nondimensional ratio of the constant pressure specific heat of air and the constant volume specific heat of air, $\kappa \;=\; C_p/C_v$, which commonly arises in the analysis of acoustic phenomenon. For nominal

[42] Taylor, G. I., 1950, 'The formation of a blast wave by a very intense explosion: II'. The atomic explosion of 1945. Proc. R. Soc., London, A201, 175 - 190.

conditions, $\kappa \approx 1.4$, but of course an atomic blast is an extreme case that may involve fairly exotic effects. The bottom line is that Taylor's analysis found $F(\kappa) \approx 1$.

Here's a significant shortcut for this problem that omits the thermodynamic $F(\kappa)$ dependence and yet arrives at Taylor's essential result: solve for the (nondimensional) radius of the blast wave as a function of time, assuming that the only relevant parameters are the density of air, ρ_a, and the energy of the expanding blast wave, E_0. The key result is the power-law time-dependence of the radius. Does your result match (128)? And does this power law conform with the observations listed above? What do you infer for the energy parameter, E_0? [43]

Suppose that you did include the specific heat at constant pressure in the VPlist, $C_p \doteq$ [mass length time temperature] = [0 2 -2 -1], which has a dimension inverse temperature, and necessarily the specific heat at constant volume, C_v, same dimensions. What changes? [44]

7.5 Planetary orbits

> *It is one of the great tasks of science to learn what are accidents and what are principles, and about this we cannot always know in advance.*[45]
>
> Steven Weinberg, 2003.

The collaboration of the Dutch astronomer Tycho Brahe (1546 - 1601) and German polymath Johannes Kepler (1571 - 1630) was a milestone of the early Scientific Revolution. Tycho was an energetic and meticulous observer of the heavens who built the most precise observing instruments of the time, while also compiling historical, astronomical data from many sources. His protege, Kepler, was an accomplished mathematician whose worldview owed much to the classical Greeks and medieval scholastics. Kepler was strongly motivated by the mystical belief that the heavens must reflect a harmony and a geometric simplicity that evidenced creation by the Deity.[46]

[43] You wouldn't be confident in this analysis absent the much more detailed and comprehensive investigation of Taylor (1950), and, the opportunity to test against observations. Since this phenomenon is very far from common experience, it will be helpful to know that the E_0 estimated in this way is roughly 8×10^{13} Joules, which is equivalent to the energy released in the detonation of about 15 kilotons of TNT. This greatly simplified model ignores the work against the ambient atmosphere and hence may underestimate the actual thermal energy released. It also ignores the energy released as radiation that would have escaped the blast wave instantaneously, another likely bias toward a low total energy estimate.

[44] If you choose, you can see some of the results of this problem computed by the script DanalysisA2.m, Sec. 3.4.

[45] Weinberg, S., 2003, 'Can science explain everything? Can science explain anything?', Ch. 2 of *Explanations*, J. Crowell, Ed., Oxford Univ. Press. 23 - 38.

[46] Holton, G., 1956, 'Johannes Kepler's universe: its physics and metaphysics', *Am. J. Phys.*, Vol. XXIV, No. 5, 340 - 351. The literature on Kepler's remarkable life and accomplishments is voluminous and still growing. One of the better online references is https://www.aps.org/archives/publications/apsnews/201407/physicshistory.cfm and also https://plato.stanford.edu/entries/kepler/.

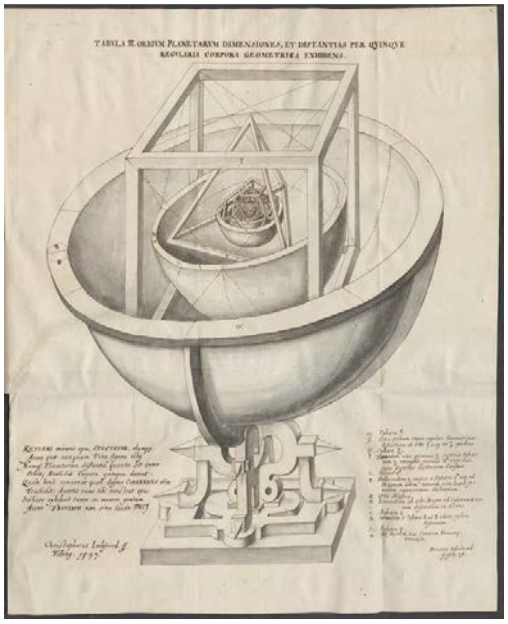

This image is in the public domain.

Figure 21: Kepler's Platonic solids model of the solar system. The outermost sphere represents the orbit of Saturn, and the next smaller sphere represents that of Jupiter. These are related by the inscribed cube which fits just inside the outer sphere, and encloses the inner sphere. Pure geometry thus defines the ratio of the radii of these spheres and, it was thought by Kepler, the orbital radii of Jupiter/Saturn. Given the freedom to choose the order of the remaining four solids, this scheme can be extended with some success to Mars and the inner planets. This model was in several respects a landmark in the Scientific Revolution; it brought the heavens down to Earth, and it supported a sun-centered solar system. Taken literally, it explained the number of planets that were then known, and it made a definite, quantitative prediction of the relationship among the planetary orbits that could be tested against observations.

Kepler came to prominence as a young mathematics professor when he published a geometric model of the solar system based upon the notion that the planetary orbital radii increased in proportion to the circumference of the five regular, Platonic solids nested on the Sun (Fig. 21).[47] The inspiration for this model seems to have come from the coincidence of there being exactly five Platonic solids, the number needed to account for the relative radii of the six known planets. The quantitative predictions of this model were within about 10% of the orbital estimates of Nicholas Copernicus — not convincingly right, but not clearly wrong.

7.5.1 Discovering a harmony in the heavens

The ambiguous match between Kepler's Platonic solids model and Copernicus' orbital estimates was no doubt part of Kepler's motivation to compute refined orbital estimates from Tycho's precise and extensive observations. The result was a significant advance in the precision of orbital estimates, with values close to modern (Table 3).[48] However, aside from Jupiter's orbital radius, the refined estimates were not very different from those made by Copernicus. Kepler's writings leave the impression that he had a clear understanding of what would constitute a meaningful departure of a model prediction from observed reality. And specifically, he found that the Platonic solids model was not a satisfactory fit to the more precise orbital estimates, as he must have hoped.

[47] This image is thanks to the Yale University Library https://search.library.yale.edu/catalog/1886333

[48] Kepler's data has been called to question for being a bit more precise than the observations should have allowed, https://www.nytimes.com/1990/01/23/science/after-400-years-a-challenge-to-kepler-he-fabricated-his-data-scholar-says.html

Historical and Modern Orbital Parameters

variable	Mercury	Venus	Earth	Mars	Jupiter	Saturn
Tycho and Kepler mean radius, Rp, AU	0.388	0.724	1	1.524	5.200	9.510
Copernican mean radius, Rp, AU	0.38	0.72	1	1.52	5.22	9.17
Modern mean radius, Rp, AU	0.387	0.723	1	1.52	5.200	9.54
Modern period, Tp, years	0.242	0.616	1	1.881	11.86	29.33
Modern planetary mass, Mp/Me	0.054	0.815	1	0.108	317.8	95.2
Modern eccentricity	0.205	0.006	0.017	0.093	0.048	0.054

Table 3: Estimates of orbital parameters by Tycho and Kepler, Copernicus, and modern values. These include the mean radius, Rp, and the period, Tp. Note that Tp is normalized with Earth's period, a year, and Rp is in units of Earth's mean radius, an Astronomical Unit, or AU. The absolute distance was not known in Kepler's era. Also included are modern estimates of planetary mass, Mp, in units of Earth's mass, Me, and the orbital eccentricity.[49]

Harmony among the planets of our solar system, if any exists, was not to be found in the relationship of the orbital radii.

A few questions for you. 1) Considering the six planetary orbital radii, Rp, of Table 3 available to Kepler, do you see a harmony i.e., some kind of regularity or pattern? 2) Evaluate the Platonic solids model given that a cube just touches the orbital sphere of Saturn at its eight corners, and encloses snugly the orbital sphere of Saturn (see Fig. 21). What is the ratio of the radii of the inner and outer spheres, and how does that compare with the ratio of the observed radii in Table (3)? Use both Copernican data and the Tycho/Kepler data. 3) Now consider the orbital radii Rp, and the orbital periods Tp, taken planet by planet; do you see a relationship Tp(Rp) that is in common to all six planets? (You may recognize your result as Kepler's third law of planetary motion.)

Kepler never gave up completely on the Platonic solids model, but his interests extended to modeling the detailed orbits of the individual planets, a key ingredient for forecasting astrology (a task that came with his post as a court astronomer). It was recognized that a circular, sun-centered orbit did not suffice for the eccentric orbit of Mars, and Kepler found that the *ad hoc* fix of adding one or a few additional suborbits (epicycles) was only a marginal improvement. After years of effort, Kepler discovered that an ellipse with the sun at one focus was a markedly better model of Mars' orbit, in terms of accuracy and simplicity. Moreover, he found that *all* of the planets moved on elliptical orbits, to within the high precision of the Tycho/Kepler analysis (Kepler's first law). Here, at last, Kepler found a genuine harmony, though of a different kind than he had sought with

the Platonic solids model. Today we expect that this same law will hold for planets and asteroids in bound orbits found anywhere in the universe.

Kepler's analysis confirmed a crucial role for the Sun, and even more that the Sun acted to 'gather' planets to itself, i.e., that the Sun was the seat of an attractive force that decreased with distance. Despite that crucial insight, Kepler did not discover a physical mechanism for planetary motion before his death in 1630. Kepler's grave site has been lost, but his moving, self-written epitaph has survived:

I measured the skies, now the shadows I measure.
Skybound was the mind, Earthbound the body rests.

Johannes Kepler

7.5.2 An orbital mechanism

The mechanism behind elliptical orbits was clarified some fifty years after Kepler's death by Newton's theory of universal gravitation. You could just as well say that Kepler's laws of planetary motion imply the central force and the inverse square dependence on radius that is the heart of Newton's universal gravity. Newton's theory is amenable to a dimensional analysis. Suppose that the orbital period, Tp, depends upon gravitational interaction between the sun with mass Ms and a planet with mass Mp, their separation distance, Rp, and Newton's gravitational constant, $G \doteq$ [-1 3 -2]. What can a dimensional analysis tell us about the orbital period, Tp? Given the following numerical data, AU = 1.49 $\times 10^{11}$ m, G = 6.67 $\times 10^{-11}$ kg^{-1} m^3 s^{-2} and Ms = 1.9880 $\times 10^{30}$ kg, what is the similarity constant? (Hint; a common geometric factor.) There will be two nondimensional variables in this analysis. What is the dependence of the (nondimensional) period upon Mp/Ms? [50] If your result is indeed universal, then it should conform also with the orbital parameters of the first four moons of Jupiter discovered by Galileo, Table (4). Jupiter has a mass Mj = 1.8973 $\times 10^{27}$ kg.

Table 4: The Galilean moons of Jupiter

	Io	Europa	Ganymede	Callisto
Orbital radius, Rm, 10^3 km	421	671	1070	1882
Period, Tm, days	1.77	3.55	7.15	16.68

[49] Kepler's data are from C. M. Linton, 2004, *From Eudoxus to Einstein: A history of mathematical astronomy*, Cambridge U. Press, page 198. Copernicus' data is from https://pages.uoregon.edu/imamura/121/lecture-3/ Modern data are from https://nssdc.gsfc.nasa.gov/planetary/factsheet/joviansatfact.html

[50] If you choose, you can see some of the results of this problem computed by DanalysisA2.m (Sec. 3.4).

Index

aerodynamic drag, 37
aerodynamic drag
    three dimensional flow effects, 42
annual cycle
    ground temperature, 55

blast wave, 74
boundary layer, 52

diffusion distance, 52
diffusion equation, 48
dimensional analysis
    benefit of, 15, 16
    premise, 14
dimensional homogeneity, 13
dimensions, 13
dinosaur, running speed, 72
drag coefficient
    inertial, 41
    viscous, 40

Froude number, 74

Kepler, 76

matrix
    rank, 30
    zero, 33
matrix,
    dimension, 26
model
    complete, 13
models
    mathematical, 8
    numerical, 11

Newtonian fluid, 48
nondimensional variables
    basis set , 29
null space basis, 27

parameters
    extra and omitted, 21
    local and global, 22
pendulum
    isochronicity, 19
    model equations, 11
    simple, 8
    time scales, 8
    VPlist , 18
    VPlist , 12
pendulum
    decay rate, 34
pendulum, simple, 9
physical model, 12
Planck length, 67
Planck units, 66

Reynolds number, 37, 41

scaling analysis, 57
similarity, 50
similarity function, 19
similarity solution, 52
solutions
    numerical, 11
Stokes' first problem, 48
Stokes' second problem, 53

units, 14

viscosity, 34
VPlist, 12
VPlist
    specificity (lack of), 21

weir, transport through, 69

zero order solution, 39

Draining a Tank

an appendix to

Dimensional Analysis of Models and Data Sets

James F. Price
Dept. of Physical Oceanography, Woods Hole Oceanographic Institution
Woods Hole, Massachusetts, 02543
http://www.whoi.edu/science/PO/people/jprice · jprice@whoi.edu

February 9, 2026

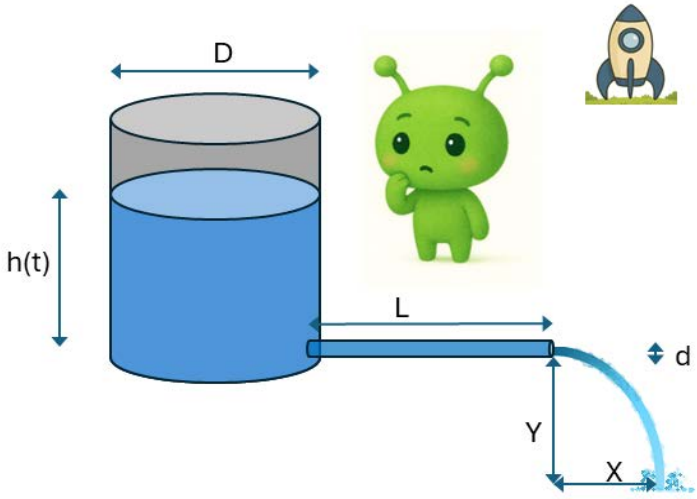

Planetary Explorer contemplating a water tank.
By the author using ChatGPT-5.

How long to drain this tank?

Here to learn Earth's ways.
All I see are water tanks —
deeper than they seem?

Summary

We can help. The objectives of this appendix are to observe and then model the time it takes a gravity-driven outflow to drain a tank. The observations come from a family of experiments that explore the effects of two real-fluid properties of water, surface tension and viscosity. Surface tension will slow the outflow as the fluid height h becomes small, and may stop it altogether depending upon the inside diameter of the orifice or pipe, d. When a pipe is present, viscous drag will reduce the outflow by a factor that depends upon the fluid viscosity, the diameter and length of the pipe, d and L, and the surface height.

The goal of this appendix is to demonstrate dimensional analysis as a guide for organizing this multi-parameter dataset into a concise and interpretable form. A clear organization of the data facilitates comparison with model predictions and highlights specific errors. This leads to a sequence of improved models. The end result is a model that is largely understandable while providing solutions that are empirically adequate over the parameter space of the present experiments.

Contents

1 Draining a tank; objectives and goal **3**
- 1.1 Why and how dimensional analysis . . . 4
- 1.2 Model development guided by observations and dimensional analysis . . . 5
- 1.3 Glossary of symbols, phrases and models . . . 8

2 A family of experiments **9**
- 2.1 Parameter space of this apparatus . . . 10
- 2.2 Making observations . . . 10
- 2.3 Inferences from the first experiments . . . 11
- 2.4 Changing the problem from h(t) to Q(h) . . . 13
- 2.5 Torricelli velocity and a zero-order model . . . 15
- 2.6 Summary to here and outlook . . . 16
- 2.7 Problems . . . 16

3 An elementary (and very successful) Model 1 **16**
- 3.1 A data-driven Model 1 . . . 16
- 3.2 Integrating to find h(t) . . . 18
- 3.3 Summary . . . 18
- 3.4 Problems . . . 19

4 Surface tension reduces transport in the small $\mathbf{h/d}$ regime **19**
- 4.1 Why do fluids exhibit surface tension? . . . 20
- 4.2 Surface tension and pressure within a cylindrical jet of water . . . 21
- 4.3 Model 2 includes a first-order effect of surface tension . . . 21
- 4.4 Summary . . . 22
- 4.5 Problems . . . 22

5 Outflow through an orifice and a pipe, starting with observations **23**
- 5.1 Reynolds numbers, external and internal, Re_x and Re . . . 25
- 5.2 The function F for orifice plus viscous pipe flow . . . 27
- 5.3 Summary . . . 27
- 5.4 Problems . . . 29

6 Models of viscous, laminar pipe flow **29**
- 6.1 Poiseuille's solution for laminar flow, Model 3 . . . 29
- 6.2 A hybrid Model 4 – Sig. Torricelli, say hello to M. Poiseuille . . . 31
- 6.3 A collapse to one independent variable . . . 34
- 6.4 Model 4 includes surface tension and viscosity appropriate to a laminar flow . . . 36
- 6.5 Summary . . . 38
- 6.6 Problems . . . 38

7 Turbulent flow accounted by Model 5 **39**
- 7.1 The inferred source of the overestimation error . . . 40
- 7.2 Historical, experimental observations of pipe flow . . . 41
- 7.3 Estimating an effective viscosity for use within a laminar flow framework . . . 45
- 7.4 At last, Model 5 . . . 46

7.5 Summary and closing remarks 47
7.6 Problems 48

8 Housekeeping **51**

9 Index **51**

1 Draining a tank; objectives and goal

"How long to drain this tank?" comes up in a wide range of contexts. Tank-draining projects are a mainstay of physics education, where they combine accessible experiments with satisfying theory.[1] Tank-draining problems continue to be a research topic in nuclear and chemical engineering when they include complex plumbing and highly exotic fluids.[2]

Though simple in concept, tank-draining problems do not admit simple solutions except in the most idealized case in which the fluid is considered to be ideal. This study goes beyond the basic case by including two real-fluid properties of water, surface tension and viscosity. Modeling these phenomena, the objective of this appendix, requires experimental observations and theory combined in roughly equal measure. The deeper goal of this appendix is to show how dimensional analysis can be the essential link between observations and a theory.

Readers are assumed to have experience with applied mathematics including linear algebra and ordinary differential equations, and classical mechanics to include a first course in fluid mechanics. For these readers, this article should be suitable for self-study.

[1] Donnelly, S. C., et al., 2024, Draining a tank through multiple orifices: An improved lab experiment in fluid mechanics, https://doi.org/10.18260/1-2-660-46367, and Rother, M. A., 2024, Modelling tank drainage using a simple apparatus. Journal of Mathematical Education in Science and Technology. 55, 2, 295 - 307. https://doi.org/10.1080/0020739X.2023.2249472 .

[2] Elgamal, M., K. Kriaa and M. Farouk, 2021, Drainage of a Water Tank with Pipe Outlet Loaded by a Passive Rotor. Water, 2021, 13, 872 https://doi.org/10.3390/w13131872

1.1 Why and how dimensional analysis

The procedure of dimensional analysis followed here is outlined briefly below and in considerably greater detail in the main text, Dimensional Analysis of Models and Data Sets.[3] If dimensional analysis strikes you as abstract in the extreme — as it does for *everyone* who is new to the idea — then Secs. 1 - 3 of the main text are strongly recommended as a prerequisite to this appendix. If you are somewhat familiar with dimensional analysis as it is usually practiced via the Buckingham Pi Theorem, then you will find that the present method is different mainly by the approach to computation, 3) below, and interpretation, 4) below.

1. **Problem definition.** A problem is defined by a so-called Variables and Parameters list, or VPlist, that starts with one dependent variable, the unknown, and includes all of the other variables and parameters that would necessarily appear in a model of the phenomenon. A remarkable property of dimensional analysis is that you do not have to know the model in any further detail; though better of course, if you do. These variables and parameters are characterized by the powers (the exponents) on their fundamental dimensions, [mass length time]. For example, the dimensions of a pipe having length, L, will be indicated by a dot-equals notation, e.g., $L \doteq [0\ 1\ 0]$, a speed $V = dL/dt$ has dimensions $V \doteq [0\ 1\ -1]$, and an acceleration has dimensions $dV/dt \doteq [0\ 1\ -2]$. The powers of each member of the VPlist (the three-element row vectors above) are collected into a dimension matrix.

2. **The practical advantages of dimensional analysis.** If the VPlist is complete, then the dependent variable may be written in a nondimensional form that is free from reference to a system of units, e.g., meters, centimeters or feet, and so is a pure number. There are two significant advantages in this that will be highlighted as we go through this analysis. First, a description in nondimensional variables is more concise (has fewer variables) than is the equivalent dimensional description. Second, a nondimensional description helps focus attention on meaningful relationships. For example, a pipe may be judged to be long or short compared to the pipe diameter, a natural scale with physical significance, or in meters or centimeters, arbitrary scales. The latter system is likely to be most useful during the design and execution of an experiment, while the use of nondimensional variables will maximize the utility of the experimental results.

3. **Automated calculation of nondimensional variables.** The nondimensional variables may be computed by solving a system of linear equations for the null space of the dimension matrix. The solution vectors of the null space correspond one-to-one with nondimensional variables.

[3] Online at https://ocw.mit.edu/courses/res-12-001-topics-in-fluid-dynamics-fall-2024/

This calculation is not difficult, but can be tedious if done by hand. The calculation is quick and sure when automated.[4]

4. **Interpretation.** The system of equations is most often undetermined, i.e., more unknowns than independent equations. In that case the initial basis set is not unique, and it will be optimal only by chance. Your task will be to transform (as necessary) the initial basis set into a form that will enhance the utility and interpretation of the analysis. Examples of this transformation will be seen throughout.

1.2 Model development guided by observations and dimensional analysis

Planetary Explorer beginning a long trek.
Image by the author using ChatGPT-5.

Seeking a better model.

A long path ahead.
Starlit by the Milky Way,
I'll take slow, sure steps.

The model development described here takes place in five steps, Fig. 1, each one motivated by a comparison of model predictions with a suite of experimental observations. Dimensional analysis is a great help in organizing the observations, and so guiding the next step in the model development.

There are two ideals for the model — sufficient transparency that we can understand what the model is and what it does, and, that the model predictions be true to the observations. These are not

[4] via Matlab: https://www2.whoi.edu/staff/jprice/wp-content/uploads/sites/199/2024/06/DanalysisA2.zip
or Python: https://www2.whoi.edu/staff/jprice/wp-content/uploads/sites/199/2024/10/DA2Python.zip

easily achieved at once. In the progression of models shown in Fig. 1, Model 4 is transparent and understandable but makes a consistent overestimate of the outflow transport. Model 5 utilizes historical, empirical turbulent pipe flow correlations to modify the viscous drag calculated by Model 4. This largely corrects the overestimation errors, but with some loss of transparency. The intent here is to be deliberate and clear about these tradeoffs.

Sec. 2. The next section describes the experiments and the resulting data that are essential to this study. The present family of experiments is defined by a four-dimensional parameter space — orifice or pipe diameter, pipe length, fluid height, and fluid viscosity. The aim of this study is not to answer any one specific tank-draining problem, helpful as that might be, but rather to model and understand the entire family of experiments defined by the available apparatus.

Sec. 3. The first experiments are made without a pipe, or orifice-only. The observed surface height, $h(t)$ is almost parabolic in time, and is described well by the most elementary model, Model 1, until h becomes very small. The observed outflow then slows and may stop altogether before the tank drains completely. In some respects this is a small detail, but it is also a qualitative error that is inherent to the ideal fluid model implicit in Model 1. How can we improve on this?

Sec. 4. At small values of h the orifice may be blocked by a stationary bubble or cap of fluid. From appearance alone this suggests an effect of surface tension, treated briefly in Sec. 4, and implemented as Model 2.

Sec. 5. The emphasis of this study is on the viscous drag that accompanies outflow through a pipe. Dimensional analysis is used to organize observations in a way that reveals the systematic and large amplitude variation of the outflow transport with pipe length, pipe diameter, viscosity and surface height. This empirical relationship is the objective of later Models 4 and 5.

Sec. 6.1 Poiseuille's historically significant and still quite useful model of fully-developed, viscous, laminar pipe flow is taken as Model 3. It shows promise for cases with longer pipes and greater viscous drag. However, it diverges toward unrealistic, excessive transport for cases with lesser drag because it takes no account of the inertial acceleration that has to accompany the movement of fluid from the tank into and through the orifice.

Sec. 6.2 A hybrid Model 4 combines Poiseuille's solution with the inertial orifice flow of Model 1 and surface tension of Model 2. A surprising result is that the solution of Model 4 can be written as a function of one nondimensional independent variable where dimensional analysis had indicated two independent variables. The collapsed, one variable description leads to a more insightful diagnosis of the advective/diffusive balance within the laminar flow regime. Model 4 gives a reasonable, semiquantitative account of the observations overall, however it displays a systematic overestimate of transport (underestimates viscous drag) for cases with larger Reynolds numbers.

Sec. 7 The inference made from this observation is that the flow is turbulent at the larger Reynolds

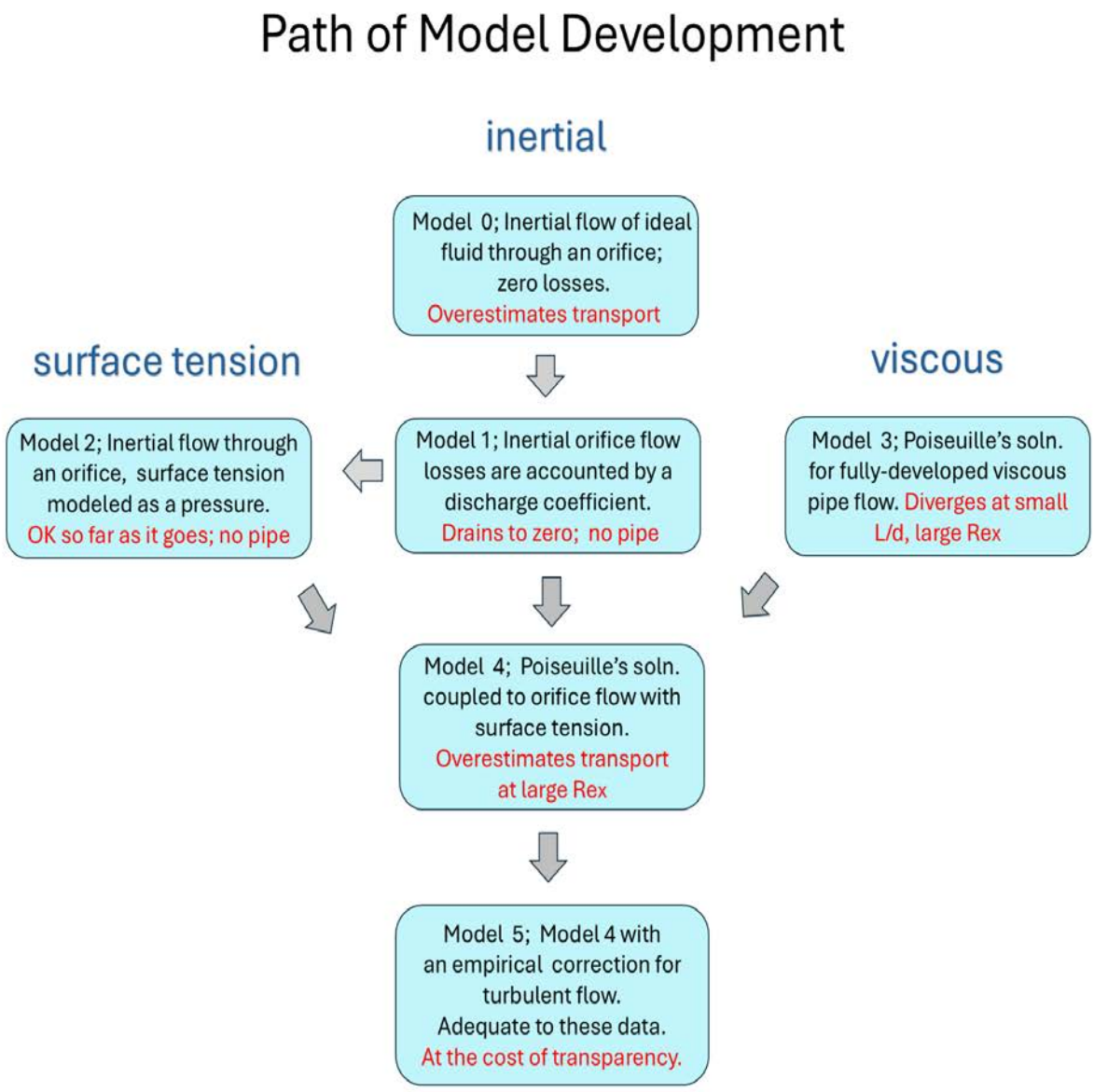

Figure 1: The sequence of models developed here, starting from very simple at the top to fairly complex at the bottom. A narrative of this model progression is in Sec. 1.2. There are at first two tracks that treat two distinct physical properties of real water. The track at left deals with surface tension, and the track at right deals with viscous effects. Surface tension and viscosity are treated separately until brought together in Model 4. The final Model 5 implements an empirical correction for the greater wall stress that occurs at larger Reynolds number consistent with the occurrence of turbulent flow. The red text in a box notes a salient shortcoming.

numbers reached in these experiments. Modeling turbulent flow relies on historical data correlations. The resulting Model 5 is adequate to these data, but at some cost in transparency, i.e., Model 5 is not understandable to the depth of Model 4.

1.3 Glossary of symbols, phrases and models

- **Symbols**
  - C orifice discharge coefficient; for this apparatus, $C \approx 0.77$, nondimensional
  - d inside diameter of the orifice and the pipe
  - D diameter of the cylindrical water tank
  - F is an unknown function
  - g acceleration of gravity, 9.8 m s^{-2} and presumed constant
  - h height of the water surface above the orifice/pipe center
  - Q observed volume transport of the outflow, m^3 s^{-1}
  - μ dynamic viscosity, for water, nominal 0.9 $\times 10^{-3}$ Pa s, temperature dependent
  - $\nu = \mu/\rho$ kinematic viscosity, for water, nominal 0.9 $\times 10^{-6}$ m^2 s^{-1}
  - ν_e effective viscosity that mimics the enhanced wall stress of turbulent flow
  - r radius of the orifice or pipe = $d/2$
  - ρ the density of fresh water, 998 kg m^{-3} and presumed constant
  - σ surface tension, for water, nominal 75×10^{-3} N m^{-1}, or 75×10^{-3} kg s^{-2}
  - W volume of fluid in the tank, m^3
  - $\doteq$ 'dot equals' is an operator that brings out the exponents on [mass, length, time], e.g., $W \doteq$ [0 3 0] and $Q = -dW/dt \doteq$ [0 3 -1].

- **Derived Symbols and Phrases**
  - $a = \pi d^2 / 4$, area of the orifice and pipe
  - $A = \pi D^2 / 4$, area of the tank
  - $E = (L/d)\, Re_x^{-1} = (L\,\nu)/\, d^2 \sqrt{2\ g\ h}$
  - $h_\sigma = \sigma /(\rho\, g\, r)$, equivalent hydrostatic head of the surface tension-induced pressure
  - $V_a = Q\,/\,a$, area-averaged velocity of the outflow, known only if Q is known
  - $V_T = \sqrt{2\, g\, h}$, Torricelli velocity, considered external when h is a known, independent variable

  - $Re \;=\; V_a\, d\,/\nu$, the most commonly encountered version of a pipe Reynolds number
  - $Re_x \;=\; V_T\, d\,/\nu$, the external Reynolds number used frequently here
  - basis set of nondimensional variables, calculated by the codes linked in Sec. 8.
  - entry length, the distance downstream from the orifice over which the flow becomes independent of distance, also said to be fully-developed
  - hydrostatic head, the height of a fluid at rest that gives a specific pressure
  - laminar flow implies a steady, one-dimensional velocity throughout the pipe, and a simple relationship between frictional drag and transport
  - turbulent flow implies unsteady, three-dimensional, and dispersive velocity, with one consequence being greater drag than in an otherwise comparable laminar flow
  - VPlist, variables and parameters in a list that defines a problem.

- **Glossary of Models**
  - Model 0, Q_0, a zero-order model of orifice transport, $Q_0 \;=\; a\, V_T$, Eq. (11)
  - Q_1 the elementary model of orifice transport, $Q_1 \;=\; C\, Q_0$, Eq. (14)
  - Q_2 as Q_1 including surface tension, $Q_2 \;=\; Q_1 \sqrt{1 - h_\sigma\,/\,h}$, Eq. (22)
  - Q_3 Poiseuille's solution for viscous, laminar flow through a pipe, Eq. (35)
  - Q_4 a solvable, hybrid model that includes Q_1, Q_2 and Q_3, Eq. (40)
  - Q_4' Model 4, but omitting surface tension, implicitly via Eq. (41)
  - Q_5 as Q_4 with a correction for turbulent flow, Eq. (62)
  - Q_5' as Q_5 but omitting surface tension.

2 A family of experiments

This study is built around a dataset generated during a series of low-tech, tabletop experiments that can be readily reproduced and extended. The tank was a polypropylene, semi-transparent laboratory beaker into which holes of known diameter, orifices, were drilled carefully a few centimeters above the bottom. For most experiments, there was a polypropylene tube connected directly to the orifice (very much like the cover page illustration) and kept horizontal. The length of this 'pipe' could be easily cut down, including to effectively zero. The fluid was ordinary tap water, whose viscosity, μ, and surface tension, σ, are well-known functions of temperature.

2.1 Parameter space of this apparatus

The immediate aim of the experiments was to document the time to drain (or more generally the draining rate) over the accessible range of the independent parameters that define this family of experiments:

- orifice or pipe diameter, $3 \leq d \leq 6.5$ mm,
- pipe length, $0 \leq L \leq 1.5$ m,
- fluid viscosity, $0.6 \times 10^{-3} \leq \mu \leq 1.5 \times 10^{-3}$ Pa s, depending upon water temperature,
- surface height, $0 \leq h \leq 0.15$ m.

Other relevant parameters that were not varied in these experiments:

- σ = 75 $\times 10^{-3}$ N m^{-1}, surface tension of fresh water at room temperature,
- $D = 0.185$ m, the tank diameter,
- $g = 9.8$ m s^{-2}, acceleration of gravity, and
- $\rho = 998$ kg m^{-3}, the nominal density of fresh water.

This apparatus is intermediate in scale — it is much larger than the scales of biological, capillary flows, and it is much smaller than the scales of a continent-spanning natural gas pipeline. The resulting flows may be characterized as low speed, low energy, and mostly *laminar*. However, in the higher range of Reynolds numbers accessed here there are fairly clear signs of weakly *turbulent* flow discussed in Sec. 7.

2.2 Making observations

Experiments began by filling the beaker with water having a measured temperature ranging from very hot to almost freezing. Once the fluid had settled (observed with dye), the orifice or pipe was uncovered, and the water allowed to drain freely. The beaker had a volumetric scale, and the elapsed time, t_i was recorded as the surface descended by discrete intervals of volume, W_i = (4.5, 4.0, 3.5 ... 0.5) $\times$ 10^{-3} m^3, and thus the direct observation was of (W_i, t_i) at about 8 - 12 times. Most experiments were complete within twenty minutes. The surface height in meters referenced to the orifice center (where $W = W_0$) is easily calculated by

$$h_i = (W_i(t) - W_0)/A, \tag{1}$$

where $A = \pi D^2/4$ is the surface area of the tank. A closely related variable is the outflow volume transport, Q, estimated by first-differencing the discrete, observed volumes and times,

$$Q_i \approx -\frac{W_{i+1} - W_i}{t_{i+1} - t_i}. \tag{2}$$

The sign convention ensures that the estimated outflow $Q > 0$, to aid visualization. The h that goes along with (2) is the midpoint average $\bar{h_i} = (h_{i+1} + h_i)/2$, and similarly for the time. From here on the subscripts and accents are dropped, and h, t and Q are treated as if continuous.

The measurements were found to be nearly repeatable, with random errors in the time estimated to be no more than 2 seconds. These small errors do not accumulate during the course of an experiment, and may be suppressed by a three-point smoothing of the observed times (applied in only a few cases). The largest source of systematic error comes from defining the inside diameter of the tube, d. For each tube, the diameter was measured by feeler gauges and often found to be slightly different, by as much as 0.1 mm, from the diameter indicated by the manufacturer (not a problem for the orifice diameter, which is well-controlled). Uncertainty in d is magnified by the sensitive dependence upon d that characterizes several aspects of tank-draining, e.g., outflow transport $Q \propto d^2$. The net uncertainty on any one estimate of Q is roughly $\pm 10\%$ of the magnitude.

These measurements were neither highly resolved nor highly precise. That is less than ideal, of course, but it is not disqualifying because the case-to-case variation with changing parameters is considerably greater than are the random or systematic errors that compromise the value of any one realization. Thus, we can with some confidence explore the parameter dependence of h and Q over a family of experiments. Dimensional analysis is especially useful in this context.

2.3 Inferences from the first experiments

The first set of experiments used room temperature water, $T = 20\,^\circ C$, and no pipe (orifice-only) and so L was effectively zero. The orifice diameter was $d = 3, 4.5$ or 6.5 mm. The surface height $h(t)$, here regarded as the dependent variable, decreased smoothly in time, Fig. 2. Notice that the variation of h with d — the signal we are after — is considerably greater than are the likely experimental errors noted above.

After several trials with dimensional analysis, it became evident that the usual tank-draining problem — *How long to drain this tank?* — was best approached indirectly.

The first issue is that in some experiments the tank never actually drained in the strong sense $h \to 0$. At the beginning of an experiment, when h was largest, the outflow makes a continuous stream, or jet, of water that traces out what appears to be a ballistic trajectory. As h becomes small, less than a few centimeters, the outflow may slow significantly and then stop when h was still

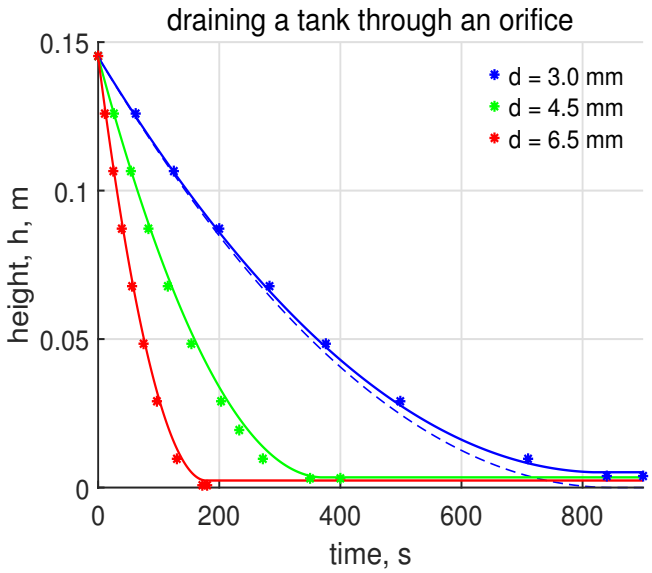

Figure 2: Surface height, $h(t)$, from three orifice-only experiments that had different orifice diameters, the red, green and blue dots. The trajectories $h(t)$ are very nearly parabolic, a rapid decrease at the beginning that markedly slows as h decreases. These experiments show that a modest increase in orifice diameter resulted in a substantially faster decrease of the surface height. Notice that the surface height stops descending short of zero. The dashed blue line is the ideal fluid Model 1 solution for the case $d = 3.0$ mm. Model 1 ignores surface tension and so this solution drains to zero. The solid lines are computed by Model 2 which acknowledges surface tension (coming in Sec. 4).

roughly 1 cm above the center of the orifice. The fluid then forms an outward protruding cap or bubble that is evidently held in place by surface tension and adhesion to the beaker. Surface dynamics of this kind is central to many small scale fluid problems and is discussed briefly in Sec. 4.

A second issue is that a response to the original problem (how long?) implies the construction of a model relationship for the time-dependent height, $h(t)$. Consider the simplest possible version of this: draining an ideal fluid (zero surface tension and zero viscosity) through an orifice (zero pipe length). In Sec. 3.1 below we will examine a very simple and effective model for this problem. But suppose we do not know the model — we can still make progress via dimensional analysis provided only that we can compile a list of the variables and parameters that would appear in an appropriate model.

- A VPlist for the surface height of an ideal fluid draining through an orifice:

1. surface height, $h \doteq [\,0 \quad 1 \quad 0\,]$, the dependent variable,
2. time, $t \doteq [\,0 \quad 0 \quad 1\,]$, an independent variable,
3. initial height, $h_0 \doteq [\,0 \quad 1 \quad 0\,]$, a parameter,
4. diameter of the orifice, $d \doteq [\,0 \quad 1 \quad 0\,]$, a parameter,
5. diameter of the tank, $D \doteq [\,0 \quad 1 \quad 0\,]$, a parameter,
6. acceleration of gravity, $g \doteq [\,0 \quad 1 \quad -2\,]$, a parameter.

If this list is indeed complete, then we can assert that there is, in principle, a relationship

$$h = F(t, h_0, d, D, g). \tag{3}$$

The function F is unknown, and it is, of course, crucial. Absent an appropriate model, experimental data are required to show what F might be.

Now consider the nondimensional counterpart of (3). This VPlist has six members having two fundamental units, length and time. Our rule-of-thumb guidance to the number of required nondimensional variables (discussed in the main text, Sec. 3) indicates that a basis set for this VPlist (notice that it is not *the* basis set) will contain six minus two = four nondimensional variables. As one possibility, the nondimensional version of (3) could be

$$\frac{h}{h_0} \;=\; F(t\sqrt{g/h_0},\; \frac{d}{D}, \frac{h_0}{D}), \tag{4}$$

which recycles the symbol F to represent an unknown function. The dependent variable is h in units that are natural to the problem, h_0.[5] Similarly, the orifice diameter d is in units of the tank diameter, D, and time is measured by the time required to free-fall a distance h_0 while accelerating at g. In place of five dimensional variables in the F of Eq. (3), there are just three nondimensional variables in the F of (4). That is a very useful, practical result from dimensional analysis, but it is not a finished result until F can be specified.

Dealing with three independent nondimensional variables is certainly possible (many real-life problems are far more extensive), and yet (4) seems unduly cumbersome given how straightforward and spare this problem appears to be. It will often happen that the first try at a VPlist will have a broader scope than is desirable for the problem at hand — in this case, slow outflow due mainly to the property that $d \ll D$. How can we change the problem and the VPlist to reflect that qualification?

2.4 Changing the problem from h(t) to Q(h)

The surface height, h, is very important in what follows. Nevertheless, h may not be the best choice for the dependent variable. The reason, shown below, is that a model of $h(t)$ necessarily requires the time, t, and the tank diameter, D, as parameters.

Suppose instead that we seek a model of the volume transport, Q, of the outflowing water, Eq. (2). A key modeling assumption appropriate to this new problem is that Q depends only (or mainly) upon local conditions, and specifically the pressure difference across the orifice. As a corollary of this, the beaker diameter is large enough compared to the orifice that the beaker may be viewed as an infinite reservoir of water that is effectively at rest. D will then have a negligible effect upon the

[5] One could just as well say that h is measured by, divided by, scaled by, or nondimensionalized by h_0.

volume transport, though it will remain an essential parameter in any model that seeks to compute the time to drain, as in (4). Since $d << D$, the flow within the tank is very slow compared to the outflow velocity, and the acceleration of the water in the tank is negligible compared to g. The pressure $P(z)$ within the beaker is then given accurately by the hydrostatic pressure,

$$\frac{\partial P}{\partial z} = -\rho g, \tag{5}$$

and so

$$P(z) = \rho g (h - z) + P_{atm}, \tag{6}$$

where z is the vertical coordinate positive up and zero at the orifice, and ρ is the constant density of the fluid.[6] P_{atm} is the ambient, atmospheric pressure which varies insignificantly over the depth of the tank. The pressure difference across the orifice is, provisionally, just

$$\delta P_{orf} = \rho g h, \tag{7}$$

the hydrostatic pressure inside the tank at the depth of the orifice. The important variable of (7) is h; g and ρ are necessary to have the units of pressure, but are global constants in this family of experiments.

- A VPlist for the pressure-driven volume outflow of an ideal fluid through an orifice:

1. outflow volume transport, $Q \doteq$ [0 3 -1], the dependent variable,
2. surface height above the orifice, $h \doteq$ [0 1 0], the independent variable,
3. diameter of the orifice, $d \doteq$ [0 1 0], a parameter,
4. acceleration of gravity, $g \doteq$ [0 1 -2], a parameter,
5. density of the fluid, $\rho \doteq$ [1 -3 0], a parameter.

A quick calculation of a null space basis from this VPlist leads to

$$\frac{Q}{d^2 \sqrt{g h}} = F(\frac{h}{d}), \tag{8}$$

which has only one independent, nondimensional variable. This represents major progress from Eq. (4). Dimensional analysis has gotten us as far as this very efficient representation of Q. To go further and specify the function F will require physics and/or observations.

[6] To here this is the usual, elementary tank-draining problem. An advanced treatment is by D'Alessio, S., 2021, Torricelli's law revisited. European J. of Physics, 42 065808.

2.5 Torricelli velocity and a zero-order model

Eq. (8) could be used as is, but it is helpful to modify it superficially by introducing two O(1) numerical factors into the left-side denominator,

$$\frac{Q}{\frac{\pi}{4}\,d^2\,\sqrt{2\,g\,h}} \;=\; F(\frac{h}{d}). \tag{9}$$

A factor $\pi/4$ multiplies d^2 to give the area of the orifice,

$$a \;=\; \frac{\pi}{4}\,d^2.$$

A factor $\sqrt{2}$ multiplies $\sqrt{g\,h}$. The latter follows from the conservation of energy of a particle falling a distance h under gravity and acquiring kinetic energy $\propto\; V^2/2 \;=\; g\,h$. The velocity of an energy-conserving free fall is then

$$\boxed{V_T \;=\; \sqrt{2\,g\,h}} \tag{10}$$

dubbed the Torricelli velocity.[7]

The product of V_T and the area of the orifice makes a sensible, physically-based natural scale for the outflow transport,

$$\boxed{Q_0 \;=\; a\,V_T \;=\; a\,\sqrt{2\,g\,h}} \tag{11}$$

In the main text[3] this sort of thing was called a zero-order model, here shortened to Model 0 and for the transport, Q_0. If h is regarded as a known, independent variable, then Q_0 is known. This Q_0 will be used throughout this study to nondimensionalize Q, and e.g., Eq. (9) becomes

$$\frac{Q}{Q_0} \;=\; F(\frac{h}{d}). \tag{12}$$

A key, implicit assumption of (12) is that the geometric properties of the tank are represented by the single nondimensional variable $h\,/\,d$. In the orifice-only cases, the actual (dimensional) transport Q comes close to Q_0 so that $F(h/d)$ is just slightly less than 1. In other cases, especially those involving long and narrow pipes that will be treated in Secs. 5 - 7, Q is much less than Q_0 and so $F \;\ll\; 1$.

---

[7] Evangelista Torricelli, 1608 - 1647, was a student and then a close associate of Galileo Galilei. His experimental investigations on a draining tank showed that the outflowing jet described a ballistic trajectory like that of a solid particle. Torricelli's research on vacuum and barometers led to an appreciation for atmospheric pressure and the crucial insight that 'we live submerged at the bottom of an ocean of air'. This included that horizontal variations of pressure were the immediate cause of winds, the start of dynamic meteorology. A derived unit of pressure, the torr, is in his honor and is 1 torr = 1 mmHg (nominal g) at 0 C. The torr is today used mainly in vacuum applications.

2.6 Summary to here and outlook

This investigation will proceed along three lines.

Experimental observations are the essential starting point. Experiments will document Q along with the relevant fluid and tank parameters.

Dimensional Analysis provides an efficient framework for analyzing the observations by defining the minimum number of independent variables, e.g., Eq. (4) vs. (3).

Theory and Modeling coming in later sections will seek to illuminate and reproduce the function F of relations like (12).

2.7 Problems

- In Sec. 2.4 the tank-draining problem was changed from modeling $h(t)$ to modeling $Q(h)$. How and why did this change the status of the variable h?
- What dimensional variables or parameters have gone missing from Eq. (8) compared with Eq. (4), and on what basis?

3 An elementary (and very successful) Model 1

3.1 A data-driven Model 1

We know all of the individual terms of (12), including most importantly Q from the observations of Fig. 2 and Eq. (2). What we do not know is the function F, and dimensional analysis alone can not tell us anything more. To find out what F looks like, let's evaluate (12) by plotting the nondimensional transport Q/Q_0 against h/d, Fig. 3, left.

It appears that $F(h/d)$ exhibits two regimes.

- At smaller values of h/d (small compared to what?), the normalized volume transport goes to zero as h/d goes to zero, and indeed the transport may vanish while h is still appreciable. This is directly related to the surface tension-induced bubble noted above, and discussed further in Sec. 4.
- At larger values of h/d, roughly $h/d > 10$, which includes most of the experimental data, the normalized volume transport is quasi-independent of h/d. In other words, at larger values of h/d, the function $F(h/d)$ is nearly a nondimensional constant, call it C.

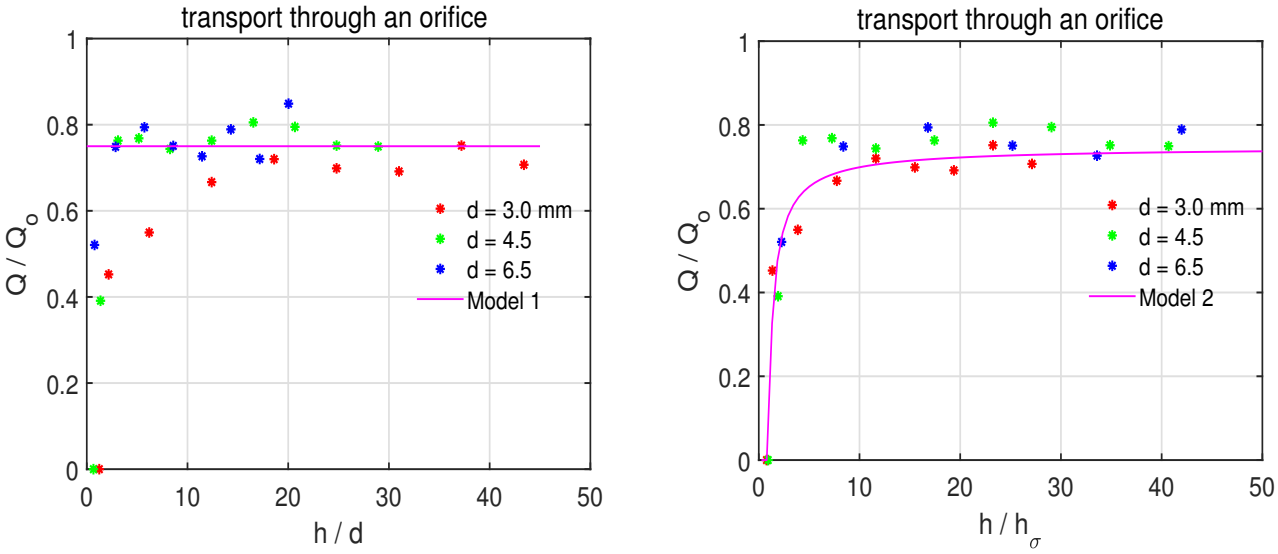

Figure 3: **(left)** Observed volume transport from the orifice-only experiments of Fig. 2. The transport is nondimensionalized consistent with Eq. (12). It is argued that there are two regimes evident here. At small h/d, the nondimensional transport decreases as h/d goes to zero. At larger h/d, the transport is approximately independent of h/d, the magenta line which is Model 1, Sec. 3.2. **(right)** This is the same data shown at left, except that the independent variable is h/h_σ, where h_σ is the pressure head due to surface tension, Eq. (19). This magenta line comes from Model 2 described in Sec. 4.3.

Dimensional analysis does not evaluate C, but the data of Fig. 3 indicate that

$$\frac{Q}{Q_0} \;=\; C \;=\; 0.77 \;\pm 0.03 \tag{13}$$

is a reasonable first approximation for these three experiments. It bears some emphasis that the step from Eq. (12) to (13) is

- empirical — C is calibrated using these observations, and 0.77 may not be appropriate to your apparatus or your fluid.
- contingent — Eq. (13) holds only for larger h/d.

The parameter C is called the 'discharge coefficient', and a value in the range $0.6 < C < 0.8$ is expected for simple, square-edged orifices of the present sort.[8] The physical process that leads to a C that is slightly less than 1 in these experiments is not primarily friction (viscosity), as one might first guess, but rather inertial acceleration on the water approaching the orifice. The evidence for this is twofold. First, C varies only weakly with viscosity (temperature) in this family of experiments. Second, dye observations show that the flow into the orifice comes from the entire hemispherical

[8] A thoughtful discussion of C is by Savage, T., Porterfield, W. R. Penney and E. C. Clausen, The draining of a tank: A laboratory experiment in fluid mechanics. ASEE Midwest Section Conference, 2021.

region inside the tank. The inflow to the orifice has to be accelerated, and some fraction of it also has to make a sharp 90 degree change in direction as it approaches and enters the orifice. Even modest fairing (rounding on the inside of the orifice) can ease this sharp change of direction and bring C close to 1.0. On this basis, the orifice flow process will be called 'inertial' to distinguish from viscous and surface tension phenomena coming in the next two sections.

3.2 Integrating to find h(t)

Given (13), a useful model of the outflow transport, dubbed Model 1, is just

$$Q_1 \;=\; C \times Q_0 \;=\; C\,\frac{\pi}{4}\,d^2\,\sqrt{2\,g\,h}. \tag{14}$$

From here and given Eqs. (1) and (2), it is straightforward to write an ODE for $h(\,t\,)$,

$$\frac{d\,h}{d\,t} \;=\; -\,\frac{Q_1}{A} \;=\; -\,C\frac{d^2}{D^2}\,\sqrt{2\,g\,h} \tag{15}$$

that may be integrated to find

$$h(t) \;=\; \left(\sqrt{h_0} \;-\; \left(0.5\,C\,(\frac{d}{D})^2\,\sqrt{2\,g}\right)\,t\right)^2. \tag{16}$$

This defines a parabolic $h(t)$ (second degree in time) that, overall, bears a striking resemblance to the experimental data shown in Fig. 2 (the dashed, blue line compared to the blue dots). In all cases the surface height decreases rapidly at the start of an experiment and then slows markedly as $h \to 0$. When a pipe is present, wall friction due to either or both laminar viscous flow and turbulent flow can change the rate quite a lot, but this pattern remains a characteristic of the $\sqrt{g\,h}$-dependence of a gravity-driven outflow transport, Eq. (11).

3.3 Summary

Model 1 makes a very good start, and for not much effort. In particular, it shows that the surface of a tank that is draining due to a gravity-driven outflow will fall (comparatively) rapidly at the start of an experiment, and then slow markedly as the pressure difference across the orifice decreases.

Model 1 leaves some room for improvement. Eq. (14) departs from the observations at smaller values of h/d, roughly $h/d < 8$, in that it indicates constant $Q_1/Q_0 \;=\; C$ all the way to h = 0. On the other hand, the observations indicate that the (nondimensional) transport slows for small h/d, and then may stop altogether before the tank is completely drained, Fig. 3. This is not a measurement

artifact. The corresponding error in Eq. (16) is that the predicted h goes to zero. Evidently something is missing from (14) and (16).

3.4 Problems

- The orifice-only outflow Model 1, Eq. (14), can be rewritten as an ordinary differential equation $dh/dt = F(h, g, d, D)$, Eq. (15). Integrate this equation given an initial value $h(t = 0) = h_0$ to find Eq. (16).[9] How does this solution compare with the expectations from dimensional analysis, Eq. (3)?

- It has been noted that a parabolic in time trajectory $h(t)$ is characteristic of a gravity-driven outflow for which $Q \propto \sqrt{g\,h}$. Suppose instead that the outflow transport is (for some reason) linear in h, i.e., $Q \propto g\,h$. What is the trajectory $h(t)$ in that case?

- Imagine that the water tank is closed on top, so that the air pressure above the water surface can be altered by a controllable air pump. What additional air pressure (above atmospheric) would be required to yield a constant Q, until the tank drains and uncovers the orifice?

- It was claimed in Sec. 3.2 that the discharge coefficient C for the present experiments is effectively a constant because it is a result of inertial (accelerated) flow. This depends upon the geometry of the orifice which doesn't change appreciably from one experiment to the next. However, this is not a universal law. Consider that the fluid being drained is honey, which has a viscosity that is roughly 5,000 times that of water. Qualitatively, how would this increased viscosity affect the magnitude of the transport? Does this imply that C must, in general, depend upon ν, even while the claim made here is that viscosity is not important for *these* orifice-only experiments? This example illustrates why nearly every claim made here has to be qualified with the tedious phrase 'for these experiments' meaning that the fluid is something like water and that the geometric dimensions are not too far from those listed in Sec. 2.1.

4 Surface tension reduces transport in the small h/d regime

It was noted above that the outflow may come to a stop before $h \to 0$. In that state the outflow appears to be blocked by a flattened bubble of fluid that caps the orifice. The inference is that surface tension has overcome the hydrostatic pressure difference (7) that would otherwise accelerate fluid through the orifice. This is not a large effect on the scales that characterize the parameter range of

[9] An excellent tutorial for this problem is https://www.youtube.com/watch?v=iKDdInE7wqE.

these experiments, i.e., the d, h, g, etc. of Sec. 2.1. However, this effect is systematic and interesting on its own merits.[10]

4.1 Why do fluids exhibit surface tension?

Surface tension is a fundamental characteristic of a fluid that has an appealing microscale explanation. The individual molecules of a fluid are free to move and jostle around but they are also cohesive, in that fluid molecules exert an intermolecular attraction (hydrogen bonding in water) that acts to clump fluid molecules together. When clumped together, water molecules are in a lower energy state than if they were separated and moving independently (as do the molecules that make up a gas). Where there is a free surface that exposes the fluid to some other, less attractive material — if water, then air — the molecules that are immediately on the free surface will not have fluid molecules on all sides, and so will be in a slightly elevated energy state; think of attracting particles that have been pulled apart. The existence of a free surface thus implies some potential energy that may be characterized as a thermodynamic property called surface tension, denoted here by σ. Surface tension can be viewed as either an energy per unit area, in SI units, Joules per meter squared, and so $\sigma \doteq [\,1\ 0\ -2\,]$, or, as a force per unit length, Newtons per meter, and having the same fundamental dimensions. Both interpretations are useful.

Water has a fairly high surface tension,

$$\sigma \approx 75 \times 10^{-3}\ \mathrm{J\ m^{-2}} = \mathrm{N\ m^{-1}},$$

compared to most other familiar fluids, e.g., isopropyl alcohol, for which $\sigma \approx 20 \times 10^{-3}$ N m^{-1}. A familiar consequence is that water tends to form into spherical drops (absent some other influence such as air drag on a falling drop) that minimize surface area, and thus the surface energy for a given volume. Surface tension, viewed as a force per unit length, acts as a membrane under tension that maintains a spherical shape. A consequence is that there is an elevated pressure inside a water drop that is proportional to σ times the Laplace curvature of the surface. The curvature of a sphere is $2/r$, with r the radius; the pressure inside a spherical water drop is thus

$$P_{drop} = 2\,\sigma/r \tag{17}$$

higher than the ambient pressure.[10]

[10] Surface physics is vitally important for microfluidic (very small scale) devices. An excellent introduction to surface tension is https://en.wikipedia.org/wiki/Surface_tension Also highly recommended and more advanced is https://web.mit.edu/1.63/www/Lec-notes/Surfacetension/Lecture1.pdf

4.2 Surface tension and pressure within a cylindrical jet of water

A vigorous outflow through a round orifice produces a cylindrical jet of water, cover page.[11] The surface curvature of a cylinder is half that of a sphere having the same radius and thus the surface-tension induced pressure within the jet is estimated to be half that of the corresponding sphere, i.e.,

$$P_\sigma \;=\; \frac{\sigma}{r}. \tag{18}$$

The pressure P_σ can be expressed as an equivalent hydrostatic pressure head,

$$\boxed{h_\sigma \;= \frac{\sigma}{\rho\, g\, r},} \tag{19}$$

which is constant for a given experiment. For the surface tension of water and if r is a few millimeters, then h_σ is O(1) cm.

From this discussion it seems plausible that the outflow transport might be dependent upon h_σ which suggests a revised form of Eq. (12),

$$\frac{Q}{Q_0} \;=\; F(\frac{h}{h_\sigma}). \tag{20}$$

When the data of Fig. 3 are nondimensionalized in this way (right panel), the normalized transport is found to decrease significantly when $h/h_\sigma < 5$, and vanishes at roughly $h/h_\sigma \leq 1$. This is consistent with the notion that the surface-tension induced pressure inhibits the outflow, an effect which is especially noticeable for the smaller diameter orifices and pipes considered here.

4.3 Model 2 includes a first-order effect of surface tension

This, in turn, suggests a revised model for orifice transport. Model 1, Eq. (14), amounts to taking the pressure outside the tank to be zero. Now we understand that there is a slightly higher pressure required to overcome the surface-tension induced pressure acting upon the jet. With that in mind, revise the Torricelli velocity to

$$V_{T\,\sigma} \;=\; \sqrt{2\,g\,(h - h_\sigma)}, \tag{21}$$

and define a Model 2 for the transport,

$$\boxed{Q_2 \;=\; C\,\frac{\pi}{4}\,d^2\,\sqrt{2\,g\,(h \;-\; h_\sigma)}} \tag{22}$$

[11] A parcel of fluid within the free-falling jet has a certain horizontal velocity, $dX\,/\,dt \;=\; V_o \;\approx\; V_T$, that is nearly conserved, and it is accelerated downward by gravity at a rate $d^2\,Y\,/\,dt^2 \;=\; -\,g$. A parcel, and thus the jet, traces a parabolic (ballistic) trajectory, $X \;\propto\; (V_o\,/\sqrt{g})\,\sqrt{-Y}$.

that is valid only for $h \geq h_\sigma$. This may be solved for

$$h(t) = h_\sigma + \left(\sqrt{h_0 - h_\sigma} - \left(0.5\, C\, (\frac{d}{D})^2 \sqrt{2\, g} \right) t \right)^2, \tag{23}$$

the solid red line of Fig. 2. Compared with Model 1 that ignored surface tension (the dashed red line), the new Model 2 solution for $h(t)$ is only slightly different overall from that of Model 1, but it does include the qualitative feature that h asymptotes to h_σ, rather than to zero, as does the solution of Model 1.

4.4 Summary

A more sensitive test of Model 2 comes from differentiating the solution (23) and evaluating $Q_2/Q_0 = F(h/h_\sigma)$, the magenta line of Fig. 3. This shows a slowing of the outflow as h/h_σ falls below about 5, and stopping altogether at about $h = h_\sigma$. These are consistent with the observations, and suggest that this first-order treatment of surface tension makes a small but useful step toward a realistic model.[12]

The first-order treatment of surface tension reflected in Eq. (21) is as far as this study will go regarding surface tension *per se*. This result will be incorporated into Models 4 and 5 developed in Secs. 6 and 7. Until then, surface tension will be set aside in order to focus attention on the viscous effects that can greatly modify the outflow transport through a pipe.

4.5 Problems

- The left and right sides of Fig. 3 give us a chance to compare two versions of a nondimensional format, $F(h/d)$ vs. $F(h/h_\sigma)$ (recall that F merely holds a place for an unspecified function). Which is the better nondimensional independent variable, h/d, or h/h_σ? What criteria could we deploy to decide this? Three suggestions: First, simplicity or transparency are always desirable, but probably not decisive. Second, if one version produces a more convincing collapse of the data toward a single curve, then that would surely count in its favor. Third, which of the inferred relations $F(h/d)$ and $F(h/h_\sigma)$ has a better-motivated, quantitative physical interpretation? Can

[12] The present treatment of surface tension overlooks a detail (within a detail). As h approaches h_σ, the outflow slows markedly, and then begins to dribble down the side of the tank: a weak outflow continues, but there is no more ballistic jet. After a short time, the dribbling stops and the orifice becomes capped over, as described above. The cap has some curvature but not so much as a sphere: $P_{\sigma-cap} \approx \sigma \,/\, r$ seems plausible for the blocked outflow. Also ignored here is the wetting properties of the solid substrate: polypropylene, does it attract or repel water? A single stage surface tension effect estimated by Eq. (22) is perhaps a fortuitous approximation. For more on these phenomena, see Ferrand, J., L. Favreau, S. Joubaud and E. Freyssingeas, 2016, Wetting effect on Torricelli's law, Phys. Rev. Lett., 117, 248001 - 248005.

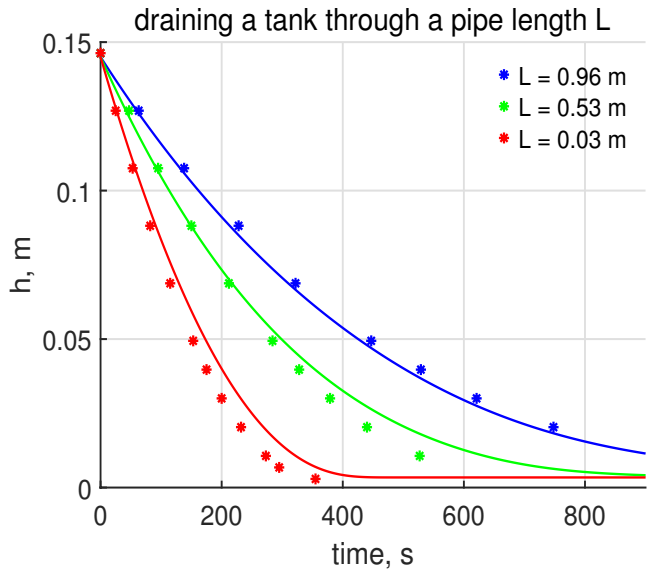

Figure 4: Surface height, $h(t)$, from three experiments in which the water was drained through pipes that had diameter $d = 4.7$ mm and one of three lengths, $L = 0.96$ m, 0.53 m, or 0.03 m, almost an orifice. The solid lines are calculations made by Model 4 discussed in Sec. 6.

you show that

$$\frac{h}{h_\sigma} \propto \frac{hydrostatic\,pressure}{surface\,tension\,pressure}.$$

This ratio of gravitational to surface tension pressure is often called a Bond or Eotvos number.

- Using dimensional analysis, show that the pressure anomaly inside a cylindrical jet of radius r is as given by Eq. (18), $P_\sigma = \sigma / r$ up to an unknown factor (happens to be 1). Two hints: for surface tension, $\sigma \doteq [1\ 0\ -2]$ and pressure, $P \doteq [1\ -1\ -2]$. Can you go from here to the equivalent height of a hydrostatic pressure and Eq. (19)?

5 Outflow through an orifice and a pipe, starting with observations

If the outflow must pass through a pipe, as on the cover page, it is expected that the volume transport will be lessened by drag (friction) between the moving water and the walls of the pipe. A few experiments show this effect clearly; for a given fluid (water at room temperature) and a given diameter of the pipe and orifice, the tank drains considerably more slowly when the pipe is longer, Fig. 4. By changing the temperature of the water, and thus the viscosity of the water, it is evident that warmer water (smaller viscosity) drains somewhat faster than does colder water, Fig. 5. The qualitative sense of these viscous effects is not surprising. To go beyond that and make a model, we have to define the magnitude of viscous effects. How can we organize the experimental data to this end?

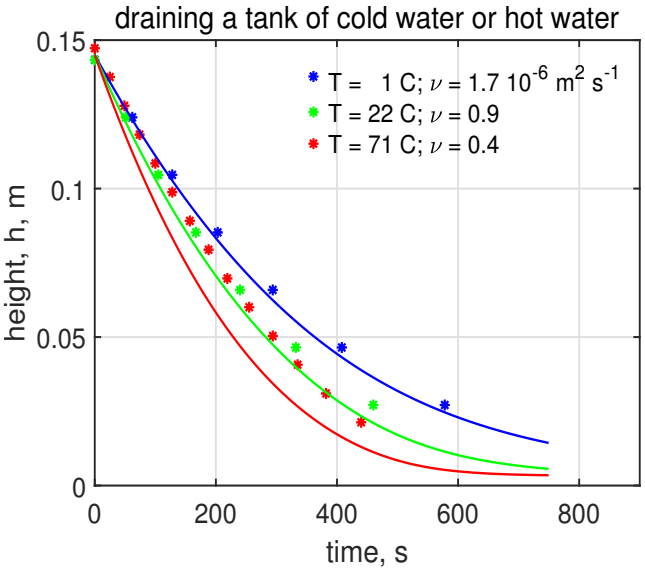

Figure 5: Surface height, $h(t)$, from three experiments that had pipe diameter and length in common, $d = 4.7$ mm and $L = 0.64$ m and thus $L/d \approx 140$. They differed by the temperature of the water, from nearly freezing (blue dots) to very hot (red dots). As a consequence, the kinematic viscosity, ν (= μ/ρ), varied by roughly a factor four. The warmest water (red dots) which had the smallest viscosity, drained considerably faster than did the cold water (not surprising), but, notice that it drained only slightly faster than did the room temperature water (green dots). This hints at something important coming in Sec. 7.2

As a guide, let's look for the relationship between the outflow transport and the (presumed) relevant variables under the assumption that the outflow transport is dependent only upon the local conditions at the orifice and the pipe (note that surface tension is omitted for now).

- A VPlist for pressure-driven outflow of water through an orifice and a pipe: (24)

1. outflow volume transport, $Q \doteq$ [0 3 -1], the dependent variable,
2. diameter of the orifice, $d \doteq$ [0 1 0], a parameter,
3. hydrostatic pressure head at the orifice, $gh \doteq$ [0 2 -2], an independent variable,
4. kinematic viscosity of the water, $\nu \doteq$ [0 2 -1], a parameter,
5. length of the pipe, $L \doteq$ [0 1 0], a parameter.

Three nondimensional variables are expected, and for this (arbitrary) ordering of the VPlist, the algorithm returns

$$\frac{Q}{L\nu} = F(\frac{d}{L}, \frac{L^2\, gh}{\nu^2}). \tag{25}$$

This is correct mathematically, i.e., it is a basis set of nondimensional variables for this VPlist. However, the important scale that normalizes the transport, $L\nu$, seems oddly out of place here. ($L\nu$ will arise again later in a context where it will make sense.) Use instead the zero-order model defined by Eq. (11), $Q_0 = \frac{\pi}{4} d^2 \sqrt{2gh}$, which presumes that inertial (rather than viscous dynamics) are dominant. This is a reminder that the purely formal method of dimensional analysis may not provide physical sense; that is a judgment and task left for us. After some reorganizing of the variables in (25) there follows an important relationship:

$$\boxed{\frac{Q}{Q_0} = F\left(\frac{L}{d}, \frac{V_T\, d}{\nu}\right)} \tag{26}$$

The left side of (26) is the now familiar nondimensional volume transport. The unknown function F on the right-hand side depends upon two nondimensional, independent variables. The first independent variable, $L\,/\,d$, is an aspect ratio, and is a straightforward reply to 'how long is this pipe?' given in natural units. In these experiments, L/d is in the range 0 - 500. The second nondimensional variable on the right side of (26) is less obvious.

5.1 Reynolds numbers, external and internal, Re_x and Re

The second independent variable

$$\text{external Reynolds number,} \quad \boxed{Re_x \;=\; \frac{V_T\, d}{\nu}} \tag{27}$$

has the form of a

$$\boxed{Reynolds\ number \;\propto\; \frac{velocity\ scale \times length\ scale}{kinematic\ viscosity}} \tag{28}$$

This ratio is important in many contexts, and Reynolds numbers come in correspondingly many versions.[13] The terms of (27) are:

- ν**, kinematic viscosity**, is straightforward when it is regarded as a fluid property, the usual intent of the Navier-Stokes equations.
- V_T**, a velocity scale** (a speed) is usually clear. In Eq. (28) the velocity is the Torricelli velocity, $V_T \;=\; \sqrt{2\,g\,h}$, which may be evaluated *a priori*, before a solution is known, presuming that h is observed or otherwise known. For that reason the Reynolds number (27) is said to be an 'external' Reynolds number. This Re_x is different from the much more often encountered

$$\text{internal Reynolds number,} \quad \boxed{Re \;=\; \frac{V_a\, d}{\nu}, \quad \text{where} \;\; V_a \;=\; \frac{Q}{a}} \tag{29}$$

The velocity V_a is the area-averaged velocity in the pipe and is known only after we know Q and so Re of Eq. (29) is said to be 'internal'. The link between these two Reynolds numbers is

$$\boxed{Re \;=\; Re_x\,\frac{Q}{Q_0}} \tag{30}$$

and hence Re will be somewhat smaller numerically than is Re_x. The internal Reynolds number will be used extensively in Sec. 7 when this analysis makes connection with the extensive historical literature on pipe flows.

[13] An excellent discussion of the Reynolds number including an interesting history is https://en.wikipedia.org/wiki/Reynoldsnumber

- L**, a length scale,** here taken to be the pipe diameter, d. The length scale is often the least obvious term in a Reynolds number. A conventional (though not altogether convincing) way to develop an interpretation of the length scale comes from a scaling analysis of the Navier-Stokes momentum equation,

$$\frac{\partial \mathbf{V}}{\partial t} \; + \; (\mathbf{V} \cdot \nabla)\, \mathbf{V} \;\; = \;\; - \nabla P/\rho \; + \; \nu \nabla^2 \mathbf{V} \; + \; \mathbf{g}. \tag{31}$$

  The goal is to compare the magnitude of the viscous term (second term on the right) to the inertial, acceleration term (second term on the left). Let V be the velocity scale, an upper bound on the magnitude of the fluid velocity expected in the problem. The kinematic viscosity ν can remain as is. The key is to identify a length scale, X, over which this velocity varies by O(1) so that, say for the x direction,

$$\frac{\partial V}{\partial x} \; \propto \; \frac{V}{X} \quad \text{and} \quad \nabla^2 \mathbf{V} \; \propto \; \frac{V}{X^2}.$$

  Under the assumption that a single length scale X is appropriate to the spatial derivatives in both the inertial term and the Laplacian of the viscous term, then it is straightforward to estimate the ratio of the inertial term(s) and the viscous term;

$$\frac{inertial}{viscous} \; \propto \; \frac{(\mathbf{V} \cdot \nabla)\, \mathbf{V}}{\nu \nabla^2 \mathbf{V}} \; \propto \; \frac{V^2/X}{\nu\, V/X^2} \; = \; \frac{V\, X}{\nu} \; = \; Re,$$

  a Reynolds number. In the case of pipe flow being considered here, the velocity varies with the radius, mainly, and thus the length scale X is identified as d.

Interpretation of Re_x: It is reassuring to find that a nondimensional number comes out to be O(1), as that implies a comparison of like things. There is no such comfort here; the numerical values of Re_x are O(10^4) (which is typical also for the Re of intermediate scale pipe flows). Taken literally, this would imply that the possible viscous force is much, much less than the inertial forces, and that some other term in the Navier-Stokes momentum balance must account for inertial accelerations (pressure gradient and/or time dependence). That is true, but nevertheless, these very large Re_x should not be interpreted to mean that viscosity may be omitted altogether (reminiscent of the air flow around a golf ball or a soccer ball, Sec. 4.5 of the main text).

What is the interpretation of Re_x for the present experiments? First, note that Re_x is the only independent variable of Eq. (26) holding ν; whatever viscous effects there are will be attributed to Re_x-dependence. Within this family of experiments, we can expect that a smaller value of Re_x should correspond to greater viscous effects, *viz.*, reduced transport.[14] The external Reynolds number thus appears to be a rough comparative measure of the ratio of inertial force (accelerations) to

[14] We usually think of a Reynolds number in association with viscous effects, but notice that viscosity happens to be in the denominator (it could have been otherwise). With that convention, smaller ν gives large Re, all else equal.

viscous force. Finally, given Eq. (30), the present Re_x can easily make contact with the vast literature on pipe flows that rely on the internal Reynolds number, Re (more on this in Sec. 7).

5.2 The function F for orifice plus viscous pipe flow

The relation (26) may be evaluated from the experimental data to provide a look at the function, $F(L/d,\ Re_x)$, Fig. 6. The coordinate system is three-dimensional since there is one nondimensional dependent variable, Q/Q_0, and two nondimensional independent variables, L/d, and Re_x, as noted above. Notice that surface tension has been excluded from these coordinates, but its effect is still present in some of the data.

A given experiment returns a handful of data points, all at the same L/d, and sampling a range of h, starting from h_0 and going to smaller h, in some experiments, to h_σ. The data points from a given experiment thus line up in strings that run parallel to the Re_x axis; larger Re_x is due to larger h. The nondimensional transport within a given experiment decreases smoothly with decreasing Re_x and thus with decreasing h. This is qualitatively consistent with the expectation that smaller Re_x (in the case of a single experiment because of small h) will generally correspond to a greater viscous effect.

The amplitude of the viscous effect, i.e., the decrease of the transport, depends also upon L/d. For the smallest values of L/d found on the left-most part of Fig. 6, this becomes the orifice-only result that $Q/Q_0 \ = \ C \ \approx \ 0.77$. In that limit, the Re_x-dependence vanishes: if L vanishes, then viscous effects effectively vanish as well. The converse is just as true; for a given Re_x, the nondimensional transport decreases significantly with increasing L/d; the decrease is especially strong at small values of L/d. In the range $L/d \ \approx \ 400$ and smaller Re_x found in the lower right corner of Fig. 6, the nondimensional transport is only about 25% of the orifice-only value, C.

5.3 Summary

Fig. 6 includes all of the data taken in these experiments (including data at small $h\,/\,h_\sigma$ that were likely affected by surface tension.) By visual inspection, it appears that the nondimensional coordinates of Eq. (26) will be a useful framework for the analysis of transport dependence upon h, L, d and ν insofar as the locus of data approximates a function $F(L/d, Re_x)$. Once we know this function, we can write an ODE for the surface height,

$$\frac{dh}{dt} \ = \ - A^{-1} Q_0 F(\, L/d,\ Re_x\,), \tag{32}$$

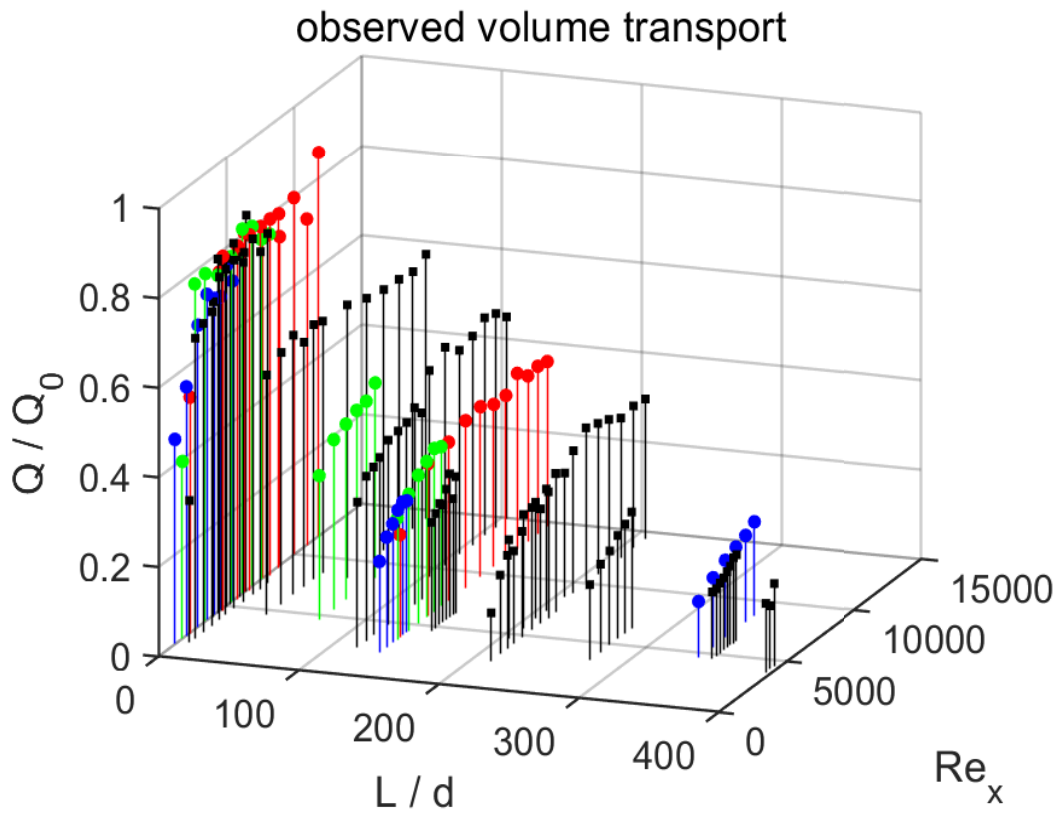

Figure 6: Observed nondimensional volume transport as a function of the pipe aspect ratio, L/d, and the external Reynolds number, $Re_x = V_T\, d\,/\,\nu$. There are 23 experiments shown here, each of which yields between five and 12 data points; 181 points in total. The data from a given experiment line up in a string that has a constant L/d, but a varying h. Each experiment thus samples a small range of Re_x. The red, green and blue dots are the data from the nine experiments of Figs. 2, 4 and 5. The black dots are from fourteen other, similar experiments. This is a rather dense and complex figure, but if you study it for just a minute you can envision that the locus of data points implies the existence of a two-dimensional surface $F(L/d,\ Re_x)$. A key objective of this study is to understand how such a surface arises and to use that understanding as a guide to model development (coming in Secs. 6 and 7). These data and a Matlab script to read and plot them are linked in Sec. 8.

a generalized version of Eq. (15). The Re_x in the argument of F above will include h. This will likely frustrate a separation of variables, but numerical solution should be fast and accurate.

To implement any solution, the function F has to be made portable. One could estimate an empirical fit to a dataset like Fig. 6, or, seek an appropriate model. The remainder of this appendix works toward the latter.

5.4 Problems

- There is no accounting for surface tension effects in the coordinate system of Fig. 6, and so it is questionable whether data that were likely affected by surface tension should be included. Where in Fig. 6 (at what L/d and Re_x) are these surface-tension-affected data?
- Can you find and then interpret the data that came from the three experiments with variable temperature shown in Fig. 5?
- Using the properties of a null space basis, recast Eq. (25) into the form preferred here, Eq. (26). The key step is choosing a scale for the dependent variable.

6 Models of viscous, laminar pipe flow

This section will develop models of laminar flow that are appropriate for the lower Re_x range of the parameter space sampled here, roughly $Re_x \leq 7000$. It is expected that at larger Re_x there will be a transition from laminar to turbulent flow with a consequence of larger wall stress (for a given Re_x) than would be predicted by a laminar flow model; much more on this in Sec. 7.

6.1 Poiseuille's solution for laminar flow, Model 3

For now, consider pipe flow alone, ignoring the necessity of a tank and orifice, and omitting surface tension. Suppose that the pressure at the ends of this horizontal pipe are known and that the pressure difference is δP_{pipe}. Additionally, assume that the flow is unchanging along the pipe, and said to be

fully developed.[15] In that case the pressure gradient, a force per unit volume, is

$$\frac{\partial P}{\partial x} \;=\; \frac{\delta P_{pipe}}{L},$$

and also uniform along the pipe. Given the pressure gradient, what is the volume transport through the pipe?

- A VPlist for the pressure-driven transport of a fully-developed, viscous pipe flow: (33)

1. volume transport, $Q \;\doteq\; [\,0 \quad 3 \quad -1\,]$, the dependent variable,
2. pressure gradient, $\partial P/\partial x \;\doteq\; [\,1 \quad -2 \quad -2\,]$, an independent variable,
3. radius of the pipe, $r \;\doteq\; [\,0 \quad 1 \quad 0\,]$, a parameter,
4. dynamic viscosity, $\mu \;\doteq\; [\,1 \quad -1 \quad -1\,]$, a parameter.

This is a subset of the VPlist that led to Eq. (26). In this VPlist there are four dimensional variables having three fundamental units, and hence there is just one nondimensional variable, the nondimensional transport, that must be a constant,

$$\frac{Q\,\mu}{r^4\;\partial P/\partial x} \;=\; constant. \tag{34}$$

The result (34) from dimensional analysis has the form of the famous and very useful Poiseuille solution for the transport of a laminar, fully-developed, viscous pipe flow,

$$\boxed{Q_3 \;= \frac{\pi}{8}\,\frac{r^4\;\delta P_{pipe}}{\mu\;L},} \tag{35}$$

also called the Hagen-Poiseuille solution.[16] This is taken to be Model 3. Two things to note: 1) the sensitive dependence of Q upon r, here $Q \;\propto\; r^4$ compared with $Q \;\propto\; r^2$ for an inviscid, inertial orifice flow of Sec. 3, and, 2) the transport is directly proportional to (is linear in) the pressure gradient and is inversely proportional to the viscosity. This seems physically plausible, but is *not*

[15] The strong acceleration of flow through the orifice and into the pipe is bound to cause some disturbance that may damp out with distance downstream. The distance downstream required to lose memory of the orifice is called the entry length; the equilibrated flow further downstream is said to be fully-developed. The effect of a finite entry length is likely to be increased drag overall. There is some evidence of that in this dataset, but it is small compared to the effects of turbulent flow taken up in Sec. 7.

[16] The dimensional analysis leading to (34) is standard textbook fare and is useful for now. However, its success in yielding the Poiseuille relation owes to a somewhat arbitrary choice in defining the variables of the VPlist (33) that will be discussed further in a problem at the end of Sec. 7.

always the case as will be seen in Sec. 7. Poiseuille's[17] solution for laminar pipe flow is closed, including the leading factor $\pi/8$ that is needed to calibrate the dimensional analysis result, (34).[18] After some rearrangement, the transport (35) can be rewritten in a nondimensional form using the zero-order model of Eq. (11) to scale the dependent variable,

$$\boxed{\frac{Q_3}{Q_0} \;=\; \frac{1}{64}\,(\frac{L}{d})^{-1}\,Re_x} \tag{36}$$

Under the conditions of its derivation, fully-developed laminar flow, the Poiseuille solution gives a very good account of experimental observations. Indeed, it works well enough that it may be used along with careful measurements to estimate fluid viscosity, μ. Does (35) suffice for the experimental configuration used here? We can learn a lot by plotting the Poiseuille solution in the coordinates of Fig. 6 (Fig. 7, upper right). This shows some promise in the range of smaller Re_x and larger L/d, which implies large viscous effects. But at larger Re_x and smaller L/d, the Poiseuille solution diverges, predicting transport that is much larger than the transport that could be accelerated through the orifice by the given pressure difference. The conclusion has to be that the Poiseuille solution taken alone, Eq. (35), Model 3, does not make a suitable model of the present system — tank, orifice, pipe, discharge into air. (No doubt M. Poiseuille could have told us as much, even without the hindsight of a fancy diagram.)

6.2 A hybrid Model 4 – Sig. Torricelli, say hello to M. Poiseuille

The fluid path from the tank to the open air can be envisioned in three parts: first, inertial (accelerated) flow from the tank into the orifice; second, viscous (and possibly turbulent) flow through a pipe; and third, escape into the open air and production of a free surface. Each of these has been discussed in isolation, and now we will seek to connect them to make a model of the system as a whole. The idea will be to ensure that the pressure is continuous from the tank to the open air, and that the transport is consistent with the pressure changes and is constant throughout.

Let the pressure across the orifice be $\rho\,g\,h \;-\; P_x$ where P_x is the unknown pressure post-orifice,

[17] Jean L. M. Poiseuille (1797 - 1869) was a French physiologist who pioneered the quantitative study of blood flow. He discovered the Poiseuille relation for viscous flow in pipes (blood vessels) experimentally. Some years later he provided the corresponding theory, including Eq. (35), one of the first complete solutions of the Navier-Stokes equations. His contributions also include the development of practical instruments for measuring blood pressure *in vivo*. The CGS unit of dynamic viscosity is the poise, P, in his honor; 1 P = 0.1 N s m^{-2}.

[18] The derivation of (35) is useful to see and can be found in most fluid mechanics texts. A very good online reference is https://en.wikipedia.org/wiki/Hagen-Poiseuille_equation

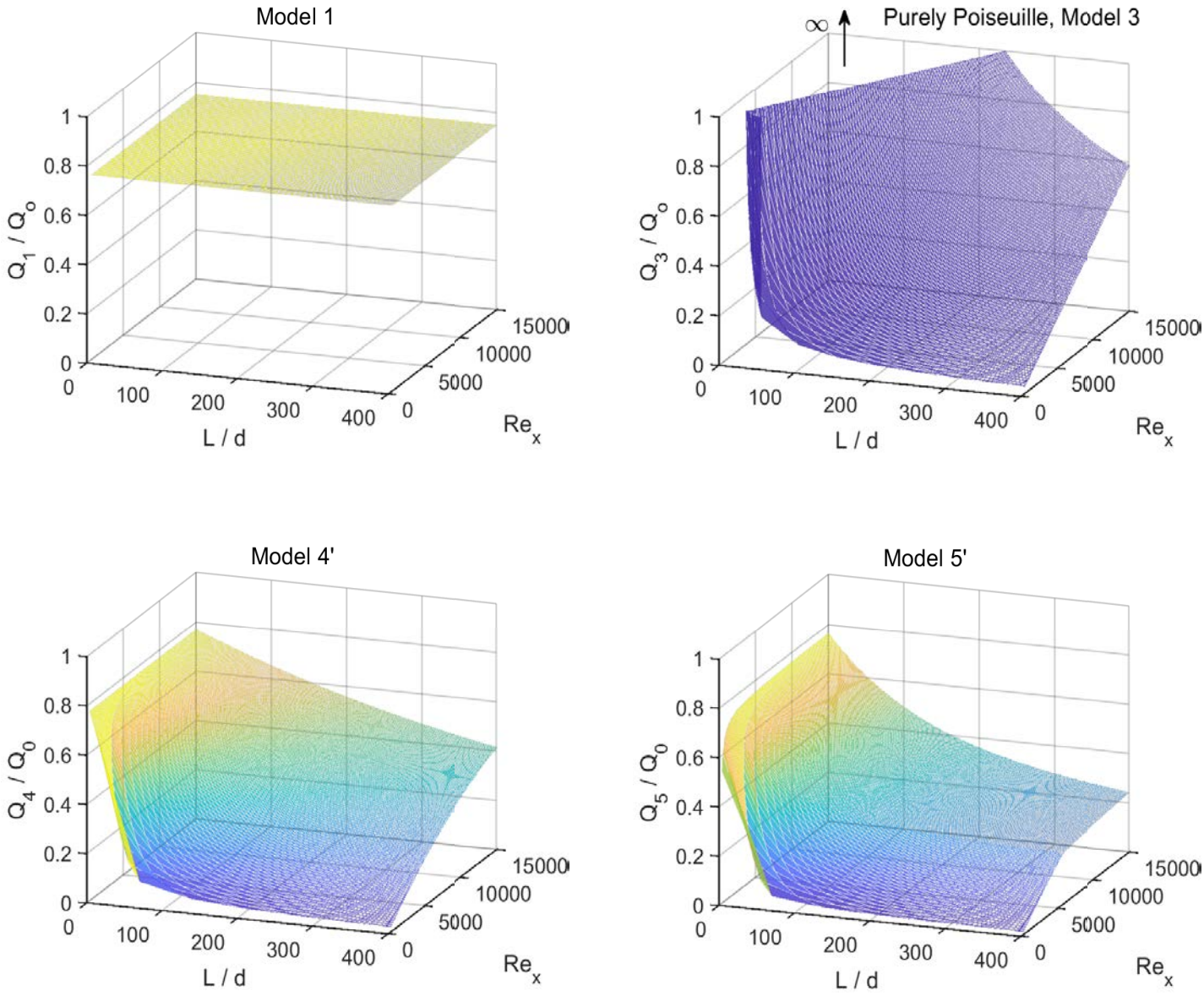

Figure 7: Four models of Q/Q_0 in the independent coordinates L/d and Re_x used in Fig. 6. This necessarily omits reference to surface tension. **Upper Left** The elementary Model 1 solution for transport through an orifice, dubbed Q_1. This solution does not depend upon L or ν and so this model defines a flat plane in this coordinate system. **Upper Right** The Poiseuille solution Q_3 for steady, fully-developed pipe flow. The transport diverges for small L/d and large Re_x, i.e., in the parameter range of smaller viscous effects, and has been clipped at 1. **Lower Left** The solution of Model 4' that combines Torricelli and Poiseuille, Eq. (41) and so has transport that is consistent with both orifice and viscous pipe flow (discussed in Sec. 6.2). The prime indicates that surface tension has been omitted. **Lower Right** Model 5' is similar to Model 4' at left, but includes a correction for the greater wall stress that occurs when the flow is turbulent at larger Re_x (Sec. 7). Notice the difference between Model 4' and Model 5' at larger Re_x and L/d but not otherwise.

or right at the start of the pipe. The transport through the orifice will then be estimated as

$$Q_{orf} \;=\; C\pi r^2\sqrt{2(g\,h \;-\; P_x/\rho)}. \tag{37}$$

This pressure difference and thus the transport through the orifice will be less, and possibly a lot less, than the orifice-only Model 1 of Sec. 3, which took the pressure P_x just beyond the orifice to be zero.

The pressure at the end of the pipe is $P_\sigma \;=\; \sigma/r$, the surface tension-induced pressure on the escaping jet of water in contact with air. The transport through the pipe will be estimated from Poiseuille's relation,

$$Q_{pipe} \;=\; \frac{\pi\, r^4}{8\,\mu\, L}(P_x - \frac{\sigma}{r}). \tag{38}$$

The one unknown in this is P_x, the pressure at the start of the pipe. This can be solved by requiring that the transport must be continuous,

$$Q_{orf} \;=\; Q_{pipe}. \tag{39}$$

Let

$$p \;=\; \frac{P_x}{\rho}, \qquad S \;=\; \frac{r^2}{8\,C\,\nu\,L}, \;\; \text{and recall} \;\; h_\sigma \;=\; \frac{\sigma}{\rho\, g\, r} \quad \text{and} \quad \nu \;=\; \frac{\mu}{\rho},$$

in which terms the continuity of transport (39) becomes

$$\sqrt{2(g\,h \;-\; p)} \;=\; S\,(p \;-\; g\,h_\sigma).$$

Squaring and rearranging into a quadratic in p gives

$$S^2\,p^2 \;+\; (2 - 2\,S^2\,g\,h_\sigma)\,p \;+\; S^2\,g^2\,h_\sigma^2 \;-\; 2\,g\,h = 0. \tag{40}$$

Once this is solved for $p \;=\; P_x/\rho$ (the positive root) the transport may be evaluated from either (37) or (38). This model and solution are called Model 4 and Q_4.

When surface tension is included, the analytic expression for Q_4 is too complex algebraically to be useful (though readily evaluated numerically in Sec. 6.4). For now, simplify by setting $h_\sigma \;=\; 0$ so that we can examine the orifice plus viscous pipe flow component, which will be dubbed Model 4'. The pressure, p, is then

$$p \;=\; \frac{P_x}{\rho} \;=\; \frac{-1 \;+\; \sqrt{1 \;+\; 2\,g\,h\,S^2}}{S^2}.$$

Substituting into (38), and after considerable rearranging:

$$\frac{{Q_4}'}{Q_0} \;=\; C\left(\,(\,1 \;+\; 1024\,C^2\,E^2\,)^{1/2} \;-\; 32\,C\,E\,\right), \tag{41}$$

where

$$E \;=\; \frac{L}{d}\, Re_x^{-1}. \tag{42}$$

The Model 4' solution, Fig. 7, lower left, is similar to the Model 3 Poiseuille solution for smaller values of the Reynolds number, roughly $Re_x < 2000$ where viscous effects are most important. It is qualitatively different at larger Re_x where the Model 3 solution diverges. The Model 4' solution gives reasonable transport in that regime because it has included the very important constraint imposed by the necessity for accelerated, inertial flow from the tank and into the orifice.

6.3 A collapse to one independent variable

The Model 4' solution (41) has the interesting property that it depends upon a single, independent nondimensional variable, E, vs. the $L\,/\,d$ and Re_x separately that we learned from dimensional analysis. The nondimensional variable E includes all of the important parameters that are expected to contribute to $Q\,/\,Q_0$ in these experiments (except for σ). A dependence upon the single nondimensional variable E is a special case of the more general result from dimensional analysis that indicated two separate, independent nondimensional variables, $L\,/\,d$ and Re_x. This important difference arises because Model 4 was built upon three physical constraints — continuity of volume transport, a solution for orifice flow, and Poiseuille's solution for laminar pipe flow — that were not incorporated into the VPlist (24). Thus the result from dimensional analysis is more general, i.e., less specific, than is the solution of a model that is otherwise consistent with the VPlist. This is a characteristic of dimensional analysis.[19]

The Eqs. (41) and (42) are somewhat surprising, and, if consistent with the observations, useful as well. To find out whether this holds within the observations we need only plot the usual $Q\,/\,Q_0$ against E and find a moderately good correlation, Figs. 8 and 9. It is always desirable to find the most compact description of a dataset or model solution, and this new version (new compared with the three-dimensional presentation of Fig. 6) meets that criterion.

The E description may be readily interpreted as the ratio of two time scales:

$$E \;=\; \frac{L\,/\,V_T}{d^2\,/\,\nu} \;\propto\; \frac{advection\ time}{diffusion\ time}. \tag{43}$$

The numerator is the time required for advection over the length of the pipe L at the speed V_T, and the denominator is the time required for diffusion across the diameter of the pipe. If the time required for diffusion is comparatively large, then E is comparatively small and viscous effects

[19]This important lack of specificity (or unintentional generality) is inherent to dimensional analysis and is discussed in greater depth in the main text, Sec. 3.

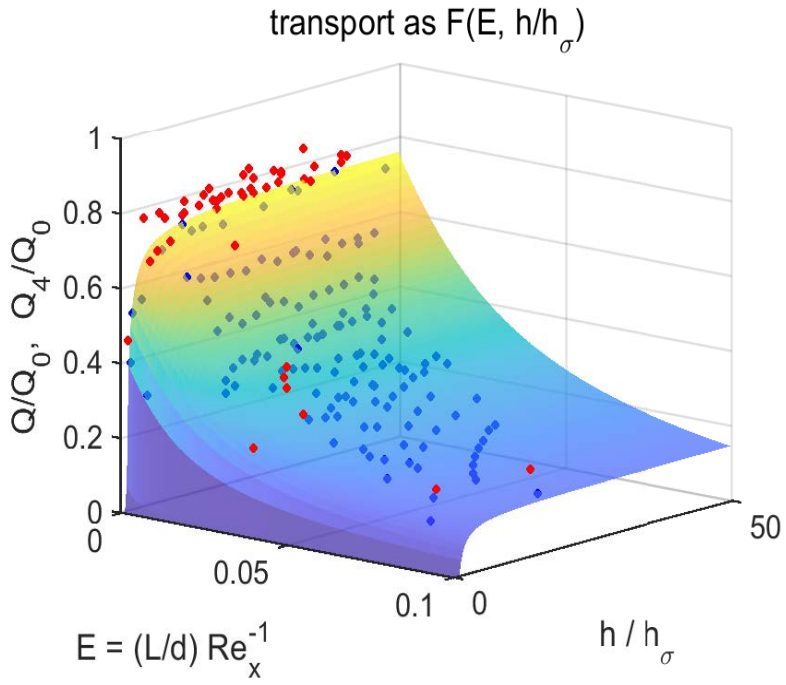

Figure 8: This surface is the Model 4 solution evaluated from Eq. (40), and the points are the full set of observations. The data points that lie below the surface are blue; those above the surface (a distinct minority) are red. The overall shape of the model surface looks reasonable compared to the data, but there is a clear tendency for Model 4 to overestimate transport. A more quantitative comparison comes in the next two figures.

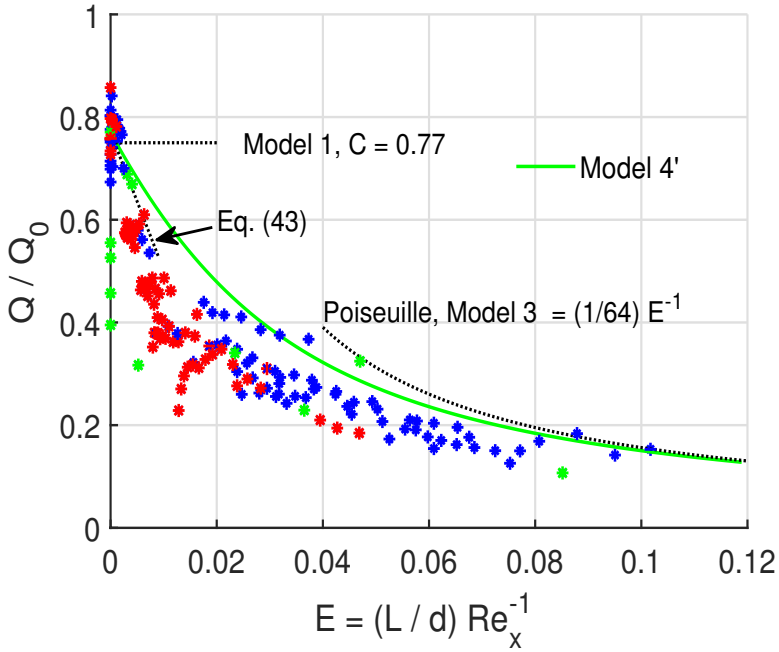

Figure 9: Observed transport (colored points) as a function of a single independent variable, $E = (L/d)\, Re_x^{-1}$. This is a projection of Fig. 8 onto a Q vs. E plane. The green line is the solution of Model 4' (which omits surface tension). The red data points have large Re_x, and the green data points are at small h/h_σ and likely affected by surface tension. The black dotted lines are the asymptotes of Q_4' for small and large E. Notice that the Model 4' solution parallels the data cloud, but sits above it, i.e., Model 4' systematically overestimates the transport, as noted in the previous figure. This will be addressed in Sec. 7.

should be less prominent. This is consistent with the observations.

The function $F(E)$ of Eq. (41) and plotted in Fig. 9 is not transparent, but it does have familiar asymptotes, Eq. (44), (45), and (46), that are sketched onto Fig. 9 as dashed, black lines.

- At $E = 0$, where there is no effect of viscosity,

$$Q_4 / Q_0 = 0.77 = C. \tag{44}$$

  This is Model 1, inertial, orifice flow.

- At small values of E, which corresponds to small (but not zero) viscous effects, the Model 4 solution goes to

$$Q_4/Q_0 \rightarrow C \left(1 - 32\,C\,E + 512\,C^2\,E^2 \ldots.\right). \tag{45}$$

  This indicates a strong decrease of transport with increasing L that is indeed observed for shorter pipes.

- At large E and large viscous effects,

$$Q_4 / Q_0 \rightarrow \frac{1}{64}\,E^{-1}, \tag{46}$$

  which is the Poiseuille solution for viscous, laminar pipe flow, and Model 3.

6.4 Model 4 includes surface tension and viscosity appropriate to a laminar flow

Now consider the solution of Eq. (40) with surface tension included, called Model 4 (no prime). The VPlist for this model is

- A VPlist for pressure-driven outflow of water through an orifice and a pipe: (47)

1. outflow volume transport, $Q \doteq$ [0 3 -1], the dependent variable,
2. hydrostatic pressure head at the orifice, $g\,h \doteq$ [0 2 -2], an independent variable,
3. diameter of the orifice and pipe, $d \doteq$ [0 1 0], a parameter,
4. length of the pipe, $L \doteq$ [0 1 0], a parameter.
5. kinematic viscosity of the water, $\nu \doteq$ [0 2 -1], a parameter,
6. surface tension of the water, $\sigma \doteq$ [1 0 -2], a parameter,
7. density of water, $\rho \doteq$ [1 -3 0], a parameter.

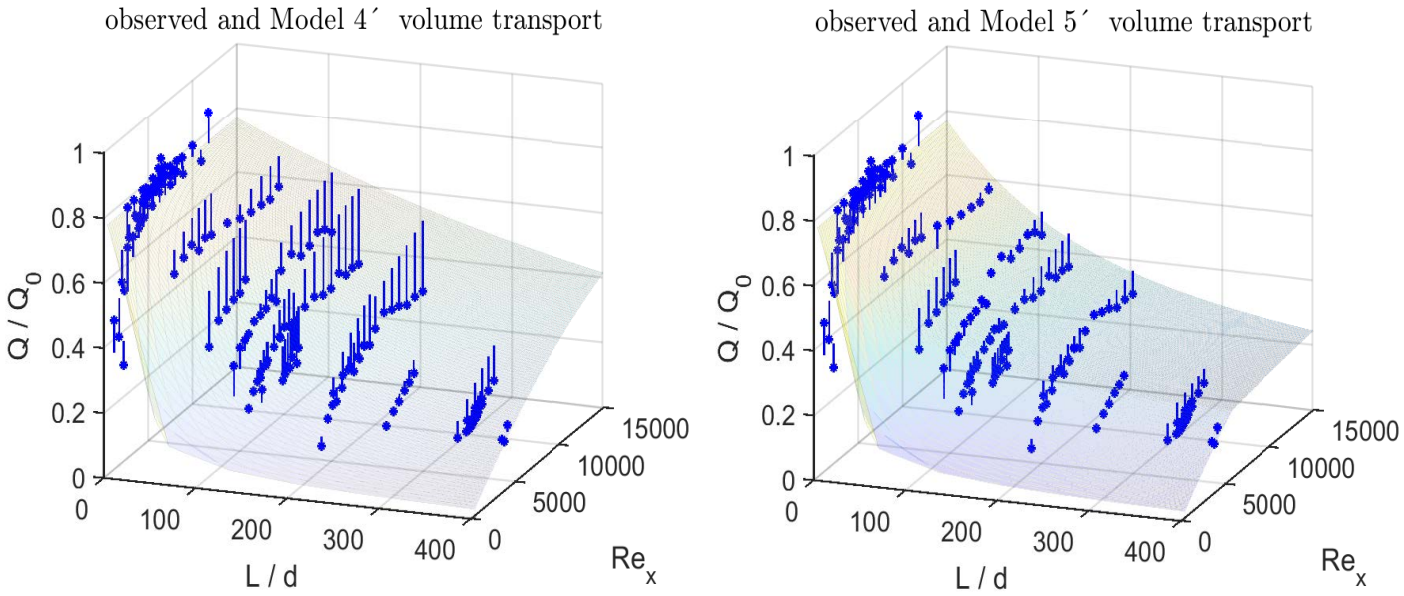

Figure 10: **(left)** Observed volume transport, blue dots, and the Model 4' solution shown as a surface in coordinates $(L\,/\,d,\ Re_x)$ as in Fig. 6. The stem goes from the data point up or down to the surface. This makes it especially clear that Model 4 overestimates transport (underestimates wall stress) at larger values of Re_x. This plot includes all of the data, including data taken at small $h\,/\,h_\sigma$ where surface tension effects are important. The model solution shown in these coordinates has to take $\sigma = 0$ and so can not replicate the reduced transport at very small h and small Re_x. **(right)** This is the same data shown at left, but here the surface is from Model 5' discussed in Sec. 7. The overestimate of transport seen at left is reduced considerably.

A basis set of nondimensional variables is, after considerable rearranging,

$$\frac{Q_4}{Q_0} \;=\; F(\frac{L}{d},\, Re_x,\, \frac{h}{h_\sigma}). \tag{48}$$

If the E-collapse discussed just above is applicable here as well, then provisionally,

$$\frac{Q_4}{Q_0} \;=\; F(E,\, \frac{h}{h_\sigma}). \tag{49}$$

To test whether this is valid we can make a three-dimensional graph of the Model 4 solution alongside *all* of the data, Fig. 8. The surface defined by Model 4 shows the variation of the nondimensional transport with E that could have been anticipated from Fig. 9; it also reveals a sharp decrease in the transport as $h/h_\sigma \to 1$ due to surface tension. This could have been anticipated from Fig. 3, right.

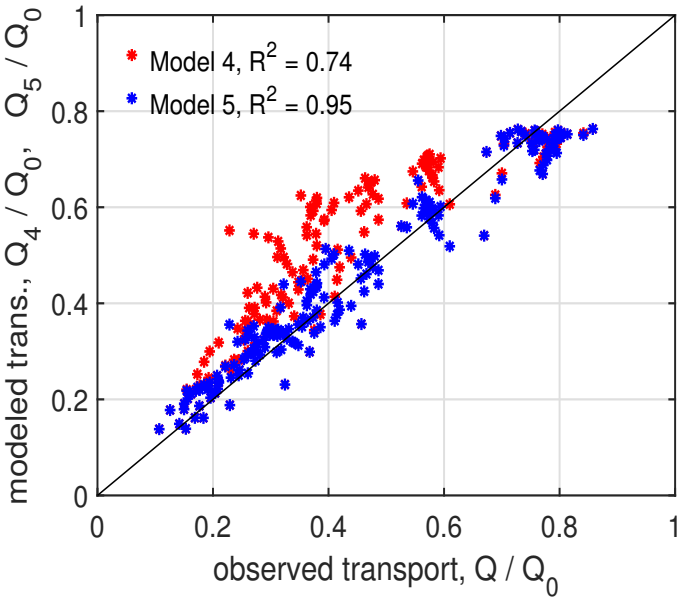

Figure 11: Modeled vs. observed transport. There are two versions of the modeled transport, the red dots are from Model 4 and the blue dots are from Model 5. Notice that Model 4 has a noticeable positive bias (predicts excess transport). This is mostly cured by the changes made to get Model 5, discussed in Sec. 7.

6.5 Summary

The Model 4 solution makes a reasonable, qualitative comparison with the observations, Fig. 8, including at small $h \,/\, h_\sigma$. It may be compared quantitatively with the full dataset and returns a coefficient of determination $R^2 = 0.74$. If the data that have large external Reynolds numbers, $Re_x \geq 7000$, are excluded from the sample, then R^2 increases somewhat to $R^2 = 0.86$. This is a more appropriate test of this laminar flow model.

Model 4 accomplishes most of what we set out to do in Sec. 1.2: it is understandable (though solution of the quadratic (40) is not transparent) and it gives semi-quantitative predictions. Given Model 4, we can interpret most of what can be seen in Fig. 6. It might be appropriate to thank Sig. Torricelli and M. Poiseuille for their remarkable contributions, and stop here. Except for one last issue: Model 4 overestimates transport by as much as 35% in some regions of parameter space. It looks like there is one more important step to take.

6.6 Problems

- Starting with the Poiseuille solution, Eq. (35), recast into the nondimensional coordinates of Fig. 6. Show that the Poiseuille solution is (this repeats Eq. (36)),

$$\frac{Q}{Q_0} = \frac{1}{64} \left(\frac{L}{d}\right)^{-1} Re_x.$$

  How does this compare with the surface plotted in Fig. 7, upper right?

- The pipes in these experiments were maintained in a horizontal orientation so that we wouldn't have to consider the angle from horizontal as yet another variable. Now imagine that the discharge end of the pipe was tipped up slightly. How would this affect the transport of the outflow? Can you connect this with the treatment of surface tension in Sec. 4?

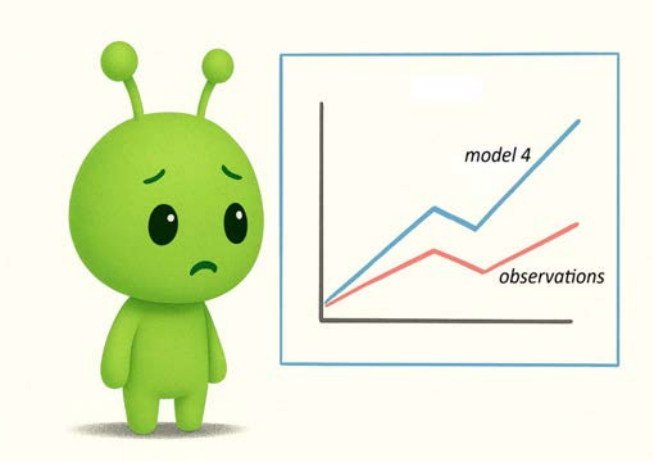

Planetary Explorer testing a new model.
Image by the author using ChatGPT-5.

Make a model, then test a model.

Models flow with grace.
Real, twisting fluids say no!
Try and try again.

7 Turbulent flow accounted by Model 5

The objective of this section is to resolve the systematic overestimation error made by Model 4. This proceeds in four steps:

7.1) Identify the source of the error — the occurrence of turbulent flow — based in large part upon its dependence upon Reynolds number.

7.2) Review historical observations that document pressure/velocity correlations in laminar and turbulent pipe flows.

7.3) Analyze these historical observations to estimate a turbulence-enhanced "effective" viscosity that may be applied within the laminar flow framework of Model 4.

7.4) Test the resulting Model 5 against observations.

7.1 The inferred source of the overestimation error

The error made by Model 4 has a telling geography, being most apparent for the largest Re_x, greater than about 7000, Fig. 10, left. A clear example of this comes from the three experiments of Fig. 5 that showed dependence of Q upon viscosity (due to different water temperature). The two experiments having cold and room temperature water sampled $2000 \leq Re_x \leq 7000$ and were predicted fairly well by the laminar flow Model 4, Fig. 12. The hot water experiment sampled $4000 \leq Re_x \leq 17000$ and in that range the Model 4-predicted transport exceeds the observed transport by an appreciable fraction, up to 50% at the largest Re_x. This discrepancy easily exceeds the uncertainty on observed Q, and it is systematic, a similar pattern is evident in other experiments that sampled larger L/d and Re_x. The upper Re_x limit for validity of the laminar flow Model 4 appears to be roughly $Re_x \approx 7000$. Using Eq. (30), this corresponds to an internal Reynolds number, $Re = V_a\, d\,/\,\nu = (Q\,/\,Q_0) \times Re_x = 0.35 \times 7000 \approx 2500$, where $Q\,/\,Q_0 = 0.35$ has been read from Fig. 12. A transition from laminar to turbulent flow at roughly this internal Reynolds number is consistent with well-known stability properties of pipe flow.[20] [21] Below $Re \approx 2000$, a laminar pipe flow will be stable, unless strongly perturbed by an outside agent; above a Reynolds number of about 3000, a laminar pipe flow will be unstable and likely to become at least intermittently turbulent. The inference made here is that the overestimation of transport by Model 4 is linked to the occurrence of turbulent flow, where Model 4 treated only laminar flow.

The chaotic, three-dimensional flow that constitutes turbulence continually mixes higher velocity fluid from the central core of the pipe into the boundary layer on the pipe walls. In a laminar flow the same process occurs by the generally much slower mechanism of molecular diffusion of momentum. Turbulent flow thus produces a higher wall stress than is found in the corresponding (same transport) laminar flow. For a given pressure difference, the occurrence of turbulent (vs. laminar) flow thus leads to reduced transport. This can be inferred from the observations of Fig. 12 where the transport is nearly independent of Re_x at larger values of Re_x. In contrast, if the flow was laminar, then we would expect a more or less linear increase of Q with Re_x, Eq. (36), and which is evident in the observations made at smaller Re_x.

---

[20] An excellent introduction to turbulent pipe flow (and fluid mechanics generally) is the text by White, F. M. and H. Xue, 2021, 'Fluid Mechanics', 9th Ed., McGraw Hill.

[21] When discussing a changeover from laminar to turbulent flow, or vice versa, it is almost irresistible to speak of a "transition to turbulent" flow, as implied here, even though what actually happens in these experiments is a change in time from (in some cases) turbulent flow to laminar flow as the surface height, h, and the velocity V_a decrease over time. This propensity for "transition to turbulence" may be partly alliteration, but also conceptual; it is much easier to envision going from a known state, laminar flow, into a chaotic state, turbulent flow vs. the other way around. Stability studies must proceed that way. Does it matter which way the transition goes? Is there hysteresis? Probably yes, especially when, as here, the Reynolds number is not far from the transition region.

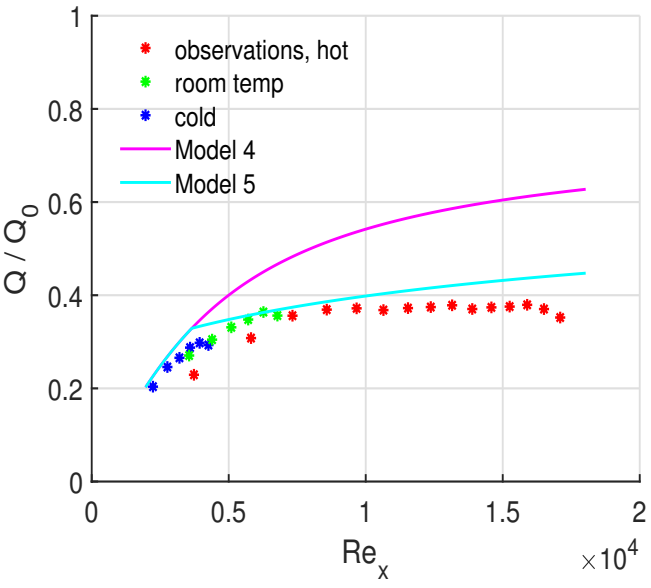

Figure 12: Red, green and blue points are the observed, nondimensional transport $Q\,/\,Q_0$ from the experiments of Fig. 5 shown here as a function of Re_x. These three experiments are at a common $L\,/\,d \;=\; 140$, but have different viscosity due to different temperature. The cyan line is the corresponding Model 4 prediction which overestimates the transport at larger Re_x. Notice the change in the nondimensional transport at very roughly $Re_x \;=\; 7000$, which corresponds to an internal Reynolds number, $Re \;=\; Re_x\,(Q\,/\,Q_0) \;\approx\; 2500$. This is interpreted to be a result of a transition from (somewhat) turbulent flow at larger Re_x to laminar flow at smaller Re_x.
A better prediction comes from Model 5, the magenta line, that implements an adjustment of the viscosity to account for turbulent flow.

7.2 Historical, experimental observations of pipe flow

There are significant engineering and economic consequences that follow from the increased flow resistance caused by turbulence, and the related phenomena have been studied intensively for more than a century and a half.[22] And yet, as Richard Feynman noted in the 1960s,

> *What we really can not do is deal with actual, wet water running through a pipe. That is the central problem which we ought to solve some day, and we have not.*[23]

By 'solve', Feynman was contrasting the empirical treatment of turbulent flows (coming below) with the Poiseuille solution from first principles that solves laminar pipe flow once and for all. A great deal has been learned regarding the remarkably complex phenomena that make up a turbulent pipe flow,[24] which goes some way to explaining why we still do not have a concise, understandable solution for turbulent pipe flow. This strongly shapes the development of a model intended to account for turbulent flow effects.

[22] If turbulence is a new or unfamiliar concept, then a must-see resource is the film by R. Stewart, 'Turbulence', available online at https://hml.mit.edu/ncfmf/

[23] R. Feynman, 'Lectures on Physics Vol. II', 1964, Addison-Wesley.

[24] An excellent, comprehensive review of the research on turbulent transition is by Avila, M, D., Barkley and B. Hof, 2023, 'Transition to turbulence in pipe flow', Ann. Rev. Fluid Mech., 55, 575-602. https://doi.org/10.1146/annurev-fluid-120720-025957

What we do have is a vast body of historical data and their analyses. Many of these experimental studies came in response to the practical need to predict the pressure drop, $\delta P/\rho \;=\; g\,h$, that will be required to drive a given fluid at a specified mean velocity, V_a, through a given pipe. Dimensional analysis of this problem is

- A VPlist for the pressure drop along a pipe: (50)

1. pressure drop expressed as a hydrostatic head, $g\,h \;\doteq\; [\,0\;\;2\;\;-2\,]$, the dependent variable,
2. mean velocity, $V_a \;\doteq\; [\,0\;\;\;1\;\;\;-1\,]$, an independent variable,
3. diameter of the pipe, $d \;\doteq\; [\,0\;\;\;1\;\;\;0\,]$, a parameter,
4. kinematic viscosity of the water, $\nu \;\doteq\; [\,0\;\;\;2\;\;\;-1\,]$, a parameter,
5. length of the pipe, $L \;\doteq\; [\,0\;\;\;1\;\;\;0\,]$, a parameter.

Three nondimensional variables are expected, and as one possibility,

$$\frac{g\,h}{V_a^2\,/\,2} \;=\; f(\frac{L}{d},\; Re), \quad \text{where} \quad Re \;=\; \frac{V_a\,d}{\nu}. \tag{51}$$

This is a complement to the problem of viscous pipe flow posed in Sec. 6. The key difference is that V_a and pressure $g\,h$, have switched places. In (51), V_a is the known, independent variable, and pressure $g\,h$ is the unknown, dependent variable. Thus the Reynolds number of (51) is the internal Reynolds number, Re, (Sec. 5.1) in place of the external Reynolds number Re_x used extensively in Sec. 6. Since pressure is the dependent variable, it has been kept to the first power, and so V_a is quadratic in this relation.

If the flow within the pipe is independent of distance downstream (i.e., fully developed) then the pressure drop should be directly proportional to the pipe length, L. In that event the parameter L/d may be taken out of the argument of f and included as a multiplying factor. This gives a widely used, simplified form

$$\boxed{\frac{g\,h}{V_a^2\,/\,2} \;=\; \frac{L}{d}\,f(\,Re\,)} \tag{52}$$

The unknown function of (52) is denoted by f, which is traditional in this role, and called the 'friction factor'. The function $f(Re)$ has been the object of hundreds of experimental programs, and the results compiled into a Moody diagram, a simplified example of which is Fig. 13.[25] There is no doubt about the practical value of the Moody diagram, but the physical interpretation of f itself does not go very deep. f is not a fluid property, but rather a joint property of the fluid, the pipe and the

[25] Estimation of the wall stress in real pipes may have to account for the surface roughness of the pipe wall. If the height of the roughness elements is ϵ, then the roughness will appear in Eq. (51) as a nondimensional parameter $\epsilon\,/\,d$. Moody diagrams generally display a near-blizzard of curves, each having a specific $\epsilon\,/\,d$, that sit above and roughly parallel to the curve for smooth pipes, the solid red line of Fig. 13. The 'pipes' used in the present experiments were new and clean and presumed to be smooth, and so roughness is neglected here; thus the impoverished Moody diagram of Fig. 13.

flow, organized by the dimensional analysis that lead to Eq. (52). f is also not a model of turbulence, but rather an empirical measure of flow resistance, larger f corresponding to greater flow resistance.

One part of the Moody diagram is clear and even familiar. In the low Re laminar flow regime, the Poiseuille solution in this framework is

$$f_{lam}(Re) \;=\; \frac{64}{Re} \tag{53}$$

the blue line at lower left of Fig. 13. The higher Re turbulent flow regime is different. One classical representation of $f(Re)$ for turbulent flow in a smooth pipe is the red solid curve at lower right, an empirical correlation of experimental data analyzed by Blasius in the 1910s,[26]

$$f_{turb}(Re) \;=\; \frac{0.316}{Re^{1/4}} \tag{54}$$

In what follows it will be necessary to have a function $f(Re)$ defined over the full range of Re. The laminar and turbulent prescriptions (53) and (54) are simply spliced together; $f(Re)$ follows the Poiseuille curve (53) for small Re up until intersection with the Blasius curve Eq. (54) at $Re \;=\; 1200$. It continues as the Blasius curve (54) thereafter with no special treatment of the transition region.[27] The spliced together function will be referred to as $f_{hist}(Re)$

The data from the present experiments may be used to evaluate $f(Re)$ via Eq. (52), which gives an interesting result, Fig. 14. The distribution is consistent in part with the historical data insofar as many of the experimental data fall close to the historical curves. That is reassuring; our little table-top apparatus is evidently not highly anomalous. But notice there are also many estimates of f that are well away from the historical curves, all in the direction of larger f. These seemingly high estimates are not measurement artifacts, but likely due to any one of several physical processes that are not accounted by a classical friction factor: surface tension, entrance effects (for short pipes) which violate the fully-developed flow restriction,[15] and hysteresis (turbulent to laminar transition).[21] Each of these phenomena is expected to enhance the flow resistance for a given Re. Surface tension was treated briefly in Sec. 4 and accounted in Model 4 and Model 5, but a treatment of the latter two phenomena is beyond the scope of this study.

[26]The original paper by Blasius is in German and hard to access, but discussed further in almost every comprehensive fluid mechanics text.

[27]There are a number of more complex formulae that serve to connect smoothly the laminar and turbulent flow branches of $f(Re)$ within the transition region.[20] A single, continuous function $f(Re)$ is desirable, but the differences compared with the present, simplified version, Eq. (53) spliced to Eq. (54), have been found to be very small in this application.

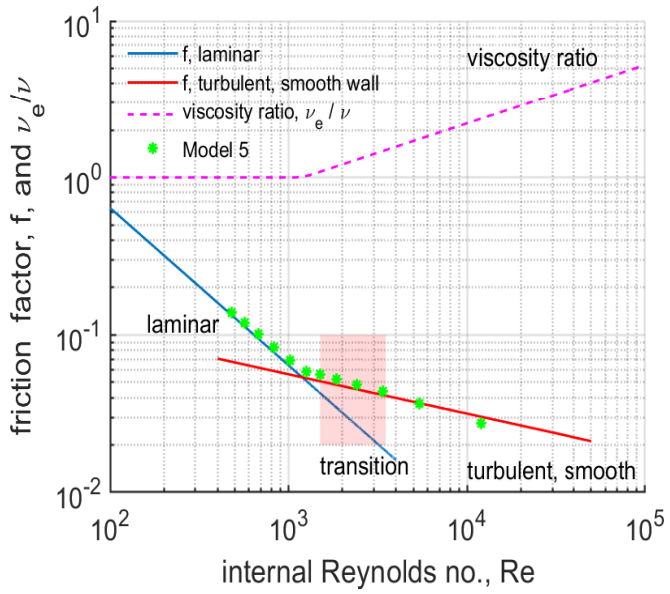

Figure 13: The friction factor, f, as a function of the internal Reynolds number, Re. The blue line at lower left comes from a laminar flow, i.e., Poiseuille's solution. The red curve at lower right is the Blasius fit to turbulent flow in a smooth pipe. The dashed, magenta line is the viscosity ratio computed from Eq. (62) and the constraint that ν_e/ν must be greater than 1. The green dots are $f(Re)$ computed by Model 5 and discussed in Sec. 7.3. The light red shading indicates the transition region, the range of Reynolds numbers, very roughly 1500 - 3500, at which a laminar flow, if gently accelerated and not subjected to large amplitude perturbations, would likely show signs of instability and a transition to turbulent flow. In practice there is not a sharp boundary on the transition region, and neither is there a clear consensus on $f(Re)$ within this region.

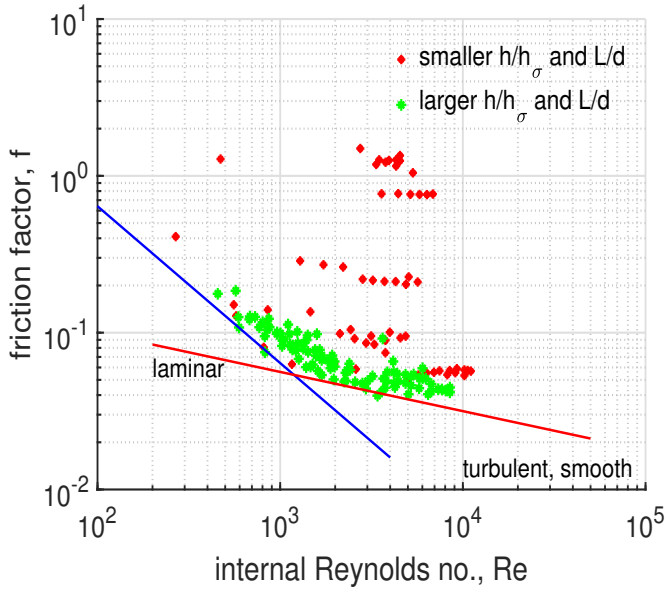

Figure 14: The friction factor, $f(Re)$, evaluated from the present experimental data, the red and green dots. The blue and red lines are as in the previous figure. The red dots represent data at smaller values of h/h_σ, likely affected by surface tension, and at smaller L/d that may be affected by entry length.[15] Neither of these phenomena is accounted by a friction factor, and it is not surprising that the red points are widely scattered. The distribution of the green points (all the rest of the data that are at larger h/h_σ and L/d) forms a cloud that is slightly above the historical curves and that more or less conforms with the change in slope of $f(Re)$ that is expected in the transition from laminar to turbulent flow at very roughly $Re \approx 2500$.

7.3 Estimating an effective viscosity for use within a laminar flow framework

To make use of the essential information provided by the historical $f(Re)$, the tactic will be to map $f(Re)$ onto a so-called effective viscosity, ν_e. The intention is that this ν_e will account for the possibility of turbulence-enhanced flow resistance within the laminar framework of Model 4. The detailed form of the mapping described next appears to be somewhat novel, but the notion of an effective viscosity to represent one or another aspect of turbulence has classical roots and an extensive history of development.[28]

The question posed here becomes: what value of effective viscosity, ν_e, will give a transport that is consistent with the piece-wise continuous $f(Re)$ of Eqs. (53) and (54)? From (52) it is evident that "Moody" scaling, Eq. (52), gives

$$Q^{Moody}(f(Re)) \;=\; (\,(\pi^2\, g\, h\; d^5)/(8\, L))^{1/2}\, \frac{1}{f(Re)^{1/2}} \tag{55}$$

for any $f(Re)$. For the special case of a laminar flow, the Moody scaling is

$$Q^{Moody}(f_{lam}(Re)) \;=\; (\,(\pi^2\, g\, h\; d^5)/(8\, L))^{1/2}\, \frac{1}{f_{lam}(Re)^{1/2}}. \tag{56}$$

The term $f_{lam}(Re)$ is known, but left as is for now. The ratio of the general Q^{Moody} to the laminar Q^{Moody} is then

$$\frac{Q^{Moody}(f(Re)}{Q^{Moody}(f_{lam}(Re))} \;=\; \sqrt{\frac{f_{lam}(Re)}{f(Re)}} \tag{57}$$

and all of the constants have dropped out. The Poiseuille scaling Eq. (35) gives $Q^{Pois}(\nu)$; first the laminar case,

$$Q^{Pois}(\nu) \;=\; \frac{\pi\, g\, h\, r^4}{8\, L\, \nu}, \tag{58}$$

where this ν is the usual (fluid property) viscosity, not dependent upon Re. Now define a general Q^{Pois} for which ν_e may be a function of Re, but still Poiseuille scaling

$$Q^{Pois}(\nu_e) \;=\; \frac{\pi\, g\, h\, r^4}{8\, L\, \nu_e}. \tag{59}$$

The ratio of this with (58) is just

$$\frac{Q^{Pois}(\nu_e)}{Q^{Pois}(\nu)} \;=\; \frac{\nu}{\nu_e}. \tag{60}$$

[28] A famous, early example is Prandtl's mixing length model, e.g., White and Xue (2021).[20] Prandtl's model treated a steady one-dimensional boundary layer flow, while the present application is to a steady, zero-dimensional system, the bulk transport. A modern, advanced treatise on turbulence including models of effective diffusivity that are far more sophisticated than considered here is by Pope S.B., 2000, 'Turbulent flows', Cambridge Univ. Press.

Now for the key step: define ν_e by requiring consistency between (57) and (60) in the sense that at a given Re, these two scaling estimates should give the same transport relative to the laminar case,

$$\frac{Q^{Moody}(f(Re))}{Q^{Moody}(f_{lam}(Re))} \;=\; \frac{Q^{Pois}(\nu_e)}{Q^{Pois}(\nu)}. \tag{61}$$

Substitution of (57) and (60) and rearranging yields a neat result,

$$\boxed{\frac{\nu_e}{\nu} \;=\; \sqrt{\frac{f(Re)}{f_{lam}(Re)}}} \tag{62}$$

The effective viscosity is thus, relative to the actual fluid viscosity, proportional to the square root of $f(Re)$ relative to the laminar $f_{lam}(Re)$ which we know from Eq. (53). Given the historical $f(Re)$, this is a closed prescription for ν_e that has not introduced new or adjustable parameters. Eq. (62) is the dashed magenta line labeled viscosity ratio in Fig. 13.

A particularly handy version of (62) comes from substitution of (53) and (54),

$$\text{on the laminar branch,} \quad Re \le 1200: \quad \boxed{\frac{\nu_e}{\nu} \;=\; 1} \tag{63}$$

$$\text{on the turbulent branch,} \quad Re \ge 1200: \quad \boxed{\frac{\nu_e}{\nu} \;=\; 7\times 10^{-2}\, Re^{3/8}} \tag{64}$$

Implementation of an effective viscosity starts with a solution of Model 4. If that solution gives $Re \le 1200$, then the flow is presumed to be laminar, $\nu_e = \nu$, and nothing more need be done. If instead $Re \ge 1200$, then the effective viscosity ν_e is evaluated from (64) and the solution recomputed with $\nu = \nu_e$. This first estimate of ν_e will be somewhat too large since the Model 4 estimate of Re will be too large. The solution is therefore iterated to arrive at an internally consistent solution in which the model-computed $f(Re)$ approximates the historical $f_{hist}(Re)$, cf. the green dots of Fig. 13. In all of this, the Reynolds numbers are evaluated with the actual fluid viscosity, ν, not the effective viscosity.[29]

7.4 At last, Model 5

Model 5 is defined by the effective viscosity relation (63) and (64) and the algorithm to implement its use in a laminar flow framework. Over most of the parameter space of these experiments the effective viscosity is less than twice the actual fluid viscosity, the dashed magenta curve of Fig. 13. The consequences for the model-computed transport are readily apparent at larger Re_x, compare the

[29] A Matlab script that implements Model 5 is linked in Sec. 8.

Model 4' solution with the Model 5' solution in Fig. 10. However, the differences are not qualitative simply because the largest Re_x sampled here is not, by most standards (Sec. 2.1), large.

The essential starting point for ν_e, the historical $f(Re)$ of Fig. 13), is well-established and can be regarded as an empirical fact within its somewhat restricted domain (that the flow is fully-developed, which probably does not hold in every experiment here). Nevertheless, the present mapping of $f(Re)$ to $\nu_e(Re)$, Eqs. (63) and (64), should be regarded as a working hypothesis, and not an inevitable, fundamental law derived from first principles: this ν_e device might work or it might not. Significantly, this model of an effective viscosity is a *testable* hypothesis in that its consequences can be readily checked against observations. The changes in transport that result from an increased viscosity ($\nu_e > \nu$) are in a direction that reduces the positive bias of Model 4, an example is in Fig. 12. The Model 4 solution begins to depart noticeably from the observations at $Re_x \approx 7000$, while the Model 5 solution stays closer to the observations, though still slightly high. When the solution of Model 5 (including surface tension) is compared directly to the entire dataset (no exclusions for surface tension or short pipes) the blue dots of Fig. 11), the coefficient of determination is found to be $R^2 = 0.95$ and hence Q_5 accounts for 95% of the variance in Q. This is a significant result, since the only adjustable parameter in Model 5 is the discharge coefficient, set to $C = 0.77$ all the way back in Model 1 (Sec. 3). The root mean square of the error, $Q - Q_5$, is 0.05 (nondimensional units), and the mean of the error is -0.008 (also nondimensional). The sign indicates that Q_5 is slightly higher than the observed Q/Q_0, on average, though the bias is significantly reduced compared to that of the Model 4 solution.

The apparent success of Model 5 could engender over confidence in the effective viscosity estimated by (63) and (64. Turbulence and viscosity are different things, different categories — turbulence is not merely an enhanced viscosity. Neither does ν_e represent a physical property of the fluid (roughly the same caution was leveled against f). Rather, this ν_e is a modeling device, or in modern vernacular, a modeling *hack*, that serves to import the historical laminar and turbulent flow relationship $f(Re)$ into the specific, laminar flow (Poiseuille model) framework developed as Model 4. This prescription for ν_e does not come close to being the model of turbulence alluded to by Feynman.

7.5 Summary and closing remarks

Model 5 appears to be empirically adequate over the rather small parameter space of these experiments (small when compared to the immense range of possible pipe flows noted in Sec. 2.1). The limited precision and resolution of the data are also at issue. The remaining differences between Model 5 and the present dataset give scant motivation or direction for further development and that means that we have finally come to the end of the development path previewed in Fig. 1. Better, more accurate and more comprehensive models are undoubtedly possible. To that end, more precise and more robust experimental apparatus that allowed greater temporal and volumetric resolution

would be highly desirable (see Rother, 2024, of footnote 1). One of the most useful improvements would be as simple as a taller tank that would yield larger outflow velocity and larger Reynolds numbers than were obtained with the modest apparatus used here.

Recall that in Sec. 1.2 there was mention of two desirable traits in a model, clarity (or understandability) and adequacy to the phenomenon and data of interest. These are likely to be in tension: here it seems that Model 4 is understandable, and Model 5 is adequate to the data. Now it's time to add one more hurdle for the study overall, *viz.*, we shouldn't feel comfortable with a model, and should not be confident applying that model, unless we understand where in parameter space the model will fail. The present dataset is not extensive enough to reveal the limits of Model 5, but we can be certain that there are such boundaries, and they may not be too far away from the boundaries of Fig. 6. The most likely point of failure is the relation Eq. (63) that maps $f(Re)$ to ν_e. And specifically, without understanding the physical basis for the Blasius correlation Eq. (54) there is no sound basis for trusting Model 5 solutions outside the range of Re that was sampled in these experiments.

7.6 Problems

- Fig. 13 showed Model 5 solutions in Moody scaling, $f(Re)$, the green dots. These approximate the historical $f_{hist}(Re)$ given by Eqs. (53) and (54). Is this comparison a test of physics or numerical implementation?

- The changes made by the implementation of an effective viscosity are evident in the shift of predicted transport closer to the one-to-one line in Fig. 11 (red dots, Model 4, to blue dots Model 5). The change is most evident in the middle range of transport values. Can you explain why this is the case?

- Up through Sec. 6 the essential nondimensional parameter was the external Reynolds number, Re_x. Then in Sec. 7 that role was taken by the much more often encountered (just plain) Reynolds number, Re, dubbed the internal Reynolds number in Sec. 6. Can you explain why the sudden changeover from Re_x to Re, aside from historical precedent?

- Fig. 6 was (probably) difficult to appreciate on first sight. What can you now understand of it?

  i) What parameter space is defined by the coordinate axes of this figure? What is the parameter space sampled by the observations? What part of the figure's parameter space was inaccessible to the experiments? (hint: think Venn diagram).
  ii) Where is there evidence of a surface tension effect? Why not in other data?
  iii) Where in this figure is the most obvious evidence of a viscous drag effect on a laminar flow?
  iv) Why does the (inferred) surface $F(L/d,\ Re_x)$ flatten out at large Re_x and large L/d?

- Advanced exploration for Earthlings. At the outset of Sec. 6 a dimensional analysis was applied to pressure-driven, viscous, fully-developed pipe flow. Repeating the VPlist here for convenience,

  Pressure-driven transport of a fully-developed, viscous pipe flow: (33r)

volume transport, $Q \doteq$ [0 3 -1], the dependent variable,
pressure gradient, $\partial P/\partial x \doteq$ [1 -2 -2], an independent variable,
radius of the pipe, $r \doteq$ [0 1 0], a parameter,
dynamic viscosity, $\mu \doteq$ [1 -1 -1], a parameter.

This VPlist yields a basis set having just one nondimensional variable that must be a constant,

$$\frac{Q\,\mu}{r^4\ \partial P/\partial x} \ = \ constant. \tag{34r}$$

The result (34r) has the form of Poiseuille's linear, laminar solution, in which transport is directly proportional to the pressure gradient. In this Sec. 7 we have seen that the transport of a pipe flow may also depend upon the properties of the flow itself, whether laminar or turbulent. Where in (33r) is the possibility of turbulence? Or said a little differently, why is a linear, laminar flow guaranteed by this specific VPlist?

The VPlist (33r) included a small choice that had larger consequences than might be anticipated. The parameters pressure gradient and dynamic viscosity both included the dimension, mass. Fair enough, they usually do. But since the dependent variable was taken to be the volume transport, Q, which does not contain a mass dimension, then the viscosity and pressure gradient were bound to appear in the resulting basis set as their ratio, call it $\quad = \mu\,(\partial P/\partial x)^{-1}$, and $\quad \doteq [0\ 1\ 1]$. The VPlist (33r) had, in effect, only three independent dimensional variables, Q, r and $\quad$, and just two dimensions, length and time. This implies that there will be only one nondimensional variable, as there is in (34r), which is consistent with Poiseuille's solution for linear, laminar flow. In other words, there is no allowance in the basis set (34r) for a turbulent flow in which transport is not directly proportional to the pressure gradient.

Let's try an experiment: starting with the VPlist (33r), divide the dynamic viscosity by the fluid density to get the kinematic viscosity, and similarly for the pressure gradient to recast as an acceleration. We are not concerned in this study with the possibility of a variable fluid density, and so these choices should be acceptable, physically.

Pressure-driven transport of a fully-developed, viscous pipe flow, omitting mass:

volume transport, $Q \doteq$ [0 3 -1], the dependent variable, (65)
pressure gradient acceleration, $(\partial P/\partial x)\,/\,\rho \doteq$ [0 1 -2], an independent variable,
radius of the pipe, $r \doteq$ [0 1 0], a parameter,
kinematic viscosity, $\nu \ = \ \mu\,/\,\rho \doteq$ [0 2 -1], a parameter.

There are four members in the revised VPlist, just as before, but now with only two dimensions, length and time. Compute the basis set of nondimensional variables and find two members,

$$\frac{Q}{d\,\nu} \ = \ F(\frac{d^3\,((\partial P/\partial x)\,/\,\rho)}{\nu^2}), \tag{66}$$

a nondimensional transport that is equal to an unknown function of a Reynolds-like number. This revised analysis can accommodate turbulent flow and laminar flow, and yet it has sprung from a reduced and seemingly simpler VPlist compared with (33r).

Below are some experiments that will help fill out this discussion. The repeated null space calculations implied here are best done with Matlab or Python codes linked in the next section.

i) Starting with the VPlist (33r), change the dependent variable to mass transport,
$Q_m \doteq [\,1\ 0\ -1\,]$, but leave all else the same. This is the complement to the example worked

above in the sense that all possible instances of mass are included in the VPlist. Compute the nondimensional basis set, and compare with Eq. (34r).

ii) Starting with the VPlist (33r), replace the dynamic viscosity with kinematic viscosity (as if dividing by a constant density) but leave all else as is. This will not go well to the extent that the nondimensional basis set will have to omit the pressure gradient, the motive power for the flow. What went wrong?

iii) There are several more variations on this mass in or mass out exercise, and it is revealing to approach them systematically. Start with the VPlist (33r), and set plausibility aside. Allow that the three variables Q, $\partial P \,/\, \partial x$, and μ can appear either with or without division by density; r continues along unbothered by all this. How many unique combinations (mass on, mass off for each relevant parameter) are there in this ensemble of VPlists? We have already considered two of them in i) and ii) above. How many of the ensemble VPlists will fail to give a sensible result, as in case ii) above? How many give the Poiseuille result, Eq. (34r)? How many give that $F = F(Re)$? Now allow physical reasoning back in. Which of the VPlists and solutions are the least arbitrary?

iv) Starting with the VPlist (33r), include the fluid density as a fifth member of the VPlist. Calculate the nondimensional variables of this augmented VPlist, and explain how your new result compares with Eq. (34r).

What's the moral of this short story / long problem? Because VPlists do not include much information to begin with, even a small and seemingly incidental omission or addition can have a qualitative effect on the result. As well, there is binary-like property to a VPlist; a parameter is either in or out, with no gradation for just a little effect of mass, for example. With that in mind, it is good practice to regard every new or unfamiliar VPlist as provisional, and to experiment with plausible variations to see if something unexpected may emerge.

- ## Farewell, Explorer.

Off to find new worlds.
With Earth's gift of fresh insight,
She will make her way.

With business finally finished (tank drained) and with a backpack full of new codes and diagrams, Planetary Explorer blasted off in search of new planets and adventures. Soon she discovered a new and somewhat barren planet, and most surprising, another tank-draining project. There were two obstacles not encountered on verdant Earth: no Matlab and no internet. Assuming that the local gravitational acceleration g can be measured independently, how might the diagrams of this appendix be used to predict the gravity-driven outflow rate on this new planet?

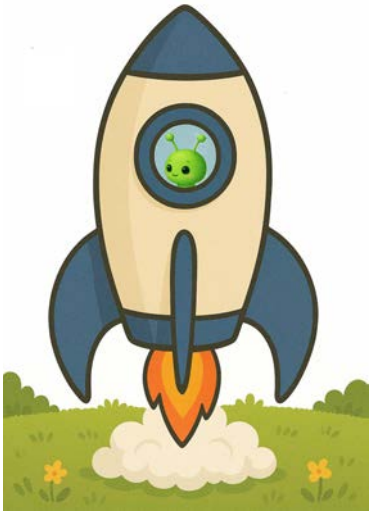

Planetary Explorer blasting off.
Image by the author using ChatGPT-5.

8 Housekeeping

Attribution and Acknowledgment: The experiments, the models and codes, the text and the technical figures were made by the author. The Planetary Explorer images were created by the author using ChatGPT-5. Administrative assistance was provided by the Dept. of Physical Oceanography, Woods Hole Oceanographic Institution.

License: Copying and distribution for educational purposes is encouraged, consistent with the Creative Commons license CC BY-NC-SA.

Citation: This essay may be cited by the web address on the Massachusetts Institute of Technology OpenCourseWare — Price, James F., 12.808 Supplemental Material, Topics in Fluid Dynamics: Lagrangian and Eulerian Representations, a Coriolis tutorial, and Dimensional Analysis of Models and Data Sets, https://ocw.mit.edu/courses/res-12-001-topics-in-fluid-dynamics-fall-2024 (date accessed).

Links to codes and data: The experimental data, the models and a Matlab script to exercise both are available at https://www2.whoi.edu/staff/jprice/wp-content/uploads/sites/199/2025/12/DA-tank.zip
There are four main files:

- Dstruct.mat, a Matlab structure that stores all of the experimental data.
- DAtank.xlsx, same as above but in an Excel table file.
- Model5.m, a Matlab function that evaluates Model 5, and with appropriate settings, Model 4.
- Dplot.m, a Matlab script that loads Dstruct.mat and makes several plots of the data, including a version of Fig. 6 along with model predictions.

Index

basis set, 3

dimensional analysis
    advantages, 3
discharge coefficient, C, 16

f
    laminar, 41
flow
    inertial, 16
    laminar, 29
friction factor, 41

Model
    0, 14
    1, 17
    2, 20
    3, 29
    4, 30
    5, 45
model
    sequence, 6
Moody diagram, 41

parabolic, 17
parameter space, 5, 8
Poiseuille solution
    via dimensional analysis, 47
Poiseuille's solution, 29
pressure
    hydrostatic, 13

Reynolds number
    external, 24
    internal, 24

scale
    natural, 14
surface tension, 18

transport, 9

velocity
    average, 24
    Torricelli, 13
viscosity , 44
    effective, 44
viscous effects, 21
VPlist, 3

Draining a Tank

an appendix to

Dimensional Analysis of Models and Data Sets

James F. Price
Dept. of Physical Oceanography, Woods Hole Oceanographic Institution
Woods Hole, Massachusetts, 02543
http://www.whoi.edu/science/PO/people/jprice · jprice@whoi.edu

February 9, 2026

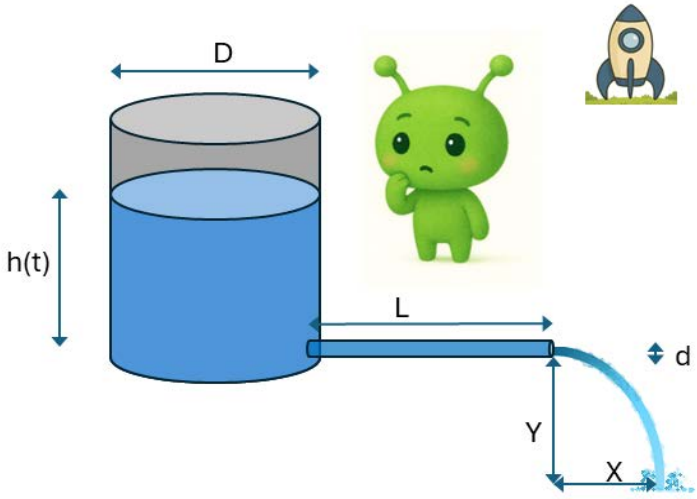

Planetary Explorer contemplating a water tank.
By the author using ChatGPT-5.

How long to drain this tank?

Here to learn Earth's ways.
All I see are water tanks —
deeper than they seem?

Summary

We can help. The objectives of this appendix are to observe and then model the time it takes a gravity-driven outflow to drain a tank. The observations come from a family of experiments that explore the effects of two real-fluid properties of water, surface tension and viscosity. Surface tension will slow the outflow as the fluid height h becomes small, and may stop it altogether depending upon the inside diameter of the orifice or pipe, d. When a pipe is present, viscous drag will reduce the outflow by a factor that depends upon the fluid viscosity, the diameter and length of the pipe, d and L, and the surface height.

The goal of this appendix is to demonstrate dimensional analysis as a guide for organizing this multi-parameter dataset into a concise and interpretable form. A clear organization of the data facilitates comparison with model predictions and highlights specific errors. This leads to a sequence of improved models. The end result is a model that is largely understandable while providing solutions that are empirically adequate over the parameter space of the present experiments.

Contents

1 Draining a tank; objectives and goal **3**
- 1.1 Why and how dimensional analysis . . . 4
- 1.2 Model development guided by observations and dimensional analysis . . . 5
- 1.3 Glossary of symbols, phrases and models . . . 8

2 A family of experiments **9**
- 2.1 Parameter space of this apparatus . . . 10
- 2.2 Making observations . . . 10
- 2.3 Inferences from the first experiments . . . 11
- 2.4 Changing the problem from h(t) to Q(h) . . . 13
- 2.5 Torricelli velocity and a zero-order model . . . 15
- 2.6 Summary to here and outlook . . . 16
- 2.7 Problems . . . 16

3 An elementary (and very successful) Model 1 **16**
- 3.1 A data-driven Model 1 . . . 16
- 3.2 Integrating to find h(t) . . . 18
- 3.3 Summary . . . 18
- 3.4 Problems . . . 19

4 Surface tension reduces transport in the small $\mathbf{h/d}$ regime **19**
- 4.1 Why do fluids exhibit surface tension? . . . 20
- 4.2 Surface tension and pressure within a cylindrical jet of water . . . 21
- 4.3 Model 2 includes a first-order effect of surface tension . . . 21
- 4.4 Summary . . . 22
- 4.5 Problems . . . 22

5 Outflow through an orifice and a pipe, starting with observations **23**
- 5.1 Reynolds numbers, external and internal, Re_x and Re . . . 25
- 5.2 The function F for orifice plus viscous pipe flow . . . 27
- 5.3 Summary . . . 27
- 5.4 Problems . . . 29

6 Models of viscous, laminar pipe flow **29**
- 6.1 Poiseuille's solution for laminar flow, Model 3 . . . 29
- 6.2 A hybrid Model 4 – Sig. Torricelli, say hello to M. Poiseuille . . . 31
- 6.3 A collapse to one independent variable . . . 34
- 6.4 Model 4 includes surface tension and viscosity appropriate to a laminar flow . . . 36
- 6.5 Summary . . . 38
- 6.6 Problems . . . 38

7 Turbulent flow accounted by Model 5 **39**
- 7.1 The inferred source of the overestimation error . . . 40
- 7.2 Historical, experimental observations of pipe flow . . . 41
- 7.3 Estimating an effective viscosity for use within a laminar flow framework . . . 45
- 7.4 At last, Model 5 . . . 46

7.5 Summary and closing remarks 47
7.6 Problems 48

8 Housekeeping **51**

9 Index **51**

1 Draining a tank; objectives and goal

"How long to drain this tank?" comes up in a wide range of contexts. Tank-draining projects are a mainstay of physics education, where they combine accessible experiments with satisfying theory.[1] Tank-draining problems continue to be a research topic in nuclear and chemical engineering when they include complex plumbing and highly exotic fluids.[2]

Though simple in concept, tank-draining problems do not admit simple solutions except in the most idealized case in which the fluid is considered to be ideal. This study goes beyond the basic case by including two real-fluid properties of water, surface tension and viscosity. Modeling these phenomena, the objective of this appendix, requires experimental observations and theory combined in roughly equal measure. The deeper goal of this appendix is to show how dimensional analysis can be the essential link between observations and a theory.

Readers are assumed to have experience with applied mathematics including linear algebra and ordinary differential equations, and classical mechanics to include a first course in fluid mechanics. For these readers, this article should be suitable for self-study.

[1] Donnelly, S. C., et al., 2024, Draining a tank through multiple orifices: An improved lab experiment in fluid mechanics, https://doi.org/10.18260/1-2-660-46367, and Rother, M. A., 2024, Modelling tank drainage using a simple apparatus. Journal of Mathematical Education in Science and Technology. 55, 2, 295 - 307. https://doi.org/10.1080/0020739X.2023.2249472 .

[2] Elgamal, M., K. Kriaa and M. Farouk, 2021, Drainage of a Water Tank with Pipe Outlet Loaded by a Passive Rotor. Water, 2021, 13, 872 https://doi.org/10.3390/w13131872

1.1 Why and how dimensional analysis

The procedure of dimensional analysis followed here is outlined briefly below and in considerably greater detail in the main text, Dimensional Analysis of Models and Data Sets.[3] If dimensional analysis strikes you as abstract in the extreme — as it does for *everyone* who is new to the idea — then Secs. 1 - 3 of the main text are strongly recommended as a prerequisite to this appendix. If you are somewhat familiar with dimensional analysis as it is usually practiced via the Buckingham Pi Theorem, then you will find that the present method is different mainly by the approach to computation, 3) below, and interpretation, 4) below.

1. **Problem definition.** A problem is defined by a so-called Variables and Parameters list, or VPlist, that starts with one dependent variable, the unknown, and includes all of the other variables and parameters that would necessarily appear in a model of the phenomenon. A remarkable property of dimensional analysis is that you do not have to know the model in any further detail; though better of course, if you do. These variables and parameters are characterized by the powers (the exponents) on their fundamental dimensions, [mass length time]. For example, the dimensions of a pipe having length, L, will be indicated by a dot-equals notation, e.g., $L \doteq [0\ 1\ 0]$, a speed $V = dL/dt$ has dimensions $V \doteq [0\ 1\ -1]$, and an acceleration has dimensions $dV/dt \doteq [0\ 1\ -2]$. The powers of each member of the VPlist (the three-element row vectors above) are collected into a dimension matrix.

2. **The practical advantages of dimensional analysis.** If the VPlist is complete, then the dependent variable may be written in a nondimensional form that is free from reference to a system of units, e.g., meters, centimeters or feet, and so is a pure number. There are two significant advantages in this that will be highlighted as we go through this analysis. First, a description in nondimensional variables is more concise (has fewer variables) than is the equivalent dimensional description. Second, a nondimensional description helps focus attention on meaningful relationships. For example, a pipe may be judged to be long or short compared to the pipe diameter, a natural scale with physical significance, or in meters or centimeters, arbitrary scales. The latter system is likely to be most useful during the design and execution of an experiment, while the use of nondimensional variables will maximize the utility of the experimental results.

3. **Automated calculation of nondimensional variables.** The nondimensional variables may be computed by solving a system of linear equations for the null space of the dimension matrix. The solution vectors of the null space correspond one-to-one with nondimensional variables.

[3] Online at https://ocw.mit.edu/courses/res-12-001-topics-in-fluid-dynamics-fall-2024/

This calculation is not difficult, but can be tedious if done by hand. The calculation is quick and sure when automated.[4]

4. **Interpretation.** The system of equations is most often undetermined, i.e., more unknowns than independent equations. In that case the initial basis set is not unique, and it will be optimal only by chance. Your task will be to transform (as necessary) the initial basis set into a form that will enhance the utility and interpretation of the analysis. Examples of this transformation will be seen throughout.

1.2 Model development guided by observations and dimensional analysis

Planetary Explorer beginning a long trek.
Image by the author using ChatGPT-5.

Seeking a better model.

A long path ahead.
Starlit by the Milky Way,
I'll take slow, sure steps.

The model development described here takes place in five steps, Fig. 1, each one motivated by a comparison of model predictions with a suite of experimental observations. Dimensional analysis is a great help in organizing the observations, and so guiding the next step in the model development.

There are two ideals for the model — sufficient transparency that we can understand what the model is and what it does, and, that the model predictions be true to the observations. These are not

[4] via Matlab: https://www2.whoi.edu/staff/jprice/wp-content/uploads/sites/199/2024/06/DanalysisA2.zip
or Python: https://www2.whoi.edu/staff/jprice/wp-content/uploads/sites/199/2024/10/DA2Python.zip

easily achieved at once. In the progression of models shown in Fig. 1, Model 4 is transparent and understandable but makes a consistent overestimate of the outflow transport. Model 5 utilizes historical, empirical turbulent pipe flow correlations to modify the viscous drag calculated by Model 4. This largely corrects the overestimation errors, but with some loss of transparency. The intent here is to be deliberate and clear about these tradeoffs.

Sec. 2. The next section describes the experiments and the resulting data that are essential to this study. The present family of experiments is defined by a four-dimensional parameter space — orifice or pipe diameter, pipe length, fluid height, and fluid viscosity. The aim of this study is not to answer any one specific tank-draining problem, helpful as that might be, but rather to model and understand the entire family of experiments defined by the available apparatus.

Sec. 3. The first experiments are made without a pipe, or orifice-only. The observed surface height, $h(t)$ is almost parabolic in time, and is described well by the most elementary model, Model 1, until h becomes very small. The observed outflow then slows and may stop altogether before the tank drains completely. In some respects this is a small detail, but it is also a qualitative error that is inherent to the ideal fluid model implicit in Model 1. How can we improve on this?

Sec. 4. At small values of h the orifice may be blocked by a stationary bubble or cap of fluid. From appearance alone this suggests an effect of surface tension, treated briefly in Sec. 4, and implemented as Model 2.

Sec. 5. The emphasis of this study is on the viscous drag that accompanies outflow through a pipe. Dimensional analysis is used to organize observations in a way that reveals the systematic and large amplitude variation of the outflow transport with pipe length, pipe diameter, viscosity and surface height. This empirical relationship is the objective of later Models 4 and 5.

Sec. 6.1 Poiseuille's historically significant and still quite useful model of fully-developed, viscous, laminar pipe flow is taken as Model 3. It shows promise for cases with longer pipes and greater viscous drag. However, it diverges toward unrealistic, excessive transport for cases with lesser drag because it takes no account of the inertial acceleration that has to accompany the movement of fluid from the tank into and through the orifice.

Sec. 6.2 A hybrid Model 4 combines Poiseuille's solution with the inertial orifice flow of Model 1 and surface tension of Model 2. A surprising result is that the solution of Model 4 can be written as a function of one nondimensional independent variable where dimensional analysis had indicated two independent variables. The collapsed, one variable description leads to a more insightful diagnosis of the advective/diffusive balance within the laminar flow regime. Model 4 gives a reasonable, semiquantitative account of the observations overall, however it displays a systematic overestimate of transport (underestimates viscous drag) for cases with larger Reynolds numbers.

Sec. 7 The inference made from this observation is that the flow is turbulent at the larger Reynolds

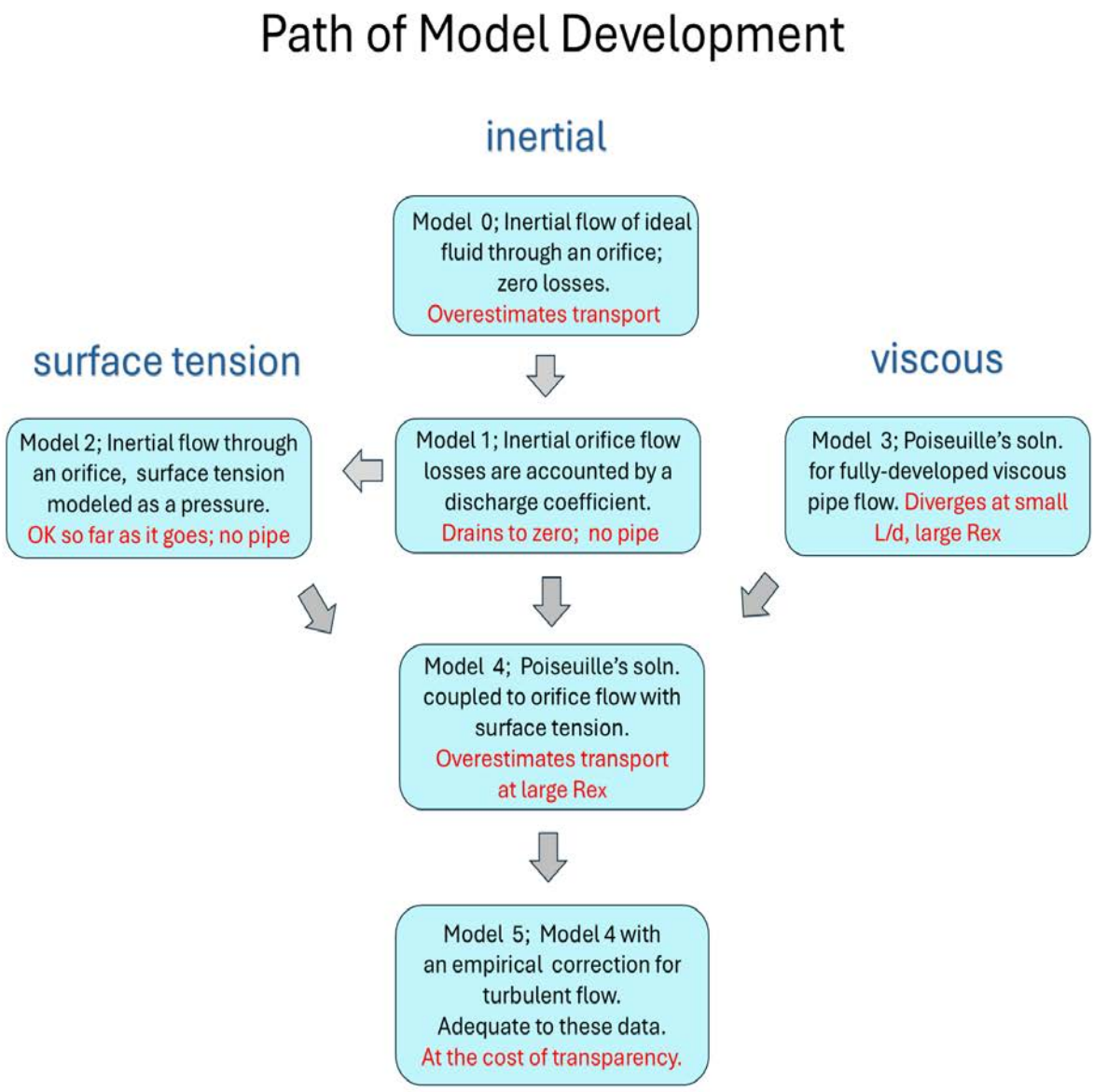

Figure 1: The sequence of models developed here, starting from very simple at the top to fairly complex at the bottom. A narrative of this model progression is in Sec. 1.2. There are at first two tracks that treat two distinct physical properties of real water. The track at left deals with surface tension, and the track at right deals with viscous effects. Surface tension and viscosity are treated separately until brought together in Model 4. The final Model 5 implements an empirical correction for the greater wall stress that occurs at larger Reynolds number consistent with the occurrence of turbulent flow. The red text in a box notes a salient shortcoming.

numbers reached in these experiments. Modeling turbulent flow relies on historical data correlations. The resulting Model 5 is adequate to these data, but at some cost in transparency, i.e., Model 5 is not understandable to the depth of Model 4.

1.3 Glossary of symbols, phrases and models

- **Symbols**
  - C orifice discharge coefficient; for this apparatus, $C \approx 0.77$, nondimensional
  - d inside diameter of the orifice and the pipe
  - D diameter of the cylindrical water tank
  - F is an unknown function
  - g acceleration of gravity, 9.8 m s^{-2} and presumed constant
  - h height of the water surface above the orifice/pipe center
  - Q observed volume transport of the outflow, m^3 s^{-1}
  - μ dynamic viscosity, for water, nominal 0.9 $\times 10^{-3}$ Pa s, temperature dependent
  - $\nu = \mu/\rho$ kinematic viscosity, for water, nominal 0.9 $\times 10^{-6}$ m^2 s^{-1}
  - ν_e effective viscosity that mimics the enhanced wall stress of turbulent flow
  - r radius of the orifice or pipe = $d/2$
  - ρ the density of fresh water, 998 kg m^{-3} and presumed constant
  - σ surface tension, for water, nominal 75×10^{-3} N m^{-1}, or 75×10^{-3} kg s^{-2}
  - W volume of fluid in the tank, m^3
  - $\doteq$ 'dot equals' is an operator that brings out the exponents on [mass, length, time], e.g., $W \doteq$ [0 3 0] and $Q = -dW/dt \doteq$ [0 3 -1].

- **Derived Symbols and Phrases**
  - $a = \pi d^2 / 4$, area of the orifice and pipe
  - $A = \pi D^2 / 4$, area of the tank
  - $E = (L/d)\, Re_x^{-1} = (L\,\nu)/\, d^2 \sqrt{2\ g\ h}$
  - $h_\sigma = \sigma /(\rho\, g\, r)$, equivalent hydrostatic head of the surface tension-induced pressure
  - $V_a = Q\,/\,a$, area-averaged velocity of the outflow, known only if Q is known
  - $V_T = \sqrt{2\, g\, h}$, Torricelli velocity, considered external when h is a known, independent variable

  - $Re \;=\; V_a\, d\,/\nu$, the most commonly encountered version of a pipe Reynolds number
  - $Re_x \;=\; V_T\, d\,/\nu$, the external Reynolds number used frequently here
  - basis set of nondimensional variables, calculated by the codes linked in Sec. 8.
  - entry length, the distance downstream from the orifice over which the flow becomes independent of distance, also said to be fully-developed
  - hydrostatic head, the height of a fluid at rest that gives a specific pressure
  - laminar flow implies a steady, one-dimensional velocity throughout the pipe, and a simple relationship between frictional drag and transport
  - turbulent flow implies unsteady, three-dimensional, and dispersive velocity, with one consequence being greater drag than in an otherwise comparable laminar flow
  - VPlist, variables and parameters in a list that defines a problem.

- **Glossary of Models**
  - Model 0, Q_0, a zero-order model of orifice transport, $Q_0 \;=\; a\, V_T$, Eq. (11)
  - Q_1 the elementary model of orifice transport, $Q_1 \;=\; C\, Q_0$, Eq. (14)
  - Q_2 as Q_1 including surface tension, $Q_2 \;=\; Q_1 \sqrt{1 - h_\sigma\,/\,h}$, Eq. (22)
  - Q_3 Poiseuille's solution for viscous, laminar flow through a pipe, Eq. (35)
  - Q_4 a solvable, hybrid model that includes Q_1, Q_2 and Q_3, Eq. (40)
  - Q_4' Model 4, but omitting surface tension, implicitly via Eq. (41)
  - Q_5 as Q_4 with a correction for turbulent flow, Eq. (62)
  - Q_5' as Q_5 but omitting surface tension.

2 A family of experiments

This study is built around a dataset generated during a series of low-tech, tabletop experiments that can be readily reproduced and extended. The tank was a polypropylene, semi-transparent laboratory beaker into which holes of known diameter, orifices, were drilled carefully a few centimeters above the bottom. For most experiments, there was a polypropylene tube connected directly to the orifice (very much like the cover page illustration) and kept horizontal. The length of this 'pipe' could be easily cut down, including to effectively zero. The fluid was ordinary tap water, whose viscosity, μ, and surface tension, σ, are well-known functions of temperature.

2.1 Parameter space of this apparatus

The immediate aim of the experiments was to document the time to drain (or more generally the draining rate) over the accessible range of the independent parameters that define this family of experiments:

- orifice or pipe diameter, $3 \leq d \leq 6.5$ mm,
- pipe length, $0 \leq L \leq 1.5$ m,
- fluid viscosity, $0.6 \times 10^{-3} \leq \mu \leq 1.5 \times 10^{-3}$ Pa s, depending upon water temperature,
- surface height, $0 \leq h \leq 0.15$ m.

Other relevant parameters that were not varied in these experiments:

- σ = 75 $\times 10^{-3}$ N m^{-1}, surface tension of fresh water at room temperature,
- $D = 0.185$ m, the tank diameter,
- $g = 9.8$ m s^{-2}, acceleration of gravity, and
- $\rho = 998$ kg m^{-3}, the nominal density of fresh water.

This apparatus is intermediate in scale — it is much larger than the scales of biological, capillary flows, and it is much smaller than the scales of a continent-spanning natural gas pipeline. The resulting flows may be characterized as low speed, low energy, and mostly *laminar*. However, in the higher range of Reynolds numbers accessed here there are fairly clear signs of weakly *turbulent* flow discussed in Sec. 7.

2.2 Making observations

Experiments began by filling the beaker with water having a measured temperature ranging from very hot to almost freezing. Once the fluid had settled (observed with dye), the orifice or pipe was uncovered, and the water allowed to drain freely. The beaker had a volumetric scale, and the elapsed time, t_i was recorded as the surface descended by discrete intervals of volume, W_i = (4.5, 4.0, 3.5 ... 0.5) $\times$ 10^{-3} m^3, and thus the direct observation was of (W_i, t_i) at about 8 - 12 times. Most experiments were complete within twenty minutes. The surface height in meters referenced to the orifice center (where $W = W_0$) is easily calculated by

$$h_i = (W_i(t) - W_0)/A, \tag{1}$$

where $A = \pi D^2/4$ is the surface area of the tank. A closely related variable is the outflow volume transport, Q, estimated by first-differencing the discrete, observed volumes and times,

$$Q_i \approx -\frac{W_{i+1} - W_i}{t_{i+1} - t_i}. \tag{2}$$

The sign convention ensures that the estimated outflow $Q > 0$, to aid visualization. The h that goes along with (2) is the midpoint average $\bar{h_i} = (h_{i+1} + h_i)/2$, and similarly for the time. From here on the subscripts and accents are dropped, and h, t and Q are treated as if continuous.

The measurements were found to be nearly repeatable, with random errors in the time estimated to be no more than 2 seconds. These small errors do not accumulate during the course of an experiment, and may be suppressed by a three-point smoothing of the observed times (applied in only a few cases). The largest source of systematic error comes from defining the inside diameter of the tube, d. For each tube, the diameter was measured by feeler gauges and often found to be slightly different, by as much as 0.1 mm, from the diameter indicated by the manufacturer (not a problem for the orifice diameter, which is well-controlled). Uncertainty in d is magnified by the sensitive dependence upon d that characterizes several aspects of tank-draining, e.g., outflow transport $Q \propto d^2$. The net uncertainty on any one estimate of Q is roughly $\pm 10\%$ of the magnitude.

These measurements were neither highly resolved nor highly precise. That is less than ideal, of course, but it is not disqualifying because the case-to-case variation with changing parameters is considerably greater than are the random or systematic errors that compromise the value of any one realization. Thus, we can with some confidence explore the parameter dependence of h and Q over a family of experiments. Dimensional analysis is especially useful in this context.

2.3 Inferences from the first experiments

The first set of experiments used room temperature water, $T = 20\,^\circ C$, and no pipe (orifice-only) and so L was effectively zero. The orifice diameter was $d = 3, 4.5$ or 6.5 mm. The surface height $h(t)$, here regarded as the dependent variable, decreased smoothly in time, Fig. 2. Notice that the variation of h with d — the signal we are after — is considerably greater than are the likely experimental errors noted above.

After several trials with dimensional analysis, it became evident that the usual tank-draining problem — *How long to drain this tank?* — was best approached indirectly.

The first issue is that in some experiments the tank never actually drained in the strong sense $h \to 0$. At the beginning of an experiment, when h was largest, the outflow makes a continuous stream, or jet, of water that traces out what appears to be a ballistic trajectory. As h becomes small, less than a few centimeters, the outflow may slow significantly and then stop when h was still

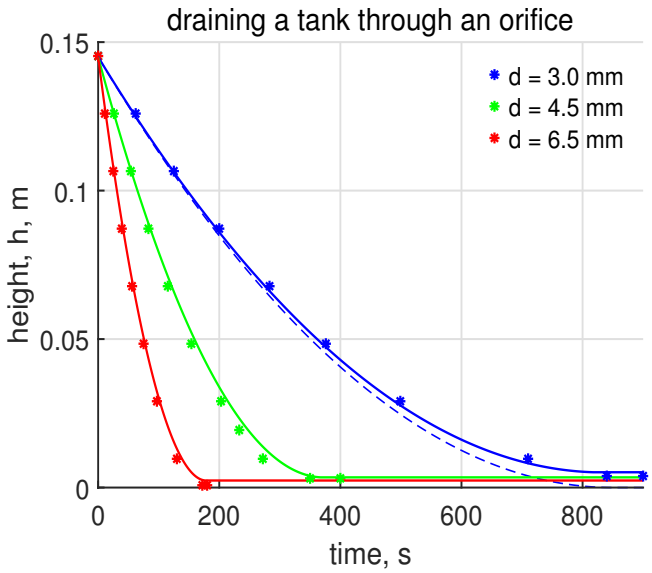

Figure 2: Surface height, $h(t)$, from three orifice-only experiments that had different orifice diameters, the red, green and blue dots. The trajectories $h(t)$ are very nearly parabolic, a rapid decrease at the beginning that markedly slows as h decreases. These experiments show that a modest increase in orifice diameter resulted in a substantially faster decrease of the surface height. Notice that the surface height stops descending short of zero. The dashed blue line is the ideal fluid Model 1 solution for the case $d = 3.0$ mm. Model 1 ignores surface tension and so this solution drains to zero. The solid lines are computed by Model 2 which acknowledges surface tension (coming in Sec. 4).

roughly 1 cm above the center of the orifice. The fluid then forms an outward protruding cap or bubble that is evidently held in place by surface tension and adhesion to the beaker. Surface dynamics of this kind is central to many small scale fluid problems and is discussed briefly in Sec. 4.

A second issue is that a response to the original problem (how long?) implies the construction of a model relationship for the time-dependent height, $h(t)$. Consider the simplest possible version of this: draining an ideal fluid (zero surface tension and zero viscosity) through an orifice (zero pipe length). In Sec. 3.1 below we will examine a very simple and effective model for this problem. But suppose we do not know the model — we can still make progress via dimensional analysis provided only that we can compile a list of the variables and parameters that would appear in an appropriate model.

- A VPlist for the surface height of an ideal fluid draining through an orifice:

1. surface height, $h \doteq [\,0 \quad 1 \quad 0\,]$, the dependent variable,
2. time, $t \doteq [\,0 \quad 0 \quad 1\,]$, an independent variable,
3. initial height, $h_0 \doteq [\,0 \quad 1 \quad 0\,]$, a parameter,
4. diameter of the orifice, $d \doteq [\,0 \quad 1 \quad 0\,]$, a parameter,
5. diameter of the tank, $D \doteq [\,0 \quad 1 \quad 0\,]$, a parameter,
6. acceleration of gravity, $g \doteq [\,0 \quad 1 \quad -2\,]$, a parameter.

If this list is indeed complete, then we can assert that there is, in principle, a relationship

$$h = F(t, h_0, d, D, g). \tag{3}$$

The function F is unknown, and it is, of course, crucial. Absent an appropriate model, experimental data are required to show what F might be.

Now consider the nondimensional counterpart of (3). This VPlist has six members having two fundamental units, length and time. Our rule-of-thumb guidance to the number of required nondimensional variables (discussed in the main text, Sec. 3) indicates that a basis set for this VPlist (notice that it is not *the* basis set) will contain six minus two = four nondimensional variables. As one possibility, the nondimensional version of (3) could be

$$\frac{h}{h_0} \;=\; F(t\sqrt{g/h_0},\; \frac{d}{D}, \frac{h_0}{D}), \tag{4}$$

which recycles the symbol F to represent an unknown function. The dependent variable is h in units that are natural to the problem, h_0.[5] Similarly, the orifice diameter d is in units of the tank diameter, D, and time is measured by the time required to free-fall a distance h_0 while accelerating at g. In place of five dimensional variables in the F of Eq. (3), there are just three nondimensional variables in the F of (4). That is a very useful, practical result from dimensional analysis, but it is not a finished result until F can be specified.

Dealing with three independent nondimensional variables is certainly possible (many real-life problems are far more extensive), and yet (4) seems unduly cumbersome given how straightforward and spare this problem appears to be. It will often happen that the first try at a VPlist will have a broader scope than is desirable for the problem at hand — in this case, slow outflow due mainly to the property that $d \ll D$. How can we change the problem and the VPlist to reflect that qualification?

2.4 Changing the problem from h(t) to Q(h)

The surface height, h, is very important in what follows. Nevertheless, h may not be the best choice for the dependent variable. The reason, shown below, is that a model of $h(t)$ necessarily requires the time, t, and the tank diameter, D, as parameters.

Suppose instead that we seek a model of the volume transport, Q, of the outflowing water, Eq. (2). A key modeling assumption appropriate to this new problem is that Q depends only (or mainly) upon local conditions, and specifically the pressure difference across the orifice. As a corollary of this, the beaker diameter is large enough compared to the orifice that the beaker may be viewed as an infinite reservoir of water that is effectively at rest. D will then have a negligible effect upon the

[5] One could just as well say that h is measured by, divided by, scaled by, or nondimensionalized by h_0.

volume transport, though it will remain an essential parameter in any model that seeks to compute the time to drain, as in (4). Since $d << D$, the flow within the tank is very slow compared to the outflow velocity, and the acceleration of the water in the tank is negligible compared to g. The pressure $P(z)$ within the beaker is then given accurately by the hydrostatic pressure,

$$\frac{\partial P}{\partial z} = -\rho g, \tag{5}$$

and so

$$P(z) = \rho g (h - z) + P_{atm}, \tag{6}$$

where z is the vertical coordinate positive up and zero at the orifice, and ρ is the constant density of the fluid.[6] P_{atm} is the ambient, atmospheric pressure which varies insignificantly over the depth of the tank. The pressure difference across the orifice is, provisionally, just

$$\delta P_{orf} = \rho g h, \tag{7}$$

the hydrostatic pressure inside the tank at the depth of the orifice. The important variable of (7) is h; g and ρ are necessary to have the units of pressure, but are global constants in this family of experiments.

- A VPlist for the pressure-driven volume outflow of an ideal fluid through an orifice:

1. outflow volume transport, $Q \doteq$ [0 3 -1], the dependent variable,
2. surface height above the orifice, $h \doteq$ [0 1 0], the independent variable,
3. diameter of the orifice, $d \doteq$ [0 1 0], a parameter,
4. acceleration of gravity, $g \doteq$ [0 1 -2], a parameter,
5. density of the fluid, $\rho \doteq$ [1 -3 0], a parameter.

A quick calculation of a null space basis from this VPlist leads to

$$\frac{Q}{d^2 \sqrt{g h}} = F(\frac{h}{d}), \tag{8}$$

which has only one independent, nondimensional variable. This represents major progress from Eq. (4). Dimensional analysis has gotten us as far as this very efficient representation of Q. To go further and specify the function F will require physics and/or observations.

[6] To here this is the usual, elementary tank-draining problem. An advanced treatment is by D'Alessio, S., 2021, Torricelli's law revisited. European J. of Physics, 42 065808.

2.5 Torricelli velocity and a zero-order model

Eq. (8) could be used as is, but it is helpful to modify it superficially by introducing two O(1) numerical factors into the left-side denominator,

$$\frac{Q}{\frac{\pi}{4}\,d^2\,\sqrt{2\,g\,h}} \;=\; F(\frac{h}{d}). \tag{9}$$

A factor $\pi/4$ multiplies d^2 to give the area of the orifice,

$$a \;=\; \frac{\pi}{4}\,d^2.$$

A factor $\sqrt{2}$ multiplies $\sqrt{g\,h}$. The latter follows from the conservation of energy of a particle falling a distance h under gravity and acquiring kinetic energy $\propto\; V^2/2 \;=\; g\,h$. The velocity of an energy-conserving free fall is then

$$\boxed{V_T \;=\; \sqrt{2\,g\,h}} \tag{10}$$

dubbed the Torricelli velocity.[7]

The product of V_T and the area of the orifice makes a sensible, physically-based natural scale for the outflow transport,

$$\boxed{Q_0 \;=\; a\,V_T \;=\; a\,\sqrt{2\,g\,h}} \tag{11}$$

In the main text[3] this sort of thing was called a zero-order model, here shortened to Model 0 and for the transport, Q_0. If h is regarded as a known, independent variable, then Q_0 is known. This Q_0 will be used throughout this study to nondimensionalize Q, and e.g., Eq. (9) becomes

$$\frac{Q}{Q_0} \;=\; F(\frac{h}{d}). \tag{12}$$

A key, implicit assumption of (12) is that the geometric properties of the tank are represented by the single nondimensional variable $h\,/\,d$. In the orifice-only cases, the actual (dimensional) transport Q comes close to Q_0 so that $F(h/d)$ is just slightly less than 1. In other cases, especially those involving long and narrow pipes that will be treated in Secs. 5 - 7, Q is much less than Q_0 and so $F \;\ll\; 1$.

---

[7] Evangelista Torricelli, 1608 - 1647, was a student and then a close associate of Galileo Galilei. His experimental investigations on a draining tank showed that the outflowing jet described a ballistic trajectory like that of a solid particle. Torricelli's research on vacuum and barometers led to an appreciation for atmospheric pressure and the crucial insight that 'we live submerged at the bottom of an ocean of air'. This included that horizontal variations of pressure were the immediate cause of winds, the start of dynamic meteorology. A derived unit of pressure, the torr, is in his honor and is 1 torr = 1 mmHg (nominal g) at 0 C. The torr is today used mainly in vacuum applications.

2.6 Summary to here and outlook

This investigation will proceed along three lines.

Experimental observations are the essential starting point. Experiments will document Q along with the relevant fluid and tank parameters.

Dimensional Analysis provides an efficient framework for analyzing the observations by defining the minimum number of independent variables, e.g., Eq. (4) vs. (3).

Theory and Modeling coming in later sections will seek to illuminate and reproduce the function F of relations like (12).

2.7 Problems

- In Sec. 2.4 the tank-draining problem was changed from modeling $h(t)$ to modeling $Q(h)$. How and why did this change the status of the variable h?
- What dimensional variables or parameters have gone missing from Eq. (8) compared with Eq. (4), and on what basis?

3 An elementary (and very successful) Model 1

3.1 A data-driven Model 1

We know all of the individual terms of (12), including most importantly Q from the observations of Fig. 2 and Eq. (2). What we do not know is the function F, and dimensional analysis alone can not tell us anything more. To find out what F looks like, let's evaluate (12) by plotting the nondimensional transport Q/Q_0 against h/d, Fig. 3, left.

It appears that $F(h/d)$ exhibits two regimes.

- At smaller values of h/d (small compared to what?), the normalized volume transport goes to zero as h/d goes to zero, and indeed the transport may vanish while h is still appreciable. This is directly related to the surface tension-induced bubble noted above, and discussed further in Sec. 4.
- At larger values of h/d, roughly $h/d > 10$, which includes most of the experimental data, the normalized volume transport is quasi-independent of h/d. In other words, at larger values of h/d, the function $F(h/d)$ is nearly a nondimensional constant, call it C.

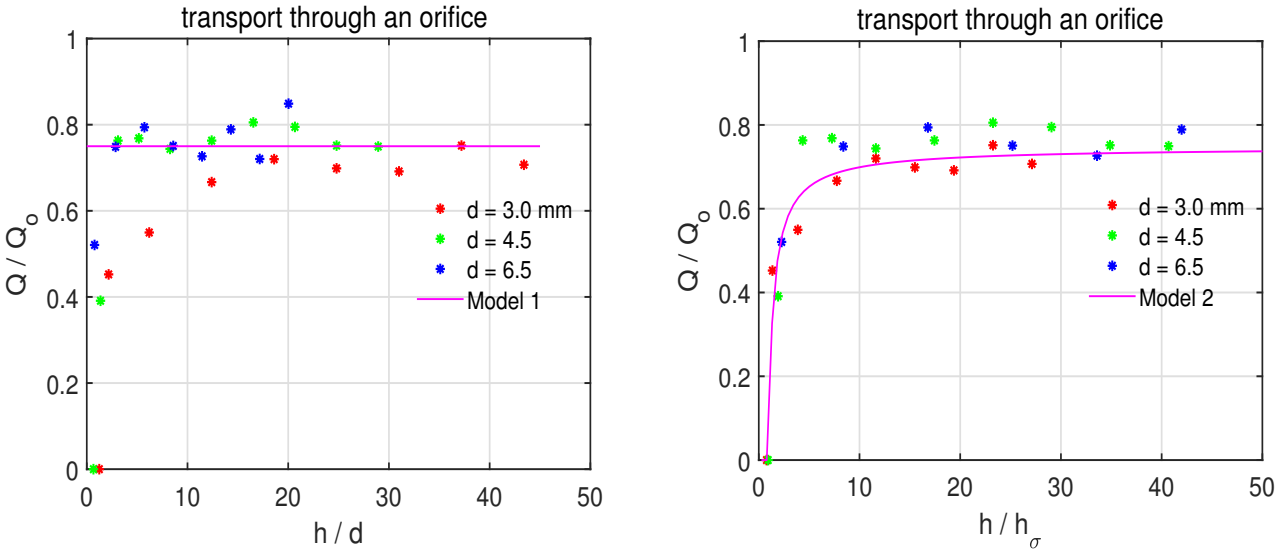

Figure 3: **(left)** Observed volume transport from the orifice-only experiments of Fig. 2. The transport is nondimensionalized consistent with Eq. (12). It is argued that there are two regimes evident here. At small h/d, the nondimensional transport decreases as h/d goes to zero. At larger h/d, the transport is approximately independent of h/d, the magenta line which is Model 1, Sec. 3.2. **(right)** This is the same data shown at left, except that the independent variable is h/h_σ, where h_σ is the pressure head due to surface tension, Eq. (19). This magenta line comes from Model 2 described in Sec. 4.3.

Dimensional analysis does not evaluate C, but the data of Fig. 3 indicate that

$$\frac{Q}{Q_0} \;=\; C \;=\; 0.77 \;\pm 0.03 \tag{13}$$

is a reasonable first approximation for these three experiments. It bears some emphasis that the step from Eq. (12) to (13) is

- empirical — C is calibrated using these observations, and 0.77 may not be appropriate to your apparatus or your fluid.
- contingent — Eq. (13) holds only for larger h/d.

The parameter C is called the 'discharge coefficient', and a value in the range $0.6 < C < 0.8$ is expected for simple, square-edged orifices of the present sort.[8] The physical process that leads to a C that is slightly less than 1 in these experiments is not primarily friction (viscosity), as one might first guess, but rather inertial acceleration on the water approaching the orifice. The evidence for this is twofold. First, C varies only weakly with viscosity (temperature) in this family of experiments. Second, dye observations show that the flow into the orifice comes from the entire hemispherical

[8] A thoughtful discussion of C is by Savage, T., Porterfield, W. R. Penney and E. C. Clausen, The draining of a tank: A laboratory experiment in fluid mechanics. ASEE Midwest Section Conference, 2021.

region inside the tank. The inflow to the orifice has to be accelerated, and some fraction of it also has to make a sharp 90 degree change in direction as it approaches and enters the orifice. Even modest fairing (rounding on the inside of the orifice) can ease this sharp change of direction and bring C close to 1.0. On this basis, the orifice flow process will be called 'inertial' to distinguish from viscous and surface tension phenomena coming in the next two sections.

3.2 Integrating to find h(t)

Given (13), a useful model of the outflow transport, dubbed Model 1, is just

$$Q_1 \;=\; C \times Q_0 \;=\; C\,\frac{\pi}{4}\,d^2\,\sqrt{2\,g\,h}. \tag{14}$$

From here and given Eqs. (1) and (2), it is straightforward to write an ODE for $h(\,t\,)$,

$$\frac{d\,h}{d\,t} \;=\; -\,\frac{Q_1}{A} \;=\; -\,C\frac{d^2}{D^2}\,\sqrt{2\,g\,h} \tag{15}$$

that may be integrated to find

$$h(t) \;=\; \left(\sqrt{h_0} \;-\; \left(0.5\,C\,(\frac{d}{D})^2\,\sqrt{2\,g}\right)\,t\right)^2. \tag{16}$$

This defines a parabolic $h(t)$ (second degree in time) that, overall, bears a striking resemblance to the experimental data shown in Fig. 2 (the dashed, blue line compared to the blue dots). In all cases the surface height decreases rapidly at the start of an experiment and then slows markedly as $h \to 0$. When a pipe is present, wall friction due to either or both laminar viscous flow and turbulent flow can change the rate quite a lot, but this pattern remains a characteristic of the $\sqrt{g\,h}$-dependence of a gravity-driven outflow transport, Eq. (11).

3.3 Summary

Model 1 makes a very good start, and for not much effort. In particular, it shows that the surface of a tank that is draining due to a gravity-driven outflow will fall (comparatively) rapidly at the start of an experiment, and then slow markedly as the pressure difference across the orifice decreases.

Model 1 leaves some room for improvement. Eq. (14) departs from the observations at smaller values of h/d, roughly $h/d < 8$, in that it indicates constant $Q_1/Q_0 \;=\; C$ all the way to h = 0. On the other hand, the observations indicate that the (nondimensional) transport slows for small h/d, and then may stop altogether before the tank is completely drained, Fig. 3. This is not a measurement

artifact. The corresponding error in Eq. (16) is that the predicted h goes to zero. Evidently something is missing from (14) and (16).

3.4 Problems

- The orifice-only outflow Model 1, Eq. (14), can be rewritten as an ordinary differential equation $dh/dt = F(h, g, d, D)$, Eq. (15). Integrate this equation given an initial value $h(t = 0) = h_0$ to find Eq. (16).[9] How does this solution compare with the expectations from dimensional analysis, Eq. (3)?

- It has been noted that a parabolic in time trajectory $h(t)$ is characteristic of a gravity-driven outflow for which $Q \propto \sqrt{g\,h}$. Suppose instead that the outflow transport is (for some reason) linear in h, i.e., $Q \propto g\,h$. What is the trajectory $h(t)$ in that case?

- Imagine that the water tank is closed on top, so that the air pressure above the water surface can be altered by a controllable air pump. What additional air pressure (above atmospheric) would be required to yield a constant Q, until the tank drains and uncovers the orifice?

- It was claimed in Sec. 3.2 that the discharge coefficient C for the present experiments is effectively a constant because it is a result of inertial (accelerated) flow. This depends upon the geometry of the orifice which doesn't change appreciably from one experiment to the next. However, this is not a universal law. Consider that the fluid being drained is honey, which has a viscosity that is roughly 5,000 times that of water. Qualitatively, how would this increased viscosity affect the magnitude of the transport? Does this imply that C must, in general, depend upon ν, even while the claim made here is that viscosity is not important for *these* orifice-only experiments? This example illustrates why nearly every claim made here has to be qualified with the tedious phrase 'for these experiments' meaning that the fluid is something like water and that the geometric dimensions are not too far from those listed in Sec. 2.1.

4 Surface tension reduces transport in the small h/d regime

It was noted above that the outflow may come to a stop before $h \to 0$. In that state the outflow appears to be blocked by a flattened bubble of fluid that caps the orifice. The inference is that surface tension has overcome the hydrostatic pressure difference (7) that would otherwise accelerate fluid through the orifice. This is not a large effect on the scales that characterize the parameter range of

[9] An excellent tutorial for this problem is https://www.youtube.com/watch?v=iKDdInE7wqE.

these experiments, i.e., the d, h, g, etc. of Sec. 2.1. However, this effect is systematic and interesting on its own merits.[10]

4.1 Why do fluids exhibit surface tension?

Surface tension is a fundamental characteristic of a fluid that has an appealing microscale explanation. The individual molecules of a fluid are free to move and jostle around but they are also cohesive, in that fluid molecules exert an intermolecular attraction (hydrogen bonding in water) that acts to clump fluid molecules together. When clumped together, water molecules are in a lower energy state than if they were separated and moving independently (as do the molecules that make up a gas). Where there is a free surface that exposes the fluid to some other, less attractive material — if water, then air — the molecules that are immediately on the free surface will not have fluid molecules on all sides, and so will be in a slightly elevated energy state; think of attracting particles that have been pulled apart. The existence of a free surface thus implies some potential energy that may be characterized as a thermodynamic property called surface tension, denoted here by σ. Surface tension can be viewed as either an energy per unit area, in SI units, Joules per meter squared, and so $\sigma \doteq [\,1\ 0\ -2\,]$, or, as a force per unit length, Newtons per meter, and having the same fundamental dimensions. Both interpretations are useful.

Water has a fairly high surface tension,

$$\sigma \approx 75 \times 10^{-3}\ \mathrm{J\ m^{-2}} = \mathrm{N\ m^{-1}},$$

compared to most other familiar fluids, e.g., isopropyl alcohol, for which $\sigma \approx 20 \times 10^{-3}$ N m^{-1}. A familiar consequence is that water tends to form into spherical drops (absent some other influence such as air drag on a falling drop) that minimize surface area, and thus the surface energy for a given volume. Surface tension, viewed as a force per unit length, acts as a membrane under tension that maintains a spherical shape. A consequence is that there is an elevated pressure inside a water drop that is proportional to σ times the Laplace curvature of the surface. The curvature of a sphere is $2/r$, with r the radius; the pressure inside a spherical water drop is thus

$$P_{drop} = 2\,\sigma/r \tag{17}$$

higher than the ambient pressure.[10]

[10] Surface physics is vitally important for microfluidic (very small scale) devices. An excellent introduction to surface tension is https://en.wikipedia.org/wiki/Surface_tension Also highly recommended and more advanced is https://web.mit.edu/1.63/www/Lec-notes/Surfacetension/Lecture1.pdf

4.2 Surface tension and pressure within a cylindrical jet of water

A vigorous outflow through a round orifice produces a cylindrical jet of water, cover page.[11] The surface curvature of a cylinder is half that of a sphere having the same radius and thus the surface-tension induced pressure within the jet is estimated to be half that of the corresponding sphere, i.e.,

$$P_\sigma \;=\; \frac{\sigma}{r}. \tag{18}$$

The pressure P_σ can be expressed as an equivalent hydrostatic pressure head,

$$\boxed{h_\sigma \;= \frac{\sigma}{\rho\, g\, r},} \tag{19}$$

which is constant for a given experiment. For the surface tension of water and if r is a few millimeters, then h_σ is O(1) cm.

From this discussion it seems plausible that the outflow transport might be dependent upon h_σ which suggests a revised form of Eq. (12),

$$\frac{Q}{Q_0} \;=\; F(\frac{h}{h_\sigma}). \tag{20}$$

When the data of Fig. 3 are nondimensionalized in this way (right panel), the normalized transport is found to decrease significantly when $h/h_\sigma < 5$, and vanishes at roughly $h/h_\sigma \leq 1$. This is consistent with the notion that the surface-tension induced pressure inhibits the outflow, an effect which is especially noticeable for the smaller diameter orifices and pipes considered here.

4.3 Model 2 includes a first-order effect of surface tension

This, in turn, suggests a revised model for orifice transport. Model 1, Eq. (14), amounts to taking the pressure outside the tank to be zero. Now we understand that there is a slightly higher pressure required to overcome the surface-tension induced pressure acting upon the jet. With that in mind, revise the Torricelli velocity to

$$V_{T\,\sigma} \;=\; \sqrt{2\,g\,(h - h_\sigma)}, \tag{21}$$

and define a Model 2 for the transport,

$$\boxed{Q_2 \;=\; C\,\frac{\pi}{4}\,d^2\,\sqrt{2\,g\,(h \;-\; h_\sigma)}} \tag{22}$$

[11] A parcel of fluid within the free-falling jet has a certain horizontal velocity, $dX\,/\,dt \;=\; V_o \;\approx\; V_T$, that is nearly conserved, and it is accelerated downward by gravity at a rate $d^2\,Y\,/\,dt^2 \;=\; -\,g$. A parcel, and thus the jet, traces a parabolic (ballistic) trajectory, $X \;\propto\; (V_o\,/\sqrt{g})\,\sqrt{-Y}$.

that is valid only for $h \geq h_\sigma$. This may be solved for

$$h(t) = h_\sigma + \left(\sqrt{h_0 - h_\sigma} - \left(0.5\, C\, (\frac{d}{D})^2 \sqrt{2\, g} \right) t \right)^2, \tag{23}$$

the solid red line of Fig. 2. Compared with Model 1 that ignored surface tension (the dashed red line), the new Model 2 solution for $h(t)$ is only slightly different overall from that of Model 1, but it does include the qualitative feature that h asymptotes to h_σ, rather than to zero, as does the solution of Model 1.

4.4 Summary

A more sensitive test of Model 2 comes from differentiating the solution (23) and evaluating $Q_2/Q_0 = F(h/h_\sigma)$, the magenta line of Fig. 3. This shows a slowing of the outflow as h/h_σ falls below about 5, and stopping altogether at about $h = h_\sigma$. These are consistent with the observations, and suggest that this first-order treatment of surface tension makes a small but useful step toward a realistic model.[12]

The first-order treatment of surface tension reflected in Eq. (21) is as far as this study will go regarding surface tension *per se*. This result will be incorporated into Models 4 and 5 developed in Secs. 6 and 7. Until then, surface tension will be set aside in order to focus attention on the viscous effects that can greatly modify the outflow transport through a pipe.

4.5 Problems

- The left and right sides of Fig. 3 give us a chance to compare two versions of a nondimensional format, $F(h/d)$ vs. $F(h/h_\sigma)$ (recall that F merely holds a place for an unspecified function). Which is the better nondimensional independent variable, h/d, or h/h_σ? What criteria could we deploy to decide this? Three suggestions: First, simplicity or transparency are always desirable, but probably not decisive. Second, if one version produces a more convincing collapse of the data toward a single curve, then that would surely count in its favor. Third, which of the inferred relations $F(h/d)$ and $F(h/h_\sigma)$ has a better-motivated, quantitative physical interpretation? Can

[12] The present treatment of surface tension overlooks a detail (within a detail). As h approaches h_σ, the outflow slows markedly, and then begins to dribble down the side of the tank: a weak outflow continues, but there is no more ballistic jet. After a short time, the dribbling stops and the orifice becomes capped over, as described above. The cap has some curvature but not so much as a sphere: $P_{\sigma-cap} \approx \sigma \,/\, r$ seems plausible for the blocked outflow. Also ignored here is the wetting properties of the solid substrate: polypropylene, does it attract or repel water? A single stage surface tension effect estimated by Eq. (22) is perhaps a fortuitous approximation. For more on these phenomena, see Ferrand, J., L. Favreau, S. Joubaud and E. Freyssingeas, 2016, Wetting effect on Torricelli's law, Phys. Rev. Lett., 117, 248001 - 248005.

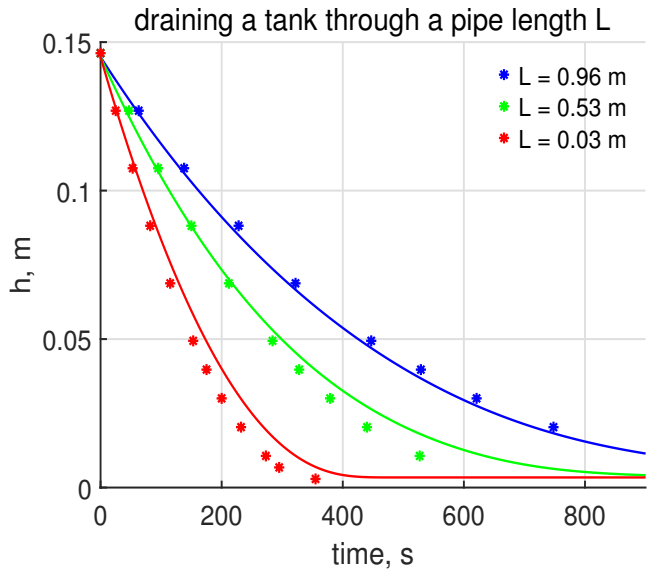

Figure 4: Surface height, $h(t)$, from three experiments in which the water was drained through pipes that had diameter $d = 4.7$ mm and one of three lengths, $L = 0.96$ m, 0.53 m, or 0.03 m, almost an orifice. The solid lines are calculations made by Model 4 discussed in Sec. 6.

you show that

$$\frac{h}{h_\sigma} \propto \frac{hydrostatic\,pressure}{surface\,tension\,pressure}.$$

This ratio of gravitational to surface tension pressure is often called a Bond or Eotvos number.

- Using dimensional analysis, show that the pressure anomaly inside a cylindrical jet of radius r is as given by Eq. (18), $P_\sigma = \sigma / r$ up to an unknown factor (happens to be 1). Two hints: for surface tension, $\sigma \doteq [1\ 0\ -2]$ and pressure, $P \doteq [1\ -1\ -2]$. Can you go from here to the equivalent height of a hydrostatic pressure and Eq. (19)?

5 Outflow through an orifice and a pipe, starting with observations

If the outflow must pass through a pipe, as on the cover page, it is expected that the volume transport will be lessened by drag (friction) between the moving water and the walls of the pipe. A few experiments show this effect clearly; for a given fluid (water at room temperature) and a given diameter of the pipe and orifice, the tank drains considerably more slowly when the pipe is longer, Fig. 4. By changing the temperature of the water, and thus the viscosity of the water, it is evident that warmer water (smaller viscosity) drains somewhat faster than does colder water, Fig. 5. The qualitative sense of these viscous effects is not surprising. To go beyond that and make a model, we have to define the magnitude of viscous effects. How can we organize the experimental data to this end?

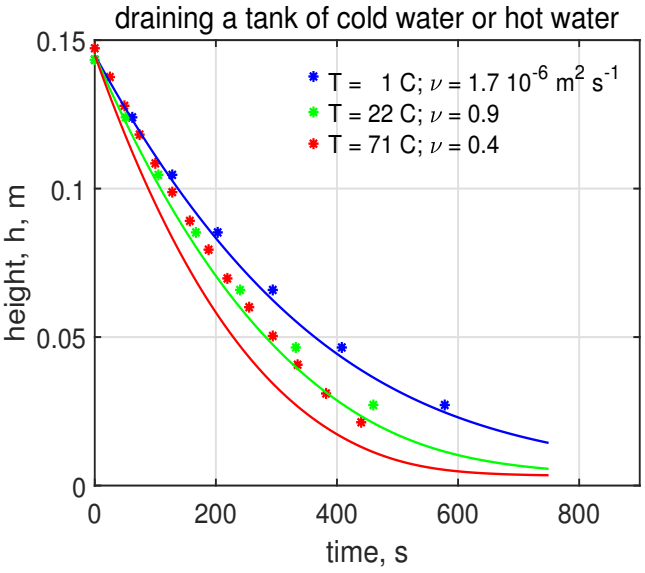

Figure 5: Surface height, $h(t)$, from three experiments that had pipe diameter and length in common, $d = 4.7$ mm and $L = 0.64$ m and thus $L/d \approx 140$. They differed by the temperature of the water, from nearly freezing (blue dots) to very hot (red dots). As a consequence, the kinematic viscosity, ν (= μ/ρ), varied by roughly a factor four. The warmest water (red dots) which had the smallest viscosity, drained considerably faster than did the cold water (not surprising), but, notice that it drained only slightly faster than did the room temperature water (green dots). This hints at something important coming in Sec. 7.2

As a guide, let's look for the relationship between the outflow transport and the (presumed) relevant variables under the assumption that the outflow transport is dependent only upon the local conditions at the orifice and the pipe (note that surface tension is omitted for now).

- A VPlist for pressure-driven outflow of water through an orifice and a pipe: (24)

1. outflow volume transport, $Q \doteq$ [0 3 -1], the dependent variable,
2. diameter of the orifice, $d \doteq$ [0 1 0], a parameter,
3. hydrostatic pressure head at the orifice, $gh \doteq$ [0 2 -2], an independent variable,
4. kinematic viscosity of the water, $\nu \doteq$ [0 2 -1], a parameter,
5. length of the pipe, $L \doteq$ [0 1 0], a parameter.

Three nondimensional variables are expected, and for this (arbitrary) ordering of the VPlist, the algorithm returns

$$\frac{Q}{L\nu} = F(\frac{d}{L}, \frac{L^2\, gh}{\nu^2}). \tag{25}$$

This is correct mathematically, i.e., it is a basis set of nondimensional variables for this VPlist. However, the important scale that normalizes the transport, $L\nu$, seems oddly out of place here. ($L\nu$ will arise again later in a context where it will make sense.) Use instead the zero-order model defined by Eq. (11), $Q_0 = \frac{\pi}{4} d^2 \sqrt{2gh}$, which presumes that inertial (rather than viscous dynamics) are dominant. This is a reminder that the purely formal method of dimensional analysis may not provide physical sense; that is a judgment and task left for us. After some reorganizing of the variables in (25) there follows an important relationship:

$$\boxed{\frac{Q}{Q_0} = F\left(\frac{L}{d}, \frac{V_T\, d}{\nu}\right)} \tag{26}$$

The left side of (26) is the now familiar nondimensional volume transport. The unknown function F on the right-hand side depends upon two nondimensional, independent variables. The first independent variable, $L\,/\,d$, is an aspect ratio, and is a straightforward reply to 'how long is this pipe?' given in natural units. In these experiments, L/d is in the range 0 - 500. The second nondimensional variable on the right side of (26) is less obvious.

5.1 Reynolds numbers, external and internal, Re_x and Re

The second independent variable

$$\text{external Reynolds number,} \quad \boxed{Re_x \;=\; \frac{V_T\, d}{\nu}} \tag{27}$$

has the form of a

$$\boxed{Reynolds\ number \;\propto\; \frac{velocity\ scale \times length\ scale}{kinematic\ viscosity}} \tag{28}$$

This ratio is important in many contexts, and Reynolds numbers come in correspondingly many versions.[13] The terms of (27) are:

- ν**, kinematic viscosity**, is straightforward when it is regarded as a fluid property, the usual intent of the Navier-Stokes equations.
- V_T**, a velocity scale** (a speed) is usually clear. In Eq. (28) the velocity is the Torricelli velocity, $V_T \;=\; \sqrt{2\,g\,h}$, which may be evaluated *a priori*, before a solution is known, presuming that h is observed or otherwise known. For that reason the Reynolds number (27) is said to be an 'external' Reynolds number. This Re_x is different from the much more often encountered

$$\text{internal Reynolds number,} \quad \boxed{Re \;=\; \frac{V_a\, d}{\nu}, \quad \text{where} \;\; V_a \;=\; \frac{Q}{a}} \tag{29}$$

The velocity V_a is the area-averaged velocity in the pipe and is known only after we know Q and so Re of Eq. (29) is said to be 'internal'. The link between these two Reynolds numbers is

$$\boxed{Re \;=\; Re_x\,\frac{Q}{Q_0}} \tag{30}$$

and hence Re will be somewhat smaller numerically than is Re_x. The internal Reynolds number will be used extensively in Sec. 7 when this analysis makes connection with the extensive historical literature on pipe flows.

[13] An excellent discussion of the Reynolds number including an interesting history is https://en.wikipedia.org/wiki/Reynoldsnumber

- L**, a length scale,** here taken to be the pipe diameter, d. The length scale is often the least obvious term in a Reynolds number. A conventional (though not altogether convincing) way to develop an interpretation of the length scale comes from a scaling analysis of the Navier-Stokes momentum equation,

$$\frac{\partial \mathbf{V}}{\partial t} \; + \; (\mathbf{V} \cdot \nabla)\, \mathbf{V} \;\; = \;\; - \nabla P/\rho \; + \; \nu \nabla^2 \mathbf{V} \; + \; \mathbf{g}. \tag{31}$$

  The goal is to compare the magnitude of the viscous term (second term on the right) to the inertial, acceleration term (second term on the left). Let V be the velocity scale, an upper bound on the magnitude of the fluid velocity expected in the problem. The kinematic viscosity ν can remain as is. The key is to identify a length scale, X, over which this velocity varies by O(1) so that, say for the x direction,

$$\frac{\partial V}{\partial x} \; \propto \; \frac{V}{X} \quad \text{and} \quad \nabla^2 \mathbf{V} \; \propto \; \frac{V}{X^2}.$$

  Under the assumption that a single length scale X is appropriate to the spatial derivatives in both the inertial term and the Laplacian of the viscous term, then it is straightforward to estimate the ratio of the inertial term(s) and the viscous term;

$$\frac{inertial}{viscous} \; \propto \; \frac{(\mathbf{V} \cdot \nabla)\, \mathbf{V}}{\nu \nabla^2 \mathbf{V}} \; \propto \; \frac{V^2/X}{\nu\, V/X^2} \; = \; \frac{V\, X}{\nu} \; = \; Re,$$

  a Reynolds number. In the case of pipe flow being considered here, the velocity varies with the radius, mainly, and thus the length scale X is identified as d.

Interpretation of Re_x: It is reassuring to find that a nondimensional number comes out to be O(1), as that implies a comparison of like things. There is no such comfort here; the numerical values of Re_x are O(10^4) (which is typical also for the Re of intermediate scale pipe flows). Taken literally, this would imply that the possible viscous force is much, much less than the inertial forces, and that some other term in the Navier-Stokes momentum balance must account for inertial accelerations (pressure gradient and/or time dependence). That is true, but nevertheless, these very large Re_x should not be interpreted to mean that viscosity may be omitted altogether (reminiscent of the air flow around a golf ball or a soccer ball, Sec. 4.5 of the main text).

What is the interpretation of Re_x for the present experiments? First, note that Re_x is the only independent variable of Eq. (26) holding ν; whatever viscous effects there are will be attributed to Re_x-dependence. Within this family of experiments, we can expect that a smaller value of Re_x should correspond to greater viscous effects, *viz.*, reduced transport.[14] The external Reynolds number thus appears to be a rough comparative measure of the ratio of inertial force (accelerations) to

[14] We usually think of a Reynolds number in association with viscous effects, but notice that viscosity happens to be in the denominator (it could have been otherwise). With that convention, smaller ν gives large Re, all else equal.

viscous force. Finally, given Eq. (30), the present Re_x can easily make contact with the vast literature on pipe flows that rely on the internal Reynolds number, Re (more on this in Sec. 7).

5.2 The function F for orifice plus viscous pipe flow

The relation (26) may be evaluated from the experimental data to provide a look at the function, $F(L/d,\ Re_x)$, Fig. 6. The coordinate system is three-dimensional since there is one nondimensional dependent variable, Q/Q_0, and two nondimensional independent variables, L/d, and Re_x, as noted above. Notice that surface tension has been excluded from these coordinates, but its effect is still present in some of the data.

A given experiment returns a handful of data points, all at the same L/d, and sampling a range of h, starting from h_0 and going to smaller h, in some experiments, to h_σ. The data points from a given experiment thus line up in strings that run parallel to the Re_x axis; larger Re_x is due to larger h. The nondimensional transport within a given experiment decreases smoothly with decreasing Re_x and thus with decreasing h. This is qualitatively consistent with the expectation that smaller Re_x (in the case of a single experiment because of small h) will generally correspond to a greater viscous effect.

The amplitude of the viscous effect, i.e., the decrease of the transport, depends also upon L/d. For the smallest values of L/d found on the left-most part of Fig. 6, this becomes the orifice-only result that $Q/Q_0 \ = \ C \ \approx \ 0.77$. In that limit, the Re_x-dependence vanishes: if L vanishes, then viscous effects effectively vanish as well. The converse is just as true; for a given Re_x, the nondimensional transport decreases significantly with increasing L/d; the decrease is especially strong at small values of L/d. In the range $L/d \ \approx \ 400$ and smaller Re_x found in the lower right corner of Fig. 6, the nondimensional transport is only about 25% of the orifice-only value, C.

5.3 Summary

Fig. 6 includes all of the data taken in these experiments (including data at small $h\,/\,h_\sigma$ that were likely affected by surface tension.) By visual inspection, it appears that the nondimensional coordinates of Eq. (26) will be a useful framework for the analysis of transport dependence upon h, L, d and ν insofar as the locus of data approximates a function $F(L/d, Re_x)$. Once we know this function, we can write an ODE for the surface height,

$$\frac{dh}{dt} \ = \ - A^{-1} Q_0 F(\, L/d,\ Re_x\,), \tag{32}$$

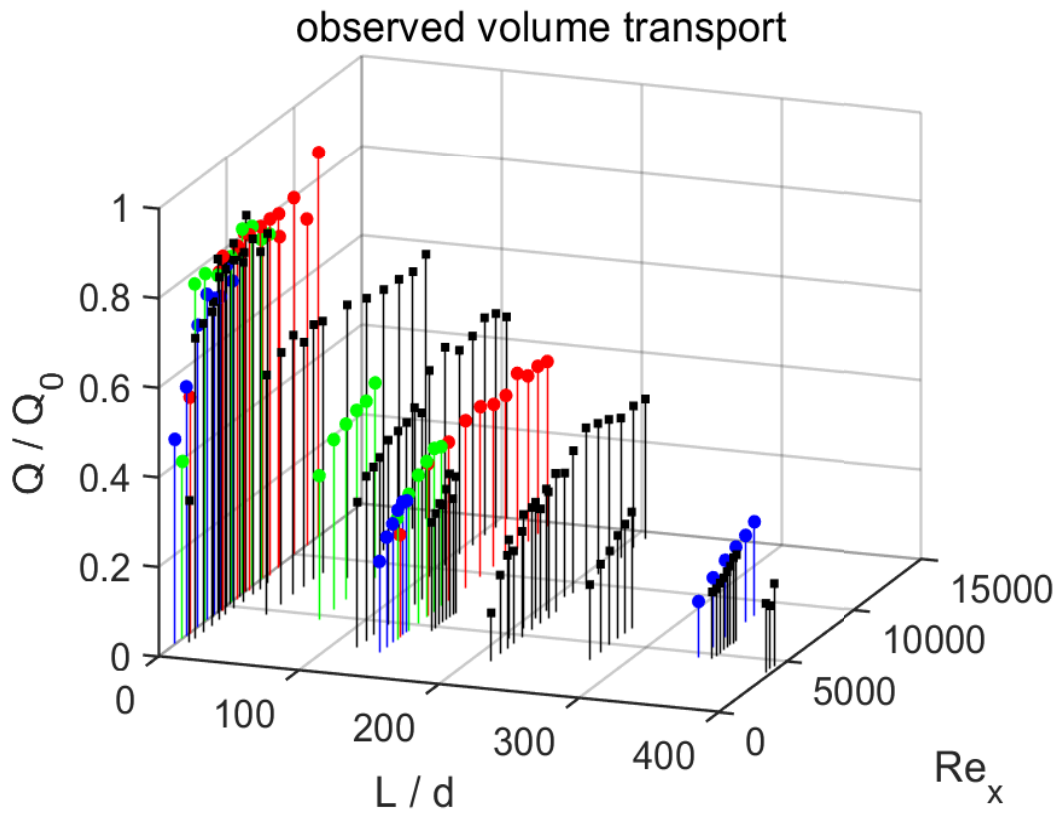

Figure 6: Observed nondimensional volume transport as a function of the pipe aspect ratio, L/d, and the external Reynolds number, $Re_x = V_T\, d\,/\,\nu$. There are 23 experiments shown here, each of which yields between five and 12 data points; 181 points in total. The data from a given experiment line up in a string that has a constant L/d, but a varying h. Each experiment thus samples a small range of Re_x. The red, green and blue dots are the data from the nine experiments of Figs. 2, 4 and 5. The black dots are from fourteen other, similar experiments. This is a rather dense and complex figure, but if you study it for just a minute you can envision that the locus of data points implies the existence of a two-dimensional surface $F(L/d,\ Re_x)$. A key objective of this study is to understand how such a surface arises and to use that understanding as a guide to model development (coming in Secs. 6 and 7). These data and a Matlab script to read and plot them are linked in Sec. 8.

a generalized version of Eq. (15). The Re_x in the argument of F above will include h. This will likely frustrate a separation of variables, but numerical solution should be fast and accurate.

To implement any solution, the function F has to be made portable. One could estimate an empirical fit to a dataset like Fig. 6, or, seek an appropriate model. The remainder of this appendix works toward the latter.

5.4 Problems

- There is no accounting for surface tension effects in the coordinate system of Fig. 6, and so it is questionable whether data that were likely affected by surface tension should be included. Where in Fig. 6 (at what L/d and Re_x) are these surface-tension-affected data?
- Can you find and then interpret the data that came from the three experiments with variable temperature shown in Fig. 5?
- Using the properties of a null space basis, recast Eq. (25) into the form preferred here, Eq. (26). The key step is choosing a scale for the dependent variable.

6 Models of viscous, laminar pipe flow

This section will develop models of laminar flow that are appropriate for the lower Re_x range of the parameter space sampled here, roughly $Re_x \leq 7000$. It is expected that at larger Re_x there will be a transition from laminar to turbulent flow with a consequence of larger wall stress (for a given Re_x) than would be predicted by a laminar flow model; much more on this in Sec. 7.

6.1 Poiseuille's solution for laminar flow, Model 3

For now, consider pipe flow alone, ignoring the necessity of a tank and orifice, and omitting surface tension. Suppose that the pressure at the ends of this horizontal pipe are known and that the pressure difference is δP_{pipe}. Additionally, assume that the flow is unchanging along the pipe, and said to be

fully developed.[15] In that case the pressure gradient, a force per unit volume, is

$$\frac{\partial P}{\partial x} \;=\; \frac{\delta P_{pipe}}{L},$$

and also uniform along the pipe. Given the pressure gradient, what is the volume transport through the pipe?

- A VPlist for the pressure-driven transport of a fully-developed, viscous pipe flow: (33)

1. volume transport, $Q \;\doteq\; [\,0 \quad 3 \quad -1\,]$, the dependent variable,
2. pressure gradient, $\partial P/\partial x \;\doteq\; [\,1 \quad -2 \quad -2\,]$, an independent variable,
3. radius of the pipe, $r \;\doteq\; [\,0 \quad 1 \quad 0\,]$, a parameter,
4. dynamic viscosity, $\mu \;\doteq\; [\,1 \quad -1 \quad -1\,]$, a parameter.

This is a subset of the VPlist that led to Eq. (26). In this VPlist there are four dimensional variables having three fundamental units, and hence there is just one nondimensional variable, the nondimensional transport, that must be a constant,

$$\frac{Q\,\mu}{r^4\;\partial P/\partial x} \;=\; constant. \tag{34}$$

The result (34) from dimensional analysis has the form of the famous and very useful Poiseuille solution for the transport of a laminar, fully-developed, viscous pipe flow,

$$\boxed{Q_3 \;= \frac{\pi}{8}\,\frac{r^4\;\delta P_{pipe}}{\mu\;L},} \tag{35}$$

also called the Hagen-Poiseuille solution.[16] This is taken to be Model 3. Two things to note: 1) the sensitive dependence of Q upon r, here $Q \;\propto\; r^4$ compared with $Q \;\propto\; r^2$ for an inviscid, inertial orifice flow of Sec. 3, and, 2) the transport is directly proportional to (is linear in) the pressure gradient and is inversely proportional to the viscosity. This seems physically plausible, but is *not*

[15] The strong acceleration of flow through the orifice and into the pipe is bound to cause some disturbance that may damp out with distance downstream. The distance downstream required to lose memory of the orifice is called the entry length; the equilibrated flow further downstream is said to be fully-developed. The effect of a finite entry length is likely to be increased drag overall. There is some evidence of that in this dataset, but it is small compared to the effects of turbulent flow taken up in Sec. 7.

[16] The dimensional analysis leading to (34) is standard textbook fare and is useful for now. However, its success in yielding the Poiseuille relation owes to a somewhat arbitrary choice in defining the variables of the VPlist (33) that will be discussed further in a problem at the end of Sec. 7.

always the case as will be seen in Sec. 7. Poiseuille's[17] solution for laminar pipe flow is closed, including the leading factor $\pi/8$ that is needed to calibrate the dimensional analysis result, (34).[18] After some rearrangement, the transport (35) can be rewritten in a nondimensional form using the zero-order model of Eq. (11) to scale the dependent variable,

$$\boxed{\frac{Q_3}{Q_0} \;=\; \frac{1}{64}\,(\frac{L}{d})^{-1}\,Re_x} \tag{36}$$

Under the conditions of its derivation, fully-developed laminar flow, the Poiseuille solution gives a very good account of experimental observations. Indeed, it works well enough that it may be used along with careful measurements to estimate fluid viscosity, μ. Does (35) suffice for the experimental configuration used here? We can learn a lot by plotting the Poiseuille solution in the coordinates of Fig. 6 (Fig. 7, upper right). This shows some promise in the range of smaller Re_x and larger L/d, which implies large viscous effects. But at larger Re_x and smaller L/d, the Poiseuille solution diverges, predicting transport that is much larger than the transport that could be accelerated through the orifice by the given pressure difference. The conclusion has to be that the Poiseuille solution taken alone, Eq. (35), Model 3, does not make a suitable model of the present system — tank, orifice, pipe, discharge into air. (No doubt M. Poiseuille could have told us as much, even without the hindsight of a fancy diagram.)

6.2 A hybrid Model 4 – Sig. Torricelli, say hello to M. Poiseuille

The fluid path from the tank to the open air can be envisioned in three parts: first, inertial (accelerated) flow from the tank into the orifice; second, viscous (and possibly turbulent) flow through a pipe; and third, escape into the open air and production of a free surface. Each of these has been discussed in isolation, and now we will seek to connect them to make a model of the system as a whole. The idea will be to ensure that the pressure is continuous from the tank to the open air, and that the transport is consistent with the pressure changes and is constant throughout.

Let the pressure across the orifice be $\rho\,g\,h \;-\; P_x$ where P_x is the unknown pressure post-orifice,

[17] Jean L. M. Poiseuille (1797 - 1869) was a French physiologist who pioneered the quantitative study of blood flow. He discovered the Poiseuille relation for viscous flow in pipes (blood vessels) experimentally. Some years later he provided the corresponding theory, including Eq. (35), one of the first complete solutions of the Navier-Stokes equations. His contributions also include the development of practical instruments for measuring blood pressure *in vivo*. The CGS unit of dynamic viscosity is the poise, P, in his honor; 1 P = 0.1 N s m^{-2}.

[18] The derivation of (35) is useful to see and can be found in most fluid mechanics texts. A very good online reference is https://en.wikipedia.org/wiki/Hagen-Poiseuille_equation

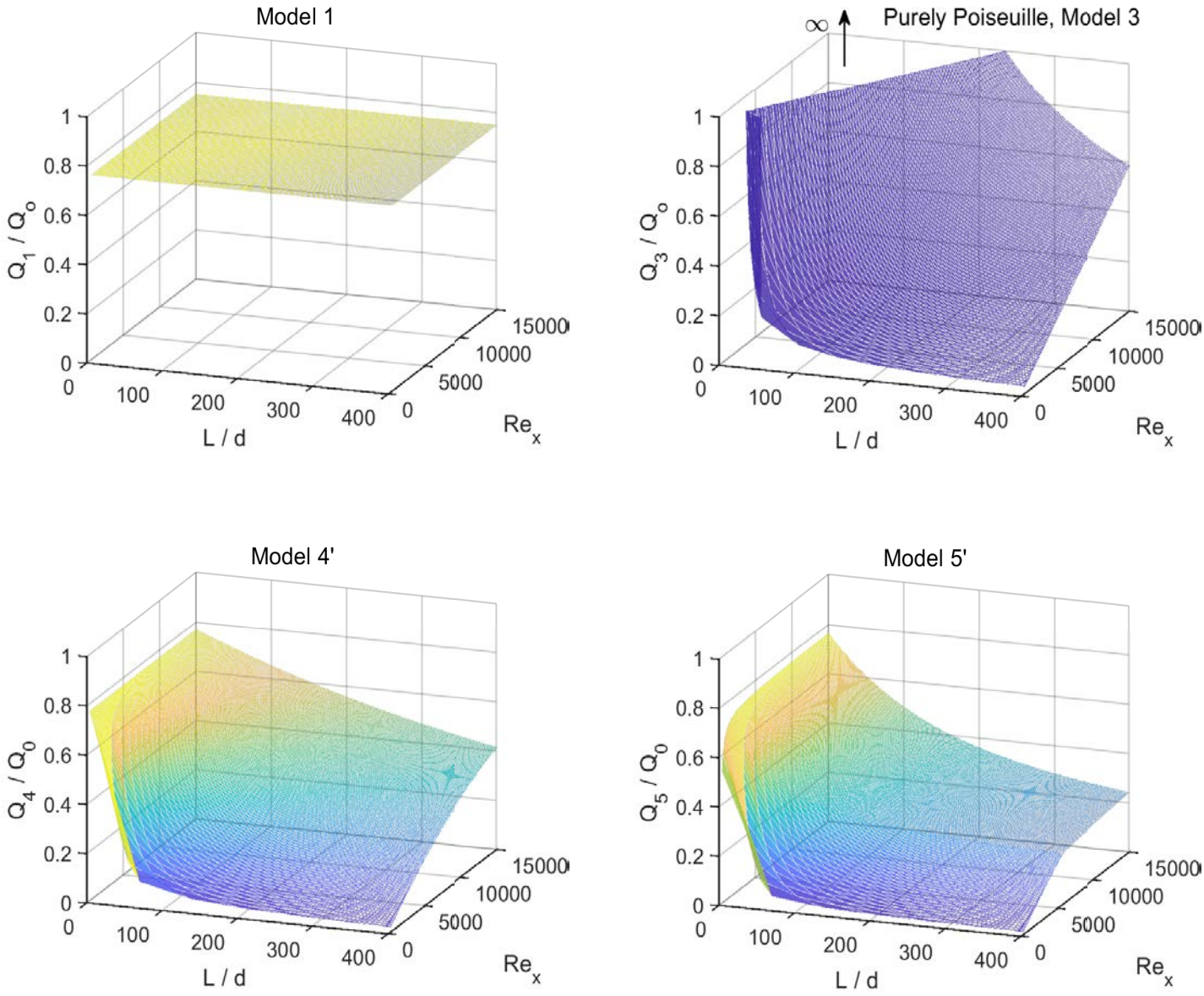

Figure 7: Four models of Q/Q_0 in the independent coordinates L/d and Re_x used in Fig. 6. This necessarily omits reference to surface tension. **Upper Left** The elementary Model 1 solution for transport through an orifice, dubbed Q_1. This solution does not depend upon L or ν and so this model defines a flat plane in this coordinate system. **Upper Right** The Poiseuille solution Q_3 for steady, fully-developed pipe flow. The transport diverges for small L/d and large Re_x, i.e., in the parameter range of smaller viscous effects, and has been clipped at 1. **Lower Left** The solution of Model 4' that combines Torricelli and Poiseuille, Eq. (41) and so has transport that is consistent with both orifice and viscous pipe flow (discussed in Sec. 6.2). The prime indicates that surface tension has been omitted. **Lower Right** Model 5' is similar to Model 4' at left, but includes a correction for the greater wall stress that occurs when the flow is turbulent at larger Re_x (Sec. 7). Notice the difference between Model 4' and Model 5' at larger Re_x and L/d but not otherwise.

or right at the start of the pipe. The transport through the orifice will then be estimated as

$$Q_{orf} \;=\; C\pi r^2\sqrt{2(g\,h \;-\; P_x/\rho)}. \tag{37}$$

This pressure difference and thus the transport through the orifice will be less, and possibly a lot less, than the orifice-only Model 1 of Sec. 3, which took the pressure P_x just beyond the orifice to be zero.

The pressure at the end of the pipe is $P_\sigma \;=\; \sigma/r$, the surface tension-induced pressure on the escaping jet of water in contact with air. The transport through the pipe will be estimated from Poiseuille's relation,

$$Q_{pipe} \;=\; \frac{\pi\, r^4}{8\,\mu\, L}(P_x - \frac{\sigma}{r}). \tag{38}$$

The one unknown in this is P_x, the pressure at the start of the pipe. This can be solved by requiring that the transport must be continuous,

$$Q_{orf} \;=\; Q_{pipe}. \tag{39}$$

Let

$$p \;=\; \frac{P_x}{\rho}, \qquad S \;=\; \frac{r^2}{8\,C\,\nu\,L}, \;\; \text{and recall} \;\; h_\sigma \;=\; \frac{\sigma}{\rho\, g\, r} \quad \text{and} \quad \nu \;=\; \frac{\mu}{\rho},$$

in which terms the continuity of transport (39) becomes

$$\sqrt{2(g\,h \;-\; p)} \;=\; S\,(p \;-\; g\,h_\sigma).$$

Squaring and rearranging into a quadratic in p gives

$$S^2\,p^2 \;+\; (2 - 2\,S^2\,g\,h_\sigma)\,p \;+\; S^2\,g^2\,h_\sigma^2 \;-\; 2\,g\,h = 0. \tag{40}$$

Once this is solved for $p \;=\; P_x/\rho$ (the positive root) the transport may be evaluated from either (37) or (38). This model and solution are called Model 4 and Q_4.

When surface tension is included, the analytic expression for Q_4 is too complex algebraically to be useful (though readily evaluated numerically in Sec. 6.4). For now, simplify by setting $h_\sigma \;=\; 0$ so that we can examine the orifice plus viscous pipe flow component, which will be dubbed Model 4'. The pressure, p, is then

$$p \;=\; \frac{P_x}{\rho} \;=\; \frac{-1 \;+\; \sqrt{1 \;+\; 2\,g\,h\,S^2}}{S^2}.$$

Substituting into (38), and after considerable rearranging:

$$\frac{{Q_4}'}{Q_0} \;=\; C\left(\,(\,1 \;+\; 1024\,C^2\,E^2\,)^{1/2} \;-\; 32\,C\,E\,\right), \tag{41}$$

where

$$E \;=\; \frac{L}{d}\, Re_x^{-1}. \tag{42}$$

The Model 4' solution, Fig. 7, lower left, is similar to the Model 3 Poiseuille solution for smaller values of the Reynolds number, roughly $Re_x < 2000$ where viscous effects are most important. It is qualitatively different at larger Re_x where the Model 3 solution diverges. The Model 4' solution gives reasonable transport in that regime because it has included the very important constraint imposed by the necessity for accelerated, inertial flow from the tank and into the orifice.

6.3 A collapse to one independent variable

The Model 4' solution (41) has the interesting property that it depends upon a single, independent nondimensional variable, E, vs. the $L\,/\,d$ and Re_x separately that we learned from dimensional analysis. The nondimensional variable E includes all of the important parameters that are expected to contribute to $Q\,/\,Q_0$ in these experiments (except for σ). A dependence upon the single nondimensional variable E is a special case of the more general result from dimensional analysis that indicated two separate, independent nondimensional variables, $L\,/\,d$ and Re_x. This important difference arises because Model 4 was built upon three physical constraints — continuity of volume transport, a solution for orifice flow, and Poiseuille's solution for laminar pipe flow — that were not incorporated into the VPlist (24). Thus the result from dimensional analysis is more general, i.e., less specific, than is the solution of a model that is otherwise consistent with the VPlist. This is a characteristic of dimensional analysis.[19]

The Eqs. (41) and (42) are somewhat surprising, and, if consistent with the observations, useful as well. To find out whether this holds within the observations we need only plot the usual $Q\,/\,Q_0$ against E and find a moderately good correlation, Figs. 8 and 9. It is always desirable to find the most compact description of a dataset or model solution, and this new version (new compared with the three-dimensional presentation of Fig. 6) meets that criterion.

The E description may be readily interpreted as the ratio of two time scales:

$$E \;=\; \frac{L\,/\,V_T}{d^2\,/\,\nu} \;\propto\; \frac{advection\ time}{diffusion\ time}. \tag{43}$$

The numerator is the time required for advection over the length of the pipe L at the speed V_T, and the denominator is the time required for diffusion across the diameter of the pipe. If the time required for diffusion is comparatively large, then E is comparatively small and viscous effects

[19]This important lack of specificity (or unintentional generality) is inherent to dimensional analysis and is discussed in greater depth in the main text, Sec. 3.

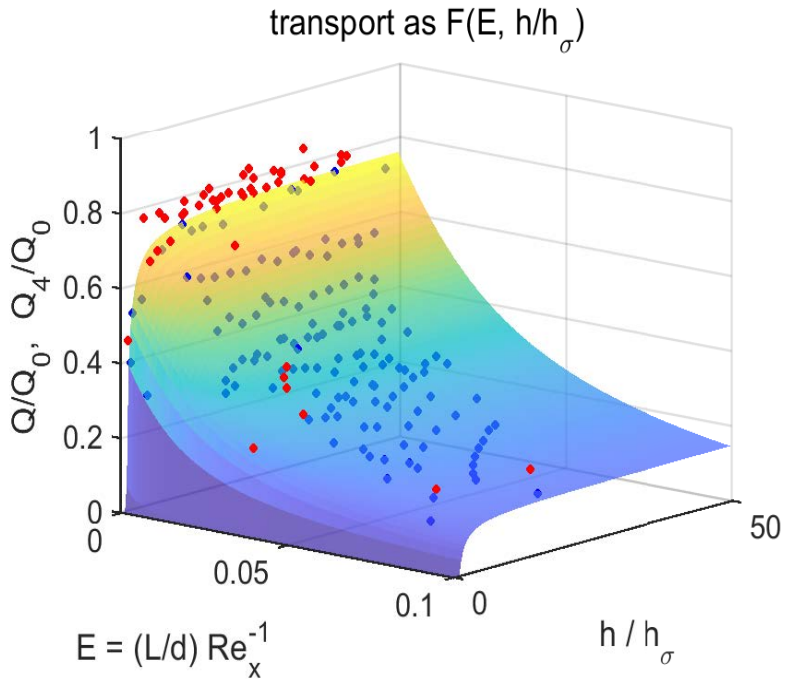

Figure 8: This surface is the Model 4 solution evaluated from Eq. (40), and the points are the full set of observations. The data points that lie below the surface are blue; those above the surface (a distinct minority) are red. The overall shape of the model surface looks reasonable compared to the data, but there is a clear tendency for Model 4 to overestimate transport. A more quantitative comparison comes in the next two figures.

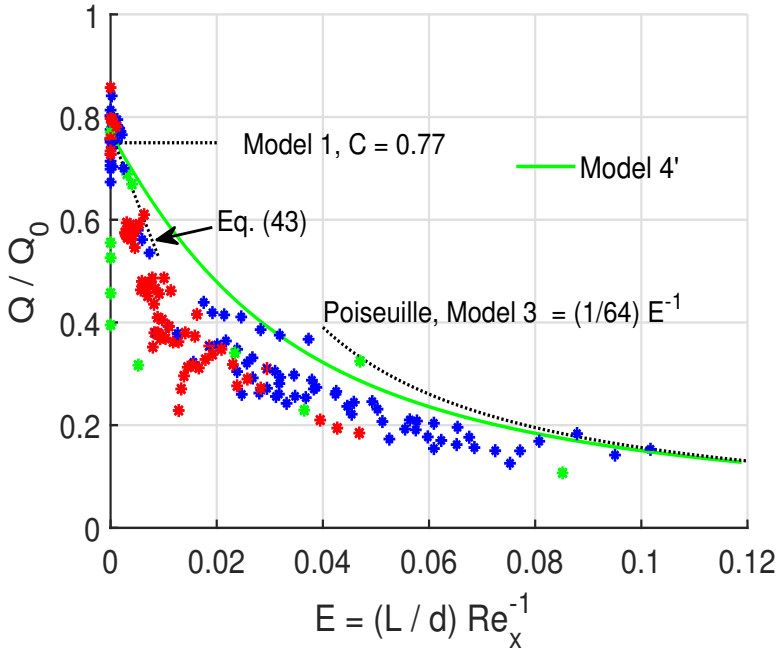

Figure 9: Observed transport (colored points) as a function of a single independent variable, $E = (L/d)\, Re_x^{-1}$. This is a projection of Fig. 8 onto a Q vs. E plane. The green line is the solution of Model 4' (which omits surface tension). The red data points have large Re_x, and the green data points are at small h/h_σ and likely affected by surface tension. The black dotted lines are the asymptotes of Q_4' for small and large E. Notice that the Model 4' solution parallels the data cloud, but sits above it, i.e., Model 4' systematically overestimates the transport, as noted in the previous figure. This will be addressed in Sec. 7.

should be less prominent. This is consistent with the observations.

The function $F(E)$ of Eq. (41) and plotted in Fig. 9 is not transparent, but it does have familiar asymptotes, Eq. (44), (45), and (46), that are sketched onto Fig. 9 as dashed, black lines.

- At $E = 0$, where there is no effect of viscosity,

$$Q_4 / Q_0 = 0.77 = C. \tag{44}$$

  This is Model 1, inertial, orifice flow.

- At small values of E, which corresponds to small (but not zero) viscous effects, the Model 4 solution goes to

$$Q_4/Q_0 \rightarrow C \left(1 - 32\,C\,E + 512\,C^2\,E^2 \ldots.\right). \tag{45}$$

  This indicates a strong decrease of transport with increasing L that is indeed observed for shorter pipes.

- At large E and large viscous effects,

$$Q_4 / Q_0 \rightarrow \frac{1}{64}\,E^{-1}, \tag{46}$$

  which is the Poiseuille solution for viscous, laminar pipe flow, and Model 3.

6.4 Model 4 includes surface tension and viscosity appropriate to a laminar flow

Now consider the solution of Eq. (40) with surface tension included, called Model 4 (no prime). The VPlist for this model is

- A VPlist for pressure-driven outflow of water through an orifice and a pipe: (47)

1. outflow volume transport, $Q \doteq$ [0 3 -1], the dependent variable,
2. hydrostatic pressure head at the orifice, $g\,h \doteq$ [0 2 -2], an independent variable,
3. diameter of the orifice and pipe, $d \doteq$ [0 1 0], a parameter,
4. length of the pipe, $L \doteq$ [0 1 0], a parameter.
5. kinematic viscosity of the water, $\nu \doteq$ [0 2 -1], a parameter,
6. surface tension of the water, $\sigma \doteq$ [1 0 -2], a parameter,
7. density of water, $\rho \doteq$ [1 -3 0], a parameter.

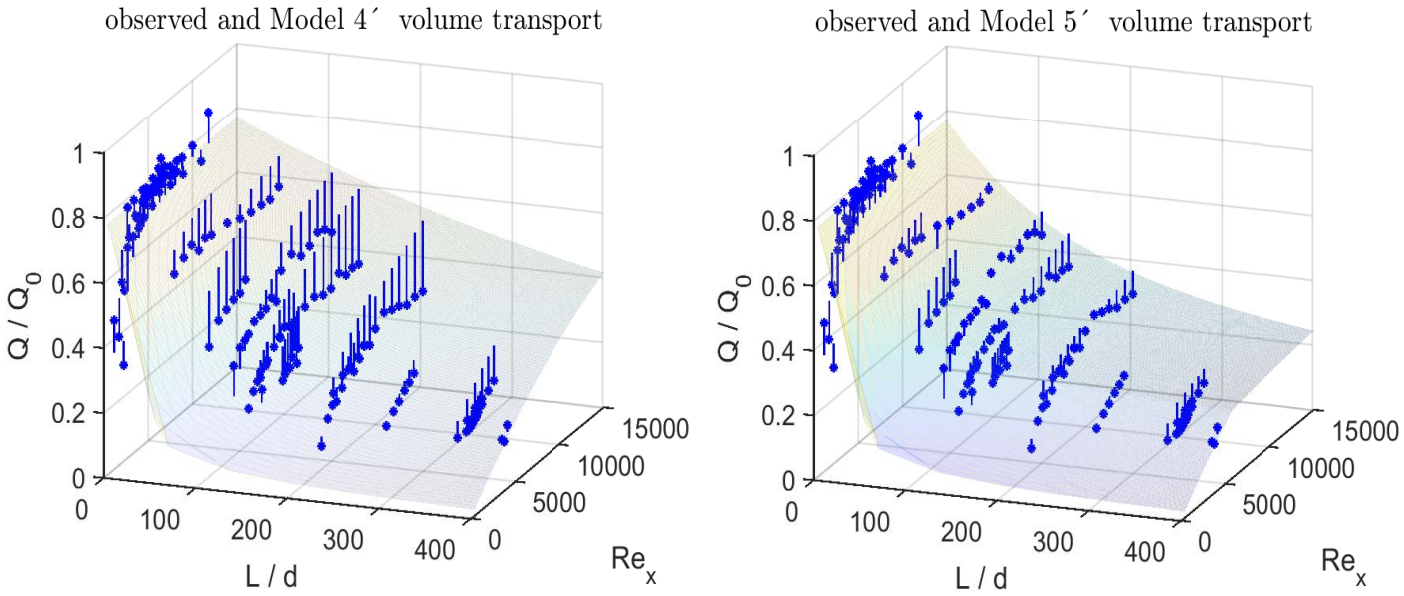

Figure 10: **(left)** Observed volume transport, blue dots, and the Model 4' solution shown as a surface in coordinates $(L\,/\,d,\ Re_x)$ as in Fig. 6. The stem goes from the data point up or down to the surface. This makes it especially clear that Model 4 overestimates transport (underestimates wall stress) at larger values of Re_x. This plot includes all of the data, including data taken at small $h\,/\,h_\sigma$ where surface tension effects are important. The model solution shown in these coordinates has to take $\sigma = 0$ and so can not replicate the reduced transport at very small h and small Re_x. **(right)** This is the same data shown at left, but here the surface is from Model 5' discussed in Sec. 7. The overestimate of transport seen at left is reduced considerably.

A basis set of nondimensional variables is, after considerable rearranging,

$$\frac{Q_4}{Q_0} \;=\; F(\frac{L}{d},\, Re_x,\, \frac{h}{h_\sigma}). \tag{48}$$

If the E-collapse discussed just above is applicable here as well, then provisionally,

$$\frac{Q_4}{Q_0} \;=\; F(E,\, \frac{h}{h_\sigma}). \tag{49}$$

To test whether this is valid we can make a three-dimensional graph of the Model 4 solution alongside *all* of the data, Fig. 8. The surface defined by Model 4 shows the variation of the nondimensional transport with E that could have been anticipated from Fig. 9; it also reveals a sharp decrease in the transport as $h/h_\sigma \to 1$ due to surface tension. This could have been anticipated from Fig. 3, right.

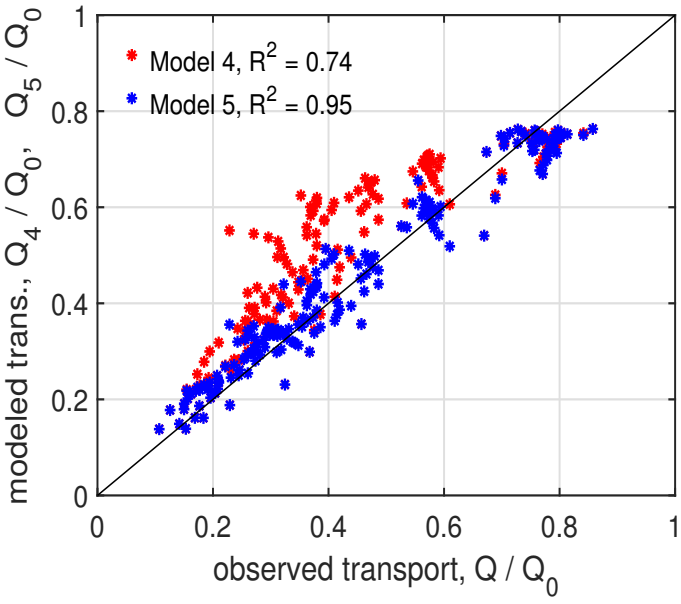

Figure 11: Modeled vs. observed transport. There are two versions of the modeled transport, the red dots are from Model 4 and the blue dots are from Model 5. Notice that Model 4 has a noticeable positive bias (predicts excess transport). This is mostly cured by the changes made to get Model 5, discussed in Sec. 7.

6.5 Summary

The Model 4 solution makes a reasonable, qualitative comparison with the observations, Fig. 8, including at small $h \,/\, h_\sigma$. It may be compared quantitatively with the full dataset and returns a coefficient of determination $R^2 = 0.74$. If the data that have large external Reynolds numbers, $Re_x \geq 7000$, are excluded from the sample, then R^2 increases somewhat to $R^2 = 0.86$. This is a more appropriate test of this laminar flow model.

Model 4 accomplishes most of what we set out to do in Sec. 1.2: it is understandable (though solution of the quadratic (40) is not transparent) and it gives semi-quantitative predictions. Given Model 4, we can interpret most of what can be seen in Fig. 6. It might be appropriate to thank Sig. Torricelli and M. Poiseuille for their remarkable contributions, and stop here. Except for one last issue: Model 4 overestimates transport by as much as 35% in some regions of parameter space. It looks like there is one more important step to take.

6.6 Problems

- Starting with the Poiseuille solution, Eq. (35), recast into the nondimensional coordinates of Fig. 6. Show that the Poiseuille solution is (this repeats Eq. (36)),

$$\frac{Q}{Q_0} = \frac{1}{64} \left(\frac{L}{d}\right)^{-1} Re_x.$$

  How does this compare with the surface plotted in Fig. 7, upper right?

- The pipes in these experiments were maintained in a horizontal orientation so that we wouldn't have to consider the angle from horizontal as yet another variable. Now imagine that the discharge end of the pipe was tipped up slightly. How would this affect the transport of the outflow? Can you connect this with the treatment of surface tension in Sec. 4?

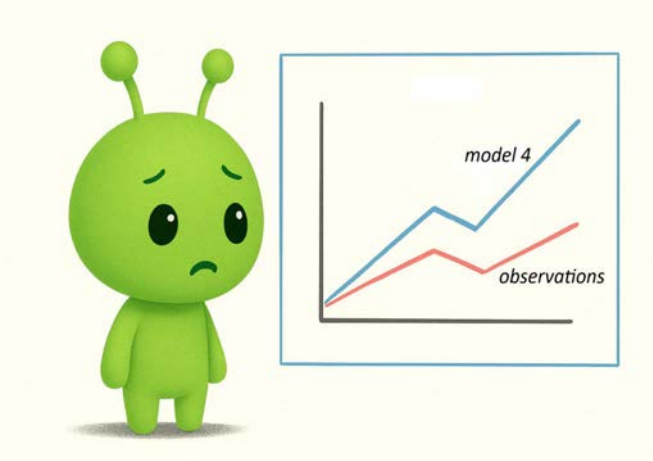

Planetary Explorer testing a new model.
Image by the author using ChatGPT-5.

Make a model, then test a model.

Models flow with grace.
Real, twisting fluids say no!
Try and try again.

7 Turbulent flow accounted by Model 5

The objective of this section is to resolve the systematic overestimation error made by Model 4. This proceeds in four steps:

7.1) Identify the source of the error — the occurrence of turbulent flow — based in large part upon its dependence upon Reynolds number.

7.2) Review historical observations that document pressure/velocity correlations in laminar and turbulent pipe flows.

7.3) Analyze these historical observations to estimate a turbulence-enhanced "effective" viscosity that may be applied within the laminar flow framework of Model 4.

7.4) Test the resulting Model 5 against observations.

7.1 The inferred source of the overestimation error

The error made by Model 4 has a telling geography, being most apparent for the largest Re_x, greater than about 7000, Fig. 10, left. A clear example of this comes from the three experiments of Fig. 5 that showed dependence of Q upon viscosity (due to different water temperature). The two experiments having cold and room temperature water sampled $2000 \leq Re_x \leq 7000$ and were predicted fairly well by the laminar flow Model 4, Fig. 12. The hot water experiment sampled $4000 \leq Re_x \leq 17000$ and in that range the Model 4-predicted transport exceeds the observed transport by an appreciable fraction, up to 50% at the largest Re_x. This discrepancy easily exceeds the uncertainty on observed Q, and it is systematic, a similar pattern is evident in other experiments that sampled larger L/d and Re_x. The upper Re_x limit for validity of the laminar flow Model 4 appears to be roughly $Re_x \approx 7000$. Using Eq. (30), this corresponds to an internal Reynolds number, $Re = V_a\, d\,/\,\nu = (Q\,/\,Q_0) \times Re_x = 0.35 \times 7000 \approx 2500$, where $Q\,/\,Q_0 = 0.35$ has been read from Fig. 12. A transition from laminar to turbulent flow at roughly this internal Reynolds number is consistent with well-known stability properties of pipe flow.[20] [21] Below $Re \approx 2000$, a laminar pipe flow will be stable, unless strongly perturbed by an outside agent; above a Reynolds number of about 3000, a laminar pipe flow will be unstable and likely to become at least intermittently turbulent. The inference made here is that the overestimation of transport by Model 4 is linked to the occurrence of turbulent flow, where Model 4 treated only laminar flow.

The chaotic, three-dimensional flow that constitutes turbulence continually mixes higher velocity fluid from the central core of the pipe into the boundary layer on the pipe walls. In a laminar flow the same process occurs by the generally much slower mechanism of molecular diffusion of momentum. Turbulent flow thus produces a higher wall stress than is found in the corresponding (same transport) laminar flow. For a given pressure difference, the occurrence of turbulent (vs. laminar) flow thus leads to reduced transport. This can be inferred from the observations of Fig. 12 where the transport is nearly independent of Re_x at larger values of Re_x. In contrast, if the flow was laminar, then we would expect a more or less linear increase of Q with Re_x, Eq. (36), and which is evident in the observations made at smaller Re_x.

---

[20] An excellent introduction to turbulent pipe flow (and fluid mechanics generally) is the text by White, F. M. and H. Xue, 2021, 'Fluid Mechanics', 9th Ed., McGraw Hill.

[21] When discussing a changeover from laminar to turbulent flow, or vice versa, it is almost irresistible to speak of a "transition to turbulent" flow, as implied here, even though what actually happens in these experiments is a change in time from (in some cases) turbulent flow to laminar flow as the surface height, h, and the velocity V_a decrease over time. This propensity for "transition to turbulence" may be partly alliteration, but also conceptual; it is much easier to envision going from a known state, laminar flow, into a chaotic state, turbulent flow vs. the other way around. Stability studies must proceed that way. Does it matter which way the transition goes? Is there hysteresis? Probably yes, especially when, as here, the Reynolds number is not far from the transition region.

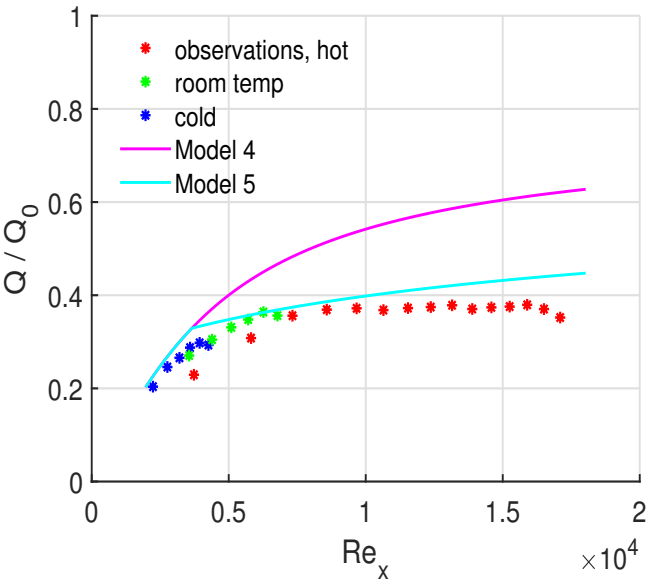

Figure 12: Red, green and blue points are the observed, nondimensional transport $Q\,/\,Q_0$ from the experiments of Fig. 5 shown here as a function of Re_x. These three experiments are at a common $L\,/\,d \;=\; 140$, but have different viscosity due to different temperature. The cyan line is the corresponding Model 4 prediction which overestimates the transport at larger Re_x. Notice the change in the nondimensional transport at very roughly $Re_x \;=\; 7000$, which corresponds to an internal Reynolds number, $Re \;=\; Re_x\,(Q\,/\,Q_0) \;\approx\; 2500$. This is interpreted to be a result of a transition from (somewhat) turbulent flow at larger Re_x to laminar flow at smaller Re_x.
A better prediction comes from Model 5, the magenta line, that implements an adjustment of the viscosity to account for turbulent flow.

7.2 Historical, experimental observations of pipe flow

There are significant engineering and economic consequences that follow from the increased flow resistance caused by turbulence, and the related phenomena have been studied intensively for more than a century and a half.[22] And yet, as Richard Feynman noted in the 1960s,

> *What we really can not do is deal with actual, wet water running through a pipe. That is the central problem which we ought to solve some day, and we have not.*[23]

By 'solve', Feynman was contrasting the empirical treatment of turbulent flows (coming below) with the Poiseuille solution from first principles that solves laminar pipe flow once and for all. A great deal has been learned regarding the remarkably complex phenomena that make up a turbulent pipe flow,[24] which goes some way to explaining why we still do not have a concise, understandable solution for turbulent pipe flow. This strongly shapes the development of a model intended to account for turbulent flow effects.

[22] If turbulence is a new or unfamiliar concept, then a must-see resource is the film by R. Stewart, 'Turbulence', available online at https://hml.mit.edu/ncfmf/

[23] R. Feynman, 'Lectures on Physics Vol. II', 1964, Addison-Wesley.

[24] An excellent, comprehensive review of the research on turbulent transition is by Avila, M, D., Barkley and B. Hof, 2023, 'Transition to turbulence in pipe flow', Ann. Rev. Fluid Mech., 55, 575-602. https://doi.org/10.1146/annurev-fluid-120720-025957

What we do have is a vast body of historical data and their analyses. Many of these experimental studies came in response to the practical need to predict the pressure drop, $\delta P/\rho \;=\; g\,h$, that will be required to drive a given fluid at a specified mean velocity, V_a, through a given pipe. Dimensional analysis of this problem is

- A VPlist for the pressure drop along a pipe: (50)

1. pressure drop expressed as a hydrostatic head, $g\,h \;\doteq\; [\,0\;\;2\;\;-2\,]$, the dependent variable,
2. mean velocity, $V_a \;\doteq\; [\,0\;\;\;1\;\;\;-1\,]$, an independent variable,
3. diameter of the pipe, $d \;\doteq\; [\,0\;\;\;1\;\;\;0\,]$, a parameter,
4. kinematic viscosity of the water, $\nu \;\doteq\; [\,0\;\;\;2\;\;\;-1\,]$, a parameter,
5. length of the pipe, $L \;\doteq\; [\,0\;\;\;1\;\;\;0\,]$, a parameter.

Three nondimensional variables are expected, and as one possibility,

$$\frac{g\,h}{V_a^2\,/\,2} \;=\; f(\frac{L}{d},\; Re), \quad \text{where} \quad Re \;=\; \frac{V_a\,d}{\nu}. \tag{51}$$

This is a complement to the problem of viscous pipe flow posed in Sec. 6. The key difference is that V_a and pressure $g\,h$, have switched places. In (51), V_a is the known, independent variable, and pressure $g\,h$ is the unknown, dependent variable. Thus the Reynolds number of (51) is the internal Reynolds number, Re, (Sec. 5.1) in place of the external Reynolds number Re_x used extensively in Sec. 6. Since pressure is the dependent variable, it has been kept to the first power, and so V_a is quadratic in this relation.

If the flow within the pipe is independent of distance downstream (i.e., fully developed) then the pressure drop should be directly proportional to the pipe length, L. In that event the parameter L/d may be taken out of the argument of f and included as a multiplying factor. This gives a widely used, simplified form

$$\boxed{\frac{g\,h}{V_a^2\,/\,2} \;=\; \frac{L}{d}\,f(\,Re\,)} \tag{52}$$

The unknown function of (52) is denoted by f, which is traditional in this role, and called the 'friction factor'. The function $f(Re)$ has been the object of hundreds of experimental programs, and the results compiled into a Moody diagram, a simplified example of which is Fig. 13.[25] There is no doubt about the practical value of the Moody diagram, but the physical interpretation of f itself does not go very deep. f is not a fluid property, but rather a joint property of the fluid, the pipe and the

[25] Estimation of the wall stress in real pipes may have to account for the surface roughness of the pipe wall. If the height of the roughness elements is ϵ, then the roughness will appear in Eq. (51) as a nondimensional parameter $\epsilon\,/\,d$. Moody diagrams generally display a near-blizzard of curves, each having a specific $\epsilon\,/\,d$, that sit above and roughly parallel to the curve for smooth pipes, the solid red line of Fig. 13. The 'pipes' used in the present experiments were new and clean and presumed to be smooth, and so roughness is neglected here; thus the impoverished Moody diagram of Fig. 13.

flow, organized by the dimensional analysis that lead to Eq. (52). f is also not a model of turbulence, but rather an empirical measure of flow resistance, larger f corresponding to greater flow resistance.

One part of the Moody diagram is clear and even familiar. In the low Re laminar flow regime, the Poiseuille solution in this framework is

$$f_{lam}(Re) \;=\; \frac{64}{Re} \tag{53}$$

the blue line at lower left of Fig. 13. The higher Re turbulent flow regime is different. One classical representation of $f(Re)$ for turbulent flow in a smooth pipe is the red solid curve at lower right, an empirical correlation of experimental data analyzed by Blasius in the 1910s,[26]

$$f_{turb}(Re) \;=\; \frac{0.316}{Re^{1/4}} \tag{54}$$

In what follows it will be necessary to have a function $f(Re)$ defined over the full range of Re. The laminar and turbulent prescriptions (53) and (54) are simply spliced together; $f(Re)$ follows the Poiseuille curve (53) for small Re up until intersection with the Blasius curve Eq. (54) at $Re \;=\; 1200$. It continues as the Blasius curve (54) thereafter with no special treatment of the transition region.[27] The spliced together function will be referred to as $f_{hist}(Re)$

The data from the present experiments may be used to evaluate $f(Re)$ via Eq. (52), which gives an interesting result, Fig. 14. The distribution is consistent in part with the historical data insofar as many of the experimental data fall close to the historical curves. That is reassuring; our little table-top apparatus is evidently not highly anomalous. But notice there are also many estimates of f that are well away from the historical curves, all in the direction of larger f. These seemingly high estimates are not measurement artifacts, but likely due to any one of several physical processes that are not accounted by a classical friction factor: surface tension, entrance effects (for short pipes) which violate the fully-developed flow restriction,[15] and hysteresis (turbulent to laminar transition).[21] Each of these phenomena is expected to enhance the flow resistance for a given Re. Surface tension was treated briefly in Sec. 4 and accounted in Model 4 and Model 5, but a treatment of the latter two phenomena is beyond the scope of this study.

[26]The original paper by Blasius is in German and hard to access, but discussed further in almost every comprehensive fluid mechanics text.

[27]There are a number of more complex formulae that serve to connect smoothly the laminar and turbulent flow branches of $f(Re)$ within the transition region.[20] A single, continuous function $f(Re)$ is desirable, but the differences compared with the present, simplified version, Eq. (53) spliced to Eq. (54), have been found to be very small in this application.

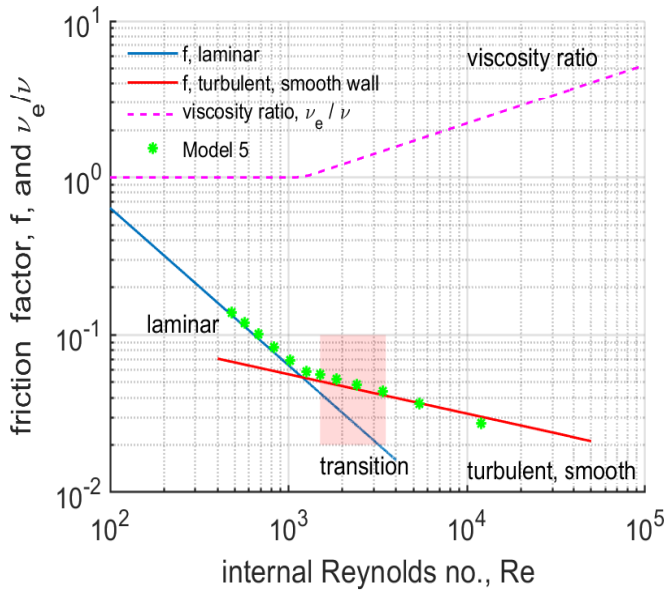

Figure 13: The friction factor, f, as a function of the internal Reynolds number, Re. The blue line at lower left comes from a laminar flow, i.e., Poiseuille's solution. The red curve at lower right is the Blasius fit to turbulent flow in a smooth pipe. The dashed, magenta line is the viscosity ratio computed from Eq. (62) and the constraint that ν_e/ν must be greater than 1. The green dots are $f(Re)$ computed by Model 5 and discussed in Sec. 7.3. The light red shading indicates the transition region, the range of Reynolds numbers, very roughly 1500 - 3500, at which a laminar flow, if gently accelerated and not subjected to large amplitude perturbations, would likely show signs of instability and a transition to turbulent flow. In practice there is not a sharp boundary on the transition region, and neither is there a clear consensus on $f(Re)$ within this region.

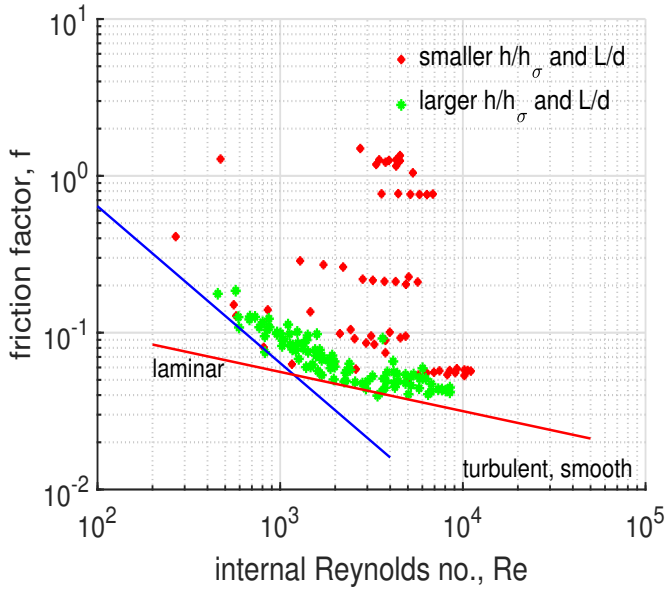

Figure 14: The friction factor, $f(Re)$, evaluated from the present experimental data, the red and green dots. The blue and red lines are as in the previous figure. The red dots represent data at smaller values of h/h_σ, likely affected by surface tension, and at smaller L/d that may be affected by entry length.[15] Neither of these phenomena is accounted by a friction factor, and it is not surprising that the red points are widely scattered. The distribution of the green points (all the rest of the data that are at larger h/h_σ and L/d) forms a cloud that is slightly above the historical curves and that more or less conforms with the change in slope of $f(Re)$ that is expected in the transition from laminar to turbulent flow at very roughly $Re \approx 2500$.

7.3 Estimating an effective viscosity for use within a laminar flow framework

To make use of the essential information provided by the historical $f(Re)$, the tactic will be to map $f(Re)$ onto a so-called effective viscosity, ν_e. The intention is that this ν_e will account for the possibility of turbulence-enhanced flow resistance within the laminar framework of Model 4. The detailed form of the mapping described next appears to be somewhat novel, but the notion of an effective viscosity to represent one or another aspect of turbulence has classical roots and an extensive history of development.[28]

The question posed here becomes: what value of effective viscosity, ν_e, will give a transport that is consistent with the piece-wise continuous $f(Re)$ of Eqs. (53) and (54)? From (52) it is evident that "Moody" scaling, Eq. (52), gives

$$Q^{Moody}(f(Re)) \;=\; (\,(\pi^2\, g\, h\; d^5)/(8\, L))^{1/2}\, \frac{1}{f(Re)^{1/2}} \tag{55}$$

for any $f(Re)$. For the special case of a laminar flow, the Moody scaling is

$$Q^{Moody}(f_{lam}(Re)) \;=\; (\,(\pi^2\, g\, h\; d^5)/(8\, L))^{1/2}\, \frac{1}{f_{lam}(Re)^{1/2}}. \tag{56}$$

The term $f_{lam}(Re)$ is known, but left as is for now. The ratio of the general Q^{Moody} to the laminar Q^{Moody} is then

$$\frac{Q^{Moody}(f(Re)}{Q^{Moody}(f_{lam}(Re))} \;=\; \sqrt{\frac{f_{lam}(Re)}{f(Re)}} \tag{57}$$

and all of the constants have dropped out. The Poiseuille scaling Eq. (35) gives $Q^{Pois}(\nu)$; first the laminar case,

$$Q^{Pois}(\nu) \;=\; \frac{\pi\, g\, h\, r^4}{8\, L\, \nu}, \tag{58}$$

where this ν is the usual (fluid property) viscosity, not dependent upon Re. Now define a general Q^{Pois} for which ν_e may be a function of Re, but still Poiseuille scaling

$$Q^{Pois}(\nu_e) \;=\; \frac{\pi\, g\, h\, r^4}{8\, L\, \nu_e}. \tag{59}$$

The ratio of this with (58) is just

$$\frac{Q^{Pois}(\nu_e)}{Q^{Pois}(\nu)} \;=\; \frac{\nu}{\nu_e}. \tag{60}$$

[28] A famous, early example is Prandtl's mixing length model, e.g., White and Xue (2021).[20] Prandtl's model treated a steady one-dimensional boundary layer flow, while the present application is to a steady, zero-dimensional system, the bulk transport. A modern, advanced treatise on turbulence including models of effective diffusivity that are far more sophisticated than considered here is by Pope S.B., 2000, 'Turbulent flows', Cambridge Univ. Press.

Now for the key step: define ν_e by requiring consistency between (57) and (60) in the sense that at a given Re, these two scaling estimates should give the same transport relative to the laminar case,

$$\frac{Q^{Moody}(f(Re))}{Q^{Moody}(f_{lam}(Re))} \;=\; \frac{Q^{Pois}(\nu_e)}{Q^{Pois}(\nu)}. \tag{61}$$

Substitution of (57) and (60) and rearranging yields a neat result,

$$\boxed{\frac{\nu_e}{\nu} \;=\; \sqrt{\frac{f(Re)}{f_{lam}(Re)}}} \tag{62}$$

The effective viscosity is thus, relative to the actual fluid viscosity, proportional to the square root of $f(Re)$ relative to the laminar $f_{lam}(Re)$ which we know from Eq. (53). Given the historical $f(Re)$, this is a closed prescription for ν_e that has not introduced new or adjustable parameters. Eq. (62) is the dashed magenta line labeled viscosity ratio in Fig. 13.

A particularly handy version of (62) comes from substitution of (53) and (54),

$$\text{on the laminar branch,} \quad Re \le 1200: \quad \boxed{\frac{\nu_e}{\nu} \;=\; 1} \tag{63}$$

$$\text{on the turbulent branch,} \quad Re \ge 1200: \quad \boxed{\frac{\nu_e}{\nu} \;=\; 7\times 10^{-2}\, Re^{3/8}} \tag{64}$$

Implementation of an effective viscosity starts with a solution of Model 4. If that solution gives $Re \le 1200$, then the flow is presumed to be laminar, $\nu_e = \nu$, and nothing more need be done. If instead $Re \ge 1200$, then the effective viscosity ν_e is evaluated from (64) and the solution recomputed with $\nu = \nu_e$. This first estimate of ν_e will be somewhat too large since the Model 4 estimate of Re will be too large. The solution is therefore iterated to arrive at an internally consistent solution in which the model-computed $f(Re)$ approximates the historical $f_{hist}(Re)$, cf. the green dots of Fig. 13. In all of this, the Reynolds numbers are evaluated with the actual fluid viscosity, ν, not the effective viscosity.[29]

7.4 At last, Model 5

Model 5 is defined by the effective viscosity relation (63) and (64) and the algorithm to implement its use in a laminar flow framework. Over most of the parameter space of these experiments the effective viscosity is less than twice the actual fluid viscosity, the dashed magenta curve of Fig. 13. The consequences for the model-computed transport are readily apparent at larger Re_x, compare the

[29] A Matlab script that implements Model 5 is linked in Sec. 8.

Model 4' solution with the Model 5' solution in Fig. 10. However, the differences are not qualitative simply because the largest Re_x sampled here is not, by most standards (Sec. 2.1), large.

The essential starting point for ν_e, the historical $f(Re)$ of Fig. 13), is well-established and can be regarded as an empirical fact within its somewhat restricted domain (that the flow is fully-developed, which probably does not hold in every experiment here). Nevertheless, the present mapping of $f(Re)$ to $\nu_e(Re)$, Eqs. (63) and (64), should be regarded as a working hypothesis, and not an inevitable, fundamental law derived from first principles: this ν_e device might work or it might not. Significantly, this model of an effective viscosity is a *testable* hypothesis in that its consequences can be readily checked against observations. The changes in transport that result from an increased viscosity ($\nu_e > \nu$) are in a direction that reduces the positive bias of Model 4, an example is in Fig. 12. The Model 4 solution begins to depart noticeably from the observations at $Re_x \approx 7000$, while the Model 5 solution stays closer to the observations, though still slightly high. When the solution of Model 5 (including surface tension) is compared directly to the entire dataset (no exclusions for surface tension or short pipes) the blue dots of Fig. 11), the coefficient of determination is found to be $R^2 = 0.95$ and hence Q_5 accounts for 95% of the variance in Q. This is a significant result, since the only adjustable parameter in Model 5 is the discharge coefficient, set to $C = 0.77$ all the way back in Model 1 (Sec. 3). The root mean square of the error, $Q - Q_5$, is 0.05 (nondimensional units), and the mean of the error is -0.008 (also nondimensional). The sign indicates that Q_5 is slightly higher than the observed Q/Q_0, on average, though the bias is significantly reduced compared to that of the Model 4 solution.

The apparent success of Model 5 could engender over confidence in the effective viscosity estimated by (63) and (64. Turbulence and viscosity are different things, different categories — turbulence is not merely an enhanced viscosity. Neither does ν_e represent a physical property of the fluid (roughly the same caution was leveled against f). Rather, this ν_e is a modeling device, or in modern vernacular, a modeling *hack*, that serves to import the historical laminar and turbulent flow relationship $f(Re)$ into the specific, laminar flow (Poiseuille model) framework developed as Model 4. This prescription for ν_e does not come close to being the model of turbulence alluded to by Feynman.

7.5 Summary and closing remarks

Model 5 appears to be empirically adequate over the rather small parameter space of these experiments (small when compared to the immense range of possible pipe flows noted in Sec. 2.1). The limited precision and resolution of the data are also at issue. The remaining differences between Model 5 and the present dataset give scant motivation or direction for further development and that means that we have finally come to the end of the development path previewed in Fig. 1. Better, more accurate and more comprehensive models are undoubtedly possible. To that end, more precise and more robust experimental apparatus that allowed greater temporal and volumetric resolution

would be highly desirable (see Rother, 2024, of footnote 1). One of the most useful improvements would be as simple as a taller tank that would yield larger outflow velocity and larger Reynolds numbers than were obtained with the modest apparatus used here.

Recall that in Sec. 1.2 there was mention of two desirable traits in a model, clarity (or understandability) and adequacy to the phenomenon and data of interest. These are likely to be in tension: here it seems that Model 4 is understandable, and Model 5 is adequate to the data. Now it's time to add one more hurdle for the study overall, *viz.*, we shouldn't feel comfortable with a model, and should not be confident applying that model, unless we understand where in parameter space the model will fail. The present dataset is not extensive enough to reveal the limits of Model 5, but we can be certain that there are such boundaries, and they may not be too far away from the boundaries of Fig. 6. The most likely point of failure is the relation Eq. (63) that maps $f(Re)$ to ν_e. And specifically, without understanding the physical basis for the Blasius correlation Eq. (54) there is no sound basis for trusting Model 5 solutions outside the range of Re that was sampled in these experiments.

7.6 Problems

- Fig. 13 showed Model 5 solutions in Moody scaling, $f(Re)$, the green dots. These approximate the historical $f_{hist}(Re)$ given by Eqs. (53) and (54). Is this comparison a test of physics or numerical implementation?

- The changes made by the implementation of an effective viscosity are evident in the shift of predicted transport closer to the one-to-one line in Fig. 11 (red dots, Model 4, to blue dots Model 5). The change is most evident in the middle range of transport values. Can you explain why this is the case?

- Up through Sec. 6 the essential nondimensional parameter was the external Reynolds number, Re_x. Then in Sec. 7 that role was taken by the much more often encountered (just plain) Reynolds number, Re, dubbed the internal Reynolds number in Sec. 6. Can you explain why the sudden changeover from Re_x to Re, aside from historical precedent?

- Fig. 6 was (probably) difficult to appreciate on first sight. What can you now understand of it?

  i) What parameter space is defined by the coordinate axes of this figure? What is the parameter space sampled by the observations? What part of the figure's parameter space was inaccessible to the experiments? (hint: think Venn diagram).
  ii) Where is there evidence of a surface tension effect? Why not in other data?
  iii) Where in this figure is the most obvious evidence of a viscous drag effect on a laminar flow?
  iv) Why does the (inferred) surface $F(L/d,\ Re_x)$ flatten out at large Re_x and large L/d?

- Advanced exploration for Earthlings. At the outset of Sec. 6 a dimensional analysis was applied to pressure-driven, viscous, fully-developed pipe flow. Repeating the VPlist here for convenience,

  Pressure-driven transport of a fully-developed, viscous pipe flow: (33r)

volume transport, $Q \doteq$ [0 3 -1], the dependent variable,
pressure gradient, $\partial P/\partial x \doteq$ [1 -2 -2], an independent variable,
radius of the pipe, $r \doteq$ [0 1 0], a parameter,
dynamic viscosity, $\mu \doteq$ [1 -1 -1], a parameter.

This VPlist yields a basis set having just one nondimensional variable that must be a constant,

$$\frac{Q\,\mu}{r^4\ \partial P/\partial x} \ = \ constant. \tag{34r}$$

The result (34r) has the form of Poiseuille's linear, laminar solution, in which transport is directly proportional to the pressure gradient. In this Sec. 7 we have seen that the transport of a pipe flow may also depend upon the properties of the flow itself, whether laminar or turbulent. Where in (33r) is the possibility of turbulence? Or said a little differently, why is a linear, laminar flow guaranteed by this specific VPlist?

The VPlist (33r) included a small choice that had larger consequences than might be anticipated. The parameters pressure gradient and dynamic viscosity both included the dimension, mass. Fair enough, they usually do. But since the dependent variable was taken to be the volume transport, Q, which does not contain a mass dimension, then the viscosity and pressure gradient were bound to appear in the resulting basis set as their ratio, call it $\quad = \mu\,(\partial P/\partial x)^{-1}$, and $\quad \doteq [0\ 1\ 1]$. The VPlist (33r) had, in effect, only three independent dimensional variables, Q, r and $\quad$, and just two dimensions, length and time. This implies that there will be only one nondimensional variable, as there is in (34r), which is consistent with Poiseuille's solution for linear, laminar flow. In other words, there is no allowance in the basis set (34r) for a turbulent flow in which transport is not directly proportional to the pressure gradient.

Let's try an experiment: starting with the VPlist (33r), divide the dynamic viscosity by the fluid density to get the kinematic viscosity, and similarly for the pressure gradient to recast as an acceleration. We are not concerned in this study with the possibility of a variable fluid density, and so these choices should be acceptable, physically.

Pressure-driven transport of a fully-developed, viscous pipe flow, omitting mass:

volume transport, $Q \doteq$ [0 3 -1], the dependent variable, (65)
pressure gradient acceleration, $(\partial P/\partial x)\,/\,\rho \doteq$ [0 1 -2], an independent variable,
radius of the pipe, $r \doteq$ [0 1 0], a parameter,
kinematic viscosity, $\nu \ = \ \mu\,/\,\rho \doteq$ [0 2 -1], a parameter.

There are four members in the revised VPlist, just as before, but now with only two dimensions, length and time. Compute the basis set of nondimensional variables and find two members,

$$\frac{Q}{d\,\nu} \ = \ F(\frac{d^3\,((\partial P/\partial x)\,/\,\rho)}{\nu^2}), \tag{66}$$

a nondimensional transport that is equal to an unknown function of a Reynolds-like number. This revised analysis can accommodate turbulent flow and laminar flow, and yet it has sprung from a reduced and seemingly simpler VPlist compared with (33r).

Below are some experiments that will help fill out this discussion. The repeated null space calculations implied here are best done with Matlab or Python codes linked in the next section.

i) Starting with the VPlist (33r), change the dependent variable to mass transport,
$Q_m \doteq [\,1\ 0\ -1\,]$, but leave all else the same. This is the complement to the example worked

above in the sense that all possible instances of mass are included in the VPlist. Compute the nondimensional basis set, and compare with Eq. (34r).

ii) Starting with the VPlist (33r), replace the dynamic viscosity with kinematic viscosity (as if dividing by a constant density) but leave all else as is. This will not go well to the extent that the nondimensional basis set will have to omit the pressure gradient, the motive power for the flow. What went wrong?

iii) There are several more variations on this mass in or mass out exercise, and it is revealing to approach them systematically. Start with the VPlist (33r), and set plausibility aside. Allow that the three variables Q, $\partial P \,/\, \partial x$, and μ can appear either with or without division by density; r continues along unbothered by all this. How many unique combinations (mass on, mass off for each relevant parameter) are there in this ensemble of VPlists? We have already considered two of them in i) and ii) above. How many of the ensemble VPlists will fail to give a sensible result, as in case ii) above? How many give the Poiseuille result, Eq. (34r)? How many give that $F = F(Re)$? Now allow physical reasoning back in. Which of the VPlists and solutions are the least arbitrary?

iv) Starting with the VPlist (33r), include the fluid density as a fifth member of the VPlist. Calculate the nondimensional variables of this augmented VPlist, and explain how your new result compares with Eq. (34r).

What's the moral of this short story / long problem? Because VPlists do not include much information to begin with, even a small and seemingly incidental omission or addition can have a qualitative effect on the result. As well, there is binary-like property to a VPlist; a parameter is either in or out, with no gradation for just a little effect of mass, for example. With that in mind, it is good practice to regard every new or unfamiliar VPlist as provisional, and to experiment with plausible variations to see if something unexpected may emerge.

- ## Farewell, Explorer.

Off to find new worlds.
With Earth's gift of fresh insight,
She will make her way.

With business finally finished (tank drained) and with a backpack full of new codes and diagrams, Planetary Explorer blasted off in search of new planets and adventures. Soon she discovered a new and somewhat barren planet, and most surprising, another tank-draining project. There were two obstacles not encountered on verdant Earth: no Matlab and no internet. Assuming that the local gravitational acceleration g can be measured independently, how might the diagrams of this appendix be used to predict the gravity-driven outflow rate on this new planet?

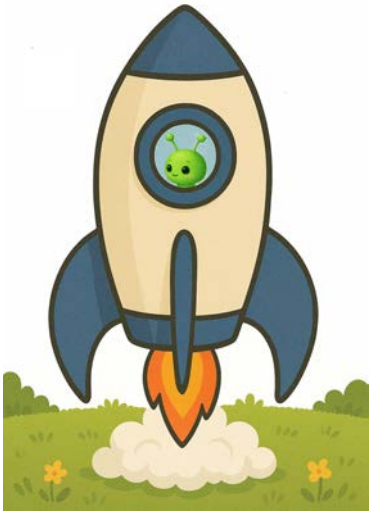

Planetary Explorer blasting off.
Image by the author using ChatGPT-5.

8 Housekeeping

Attribution and Acknowledgment: The experiments, the models and codes, the text and the technical figures were made by the author. The Planetary Explorer images were created by the author using ChatGPT-5. Administrative assistance was provided by the Dept. of Physical Oceanography, Woods Hole Oceanographic Institution.

License: Copying and distribution for educational purposes is encouraged, consistent with the Creative Commons license CC BY-NC-SA.

Citation: This essay may be cited by the web address on the Massachusetts Institute of Technology OpenCourseWare — Price, James F., 12.808 Supplemental Material, Topics in Fluid Dynamics: Lagrangian and Eulerian Representations, a Coriolis tutorial, and Dimensional Analysis of Models and Data Sets, https://ocw.mit.edu/courses/res-12-001-topics-in-fluid-dynamics-fall-2024 (date accessed).

Links to codes and data: The experimental data, the models and a Matlab script to exercise both are available at https://www2.whoi.edu/staff/jprice/wp-content/uploads/sites/199/2025/12/DA-tank.zip
There are four main files:

- Dstruct.mat, a Matlab structure that stores all of the experimental data.
- DAtank.xlsx, same as above but in an Excel table file.
- Model5.m, a Matlab function that evaluates Model 5, and with appropriate settings, Model 4.
- Dplot.m, a Matlab script that loads Dstruct.mat and makes several plots of the data, including a version of Fig. 6 along with model predictions.

Index

basis set, 3

dimensional analysis
    advantages, 3
discharge coefficient, C, 16

f
    laminar, 41
flow
    inertial, 16
    laminar, 29
friction factor, 41

Model
    0, 14
    1, 17
    2, 20
    3, 29
    4, 30
    5, 45
model
    sequence, 6
Moody diagram, 41

parabolic, 17
parameter space, 5, 8
Poiseuille solution
    via dimensional analysis, 47
Poiseuille's solution, 29
pressure
    hydrostatic, 13

Reynolds number
    external, 24
    internal, 24

scale
    natural, 14
surface tension, 18

transport, 9

velocity
    average, 24
    Torricelli, 13
viscosity , 44
    effective, 44
viscous effects, 21
VPlist, 3

a Coriolis tutorial, Part 1:
the Coriolis force, inertial and geostrophic motion

James F. Price
Woods Hole Oceanographic Institution
Woods Hole, Massachusetts, 02543
https://www2.whoi.edu/staff/jprice/ jprice@whoi.edu

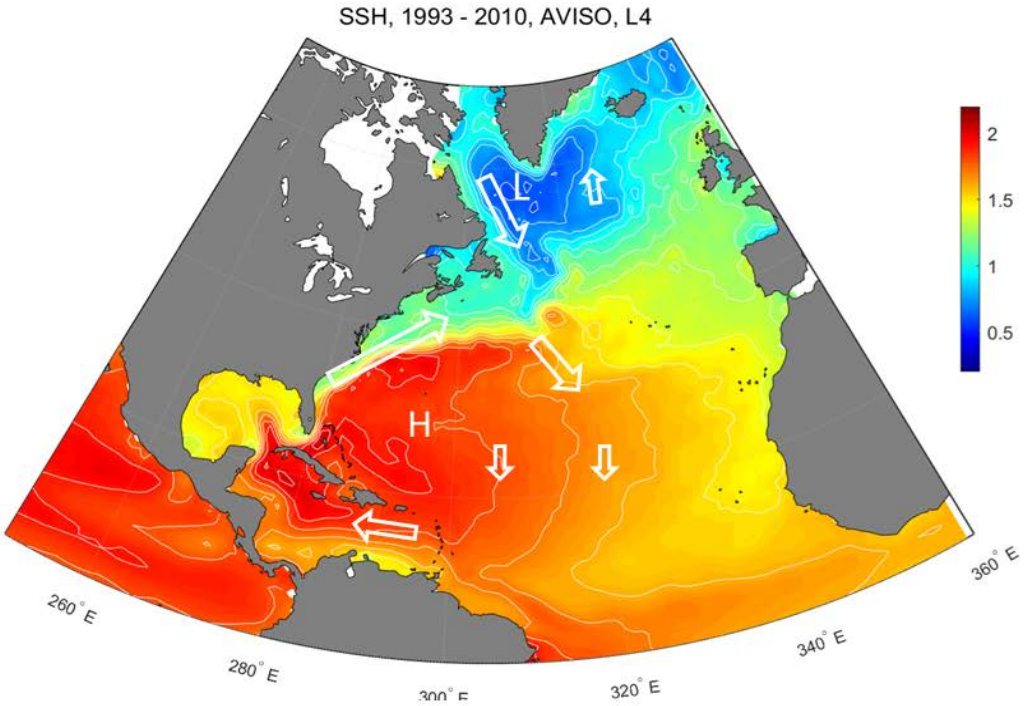

Figure 1: The decadal average sea surface height (SSH) of the North Atlantic. Colorbar at right is in meters. The principal features are a high over the subtropics and a low over the subpolar region. The inferred geostrophic current is sketched at a few locations. Geostrophic currents are almost parallel to lines of SSH, with higher SSH to the right of the current in the northern hemisphere. The upper-ocean circulation of the subtropical basin is thus a clockwise turning, horizontal gyre. The first goal of this essay is to understand how Earth's rotation leads to the Coriolis force, and the second goal is to begin to consider some of the consequences of rotation, including a very simple analog of the geostrophic relationship between SSH and upper-ocean currents.

Abstract: This essay is the first of a five part introduction to the Coriolis force and its consequences for the atmosphere and ocean. It is intended for students who are near the beginning of a quantitative study of geophysical fluid dynamics and who have some background in classical mechanics and applied mathematics.

The equation of motion appropriate to a steadily rotating reference frame includes two terms that account for accelerations that arise from the rotation of the reference frame, a centrifugal force and a Coriolis force. In the special case of an Earth-attached reference frame, the centrifugal force is subsumed into the gravity field. The Coriolis force has a very simple mathematical form, $-2\mathbf{\Omega}\times\mathbf{V}'M$, where $\mathbf{\Omega}$ is Earth's rotation vector, $\mathbf{V}'$ is the velocity observed from the rotating frame and M is the parcel mass. The Coriolis force is perpendicular to the velocity and so tends to change velocity direction, but not velocity amplitude. Hence the Coriolis force does no work. Nevertheless the Coriolis force has a profound importance for the circulation of the atmosphere and oceans.

Two direct consequences of the Coriolis force are considered here. If the Coriolis force is the only force acting on a moving parcel, then the velocity vector of the parcel will be turned anti-cyclonically (clockwise in the northern hemisphere) at the rate $-f$, where $f = 2\Omega\sin(\text{latitude})$ is the Coriolis parameter. These free motions, often termed inertial oscillations, are a first approximation of the upper ocean currents generated by a transient wind event. If the Coriolis force is balanced by a steady force, say a horizontal component of gravity as in Fig.1, then the associated geostrophic wind or current will be in a direction that is perpendicular to the gradient of the SSH and thus parallel to isolines of SSH. In the northern hemisphere, higher SSH is to the right of the current. This is said to be a geostrophic balance, and is the defining characteristic of the large scale, low frequency, extra-tropical circulation of the atmosphere and the oceans.

More on Figure 1: The mean of sea surface height (SSH) over almost two decades as observed by satellite altimetry and compiled by the Aviso project, http://www.aviso.oceanobs.com/duacs/ SSH is a constant pressure surface that is displaced slightly but significantly from level and hence there is a horizontal component of gravity along this surface that is proportional to the gradient of SSH. What keeps the SSH displaced away from level? We can be confident that the horizontal gravitational force associated with this tilted SSH is balanced locally (at a given point) by the Coriolis force acting upon currents that flow nearly parallel to isolines of SSH. This geostrophic relationship is a central topic of this essay. Notice that by far the largest gradients of SSH and so the largest geostrophic currents are found on the western boundary of the gyres. This east-west asymmetry is a consequence of Earth's rotation and nearly spherical shape, taken up in Part 4 of this series.

Contents

1 Large-scale, low frequency flows of the atmosphere and ocean **4**

1.1 Models and reference frames 6

1.1.1 Classical mechanics observed from an inertial reference frame 7

1.1.2 Classical mechanics observed from a rotating, noninertial reference frame 8

1.2 The goals and the plan of this essay 9

1.3 About these essays 10

2 Noninertial reference frames **12**

2.1 Kinematics of a linearly accelerating reference frame 12

2.2 Kinematics of a rotating reference frame 15

2.2.1 Transforming the position, velocity and acceleration vectors 15

2.2.2 Stationary $\Rightarrow$ Inertial; Rotating $\Rightarrow$ Earth-Attached 21

2.2.3 Remarks on the transformed equation of motion 24

2.3 Problems 25

3 Inertial and noninertial descriptions of elementary motions **25**

3.1 Switching sides 26

3.1.1 One-dimensional, vertical motion with gravity 26

3.1.2 Two-dimensional, circular motion; polar coordinates 27

3.2 To get a feel for the Coriolis force 32

3.2.1 At rest in the rotating frame 33

3.2.2 A cautious walk in the rotating frame 33

3.3 An elementary projectile problem 35

3.4 Appendix to Section 3; Spherical Coordinates 38

3.5 Problems 41

4 A reference frame attached to the rotating Earth **42**

4.1 Cancellation of the centrifugal force by Earth's (slightly chubby) figure 42

4.2 The equation of motion for an Earth-attached reference frame 45

4.3 Coriolis force on motions in a thin, spherical shell 45

4.4 One last look at the inertial frame equations 47

4.5 Problems 50

5 A dense parcel released onto a rotating slope with friction **52**

5.1 The nondimensional equations; Ekman number 54
5.2 (Near-) Inertial motion 56
5.3 (Quasi-) Geostrophic motion 60
5.4 Energy balance 62
5.5 Problems 64

6 Summary and Closing Remarks **66**
6.1 What is the Coriolis force? 66
6.2 Consequences of the Coriolis force for the circulation of the atmosphere and ocean . . . 66
6.3 What comes next? 67
6.4 Supplementary material 68
Index 69

1 Large-scale, low frequency flows of the atmosphere and ocean

The large-scale, low frequency flows of Earth's atmosphere and ocean take the form of circulations around centers of high or low gravitational potential (the height of a constant pressure surface relative to a known level, the sea surface height, SSH, of Fig. (1), or the 500 hPa height of Fig. (2). Ocean circulation features of this sort include gyres that extend across ocean basins, and in the atmosphere, a broad belt of westerly wind that encircles the mid-latitudes in both hemispheres. Smaller scale circulations often dominate the weather. Hurricanes and mid-latitude storms have a more or less circular flow around a low, and many regions of the ocean are filled with slowly revolving eddies having a diameter of several hundred kilometers. The height anomaly that is associated with these circulation features is the direct result of a mass excess or deficit (high or low height anomaly).

What is at first surprising and deserving of an explanation is that large scale mass anomalies implicit in the SSH and height fields of Figs. (1) and (2) persist for many days or weeks, even in the absence of an external momentum or energy source. The winds and currents that would be expected to accelerate down the height gradient (in effect, downhill) and disperse the associated mass anomaly do not occur. Instead, large-scale, low frequency winds and currents outside of the near-equatorial region are observed to flow in a direction almost parallel to lines of constant height; the sense of the flow is clockwise around highs (northern hemisphere) and anti-clockwise around lows. The flow direction is reversed in the southern hemisphere, anti-clockwise around highs and clockwise around lows. From

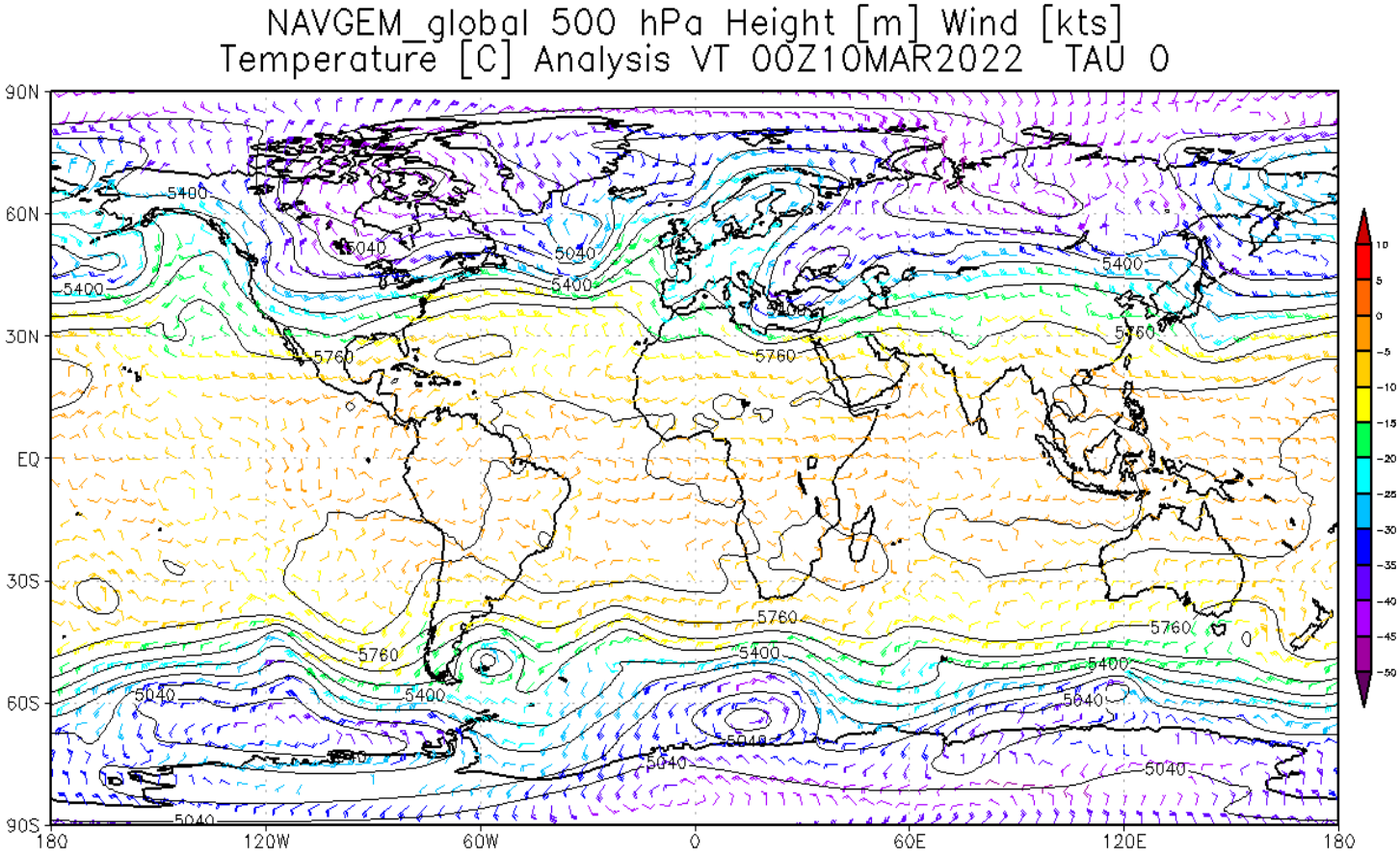

Figure 2: A weather chart at 500 hPa, a middle level of the atmosphere, on 10 March, 2022 produced by the NAVy Global Environmental Model, NAVGEM (thanks to the Naval Research Laboratory, Monterey CA, and Fleet Numerical Oceanography Center, https://www.nrlmry.navy.mil/metoc/nogaps/). The solid contours are the height (meters) of the 500 hPa pressure surface above sea level contoured at 120 m intervals. The horizontal wind is shown as barbs (one thin barb = 10 knots $\approx$ 5 m s^{-1}, one heavy barb = 50 knots). The color is temperature, deg C, with a scale at right. Several important phenomena are evident on this map: (1) The largest scale of variation is a high at low latitudes, roughly 5800 m near the equator, and a low at either pole, roughly 5050 m. (2) The zonal winds at mid-latitudes are mainly westerly in both hemispheres, i.e., from west to east, though with considerable variability in the north-south component, e.g., a prominent ridge over central Europe on this day. The broad band of westerly winds includes the jet stream(s), where wind speed is typically $\approx$ 30 m s^{-1}. (3) Within the westerly wind band, the 500 hPa surface generally slopes upward toward lower latitude, roughly 200 m per 1000 km. There is thus a small, but significant component of gravity along the 500 hPa surface directed from south to north in the northern hemisphere, and reversed in the southern hemisphere. (4) The wind and height fields outside of near-equatorial regions (roughly $\pm$ 10 degrees of latitude) thus exhibit a geostrophic relationship: wind vectors are nearly parallel to the contours of constant height, greater height is to the right of the wind vector in the northern hemisphere and to the left in the southern hemisphere, and faster winds are found in conjunction with larger height gradients.

This image is in the public domain.

this we can infer that the horizontal gravitational force along a pressure surface must be balanced approximately by a second force that acts to deflect horizontal winds and currents to the right of the velocity vector in the northern hemisphere and to the left of the velocity vector in the southern hemisphere (you should make a sketch of this[1]). This deflecting force is called the Coriolis force,[2] and is the theme of this essay. A quasi-steady balance between the horizontal gravitational force (or equivalently, the horizontal component of the pressure gradient) and the Coriolis force is called a geostrophic balance. An approximate or quasi- geostrophic balance is the defining characteristic of large scale, low frequency atmospheric and oceanic flows.[3]

We attribute profound physical consequences to the Coriolis force, and yet cannot point to a physical interaction as the cause of the Coriolis force in the straightforward way that height anomalies are related to the mass field. Rather, the Coriolis force arises from motion itself, combined with the necessity that we observe the atmosphere and ocean from an Earth-attached and thus rotating, noninertial reference frame. In this respect the Coriolis force is very different from other important forces acting on geophysical fluids, e.g., friction and gravity, that arise from an interaction of physical objects. The goals of this essay (elaborated below) are, first, to explain the origin and basic properties of the Coriolis force, and then to examine some of its direct consequences for the atmosphere and ocean, including a very simple analogue of geostrophic motion.

1.1 Models and reference frames

These essays proceed inductively, developing and adding new concepts one by one rather than deriving them from a comprehensive starting point. In that spirit, the first physical model considered here in Part 1 will be a single, isolated fluid particle, or 'parcel'. This is a very drastic and for most purposes untenable idealization of a fluid. Winds and currents, like all macroscopic fluid flows, are effectively a continuum of parcels that interact in three-dimensions; the motion of any one parcel is connected by pressure gradients and by friction to the motion of essentially all of the other parcels that make up the flow. This global dependence is at the very heart of fluid mechanics, but can be set aside here because the Coriolis force on a given parcel depends only upon the velocity of that parcel. What will have to go missing in this single parcel model is that the external forces on a parcel (the $\mathbf{F}$ below) must be

[1] And then you will surely be wondering, What's it do right on the equator?, taken up in Sec. 6, Homework Problem 12.

[2] After the French physicist and engineer, Gaspard-Gustave de Coriolis, 1792-1843, whose seminal contributions include the systematic derivation of the rotating frame equation of motion and the development of the gyroscope. An informative history of the Coriolis force is by A. Persson, 'How do we understand the Coriolis force?', *Bull. Am. Met. Soc.*, **79**(7), 1373-1385 (1998).

[3] To be sure, it's not quite this simple. This 'large scale, low frequency' is a shorthand for (1) large spatial scale, (2) low frequency, (3) extra-tropical, and (4) outside of frictional boundary layers. It is important to have a quantitative sense what is meant by each of these (which turn out to be linked in interesting ways) and we will come to this in Parts 2 and 3. For now, suffice it to say that this present use of 'large scale' encompasses everything that you can readily see in Figs. 1 and 2, except for the equatorial region, roughly ± 10 deg of latitude.

prescribed in a way that can take no account of, e.g., the mass and pressure fields that evolve as part of a real fluid flow. The phenomena that may be treated with a single parcel model are thus severely limited, but are nevertheless a recognizable subset of the phenomena that arise in more realistic fluid models (coming in Part 2) and in the real ocean and atmosphere (Figs. 1 and 2, and in Sec. 5).

1.1.1 Classical mechanics observed from an inertial reference frame

If a parcel is observed from an inertial reference frame[4] then the classical (Newtonian) equation of motion is just

$$\frac{d(M\mathbf{V})}{dt} = \mathbf{F} + \mathbf{g}_* M,$$

where d/dt is an ordinary time derivative, $\mathbf{V}$ is the velocity in a three-dimensional space, and M is the parcel's mass. The parcel mass will be presumed constant in all that follows, and the equation of motion rewritten as

$$\frac{d\mathbf{V}}{dt} = \mathbf{F}/M + \mathbf{g}_*, \tag{1}$$

where $\mathbf{F}$ is the sum of the forces that we can specify *a priori* given the complete knowledge of the environment, e.g., frictional drag with the sea floor, and $\mathbf{g}_*$ is gravitational mass attraction.[5] These are said to be central forces insofar as they act in a radial direction between parcels, or in the case of gravitational mass attraction, between parcels and the center of mass of the Earth.

In this essay we are especially concerned with identifying the acceleration that would be observed in a given reference frame. Unless it is noted otherwise, this acceleration will be written on the left-hand side of an equation of motion, as in Eqn. (1), even if the acceleration is considered to be the known quantity. The forces, i.e., everything else, will then be written be on the right-hand side of the equation as

$$observed\ acceleration \ = \ sum\ of\ the\ forces/M. \tag{2}$$

[4] 'Inertia' has Latin roots *in+artis* meaning without art or skill and secondarily, resistant to change. Since Newton's *Principia*, physics usage has emphasized the latter: a parcel having inertia will remain at rest, or if in motion, continue without change unless subjected to an external force. A 'reference frame' is comprised of a coordinate system that serves to arithmetize the position of parcels, a clock to tell the time, and an observer who makes an objective record of positions and times as seen from that reference frame. A reference frame may or may not be attached to a physical object. In this essay we suppose purely classical physics so that measurements of length and of time are identical in all reference frames; measurements of position, velocity and acceleration *are* reference frame-dependent, as discussed in Section 2. This common sense view of space and time begins to fail when velocities approach the speed of light, which is not an issue here. An 'inertial reference frame' is one in which all parcels have the property of inertia and in which the total momentum is conserved, i.e., all forces occur as action-reaction force pairs. How this plays out in the presence of gravity is discussed briefly in Sec. 3.1.

[5] In all of this it is taken for granted that inertial mass (the mass property that is inversely proportional to acceleration for a given force) is exactly equal to gravitational mass (the mass property that is relevant in gravitational attraction). This is oftentimes referred to as the Equivalence Principal, and sometimes as the Universality of Free Fall. The simplest and most important rationalization for this is that inertial mass and gravitational mass are not merely equal numerically, but are one and the same thing.

The left and right-hand sides of an equation of motion will be called 'acceleration' and 'force(s)', even though all of the terms necessarily have the physical dimensions of acceleration, $[length\ time^{-2}]$. (This is not the usual convention in geophysical fluid dynamics, where the Coriolis force/M is most often written on the left side of the equation of motion.)

This inertial frame equation of motion (1) has two fundamental properties that are noted here because we are about to give them up:

Global conservation. For each of the central forces acting on the parcel there will be a corresponding reaction force acting on the environment that sets up the force. Thus the global time rate of change of momentum (global means the parcel plus the environment) due to the sum of all of the central forces $\mathbf{F}+\mathbf{g}_* M$ is zero, and so the global momentum is conserved. Usually our attention is focused on the local problem, i.e., the parcel only, with this global conservation taken for granted and not analyzed explicitly.

Invariance to Galilean transformation. Eqn. (1) should be invariant to a steady, linear translation of the reference frame, often called a Galilean transformation, because only relative motion has physical significance. Thus a constant velocity added to $\mathbf{V}$ will cause no change in the time derivative, and should as well cause no change in the forces $\mathbf{F}$ or $\mathbf{g}*M$. Like the global balance just noted, this fundamental property is not invoked frequently, but is a powerful guide to the form of the forces $\mathbf{F}$. For example, a frictional force that satisfies Galilean invariance should depend upon the difference of the parcel velocity with respect to a surface or adjacent parcels, and not the parcel velocity only.

1.1.2 Classical mechanics observed from a rotating, noninertial reference frame

When it comes to the analysis of the atmosphere or ocean, we always use a reference frame that is attached to the rotating Earth — true (literal) inertial reference frames are not accessible to most kinds of observation and wouldn't be desirable even if they were. Some of the reasons for this are discussed in a later section, 4.3, but for now we are concerned with the consequence that, because of the Earth's rotation, Fig. 3, an Earth-attached reference frame is significantly *noninertial* for the large-scale, low-frequency motions of the atmosphere and ocean: Eqn. (1) does not hold for large scale winds and ocean currents, even as a first approximation. The equation of motion appropriate to an Earth-attached, rotating reference frame (derived in detail in Sections 2 and 4.1) is instead

$$\frac{d\mathbf{V}'}{dt} = -2\boldsymbol{\Omega}\times\mathbf{V}' + \mathbf{F}'/M + \mathbf{g}, \tag{3}$$

where the prime on a vector indicates that it is observed from the rotating frame, $\boldsymbol{\Omega}$ is Earth's rotation vector (Fig. 3), which has the dimensions $[time^{-1}]$, and $\mathbf{g}$ is gravitational mass attraction plus the centrifugal force associated with Earth's rotation and called simply 'gravity' (discussed further in Section 4.1). Our obsession here will be the new term, $-2\boldsymbol{\Omega}\times\mathbf{V}'$, often called the Coriolis force in geophysics (though here it has the dimensions $[length\ time^{-2}]$ of an acceleration).

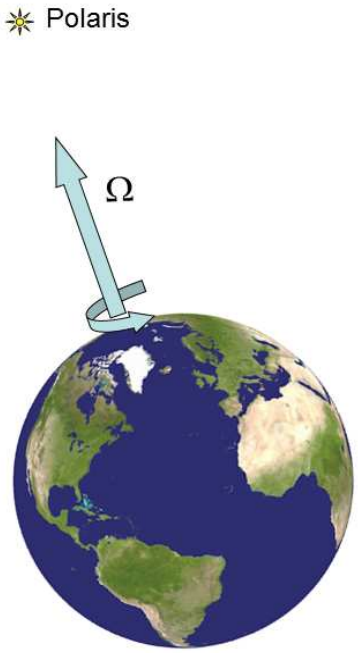

Figure 3: Earth's rotation vector, $\mathbf{\Omega}$, maintains a nearly steady bearing close to Polaris, commonly called the Pole Star or North Star. Earth thus has a specific orientation with respect to the universe at large, and, in consequence, all directions are not equal. This is manifest as a marked anisotropy of most large-scale circulation phenomena, e.g., the east-west asymmetry of ocean gyres noted in Fig. 1 and the westward propagation of low frequency waves and eddies studied in Part 3.

1.2 The goals and the plan of this essay

Eqn. (2) applied to geophysical flows is not the least bit controversial and so the practical thing to do is to accept the Coriolis force as given (as we do many other concepts) and get on with the applications. You can do that here by going directly to Sec. 5. However, that shortcut is very likely to leave you wondering ... **What is the Coriolis force?** ... in the conceptual and in the physical sense, and for example, is it appropriate to call $-2\mathbf{\Omega}\times\mathbf{V}'$ the Coriolis 'force'? The classical mechanics literature applies a bewildering array of names to this term, that it is the Coriolis effect, a pseudo force, a virtual force, an apparent force, an inertial force (we will use this as well), a noninertial force (which makes more literal sense), and most equivocal of all, a fictitious correction force.[6] A case can be made for each of these terms, but the choice here will be just plain Coriolis force, since we are going to be most concerned with what the Coriolis force does in the context of geophysical flows.

The plan for Secs. 1 - 4 is to take a slow and careful journey from Eqn. (1) to Eqn. (2) so that at the end we should be able to explain the origin and basic properties of the Coriolis force, the first goal of

[6]The latter is by by J. D. Marion, *Classical Mechanics of Particles and Systems* (Academic Press, NY, 1965), who describes the plight of a rotating observer as follows (the double quotes are his): '... the observer must postulate an additional force - the centrifugal force. But the "requirement" is an artificial one; it arises solely from an attempt to extend the form of Newton's equations to a non inertial system and this may be done only by introducing a fictitious "correction force". The same comments apply for the Coriolis force; this "force" arises when attempt is made to describe motion relative to the rotating body.' Rotating observers do indeed have to contend with inertial forces that are not found in otherwise comparable inertial frames, but these inertial forces are not *ad hoc* corrections as Marion's quote (taken out of context) might seem to imply.

this essay.[7] We have already noted that the Coriolis force arises from the rotation of an Earth-attached reference frame. The origin of the Coriolis force is thus a matter kinematics, i.e., mathematics, rather than physics, and taken up in Section 2. This is part of the reason why the Coriolis force can be hard to grasp, conceptually.[8] Several very simple applications of the rotating frame equation of motion are considered in Section 3. These illustrate the often marked difference between inertial and rotating frame descriptions of the same phenomenon, and they also show that the rotating frame equation of motion (2) does *not* retain the fundamental properties of the inertial frame Eqn. (1) noted above. Eqn. (2) applies on a rotating Earth or a planet, where the centrifugal force associated with planetary rotation is canceled (Section 4). The rotating frame equation of motion thus treats only the comparatively small relative velocity, i.e., winds and currents. This is a huge advantage compared with the inertial frame equation of motion, which has to treat all of the motion, including that due to Earth's rotation, and more than compensates for the admittedly peculiar properties of the Coriolis force which comes along with the rotating frame.

The second goal of this essay is to begin to address ... **What are the consequences of Earth's rotation and the Coriolis force for the circulation of the atmosphere and ocean?** This is an almost open-ended question that makes up much of the field of geophysical fluid dynamics. A first small step is taken in Section 5 by analyzing the motion of a parcel released onto a sloping surface, e.g., the sea surface or 500 hPa pressure surface (if they are considered to be fixed), and including a simplified form of friction. The resulting motion may include inertial oscillations, the free oscillation of the rotating frame momentum equations, and a steady motion, called geostrophic flow, that is a first approximation of the currents and winds of Figs. (1) and (2).

1.3 About these essays

This essay is the first in a five part series,

Part 1: the Coriolis force, inertial and geostrophic motion,

Part 2: a rotating shallow water model, potential vorticity conservation and geostrophic adjustment,

[7] 'Explanation is indeed a virtue; but still, less a virtue than an anthropocentric pleasure.' B. van Frassen, 'The pragmatics of explanation', in *The Philosophy of Science*, Ed. by R. Boyd, P. Gasper and J. D. Trout. (The MIT Press, Cambridge Ma, 1999). This pleasure of understanding is the deep motivation of this essay, but clearly the Coriolis force has great practical significance for the atmosphere and ocean, and for those of us who seek to understand and predict their motions.

[8] All this talk of 'forces, forces, forces' seems a little quaint and it is certainly becoming tedious. Modern dynamics is more likely to be developed around the concepts of energy, action and minimization principles, which are very useful in some special classes of fluid flow. However, it remains that the majority of fluid mechanics proceeds along the path of Eqn. (1) laid down by Newton. In part this is because mechanical energy is not conserved in most real fluid flows and in part because the interaction between a fluid parcel and its surroundings is often at issue, friction for example, and is usually best-described in terms of forces. Sometimes, just to avoid saying Coriolis force yet again, we will use instead 'rotation'.

Part 3: beta-effects, westward propagation,

Part 4: the Sverdrup relation and wind-driven ocean circulation, and,

Part 5: on the seasonally-varying Arabian Sea.

These have been written for students who are near the beginning of a quantitative study of geophysical fluid dynamics. Some background in classical mechanics and applied mathematics is assumed, roughly second year, undergraduate level physics and applied mathematics.

This Part 1 essay introduces the basics — the kinematics of a rotating reference frame and the properties of the resulting Coriolis force. Rotating reference frames are a topic included in many classical mechanics courses and textbooks and there is nothing fundamental and new regarding the Coriolis force added here.[9] The hope is that this essay will make a useful supplement to these sources by providing more of the relevant physics background and greater mathematical detail than is possible in a wide-ranging fluid dynamics text, and by emphasizing geophysical phenomena that are missed or outright misconstrued in many classical mechanics texts.[10,11] Ocean and atmospheric sciences are all about fluids in motion on a grand scale, and the electronic version of this essay includes links to animations and to source codes of numerical models that provide a more vivid depiction of these motions than is possible in a hardcopy.

The first version of this essay was released in 2003, and since then the text and models have been revised and expanded many times. The most up-to-date version of the essays and codes will be posted to the author's web site, https://www2.whoi.edu/staff/jprice and look for the page Education Projects. Comments and questions are encouraged and may be addressed to jprice@whoi.edu

[9]Classical mechanics texts in order of increasing level: A. P. French, *Newtonian Mechanics* (W. W. Norton Co., 1971); A. L. Fetter and J. D. Walecka, *Theoretical Mechanics of Particles and Continua* (McGraw-Hill, NY, 1990); C. Lanczos, *The Variational Principles of Mechanics* (Dover Pub., NY, 1949). Textbooks on geophysical fluid dynamics emphasize mainly the consequences of Earth's rotation; excellent introductions at about the level of this essay are by J. R. Holton, *An Introduction to Dynamic Meteorology, 3rd Ed.* (Academic Press, San Diego, 1992), and by B. Cushman-Roisin, *Introduction to Geophysical Fluid Dynamics* (Prentice Hall, Engelwood Cliffs, New Jersey, 1994). Somewhat more advanced and highly recommended for the topic of geostrophic adjustment is A. E. Gill, *Atmosphere-Ocean Dynamics* (Academic Press, NY, 1982), for waves generally, J. Pedlosky, *Waves in the Ocean and Atmosphere*, (Springer, 2003) and also J. C. McWilliams, *Fundamentals of Geophysical Fluid Dynamics*, (Cambridge Univ. Press, 2006).

[10]There are several essays or articles that, like this one, aim to clarify the Coriolis force. A fine treatment in great depth is by H. M. Stommel and D. W. Moore, *An Introduction to the Coriolis Force* (Columbia Univ. Press, 1989); the present Section 4.1 owes a great deal to their work. A detailed analysis of dropped particle motion is by M. S. Tiersten and H. Soodak, 'Dropped objects and other motions relative to a noninertial earth', *Am. J. Phys.*, **68**(2), 129–142 (2000). A useful web page for general science students is http://www.ems.psu.edu/%7Efraser/Bad/BadFAQ/BadCoriolisFAQ.html

[11]The Coriolis force also has engineering applications; it is exploited to measure the angular velocity required for vehicle control systems, http://www.siliconsensing.com, and to measure mass transport in fluid flow, http://www.micromotion.com.

Financial support during the preparation of these essays was provided by the Academic Programs Office of the Woods Hole Oceanographic Institution. Additional salary support has been provided by the U.S. Office of Naval Research. Terry McKee of WHOI is thanked for her expert assistance with Aviso data. Tom Farrar of WHOI, Pedro de la Torre of KAUST, Adam Laux of Siena Italy, Ru Chen of MIT/WHOI, Peter Gaube of OSU/COAS, Jennifer Van Wakeman of OSU/COAS, Iam-Fei Pun of WHOI and Ted Price of Yale Univ. are all thanked for proof-reading a draft of this essay. Jiayan Yang, Xin Huang and Dennis McGillicuddy of WHOI are thanked for their insightful comments and suggestions on Part 3.

These essays and associated materials may be cited by the MIT OpenCourseWare address: Price, James F., 12.808 Supplemental Material, Topics in Fluid Dynamics: Dimensional Analysis, a Coriolis tutorial, and Lagrangian and Eulerian Representations (Spring 2022), https://ocw.mit.edu/courses/res-12-001-topics-in-fluid-dynamics-spring-2022 (date accessed). License: Creative Commons, CC BY-NC-SA. For rights and obligations under this license see https://creativecommons.org/licenses/

2 Noninertial reference frames

The first step toward understanding the origin of the Coriolis force is to describe the origin of inertial forces in the simplest possible context, a pair of reference frames that are represented by displaced coordinate axes, Fig. (4). Frame one is labeled X and Z and frame two is labeled X' and Z'. It is helpful to assume that frame one is stationary and that frame two is displaced relative to frame one by a time-dependent vector, $\mathbf{X_o}(t)$. The measurements of position, velocity, etc. of a given parcel will thus be different in frame two vs. frame one. Just how the measurements differ is a matter of kinematics; there is no physics involved until we define the acceleration of frame two, and then use the accelerations to write an equation of motion appropriate to frame 2, e.g., Eqn. (2).

2.1 Kinematics of a linearly accelerating reference frame

If the position vector of a given parcel is $\mathbf{X}$ when observed from frame one, then from within frame two the same parcel will be observed at the position

$$\mathbf{X}' = \mathbf{X} - \mathbf{X_o}.$$

The position vector of a parcel thus depends upon the reference frame. Suppose that frame two is translated and possibly accelerated with respect to frame one, while maintaining a constant orientation (rotation will be considered shortly). If the velocity of a parcel observed in frame one is $d\mathbf{X}/dt$, then in

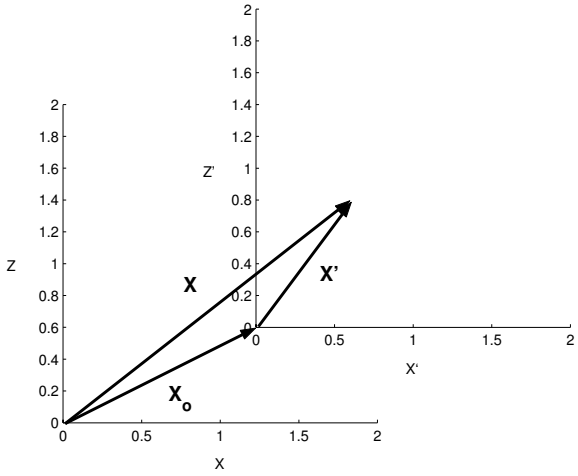

Figure 4: Two reference frames are represented by coordinate axes that are displaced by the vector $\mathbf{X_o}$ that is time-dependent. In this Section 2.1 we consider only a relative translation, so that frame two maintains a fixed orientation with respect to frame one. The rotation of frame two will be considered beginning in Section 2.2.

frame two the same parcel will be observed to have velocity

$$\frac{d\mathbf{X}'}{dt} = \frac{d\mathbf{X}}{dt} - \frac{d\mathbf{X_o}}{dt}.$$

The accelerations are similarly $d^2\mathbf{X}/dt^2$ and

$$\frac{d^2\mathbf{X}'}{dt^2} = \frac{d^2\mathbf{X}}{dt^2} - \frac{d^2\mathbf{X_o}}{dt^2}. \tag{4}$$

We are going to assume that frame one is an inertial reference frame, i.e., that parcels observed in frame one have the property of inertia so that their momentum changes only in response to a force, $\mathbf{F}$, i.e., Eqn. (1). From Eqn. (1) and from Eqn. (4) we can easily write down the equation of motion for the parcel as it would be observed from frame two:

$$\frac{d^2\mathbf{X}'}{dt^2} = -\frac{d^2\mathbf{X_o}}{dt^2} + \mathbf{F}/M + \mathbf{g}_*. \tag{5}$$

The term $-(d^2\mathbf{X_o}/dt^2)$ appearing in the frame two equation of motion (5) will be called an 'inertial force', and when this term is nonzero, frame two is said to be 'noninertial'. As an example, suppose that frame two is subject to a constant acceleration, $d^2\mathbf{X_o}/dt^2 = \mathbf{A}$ that is upward and to the right in Fig. (4). From Eqn. (4) it is evident that all parcels observed from within frame two would then appear to accelerate with a magnitude and direction $-\mathbf{A}$, downward and to the left, and which is, of course, exactly opposite the acceleration of frame two with respect to frame one. Clearly, the origin of the inertial force is the acceleration of the reference frame, $\mathbf{A}$, and not an interaction with other objects, e.g., by friction or collisions.

Inertial forces that arise in this way are exactly proportional to the mass of the object, and in this key respect are indistinguishable from gravitational mass attraction. If an inertial force is dependent only upon position, as is the centrifugal force due to Earth's rotation (Section 4.1), then it might as well

be added with gravitational mass attraction $\mathbf{g}_*$ to give a single, time-independent acceleration field, usually termed 'gravity' and denoted by $\mathbf{g}$. Indeed, this gravity field — mass attraction plus centrifugal acceleration — is the acceleration field that may be observed directly, for example by observing a plumb line.[12]

Since there is no interaction between particles involved in an inertial force, there is also no action-reaction force pair associated with an inertial force. Global momentum conservation thus does not hold in the presence of inertial forces. There is something highly equivocal about the phenomenon we are calling an 'inertial force', and so you can appreciate why some authors have deemed them to be 'virtual' or 'fictitious correction' forces.[6]

Whether an inertial force is problematic or not depends entirely upon whether the acceleration $d^2\mathbf{X_o}/dt^2$ is known or not. If it should happen that the acceleration of frame two is not known, then all bets are off. For example, imagine observing the motion of a plumb bob within an enclosed trailer that was moving along in irregular, stop-and-go traffic. The bob would be observed to lurch forward and backward unexpectedly, and we would soon conclude that studying dynamics in such an uncontrolled, noninertial reference frame was going to be a very difficult endeavor. Inertial forces could be blamed if it was observed that all of the physical objects in the trailer, observers included, experienced exactly the same unaccounted acceleration. In many cases the relevant inertial forces are known well enough to use noninertial reference frames with great precision, e.g., the topography of Earth's gravity field must be known to within a few centimeters to interpret sea surface altimetry data of the kind seen in Fig. (1)[13] and the Coriolis force can be readily calculated as in Eqn. (2) knowing only Earth's rotation vector and the parcel velocity.

In the specific example of a translating reference frame sketched in Fig. (4), one could just as well transform the observations made from frame two back into the inertial frame one, use the inertial frame equation of motion to make a calculation, and then transform back to frame two if required. By that tactic we could avoid altogether the seeming delusion of an inertial force. However, when it comes to the observation and analysis of Earth's atmosphere and ocean, there is really no choice but to use an Earth-attached and thus rotating and noninertial reference (discussed in Section 4.3). That being so, we have to contend with the Coriolis force, an inertial force that arises from the rotation of an Earth-attached frame. The kinematics of rotation add a small complication that is taken up in the next Section 2.2. But the key point is this — if you followed the development of Eqn. (5), then you already

[12] A plumb bob is nothing more than a weight, the bob, that hangs from a string, the plumb line (and *plumbum* is the Latin for lead, Pb). When a plumb bob is at rest in a given reference frame, the plumb line is parallel to the local acceleration field of that reference frame. If the bob is displaced and released, it will oscillate as a simple pendulum. The observed period of small amplitude oscillations, P, can be used to infer the magnitude of the acceleration, $g = L/(P/2\pi)^2$, where L is the length of the plumb line. If the reference frame is attached to the rotating Earth (and it probably will be!), then the motion of the bob will be effected also by the Coriolis force, in which case the device is often termed a Foucault pendulum discussed in a later section, 4.5.

[13] Earth's gravity field is the object of extensive and ongoing survey by some truly remarkable technology and methods, see http://www.csr.utexas.edu/grace/

understand the origin of inertial forces, including the Coriolis force.

2.2 Kinematics of a rotating reference frame

The Coriolis force will arise in the equivalent of Eqn. (5) for the case of a steadily rotating reference frame. Reference frame one will again be assumed to be stationary and defined by a triad of orthogonal unit vectors, $\mathbf{e_1}$, $\mathbf{e_2}$ and $\mathbf{e_3}$ (Fig. 5). A parcel P can then be located by a position vector $\mathbf{X}$

$$\mathbf{X} = \mathbf{e_1} x_1 + \mathbf{e_2} x_2 + \mathbf{e_3} x_3, \tag{6}$$

where the Cartesian (rectangular) components, x_i, are the projection of $\mathbf{X}$ onto each of the unit vectors in turn. It is useful to rewrite Eqn. (6) using matrix notation. The unit vectors are made the elements of a row matrix,

$$\mathbb{E} = [\mathbf{e_1}\ \mathbf{e_2}\ \mathbf{e_3}], \tag{7}$$

and the components x_i are taken to be the elements of a column matrix,

$$\mathbb{X} = \begin{bmatrix} x_1 \\ x_2 \\ x_3 \end{bmatrix}. \tag{8}$$

Eqn. (6) may then be written in a way that conforms with the usual matrix multiplication rules as

$$\mathbf{X} = \mathbb{E}\mathbb{X}. \tag{9}$$

The vector $\mathbf{X}$ and its time derivatives are presumed to have an objective existence, i.e., they represent something physical that is unaffected by our arbitrary choice of a reference frame. Nevertheless, the way these vectors appear clearly does depend upon the reference frame (Fig. 5) and for our purpose it is essential to know how the position, velocity and acceleration vectors will appear when they are observed from a steadily rotating reference frame. In a later part of this section we will identify the rotating reference frame as an Earth-attached reference frame and the stationary frame as one aligned on the distant fixed stars. It is assumed that the motion of the rotating frame can be represented by a time-independent rotation vector, $\mathbf{\Omega}$. The $\mathbf{e_3}$ unit vector can be aligned with $\mathbf{\Omega}$ with no loss of generality, Fig. (5a). We can go a step further and align the origins of the stationary and rotating reference frames because the Coriolis force is independent of position (Section 2.2).

2.2.1 Transforming the position, velocity and acceleration vectors

Position: Back to the question at hand: how does this position vector look when viewed from a second reference frame that is rotated through an angle θ with respect to the first frame? The answer is

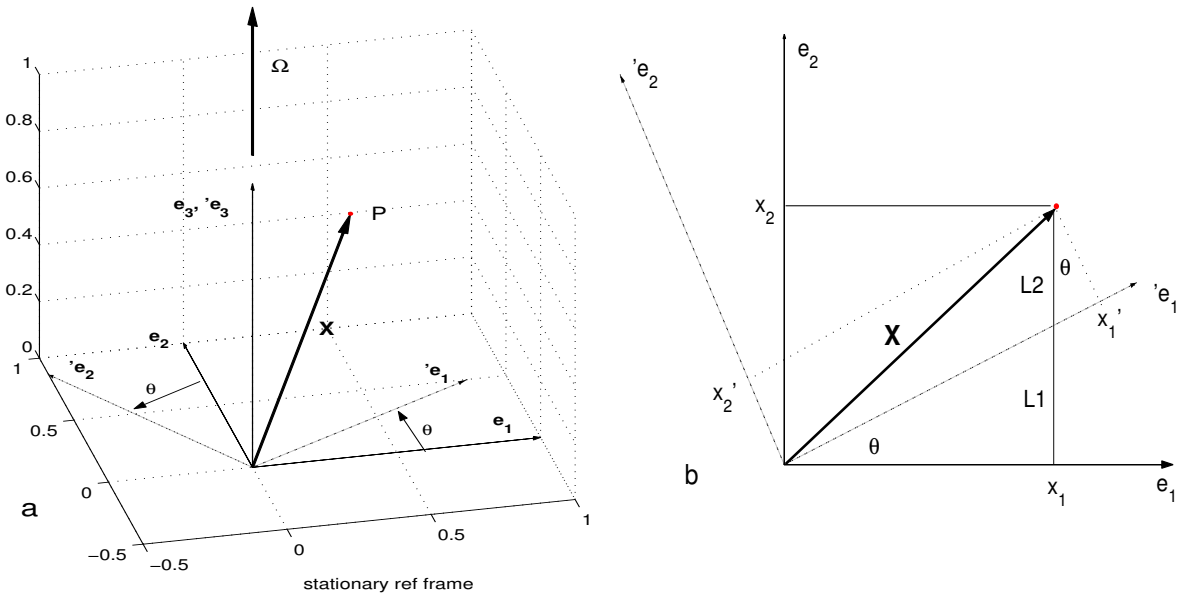

Figure 5: **(a)** A parcel P is located by the tip of a position vector, **X**. The stationary reference frame has solid unit vectors that are presumed to be time-independent, and a second, rotated reference frame has dashed unit vectors that are labeled $\mathbf{`e_i}$. The reference frames have a common origin, and rotation is about the $\mathbf{e_3}$ axis. The unit vector $\mathbf{e_3}$ is thus unchanged by this rotation and so $\mathbf{`e_3} = \mathbf{e_3}$. This holds also for $\mathbf{\Omega}' = \mathbf{\Omega}$, and so we will use $\mathbf{\Omega}$ exclusively. The angle θ is counted positive when the rotation is counterclockwise. **(b)** The components of **X** in the stationary reference frame are x_1, x_2, x_3, and in the rotated reference frame they are x_1', x_2', x_3'.

that the vector 'looks' like the components appropriate to the rotated reference frame, and so we need to find the projection of **X** onto the unit vectors that define the rotated frame. The details are shown in Fig. (5b); notice that $x_2 = L1 + L2$, $L1 = x_1 \tan\theta$, and $x_2' = L2\cos\theta$. From this it follows that $x_2' = (x_2 - x_1\tan\theta)\cos\theta = -x_1\sin\theta + x_2\cos\theta$. By a similar calculation we can find that $x_1' = x_1\cos\theta + x_2\sin\theta$. The component x_3' that is aligned with the axis of the rotation vector is unchanged, $x_3' = x_3$, and so the set of equations for the primed components may be written as a column vector

$$\mathbb{X}' = \begin{bmatrix} x_1' \\ x_2' \\ x_3' \end{bmatrix} = \begin{bmatrix} x_1\cos\theta + x_2\sin\theta \\ -x_1\sin\theta + x_2\cos\theta \\ x_3 \end{bmatrix}. \tag{10}$$

By inspection this can be factored into the product

$$\mathbb{X}' = \mathbb{R}\mathbb{X}, \tag{11}$$

where $\mathbb{X}$ is the matrix of stationary frame components and $\mathbb{R}$ is the rotation matrix,[14]

$$\mathbb{R}(\theta) = \begin{bmatrix} \cos\theta & \sin\theta & 0 \\ -\sin\theta & \cos\theta & 0 \\ 0 & 0 & 1 \end{bmatrix}. \tag{12}$$

This θ is the angle displaced by the rotated reference frame and is positive counterclockwise. The position vector observed from the rotated frame will be denoted by $\mathbf{X}'$; to construct $\mathbf{X}'$ we sum the rotated components, $\mathbb{X}'$, times a set of unit vectors that are fixed and thus

$$\mathbf{X}' = \mathbf{e_1}x_1' + \mathbf{e_2}x_2' + \mathbf{e_3}x_3' = \mathbb{E}\mathbb{X}' \tag{13}$$

For example, the position vector $\mathbf{X}$ of Fig. (5) is at an angle of about 45° counterclockwise from the $\mathbf{e_1}$ unit vector and the rotated frame is at $\theta = 30°$ counterclockwise from the stationary frame one. That being so, the position vector viewed from the rotated reference frame, $\mathbf{X}'$, makes an angle of 45° - 30° = 15° with respect to the $\mathbf{e_1}$ (fixed) unit vector seen within the rotated frame, Fig. (6). As a kind of verbal shorthand we might say that the position vector has been 'transformed' into the rotated frame by Eqs. (10) and (13). But since the vector has an objective existence, what we really mean is that the components of the position vector are transformed by Eqn. (10) and then summed with fixed unit vectors to yield what should be regarded as a new vector, $\mathbf{X}'$, the position vector that we observe from the rotated (or rotating) reference frame.

Velocity: The velocity of parcel P seen in the stationary frame is just the time rate of change of the position vector seen in that frame,

$$\frac{d\mathbf{X}}{dt} = \frac{d}{dt}\mathbb{E}\mathbb{X} = \mathbb{E}\frac{d\mathbb{X}}{dt},$$

since $\mathbb{E}$ is time-independent. The velocity of parcel P as seen from the rotating reference frame is similarly

$$\frac{d\mathbf{X}'}{dt} = \frac{d}{dt}\mathbb{E}\mathbb{X}' = \mathbb{E}\frac{d\mathbb{X}'}{dt},$$

which indicates that the time derivatives of the rotated components are going to be very important in what follows. For the first derivative we find

$$\frac{d\mathbb{X}'}{dt} = \frac{d(\mathbb{R}\mathbb{X})}{dt} = \frac{d\mathbb{R}}{dt}\mathbb{X} + \mathbb{R}\frac{d\mathbb{X}}{dt}. \tag{14}$$

The second term on the right side of Eqn. (14) represents velocity components from the stationary frame that have been transformed into the rotating frame, as in Eqn. (11). If the rotation angle θ was

[14] A concise and clear reference on matrix representations of coordinate transformations is by J. Pettofrezzo *Matrices and Transformations* (Dover Pub., New York, 1966). An excellent all-around reference for undergraduate-level applied mathematics including coordinate transformations is by M. L. Boas, *Mathematical Methods in the Physical Sciences, 2nd edition* (John Wiley and Sons, 1983).

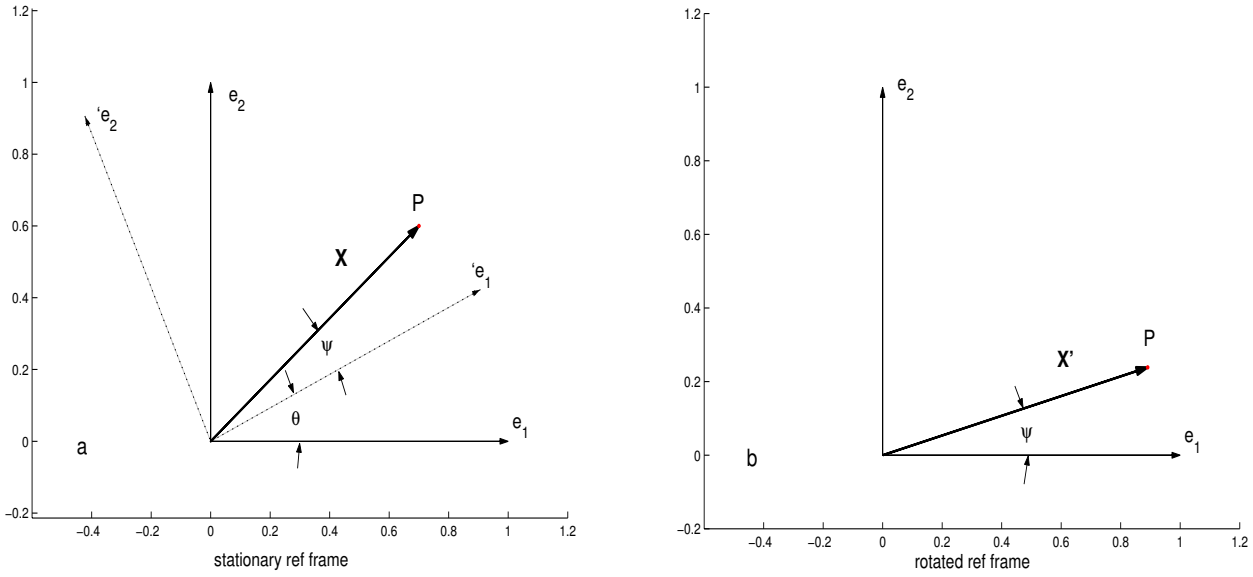

Figure 6: **(a)** The position vector $\mathbf{X}$ seen from the stationary reference frame. **(b)** The position vector as seen from the rotated frame, denoted by $\mathbf{X}'$. Note that in the rotated reference frame the unit vectors are labeled $\mathbf{e_i}$ since they are fixed; when these unit vectors are seen from the stationary frame, as on the left, they are labeled $\mathbf{`e_i}$. If the position vector is stationary in the stationary frame, then $\theta + \psi = constant$. The angle ψ then changes as $d\psi/dt = -d\theta/dt = -\Omega$, and thus the vector $\mathbf{X}'$ appears to rotate at the same rate but in the opposite sense as does the rotating reference frame.

constant so that $\mathbb{R}$ was independent of time, then the first term on the right side would vanish and the velocity components would transform exactly as do the components of the position vector. In that case there would be no Coriolis force.

When the rotation angle is time-varying, as it will be here, the first term on the right side of Eqn. (14) is non-zero and represents a velocity component that is induced solely by the rotation of the reference frame. For an Earth-attached reference frame

$$\theta = \theta_0 + \Omega t,$$

where Ω is Earth's rotation rate measured with respect to the distant stars, effectively a constant defined below (and θ_0 is unimportant). Though Ω may be presumed constant, the associated reference frame is nevertheless accelerating and is noninertial in the same way that circular motion at a steady speed is accelerating because the direction of the velocity vector is continually changing (cf. Fig. 10). Given this $\theta(t)$, the time-derivative of the rotation matrix is

$$\frac{d\mathbb{R}}{dt} = \Omega \begin{bmatrix} -\sin\theta(t) & \cos\theta(t) & 0 \\ -\cos\theta(t) & -\sin\theta(t) & 0 \\ 0 & 0 & 0 \end{bmatrix}, \tag{15}$$

which has the elements of $\mathbb{R}$, but shuffled around. By inspection, this matrix can be factored into the

product of a matrix $\mathbb{C}$ and $\mathbb{R}$ as

$$\frac{d\mathbb{R}}{dt} = \Omega\, \mathbb{C}\mathbb{R}(\theta(t)), \tag{16}$$

where the matrix $\mathbb{C}$ is

$$\mathbb{C} = \begin{bmatrix} 0 & 1 & 0 \\ -1 & 0 & 0 \\ 0 & 0 & 0 \end{bmatrix} = \begin{bmatrix} 1 & 0 & 0 \\ 0 & 1 & 0 \\ 0 & 0 & 0 \end{bmatrix} \mathbb{R}(\pi/2). \tag{17}$$

Multiplication by $\mathbb{C}$ acts to knock out the component $(\,)_3$ that is parallel to $\mathbf{\Omega}$ and causes a rotation of $\pi/2$ in the plane perpendicular to $\mathbf{\Omega}$. Substitution into Eqn. (14) gives the velocity components appropriate to the rotating frame

$$\frac{d(\mathbb{R}\mathbb{X})}{dt} \;=\; \Omega\mathbb{C}\mathbb{R}\mathbb{X} + \mathbb{R}\frac{d\mathbb{X}}{dt}, \tag{18}$$

or using the prime notation $(\,)'$ to indicate multiplication by $\mathbb{R}$, then

$$\frac{d\mathbb{X}'}{dt} = \Omega\mathbb{C}\mathbb{X}' + \left(\frac{d\mathbb{X}}{dt}\right)' \tag{19}$$

The second term on the right side of Eqn. (19) is just the rotated velocity components and is present even if Ω vanished (a rotated but not a rotating reference frame). The first term on the right side represents a velocity that is induced by the rotation rate of the rotating frame; this induced velocity is proportional to Ω and makes an angle of $\pi/2$ radians to the right of the position vector in the rotating frame (assuming that $\Omega > 0$).

To calculate the vector form of this term we can assume that the parcel P is stationary in the stationary reference frame so that $d\mathbf{X}/dt = 0$. Viewed from the rotating frame, the parcel will appear to move clockwise at a rate that can be calculated from the geometry (Fig. 7). Let the rotation in a time interval δt be given by $\delta\psi = -\Omega\delta t$; in that time interval the tip of the vector will move a distance $|\delta\mathbf{X}'| = |\mathbf{X}'|\sin(\delta\psi) \approx |\,\mathbf{X}'|\delta\psi$, assuming the small angle approximation for $\sin(\delta\psi)$. The parcel will move in a direction that is perpendicular (instantaneously) to $\mathbf{X}'$. The velocity of parcel P as seen from the rotating frame and due solely to the coordinate system rotation is thus $\lim_{\delta t\to 0}\frac{\delta\mathbf{X}'}{\delta t} = -\mathbf{\Omega}\times\boldsymbol{X'}$, the vector cross-product equivalent of $\Omega\mathbb{C}\mathbb{X}'$ (Fig. 8). The vector equivalent of Eqn. (19) is then,

$$\boxed{\frac{d\mathbf{X}'}{dt} = -\mathbf{\Omega}\times\boldsymbol{X'} + \left(\frac{d\mathbf{X}}{dt}\right)'} \tag{20}$$

This and a handful of other equations upcoming are boxed to indicate their special importance.

The relation between time derivatives given by Eqn. (20) applies to velocity vectors, acceleration vectors, etc., and may be written as an operator equation,

$$\frac{d(\;)'}{dt} = -\mathbf{\Omega}\times(\;)' + \left(\frac{d(\;)}{dt}\right)' \tag{21}$$

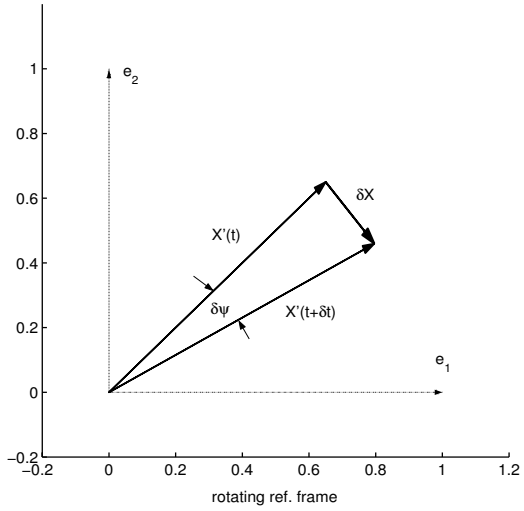

Figure 7: The position vector $\mathbf{X}'$ seen from the rotating reference frame. The unit vectors that define this frame, $\mathbf{`e_i}$, appear to be stationary when viewed from within this frame, and hence we label them with $\mathbf{e_i}$ (not primed). Assume that $\Omega > 0$ so that the rotating frame is turning counterclockwise with respect to the stationary frame, and assume that the parcel P is stationary in the stationary reference frame so that $d\mathbf{X}/dt = 0$. Parcel P as viewed from the rotating frame will then appear to move clockwise on a circular path.

that is valid for all vectors regardless of their position with repsect to the axis of rotation.[15] From left to right the terms are: 1) the time rate of change of a vector as seen in the rotating reference frame, 2) the cross-product of the rotation vector with the vector and 3) the time rate change of the vector as seen in the stationary frame and then rotated into the rotating frame. Notice that the time rate of change and prime operators of (21) do not commute, the difference being the cross-product term which represents a time rate change in the *direction* of the vector, but not its magnitude. The left hand side, term 1), is the time rate of change that we observe directly or seek to solve when working from the rotating frame.

Acceleration: Our goal here is to relate the accelerations seen in the two reference frames and so differentiating Eqn. (19) once more and after rearrangement of the kind used above

$$\frac{d^2\mathbb{X}'}{dt^2} = 2\Omega\mathbb{C}\frac{d\mathbb{X}'}{dt} + \Omega^2\mathbb{C}^2\mathbb{X}' + \left(\frac{d^2\mathbb{X}}{dt^2}\right)' \tag{22}$$

The middle term on the right includes multiplication by the matrix $\mathbb{C}^2 = \mathbb{C}\mathbb{C}$,

$$\mathbb{C}^2 = \begin{bmatrix} 1 & 0 & 0 \\ 0 & 1 & 0 \\ 0 & 0 & 0 \end{bmatrix} \mathbb{R}(\pi/2) \begin{bmatrix} 1 & 0 & 0 \\ 0 & 1 & 0 \\ 0 & 0 & 0 \end{bmatrix} \mathbb{R}(\pi/2) = \begin{bmatrix} 1 & 0 & 0 \\ 0 & 1 & 0 \\ 0 & 0 & 0 \end{bmatrix} \mathbb{R}(\pi) = \begin{bmatrix} -1 & 0 & 0 \\ 0 & -1 & 0 \\ 0 & 0 & 0 \end{bmatrix},$$

that knocks out the component parallel to the rotation vector $\mathbf{\Omega}$ and reverses the other two components; the vector equivalent of $\Omega^2\mathbb{C}^2\mathbb{X}'$ is thus $-\mathbf{\Omega}\times\mathbf{\Omega}\times\mathbf{X}'$ (Fig. 8). The vector equivalent of Eqn. (22) is

[15] Imagine arrows taped to a turntable with random orientations. Once the turntable is set into (solid body) rotation, all of the arrows will necessarily rotate at the same rotation rate regardless of their position or orientation. The rotation will, of course, cause a translation of the arrows that depends upon their location, but the rotation rate is necessarily uniform, and this holds regardless of the physical quantity that the vector represents. This is of some importance for our application to a rotating Earth, since Earth's motion includes a rotation about the polar axis, as well as an orbital motion around the Sun and yet we represent Earth's rotation by a single vector.

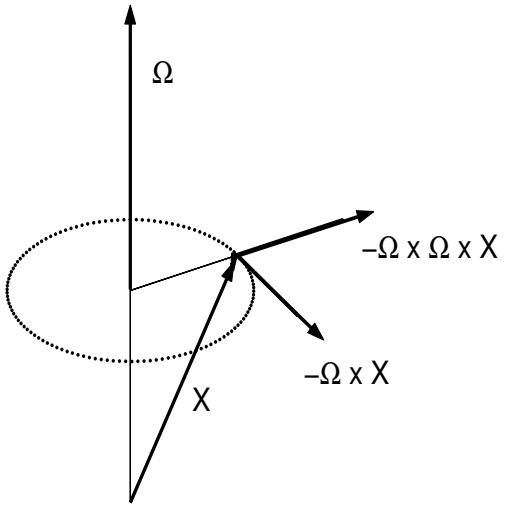

Figure 8: A schematic showing the relationship of a vector $\mathbf{X}$, and various cross-products with a second vector $\mathbf{\Omega}$ (note the signs). The vector $\mathbf{X}$ is shown with its tail perched on the axis of the vector $\mathbf{\Omega}$ as if it were a position vector. This helps to visualize the direction of the cross-products, but it is important to note that the relationship among the vectors and vector products shown here holds for all vectors, regardless of where they are defined in space or the physical quantity, e.g., position or velocity, that they represent.

then[16]

$$\boxed{\frac{d^2\mathbf{X}'}{dt^2} = -2\mathbf{\Omega}\times\frac{d\mathbf{X}'}{dt} - \mathbf{\Omega}\times\mathbf{\Omega}\times\mathbf{X}' + \left(\frac{d^2\mathbf{X}}{dt^2}\right)'} \tag{23}$$

Note the similarity with Eqn. (3). From left to right the terms are 1) the acceleration as seen in the rotating frame, 2) the Coriolis term, 3) the centrifugal[17] term, and 4) the acceleration as seen in the stationary frame and then rotated into the rotating frame. As before, term 1) is the acceleration that we directly observe or seek to solve for when working from the rotating reference frame.

2.2.2 Stationary ⇒ Inertial; Rotating ⇒ Earth-Attached

The third and final step in this derivation of the Coriolis force is to define the inertial reference frame one, and then the rotation rate of frame two. To make frame one inertial it is presumed that the unit

[16]The relationship between the stationary and rotating frame velocity vectors given by Eqs. (19) and (20) is clear visually and becomes intuitive given just a little experience. It is not so easy to intuit the corresponding relationship between the accelerations given by Eqs. (22) and (23). To understand the transformation of acceleration there is really no choice but to understand (be able to reproduce and then explain) the mathematical steps going from Eqn. (19) to Eqn. (22) and/or from Eqn. (20) to Eqn. (23).

[17]'Centrifugal' and 'centripetal' have Latin roots, *centri+fugere* and *centri+peter*, meaning center-fleeing and center-seeking, respectively. Taken literally these would indicate merely the sign of a radial force, for example. However, they are very often used to mean specifically a term of the sort $\Omega^2 r$, seen on the right side of Eq. (23), i.e., the centrifugal force in an equation of motion written for a rotating, non-inertial reference frame. The same kind of term, though with the rotation rate written as ω and referring to the angular coordinate of the parcel rather than the reference frame, will also arise as the acceleration observed from an inertial reference frame. In that case $\omega^2 r$ is the centripetal acceleration that must accompany every curving trajectory. This seeming change of identity from an inertial force to an acceleration will be discussed further in Sec. 3.2.

vectors $\mathbf{e_i}$ could in principle be aligned on the distant, 'fixed stars'.[18] The rotating frame two is presumed to be attached to Earth, and the rotation rate Ω is then given by the rate at which the same fixed stars are observed to rotate overhead, one revolution per *sidereal* day (Latin for from the stars),

$$\boxed{\Omega \;=\; 2\pi/(23 \text{ hrs}, 56 \text{ min and } 4.09 \text{ sec}) \;=\; 7.2921\times10^{-5} \text{ rad s}^{-1}} \tag{24}$$

A sidereal day is only about four minutes less than a solar day, and so in a purely numerical sense, $\Omega \approx \Omega_{solar} = 2\pi/24$ hours = 7.2722×10^{-5} rad s^{-1} which is certainly easier to remember than is Eqn. (24). For the purpose of a rough estimate, the small numerical difference between Ω and Ω_{solar} is not significant. However, the difference between Ω and Ω_{solar} can be told in numerical simulations and in well-resolved field observations. And too, on Mach's Principle,[18] the difference between Ω and Ω_{solar} is highly significant.

Earth's rotation rate is very nearly constant, and the axis of rotation maintains a nearly steady bearing on a point on the celestial sphere that is close to the North Star, Polaris (Fig. 3). The Earth's rotation vector thus provides a definite orientation of Earth with respect to the universe, and Earth's rotation rate has an absolute magnitude. The practical evidence of this comes from rotation rate sensors[11] that read out Earth's rotation rate with respect to the fixed stars as a kind of gage pressure, called 'Earth rate'.[19]

[18]Fixed is a matter of degree. The Sun and the planets certainly do not qualify as fixed, but even some nearby stars move detectably over the course of a year. The intent is that the most distant stars should serve as sign posts for the spatially-averaged mass of the universe as a whole on the hypothesis that inertia arises whenever there is an acceleration (linear or rotational) with respect to the mass of the universe. This grand idea was expressed most forcefully by the Austrian philosopher and physicist Ernst Mach, and is often termed Mach's Principle (see, e.g., J. Schwinger, *Einstein's Legacy* Dover Publications, 1986; M. Born, *Einstein's Theory of Relativity*, Dover Publications, 1962). Mach's Principle seems to be in accord with all empirical data, including the magnitude of the Coriolis force. Mach's principle is probably best thought of as a (profound) relationship, rather than the fundamental mechanism of inertia. A new hypothesis takes the form of so-called vacuum stuff (or Higgs field) that is presumed to pervade all of space and so provide a local mechanism for resistance to accelerated motion (see P. Davies, 'On the meaning of Mach's principle', http://www.padrak.com/ine/INERTIA.html). The debate between Newton and Leibniz over the reality of absolute space — which had seemed to go in favor of relative space, Leibniz and Mach's Principle — has been renewed in the search for a physical origin of inertia. When this is achieved, we can then point to a physical origin of the Coriolis force.

Observations on the fixed stars are a very precise means to define rotation rate, but can not, in general, be used to define the linear translation or acceleration of a reference frame. The only way to know if a reference frame that is aligned on the fixed stars is inertial is to carry out mechanics experiments and test whether Eqn.(1) holds and global momentum is conserved. If yes, the frame is inertial.

[19]For our present purpose $\mathbf{\Omega}$ may be presumed constant. In fact, there are small but observable variations of Earth's rotation rate due mainly to changes in the atmospheric and oceanic circulation and due to mass distribution within the cryosphere, see B. F. Chao and C. M. Cox, 'Detection of a large-scale mass redistribution in the terrestrial system since 1998,' Science, **297**, 831–833 (2002), and R. M. Ponte and D. Stammer, 'Role of ocean currents and bottom pressure variability on seasonal polar motion,' *J. Geophys. Res.*, **104**, 23393–23409 (1999). The direction of $\mathbf{\Omega}$ with respect to the celestial sphere also varies detectably on time scales of tens of centuries on account of precession, so that Polaris has not always been the pole star (Fig. 3), even during historical times. The slow variation of Earth's orbital parameters (slow enough to be assumed to vanish for our purpose) are an important element of climate, see e.g., J. A. Rial, 'Pacemaking the ice ages by frequency modulation of

Assume that the inertial frame equation of motion is

$$\frac{d^2\mathbb{X}}{dt^2} = \mathbb{F}/M + \mathbb{G}_* \text{ and } \frac{d^2\mathbf{X}}{dt^2} = \mathbf{F}/M + \mathbf{g}_* \tag{25}$$

($\mathbb{G}_*$ is the component matrix of $\mathbf{g}*$). The acceleration and force can always be viewed from another reference frame that is rotated (but not rotating) with respect to the first frame,

$$\left(\frac{d^2\mathbb{X}}{dt^2}\right)' = \mathbb{F}' + \mathbb{G}'_* \text{ and } \left(\frac{d^2\mathbf{X}}{dt^2}\right)' = \mathbf{F}' + \mathbf{g}'_*, \tag{26}$$

as if we had chosen a different set of fixed stars or multiplied both sides of Eqn. (22) by the same rotation matrix. This equation of motion preserves the global conservation and Galilean transformation properties of Eqn. (25). To find the rotating frame equation of motion, eliminate the rotated acceleration from Eqn. (26) using Eqs. (22) and (23) and then solve for the acceleration seen in the rotating frame: the components are

$$\frac{d^2\mathbb{X}'}{dt^2} = 2\Omega\mathbb{C}\frac{d\mathbb{X}'}{dt} - \Omega^2\mathbb{C}^2\mathbb{X}' + \mathbb{F}' + \mathbb{G}'_* \tag{27}$$

and the vector equivalent is

$$\boxed{\frac{d^2\mathbf{X}'}{dt^2} = -2\boldsymbol{\Omega}\times\frac{d\mathbf{X}'}{dt} - \boldsymbol{\Omega}\times\boldsymbol{\Omega}\times\mathbf{X}' + \mathbf{F}' + \mathbf{g}_*{}'.} \tag{28}$$

Eqn. (28) has the form of Eqn. (4), the difference being that the noninertial reference frame is rotating rather than translating. If the origin of this noninertial reference frame was also accelerating, then there would be a third inertial force term, $-(d^2\mathbf{X_o}/dt^2)$. Notice that we are not yet at Eqn. (2); in Section 4.1 the centrifugal force and gravitational mass attraction terms will be combined into the time-independent inertial force **g**.

Earth's orbital eccentricity,' *Science*, **285**, 564–568 (1999).

As well, Earth's motion within the solar system and galaxy is much more complex than a simple spin around a perfectly stable polar axis. Among other things, the Earth orbits the Sun in a counterclockwise direction with a rotation rate of 1.9910 $\times 10^{-7}$ s^{-1}, which is about 0.3% of the rotation rate Ω. Does this orbital motion enter into the Coriolis force, or otherwise affect the dynamics of the atmosphere and oceans? The short answer is no and yes. We have already accounted for the rotation of the Earth with respect to the fixed stars. Whether this rotation is due to a spin about an axis centered on the Earth or due to a solid body rotation about a displaced center is not relevant for the Coriolis force *per se*, as noted in the discussion of Eqn. (21). However, since Earth's polar axis is tilted significantly from normal to the plane of the Earth's orbit around the Sun (the tilt implied by Fig. 3), we can ascribe Earth's rotation Ω to spin alone. The orbital motion about the Sun combined with Earth's finite size gives rise to tidal forces, which are small but important spatial variations of the centrifugal/gravitational balance that holds for the Earth-Sun and for the Earth-Moon as a whole (described particularly well by French[9], and see also Tiersten, M. S. and H Soodak, 'Dropped objects and other motions relative to the noninertial earth', *Am. J. Phys.*, **68** (2), Feb. 2000, 129-142).

2.2.3 Remarks on the transformed equation of motion

Once the transformation rule for accelerations, Eqn. (23), is in hand, the path to the rotating frame equation of motion is short and direct — if Eqn. (26) holds in a given reference frame (say an inertial frame, but that is not essential) then Eqs. (27) and (28) hold exactly in a frame that rotates at the constant rate and direction given by $\mathbf{\Omega}$ with respect to the first frame. The rotating frame equation of motion includes two terms that are dependent upon the rotation vector, the Coriolis term, $-2\mathbf{\Omega}\times(d\mathbf{X}'/dt)$, and the centrifugal term, $-\mathbf{\Omega}\times\mathbf{\Omega}\times\mathbf{X}'$. These terms are sometimes written on the left side of an equation of motion as if they were going to be regarded as part of the acceleration, i.e.,

$$\frac{d^2\mathbf{X}'}{dt^2} + 2\mathbf{\Omega}\times\frac{d\mathbf{X}'}{dt} + \mathbf{\Omega}\times\mathbf{\Omega}\times\mathbf{X}' = \mathbf{F}'/M + \mathbf{g}*'. \tag{29}$$

Comparing the left side of Eqn. (29) with Eqn. (23), it is evident that the rotated acceleration is equal to the rotated force,

$$\left(\frac{d^2\mathbf{X}}{dt^2}\right)' = \mathbf{F}'/M + \mathbf{g}*',$$

which is well and true and the same as Eqn. (26).[20] However, it is crucial to understand that the left side of Eqn. (29), $(d^2\mathbf{X}/dt^2)'$ is *not* the acceleration that is observed from the rotating reference frame, $d^2\mathbf{X}'/dt^2$. When Eqn. (29) is solved for $d^2\mathbf{X}'/dt^2$, it follows that the Coriolis and centrifugal terms are, figuratively or literally, sent to the right side of the equation of motion where they are interpreted as if they were forces.

When the Coriolis and centrifugal terms are regarded as forces — and it is argued here that they should be when observing from a rotating reference frame — they have all of the peculiar properties of inertial forces noted in Section 2.1. From Eqn. (29) (and Eqn. 4) it is evident that the centrifugal and Coriolis terms are exactly proportional to the mass of the parcel observed, whatever that mass may be. The acceleration associated with these inertial forces arises from the rotational acceleration of the reference frame, combined with relative velocity for the Coriolis force. They differ from central forces $\mathbf{F}$ and $\mathbf{g}*M$ in the respect that there is no physical interaction that causes the Coriolis or centrifugal force and hence there is no action-reaction force pair. As a consequence the rotating frame equation of motion does not retain the global conservation of momentum that is a fundamental property of the inertial frame equation of motion and central forces (an example of this nonconservation is described in Section 3.4). Similarly, we note here only that invariance to Galilean transformation is lost since the Coriolis force involves the velocity rather than velocity derivatives. Thus $\mathbf{V}'$ is an absolute velocity in the rotating reference frame of the Earth. If we need to call attention to these special properties of the Coriolis force, then the usage Coriolis *inertial* force seems appropriate because it is free from the taint

[20] Recall that $\mathbf{\Omega} = \mathbf{\Omega}'$ and so we could put a prime on every vector in this equation. That being so, it would be better to remove the visually distracting primes and then make note that the resulting equation holds in a steadily rotating reference frame. We will keep the primes for now, since we will be considering both inertial and rotating reference frames until Section 5.

of unreality that goes with 'virtual force', 'fictitious correction force', etc., and because it gives at least a hint at the origin of the Coriolis force. It is important to be aware of these properties of the rotating frame equation of motion, and also to be assured that in most analysis of geophysical flows they are of no great practical consequence. What is most important is that the rotating frame equation of motion offers a very significant gain in simplicity compared to the inertial frame equation of motion, discussed further in Section 4.

The Coriolis and centrifugal forces taken individually have simple interpretations. From Eqn. (28) it is evident that the Coriolis force is normal to the velocity, $d\mathbf{X}'/dt$, and to the rotation vector, $\mathbf{\Omega}$. The Coriolis force will thus tend to cause the velocity to change direction but not magnitude, and is appropriately termed a deflecting force as noted in Section 1 (the purest example of this deflection occurs in an important phenomenon called inertial motion, described in Section 5.2.) The centrifugal force is in a direction perpendicular to and directed away from the axis of rotation. It is independent of time and is dependent upon position. How these forces effect dynamics in simplified conditions will be considered in Sections 3, 4.3 and 5.

2.3 Problems

(1) It is important that Eqs. (10) through (13) have an immediate and concrete meaning for you. Some questions/assignments to help you along: Verify Eqs. (10) and (13) by some direct experimentation, i.e., try them and see. Show that the transformation of the vector components given by Eqs. (11) and (12) leaves the magnitude of the vector unchanged, i.e., $|\mathbf{X}'| = |\mathbf{X}|$. Verify that $\mathbb{R}(\theta_1)\mathbb{R}(\theta_2) = \mathbb{R}(\theta_1 + \theta_2)$ and that $\mathbb{R}\theta^{-1} = \mathbb{R}(-\theta)$, where $\mathbb{R}^{-1}$ is the inverse (and also the transpose) of the rotation matrix.

(2) Show that the unit vectors that define the rotated frame can be related to the unit vectors of the stationary frame by $\grave{}\,\mathbb{E} = \mathbb{E}\mathbb{R}^{-1}$ and hence the unit vectors observed from the stationary frame turn the opposite direction of the position vector observed from the rotating frame (and thus the reversed prime). The components of an ordinary vector (a position vector or velocity vector) are thus said to be *contravariant*, meaning that they rotate in a sense that is opposite the rotation of the coordinate system. What, then, can you make of $\grave{}\,\mathbb{E}\mathbb{X}' = \mathbb{E}\mathbb{R}^{-1}\mathbb{R}\mathbb{X}$?

(3) What is the rotation rate of the Moon? Hint, make a sketch of the Earth-Moon orbital system and consider what we observe of the Moon from Earth. What would the Coriolis and centrifugal forces be on the Moon?

3 Inertial and noninertial descriptions of elementary motions

The object of this section is to evaluate the equations of motion (25) and (28) for several examples of elementary motions. The goal will be to understand how the accelerations and the inertial forces — gravity, centrifugal and Coriolis — depend upon the reference frame. Though the motions considered

A characterization of the forces on geophysical flows.

	central?	inertial?	Galilean invariant?	position only?
contact forces	yes	no	yes	no
grav. mass attraction	yes	yes	yes	yes
centrifugal	no	yes	yes	yes
Coriolis	no	yes	no	no

Table 1: Contact forces on fluid parcels include pressure gradients (normal to a surface) and frictional forces (mainly tangential to a surface). The centrifugal force noted here is that associated with Earth's rotation. 'position only' means dependent upon the parcel position but not the parcel velocity, for example. This table ignores electromagnetic forces since they are usually small.

here are truly elementary, nevertheless the analysis is slightly subtle in that the acceleration and inertial force terms may change identity, as if be fiat, when observing from one reference frame or another. To appreciate that there is more to this analysis than an arbitrary relabeling of terms, it will be very helpful for you to make a sketch of each case, starting with the observed acceleration.

3.1 Switching sides

3.1.1 One-dimensional, vertical motion with gravity

Consider a parcel of fixed mass M that is in contact with the ground and at rest. For the purpose here, a reference frame that is attached to the ground may be considered to be inertial. The vertical component of the equation of motion is then, in general,

$$\frac{d^2z}{dt^2} \;=\; F_z/M - g,$$

where the observed acceleration is written on the left hand side and the forces are listed on the right side. The forces acting on this parcel include the vertical component of a contact force, F_z, that acts over the surface of the parcel. To measure the contact force, the parcel could (in principal) be enclosed in a wrap-around strain gage that reads out the tangential and normal stresses acting on the surface of the parcel. In this case, the strain gauge will read a contact force that is upwards, $F_z > 0$. The other force acting on this parcel is due to gravity, $\mathbf{g}M$, an inertial force that acts throughout the body of the parcel (in this section there is no need to make a distinction between g and $g*$) (Table 1). To make an independent measure of $\mathbf{g}$, the direction may be observed as the direction of a stationary plumb line, and the magnitude of $\mathbf{g}$ may be inferred from the period of small oscillations.[12] For the conditions prescribed, a parcel at rest, the equation of motion for a ground-attached reference frame is just

$$\text{ground} - \text{attached frame}: \quad 0 \;=\; F_z - gM, \tag{30}$$

a static force balance between the upward contact force, F_z, and the downward force due to gravity, i.e., the parcel's weight (you were warned that this would be elementary).

Now suppose that the same parcel is observed from a reference frame that is in free-fall and accelerating downwards at the rate $-g$ with respect to the ground-attached frame.[21] When viewed from this free-falling reference frame, the parcel is observed to be accelerating upward at the rate

$$\frac{d^2z'}{dt^2} \;=\; g > 0.$$

In this free-falling frame, there is no gravitational force (imagine astronauts free-falling (floating) in space and attempting pendulum experiments ..... 'Houston, we have a pendulum problem') and so the only force recognized as acting on the parcel is the upward contact force, F_z, which is unchanged from the case before, i.e., the contact force is invariant. The equation of motion for the parcel observed from this free-falling reference frame is then, with the observed acceleration on the left,

$$\text{free}-\text{falling frame}: \quad \frac{d^2z'}{dt^2} = g \;=\; F_z/M. \tag{31}$$

Notice that in going from the inertial frame and Eqn. (30) to the free-falling frame and Eqn. (31), the term involving g has seemed to switch sides; gM is the force of gravity (an inertial force) in the ground-attached reference frame, Eqn. (30), and appears as an acceleration in the free-falling reference frame, Eqn. (31). Exactly this kind of switching sides will obtain when we consider rotating reference frames and the centrifugal and Coriolis forces.

3.1.2 Two-dimensional, circular motion; polar coordinates

Now consider the purely horizontal motion of a parcel so that gravity and the vertical component of the motion are ignored. It will be advantageous to utilize polar coordinates, which are reviewed here briefly. If you are familiar with polar coordinates, then jump ahead to Eqns. (36) and (37).

Presume that the motion is confined to a plane defined by the usual cartesian coordinates x_1 and x_2 and unit vectors $\mathbf{e_1}$ and $\mathbf{e_2}$. Thus the position of any point in the plane may be specified by (x_1, x_2) and vectors by their projection onto $\mathbf{e_1}$ and $\mathbf{e_2}$. Alternatively, a position may also be defined by polar coordinates, the distance from the origin, r, and an angle, λ between the radius vector and (arbitrarily)

[21] Gravitational mass attraction is an inertial force and a central force that has a very long range. Consider two gravitating bodies and a reference frame attached to one of them, say parcel one, which will then be observed to be at rest. If parcel two is then found to accelerate towards parcel one, the total momentum of the system (parcel one plus parcel two) will not be conserved, i.e., in effect, gravity would not be recognized as a central force. A reference frame attached to one of the parcels is thus noninertial. To define an inertial reference frame in the presence of mutually gravitating bodies we can use the center of mass of the system, and then align on the fixed stars. This amounts to putting the entire system into free-fall with respect to any larger scale (external to this system) gravitational mass attraction. For more on gravity and inertial reference frames see http://plato.stanford.edu/entries/spacetime-iframes/.

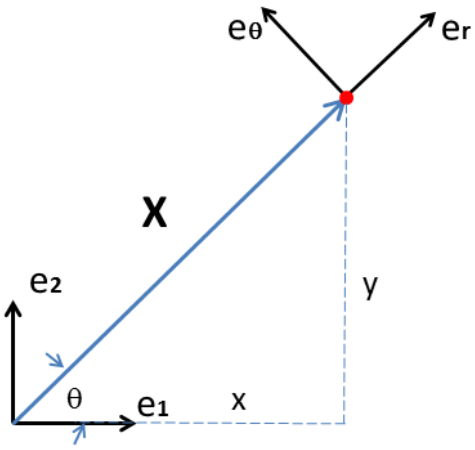

Figure 9: The unit vectors $\mathbf{e_1}, \mathbf{e_2}$ define a cartesian reference frame. The unit vectors for a polar coordinate system, $\mathbf{e_r}$ and $\mathbf{e}_\lambda$, are defined at the position of a given parcel (red dot) with $\mathbf{e_r}$ in the direction of the line segment from the origin to the parcel position. These polar unit vectors are in general time-dependent because the angle λ is time-dependent.

$\mathbf{e_1}$. The angle λ increases anti-clockwise (Fig. 9). To insure that the polar coordinates are unique we will require that

$$r \geq 0 \quad \text{and} \quad 0 \leq \lambda < 2\pi.$$

The position vector is then

$$\mathbf{X} = r\mathbf{e_r},$$

where the unit vector $\mathbf{e_r}$ has an origin at the parcel position and is in the direction of a line segment from the origin to the parcel position. The direction of $\mathbf{e_r}$ is thus λ. The unit vector $\mathbf{e}_\lambda$ is orthogonal and to the left of $\mathbf{e_r}$. The conversion from cartesian to polar coordinates is

$$r = \sqrt{x^2 + y^2} \quad \text{and} \quad \lambda = \tan^{-1}(y/x),$$

and back,

$$x = r\cos\lambda \quad \text{and} \quad y = r\sin\lambda.$$

The polar system unit vectors are time-dependent because λ is in general time-dependent. To find out how they vary with $\lambda(t)$ we start by writing their expression in terms of the time-independent cartesian unit vectors as

$$\mathbf{e_r} = \cos\lambda\,\mathbf{e_1} + \sin\lambda\,\mathbf{e_2}, \quad \text{and,} \quad \mathbf{e}_\lambda = -\sin\lambda\,\mathbf{e_1} + \cos\lambda\,\mathbf{e_2}. \tag{32}$$

From Eqn (32) the time rate changes are

$$\frac{d\mathbf{e_r}}{dt} = \omega \mathbf{e}_\lambda \quad \text{and} \quad \frac{d\mathbf{e}_\lambda}{dt} = -\omega \mathbf{e_r}, \tag{33}$$

where $\omega = d\lambda/dt$. The d/dt operating on a polar unit vector induces a rotation of 90 degrees in the direction of ω, and stretching by the factor ω. With these results in hand the parcel velocity is readily computed as

$$\frac{d\mathbf{X}}{dt} = \frac{dr}{dt}\mathbf{e_r} + r\frac{d\mathbf{e_r}}{dt} = \frac{dr}{dt}\mathbf{e_r} + r\omega\mathbf{e}_\lambda \tag{34}$$

which shows the polar velocity components

$$U_r = \frac{dr}{dt} \quad \text{and} \quad U_\lambda = r\omega.$$

A second, similar differentiation yields the the acceleration,

$$\frac{d^2\mathbf{X}}{dt^2} \;=\; \left(\frac{d^2r}{dt^2} - r\omega^2\right)\mathbf{e_r} + \left(2\omega\frac{dr}{dt} + r\frac{d\omega}{dt}\right)\mathbf{e}_\lambda, \tag{35}$$

and the equation of motion sorted into radial and tangential components,

$$\frac{d^2r}{dt^2} - r\omega^2 \;=\; F_r/M, \tag{36}$$

$$2\omega\frac{dr}{dt} + r\frac{d\omega}{dt} \;=\; F_\lambda/M. \tag{37}$$

Notice that there are terms $-r\omega^2$ and $2\omega\frac{dr}{dt}$ on the left-hand side of (36) and (37) that have the form of centrifugal and Coriolis terms and are sometimes said to be such, e.g., the excellent applied mathematics text by Boas.[14] However, the angular velocity ω in these equations is that of the parcel position, not the rotation rate of the reference frame, and these terms are an essential part of the acceleration seen in the inertial reference frame. Casual labeling may be harmless in most contexts, but for the goals here it is an error: these equations have been written for an inertial reference frame where centrifugal and Coriolis forces ***do not arise***.

To see this last important point, consider uniform circular motion, $r = const$ and $\omega = d\lambda/dt = const$. The radial acceleration is then from Eqn (36), $-r\omega^2 < 0$, which is the centripetal (center-seeking) acceleration of uniform circular motion (d/dt operating twice on $\mathbf{e_r}$ times a constant r, or, Fig. 10). To say it a little more emphatically, $-r\omega^2$ is the entire acceleration observed in the case of uniform circular motion. This radial acceleration implies a centripetal radial force, $F_r \;=\; -r\omega^2 M < 0$, and the radial component balance Eqn (36) reduces to

$$\text{uniform circular motion, inertial frame}: \quad -r\omega^2 \;=\; F_r/M. \tag{38}$$

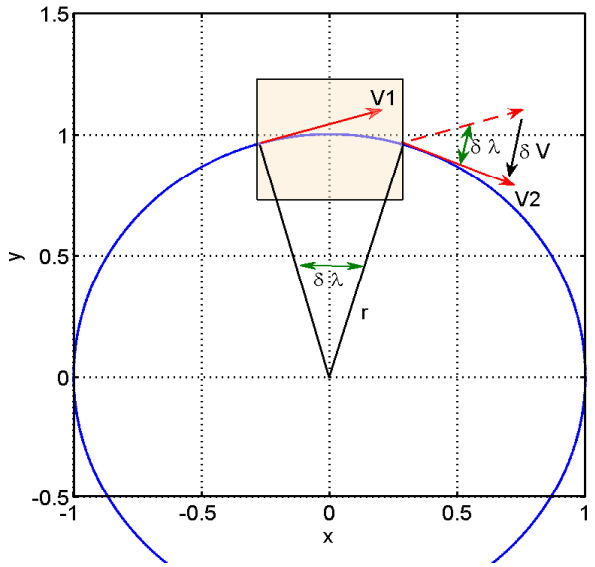

Figure 10: The velocity at two times along a circular trajectory (thin blue line) having radius r and frequency ω. The angular distance between the two times is $\delta\lambda = \delta t\omega$ and the velocity change is $\delta\mathbf{V} = \mathbf{V_2} - \mathbf{V_1}$. In the limit $\delta t \to 0$, the time rate change of velocity $\delta\mathbf{V}/\delta t$ is toward the center of curvature, i.e., a *centripetal acceleration*. If the motion is steady and circular, then $d\mathbf{V}/dt = -|\mathbf{V}|\omega\mathbf{e_r} = -r\omega^2\mathbf{e_r}$, where $\mathbf{e_r}$ is the radial unit vector. The centripetal acceleration may also be written $-(U_\lambda^2/r)\mathbf{e_r}$, where $U_\lambda = \omega r$ is the azimuthal speed. The shaded rectangle is a control volume used in a later problem to find the equivalent of centripetal acceleration in cartesian coordinates, $u\partial v/\partial x$, for the particular position shown here.

The azimuthal component Eqn. (37) vanishes term by term.

We can rewrite Eqns. (36) and (37) in a way that will help develop a physical interpretation by noting that $r\omega^2 = U_\lambda^2/r$ and that the angular momentum is $L = rU_\lambda M$ and thus

$$\boxed{\frac{d^2r}{dt^2} - \frac{U_\lambda^2}{r} = F_r/M} \tag{39}$$

and

$$\boxed{\frac{1}{M}\frac{dL}{dt} = rF_\lambda/M} \tag{40}$$

Two points: 1) The centripetal acceleration of Eqn.(39) depends quadratically upon the tangential velocity, U_λ, times the radius of curvature, $1/r$, and 2) The angular momentum of Eqn.(40) can change only if there is a torque, rF_λ, exerted upon the parcel, with the moment arm being the distance to the origin, r.

It is straightforward to find the corresponding rotating reference frame equation of motion. The origin of the rotating frame may be set at the origin of the fixed frame, and hence the radius is the same, $r' = r$. The unit vectors are identical since they are defined at the location of the parcel, $\mathbf{e}'_\mathbf{r} = \mathbf{e_r}$ and $\mathbf{e}'_\lambda = \mathbf{e}_\lambda$. The components of the force F are also identical in the two frames, $F'_r = F_r$ and $F'_\lambda = F_\lambda$. Differences arise when the angular velocity ω of the parcel is decomposed into the presumed constant angular velocity of the rotating frame, Ω, and a relative angular velocity of the parcel when viewed from the rotating frame, i.e., ω', i.e.,

$$\omega = \Omega + \omega'.$$

An observer in the rotating reference frame will see the parcel motion associated with the relative angular velocity, but not the angular velocity associated with rotation of the reference frame, Ω. Substituting this into the inertial frame equations of motion above, and rearrangement to keep the observed acceleration on the left hand side while moving terms containing Ω to the right hand side yields the rather formidable-looking rotating frame equations of motion:

$$\frac{d^2r'}{dt^2} - r'\omega'^2 \;=\; r'\Omega^2 + 2\Omega\omega' r' + F'_r/M, \tag{41}$$

$$2\omega'\frac{dr'}{dt} + r'\frac{d\omega'}{dt} \;=\; -2\Omega\frac{dr'}{dt} + F'_\lambda/M. \tag{42}$$

We can write these using the rotating frame velocity components, $U'_r = dr'/dt$ and $U'_\lambda \;=\; \omega' r'$ and angular momentum, $L' = r'U'_\lambda M$, as

$$\boxed{\frac{d^2r'}{dt^2} - \frac{U'^2_\lambda}{r} \;=\; r'\Omega^2 + 2\Omega U'_\lambda + F'_r/M} \tag{43}$$

$$\boxed{\frac{1}{rM}\frac{dL'}{dt} \;=\; -2\Omega U'_r + F'_\lambda/M} \tag{44}$$

There is a genuine centrifugal force term $\propto \Omega^2 > 0$ in the radial component (43), and there are Coriolis force terms, $\propto 2\Omega$, on the right hand sides of both (43) and (44). This makes the third time that we have derived the centrifugal and Coriolis terms — in Cartesian coordinates, Eqn. (27), in vector form, Eqn. (28), and here in polar coordinates. It is worthwhile for you to verify the steps leading to these equations, as they are perhaps the most direct derivation of the Coriolis force and most easily show how the factor of 2 arises in the Coriolis term.

Now let's use these rotating polar coordinates to analyze the simple but important example of uniform circular motion whose inertial frame description was Eqn (38). Assume that the reference frame rotation rate is ω, the angular velocity of the parcel seen in the inertial frame. Thus $d\omega'/dt = 0$, and the parcel is stationary in the rotating frame; we might call this a co-rotating frame. It follows that $d(\;)/dt = U_\lambda = U_r = 0$ and so the azimuthal component Eqn. (42) vanishes term by term. All that is left of the radial component Eqn. (43) is

$$\mathrm{co-rotating,\ non-inertial\ frame:}\quad 0 \;=\; r'\omega^2 + F'_r/M \tag{45}$$

and recall that $r' = r$. The term $r'\omega^2 > 0$ is a centrifugal (center fleeing) force that is balanced by a centripetal contact force, F'_r, which is the same contact force observed in the inertial frame, $F'_r = F_r = -r'\omega^2 M$, consistent with Eqn. (45). Thus Eqns. (38) and (45) comprise another example of switching sides: an acceleration seen in an inertial frame — in this case a centripetal acceleration on the

left side of Eqn. (38) — is transformed into an inertial force — a centrifugal force on the right side of (45) — when the same parcel is observed from a non-inertial, co-rotating reference frame.

Before moving on to an application below, it may be prudent to note that a rotating frame description is not always so adept as it may appear above. For example, assume that the parcel is at rest in the inertial frame, and that the horizontal component of the contact force vanishes. The inertial frame equation of motion in polar coordinates Eqns. (36) and (37) vanishes term by term; clearly, nothing is happening in an inertial frame. Now suppose that the same parcel is viewed from a steadily rotating reference frame, say rotating at a rate Ω, and at a distance r' from the origin. Viewed from this frame, the parcel will appear to be moving in a circle of radius $r' = constant$ and in a direction opposite the rotation of the reference frame. The parcel's rotation rate is $\omega' = -\Omega$, just as in Figure (7). With these conditions the tangential component equation of motion vanishes term by term ($\mathbf{F} = 0$), but three of the radial component terms are nonzero,

$$-r'\omega'^2 \;=\; r'\Omega^2 + 2\Omega\omega' r', \tag{46}$$

and indicate an interesting balance between the centripetal acceleration, $-r'\omega'^2$ (the observed acceleration is listed on the left hand side), and the sum of the centrifugal and Coriolis inertial forces (the right hand side, divided by M, and note that $\omega' = -\Omega$). Interesting perhaps, but also a bit alarming; a parcel that is at rest and doing nothing in an inertial frame has acquired a rather complex momentum balance when observed from a rotating reference frame. It is tempting to deem the Coriolis and centrifugal terms that arise in this example to be 'virtual', or 'fictitious, correction' forces to acknowledge this discomfort.[6] But labeling terms this way wouldn't add anything useful, and it might obscure the fundamental issue — accelerations and inertial forces are relative to a reference frame. This applies just as well to centrifugal and Coriolis forces as it does to gravitational mass attraction.

3.2 To get a feel for the Coriolis force

A centrifugal force is often encountered in daily life. For example, a runner having a speed $V = 5$ m s^{-1} and making a moderately sharp turn, radius $R = 15$ m, will easily feel the centrifugal force, $(V^2/R)M \approx 0.15gM$ or 15% of her weight. It is unlikely that a runner would think of this centrifugal force as virtual or fictitious.

The Coriolis force associated with Earth's rotation is by comparison very, very small, only about $2\Omega VM \approx 10^{-4}gM$ for the same runner, and not noticeable. To experience the Coriolis force in the same direct way that we can experience (feel) the centrifugal force, requires a platform having a rotation rate that exceeds Earth's rotation rate by a factor of about 10^4. A typical merry-go-round has a rotation rate $\Omega = 2\pi/12$ rad s^{-1} = 0.5 rad s^{-1} that is ideal.

In what follows, the heretofore nondescript 'parcel' is presumed to be a sentient being i.e., a rider (is that you?). Motion is observed by a separate observer who can be either external to the

merry-go-round, and thus is an inertial reference frame, or riding on the merry-go-round, and thus in a non-inertial reference frame. To calculate the forces on this rider, assume a mass, $M = 75$ kg, the standard airline passenger before the era of super-sized meals and passengers.

3.2.1 At rest in the rotating frame

To start, let's presume that we are standing quietly at the radius $r = 6$ m of a merry-go-round that it is rotating at a steady rate, $\Omega = 0.5$ rad s^{-1}. How does the description of our motion depend upon the reference frame, and what are the forces involved?

Viewed from an inertial frame outside of the merry-go-round, the radial component balance Eqn. (37) is, with $\omega = \Omega$ and $dr/dt = d\omega/dt = F_\theta = 0$

$$-r\Omega^2 M \;=\; F_r, \tag{47}$$

in which a centripetal acceleration ($\times M$) is balanced by an inward-directed contact force, $F_r = -r\Omega^2 M = -112$ N, equivalent to the weight of a mass $F_r/g = 11.5$ kg (equivalent to about 28 lbs) and which is quite noticeable. This contact force is exerted by the merry-go-round on us, say through a hand rail.

Viewed from a rotating, non-inertial reference frame, i.e., from the merry-go-round, there is no acceleration, and the radial force balance is Eqn. (45) with $r' = r$,

$$0 \;=\; r'\Omega^2 M + F_r'. \tag{48}$$

The physical conditions are unchanged and thus the contact force exerted by the merry-go-round is exactly as before, $F_r' = F_r = -112$ N. As noted by examples in Sec. 3.1, the acceleration seen in the inertial frame Eqn. (47) has become an inertial force, $r'\Omega^2 M$, a centrifugal force, in the rotating frame, Eqn. (48). Within the rotating frame, the centrifugal force is quite vivid; it appears that we are being pushed outwards, or centrifugally, by a force that is distributed throughout our body. To maintain a fixed position, this centrifugal force must be opposed by a centripetal contact force, F_r', exerted by the hand rail.

3.2.2 A cautious walk in the rotating frame

Most merry-go-rounds have signs posted that caution riders to remain in their seats after the ride begins. This is a good and prudent rule, of course. But if the goal is to get a feel for the Coriolis force, then we may decide to go for a very cautious walk on the merry-go-round.

Azimuthal relative velocity. Let's assume that we begin to walk azimuthally, so that $r = 6$ m and constant. A reasonable walking pace under the circumstance is about $U_w = 1.5$ m s^{-1}, which

corresponds to a relative rotation rate $\omega' = 0.25$ rad s^{-1}, and recall that $\Omega = 0.5$ rad s^{-1}. If the direction is in the direction of the merry-go-round rotation, then $\omega = \Omega + \omega' = 0.75$ rad s^{-1}. From the inertial frame, Eqn. (37), the centripetal force required to maintain $r = constant$ when moving at this greater angular velocity is

$$F_r \;=\; -r\omega^2 M \;=\; -r(\Omega+\omega')^2 M \;=\; -253 \text{ N},$$

which is roughly twice the centripetal force experienced when stationary. If we then reverse direction and walk at the same speed against the direction of rotation of the merry-go-round, $\omega' = -0.25$ rad s^{-1}, then F_r is reduced to about -28 N. This pronounced variation of F_r with ω_w is a straightforward consequence of the quadratic dependence of centripetal acceleration upon azimuthal velocity.

When our motion is viewed and analyzed from within the rotating frame of the merry-go-round, we distinguish between the rotation rate of the merry-go-round, Ω, and the relative rotation rate, ω', due to the presumed relative motion. The radial component of the rotating frame equation of motion (41) reduces to

$$-r'\omega' M \;=\; r'\Omega^2 M + 2\Omega\omega' r' M + F_r'. \tag{49}$$

The term on the left is a centripetal force, the first term on the right is the centrifugal force due to the merry-go-round's rotation, and the second term on the right, $2\Omega\omega' M$, is a Coriolis force. For these conditions, the Coriolis force is substantial, $2r'\Omega\omega' M \pm 112$ N, with the sign determined by the direction of motion relative to Ω. If $\Omega > 0$ and $\omega' > 0$, i.e., walking in the anti-clockwise direction of the merry-go-round rotation, then the radial Coriolis force is positive and to the right of the relative velocity.

Radial relative velocity. Now consider going for a very cautious walk in the radial direction so that $\omega' = 0$ and the rotation rate remains constant at $\Omega = 0.5$ rad sec^{-1}. Presume a modest radial speed $dr'/dt = 1$ m s^{-1} and positive. In practice, even this slow pace is difficult to maintain for more than a few steps, but that will suffice.

Viewed from an inertial frame, the azimuthal component of the equation of motion, Eqn. (37), reduces to

$$2\Omega\frac{dr}{dt}M \;=\; F_\lambda, \tag{50}$$

where $F_\lambda \approx 75$ N (or about 16 pounds) for the given data. The sense of F_λ is positive, or anti-clockwise. The left hand side of (50) has the form of a Coriolis force, but don't jump to that conclusion; this is an inertial frame description, so there is no Coriolis force. The inertial frame description may be cast as a balance of angular momentum, $L = r^2\Omega M$ and hence $L \propto r^2$ since Ω and M are constant in this case. When $dr/dt > 0$ the angular momentum is necessarily increasing and must be provided by a positive torque, i.e., $rF_\lambda > 0$. If instead the radial motion was inward, so that $dr/dt < 0$, then the angular momentum would be decreasing, and F_λ would be negative. Be sure that the sense (the direction) of F_λ is clear before going on to consider this motion from the rotating frame.

From within the rotating frame, and given that the motion is constrained to be radial only, the azimuthal component of the equation of motion reduces to a force balance,

$$0 = -2\Omega\frac{dr'}{dt}M + F'_\lambda, \tag{51}$$

where $-2\Omega\frac{dr'}{dt}M$ is now a Coriolis force and $F'_\lambda = F_\lambda$ is the same contact force as before. For example, if the radial motion is outward, $\frac{dr'}{dt} \geq 0$, then the azimuthal Coriolis force is clockwise, $-2\Omega\frac{dr'}{dt}M \leq 0$, which is to the right of and normal to the radial velocity. If the radial motion is inward, then the Coriolis force is reversed, and again is to the right of the radial motion.

Be careful! If you have the opportunity to do this experiment you will learn with the first few steps whether the Coriolis force is better described as a real force, or as a fictitious correction force. Be sure to ask permission of the merry-go-round operator before you start walking around, and exercise genuine caution. The Coriolis force is an inertial force and so is distributed throughout your body, unlike the contact force which acts only where you are in contact with the merry-go-round, i.e., through a secure grip on a hand rail. The radial Coriolis force associated with azimuthal motion feels much like an increase or slackening of the centrifugal force, and is not especially difficult to compensate. Be warned, though, that the azimuthal Coriolis force associated with radial motion is startling, even presuming that you are the complete master of this analysis. (If you do not have access to a merry-go-round or if you judge that this experiment is unwise, then see Stommel and Moore[10] for alternate ways to accomplish some of the same things.)

3.3 An elementary projectile problem

A very simple projectile problem analyzed from inertial and rotating reference frames can reveal some other aspects of rotating frame dynamics. Assume that a projectile is launched with velocity $(U_0, V_0, W_0) = (0, 1, 1)$ and from the origin $(x, y) = (0, 0)$. The only force presumed to act on the projectile after launch is the downward force of gravity, $-gM\mathbf{e_3}$, which is the same in either reference frame.

From the inertial frame. The equations of motion and initial conditions in Cartesian components are linear and uncoupled;

$$\frac{d^2x}{dt^2} = 0; \quad x(0) = 0, \quad \frac{dx}{dt} = 0, \tag{52}$$

$$\frac{d^2y}{dt^2} = 0; \quad y(0) = 0, \quad \frac{dy}{dt} = V_0,$$

$$\frac{d^2z}{dt^2} = -g; \quad z(0) = 0, \quad \frac{dz}{dt} = W_0,$$

where M has been divided out. These are readily integrated to yield the solution for the time interval when the parcel is in flight;

$$\begin{aligned} 0 &< t < \frac{2W_0}{g}, \\ x(t) &= 0, \\ y(t) &= y_0 + tV_0, \\ z(t) &= t(W_0 - \frac{1}{2}gt). \end{aligned} \tag{53}$$

The horizontal displacement (x, y) is sketched as the blue curve of Fig. (11), a linear displacement toward positive y until to $t = 2\pi$ when the parcel returns to the ground. The vertical displacement (not shown) is a simple up and down, with constant downward acceleration.

From the rotating frame. How would this same motion look when viewed from a rotating reference frame? Set the origin of the rotating frame coincident with the origin of the inertial frame and assume that the rotation is about the $\mathbf{e_3}$ (vertical, or z) axis at a constant Ω. The equations of motion, with $\mathbf{F} = 0$, are (Eqn. (28),

$$\begin{aligned} \frac{d^2x'}{dt^2} &= -2\Omega v' + x'\Omega^2; \quad x'(0) = 0, \quad \frac{dx'}{dt} = 0, \\ \frac{d^2y'}{dt^2} &= 2\Omega u' + y'\Omega^2; \quad y'(0) = 0, \quad \frac{dy'}{dt} = V_0, \\ \frac{d^2z'}{dt^2} &= -g; \quad z'(0) = 0, \quad \frac{dz'}{dt} = W_0. \end{aligned} \tag{54}$$

The z component equation is unchanged since the rotation axis was aligned with z. This is quite general; motion that is parallel to the rotation vector $\mathbf{\Omega}$ is unchanged by rotation.

The horizontal components of the rotating frame equations (54) include Coriolis and centrifugal force terms that are coupled but linear, and so we can integrate this system almost as easily as the inertial frame counterpart,

$$\begin{aligned} 0 &< t < \frac{2W_0}{g}, \\ x'(t) &= -tV_0 \sin(-\Omega t), \\ y'(t) &= tV_0 \cos(-\Omega t), \\ z'(t) &= t(W_0 - \frac{1}{2}gt) \end{aligned} \tag{55}$$

and find the black trajectory of Fig. (11). The rotating frame trajectory rotates clockwise, or opposite the reference frame rotation, and makes a complete rotation in time = $2\pi/\Omega$. When it intersects the inertial frame trajectory we are reminded that the distance from the origin (radius) is not changed by

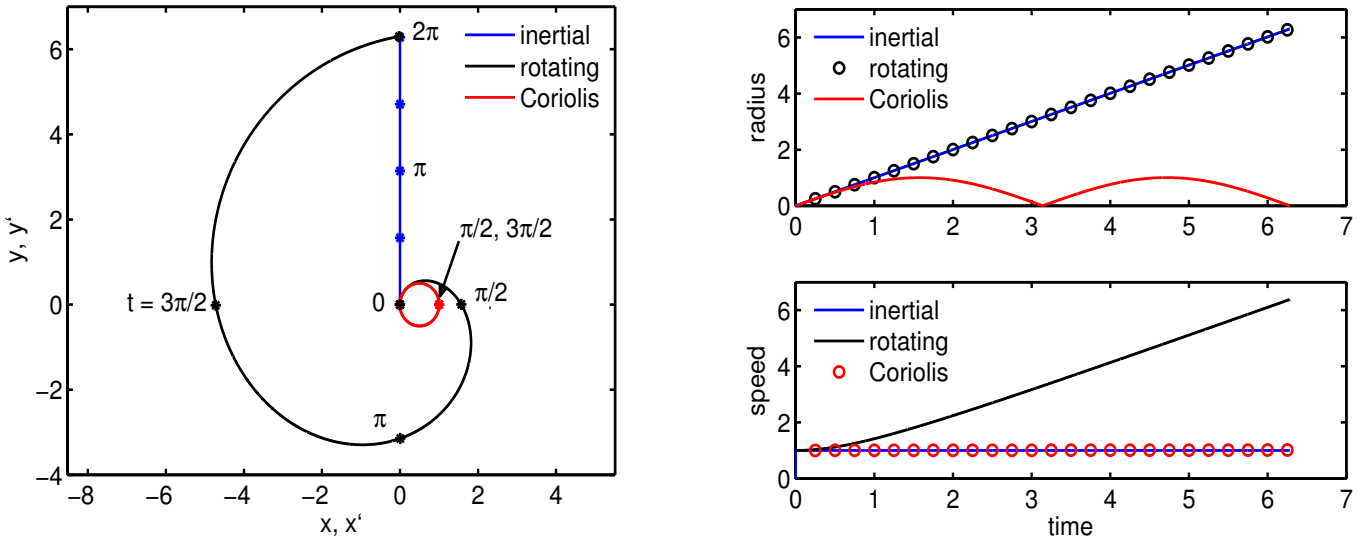

Figure 11: **(left)** The horizontal trace of a parcel launched from $(0,0)$ in the positive y-direction as seen from an inertial reference frame (blue line) and as seen from a rotating frame (black line). The elapsed time is marked at intervals of $\pi/2$. The rotating frame was turning anti-clockwise with respect to the inertial frame, and hence the black trajectory turns clockwise with time at the same rate, though in the opposite direction. For comparison, the red trajectory was computed with the Coriolis force only (no centrifugal force; the motivation for this will come in Sec. 4). This an inertial motion that makes two complete clockwise orbits in time = 2π, twice the rate of the reference frame rotation. Videos from comparable laboratory experiments may be viewed at https://spinlab.ess.ucla.edu/ **(right) (upper)** The radius (distance from origin) and **(lower)** speed for the three trajectories. Notice that 1) the inertial and rotating trajectories have equal radius, while the radius of the Coriolis trajectory is much less, and 2) the inertial and Coriolis trajectories show the same, constant speed, while the rotating trajectory has a greater and increasing speed on account of the centrifugal force.

rotation, $r' = r$, since the coordinate systems have coincident origins. We know the inertial frame radius, $r = tV_0$, and hence we also know

$$r' = tV_0. \tag{56}$$

The angular position of the parcel in the inertial frame is $\lambda = \pi/2$ and constant, since the motion is purely radial. The relative rotation rate of the parcel seen from the rotating frame is $\omega' = -\Omega$, and thus

$$\lambda' = \pi/2 - \Omega t, \tag{57}$$

which, together with Eqn. (56), gives the polar coordinates of the parcel position. Both the radius and the angle increase linearly in time, and the rotating frame trajectory is Archimedes spiral.

When viewed from the rotating frame, the projectile is observed to be deflected to the right which we can attribute to the Coriolis force. Notice that the horizontal speed and thus the kinetic energy

increase with time (Fig. 11, right). This cannot be attributed to the Coriolis force, which is always perpendicular to the velocity and so can do no work. The rate of increase of rotating frame kinetic energy (per unit mass) is

$$\begin{aligned} \frac{d\mathbf{V'^2}/2}{dt} &= \frac{d(V_0^2 + r'^2\Omega^2)/2}{dt} \\ &= \frac{dr'}{dt} r'\Omega^2 \end{aligned} \tag{58}$$

which may be interpreted as the work done by the centrifugal force, $r'\Omega^2$, on the radial velocity, dr'/dt. In fact, if the projectile had not returned to the ground, its speed (observed from the rotating reference frame) would have increased without limit so long as the radius increased. It was noted earlier that a rotating, non-inertial reference frame does not, in general, conserve global momentum, and now it is apparent that energy is also not conserved. Nevertheless, we can provide a complete and internally consistent accounting of the energy changes seen in a rotating frame, as in Eqn. (58).

3.4 Appendix to Section 3; Spherical Coordinates

Spherical coordinates can be very useful when motion is more or less confined to the surface of a sphere, e.g., the Earth, approximately. We will have occasion to use spherical coordinates later on, and so will go ahead and write them down here while polar coordinates are still fresh and pleasing(?). The method for finding the equation of motion in spherical coordinates is exactly as above, though with the need for an additional angle. There are many varieties of spherical coordinates; we will use 'geographic' spherical coordinates in which the longitude (also called azimuth) is measured by λ, where $0 \leq \lambda \leq 2\pi$, increasing anti-clockwise (Figure 12), the latitude (also called elevation) is measured by ϕ, where $-\pi/2 \leq \phi \leq \pi/2$, increasing anti-clockwise and with a zero at the equator and distance from the origin by r. The conversion from spherical to cartesian coordinates is:

$$x = r\cos^2\phi, \quad y = r\cos\phi\sin\lambda, \quad z = r\sin\phi,$$

and the reverse,

$$\lambda = \tan^{-1}(y/x), \quad \phi = \sin^{-1}(z/\sqrt{x^2+y^2+z^2}), \quad r = \sqrt{x^2+y^2+z^2}.$$

The spherical system unit vectors (Fig. 13) written in Cartesian coordinates are:

$$\mathbf{e}_\lambda = -\sin\lambda\mathbf{e_1} + \cos\lambda\mathbf{e_2}, \tag{59}$$

$$\mathbf{e}_\phi = -\cos\lambda\sin\phi\mathbf{e_1} - \sin\lambda\sin\phi\mathbf{e_2} + \cos\phi\mathbf{e_3}, \tag{60}$$

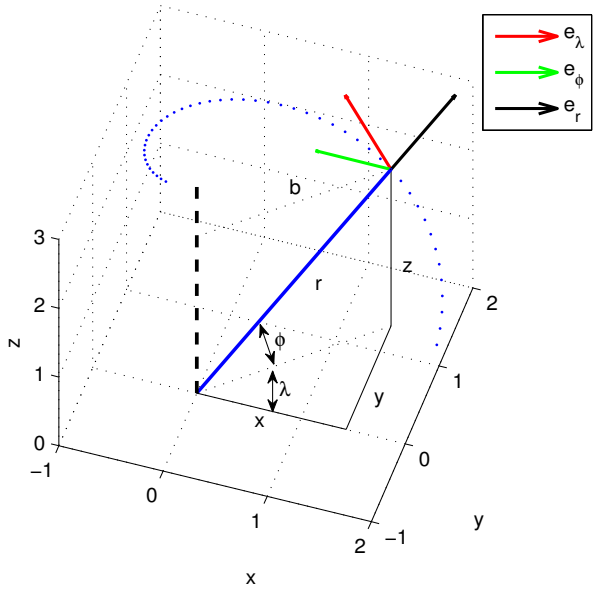

Figure 12: A three-dimensional trajectory (blue dots) with, for one point only, the radius (blue line) and the spherical unit vectors (red, green and black). The spherical system coordinates are: (1) the longitude, λ, the angle between the projection of the radius onto the (x,y) plane and the x axis; (2) the latitude, ϕ, the angle between the radius and the (x,y) plane, and (3) the radius magnitude, r. The black dashed center line will be the axis of rotation (pole) when reference frame rotation is considered. The perpendicular distance from the pole to a given point, labeled b, is then very important. The (x,y,z) components of this point are also shown.

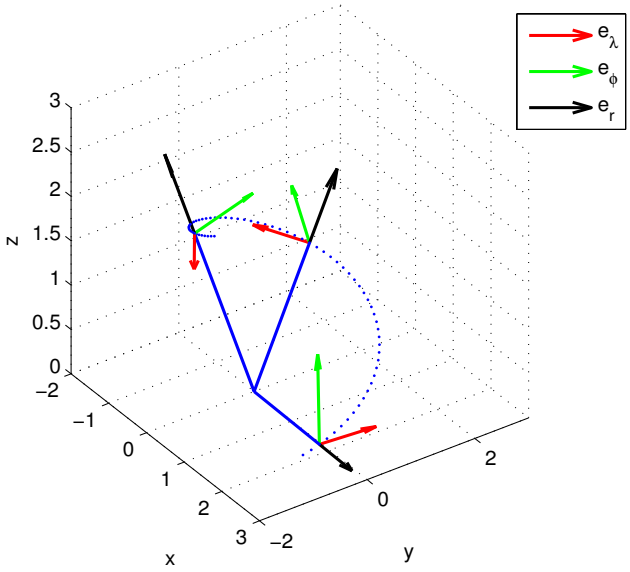

Figure 13: A three-dimensional trajectory (blue dots) that begins at lower center and then turns counterclockwise as it moves toward positive z. Radials from the origin $(0,0,0)$ are the blue lines shown at three points along the trajectory. The spherical system unit vectors are in red, green and black at the same points. Notice that these change direction along the trajectory and that the black vector, $\mathbf{e_r}$, remains aligned with the radial.

$$\mathbf{e_r} = \cos\lambda\cos\phi\,\mathbf{e_1} + \sin\lambda\cos\phi\,\mathbf{e_2} + \sin\phi\,\mathbf{e_3}. \tag{61}$$

Notice that when $\phi = 0$ these reduce to the polar coordinate system.

The position and velocity vectors are

$$\mathbf{X} = r\mathbf{e_r}, \tag{62}$$

and

$$\frac{d\mathbf{X}}{dt} = \frac{dr}{dt}\mathbf{e_r} + r\frac{d\phi}{dt}\mathbf{e}_\phi + r\cos\phi\frac{d\lambda}{dt}\mathbf{e}_\lambda, \tag{63}$$

where the velocity components are

$$U_\lambda = r\cos\phi\frac{d\lambda}{dt}, \quad U_\phi = r\frac{d\phi}{dt}, \quad \text{and} \quad U_r = \frac{dr}{dt}.$$

These bear obvious similarity to the now familiar polar velocity, though with the moment arm $r\cos\phi = b$ in the longitudinal component in place of r only. Continuing on to find the acceleration and then the equation of motion in λ, ϕ and r components:

$$(2\frac{dr}{dt}\frac{d\lambda}{dt}\cos\phi \;-\; 2r\frac{d\phi}{dt}\frac{d\lambda}{dt}\sin\phi \;+\; r\cos\phi\frac{d^2\lambda}{dt^2})M \;=\; F_\lambda, \tag{64}$$

$$(2\frac{dr}{dt}\frac{d\phi}{dt} + \; r\frac{d^2\phi}{dt^2} \;+\; r\cos\phi(\frac{d\lambda}{dt})^2\sin\phi)M \;=\; F_\phi, \tag{65}$$

$$(\frac{d^2r}{dt^2} \;-\; r\cos\phi(\frac{d\lambda}{dt})^2\cos\phi \;-\; r(\frac{d\phi}{dt})^2)M \;=\; F_r. \tag{66}$$

These may be rewritten in a more compact and revealing form be defining angular momentum for the λ and ϕ coordinates:

$$L_\lambda = (r\cos\phi)^2\frac{d\lambda}{dt}M, \;\text{ and }\; L_\phi = r^2\frac{d\phi}{dt}M,$$

and centripetal accelerations ($\times M$) for the λ and ϕ components:

$$C_\lambda \;=\; -r\cos\phi(\frac{d\lambda}{dt})^2M \;\text{ and }\; C_\phi \;=\; -r(\frac{d\phi}{dt})^2M.$$

In these variables the equations of motion are:

$$\frac{1}{r\cos\phi}\frac{dL_\lambda}{dt} \;=\; F_\lambda, \tag{67}$$

$$\frac{1}{r}\frac{dL_\phi}{dt} \;-\; C_\lambda\sin\phi \;=\; F_\phi, \tag{68}$$

$$\frac{d^2r}{dt^2}M \;+\; C_\lambda \cos\phi + C_\phi \;=\; F_r. \tag{69}$$

The rotating frame equations follow from the substitution

$$\frac{d\lambda}{dt} = \Omega + \frac{d\lambda'}{dt},$$

and rearranging the way we did for the polar coordinates:

$$(2\frac{dr'}{dt}\frac{d\lambda'}{dt}\cos\phi' \;+\; r\cos\phi'\,\frac{d^2\lambda'}{dt^2} \;-\; 2r'\frac{d\phi'}{dt}\frac{d\lambda'}{dt}\sin\phi')M \;=\; -2\Omega\frac{dr'}{dt}\cos\phi' \;+\; 2\Omega r'\frac{d\phi'}{dt}\sin\phi' \;+\; F'_\lambda, \tag{70}$$

$$(2\frac{dr'}{dt}\frac{d\phi'}{dt} \;+\; r'\cos\phi'\,(\frac{d\lambda'}{dt})^2\sin\phi' \;+\; r'\frac{d^2\phi'}{dt^2})M \;=\; \;-\; r'\cos\phi'\Omega^2\sin\phi' \;-\; 2\Omega\, r\cos\phi'\,\frac{d\lambda'}{dt}\sin\phi' \;+\; F'_\phi, \tag{71}$$

$$(\frac{d^2r'}{dt^2} \;-\; r'\cos\phi'\,(\frac{d\lambda'}{dt})^2\cos\phi' \;-\; r'(\frac{d\phi'}{dt})^2)M \;=\; r'\cos\phi'\,\Omega^2\cos\phi' \;+\; 2\Omega r'\cos\phi'\frac{d\lambda'}{dt}\cos\phi' \;+\; F'_r. \tag{72}$$

We can tidy these up a little by rewriting in terms of $L'_\lambda = (r'\cos\phi')^2\frac{d\lambda'}{dt}M$, etc.,

$$\frac{1}{r'\cos\phi'}\frac{dL'_\lambda}{dt} \;=\; -2\Omega U'_r\cos\phi M \;+\; 2\Omega\sin\phi U'_\phi M + F'_\lambda, \tag{73}$$

$$\frac{1}{r'}\frac{dL'_\phi}{dt} \;-\; C'_\lambda\sin\phi \;=\; -r'\cos\phi'\sin\phi'\Omega^2 M - 2\Omega\sin\phi' U_\lambda M \;+\; F'_\phi, \tag{74}$$

$$\frac{d^2r'}{dt^2}M \;+\; C_\lambda\cos\phi \;+\; C_\phi \;=\; r'\cos^2\phi\Omega^2 M \;+\; 2\Omega\cos\phi U_\lambda M \;+\; F'_r. \tag{75}$$

3.5 Problems

(1) Given that we know the inertial frame trajectory, Eqns. (53), show that the rotating frame trajectory may be computed by applying a time-dependent rotation operation via Eqn. (12), $\mathbb{X}' = \mathbb{R}\mathbb{X}$ and with $\theta = \Omega t$, with the result Eqns. (55). So for this case — a two-dimensional planar domain and rotation vector normal to the plane, we can either integrate the rotating frame equations of motion, or, rotate the inertial frame solution. This will not be the case when we finally get to an Earth-attached, rotating frame.

(2) In the example of Sec. 3.2, walking on a merry-go-round, it was suggested that you would be able to feel the Coriolis force directly. Imagine that you are riding along on the projectile of Sec 3.3 (don't try this one at home) — would you be able to feel the Coriolis force?

(3) The centrifugal force produces a radial acceleration on every object on the merry-go-round and thus contributes to the direction and magnitude of the time-independent acceleration field observed in a rotating frame, an important point returned to in Section 4.1. For example, show that a plumb line makes an angle to the vertical of $\arctan(r'\Omega^2/g)$, where the vertical direction and g are in the absence of rotation.

(4) Your human pinball experiments on the merry-go-round (Sec. 3.2) were illuminating, and something you were eager to share with your father, Gustav-Gaspard, and younger brother, Gustav-Gaspard Jr. Your father is old school — he doesn't believe in ghosts or magic or virtual forces — and engaged in a heated debate with GG Jr. regards just what happened on the merry-go-round: was it a Coriolis force that pushed every moving object sideways — this is GG Jr.'s assertion — or was it simply a torque required to change angular momentum, as your father insists?

(5) The spherical system equations (64) - (66) are fairly forbidding upon a first or second encounter and you certainly can not expect to spot errors without considerable experience (and in fact, errors (probably typographical) are common in the literature). How can we check that the equations listed here are correct? One straightforward if slightly tedious way to check the equations is to define a 3-dimensional trajectory in the spherical system, $\mathbf{X}(\lambda,\phi,r)$, convert to the familiar $\mathbf{X}(x,y,z)$ coordinates, and compute the velocity, acceleration, Coriolis force, etc. in the cartesian coordinates. Then compute the same quantities using the spherical system, and compare the results directly. The script sphere_check.m (Sec. 6.3) does just this. You can use that script to define a new trajectory (your choice), and check the results for yourself.

4 A reference frame attached to the rotating Earth

4.1 Cancellation of the centrifugal force by Earth's (slightly chubby) figure

If Earth was a perfect, homogeneous sphere (it is not), the gravitational mass attraction at the surface, $\mathbf{g}*$, would be directed towards the center (Fig. 14). Because the Earth is rotating, every parcel on the surface is also subject to a centrifugal force

$$\boldsymbol{C} \;=\; -\boldsymbol{\Omega}\times\boldsymbol{\Omega}\times\mathbf{X} \tag{76}$$

of magnitude $\Omega^2 R_E\cos\phi$, where R_E is Earth's nominal radius, and ϕ is the latitude. The vector $\boldsymbol{C}$ is perpendicular to the Earth's rotation axis, and is directed away from the axis. This centrifugal force has a component parallel to the surface, a shear force, Eqn. (71),

$$C_\phi = \Omega^2 R_E\cos\phi\sin\phi, \tag{77}$$

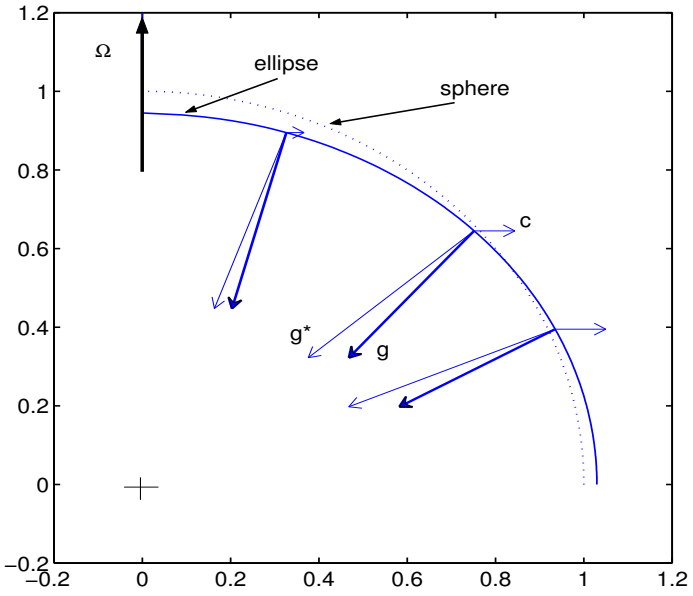

Figure 14: Cross-section through a hemisphere of a gravitating and rotating planet. The gravitational acceleration due to mass attraction is shown as the vector $\mathbf{g}*$ that points to the center of a spherical, homogeneous planet. The centrifugal acceleration, $\mathbf{C}$, associated with the planet's rotation is directed normal to and away from the rotation axis, and is to scale for the planet Saturn. The combined gravitational and centrifugal acceleration is shown as the heavier vector, $\mathbf{g}$. This vector is in the direction of a plumb line, and defines vertical. A surface that is normal to $\mathbf{g}$ similarly defines a level surface, and has the approximate shape of an oblate spheroid (the solid curve). The ellipse of this diagram has a flatness $F = 0.1$ that approximates Saturn; for Earth, $F = 0.0033$.

that is directed towards the equator (except at the equator where the 3-d vector centrifugal force is vertical).[22] C_ϕ is very small compared to $g*$, $C_\phi/g* \approx 0.002$ at most, but it has been present since the Earth's formation. A fluid can not sustain a shear without deforming, and over geological time this holds as well for the Earth's interior and crust. Thus it is highly plausible that the Earth long ago settled into a rotational-gravitational equilibrium configuration in which this C_ϕ is exactly balanced by a component of the gravitational (mass) attraction that is parallel to the displaced surface and poleward, i.e., centripetal.

To make what turns out to be a pretty rough estimate of the displaced surface, η_Ω, assume that the gravitational mass attraction remains that of a sphere and that the meridional slope $(1/R_E)\partial\eta_\Omega/\partial\phi$ times the gravitational mass attraction is in balance with the tangential component of the centrifugal force (Eqn. 71),

$$\frac{g*}{R_E}\frac{\partial\eta}{\partial\phi} = \Omega^2 R_E \cos\phi \sin\phi\,. \tag{78}$$

[22] Ancient critics of the rotating Earth hypothesis argued that loose objects on a spinning sphere should fly off into space, which clearly does not happen. Even so, given the persistent centrifugal force due to Earth's rotation it is plausible that we might drift towards the equator. Alfred Wegner proposed just this as the engine of Earth's moving continents, which may have helped delay the acceptance of his otherwise remarkable inference that continents move (see D. McKenzie, 'Seafloor magnetism and drifting continents', in *A Century of Nature*, 131-137. Ed. by L. Garwin and T. Lincoln, The Univ. of Chicago Press, Chicago, Il, 2003.).

This may then be integrated with latitude to yield the equilibrium displacement,

$$\begin{aligned} \eta_\Omega(\phi) &= \int_0^\phi \frac{\Omega^2 R_E^2}{g*} \cos\phi \sin\phi \, d\phi \\ &= \frac{\Omega^2 R_E^2}{2g*} \sin\phi^2 \; + \; constant. \end{aligned} \tag{79}$$

When this displacement is added onto a sphere the result is an oblate (flattened) spheroid, Fig. (14), which is consistent qualitatively (but not quantitatively) with the observed shape of the Earth.[23] A convenient measure of flattening is $J = (R_{eqt} - R_{pol})/R_{eqt}$, where the subscripts refer to the equatorial and polar radius. Earth's flatness is $J = 0.0033$, which seems quite small, but is nevertheless highly significant in ways beyond that considered here.[24,25]

Closely related is the notion of 'vertical'. A direct measurement of vertical can be made by means of a plumb line; the plumb line of a plumb bob that is at rest is parallel to the local gravity and defines the direction vertical. Following the discussion above we know that the time-independent, acceleration field of the Earth is made up of two contributions, the first and by far the largest being mass attraction, $\mathbf{g}*$, and the second being the centrifugal acceleration, $\mathbf{C}$, associated with the Earth's rotation, Fig. (14). Just as on the merry-go-round, this centrifugal acceleration adds with the gravitational mass attraction to give the net acceleration, called 'gravity', $\mathbf{g} = \mathbf{g}* + \mathbf{C}$, a time-independent vector (field) whose direction is observable with a stationary plumb line and whose magnitude may be inferred by observing the period of small amplitude oscillations when the plumb bob is displaced and released, i.e., a pendulum. A surface that is normal to the gravitational acceleration vector is said to be a level surface in as much as the acceleration component parallel to that surface is zero. A resting fluid can sustain a

[23]The idea behind Eqn. (79) is a good start, but doesn't go far enough. The pole-to-equator rise given by Eqn. (79) is about 11 km whereas precise observations show that Earth's equatorial radius, $R_{eqt} = 6378.2$, is greater than the polar radius, $R_{pol} = 6356.7$ km, by about 21.5 km. The calculation (79) is a first approximation insofar as it ignores the gravitational mass attraction of the equatorial bulge, which is toward the equator and thus also has a centrifugal component. Thus still more mass must be displaced equatorward in order to increase η_Ω enough to reach a rotational-gravitational equilibrium. The net result is roughly a factor of two greater amplitude than Eqn. (79) indicates.

A comprehensive source for physical data on the planets is C. F. Yoder, 'Astrometric and geodetic data on Earth and the solar system,' Ch. 1, pp 1–32, of *A Handbook of Physical Constants: Global Earth Physics (Vol. 1)*. American Geophysical Union (1995).

[24]To note just two: 1) Earth's ellipsoidal shape must be accounted for in highly precise, long range navigation systems (GPS), while shorter range or less precise systems can approximate the Earth as spherical. 2) Because the Earth is not perfectly spherical, the gravitational tug of the Sun, Moon and planets can exert a torque on the Earth and thereby perturb Earth's rotation vector. The resulting, slow variations lead to dramatic changes in Earth's climate.[19]

[25]The flatness of a rotating planet is given roughly by $J \approx \Omega^2 R/g$. If the gravitational acceleration at the surface, g, is written in terms of the planet's mean radius, R, and density, ρ, then $J = \Omega^2/(\frac{4}{3}\pi G\rho)$, where $G = 6.67\times10^{-11}$ m^3 kg^{-1} s^{-2} is the universal gravitational constant. The rotation rate and the density vary a good deal among the planets, and consequently so does J. The gas giant, Saturn, has a rotation rate a little more than twice that of Earth and a very low mean density, about one eighth of Earth's. The result is that Saturn's flatness is large enough, $J \approx 0.10$, that it can be discerned through a good backyard telescope or in a figure drawn to scale, Fig. (14).

normal stress, i.e., pressure, but not a shear stress. Thus a level surface can also be defined by observing the free surface of a water body that is at rest in the rotating frame.[26] In sum, the measurements of vertical and level that we can readily make necessarily lump together gravitational mass attraction with the centrifugal force due to Earth's rotation.

4.2 The equation of motion for an Earth-attached reference frame

Now we are going to apply the inference made above, that there exists a tangential component of gravitational mass attraction that exactly balances the centrifugal force due to Earth's rotation and that we define vertical in terms of the measurements that we can readily make; thus

$$\mathbf{g} = \mathbf{g}* + \mathbf{\Omega}\times\mathbf{\Omega}\times\mathbf{X}. \tag{80}$$

The equations of motion for a rotating/gravitating planet are then,

$$\boxed{\frac{d\mathbf{V}'}{dt} = -2\mathbf{\Omega}\times\mathbf{V}' + \mathbf{F}'/M + \mathbf{g}} \tag{81}$$

which is Eqn. (2), at last! The happy result is that the rotating frame equation of motion applied in an Earth-attached reference frame does not include the centrifugal force associated with Earth's rotation (and neither do we tend to roll towards the equator).

Vector notation is handy for many derivations and for visualization, but when it comes time to do a calculation we will need the component-wise equations, usually Earth-attached, rectangular coordinates. The east unit vector is $\mathbf{e_x}$, north is $\mathbf{e_y}$, and the horizontal is defined by a tangent plane to Earth's surface. The vertical direction, $\mathbf{e_z}$, is thus radial with respect to the (approximately) spherical Earth. The rotation vector $\mathbf{\Omega}$ makes an angle ϕ with respect to the local horizontal x', y' plane, where ϕ is the latitude of the coordinate system and thus

$$\mathbf{\Omega} = \Omega\cos\phi\,\mathbf{e_y} + \Omega\sin\phi\,\mathbf{e_z}.$$

If $\mathbf{V}' = u'\mathbf{e_x} + v'\mathbf{e_y} + w'\mathbf{e_z}$, then the full, three-dimensional Coriolis force is

$$-2\mathbf{\Omega}\times\mathbf{V}' = -(2\Omega\cos\phi\,w' - 2\Omega\sin\phi\,v')\mathbf{e_x} - 2\Omega\sin\phi\,u'\mathbf{e_y} + 2\Omega\cos\phi\,u'\mathbf{e_z}. \tag{82}$$

4.3 Coriolis force on motions in a thin, spherical shell

Application to geophysical flows is made somewhat simpler by noting that large scale geophysical flows are very flat in the sense that the horizontal component of wind and current are very much larger

[26] The ocean and atmosphere are *not* at rest, and the observed displacements of constant pressure surfaces, e.g., the sea surface and 500 hPa surface, are invaluable, indirect measures of that motion that may be inferred via geostrophy, Sec 5.

than the vertical component, $u' \propto v' \gg w'$, in part because the oceans and the atmosphere are quite thin, having a depth to width ratio of about 0.001. As well, the ocean and atmosphere are stably stratified in the vertical, which greatly inhibits the vertical component of motion. For large scale (in the horizontal) flows, the Coriolis term multiplying w' in the x component of Eqn. (82) is thus very much smaller than the terms multiplied by u' or v' and as an excellent approximation the w' terms may be ignored; very often they are ignored with no mention made. The Coriolis term that appears in the vertical component is usually much, much smaller than the gravitational acceleration, and it too is often dropped without mention. The result is the thin fluid approximation of the Coriolis force in which only the horizontal Coriolis force acting on horizontal motions is retained,

$$\boxed{-2\mathbf{\Omega}\times\mathbf{V}' \approx -\mathbf{f}\times\mathbf{V}' = fv'\mathbf{e_x} - fu'\mathbf{e_y}} \tag{83}$$

where $\mathbf{f} = f\mathbf{e_z}$, and f is the very important Coriolis parameter,

$$\boxed{f = 2\Omega\sin\phi} \tag{84}$$

and ϕ is the latitude. Notice that f varies with the sine of the latitude, having a zero at the equator and maxima at the poles; $f < 0$ in the southern hemisphere. The horizontal, component-wise momentum equations written for the thin fluid form of the Coriolis force are:

$$\boxed{\begin{aligned} \frac{du}{dt} &= \quad fv - g\frac{\partial\eta}{\partial x} \\ \frac{dv}{dt} &= -fu - g\frac{\partial\eta}{\partial y} \end{aligned}} \tag{85}$$

where the force associated with a tilted constant pressure surface is included on the right.[27]

For problems that involve parcel displacements, L, that are very small compared to the radius of the Earth, R_E, a simplification of f itself is often appropriate. The Coriolis parameter may be expanded in a Taylor series about a central latitude ϕ_0 where the north coordinate $y = y_0$,

$$f(y) = f(y_0) + (y - y_0)\frac{df}{dy}\,|_{y_0} + HOT. \tag{86}$$

If the second term involving the first derivative $df/dy = 2\Omega\cos\phi/R_E$, often written as $df/dy = \beta$, is demonstrably much smaller than the first term, which follows if $L \ll R_E$, then the second and higher terms may be dropped to leave

$$f = f(y_0), \tag{87}$$

and thus f is taken as constant. This is called the f-plane approximation. While the f-plane approximation is very useful in a number of contexts, there is an entire class of low frequency motions

[27] This system has what will in general be three unknowns: u, v and η. For now we will take η as known, i.e., the height of the sea floor in Sec. 5. In a genuine fluid model, which we will come to in Part 2, η will be connected to the flow by the conservation of mass.

known as Rossby waves that go missing and which are of great importance for the real atmosphere and ocean. We will come to this phenomena in Part 3 by keeping the second order term of (86), and thus represent $f(y)$ by

$$f(y) = f(y_0) + \beta(y - y_0), \tag{88}$$

often called a β-plane approximation.

4.4 One last look at the inertial frame equations

We have noted that the rotating frame equation of motion has some inherent awkwardness, viz., the loss of Galilean invariance and global momentum conservation that accompany the Coriolis force. Why, then, do we insist upon using the rotating frame equations for nearly all of our analyses of geophysical flow?

The reasons are several, any one of which would be compelling, but beginning with the fact that the definition and implementation of an inertial frame (outside of the Earth) is simply not a viable option; whatever conceptual clarity might be gained by avoiding the Coriolis force would be more than offset by difficulty with observation. Consider just one aspect of this: the inertial frame velocity,

$$\mathbf{V} = \mathbf{V}_\Omega + \mathbf{V}', \tag{89}$$

is dominated by the planetary velocity due to the solid-body rotation $V_\Omega = \Omega R_E \cos\phi$, where R_E is earth's nominal radius, 6365 km, and thus $V_\Omega \approx 450$ m s^{-1} near the equator. A significant wind speed at mid-level of the atmosphere is $V' \approx 30$ m s^{-1} (the westerlies of Fig. 2) and a fast ocean current is $V' \approx 1$ m s^{-1} (the western boundary current of Fig. 1). An inertial frame description must account for $\mathbf{V}_\Omega$ and the associated, very large centripetal force, and yet our interest is almost always the comparatively small relative motion of the atmosphere and ocean, $\mathbf{V}'$, since it is the relative motion that transports heat and mass over the Earth. In that important regard, the planetary velocity $\mathbf{V}_\Omega$ is invisible to us Earth-bound observers, no matter how large it is. To say it a little differently — it is the relative velocity that we measure when observe from Earth's surface, and it is the relative velocity that we seek to know for almost every practical purpose. The Coriolis force follows.

The reservations regards practical use of the inertial frame equations apply mainly to observations. Given that we presume to know exactly the centripetal force required to balance the planetary velocity, then in principle a calculation based upon the inertial frame equations should be quite doable. To illustrate this, and before we turn away completely and finally from the inertial frame equations, it is instructive to analyze some very simple motions using the inertial frame, spherical equations of motion (Sec. 3.4). This is partly repetitious with the discussions of Secs. 3.2 and 3.3. It will differ importantly insofar as the setting will be a rotating planet, Fig. (15). As before we will analyze the motion of a single parcel, but just for the sake of visualization it is helpful to imagine that this parcel is part of a torus of fluid, Fig. (15), that encircles a rotating planet. It is presumed that the torus will move in a completely coherent way, so that the motion of any one parcel will be the same as all other parcels.

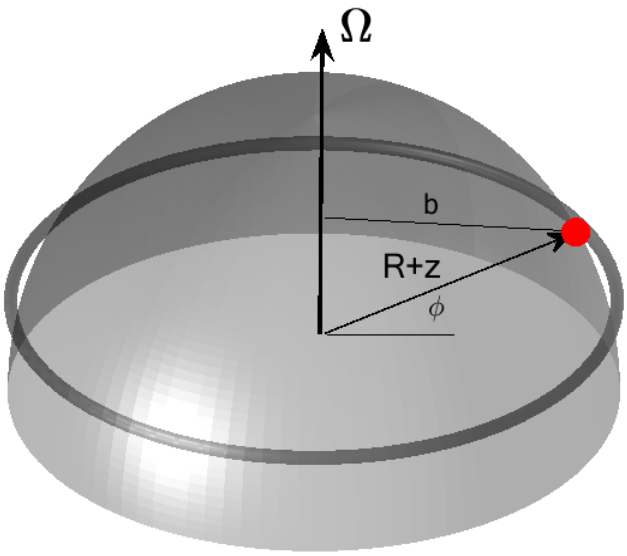

Figure 15: A schematic showing a rotating planet and an encircling tube of fluid whose motion includes a rotation at the same rate as the underlying planet, i.e., a planetary velocity. A single parcel whose motion is identical with the tube at large is denoted by the red dot. This analysis will use spherical coordinates, Sec. 3.4. Here the radial distance from the center will be written $r = R + z$, where $z \ll R$. Not shown here is the longitude (or azimuth) coordinate, λ, which is the same as in the spherical system.

The only two forces acknowledged here will be gravity, certainly in the vertical component, and also the horizontal gravitational acceleration associated with Earth's oblate figure (equatorial bulge). The basic state velocity is that due to planetary rotation, $U_\lambda = (R+z)\cos\phi\,\Omega$ and which is azimuthal, or eastward. With these in mind, the inertial frame, spherical system equations of motion are:

$$\frac{1}{(R+z)\cos\phi}\frac{dL_\lambda}{dt} \;=\; 0, \tag{90}$$

$$\frac{1}{(R+z)}\frac{dL_\phi}{dt} \;-\; C_\lambda \sin\phi \;=\; -(R+z)\cos\phi\,\Omega^2\sin\phi, \tag{91}$$

$$\frac{d^2z}{dt^2} \;+\; C_\lambda\cos\phi + C_\phi \;=\; -g. \tag{92}$$

Northward motion: For the first example, presume that the parcel stays in contact with a frictionless planet so that $r = R$ and constant. The longitudinal angular velocity may be written

$$\frac{d\lambda}{dt} \;=\; \Omega + \frac{d\lambda'}{dt}$$

and the tangential or λ-component angular momentum is

$$L_\lambda \;=\; (R\cos\phi)^2(\Omega + \frac{d\lambda'}{dt}).$$

The λ component equation of motion (Eqn. 67) is just conservation of this angular momentum,

$$\frac{dL_\lambda}{dt} \;=\; 0,$$

and hence

$$-2R\sin\phi\frac{d\phi}{dt}(\Omega+\frac{d\lambda'}{dt}) \;+\; R\cos\phi\frac{d^2\lambda'}{dt^2} = 0.$$

Factoring out the Ω term and moving it to the right gives,

$$\begin{aligned}\frac{1}{R\cos\phi}\frac{dL'_\lambda}{dt} \;&=\; 2\Omega\sin\phi R\cos\phi\frac{d\phi}{dt}\\ &= fU_\phi,\end{aligned} \tag{93}$$

which is the corresponding rotating frame equation of motion. But the inertial frame interpretation is via angular momentum conservation: as the parcel (or torus) moves northward, $d\phi/dt \geq 0$ say, it acquires some positive or eastward L'_λ specifically because the perpendicular to the rotation axis, b, shrinks northward. The initial angular momentum includes a very large (dominant) contribution from the Earth's rotation, i.e., $\Omega \gg d\lambda'/dt$. You may very well feel that the inertial frame derivation is based upon much more familiar, 'physical' principles than is the rotating frame version. However, the inference of an eastward relative acceleration associated with northward motion is exactly the same from both perspectives, as it should be.

Eastward motion: The inertial frame ϕ component equation of motion includes a significant contribution from the planetary velocity and centripetal force; if in steady state, assuming that $U'_\phi = 0$ for the moment, then Eqn. (68) is just,

$$\begin{aligned}-C_\lambda\sin\phi \;&=\; F_\phi\\ &=\; -R\cos\phi\Omega^2\sin\phi,\end{aligned} \tag{94}$$

a steady balance between the ϕ component of the centripetal acceleration and the centripetal force associated with the equatorial bulging noted in Sec. 4.1. Now suppose that there is comparatively small relative λ component velocity so that

$$\frac{d\lambda}{dt} = \Omega \;+\; \frac{d\lambda'}{dt}$$

and substitute into the ϕ component equation of motion, Eqn. (68),

$$\frac{1}{r}\frac{dL_\lambda}{dt} \;+\; R\cos\phi(\Omega^2+2\Omega\frac{d\lambda'}{dt} \;+\; (\frac{d\lambda'}{dt})^2)\sin\phi \;=\; -R\cos\phi\Omega^2\sin\phi.$$

Rearranging and moving the 2Ω term to the right side yields

$$\begin{aligned}\frac{1}{R}\frac{dL'_\lambda}{dt} \;-\; C'_\lambda\sin\phi \;&=\; 2\Omega\sin\phi R\cos\phi\frac{d\phi'}{dt}\\ &=\; fU'_\phi.\end{aligned} \tag{95}$$

Again, this is the rotating frame equivalent. A significant difference with the example of northward motion noted above is that the induced acceleration comes from an out-of-balance centripetal force and acceleration. As in the previous case, the basic state is that due to Earth's rotation and resulting gravitational-rotational equilibrium.

Vertical motion: Imagine a parcel that is released from (relative) rest at a height h and allowed to free fall. The initially purely vertical motion has no appreciable consequences for either the ϕ or r component equations of motion, but it does appear in the λ component equation multiplied by Ω (Eqn. 67). The vertical acceleration, ignoring air resistance is just

$$\frac{d^2z}{dt^2} = -g, \tag{96}$$

with g the presumed constant acceleration of gravity, 9.8 m sec^{-2}. Integrating once to find the vertical velocity, $w = -gt$, and once more for the displacement, $z = h - 1/2gt^2$. The time of flight is just $T = \sqrt{2h/g}$.

The only force acting on the parcel is the radial force of gravity, and hence the parcel will conserve angular momentum. The λ-component angular momentum conservation, Eqn. (67), is then just

$$\frac{d}{dt}\left((R\ +\ z)^2\cos^2\phi(\Omega\ +\ \frac{d\lambda'}{dt})\right)\ =\ 0. \tag{97}$$

Expanding the derivative and cancelling terms gives

$$2\frac{dz}{dt}\cos\phi(\Omega+\frac{d\lambda'}{dt})+(R+z)\cos\phi\frac{d^2\lambda'}{dt^2}=0$$

Rewriting in terms of $u' = R\cos\phi\frac{d\lambda'}{dt}$ and $w' = \frac{dz}{dt}$ and assuming that z is O(100), then $z \ll R$, and the relative speed u' is very, very small compared to the planetary rotation speed, $u' \ll \Omega R$. To an excellent approximation Eqn. (97) is

$$\frac{du'}{dt} \approx -2\Omega\cos\phi w'. \tag{98}$$

Thus, as the parcel falls, $w' \leq 0$, and moves into orbit closer to the rotation axis, it is accelerated to the east at a rate that is proportional to twice the rotation rate Ω and the cosine of the latitude. Viewed from an inertial reference frame, this eastward acceleration is the expected consequence of angular momentum conservation, where the angular momentum is that due to planetary rotation. The complementary rotating frame description of this motion is that eastward acceleration is due to the Coriolis force acting upon the relative vertical velocity.

4.5 Problems

(1) The rather formal notions of vertical and level raised in Sec. 4.2 turned out to have considerable practical importance beginning on a sweltering August afternoon when the University Housing

Office notified your dear younger brother, GG Jr., that because of an unexpectedly heavy influx of freshmen, his old and comfortable dorm room was not going to be available. As a consolation, they offered him the use of the merry-go-round (the one in Section 3.3, and still running) at the local, failed amusement park just gobbled up by the University. He shares your enthusiasm for rotation and accepts, eagerly. The centrifugal force, amusing at first, was soon a huge annoyance. GG suffered from recurring nightmares of sliding out of bed and over a cliff. Something had to be done, so you decide to build up the floor so that the tilt of the floor, combined with gravitational acceleration, would be just sufficient to balance the centrifugal force, as in Eqn. (78). What shape $\eta(r)$ is required, and how much does the outside edge ($r = 6$ m, $\Omega = 0.5$ rad s^{-1}) have to be built up? How could you verify success? Given that GG's bed is 2 m long and flat, what is the axial traction, or tidal force? Is the calibration of a bathroom scale effected? Guests are always impressed with GG's rotating dorm room, and to make sure they have the full experience, he sends them to the refrigerator for another cold drink. Describe what happens next using Eqn. (81). Is their experience route-dependent?

(2) In most of what follows the Coriolis force will be represented by the thin fluid approximation Eqn. (83) that accounts only for the horizontal Coriolis force due to horizontal velocity. This horizontal component of the Coriolis force is proportional to the Coriolis parameter, f, and thus vanishes along the equator. This is such an important and striking result that it can be easy to forget the three-dimensional Coriolis force. Given an eastward and then a northward relative velocity, make a sketch that shows the 3-d Coriolis force at several latitudes including the pole and the equator (and recall Fig. 8), and resolve into (local) horizontal and vertical components. The vertical component of the Coriolis force is negligible for most geophysical flow phenomena, but it is of considerable importance for gravity mapping, where it is called the Eotvos effect (see https://en.wikipedia.org/wiki/Eotvos_effect).

(3) The vertical component of the Coriolis force has a small but observable effect on the motion of free projectiles. Consider the Coriolis deflection of a long-range rifle shot, say range is $L = 1$ km and with a trajectory that is nearly flat. Assuming mid-latitude; estimate the horizontal deflection and show that it is given by $\delta y \approx \delta t\ f\ L/2$, where δt is the time of flight, 2 sec. Show that the vertical deflection is similar and given approximately by $\delta z \approx \delta t\ f_{vert}\ L\ cos(\psi)/2$, where $f_{vert} = 2\Omega cos\phi$ and ψ is the direction of the projectile motion with respect to east (north is $\pi/2$). How do these deflections vary with latitude, ϕ, and with the direction, ψ?

(4) The effect of Earth's rotation on the motion of a simple (one bob) pendulum, called a Foucault pendulum in this context, is treated in detail in many physics texts, e.g. Marion[6], and need not be repeated here. Foucault pendulums are commonly displayed in science museums, though seldom to large crowds (see *The Prism and the Pendulum* by R. P. Crease for a more enthusiastic appraisal). It is, however, easy and fun (!) to make and observe your own Foucault pendulum, nothing more than a simple pendulum having two readily engineered properties. First, the e-folding time of the motion due to frictional dissipation must be long enough that the precession will become apparent before the motion dies away, 20 min will suffice at mid-latitudes. This can be achieved using a dense, smooth and symmetric bob having a weight of about half a kilogram or more, and suspended on a fine, smooth monofilament line. It is helpful if line is several meters or more in length. Second, the pendulum should not interact appreciably with its mounting. This is harder to evaluate, but generally requires a very rigid support, and a bearing that can not exert appreciable torque, for example a fish hook bearing on a very hard steel surface. The precession is easily masked by any initial motion you might inadvertently impose, but after several careful trials

you will very likely begin to see the Earth rotate under your pendulum. Can you infer your latitude from the observations? The rotation effect is proportional to the rotation rate, and so you should plan to bring a simple and rugged pocket pendulum (a rock on a string will do) on your merry-go-round ride (Section 3.2). How do your observations (even if qualitative) compare with your solution for a Foucault pendulum? (Hint - consider the initial condition.)

(5) In Sec. 4.4 we used the spherical system equations of motion as the starting point for an analysis of some simple motions. The spherical system is an acquired taste, which I am betting you have not acquired. There is a simpler way to come to several of the results of that section that you may find more appealing. When observed from an inertial reference frame, the eastward velocity of the parcel is $U = \Omega b + u'$ where $b = (R+z)\cos\phi$ is the perpendicular distance to the rotation axis. The parcel has angular momentum associated with this eastward velocity, $L = Ub$. For what follows here we can think of the angular momentum as a scalar. Presume that the parcel motion is unforced, aside from gravity. Show that conservation of this angular momentum under changing ϕ and z leads immediately to the inference of a Coriolis force. In fact, you can think of this as your (partial) derivation of the Coriolis force (partial since it does not include the planetary centripetal acceleration, the second case considered in Sec. 4.4).

(6) The Coriolis force on most everyday (every weekend) motions is not noticeable. For example, golfers worry about about all kinds of environmental and fluid dynamical issues, but never the Coriolis force. A good golf drive may go 250 m, and stay in the air for about 5 sec. Can you explain quantitatively why this motion is not much affected by the Coriolis force? Contrast this with the very large effects upon winds and ocean currents.

5 A dense parcel released onto a rotating slope with friction

The second goal of this essay is to begin to understand the consequences of rotation for the atmosphere and ocean. As already noted in Sec. 1, the consequences of rotation are profound and wide ranging and will likely be an enduring topic of your study of the atmosphere and ocean. In this section we can take a rewarding and nearly painless first step toward understanding the consequences of rotation by analyzing the motion of a dense parcel that is released onto a rotating, sloping sea floor. This simple problem serves to illustrates two fundamental modes of the rotating momentum equations — inertial motion and geostrophic motion — that will recur in much more comprehensive models and in the real atmosphere and ocean.

The sea floor is presumed to be at a depth $z = -b(y)$ that increases uniformly in the y direction as $db/dy = \alpha$, a small positive constant, O(10^{-2}). The fixed buoyancy of the parcel is $g' = -g\frac{\delta\rho}{\rho_o}$, where $\delta\rho$ is the density anomaly of the parcel with respect to its surroundings, say 0.5 kg m^{-3}, and ρ_o is a nominal sea water density, 1030 kg m^{-3}. (Notice that a prime superscript is used here to denote buoyancy, or reduced gravity. The prime previously used to indicate rotating frame velocity will be omitted, with rotating frame understood.) The component of the buoyancy parallel to the sea floor, $g'\alpha$, thus provides a constant force (per unit mass, understood from here on) in the y direction. Absent rotation, the parcel would accelerate down hill in the positive y direction. With rotation, the parcel

velocity V will be significantly altered in a time T_r in the scale analysis sense (rough magnitude only) that

$$f\ V\ T_r \approx V$$

and hence

$$\boxed{T_r = \frac{1}{f}} \tag{99}$$

The important time scale $1/f$ is dubbed the rotation time. For a mid-latitude, $1/f \approx 4$ hours. In other words, for rotation to be of first order importance, the motion has to persist for several hours or more. Thus the flight path of a golf ball (requiring about 3 seconds) is very little affected by Earth's rotation when compared to other curves and swerves, and as we knew from a more detailed calculation in Sec. 3. Given that the motion will be nearly horizontal and that we seek the simplest model, rotation will be modeled by the thin fluid form of the Coriolis force, and the Coriolis parameter f will be taken as constant (the f-plane approximation).

Since the parcel is imagined to be in contact with the bottom, it is plausible that the momentum balance should include bottom friction. Here the bottom friction will be represented by the simplest linear (or Rayleigh) law in which the friction is presumed to be proportional to and antiparallel to the velocity difference between the parcel velocity and the bottom, i.e., bottom friction $= -r(\mathbf{V} - \mathbf{V_{bot}})$. The ocean bottom is at rest in the rotating frame and hence $\mathbf{V_{bot}} = 0$ and omitted from here on. From observations of ocean density currents (looking ahead to Fig. 16), a reasonable order of magnitude of the friction coefficient is $r\ =\ \mathrm{O}(10^{-5})\ \mathrm{s}^{-1}$.[28]

The equations of motion for the parcel including rotation and this simplified bottom friction are

$$\begin{aligned} \frac{d^2x}{dt^2} &= \frac{du}{dt} &&= \quad fv - ru, \\ \frac{d^2y}{dt^2} &= \frac{dv}{dt} &&= -fu - rv + g'\alpha, \end{aligned} \tag{100}$$

with vector equivalent,

$$\frac{d\mathbf{V}}{dt} = -f\mathbf{k}\times\mathbf{V} - r\mathbf{V} + g'\nabla b. \tag{101}$$

Initial conditions on the position and the velocity components are

$$x(0) = X_0, \quad y(0) = Y_o \quad \text{and} \quad u(0) = U_o, \quad v(0) = 0. \tag{102}$$

[28]This use of a linear friction law is purely expedient. A linear friction law is most appropriate in a viscous, laminar boundary layer that is in contact with a no-slip boundary. In that case $\tau = \mu\frac{\partial U}{\partial z}$ within the laminar boundary layer, where μ is the viscosity of the fluid. However, the laminar boundary layer above a rough ocean bottom is very thin, $\mathrm{O}(10^{-3})$ m, and above this the flow will in general be turbulent. If the velocity that is used to estimate or compute friction is measured or computed within the much thicker turbulent boundary layer, as it almost always has to be, then the friction law is likely better approximated as independent of the viscosity and quadratic in the velocity, i.e., $\tau = \rho C_d U^2$, where C_d is the drag coefficient. Typically, $C_d = 1 - 3\times 10^{-3}$, but depending upon bottom roughness, mean speed, and more.

In most of what follows we will presume $U_o = 0$. Integrating once gives the solution for the velocity components,

$$u(t) = \frac{g'\alpha}{r^2+f^2}\left[f - \exp(-rt)(f\cos(-ft) - r\sin(-ft))\right], \tag{103}$$
$$v(t) = \frac{g'\alpha}{r^2+f^2}\left[r - \exp(-rt)(f\sin(-ft) + r\cos(-ft))\right].$$

If the position (trajectory) is required, it may be computed by integrating the velocity

$$x(t) = X_o + \int_0^t u dt \quad \text{and} \quad y(t) = Y_o + \int_0^t v dt,$$

and if the depth is required,

$$z(t) = Z_o - \alpha y(t).$$

5.1 The nondimensional equations; Ekman number

The solution above is simple by the standards of fluid dynamics, but it does contain three parameters along with the time, and so has a fairly large parameter space. We will consider a couple of specific cases motivated by observations, but our primary intent is to develop some understanding of the effects of rotation and friction over the entire family of solutions. How can the solution be displayed to this end?

A very widely applicable approach is to rewrite the governing equations and (or) the solution using nondimensional variables. This will serve to reduce the number of parameters to the fewest possible while retaining everything that was present in the dimensional equations. Lets start with the x-component momentum equation, and hence u will be the single dependent variable and it has units length and time, l and t. Time is the sole independent variabil, and obviousl its units are em t. There are three independent parameters in the problem; 1) the buoyancy and bottom slope, $g'\alpha$, which always occur in this combination and so count as one parameter, an acceleration with units l and t and dimensions $l\ t^{-2}$. 2) the Coriolis parameter, f, an inverse time, dimensions t^{-1}, and 3) the bottom friction coefficient, r, also an inverse time scale, t^{-1}. Thus there are five variables or parameters having two fundamental units. Because we anticipate that rotation will be of great importance in the parameter space of most interest, the inverse Coriolis parameter or rotation time, will be used to scale time, i.e., $t_* = tf$. You can think of this as measuring the time in units of the rotation time. A velocity (speed) scale is then estimated as the product of this time scale and the acceleration $g'\alpha$,

$$\boxed{U_{geo} = \frac{g'\alpha}{f}} \tag{104}$$

the very important geostrophic speed. Measuring the velocity in these units then gives the nondimensional velocity, $u_* = u/U_{geo}$ and similarly for the v component. Rewriting the governing equations in terms of these nondimensional variables

$$\frac{du_*}{dt_*} = v_* - Eu_*, \tag{105}$$

$$\frac{dv_*}{dt_*} = -u_* - Ev_* + 1, \tag{106}$$

where E is the Ekman number,

$$\boxed{E = \frac{r}{f}} \tag{107}$$

the nondimensional ratio of the friction parameter to the Coriolis parameter. There are other forms of the Ekman number that follow from different forms of friction parameterization. They all have in common that small E indicates small friction compared to rotation. The initial condition is presumed to be a state of rest, $u_*(0) = 0,\ v_*(0) = 0$ and the solution of these equations is

$$u_*(t_*) = \frac{1}{1+E^2}\left[1 - \exp(-Et_*)(\cos(-t_*) - E\sin(-t_*))\right], \tag{108}$$

$$v_*(t_*) = \frac{1}{1+E^2}\left[E - \exp(-Et_*)(\sin(-t_*) + E\cos(-t_*))\right],$$

and for completeness,

$$t_* = tf, \quad U_{geo} = \frac{g'\alpha}{f}, \quad u_* = \frac{u}{U_{geo}} \quad \text{and} \quad v_* = \frac{v}{U_{geo}}.$$

The geostrophic scale U_{geo} serves only to scale the velocity amplitude, and thus the parameter space of this problem has been reduced to a single independent, nondimensional variable, t_*, and one nondimensional parameter E.[29]

The solution Eqn. (108) can be written as the sum of a time-dependent part, termed an *i*nertial motion (or just as often, inertial 'oscillation') that is here damped by friction,

$$\begin{bmatrix} u_* \\ v_* \end{bmatrix}_i = -\frac{\exp(-Et_*)}{1+E^2}\begin{bmatrix} \cos(-t_*) - E\sin(-t_*) \\ \sin(-t_*) + E\cos(-t_*) \end{bmatrix}, \tag{109}$$

and a time-independent motion that is the single parcel equivalent of *g*eostrophic motion

$$\begin{bmatrix} u_* \\ v_* \end{bmatrix}_g = \frac{1}{1+E^2}\begin{bmatrix} 1 \\ E \end{bmatrix}, \tag{110}$$

[29]On first encounter, this kind of dimensional analysis is likely to seem abstract, arbitrary and abstruse, i.e., far more harmful than helpful. The method and the benefits of dimensional analysis will become clearer with experience, mainly, and an attempt to help that along is 'Dimensional analysis of models and data sets', by J. Price, *Am. J. Phys.*, **71**(5), 437–447 (2003) and available online in an expanded version from the author's web page (Sec. 1.3).

also damped by friction. Since the IC was taken to be a state of rest, $U_o = 0$, the dimensional amplitude is directly proportional to the geostrophic velocity scale, U_{geo}. Since the model and solution are linear, the form of the solution does not change with U_{geo}.

Our discussion of the solution will generally refer to the velocity, Eqns. (109) and (110), which are simple algebraically. However, the solution is considerably easier to visualize in the form of the parcel trajectory, computed by integrating the velocity in time (Fig. 16, left, and see the embedded animation or better, run the script partslope.m to make your own).

Immediately after the parcel is released from rest it accelerates down the slope. The Coriolis force acts to deflect the moving parcel to the right, and by about $t = 1/f$, or $t_* = 1$, the parcel has been turned by 1 radian, or about 50°, with respect to the buoyancy force. The time required for the Coriolis force to have an appreciable effect on a moving object is thus $1/f$, the very important rotation time scale noted previously. The Coriolis force continues to turn the parcel to the right, and by about $t_* = \pi$ the parcel velocity is directed up the slope. If $E = 0$ and there is no friction, the parcel will climb back to its starting depth at $t_* = 2\pi$ (or $t = 2\pi/f$) where it will stop momentarily, before repeating the cycle. In the meantime it will have moved a significant distance along the slope. When friction is present, $0 < E < 1$, the parcel still makes at least a few oscillations up and down slope, but with decreasing amplitude with time, and will gradually slide down the slope. The clockwise-turning looping motion is associated with near-inertial motion Eqn. (109) and the steadily growing displacement along the slope, in the positive x direction mainly, is associated with quasi-geostrophic motion, Eqn. (110). In fact, these specific trajectories may be viewed as nothing but the superposition of inertial and geostrophic motion, damped by friction when $E > 0$.

5.2 (Near-) Inertial motion

In Eqn. (109) we already have a solution for inertial motion, but it is helpful to take a step back to the dimensional form of the momentum equations, (4.3) and point out the subset that supports pure inertial motion:

$$\boxed{\begin{aligned} \frac{du}{dt} &= fv \\ \frac{dv}{dt} &= -fu \end{aligned}} \tag{111}$$

The Coriolis force can not generate a velocity, and so to get things started we have to posit an initial velocity, $u(t = 0) = U_o$ and $v(t = 0) = 0$. The solution is pure inertial motion,

$$u = U_o \cos(-ft), \quad \text{and} \quad v = U_o \sin(-ft), \tag{112}$$

which is the free mode of the f-plane momentum equations, i.e., when the Coriolis force is left on it its own. The speed of a pure inertial motion is constant in time, and the velocity vector rotates at a steady

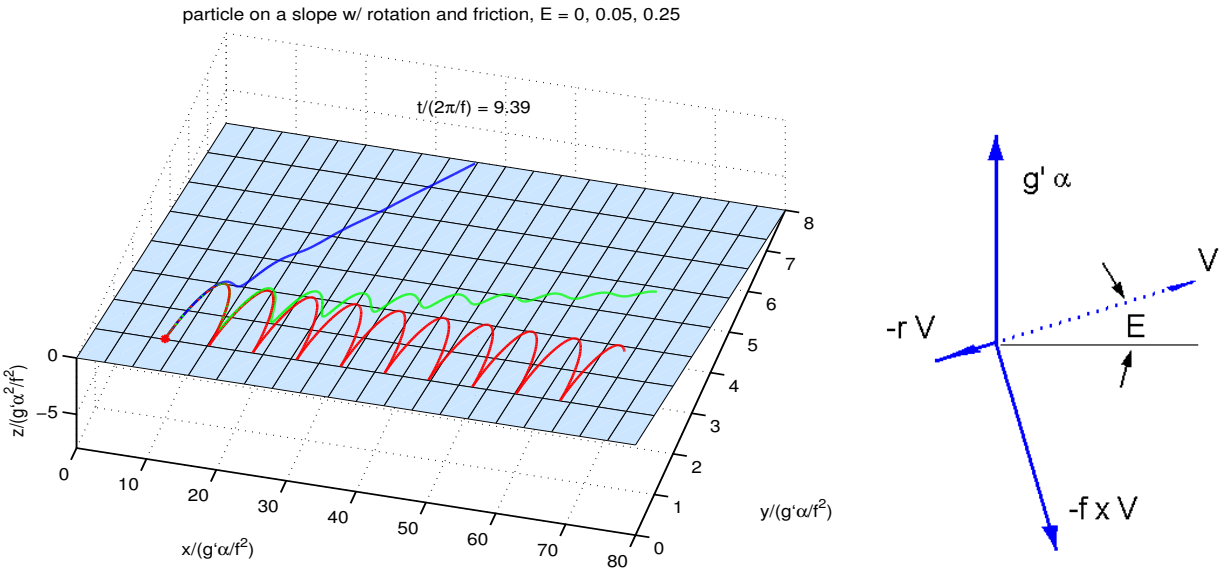

Figure 16: **(left)** Trajectories of three dense parcels released from rest onto a rotating slope. The buoyancy force is toward positive y (up in this figure). These parcels differ by having rather large friction (blue trajectory, $E = r/f = 0.25$), moderate, more or less realistic friction (green trajectory, $E = 0.05$) and no friction at all (red trajectory, $E = 0$). The elapsed time in units of inertial periods, $2\pi/f$, is at upper left. At mid-latitude, an inertial period is approximately one day, and hence these trajectories span a little more than one week. The along- and across-slope distance scales are distorted by a factor of almost 10 in this plot, so that the blue trajectory having $E = 0.25$ makes a much shallower descent of the slope than first appears here. Notice that for values of $E \ll 1$ (red and green trajectories), the motion includes a looping inertial motion, and a long-term displacement that is more or less along the slope, the analog of geostrophic motion. This is presumed to be a northern hemisphere problem, $f > 0$, so that shallower bottom depth is to the right when looking in the direction of the long-term motion. Experiments that test different r or different initial conditions may be carried out via the Matlab script partslope.m (linked in Sec. 6.3). **(right)** The time-mean horizontal velocity (the dotted vector) and the time-mean force balance (solid arrows) for the case $E = 0.25$ (the blue trajectory). The Coriolis force (/M) is labeled $-\mathbf{f}\times\mathbf{V}$. The angle of the velocity with respect to the isobaths is $E = r/f$, the Ekman number.

rate $f = 2\Omega \sin\phi$ in a direction opposite the rotation of the reference frame, Ω; inertial rotation is clockwise in the northern hemisphere and anti-clockwise in the southern hemisphere.

Inertial motion is a striking example of the non-conservation property inherent to the rotating frame equations: the velocity of the parcel is continually accelerated (deflected) with nothing else showing a reaction force; i.e., there is no evident physical cause for this acceleration, and global momentum is not conserved.[30, 31]

The trajectory of a pure inertial motion is circular (Fig. 11),

$$x(t) = \int u(t)dt = \frac{U_o}{f}\sin(-ft), \tag{113}$$

$$y(t) = \int v(t)dt = -\frac{U_o}{f}\cos(-ft), \tag{114}$$

up to a constant. The radius of the circle is $r = \sqrt{x^2+y^2} = |U_o|/f$. A complete orbit takes time $2\pi/f$, a so-called inertial period: just a few minutes less than 12 hrs at the poles, a little less than 24 hrs at 30 N or S, and infinite at the equator. (Infinite is, of course, unlikely physically, and suggests that something more will arise on the equator; more on this below). Though inertial motion rotates in the sense opposite the reference frame, it is clearly not just a simple rotation of the inertial frame solution (cf., Fig. 11). In most cases (equator aside) the displacement associated with an inertial motion is not large, typically a few kilometers in the mid-latitude ocean. Inertial motion thus does not, in general, contribute directly to what we usually mean by 'circulation', *viz.*, significant transport by fluid flow.

The centripetal acceleration associated with circular, inertial motion is $-U_o^2/r$ (Fig. 10). This centripetal acceleration is provided by the Coriolis force, and hence the radial momentum balance of this pure inertial motion is just

$$\frac{-U_o^2}{r} = fU_o. \tag{115}$$

[30] To discern a physical cause of inertial motion we could analyze the inertial frame equivalent motion as in Sec. (3.4), a combination of angular momentum conservation (northward relative motion) and the slightly out of balance centripetal acceleration (eastward relative motion). See also D. R. Durran, 'Is the Coriolis force really responsible for the inertial oscillation?' *Bull. Am. Met. Soc.*, **74**(11), 2179–2184 (1993).

[31] The Coriolis force is isomorphic to the Lorentz force, $q\mathbf{V}\times\mathbf{B}$, on a moving charged particle having charge q and mass M in a magnetic field $\mathbf{B}$. The charged particle will be deflected into a circular orbit with the cyclotron frequency, qB/M, analogous to an inertial oscillation at the frequency f. A difference in detail is that geophysical flows are generally constrained to occur in the local horizontal plane, while a charged particle may have an arbitrary three dimensional velocity with respect to $\mathbf{B}$. What happens when $\mathbf{V}$ is parallel to $\mathbf{B}$? Where on Earth does it happen that $\mathbf{V}$ (a horizontal current) may be parallel to Ω? Still another example of such a force law comes from General Relativity which predicts that a rotating object will be accompanied by a gravitomagnetic field that gives rise to a Coriolis-like gravitational force on moving objects. The Gravity Probe B mission, one of the most challenging physics experiments ever conducted, has apparently confirmed the presence of a gravitomagnetic field around Earth, see http://einstein.stanford.edu/

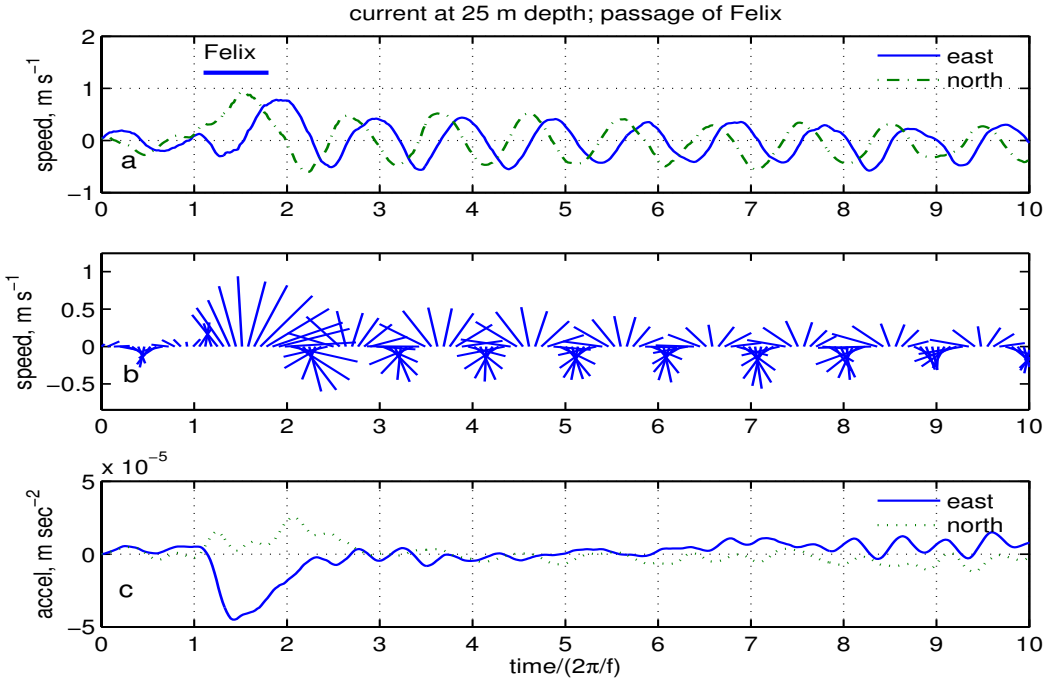

Figure 17: Ocean currents measured at a depth of 25 m by a current meter deployed southwest of Bermuda. The time scale is inertial periods, $2\pi/f$, which are nearly equal to days at this latitude. Hurricane Felix passed over the current meter mooring between $1 < t/(2\pi/f) < 2$ and the strong and rapidly changing wind stress produced energetic, clockwise rotating currents within the upper ocean. **(a)** East and north current components. Notice that the maximum north leads maximum east by about a quarter inertial period, and hence the velocity vector is rotating clockwise. **(b)** Current vectors, with north 'up'. To a first, the fluctuating current seen here is an inertial inertial oscillation. A more refined description is to note that it is a near-inertial oscillation; the frequency is roughly 5% percent higher than f and the amplitude e-folds over about 10 days (by inspection). These small departures from pure inertial motion are indicative of wave-like dynamics considered in Part 2. **(c)** Acceleration estimated from the current meter data as $d\mathbf{V}'/dt + 2\boldsymbol{\Omega}\times\mathbf{V}'$, as if the measurements were made on a specific parcel. The large acceleration to the west northwest corresponds in time to the passage of Felix and the direction of the estimated acceleration is very roughly parallel to the wind direction (not shown here). Notice the much smaller oscillations of the acceleration having a period of about 0.5 inertial periods (especially the last several inertial periods). These are likely due to pressure gradients associated with the semidiurnal tide. This is a small part of the data described in detail by Zedler, S.E., T.D. Dickey, S.C. Doney, J.F. Price, X. Yu, and G.L. Mellor, 'Analysis and simulations of the upper ocean's response to Hurricane Felix at the Bermuda Testbed Mooring site: August 13-23, 1995', *J. Geophys. Res.*, **107**, (C12), **25**-1 - **25**-29, (2002), available online at http://www.opl.ucsb.edu/tommy/pubs/SarahFelixJGR.pdf.

Interestingly, there are two quite different flows that are consistent with a single parcel undergoing inertial motion given by Eqns. (114) and (115): 1) a *vortical inertial motion* associated with a steady, anticyclonic eddy (or vortex), and 2) a time-dependent but spatially quasi-homogeneous *inertial oscillation.* To treat either of these at a useful depth will require a more comprehensive two-dimensional *fluid* model that we will come to in Part 2.[32] For now, suffice it to say that vortical inertial motion is very rarely (never ?) observed in the ocean or atmosphere, while near-inertial oscillations are very widely observed in the upper ocean following a sudden shift in the wind speed or direction, (Fig. 17).

Observed near-inertial oscillations differ from pure inertial motion in that their frequency is usually slightly higher than f or 'blue shifted'. As we will see in Part 2, near-inertial oscillations may be thought of as the long wave length limit of gravity waves in the presence of rotation (inertial-gravity waves) and the slight blue shift is characteristic of the gravity wave dynamics. The amplitude of observed near-inertial oscillations also changes with time; in the case of Fig. (17), the current amplitude e-folds in about one week following the very strong, transient forcing caused by a passing hurricane. This decay is likely a consequence of energy dispersion in space by wave propagation, and almost certainly not the dissipation process modeled here as $-r\mathbf{V}$.

5.3 (Quasi-) Geostrophic motion

The long-term displacement of the parcel is associated with the time-independent part of the solution, Eqn. (110), which is the parcel equivalent of damped, geostrophic motion. Again it is helpful to take a short step back to the dimensional momentum equations (Sec. 4.3) and point out the subset that supports pure geostrophic motion, $r = 0$ and $d/dt = 0$, in which case the x-momentum equation vanishes term by term, and the y-component is algebraic,

$$\boxed{0 = -fu + g'\alpha} \tag{116}$$

where we have assumed reduced gravity and in this case $\alpha = \partial\eta/\partial y$. Thus pure geostrophic motion is in the x-direction only,

$$u = \frac{g'\alpha}{f},$$

[32] A preview. The $d(\ )/dt$ of Eqn. (111) is time rate of change following a given parcel and is thus Lagrangian. In order to discern the difference between a vortical inertial motion and an inertial oscillation we would need to compute trajectories of some additional, different parcels, but there is presently no clear motivation for proceeding that way. Analysis in an Eulerian frame is helpful: the time derivative is then $d(\ )/dt = \partial(\ )/\partial t + \mathbf{V}.\nabla(\ )$, a local time rate of change and an advective rate of change. If the balance is between the local time rate change and the Coriolis force, then the solution will be a spatially homogeneous *inertial oscillation*. If the balance is between the advective rate of change and the Coriolis force, then the solution will be a steady, spatially-dependent *vortical inertial motion*. A map of the velocity field would be completely different in these two flows, and yet the trajectory af a given parcel may be identical, Eqn. (114).

which is the geostrophic velocity scale, U_{geo}. In a more general vector form, good for any steady, horizontal force $\mathbf{G}$,

$$\boxed{\mathbf{V}_{geo} = -\frac{1}{\rho_o f}\mathbf{k}\times\mathbf{G}} \tag{117}$$

where $\mathbf{k}$ is the vertical unit vector. In practice we usually reserve the distinction 'geostrophic' for the case that the force is a horizontal pressure gradient, $\mathbf{G} = -\nabla P$ or equivalently a geopotential gradient, $\propto -g\nabla\eta$. If the force is the vertical divergence of a horizontal wind stress, $\mathbf{G} = \partial\tau/\partial z$, then the steady velocity is often termed an Ekman velocity.

Simple though (117) is, there are several important points to make regarding geostrophy:

1) Perhaps the key point is that when the Coriolis force is present along with a persistent applied force, there can exist (likely will exist) a steady velocity that is perpendicular to the applied force provided that the forcing persists for a sufficient time, several or more rotation times. Looking in the direction of the applied force, $\mathbf{V}_{geo}$ is to the right in the northern hemisphere, and to the left in the southern hemisphere.

2) For a given $\mathbf{G}$, the geostrophic wind or current goes as $1/f$, and hence will be larger at a lower latitude. Clearly something beyond pure geostrophy will be important on or very near the equator where $f = 0$. With that important proviso, we can use Eqn. (117) to evaluate the surface geostrophic current that is expected to accompany the tilted sea surface of Fig. (1) outside of a near-equator zone, say ± 5 degrees of latitude.

3) A pure geostrophic balance is sometimes said to be degenerate, insofar as it gives no clue to either the origin of the motion or to the future evolution of the motion. Some other dynamics has to be added before these crucial aspects of the flow can be addressed. Nevertheless, geostrophy is a very important and widely used diagnostic relationship as noted above, and is the starting point for more comprehensive models.

4) An exact *instantaneous* geostrophic balance does not hold, in general, even in the idealized case, $E = 0$, because of nearly ubiquitous inertial motions. However, if we are able to time-average the motion over a long enough interval that the oscillating inertial motion may be averaged out, then the remaining, time-average velocity will be closer to geostrophic balance. Said a little differently, geostrophic balance may be present on time-average even if not instantaneously.

5) Because geostrophic motion may be present on long-term average (unlike inertial motion), the parcel displacements and transport associated with geostrophic motion may be very large. Thus, geostrophic motion makes up most of the circulation of the atmosphere and oceans.

An exact geostrophic balance is an idealization (albeit a very useful one) insofar as many processes can cause small departures, e.g., time dependence, advection, friction, and more. In the parcel on a slope experiments we can see that quasi-geostrophy, a phrase often used to mean near-geostrophy, will hold provided that the applied force varies slowly compared to the rotation time scale, $1/f$, and that the Ekman number is not too large, say $E \leq 0.1$, which commonly occurs. Aside from the startup transient, the former condition holds exactly in these experiments since the bottom slope is spatially uniform and unlimited in extent. The more realistic shallow water (fluid) model of Part 2 will supplant this latter condition with the requirement that the horizontal scale L of a layer thickness (mass) anomaly must exceed the rotation length scale, C/f, where C is the gravity wave speed dependent upon stratification. [33] Trajectories having larger E show a steeper descent of the slope, from Eqn. (110), $v_*/u_* = E$. It is important to note that friction is large or small depending upon the ratio r/f and not simply r alone. In other words, for a given r, frictional effects are greater at lower latitudes (smaller f). Very near the equator, E will thus be large for almost any r, and on that basis alone geostrophic motion would not be expected near the equator. Friction may be somewhat important in this regard, but a more comprehensive fluid model treated in Part 3 Sec. 3 shows that gravity wave dynamics is likely to be more important than is friction alone.

5.4 Energy balance

Energy balance makes a compact and sometimes useful diagnostic; it is compact since energy is a scalar vs. a vector momentum, and it is more or less useful depending mainly upon how well the dissipation processes may be evaluated. In this model problem, the energy source is the potential energy associated with the dense parcel sitting on a sloping bottom and we have the luxury of knowing the dissipation (bottom drag) exactly. As the parcel descends the slope, it will release potential energy and so generate kinetic energy and thus motion.

To find the energy balance equation, multiply the x-component momentum equation (105) by u_* and the y-component equation by v_* and add:

$$\frac{d(u_*^2+v_*^2)/2}{dt_*} \quad - v_* \quad = \quad -E(u_*^2+v_*^2). \tag{118}$$

The term on the left is the time rate change of kinetic energy; the term on the right of (118) is the rate of work by bottom friction, always negative since bottom friction opposes the velocity. The second term on the left is the rate of work by the buoyancy force (in nondimensional units), which is also the rate of change of potential energy. The dimensional potential energy is just $PE = g'(z-Z_0) = -g'\alpha(y-Y_0)$

[33] A subtle distinction between the present single parcel model result and the usual idea of geostrophy is that the single parcel model is Lagrangian, i.e., the dependent variables are the position and velocity of a specific parcel, not the velocity at a point in space as is implicit in Fig. 1, say, which is an Eulerian representation. These two representations merge only in the highly idealized case that all fields are spatially uniform.

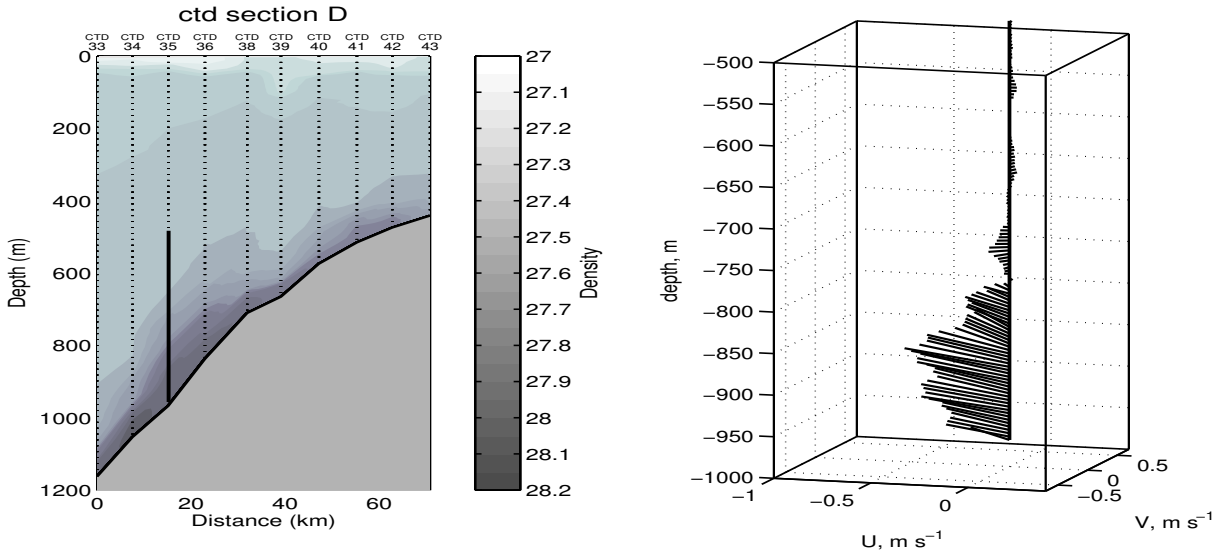

Figure 18: Observations of a dense bottom current, the Faroe Bank Channel Overflow, found on the southern flank of the Scotland-Iceland Ridge. **(left)** A section made across the current showing dense water that has come through the narrow Faroe Bank Channel (about 15 km width, at latitude 62 N and about 90 km to the northeast (upstream) of this site). This dense water will eventually settle into the deep North Atlantic where it makes up the Upper North Atlantic Deep Water. The units of density are kg m^{-3}, and 1000 has been subtracted away. By inspection of these data, the reduced gravity of the dense water is $g' = g\ \delta\rho/\rho_0 \approx g\ 0.5/1000 = 0.5\times10^{-2}$ m s^{-2}, and the bottom slope is roughly $\alpha = 1.3\times10^{-2}$. **(right)** A current profile measured at the thick vertical line shown on the density section. The density section was aligned normal to the isobaths and the current appeared to be flowing roughly along the isobaths. The core of the dense water has descended roughly 200 m between this site and the Faroe Bank Channel.

with Z_o the initial depth, and

$$v_* = \frac{vf}{g'\alpha} = -\frac{dz}{dt}\frac{f}{g'\alpha^2} = \frac{-dPE}{dt}\frac{1}{fU_{geo}^2} = \frac{-dPE_*}{dt_*},$$

the rate of change of potential energy in nondimensional units, fU_{geo}^2. It can be helpful to integrate (118) with time to compute the change in energy from the initial state:

$$\begin{array}{ccccccc} (u_*^2+v_*^2)/2 & - & \int_o^t v_* dt_* & = & - & \int_o^t E(u_*^2+v_*^2)dt_*, \\ KE & + & PE & = & & FW, \end{array} \tag{119}$$

where KE is the kinetic energy, PE is the change in potential energy as the parcel is displaced up and down the slope, and FW is the net frictional work done by the parcel, always a loss (Fig. 19).

The Coriolis force does no work on the parcel since it is perpendicular to the velocity, and hence does not appear directly in the energy balance. Rotation nevertheless has a profound effect on the

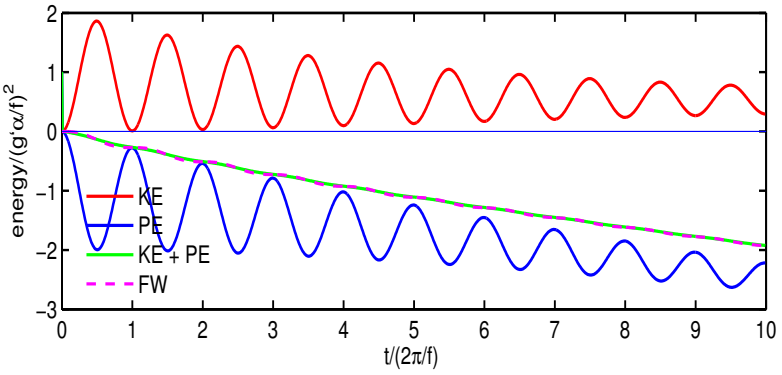

Figure 19: The energy balance for the trajectory of Fig. (16) having $E = 0.2$. These data are plotted in a nondimensional form in which the energy or work is normalized by the square of the velocity scale, $U_{geo} = g'\alpha/f$, and time is nondimensionalized by the inertial period, $2\pi/f$. Potential energy was assigned a zero at the initial depth of the parcel. Note the complementary inertial oscillations of PE and KE, and that the decrease of total energy was due to work against bottom friction (the solid green and dashed red lines that overlay one another).

energy balance. The inertial oscillations that carry the parcel up and down the slope show up in the energy balance as a reversible (aside from friction) interchange of kinetic and potential energy, exactly analogous to a simple pendulum. The most profund consequence of rotation is that it inhibits the release of potential energy. In the important limit that $E \to 0$, and aside from inertial motion, the parcel velocity will be perpendicular to the buoyancy force, as in Eqn. (117), and the parcel will coast along an isobath in steady, energy-conserving geostrophic motion. If there is some friction, as there is in the case shown, then the cross-isobath component of the motion carries the parcel to greater bottom depth and thus releases potential energy at a rate that is proportional to the Ekman number, Eqn. (107), $v_*/u_* = E = r/f$. Whether friction or rotation is dominant, and thus whether the motion is rapidly dissipated or long-lived, depends solely upon the Ekman number in this simplified system (Fig. 16b).

5.5 Problems

(1) Draw the vector force balance for inertial oscillations (include the acceleration) with and without bottom friction as in Fig. (16, right).

(2) What value of r is required to mimic the observed decay of near-inertial oscillations of Fig. (17)? Does the same model solution account also for the small, super-inertial frequency shift noted in the field data?

(3) Write the non-dimensional form of the pure inertial motion model and solution, Eqn. (114). This model is so reduced that there is, admittedly, not much to gain by nondimensionalizing Eqn. (111).

(4) The parcel displacement, Eq. (114), $\delta = U_o/f$ associated with an inertial motion goes as $1/f$, and hence $\delta \to \infty$ as $f \to 0$, i.e., as the latitude approaches the equator. We can be pretty sure that something will intervene to preclude infinite displacements. One possibility is that the north-south variation of f around the equator will become relevant as the displacement becomes large, i.e., the $f-$plane assumption that $\delta \ll R_E$ noted with Eqn. (87) will break down. Suppose that we keep the first order term in $f(y)$, and assume $f = \beta y$, i.e., an equatorial beta-plane. Describe the equatorial inertial oscillations of a parcel initially on the equator, and given an impulse U_o directed

toward the northeast. How about an impulse directed toward the northwest? You should find that these two cases will yield quite different trajectories. This is an example, of which we will see more in Part 2, of the anisotropy that arises from rotation and Earth's spherical shape.

(5) In Sec. 5.1 it was noted that dimensional analysis may be somewhat arbitrary, as there are usually several possible ways to nondimensionalize any given model. For example, in this parcel on a slope problem the time scale $1/r$ could be used to nondimensionalize (that is, to scale or measure) the time. How would this change the solution, Eqn. (108) and the family of trajectories?

(6) Assuming small Ekman number, how long does it take for a geostrophic balance to arise after a parcel is released? Are the time-averaged solutions of the single parcel model the solutions of the time-averaged model equations? Suppose the model equations were not linear, say that friction is $\propto U^2$, then what?

(7) Inertial oscillations do not contribute to the long-term displacement of the parcel, though they can dominate the instantaneous velocity. Can you find an initial condition on the parcel velocity that prevents these pesky inertial oscillations? You can test your ideas against solutions from partslope.m (Section 7).

(8) Explain in words why a geostrophic balance (or a near geostrophic balance) is expected in this problem, given only small enough E and sufficient space and time.

(9) Make a semi-quantitative test of geostrophic balance for the westerly wind belt seen in Fig. (2). Sample (by eye) the sea surface height of Fig. (1) along an east-west section at 33 ^{o}N, including at least a few points in the western boundary region. Then estimate the east-west profile of the inferred geostrophic current (and note that the buoyancy of the sea surface is effectively the full g since the density difference is between water and air). What is the current direction? Using this result as a guide, sketch the (approximate) large-scale pattern of surface geostrophic current over the subpolar gyre and lower subtropics on Fig. (1). You can check your result against observed surface currents, http://oceancurrents.rsmas.miami.edu/atlantic/florida.html

(10) Assuming that the descent of the dense water from Faroe Bank Channel to the site observed in (Fig. 18) was due mainly to bottom friction, which trajectory of Fig. (16) is analogous to this current? Said a little differently, what is the approximate Ekman number of this current?

(11) An important goal of this essay has been to understand geostrophic balance, the characteristic feature of many large scale geophysical flows. However, it has also been noted that pure geostrophy is a dead end insofar as it gives no clue to the origin or the evolution with time. To predict the evolution of a flow we have to understand what are usually small departures from pure geostrophy, here limited to time-dependence, e.g., inertial motion, and friction. With that in mind, compare the relative importance of friction in the time-average momentum balance, Fig. (16), right, and in the energy balance, Fig. (19).

(12) The Coriolis parameter, f, changes signs crossing the equator, and thus a northern hemisphere inertial motion turns clockwise in time, and a southern hemisphere inertial motion turns anticlockwise. You are in very good company if you are wondering ... 'What's it do right on the equator?' (see S. Adams, *It's Obvious You Won't Survive by Your Wits Alone*, p. 107, Andrews and McNeil Press, Kansas City, Kansas, 1995). By symmetry, the horizontal component of the Coriolis force must vanish right on the equator and hence the contrast between mid-latitude phenomena and equatorial phenomena is of great interest and taken up in the Part 3 essay. To start on this, how would you characterize the near-equatorial ($\pm$10 deg of latitude) wind and height

relationship of the 500 hPa winds evident in Fig. 2? You may find it helpful to see an animation of these charts available online at http://www.nrlmry.navy.mil/metoc/nogaps/.

6 Summary and Closing Remarks

6.1 What is the Coriolis force?

The winds and currents of Earth's atmosphere and oceans are necessarily observed and analyzed from the perspective of an Earth-attached and thus a rotating, non-inertial reference system. The inertial frame equation of motion transformed to a general rotating frame includes two terms due to the rotation, a centrifugal force term and a Coriolis term, $-2\mathbf{\Omega}\times\mathbf{V}'M$ (Section 2). There is nothing *ad hoc* or discretionary about the appearance of these terms in a rotating frame equation of motion. In the case of an Earth-attached frame, the centrifugal force is cancelled by the aspherical gravitational mass attraction associated with the slightly out of round shape of the Earth (Section 4). The Coriolis force remains, and is of first importance for large scale, low frequency winds and currents.

It is debatable what the Coriolis term should be called, whether a force as done here, or an acceleration. The latter is sensible insofar as the Coriolis force on a parcel is exactly proportional to the mass of the parcel, regardless of what the mass may be. This is a property shared with gravitational mass attraction, but not with central forces that arise from the physical interaction of objects. Nevertheless, we chose the Coriolis 'force' label, since we are especially concerned with the consequences of the Coriolis term.

Because the atmosphere and the oceans are thin when viewed in the large and also stably stratified, the horizontal component of winds and currents is generally much, much larger than is the vertical component. In place of the full three-dimensional Coriolis, it is usually sufficient to consider only the horizontal component acting upon the horizontal wind or ocean currents,

$$-2\mathbf{\Omega}\times\mathbf{V}' \approx -\mathbf{f}\times\mathbf{V}' = fv'\mathbf{e_x} - fu'\mathbf{e_y}$$

where $\mathbf{f} = f\mathbf{e_z}$, and

$$f = 2\Omega\sin(latitude)$$

is the Coriolis parameter, which will arise very, very often in a study of geophysical fluid dynamics.

6.2 Consequences of the Coriolis force for the circulation of the atmosphere and ocean

Here in Part 1 we have made a small start toward understanding the profound consequences of the Coriolis force with an analysis of a dense parcel released onto a slope (Section 5). This revealed two

kinds of motion that depend directly upon the Coriolis force. There is a free oscillation, usually called an inertial oscillation, in which an otherwise unforced current rotates at the inertial frequency, f. These inertial oscillations are a prominent phenomenon of the upper ocean current following the passage of a storm. A crucial, qualitative effect of rotation is that it makes possible a steady motion for which an external force (wind stress or geopotential gradient) is balanced by the Coriolis force acting upon a geostrophic current,

$$\mathbf{V}_{geo} = -\frac{g}{\rho_o f}\mathbf{k}\times\nabla\eta.$$

A characteristic of geostrophic motion is that the velocity is perpendicular to the applied force; in the northern hemisphere, high SSH is to the right of a geostrophic current (Fig.1). It would be easy to over-interpret the results from our little single parcel model, but, a correct inference is that Earth's rotation — by way of the Coriolis force — is a key to understanding the persistent, large scale circulation of both the atmosphere and the ocean (outside of equatorial regions).

6.3 What comes next?

This introduction to the Coriolis force continues in Parts 2, 3, 4 and 5 with an emphasis on the consequences of rotation for the atmosphere and ocean. Specific goals are to understand

Part 2: a rotating shallow water model, potential vorticity balance and geostrophic adjustment. What circumstances lead to a near geostrophic balance? As we have noted throughout this essay, a near geostrophic balance is almost inevitable for large scale, low frequency motions of the atmosphere or ocean. The essential piece of this is to define large scale and low frequency, which depends upon the stratification and the Coriolis parameter, f, and so varies substantially with latitude.

The plan/method of Part 2 is to construct a model of a single fluid layer, often called the shallow water model, and to conduct a sequence of initial value experiments that may or may not evolve into geostrophic balance. The potential vorticity of the initial state is a key diagnostic. The tools and methods introduced in Part 2 are thus a very considerable advance over those employed here in Part 1, and are more likely to be directly useful in your own research. Everything that you have learned in Part 1 regarding the Coriolis force acting on a single parcel will be essential background for understanding the more comprehensive models and experiments introduced in Part 2 and on.

Part 3: β-effects, and westward propagation. The single new feature introduced in Part 3 is the explicit recognition that the Coriolis parameter varies with latitude, in the beta-plane approximation, $f = f_o + \beta y$ with y the north coordinate. The resulting beta-effects includes some of the most interesting and important phenomena of geophysical flows — a pronounced east-west asymmetry in many large scale phenomenona, and westward propagation of eddies in the ocean and long waves in the westerlies (Fig. 2).

Part 4: wind-driven ocean circulation and the Sverdrup relation. The goals are to learn how the

Sverdrup relation is established following the onset of a wind field applied to an ocean basin, and to understand some important properties of the wind-driven, upper-ocean gyres, e.g., the marked east-west asymmetry.

Part 5: on the seasonally-varying wind-driven circulation of the Arabian Sea. This capstone project that brings together many of the results from the previous essays applied to the Arabian Sea. As the title implies, this is mostly oceanographic, though some details of the South Asia Monsoon winds are highly significant.

6.4 Supplementary material

Matlab scripts that will help you do the homework problems may be downloaded from https://www2.whoi.edu/staff/jprice/aCt-codes which includes the following:

rotation_1.m solves for the three-dimensional motion of a parcel as seen from an inertial and from a rotating reference frame. Used to make Fig. 11.

rotation_2.m solves for the inertial oscillation of a parcel moving freely on a rotating, parabolic surface so that centrifugal force is cancelled, and as seen from an inertial and from a rotating reference frame.

partslope.m solves for the motion of a single dense parcel on a slope and subject to buoyancy, bottom friction and Coriolis forces as in Section 5. It is easy to specify a new experiment by changing the initial velocity, bottom slope, etc.

sphere_check.m used to check the spherical system equations of motion, and useful as an introduction to spherical coordinates (Sec. 3.4).

Index

bottom friction, 53

central force, 7
centrifugal, 21
centripetal, 21
centripetal acceleration, 29
Coriolis force, 6
Coriolis force
    peculiar properties of, 24
    thin-fluid, horizontal only, 45
    three dimensional, cartesian, 45
Coriolis parameter, 45
    β-plane approximation, 46
    f-plane approximation, 46

Earth flatness, 43
Earth rotation rate, 22
Earth rotation vector, 9
Ekman number, 54

fixed stars and Mach's principal, 21
Foucault pendulum, DIY, 51

Galilean transformation, 8
geostrophic balance, 6
geostrophic motion
    near-geostrophic, 61
geostrophic motion , 60
geostrophic speed, 54

inertial force, 13
inertial motion, 35, **57**
    inertial oscillations, 58
    near-inertial oscillations, 60
    vortical inertial motion, 58
inertial reference frame, 7

large scale cicrculation, 6
level (horizontal) surface, 44

nondimensional variables, 54

plumb bob, 13
plumb line, 13
polar coordinates, 27

reduced gravity, 52
rotation time scale, 52

single parcel model, 6
spherical coordinates, 38

vector
    cross-product, 19
vector cross-product, 20
vector transformed, 17
vertical, 44

a Coriolis tutorial, Part 2:

a rotating shallow water model and geostrophic adjustment

James F. Price
Woods Hole Oceanographic Institution
Woods Hole, Massachusetts, 02543
https://www2.whoi.edu/staff/jprice/ jprice@whoi.edu

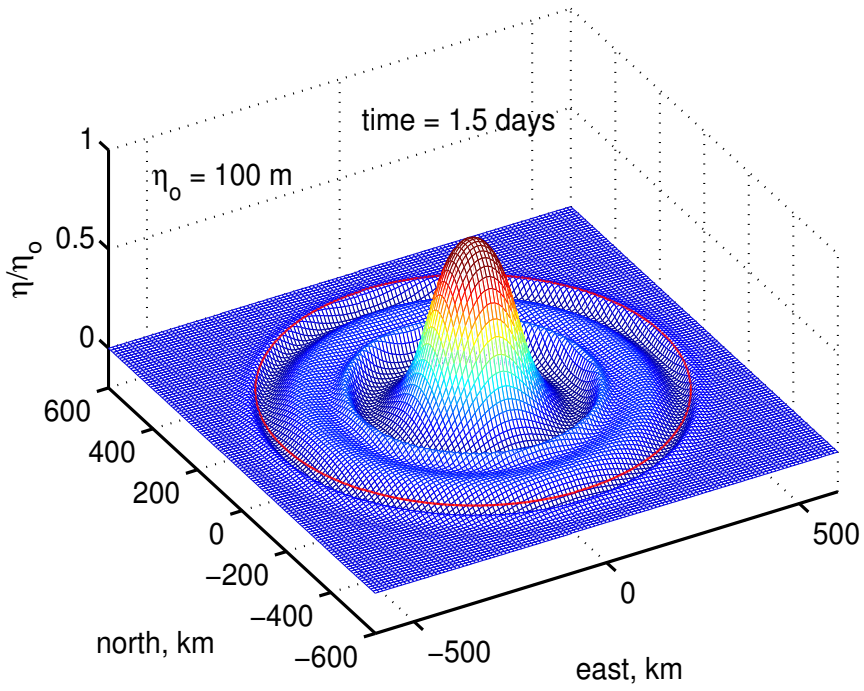

Figure 1: A snapshot taken 1.5 days after the start of a numerical experiment on geostrophic adjustment: a thickness anomaly of a dense fluid was released from rest onto an $f-$plane centered on 30^oN and allowed to evolve freely under the effects of gravity and rotation. The thickness anomaly slumps noticeably within the first half day, which excites inertia-gravity waves that expand isotropically. The leading edge propagates at the rate of a long, non-dispersive baroclinic gravity wave, roughly 275 km day^{-1} in this case. After about ten days the inertia-gravity wave radiation was largely completed, leaving most of the height anomaly seen here in a near geostrophic balance. An animation of this experiment is online at https://scienceweb.whoi.edu/PO/people/jprice/education/ga2d-h100-f.mp4 The goal of this Part 2 essay is to understand how the geostrophic adjustment process varies with the environment, the radius of the initial height anomaly, and the initial potential vorticity.

Abstract: This is the second of a four-part introduction to the effects of Earth's rotation on the fluid dynamics of the atmosphere and ocean. Part 1 derived the Coriolis force, $\propto -f\mathbf{k}\times\mathbf{V}$, where f is the Coriolis parameter, $\mathbf{k}$ is the vertical unit vector, and $\mathbf{V}$ is horizontal wind or current, and went on to analyze some of its basic properties in the context of a very simple, single parcel model. The goal and plan of this Part 2 is to develop further insight into the consequences of the Coriolis force by analyzing a sequence of experiments in which a thickness anomaly of horizontal scale L is released from rest and allowed to evolve under the influence of gravity and the Coriolis force. These geostrophic adjustment experiments are posed in a single layer fluid model, often called the shallow water model.

The initial gravitational slumping produces gravity waves (see the cover graphic). If there is no rotation, i.e., if $f = 0$, gravity waves will disperse the mass anomaly in a time L/C, where C is the gravity wave phase speed. When rotation is present, and if L exceeds several times the radius of deformation, $R_d = C/f$, and assuming that the eddy has a potential vorticity anomaly, then the Coriolis force will arrest the gravitational slumping and yield a geostrophically balanced eddy, an anti-cyclone if the thickness anomaly was a mass excess (high pressure). If f is presumed to be constant and if there is no friction, then a geostrophically balanced eddy could be exactly steady. Curvature effects on a two-dimensional eddy are measured by the Rossby number, U/fL, with U the azimuthal current. If the Rossby number is appreciable, then the actual, balanced current will exceed the geostrophic current in the case of an anticyclone.

These and other low frequency phenomenon are often best interpreted in the context of potential vorticity conservation, the geophysical fluid equivalent of angular momentum conservation. Earth's rotation contributes planetary vorticity = f, that is generally considerably larger than the relative vorticity of winds and currents. Small changes in the thickness of a fluid column may thus cause significant changes in the relative vorticity of winds and currents.

Contents

1 Large-scale flows of the atmosphere and ocean **4**

1.1 The goal, and a plan to investigate the adjustment to geostrophic balance 4

1.2 Recurring themes 5

2 A shallow water model **7**

2.1 Conservation equations of an ideal fluid layer 9

2.1.1 Mass Conservation 9

2.1.2 Momentum conservation 11

2.2 Shallow water model compared to a single parcel model . . . 13
2.3 Solving and diagnosing the shallow water system . . . 15
2.3.1 Wave velocities and fluid velocities . . . 15
2.3.2 Energy balance . . . 17
2.3.3 Potential vorticity balance . . . 18
2.3.4 Finite amplitude effects . . . 23
2.4 Boundary and initial conditions define the problem . . . 24
2.5 Appendix to Sec. 2: Normal modes of a two layer model ocean . . . 25
2.5.1 Barotropic mode . . . 28
2.5.2 Baroclinic mode . . . 31
2.5.3 Reduced gravity approximation of the baroclinic mode . . . 32
2.6 Problems . . . 32

3 Gravitational adjustment **35**
3.1 Just gravity waves . . . 35
3.2 An exact solution of the linear, one-dimensional wave equation . . . 37
3.3 The choice of scales . . . 38
3.4 Energy and potential vorticity balances . . . 39
3.5 Finer details of the solution; finite amplitude effects . . . 40
3.6 Problems . . . 42

4 Geostrophic adjustment on an f-plane **43**
4.1 Dispersion relation for waves on an f-plane . . . 43
4.2 Intrinsic scales of the f-plane . . . 46
4.3 Gravity, inertial and geostrophic motions . . . 47
4.4 The steady state inferred from potential vorticity conservation . . . 50
4.5 If there is no potential vorticity anomaly . . . 54
4.6 Problems . . . 55

5 In two horizontal dimensions **56**
5.1 Adjustment is not greatly altered by the additional dimension . . . 56
5.2 Curvature and Rossby number . . . 56
5.3 Problems . . . 61

6 Closing remarks **62**
6.1 Summary of Part 2 . . . 62

6.2 What comes next? 63
6.3 Supplementary material 63
Index 65

1 Large-scale flows of the atmosphere and ocean

This essay continues a four-part introduction to fluid dynamics on a rotating Earth. It is written for students who have some preparation in classical dynamics and applied mathematics and who are beginning a quantitative study of geophysical fluid dynamics. Part 1 examined the origin and the fundamental properties of the Coriolis force, and went on to consider a few of its consequences in the context of a single parcel model. The Coriolis force, often called simply 'rotation', admits two new modes of motion, a free oscillation usually called an inertial oscillation, and if there is a steady or time-mean external force, a steady or time-mean motion that is an analogue of geostrophic motion in the atmosphere and ocean.

1.1 The goal, and a plan to investigate the adjustment to geostrophic balance

The broad goal of this Part 2 is to develop insight for one of the most profound consequences of rotation, and specifically: **What circumstances lead to geostrophic balance?** It was noted in Part 1 that geostrophy was characteristic of most large scale and low frequency circulation, and now it is time to flesh out what we mean by 'large scale and low frequency' and to observe in some detail how geostrophy arises.

The plan is to solve and analyze a sequence of experiments in which a mass anomaly is released and allowed to evolve freely under the influence of gravity and rotation: gravity alone in Section 3, and gravity and rotation together in Section 4. As we will see first in Sec. 4, a nearly steady, nearly geostrophic state will arise spontaneously, provided that the mass anomaly has a sufficiently large horizontal scale, about 100 kilometers or greater at mid-latitudes. On the other hand, mass anomalies having a smaller horizontal scale, or having an initial current field that is characteristic of a gravity wave, will be dispersed into gravity waves. The essential results may be developed in a one-dimensional

domain, which makes it especially easy to conduct new experiments. However, oceanic and atmospheric eddies are more nearly circular than linear in plan view (Fig. 2) and will be modified somewhat by flow curvature, considered in Section 5. Results are summarized in Section 6, which then takes a look ahead to new phenomena that arise when the spatial variation of f is acknowledged.

1.2 Recurring themes

The discussion of the geostrophic adjustment experiments coming next will be based upon four noteworthy topics and themes that you will encounter over and over again in your study of the atmosphere and ocean:

Wave Dynamics As previewed in the cover graphic, many of the phenomena that arise in these experiments are wave-like. There are gravity waves that are more or less modified by rotation depending upon their wavelength and f, and nearly geostrophic eddies[1] that may also exhibit wave-like propagation (when the β-effect is included in Part 3). The language and concepts appropriate to waves — dispersion relations, phase speed, group speed — are thus very useful for describing the phenomena that arise in the these experiments.

Potential Vorticity Balance The dynamics of low frequency, quasi-geostrophic atmospheric and oceanic phenomena is revealed most effectively by analyzing the balance of potential vorticity, essentially the angular momentum of a rotating fluid, Sec. 2.2.3, rather than by the balance of linear momentum, which was all that was possible for the point-like parcel of Part 1. This use of potential vorticity balance was introduced by Rossby and colleagues in the 1930s[2] and remains an invaluable tool for the analysis and prediction of large scale and low frequency geophysical flows. Potential vorticity balance will be a central theme here and in Part 3.

Linear and Nonlinear, Finite Amplitude Waves that arise in linear systems, or in the limit that amplitude goes to zero in the solution of a nonlinear system, will have the most accessible description, e.g., by way of a dispersion relation. On the other hand, many geophysical phenomenon have an amplitude large enough that linear dynamics would not seem to be valid. Nevertheless, linear theory will generally be the starting point for an analyses that may then go on to include finite amplitude effects by way of more comprehensive (numerical) solution methods.

[1]The term 'eddy' is widely used in fluid dynamics, and with a wide range of meanings. Here eddy means a flow feature having a more or less circular planform, but with no particular dynamics or time-dependence implied. To characterize a movement as 'propagation' is suggestive of wave propagation, which is intended.

[2]Much of the pioneering research on the topics discussed in this essay appeared in a series of classic papers by Carl G. Rossby and colleagues published in the late 1930s. A scientific biography of Rossby and a bibliography of his classic papers is avilable at http://www.nasonline.org/publications/biographical-memoirs/memoir-pdfs/rossby-carl-gustaf.pdf

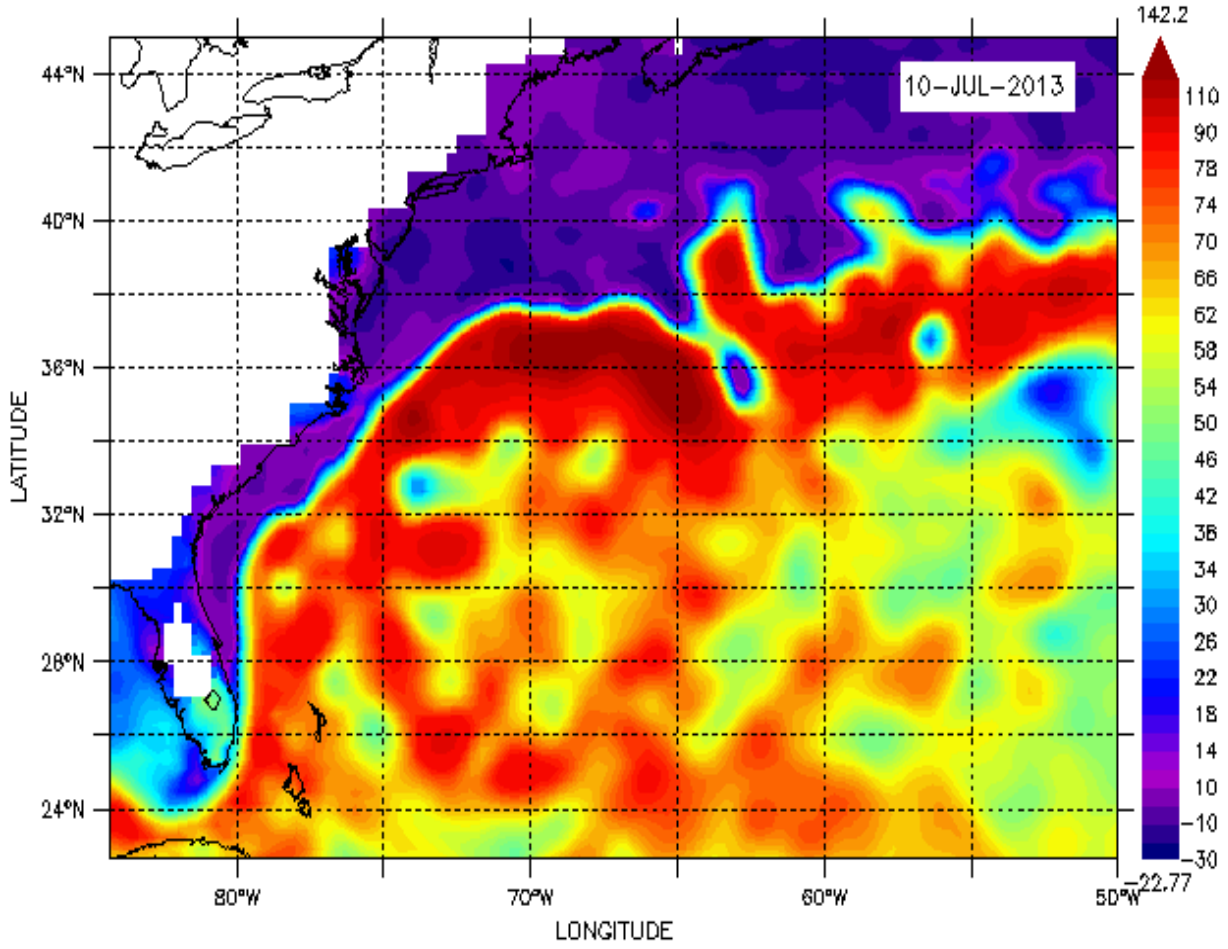

Figure 2: A snapshot of sea surface height, SSH, over the North Atlantic ocean from July, 2013 (thanks to the Aviso project, https://www.aviso.altimetry.fr/en/home.htm). Compared with the year-long mean of Fig. (1), Part 1, this field shows considerable variability on scales of several hundred kilometers, often termed the oceanic mesoscale (*meso* is Greek for middle) especially in subtropical and higher latitudes. These mesoscale eddies persist as identifiable features for many weeks or months and have an SSH amplitude of about $\pm$ 0.1 m. The corresponding thermocline displacements are about $\pm$ 50 m (not evident in this figure). The specific goal of this essay is to understand how Earth's rotation makes possible long-lived eddies of this kind.

Numerical Models and Solutions The shallow water system used here is kept as simple as possible but is nevertheless nonlinear, as are all more or less complete fluid models. Solving this nonlinear system, even for an idealized problem, usually requires more than just pencil and paper, *viz.*, a numerical code or model that serves to time-step a finite difference representation of the shallow water equations. In this and in many other ways, numerical models are an essential part of atmospheric and oceanic science, and for example, nearly all of the PhD students in the MIT/WHOI Joint Program (Physical Oceanography) use numerical models during their thesis research. For many of these students, that is also their first, hands-on experience. An implicit goal of this essay is to introduce some aspects of the practice of numerical modelling, especially hypothesis testing and solution interpretation. To that end, some of the homework assignments suggested here will require the generation of new numerical solutions. Source codes that are directly applicable to these problems are available on an anonymous ftp site linked in Sec. 6.3. By introducing some of the methods (and limitations) of numerical research, this essay is intended to supplement the excellent GFD texts available today by, among others, Cushman-Roisin, Gill and Pedlosky, that treat many of the same gesotrophic adjustment problems via mainly analytic solution methods.[3]

2 A shallow water model

This section derives the shallow water model, the conservation equations appropriate to a single fluid layer that varies in the horizontal, (x,y), but not in the vertical, z.[4] This layer is presumed to have a nominal thickness, H (Fig. 3). The vertical displacement of the upper surface (relative to a level surface) is $\eta(x,y,t)$ and will vary with horizontal position and with time. The thickness of the layer is thus imn general, $h(x,y,t) = H + b(x,y) + \eta(x,y,t)$ with b the variable lower boundary of the layer, or the sea floor. In this essay, only the case $b = 0$ (flat bottom) will be considered. The fluid above is presumed to be at rest, and to have a uniform density ρ_o, and pressure, P_a, that is uniform horizontally. The fluid within the lower layer has a greater density than the fluid above, $\rho_o + \delta\rho$ where $\delta\rho$ is a specified constant noted below.

Compared with the single parcel model of Part 1, this single layer model is a very big step toward a

[3] An introduction to geophysical fluid dynamics at about the level of this essay is by B. Cushman-Roisin, *Introduction to Geophysical Fluid Dynamics* (Prentice Hall, Engelwood Cliffs, New Jersey, 1994). Somewhat more advanced and highly recommended for the topic of geostrophic adjustment is A. E. Gill, *Atmosphere-Ocean Dynamics* (Academic Press, NY, 1982) and for waves generally, J. Pedlosky, *Waves in the Ocean and Atmosphere* (Springer, 2003).

[4] You may have noticed that this is a lengthy and mathematically dense section, and if so, the little voice in your head may be asking ... *do we really have to know all of this?* This is essential background for understanding the shallow water model and I hope that you will be sufficiently motivated to work through this material some day. If you are not ready for that task now, then jump ahead to Section 3 where discussion of the experiments begins in earnest.

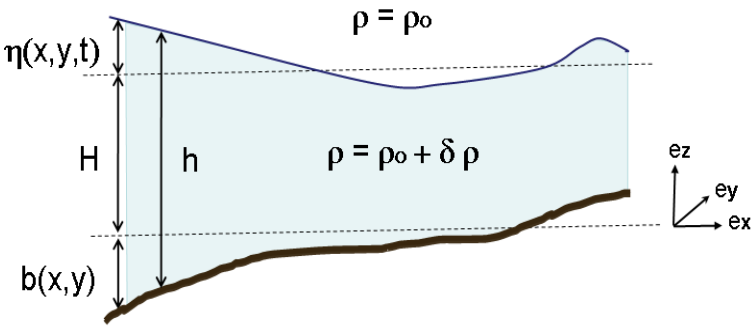

Figure 3: Schematic of a single fluid layer (light blue) sitting on a variable-depth lower, solid boundary, e.g., the sea floor. The horizontal dashed lines are level surfaces (perpendicular to gravity). This layer could be a homogeneous ocean, in which case the fluid above is the atmosphere and $\delta\rho \gg \rho_o$. In that case η is the displacement of the sea surface (as in Figs. 1 and 2). Or, it could be a relatively dense layer within a stratified ocean, in which case the fluid above is just slightly less dense, $\delta\rho \ll \rho_o$, and η is the displacement of a density surface. In either case, it is presumed that the fluid above the active layer does not impose a horizontally-varying pressure upon the active layer.

realistic model of the atmosphere or ocean. There are, however, two important idealizations and simplifcations that facilitate both the solution and its analysis, though at the expense of generality.

Single layer. The horizontal velocity $\mathbf{V}$ is implicitly depth-independent since it is represented by a two component vector field i.e., $\mathbf{V}(x,y,t) = [u(x,y,t), v(x,y,t)]$, vs. the true three-dimensional $\mathbf{V}(x,y,z,t)$, a bigger help than it may first appear. For this neglect of vertical structure to be a valid approximation, the nominal layer thickness, H, must be somewhat less than the horizontal scale of the motion. A single layer model of this kind is often and appropriately termed a shallow water model, even when H is taken to be the full depth of the ocean. The most convincing justification for the shallow water model comes from the analysis of a two layer model that includes both external (barotropic) and internal (baroclinic) normal modes (see the appendix to this section). The two layer model makes clear that a shallow water model is appropriate to a study of either barotropic or baroclinic normal modes, but not both at once. This is not a significant shortcoming given the broad goal of this study and, moreover, it wouldn't matter which normal mode was chosen. But given that a specific goal is to model the oceanic mesoscale eddies seen in Fig. 2, then as nominal values, $H = 500$ m and $\delta\rho = 2$ kg m^{-3}, are appropriate to the baroclinic motions of the ocean's main thermocline. Ocean mesoscale eddies have a radius $L \approx 100$ km, and hence this layer thickness is indeed 'shallow' in the sense that $H/L \ll 1$.

It is notable that oceanic eddies are mainly upper ocean phenomenon, i.e., strongest above the

main thermocline. They certainly are not resting on the sea floor, as the layer of Fig. (3) seems to be doing. The reduced gravity approximation discussed in Sec. 2.4 shows that such a single layer model will be most appropriate provided that the gravity wave speed of the model is made equal to the gravity wave speed of the baroclinic eddies of interest (and the sea floor is taken to be flat).

If the intent was to utilize the shallow water model to make a realistic simulation of a given, observed flow phenomenon, then three additional approximations or simplifications would have to be valid: 1) that the initial state was free of vertical shear, $\partial \mathbf{V}/\partial z = 0$, 2) that the fluid of interest was outside of frictional boundary layers, and 3) that the horizontal density variation within the layer was effectively zero. Most real geophysical flows violate all three of these conditions to some degree, especially 1) and 3). A realistic simulation is likely to require greater resolution in the vertical, e.g., some number of shallow layers stacked one on top of another to represent vertical shear, boundary layers, stratification, etc. However, consistent with the inductive method laid down in Part 1, one layer will be sufficient for now.

Ideal fluid. The physical processes allowed into this model are those of an ideal fluid, *viz.*, pressure and pressure horizontal variations, and transport by the fluid flow. The wide range of physical processes associated with the thermodynamic properties of a real fluid, e.g., compressibility, diffusion and viscosity, are omitted. This too may seem a bit high-handed, but is consistent with building the simplest model that will help us understand some of the consequences of Earth's rotation.

2.1 Conservation equations of an ideal fluid layer

2.1.1 Mass Conservation

The starting point is the assertion that mass (volume, really, since density is presumed constant) can be neither created nor destroyed by classical fluid dynamical processes. The positive assertion of this is that the mass of the layer at a given point can change only by virtue of mass fluxes associated with the (horizontal) fluid velocity within the layer. This is oftentimes referred to as the continuity requirement.

To find the corresponding mathematical form of this physical assumption, the mass balance will be evaluated over a control volume that spans the full thickness of the layer, Fig. (4). The mass of the layer contained within the control volume is

$$M = \rho \bar{h} dc, \tag{1}$$

where ρ is the constant density within the layer, and $\bar{h}$ is the average thickness over the interval x to $x+d$ and c is the width (the dimension into the page). The mass flux due to fluid flow through a given

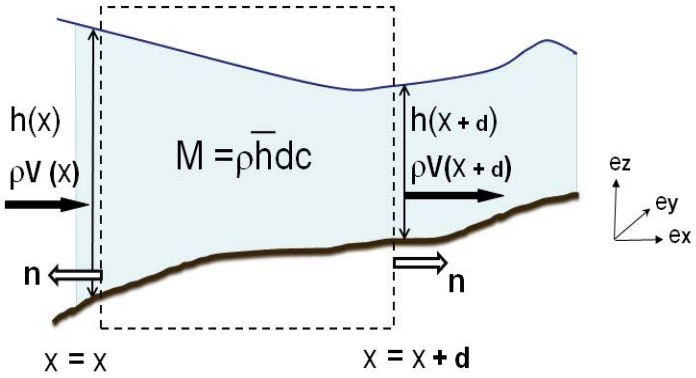

Figure 4: A control volume defined by thin dashed lines. The average thickness is $\bar{h}$, the length is d, and the width in the y-direction is c (y is normal to the page and is not shown). The statement of mass conservation appropriate to the problems considered here is that the mass of the active layer within the control volume, M, can change only because of mass fluxes due to fluid flow normal to the sides of the control volume, $-\rho A\mathbf{V}\cdot n$, where A is the area. The layer thickness variation shown here is exaggerated; changes of layer thickness of even a few percent can be significant.

surface of area A is just

$$\text{mass flux} = -\rho A\mathbf{V}\cdot\mathbf{n}, \tag{2}$$

where $\mathbf{n}$ is the outward unit normal of the surface. For the left-facing side of the control volume in Fig. (4), $\mathbf{n} = (-1,0,0)$ and the mass flux = ρhcu, where u is the x-component of the fluid velocity and hc is the area. These are evaluated at the x of the left-facing side. Noting that the unit normal on the right-facing side at $x+d$ is $\mathbf{n} = (1,0,0)$, then the sum of the mass fluxes through both x-facing sides is

$$\frac{\partial M}{\partial t} = \rho(h(x)u(x) - h(x+d)u(x+d))c. \tag{3}$$

By our construction of mass conservation, this net mass flux is equal to the time rate of change of mass within the control volume. The mass $M(x,y,t)$ varies with position and time, but notice that the time derivative of (3) is a partial derivative, since M is the mass of a control volume that is fixed in space. Inserting the definition of M, and dividing through by ρ, c and d gives

$$\frac{\partial \bar{h}}{\partial t} = \frac{1}{d}(h(x)u(x) - h(x+d)u(x+d)).$$

Now let d go to zero, and the right-hand side also becomes a partial derivative

$$\frac{\partial h}{\partial t} = -\frac{\partial (hu)}{\partial x}, \tag{4}$$

the one-dimensional, differential statement of mass conservation (though since the constant density and area are divided out, the units are length per time). Thus, the mass inside the control volume will change if and only if there is a *divergence* of the mass flux associated with the fluid flow; the mass flux alone is not relevant insofar as the M at a given position is concerned. Had variations in the y-direction (normal to the page) been considered, then there would arise an additional term, $-\partial(hv)/\partial y$, and the two-dimensional form of mass conservation for a shallow water model is

$$\frac{\partial h}{\partial t} = -\left(\frac{\partial (hu)}{\partial x} + \frac{\partial (hv)}{\partial y}\right) \tag{5}$$

$$= -\nabla\cdot(h\mathbf{V}). \tag{6}$$

This way of writing mass conservation is sometime said to be the flux form or conservative form, and is generally preferred for implementation in a numerical model. For purposes other than numerical integration it may be useful to expand the divergence operator and combine the partial time derivative and the advection term into the material derivative,

$$\frac{D(\ )}{Dt} \equiv \frac{\partial(\ )}{\partial t} + u\frac{\partial(\ )}{\partial x} + v\frac{\partial(\ )}{\partial y}, \tag{7}$$

about which more below. The mass balance (thickness balance) written using the material derivative is

$$\frac{Dh}{Dt} = \frac{\partial h}{\partial t} + u\frac{\partial h}{\partial x} + v\frac{\partial h}{\partial y} = -h\left(\frac{\partial u}{\partial x} + \frac{\partial v}{\partial y}\right). \tag{8}$$

2.1.2 Momentum conservation

At a given point, the momentum of the layer $\rho h\mathbf{V}$, can change only by the relative few prescribed processes, by momentum fluxes associated with the fluid velocity, by pressure variations, and by the Coriolis force, an inertial force that acts throughout the body of the fluid. There may also be an external force, $\mathbf{F}$, (not to be confused with the lower case f) that acts as a stress, a tangential force per area on the upper or lower boundaries.

Momentum flux by the flow. The x component of momentum (per unit area) is ρhu, and the momentum flux due to the x-component of the velocity is just

$$\text{momentum flux by the flow } = \rho hu^2,$$

which, notice, is proportional to kinetic energy.

Hydrostatic pressure and pressure flux. The phenomena of interest here are somewhat slowly varying, and the accelerations of the fluid are much, much less than the acceleration of gravity,

$$\frac{\partial^2 h}{\partial t^2} \ll g.$$

In that case the vertical component of momentum balance is the hydrostatic pressure relation,

$$\frac{\partial p}{\partial z} = -g\rho,$$

and the hydrostatic pressure within the layer ($z < h$) is

$$P(x,y,z) = P_a(z) - g\rho_o z + g\delta\rho(h(x,y,t) - z). \tag{9}$$

Thus the horizontally-varying pressure in this model is due solely to variation in the mass field, i.e., the layer thickness. $P_a(z)$ is the z-dependent but horizontally uniform pressure in the fluid above the active layer and the second term on the right is the hydrostatic pressure due to the constant density ρ_o. Neither of these z-dependent terms contribute to horizontally-varying momentum fluxes and may be ignored in what follows. The third term represents the pressure anomaly associated with the horizontally-varying layer thickness, h and notice that a relatively large layer thickness indicates a high pressure anomaly within the layer. The momentum flux due to the anomaly of hydrostatic pressure on an x-facing side of the control volume having width c is then

$$\text{pressure flux } = g\delta\rho c \int_0^h (h-z)dz \;=\; g\delta\rho c\frac{h^2}{2}.$$

The momentum flux. Summing these two terms gives the x-component momentum flux on an x-facing side of the control volume,

$$\text{momentum flux } \;=\; \rho chu^2 + g\delta\rho c\frac{h^2}{2}. \tag{10}$$

The first term on the right is the flux of u-momentum due to the u-component of the velocity and so is proportional to u^2, and the second term is the layer-averaged anomaly of the hydrostatic pressure $\propto h/2$ acting over the face of the control volume, ch. When the body force due to the Coriolis force is included, $-\mathbf{f}\times\mathbf{V} = (fv, -fu)$, and when the operations noted above to go from Eqn. (3) to Eqn. (6) are repeated here, the conservative (or flux) form of the shallow water momentum (per mass $\times$ area) equations are

$$\frac{\partial(hu)}{\partial t} = -\frac{\partial(huv)}{\partial y} - \frac{\partial(hu^2 + \frac{1}{2}g'h^2)}{\partial x} + fhv + F_x, \tag{11}$$

$$\frac{\partial(hv)}{\partial t} = -\frac{\partial(huv)}{\partial x} - \frac{\partial(hv^2 + \frac{1}{2}g'h^2)}{\partial y} - fhu + F_y, \tag{12}$$

where $g' = g\delta\rho/\rho$ is the reduced gravity (also buoyancy per unit volume). If the upper surface of the layer is the sea surface, then $\delta\rho \approx \rho$, and $g' \approx g$; if the upper surface is within the comparatively weakly stratified ocean, then $\delta\rho \ll \rho$ and so $g' \ll g$.

The external force shown here as $\mathbf{F} = (F_x,\ F_y)$ could represent wind stress, in which case we would probably say that $\mathbf{F} = \mathbf{F}(x,y)$ is a specified function of space only. Or, it could represent a bottom drag, in which case $\mathbf{F} \propto -r\mathbf{V}$ as in the single parcel model of Part 1. Notice that F must have dimensions of force/mass, though it will be referred to as 'force'. Our main interest is what the fluid flow does, rather than $\mathbf{F}$, and so unless it is noted otherwise, presume that $\mathbf{F}$ vanishes.

The shallow water mass and momentum balances written using the material derivative are then (repeating Eqn. 8),

$$\frac{Dh}{Dt} = \frac{\partial h}{\partial t} + u\frac{\partial h}{\partial x} + v\frac{\partial h}{\partial y} = -h\left(\frac{\partial u}{\partial x} + \frac{\partial v}{\partial y}\right), \tag{13}$$

$$\frac{Du}{Dt} = \frac{\partial u}{\partial t} + u\frac{\partial u}{\partial x} + v\frac{\partial u}{\partial y} = -g'\frac{\partial h}{\partial x} + fv + \frac{F_x}{h}, \tag{14}$$

$$\frac{Dv}{Dt} = \frac{\partial v}{\partial t} + u\frac{\partial v}{\partial x} + v\frac{\partial v}{\partial y} = -g'\frac{\partial h}{\partial y} - fu + \frac{F_y}{h}. \tag{15}$$

The vector equivalents are

$$\boxed{\frac{Dh}{Dt} = \frac{\partial h}{\partial t} + \mathbf{V}\cdot\nabla h = -h\nabla\cdot\mathbf{V}} \tag{16}$$

$$\boxed{\frac{D\mathbf{V}}{Dt} = \frac{\partial \mathbf{V}}{\partial t} + \mathbf{V}\cdot\nabla\mathbf{V} = -g'\nabla h - f\mathbf{k}\times\mathbf{V} + \frac{\mathbf{F}}{h}} \tag{17}$$

The Coriolis force is written in the usual form, i.e., the horizontal component only. Moreover, here in Part 2, f will be taken as a constant, though we know that f varies with latitude. This choice to employ a constant f, or f-plane model, is purely for simplicity and convenience. Once we learn some of the consequences of a constant f here in Part 2, then in Parts 3 and 4 we can go on to learn the surprising and important consequences of f(latitude).

2.2 Shallow water model compared to a single parcel model

The shallow water model equations (16) and (17) define a complete if somewhat simplified model of an idealized, two-dimensionally varying fluid. Before plunging into their solutions it is useful to consider how these shallow water equations compare with the equation of motion appropriate to the single *parcel*

of Part 1, Sec. 5 (repeated here but omitting the bottom friction term from the latter and ignoring **F** of the former),

$$\frac{d\mathbf{V}}{dt} = \; g'\nabla b - f\mathbf{k}\times\mathbf{V}.$$

1) The Coriolis terms are identical in the two systems. The Coriolis force is an inertial force that depends solely upon the fluid velocity relative to the rotation vector, and makes no distinction of the physical properties of the material. And, of course, absent that fundamental property, it would not have been appropriate to use a single parcel model as the starting point in Part 1.

2) The pressure gradient term of the shallow water model, $-g'\nabla h$, has the form of the buoyancy force on a dense parcel sitting on a slope, $g'\nabla b$ (sign aside). A crucial difference is that the bottom slope of the single parcel model is prescribed and fixed, while the gradient of layer thickness in the shallow water model is a dependent variable, dependent upon space and time via the mass balance, Eqn. (16). Mass balance has no counterpart in the single parcel model. In an ideal fluid model such as this one, the variable pressure is the only way that a fluid parcel interacts with the rest of the fluid domain. For example, if fluid begins to pile up (converge) at a given location, then the layer thickness and the hydrostatic pressure will go up until the pressure gradient is sufficient to push fluid away from that location. The rate at which the fluid responds to a convergence determines the speed of gravity wave propagation (Sec. 3.1).

3) The time derivatives have quite different meanings implicit in the use of different symbols: the ordinary time derivative d/dt of the single parcel model is the time rate change of a specific, material parcel, which in a fluid dynamics context would often be termed a Lagrangian coordinate system. Different parcels have different initial conditions and subsequent forcing, and to solve for a fluid flow requires solving for many such (interacting) parcels. The material derivative D/Dt of the present shallow water model is equal to the time rate of change following a moving parcel at the instant the parcel is coincident with the spatial position where D/Dt is evaluated. The independent coordinates of our shallow water model are fixed spatial coordinates and time, which in fluid dynamics is often referred to as an Eulerian coordinate system. The fluid present at a fixed location changes due in part to the fluid flow via the advection process represented by the term $\mathbf{V}\cdot\nabla(\;)$. Advection is the product of two dependent variables, velocity times thickness gradient in Eqn. (16) or velocity times the velocity gradient in Eqn. (17) and so is nonlinear. Advection and this associated nonlinearity are right at the heart of fluid dynamics and are a significant reason why numerical methods and numerical models are essential tools of atmospheric and oceanic sciences.

2.3 Solving and diagnosing the shallow water system

Equations (16) - (35) are a coupled set of nonlinear, partial differential equations in three dependent variables, the two components of the horizontal velocity, $\mathbf{V} = (u,\ v)$, and the thickness, h. The parameters g and $\delta\rho$ are constants for any given problem, and the Coriolis parameter f is at most a specified function of the north-south coordinate, y, about which much more below.

The shallow water model is nonlinear because of the advection terms of the material derivative noted above, e.g., the east-west advection of north-south momentum is $u\ \partial v/\partial x$, which is the product of two dependent variables. Solutions of a shallow water system including these nonlinear terms are necessarily generated by numerical methods: the one-dimensional experiments shown here were solved by the Matlab script geoadj_1d.m, and the two-dimensional experiments by the Fortran code geoadj_2d.for, both of which are linked in Sec. 6.3.[5] In common with any numerical model, these models produce (putative) solutions in the form of very large data files, $u(x_i, y_i, t_j), v(x_i, y_i, t_j)$..., where x_i, t_i are discretized position and time. To verify that this mass of data is faithful to the model equations and to the boundary/initial conditions, and then to go on and learn something useful requires as much thought and effort as does generating the model and solution in the first place. To wit, we will seek to 1) construct useful visualizations of the solutions (this can be the artful side of numerical modelling), 2) diagnose the balances of energy and potential vorticity, 3) interpret the wave-like properties of the solution using the dispersion relation of the corresponding, linearized system, and then 4) form and test hypotheses regarding parameter dependence by conducting further numerical experiments (that will be the homework, actually).

2.3.1 Wave velocities and fluid velocities

A qualitative difference between a shallow water model and the single parcel model of Part 1 is that a shallow water model supports wave motions — relatively fast-moving gravity waves will arise in all of our experiments, and much lower frequency Rossby waves will arise when there is a north-south variation of f (deferred to Part 3). If the layer thickness anomaly is a simple harmonic motion varying with x and t only, $\eta(x,t) \propto \eta_o sin(kx - \omega t)$, then a constant phase propagates at the rate of the

$$\text{wave phase speed,}\ \ C_p = \frac{\omega}{k}, \tag{18}$$

where wave frequency is $\omega = 2\pi/(\text{wave period})$, or waves per time, and the wavenumber is $k = 2\pi/(\text{wave length})$, or waves per space interval. This wave propagation velocity is often readily

[5] The details of the numerical methods are all-important in setting the efficiency and the accuracy of the solutions, but not something that will be discussed here. An excellent, concise reference on numerical methods suitable for the shallow water model is https://www.mathworks.com/company/newsletters/articles/introducing-cleves-laboratory and look for waterwave

apparent (as in the cover graphic). In many cases the thickness anomaly will be the result of a superposition of waves, i.e., waves of different wave numbers and frequencies, and in that case the envelope of the superposition will move at the

$$\text{wave group speed, } C_g = \frac{\partial \omega}{\partial k}, \tag{19}$$

This makes clear that the dispersion relation, $\omega(k)$, is going to be very important. The dispersion relation is determined by the physics of the wave medium, specifically the relationship of restoring force to wavelength. This differs greatly between pure gravity waves (Sec. 3.1), gravity waves in the presence of rotation (Sec. 3.2), and Rossby waves (Part 3). The motion of the fluid is, in general, qualitatively different from the phase speed of waves that may be propagating through the fluid. Fluid velocity is usually much less than the gravity wave speed and is often much greater than the Rossby wave speed (Rossby waves in Part 3). To see the fluid motion one can simply plot the field of the instantaneous velocity vectors, which shows the

$$\text{Eulerian fluid velocity : } \mathbf{V}(x_i, y_i, t_j) = (u(x_i, y_i, t_j), v(x_i, y_i, t_j)), \tag{20}$$

at the fixed positions (x_i, y_i) and the times, t_j. This Eulerian velocity field is the direct output of the numerical model, useful in itself, and the starting point for much else. The fluid velocity is generally proportional to the amplitude of the motion; in the problems discussed here, $V \propto \eta_o$, where η_o is the initial interface displacement. Wave speeds, on the other hand, are independent of amplitude in linear approximation, and generally only weakly dependent upon amplitude in nonlinear models (more on this below).

To see the transport of fluid over a long term we can compute the evolution of a passive tracer, say s, that is carried along with the flow without in any way altering the flow. This tracer may be embedded in the fluid at the starting time, $s_o = s(x, y, t_o)$ in any way that will serve to highlight the features of interest. This tracer is then presumed to be conserved following the flow,

$$\frac{Ds}{Dt} = 0, \tag{21}$$

or, expanding the material derivative,

$$\frac{\partial s}{\partial t} = -(u\frac{\partial s}{\partial x} + v\frac{\partial s}{\partial y}) = -\mathbf{V} \cdot \nabla s. \tag{22}$$

The tracer value at a fixed location will thus change in time due solely to advection by the flow. Diffusion of tracer is omitted in this ideal fluid model, though some inadvertent 'numerical diffusion' will always be present in numerical solutions. Thus Eqn. (21) would hold exactly only in a perfect numerical solution (and you may never see one).

The trajectories of discrete fluid parcels, or 'floats', make a useful complement to the continuous tracer. The trajectory of the ith float, (x^i, y^i), is found by integrating the (Eulerian) fluid velocity at the moving location of the float,

$$x^i(t) = x^i_o + \int_{to}^{t} u(x^i, y^i, t)dt \quad \text{and} \quad y^i(t) = y^i_o + \int_{to}^{t} v(x^i, y^i, t)dt. \tag{23}$$

Which specific fluid parcel or float is being tracked in this way is given by the initial position, i.e., the ith float starts at $x^i_o = x^i(t = t_o)$. The float will likely be found between the discrete grid points of the numerical model's Eulerian velocity field and so in practice this will require some interpolation. The trajectory is the fundamental dependent variable of a Lagrangian description (rather than the velocity as in the Eulerian description). But if needed, the Lagrangian velocity may be computed from the trajectories via

$$\text{Lagrangian fluid velocity}: \quad \mathbf{U}^i(t) = \left(\frac{\partial x^i(t)}{\partial t}, \ \frac{\partial y^i(t)}{\partial t} \right). \tag{24}$$

Tracer evolution by advection Eqn. (21) and float trajectories by Eqn. (23) are very closely related, and, for example, the tracer concentration at the moving location of a float should be exactly conserved (numerical diffusion and tracking errors aside).

The relationship between the Eulerian and the Lagrangian velocities depends very much upon the length of time that a float is tracked, the $t = t_0 + \Delta t$ of Eqn. (23). If Δt is so brief that the float moves only an infinitesimal distance compared to the scale over which the Eulerian velocity varies in space, then the Lagrangian velocity will converge to the Eulerian velocity at the starting point. Much more interesting is the case that Δt is very long, in Part 3 up to a year, in which case any given float may wander into regions having very different Eulerian velocity, which is also likely changing in time. In that event, and aside from special cases, the Lagrangian velocity will likely bear no simple relationship to the Eulerian velocity.

2.3.2 Energy balance

Energy conservation is a fundamental physical law that can sometimes be of use in analyzing a fluid flow, especially if, as here, dissipation and thermal (internal) energy may be neglected. In that case the mechanical energy, $E = KE + PE$, is conserved, where E is the sum of kinetic energy (per unit mass), $KE = \frac{1}{2}h\mathbf{V}^2$, and potential energy (per unit mass), $PE = g' \int_0^\eta z dz = \frac{1}{2}g'\eta^2 + const$. To find the rate of change of KE, take the dot product of the momentum equation with the velocity times thickness, and the rate of change of PE is found by multiplying the continuity equation by the thickness anomaly times reduced gravity. The mechanical energy balance is

$$\boxed{\frac{DE}{Dt} = -g'\nabla\cdot(\eta h\mathbf{V}) + \mathbf{F}\cdot\mathbf{V}} \tag{25}$$

The flux term on the right-hand side is the product of pressure anomaly, thickness and velocity, i.e., pressure work (actually, pressure work rate, or power). For example, if the pressure anomaly is positive on the (imaginary) boundary of a control volume where the velocity is directed outward, say, then the fluid inside the control volume will do pressure work on the fluid outside of the control volume. The energy within the control volume will thus decline, while the energy outside the control volume will increase. The pressure-work term thus accounts for the outward energy transport associated with wave radiation through an open boundary, for example. The fluid flow can also transport energy at the rate $\mathbf{V}$, a process accounted by the advection term, $\mathbf{V}\cdot\nabla E$, of the total derivative. Finally, note that an external force $\mathbf{F}$ can either increase or decrease energy depending upon whether it has a component parallel or anti-parallel to the fluid velocity.

2.3.3 Potential vorticity balance

Throughout Part 1, our perspective on dynamics was through the *linear* momentum balance (linear here in the geometric sense), and rotation appeared by way of the Coriolis *force*. That was all that was possible given a single parcel model. Momentum balance is always relevant, but may not always be highly revealing. Given the present fluid model, there is another and complementary point of view, *angular* momentum balance, that has proven immensely fruitful for understanding some of the most important low frequency (frequencies less than f) phenomena of geophysical fluid dynamics. Two main reasons, to get a little ahead in this short story, are that 1) Earth's rotation provides a very large background angular momentum that is made visible by small changes in the thickness or latitude of a fluid column, and, 2) the angular momentum balance amounts to a kind of filter that eliminates high frequency gravity wave motions and so serves to highlight the processes that cause departures from geostrophic balance and that lead to low frequency currents and winds, i.e., large scale circulation.

Back a step or two..... to analyze the motion of a rotating, solid object, say a gyroscope, you might begin by computing the linear momentum balance of the component pieces. This would require an accounting of radial accelerations and internal stresses on each piece and would likely be a fairly arduous task. Assuming that the gyroscope is not at risk of breaking up, then at some point you might decide to take the structure for granted, and focus your effort toward analyzing the angular (azimuthal) momentum balance of the gyroscope as a whole. As a first step you would define a coordinate system that gave the most compact and least complex accounting of the moment of inertia of the gyroscope and then consider the processes that cause the angular momentum to change with time. The physical content of your angular momentum analysis would not be fundamentally different from the linear momentum description, but it would likely be a great deal simpler in the same way that choosing appropriate variables and an appropriate coordinate system can facilitate any mathematical analysis. The same considerations apply to an analysis of a fluid flow: as we will see in examples here, an angular momentum analysis and description will often (but not always!) be a good deal simpler and so

provide a great deal more insight than does the otherwise equivalent linear momentum analysis.

The fluid flow equivalent of angular velocity is the curl of the fluid velocity,

$$\boxed{\xi \equiv \nabla \times \mathbf{V}}$$

called the vorticity. If the fluid velocity is a three-dimensional vector, then the vorticity is also a three-dimensional vector. In the special case of the shallow water model, the velocity varies only in the two horizontal dimensions, and so the shallow water vorticity,

$$\xi = \nabla \times \mathbf{V} = (\frac{\partial v}{\partial x} - \frac{\partial u}{\partial y})_z, \tag{26}$$

has a vertical component only and is effectively a scalar. You can visualize vorticity as the rotation of small (but not quite point-like) two-dimensional parcels, e.g., cylinders, that make up the fluid.[6] As we will see, however, vorticity in a plane wave will arise from horizontal shear in the direction normal to the velocity, e.g., $\xi = \partial v/\partial x$ or $\xi = -\partial u/\partial y$ are quite possible, and so spinning cylinders are not always apropos. If the direction of rotation is the same as Earth's rotation, the vorticity is said to be *cyclonic* (from the Greek *kyklon*, for circular motion). Cyclonic rotation is thus counterclockwise in the northern hemisphere and clockwise in the southern hemisphere. Anticyclonic is the reverse. Notice that vorticity has units of inverse time, or frequency, the same as the Coriolis parameter, f. There is an important sense in which ξ may be compared to and even added to f, as discussed below.

The vorticity of a fluid is unlike the angular momentum associated with a solid object in that it is defined at every point in a fluid, i.e., in principle there is a vorticity field that accompanies every fluid flow (although it could be zero), just as there is a velocity field and a thickness field in the shallow water model. The governing equation for this vorticity field may be found by taking the curl of the momentum equation, $\partial/\partial x$ of the y-component minus $\partial/\partial y$ of the x-component. A consequence of applying the curl operator is that all of the forces that are derivable from a potential are eliminated, most notably the pressure gradient in the shallow water model, i.e.,

$$\nabla \times \nabla(\eta(x,y)) = \frac{\partial^2 \eta}{\partial x \partial y} - \frac{\partial^2 \eta}{\partial y \partial x} = 0.$$

A divergence term $\partial u/\partial x + \partial v/\partial y$ will arise and may be eliminated using the thickness (continuity) equation, (16). After a little further rearrangement, the result is a balance equation for a scalar, q, called the potential vorticity,

$$\boxed{\frac{Dq}{Dt} = \frac{\partial q}{\partial t} + \mathbf{V} \cdot \nabla q = \frac{1}{h} \nabla \times \frac{\mathbf{F}}{h}} \tag{27}$$

[6] An essential resource for all students of fluid mechanics is the collection of fluid mechanics films made in the 1960s by Ascher Shapiro and colleagues and now available online at http://web.mit.edu/hml/ncfmf.html These films will seem a little old-fashioned today, but they are nevertheless very highly recommended in that they provide excellent visualizations of many key concepts of fluid mechanics, including vorticity and Eulerian and Lagrangian coordinate systems, that are timeless. A more modern film collection, many of which emphasize rotational effects, is https://spinlab.ess.ucla.edu/

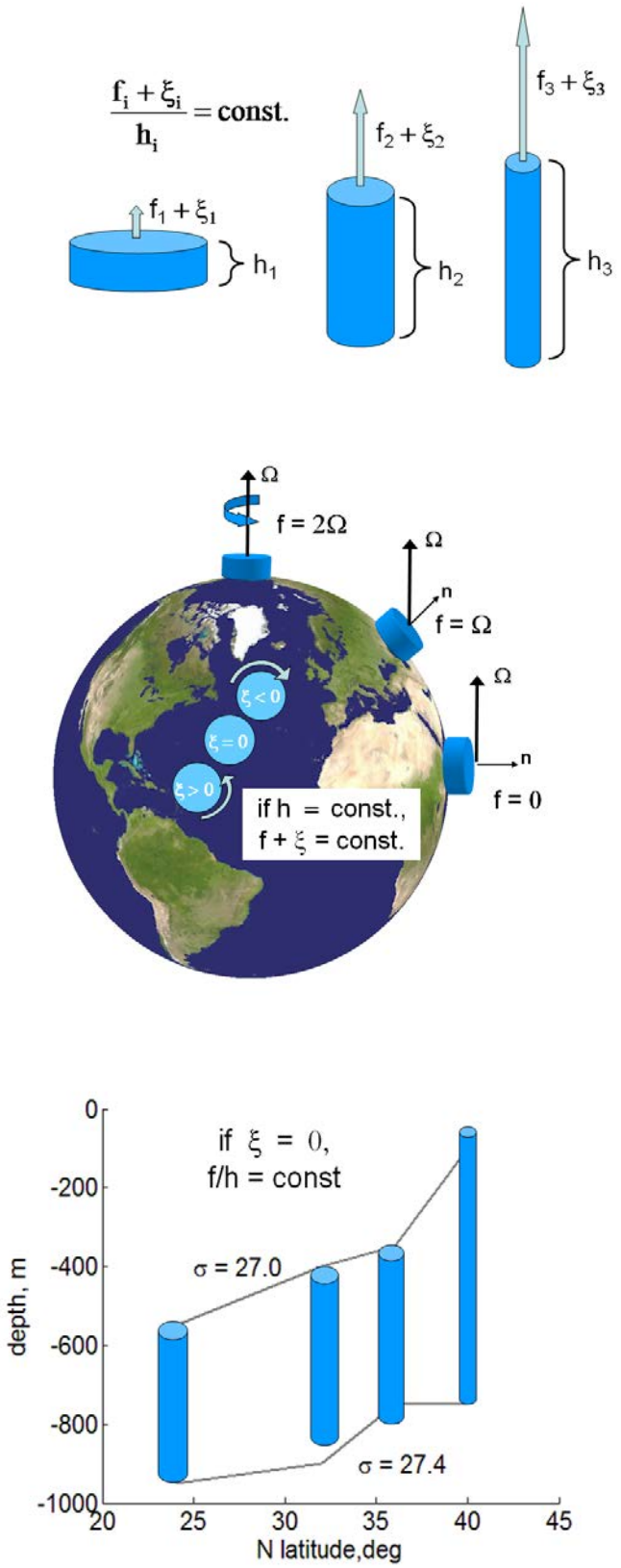

Figure 5: Some illustrations of q-conservation, $Dq/Dt = 0$, by fluid columns that have a constant volume but may have a variable thickness, h and that are free of external torques, $\nabla \times \mathbf{F} = 0$. **(upper)** If h is variable, then the absolute vorticity, $f + \xi$, will change in proportion to h. This is true whether the absolute vorticity $\approx \xi$, because $f \ll \xi$ as in small scale or engineering flows, or if $\xi \ll f$ and ξ is effectively zero, as in a gyre-scale flow, illustrated in the lower panel. **(middle)** The columns perched at upper and right on the Earth are intended to show that the planetary vorticity due solely to Earth's rotation is given by $\nabla \times \mathbf{V}_\Omega = 2\mathbf{\Omega} \cdot \mathbf{n} = 2\Omega \sin(\text{latitude}) = f$. The planetary velocity $\mathbf{V}_\Omega$ and thus the planetary vorticity f are apparent to an inertial observer, implicit in this view from space. We Earth-bound observers will see only the relative velocity $\mathbf{V}$, i.e., winds and ocean currents, and the relative vorticity, ξ. The planetary vorticity is not directly observable (though the stars turning overhead are a mirror image). The three columns in the North Atlantic are shown end-on to illustrate the sense of relative vorticity that would be acquired by a q-conserving column that was displaced north or south away from a reference site where $\xi = 0$ while holding h constant. This and the next mechanism involve $f(\text{latitude})$ that will be taken up in Part 3. **(lower)** If the relative vorticity ξ is much, much less than f and remains effectively zero, as in a gyre-scale flow, then a change in the latitude of a column will be accompanied by a change in the thickness of a column in the sense shown here, i.e., smaller h in the direction of smaller $|f|$. The solid lines are depths of the 27.0 and 27.4 potential density surfaces along a plausible trajectory through the main thermocline of the eastern subtropical North Atlantic. These data are after Fig. 4 of Luyten J. R. et al., 1983: 'The ventilated thermocline', *J. Phys. Oceanogr.* 13, 292 - 309.

where

$$\boxed{q = \frac{f+\xi}{h}} \tag{28}$$

Up until Part 3 our interest will be the fluid only, $\mathbf{F} = 0$, in which case we have a q-conservation law

$$\boxed{\frac{Dq}{Dt} = 0} \tag{29}$$

The terms in potential vorticity balance are:

$\xi = \nabla \times \mathbf{V}$ is often called the *relative* vorticity in this context, since it is the vorticity of the relative velocity, i.e., the winds and currents observed from an Earth-attached reference frame. In Part 1, Sec. 4 the relative velocity was denoted by $\mathbf{V}'$, though by now the prime superscript has been dropped.

$f = \nabla \times \mathbf{V}_\Omega$ is the *planetary* vorticity of the planetary velocity, $\mathbf{V}_\Omega = \mathbf{\Omega} \times \mathbf{X}$, due to Earth's rotation, Fig. (5), where $\mathbf{X}$ is the position vector (Sec. 4.3, Part 1). f may be written in several forms, $f = \nabla \times \mathbf{\Omega} \times \mathbf{X} = 2\mathbf{\Omega} \cdot \mathbf{n} = 2\Omega \sin(\text{latitude})$,

$f + \xi = \nabla \times (\mathbf{V}_\Omega + \mathbf{V})$ is appropriately termed the *absolute* vorticity, since it is indeed the vorticity of the absolute velocity, $\mathbf{V}_\Omega + \mathbf{V}$, i.e., the velocity that would be observed from an inertial reference frame, and finally,

h is the layer (or column) thickness.

The conservation equation (29) states that q is conserved following an ideal fluid parcel (or fluid column since this is a single layer model). By ideal we mean that there is no external torque due to wind stress or bottom friction. What is most important is to notice what is missing from (29): there is no process comparable to pressure work found in the energy balance, Eqn. (25), that transmits energy at the speed of gravity waves — q is transported with the fluid, exactly as a passive tracer, Eqn. (21), and not at the gravity wave velocity as is energy. Thus the potential vorticity of an ideal fluid has the conservation property of a tracer (or dye) that, once put into a fluid, remains with the fluid no matter how complex the flow may be. This includes during the process of geostrophic adjustment. But unlike a passive tracer, the potential vorticity includes an important part of the velocity field, the part having relative vorticity. In some cases it may be sufficient to calculate the evolution of a flow from q-conservation only, the steady state of an adjustment process is an important example in Sec 4.4, which

is a marked simplification over solving the full shallow water system. However, the pure gravity wave experiment in Sec. 3.1 will show that q conservation can be irrelevant if the dynamics is such that there is no vorticity.

Potential vorticity is a generalized angular momentum insofar as it accounts for a variable moment of inertia (variable thickness) as well as the planetary vorticity f due to Earth's rotation. The planetary vorticity is extremely important in this regard, because f is considerably larger than is the ξ of large scale flows, usually by a factor of 10 and often much more. A fluid column having potential vorticity will exhibit a kind of gyroscopic rigidity in the sense that it will respond to changes in the parcel configuration (thickness) or to changes in latitude and thus f. For example, suppose that a fluid column has absolute vorticity $(f_1 + \xi_1)$ and thickness h_1 in an initial state, and is then stretched from h_1 to h_2. Assuming that the stretching occurs without frictional or external torques, then the conservation law (29) applies and the absolute vorticity of the column will change to $(f_2 + \xi_2) = (f_1 + \xi_1)h_1/h_2$ (Fig. 5). Whether the change in absolute vorticity is due mainly to a change in the relative vorticity or due to a change in the planetary vorticity (latitude) can not be told without some additional information; sometimes knowing just the horizontal scale of the motion will suffice (Sec. 2, Part 3).

You may be wondering why we should make such a fuss over potential vorticity when the numerical model solves the more general shallow water equations. It is true that the winds or currents that might be inferred from a q-conservation argument can always be computed by the shallow water model and so q-conservation is redundant insofar as computation alone is concerned. The value of potential vorticity becomes evident when it is time to describe, interpret and understand a numerical model solution or a set of field observations: a potential vorticity-based description will often be simpler and yield far more insight than would the corresponding momentum plus continuity description. Of course, this presumes that potential vorticity concepts are a part of our working, fluid dynamics vocabulary. We can take a useful step in that direction by using potential vorticity balance to help describe and interpret the geostrophic adjustment experiments that follow in Sec. 4 and in Part 3.[7]

[7]Before ending this discussion it should be noted that the shallow water potential vorticity is not the most general form of potential vorticity, just as the shallow water model is not the most general fluid model. If the fluid velocity is a three component vector, which it generally is in the ocean and atmosphere, then so too is the vorticity. The three-dimensional vorticity equation includes a term that represents a change in the direction of the vorticity vector, e.g., from the horizontal into the vertical, often called 'tipping'. If the fluid flow is baroclinic, which the atmosphere and ocean generally are, then there is an additional term that arises from the cross-product of the density and pressure gradients, called the 'solenoidal' term. The corresponding three-dimensional and baroclinic potential vorticity that takes account of these additional processes is often called the Ertel potential vorticity; it reduces to the shallow water potential vorticity when the flow is appropriately two-dimensional and barotropic. By and large, the simpler shallow water potential vorticity will be adequate for an analysis of most large (horizontal) scale phenomenon, e.g., gyre-scale flows and even mesoscale eddies, once they are formed. However, it will not be adequate for analysis of small scale phenomenon, e.g., boundary layer roll vortices and three-dimensional turbulence. Knowing where this transition may occur requires a thorough understanding of Ertel potential vorticity. A very insightful discussion of some of these more advanced concepts is available online at http://www.damtp.cam.ac.uk/user/mem/

2.3.4 Finite amplitude effects

The phrases 'nonlinear' and 'finite amplitude' are often used interchangeably. Here, however, linear and nonlinear will be reserved for model equations, which are either one or the other with no gradation. The shallow water system is nonlinear because of the six terms that are the products of dependent variables, e.g., in the thickness equation (13) the terms $u\partial h/\partial x$ and $h\partial u/\partial x$ are nonlinear and so the model system is nonlinear when these are retained. [8]

Finite amplitude effects are the departures from linear dependence upon amplitude. Finite amplitude effects do not arise in the solution of a linear model, and are a matter of degree in the solution of a nonlinear model. For example, in the problems studied here, the amplitude is largely determined by η_o, the initial thickness anomaly. If the shallow water equations were linear (they aren't) then the solution $\eta(x,y,t)/\eta_o$ would be invariant to changes in η_o. Even in a nonlinear model, we can expect that $\eta(x,y,t)/\eta_o$ should be invariant to η_o in the limit of very small η_o (say $\eta_o = 1$ m with H = 500 m) simply because the nonlinear terms noted above will be very, very small compared to the dominant linear terms. The amplitude of the base case, $\eta_o = 50$ m, has been chosen to correspond with the observed SSH signature of mesoscale eddies (Fig. 1). At this amplitude, there are several interesting and important finite amplitude phenomena, including very large float (material) displacements given sufficient time. Nevertheless, a great deal of what we can see in a solution for $\eta(x,y,t)$ and $\mathbf{V}(x,y,t)$ can be attributed to linear wave dynamics and especially to the dispersion property of the waves supported by the linear shallow water system. (more on this below and in Part 3). The linear subset of the shallow water model results when $D(\ )/Dt$ is replaced everywhere by $\partial(\ )/\partial t$, and the variable layer thickness h is replaced by the constant initial thickness, H. In Cartesian components the linear shallow water model is

$$\begin{aligned}
\frac{\partial h}{\partial t} &= -H(\tfrac{\partial u}{\partial x} + \tfrac{\partial v}{\partial y}),\\
\frac{\partial u}{\partial t} &= -g'\tfrac{\partial h}{\partial x} + fv,\\
\frac{\partial v}{\partial t} &= -g'\tfrac{\partial h}{\partial y} - fu.
\end{aligned} \tag{30}$$

The stratification is represented in this one layer model by g' and H and assumed homogeneous. The stratification determines the phase speed of waves. The f is these equation is in general dependent

[8] Terms like $u\ \partial h/\partial x$ that are the product of two dependent variables are sometimes said to be 'bilinear' or 'semi-linear'. Model equations having such terms are nonlinear in the most important sense that a superposition of valid solutions does not yield a new valid solution. However, some solution methods are applicable to semi-linear systems, e.g., the method of characteristics, that are not applicable to more comprehensively nonlinear systems.

upon latitude (or north distance, y); the spatial variation of f determines the kinds of waves that are possible.

2.4 Boundary and initial conditions define the problem

The mass and momentum equations (16) and (17) could be used to model a wide range of phenomena. The definition of a specific, solvable problem follows from the specification of an initial condition on h and $\mathbf{V}$ throughout the model domain, and the definition of boundary conditions along the edges of the domain.

The problems studied here are variants on the classical problem of geostrophic adjustment[??] and specifically, geostrophic adjustment of a mesoscale eddy-like feature at mid-latitude. The stratification is chosen to be typical of the subtropical main thermocline,

$$H = 500 \text{ m} \text{ and } \delta\rho = 2 \text{ kg m}^{-3}, \tag{31}$$

and the resulting gravity wave speed,

$$C = \sqrt{g(\delta\rho/\rho_o)H} \approx 3.1 \text{ m s}^{-1},$$

is that of an internal or baroclinic gravity wave (Sec. 2.4.2). The initial condition is either a one-dimensional ridge with half-width L,

$$\eta(x,t=0) = \eta_o \text{ if } |x| \leq L, \text{ or else } \eta(x,t=0) = 0, \tag{32}$$

(here in Sec. 3) or a two-dimensional eddy with radius = L (in Sec. 4).[9] The half-width and the amplitude of the initial interface displacement are chosen to be comparable to observed mid-latitude mesoscale eddies (Fig. 1),

$$L = 100 \text{ km} \quad \text{and} \quad \eta_0 = 50 \text{ m}. \tag{33}$$

The initial velocity can be one of several forms, the default being a state of rest,

$$\mathbf{V}(x,t=0) = 0. \tag{34}$$

[9] The initial ridge given by Eqn. (32) has a very sharp edge, which in (numerical) practice is smoothed over a few horizontal grid points. Nevertheless, when released suddenly, this initial condition tends to produce energetic gravity waves that are not highly realistic of most natural phenomenon. Wind or tidal forcing acting on the ocean are by comparison rather slowly varying in time and space, and so less apt to produce energetic gravity waves. The initial condition may be easily changed to something smoother, and for that matter, the models may be readily configured to allow realistic wind or tidal forcing as in Part 3.

If the initial velocity and vorticity vanish, then the initial ridge has a potential vorticity $q = f/(H + \eta_o)$ compared with f/H in the outlying fluid. This potential vorticity anomaly is preserved during geostrophic adjustment, the full import of which will become clear in Sec. 4.5.

The computational domain will be either one-dimensional, having a width of several thousand kilometers, where that is appropriate (Secs. 3 and 4, where f is presumed to be a constant), or two-dimensional and 4000 km on a side (Sec. 5). There is no attempt to compute the fluid state outside of the computational domain, and so something other than the momentum and continuity equations will have to be imposed on the boundaries.

The only energy in the initial state is associated with the initial eddy which is placed near the center of the model domain. It is then reasonable that waves will be radiated outward only, i.e., that nothing will come into the model domain from the outside. A plausible and generally effective representation of this one-way, outward transfer is made by imposing a radiation boundary condition along the boundaries:

$$\frac{\partial \psi}{\partial t} = -U_{rad}\frac{\partial \psi}{\partial n}, \tag{35}$$

where ψ is thickness or a velocity component, n is the direction normal and outward from the boundary and U_{rad} is the appropriate velocity component normal to the boundary. This amounts to imposing a one-dimensional advection process normal to the boundary and at the speed U_{rad}, which is very important to the success of (35). The appropriate value of U_{rad} depends upon the dominant process local to the boundary, and that may change with time. Here, during the first 20 days of an experiment, U_{rad} is taken to be the gravity wave speed, $U_{rad} = C = \sqrt{g'H}$, the fastest wave speed in the shallow water system (Sec. 3.1). This serves well to usher along the gravity waves that first reach a distant boundary. But after that comes trouble ... very, very slowly ... in the form of low frequency Rossby waves (in Part 3).

2.5 Appendix to Sec. 2: Normal modes of a two layer model ocean

The shallow water model applied to a homogeneous (unstratified and so *barotropic*) ocean stands on its own. But if the shallow water model is applied to internal or *baroclinic* motions (defined below), then some discussion of the correspondence between observed and modelled layer thicknesses and phase speeds seems necessary.[10] In that vein it is useful to examine briefly the wave properties of a simple two

[10]The terms barotropic and baroclinic describe the dependence of density upon pressure. A barotropic fluid is one in which the density can be written as a function of the pressure only, $\rho = \rho(P)$. This would hold always in a fluid that was homogeneous, for example, in the (single layer) shallow water model. It would also hold in a fluid that was density stratified, provided that the density surfaces and pressure surfaces were everywhere parallel. This would likely be true in a resting state, but not when motion causes vertical displacements of density surfaces that will often greatly exceed the associated

layer model. For this purpose rotation and nonlinearity may be ignored, and the motion presumed to be in one horizontal dimension only (x,t). The stratification is represented by two homogeneous layers, Fig. (6), an upper layer 1, having an undisturbed thickness H_1 and density ρ_1, and a lower layer, 2, with undisturbed thickness H_2 and slightly greater density, $\rho_2 = \rho_1 + \delta\rho$. If this was meant to represent the open ocean, then the interface between the layers would correspond with the middle of the main thermocline and typical values would be $H_1 = 500$ m, $H_2 = 3500$ m, $\rho_1 = 1030$ kg m^{-3} and $\rho_2 = \rho_1 + \delta\rho$ with $\delta\rho = 2$ kg m^{-3}.

The interest here is in large scale, fairly slowly varying motions for which vertical accelerations are very, very gentle, $\ll g$, and the pressure is consequently hydrostatic, i.e., due to the weight of the fluid overhead. The bottom pressure is $P_b = g(\rho_1 h_1 + \rho_2 h_2)$, and the pressure within the layers varies as

$$P_1(x,z,t) = g\rho_1(h_1(x,t) + h_2(x,t) - z) \quad \text{and} \quad P_2(x,z,t) = g\rho_1 h_1(x,t) + g\rho_2(h_2(x,t) - z),$$

where $h(x,t)$ is the space and time-varying layer thickness. The pressure gradient divided by the density is then in each layer,

$$\frac{1}{\rho_1}\frac{\partial P_1}{\partial x} = g(\frac{\partial h_1}{\partial x} + \frac{\partial h_2}{\partial x}) \quad \text{and} \quad \frac{1}{\rho_2}\frac{\partial P_2}{\partial x} = g\frac{\rho_1}{\rho_2}\frac{\partial h_1}{\partial x} + g\frac{\partial h_2}{\partial x}. \tag{36}$$

With these results in hand, the momentum and continuity equations for the velocity and layer thicknesses are (anticipating a matrix format):

$$\begin{aligned}
\frac{\partial u_1}{\partial t} + g\frac{\partial h_1}{\partial x} + g\frac{\partial h_2}{\partial x} &= 0,\\
H_1\frac{\partial u_1}{\partial x} + \frac{\partial h_1}{\partial t} &= 0,\\
g\frac{\rho_1}{\rho_2}\frac{\partial h_1}{\partial x} + \frac{\partial u_2}{\partial t} + g\frac{\partial h_2}{\partial x} &= 0,\\
H_2\frac{\partial u_2}{\partial x} + \frac{\partial h_2}{\partial t} &= 0.
\end{aligned} \tag{37}$$

Notice that the thickness of a given layer can vary only if there is divergence within that layer, and, that the pressure gradient has a dependence upon both layer thicknesses. Thus the pressure gradient couples the layers together.

displacement of pressure surfaces. In that case, the fluid would be described as baroclinic, meaning that density and pressure surfaces intersect, and so density varied with more than the pressure, i.e., with horizontal position and time at a given pressure. Thus, barotropic is a special case in which density surfaces are always parallel with pressure surfaces, while baroclinic is all else. The distinction is important in that the pressure gradient can (will) generate vertical shear in a baroclinic fluid, but not in a barotropic fluid. Thus a shallow water model will be realistic model of a barotropic fluid and flow. A shallow water solution will require some interpretation if, as here, it is meant to represent a baroclinic phenomenon, e.g., ocean mesoscale eddies.

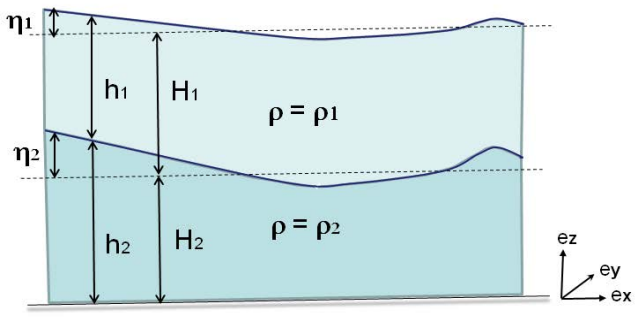

Figure 6: A two layer model appropriate to the stratified ocean. The dashed lines are level surfaces. The undisturbed layer thicknesses are H_1 and H_2, and the actual thicknesses are h_1 and h_2. The upper surfaces of the layers are displaced to $\eta_1 = h_1 + h_2 - (H_1 + H_2)$ and $\eta_2 = h_2 - H_2$. The pressure of the atmosphere above is presumed horizontally uniform and so negligible.

To find the wave properties of this system, presume that a wave may exist in both layers: $u_1(x,t) = U_1 cos(kx - \omega t)$, $u_2(x,t) = U_2 cos(kx - \omega t)$, $h_1(x,t) = H_1 + \Gamma_1 cos(kx - \omega t)$ and $h_2(x,t) = H_2 + \Gamma_2 cos(kx - \omega t)$. The U_1, Γ_1, U_2, Γ_2 are constant but to this point unknown amplitudes. Notice that the wave frequency and wavenumber are the same in the two layers, which is implicit in 'a wave', and are also unknown. After substitution of this wave form, the governing equations (37) may be written in matrices as

$$\begin{pmatrix} -\omega & gk & 0 & gk \\ H_1 k & -\omega & 0 & 0 \\ 0 & gk\frac{\rho_1}{\rho_2} & -\omega & gk \\ 0 & 0 & H_2 k & -\omega \end{pmatrix} \begin{pmatrix} U_1 \\ \Gamma_1 \\ U_2 \\ \Gamma_2 \end{pmatrix} = 0.$$

The simplest and most insightful description of a multi-part, linear system such as this will often be in terms of the normal mode frequencies and structure, also called the eigenvalues and eigenvectors. The normal modes are independent of one another, and hence the governing equations written in terms of the normal modes will be decoupled, which is not the case with Eqns. (37) written in the layer-wise thickness and velocity. To find the frequencies of the normal modes it is necessary to solve the characteristic equation of the coefficient matrix (same as saying that the determinant must vanish), which is a fourth order polynomial in ω

$$\omega^4 - gk^2(H_1 + H_2)\omega^2 + g^2 k^4 H_1 H_2 (\frac{\rho_2 - \rho_1}{\rho_2}) = 0.$$

This characteristic equation is bi-quadratic (the cubic and linear terms vanish) and can be readily solved

as a quadratic equation for ω^2,

$$\omega^2 = \frac{gk^2(H_1+H_2)}{2} \pm \frac{\sqrt{g^2k^4(H_1+H_2)^2 - 4g^2k^4H_1H_2(\frac{\rho_2-\rho_1}{\rho_2})}}{2}. \tag{38}$$

In the oceanic case in which $\frac{\rho_2-\rho_1}{\rho_2} \ll 1$ this may be simplified by factoring the term under the square root and then using the binomial theorem that $(1+\varepsilon)^{1/2} \approx 1+\varepsilon/2$ when $\varepsilon \ll 1$ as applies here,

$$\omega^2 = \frac{gk^2(H_1+H_2)}{2} \pm gk^2\frac{(H_1+H_2)}{2}\left(1 - 2\frac{H_1H_2}{(H_1+H_2)^2}(\frac{\rho_2-\rho_1}{\rho_2})\right). \tag{39}$$

2.5.1 Barotropic mode

The larger of the two roots of Eqn. (39) is the frequency squared of the external or *barotropic* mode,

$$\omega_{btr}^2 = gk^2(H_1+H_2) - gk^2\frac{H_1H_2}{(H_1+H_2)}(\frac{\rho_2-\rho_1}{\rho_2}). \tag{40}$$

Since the trailing factor involving the density difference is very, very small, ≈ 0.002, an excellent approximation of this frequency is

$$\omega_{btr} \approx \pm k\sqrt{g(H_1+H_2)}. \tag{41}$$

If the intent is to reproduce this dispersion relationship within a shallow water model, then the single-layer equivalent gravity and layer thickness are simply

$$g_e = g, \quad \text{and} \quad H_e = H_1+H_2, \tag{42}$$

which might have been guessed without help from a two layer model. This is the barotropic mode. The same kind of result is slightly less obvious for the baroclinic mode coming next.

By putting the appropriate frequency (41) back into the governing equations (37) we can solve for the ratio of the amplitude of the layer thicknesses changes,

$$\frac{\Gamma_1}{\Gamma_2} = \frac{\rho_2}{2\rho_1}\left((H_1 + (H_1^2+H_2^2-2H_1H_2+4H_1H_2\frac{\rho_1}{\rho_2})^{1/2})/H_2 - 1\right). \tag{43}$$

Noting that ρ_1/ρ_2 is very close to 1, then as a very good approximation,

$$\frac{\Gamma_1}{\Gamma_2} \approx \frac{H_1}{H_2}. \tag{44}$$

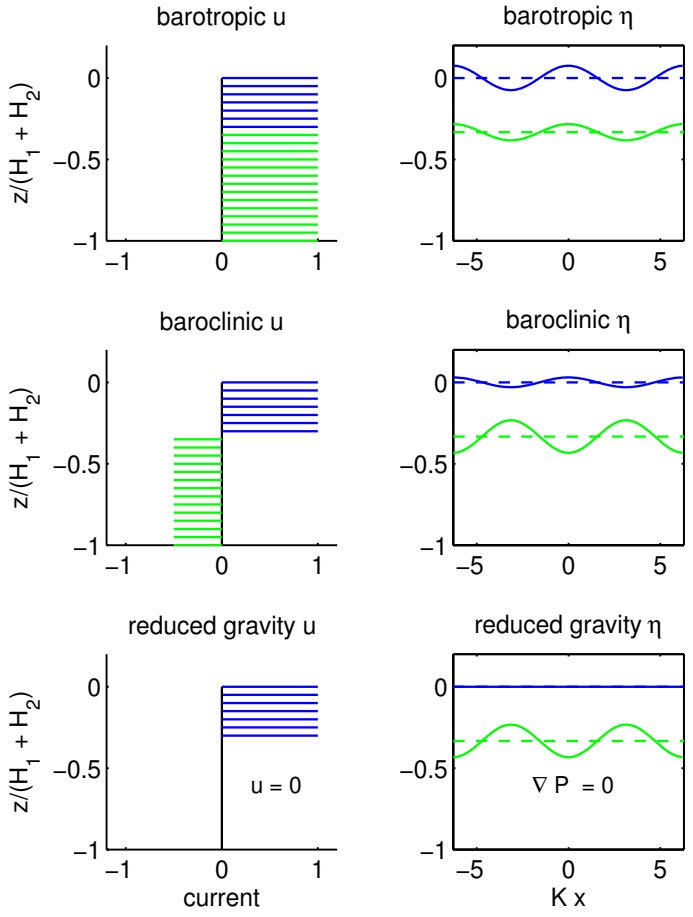

Figure 7: Normal modes of a two-layer ocean. **(upper)** The barotropic normal mode; current profile (upper left, arbitrary amplitude) and the sea surface and interface displacements (upper right, blue and green lines). **(middle)** The baroclinic normal mode. The currents and the sea surface and interface displacements have a self-consistent structure, but the thicknesses, $H_1 = 500$ m and $H_2 = 1000$ m, and the density difference, $\delta\rho = 300$ kg m^{-3}, were chosen to make this structure legible rather than realistic of the ocean thermocline. **(lower)** The reduced gravity approximation of the baroclinic mode uses only the density interface to compute the pressure gradient in the upper layer on the assumption that the lower layer currents and pressure gradient vanish. This would not be a good approximation for the stratification shown in this figure because H_1/H_2 is not $\ll 1$.

In this linear model the amplitude of either Γ_1 or Γ_2 is arbitrary, but the ratio Γ_1/Γ_2 is determined by the dynamics. Eqn. (44) indicates that the layer thicknesses oscillate in phase and with an amplitude that is proportional to the undisturbed layer thickness. For some purposes it is helpful to know the displacement of the upper surfaces of the layers; the sea surface, sometimes called the free surface, is displaced from its resting (level) height by

$$\eta_1 = (h_1 + h_2) - (H_1 + H_2),$$

and the density interface between the layers by

$$\eta_2 = h_2 - H_2.$$

In the barotropic mode, the amplitude of the vertical displacement of the free surface compared to the displacement of the interface is then, using Eqn. (44),

$$\frac{\Gamma_1 + \Gamma_2}{\Gamma_2} = \frac{H_1 + H_2}{H_2} \approx 1.14, \tag{45}$$

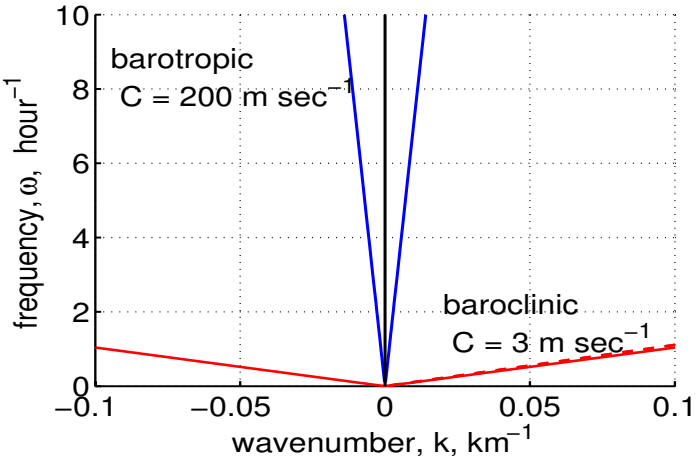

Figure 8: The dispersion relation for gravity waves of a two layer, nonrotating model of a stratified ocean. The solid lines are the full dispersion relation, and the dashed red line is an approximation discussed in the main text. At a common wavenumber, the barotropic and baroclinic modes have vastly different frequencies and phase speeds.

for our nominal, open ocean stratification. The vertical displacement is thus a maximum at the sea surface and decreases linearly to zero at the bottom (Fig. 7, upper). The displacements $\eta_1(x,t)$ and $\eta_2(x,t)$ have a $cos(kx-\omega t)$ time- and space-dependence that is common to both layers, which is what distinguishes a mode from an arbitrary motion. The pressure gradient is due almost entirely to the displacement of the free surface, and the currents are the essentially the same in the two layers (uniform with depth). The density interface η_2 moves up and down exactly as does the pressure at that level, and thus the density could be written as a function of the pressure in the initial state and during the subsequent motion. This kind of wave motion in which $\rho = \rho(P)$ everywhere in the fluid is, as here, termed barotropic.

The phase speed of a barotropic wave for a nominal, open ocean depth $H_1 + H_2 = 4000$ m is very fast,

$$C_{btr} = \frac{\omega_{btr}}{k} = \sqrt{g(H_1+H_2)} \approx 200 \text{ m sec}^{-1} \approx 680 \text{ km hour}^{-1},$$

or comparable to that of a jet transport. High frequency (5 to 20 min period) barotropic waves of this kind (in some circumstances called *tsunamis*, Japanese for harbor wave) are the primary oceanic response to a rapid vertical displacement of the sea floor (a few meters in a few minutes over a large horizontal scale). Because the fluid velocity associated with open ocean tsunami waves is comparatively gentle, a few centimeters per second, these waves undergo very little dissipation, and, aside from two-dimensional spreading, may arrive on a distant shore with a significant amplitude. Lower frequency barotropic waves (periods 1/2 to 1 day) are the principal components of the open ocean, astronomical tides. These near-daily frequency waves gravity waves are modified substantially by Earth's rotation and are often called inertia-gravity waves (Sec. 4, also called Poincare waves).[11]

[11] An excellent resource for tsunami waves is http://www.tsunami.noaa.gov/ A classic paper on open ocean tides is by http://articles.adsabs.harvard.edu//full/1944MNRAS.104..244P/0000254.000.html

2.5.2 Baroclinic mode

The smaller of the two roots of Eqn. (39) is labeled the internal or *baroclinic* normal mode, and

$$\omega_{bcl} = \pm k\sqrt{g\frac{H_1H_2}{(H_1+H_2)}(\frac{\rho_2-\rho_1}{\rho_2})}. \tag{46}$$

Baroclinic gravity waves have a much lower frequency and phase speed than does a barotropic wave of the same wavelength,

$$\frac{\omega_{bcl}}{\omega_{btr}} = \frac{C_{bcl}}{C_{btr}} \approx \sqrt{\frac{g'H_1H_2}{g(H_1+H_2)^2}} \approx \frac{1}{70},$$

mainly because the reduced gravity, $g' = g(\rho_2-\rho_1)/\rho_2 = g(2/1000)$, is very much less than the full gravity, g. If the intent is to model the baroclinic dispersion relation using a shallow water model, then

$$g_e = g' \text{ and } H_e = \frac{H_1H_2}{(H_1+H_2)} \tag{47}$$

will give an appropriate phase speed.[12] It is usually the case that H_2 exceeds H_1 by a factor of 5 - 10, and as a fair approximation, $H_e \approx H_1$. The baroclinic, long gravity wave phase speed is then, for the nominal stratification,

$$C_{bcl} = \frac{\omega_{bcl}}{k} = \sqrt{g'H_1} \approx 3.1 \text{ m sec}^{-1} \approx 270 \text{ km day}^{-1},$$

the red line of Fig. (8).

The ratio of layer thicknesses in the baroclinic mode is

$$\frac{\Gamma_1}{\Gamma_2} = \frac{\rho_2}{2\rho_1}\left((H_1 - (H_1^2+H_2^2-2H_1H_2+4H_1H_2\frac{\rho_1}{\rho_2})^{1/2})/H_2 - 1\right). \tag{48}$$

Making the same approximation noted earlier for the barotropic mode,

$$\frac{\Gamma_1}{\Gamma_2} \approx -\frac{\rho_2}{\rho_1} \approx -1, \tag{49}$$

and hence the layer thicknesses oscillate out of phase, and with nearly equal amplitude (Fig. 7, middle). There is a small but very important displacement of the free surface,

$$\frac{\Gamma_1+\Gamma_2}{\Gamma_2} \approx -\frac{\rho_2-\rho_1}{\rho_1} = -0.0017,$$

[12]Most authors define the equivalent depth from phase speed only, i.e., $H_e = C_{bcl}^2/g$ with g the full gravity. With that definition, the baroclinic $H_e \approx 1$ m (!). In other words, the baroclinic gravity wave mode has the phase speed of a 1 m thick, homogeneous (barotropic) layer. In a linear shallow water model and problem, the phase speed is all that matters and this can be a useful definition. However, if the shallow water model includes finite amplitude effects and is intended to simulate realistic amplitudes, then the actual layer thickness is relevant, and the equivalent values of Eqn. (47) seem more apt.

for the given stratification. An interface (thermocline) displacement of 50 m will thus be accompanied by a free surface displacement of about $50 * (\delta\rho/\rho_o) \approx 10$ cm, which is readily detectable to satellite-based, altimetric methods, as in Fig. (2). The currents in the upper and lower layers are exactly out of phase, and their ratio is such that the net transport vanishes.

2.5.3 Reduced gravity approximation of the baroclinic mode

The transport (depth integrated velocity) of the baroclinic normal mode = $u_1H_1 + u_2H_2 = 0$. Thus the upper and lower layer currents are in the ratio $u_1/u_2 = -H_2/H_1$. In the limit that $H_1/H_2 \to 0$, the lower layer current and pressure gradient are much, much less than in the upper layer. In that case, an approximation of Eqn. (36) is that

$$\frac{\partial h_2}{\partial x} = -\frac{\rho_1}{\rho_2}\frac{\partial h_1}{\partial x},$$

which may be used to eliminate the h_2 term from the upper layer pressure gradient,

$$\frac{\partial P_1}{\partial x} = g\left(\frac{\rho_2 - \rho_1}{\rho_2}\right)\frac{\partial h_1}{\partial x} = g'\frac{\partial h_1}{\partial x}.$$

The density interface can thus be used as a proxy for the sea surface insofar as the pressure gradient in the upper layer is concerned, provided that the full gravity that multiplies the sea surface slope is replaced by the much smaller reduced gravity, g', multiplying the much greater slope of the density interface. In that way all reference to the lower layer may be eliminated from the upper layer equations. This is sometimes referred to as a one and a half layer model, where the half refers to the deep, resting lower layer, and it is also called the reduced gravity approximation, (Fig. 7, lower). This is an appropriate interpretation of the shallow water model when applied to a simulation of baroclinic, mesoscale eddies which are mainly upper ocean (layer one) phenomena, and plausible for modelling some aspects of the wind-driven circulation of subtropical gyres (Fig. 9 and more in Part 4). The reduced gravity approximation may also be used in a multi-layered model, so long as it is appropriate to approximate the deep flow and pressure gradient as vanishing.

2.6 Problems

(1) What is the interpretation of $d/dt = 0$ in a Lagrangian system? How about $\partial/\partial t = 0$ and $D/Dt = 0$ in an Eulerian system? The material derivative and some aspects of advection are discussed in greater detail in 'Lagrangian and Eulerian representations...'. Price, James F., 12.808 Supplemental Material, Topics in Fluid Dynamics: Dimensional Analysis, the Coriolis Force, and Lagrangian and Eulerian Representations, https://ocw.mit.edu/resources/res-12-001-topics-in-fluid-dynamics-spring-2010/

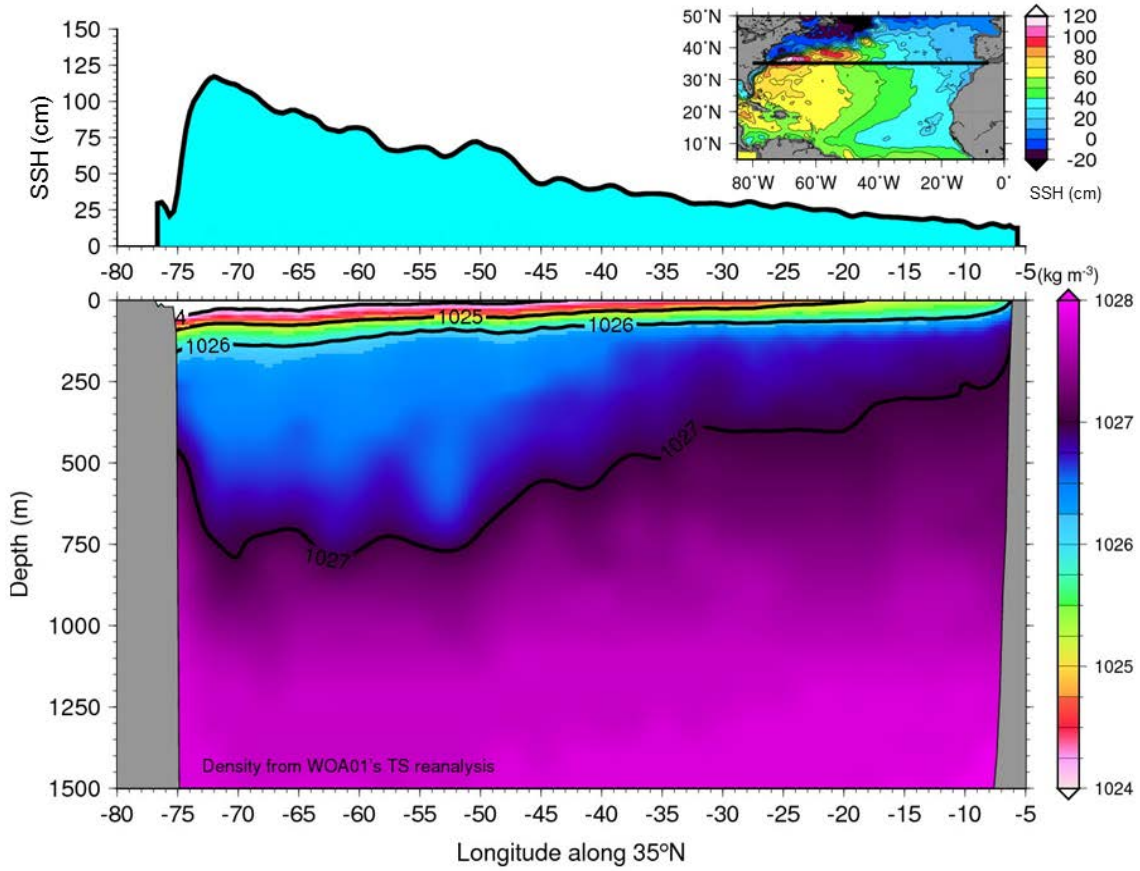

Figure 9: A cross section of the North Atlantic subtropical thermocline, sliced east-west along 35^oN, and viewed looking toward the north. The upper panel is SSH as in Fig.1, but here the monthly average for September over about twenty years of measurement. The lower panel is the long-term, September average of density along 35^oN from the World Ocean Atlas 2001 (http://www.nodc.noaa.gov/OC5/WOA01/pr_woa01.html). The tilt of the thermocline mirrors the tilt of the sea surface so that high SSH corresponds to a thick, warm upper layer. A result is that the pressure gradient and geostrophic velocity are comparatively small in the abyssal ocean, roughly 1500 - 2500 m depth, suggestive of a reduced gravity approximation (Section 2.4.3). Not shown in this figure are bottom-trapped density currents found at depths in excess of about 3000 m that make up the lower limb of the meridional overturning circulation. This figure was kindly provided by Iam-Fei Pun of WHOI.

(2) If phase speed and group speed are not already familiar to you, then the very brief discussion of Sec. 2.2.1 will probably not suffice. An excellent primary reference is Chapters 1 and 2 of Pedlosky's 'Waves in the Ocean and Atmosphere' (footnote 3). For a quick refresher, you might take a look at the script twowaves.m (Sec. 6.3), which allows you to define an arbitrary dispersion relationship between two waves that are then superimposed. The envelope of the superposition, and thus a wave form or pulse, propagates at the group speed, $C_g = \delta\omega/\delta k$, where δ is the difference between the two waves.

(3) You will feel much more at ease with the important energy and potential vorticity conservation laws if you will take the time to derive them yourself. There are no special techniques or approximations required, though the full shallow water equations entail a fair degree of manipulation. It will be helpful to start with the linear shallow water equations (see the next section) and then add just one of the advection terms, say $u\partial h/\partial x$. Performing this derivation does not aid applications, but it does help answer two important questions. 1) Does the linear shallow water system yield a self-consistent energy and vorticity balance? 2) Does the q conservation law include all of the phenomena of the shallow water system? How about energy conservation? (This second question will be answered in Sec. 3.1.)

(4) Some q-conservation problems for you: 1) A right cylinder having a radius r and height h has a moment of inertia $I = Mr^2/2$ where M is the mass of the cylinder. The angular momentum due to rotation at a rate ω about the central axis is $L = I\omega$. Show that conservation of angular momentum under changes of h and r that are mass (volume) conserving can be summarized with a vorticity conservation law like Eqn. (29). 2) Because $f \gg \xi$, generally, a change in thickness of 10% is often highly significant for the relative vorticity, as is a change in latitude of only a few degrees. Assume that a fluid column having a radius of 50 km and a thickness of 700 m is moved from 40^oN to 25^oN and that it conserves q. If all of the change in f is accounted by changes in ξ (no thickness change), estimate the magnitude of the resulting current. Now suppose that the change in f is accommodated entirely by a change in thickness.....how much?

(5) The algebra required for a three layer model is a bit tedious and is a good application for symbolic mathematics; see twolayer_eig.m linked in Sec. 6.3.

(6) Some modal questions for you: 1) Any arbitrary configuration of layer thicknesses may be decomposed into the normal modes. What would you infer is the two layer model composition of the offhand sketch of layer thicknesses in Fig. (6)? 2) In place of two active layers, suppose three layers of equal thickness. What would you guess for the modal structure of η? Check your answer against the (numerical) eigenvectors of twolayer_eig.m (Sec. 6.3). 3) The reduced gravity approximation is counterintuitive in that the density interface displacement is used to compute the hydrostatic pressure anomaly in the layer *above* the density interface. Rather than try to explain that while developing the shallow water model in Sec. 2.1, this valuable and sensible approximation (or interpretation) was deferred to this appendix. The essential, physical connection between pressure and mass or thickness anomaly is that a comparatively thick upper layer is a region of high pressure anomaly, as in Fig. (9). What do you think would happen if, due to a sign error in the code of a numerical model (we all make them) this relationship was reversed?

3 Gravitational adjustment

The sequence of experiments described here and in Part 3 differ mainly in the way that Earth's shape and rotation are represented. Of course, we know that the Earth is approximately spherical and that the Coriolis parameter varies significantly with latitude. Nevertheless, in the first experiments described here in Sec. 3, the model domain is presumed to be flat and not rotating, i.e.,

$$f = 0,$$

and there is no Coriolis force. In that case the shallow water model supports pure gravity waves only. Then, in Sections 4 and 5, the Earth will be approximated as rotating but flat, i.e.,

$$f = f_o = constant,$$

in which case there are gravity waves, inertial oscillations and geostrophic motions all at once. With an understanding of those experiments in hand, we will then be ready in Part 3 for the realistic case, spatially varying f,

$$f = 2\Omega sin(\text{latitude}),$$

first a mid-latitude case and then an equatorial case. These latter two experiments will include all of the phenomena that arose before, plus a low frequency wave called a planetary wave or Rossby wave.

3.1 Just gravity waves

The experiment starts at $t = 0$ when the thickness anomaly of dense water is released. Within the first tens of minutes the ridge begins to slump under the force of gravity, releasing potential energy and generating currents (kinetic energy). In this experiment, the motions take the form of two equal, outgoing solitary 'wave pulses' of amplitude $\eta_o/2$ and width $2L$. These pulses move at a steady speed that is very close to the (baroclinic) gravity wave speed, $C = \sqrt{g'H}$, and hence they run off of the model domain in just a few days. Other than these two discrete wave pulses, there is nothing. If you (like the author) had expected the response to look something like the waves excited on the surface of a pond by an errant golf ball, or tsunami waves generated on the surface of the ocean by a moving sea floor, then this solution will seem strange indeed. This raises a string of questions, some that should arise in any numerical study, and others that are specific to this case. In the first place, how can we know that this numerical solution is faithful to the model equations? [13] And then, these pulses look nothing like elementary gravity waves and so is it appropriate to call them 'wave' pulses?

[13] Looking at the plot of a numerical solution is a little bit like looking at Saturn through a new, homemade telescope (Fig. 11, Part 1). Barring catastrophic errors, the largest eddies and the rings will be obvious and unmistakable. However, at

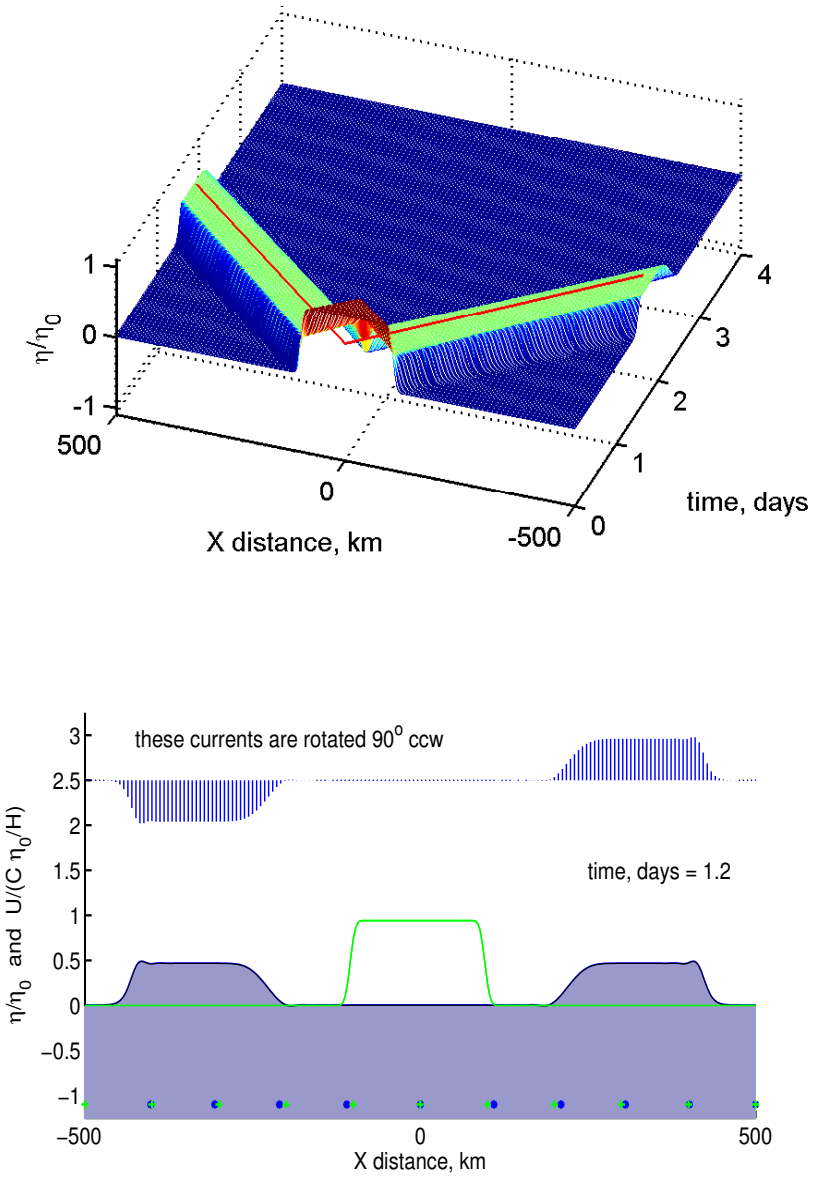

Figure 10: An experiment in gravitational adjustment (no rotation) solved by the numerical model geoadj_1d.m linked in Sec. 6.3. **(upper)** The nondimensional (scaled) thickness anomaly, $\eta(x,t)/\eta_0$, following the release of a rectangular ridge that had an initial amplitude $\eta_0 = 50$m. The thin red lines have a slope given by the gravity wave speed, $C = \sqrt{g'H} = 3.1$ m s^{-1} in this experiment. This solution was computed by the numerical model, geoadj_1d.m (Sec. 6.3). **(lower)** A snapshot of the solution at $t = 1.2$ days. The green line shows the initial thickness anomaly. The current, which is shown by the array of vectors plotted above, is in the x-direction only and has been rotated 90^o counterclockwise to be made visible here. The current is scaled with $C\eta_o/H$ (= 0.3 m s^{-1} for the case $\eta_o = 50$ m). The blue dots and green crosses at depth = -1.1 show the present positions and the initial positions of floats.

3.2 An exact solution of the linear, one-dimensional wave equation

There is a well-known, exact analytic solution for the initial value problem of the linear one-dimensional wave equation that can serve as a very useful reference for some aspects of this numerical solution. The wave equation of the linear, nonrotating shallow water system, Eqns. (30) with $f = 0$ and $v = 0$) is readily found by eliminating u in favor of η (recall that $\eta = H + h$ with H a constant and so $\partial h/\partial t = \partial \eta/\partial t$),

$$\frac{\partial^2 \eta}{\partial t^2} = g' H \frac{\partial^2 \eta}{\partial x^2}. \tag{50}$$

Given that the initial data is

$$\eta(x, t = 0) = \eta_o(x), \tag{51}$$

then the d'Alembert solution

$$\eta(x,t) = \frac{1}{2}\eta_o(kx - \omega t) + \frac{1}{2}\eta_o(kx + \omega t), \tag{52}$$

solves (50) and (51) provided that

$$\omega = k\sqrt{g'H}. \tag{53}$$

The relationship $\omega(k)$ given by Eqn. (53) is called the dispersion relation, and is the crucial and distinguishing property of a wave system. This is a particularly simple dispersion relation, $\omega(k)$ being a straight line with slope $\sqrt{g'H}$, Fig. (8). Waves of all wavenumber thus have the same phase speed,

$$\boxed{C_p = \frac{\omega}{k} = \sqrt{g'H} = C} \tag{54}$$

and the same group speed,

$$\boxed{C_g = \frac{\partial \omega}{\partial k} = \sqrt{g'H} = C} \tag{55}$$

Because all of the waves in this system (that is to say, waves of all wavenumbers) have the same phase speed, this system (shallow water, linear, nonrotating) is said to be nondispersive. As a consequence, the initial shape, $\eta_o(x)$, is retained in the propagating wave pulses. Examples of dispersive wave systems arise in later problems. Notice that the phase and group speed in this linear model are dependent upon the stratification g' and H only, and are independent of the amplitude of the motion.

some level of detail an active skepticism is healthy, even essential to avoid over-interpretation or outright error. For example, would you notice that Saturn is somewhat flattened if you didn't anticipate it? How could you discern genuine flatness from an optical distortion? One way would be to observe other, better-known phenomenon, e.g., the Moon, to calibrate the instrument's performance and extrapolate from there. Something like that can be done for numerical solutions by verifying that they follow adequately the conservation laws for energy and potential vorticity, among others, and that they reproduce known solutions well enough. The qualifications used here are deliberate; numerical solutions will never be perfect, and they don't need to be. You do have to verify that they are good enough for the problem at hand.

Gravity waves are the only possible nontrivial motion in this system. There is nothing that picks out a favored direction, and hence it is isotropic (from Greek *iso* + *tropos*, equal in all directions). Thus by symmetry half of the initial ridge propagates in one direction, and half goes the other.

The current that accompanies the wave pulses is in the direction of the pulse propagation, i.e., toward positive x within the right-traveling pulse. The velocity and the pressure gradient within the pulses is thus colinear (parallel or anti-parallel), a relationship often termed longitudinal in this context, and that is characteristic of pure gravity wave motion. On the other hand, geostrophic motion is transverse insofar as the velocity and the pressure gradient are approximately normal to one another (Part 1, Sec. 5 and other examples coming soon). The observed velocity/pressure gradient relationship thus provides a useful qualitative clue to dynamics at the level of the momentum balance.

Perhaps the two most important points are that 1) comparison with the exact d'Alembert solution shows that the numerical solution of Fig. (10) is qualitatively correct (more details below), and 2) the isolated pulses seen in the numerical solution are gravity waves in all respects save their appearance (and our prejudice that waves should look sinusoidal). Their structure is that of the initial condition and is retained because of the nondispersive property of shallow water, nonrotating gravity waves combined with the one-dimensional geometry of this specific problem.

3.3 The choice of scales

There is usually more than one way to plot a model solution (Fig. 10). It is highly desirable to use coordinates that will allow for use by the broadest possible audience. This generally requires the use of nondimensional coordinates, i.e., that independent variables, distance, time, etc. be reported in units that are intrinsic (natural) to the model system rather than in meters or seconds. In that respect, a curious feature of the linear, nonrotating shallow water model, Eq. (50), is that the gravity wave speed, $C = \sqrt{g'H}$, is the only intrinsic scale; there is no intrinsic horizontal length scale or time scale, as there will be when rotation is included in Sec. 3.1. Dimensional scales that are convenient for the specific initial condition, kilometers for horizontal distance and days for time, were therefore chosen for Fig. (10) and will be retained in all later plots to facilitate comparison with this first experiment.

The scales for the dependent variables, η and u, were chosen with the goal that the scaled (nondimensional) variables should be independent of the initial amplitude, η_0, in the limit of small amplitude. The obvious scale for the thickness anomaly is η_0, the initial value. Thus the thickness anomaly is plotted as η/η_o. (To preserve the important sign of η_o it is necessary to use the absolute value, $\eta/\mid \eta_o \mid$, though the plot legends do not show this.) The appropriate scale for the fluid speed is less obvious. The gravity wave speed $C = \sqrt{g'H}$ seems a promising candidate at first. However, C depends only upon the fluid properties and is independent of the amplitude, here η_o, while the fluid

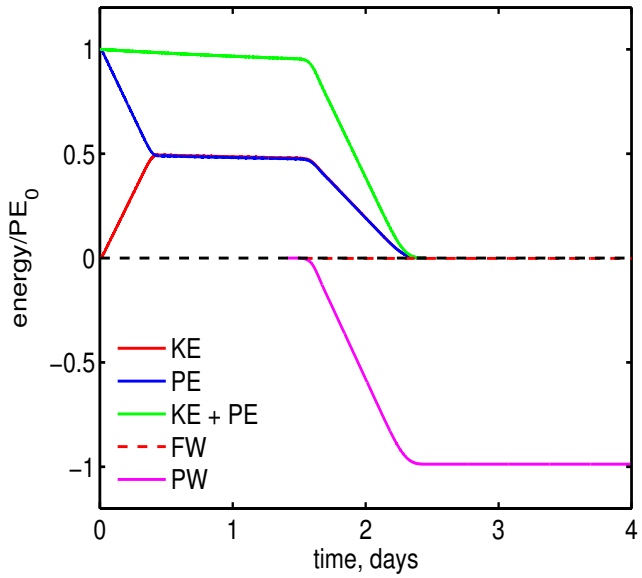

Figure 11: The energy balance for the gravitational adjustment problem (no rotation, Sec. 3.1) evaluated over a control volume $-500 \le x \le 500$ km. Energy is nondimensionalized with the initial potential energy, PE_0, and time is in days. The first four curves shown here have the same meaning as the curves with the same name (and color) in the parcel on a slope problem of Part 1, Sec. 5. Frictional work (FW) is vanishingly small since the frictional parameter r was effectively zero in this experiment.

speed should increase roughly linearly with η_o. Hence, C alone is evidently not an appropriate scale for the fluid speed. As a guess let's try instead $C\eta_o/H$, i.e., plot $u/(C\eta_o/H)$ (Fig. 10). Note that the current amplitude is about 0.5 in these nondimensional units. If this is indeed an appropriate scaling, then the nondimensional (or normalized) fluid speed should remain about 0.5 when η_o is varied within a small amplitude regime. At a large enough amplitude, the nondimensional speed will depart from this linear scale, which can be interpreted as a finite amplitude effect.

3.4 Energy and potential vorticity balances

The energy balance (Sec. 2.3.2) was evaluated over a domain $-500 \le x \le 500$ km (Fig. 11). Several features of this energy balance are in common with the parcel on a slope (Part 1, Sec. 5.3). First, the only source of energy is the potential energy, PE, stored in the initial ridge, as is true in all of the geostrophic adjustment problems that follow. Second, after the ridge is released and begins to slump, the decrease of PE is accompanied by a closely comparable increase of kinetic energy, KE. Thus the total energy, KE + PE, is approximately conserved in this ideal shallow water model, aside from small losses (a few percent per week) due to numerical viscosity and to a small but numerically necessary horizontal diffusion (discussed below).

Other aspects of this energy balance are quite different from that of the single parcel experiment. Notice that once the outward-going wave pulses are fully separated, $t \ge 2L/C = 0.8$ days, the kinetic energy and potential energy are thereafter equal. This kind of energy equipartition is a characteristic of

(nonrotating) linear gravity wave motion and so provides a useful check on the numerical solution in the much more common case that an exact analytic solution is not available. A second difference is the domain over which the energy balance was diagnosed. There was no choice about where to evaluate the energy balance for a single parcel; of course the balance was computed for the moving parcel. In fluid dynamics parlance that would likely be called a Lagrangian (material-following) balance. Given the present fluid model, there are a number of other ways that an energy balance could be evaluated. The balance could follow a wave pulse, or it could follow any specific fluid column. Here, the energy balance is evaluated over a fixed control volume, which is oftentimes called an Eulerian balance. As one consequence, energy could leave the control volume through the sides beginning at $t \approx 1.6$ days when the wave pulses reach the edges of the control volume. This energy flux is accounted by the pressure work term of Eqn (25).

Potential vorticity is interesting in quite a different way — there isn't any potential vorticity anomaly in this case! There is no planetary vorticity since $f = 0$, there is no relative vorticity in the initial condition since the ridge begins at rest, and there is no vorticity produced by the subsequent gravity wave processes because the pressure gradient in a shallow water model has zero curl.[14] Potential vorticity analysis is very often invaluable for the analysis of low frequency phenomenon (next sections), but it is not relevant to shallow water gravity waves.

3.5 Finer details of the solution; finite amplitude effects

On first seeing this solution the question came up — in what ways and to what degree can we trust this numerical solution? If we were attempting to make a realistic simulation of an observed, physical phenomenon (we aren't) then we would have to consider the assumptions made in formulating the shallow water model. But here the issue is much narrower .... how can we test that the plots in front of us represent an acceptably accurate solution to the problem posed? Comparison of the numerical solution with the exact D'Alembert solution suggests that wave propagation aspects are simulated reasonably well in the sense that the pulses move at nearly the phase speed C, and without significant dispersion, as they should in a small amplitude limit. Energy is also balanced fairly closely, though there is an unaccounted loss of a few percent in the first week. This implies that the amplitude generally must be slightly low as well.

A close look reveals two other, small but systematic differences between the numerical solution and the exact, linear d'Alembert solution insofar as the numerical wave pulses do not retain the exact

[14] In a shallow water model the fluid density is presumed constant in space and in time. If instead the density varies in space, then the pressure gradient divided by the variable density may have a curl, often called a solenoidal term. This term will produce vorticity having a component normal to the plane of the pressure and density gradients. This baroclinic process can be important in a more general three-dimensional fluid, but can not arise here.

shape of the initial ridge. First, the numerical $\eta(x,t)$ shows a small scale spatial oscillation (wavelength several times the numerical grid interval) that is characteristic of a finite-differencing error.[15] A second and more interesting difference is that the leading edge of a numerical wave pulse is steepened slightly, while the trailing edge is elongated or rarefied. This appears to be a genuine, finite amplitude effect due to nonlinear processes — horizontal advection and large variations in layer thickness — that are present in the nonlinear numerical model and solution, but not in the linear D'Alembert solution.

It is very useful to be able to make an *a priori* (before the event) estimate of the nonlinear terms and so to form a hypothesis regarding how finite amplitude effects may vary with the amplitude, η_o. For a longitudinal wave in which the wave and fluid velocity are colinear,
$u \propto u_o \cos(kx-\omega t)$, $h \propto h_o \cos(kx-\omega t+\phi)$, the ratio of the nonlinear thickness advection term to the linear local time rate of change may be estimated as

$$\frac{\text{nonlinear}}{\text{linear}} = \frac{u\partial h/\partial x}{\partial h/\partial t} = \frac{u_o k}{\omega} = \frac{u_o}{C}, \tag{56}$$

the ratio of the fluid speed to the wave phase speed. This ratio arises very widely and is often called the Froude number,

$$\boxed{F = \frac{u_o}{C}} \tag{57}$$

Given the (tentative) scale estimate of the current amplitude, $u_o \approx C\eta_o/H$ (Sec. 3.1), the Froude number can be written in external parameters and easily evaluated (recall that for the base case, $\eta_0 = 50$ m and $H = 500$ m) as

$$F = \frac{\eta_0}{H} = 0.1.$$

The other nonlinear term in the thickness equation may be readily factored into nonlinear and linear terms, $h(\partial u/\partial x) = (\eta + H)(\partial u/\partial x)$. Under the assumption that the variable η will be no larger than the initial value η_o, then again

$$\frac{\text{nonlinear}}{\text{linear}} = \frac{\eta(\partial u/\partial x)}{H(\partial u/\partial x)} = \frac{\eta}{H} \approx \frac{\eta_o}{H}.$$

The important ratio, η_o/H, called simply the 'amplitude', happens to be equal to the Froude number in this case, but not generally. These simple estimates indicate that nonlinear terms are small but not

[15] This error can be made larger or smaller depending upon the smoothness of the initial condition. If allowed to grow unchecked, this grid scale noise can readily swamp the 'physical' content of a numerical solution, i.e., the part that is faithful to the model equations. A simple cure is to include the smallest possible horizontal diffusion of thickness and momentum that will serve to damp high frequency variability. That has been done in these numerical solutions, though mention of it was left out of the previous discussion. The issue then becomes whether this *ad hoc* diffusion impacts significantly the aspects of the solution that are of interest. In this experiment, a thickness diffusion $D = 5$ m^2 sec^{-1} was sufficient to prevent runaway growth of the grid scale noise, though not enough to crush it completely. Over the short duration of this experiment, $T = 5$ days, this diffusion causes a small but acceptable spreading of the ridge judging from $\sqrt{DT^2} \approx 1.5$ km $\ll L$.

negligible compared to comparable linear terms in the base case in which $\eta_o/H \approx 0.1$. It is then plausible, but not certain from this analysis, that there should occur modest but detectable finite amplitude effects in the corresponding numerical solution.

A complementary estimate of finite amplitude effects comes from considering that the gravity wave speed likely depends upon the actual fluid thickness, $h = H + \eta$ and not just the nominal thickness as in the linear wave speed, Eqn. (54). A wave pulse, which has one sign, might then propagate at a speed given by the average thickness taking account of the pulse amplitude,

$$C_{pulse} = \sqrt{g'(H + \eta_o/4)} \approx C(1 + \eta_o/8H), \tag{58}$$

in the specific case considered here. Taking this thickness-dependent view of wave speed one step further, the observed steepening appears to be consistent with the idea that the thickest part of a wave pulse should propagate faster than in the undisturbed fluid, which should in consequence produce a steepened wave pulse front.

3.6 Problems

(1) Some important things went by rather quickly in Sec. 3.2. You should verify that 1) any function whose argument is $(kx \pm \omega t)$ satisfies the elementary wave equation provided that $\omega/k = \sqrt{g'H}$, and 2) the initial data is satisfied by Eqn. (52) for any $\eta_o(x)$. However, if $\eta_o \ll H$ does not hold, then the assumption that the system is linear would not be appropriate.

(2) The analysis of Sec. 3.2 lead to the (plausible) hypothesis that the wave pulses found in the numerical solution have the properties and parameter dependence of elementary gravity waves (if not their expected appearance). How can you test this, given the opportunity to specify the parameters of new numerical experiments via geoadj_1d.m (Sec. 6.3)? For now, exclude finite amplitude effects by keeping the amplitude small, $\eta_o/H \leq 0.1$, say, and omit friction, which will be discussed below.

(3) Friction was omitted from the discussion of energy balance in Sec. 3.4, but it is included in the numerical model via a linear damping of the velocity, $-r\mathbf{V}$, sometimes called Rayleigh damping. In the solution shown here r was set to a small enough value that frictional effects were negligible. Some friction questions: 1) What value of r is required to damp an outgoing wave pulse to half initial amplitude as it arrives at $x = 500$ km? 2) How does the required r vary with the nominal layer thickness, H? 3) Can you define a nondimensional number analogous to the Ekman number, $E = r/f$ (Part 1, Sec. 5) that serves to predict the amplitude of this damping effect?

(4) You can investigate finite amplitude effects systematically by experimenting with a much smaller and a much larger value for the initial thickness anomaly, say $\eta_o = 2$ and then $\eta_o = 200$ m (in the setup of the numerical model geoadj_1d.m). Some questions: 1) It is expected that finite amplitude effects should increase with η_o. But what if the nominal layer thickness, H, is increased apace with η_o so that the ratio, η_o/H remains constant? 2) Can you verify that wave front steepening (and rarefaction) is

large or small depending upon the Froude number, and conversely is independent of, e.g., the density difference, $\delta\rho$, when all else is held constant? 3) Does the scale for current speed, $C\eta_o/h$, account for the change in the actual (dimensional) current amplitude at small values of η_o/H? How about at very large values of η_o/H? 4) Test the estimated finite amplitude wave pulse speed Eqn. (58) using numerical solutions. 5) Instead of a ridge, suppose the initial interface displacement is a trough, $\eta_0 < 0$. Use the previous result 4) to explain the steepening and rarefaction seen in this case.

4 Geostrophic adjustment on an f-plane

The one new feature of the next experiment is that Earth's rotation is included, though in a simplified form, an f-plane, in which the Coriolis parameter is presumed to be constant. The latitude is taken to be 30^o N, and so

$$= 2\Omega \sin(\text{latitude}) \;=\; \Omega \;=\; 7.292 \times 10^{-5}\ \text{sec}^{-1}.$$

The inertial period is $2\pi/f \approx 1$ day (1 day less about 4 minutes). The one-dimensional domain and initial condition, including the initial state of rest, are unchanged from before.

We can compare the new experiment, Fig. (12), with the non-rotating experiment of the previous section, Fig. (10), and it is clear that the effects of rotation are very, very significant. We will discuss the details below, once we have a few more analysis tools in place. For now, note that there are still gravity waves that propagate away from the ridge, however their amplitude is much less than in the nonrotating case, and some wavelike motion persists for at least a week. The ridge subsides and spreads laterally in the first few days, but most of it remains in place, about 75% based upon a potential energy balance (Fig. 15). There are counter-flowing currents whose direction is such that the Coriolis force tends to oppose the pressure gradient associated with the sloping layer thickness, i.e., $0 \approx fv - g'\partial\eta/\partial x$, and after only a few days, the remaining ridge is in approximate geostrophic balance. In this f-plane experiment, an exact geostrophic balance is possible in principle (though not, in general, in a numerical solution).

4.1 Dispersion relation for waves on an f-plane

The waves in this rotating experiment are clearly very different from the pure gravity waves of the nonrotating case. The dispersion relationship that links the wave frequency ω and the wave number k makes a concise and very useful characterization of their properties. To find the dispersion relation, postulate a plane wave with wave vector, $\mathbf{K} = k_x\mathbf{e_x} + k_y\mathbf{e_y}$, which has a magnitude $K = \sqrt{k_x^2 + k_y^2} = 2\pi/\lambda$ with λ the wave length. A propagating plane wave having frequency ω is then $u(x,y,t) = U exp(i(k_x x + k_y y - \omega t))$ and similarly for v and η, where U, V, Γ are the constant but

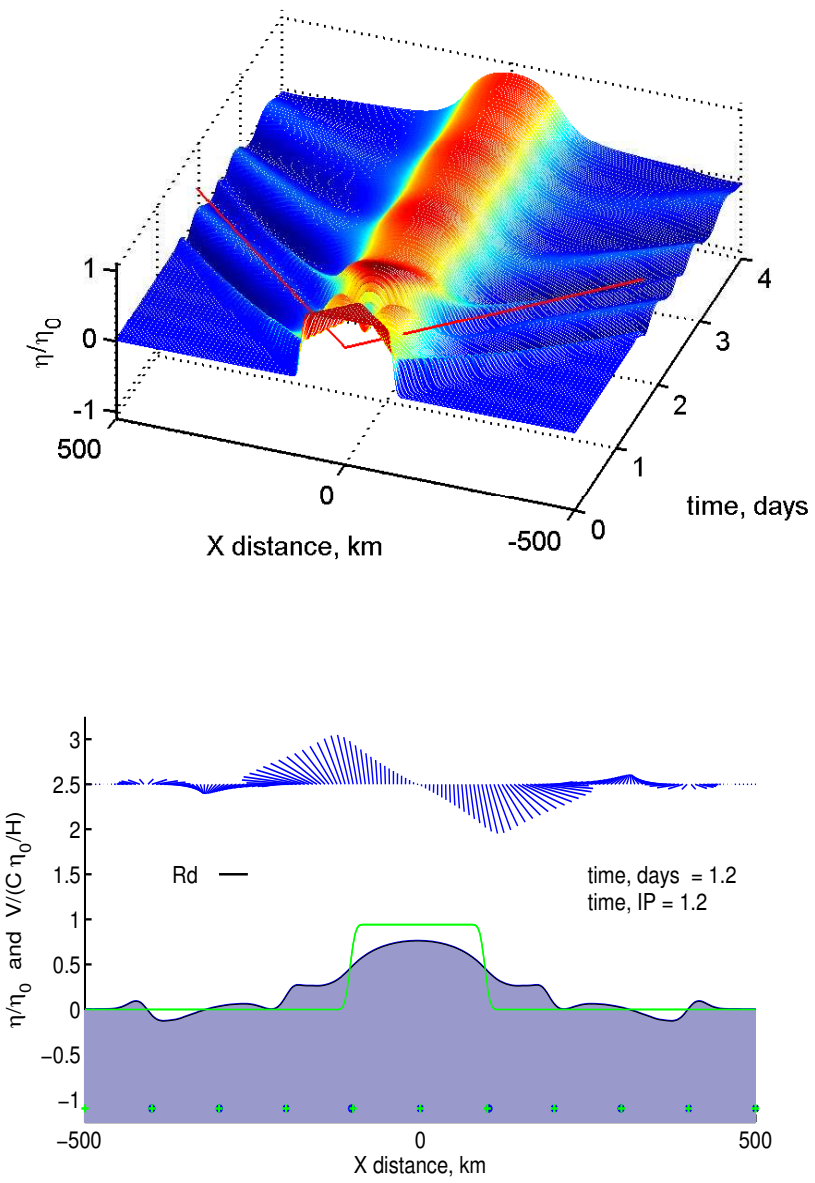

Figure 12: An experiment in geostrophic adjustment in one-dimension on an f-plane. **(upper)** The layer thickness anomaly, $\eta(x,t)/\eta_0$, of a rotating fluid layer following the release of a rectangular ridge having amplitude $\eta_0 = 50$ m. This solution was computed by the numerical model geoadj_1d.m Time and horizontal distance are shown in days and kilometers to make a direct comparison with the nonrotating experiment shown in Fig. (10). The thin red lines have a slope given by the gravity wave speed, $C = \sqrt{g'H} = 275$ km days^{-1} in this case. **(lower)** A snapshot of the solution at $t = 1.2$ days. The green line shows the initial displacement η_o. The current, which is shown by the array of vectors plotted above, is scaled with $C\eta_o/H = 0.30$ m s^{-1} for the parameters of this experiment. The blue dots and the green crosses at depth = -1.1 show the present and initial positions of floats. The floats do not move far in this experiment, and finite amplitude effects are small but detectable. Note the counter-flowing jets along the flanks of the partially subsided ridge. When the Coriolis force acting on these jets is sufficient to prevent the ridge from slumping further, the ridge is in a more or less steady, geostrophic balance.

unknown amplitudes of the velocity components and η. Substitution into the linear shallow water equations (30) and rewriting the resulting algebraic equations in a matrix format yields

$$\begin{bmatrix} -i\omega & -f & ig'k_x \\ f & -i\omega & ig'k_y \\ iHk_x & iHk_y & -i\omega \end{bmatrix} \begin{bmatrix} U \\ V \\ \Gamma \end{bmatrix} = 0. \tag{59}$$

This homogeneous system has nonzero solutions for $[U\ V\ \Gamma]$ only if it has a vanishing determinant,

$$\omega^3 - \omega(g'HK^2 + f^2) = 0, \tag{60}$$

which is to say, only if ω and K are related by a dispersion relation. The roots of (60) correspond to

$$\text{steady, geostrophic motion}: \quad \omega = 0, \text{ and} \tag{61}$$

$$\text{gravity wave motion modified by rotation}: \quad \omega = \pm\sqrt{g'HK^2 + f^2}. \tag{62}$$

Along with the dispersion relation, it is also helpful to find the polarization relation that relates the thickness and velocity components. Again we will presume a plane wave, but here there is no loss in assuming that propagation is in the x-direction only, i.e., $k_y = 0$. The thickness anomaly of a propagating plane wave can then be written $\eta(x,t) = \Gamma\cos(k_x x - \omega t)$. To find the corresponding $u(x,t)$ we can eliminate v from Eqn. (30),

$$\frac{\partial^2 u}{\partial t^2} \;=\; -f^2 u \;-\; f\frac{\partial \eta}{\partial y} \;-\; \frac{\partial^2 \eta}{\partial x \partial t}. \tag{63}$$

Substitution of the presumed $\eta(x,t)$ into (63) then gives,

$$u(x,t) \;=\; \frac{k_x \omega}{f^2 - \omega^2}\Gamma\cos(k_x x - \omega t). \tag{64}$$

Similar treatment for the other velocity component yields

$$v(x,t) \;=\; \frac{k_x f}{f^2 - \omega^2}\Gamma\sin(k_x x - \omega t). \tag{65}$$

For the wave solution, $\omega > f$, the velocity vector rotates clockwise around an ellipse whose major axis is in the direction of the wavevector, here x, and whose major/minor axes is in the ratio

$$\frac{U}{V} = \frac{\omega}{f}.$$

Since $\omega \geq f$, the ellipse is more or less elongated or polarized in the wave vector direction depending upon frequency.

4.2 Intrinsic scales of the f-plane

The rotating, shallow water model has just three external parameters: the Coriolis parameter, f, that provides a natural time scale, the rotation time, $1/f$, noted in Part 1. The reduced gravity, $g' = g\delta\rho/\rho_o$, is an acceleration, and the layer thickness, H, a degenerate length scale since there is no variation over the layer. The initial condition adds two lengths, η_o and L. The Coriolis parameter f is an obvious (inverse) time scale for normalizing the frequency of the dispersion relation Eqn. (62), and thus a given frequency can be said to be high or low compared to f. By that rearrangement to nondimensional form the dispersion relation (62) then reads

$$\frac{\omega}{f} = \pm\sqrt{\tfrac{g'H}{f^2}K^2 + 1}, \tag{66}$$

$$= \pm\sqrt{R_d^2K^2 + 1}, \tag{67}$$

in which the wavenumber K is automatically scaled by the very important length scale,

$$\boxed{R_d = \frac{C}{f}}$$

called the radius of deformation. Just as f^{-1} is the intrinsic time scale of a rotating shallow water model, R_d is the intrinsic horizontal length scale of this model. It is often the case that the initial condition or external forcing bring an external length scale to the problem, in this case the ridge width L, and the radius of deformation is the appropriate length scale for comparison. Thus a given ridge width is large or small as L/R_d is greater than or less than 1.[16] After this very simple but significant rearrangement to nondimensional coordinates, the dispersion relation (Figs. 13 and 14) holds for all values of f, g' and H, i.e., for all shallow water, f-plane models.

The value of R_d depends upon the stratification through C and the latitude through f. Over the open, subtropical oceans, $C \approx 3$ m sec^{-1} and not highly variable; $C \approx 2$ m sec^{-1} at subpolar latitudes. The more significant geographic variation of R_d comes from the latitudinal variation of $f^{-1} \propto 1/\sin(latitude)$. Notice that the equator is a special and an especially important case that will be considered in Part 3. In the ocean thermocline at 30^{o}N, $R_d \approx 40$ km. The R_d of the atmosphere at this latitude is much larger, $R_d \approx 1000$ km, because the atmosphere is both thicker than the ocean thermocline, and more strongly stratified. This very large disparity in R_d is reflected directly in the dominant horizontal scales of the variability seen in the atmosphere and ocean (cf. Figs. 1 of Part 1 and Part 2), i.e., much larger horizontal scales are observed in the atmosphere.

[16] Four remarks. 1) A more compelling physical interpretation of R_d as a length scale will come just below. 2) The important ratio of frequencies, ω/f, is sometimes referred to as the temporal Rossby number, for which there seems to be no widely accepted symbol. 3) The ratio KR_d is the layered model equivalent of the square root of the Burger number, $B = N^2/f^2$,

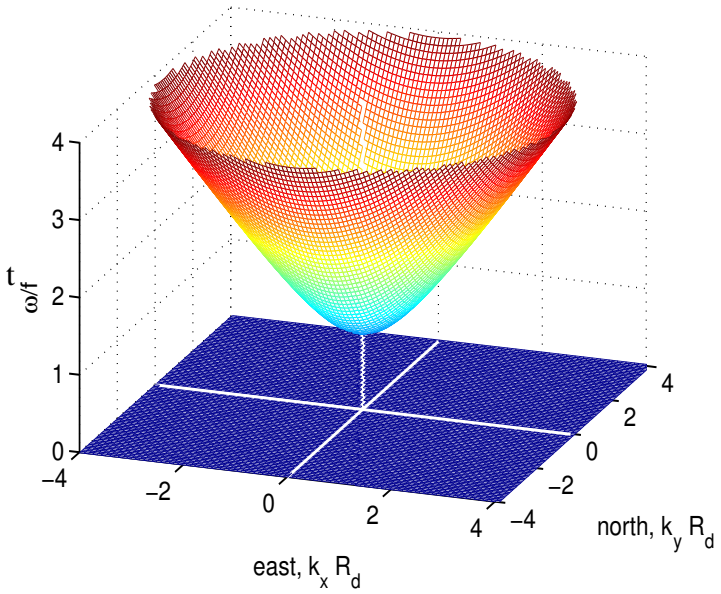

Figure 13: The dispersion relation for plane waves supported by the rotating, shallow water model. The frequency is normalized by the Coriolis parameter, f, and the wavenumber (an inverse length) by the inverse radius of deformation, R_d, discussed in the text. The colors are indicative of frequency only. A wavenumber vector $\mathbf{K}$ having an origin at $(0,0)$ and that terminates on either the bowl shaped surface or lies in the plane $\omega = 0$ is a solution, i.e., a possible free wave or geostrophic motion. This dispersion relation is symmetric about the ω axis (isotropic); the frequency of waves depends upon the magnitude of the wavenumber, $\mathbf{K}$, but not the direction of the wave vector.

4.3 Gravity, inertial and geostrophic motions

The non-zero ω/f root (the multi-colored parabola of Fig. 13 and the similar line of Fig. 14, upper) corresponds to gravity waves that are modified by rotation. There are three important limits in the dispersion relation that correspond with modes of the shallow water momentum equation.

High frequency, $\omega/f \gg 1$: In the short wave, high frequency limit, say $\omega/f \geq 5$, the dispersion relation asymptotes to pure gravity wave motion in which the phase and group speed are $C = \sqrt{g'H}$, as in the non-rotating, shallow water model (Sec. 3.1).[17] Pure gravity waves have the fastest group speed, $C_g \approx C$, and would be expected to arrive first in the far field, just as observed in the numerical solution. For these waves, the velocity is fairly strongly polarized in the direction of the wave propagation, as $U/V = \omega/f$, which may be called longitudinal.

Inertia-gravity waves: $1 < \omega/f < 5$ Intermediate scale waves fall somewhere between the limiting cases of pure gravity wave and pure inertial oscillation ($\omega/f = 1$, coming next), and are appropriately called inertia-gravity waves (or, rarely, gravity-inertia waves). Their phase speed depends upon K.

---

where $N^2 = (g/\rho)(\partial\rho/\partial z)$ is the static stability, times the aspect ratio H/λ. 4) There is no guarantee that the value 1 will always mark the boundary between large and small values of a given nondimensional number as factors of π or even $2\pi^2$ are sometimes relevant.

[17] If the wavelength is less than the layer thickness, H, then the wave motion will become a short gravity wave that is surface-trapped. These are the high frequency, wind-generated waves that make up most of the sea state and they are outside the domain of the shallow water model. Their frequency can be high enough that the pressure is nonhydrostatic.

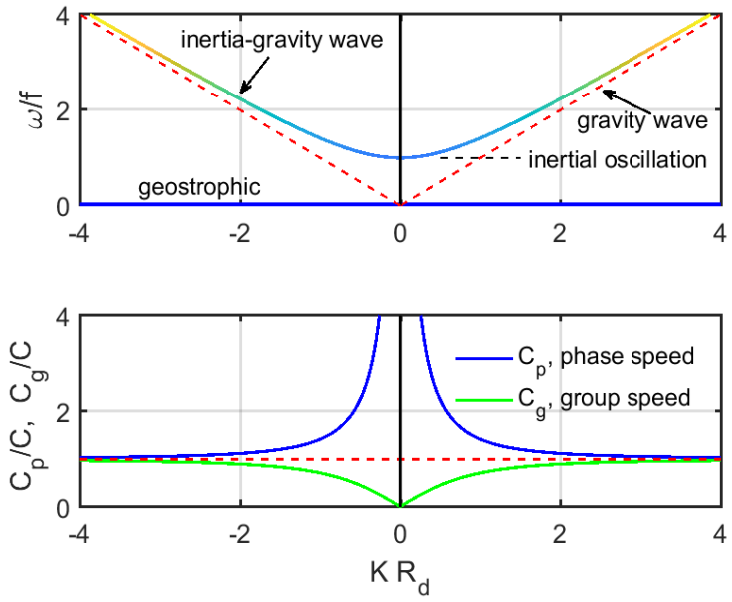

Figure 14: **(upper)** The dispersion relation for plane waves supported by the rotating, shallow water model. This is a slice through the isotropic surfaces of the previous figure. The blue line at zero frequency is the steady, geostrophic solution and the multi-colored parabola is the dispersion relation for inertia-gravity waves. The straight red dashed lines are for pure gravity waves ($f = 0$); in these nondimensional coordinates their slope is ± 1 for right- and left-going waves.**(lower)** The phase and group speeds of the inertia-gravity waves (blue and green lines) normalized by the gravity wave speed, C. Inertia-gravity waves are dispersive in that their phase speed varies with K. For short waves, $KR_d \gg 1$, the group speed asymptotes to that of pure gravity waves (the dashed red line) and in that limit $C_g = C_p = C$. The group speed goes to zero for very long waves, $KR_d \ll 1$, that have frequencies near f, i.e., near-inertial oscillations. The phase speed becomes infinite as $KR_d \to 0$.

Hence the inertia-gravity waves of an $f-$plane are dispersive, so that the shape of $\eta_0(x)$ is not, in general, preserved as these waves propagate away from a source (cf. the nonrotating, pure gravity wave experiment of Sec. 3.1). Instead, the initial form $\eta_0(x)$ will become more or less spread out, or 'dispersed', over time as waves of different wavelengths propagate at different C_g.[18]

Lowest possible wave frequency, $\omega/f \downarrow 1$: In the long wave limit, i.e., as KR_d becomes very small, inertia-gravity waves asymptote to inertial oscillations and the frequency approaches f. In this limit the phase speed is very large, infinite at $\omega/f = 1$. The entire field of motion consists of clockwise-rotating velocity having uniform phase, and thus no divergence and no associated η or pressure anomaly. It is appropriate to call this an inertial oscillation, to distinguish from vortical inertial motion that we will see in Sec. 5. Exact inertial oscillation, like exact geostrophic motion, amounts to a kind of frozen state that is unable to evolve. Consistent with this, the group speed in the limit $\omega/f \to 0$ is zero. Exact

[18]The linear initial value problem can also be solved usefully via Fourier transform. An example is carried out by the script ftransform.m (Sec. 6.3), which allows the choice of a dispersion relation. Somehow one must specify what fraction of the initial thickness anomaly will be dispersed into waves: in the non-rotating gravity wave case, all of the initial thickness anomaly η_o goes into propagating waves, but in the rotating case, a more or less significant fraction of η_o remains in the geostrophically balanced end-state as we will discuss shortly.

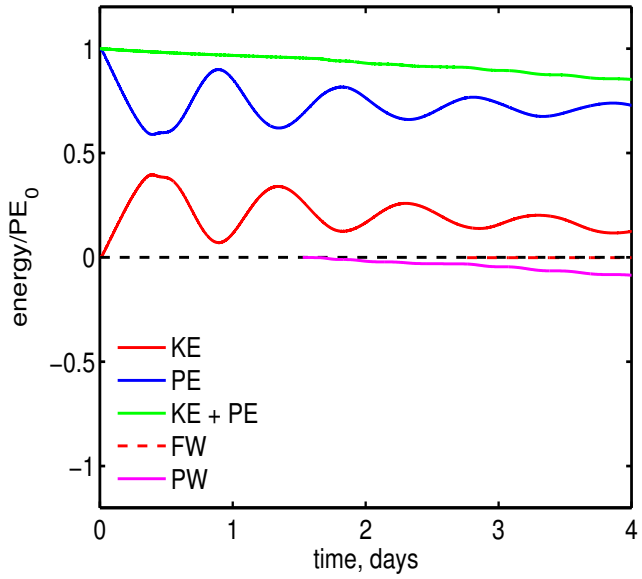

Figure 15: Energy balance of the f-plane geostrophic adjustment problem evaluated over $-500 \le x \le 500$ km. The energy and work terms are nondimensionalized with the initial potential energy, PE_0, and time is in days. At 30^o N, 1 day $\approx$ 1 inertial period. These data may be compared directly with that of the non-rotating experiment (Fig. 11) and are remarkably different. In this rotating experiment, very little energy was radiated out the sides of the domain, PW $\ll$ KE + PE, and was instead retained within the geostrophically balanced ridge as potential energy, mainly, plus significant kinetic energy. Notice that the decrease of total energy is slightly greater than the wave radiation through the sides, evidence of a small but likely growing numerical error.

inertial motion requires an infinite horizontal scale, and hence can not be realized in a finite ocean basin, or for any number of other reasons, e.g., the latitudinal variation of f and the existence of other ocean currents. While exact inertial oscillations are not expected in the ocean, rotary currents that turn in the direction of an inertial motion and that have frequencies within 5-10 percent of f — near-inertial oscillations — are very common, for example whenever there is a rapidly changing wind stress on the ocean surface (an example was noted in Section 5 of Part 1).

Notice that there is a low frequency range, $0 < \omega < f$, within which there are no free motions possible in this f-plane system.

Steady, geostrophic motion, $\omega = 0$: The root $\omega/f = 0$ corresponds to exactly steady, geostrophic motion (the blue plane of Fig. 14, upper). In this f-plane model, the corresponding wavenumber can have any orientation and any magnitude (this will not be true when the latitudinal variation of f is acknowledged in Part 3). At first this may seem a trivial solution, but it is instead the f-plane approximation of the slowly-varying and nearly geostrophic motion that makes up most of the atmosphere and ocean circulation. The polarization relation shows that the velocity associated with a plane wave thickness anomaly (not propagating) is solely in the y direction, parallel to constant thickness, and perpendicular (transverse) to the wave vector.

4.4 The steady state inferred from potential vorticity conservation

The dispersion relation is an invaluable guide to the properties of the waves that arise in a geostrophic adjustment experiment, but it can't tell us everything we might want to know. For example, the dispersion relation alone gives no hint to the amplitude of any process, i.e., it does not tell how much of the initial ridge will disperse into waves vs. survive into a geostrophic steady state. Notice too that a given wavenumber in Fig. (13) can be either a time-dependent wave, or, a steady geostrophic motion. What distinguishes these two very different kinds of motion? These important and fundamental questions lead to an analysis of potential vorticity conservation, described next.

A key result of this experiment is that most of the ridge survived the adjustment process, e.g., about 75% of the initial potential energy (Fig. 15). The conservation of potential vorticity provides real insight into why this was the case in this experiment, and why it will not be in others. In words, the $q-$conservation law Eqn. (29) states that q of a parcel (column) is unchanged by the process of geostrophic adjustment, or,

$$q(\alpha) = q_o(\alpha), \tag{68}$$

where α is a parcel tag. Assuming that q_o is known, then the task is to follow the parcels (all of the parcels) during the adjustment process. However, if the amplitude is small in the sense that parcel displacements are small compared to the scales over which the currents vary significantly, then a very helpful approximation of (68) is that

$$q(x) = q_0(x), \tag{69}$$

with x the usual (Eulerian) spatial coordinate. In other words, if the horizontal displacements during the adjustment process are small, then q will be conserved in place, approximately, and q conservation is linear. This may be checked by comparing the horizontal displacement of floats against the width of the adjusted portion of the ridge. In the base case (Fig. 12) there is a detectable, outward displacement of floats during the adjustment process, but the float displacement is small compared to the width of the adjusted portion of ridge, the radius of deformation, discussed below. As well, the geostrophic currents that form along the edge of the adjusted ridge are in a direction that is perpendicular to the thickness and velocity gradients and so cause no horizontal advection. The result is that q is indeed conserved in place, approximately, (Fig. 16, upper) as presumed in Eqn. (69). Note that the changes of v and η that occur during adjustment are significant so that linear q conservation is by no means trivial (Fig. 16).

The potential vorticity in this one-dimensional (x-dependent only) case is just

$$q = \frac{f + \partial v/\partial x}{H + \eta}.$$

The initial state included the ridge within which the layer thickness was $H + \eta_0$, and elsewhere the thickness was H. The ridge was presumed to be at rest, and so the initial relative vorticity vanishes. The

q distribution in the initial and in the final state is then, within the initial ridge,

$$\frac{f+\partial v/\partial x}{H+\eta} = \frac{f}{H+\eta_0} \text{ if } |x| \leq L, \tag{70}$$

and outside of the ridge

$$\frac{f+\partial v/\partial x}{H+\eta} = \frac{f}{H} \text{ if } |x| > L. \tag{71}$$

Note that both $v(x)$ and $\eta(x)$ are unknowns, but in addition, we have come to expect that the steady state should be in geostrophic balance, and hence we have also the geostrophic relationship between v and η, *viz.*

$$0 = fv_{geo} - g'\frac{\partial \eta_{geo}}{\partial x}.$$

When this v_{geo} is substituted into the q conservation law, say for the region $x \geq L$, Eqn. (71), there follows a second order, ordinary differential equation in $\eta_{geo}(x)$:

$$\frac{g'H}{f^2}\frac{d^2\eta_{geo}}{dx^2} - \eta_{geo} = 0.$$

The boundary conditions on η may be applied over four segments, $x \leq -L$, $-L < x \leq 0$, $0 < x \leq L$ and $x \geq L$. For example for the right-most segment, $x \geq L$, the boundary conditions are

$$\eta_{geo}(L) = \eta_0/2 \text{ and } \eta_{geo}(\infty) = 0.$$

The solution for this segment only is then

$$\eta_{geo}(x) = \frac{\eta_o}{2}\exp\left(-\frac{x-L}{R_d}\right). \tag{72}$$

By matching the solutions of the four segments, $\eta_{geo}(x)$ may be constructed across the entire ridge with a result that compares fairly well with the the numerical solution (Fig. 16, middle). Two notable features of this solution:

1) The horizontal length scale is $\mathbf{R_d}$: Compared with the initial ridge, the adjusted ridge is 'deformed' over the horizontal e-folding scale R_d. The width of the adjusted portion of the ridge is then about $3R_d$. This result suggests a clear physical interpretation of R_d. Recall from Part 1, Sec. 5.3 that $1/f$ is the time it takes for rotation to turn a parcel (started from rest) by one radian with respect to an impulsively-applied force. R_d is then the distance that a gravity wave will propagate in the time $1/f$, and hence R_d is proportional to the distance that the ridge will spread outward (as a gravity wave) before being arrested by the Coriolis force. Implicit in this is a definite meaning to the phrase 'large scale' as applied to a mass anomaly of half-width or radius L: the appropriate standard against which to compare (or measure) a horizontal length is R_d. The radius of deformation varies quite a lot with latitude, as noted earlier, and is very large (though not infinite) as f vanishes. The nonrotating

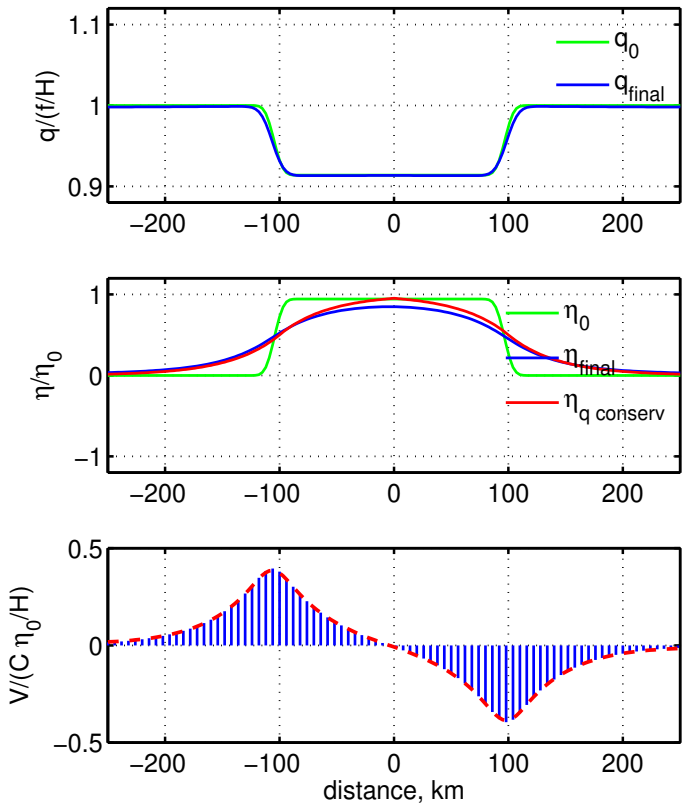

Figure 16: Elements of the potential vorticity balance for the $f-$plane geostrophic adjustment experiment. **(upper)** Initial (green) and final (blue) $q(x)$ (the latter is at $time = 6$ days). Note that q of the numerical solution is almost unchanged by the process of geostrophic adjustment, as should have been the case, despite that there are large changes in the thickness and the current. **(middle)** The initial and final thickness anomaly (green and blue lines). The red line, η_{geo}, is the steady state thickness anomaly computed from Eqn. (72) under the assumption of geostrophy and q conservation. **(lower)** Time-mean current (blue vectors). The velocity maxima, or jets, at $x = \pm$ 100 km = $\pm L$, coincide with the adjusted part of the initial ridge. These jets are in a near geostrophic balance as evidenced by a very close match with the geostrophic velocity, $(g'/f)\partial\eta_{final}/\partial x$ (dashed red line).

(gravitational) adjustment experiment of Sec. 3 can now be seen as the limit $R_d/L \to \infty$ in which rotational effects are expected to be negligible — literally zero in that case — compared to the spreading of an unbalanced thickness anomaly by gravity wave processes.

2) q-conservation and the geostrophic jets: The result Eqn. (72) gives an essentially complete account of the geostrophic jets. The jets have a relative vorticity $\partial v/\partial x$ (Fig. 16, lower) that follows from the effect of column thickness change and q conservation. For example, over the right-most segment, $x > L$, the layer thickness increased (the water column was stretched) from H to $H + \eta(x,t)$ during the adjustment process (Fig. 16, middle). The initial potential vorticity was just f/H since there was no initial velocity and no relative vorticity. To maintain constant q during the adjustment process, the relative vorticity $\xi = \partial v_{geo}/\partial x = f\eta/H > 0$ of the jet must thus be positive, or cyclonic, in this region. Stretching of the water column appears to produce positive relative vorticity by concentrating the planetary vorticity (Fig. 5, upper). To an Earth-bound, rotating observer, who sees stars turning overhead but not the rotation due to planetary velocity, it looks as if this relative vorticity has come out of nowhere. To an inertial observer for whom the same stars stand still, this looks like familiar angular momentum conservation, albeit of a deformable object.

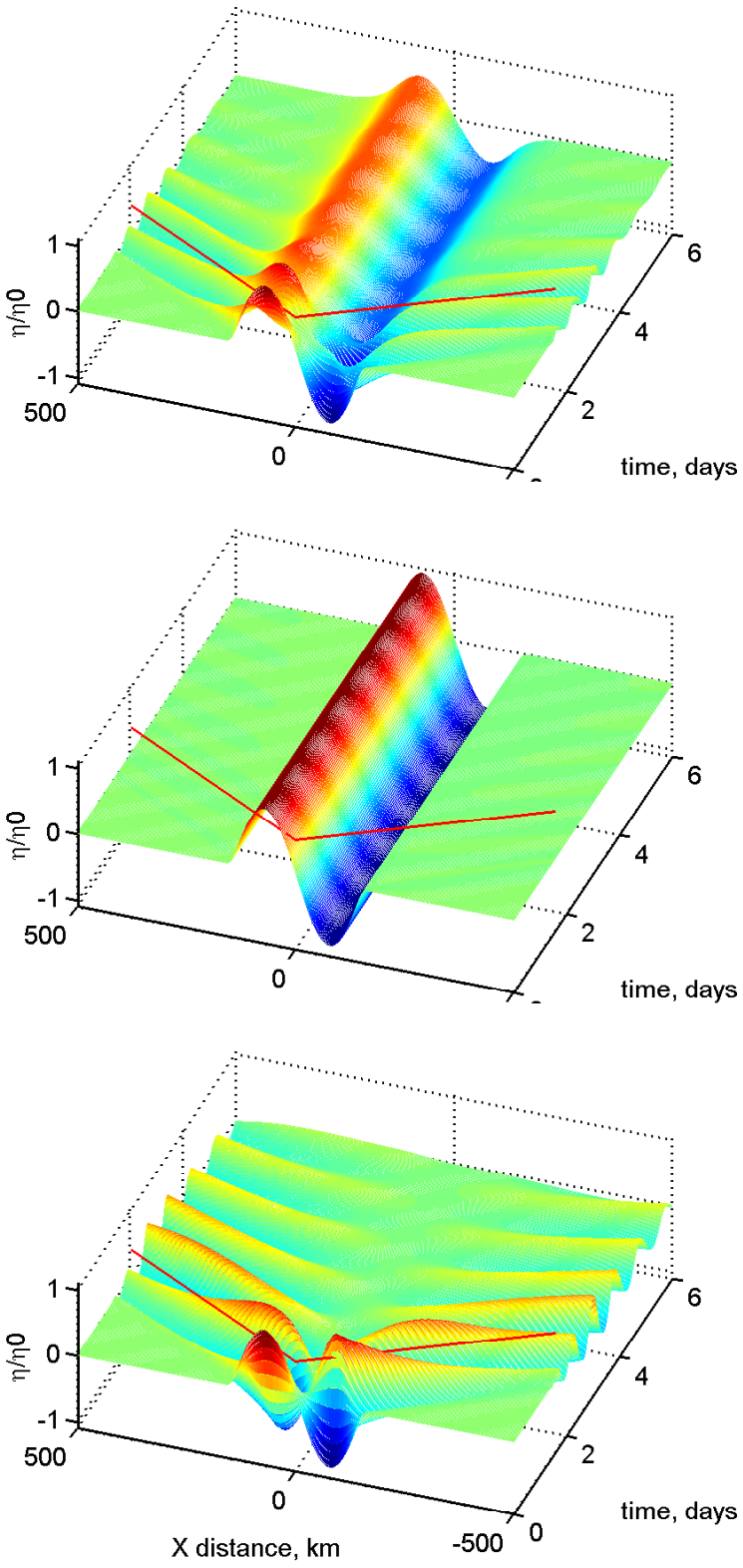

Figure 17: Three experiments in geostrophic adjustment in which the initial thickness anomaly was a single wave $\eta_0 sin(\pi x/L)$. The initial velocity was either **(top)** vanishing, as in the previous experiments, **(middle)** geostrophically balanced with the initial thickness anomaly, in which event nothing happens when the ridge is released, or **(bottom)** the velocity that gave vanishing q anomaly with respect to the outlying fluid. In this last case all of the initial ridge is dispersed by inertia-gravity waves; there is no geostrophic steady state. These experiments were carried out with geoadj_1d_uic.m, linked in Sec. 6.3.

4.5 If there is no potential vorticity anomaly

Note that if the initial q was spatially uniform (no q anomaly) the geostrophic, q-conserving solution (72) would be $\eta(x) = 0$, i.e., vanishing geostrophic steady state. In the experiment just described the initial ridge *was* a q anomaly because the initial velocity was assumed to vanish and hence the q of the initial ridge was $f/(\eta_o + H)$ compared with f/H outside the ridge. A vanishing initial velocity is the simplest initial state to define and a reasonable place to start experimenting, but it is not necessarily the most realistic or common initial condition. An experiment that allows a more general initial condition that includes velocity will make clear that insofar as the possible steady (adjusted) state is concerned, the initial ridge is defined by q its anomaly, generally, and not by η alone, as it may have seemed from this first rotating experiment.

For this more general case it is preferable to assume an initial $\eta_o(x)$ that has zero mean (though still called a ridge), e.g.,

$$\eta(x,t=0) = \eta_0 sin(\pi x/L) \text{ if } |x| < L, \text{ and } \eta(x,t=0) = 0 \text{ otherwise.}$$

Now consider one of three initial velocity fields that vanish outside of the thickness anomaly:

$$\text{vanishing velocity, } V(x,t=0) = 0, \text{ just as before,}$$

$$\text{geostrophic velocity, } V(x,t=0) = (g'/f)\partial\eta(x,t=0)/\partial x, \quad \text{or,}$$

$$\text{vanishing } q \text{ anomaly } V(x,t=0) = \int_{-L}^{x} f\eta(x,t=0)/H dx.$$

The first of these experiments (Fig. 17, upper) is very much like our previous experiment in that about two thirds of the initial ridge survives into a steady, geostrophic state. The second experiment is a non-event (Fig. 17, middle); nothing happens when a geostrophically-balanced ridge is released onto an f-plane (this would not be true if the latitudinal variation of f was retained, Part 3).

The third experiment is the important and perhaps most surprising one: a ridge having zero q anomaly is completely dispersed by inertia-gravity waves, with nothing surviving into a steady state (Fig. 17, lower).[19] This holds regardless of the width of the ridge. Evidently the width of a ridge is best defined from it's q anomaly, and not by the width of η alone, insofar as the possibility of a geostrophic end state is concerned.

The initial condition of this last experiment, vanishing initial q anomaly, may seem a special, contrived case, but it is a very, very common circumstance: tidal waves in the open ocean have large spatial scales, wavelengths of hundreds to thousands of kilometers, and yet tidal waves propagate as

[19] An animation of this third case is https://scienceweb.whoi.edu/PO/people/jprice/education/zeroq1d.mp4

almost free waves that show no sign of adjusting to the kind of geostrophic balance that characterizes mesoscale eddies and gyres. The reason is that tidal waves are generated by a small gravitational/centrifugal imbalance, the tidal force, that does not exert a torque on the ocean, and so do does not by itself generate a potential vorticity anomaly. Thus the difference between two identical wavenumbers of the dispersion relation, (Fig. 13), one being a steady geostrophic motion and the other being a wave, is evidently the association (or not) of a potential vorticity anomaly with the former but not the latter.

4.6 Problems

(1) Geostrophic balance is the final, steady state of the experiment in Fig. (12). How long would you say it takes for geostrophy to hold in this experiment? Recall from Part 1 that the time scale required for rotation to deflect a moving parcel significantly was $1/f \approx 1/4$ days at mid-latitudes. On the other hand, energetic near-inertial oscillations evidently persist for roughly five days. Are you thinking about an instantaneous geostrophic balance, or a time-mean geostrophic balance?

(2) Go back to the linear shallow water system Eqns. (30) and identify which of the terms are relevant in each of the three limits of the dispersion relation discussed in Sec. 4.3.

(3) Using the Matlab scripts geoadj_1d.m and geoadj_1d_uic.m to generate new solutions, 1) find experimentally how the width of a geostrophic jet varies with latitude and with H and g'. What do you expect if the latitude is from the southern hemisphere? Before trying these experiments in the numerical model, do a thought experiment and test your developing intuition against the numerical solution.

(4) Show that a plausible velocity scale for a geostrophic jet is $C\eta_o/H$. How/why does the jet speed vary with H? Show that a reasonable *a priori* estimate of parcel displacement is $C\eta_o/Hf$ and that the condition for linearity with respect to horizontal advection is then the familiar one, $\eta_o/H \ll 1$. Suppose that the initial thickness anomaly is made very large, say $\eta_o = 200$ m. How does this alter the potential vorticity balance during the adjustment process?

(5) The power of the potential vorticity analysis becomes evident when one considers different kinds of initial conditions, say $\eta_o = 0$, but with an unbalanced current, $u = u_o$ if $\mid x \mid \leq L$, and otherwise $u = 0$ (recall that u is the velocity component in the x-direction). Then assume the same profile but with the initial velocity directed in the y direction. Which of these initial states has vorticity, and thus a potential vorticity anomaly that should remain in the adjusted state? Solutions for these initial velocity distributions can be generated by geoadj_1d_uic.m.

(6) The solution shown here in Sec. 4 was made with a vanishingly small value of the linear damping coefficient. What happens to the wave response and to the geostrophic currents when damping is made significant? Connect the results you obtain here with the Ekman number developed in Part 1, Sec. 5.

5 In two horizontal dimensions

In this section we will consider briefly a two dimensional f-plane geostrophic adjustment experiment that introduces one new effect, flow curvature, and an important new nondimensional number, the Rossby number, that measures its magnitude. Aside from being two-dimensional, the configuration is unchanged from the basic case of Sec. 4: the initial thickness anomaly is taken to be a right cylinder having a radius $L = 100$ km that is typical of mesoscale eddies, and an amplitude 100 m. The stratification and central latitude are as before, $H = 500$ m, $g' = 2 \times 10^{-2}$ m sec^{-1} and hence $C = \sqrt{g'H} \approx 3.2$ m sec^{-1} (about 300 km day^{-1}), and $f = 7.29 \times 10^{-5}$ sec^{-1}.[20]

5.1 Adjustment is not greatly altered by the additional dimension

The slumping of the thickness anomaly produces inertia-gravity waves that propagate isotropically away from the center (cover graphic). The dispersion properties of these waves are familiar from the one-dimensional f-plane case. The wave front expands at a rate very close to the gravity wave speed, about 300 km day^{-1} (Fig. 1). The amplitude at the wave front is a small fraction of η_0, and decreases with time due to geometric spreading $\propto 1/r$ (not present in one dimension). The frequency at the wave front is roughly $2f$, and the current is at first polarized in the radial direction. With increasing time, the frequency decreases toward f, and the current vector rotates as a near-inertial motion. Near the initial eddy, weak near-inertial motion persists for several weeks.

Most of this eddy remained in place after the geostrophic adjustment process was essentially complete, several weeks after start. The resulting current was then nearly steady and anti-cyclonic (clockwise) around the eddy center, a high (Fig. 18). The initial condition was azimuthally symmetric, and nothing about the $f-$plane dynamics would change that (not the case when the β-effect is acknowledged, Part 3). Potential vorticity and energy balances are as expected from the one-dimensional cases of Sec. 4; e.g., potential vorticity stays with the fluid as prescribed in the initial condition.

5.2 Curvature and Rossby number

Once the motion reaches an azimuthally symmetric steady state we can diagnose some of its properties using the single parcel model of Part 1 (though, of course, we could not use the single parcel model to

[20] The numerical model used to solve these two dimensional problems is written in Fortran, geoadj_2d.for, linked in Sec. 6.3.

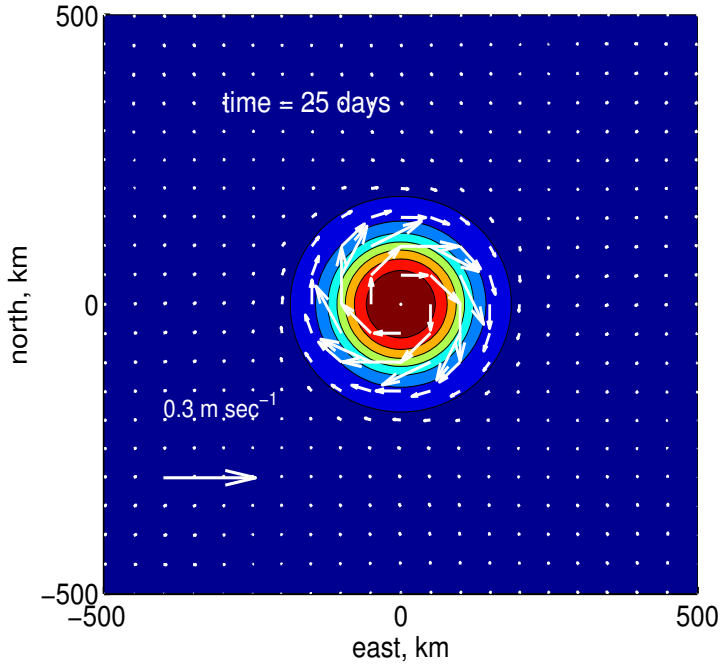

Figure 18: Velocity and interface displacement (color contours) from a two-dimensional f-plane experiment. This is a snapshot at 25 days. This eddy is a high in thickness (about 70 m at the center) and pressure and so the balanced flow is anti-cyclonic (clockwise). The big vector at lower left has a magnitude $0.5C\eta_0/H = 0.3$ m sec^{-1} and serves as a speed scale.

calculate the adjustment process in the first place). The radial component equation of motion for a rotating, polar system is (Part 1, Sec. 3.1, Eqn. 40)

$$\frac{d^2r}{dt^2} - r\omega^2 \;=\; r\Omega^2 + 2\Omega\omega r \;+\; F_r/M,$$

where we have dropped the primes used in Part 1 to indicate a rotating reference frame. The upper case Ω is the rotation rate of the reference frame, and the lower case ω is that of the parcel. Given that the flow is in steady state, the radial acceleration vanishes. The centrifugal force due to the reference frame rotation (first term on the right) also vanishes (as described in Part 1, Sec. 3). The azimuthal current is $U_\lambda \;=\; \omega r$, $f = 2\Omega$, and the external force F is the radial pressure gradient, $\propto \partial\eta/\partial r$. With these identifications, the equation of motion is

$$-\frac{U_\lambda^2}{r} \;=\; fU_\lambda \;-\; g'\frac{\partial\eta}{\partial r},$$

in which the centripetal acceleration equals the sum of the Coriolis force and the pressure gradient. It is easier to envision the steady force balance that would follow from adopting a co-rotating frame in which the parcel is not accelerating. In that case, the equation of motion is

$$0 \;=\; \frac{U_\lambda^2}{r} \;+\; fU_\lambda \;-\; g'\frac{\partial\eta}{\partial r}. \tag{73}$$

The Coriolis force will be positive (outward) if the current is cyclonic, or negative (inward) if the flow is anticyclonic. The pressure gradient force, $\propto -\partial\eta/\partial r$, may also have either sign, positive if a high, and

negative if a low. If the balance was just between these two terms, then the velocity would be the geostrophic velocity,

$$U_\lambda \;=\; U_{geo} \;=\; \frac{g'}{f}\frac{\partial \eta}{\partial r}.$$

The interesting term is the centrifugal force which is always positive (always outwards), with important consequences. The magnitude of the centrifugal force may be assessed by comparison to the Coriolis force,

$$\frac{centrifugal}{Coriolis} = \frac{U_\lambda^2/r}{fU_\lambda} = \frac{U_\lambda}{fr},$$

often written

$$\boxed{R_o = \frac{U_\lambda}{fr}} \tag{74}$$

an important nondimensional number called the Rossby number.[21] To estimate R_o for this eddy we could use the initial radius, $r = 100$ km, where the current is strongest (Fig. 18), and an estimate of the current, $U_\lambda \approx -0.2$ m s^{-1}, negative since clockwise or anticyclonic: $R_o \approx -0.03$. The centrifugal force is thus very small compared to the Coriolis force. In some applications the sign of R_o has no significance, but here it does if we use R_o to rewrite Eqn. (73),

$$0 = \; fU_\lambda(1+R_o) - g\frac{\partial \eta}{\partial r},$$

or,

$$U_\lambda \;=\; \frac{1}{1+R_o}U_{geo}.$$

In the case of a high pressure, anti-cyclone, Fig. (18), the centrifugal force adds constructively to the pressure gradient force, and in steady state, this combined centrifugal plus pressure gradient force must be balanced by a centripetal Coriolis force. The magnitude of the azimuthal velocity in a steady, high pressure anticyclone exceeds the geostrophic speed by a factor $1/(1+R_o) \approx 1.03$. Such a small effect of curvature is not apparent in Fig. (18) but evident on closer inspection, Fig. (19). A steady flow in which geostrophy is modified by curvature in this way is said to be in gradient balance or sometimes just 'balanced', with geostrophy modified by curvature being understood.

In the case of our nominal oceanic mesoscale eddy the effects of curvature are not very important or interesting. What is interesting is the insight that the gradient balance (73) can provide regarding

[21] This is a specific form of Rossby number. A more general form could be written $R_o = U/fL$, where U is a characteristic velocity (whose sign is usually not relevant), and L is the spatial scale over which the velocity varies significantly. For example, the ratio of momentum advection to the Coriolis force in the shallow water model is $U(\partial U/\partial x)/fU \approx (U^2/L)/fU = U/fL = R_o$, where equality here means same order of magnitude. Small R_o thus implies a small magnitude of momentum advection compared to the Coriolis force. An assertion of small R_o is often made at the start of a linear approximation.

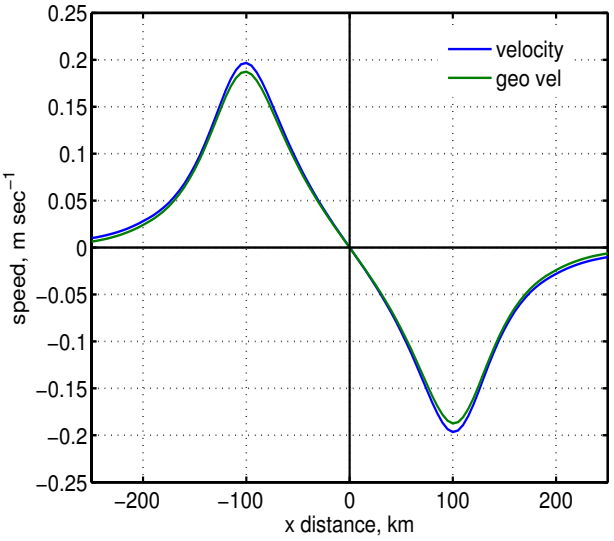

Figure 19: A slice across the adjusted eddy of Fig. (18). The geostrophic north-south velocity computed from the thickness field is the green line and the actual velocity is the blue line. The actual velocity of this high, anticyclone is only very slightly larger than the geostrophic velocity, just as expected from the small Rossby number, $R_o \approx -0.03$.

eddies generally. To that end we can treat Eqn. (73) as a quadratic equation for the unknown U_λ and with parameters f, r and $-g'\frac{\partial \eta}{\partial r}$;

$$U_\lambda = \frac{-f \pm \sqrt{f^2 + \frac{4g'}{r}\frac{\partial \eta}{\partial r}}}{2/r}. \tag{75}$$

This is a little difficult to interpret and can benefit from streamlining by dimensional analysis. There are four variables or parameters having two fundamental dimensions, length and time. Hence it should be possible to rewrite (75) in terms of one nondimensional dependent variable, and one nondimensional parameter. One possibility is

$$R_o = \frac{U_\lambda}{fr} = -\frac{1}{2} \pm \sqrt{\frac{1}{4} - \Pi}, \tag{76}$$

plotted as the blue and red lines in Fig. (20). The dependent variable is the Rossby number (74), and the independent variable is, from the second term in the radical of Eqn. (75),

$$\Pi = -\frac{g'}{rf^2}\frac{\partial \eta}{\partial r},$$

the nondimensional pressure gradient. The normalizing factor is rf^2, the centripetal acceleration of an inertial motion. The signs of R_o and Π are significant: $R_o > 0$ indicates a cyclonic (anticlockwise) flow, while $\Pi > 0$ indicates high pressure, which, if geostrophic, would be anticyclonic.

There are several noteworthy features of (76):

1) The upper left quadrant ($\Pi > 0$ and $R_o \geq 0$) of Fig. (20) is empty. There is no steady, gradient balance for a high pressure cyclone, since all three of the forces in such an eddy would be outward.

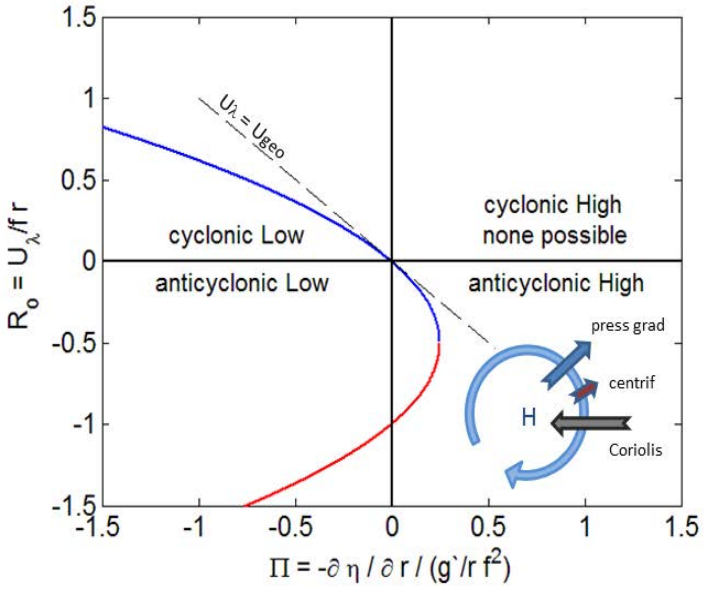

Figure 20: The blue and red line is the locus of possible solutions for gradient balanced flow over a large range of the nondimensional pressure gradient, Π. The blue line goes through the pure geostrophic case, (Π, R_o) = (0, 0), and includes the most commonly observed eddies. Red denotes high anticyclonic solutions that are uncommon and often called anomalous, but not impossible insofar as gradient balance alone is concerned. The schematic force balance for a high anticyclone is in the appropriate quadrant. The high anticyclone of Fig. (18) has a very small Rossby number, about -0.03, so that the centrifugal force is much smaller than the Coriolis force and hence it falls on the blue curve, close to the origin and close to the line $U_\lambda = U_{geo}$.

2) The large negative Π solutions, say $\Pi < 1$, are low pressure eddies for which the flow can be of either sign. For these intense eddies, the Coriolis force is of little importance, and the balance is mainly between the pressure gradient (inward) and the centrifugal force (outward), a so-called cyclostrophic balance. Tornadoes are the star examples from nature, but cyclostrophic eddies or vortices abound in everyday flows for which the spatial and time scales are small enough that the Coriolis force is unimportant; the vortices that spill off the edges of a paddle or the vortex that forms in the convergent flow above a drain are cyclostrophic eddies of this sort.

The cyclonic and anticyclonic branches differ importantly in that the cyclonic branch goes through the geostrophic state, (0, 0), while the anticyclonic branch does not. This has implications for the formation of such eddies. A cyclonic cyclostrophic eddy could result from the intensification (by vortex

stretching) of a larger scale, quasi-geostrophic flow whose absolute vorticity would be mainly planetary. Tornadoes are most often cyclonic. On the other hand, an anticyclonic eddy is more likely to be formed straightaway by intensification of whatever sign of relative vorticity might happen to be present at the site of a convergence (vortex stretching) event. Dustdevils, small scale versions of tornadoes formed by intense heating of the ground and subsequent convection, are about equally anticyclonic and cyclonic.

3) While the allowable negative (low) Π has no upper limit, the maximum possible (high) Π is 1/4 where $R_o = -1/2$. At that point the inward Coriolis force is balanced by the sum of outward pressure gradient and centrifugal forces, which are equal. Still larger positive Π implies larger centrifugal force which precludes a balance. This upper limit on Π has a real significance that can be seen in most synoptic weather maps: high pressure centers are invariably regions with very low pressure gradient and correspondingly low and often almost vanishing winds, i.e., high pressure centers give fair weather.

4) The anticyclonic high regime has two possible solutions for $0 < \Pi < -1/4$, a small magnitude R_o and a larger R_o solution ($R_o < 0$ in both cases). The former is predominantly geostrophic, with more or less minor effect of curvature. This is by far the most commonly encountered anticyclone, and our nominal oceanic eddy is of this sort. The larger magnitude R_o solution has stronger flow and the balance includes a significant contribution from the centrifugal force. This is often referred to as an anomalous anticyclonic high, on the basis that most winds or currents will generally be at least approximately geostrophic (small R_o), and indeed, large R_o anticyclones are very seldom observed in nature.[22]

5) An interesting case is anticyclonic flow at $(\Pi,\ R_o) = (0,\ -1)$ in which the balance is between the outward centrifugal force and inward Coriolis force (vanishing pressure gradient). This is one of the two kinds of inertial motion noted in Part 1, Sec. 5, vortical inertial motion, $U_\lambda = -fr$. Though possible as a steady gradient balance, such a flow would be highly unstable (see footnote above), and unlikely to persist in nature long enough to be observed.

5.3 Problems

(1) The discussion of curvature made allusion to centrifugal force acting on a parcel and is thus inherently Lagrangian. Our shallow water model is Eulerian, and there must be an equivalent

[22]This analysis considers only the possibility of a steady momentum balance, and on that basis an intense, high anticyclone is indeed possible. However, such eddies are rarely ever observed in nature. One contributing reason is that intense, high anticyclones tend to be vulnerable to centrifugal instability. Small perturbations in the azimuthally symmetric flow of an otherwise steady but unstable eddy may quickly escalate into chaotic flow that modifies the eddy away from its unstable configuration. Thus, even if an intense anticyclone was somehow formed, it would not survive. This goes beyond the present scope; see the excellent introduction by McWilliams (2006) and the review article by Chomaz, J. M, S. Ortiz, F. Gallaire and P. Billiant, 'Stability of quasi two-dimenional vortices', Lect. Notes Phys., **805**, 35-39 (2010), DOI 10.1007/978-3-642-11587-5_2

representation of this process in the Cartesian form of the Eulerian momentum equations, Eqns. (14) and (15). Can you discern what term(s) represent curvature? Hint: consider a control volume (in 2-d) set on the northern edge of the eddy and estimate the net east-west advection of north-south momentum into this control volume.

(2) Using Fig. (20), show that the actual velocity of a balanced anticyclone having $\Pi \leq 1$ exceeds the geostrophic velocity, and the reverse for cyclones. How about very intense, anticyclonic lows? What is the asymptote of R_o at very large positive Π? Why is the other sign, $-\Pi$, completely different?

(3) Sketch in the schematic force balance for the three quadrants of Fig. (20) not already noted. Describe the balance at (Π, R_o) = (0, 0) and (0, -1).

(4) Fill in the algebra needed to go from Eqn. (75) to Eqn. (76), which is one possible way to nondimensionalize the solution for balanced flow, in effect, $R_o(\Pi)$. Show that another equally efficient form is U_λ / U_{geo} is some function of Π.

6 Closing remarks

6.1 Summary of Part 2

In Section 1 we asked, **What circumstances lead to a geostrophic balance?** To develop some insight we analyzed several experiments on geostrophic adjustment posed in a numerical, shallow water model. The first experiment started with a thickness anomaly having a horizontal scale $L = 100$ km and amplitude, $\eta_0 = 50$ m, comparable to observed mesoscale eddies. Once released, the anomaly was free to evolve according to the physical processes allowed into the shallow water model.

1) When rotation is omitted by setting $f = 0$, the anomaly is quickly and completely dispersed in space by the propagation of shallow water gravity waves. These waves are nondispersive, having phase speed and group speed $C = \sqrt{g'H} \approx 3$ m sec^{-1} for the stratification typical of the mid-latitude oceans. These gravity waves are the only possible nontrivial free motions when $f = 0$. In the one-dimensional, gravitational adjustment problem of Sec. 3, the solution consists of discrete, propagating pulses that retain the shape of the initial ridge and so look nothing like elementary (sine) waves.

A given experiment is characterized also by the amplitude of the initial thickness anomaly, η_0/H. If the initial amplitude is small, $\eta_o/H \ll 1$, the pulses propagate at very nearly the expected gravity wave speed, C. For a larger initial amplitude, say $\eta_o/H \geq 0.2$, finite amplitude effects include distortions (from linear) in the shape of the pulses, and a systematic change in the propagation speed

depending upon the sign of η_o, greater when the layer is thicker.

2) When rotation is included by an f-plane approximation, the transient response includes gravity waves that are more or less modified by rotation, and a possible geostrophic steady state. The wave frequency depends upon wavelength compared to the radius of deformation, $R_d = C/f$, the intrinsic horizontal length scale of a rotating, shallow water system. The highest frequency and shortest waves are nondispersive gravity waves, while longer wavelengths are near-inertial gravity waves having very large phase speed but very small group speed. Aside from the short wave, high frequency limit, inertia-gravity waves are highly dispersive and so the radiating waves do not retain the structure of the initial thickness anomaly.

3) If the initial ridge is a potential vorticity anomaly with respect to the outlying fluid, and if the width of the initial ridge is comparable to or greater than R_d, then some fraction of the ridge will survive the adjustment process and reach geostrophic balance. In the case of a one-dimensional ridge, the geostrophic current takes the form of jets whose half-width is R_d. In an inviscid f-plane experiment, geostrophic balance can be exact, and exactly steady, i.e., geostrophy can persist forever on an $f-$plane. (As we will see in Part 3, this is not the case when the latitudinal variation of f is also considered.) In a two-dimensional experiment that begins with a cylindrical thickness anomaly (Fig. 1 and Sec. 5), a steady, balanced flow may result, and the azimuthal current U_λ deviate from geostrophic speed by a factor proportional to the Rossby number, U_λ/fL.

6.2 What comes next?

An understanding of geostrophy is an essential second step in a study of the atmosphere and ocean, but be assured that there is much, much more to learn about how such geostrophic features come to exist in the first place, and how they evolve in time. In Part 3 we will take up a fundamental question that comes from a closer look at the large scale mass (pressure) and circulation fields of the ocean and atmosphere, *viz.*, **How do small departures from geostrophic balance lead to time-dependence and to the marked east-west asymmetry of low frequency phenomenon?** The plan is again to solve experiments in geostrophic adjustment, but the next time taking account of the (surprisingly) important latitudinal variation of f.

6.3 Supplementary material

The most up-to-date version of this essay may be downloaded from the author's public access web site: https://www2.whoi.edu/staff/jprice/ and look under Education Projects. Matlab and Fortran source

codes useful for the homework are at https://www2.whoi.edu/staff/jprice/codes-aCt-P1P2/ which includes the following,

twowaves.m shows the result of superposing two sine waves whose dispersion relation may be specified arbitrarily.

twolayer_eig.m solves for eigenmodes of two and three layer models using symbolic math.

ftransform.m solves an initial value problem in one-dimension and without rotation. Shows the wave forms that result from dispersion that is normal, anomalous or none.

geoadj_1d.m is a shallow water model used for the one-dimensional geostrophic adjustment experiments of Secs. 3.1 and 3.2. The latitude, thickness anomaly, friction, etc. may be easily varied from experiment to experiment. These all assume that the initial velocity vanishes.

geoadj_1d_uic.m as above, but in this script the initial condition includes several choices for the initial current, including vanishing potential vorticity.

geoadj_2d.for is a two-dimensional shallow water model used to do the geostrophic adjustment experiment of Sec. 5. Written in a very simple Fortran. Solutions like those shown in Sec. 5 can be generated on a reasonably capable PC in a few minutes. Model parameters including latitude, the kind of f model, eddy amplitude, etc. are entered from the keyboard. Output is saved to disk.

galook.m is a Matlab script used to plot the data generated and saved by geoadj_2d.for.

Index

barotropic
    phase speed, 31

a priori, 42

baroclinic, 26
baroclinic mode, 32
barotropic
    mode, 29
Burger number, 48

curvature, 58

d'Alembert solution, 38
dispersion relation, 16
    inertia-gravity waves, 44

energy balance, 18, 50
Eulerian velocity field, 17

f-plane, 44
floats, 17
flux form, 12
Froude number, 42

geostrophic motion, 50
gravitational adjustment, 36

hydrostatic pressure, 13

ideal fluid, 10
inertial motion
    inertial oscillation, 49
    vortial inertial motion, 62

Lagrangian velocity, 18
longitudinal relationship, 39

mass conservation, 12
mass or thickness balance, 12
material derivative, 12
momentum flux, 12

nondispersive, 38
normal mode, 28

passive tracer, 17
polarization, 46
potential vorticity, 19
    and gravity waves, 41
potential vorticity conservation, 51
potential vorticity conservation equation, 22

radius of deformation, 47
reduced gravity approximation
    justification, 33
Rossby number, 59
rotation time, 47

shallow water criterion, 9
shallow water equations, 14
shallow water model, 8

transverse relationship, 39

vorticity, 19
    absolute vorticity, 22
    planetary vorticity, 22
    relative vorticity, 22
vorticity field, 20

wave group speed, 16
wave phase speed, 16

MIT OpenCourseWare
https://ocw.mit.edu

Resource: Topics in Fluid Dynamics

James Price

For information about citing these materials or our Terms of Use, visit: https://ocw.mit.edu/terms.

a Coriolis tutorial, Part 3:

β-effects; westward propagation

James F. Price

Woods Hole Oceanographic Institution,
Woods Hole, Massachusetts, 02543
https://www2.whoi.edu/staff/jprice/ jprice@whoi.edu

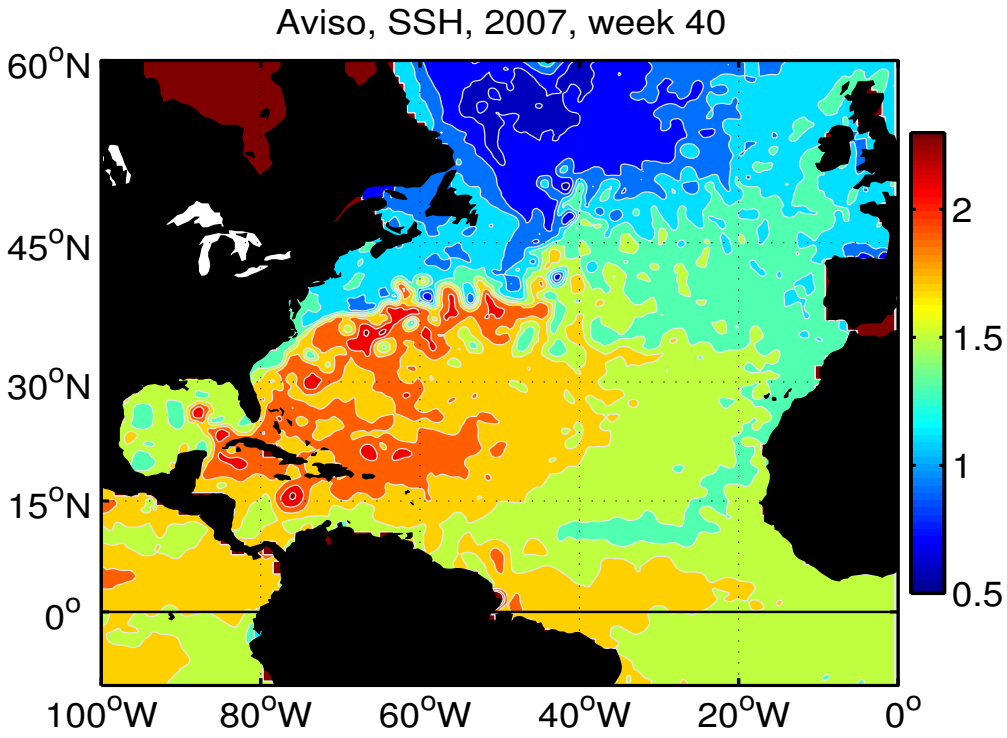

Figure 1: Sea surface height (SSH) over the North Atlantic observed by satellite altimetry. SSH variability occurs primarily on two spatial scales — basin scale gyres (thousands of kilometers), an SSH high in the subtropics and a low in the subpolar basin — and mesoscale eddies (several hundred kilometers) that are both highs and lows of SSH. The basin scale gyres are clearly present instantaneously, as here, and on long term time average, while mesoscale eddies are significantly time-dependent, including marked westward propagation. To see an animation, https://www2.whoi.edu/staff/jprice/Aviso-NA2007/ The goal of this essay is to learn how the northward increase of the Coriolis parameter leads to a westward propagation tendency for most large scale, low frequency phenomena, including the gyres and mesoscale eddies seen here.

Abstract: This is the third of a five-part introduction to the effects of Earth's rotation on the fluid dynamics of the atmosphere and ocean. The goal is to understand some of the very important beta effects (β-effects) that follow from the northward increase of the Coriolis parameter, f(latitude). The first problem considered is mid-latitude geostrophic adjustment configured as in Part 2 but with f represented by the linear approximation, $f = f_o + \beta y$, often called a β-plane. The short term (less than one week) adjustment is much the same as found on an f-plane, *viz*, spreading inertia-gravity waves that leave behind a nearly geostrophic eddy. On an f-plane, such an eddy could be exactly steady (absent diffusion or friction). On a β-plane, the same eddy will spontaneously translate westward at a slow and almost steady rate, about 3 km per day at 30^o latitude (south or north) and given scales that are typical of oceanic mesoscale eddies. This westward eddy translation has a great deal in common with the propagation of an elementary, long Rossby wave, and it is also consistent with the observed propagation of oceanic mesoscale eddies.

A similar adjustment experiment set in an equatorial region gives quite different results. Even fairly large, unbalanced thickness anomalies are rapidly dispersed into east and west-going waves. The west-going waves include the equivalent of inertia-gravity and Rossby waves. Long equatorial Rossby waves are nondispersive and have a phase and group speed of about 100 km per day, or 30 times the mid-latitude Rossby wave speed. The east-going Kelvin wave is still more impressive, as it carries the majority of the thickness anomaly in a single, nondispersive pulse that propagates eastward at the gravity wave speed, 300 km per day. Kelvin waves may thus transmit signals (say, an anomaly of upper ocean thickness) from mid-ocean to the eastern boundary within about a month.

These and other low frequency phenomenon are often interpreted most fruitfully as an aspect of potential vorticity conservation, the geophysical fluid equivalent of angular momentum conservation. Earth's rotation contributes planetary vorticity, f, that is generally considerably larger than the relative vorticity of winds and currents. Small changes in the latitude of a fluid column may convert planetary vorticity to a significant change of relative vorticity, or, if the horizontal scale of the motion is large compared to the radius of deformation, to a change in layer thickness (vortex stretching). The latter is the principal mechanism of westward propagation of long Rossby waves and of mid-latitude mesoscale eddies.

More on Figure 1: A one week average of SSH over the North Atlantic. This SSH is with respect to a level surface, with tides and high frequency variability removed. The color bar at right is in meters. These data were compiled and analyzed by the Aviso Project, https://www.aviso.altimetry.fr/ A slowly-varying, tilted SSH implies a near-surface geostrophic current that is approximately parallel to isolines of SSH. Along with geostrophic currents, there may also be wind-driven Ekman currents that are not directly visible here. Compared with the year-long mean of Fig. 1, Part 1, this field shows considerable variability on scales of several hundred kilometers, often termed the oceanic mesoscale and emphasized in this essay.

Contents

1 Large-scale flows of the atmosphere and ocean are markedly anisotropic **4**

1.1 Mesoscale Eddies . . . 4

1.2 Other phenomena . . . 5

1.2.1 Equatorial variability . . . 5

1.2.2 Upper Ocean Gyres . . . 6

1.3 Goals and the plan of this essay . . . 6

1.4 Acknowledgments . . . 7

2 Adjustment and propagation on a mid-latitude β-plane **8**

2.1 High frequency beta-effects on inertia-gravity wave propagation . . . 8

2.2 Low frequency beta-effect; westward propagation of nearly geostrophic eddies . . . 9

2.3 Planetary Rossby waves . . . 14

2.3.1 Beta and relative vorticity; short Rossby waves . . . 18

2.3.2 Beta and vortex stretching; long Rossby waves . . . 19

2.4 Finite amplitude effects, and the dual identity of mesoscale eddies . . . 21

2.4.1 Eddy propagation seen in the η and $\mathbf{V}$ fields . . . 22

2.4.2 Fluid transport seen in tracer fields and float trajectories . . . 22

2.5 Rossby waves $\rightarrow$ Eddies . . . 28

2.6 Appendix: Some of the varieties of Rossby wave-like phenomenon . . . 31

2.6.1 Westerly waves . . . 31

2.6.2 Basin-scale Rossby waves . . . 32

2.6.3 Topographic eddies and waves . . . 33

2.6.4 Tropical cyclones . . . 34

2.7 Problems . . . 35

3 Adjustment on an equatorial β-plane **36**

3.1 An equatorial adjustment experiment . . . 37

3.2 An equatorial radius of deformation . . . 38

3.3 Dispersion relation of equatorially-trapped waves . . . 40

3.3.1 Westward-going gravity and Rossby waves . . . 41

3.3.2 Kelvin wave . . . 43

3.4 Problems . . . 46

4 Summary and Remarks **46**
4.1 Mid-latitude mesoscale eddies 47
4.2 Equatorial Adjustment 48
4.3 Remarks 48
4.4 What's next? 49
Index 50

1 Large-scale flows of the atmosphere and ocean are markedly anisotropic

A thorough-going understanding (intuition) of the Coriolis force and geostrophy are a good starting point for a study of the atmosphere and ocean. However, geostrophy is nowhere near the end of the road: an exact geostrophic balance, i.e., geostrophy on an f-plane as used in Part 2, implies exactly steady winds and currents that never evolve. Moreover, f-plane phenomena are intrinsically isotropic, showing no favored direction. In sharp contrast to these properties of an f-plane model, observations from the atmosphere and the ocean show that nearly all large scale winds and currents evolve slowly but continually, even absent external forcing, and that they often exhibit a marked east-west anisotropy of one or more properties. Three important examples of this east-west asymmetry evident in Fig. 1 are:

1.1 Mesoscale Eddies

The SSH data of Fig. 1 (and especially its animation linked in the caption) reveal a number of important, characteristic properties of the mesoscale eddy field:

1. **Space and time scales.** Any given snapshot of SSH will reveal variability in the form of more or less round SSH anomalies having a radius $L \approx 200$ km, an SSH amplitude of typically $\pm$ 0.1 m and currents $U \approx 0.1$ m sec^{-1} — mesoscale eddies. Direct measurements of ocean currents within eddies indicate that their momentum balance is close to being geostrophic, as we would have expected given their modest amplitude and typically small Rossby number, $R_o \leq 0.05$ (Sec. 5, Part 2). A given eddy, i.e., a specific SSH anomaly, can often be identified and tracked for many months. Highs and lows of SSH — anti-cyclones and cyclones — are about equally common.

2. **Westward propagation.** Aside from regions having strong mean currents, e.g., the North Brazil current or the Gulf Stream and its extension into the subpolar gyre, mesoscale eddies propagate westward, slowly, but relentlessly. On average over all ocean basins, the eddy propagation speed at 30 deg latitude has been estimated from satellite altimetric data to be $3.5 \pm 1.5 \times 10^{-2}$ m sec^{-1} or about 3 km day^{-1}. The observed eddy propagation speed decreases somewhat toward higher latitude, and increases markedly toward lower latitudes down to about 15 deg. At still lower latitudes, the SSH signature of mesoscale eddies is much reduced.[1]

3. **Geography and seasonality.** Mesoscale eddies are very widespread but their amplitude shows considerable spatial variability. The largest SSH amplitudes, up to about about ± 0.2 m, are found near the western boundaries of the subtropical and subpolar basins. Eddy amplitudes are considerably less in the eastern half of the subtropical North Atlantic, and mesoscale eddies are less common in the equatorial region, outside of the North Brazil current. There is very little evidence of seasonality of eddy amplitude or other properties, suggesting that direct forcing by the atmosphere is not the primary generation process (the equatorial region again being a partial exception).

1.2 Other phenomena

1.2.1 Equatorial variability

SSH variability seen in the equatorial region ($\pm 10^o$ of the equator) is quite different from that seen at higher latitudes. Mesoscale eddies are, by comparison with higher latitudes, uncommon. SSH variability occurs primarily in zonally elongated and meridionally compressed features that are displaced from the equator by 5 to 10^o and that appear to have significant seasonality. There are occasional events of rapid eastward propagation along the equator, several hundred kilometers per day, sometimes spanning almost the entire basin.

[1] A comprehensive analysis of mesoscale eddies observed in altimetric data is by Chelton, D.B., Schlax, M.G., Samelson, R.M.,2011, Global Observations of Nonlinear Mesoscale Eddies, *Progress in Oceanography*, doi: 10.1016/j.pocean.2011.01.002. Other recent analyses of the oceanic mesoscale are by Fu, L., D. B. Chelton, P. Le Traon and R. Morrow, 'Eddy dynamics from satellite altimetry', *Oceanography Mag.*, 2010, and by Zang, X. and C. Wunsch, 1999, *J. Phys. Oceanogr.*, 29, 2183-2199. Fu, L-L., 2009, 'Pattern and velocity propagation of the global ocean eddy variability', *J. Geophys-Res Oceans*, 114, C11017, doi:10.1029/2009JC005349 describes the often very large effect of the time-mean ocean circulation upon eddy propagation.

1.2.2 Upper Ocean Gyres

Fig. 1 is centered on the North Atlantic subtropical gyre, a high pressure (high SSH) clockwise rotating, basin-filling circulation that is driven by the overlying winds. A striking characteristic of all wind-driven ocean gyres is that they are strongly compressed onto the western side of the basin, often termed western intensification. This and other aspects of wind-driven circulation will be deferred to Part 4.

1.3 Goals and the plan of this essay

The goal of this essay is to take a significant step beyond f-plane geostrophy and address .... **What process(es) lead to the time-dependence and marked east-west asymmetry of most large-scale flow phenomena?** There are many processes that can cause departures from geostrophy and time-dependence, including drag on an upper or lower boundary, which will be considered here in a simplified form. However, another process(es), called the β-effect(s), is the emphasis here. β-effects are ubiquitous in that they arise merely from north-south flow in combination with the northward increase of the Coriolis parameter,

$$f(\phi) = 2\Omega \sin(\phi), \tag{1}$$

where ϕ is the latitude. The $f(\phi)$ above can often be used as is, but for our purpose it is helpful to use the linear approximation that

$$f(y) = f(\phi_o) + \frac{df}{dy} y + HOT, \tag{2}$$

where $y = R_E(\phi - \phi_o)$ is the north-south (Cartesian) coordinate, R_E is Earth's nominal radius, approx. 6370 km. The coefficient of the linear term is very often written as

$$\boxed{\beta = \frac{df}{dy} = \frac{2\Omega}{R_E}\cos\phi_0} \tag{3}$$

When the higher order terms (HOT) of (2) are ignored, the resulting linear model

$$\boxed{f(y) \;=\; f(\phi_o) \;+\; \beta y} \tag{4}$$

is often called a β-plane. β is positive in both hemispheres, has a maximum at the equator, and goes to zero at the poles. At 30^o N, say, $\beta = 2.29 \times 10^{-11}\mathrm{m}^{-1}\mathrm{s}^{-1}$, which looks to be very small. However, the appropriate comparison is βL with the constant term $f_o = f(\phi_o)$ of (2), where L is the horizontal scale of the motion, and then it is apparent that the β term is $\propto L/R_E$. The β term is still small for mesoscale-sized phenomena, $L = O(10^5)$ m. However, β effects may be systematic and persistent, and may thus become important over a long term, say months.

The plan is to solve and analyze a sequence of idealized adjustment experiments posed in a shallow water (single layer fluid) numerical model in which the Coriolis parameter is represented by the β-plane approximation, Eqn. (4). The shallow water momentum and continuity equations were written in Sec. 2, Part 2 and will not be repeated until some new terms are added in Part 4. The configuration is an open domain, very much like that of Part 2. Mid-latitude, mesoscale eddies are treated in Sec. 2, and a similar equatorial adjustment experiment is considered in Sec. 3.

The emphasis here is on β-effects rather then the shallow water model *per se* or its analysis, but there two aspects of the model and method that you should watch for. First, the shallow water equations solved here are nonlinear, in common with all but the most simplified fluid models. Whether the solution exhibits appreciable finite amplitude phenomena depends upon the amplitude of the initial eddy (Sec. 2) or wind stress (Part 4). Amplitudes are chosen to be realistic of the phenomena of Fig. 1, and as a result, finite amplitude effects are appreciable but generally not dominant. However, this depends very much on the specific phenomenon under consideration, i.e., whether eddy propagation, which looks to be nearly linear, or parcel displacement caused by the eddy, which is significantly nonlinear. Second, the primary analysis method is diagnosis of the potential vorticity balance, i.e. q-balance. This was very fruitful for understanding the geostrophic adjustment phenomena of Part 2, and it is almost indispensable for interpretation of the upcoming experiments. Gaining some fluency with the concepts of q-balance will be invaluable for your study of oceanic and atmospheric dynamics, and an implicit goal of this essay is to help you make a start.

1.4 Acknowledgments

Financial support during the preparation of these essays was provided by the Academic Programs Office of the Woods Hole Oceanographic Institution. Additional salary support has been provided by the U.S. Office of Naval Research.

These essays and associated materials may be cited by the MIT OpenCourseWare address: Price, James F., 12.808 Supplemental Material, Topics in Fluid Dynamics: Dimensional Analysis, a Coriolis tutorial, and Lagrangian and Eulerian Representations (Spring 2022), https://ocw.mit.edu/courses/res-12-001-topics-in-fluid-dynamics-spring-2022 (date accessed).
License: Creative Commons, CC BY-NC-SA. For rights and obligations under this license see https://creativecommons.org/licenses/

2 Adjustment and propagation on a mid-latitude β-plane

We can begin to understand some of the observed properties noted in Sec. 1.1 by studying the evolution of a single eddy made by geostrophic adjustment, just as in Part 2, with the only new wrinkle being $f(\phi)$ given by Eqns. (3) and (4) vs. an f-plane in Part 2. As well, the integrations are continued for a much longer duration, up to a year. The spatial domain of the model is two-dimensional, with $(x,\ y)$ the east and north coordinates, and the domain is 3000 km on a side. The undisturbed layer thickness, H = 500 m. The initial condition is taken to be a right cylinder of radius $L = 100$ km, and thickness anomaly, $\eta_0 = 50$ m. This corresponds to an SSH anomaly of about 0.1 m (from the reduced gravity approximation, Sec. 2, Part 2), which is typical of observed SSH mesoscale variability. The initial velocity is everywhere at rest. The initial eddy is thus a potential vorticity anomaly compared to the outlying fluid, i.e., inside the initial eddy, $q = f/(\eta_0 + H)$, while outside, $q = f/H$. Everything that we saw and learned from the f-plane adjustment experiments in Part 2 will recur here, but alongside several new and very important phenomena — β-effects — that owe their existence to the inclusion of the β term in (2). There are two kinds of beta-effects noted here, high frequency beta effects upon inertia-gravity waves which is discussed very briefly, and low frequency beta effects that are the central topic.[2]

2.1 High frequency beta-effects on inertia-gravity wave propagation

In the case of a mesoscale eddy having radius $L = 100$ km, the spatial variation of f is small, $\beta\delta y/f_o = 2L/R_E \approx 0.03$, and so it is not surprising that the first few days of the geostrophic adjustment process are very similar to that seen in the f-plane experiments of Part 2, including, initially, isotropic radiation of inertia-gravity waves Fig. (2), and the animation linked in the caption. But after about a week, the inertia-gravity wave field develops a noticeable north-south asymmetry. The waves that propagate poleward (northward in this case) are propagating toward higher f. Within a few thousand kilometers these waves reach a latitude at which their intrinsic frequency approaches f. Recall from Part 2 that free inertia-gravity waves can not exist at a latitude where their frequency is less than the local inertial frequency, f, and this is true on a β-plane as well. Poleward-traveling inertia-gravity waves are thus reflected equatorward. After about ten days have passed, the region that is poleward (northward) of the eddy is nearly free of inertia-gravity waves, while the equatorward side is still fairly energetic. This β-induced refraction of inertia-gravity waves is an interesting and important process of the ocean's internal wave sea state. However, the emphasis here is on low frequency phenomenon, and this particular high-frequency β-effect will not be discussed in depth.

[2]These experiments start with a mesoscale eddy-sized q anomaly. This raises the important question — why are there such thickness anomalies in the first place? — considered very briefly in Sec. 2.5.

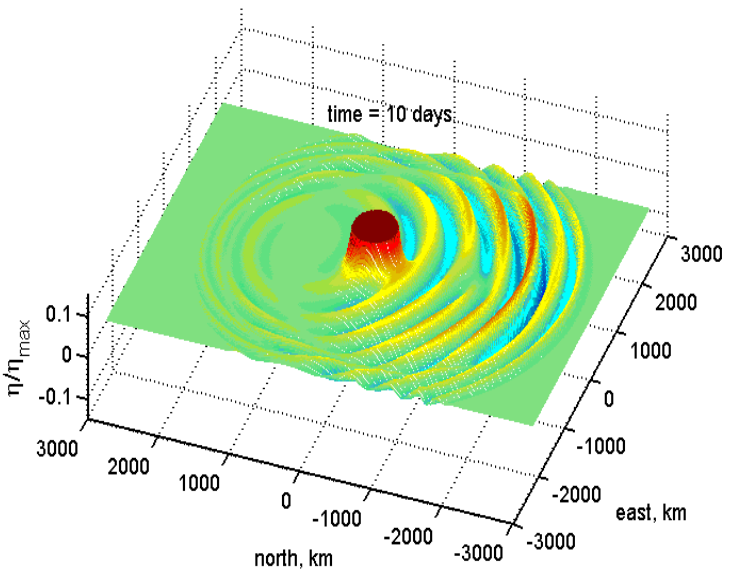

Figure 2: A snapshot of scaled thickness anomaly ($\eta_{max} = \eta_0 = 50$ m) 10 days after the start of a β-plane adjustment experiment. Poleward (north) is to the left in this figure. The vertical scale is severely truncated to emphasize the comparatively small amplitude inertia-gravity waves. By this time the wave amplitude is much reduced on the poleward side of the eddy. This north-south asymmetry in wave amplitude is due to a beta-induced reflection of the poleward-traveling, inertia-gravity waves. An animation of this data is igwaves-beta.mp4 in the P3 video collection https://www2.whoi.edu/staff/jprice/P3-videos

2.2 Low frequency beta-effect; westward propagation of nearly geostrophic eddies

Over a longer time, this experiment reveals a wholly new process that follows from the seemingly small change made to the Coriolis parameter — the eddy peak moves almost due westward at a slow but steady rate, -0.03 m sec^{-1} or roughly 3 km per day (Fig. 3). This westward propagation is significant in that it is 1) a robust and well-resolved feature of the numerical solution, and 2) closely comparable to the observed, westward propagation of ocean mesoscale eddies at this latitude (Fig. 1). Notice that the eddy peak just about keeps pace with the thin red line of Fig. (3) that is translated westward at the long Rossby wave speed appropriate to the present stratification and central latitude, $-\beta R_d^2 = -0.036$ m sec^{-1}, discussed in detail in Sec. 2.4.

The eddy peak in η remains well-defined, though the amplitude diminishes over time, especially at the beginning of the experiment. A spreading wake of decidedly wavy-looking ridges and troughs appears to trail behind the eddy peak, and eventually extends slightly eastward of the initial eastward edge, $x = 100$ km. The energy present in these waves must have come from the initial potential energy of the raised interface, and hence the spreading of energy away from the eddy peak is consistent with the decrease in the eddy peak amplitude.

The primary goals for the remainder of this section are to develop an understanding of the westward

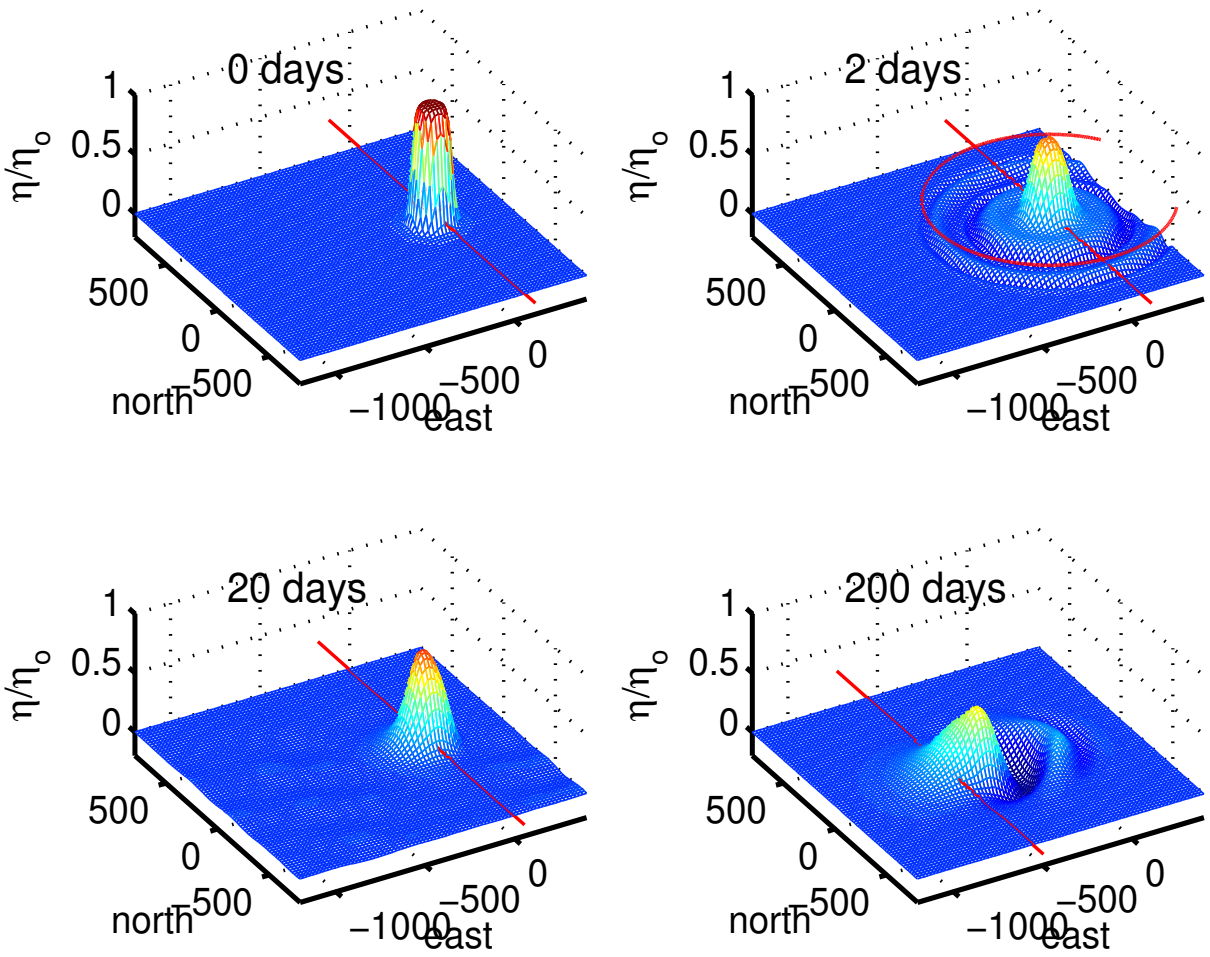

Figure 3: A numerical experiment in geostrophic adjustment on a β-plane solved by the numerical model geoadj_2d.for The normalized anomaly of layer thickness, η/η_0 ($\eta_o = 50$ m), is shown at four times: (upper left) the initial state of rest at $time = t = 0$, (upper right) 2 days after the eddy was released, and while inertia-gravity waves were prominent, (lower left) at 20 days, and (lower right) at 200 days, by which time the beta-induced westward propagation of the eddy peak is pronounced. The figures are annotated with a thin red circle having a radius $r = L + C\,t$ that expands at the gravity wave speed, $C = \sqrt{g'H} \approx 300$ km day^{-1} and so is off the model domain in about five days. There is also a thin red line oriented north-south that moves westward at the long Rossby wave speed, $-\beta R_d^2$, which is about 3 km day^{-1} for this experiment (Sec. 2.3). It can be very helpful to see these data animated, see pos50-h.mp4 in https://www2.whoi.edu/staff/jprice/P3-videos

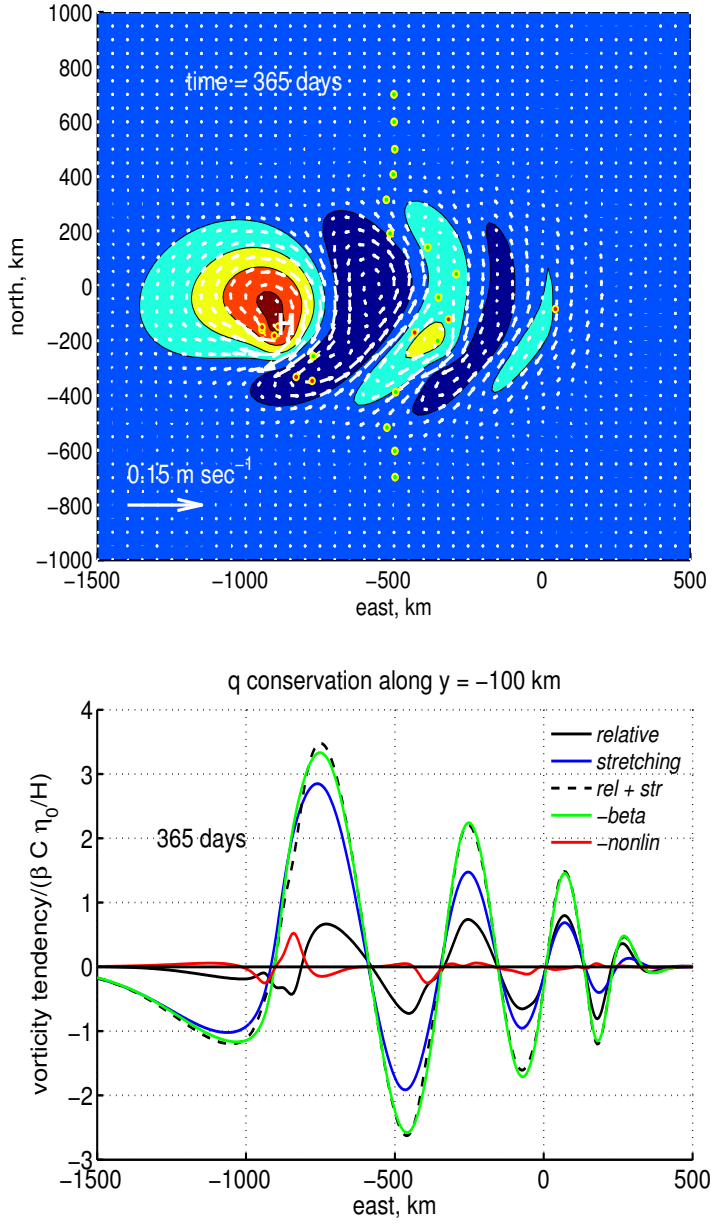

Figure 4: **(upper)** A snapshot of the horizontal velocity and thickness anomaly η (color contours, proportional to pressure) from the β-plane geostrophic adjustment experiment of Fig. (3). The north coordinate, y, was centered on 30^oN; the east coordinate, x, increases to the right. The big vector at lower left has a magnitude $0.5C\eta_0/H$ and serves as a scale for speed. This is a snapshot at 365 days; an animation is pos50-u.mp4 in the P3-videos collection. The red and green dots are floats (passive fluid parcels) that will be discussed in Sec. 2.5. **(lower)** The potential vorticity balance (8) evaluated at $time = 365$ days along the line $y = -100$ km through the eddy peak in η. Here the β term has been moved to the right side of the equation, as *relative + stretching = -beta - nonlin* which helps show that (negative) *beta* term (green line) is closely balanced by the sum of the time rate of change of *relative* vorticity (black line) and vortex *stretching* (blue line; the sum *relative + stretching* is the black dashed line). Notice that the horizontal scale of the motion decreases from west to east, while the ratio relative/stretching (black/blue) increases from west to east. This systematic variation of horizontal scale and q-conservation mechanism is characteristic of a dispersing Rossby wave pulse discussed in Sec. 2.3.

propagation of the eddy peak and the spreading (dispersion) of energy. The implicit assumption is that if we can understand these aspects of the numerical experiment, then we will have developed also a candidate understanding of the westward propagation of oceanic mesoscale eddies.[3]

The westward propagation of the eddy peak seen in Fig. (3) is reminiscent of the propagation of the wave pulses of Sec. 3 Part 2 insofar as the eddy peak propagates steadily and as a somewhat coherent feature (though with appreciable decay discussed below). This westward propagation is very slow, however, only about one percent of the gravity wave speed, C. At a fixed point, the time rate of change, and thus the frequency, ω, is correspondingly very low, about 1% of f. Is there a useful wave description of this westward propagation? The corresponding wave motion is certainly not contained within the f-plane model, since no free motion exists in the low frequency band $0 \leq \omega \leq f$ (Sec. 4, Part 2) and even more to the point, a balanced eddy stays where it is put on an f-plane (Sec. 5, Part 2). An analysis of westward propagation will evidently require taking explicit account of the one new feature of this experiment, the northward variation of f represented in Eqn. (2) by βy. The straightforward and appealing technique of looking for plane wave solutions directly in the governing equations (Sec. 4, Part 2) does not go through when $f = f(y)$ since the coefficients in the linear shallow water equations are then not constants.

How to proceed? Two clues: 1) In the shallow water model integrated here the potential vorticity should be conserved following parcels since there is no external forcing (and aside from real or inadvertent numerical diffusion). In that sense the conservation of potential vorticity is already known,

$$\frac{Dq}{Dt} = \frac{D}{Dt}\left(\frac{\xi + f}{h}\right) = 0. \tag{5}$$

It remains to learn how the various terms of (5) achieve this balance, and doing so yields considerable insight into the mechanism of westward propagation (Sec. 2.4). 2) The velocity and pressure fields associated with the propagating eddy are transverse and nearly geostrophic; it is hard to see any discrepancy between the velocity direction and the local pressure isolines, though exact geostrophic momentum balance clearly can not hold. Nevertheless, geostrophy might be used to eliminate one of η or ξ and so to arrive at a governing equation for the slowly evolving, nearly geostrophic flow seen in this experiment.

The shallow water q-conservation equation (5) expanded and noting that $h = H + \eta$ and

[3] Westward propagation persists until the eddy peak reaches the western boundary of the computational domain. The subsequent evolution of the eddy depends entirely upon the boundary condition imposed on the western edge of the domain. The radiation boundary condition used here (Sec. 2.2, Part 2), $\partial(\ )/\partial t = -U_{rad}\partial(\ )/\partial x$ with $U_{rad} = C = \sqrt{g'H} = 3$ m sec^{-1}, is effective at minimizing the undesirable reflection of the fast-moving gravity waves. However, this comparatively large U_{rad} will act to push the eddy through the western boundary much more rapidly than it would otherwise go. Since the gravity wave and Rossby wave processes are so distinct in this experiment, it is sufficient to simply reset U_{rad} to the long Rossby wave speed, $U_{rad} = \beta R_d^2 \approx 0.03$ m sec^{-1} (Sec. 2.2) after enough time has elapsed, 30 days.

$Df/Dt = \partial f/\partial t + v\partial f/\partial y = \beta v$ is

$$\frac{D\xi}{Dt} - \frac{D\eta}{Dt}\frac{\xi+f}{(H+\eta)} + \beta v = 0, \tag{6}$$

$$nonlin\ relative + nonlin\ stretching + beta = 0.$$

The terms are the material time rate change of *relative* vorticity, the material time rate change of thickness, here called vortex *stretching*, and the very important *beta* effect due to meridional flow through a y-varying f. Since this D/Dt is the material derivative, the first two terms are nonlinear. As we will see shortly, the dominant terms for this experiment are three linear terms that are embedded in (6), and it is very helpful to sort them out. The important *beta* term is linear as is. The *nonlin relative* term is easily factored into a local time rate of change, which is linear, and an advection term that is nonlinear,

$$\frac{D\xi}{Dt} = \frac{\partial\xi}{\partial t} + \mathbf{V}\cdot\nabla\xi.$$

The *nonlin stretching* term may be expanded into

$$\frac{D\eta}{Dt}\frac{\xi+f}{(H+\eta)} = \frac{\partial\eta}{\partial t}\frac{f}{H} - \frac{\partial\eta}{\partial t}\frac{\eta f}{(H+\eta)^2} + \frac{\partial\eta}{\partial t}\frac{\xi}{H+\eta} + \mathbf{V}\cdot\nabla\eta\frac{\xi+f}{H+\eta}, \tag{7}$$

where the first term on the right side of (7) is linear and usually the largest term, and the next three terms are all nonlinear. Substituting these expansions into (6) and collecting the linear terms on the left yields[4]

$$\frac{\partial\xi}{\partial t} - \frac{f}{H}\frac{\partial\eta}{\partial t} + \beta v = -\mathbf{V}\cdot\nabla\xi + \frac{\partial\eta}{\partial t}\frac{\eta f}{(H+\eta)^2} - \frac{\partial\eta}{\partial t}\frac{\xi}{H+\eta} - \mathbf{V}\cdot\nabla\eta\frac{\xi+f}{H+\eta}, \tag{8}$$

$$relative + stretching + beta = -nonlin.$$

The terms of Eqn. (8) evaluated along an east-west slice through the eddy peak η, along $y = -100$ km, and for the $time = 365$ days are in Fig. (4), bottom. The nonlinear term (red line) is appreciable near the eddy peak, but over most of the domain and including within the eddy, the β term is very nearly balanced by the sum of the relative and stretching vorticity terms, which are in phase. Thus the q balance of this phenomenon approximates the linear q balance,

$$\boxed{\frac{\partial\xi}{\partial t} - \frac{f}{H}\frac{\partial\eta}{\partial t} + \beta v = 0} \tag{9}$$

$$relative + stretching + beta = 0.$$

[4]Notice that the dimension of these terms is *vorticity time*$^{-1}$, i.e., it is a vorticity tendency equation. Eqn. (6) will nevertheless be referred to as a *potential* vorticity conservation equation, since that was the essential origin.

Many of the large scale, low frequency phenomena of the atmosphere and ocean have a significant overlap with this linear q-balance, even when, as here, they may also exhibit finite amplitude effects and be subject to external forcing. The upcoming Sec. 2.3 will examine the free waves that are supported by Eqn. (9), planetary Rossby waves, and finite amplitude (nonlinear) effects will be discussed in Sec. 2.4.

Assuming that the object will be motions having very low frequency, $\omega/f \ll 1$, and modest amplitudes, $\eta/H \ll 1$, then the velocity and pressure will be nearly geostrophic. In that case the geostrophic relations for north-south velocity, $v = (g'/f)\partial\eta/\partial x$, and vorticity, $\xi = (g'/f)\nabla^2\eta$, may be substituted in to Eqn. (9) to eliminate the velocity components in favor of η. After a little rearrangement there comes a linear, third order governing equation for η,

$$(\frac{g'H}{f^2}\nabla^2 \; - \; 1)\frac{\partial\eta}{\partial t} \; - \; \frac{\beta g'H}{f^2}\frac{\partial\eta}{\partial x} \; = \; 0, \tag{10}$$

$$relative + stretching + beta = 0.$$

Notice that the time derivative of η is proportional to the first derivative of η in one direction, east-west. The dynamics of a β-plane is evidently anisotropic (not the same in all directions), which is a significant difference from an f-plane. This crucial dependence upon direction can be attributed to Earth's rotation vector (Part 1), which defines a specific direction for geophysical flow phenomena that are 1) low frequency enough to be significantly effected by the Coriolis force and 2) that have sufficiently large horizontal scale to be effected by the spatial variation of f due to Earth's nearly spherical shape.

2.3 Planetary Rossby waves

It is of considerable interest to learn how the balance of potential vorticity depends upon the horizontal spatial scales and the time scale of the motion. To learn the result for the important case of linear and nearly geostrophic potential vorticity, Eqn. (10), we need only substitute an elementary plane wave form,

$$\eta(x,t) \; = \; \eta_0 \exp(i(k_x x + k_y y - \omega t)) \tag{11}$$

into Eqn. (10). A spatial derivative in the x direction thus brings out the east-west component of the wavenumber, k_x, and a partial time derivative brings out the frequency, ω (assumed to be positive in all that follows). Solving for ω yields the dispersion relation for planetary Rossby waves, [5] Fig. (5),

$$\boxed{\omega \; = \; -\beta R_d \quad \frac{R_d k_x}{1 + R_d^2(k_x^2 + k_y^2)}\Bigg)\Bigg(} \tag{12}$$

[5]The terms 'eddy' and 'wave' are widely used, sometimes almost interchangeably. In fluid mechanics parlance, the most general use of 'eddy' is to denote any kind of departure from a spatial or a temporal mean. Here, eddy will be used to denote a flow feature having a quasi-circular planform and a thus more or less closed circulation. Mesoscale eddies are an example, and of course they are also a departure (anomaly) from a time or space average that would be appropriate for defining a basin-scale

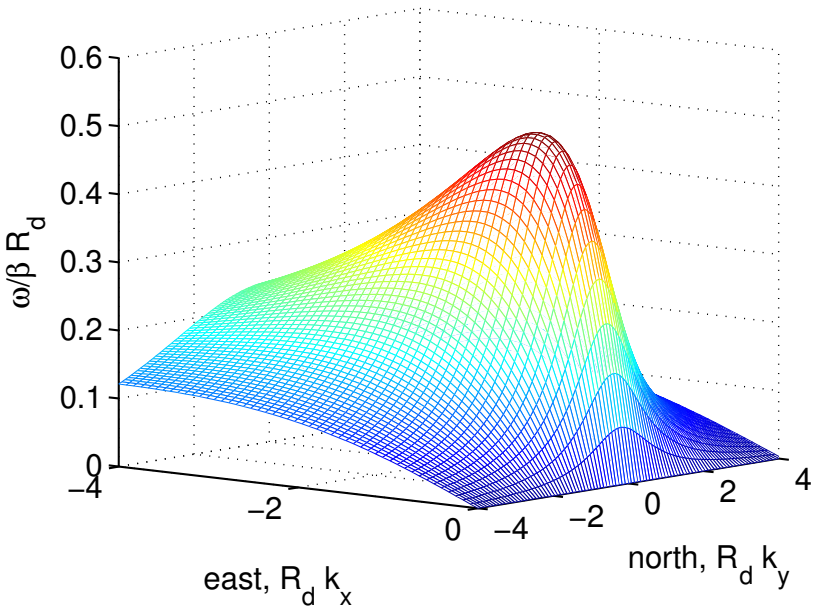

Figure 5: The dispersion relation for planetary Rossby waves, Eqn. (12). Frequency is normalized by $\beta R_d = 2\pi/85$ days, evaluated for a baroclinic midlatitude ocean. This surface is symmetric in the north-south component of the wavenumber vector, k_y. The east-west component can only be negative, i.e., $k_x < 0$ for planetary Rossby waves.

Notice that as was the case for inertia-gravity waves, the dispersion relation depends upon the stratification through R_d and Earth's rotation through f; notably, this dispersion relation also depends upon β.

The dispersion relation (12) is a very useful characterization of the linear, quasi-geostrophic vorticity balance Eqn. (10) and will be discussed here at some length. However, it is worth noting that plane Rossby waves — the literal interpretation of (11) — are generally *not* a prominent phenomena of the oceans. For example, there are no plane (long-crested) Rossby waves evident in Fig. 1, though in other years and other oceans, there may be, Sec. 2.6.2). Long-crested Rossby waves are not readily generated by winds and other forcing mechanisms, which generally have shorter space scales, and, even when they are, long-crested waves are likely to be unstable and evolve spontaneously into mesoscale eddies (an example is in Sec. 2.5). The perspective on Rossby waves taken here is that while Rossby waves are important in their own right, they are most important as the archetype of low frequency, nearly geostrophic motions generally, and including mesoscale eddies. The dispersion relation (12) is our handy guide to the relationship of time and space scales of such motions.

---

gyre. The term 'wave' might be applied reasonably to any phenomenon that results in the transmission of energy through a fluid (or solid) medium, though without necessarily transporting material. Mesoscale eddies on a beta-plane likely have just this property (Sec. 2.5) and so would qualify as waves in this (quite sensible) generalized sense. Here, however, the word 'wave' will be reserved here for an elementary plane motion of the sort Eqn. (11). Why this specific distinction between waves and eddies should be made clear in Sec. 2.7. (For a broad perspective on this issue see Scales, J. A. and R Sneider, 'What is a wave?', *Nature*, 401, 21 October, 1999, 739-740.)

Rossby waves are altogether different from the inertia-gravity waves of Part 2. In the first place, they have a very low frequency, and are very slowly moving; the factor in parentheses is O(1) for the wavenumbers and R_d of interest here and the frequency is determined largely by the leading factor, $\beta R_d \approx f R_d/R_E$ which is O(0.01)f, when $R_d = 40$ km, appropriate to the subtropical baroclinic ocean. This is the order of the frequency of both the numerical eddy and observed mesoscale eddies (Fig. 1). The frequency of Rossby waves is strongly dependent upon the wavenumber vector, i.e., both the magnitude and the direction. (This is in marked contrast to the isotropic dispersion relation of inertia-gravity waves on an f-plane noted in Part 2.) The east-west component k_x must be negative and so planetary Rossby waves propagate phase to the west only. For a given wavenumber magnitude, the frequency is a maximum when the wave vector is directed due west, $k_y = 0$, and the frequency is zero if the wave vector is directed due north or due south, $k_x = 0$. In that case the currents are purely east-west or zonal, and hence not subject to a β-effect. Zero frequency implies steady and exactly geostrophic motion, and any purely zonal motion satisfies Eqn. (12) regardless of k_y. The dispersion relation (Fig. 5) is symmetric north-south, and the north-south component of phase velocity can have either sign. The east-west component of phase speed is always negative, i.e., always westward (Fig. 6), a fundamental property of planetary Rossby waves.

The numerical (and the real) mesoscale eddies propagate almost due west, and hence it is helpful to simplify the dispersion relation to the case of an east-west wave vector, i.e., $(k_x, k_y) = (k_x, 0)$, Fig. (6),

$$\omega = -\beta R_d \left(\frac{R_d k_x}{1 + R_d^2 k_x^2} \right) \left(\right. \tag{13}$$

The phase speed in the east-west direction is

$$Cp \;=\; \frac{\omega}{k_x} = -\beta R_d^2 \left(\frac{1}{1 + R_d^2 k_x^2} \right) \left(\right. \tag{14}$$

and always negative (westward). The maximum phase speed occurs with the longest waves, and is up to βR_d^2, a stately 3 kilometers per day. The phase speed is, of course, a fundamental property of any wave, but nevertheless, the group speed is more evident in the experiments conducted here in which the waves spread from a confined region. The east-west group speed is

$$Cg \;=\; \frac{\partial \omega}{\partial k_x} \;=\; -\beta R_d^2 \left(\frac{1}{1 + R_d^2 k_x^2} \right) \left(1 \left(-2 \frac{R_d^2 k_x^2}{1 + R_d^2 k_x^2} \right) \right) \left(\right. \tag{15}$$

which may be written

$$Cg \;=\; Cp \left(1 - 2 \frac{R_d^2 k_x^2}{1 + R_d^2 k_x^2} \right) \left(\right. \tag{16}$$

The group speed is westward for long waves, $R_d k_x \geq -1$, and also has a maximum magnitude of βR_d^2.

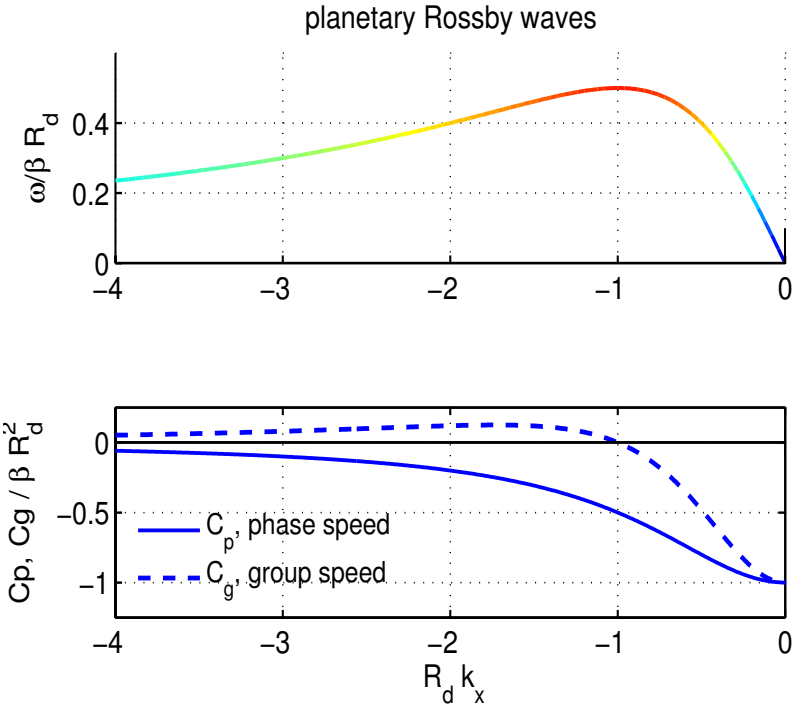

Figure 6: **(upper)** The dispersion relation for midlatitude, baroclinic, oceanic Rossby waves (Fig. 5) sliced along $k_y = 0$. Frequency is normalized by βR_d as before. **(lower)** Zonal phase and group speeds of planetary Rossby waves normalized by $\beta R_d^2 = 0.036$ m sec^{-1}. The phase speed (solid line) is always negative, i.e., always westward. The group speed (dashed line) is also westward for long waves, $R_d k_x \geq -1$, and is eastward and small for medium to short waves, $R_d k_x \leq -1$.

The phase and the group speed are proportional to β and so increase toward the equator. The group speed is eastward but rather slow even by Rossby wave standards for medium and short waves, $k_x R_d < 1$. The maximum eastward group speed is about $0.15\beta R_d^2$, or only about 1/2 kilometer per day at mid-latitudes, and occurs at $R_d k_x = -\sqrt{3}$. There is clear evidence of this slow eastward energy propagation in the idealized experiments that follow, but admittedly it is hard to see evidence of it in the real ocean.

In the preliminary discussion of the q-balance of Fig. (4), lower, it was noted that the β term is nearly balanced by the in-phase sum of relative vorticity and stretching vorticity. The next issue is the ratio of these two terms and the correlation of the ratio with the horizontal scale of the motion and the east-west distance from the starting point. This may be estimated from Eqn. (10) using that ∇^2 operating on a plane wave $\propto cos(k_x x - \omega t)$ gives $-k_x^2$ and thus,

$$\frac{relative}{stretching} = \frac{\frac{g'H}{f^2}\frac{\partial \nabla^2 \eta}{\partial t}}{\frac{-\partial \eta}{\partial t}} = \frac{g'H}{f^2}k_x^2 = R_d^2 k_x^2. \tag{17}$$

Relative vorticity is thus more important for waves which have a short horizontal scale, i.e. $R_d k_x \gg 1$, while stretching vorticity dominates for longer waves, $R_d k_x \ll 1$. The eddy of our geostrophic adjustment experiment has an initial scale $R_d k_x \approx 1$, so that relative and stretching vorticity terms are comparable in the initial q balance. By 365 days, the eddy has dispersed, especially east to west, and the q-balance has

become sorted out so that the ratio Eqn. (17) is about 4 in the vicinity of the eddy peak near $x = -1000$ km, and the ratio is about 1/4 in the region around x = 300 km. The east-west scale of the motion also varies systematically, being considerably larger toward the west than in the east. This east-west variation of the q-balance and of the horizontal scale of the motion are consistent with the Rossby wave dispersion relation.

2.3.1 Beta and relative vorticity; short Rossby waves

The presence of a wave implies a restoring force that is related to the configuration of the system. In the common case of simple harmonic waves in a fluid or solid, the restoring force is proportional to the displacement of a parcel away from equilibrium. The restoring force of a gravity wave is straightforward — gravity acting upon a displaced sea surface or internal density interface. The restoring 'force' of a Rossby wave must be related to the presence of β and the north-south displacement of parcels in a y-varying f. The restoring force provided by the β-effect is somewhat indirect compared to gravity acting on a displaced density surface, but nevertheless results in two quite different mechanisms of westward propagation and two kinds of Rossby waves, short Rossby waves and long Rossby waves. To follow along with the discussion below it will be helpful for you to make sketches of $\eta(x,t) = \eta_o cos(k_x x - \omega t), v(x,t)$, etc., and fill in the very brief calculations outlined here.

Suppose that the motion (waves) is in the short wave limit $R_d k_x \gg 1$. If $R_d k_x = 5$, say, then for $R_d = 40$ km, $\lambda \approx 50$ km would suffice. In that case, the relative vorticity term is considerably greater than the stretching vorticity term and the conservation of q may be approximated by the conservation of absolute vorticity

$$\xi + f = constant,$$

or in time-differentiated, linear form,

$$\frac{\partial \xi}{\partial t} + \beta v = 0, \tag{18}$$

a balance between *relative* vorticity and *beta*. A northward meridional current, $v > 0$, thus induces a negative change in the relative vorticity, $\frac{\partial \xi}{\partial t} < 0$, and the converse for a southward meridional current.

To see the westward phase propagation that results from this $q-$mode, assume that the meridional velocity has the form of a propagating plane wave,

$$v(x,y,t) = V cos(k_x x - \omega t),$$

with wavenumber directed due east-west. The zonal current then vanishes, and the relative vorticity is due solely to the east-west horizontal shear of the meridional velocity, $\xi = \partial v / \partial x$ (not the solid body

rotation that is often depicted in qualitative diagrams, e.g., the spinning cylinder in Part 2, Fig. (4), middle). Substitution of this plane wave form into the reduced $q-$conservation equation (18) then yields

$$\boxed{\omega = -\frac{\beta}{k_x}} \tag{19}$$

which is the short wavelength limit of Eqn. (14). The phase speed of short Rossby waves is then

$$\boxed{Cp_{shortRo} = -\frac{\beta}{k_x^2}} \tag{20}$$

and westward. $Cp_{shortRo}$ is obviously dependent upon k_x so that short Rossby waves are highly dispersive. Their group speed is

$$\boxed{Cg_{shortRo} = \frac{\beta}{k_x^2}} \tag{21}$$

and eastward, and notice equal in magnitude to the phase speed (Fig. 6).

The dispersion relation (19) is remarkable for what it omits: the dispersion relation (dynamics) of short Rossby waves does not depend upon the stratification or even the water column thickness; it depends only upon β and the zonal wavenumber, k_x. The motion is purely horizontal and nondivergent and so short Rossby waves are sometimes referred to as nondivergent Rossby waves. This is the $q-$conservation mechanism and the dispersion relation that C. G. Rossby inferred for westerly waves in the atmosphere (Secs. 1 and 2.6.1).

The group speed of short Rossby waves is very small, hundreds of meters per day as noted before, so that it takes quite some time for these waves to emerge from the initial eddy. But by day 365 there is clear evidence of slow, eastward energy propagation in the region $x > 200$ km (Fig. 4, lower). The horizontal scale in that easternmost region is, by inspection, $\lambda \approx 150$ km, and thus $R_d k_x \approx -2$, which is near the maximum eastward Cg. The linear q balance in that region is characterized by $relative/stretching \approx 4$. The very slow eastward extension of the eddy disturbance into the region east of the initial eddy position thus appears to be consistent with the slow eastward group speed and q balance of short(ish) Rossby waves.

2.3.2 Beta and vortex stretching; long Rossby waves

Another and very important mode of q-conservation holds for motions having a large horizontal scale in the sense that $R_d k_x \ll 1$. For the present case, $\lambda \geq 500$ km suffices. The change of relative vorticity is

negligible for such large scale motions, and the q balance may be approximated as (Fig. 4, lower, Part 2)

$$\frac{f}{H+\eta} = constant. \tag{22}$$

The linearized time rate of change is a balance between *beta* and vortex *stretching*,

$$\beta v \; - \; \frac{f}{H}\frac{\partial \eta}{\partial t} \; = \; 0. \tag{23}$$

To see how this q-mode may support a wave, presume a zonally propagating thickness anomaly

$$\eta(x,y,t) = \eta_0 cos(k_x x - \omega t)$$

that is in geostrophic balance with a north-south (meridional) current,

$$v(x,y,t) = \frac{g'}{f(y)}\frac{\partial \eta}{\partial x}.$$

Substitution into the reduced q-conservation equation and rearrangement yields

$$\frac{\partial \eta}{\partial t} = \frac{g' H \beta}{f^2}\frac{\partial \eta}{\partial x},$$

a first order wave equation. Substitution of the presumed plane wave form yields the dispersion relation

$$\boxed{\omega = -\beta \frac{g' H}{f^2} k_x} \tag{24}$$

the small $R_d k_x$ limit (i.e., the long Rossby wave limit) of Eqn. (14). The phase speed and the group speed are the same,

$$\boxed{Cp_{longRo} \; = \; Cg_{longRo} \; = \; -\beta R_d^2} \tag{25}$$

and independent of k_x. Long Rossby waves are thus nondispersive.

The dispersion relation of long Rossby waves depends upon stratification. Because the q-conservation mechanism of long Rossby waves is the β-induced divergence of the north-south (or meridional) geostrophic current, long Rossby waves are sometimes called divergent Rossby waves. Unlike the short Rossby wave, they can have a significant effect upon layer thickness, as we will see in Sec. 4. Notice especially the crucial f^{-2} dependence of the long Rossby wave phase and group speed. This will appear as a key, qualitative property at several junctures in this essay. An approximate $q-$balance of this sort is evident in the vicinity of the eddy peak, $-1200 \leq x \leq -800$ km, where the stretching term is about four times the magnitude of the relative vorticity term (Fig. 4, lower). The

wavelength is about $\lambda \approx 800$ km, and hence $R_d k_x \approx 0.3$, which is consistent with the ratio relative/stretching. The eddy peak at 365 days thus has a horizontal scale that is near the non-dispersive range of the Rossby wave dispersion relation (Fig. 6) and consistent with this, the eddy peak continues propagating westward with little further change and at a rate, 80 to 90% of βR_d^2, the long (Rossby) wave speed.

Though the eddy peak certainly does not have the appearance of a plane wave, it nevertheless has the q-balance and propagation characteristics of a (fairly) long elementary Rossby wave. Moreover, the propagation speed of the numerical eddy is consistent with the observed speed of oceanic mesoscale eddies at latitude 30^o. Most importantly, the satellite altimetry observations of Fig. (1) allow this result to be extended over a significant range of latitude.[6,7]

2.4 Finite amplitude effects, and the dual identity of mesoscale eddies

To now our discussion of eddy phenomena has emphasized that linear Rossby wave theory gives a very useful account of the westward propagation and dispersion seen in the η and $\mathbf{V}$ fields. This section will take a more in-depth look at the experiments and reveals two ways in which a linear description is incomplete: 1) First of all, there are modest but detectable finite amplitude effects on wave propagation in the base case experiment which has a realistic amplitude. 2) More striking is that fluid (tracer) transport by these eddies can be qualitatively different from the wave-like motion of the eddy peak and is entirely a finite amplitude effect. In this respect, mesoscale eddies have a kind of dual identity — Rossby wave-like when viewed in the η field, and yet capable of transporting tracer for significant distances depending upon amplitude. To highlight these phenomena and their dependence upon amplitude, it is helpful to compare the solutions from two new experiments made by setting the initial amplitude very small, $\eta_o = 1$ m (Fig. 7), so that all finite amplitude effects should vanish, and then much larger, $\eta_o = 100$ m (Fig. 8),

[6] A recent, comprehensive modelling study of the SSH climatology is by Early, J. J., R. M. Samelson and D. B. Chelton, 2011, 'The evolution and propagation of quasigeostrophic ocean eddies', *J. Phys. Oceanogr.,* doi: 10.1175/2011JPO4601.1 and references therein. Also highly recommended is http://jeffreyearly.com/science/qg-eddies-paper/ A notable, early theoretical/numerical study is by McWilliams, J. C. and G. R. Flierl, 1979, 'On the evolution of isolated, nonlinear vortices', *J. Phys. Oceanogr.*, 9, 1155-1182. A collection of research reviews is by Hect, M. W. and Hasumi, H., 2008, 'Ocean modelling in an eddying regime', *Geophys. Mono. Ser.*, **177**, American Geophys. Union.

[7] The discussion here was organized around two of the three modes of the linear potential vorticity balance that correspond with limits of the Rossby wave dispersion relation. Just to be complete, the third mode of vorticity balance is between stretching and relative vorticity, as in Fig. (4), upper, Part 2. In this mode, a change in relative vorticity occurs in phase with stretching, and thus when stretching stops, so does the change of relative vorticity. There is no mechanism for wave propagation associated with this mode, but it makes an important appearance in several numerical experiments; the geostrophic jets of Sec. 4.4, Part 2 exhibit this mode of q conservation, and there will be another example in Sec. 3.3 associated with Kelvin waves.

so that finite amplitude effects should be fairly pronounced.[8]

2.4.1 Eddy propagation seen in the η and V fields

The overall appearance of the normalized interface displacement $\eta(x,y,t)/\eta_o$ and the normalized current $\mathbf{V}/(C\eta_o/H)$ are not greatly different between these two experiments, but there are differences in detail. Most notably, the amplitude of the eddy peak is preserved somewhat longer in the large amplitude experiment and the waves found to the east of the peak have less symmetry when compared to the small amplitude experiment.

The zonal propagation speed of the eddy peak is also altered by finite amplitude effects: the zonal eddy peak speed is about 80% of $C_{longRo} = -\beta R_d^2$ in the small amplitude experiment (Fig. 9, dashed lines, and Fig. 10) and is about 90% of C_{longRo} in a large amplitude experiment, $\eta_o/H = 0.2$. For still larger amplitudes there is little further increase and so it appears that the long Rossby wave speed is a speed limit for the zonal motion of these eddies.

Finite amplitude effects cause a noticeable meridional motion of the eddy peak. Large amplitude anti-cyclones ($\eta_o/H = 0.1$, solid red line of Fig. 9) show a small component of motion toward the equator, about 10% of the westward propagation speed. Large amplitude cyclonic eddies show a similar poleward motion (the solid blue line of Fig. 9). These modest but detectable finite amplitude effects on the speed and direction of the eddy propagation seen in η are consistent with the observed propagation of oceanic mesoscale eddies seen in SSH (Fig. 1).[6]

2.4.2 Fluid transport seen in tracer fields and float trajectories

There is another very important class of eddy phenomena, the long term transport of fluid, often called the Lagrangian velocity, Part 2 Sec. 2, that is strongly dependent upon eddy amplitude. To see the fluid motion we have to analyze a tracer field or compute the trajectories of floats (passive particles). It was noted in Part 2 that the ideal (no external forcing) shallow water model has a natural, built-in tracer, the field of potential vorticity, q, which follows a conservation law, $Dq/Dt = 0$, i.e., q is conserved on fluid parcels. The initial condition on q (Fig. 11, left) in these experiments is a uniformly sloping background due to the northward increase of f, and a circular, low-q anomaly centered on $(x,\ y) = (0,\ 0)$ that is the

[8] This takes a short-cut. By the present definition of finite amplitude (Part 2, Sec. 2.3.4) we should first verify that there is indeed a linear regime at small amplitude by comparing the solutions from two (putatively) small amplitude experiments, say $\eta_o = 1$ m with $\eta_o = 2$ m, to verify that the scaled ηs and $\mathbf{V}$s are indistinguishable. They are.

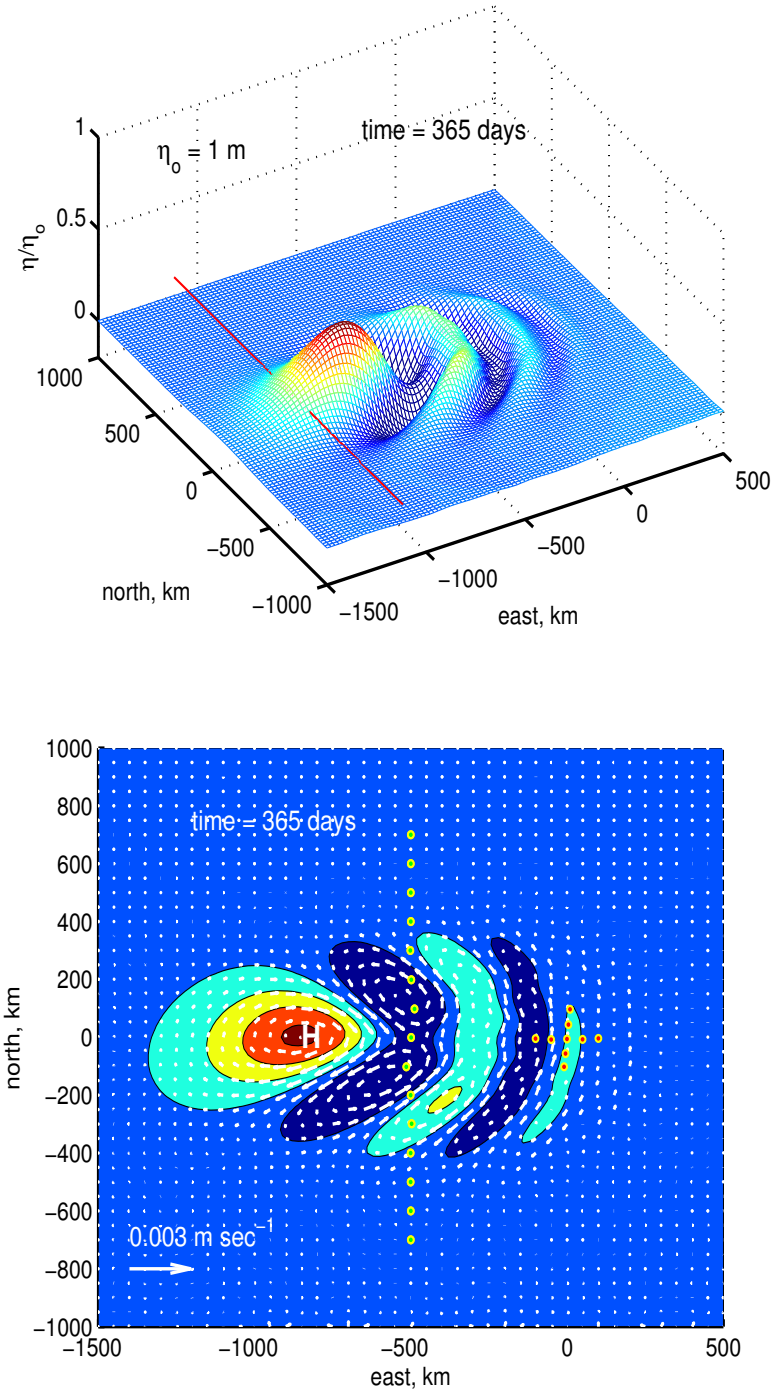

Figure 7: A small amplitude experiment in which $\eta_0 = 1$ m and $\eta_0/H = 0.002$ so that finite amplitude effects are negligible (a large amplitude experiment is next). **(upper)** The normalized interface displacement $\eta(x,y,t)/\eta_0$. **(lower)** The velocity field (vectors), thickness (color contours) and floats (red and green dots). The big vector at lower left has a magnitude $0.5C\eta_0/H$ and serves as scale for the velocity. The red floats were started within the eddy, while the green floats were set on a north-south line at $x = -500$ km and well to the west of the initial eddy. None of the floats moved an appreciable distance during the course of this year-long experiment, while the eddy peak propagated westward as if a linear wave. An animation of these data is pos1-u.mp4 in P3-videos.

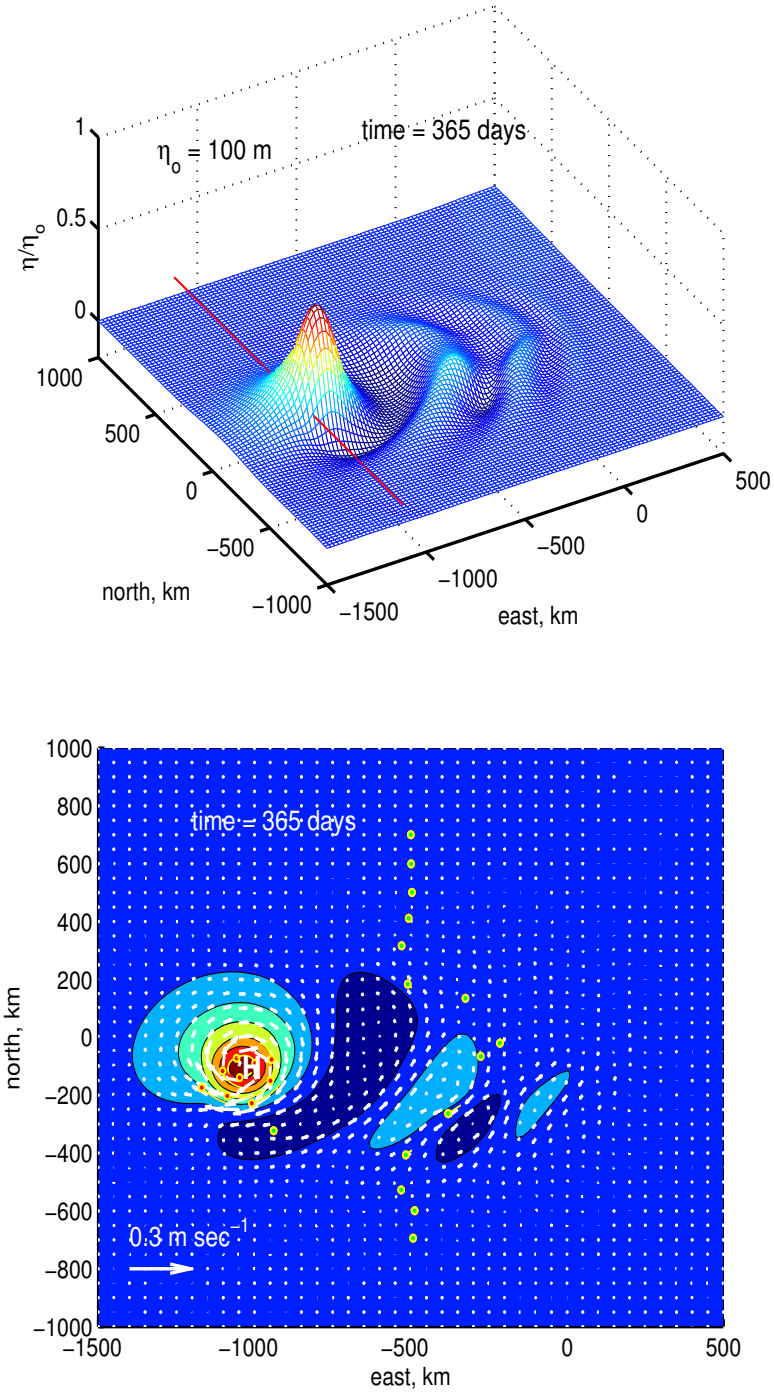

Figure 8: A large amplitude experiment, $\eta_0 = 100$ m and $\eta_0/H = 0.2$ so that finite amplitude effects are appreciable. **(upper)** Compared with the previous, small-amplitude experiment, Fig. (7), the (normalized) $\eta(x,y,t)$ eddy peak retained a somewhat larger fraction of its initial value. **(lower)** The velocity field and the floats of the large amplitude experiment. As before, the big vector at lower left has a magnitude $0.5C\eta_0/H$ and serves as the scale for velocity. The red floats, which were started within the eddy, were trapped by the eddy for the year-long duration of this experiment. The green floats, which were started well outside of the eddy along a north-south line at $x = -500$ km, were displaced mainly to the east as the eddy propagated by their initial longitude. The qualitative difference in these float trajectories compared to those of Fig. (7) shows that tracer (float) transport is a finite amplitude phenomenon. The animations provide a much more vivid sense of the differences between this and the previous experiment; this one is pos100-u.mp4

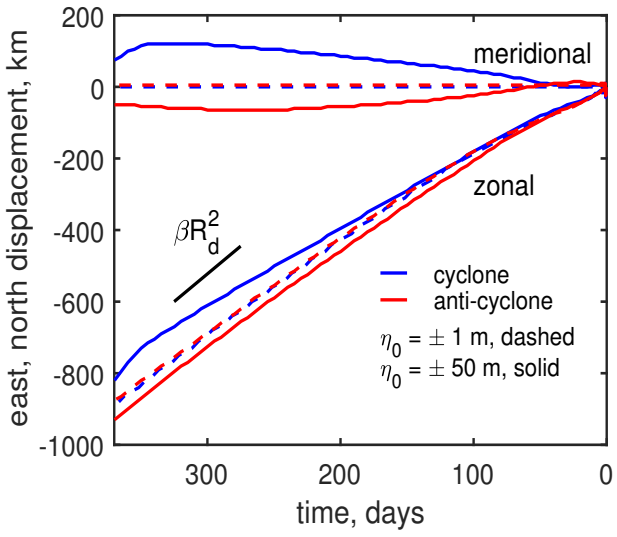

Figure 9: Time series of northward (here, poleward) and eastward displacement of the eddy peak (the maximum of $\mid \eta \mid$) for four experiments in which the amplitude and the sign of the initial displacement was $\eta_0 = \pm$ 1 m (two dashed lines that are almost identical) or $\pm$50 m (the solid red and blue lines). Blue curves are from the cyclones and red curves are from anti-cyclones. In all cases the zonal displacement is dominantly westward and at about 80 to 90% of the long Rossby wave speed, βR_d^2, evaluated at 30^{o}N. The strong cyclone (solid blue line) shows a small meridional poleward displacement (upper set of curves), while the strong anti-cyclone (solid red line) shows a small meridional equatorward displacement.

initial (thick) eddy. It is interesting to solve in parallel for the evolution of a passive tracer, $Ds/Dt = 0$, whose initial condition can be set arbitrarily; one simple choice is $s_o = 1$ inside the radius of the initial eddy, and zero otherwise (Fig. 12, left). The motion of the eddy center is readily apparent in the evolution of either of these tracer fields and is exactly the same in these two fields, as it should be. In the base case experiment, which has a fairly large amplitude, $\eta_o/H = 0.1$, the q or s anomaly moves mainly westward and slightly southward, very much like the eddy peak in this experiment. It bears emphasis that the tracer and the eddy q anomaly can move only by virtue of the fluid motion (not wave motion). Thus the appearance of the eddy's low q anomaly is associated with a noticeable contribution by the *nonlin* term to q conservation (Fig. 4, lower). The main contribution to *nonlin* is from horizontal advection of relative vorticity (the first term on the right side of Eqn. (8)).

The background (non-eddy) parts of these two tracer fields are somewhat different. The q field at the latitude of the eddy shows rather large meridional displacements of constant q lines. The passive tracer shows something similar only where there happens to be a meridional tracer gradient, near the eddy center and in a long, thin filament of tracer that extends from the eddy center back toward the starting location. This loss of tracer from the eddy into the filament is accompanied by a slow decrease of the eddy radius, mainly. The same filament is present also in the q field, although not apparent against the background of Fig. (11).[9]

[9]This tracer filament is very interesting insofar as it may show how discrete eddies may act to disperse tracer properties. However, this filament is also just the kind of thing that is especially challenging for a numerical solution. Specifically, the width of the numerical filament (i.e., the filament within a numerical solution) can never be less than several times the horizontal

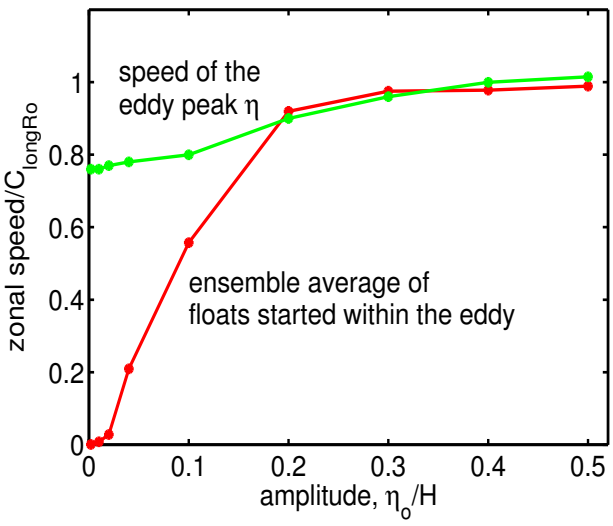

Figure 10: Average zonal speed of the eddy peak of η (green line; all anticyclones) and of an ensemble of floats that were launched within the eddy (red line) for nine experiments having amplitude $0.001 < \eta_o/H < 0.5$, the independent variable. The average is over the first year of the experiment. Speeds are normalized by the long Rossby wave speed at the average latitude of the eddy peak. The normalized eddy peak speed depends somewhat upon the eddy amplitude, while the ensemble-averaged float speed is very sensitive to eddy amplitude up to $\eta_o/H \approx 0.2$. These are robust results in a numerical solution sense, and an interesting comparison of two important properties of (numerical) mesoscale eddies. However, the eddy peak speed and the ensemble-averaged float speed (or Lagrangian velocity) are, in general, qualitatively different things, e.g., the float speed depends upon the averaging interval in the intermediate amplitude cases in which some fraction of the floats is lost from the eddy during the first year (as in Fig. 4, upper).

Fluid motion may be easier to quantify when diagnosed from the motion of discrete, passive parcels, or 'floats' (Sec. 2.3.3, Part 2), that are set in the initial state. A cluster of nine (red) floats was started within the eddy to serve as a tag on the eddy, and a line of (green) floats was placed along a north-south line 500 km west of the eddy initial position (Fig. 7, lower) to show the motion of the ambient fluid as the eddy passes through their longitude. In the small amplitude experiment, $\eta_0/H = 0.002$ (Fig. 7), all of these floats appear to be essentially frozen in space for the full duration of the experiment. At the same time, the eddy marked by η moves westward as would a linear Rossby wave. The ensemble average speed of the red floats launched within the eddy is thus about zero, while the eddy peak defined by η propagates at about 80% of C_{longRo}. This qualitative difference between float (and thus fluid) motion and

grid interval, 5 km, which may be considerably greater then the natural, physical horizontal scale of the filament. Small changes in the diffusion (deliberate or numerical) or even in the method used to estimate and time-step the advection terms of the tracer equation can thus cause a significant difference in the width of the filament and thus in the tracer concentration along the filament, even while leaving the eddy propagation almost unaffected. Eddy propagation thus appears to be a robust and well-resolved process in these numerical solutions, while the width and tracer concentration along this very thin tracer filament are not.

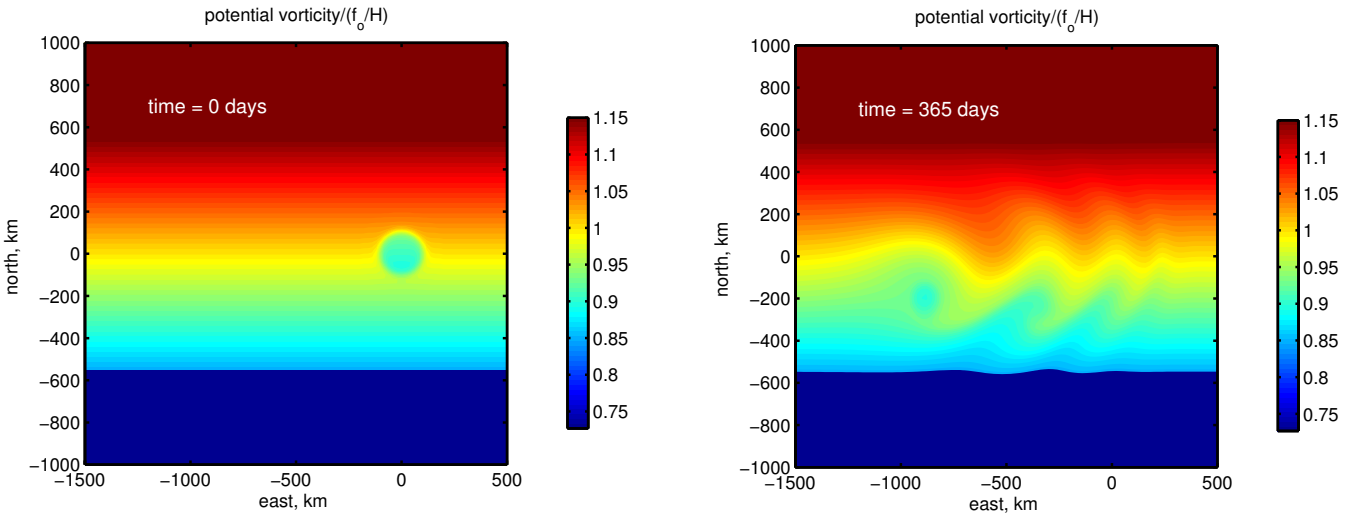

Figure 11: Potential vorticity from the experiment $\eta_o = 50$ m. **(left)** The initial condition. The eddy is the pale blue, low q anomaly centered on $(x,y) = (0,0)$. **(right)** At 365 days. The eddy center marked by the potential vorticity anomaly is now at $(x,y) = (-900,-200)$ km, which is about 100 km equatorward of the eddy peak seen in η at this time.

the motion of the eddy peak seen in η also leads to the depiction of the eddy peak motion as 'propagation', and implicitly, wave propagation.

The float movement (and the transport of tracers and fluid) is very different in the large amplitude experiment, $\eta_o/H = 0.2$, (Fig. 8, lower), even while the westward propagation of the eddy peak is changed only slightly. The large amplitude azimuthal current within the eddy effectively traps the red floats on the side of the eddy where the current is westward, in the direction of the eddy propagation (the south side of the anticyclone of Fig. (8, lower). The eddy then advects the floats to the west-southwest over a distance of almost 1000 km within the first year. The long-term, ensemble mean Lagrangian velocity of these specific floats is thus the same as the speed of the eddy peak (Fig. 10), about 95% of C_{longRo}. In an intermediate amplitude experiment, roughly $0.03 \leq \eta_o/H \leq 0.2$, e.g., Fig. (4, upper), some fraction of the red floats are lost from the eddy as it shrinks in radius during the first year, and hence the ensemble-average float speed is intermediate between 0 and the eddy peak speed. The ensemble-average float speed thus depends entirely upon the residence time of the floats within the eddy, which in turn depends upon the initial amplitude of the eddy and the rate at which it decays and disperses. This significant dependence of the float speed with amplitude fits the present definition of a finite amplitude phenomenon.[10]

[10]The meridional drift of large amplitude eddies has been studied extensively in the context of tropical cyclone motion, see http://www.aoml.noaa.gov/general/WWW000/nhurr00.html . In brief, the present eddies have a horizontal scale $KR_d \leq 1$ that

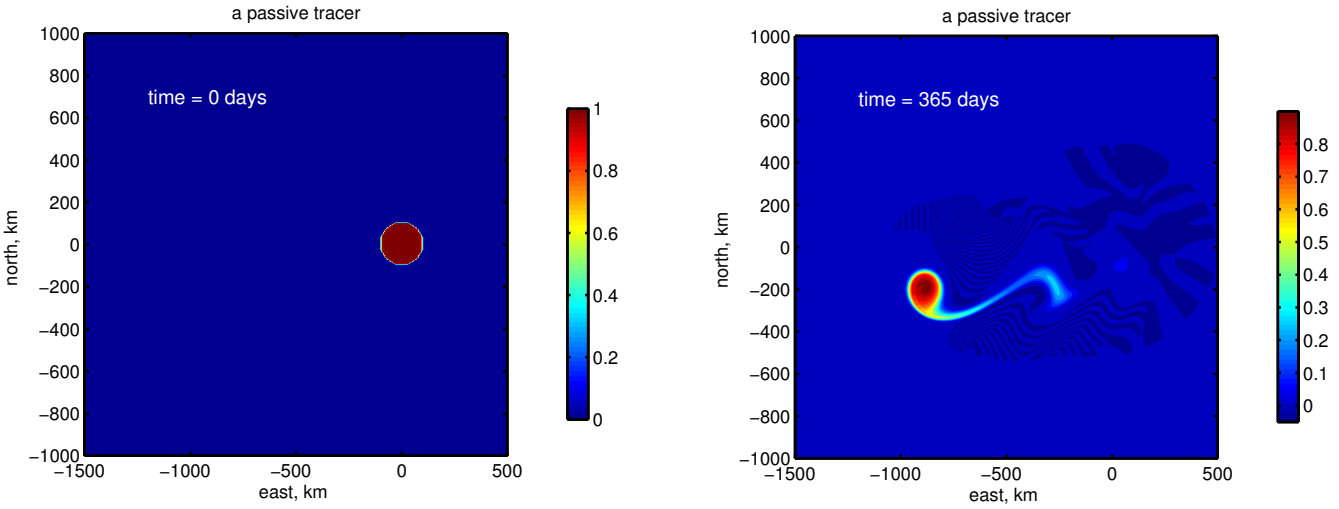

Figure 12: The evolution of a passive tracer inserted into the experiment $\eta_o = 50$ m. **(left)** The initial condition; $s = 1$ within the initial eddy, $s = 0$ otherwise. **(right)** At 365 days. Notice that the eddy center marked by tracer is at about $(x, y) = (-900, -200)$ km, and the same as seen in the q field of the previous figure. Notice too the thin, wispy trail of tracer left behind the westward-propagating eddy. This corresponds with the line of (red) floats dropped off by the eddy Fig. (4, upper) and with a faint local minimum of potential vorticity.

2.5 Rossby waves → Eddies

This essay has discussed Rossby waves (elementary, plane Rossby waves) and mesoscale eddies on a more or less equal footing. This may have left you wondering if these phenomenon are equally important and whether there may be connections between them, even aside from their common vorticity balance. One interesting connection is that under common circumstances, Rossby waves are expected to evolve spontaneously into mesoscale eddies, i.e., Rossby waves are very often unstable. The topic of fluid flow instabilities is beyond the scope of this essay, but a simple example of Rossby wave instability will serve to illustrate the phenomenon and (ideally) may stoke your appetite for more.[11]

---

is not completely large scale, i.e., the beta effect is not balanced solely by divergence. There is some relative vorticity generated by the meridional velocity of the eddy and an induced cyclonic vorticity on the northeast side of the eddy and cyclonic vorticity on the southwest side. The net result is a markedly asymmetric velocity field with a strong southwest current on the southern side of the eddy, readily evident in Fig. 8, bottom. This current acts to self-advect the eddy center toward the southwest. For a large amplitude cyclone the strongest current is on the northeast quadrant and is directed northwest. The amplitude of this current is much, much greater than the resulting southwest drift of an anti-cyclonic eddy (noted in the discussion above), evidently because it is on the periphery of the eddy, and is directed mainly along lines of constant h.

[11] See Isachsen, P. E., J. H LaCasce and J. Pedlosky, 'Rossby wave instability and apparent phase speeds in large ocean basins', *J. Phys. Oceanogr.*, 2007, 1177-1191, DOI: 10.1175/JPO3054.1 and references therein.

The model is initialized with a rather special state: a north-south oriented ridge/trough that mimics one isolated wave,

$$\eta(x,y,t=0) \;=\; \eta_o \frac{f}{f_o} \sin(2\pi x/\lambda) \quad \text{if} \quad |\,x\,| < \lambda/2, \tag{26}$$

and otherwise

$$\eta(x,y,t=0) \;=\; 0 \quad \text{if} \quad |\,x\,| > \lambda/2.$$

The wavelength is $\lambda = 600$ km. The currents are initialized with the corresponding geostrophic velocity. The evolution of this system is dependent upon amplitude, and so it is desirable to make the initial current the same at all latitudes. The amplitude was therefore scaled with f/f_o, with f_o appropriate to 30^oN. In the first experiment the amplitude is very small, $\eta_o = 1$ m and thus $\eta_o/H = 0.002$; in a second experiment the amplitude is very large, $\eta_o 100$ m and thus $\eta_o/H = 0.2$. In an attempt to minimize the effect of northern and southern boundaries of the model domain, the amplitude was tapered to zero approaching the equator and also at very high latitude (off of the model domain shown here).

Once this feature is released onto a β-plane we would expect westward propagation as a (fairly) long Rossby wave, and indeed that happens. There is quite noticeable dispersion since the isolated sinusoid Eqn. (26) is not a pure harmonic. As well, while the initial wavelength is long, $kR_d \approx 0.4$, it is not extremely so. When the initial amplitude is very small, $\eta_o/H \ll 1$, (middle panel of Fig. 13), the wave remains easily identifiable for O(1000) days and the leading edge just about keeps pace with the expected long Rossby wave speed. When the amplitude is very large, $\eta_o/H = 0.2$ (lower panel of Fig. 13), the evolution is dramatically different. Within a few hundred days there appears a semi-regular train of lumps and bumps along the length of the wave, and by about 500 days the original long-crested wave evolves into a semi-regular array of mesoscale eddies. These eddies have a scale (diameter) of about 250 km in the northern (high latitude) portion of the domain, and somewhat larger, about 400 km in the low latitude part of the domain. These eddies are in the small wavenumber region of kR_d space, and so they too propagate westward at a rate that is just slightly less than the initial Rossby wave propagation. Even though the initially smooth and continuous wave breaks up rather dramatically, westward propagation nevertheless continues almost unabated.

The details of when and where the eddies form in this experiment depends sensitively upon the way that the initial wave is perturbed. Here the perturbation results mainly from the low latitude end of the wave, which recall was tapered to fit into the model domain. The real ocean is filled with all manner of perturbations having a wide range of time and space scales, though probably nothing quite like the tapering employed here. In any event, the result of the instability — mesoscale eddies — is not sensitive to the form of the perturbation.

Theory (see Isachsen et al.[11]) indicates that the scale of the most rapidly growing instability is proportional to the local radius of deformation, consistent with the y-dependent diameter of the mature

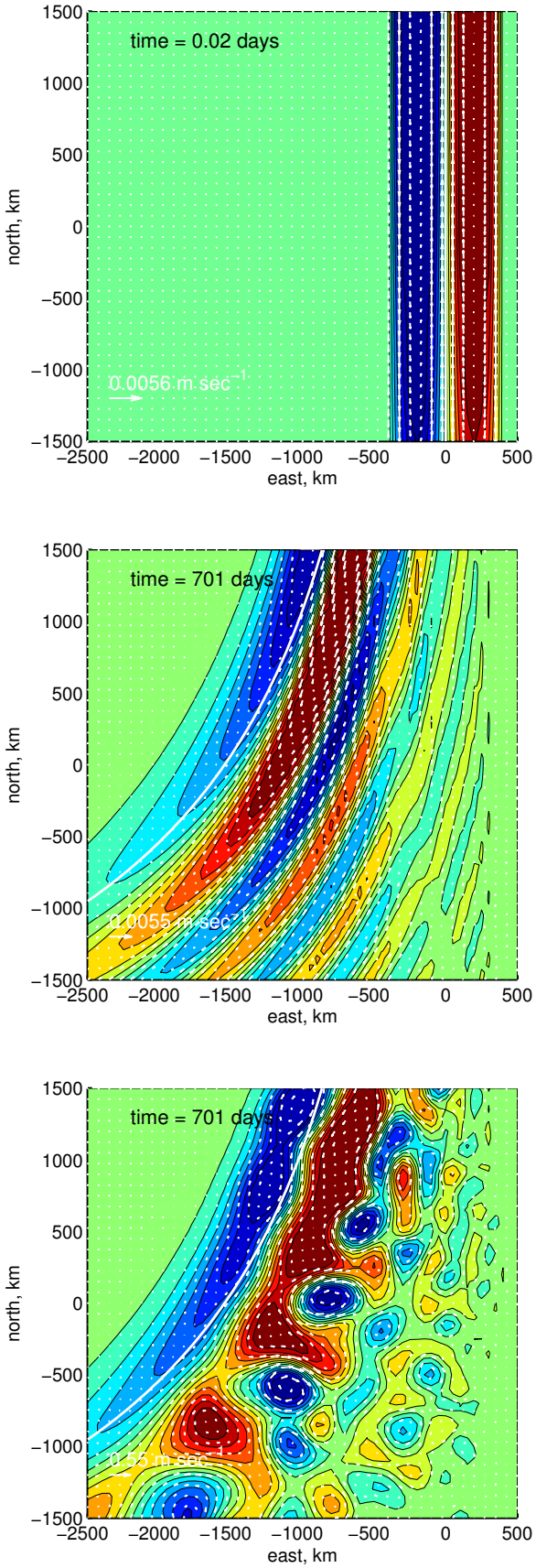

Figure 13: Two experiments that were initialized with a single meridionally-oriented wave in geostrophic balance. **(upper)** The initial condition. **(middle)** The normalized thickness anomaly and currents of a small amplitude case that had $\eta_o = 1$ m. The white parabola was started at $x = 0$ and then displaced westward at the y-dependent long Rossby wave speed. The leading ridge/trough just about keep pace with this westward speed but there is also significant dispersion, with shorter wavelengths lagging well behind. **(lower)** A large amplitude experiment having $\eta_o = 100$ m.

eddies found here. The rate at which the instability grows (once triggered by some kind of perturbation) is expected to be proportional to the amplitude of the initial wave. The two cases of Fig. (13) are extreme, $\eta_o = 1$ m and $\eta_o = 100$ m. In the former case the growth is so slow that there is little evidence of eddy formation even after almost two years. However, in the large amplitude case, which is closer to being realistic of the ocean, the growth is fairly fast, with eddies becoming apparent within several hundred days of the start of the experiment.

2.6 Appendix: Some of the varieties of Rossby wave-like phenomenon

2.6.1 Westerly waves

The westerly wind belts that encircle the mid-latitudes in both hemispheres are nearly always perturbed by wave-like undulations, appropriately termed westerly waves, that are a very significant factor in the day-to-day variation of weather (Fig. 1, Part 1). The longest such waves having wavelengths of O(10,000 km) are often observed to be almost stationary with respect to Earth despite that they are embedded in the eastward flowing westerly wind belt where the spatially-averaged wind is $\bar{U} \approx 30$ m s^{-1}. The longest waves have a westward propagation speed that is just sufficient to stem this eastward advection and may appear to be nearly stationary with respect to the Earth. Quasi-stationary waves of this sort are very common in fluid flows around fixed obstacles: 'rapids' on the surface of a river and ripples on the flow of water from a faucet are familiar examples.

On the other hand, the shortest westerly waves, which may dominate the instantaneous pattern of the westerlies at other times (the web site noted in footnote 3, Part 1 shows instances of this) clearly propagate from west to east. In some cases short waves move eastward at a speed that is not much less than $\bar{U}$. Short westerly waves (which have wavelengths of several thousand kilometers) thus appear to be almost passively advected by the westerly wind. Rossby proposed that westerly waves propagate zonally within a zonal mean flow, $\bar{U}$, as

$$C_w = \bar{U} - \frac{\beta}{k_x^2}, \tag{27}$$

which is the short (non-divergent) limit of the Rossby wave dispersion relation Eqn. (12) plus advection. This relation, and the analysis that led to it, proved to have great merit both as a fundamental explanation of the observations and as a practical guide for weather forecasting.[12]

[12] A superb animation of westerly waves is at https://oceanservice.noaa.gov/facts/rossby-wave.html

2.6.2 Basin-scale Rossby waves

Satellite altimetry has revealed that most ocean basins are full of low frequency variability. In the lower subtropics, a portion of the low frequency variability takes the form of very long-crested, westward propagating, baroclinic features that are unambiguously planetary Rossby waves. These long-crested waves originate on or near the eastern boundary, and then may propagate a very long distance into the open ocean (Fig. 14). This phenomenon makes clear that something very close to an elementary Rossby waves can indeed occur in the ocean, provided that some mechanism has the appropriate (long) time and (long) space scales needed to generate them in the first place.

A remarkable occurrence of such a long-crested Rossby wave was observed in the Pacific ocean in the decade following the very large amplitude ENSO event of 1982-1983.[13] The ENSO event began with a slackening of easterly winds over the western tropical Pacific ocean that allowed the very thick western tropical thermocline to relax back toward a lower energy state, something like the release of our raised eddy of Secs. 4.1 and 4.2, though on a much larger scale. The fastest response was a positive (relative high of SSH and a thick upper layer) Kelvin wave pulse that propagated from the western Pacific to the eastern boundary of the Pacific (roughly 15,000 km) within about two months; $C \approx 3$ m sec^{-1}. The equatorial Kelvin wave was scattered into positive boundary Kelvin waves that propagated north and south along the eastern boundary at a similar speed. The arrival of a positive Kelvin wave is accompanied by warm poleward currents and a thickened thermocline that have very significant consequences for coastal ecosystems (El Nino of the eastern South Pacific). The thickened thermocline along the eastern boundary was the proximal forcing mechanism of baroclinic Rossby wave(s) that began propagating westward across the Pacific basin. The meridional extent of the waves (distance along the wave crest) was more than 3000 km in both hemispheres, the meridional extent of the boundary Kelvin wave disturbance. Wave crests were strongly refracted toward the west at low latitudes (Fig. 14), consistent with the wave speed of long (divergent, non-dispersive) baroclinic Rossby waves, $C \propto \beta/f^2$, i.e., faster westward propagation at lower latitudes (but not in excess of C). The initial, high SSH wave pulse that started the 1982-1983 ENSO event was detectable for at least a decade after its generation, by which time it had reached the western boundary near Japan, where it altered the path of the Kuroshio current. This kind of very large scale, low frequency variability is predictable for years ahead, once it has formed.

One question these observations raise is, how could such a long-crested wave survive the instability process noted in Sec. 2.7? The satellite SSH observations that were made in the 1980s were not as well resolved spatially as those made more recently, but a second look at the field of (Fig. 14) suggests that the wave front may very well have fractured into mesoscale eddies. As we have seen, these eddies propagate to the west very much like the original, long-crested Rossby wave.

[13] Jacobs, G. A., H. E. Hurlburt, J. C. Kindle, E. J. Metzger, J. L. Mitchell, W. J. Teague, and A. J. Wallcraft, 1994: 'Decade-scale trans-Pacific propagation and warming effects of an El Nino anomaly', *Nature*, Vol. 370, pp. 360-363.

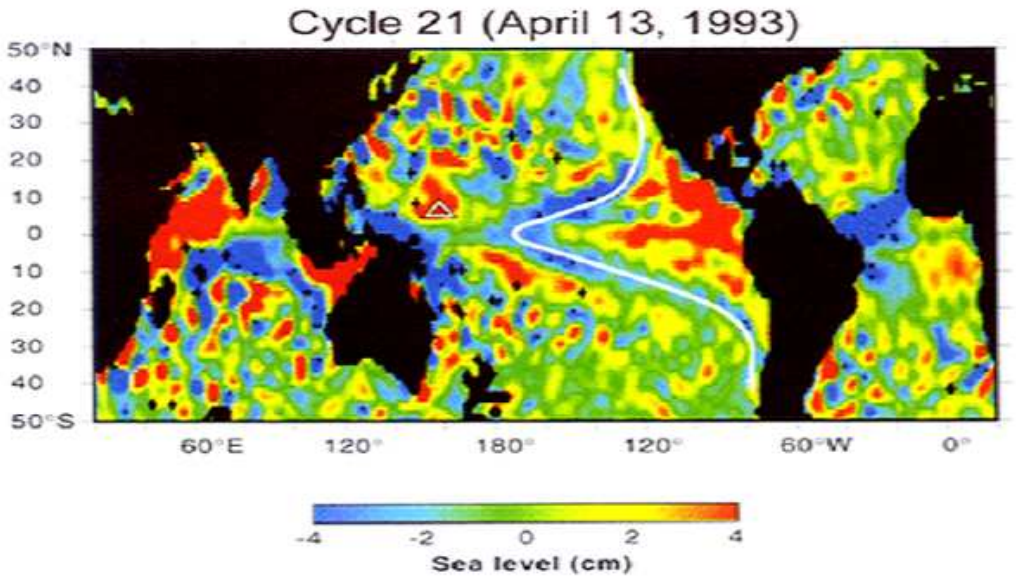

Figure 14: A snapshot of SSH observed by TOPEX/POSEIDON satellite altimetry in the Spring of 1993. The subtropics in both hemispheres of the Pacific basin showed long-crested, westward propagating baroclinic Rossby waves that started on the eastern boundary. The white line is along a relative low of SSH. The westward refraction of the wave crest at low latitudes is consistent with the latitudinal dependence of a long (divergent and non-dispersive) baroclinic Rossby wave. Notice that there is similar variability evident also in the Atlantic basin (though evidently not in 2007, Fig. 2). This figure is reproduced with permission from Dudley Chelton, and is from Chelton and Slax (1994), https://oregonstate.app.box.com/s/oetv6qnepc9go6ruhp4cnqab2e6gbi9d

2.6.3 Topographic eddies and waves

The variation of bottom depth has been omitted from our analysis, mainly for simplicity. This would be an acceptable approximation in cases where the flow of wind or ocean currents at the ground or sea floor was very weak, as in the mesoscale eddies of Sec. 2 or the open ocean, equatorial phenomenon of Sec. 3. However, there are common circumstances where strong currents occur near the bottom even in the deep, stratified ocean, e.g., under the Gulf Stream, and circumstances where the flow is barotropic (depth-independent) and hence in contact with the bottom, e.g., on continental shelves. The relevant, background potential vorticity is then $f/(H+b)$, with $H+b(x,y)$ the nominal thickness. The essential difference between column thickness that varies with b vs. η is that b is spatially dependent but time independent. A fluid column that moves across bottom contours will then necessarily be stretched (or squashed), inducing relative vorticity, exactly as does flow across lines of constant f.

The ratio of planetary to topographic vorticity change over a typical continental shelf is

$$\frac{\text{planetary}}{\text{topographic}} = \frac{\frac{1}{f}\frac{\partial f}{\partial y}}{\frac{1}{h}\frac{\partial h}{\partial y}} = \frac{h}{\alpha R_E} \text{ is } O(10^{-1}),$$

given a bottom slope $\alpha = 10^{-3}$ and nominal depth $H = 200$ m. The magnitude of the topographic term can easily exceed the planetary β term since the bottom depth typically varies on much shorter spatial scales than does f (radius of Earth, R_E). Topographic effects would prevail over the (planetary) β-effect over most of the deep, open ocean as well, except that stratification largely shields the upper water column from direct bottom slope effects. Assuming that topographic variation dominates the gradient of the background potential vorticity, $q = f/H$, and that the flow is depth-independent, then the frequency of topographic Rossby waves is given by

$$\frac{\omega}{f} = \frac{\alpha g}{fC}\left(\left(\frac{R_d K}{1+R_d^2 K^2}\right)\right($$

where $R_d = C/f$ is the barotropic radius of deformation, with $C = \sqrt{gH}$ computed from a nominal H and the full gravity. For a nominal shelf, $C \approx 45$ m s^{-1} and $R_d \approx 900$ km (mid latitudes). These waves often have considerably higher frequencies than do planetary Rossby waves, with 5 - 20 day periods being common. They have correspondingly greater phase and group speeds as well. Just as planetary Rossby waves propagate phase westward - with higher background potential vorticity to the right of the wave vector - so too these topographic Rossby waves propagate phase with shallower water and thus larger f/H on their right.[14]

2.6.4 Tropical cyclones

One of the most remarkable instances of Rossby wave dynamics occurs in conjunction with tropical cyclones (TC), intense vortical flows around low pressure anomalies. Most TCs begin with a convective cloud cluster, that may become organized into a vortex and grow in amplitude and scale if the mesoscale shear environment includes sufficient cyclonic vorticity. Mature TCs typically have a radius of several hundred kilometers, which is quite small compared to the atmospheric radius of deformation, about 1000 km.

Some tropical cyclones (about 1 in 6) have been observed to develop a marked, eastward-extending Rossby wave wake in the troposphere. The wavelength along the wake is typically several thousand

[14] An excellent description of short-crested, baroclinic, topographic waves (or eddies) observed under the Gulf Stream is available at http://www.po.gso.uri.edu/dynamics/wbc/TRW.html

kilometers, and consists of alternate cyclonic and anti-cyclonic disturbances. The cyclonic features have been observed to act as the vorticity trigger for subsequent TC genesis, so that TCs, particularly in the western North Pacific, may develop in a semi-regular sequence at intervals of several thousand kilometers. The spatial scale is evidently set by the Rossby wave properties of the eastward extending wake.[15]

2.7 Problems

(1) A little more on high frequency beta-effects. Imagine an f-plane, and an initial condition that is an unbalanced and unforced northward current in a surface layer of thickness h. How would the resulting free inertial motions evolve at two sites at different latitudes? Now suppose that this experiment is repeated but on a beta-plane and taking account of the possible pressure gradient that would follow from divergence of the upper layer current. How would the inertial oscillations evolve? Now suppose that the initial condition is consistent with generation by a wind with some duration so that $v \propto \tau/(f(y)h)$. If you followed this, then you can appreciate that there are two high frequency beta-effects; a y-dependent frequency of inertial motions, and a $1/f(y)$ dependence of wind-driven current amplitude.

(2) Eqn. (13) is the third time that the radius of deformation has arisen as the appropriate length scale against which to compare (or measure) horizontal scales, in that case the wavelength of Rossby waves. Does this reflect an excess of enthusiasm for R_d, or is there really nothing else as suitable? What about the layer thickness, H? Surely it too is an intrinsic length scale.

(3) Rossby waves exhibit normal dispersion in that longer waves have greater phase speed. It can happen that shorter waves have a greater phase speed, a property dubbed anomalous dispersion. An example of anomalous dispersion that you can readily investigate is that of capillary waves generated by the movement of a small object across the surface of still water. If the object moves more slowly than the slowest gravity/capillary wave, there are no waves. But when the speed of the moving object exceeds this minimum wave speed, a wave pattern will suddenly appear around and in front of the object. Short capillary waves lead the pack. Here's a question for you to answer experimentally: at what speed does this occur? (A factor of two is fine.) Anomalous and normal dispersion may be investigated also via numerical experiments that solve an initial value problem, ftransform.m (Sec. 7, Part 2).

(4) A couple of dispersion relation questions for you: 1) Sketch the dispersion relations for the short and long Rossby waves limits onto Fig. (6, upper). Use parameters appropriate to 30^o N; f = 7.29x10^{-5} sec^{-1}, $C = 3$ m sec^{-1}, and β = 1.98x10^{-11} sec^{-1} m^{-1}. 2) Discuss the phase and group speed in the case that $KR_d = 1$, and interpret Fig. (4, lower).

(5) Westward energy propagation is the dominant outcome of the β plane experiments and got most of our attention, but there is noticeable eastward energy propagation as well. Starting with Eqn. (13), show that the maximum eastward C_g is $C_{longRo}/8$ and occurs at $R_d k_x = \sqrt{3}$.

[15] This phenomenon is an active area of research, see Krouse, K. D. , A H. Sobel and L. M. Polavni, 2008, 'On the wavelength of the Rossby waves radiated by tropical cyclones', *J. Atmos. Res.*, 65, 644-654, and references therein.

(6) Evaluate the long Rossby wave speed over the latitude range 10 to 50^o. In this you may assume that the gravity wave speed C is constant, $C = 3$ m sec^{-1} (though in fact it decreases somewhat poleward of the subtropics). You will notice that the latitudinal dependence of the long Rossby wave speed is quite pronounced. Can you explain in a few words where this f^{-2} dependence originates?

(7) Some eddy propagation questions. 1) How does your result from the problem 4) above compare with the eddy propagation speed found in the numerical experiments? The experiment of Fig. (3) takes care of 30^o N, so you will need to find the numerical result for other latitudes. Much better that you design and run the experiments yourself, but in case that is not feasible, some animations for other latitudes are linked in Sec. 7, Part 2. We noted in the discussion of Fig. 1 that the observed propagation speed of oceanic mesoscale eddies varies significantly with latitude, being considerably faster towards lower latitude. On average over all ocean basins the observed[1] (latitude, zonal speeds) are (10^o, -14 ± 4 cm sec^{-1}), (20^o, -5.0 ± 1.5 cm sec^{-1}), (30^o, -3.5 $\pm$1.5 cm sec^{-1}), (40^o, -1.5 $\pm$1 cm sec^{-1}) and (50^o, -0.8 $\pm$ 0.5 cm sec^{-1}). How does this compare with your results above?

(8) The natural way to think of conservation is following a given parcel or water column, i.e., a Lagrangian description. Our model equations are, however, Eulerian. 1) Go back and make an explicitly Lagrangian description of the two q conservation modes discussed above (short and long Rossby waves), and then make the corresponding Eulerian description.

(9) The discussion in the main text emphasized the trajectories of the floats that were set inside the initial eddy (the red floats). What happens to the green floats that were launched outside and to the west of the eddy? Consider the small and large amplitude experiments, Figs. (7) and (8) and their animations.

3 Adjustment on an equatorial β-plane

The temporal and spatial variability of equatorial SSH is very different from that seen at subtropical and higher latitudes. Mesoscale eddies are uncommon (though appear seasonally in some years in the Pacific), and a gyre-like structure is not readily apparent.[16] The main features are:

1) The primary variability of SSH is in zonally elongated features. These have a meridional scale of several hundreds of kilometers, and widths that may span most of the Atlantic basin. These features exhibit strong seasonality.

2) SSH variability has small amplitude. Aside from the western boundary current, the amplitude of SSH variability is typically $\pm$ 0.05 m, compared with $\pm$ 0.1 to 0.2 m for mesoscale eddies of the

[16]Most of the equatorial phenomena described here are seen much better in multi-year records: a superb animation of 18 years of satellite-derived altimetric data including the Pacific and Indian oceans is available from http://podaac.jpl.nasa.gov/node/430

subtropics and ± 1 m over the subtropical and subpolar gyres. f is, of course, much smaller, and so this does not mean that currents are also small amplitude.

3) Episodic, eastward propagation over distances that may span most of the basin.[16] The propagation speed of these eastward-going events is comparable to the gravity wave speed, several hundred km per day.

3.1 An equatorial adjustment experiment

The plan for this section is to carry out a geostrophic adjustment experiment on an equatorial beta-plane ocean and compare the results to previous experiments. As before, the motive is to gain some insight into the properties and mechanisms of the observed SSH noted above. To be sure, the results of this adjustment experiment can account for only a part of these equatorial phenomena, much of which is due instead to forcing by the large-scale, time-dependent equatorial winds. Hence, some of the discussion is deferred to Part 4. Here in Part 3 we will emphasize the properties of equatorial waves, which are of first importance in understanding variability generally.[17]

The β-plane is set to $f_0 = 0$ and $f = \beta y$, i.e., an equatorial β-plane. The stratification was changed somewhat to reflect the shallower main thermocline of equatorial regions, H = 250 m, and larger density contrast across the main thermocline, $\delta\rho = 3$ kg m^{-3}. The gravity wave speed $C = \sqrt{g'H} \approx 2.5$ m sec^{-1}. The initial condition is a raised, cylindrical thickness anomaly with radius $L = 200$ km that is centered on the equator. Though this eddy is twice the size used previously, it is nevertheless small compared to the intrinsic horizontal scale of the equatorial ocean. The domain is a box 5000 km by 5000 km. The northern and southern sides are treated with a radiation boundary condition that allows the passage of gravity waves off of the model domain. The eastern and western sides are defined by zero normal flow, $u(x = \pm 2500) = 0$. Waves reaching the zonal boundaries are thus reflected and scattered.

Soon after the equatorial thickness anomaly is released, Fig. (15), gravity waves propagate away in all directions. The leading edge of the expanding wave front is nearly circular, and grows in radius at the gravity wave speed $C = \sqrt{g'H}$, as seen before. Within about a week, gravity wave motions dispersed (spread) the eddy energy over most of the model domain. The initial thickness anomaly collapsed within about $L/C \leq 1$ day, very much as would be expected in the complete absence of rotation (Sec. 3.1, Part 2). The initial condition was symmetric about the equator, and this north-south symmetry is maintained in all that follows. However, the waves showed some significant east-west anisotropy, with preferred

[17] The GFD text by Gill noted in footnote 1 of Part 2 has a very useful discussion on equatorial dynamics. One of the seminal research papers on equatorial dynamics is also highly recommended: Matsuno, T., 1966, 'Quasi-geostrophic motions in an equatorial area', *J. Met. Soc. Japan*, 44(1), 25-43.

propagation along the equator and especially eastward, as will be discussed further below. These very significant details aside, this equatorial adjustment process looks more like the pure gravity wave experiment of Sec. 3 Part 2 than the mid-latitude f- or β-plane experiments. Beta is almost the same in this experiment as in the mid-latitude experiments of Sec. 2, and so it isn't β alone that matters but mainly f_o (which is zero here).

3.2 An equatorial radius of deformation

In the $f-$plane and mid-latitude $\beta-$plane experiments of previous sections, the radius of deformation, $R_d = C/f_0$, was the intrinsic horizontal scale against which to measure the radius of the initial eddy, wavelengths, etc. On an equatorial $\beta-$plane, $f_0 = 0$, and so the equivalent radius of deformation, R_{deq}, is bound to be somewhat different. How might this R_{deq} be deduced? Three possibilities: 1) Look for the radius of deformation in a solution involving transcendental functions of the north-south coordinate. An example is coming in the next section, but very often an explicit solution will not be available, and then something more general will be required. 2) Apply the method of dimensional analysis to deduce a length scale from the parameters that define the ocean model. Dimensional analysis works particularly well in this instance because there are only two parameters that define a shallow water, equatorial β-plane, the gravity wave speed, C [length time^{-1}] and of course β [length^{-1} time^{-1}]. The simplest, dimensionally consistent form of a length is

$$R_{deq} = \sqrt{C/\beta}, \tag{28}$$

which turns out to be correct. This result came awfully easily, but without the slightest hint of a physical interpretation. 3) Finally, recall that the long Rossby wave speed increases toward lower latitude as $\beta R_d^2 = \beta C^2/f^2$ and on an equatorial beta-plane, $\beta C^2/(\beta y)^2$. This cannot hold hold all the way to the equator, $y = 0$, since the fastest possible wave in the shallow water model is the gravity wave speed, C. At what y does the long Rossby wave speed equal the gravity wave speed? Again the answer is $y = \sqrt{C/\beta}$, and now with a very slim hint at an interpretation.

Given the (baroclinic) gravity wave speed, $C \approx 2.5$ m sec^{-1}, $R_{deq} = 340$ km. The local inertial period at that y is $2\pi/f = 4$ days. From this it appears that the eddy defined in the initial condition, radius L = 200 km, is small insofar as $L/R_{deq} \approx 1/2$ and it has been noted that the initial eddy was entirely dispersed into waves. The same result obtains even for a much larger eddy, $L = 500$ km, see https://www2.whoi.edu/staff/jprice/eqtr-largeeddy

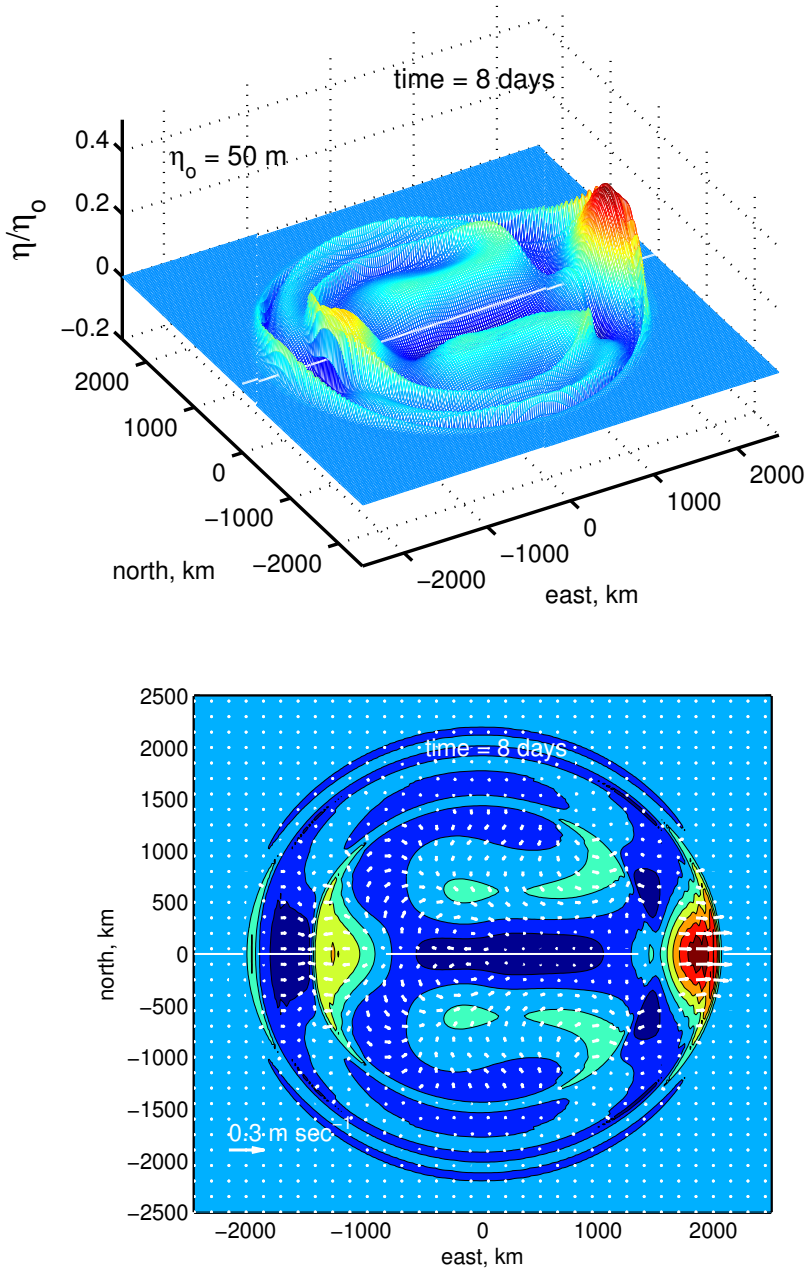

Figure 15: A snapshot from an equatorial adjustment experiment at time = 8 days after releasing a raised eddy centered on $(east, north) = (x, y) = (0, 0)$. The model domain extended 2500 km north and south of the equator (the thin white line), and sidewalls were placed at $x = \pm$ 2500 km. East is to the right. (The Pacific Ocean has more than three times this width.) **(upper)** The thickness anomaly, η. Notice that the largest feature is a positive bump centered on the equator and propagating eastward, evidently a Kelvin wave pulse as discussed in the main text. An animation of these data is eqtr-eta.mp4 in P3-videos. **(lower)** A plan view of the velocity, and color contours of η. Notice that velocity is generally normal to the η contours, indicating that these fields are mostly gravity wave motion. An animation of this data is eqtr-velocity.mp4

3.3 Dispersion relation of equatorially-trapped waves

Wave properties of the equatorial β-plane are clearly very important, and it wouldn't be exaggerating to say that waves of one kind or another are all that there is this adjustment experiment. For the purpose of examining wave properties it will be necessary to work with the linear shallow water system; substituting $f = \beta y$,

$$\frac{\partial h}{\partial t} \;=\; H(\frac{\partial u}{\partial x} \;+\; \frac{\partial v}{\partial y}), \tag{29}$$

$$\frac{\partial u}{\partial t} \;=\; -\,g'\frac{\partial h}{\partial x} \;+\; \beta y v, \tag{30}$$

$$\frac{\partial v}{\partial t} \;=\; -\,g'\frac{\partial h}{\partial y} \;-\beta y u. \tag{31}$$

Presuming the existence of zonally propagating waves that have an unknown y-dependence, then for the meridional velocity (this follows very closely the classic paper by Matsuno[17]);

$$v(x,y,t) \;=\; V(y)cos(kx_x - \omega t), \tag{32}$$

and similarly for $U(y)$ and $\Upsilon(y)$. By substitution into the linear shallow water equations and after eliminating $U(y)$ and $\Upsilon(y)$ by cross-differentiating and adding (as in the derivation of the potential vorticity balance) there results a second order, ordinary differential equation for $V(y)$,

$$\frac{d^2V}{dy^2} \;-\; \left(\frac{\beta^2y^2}{C^2} - \frac{\omega^2}{C^2} + \frac{\beta k_x}{\omega} + k^2\right)\Big(V \;=\; 0, \tag{33}$$

and a dispersion relation discussed below. To be physically realizable,

$$V(y) \to 0 \;\text{ as }\; \mid y \mid \;\; \to \infty. \tag{34}$$

Eqns. (33) and (34) have the form of a Shrodinger equation for a quantum harmonic oscillator, and the solutions are the set of eigenfunctions

$$V_n(y) = exp(-\frac{y^2}{2R_{deq}^2})H_n(\frac{y}{R_{deq}})$$

where H_n is the nth (physicist's) Hermite polynomial. The first five are $H_0 = 1$, $H_1 = 2y$, $H_3 = 4y^2 - 2$, and $H_4 = 8y^3 - 12y$. The eigenfunctions $V_n(y)$ are meridional normal modes that are numbered n = 0, 1, 2 etc. (Fig. 16, right). The Kelvin mode labeled $n = -1$ requires a separate discussion to follow. The eigenfunctions of the interface displacement, $\Upsilon_n(y)$, may be computed from the $V_n(y)$ as,[17]

$$\Upsilon_n(y) \;=\; 0.5(\omega R_{deq}/C - k_x R_{deq})V_{n+1}(y) \;-\; n(\omega R_{deq}/C + k_x R_{deq})V_{n-1}(y). \tag{35}$$

The odd numbered $\Upsilon_n(y)$ are symmetric about the equator, i.e., $\Upsilon_n(y) = \Upsilon_n(-y)$ (Fig. 16, right), while the even-numbered modes are anti-symmetric, $\Upsilon_n(y) = -\Upsilon_n(-y)$. This symmetry is very consequential for the excitation of the normal modes.

The dispersion relation $\omega(k)$ is

$$\omega^3 - \left(C^2 k_x^2 + \frac{(2n+1)C^2}{R_{deq}^2} \right) \omega - \beta C^2 k_x = 0, \tag{36}$$

where k is the zonal wavenumber (there is no north-south wavenumber by virtue of Eqn. 32), and n is the (meridional) mode number. This dispersion relation is cubic and so looks a bit complicated. However, its graph, Fig. (16, left) reveals two familiar wave types — higher frequency waves that are close analogs of the mid-latitude inertia-gravity waves, and lower frequency Rossby waves. As in the mid-latitude β-plane experiment, there is a significant frequency gap between the lowest frequency inertia-gravity wave, $\omega R_{deq}/C \approx 1.7$ (dimensional period = 5.4 days), and the highest frequency Rossby wave, $\omega R_{deq}/C \approx 0.3$ (period = 30 days).

The equatorial β-plane also supports two important wave types that are not found in the mid-latitude, open ocean. 1) The mode $n = 0$, appropriately called a mixed Rossby-gravity wave, has a $\omega(k)$ that closely parallels the Rossby wave modes for negative wave numbers (west-going waves), and parallels the inertia-gravity waves for positive wave numbers (east-going waves). The group speed of these waves is eastward at all frequencies. Depending upon the wavenumber, Rossby-gravity waves can have a frequency that is intermediate between the low frequency Rossby waves and the higher frequency inertia-gravity waves. Hence, there is no frequency gap in the family of free equatorial waves, as occurs at mid-latitudes. Unfortunately, these waves are not observed in the present experiment, because the mixed Rossby-gravity wave mode is anti-symmetric in $\eta(y)$ and so is not excited by the symmetric, initial thickness anomaly used here. 2) Second, the equatorial beta-plane also supports an eastward-going Kelvin wave, of which more below.

3.3.1 Westward-going gravity and Rossby waves

The most noteworthy wave motions appear to be trapped near the equator (Figs. 15 and 16). First, consider the wave motion(s) that are farthest west of the origin, $-2000 < x < -1800$ km, at time = 8 days. The velocity is almost normal to isolines of η and thus longitudinal and gravity wave-like. The meridional structure is a single maximum of meridional extent approx. R_{deq}, that is symmetric about the equator and thus meridional mode n = 1. The dominant wavelength is very roughly λ = 1000 km so that $kR_{deq} \approx 2$. In this $R_{deq}k_x$ range, the dispersion relationship for gravity waves is dispersive, and the group speed is slightly less than the maximum possible, $\sqrt{g'H}$. The $\eta(x)$ profile looks wave-like, vs. pulse-like

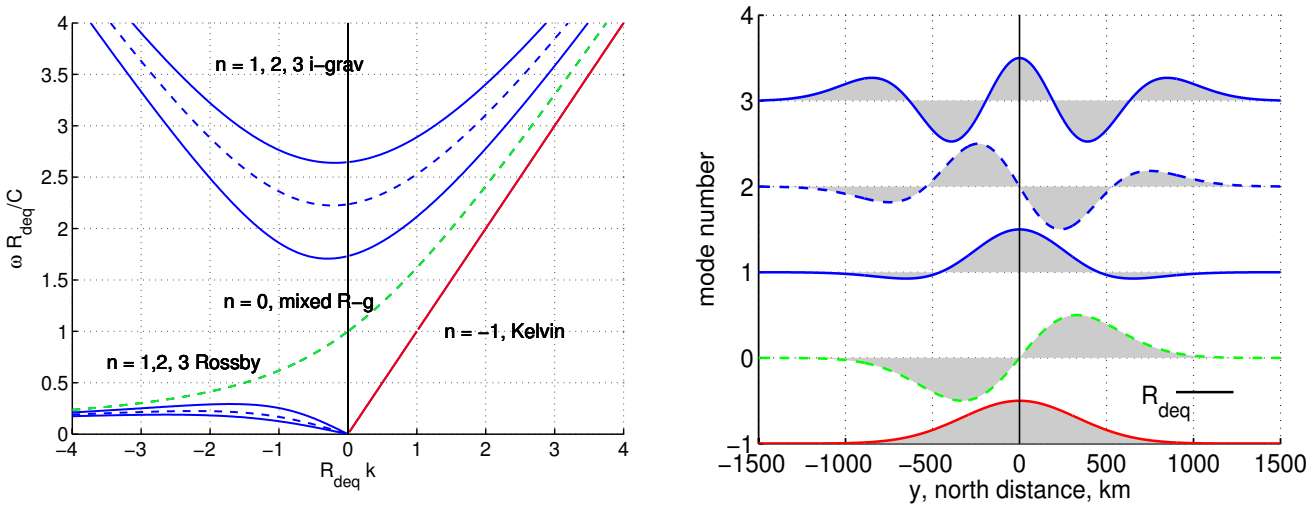

Figure 16: **(left)** Dispersion diagram for the trapped waves on an equatorial β-plane. The modes are numbered $n = -1, 0, 1...$ etc. The Kelvin wave $n = -1$ is in red, the mixed Rossby-gravity wave is in green dashed, and the inertia-gravity and Rossby waves are in blue. Modes that are symmetric in $\eta(y)$ are solid, while modes that are anti-symmetric are dashed. Note that the equatorial radius of deformation is used to nondimensionalize the zonal wavenumber, k_x, and the equatorial inertial period R_{deq}/C used to nondimensionalize the frequency. **(right)** The meridional modes of η, $\Upsilon_n(y)$, computed from the $V(y)$ modes and Eqn. (35) using $\omega R_{deq}/C \approx 2$ and $R_{deq}k_x \approx -1$, appropriate to westward propagating inertia-gravity waves. For Rossby wave values, the details are different, but the symmetry properties of the modes remain the same. The colors correspond to those at left, e.g., the Kelvin wave is in red. The amplitudes are arbitrary. Notice that lower numbered modes are effectively trapped near the equator, while higher modes may have an appreciable amplitude at higher latitudes.

(Figs. 17 and 18) Thus the leading, west-going waves appear to be equatorially-trapped gravity waves.

A somewhat larger amplitude westward-going feature trails behind the leading gravity waves; at time = 8 days a local maximum is centered on $(x, y) = (-1200, 0)$ km. The meridional structure is very similar to that noted above, mode $n = 1$, and Gaussian with north-south scale R_{deq}. The group speed is evidently about half or less of the fastest westward-going gravity waves noted just above. A qualitative difference with the gravity waves is that the velocity has some component along isolines of thickness, rather than normal as for gravity waves, and hence the velocity is somewhat geostrophic. These properties are consistent with a meridional mode 1 equatorial Rossby wave. Equatorial Rossby waves have a dispersion relation that is the low frequency limit of Eqn. (36),

$$\omega = -\frac{Ck_x}{R_{deq}^2 k_x^2 + (2n+1)}. \tag{37}$$

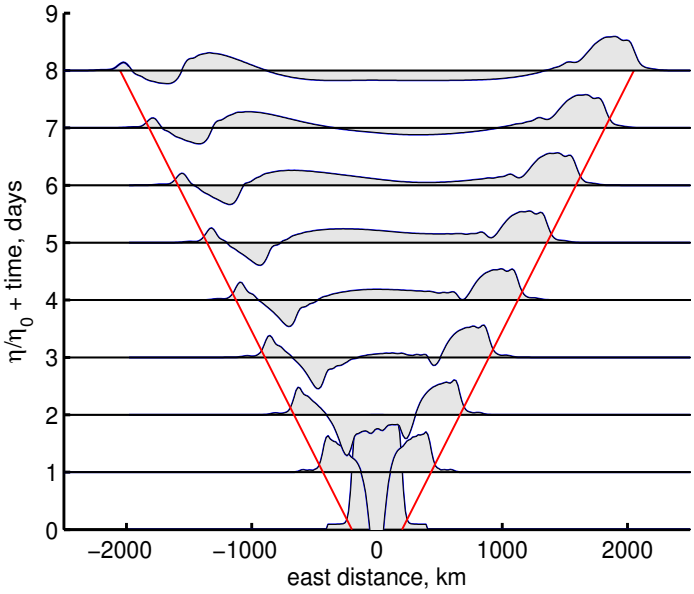

Figure 17: A series of slices through the numerical solution Fig. (15) along the equator showing $\eta(x, y = 0$,time = 0, 1, 2... days) normalized by $\frac{1}{2}\eta_0$. The red lines have a slope = $dx/dt = \pm C = \pm\sqrt{g'H}$. Notice that the westward-going, gravity wave packet changes shape with time and has only a small mean value. The eastward-going Kelvin wave pulse maintains a nearly constant shape and has an appreciable mean value. This illustrates the often qualitative difference between dispersive (westward-going) and nondispersive (eastward-going) wave propagation.

The long wave limit, $R_{deq}^2 k_x^2 \ll 1$, for $n = 1$ has phase and group speed

$$C_p = C_g = \frac{C\omega}{k_x} = -C/3$$

or about 100 km per day and westward. These long Rossby waves are nondispersive (although for the west-going waves considered as a whole there is clearly a significant range of phase and group speeds). It is notable that long equatorial Rossby waves have phase and group speed that are greater by a factor of about 30 than that of mid-latitude, long Rossby waves. This has great significance for the response of the equatorial ocean to seasonally varying wind stress, as we will discuss in Part 4.

3.3.2 Kelvin wave

The eastward-going motion is made up mainly of a very prominent isolated maxima in η that has the propagation properties of an equatorial Kelvin wave. This Kelvin wave pulse is important and interesting on two counts: first, it is the biggest feature in the solution, and second, it does not appear as a solution of the modal equation (33).

Suppose we did not know that this feature was a Kelvin wave — could we infer the dynamics from the properties evident in the numerical solution? Several useful clues are evident in a sequence of equatorial slices through the solution, Fig. (17), and in a magnified plan view, Fig. (18).

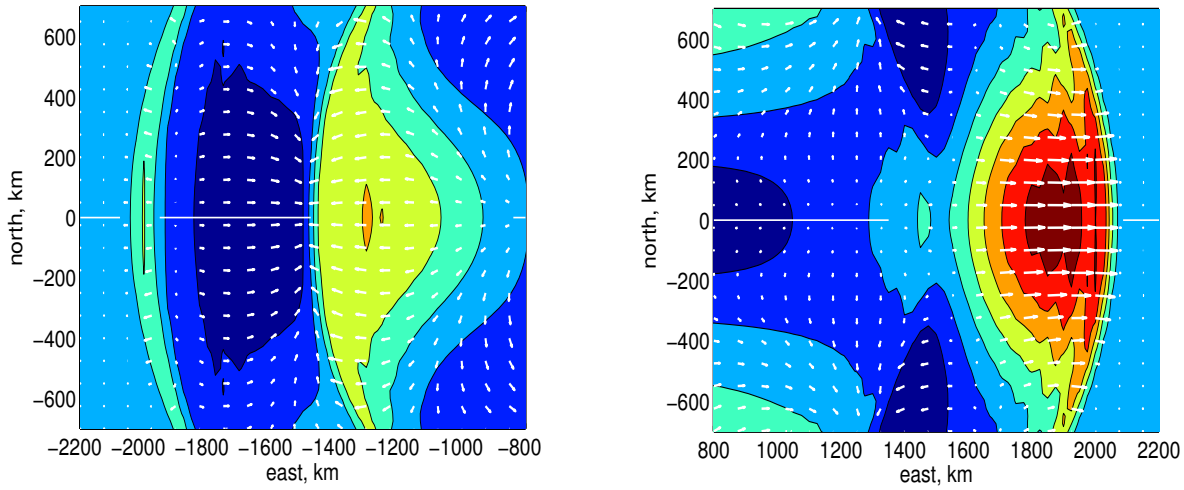

Figure 18: Enlarged snapshot views at time = 8 days of the equatorially-trapped, westward- and eastward-going local maxima from Fig. (15). **(left)** The westward-going pulse is dispersed into faster-moving gravity waves and slower moving, somewhat larger amplitude Rossby wave(s). Both kinds of westward propagating waves are evidently meridional mode 1 (Gaussian). **(right)** The eastward-going wave pulse has the properties of a Kelvin wave; the north-south structure is Gaussian, as at left, and the fluid velocity (the field of small white arrows) is directed almost exclusively east-west and

1. The pressure/velocity relationship is mainly longitudinal and the velocity is almost entirely zonal (east-west). Hence there is little or no β effect. These characteristics are consistent with a gravity wave, but not a Rossby wave.

2. Once this feature is separated from the initial eddy, the zonal wave form $\eta(x)$ remains almost constant as it propagates eastward at a speed very close to the gravity wave speed, $C = \sqrt{g'H}$. This is evidence of a nondispersive gravity wave motion as in Part 2, Sec. 3.1.

3. The meridional profile $\eta(y)$ is symmetric across the equator and is nearly self-similar, suggesting an equatorially-trapped wave mode. The half-width in y is about 400 km, or roughly R_{deq}.

The most telling/important clue to the dynamics is perhaps the first one, that $v = 0$. When this is implemented in the linear shallow water equations the result is a significantly reduced set:

$$\frac{\partial \eta}{\partial t} = H\frac{\partial u}{\partial x}, \tag{38}$$

$$\frac{\partial u}{\partial t} = -g'\frac{\partial \eta}{\partial x}, \tag{39}$$

$$0 \;=\; -g'\frac{\partial \eta}{\partial y} - \beta y u. \tag{40}$$

Eqns. (38) and (39) are exactly the pure gravity wave (nonrotating) system of Sec. 3.1 Part 2 and lead to the same elementary wave equation in (x,t);

$$\frac{\partial^2 \eta(x,y,t)}{\partial t^2} \;=\; g'H\frac{\partial^2 \eta(x,y,t)}{\partial x^2}, \tag{41}$$

and the familiar phase speed,

$$\frac{\omega}{k} \;=\; \sqrt{g'H} \;=\; C.$$

This phase speed does not depend upon k_x, and so this wave is nondispersive, which is consistent with the observed wave form Fig. (18). Eqn. (40) indicates a geostrophic balance for the east-west component of the velocity. Substitution of the updated Eqn. (32) into Eqn. (40) gives

$$0 \;=\; \frac{d\Upsilon(y)}{dy} \;-\; \frac{\beta\omega}{g'Hk_x} y\Upsilon(y). \tag{42}$$

Together with the boundedness requirement, this yields the $y-$dependence of the pulse shape, a Gaussian $\propto exp(-y^2/2R_{deq}^2)$, where $R_{deq} = \sqrt{C/\beta}$. Combining these two results gives a partial solution

$$\eta(x,y,t) \;=\; \eta_0(x)\exp\left(\frac{-y^2}{2R_{deq}^2}\right)\cos(k_x x - \omega t), \tag{43}$$

where $\eta_0(x)$ is the zonal width of the Kelvin wave pulse. The important qualitative results from this brief analysis are: 1) an equatorial Kelvin wave propagates eastward only, 2) it is non-dispersive, 3) it is symmetric across the equator (Fig. 16, right) and 4) it has a Gaussian zonal profile and zonal scale R_{deq}. The meridional profile is always the Gaussian of (43), regardless of the initial eddy size. However the width of the wave pulse, $\eta_0(x)$, is proportional to the width of the initial eddy, rather short in this experiment.

Because an equatorial Kelvin wave has zero meridional fluid velocity, it is not represented in the second order equation (33) for the meridional structure $V(y)$. Thus Eqn. (33) contains only a subset of the shallow water system, that having meridional velocity. The Kelvin wave has to be added to the solutions of Eqn. (33) in order to make a complete set and, more to the point, to account for the phenomenon seen in our numerical experiment. The Kelvin wave is usually assigned the label $n = -1$, since it's dispersion properties $\omega(k)$ fit Eqn. (36) for that n. Since there is no meridional flow across the equator, the equator could just as well be replaced by a (frictionless) wall insofar as the Kelvin wave alone is concerned.

The Kelvin wave is clearly a very important part of the adjustment process: inertia-gravity and

Rossby waves carry energy away from the collapsing eddy, but the Kelvin wave pulse carries energy along with roughly 2/3 of the excess layer thickness (initial eddy volume) towards the east. When the Kelvin wave pulse reaches the eastern boundary it is partially reflected back to the west in the form of equatorially-trapped inertia-gravity and Rossby waves. Most of the volume contained within the equatorial Kelvin wave is scattered onto boundary-trapped Kelvin waves that propagate north and south along the eastern boundary of the model domain (to see this you will need to view the animation linked in the caption to Fig. 15).[18]

3.4 Problems

(1) Some Kelvin wave questions for you. 1) In our geostrophic adjustment experiment the initial eddy had a positive η (easier to plot); suppose instead the initial eddy was a depression in the layer thickness; what differences might be expected for the Kelvin wave? Consider also finite amplitude effects that you can check with the numerical model. 2) Is it possible to have an equatorial Kelvin wave that propagates westward? 3) The zonal velocity of a Kelvin wave is in geostrophic balance with the tilted interface. Can you show that the resulting $u(y)$ is also consistent with one of the potential vorticity conservation modes discussed in Sec. 2.2.3, Part 2? 4) How would the Kelvin wave change if the initial eddy was made larger or smaller in the horizontal?

(2) The north-south symmetry of the initial condition chosen here had significant consequences for the waves that were generated during geostrophic adjustment. Suppose that the initial eddy was displaced off of the equator - what might be different? This is something you can check with a numerical experiment.

4 Summary and Remarks

This essay started with the question **What processes lead to the marked east-west asymmetry that is observed to characterize most large scale circulation (low frequency) phenomena?** Important examples of this asymmetry evident in Fig. (1) include the westward propagation of mesoscale eddies and the very marked westward intensification of the wind-driven gyres. This essay has emphasized the low frequency β-effect that arises from the northward variation of f combined with a balanced meridional velocity.

[18] An excellent online reference for the role of equatorial waves in the ENSO phenomenon is available at http://iri.columbia.edu/climate/ENSO/theory/index.html More on the equatorial Kelvin wave may be found at http://science.nasa.gov/science-news/science-at-nasa/2002/05mar_kelvinwave/ (you may have to type this in to your browser).

4.1 Mid-latitude mesoscale eddies

The first experiments considered in Sec. 2 included the geostrophic adjustment of a mesoscale-size thickness anomaly released onto a mid-latitude β-plane.

1) The short-term (several days) geostrophic adjustment process is little altered by β. The inertia-gravity waves that propagate poleward are, however, reflected when they reach a latitude where f is comparable to their intrinsic (initial) frequency. This βinduced reflection is an interesting and important process for inertia-gravity waves found in the open ocean, but it has no evident effect upon the adjusted eddy.

2) The long-term (weeks to months) evolution of a nearly balanced eddy includes β-induced westward propagation that is absent on an f-plane. For typical, subtropical C and f (30^o N) the eddy peak moves westward at about 3 km day^{-1}. The propagation speed increases sharply toward lower latitude. The numerical eddies studied here appear to make a good analog of oceanic mesoscale eddies (Fig. 1) insofar as they reproduce approximately the latitudinally-dependent zonal propagation of the eddies observed in SSH (problem 2.9.8). The β-effect acting upon nearly geostrophic eddies is a highly plausible mechanism for the observed, westward propagation of oceanic mesoscale eddies.

3) The β-plane shallow water system supports a low frequency wave, a planetary Rossby wave, that make a very useful analog of mesoscale eddies. Outside of the tropics, baroclinic, planetary Rossby waves have a low frequency, typically only about one percent of f, and currents that are nearly geostrophic. Rossby waves are markedly anisotropic in that they propagate phase westward only. Elementary (plane) Rossby waves are not commonly observed in the ocean or atmosphere but they are of great interest here because they have time and space scales in common with mesoscale eddies, and long baroclinic Rossby waves exhibit a very similar potential vorticity balance, β balanced by stretching. The phase and group speed of long, nondispersive Rossby waves is $-\beta/R_d^2$ (westward), which is just slightly greater than the propagation speed of the numerical mesoscale eddies, including the marked latitudinal dependence.

4) Insofar as westward propagation alone is concerned, the numerical eddies look to be an essentially linear phenomenon. However, their amplitude measured by thickness anomaly is appreciable, $\delta h/H \approx 0.1$, and their typical currents are several times greater than their propagation speed. As a consequence, they are likely able to trap and transport tracer for an appreciable distance. Insofar as transport goes, the numerical eddies exhibit important finite amplitude effects.

4.2 Equatorial Adjustment

5) The equatorial region — aside from the western boundary — appears to be almost free of mesoscale eddy variability ($L \propto$ several hundred km).[19] An adjustment experiment set up in an equatorial ocean suggests one reason for this may be that anomalies with horizontal scales $L < 500$ km will disperse into gravity and Rossby waves before adjusting to geostrophy. This is an extension of the main result from Sec. 4 Part 2 that the fraction of an initial anomaly that survives geostrophic adjustment is dependent upon the ratio L/R_{deq}, where the equatorial radius of deformation is $R_{deq} = \sqrt{C/\beta} = 250$ km and about five times greater than the mid-latitude equivalent.

6) Eastward propagation of a Kelvin wave is the most prominent feature of the equatorial adjustment experiments studies here (in part due to the symmetric initial condition) and is an occasional and sometimes very prominent feature also of the real equatorial oceans. The Kelvin wave has phase and group speed equal to the gravity wave speed, and is nondispersive. A Kelvin wave that is generated in mid-ocean (say by a rapid change in the winds) will thus reach the eastern boundary in a matter of weeks. There it is scattered into boundary Kelvin waves that propagate north and south along the eastern boundary of both hemispheres, and to a lesser extent, into westward traveling, dispersive, equatorially-trapped gravity and Rossby waves.

7) The equatorial ocean differs from the midlatitude beta-plane ocean in that the frequency gap between inertia-gravity waves and Rossby waves is much smaller; the inertia-gravity waves have a comparatively low (dimensional) frequency, and the Rossby waves a comparatively high frequency and fast group speed. As we will see in Part 4, this has the consequence that the equatorial and topical oceans adjust comparatively very rapidly to wind stress, including annual variations.

4.3 Remarks

An important result implicit in 1) above is that a mid-latitude β-plane supports two distinctly different, and for the most part non-interacting kinds of waves and associated dynamics: fast time-scale inertia-gravity waves and slow time-scale, quasi-geostrophic Rossby waves and eddies. This has practical importance on several levels. Insofar as westward propagation of midlatitude mesoscale eddies is concerned, it would have been simpler to start the experiment with a balanced eddy and forego the geostrophic adjustment and inertia-gravity waves. There is a pedagogic aspect as well. It is sensible to

[19] Mesoscale eddy-like features do appear seasonally some years, in especially the North Pacific equatorial ocean. These eddies are thought to result from an instability of the wind-driven equatorial current system and are termed Tropical Instability Waves. An excellent, brief introduction is http://en.wikipedia.org/wiki/Tropical_instability_waves

introduce geostrophic adjustment and Rossby wave dynamics as separate topics, rather than conflate them as they have been here. The rationale for considering these phenomenon in the same experiment is partly that the clear separation of time scales and dynamics that characterizes mid-latitudes does not extend to the equatorial region where inertia-gravity waves and Rossby waves have overlapping time and space scales.

The present numerical experiments start from a highly idealized initial condition, a right cylinder of thickness anomaly having a specified radius and that is released into a still ocean. The sudden release of this anomaly produces a fairly broad wavenumber and frequency spectrum, including gravity waves and short Rossby waves having eastward (but very small) group speed. This is not realistic of actual oceanic mesoscale eddies that are formed from a comparatively slowly growing instability of larger-scale, nearly geostrophic currents, e.g., a Rossby wave Sec. 2.7, and so are close to geostrophic balance from the outset. A fairly crude representation of this follows form initializing an adjustment experiment with a very large eddy, say radius $L = 1000$ km, or more to the point, $L = 20R_d$. The central portion of this eddy remains flat and at rest after the edges have adjusted to geostrophy. The subsequent evolution of this eddy is quite different from the propagation of a long Rossby wave, and neither is it anything like a small, wind-driven gyre. The southerly flow along the western edge of the initial (large) eddy is unstable and spontaneously forms smaller eddies having a diameter of about 300 km. These eddies are very similar to the eddies made here by geostrophic adjustment from a state of rest, although a little larger. This eddy formation process likely has some important elements in common with the formation of real oceanic mesoscale eddies, though this particular experiment lacks adequate vertical resolution.

In regions having intense currents, e.g., the Gulf Stream and extension of Fig. 1, the ocean is teeming with mesoscale eddies, that are not isolated from one another in a homogeneous environment as presumed here. As well, there are other kinds of oceanic variability and of course, sea floor topography. Interactions between neighboring eddies and between eddies and the atmosphere give rise to phenomena that modify the eddies and the larger scale environment significantly.[20]

4.4 What's next?

Part 4 will study basin scale, wind-driven flow using the same shallow water model used here, but augmented with a body force that mimics wind stress and boundary conditions that define a closed basin. The aim will be to elucidate the mechanism(s) that lead to western intensification of the major ocean

[20]McGillicuddy, D., et al., 'Eddy/wind interactions stimulate extraordinary mid-ocean plankton blooms', *Science*, 316, 1021 (2007), DOI: 10.1126/science.1136256 See also Chelton, D. B., P. Gaube, M. G. Schlax, J. J. Early and R. M. Samelson, 'The influence of nonlinear mesoscale eddies on near-surface oceanic cholorphyll', *Science*, 334, 21 Oct 2011, 328-332, doi: 10.1126/science.1208897

gyres. It will become clear that eddies and gyres are close cousins in that they share the beta-effect. In the case of eddies, the beta effect is balanced by time dependence; in the case of the wind-driven gyres, the beta effect is balanced the divergence of Ekman transport associated with wind stress curl. The final, Part 5, studies the very interesting response of the Arabian Sea to the South Asia Monsoon winds.

Index

anisotropic, 14

beta, 7
beta effects, 6
beta-effects
    high frequency, 8
    low frequency, 14
beta-plane
    equatorial, 37

eddies and waves, 14
eddy propagation
    meridional, 22
eddy properties, 5
eddy westward propagation, 5
equatorial waves
    dispersion relation, 41

floats, 26

Kelvin wave, 43

passive tracer, 22
potential vorticity balance, 11
propagation
    finite amplitude effects upon, 22

radiation boundary condition, 12
radius of deformation
    equatorial, 38
Rossby wave
    short wave limit, 18
    basin scale, 32
    dispersion relation, 15
    equatorial, 42
    instability, 28
    long wave limit, 19
    topographic, 33
    westward phase speed, 16
Rossby waves, 14

westerly waves, 31

a Coriolis tutorial, Part 4:
wind-driven ocean circulation and the Sverdrup relation

James F. Price

Woods Hole Oceanographic Institution,
Woods Hole, Massachusetts, 02543
https://www2.whoi.edu/staff/jprice/ jprice@whoi.edu

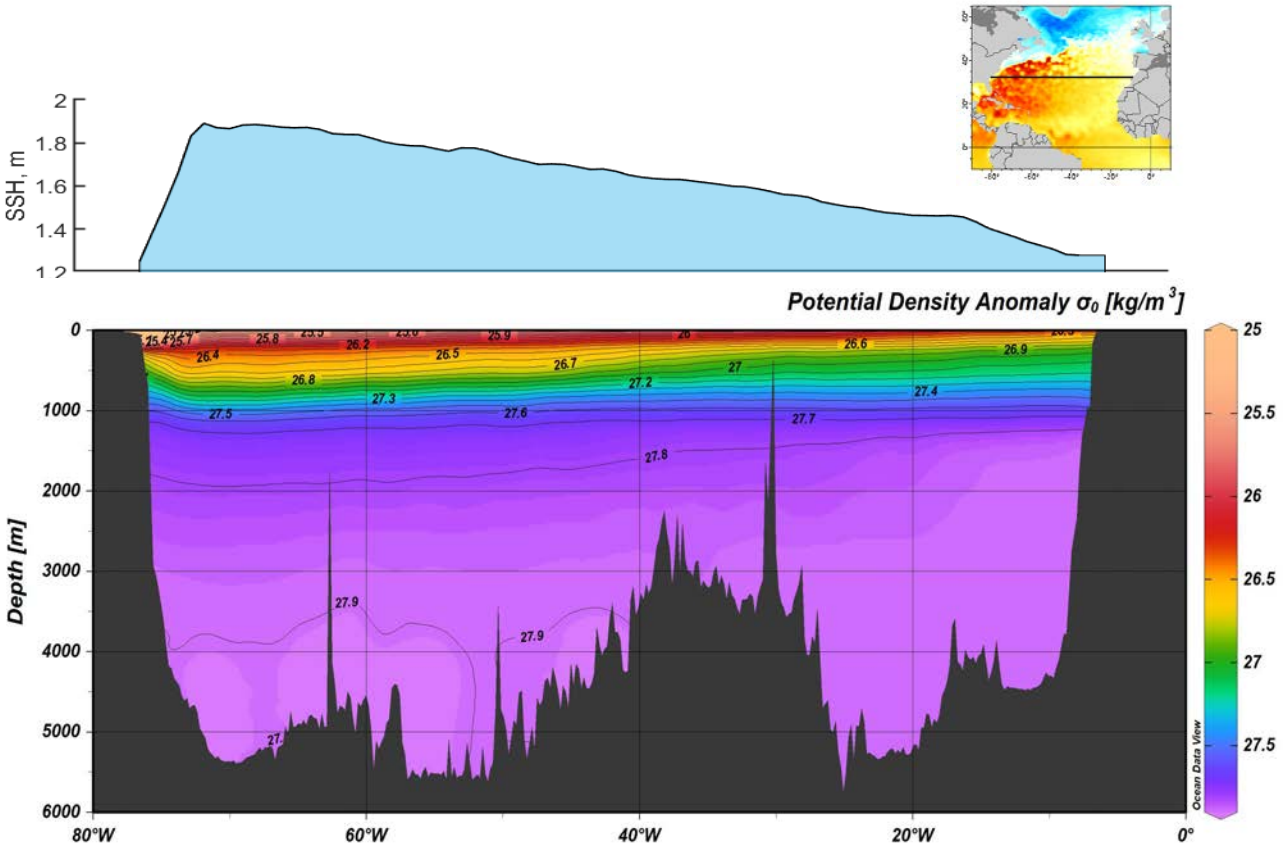

Figure 1: This section across the subtropical North Atlantic at 32 N shows the remarkable east-west asymmetry that is characteristic of wind-driven, upper ocean gyres. **(upper)** Sea surface height (SSH) from satellite altimetry, and **(lower)** potential density anomaly from *in situ* observations; both are averaged over several decades. Within a narrow western boundary region the SSH slope is positive and very large, and the inferred geostrophic current, the Gulf Stream, is northward and very fast. Over the interior of the basin, the SSH slope is negative and much smaller and the inferred geostrophic flow is southward and very slow. The associated baroclinic transport within the basin interior is consistent with the overlying, negative wind stress curl and the Sverdrup relation, a focus of this essay.

Abstract. This essay seeks to develop insight for several major features of the observed, upper ocean circulation, *e.g.,* western intensification of the major gyres and the geography of seasonal variability. A key element in this is understanding Sverdrup relation between meridional transport and the wind stress curl. To see how Sverdrup flow arises, shallow water models are solved for the circulation of a model ocean that is started from rest and driven by a specified wind stress: westerlies at mid-latitudes and easterlies in subpolar and tropical regions. This gives three regions of stress curl, negative over the subtropics, and positive over subpolar and tropical regions. The model used most extensively has just one active layer and makes the reduced gravity approximation. This is a minor extension of the model used in Parts 2 and 3 and is here dubbed 1l-rg. The dynamics of this model are baroclinic only. A second model includes three active layers, including a thick, active abyssal layer and a free sea surface and hence, 3l-fs. This more complete model includes the baroclinic dynamics of the 1l-rg model as well as fast, barotropic dynamics.

Baroclinic response in the 1l-rg solution. The developing baroclinic circulation can be described in terms of four stages. Stage 1 is the direct, local response to the imposed wind stress and includes inertia-gravity oscillations and Ekman transport within the upper, surface layer. The inertial-gravity oscillations die away after a couple of weeks with no evident lasting effect. The Ekman transport remains, and is very consequential for the long term ocean circulation. Ekman transport varies spatially on account of the latitudinal variation of wind stress and of the Coriolis parameter, f. The resulting divergence of Ekman transport modifies the thickness of the upper layer field and thus the mass field, the pressure field, and hence the circulation. Over the central subtropics, where wind stress curl is negative, the Ekman transport is convergent, which leads to a slowly thickening thermocline (about 30 meters per year in the central subtropics) and a high pressure in the upper ocean. This induces a nearly geostrophic zonal current which increases in step with the thickness field and dubbed the Stage 2 response. The amplitude is proportional to $1/f^2$ and so is much larger at lower latitudes. This local response to wind stress curl goes on for about three years (subtropical gyre) until the zonal thickness gradient balances the Ekman convergence and yields a steady state thickness and flow field. The circulation is then a baroclinic Sverdrup flow, dubbed Stage 3. The transition from Stage 2 to Stage 3 sweeps westward across the basin at the rate of a long baroclinic Rossby, $-\beta C^2/f^2 = -3$ km day^{-1} in the subtropics. Baroclinic Sverdrup flow thus occurs much sooner in the tropics (a few months) than in the subtropics (a few years) or the subpolar region (a few decades).

Even after the subtropical gyre reaches steady-state Sverdrup flow, the layer thickness continues to increase very slowly and uniformly (spatially) over the next several decades as the subtropical region absorbs water expelled from the subpolar region where the wind stress curl is positive and the upper layer becomes dramatically thinner. A basin-wide steady state, Stage 4, arises only after the subpolar gyre has also been swept by a slowly moving long baroclinic Rossby wave. Along the northern boundary of the 1l-rg model, that requires about 30 years.

The observed, basin-scale horizontal structure of the wind-driven ocean circulation, including western intensification and several of the qualitative differences between tropical, subtropical and subpolar gyres, have a plausible analog in solutions of the baroclinic shallow water model. In particular, the Sverdrup relation plus the observed pattern of wind stress curl provide a concise and convincing

explanation of the sense of the circulation over the North Atlantic: equatorward (southward) meridional flow in the subtropics of the North Atlantic, where the wind stress curl is negative, and the opposite signs in the tropical and subpolar regions. The Sverdrup relation is valid where the dominant terms of the potential vorticity balance are just two: the advection of planetary vorticity by a very slow meridional flow, and the curl of the wind stress. In practice, this holds in the interior of a basin, where the currents and friction are very weak, but not within zonal or meridional boundaries.

These experiments are carried out within a closed basin, and so the net transport through any given basin-wide zonal section must vanish in steady state. The meridional Sverdrup transport in the interior of the basin is balanced in this volumetric sense by a very intense western boundary current (wbc) having a width of order the baroclinic radius of deformation, O(100 km) in the subtropics. The baroclinic transport of a wbc reaches approximate steady state after the ocean interior to the east of the wbc has reached steady baroclinic Sverdrup flow, about three to five years in the subtropical gyre. The wbc thus follows the interior circulation, despite that it is far more energetic.

The meridional transport must vanish on zonal boundaries, and in the present model the affected zonal boundary regions are fairly wide, 500 - 1000 km in north-south extent. Within these wide zonal boundary regions, the meridional transport has the sign of the expected Sverdrup transport, but considerably reduced amplitude, going to zero on the boundary.

The annual cycle of wind stress is significant in most regions. To see the consequence, experiments are carried out with a zonal wind stress that includes a large, $\pm 50\%$, annual cycle. The ocean's response is, in most respects, unimpressive, but this depends very much upon latitude. In the subtropical gyre, the resulting annual cycle of the baroclinic wbc transport is only about $\pm 4\%$ of the mean transport. The annual cycle of wbc transport is even smaller in the subpolar gyre, and somewhat greater though still not prominent in the tropical gyre. There is, however, an appreciable baroclinic response in the eastern half of the tropical gyre. There the annual cycle of upper ocean (baroclinic) zonal currents is about $\pm 50\%$ of the mean, or roughly proportional to the wind stress variation. This vigorous seasonal cycle of tropical zonal currents appears to be a mainly local response to the varying stress curl, here called the Stage 2 response, but includes a contribution from an annual period, eastern boundary Rossby wave as well.

A barotropic and then a baroclinic response, 3l-fs. What happens when the same start up experiment is carried out with the three layer, free surface model, 3l-fs? In one key respect the results are strikingly different from those described above — the circulation comes to a nearly steady, *barotropic* Sverdrup flow within just a few weeks, even at subpolar latitudes. The comparatively very short response time of the barotropic circulation is consistent with the very fast zonal propagation of barotropic long Rossby waves, about -1200 km day^{-1} at 30 N. The basin-scale pattern of the barotropic transport, including the western boundary currents and the zonal boundary regions, is very similar to that of the baroclinic Sverdrup flow found in the 1l-rg model solution. This barotropic Sverdrup transport is almost depth-independent (as barotropic usually implies) and occurs mainly within the thick abyssal layer. The amplitude of upper ocean currents and the associated SSH anomaly are thus quite small compared to the observed SSH.

Over the following several years a baroclinic adjustment occurs in the 3l-fs model solution in just the way it does in the 1l-rg solution. In the central subtropical gyre, a first mode, long baroclinic Rossby

wave arrives from the east after about three years. As it passes, the abyssal layer comes to rest, and the Sverdrup transport is thereafter confined to the two upper ocean layers, i.e., the Sverdrup transport is then baroclinic. After about another five years and the passage of a second mode wave, the Sverdrup transport is extinguished in the unforced, lower thermocline layer and thereafter is present only in the uppermost, wind-forced layer. The amplitude of the across-basin SSH anomaly is then fairly realistic, about 1 m across the subtropical gyre. This is more the result of a felicitous choice for the initial surface layer thickness, 250 m, than it is a genuine prediction of the vertical structure of the Sverdrup flow.

More on Fig. (1) These SSH data were processed and compiled thanks to the AVISO Project https://www.aviso.altimetry.fr and served by the NOAA ERDDAP web archive, https://coastwatch.pfeg.noaa.gov/erddap/griddap/, an invaluable source for a wide variety of oceanographic data. This is the AVISO Level 4 analysis, compiled from multiple satellite missions, and SSH is relative to a carefully mapped geoid. The lower panel is the grand average of potential density from *in situ* measurements extracted from the World Ocean Atlas 2018, http://www.nodc.noaa.gov/OC5/WOA18/pr_woa18.html. The very long-time averaging of these data has suppressed the large amplitude, time-dependent signal of mesoscale eddies that is very prominent in the synoptic data of, e.g., Fig.(1), Part 3. Notice that the tilt of the thermocline mirrors the tilt of SSH so that high SSH corresponds to a thick, low density upper layer. The result is a comparatively small horizontal gradient of hydrostatic pressure at depths below about 1200 m, which is suggestive of a reduced gravity approximation that will be utilized in many of the numerical experiments discussed here. This handsome presentation was made possible by Ocean Data View, https://odv.awi.de/

Contents

1 Earth's rotation has a profound influence on the large-scale, low frequency flows of the atmosphere and the ocean **7**

1.1 The goal: Insight for the link between the winds and ocean circulation 7

1.2 Objectives and plan of this essay 9

1.3 About this essay 11

2 Worldwide, there are seven major gyres **12**

2.1 O1, The SSH signature of the major upper ocean gyres is well correlated with the wind stress curl 12

2.2 O2, Upper ocean gyres are markedly asymmetric east to west . . . 13
2.3 O3, Subtropical and subpolar gyres are quasi-steady annually, while tropical ocean circulation shows significant seasonal variation . . . 17
2.4 O4, The geostrophic flow of the subtropical gyre is somewhat surface intensified . . . 21
2.5 Appendix: Notable phenomena that are not addressed here . . . 23

3 A review of the low frequency beta effect and the Sverdrup relation 24
3.1 Balanced meridional motion is divergent horizontally . . . 25
3.1.1 Free, time-dependent motions propagate westward . . . 27
3.1.2 Forced, steady meridional motion is Sverdrup flow . . . 28
3.2 Depth dependence of Sverdrup flow . . . 29
3.3 The Sverdrup relation is valid widely, but not everywhere . . . 34

4 Shallow water models of wind-driven circulation 36
4.1 Boundary conditions for a closed basin . . . 36
4.2 Initial density and velocity . . . 37
4.3 Wind stress and its curl . . . 37
4.4 An expedient parameterization of drag on ocean currents . . . 39
4.5 Momentum and vorticity balances . . . 40
4.6 Models of stratification and pressure . . . 41
4.6.1 Single layer, reduced gravity model, 1l-rg . . . 41
4.6.2 Three layer, free surface model, 3l-fs . . . 42
4.7 Appendix to Sec. 3: Normal modes of the 3l-fs model; one fast, two slow . . . 44

5 The baroclinic circulation of the 1l-rg solution develops in four stages 46
5.1 Stage 1: Short time, local response to the wind . . . 46
5.1.1 Time scales: fast, slow, and steady . . . 46
5.1.2 Ekman currents and transport. . . . 48
5.1.3 Latitudinal dependence; trouble on the equator? . . . 49
5.2 Stage 2: Locally wind-forced, zonal geostrophic currents . . . 49
5.2.1 Divergent Ekman transport changes the mass field . . . 49
5.2.2 Zonal geostrophic currents accompany the changing mass field . . . 52
5.3 Stage 3: Blocking at the boundaries and the onset of meridional Sverdrup flow . . . 55
5.4 Stage 4: Inter-gyre exchange, and basin-wide steady state . . . 56
5.5 Western boundary currents . . . 58
5.6 Appendix to Sec. 4 . . . 62
5.6.1 A local model of wind-driven inertial and Ekman motions . . . 62
5.6.2 Simple models of a western boundary current . . . 65

6 The (almost) steady circulation **67**
6.1 A streamfunction depiction of the circulation . . . 69
6.2 Dynamics of the steady circulation: the balance of potential vorticity . . . 71
6.2.1 Sverdrup interior . . . 73
6.2.2 Western boundary currents . . . 73
6.2.3 Zonal boundary regions . . . 75
6.3 Appendix to Sec. 6: A (Lagrangian) trip around the subtropical gyre . . . 77
6.3.1 Momentum balance and energy exchanges . . . 79
6.3.2 Potential vorticity balance along a trajectory . . . 80

7 Experiments with other wind fields and basin configurations **81**
7.1 Annually-varying winds and the baroclinic circulation . . . 81
7.2 A wind stress field with no curl . . . 86
7.3 Meridional winds over a basin without sidewalls (a channel) . . . 86

8 Barotropic and baroclinic circulation of the three layer, free surface model, 3l-fs **89**
8.1 Inertial motion and Ekman transport in the surface layer . . . 91
8.2 Transient, barotropic flows . . . 94
8.3 Basin scale circulation; barotropic Sverdrup flow . . . 95
8.4 Baroclinic adjustment to a surface intensified, steady state . . . 98

9 Summary and closing remarks **101**
9.1 O1: Upper ocean gyres seen in SSH are correlated with the wind stress curl . . . 101
9.2 O2: Upper ocean gyres are markedly asymmetric east to west . . . 101
9.3 O3: Subtropical and subpolar gyres are quasi-steady while tropical circulation shows significant seasonal variation . . . 104
9.4 O4: The Sverdrup flow of the subtropical gyre is somewhat surface intensified . . . 105

10 Supplemental material **106**
10.1 Links to models and updated manuscripts . . . 106
10.2 Homework problems . . . 106

10 Index **108**

1 Earth's rotation has a profound influence on the large-scale, low frequency flows of the atmosphere and the ocean

This essay is the fourth in a five-part introduction to fluid dynamics on a rotating Earth. The broad goal of these essays is to help illuminate the effects of Earth's rotation, which include some of the most important and subtle phenomena of geophysical fluid dynamics. The first of these essays introduced the Coriolis force, the second examined geostrophic adjustment, and the third studied the phenomenon of westward propagation. These topics are about equally relevant for students of atmospheric and oceanic science.

1.1 The goal: Insight for the link between the winds and ocean circulation

The present essay continues this introduction to rotation effects, but now with a decidedly oceanic bent — large-scale, long-term mean upper ocean circulation — and especially the quasi-steady, horizontally rotating gyres that fill the subpolar and subtropical basins (Fig. 2). The broad goal is to learn how the upper ocean circulation is linked to the wind (Fig. 3) and the specific goal is to develop insight for four Observed properties:

O1: SSH anomaly of the gyres is correlated with the overlying wind stress curl,

O2: The gyres are strongly asymmetric east-to-west, implying a special direction,

O3: The subtropical and subpolar gyres are unresponsive to annually-varying wind, while the tropical ocean circulation varies significantly,

O4: The circulation of the subtropical gyre is somewhat surface intensified.

These are each elaborated and quantified in Sec. 2 by inspection of several kinds of remotely sensed data sets, especially SSH and wind stress and supplemented by some *in situ* and reanalysis data sets.

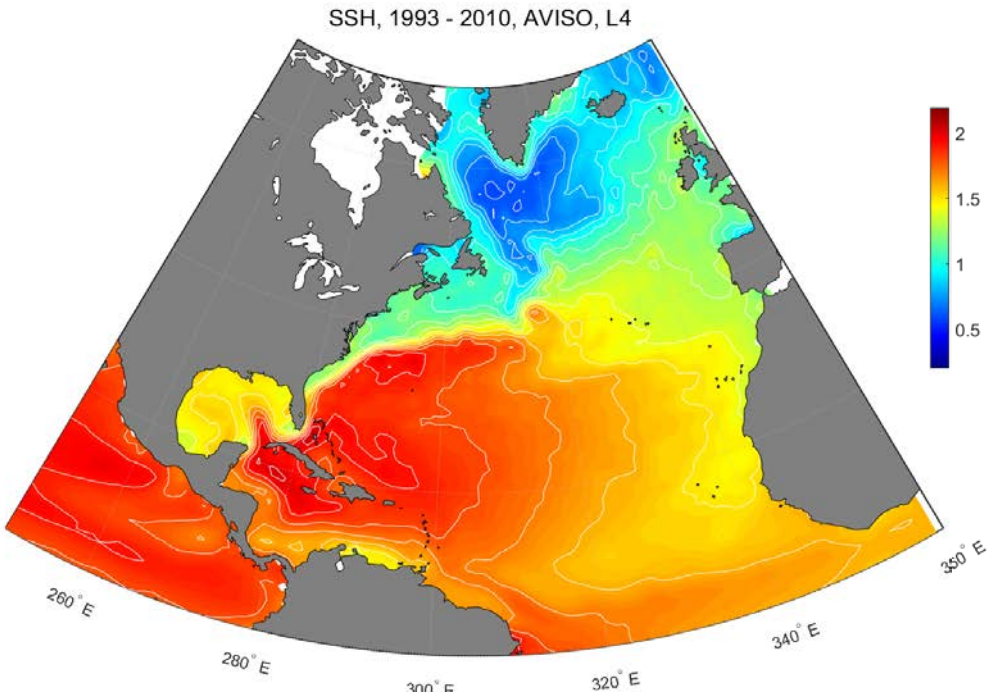

Figure 2: Sea surface height of the North Atlantic, averaged almost two decades of satellite altimetry compiled by the AVISO Project (this repeats Fig. 1 of Part 1). The color scale at right is in meters. Major features discussed here are an SSH high that fills the subtropical basin, and a SSH low in the subpolar basin. The inferred geostrophic current of the subtropical basin is a clock-wise turning gyre that is strongly asymmetric: very slow southward flow over most of the basin, and a fast north-northeastward flow in a very narrow western boundary current. The goal of this essay is to describe the connection between these circulation phenomena and the overlying wind stress. The centerpiece of this is the Sverdrup relation.

The conceptual centerpiece of this study is the **Sverdrup relation**,[1]

$$\boxed{\int_{-d_o}^{0} v(z)\,dz \;=\; M^{Sv} \;\equiv\; \frac{1}{\rho_o \beta}\nabla\times\tau(x,y)} \tag{1}$$

which is a highly distilled description of vorticity and volume conservation in a wind-driven ocean on a beta-plane. The left hand side is the meridional (north-south) component of volume transport per unit

[1]Sverdrup's pioneering paper that introduced the equivalent of Eqn. (1) is unfortunately not easily read or appreciated, but nevertheless: Sverdrup, H. U., 1947, 'Wind-driven currents in a baroclinic ocean, with application to the eastern Pacific', *Proc. Natl. Acad. Sci. U. S. A.*, **33**, 318-326, which is available online at http://www.pnas.org/content/33/11/318 The first model of a western-intensified, wind-driven gyre was by Stommel, H., 1948, and the time-dependent, gyre spin-up problem was discussed by Stommel, H., 1957, 'A survey of ocean current theory', *Deep Sea Res.*, **4**, 149-184. Be sure to see also Stommel's masterpiece, 'The Gulf Stream', 1966, Univ. of California Press. Time-dependence was treated in greater detail by Anderson, D. L. T. and Gill A. E., 1975, 'Spin-up of a stratified ocean with applications to upwelling', *Deep-Sea Research* **22**. The GFD texts noted in Part 1 each have very good discussion of the Sverdrup interior. Ch. 1 of Pedlosky, J.,1998, 'Ocean Circulation Theory', and Ch. 10 of Marshall, J. and R. A. Plumb, 2008, 'Atmosphere, Ocean and Climate Dynamics', and Ch. 14 of Vallis, G., 2006, 'Atmospheric and Oceanic Fluid Dynamics', are all highly recommended.

width and the righthand side is the curl of the wind stress, $\tau(x,y)$, a horizontal vector field that is here presumed to be known from observations (Fig. 3). The Sverdrup relation is one of the true bedrocks of ocean circulation theory; it has been repeatedly tested successfully against observations, and has been widely accepted for at least 50 years. The Sverdrup relation is also abstract to the point of being abstruse, and taken alone can not explain much of O1 - O4. For example, the Sverdrup relation is local in space (x,y) and so does not account for the striking asymmetry of the gyres (Fig. 1). The Sverdrup relation makes no reference to time or depth, and so neither can it explain O3 or O4.

1.2 Objectives and plan of this essay

The premise (and the promise) of this essay is that significant insight for the observations O1 - O4 will follow as we learn how the Sverdrup relation arises in a spin-up problem posed in a closed basin. A beta-plane approximation is used to represent the very important latitudinal variation of the Coriolis parameter, f. The objectives of this essay are then to:

i) Solve for the stratification and currents from the start up to a steady state, and characterize the processes that shape the large scale response. The initial response to stress curl and the resulting divergence of Ekman transport is local, and includes a slow but steady increase of SSH over the subtropical gyre. The amplitude depend strongly upon latitude (relevant to O1).

ii) Show that the low frequency beta effect eventually halts the local response, and the resulting steady state is then consistent with the Sverdrup relation. The time this takes varies greatly with latitude, being much faster at lower latitudes (relevant to O3).

iii) Show that the Sverdrup relation holds over most of the interior of a model ocean basin and hence the sign of the wind stress curl determines the sense (clockwise or anti-clockwise) of wind-driven gyres (relevant to O1).

iv) Observe that the Sverdrup relation necessarily fails near (most) solid boundaries and is supplanted by western or zonal boundary current dynamics (relevant to O2).

v) Consider some of the processes that determine the depth of the upper ocean circulation, the d_o of Eqn. (1) (relevant to O4). Just to be clear at the outset, the depth of Sverdrup transport appears to be beyond the simple theory used here, but it is worthwhile to preview the issues involved in making a more complete theory/model.

These are among the foundational problems of physical oceanography and have been addressed many times over, and from a variety of perspectives. This essay will work towards these objectives by an analysis of solutions from two shallow water (layered) models. The first model is familiar from Parts 2 and 3 — one active layer and pressure anomaly computed from the baroclinic density field assuming a

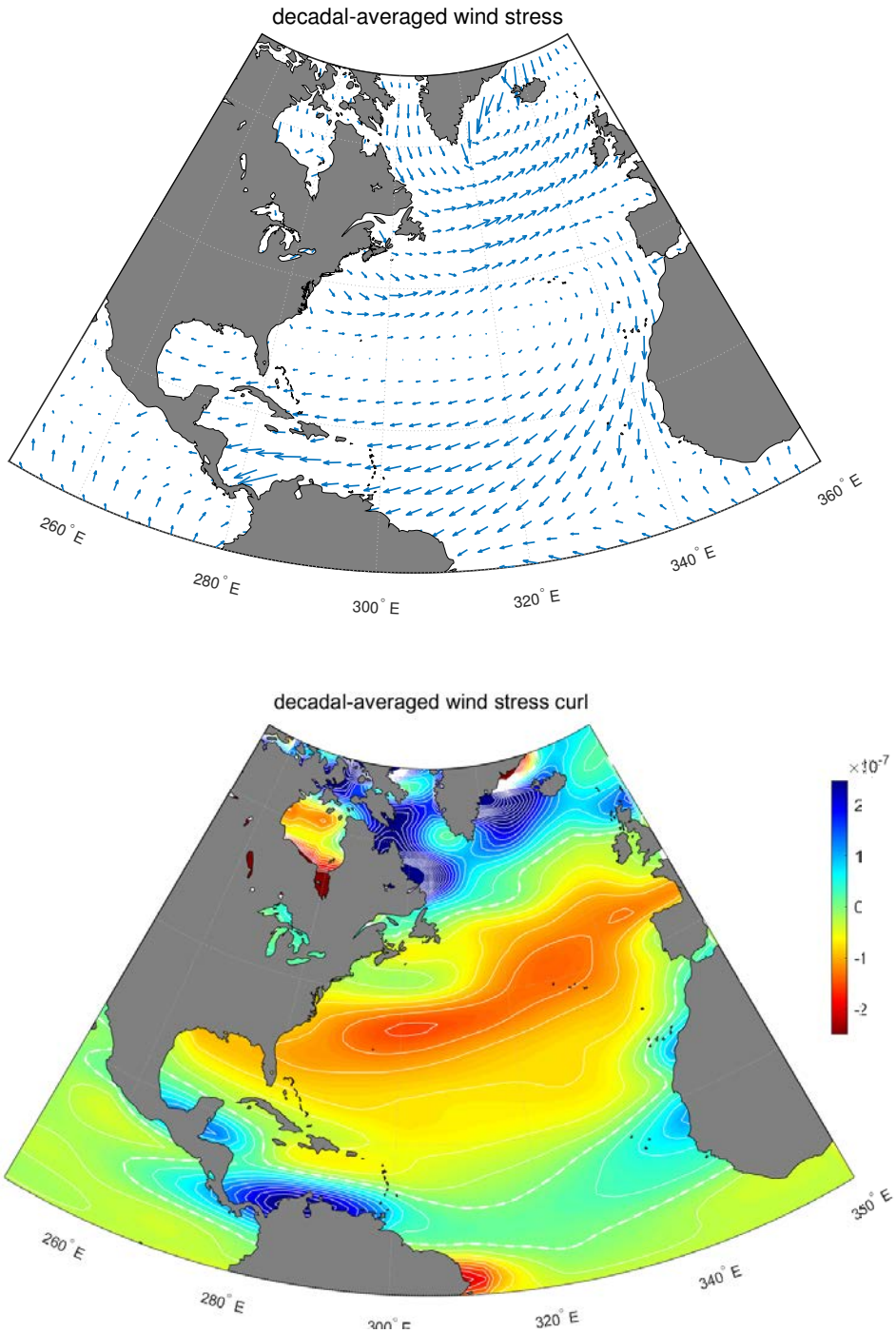

Figure 3: **(upper)** Wind stress computed from about ten years of NASA QuickSCAT scatterometry (1999 - 2009) and served by NOAA ERDDAP, https://coastwatch.pfeg.noaa.gov/erddap/griddap/ The largest magnitude of stress is 0.2 Pa east of Greenland. **(lower)** Wind stress curl, with a colorbar at right in units [Pa m^{-1}]. The heavy dashed contour is the zero. The basin-scale variation of wind stress curl includes a very extensive region of negative stress curl over the subtropics. There is positive stress curl over the subpolar region and within a narrow band over the tropics. There are pronounced, smaller spatial scale variations of stress and stress curl that are evidently associated with topography, e. g., around Greenland. Notice the similarity of the wind stress curl with the long-term average SSH of Fig. (1).

quiescent abyssal ocean. This is dubbed the 1l-rg model (Sec. 4), and can be thought of as a baroclinic only model. This 1l-rg model configuration is comparatively simple and economical and is appropriate to the first three objectives of this essay. A second model has three active layers and a free (moving) sea surface and dubbed 3l-fs. This model includes the baroclinic dynamics of the first model, as well as a very fast barotropic response that makes this model somewhat burdensome computationally. This model can help us understand some aspects of depth-dependence, but not all. For both models the shallow water model equations are extended to include wind forcing and dissipation. These new features are described in Section 4, which may be skipped by readers not interested in the fine details (but who should nevertheless take a look at the wind stress field in Sec. 4.3). The experiments are started from a state of rest and continue until the circulation reaches a basin-wide steady state, requiring about 30 years of ocean time (and a few hours (1l-rg) or a few days (3l-fs) of computer time on an ordinary personal workstation). The transient baroclinic circulation is described in Section 5 in terms of four overlapping stages, and e.g., Stage 3 begins with the onset of baroclinic Sverdrup flow. The steady circulation varies a great deal over the basin. Over the majority of the basin, the steady potential vorticity balance is that of the Sverdrup relation. However, near the western boundary, the balance includes a significant torque due to drag on an energetic western boundary current, discussed in Section 6. Section 7 considers several experiments with other wind fields including one with an annual cycle, especially relevant to study of the annual variation of tropical ocean circulation noted in O3 above. Section 8 describes the solutions from the free surface model, 3l-fs, that includes a barotropic response. You could say that this second model solution changes everything, or, you could equally well argue that it changes almost nothing. Closing remarks are in Section 9, and links to the model code and a few homework problems are in Section 10.

1.3 About this essay

This essay has grown out of 'a Coriolis tutorial' that was first published online in 2002. It has been revised many times since then, and future revisions are likely (especially in response to questions and comments, which are encouraged). The most recent update of this essay will be posted on the Education Projects page of https://www2.whoi.edu/staff/jprice/

These essays and associated materials may be cited by the MIT OpenCourseWare address: Price, James F., 12.808 Supplemental Material, Topics in Fluid Dynamics: Dimensional Analysis, a Coriolis tutorial, and Lagrangian and Eulerian Representations (Spring 2022), https://ocw.mit.edu/courses/res-12-001-topics-in-fluid-dynamics-spring-2022 (date accessed). License: Creative Commons, CC BY-NC-SA. For rights and obligations under this license see https://creativecommons.org/licenses/

Financial support was provided by the Academic Programs Office of the Woods Hole Oceanographic Institution, and by the U.S. Office of Naval Research.

2 Worldwide, there are seven major gyres

The world ocean includes seven, major upper ocean gyres - five in the subtropics that are relative highs of SSH, and two in subpolar regions, both lows, Table 1 and Fig. (4).

2.1 O1, The SSH signature of the major upper ocean gyres is well correlated with the wind stress curl

Evidence that these gyres are wind-driven is the striking visual correlation between the large scale distributions of SSH anomaly and the wind stress curl over especially the North Atlantic ocean (Figs. 1 and 2), and also worldwide (Figs. 3 and 4). The North Atlantic subtropical high of SSH underlies the extensive region of negative stress curl that arises mainly from meridional shear along the southern side of the westerly wind belt and the easterly trade winds. Notice that the boundary between the subpolar and subtropical gyres as seen in SSH trends poleward with east distance, as does the axis of the westerly winds and thus the zero of wind stress curl, cf. Fig. (4). The subpolar low of SSH underlies the region of positive stress curl along the north side of the westerly wind belt. A very similar pattern holds as well in the North Pacific and thus the correlation between SSH and wind stress curl is negative.

The southern hemisphere oceans also display such a correlation, but the sign is reversed, e.g., high SSH in the subtropical South Pacific underlies positive wind stress stress curl and so on. This implies that the link between SSH and wind stress curl is going to involve mainly f, the Coriolis parameter (which, of course, changes sign between the hemispheres), rather than β, which does not.[2] Results coming below indicate that this correlation of SSH with wind stress curl is not merely coincidental, but neither is it the most fundamental and important link between wind stress and circulation which is instead given by the Sverdrup relation, Eqn. (1), which, notice, involves β but not f.

These seven gyres have some very important features in common, especially their relationship to the overlying wind stress (cf. Fig. 4) of the westerly wind belts (eastward wind and wind stress that extend across the entirety of ocean basins and, indeed, encircle both hemispheres. The gyres are also unique in that the shape of their respective basins and sea floor topography vary enormously from one to the next. There is also a very important effect in the Atlantic and even more the North Atlantic, associated with the global-scale thermohaline circulation, about which more later.

[2] You must be thinking ..... hmmmm .... what's it do right on the equator? If this SSH/stress curl relationship is not possible on or very near the equator (from symmetry), then perhaps the wind stress (rather then the wind stress curl) is relevant. What can you discern from inspection of Fig. 3, upper, and Fig. 4, upper ?

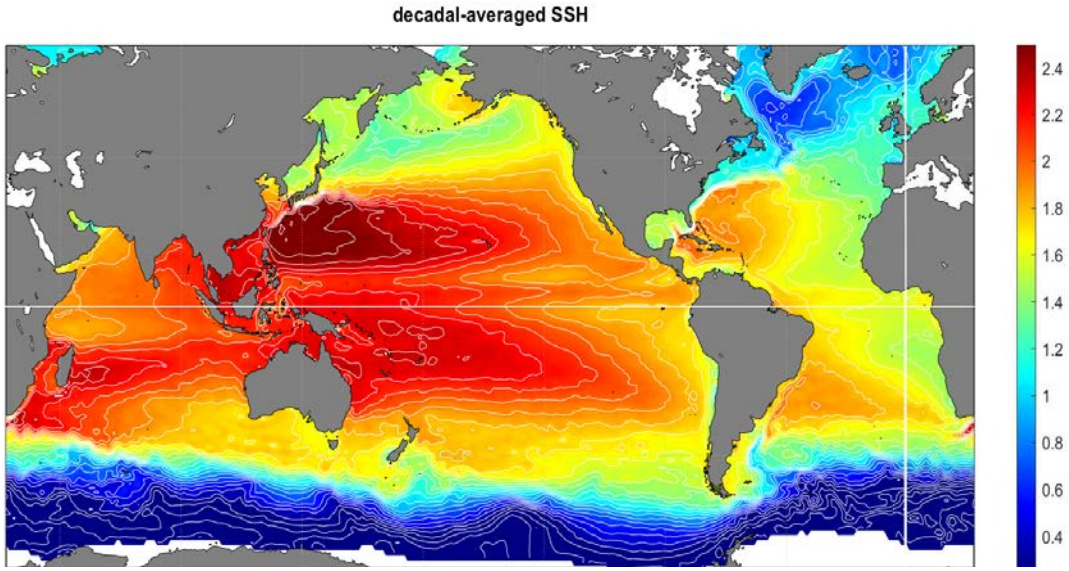

Figure 4: **(upper)** Time mean sea surface height relative to a geoid (absolute SSH) computed over almost two decades of satellite altimetric measurement. These altimeter data were compiled and processed by the AVISO project and served by the NOAA ERDDAP web page. The colorbar at right is in meters. Seven major upper ocean gyres are evident here as regional highs or lows of SSH. **(lower)** Time mean of the wind stress curl computed over about 10 years of satellite scatterometry by NASA QuickSCAT SeaWinds and served by NOAA ERDDAP. The colorbar at right is in Pa m^{-1}.

2.2 O2, Upper ocean gyres are markedly asymmetric east to west

SSH sampled along 32 N across the North Atlantic subtropical gyre shows two distinctly different regions of SSH zonal slope, $\partial\eta/\partial x$ (Fig. 6, upper). Going from the western boundary toward the east,

SEVEN GYRES

Basin/Gyre	f	$\nabla \times \tau$	SSH	N^{Sv}	WBC	WBC sense
North Pacific subpolar	+	+	L	30	Oyashio	equatorward
North Atlantic subpolar	+	+	L	25	East Greenland - Labrador	equatorward
North Pacific subtropical	+	-	H	-55	Kuroshio	poleward
North Atlantic subtropical	+	-	H	-30	Gulf Stream	poleward
South Pacific subtropical	-	+	H	55	East Australian	poleward
South Atlantic subtropical	-	+	H	25	Brazil	poleward
South Indian subtropical	-	+	H	40	Agulhas - Mozambique	poleward

Table 1: The seven major semi-permanent gyres and their western boundary currents. The first three entries are sign only. The Sverdrup volume transport, N^{Sv}, in Sverdrups, has been estimated from long-term average wind stress curl that was integrated across the basin at the central latitude of the gyre as seen in SSH (Sec. 1.2). The sign is the usual, positive north.

there is a narrow region adjacent to the western boundary of width L_{wb} that is O(100 km) within which the SSH increases eastward to a maximum $\delta\eta \approx 1$ m. The inferred geostrophic current in this western boundary current, the Gulf Stream, is poleward (northward) and swift, $U_{wb} \approx g\delta\eta/(L_{wb}f)$ is O(1 m sec^{-1}). To the east, there is a broad interior region, essentially all the rest of the basin, width $L_i \approx 7000$ km, over which there is a gradual decrease of η to approx. zero on the eastern boundary. The inferred geostrophic current in the interior is equatorward (southward) and very slow compared to the the western boundary current, $U_i \approx U_{wb}L_{wb}/L_i$ is O(0.01 m sec^{-1}) when averaged over zonal scales of O(1000 km). This slow southward flow of the interior is consistent with Sverdrup transport, about which much more below. A similar structure of rapid western boundary current and very slow interior flow is found also in the subpolar gyre of the North Atlantic, though with the sense of the SSH anomaly and the circulation reversed, and in the other five gyres (Fig. 7).[3] From this brief inspection, it is evident that the east-west asymmetry of upper ocean circulation, often called western intensification, is very pronounced,

$$\frac{L_i}{L_{wb}} \approx \frac{U_{wb}}{U_i} \text{ is } O(100).$$

[3]If you look carefully you will notice that the expected poleward-flowing, western boundary current of the South Pacific subtropical gyre, the East Australian Current, seems to be missing from Fig. (7). This is evidently an artifact of the heavy time averaging inflicted upon these data. The East Australian Current is readily apparent in SSH data sampled at a higher resolution, 1/4 degree vs. 1 degree used here, and omitting decadal time-averaging.

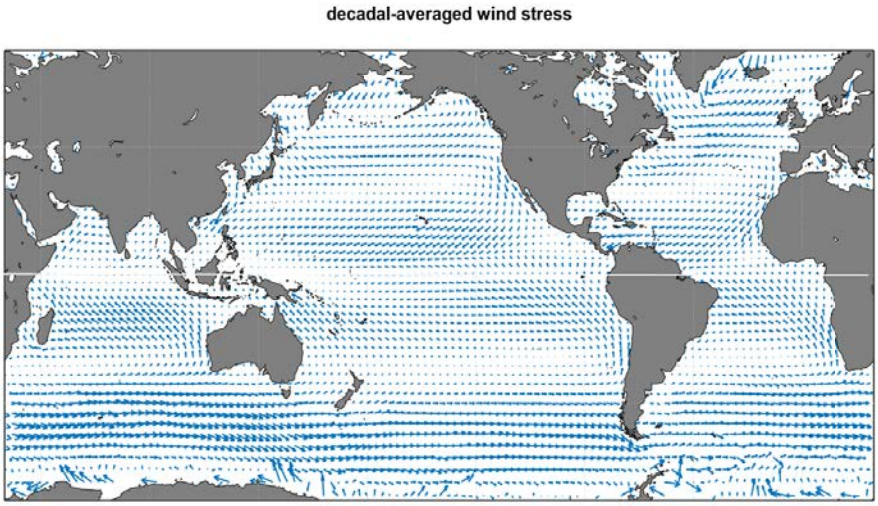

Figure 5: **(upper)** Time mean of the wind stress computed over about 10 years of satellite scatterometry measurement by NASA QuickSCAT SeaWinds and served from the NOAA ERDDAP web page. The largest magnitude of stress is about 0.25 Pa in the Southern Ocean west of Australia. **(lower)** Time mean of the east component of wind stress. East going stress (associated with westerly wind) is in red, and west going stress (easterly wind) is in blue. The largest scale of variability in the wind stress curl field comes from the meridional shear between the westerly winds (eastward stress) and the easterly trade winds (westward stress) and on the poleward side, the subpolar easterlies.

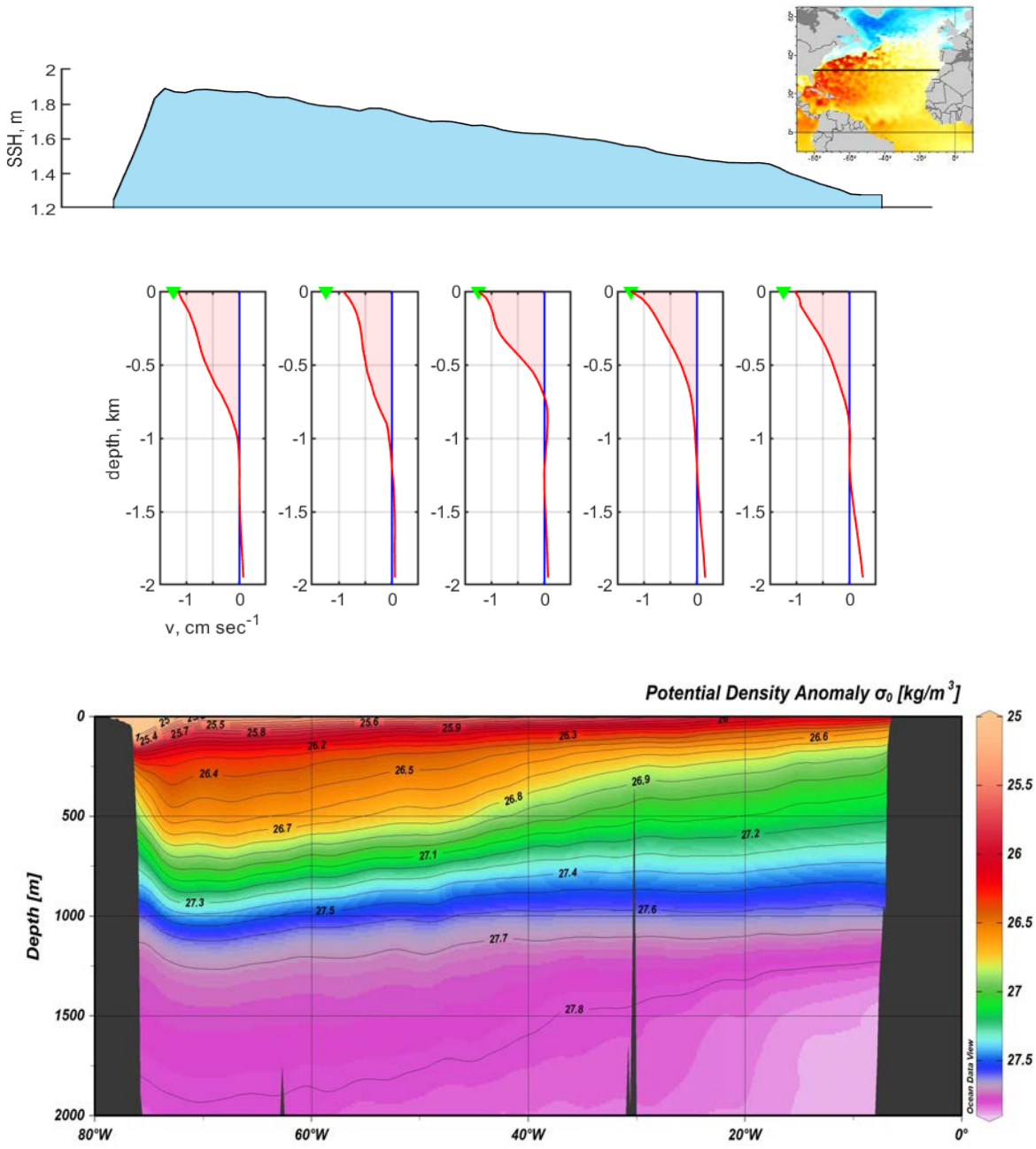

Figure 6: This section across the subtropical North Atlantic at 32 N shows the remarkable east-west asymmetry that is characteristic of wind-driven, upper ocean gyres. **(upper)** Sea surface height (SSH) from long-term averaged satellite altimetry as in Fig. (1). **(middle)** Profiles of the meridional geostrophic current referenced to 1200 m depth. These are lined up with the density section; the westernmost profile does not include the western boundary current. **(lower)** Potential density from *in situ* observations and averaged over several decades, as in Fig. (1), but here the upper 2000 m only. The density data were extracted from the World Ocean Atlas 2018, https://www.ncei.noaa.gov/products/world-ocean-atlas and displayed thanks to Ocean Data View, https://odv.awi.de

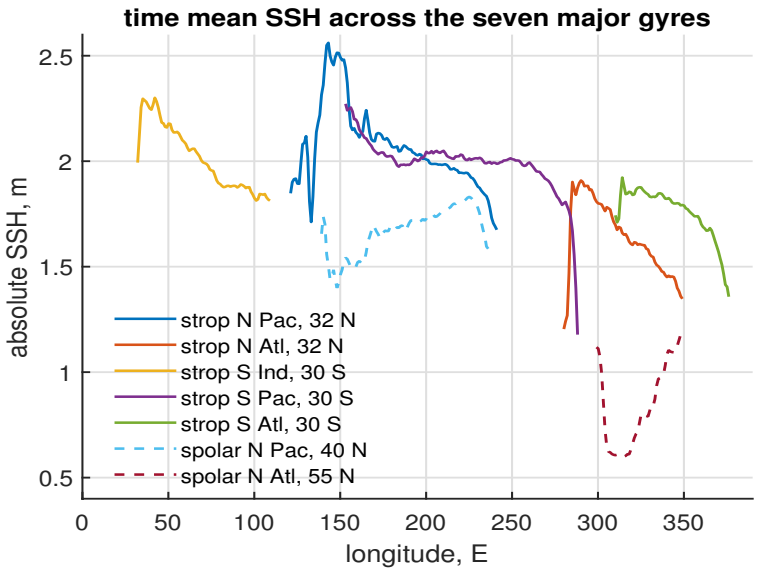

Figure 7: A longitudinal slice through each of the seven major (semi-permanent) upper ocean gyres, at the latitude noted in the legend. These sections go from coast to coast. The five subtropical gyres (solid lines) are relative highs of SSH that fill their respective basins, and have well-defined, narrow western boundary currents. The two subpolar gyres (dashed lines) are relative lows of SSH, also with narrow western boundary currents. Notice the marked dip in SSH near the eastern boundary of especially the subtropical South Pacific and South Atlantic gyres, the signature of major coastal upwelling regions.

2.3 O3, Subtropical and subpolar gyres are quasi-steady annually, while tropical ocean circulation shows significant seasonal variation

The subtropical gyre is always present in the sense that every basin-wide snapshot of SSH (examples in Part 3) and every across-basin hydrographic section will show an easily recognizable, poleward-flowing Gulf Stream near the western boundary and an equatorward Sverdrup flow over most of the rest of the basin. Said a little differently, the subtropical gyre is clearly evident not only in a long-term average, but also instantaneously, despite that there are always significant, time-dependent perturbations due to mesoscale eddies.[4] These comments hold just as well for the subpolar gyre.

Minimal seasonal variation of the subtropics and subpolar regions. One might reasonably expect

[4]Mesoscale eddies are ubiquitous, and impose large amplitude, but comparatively short time (periods of several months) and space (several hundred kilometers) scale variations on the gyre-scale SSH and currents, Fig. (1), Part 3. Thus the near-instantaneous (time and space) meridional geostrophic current in the basin interior is just about as likely to be northward as southward. The very smooth, almost linear slope of interior SSH seen in Fig.(2), upper, arises only upon long-term (decadal) averaging. Similarly, any single estimate of the instantaneous Gulf Stream transport may vary by $\pm 15\%$ around the long term mean due to superimposed, apparently random mesoscale eddy variability; Rossby, T, C. Flagg and K. Donohue, 2010, 'On the variability of Gulf Stream transport from seasonal to decadal', *J. Mar. Res., 68,* 503-522.

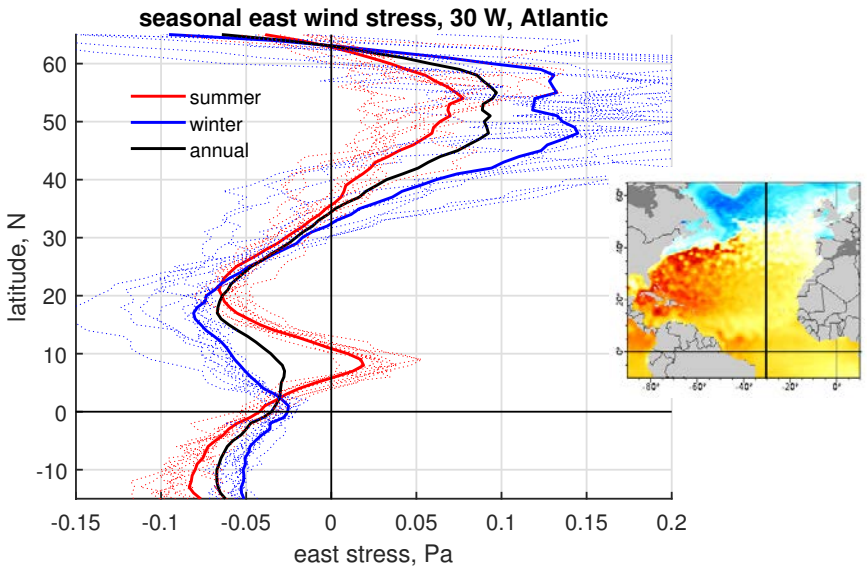

Figure 8: The east component of wind stress sampled along 30 W of the North Atlantic. Data are from a decade of scatterometry observation, QuikSCAT SeaWinds, served by the NOAA ERDDAP web page. The heavy red and blue lines are the summer and winter composite averages, and the thinner dashed lines are the individual monthly estimates. At mid-latitudes, the seasonal cycle is mainly a pronounced strengthening of the westerlies in winter, along with a very substantial increase in monthly variability (storminess). At tropical latitudes, the biggest feature is a shift in latitude of the near-equatorial easterly minimum (the doldrums) — northward during northern hemisphere summer and returning to the equator during winter. The result is a fairly substantial annual cycle of wind stress and wind stress curl in the lower subtropics.

that the upper ocean circulation would show a significant seasonal variation (i.e., an annual cycle) since the wind stress and the wind stress curl that are the ultimate source of the circulation vary quite a lot with season, in some regions up to $\pm 50\%$ (Figs. 8 and 9). However, the systematic, seasonal (annual) variation of the subtropical gyre, represented here by the seasonal average zonal profile of SSH (Fig. 10) or by the Gulf Stream transport is quite small, only about 5 to 10% of the time-mean.[4] The same comments hold for the subpolar gyre. This almost complete *absence* of significant seasonal variation in the subtropical and subpolar gyres indicates that the response time of these gyres to a changing wind stress must be considerably longer than a season.

Pronounced seasonal variation of the tropical ocean circulation. The time-mean and the seasonal variation of the tropical Atlantic circulation (within about 15 degrees of the equator) is markedly different in character from the subtropical and subpolar circulation described above. The dominant features of the tropical North Atlantic SSH are several comparatively narrow, zonally elongated ridges and troughs (just barely evident in Fig. (1), which is scaled appropriately for the entire North Atlantic; cf., Fig. 11). The magnitude of the near-surface current associated with these tropical ocean features is comparable to that found in the subtropical and subpolar gyres, though the SSH amplitude is considerably less, typically only about 0.1 m, consistent with geostrophy at low latitudes. The associated, zonal geostrophic currents

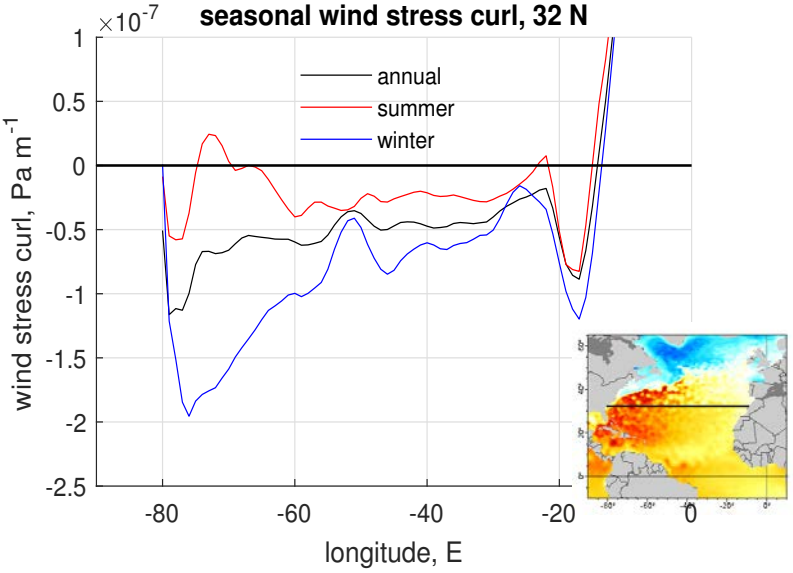

Figure 9: Longitudinal profile of wind stress curl along 32 N, as in Fig. (10) above. The black line is the annual mean, and the red and blue lines are the mean for summer and winter respectively. Notice that the wintertime curl is considerably greater in magnitude (more negative) than is the summertime curl. This wind stress data was downloaded from the SODA3 reanalysis that is archived on the NOAA ERDDAP web site.

have alternate signs: between about 25 N and 15 N there is a rather diffuse, westward flowing North Equatorial Current (NEC), essentially the southern part of the subtropical gyre, a little farther south between about 12 N and 5 N there is an eastward flowing North Equatorial Countercurrent (NECC), and still farther south, a northwestward flowing South Equatorial Current (SEC) that crosses the equator from south to north. The connection of these zonal currents with a western boundary current and with a gyre-like circulation is not clear from observations.[5]

In marked contrast to the quasi-steady subtropical and subpolar gyres noted above, these tropical ocean circulation features exhibit systematic, large amplitude seasonality: the North Equatorial Current

[5]There is a significant, northward-flowing western boundary current evident in Fig. 2 that crosses the equator and continues northwestward along the coast of South America. This North Brazil Current is the shallow side of the the global-scale, overturning circulation that imports warm South Atlantic water into the North Atlantic basin and returns cold water at great depth. The meandering North Brazil Current frequently sheds large (several hundred kilometer diameter) eddies that transport a significant part of the warm water flow. The presence of the strong and highly variable North Brazil Current makes it difficult to discern a relationship between a western boundary current and the mainly zonal currents to the east. A concise discussion of equatorial ocean circulation including the annual variability of winds and currents is by Philander, S. G., 2001, 'Atlantic ocean equatorial currents', Academic Press, doi:10.1006/rwos.2001.0361. An excellent depiction of surface currents generally is provided by http://oceancurrents.rsmas.miami.edu/atlantic/north-brazil.html

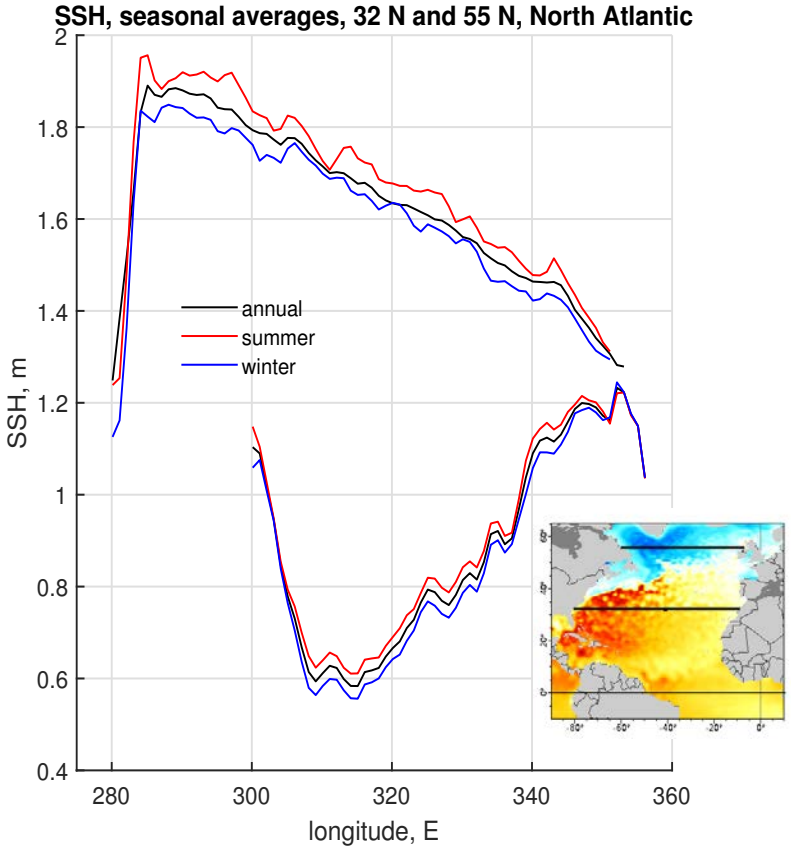

Figure 10: Longitudinal profile of decadal-averaged absolute SSH across the subtropical North Atlantic at 32 N (n.b., the upper set of curves) and at 55 N (the lower set of curves). Data are from the AVISO project via ERDDAP, and span the years 1992-2012. The black line is the annual mean, and the red and blue lines are the mean for summer and winter respectively. Note that in both gyres, the summertime SSH is slightly higher than the wintertime SSH, but the zonal slope of SSH is essentially unchanged from summer to winter. (For a little more on this, see homework problem 3 of Sec. 9.2)

and the South Equatorial Current are strongest in summer and disappear almost completely in winter, while the North Equatorial Counter Current fluctuates annually by about $\pm 40\%$ of its mean (Fig. 11). (A more compelling view of this annual variability is available by following the links to animations noted in the caption of Fig. 2, and see also the references in footnote 5.) A time-mean can always be defined, however the seasonal variability of these near-equatorial currents is more impressive and perhaps more significant than is the mean. This marked difference between the tropics and higher latitudes is emblematic of a very significant latitudinal dependence of the ocean's response to a changing wind stress, something that will be encountered at several turns in this essay. The most dramatic example of this is the monsoonal variation of circulation in the Arabian Sea, discussed at some depth in Part 5: on the seasonally-varying Arabian Sea.

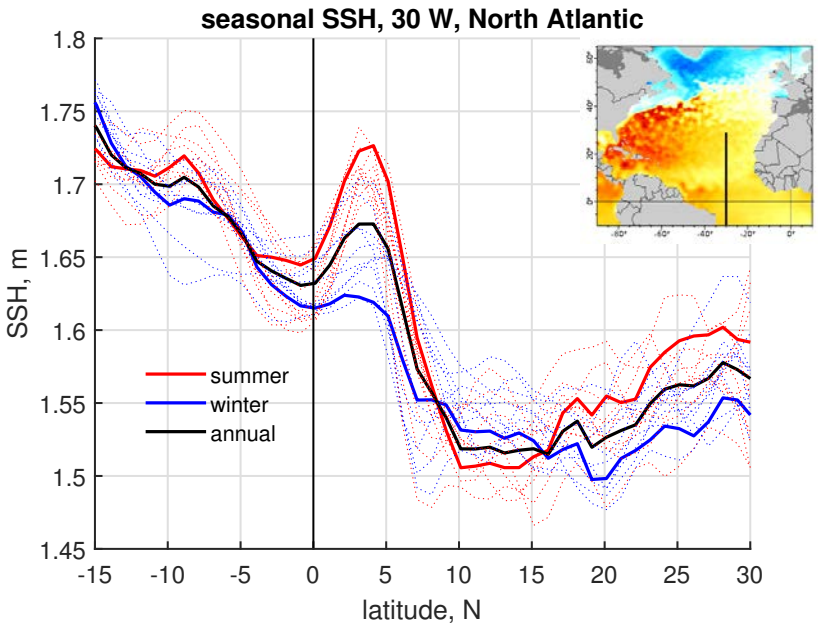

Figure 11: The summer and winter seasonal averages of SSH over 20 years of satellite altimetry along 30 W in the tropical North Atlantic. These SSH data were compiled by the AVISO project and served by NOAA's ERDDAP web page. Notice the large summer to winter change in the ridge near 7 N which supports the eastward flowing NECC on its north side during summer, and the westward flowing SEC on the south side. More subtle, but also significant, is the summer maximum of the northward slope of SSH between about 15 N and 25 N. This supports the westward flowing NEC.

2.4 O4, The geostrophic flow of the subtropical gyre is somewhat surface intensified

The SSH field gives us a good sense of the near-surface geostrophic flow, and the density section of Fig. (3) together with the thermal wind relation,

$$\frac{\partial v}{\partial z} = -\frac{g}{f\rho_o}\frac{\partial \rho}{\partial x}, \tag{2}$$

provides an opportunity to estimate the vertical extent of the underlying geostrophic flow (Fig. 6). Thermal wind may be integrated upward from a depth d_o,

$$v(z) = -\frac{g}{f\rho_o}\int_{-d_o}^{z}\frac{\partial \rho}{\partial x}dz + v(d_o). \tag{3}$$

The integration constant $v(d_o)$ may be evaluated in a variety of ways. The classic method is to set $v(d_o) = 0$ at a depth where the horizontal density gradient vanishes (isopycnals are level) and hence the thermal wind also vanishes. The velocity at that depth is then either barotropic, which is possible but not common, or the velocity vanishes, and d_o is said to be the 'depth of no motion'. Inspection of Fig. (6),

lower, suggests that $d_o = 1200$ m is a plausible guess for most of the interior of the subtropical gyre and yields the profiles of Fig. (6), upper. The long-term average SSH (Fig. 2) may also be used to make an independent estimate of the near-surface geostrophic current, and yields -1.2 cm sec^{-1}, averaged over the interior of the basin, -65 E to -10 E. This is (remarkably) consistent with the near-surface values of the thermal wind profiles, -1.1 to -1.4 cm sec^{-1}, suggesting that a depth of no motion at around 1200 m is indeed appropriate, on average, for the interior portion of this section. Hence, these current profiles may be regarded as absolute. It is important to note that there is no claim to know *why* $d_0 = 1200$ m in this instance, and hence there is no basis to argue that the same d_o will be appropriate for any other region, including the western boundary current region of this section.

A second characterization of meridional currents is available from the Simple Ocean Data Assimilation version 3, SODA3,[6] an ocean reanalysis run for the years 1985 to 2015 (Fig. 12). The reanalysis data were sampled along 32 N, and then time-averaged over two decades (Fig. 12). Reanalysis is a complex process (name notwithstanding) that uses extensive oceanic and atmospheric data sets (all available hydrographic data, satellite-observed SST, wind stress from scatterometry and air-sea heat exchange from other reanalyses) to continually update an Ocean General Circulation Model (OGCM). The aim is to produce a dynamically consistent solution including four-dimensional temperature, salinity and currents at high spatial and temporal resolution. The resulting SODA3 currents are absolute, and so there is no need to fuss with a level of no motion. As well, the OGCM includes a wind-forced Ekman layer within the upper 50 m, roughly.

These current profiles are used to investigate volume transport in a later section 1.2.1, but for now the aim is to define the depth scale (vertical extent) of the subtropical gyre circulation. There is very weak (or vanishing) meridional flow at depths of ≈ 1200 m, as expected from the nearly flat isopycnals around that depth. The meridional geostrophic current becomes more southerly approaching the surface, and has a near-surface value of about -1.3 cm sec^{-1} on average across this section. The profiles are quasi-linear in depth, and so a plausible measure of the vertical extent (i.e., the depth scale) is the half amplitude, $d_{1/2} \approx 500$ m on the western side of the section, and somewhat less, about 300 m on the eastern side. This eastward shoaling of the current is significant, but if you had to pick a single number, then

$$d_{1/2} \approx 400 \text{ m}$$

is about right for the subtropical gyre. The meridional current of the subtropical gyre interior is significantly surface-intensified in as much as it occupies only about the shallowest 10% of the water column. This will be termed the 'upper ocean', and is the part of the water column that is kept in motion by the direct and indirect effects of the overlying wind field.[7] Notice that the upper ocean so defined is roughly coincident with the main thermocline. It is, of course, very helpful to have a number in mind for

[6] Carton, J. A., G. A. Chepurin and L. Chen, 2018. SODA3: A new ocean climate reanalysis. *J. Clim.*, Vol. 31, 6967-6983.

[7] In the deep, cold 'abyssal' ocean below the main thermocline, the horizontal and vertical density gradients are much smaller and the inferred circulation is comparably very slow. Abyssal ocean circulation also owes, ultimately, to interaction with the atmosphere, including heat and fresh water exchanges that are excluded from this study. It also has a truly global extent, rather than merely basin-wide.

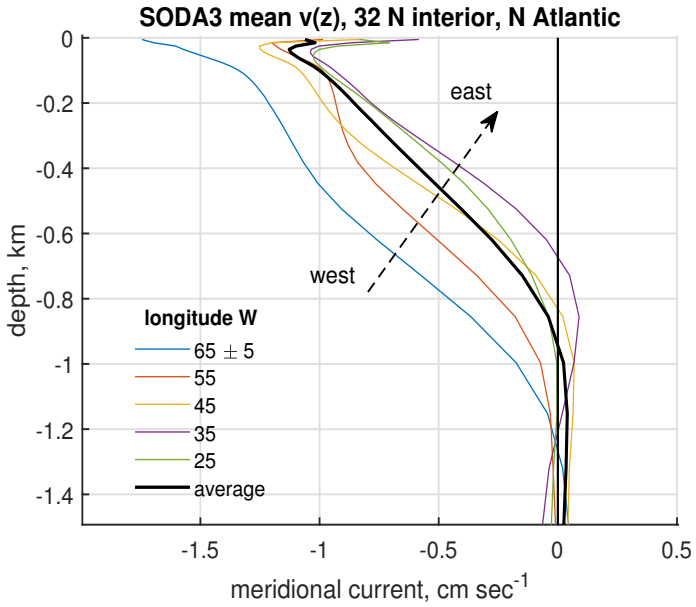

Figure 12: Profiles of long time-averaged meridional current from the SODA3 reanalysis sampled along 32 N in the subtropical North Atlantic. These data were downloaded from the NOAA ERDDAP server. Profiles are plotted every 10 deg of longitude from 65 W to 25 W. These profiles include an Ekman current in the shallowest $\approx$ 50 m, which is not present in the thermal-wind inferred profiles of Fig. (6), upper. Otherwise, these are very similar to thermal wind profiles computed from time-averaged density field data. Notice that the half-amplitude thickness of the current decreases from west to east, roughly 500 m to 300 m.

the depth (vertical extent) of the wind-driven circulation, but it is also very important to know why, i.e., what it depends upon and how it might vary from one region to the next.

2.5 Appendix: Notable phenomena that are not addressed here

Eastern boundary upwelling. One significant feature of the zonal SSH profiles that will not be treated here but that deserves much more than a passing mention is the pronounced low of SSH close to the eastern boundary of four of the subtropical gyres (the exception being the South Indian Ocean gyre). This low SSH is especially prominent in the subtropical gyres of the South Pacific and the South Atlantic. These SSH eastern boundary lows are the signature of two of the ocean's most important coastal upwelling regions, often named for their associated upper ocean current, the equatorward Humboldt Current off of Chile and Peru, and the equatorward Benguela Current off of South Africa and Namibia. These Eastern Boundary Upwelling (EBU) regions extend for hundreds of kilometers along the coast, and are marked by SST that is much cooler than is found in the interior offshore, as well as an uplifted thermocline. This is the consequence of a more or less persistent upward-going, vertical flow (or upwelling) of subsurface waters into the near surface, as much as 5 to 10 m day^{-1} or O(50) times the rate of typical open ocean Ekman suction. Thermocline water is high in nutrients that fuels very intense biological productivity in EBU regions, an order of magnitude greater than is typical of the open ocean. The proximate cause of EBU upwelling is alongshore, equatorward winds (Fig. 3) that produce a divergent Ekman transport next to the coast, and is strengthened by negative stress curl offshore (southern hemisphere). The direction and amplitude of the prevailing wind stress is the most important cause of an EBU, but it is also significant that they are found along the eastern boundaries of subtropical gyres where

cool, nutrient rich thermocline water is unusually close to the sea surface.

North Indian Ocean. The only large ocean basin that is missing from Table 1 is the North Indian Ocean. The long-term mean wind stress and wind stress curl over this basin are somewhat smaller than are found over other ocean basins. Given this, and the low (tropical) latitude of this ocean basin, it is not surprising that the time-mean SSH does not show an obvious, gyre-like structure.

What the North Indian Ocean may lack in a time-mean circulation it more than makes up with very strong seasonal circulation that is associated with seasonally reversing, or monsoonal, winds that are very different from the mainly zonal winds that drive midlatitude circulations. The summertime, Southwest monsoon winds of the Arabian Sea include what are typically quite strong southwesterly winds along the coast of Somalia and Oman. The ocean circulation responds vigorously to the onset of Southwest Monsoon winds, within a month, with a strong flow to the northeast along the coast of Somalia. This Somali Current has surface current speeds in excess of 2 m $\sec^{-1}$, a depth (thickness) of about 250 m, and a transport of roughly 30 Sv, which is comparable to that of some semi-permanent western boundary currents. This monsoon response is examined in some depth in Part 5, where the conclusion is that the summertime circulation of the Arabian Sea is not unlike that of the subtropical North Atlantic, including that its amplitude is approximately consistent with the Sverdrup relation.

3 A review of the low frequency beta effect and the Sverdrup relation

In Part 3 and here, the northward increase of f

$$f \;=\; 2\Omega \sin\left(latitude\right) \tag{4}$$

is represented by the β-plane approximation, a linear expansion of f around a central latitude,

$$\beta - \text{plane approximation}: \quad f_1 \;=\; f_o \;+\; \beta(y - y_o), \tag{5}$$

with y the north coordinate and $R_e = 6360$ km the Earth's mean radius. The coefficient

$$\beta \;=\; (2\Omega/R_e)\cos\left(lat_o\right) \tag{6}$$

is constant for a specific model. For this study, $lat_o = 30^o$ N and hence $f_o = 7.29 \times 10^{-5}$ $\sec^{-1}$, and $\beta = 1.98 \times 10^{-11} \sec^{-1}$ m^{-1}.

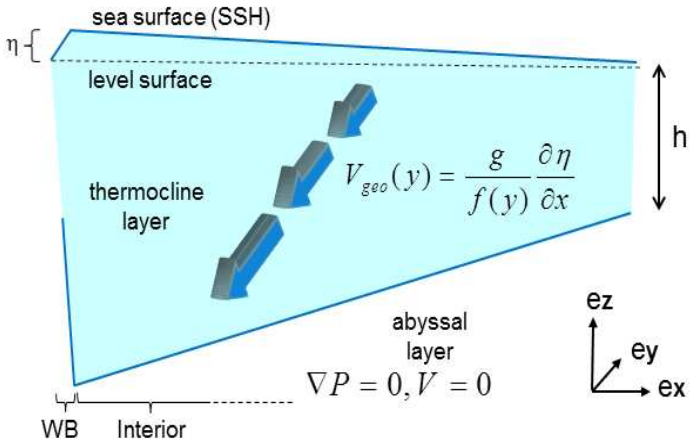

Figure 13: A schematic cross section of the North Atlantic subtropical thermocline, sliced east-west and viewed looking toward the north as in Fig. (6). The upper ocean (thermocline and above) is modeled as a single active layer. The tilt of the thermocline compensates the tilted sea surface so that the horizontal pressure gradient and velocity are vanishingly small in the very thick abyssal layer. The comparatively narrow western boundary region is noted at lower left, and the much wider interior region is all of the rest. The meridional geostrophic current in the interior is equatorward. The three bold arrows are meant to depict the geostrophic current amplitude at three latitudes and increase toward the equator, simply because because f decreases toward the equator. A meridional geostrophic current is thus divergent, $\partial v_{geo}/\partial y > 0$, which is here said to be the beta effect. In this example of equatorward flow, the resulting layer thickness tendency due to the beta effect alone is thus $\partial h/\partial t < 0$, i.e., thinning.

3.1 Balanced meridional motion is divergent horizontally

A beta-plane approximation is sufficient to reveal one of the most important consequences of the northward variation of f, that balanced meridional motion is divergent horizontally. To see how this arises, consider a vertically integrated continuity equation, or thickness balance, for a single layer (as in a reduced gravity, shallow water model, Part 2),

$$\frac{\partial h}{\partial t} = -(\frac{\partial hu}{\partial x} + \frac{\partial hv}{\partial y}). \tag{7}$$

Geostrophy for this model is just

$$-fv = -\frac{1}{\rho_o}\frac{\partial P}{\partial x} \quad \text{and} \quad fu = -\frac{1}{\rho_o}\frac{\partial P}{\partial y}. \tag{8}$$

Now substitute the geostrophic velocity components Eq. (8) and $f(y)$ from (5), to find

$$\boxed{\frac{\partial h_{geo}}{\partial t} = \frac{\beta h}{f} v_{geo}} \tag{9}$$

on the assumption that $\partial^2 P/\partial x\partial y = \partial^2 P/\partial y\partial x$. The subscript *geo* on the left side is just to emphasize that this is the geostrophic contribution only. This thickness tendency is due to the horizontal divergence of a balanced meridional velocity in the presence of a northward increase of f, here said to be the low frequency beta effect (to distinguish from the high frequency beta-effect on inertia-gravity waves noted Part 3).[8] In the example of Fig. (13), a balanced (geostrophic) current is presumed to be southerly, and thus increases in the direction of flow on account of the decrease of f toward the equator. The resulting horizontal divergence $\partial v/\partial y > 0$. Absent some other effect, the layer thickness in this example must then decrease, $\partial h/\partial t < 0$. It is easy to show that if the balanced current is instead poleward, then $\partial v/\partial y < 0$ and the layer will thicken on account of a beta-induced convergence of the horizontal velocity.

Exactly the same thing will happen if there is an applied wind stress and an Ekman current,

$$\boxed{fhu_{Ek} = \frac{1}{\rho_o}\tau_y \quad \text{and} \quad fhv_{Ek} = -\frac{1}{\rho_o}\tau_y} \tag{10}$$

Substituting these into the thickness balance yields

$$\frac{\partial h_{Ek}}{\partial t} = \frac{1}{\rho_o}\left(\frac{1}{f}\frac{\partial \tau_y}{\partial x} - \frac{\partial}{\partial y}(\frac{\tau_x}{f})\right). \tag{11}$$

Expanding the derivative on the rightmost term brings out a term that involves beta,

$$\frac{\partial h_{Ek}}{\partial t} = \frac{\beta h}{f}v_{Ek} + \frac{1}{\rho_o f}\left(\frac{\partial \tau_y}{\partial x} - \frac{\partial \tau_x}{\partial y}\right). \tag{12}$$

The wind stress field may (usually will) have some curl, while the pressure gradient field can not.

The geostrophic and Ekman velocities appear in parallel forms here and so it is useful to define their sum to be the balanced velocity,[9]

$$v_{bal} = v_{geo} + v_{Ek} \tag{13}$$

and the sum of (9) and (12) is the corresponding thickness balance,

$$\boxed{\frac{\partial h_{bal}}{\partial t} = \frac{\beta h}{f}v_{bal} + \frac{1}{\rho_o f}\left(\frac{\partial \tau_y}{\partial x} - \frac{\partial \tau_x}{\partial y}\right)} \tag{14}$$

The thickness equation (14) has three modes by which is meant notable two term balances. The first and third terms define a forced, time-dependent balance in which the Ekman convergence associated with

[8]There does not appear to be a wide consensus on the meaning of the phrase 'beta effect'. Many authors, including the Glossary of the American Meteorological Society, use the term to signify anything that happens on a beta plane that would not have happened on an otherwise similar f-plane. By that usage, the divergence of balanced meridional flow would be *a* beta effect.

[9]This use of 'balanced' is evidently not conventional. A balanced velocity is usually meant to indicate a steady, vortical flow in which geostrophy is modified by centrifugal force.

wind stress curl thickens or thins the surface layer locally. This is a very important process insofar as it changes the mass field and thus the pressure field, and will figure prominently in discussion of the Stage 2 response of Sec. 4.2.1. The first and second terms define a time-dependent, free (unforced) balance that describes the mechanism of westward propagation, and the second and third terms define a forced, steady flow which is Sverdrup balance, albeit in a one layer model.

3.1.1 Free, time-dependent motions propagate westward

The mechanism of westward propagation may be understood as the second mode noted above, the balance between time-dependence and the beta effect. To see this, rewrite the beta term using the geostrophic velocity, to find a first order wave/advection equation (Sec. 10.2, Problem 2),

$$\frac{\partial h_{geo}}{\partial t} \;=\; \beta R_d^2 \frac{\partial h}{\partial x}, \tag{15}$$

where

$$R_d \;=\; \frac{\sqrt{g'h}}{f} \;=\; \frac{C}{f}$$

is the radius of deformation. C is the gravity wave speed; in the subtropics, $C \approx 3$ m sec^{-1}, and at 30^o N, $R_d \approx 40$ km. Eqn. (18) is appropriate for free motions, e.g., elementary waves $h(x,t) \;\propto\; sin(kx - \omega t)$, and so may be characterized by a dispersion relation that connects the wavenumber, $k = 2\pi/\lambda$, and the frequency, ω,

$$\omega \;=\; -k\beta R_d^2. \tag{16}$$

This is the long wave limit of baroclinic Rossby waves (Part 3, Sec. 2.3). In this limit, phase and group speeds are equal to the long Rossby wave speed,

$$\boxed{C_{longRo} \;=\; \frac{\omega}{k} \;=\; \frac{\partial \omega}{\partial k} \;=\; -\beta R_d^2 \;\leq\; 0.} \tag{17}$$

C_{longRo} is independent of k and ω, and so this propagation is nondispersive and westward. Eqn. (15) is thus a first order wave/advection equation,

$$\boxed{\frac{\partial h_{geo}}{\partial t} \;=\; -C_{longRo}\frac{\partial h}{\partial x}} \tag{18}$$

C_{longRo} varies quite a lot with f, but at a fixed site, C_{longRo} is equivalent to a constant, westward advection velocity. Using values from 30^o N, $C_{longRo} \;\approx -3$ km day^{-1}, which is consistent with the observed propagation of mesoscale eddies discussed in Part 3.

What is most important is that all free (unforced) large scale ($\lambda >> R_d$), low frequency ($\omega << f$) phenomena will propagate westward, regardless of planform. If there are indeed no small horizontal

scales involved (and so no dispersion), then the planform will be conserved and will appear to be shifted steadily westward, as if by advection, at the constant rate, C_{longRo}. It seems appropriate to call such westward propagating phenomena 'Rossby waves', even if they may look nothing at all like an elementary wave. An appreciation for this generalized Rossby wave propagation is a key concept needed to understand the response of an ocean circulation to a transient wind. (For a little more on this see Homework problem 2, Sec. 10.2.)

3.1.2 Forced, steady meridional motion is Sverdrup flow

The third mode of (14) is forced, steady motion,

$$\boxed{hv_{bal} \;=\; \frac{1}{\beta\rho_o}\left(\frac{\partial\tau_y}{\partial x} - \frac{\partial\tau_x}{\partial y}\right)} \tag{19}$$

or in a more streamlined notation,

$$M^y_{bal} \;=\; \frac{1}{\rho_o\beta}\nabla\times\tau,$$

which is none other than the Sverdrup relation for this single layer model in which

$$M^y_{bal} \;=\; h(v_{geo} \,+\, v_{Ek}) \;=\; M^y_{geo} \,+\, M^y_{Ek}.$$

Thus the mechanism behind the Sverdrup relation can be viewed as the mass (volume) balance between the beta-induced divergence of a balanced meridional current (geostrophic plus Ekman) and the wind stress curl component of Ekman transport divergence. To say it a little differently, if there is a steady state in the presence of a wind stress curl, then a beta effect acting upon a meridional transport will be implied. The sense and the magnitude of this meridional transport is given by the Sverdrup relation. In the single layer model considered here, the Sverdrup transport is, by default, present entirely within the single active layer, which is also the Ekman layer. Surprisingly, this is also a plausible outcome in a much more capable model of Sec. 6, though not necessarily what is in the ocean.

There is yet another way to see the Sverdrup relation that combines the previous two descriptions of modes. It has been empahsized that every large scale zonal gradient of thickness should have a tendency to propagate westward. Mesoscale eddies conform to this notion — why not same for the basin-scale meridional gradient seen in Fig. 1? If the gyre was a free motion, it would certainly propagate westward, and the result at a given site would be a thinning of the upper ocean layer as given by Eqn. (15). However, the basin scale flow i.e., the gyre, is subject also to wind stress curl, which will tend to thicken the upper ocean layer, Eqn. (11). If these two tendencies just offset one another, then

$$\frac{\partial h_{geo}}{\partial t} \,+\, \frac{\partial h_{Ek}}{\partial t} \;=\; 0,$$

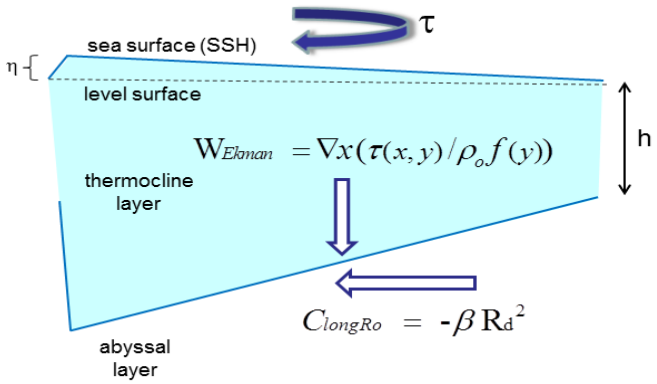

Figure 14: A schematic cross section of the North Atlantic subtropical thermocline, sliced east-west and viewed looking toward the north as in Fig. (6). The beta effect acting upon the associated meridional geostrophic current will produce a westward translation of the thickness gradient at a rate $-C_{longRo}$ and thus a thinning of the layer. The wind stress over the subtropical gyre produces an Ekman transport that is convergent and that would tend to thicken the thermocline layer. The Sverdrup relation may be viewed as a steady balance between this positive thickness tendency and the negative thickness tendency associated with the beta effect and westward propagation.

or using (11) and (15),

$$C_{longRo}\frac{\partial h}{\partial x} = \frac{1}{\rho_o}\left(\frac{1}{f}\frac{\partial \tau_y}{\partial x} - \frac{\partial}{\partial y}(\frac{\tau_x}{f})\right).$$

This can be rearranged a little to find the geostrophic form of the Sverdrup relation,

$$\boxed{M^y_{geo} = \frac{1}{\rho_o \beta}\nabla \times \frac{\tau}{f}} \tag{20}$$

in which the curl operates on wind stress divided by $f(y)$.

The large scale thickness field of the subtropical gyre interior may thus be viewed as an arrested, long Rossby wave. The westward translation expected from the β-effect and the first order wave equation is balanced by a wind stress-induced convergence of the Ekman transport. Wind-driven gyres and mesoscale eddies are closely related in as much as they have the same β-effect acting upon meridional flows (this seems obviously true), the difference is that wind stress does not vary appreciably on the horizontal scale of a mesoscale eddy and hence the westward propagation of eddies.

3.2 Depth dependence of Sverdrup flow

The depth dependence of the circulation is, of course, very important, but not something that will be treated here well enough to develop much insight. It is helpful to consider briefly what amounts to the complement of a single-layered model, a three-dimensional system that is presumed to be quasi-steady, linear and inviscid and that admits depth-dependence. The three dimensional velocity components of this

system are u, v, and w, and e.g., u is $u(x,y,z)$ (note that this holds for the present section only). The three dimensional density, continuity and momentum equations of this system are

$$\left[\frac{\partial \rho}{\partial t}\right] \;=\; -w\frac{\partial \rho}{\partial z} \;+\; \left[A\frac{\partial^2 \rho}{\partial z^2}\right] \tag{21}$$

$$0 \;=\; \frac{\partial u}{\partial x} + \frac{\partial v}{\partial y} + \frac{\partial w}{\partial z}, \tag{22}$$

$$0 \;=\; -fv \;-\; \frac{1}{\rho_o}\frac{\partial p}{\partial x} \;+\; \frac{1}{\rho_o}\frac{\partial \tau^x}{\partial z}, \tag{23}$$

$$0 \;=\; \quad fu \;-\; \frac{1}{\rho_o}\frac{\partial p}{\partial y} \;+\; \frac{1}{\rho_o}\frac{\partial \tau^y}{\partial z}, \tag{24}$$

$$0 \;=\; \quad \frac{\partial p}{\partial z} \;+\; g\rho. \tag{25}$$

The Coriolis parameter f is $f(y)$ via the β-plane approximation, Eqn. (5), which is crucially important in what follows. There are two steady forces recognized here, the horizontal gradient of the hydrostatic pressure, p,

$$p(x,y,z) = \int_{-z}^{\eta(x,y)} g\,\rho(x,y,z)\,dz,$$

which, like the velocity components, is regarded as an unknown. A second important force is the vertical gradient of a turbulent momentum flux,

$$\tau^x(x,y,z) \;=\; \rho_o < u'(x,y,z,t)w'(x,y,z,t) >$$

where the brackets $< \quad >$ indicate a time average over tens of minutes. The small scale, three-dimensional motions $u',\ w'$ that propagate a turbulent momentum flux are outside the scope of a large scale circulation model. The surface value, $\tau_o \;=\; \tau(x,y,z=0)$, is presumed to be known from observations of wind over the oceans, i.e., τ_o is said to be the wind stress (Fig. 3).

Given that the momentum balances are steady and linear, the right hand side of (23) and (25) may be written in terms of geostrophic and Ekman velocity components, say for the meridional component,

$$v_{geo} \;=\; \frac{1}{\rho_o f}\frac{\partial p}{\partial x} \quad \text{and} \quad v_{Ek} \;=\; -\frac{1}{\rho_o f}\frac{\partial \tau^x}{\partial z}$$

with no loss of generality, and define the sum to be the balanced velocity,

$$v_{bal} \;=\; v_{geo} \;+\; v_{Ek},$$

just as before. The meridional transports associated with these velocities are

$$M^y_{bal} \;=\; M^y_{geo} \;+\; M^y_{Ek} \tag{26}$$

where

$$M^y_{geo} \;=\; \int_{-d_{geo}}^{0} v_{geo}\, dz \quad \text{and} \quad M^y_{Ek} \;=\; \int_{-d_{Ek}}^{0} v_{Ek}\, dz \;=\; -\frac{1}{\rho_o}\frac{\tau^x_o}{f}. \tag{27}$$

The lower limit of depth in these transport integrals is significant. The geostrophic velocity of the major, upper ocean gyres is appreciable down to the depth of the lower main thermocline, d_{geo} is O(1000 m), and geostrophic currents associated with the global-scale overturning circulation extend over the full depth water column, noted in the discussion of Fig. (1). The Ekman velocity will be significant within an upper ocean surface layer that is mixed by the turbulent stress imposed at the surface by the wind. In density-stratified regions, such as the subtropical gyre, this Ekman layer may be as deep as the top of the seasonal thermocline, d_{Ek} is O(100 m), and hence almost always much less than d_{geo}. This important effect of stratification is something to come back to when it is time to consider what is missing from a shallow water model (Sec. 8.3).

Vorticity balance. Assuming that the wind stress on the sea surface is given, then the Ekman transport is also known. The geostrophic transport remains completely unconstrained, however, and so we can not go any further with momentum balance and continuity alone. To find out what can be learned about this system, it is very helpful to form the vorticity balance: take the partial x derivative of (25) and subtract the y derivative of (23); then eliminate the horizontal divergence $\partial u/\partial x + \partial v/\partial y$ using the continuity equation (22). This eliminates the unknown pressure and yields the steady, linear vorticity balance,

$$\beta v_{bal} \;=\; f\frac{\partial w}{\partial z} \;+\; \frac{1}{\rho_o}\frac{\partial}{\partial z}\left(\frac{\partial \tau^y}{\partial x} \;-\; \frac{\partial \tau^x}{\partial y}\right), \tag{28}$$

that holds at all z where (23) - (22) are valid. The detailed depth-dependence of w and of the wind stress-induced momentum flux are not knowable within this system alone, but some relevant boundary values are known; depth-integrate (28) from some depth $z = -d$ up to the sea surface where the wind stress is presumed known, τ_o , and the vertical velocity must vanish, *to wit*, the depth integral of (28) is

$$\beta \int_{-d}^{0} v_{bal} dz \;=\; -fw(-d) \;+\; \frac{1}{\rho_o}\left(\frac{\partial \tau^y}{\partial x} \;-\; \frac{\partial \tau^x}{\partial y}\right)\Bigg|_{-d}^{0}. \tag{29}$$

If d is deeper than the depth of the surface layer (Ekman layer), then $\tau(-d) = 0$ and all of the wind stress is absorbed within the volume of the integral and so

$$\beta \int_{-d}^{0} v_{bal} dz \;=\; -fw(-d) \;+\; \frac{1}{\rho_o}\left(\frac{\partial \tau^y_o}{\partial x} \;-\; \frac{\partial \tau^x_o}{\partial y}\right). \tag{30}$$

Rewriting this using symbols already introduced,

$$\boxed{\beta M^y_{-d} \;=\; -fw(-d) \;+\; \frac{1}{\rho_o}\nabla\times\boldsymbol{\tau_o}} \tag{31}$$

(and run out of space for subscripts, and so M_{bal} will be understood.) This is very close to the classic Sverdrup relation (1), but includes the vortex stretching effect of the vertical velocity at $z = -d$, $fw(-d)$. With this term included, (31) is as general as Eqns. (23) - (22), and M^y_{-d} of (31) is the balanced meridional transport above $z = -d$ regardless of what the ultimate cause may be, i.e., whether wind-driven locally in the Sverdrup sense or a geostrophic flow associated with the global-scale overturning circulation.

About vertical velocity, w(z). The depth-integrated vorticity equation (31) is not closed as there are two unknowns, the transport M^y_{-d} that we seek, and the vortex stretching term, $fw(-d)$, at the base of the control volume. To estimate the transport requires some form of $w(z)$.

In theories of small scale, three-dimensional motions, e.g., short wind waves on the sea surface, the vertical velocity is treated exactly on par with the horizontal velocity. However, in large scale circulation models, which deal only with low frequency motions, the vertical velocity is treated very differently. The vertical momentum balance is hydrostatic, Eqn. (22), to a very high approximation, and hence $\partial w/\partial t$ is inaccessible, effectively. Instead, $\partial w/\partial z$ is computed diagnostically from the divergence of the horizontal velocity on the basis that the motion is non-divergent in three dimensions. In a somewhat similar way it is not possible to observe the large scale, low frequency vertical velocity in any kind of widely used field measurement as it is simply too small; a very significant vertical velocity is a mere 10 m year^{-1}. A diagnostic computation via the observed horizontal velocity is also problematic given the very small values of horizontal convergence compared with estimation errors. The saving grace in all of this is that we can claim to know the boundary values of the vertical velocity at the sea surface, $w(z = 0) = 0$, as already noted, and at the sea floor, $w(z = -b) = 0$, with b the depth of a presumably flat sea floor.

The model experiments discussed in Secs. 3 and 6 indicate two possible forms for $w(z)$ and d discussed briefly. The point is to show that a very wide range of velocity profiles can be consistent with Sverdrup transport. First, rearrange Eq. (28) to solve for fw, and integrate from the surface downward,

$$fw(z) \;=\; \beta \int_0^z v_{bal}\, dz \;+\; \frac{1}{\rho_o}\left(\frac{\partial \tau^y_o}{\partial x} \;-\; \frac{\partial \tau^x_o}{\partial y}\right) - \frac{1}{\rho_o}\left(\frac{\partial \tau^y(z)}{\partial x} \;-\; \frac{\partial \tau^x(z)}{\partial y}\right). \tag{32}$$

For this purpose, imagine a thick surface layer and specify that the depth-dependence of $\tau(z)$ is a linear decrease from the surface value to zero at the depth of the surface layer, $z = z_{Ek} = -0.2$. This linear decrease is equivalent to a constant wind stress acceleration within the surface layer. Assume that the local wind stress is zero, and that the wind stress field has negative curl. This will cause a converging Ekman transport and a downward vertical velocity (the blue line of Fig. (15 left)), often called Ekman pumping, that is zero at the sea surface and has a maximum at the base of the Ekman layer, $z = -0.2$. At depths below the surface layer, there is no additional divergence due to the Ekman transport, and hence the vertical velocity due solely to the wind stress curl is constant down to the sea floor. In order that w vanish at the sea floor, some additional source of divergence and thus another contribution to the vertical velocity is required — the beta effect acting upon a balanced meridional current (geostrophic only below the Ekman layer). Assuming that the vertical velocity due to Ekman pumping is downward (negative)

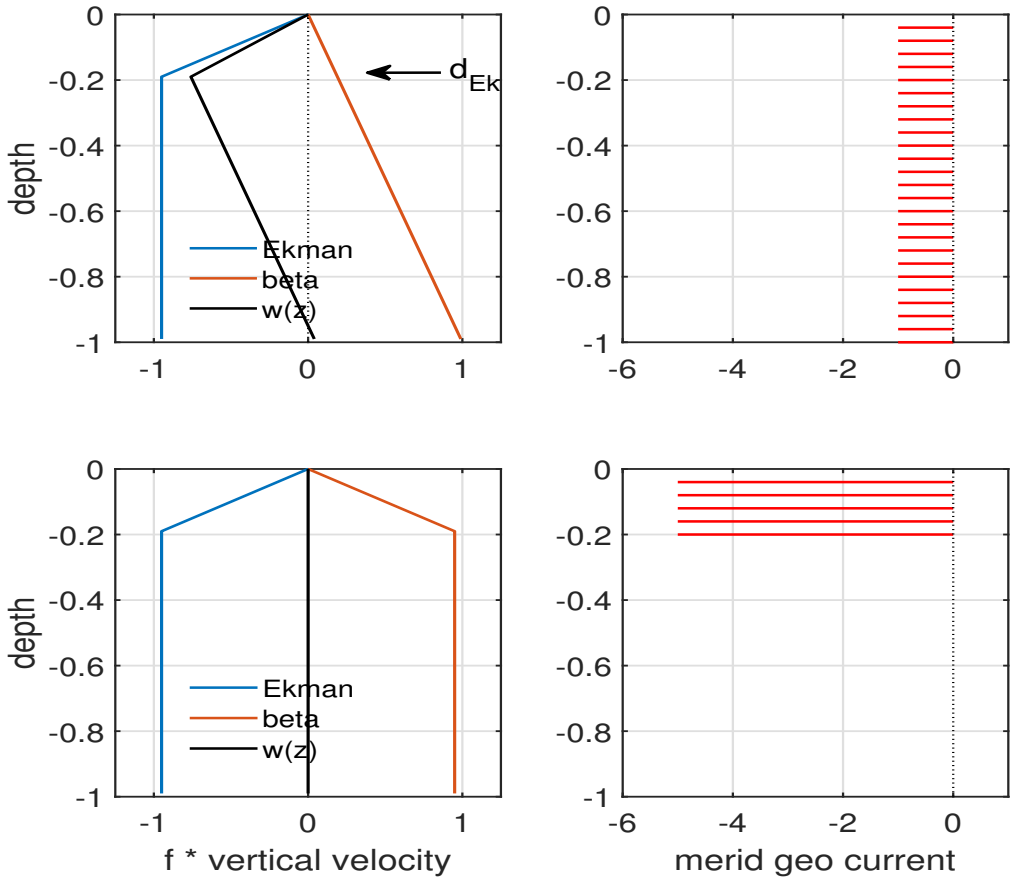

Figure 15: Schematic vertical velocity and gesotrophic velocity profiles that will be encountered in upcoming model experiments. In both cases the depth of the Ekman layer is taken to be $-d_{Ek}$ = -0.2, and the presumed flat sea floor is at $z = -1$. The Ekman transport is presumed to vanish. The vertical velocity associated with wind stress curl is the blue line, which vanishes at the sea surface. In these examples the Ekman-induced vertical velocity is downward, as in the subtropical gyre, and hence the balanced (geostrophic) current must be southward. **(upper)** Barotropic Sverdrup transport. Assuming a geostrophic current that is uniform with depth (sketched at right), the vertical velocity associated with the beta effect is the red line, which vanishes at the sea surface. The sum of the Ekman and the beta-induced vertical velocity is $w(z)$, the black line, which must vanish at the sea surface and at the sea floor. This determines the amplitude of the geostrophic current, -1 in this case. **(lower)** Baroclinic and surface-trapped Sverdrup transport. In this example, the geostrophic current is confined to the surface layer. In this case, w vanishes throughout the water column, and the geostrophic current has an amplitude of -5.

then the countervailing vertical velocity due to the beta effect must be upwards (positive) requiring that $\partial v/\partial y > 0$ and thus a southward flow (Fig. 13). Just how that southward (Sverdrup) flow is distributed in the water column is the issue. Inspection of field data in Sec. 1.1.2 led to the purely empirical result $w(d_o) = 0$ at $d_o = 1200$, and here are two other extreme possibilities that will rise in model experiments to come. For this purpose, assume that $f = \beta = 1$ and that the water column has a thickness of 1. Just for illustration, assume that the wind stress curl yields a vertical velocity $w(-0.2) = -1$. In order to satisfy the sea floor boundary condition, the beta term integrated down to the sea floor must then be the opposite, +1.

Barotropic Sverdrup transport, $\mathbf{d = b}$. One possibility is that the balanced current could be uniform with depth and with an amplitude -1, Fig. (15, upper). In that case $d = b$, and the transport integral over the full water column is given by the Sverdrup relation. While the vertical velocity will tehn vanish at the sea floor, at most depths above the sea floor w will be non zero. The velocity may be almost exactly geostrophic and the transport very accurately Sverdrupian, and yet the system will not be in a true steady state since the density will still be evolving, albeit slowly, on account of vertical advection, Eqn. (21). This is what we will find at short times (weeks to months) in experiments with a three layer model that includes an active lower layer and a free sea surface (Section 6). Hence, barotropic Sverdrup transport is quite possible, though it is not observed in the long-term averages of ocean field data.

Surface-trapped, baroclinic Sverdrup transport, $\mathbf{d = d_{Ek}}$. Another possibility consistent with the Sverdrup relation is that the balanced current could be baroclinic and confined to the surface layer. In that event, the current must have an amplitude of -5. This configuration yields a vertical velocity that is zero throughout the water column and so could be literally steady. This surface-trapped Sverdrup regime occurs by default in the single layer model as noted in Sec. 1.5.2, and it also arises in the solution of the three-layer model at very long times (decades after startup, Sec. 6). Interesting though it is, this surface trapped solution is not consistent with the inferred depth scale from field observations, since it is edthat d_{Ek} is O(100) m, and considerably less than the roughly 500 m inferred from field data (Sec. 1.1.2).

3.3 The Sverdrup relation is valid widely, but not everywhere

The limitations of the Sverdrup relation are emphasized in much of what follows, but there should be no doubt of its utility — given only the Sverdrup relation and the curl of the wind stress, one can predict meridional transport that is in accord with some of the major features of the upper ocean circulation. Notably, the meridional transport expected from a negative stress curl (clockwise rotating wind stress as occurs over the subtropics of the North Atlantic, Fig. 3) will be accompanied by a high of SSH and southward meridional flow, as indeed does occur, and evident from Figs. 1 and 2. A counterclockwise wind field and thus positive stress curl is expected to produce northward meridional flow and a low of SSH, which is consistent with observations of the subpolar basin (Fig. 2).

An informal, semi-quantitative test of the Sverdrup relation may be made using the absolute current profiles of Fig. (4) together with a more detailed look at the wind stress curl along 32 N (Fig. 9). The current profiles have a transport per unit width

$$M^y \;=\; \int_{-d_o}^{0} v\, dz$$

of from -5 to -3 $m^2\ sec^{-1}$, with larger values toward the western side of the basin. The annual average wind stress curl is about $\nabla \times \tau = -1.0$ to -0.5×10^{-7} N m^{-2}, and again with larger values to the west (Fig. 9). The expected Sverdrup transport is thus about -5.1 to -2.5 $m^2\ sec^{-1}$, which is roughly consistent with the observed, upper ocean meridional transport. It appears that

$$M^y \;\approx\; M^{Sv}$$

regionally, across the center of the North Atlantic subtropical gyre.

The basin-wide volume transport will often be of special interest,

$$N^y \;=\; \int_{basin} \int_{-d_o}^{0} v\, dz\, dx \;\approx\; -28 \text{ Sv},$$

and of course it is southward. The very widely used (though non-SI) unit of volume transport is (what else?) the Sverdrup, 1 Sv = 10^6 $m^3\ sec^{-1}$. The basin-wide Sverdrup transport estimated from the long term averaged wind stress curl at this latitude is similar,

$$N^{Sv} \;=\; \frac{1}{\rho_o \beta} \int_{basin} \nabla \times \tau \; dx \;\approx\; -30 \text{ Sv}.$$

(This comparison ignores the contribution of Ekman transport to the Sverdrup transport which is very small at this latitude, but not everywhere. More on this below.) From this generally favorable comparison of observed (geostrophic) and Sverdrup transports, both basin-wide and regionally, we can be fairly confident that the Sverdrup relation plus the known wind stress curl gives a good account of the meridional, upper ocean transport in the interior part of the North Atlantic subtropical gyre. Notice that to evaluate the observed transport required the specification of the lower limit of Sverdrup flow, here $d_o \approx 1200$ m.

Modern observational methods and analyses have made it possible to make very detailed, quantitative tests of the Sverdrup relation over almost the entire, global ocean.[10] In a nutshell, these studies concur that the Sverdrup relation is reasonably accurate (to within about 25%) over most of the interior of the North Atlantic and North Pacific subtropical gyres, provided that winds and currents are

[10]Three excellent, observation-based studies of the Sverdrup relation are by Gray, A. R. and Riser, S. C., 2014, 'A global analysis of Sverdrup balance using absolute geostrophic velocities from Argo', *J. Phys. Oceanogr.*, 1213-1229, doi: 10.1175/JPO-D-12-0206.1, and by Wunsch, C., 2011, 'The decadal mean ocean circulation and Sverdrup balance', *J. Mar. Res.*, **69**, 417-434. online at dspace.mit.edu/openaccess-disseminate/1721.1/74048 and by Thomas, M. D. et al., 2014, 'Spatial and temporal scales of Sverdrup balance', *J. Phys. Oceanogr.*, **44**, 2644-2660. doi: 10.1175/JPO-D-13-0192.1

averaged over multi year periods and over horizontal scales of O(500 km) or greater, as done above. The Sverdrup relation is not valid near western boundary currents (wbc), which is no surprise, nor is it valid in the northeastward extension of the subtropical wbc (Gulf Stream) into the subpolar basin (North Atlantic Current). The subpolar gyres of the North Pacific and North Atlantic have the expected sense of the circulation (counterclockwise), but there is a poor correlation between the magnitude of the Sverdrup transport and the observed meridional transport. The difference is especially marked in the northerly half of the North Pacific subpolar gyre, where the observed meridional transport is considerably less than the expected Sverdrup transport.

4 Shallow water models of wind-driven circulation

The shallow water model introduced in Part 2 can be made into a useful tool for studying some important facets of the wind-driven circulation by 1) defining an appropriate domain and boundary conditions, 2) adding a new term that represents wind forcing, and 3) including a very simple form of dissipation. A straightforward extension to multiple layers including an active sea surface is also described.

4.1 Boundary conditions for a closed basin

The ocean domain is taken to be a square basin with sides of length $2L$ centered on 30 ^{o}N. Rotation is treated by a β-plane approximation and the basin size is then chosen so that the southern boundary will correspond to the equator, $f = 0$. Given $\beta(30^o)$, this requires $L = 3600$ km. The resulting basin width, $2L = 7200$ km, is roughly comparable to the average width of the North Atlantic Ocean, but is only about half the width of the mighty Pacific Ocean. The intention is to model a circulation that is self-contained within this basin, and so the boundaries are made impermeable by setting the normal component of velocity to zero,

$$\mathbf{V}\cdot\mathbf{n} = 0, \tag{33}$$

on all of the boundaries.

What this formulation ignores is that the southern and northern boundaries of the real North Atlantic basin are, of course, open, and there is a significant poleward flow of warm water from the southern hemisphere into and through the North Atlantic basin. In the equatorial region this occurs largely within a western boundary current, usually called the North Brazil Current (Fig. 2 and footnote 5). Within the subtropical gyre this warm upper ocean flow makes up a part of the Gulf Stream, and is in some respects indistinguishable from the basin-scale wind-driven, Sverdrup flow. At the northern boundary, some of this warm flow continues poleward into the Norwegian-Greenland Sea as the North Atlantic Current (or

Drift). This shallow, warm, poleward flow is balanced volumetrically by a deep, cold equatorward flow, also in western boundary currents. The resulting meridional flux of warm and cold water is a very important consequence of the global-scale, meridional overturning circulation. The overturning circulation is not driven directly by basin-scale winds, as are the upper ocean gyres of Fig. 2, and an overturning circulation does not arise in the present experiments.

4.2 Initial density and velocity

There are three sensible ways to initialize density stratification and velocity depending upon the scope and goals of the experiment.

First, imagine that the aim is to model all aspects of the circulation, including the existence and scale of the main thermocline. In that case it would be appropriate to start with a homogeneous ocean, and to apply surface fluxes of heat, fresh water and wind stress that might eventually yield a main thermocline. An ambitious and interesting problem, but not attempted here.

Second, suppose the goal is to make the best possible estimate of the circulation, using every available asset, including first order observations of density, SSH, etc. This is the reanalysis project, and is an appropriate way to model and estimate higher order properties of the circulation such as meridional heat transport and secular changes. Not the present goal.

Third, the middle ground occupied here is to take for granted that the main thermocline exists, but that it is flat, initially, throughout the basin, and that the velocity is zero,

$$h(x,y,t=0) = constant \;\; and \;\; \mathbf{V}(x,y) = 0 \;\; \text{for all} \;\; (x,y). \tag{34}$$

For a single layer model, $h = 500$ m, and the density difference $\delta\rho$ = 2 kg m^{-3} are reasonable, but more on the stratification in Sec. 3.6. The aim of these experiments will be to see how and how fast this stratification and velocity will adjust to an imposed wind stress.

4.3 Wind stress and its curl

The energy source in these experiments is a wind stress, $\tau(x,y)$, a tangential force per unit area imposed on the sea surface (the subscript $_o$ needed in Sec. 1.3 has been dropped since only the surface value of wind stress will be relevant from here on). The wind stress field has to be specified from outside the model, and here it will be represented by an idealization of the time-mean wind stress that has been

computed from observed winds over the oceans, Figs. (8 and 3).[11] So far as the Sverdrup relation is concerned, the crucial property of the wind stress field is the curl, $\nabla \times \tau(x,y)$. The shallow water model requires the wind stress itself, and here, just to keep it simple, we will specify the zonal component τ^x only, and assume that τ^x is independent of x, thus

$$\tau^x(y) \;=\; \xi \sin(n\pi y/L), \tag{35}$$

where the amplitude ξ is a positive constant. For the standard case of Sec. 3, $n \;=\; 1$, and the wind stress is eastward over the northern half of the basin, which mimics westerly winds, and westward on the southern half of the basin, i.e., easterlies (Fig. 16). The amplitude is taken to be $\xi = 0.1$ Pa, or about what is estimated for the mean wind stress by the westerlies. In the experiment of Sec. 3, this wind stress field is assumed to be constant in time once it is switched on. (In Sec. 5.1, the amplitude, ξ, will be made to oscillate with an annual cycle, and in Sec. 5.3 the wind stress will be made meridional.)

A very important parameter of (35) is the meridional length scale of the wind field; for n = 1,

$$L_\tau = L/n\pi \approx 1200 \text{ km}.$$

This is comparable to though a little less than two other important horizontal scales in this problem, the basin scale

$$L = 3600 \text{ km},$$

and the planetary scale on which f varies,

$$R_f \;=\; R_E/2 \approx 3300 \text{ km},$$

where R_E is the radius of the Earth. All of these length scales are much greater than the natural horizontal length scale of the baroclinic ocean, the baroclinic radius of deformation at latitude = 30 deg,

$$R_d \approx 40 \text{ km}.$$

The wind stress is applied to the surface layer of the model ocean as if it was a body force absorbed evenly throughout the surface layer. Thus the acceleration due to wind stress alone is just

$$\frac{D\mathbf{v_1}}{Dt} \;=\; \frac{\tau}{\rho_o h_1}, \tag{36}$$

which is a valid approximation of the full momentum balance for very short times, $t \ll 1/f$, a few hours or less. In a shallow water model, $d_{Ek} = h_1$, and here we have chosen $h \;=\; 250$ m (three layer model), or

[11] There are now more than a dozen wind stress climatologies that are consistent at the semi-quantitative level needed here (see Townsend, T. L., H. E. Hurlburt and P. J. Hogan, 2000, 'Modeled Sverdrup flow in the North Atlantic from 11 different wind stress climatologies', *Dyn. Atmos. Oceans*, **32**, 373-417.) The differences in detail between the various wind stress climatologies make an easily detectable and in some ways important difference in the computed Sverdrup flow, as does the basin topography.

500 m (single layer reduced gravity model), in order to have a realistic baroclinic wave speed. In the real, stratified ocean, d_{Ek} is less than this, typically 25 - 100 m. The Ekman current in this model is thus considerably weaker than in the real ocean, but the Ekman transport and the Sverdrup transport are the same whether the wind stress is absorbed in a comparatively thin surface layer (as actually occurs) or over the entire upper ocean layer that is wind-driven in the Sverdrup sense, as happens in a shallow water model.

The curl of this wind stress is

$$\nabla \times \tau(x,y) \;=\; -\frac{\partial \tau^x}{\partial y} \;=\; -\frac{n\pi\xi}{L}\cos(\pi y/L), \tag{37}$$

has an amplitude $\xi/L_\tau \;\simeq\; 0.8\times 10^{-7}$ N m^{-3} ($n \;=\; 1$). This is comparable to typical values of stress curl seen in Fig. (3), but less than the maximum values, which are roughly 2×10^{-7} N m^{-3}. The sign of the wind stress curl defines three regions: a central subtropical region where the stress curl is negative (clockwise turning), and tropical and subpolar regions where the curl is positive (anti-clockwise), Fig. (16).

This idealized stress field is perhaps least realistic for the tropical region insofar as τ^x goes to zero on the equator where observations indicate a fairly weak but nonzero westward wind stess. This error in the tropical winds is left in place because the goal is not so much a realistic simulation of the observed ocean circulation — which would require much more than just a better wind field — but rather to investigate how the wind-driven circulation varies with latitude. The idealized stress field Eqn. (35) is appropriate to this goal since the wind stress curl magnitude of (35) is the same over the three regions (tropical, subtropical and subpolar). β is also the same, and hence so too is the Sverdrup transport. The actual transport of the subpolar and tropical gyres is, however, *not* the same as Sverdrup transport because of zonal boundary effects that extend many hundreds of kilometers into the tropical and subpolar gyres (Sec. 5.2.3).

4.4 An expedient parameterization of drag on ocean currents

With a wind stress included, and if the intention is to integrate up to a possible steady state, then there has to be some mechanism to dissipate the energy and potential vorticity that are supplied by the wind. The present model follows the classic treatment by Stommel (1948)[1] in choosing a linear drag that is proportional to and anti-parallel to the velocity,

$$drag \;=\; -rh_o\mathbf{V}, \tag{38}$$

sometimes called Stokes drag. This has the dimensions of a stress/density, and the resulting acceleration is $-rh_o\mathbf{V}/h$ (as in the single particle model of Part 1, Section 5, aside from varying layer thickness). The

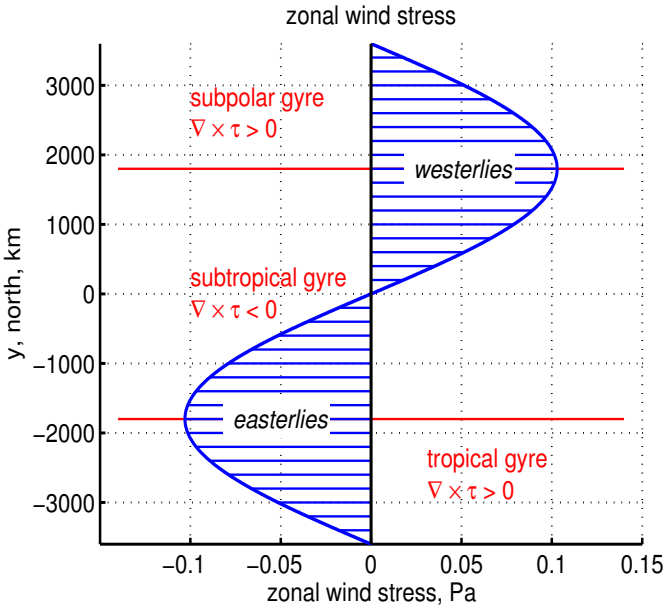

Figure 16: An idealized, zonal wind stress field that is applied to the shallow water model. The horizontal red lines appear in subsequent figures to show the axes of the easterly and westerly wind maxima, and thus the boundaries of the stress curl — negative (clockwise) in the large subtropical region between the westerly and easterly axes, and positive (anti-clockwise) over the smaller tropical and subpolar regions. These red lines correspond closely to the gyre boundaries.

coefficient r is taken to be $r = 1/(15 \text{ days})$, the smallest value of r that will allow the ocean circulation in this system (wind stress included) to reach a near steady state. Given a nominal layer thickness, $h \approx h_o$, the Ekman number at 30 ^{o}N is $E = r/f \approx 0.01$. This E seems quite small, but nevertheless, the model dynamics are almost certainly much more viscous overall than is the real ocean. Some later experiments will reveal find how this value of r is related to the natural width of the western boundary current, the radius of deformation.

In some contexts it might be argued that the Stokes drag represented by Eqn. (38) is a crude treatment of bottom drag. However, that is not plausible here since the active layer is not imagined to be in contact with a sea floor. It is probably better to think of the Stokes drag as nothing more than the simplest form of a drag or dissipation process that permits a steady state in this model.

4.5 Momentum and vorticity balances

With wind stress and drag included, the shallow water continuity (thickness balance) and momentum equations (derived in Part 2) are

$$\frac{Dh}{Dt} = \frac{\partial h}{\partial t} + \mathbf{V}\cdot\nabla h = -h\nabla\cdot\mathbf{V}, \tag{39}$$

$$\frac{D\mathbf{V}}{Dt} = \frac{\partial \mathbf{V}}{\partial t} + \mathbf{V}\cdot\nabla\mathbf{V} = -\nabla P/\rho_o - f\mathbf{k}\times\mathbf{V} + \frac{\tau}{\rho_o h} - \frac{rh_o}{h}\mathbf{V}. \tag{40}$$

The P is hydrostatic pressure anomaly defined in the next subsection. Notice that the thickness balance (39) is adiabatic in the sense that the thickness can change only by way of a divergent thickness flux, and

hence the net (basin integral) thickness is conserved.[12] This is not true for the momentum balance because of the wind stress source term and the Stokes drag dissipation term.

The shallow water potential vorticity is

$$q \;=\; \frac{\nabla\times\mathbf{V} \;+\; f}{h}, \tag{41}$$

and the q-balance is

$$\frac{Dq}{Dt} \;=\; \frac{\partial q}{\partial t} \;+\; \mathbf{V}\cdot\nabla q \;=\; \frac{1}{\rho_o h}\nabla\times\frac{\tau}{h} \;-\; \frac{r h_o}{h}\nabla\times\frac{\mathbf{V}}{h}. \tag{42}$$

Part 3 studied free Rossby waves that could be described via the mechanisms of q conservation, $Dq/Dt = 0$. Rossby wave-like motions are possible also in (42) and are a crucial part of the time-dependent dynamics discussed in Sec. 3.3.

4.6 Models of stratification and pressure

The last task is to connect the hydrostatic pressure P with the mass field, i.e., the stratification. Two models are used here.

4.6.1 Single layer, reduced gravity model, 1l-rg

The stratification model used most extensively exactly the shallow water, single layer, reduced gravity model of Parts 2 and 3, *viz.*, a single active upper ocean layer above a quiescent (infinitely deep) abyssal layer. In that event, the hydrostatic pressure anomaly within the upper ocean layer is just

$$P = g\delta\rho(h-h_o) \tag{43}$$

which gives a high pressure (anomaly) where the layer thickness is large. The equivalent SSH, which is useful for comparison to the observed SSH (Figs. 1 and 2) is just

$$\eta_1 = \frac{\delta\rho}{\rho_0}(h-h_o). \tag{44}$$

[12] This adiabatic property is especially convenient for some diagnostics of the time-changing stratification. However, it is also a liability, insofar as the layer thickness given by (39) can vanish under some plausible forcing regimes, especially at high latitudes. Vanishing layer thickness means instant death for a numerical integration. A partial remedy is to start with a fairly thick initial layer, 500 m, as is done here. Better would be the inclusion of a vertical mixing process that kept the upper layer thickness finite at all times, but which is not attempted here.

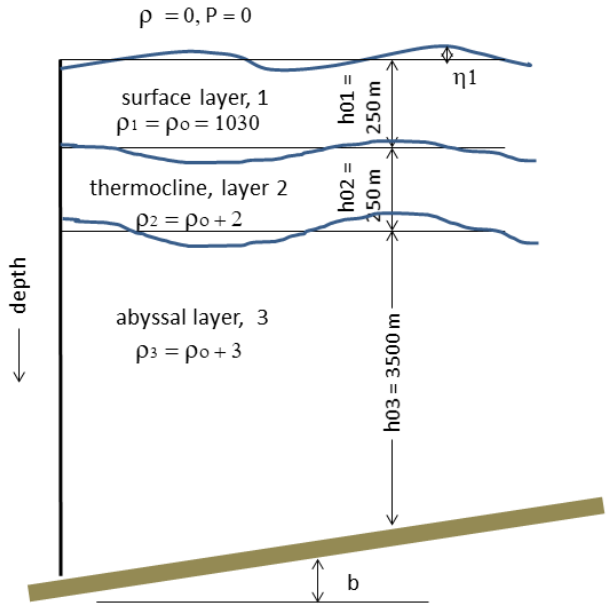

Figure 17: A three layer representation of the density stratification of the open ocean. The density and the thickness of each layer is noted. These thickness and density values are most apropos the subtropical ocean, but are presumed to hold throughout the basin. In this study the bottom depth b is presumed constant, i.e., a flat bottom.

The initial thickness is chosen to be fairly large, $h_o = 500$ m, and the density difference fairly small, $\delta\rho = 2$ kg m^{-3}. The nominal gravity wave speed is thus $= \sqrt{g\delta\rho h_o/\rho} = 3$ m sec^{-1}, which is a realistic baroclinic gravity wave speed for the subtropics, but a little high for the tropics and subpolar regions of the ocean. The radius of deformation at 30^o is $R_d = 42$ km, and the equatorial radius of deformation is $R_{deq} = \sqrt{C/\beta} = 400$ km.

4.6.2 Three layer, free surface model, 3l-fs

In this somewhat more realistic model, the stratification is represented by two upper ocean layers, and a comparatively thick abyssal layer (Fig. 17). This is still quite a truncated representation of the ocean's stratification, but it is sufficient to make a few important points (Sec. 8). The surface layer, h_1, is presumed to absorb all of the wind stress. Layer 2 is the thermocline, which follows the same momentum balance as does layer 1, though with zero wind stress, and layer 3 is the thick abyssal layer, same comment. In general, the thickness of the abyssal layer should include a significant term due to the spatially variable sea floor depth, which for now is taken to be uniform, $b = 0$. This three layer model is a straightforward generalization of the shallow water (layered) model of Parts 2 and 3, sometimes referred to as a stacked shallow water model. The initial thickness and the constant density difference, $\delta\rho$, across the top of these layers is taken to be

h_{0i}, m	ρ_i, kg m^{-3}	$\delta\rho_i$, kg m^{-3}
250	1030	1030
250	1032	2
3500	1033	1

The density and pressure of the overlying atmosphere are presumed to vanish and hence the density contrast across the sea surface, the top of layer 1, is $\delta\rho_1 = \rho_o = 1030$ kg m^{-3}, the nominal density of sea water. The density contrast across the top of layers 2 and 3 is very much less, $\delta\rho_2 = 2$ kg m^{-3} and $\delta\rho_3 = 1$ kg m^{-3}. In that sense, the ocean is very weakly stratified internally. Nevertheless, this internal stratification is of first importance for many oceanic phenomenon. The surface layer thickness is taken to be 250 m to delay the occurrence of $h \to 0$, and so is too large by a factor of about five. Hence the wind-driven surface layer currents in this model are weak compared to observations.

Layer thickness is a conserved quantity, barring vertical mixing (which undoubtedly occurs), meaning that the thickness of a given layer can change only if there is a divergence of volume flux within that layer, i.e.,

$$\frac{\partial h_1}{\partial t} = -\left(\frac{\partial (h_1 u_1)}{\partial x} + \frac{\partial (h_1 v_1)}{\partial y}\right), \tag{45a}$$

$$\frac{\partial h_2}{\partial t} = -\left(\frac{\partial (h_2 u_2)}{\partial x} + \frac{\partial (h_2 v_2)}{\partial y}\right), \tag{45b}$$

$$\frac{\partial h_3}{\partial t} = -\left(\frac{\partial (h_3 u_3)}{\partial x} + \frac{\partial (h_3 v_3)}{\partial y}\right). \tag{45c}$$

The horizontally-varying pressure anomaly is due to the displacement of the density surfaces away from their nominal, resting, flat state. From the bottom up, the interface displacements are

$$\eta_3 = h_3 - h_{o3} - b, \tag{46a}$$

$$\eta_2 = \eta_3 + h_2 - h_{o2}, \tag{46b}$$

$$\eta_1 = \eta_3 + \eta_2 + h_1 - h_{o1}. \tag{46c}$$

The motions of interest have very gentle accelerations compared to g, and so the pressure anomaly that accompanies the displaced density field may be assumed hydrostatic, i.e., due to the weight of the overlying water column. The hydrostatic pressure anomaly within each layer is then, from the surface layer down,

$$P_1 = g\,\rho_o\,\eta_1, \tag{47a}$$

$$P_2 = P_1 + g\,\delta\rho_2\,\eta_2, \tag{47b}$$

$$P_3 = P_2 + g\,\delta\rho_3\,\eta_3. \tag{47c}$$

The height of a given density interface thus depends upon the thickness of the fluid layers below, while the pressure depends upon the displaced density surfaces above. This bottom-up density/thickness relationship and top-down pressure/density relationship is what you would expect physically from hydrostatic pressure.

4.7 Appendix to Sec. 3: Normal modes of the 3l-fs model; one fast, two slow

The description of the motions that develop in the 3l-fs system may be aided by reference to the normal modes of the system. In fact, the normal modes show up fairly distinctly in the solutions that follow. A method for computing the normal modes was discussed in Part 2, Sec. 4.2 (and implemented via the Matlab script twolayer_eig.m available online, Sec 7.1) and so we will go straight to the results, the eigenvectors of velocity and thickness, and the eigenvalues that are the gravity wave (non-rotating) phase speeds of the modes,

Barotropic mode
gravity wave phase speed $C \approx \sqrt{g(h_1+h_2+h_3)}$ = 200 m sec^{-1}
radius of deformation at 30^o N, $R_d = C/f = 2800$ km
long Rossby wave speed at 30^o N, $\beta R_d^2 = 142$ m sec^{-1} = 1230 km day^{-1}.

$$\begin{pmatrix} u & h \\ 1 & 0.07 \\ 1 & 0.07 \\ 1 & 1 \end{pmatrix}$$

Baroclinic mode 1
phase speed $\approx \sqrt{g(\delta\rho_2+\delta\rho_3)(h_1+h_2)/\rho_o}$ = 2.9 m sec^{-1}
radius of deformation, 42 km
long Rossby wave speed, 0.033 m sec^{-1} = 2.9 km day^{-1}.

$$\begin{pmatrix} u & h \\ 1 & -0.7 \\ 0.41 & -0.3 \\ -0.1 & 1 \end{pmatrix}$$

Baroclinic mode 2
phase speed $\approx \sqrt{g\ \delta\rho_3\ h_1/\rho_o} = 1.5$ m sec^{-1}
radius of deformation, 22 km
long Rossby wave speed, 0.009 m sec^{-1} = 0.8 km day^{-1}.

$$\begin{pmatrix} u & h \\ 1 & 1 \\ -1 & -1 \\ 0 & 0 \end{pmatrix}$$

The eigenvectors of velocity are normalized so that the surface layer has an amplitude of 1; the thickness eigenvectors are normalized so that the largest amplitude in any layer is 1, Fig. (18).

Compared with the reduced gravity model, the crucial new property of this system is that it supports a barotropic gravity wave having a very, very fast phase speed, 200 m sec^{-1} $\approx$ 1700 km day^{-1}. Thus, a barotropic gravity wave can traverse an entire ocean basin in a few days, vs many months for a baroclinic wave. The corresponding long Rossby wave is almost as fast, $\approx$ 1200 km day^{-1}. The interface displacements of a barotropic mode are in phase with depth, but are largest at the sea surface and decrease linearly to zero at the bottom (not apparent in this figure). The pressure gradient is thus determined almost entirely by the displacement of the sea surface, and the associated barotropic velocity is essentially uniform with depth. When we say 'barotropic', this is what is intended. Such a barotropic motion is the only thing possible in a model having no internal stratification whatever. In this case there is internal stratification, and so there are also two baroclinic normal modes that, are, by comparison, quite sluggish, having phase speeds approx. 3 m sec^{-1} and 1.5 m sec^{-1}. The velocity in these baroclinic normal modes is depth-dependent, and has vanishing transport when integrated over the full water column. This is the

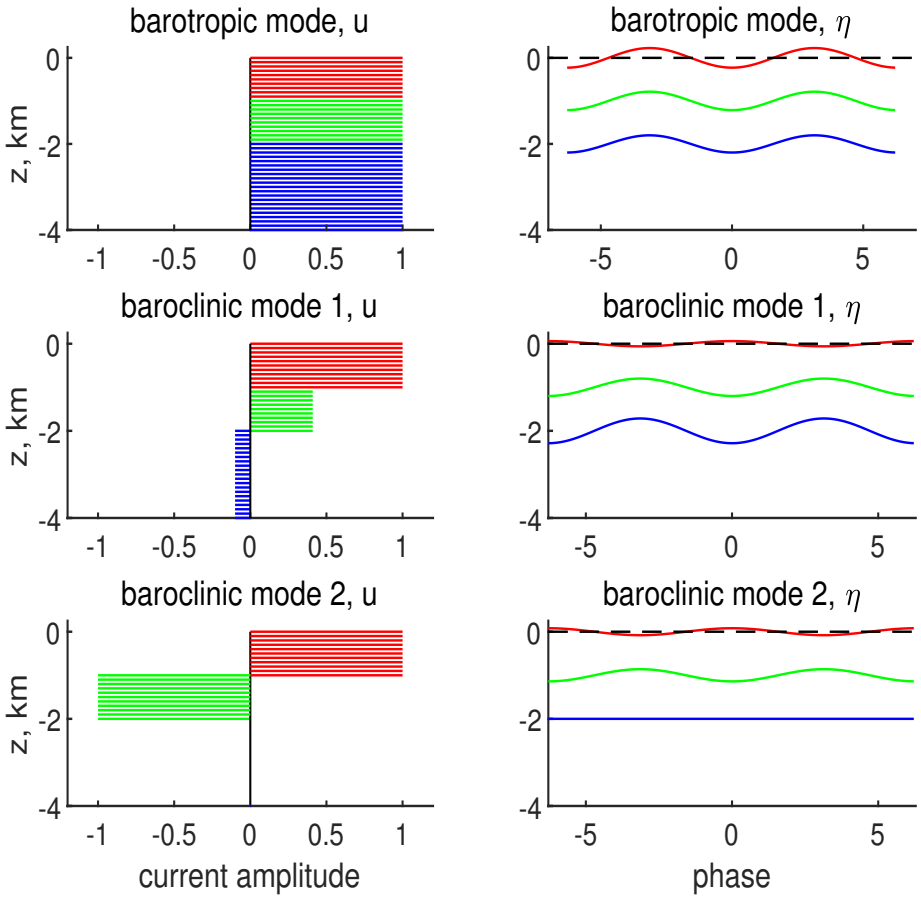

Figure 18: **(left)** Eigenvectors of the velocity from the three layer model. The layer-to-layer relative amplitudes of the velocity eigenvectors are meaningful, but their apparent thickness and thus depth is not to scale in this figure (the upper layer thicknesses have been quadrupled for the purpose of illustration). **(right)** Interface displacement computed from the eigenvectors of thickness by integrating from the bottom up, as in Eqn. (46). The amplitude of the interface displacements is schematic only but the phases are meaningful. For example, in the first baroclinic mode, the surface layer and the thermocline move up and down in phase in a 'sinuous' mode. Baroclinic mode 2 is confined almost entirely to the thermocline and surface layers, and is a 'varicose' mode in which the thickness changes in these layers are of almost equal magnitude and are out of phase.

usual meaning of 'baroclinic'. Baroclinic and barotropic waves can co-exist, or be present in isolation.

These normal modes are orthogonal and span the space, in the sense that any free motions (e.g., any wave) that can occur in the three layer model can be formed as the linear sum of these modes. Since all of the eigenvectors are required to make a complete set, there is no one that is more important than the others. However, the first baroclinic mode does have the most prominent role in the basin-scale adjustment process to an imposed wind, *viz.* the changeover from a (largely) barotropic state that forms very quickly after the wind starts, to a baroclinic, surface intensified state (Sec. 3.3) at much longer times. This is implicit in the choice of parameters of the single layer, reduced gravity model that was intended to mimic the first baroclinic mode of this more complete multi-layered model or of the real ocean.

5 The baroclinic circulation of the 1l-rg solution develops in four stages

Now, finally, we are ready to integrate and find some solutions (!). First up will be the single layer, reduced gravity model (secs. 5, 6 and 7), and then the more complex three layer model (Sec. 8).[13] The wind stress is switched on to full amplitude at time = 0 and held constant for 30 years. This long time is necessary to allow the solution to reach a (nearly) basin-wide steady state.[14] The circulation develops in four more or less distinct, temporal (but noncontiguous) stages that are characterized by the onset of specific phenomenon.

5.1 Stage 1: Short time, local response to the wind

5.1.1 Time scales: fast, slow, and steady

During the first few hours, the current is accelerated down wind at a rate $du/dt = \tau/(\rho_o h)$ (Eqn. 36). The Coriolis force turns the current to the right (northern hemisphere) after a time $1/f$, and hence a scale

[13] It would be more efficient of space on paper to if jump straight to the more complex model. But for the purposes of an introduction to this material, it seems (to this author) that it is preferable to start slowly and as simply as possible, and then add complexity. Be assured that everything that you may learn about the 1l-rg solution will be valuable in understanding the more complete results that will follow in Sec. 8.

[14] The wind has been blowing over the real oceans for a very long time. While the resulting circulation is seldom completely steady, nevertheless it isn't time-dependent because of an adjustment to a switched on wind, as occurs in these model experiments. The aim in integrating the model for so long is to be sure to get past the start up transient.

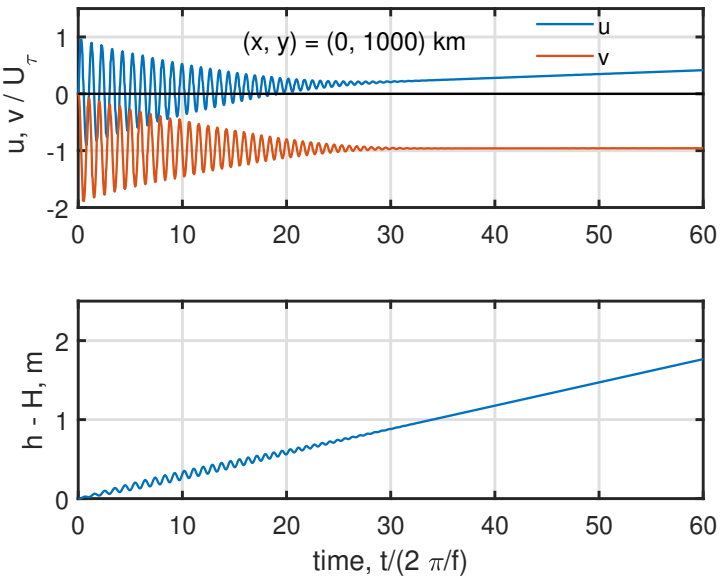

Figure 19: The short time evolution of currents. These data were sampled at 20 min. intervals on the northern side of the subtropical gyre, $(x,y) = (0,1000)$ km. This site was chosen since there is an appreciable wind stress, $\tau^x = 0.08$ N m^{-2}, which is eastward, and also a significant divergence of the Ekman transport. **(upper)** A time series of east and north current components, u and v. These are shown in units of the wind-driven velocity scale, U_τ. The high frequency oscillations are near-inertial motion; the time-mean (steady) v is southward Ekman flow which in these units has the value -1. **(lower)** Layer thickness anomaly, $h - h_o$, which shows a steady increase at about 15 m year^{-1}. This increase in layer thickness is caused by the convergence of Ekman transport, and the slow increase of the east current seen above is the associated zonal geostrophic flow (discussed in Sec 4.2). Notice the very small but dynamically significant oscillations of thickness in the first several weeks. These are evidence that the high frequency oscillations seen here are best described as near-inertial (very long wavelength) gravity wave motions.

estimate of the wind driven current amplitude that accounts for rotation is just

$$U_\tau = \frac{\tau}{\rho_o \, h f}. \tag{48}$$

The current components and the thickness sampled at a site on the northern side of the subtropical gyre (Fig. 19) display show three distinct time scales. There are fast time scale near-inertial motions having a period $1/f$, which is about a day at mid-latitudes. There is a very slow increase of the zonal current and of the layer thickness that here looks like a linear trend. Over a much longer time (shown below), this will emerge as a low frequency Rossby wave-like motion, and/or a part of the developing basin-scale circulation that is of primary interest. There is also a steady current in the meridional component, Ekman flow, that is the key intermediary between the wind and the basin-scale circulation.

Given the main interest is the large scale, low frequency circulation, then it is reasonable to ask whether it is desirable or necessary to also compute the high frequency phenomenon, the inertial motion. The shallow water system naturally includes both kinds of motions, but the high frequencies can be

suppressed easily enough by ramping up the wind stress over a few weeks (vs. the nominal, impulsive start). The resulting low frequency and steady circulation is the same either way the integration is started.[15] Thus, while inertial motion is ubiquitous in the oceans and is very important in some contexts, nevertheless it is not important here, and further discussion has been moved to an Appendix at the end of this section.

5.1.2 Ekman currents and transport.

The wind-driven current has a time-mean (Eqn. 60) that is consistent with Ekman balance modified very slightly by friction,

$$\begin{pmatrix} u \\ v \end{pmatrix} / U_\tau \approx -\left(\frac{1}{1+E^2}\right)\begin{pmatrix} E \\ -1 \end{pmatrix}. \tag{49}$$

This approximate solution for Ekman flow is indistinguishable from the solution computed by the shallow water model. The Ekman currents are present within hours of the start-up, and persist for the duration of the experiment since the wind stress is held steady. The amplitude of the Ekman current is $\propto U_\tau$, and is unrealistically small in the 1l-rg model because the layer thickness, $h_o \approx 500$ m, is much greater than a plausible Ekman layer thickness, more like 50 m. The direction of the Ekman current is approximately perpendicular and to the right of the wind stress, and so is southward at the site shown in Fig. (46) where the wind stress is eastward.

The Ekman transport is

$$M^y_{Ek} = hV_{S1} = -\frac{\tau^x}{\rho_o f} = -\frac{\xi}{\rho_o f}\sin(\pi y/L), \tag{50}$$

and is independent of the layer thickness. At the site shown in Fig. (46), which is equivalent to about 41 N, the Ekman transport is $M^y_{Ek} \approx -1.3$ m^2 sec^{-1}, which is a significant magnitude. To find the consequent *volume* transport, $[l^3\ t^{-1}]$, this M has to integrated over a horizontal distance, say the width of the North Atlantic basin, to find a volume transport (symbol N) at this y (latitude) of about $N_{Ek} = M_{Ek}2L = -10\times10^6$ m^{3}sec^{-1}, or 10 Sv, southward. This is a significant fraction of the total meridional transport at this latitude. Moreover, Ekman transport will be made up from the shallowest and generally the warmest water in the water column, and so makes a very important contribution to the heat flux carried by the ocean circulation. While Ekman transport is significant in its own right, it has an even more important indirect role in generating the changes in layer thickness that lead to geostrophic and Sverdrup transports, discussed in Sec. 5.2 and forward.

[15] This important result (no memory of the startup scenario) is consistent with the fundamental notion of the quasi-geostrophic system that the important low frequency motions are not far from geostrophic balance. The quasi-geostrophic system makes approximations (constant layer thickness, and a constant, background f, though with β) that are not consistent with some aspects of the shallow water solutions found here. Most GFD texts[2] include a discussion of quasi-geostrophic theory, and a superb online source aimed mainly at meteorologists is http://www.meteor.iastate.edu/classes/mt411/powerpoint/METR4424qgtheory.pdf

5.1.3 Latitudinal dependence; trouble on the equator?

It is notable that the amplitude of Ekman transport goes as $1/f$, and so for a given wind stress, the Ekman transport is considerably larger in the tropics than in the subpolar region. The same applies for a given pressure gradient and the amplitude of geostrophic currents.

The (near) equatorial region is noteworthy with respect to this latitudinal dependence insofar as $1/f$ is singular, and hence geostrophy and the Ekman relation imply a blowup of equatorial currents. However, the Coriolis force is not a dominant process on or very near the equator, as the Ekman and geostrophic relations presume, and happily, no such a blowup occurs in the numerical model solution. A somewhat trivial and parochial reason is that the wind stress given by Eqn. (35) has been assumed to vanish on the equator. But even with a significant equatorial stress included, which is more realistic of the real ocean, near-equatorial wind-forced currents are effectively limited by a rapid baroclinic response manifested in (or by) equatorial Kelvin wave propagation (Part 3, Sec. 4), which sets up a basin-wide pressure gradient that opposes the wind stress within only a couple of weeks. In other words, something else happens, a Kelvin wave and more, that was not anticipated by the rotational scaling Eqn. (48). In the experiments that discussed here, the circulation very near the equator is a consequence mainly of the larger scale circulation in the tropical gyre, which is the main interest, and so there is not occasion to discuss the (very interesting) equatorial phenomena.

5.2 Stage 2: Locally wind-forced, zonal geostrophic currents

5.2.1 Divergent Ekman transport changes the mass field

While Ekman transport is significant in its own right, it has an even more important indirect role by generating changes in layer thickness (mass field) and thus the pressure field. This indirect effect of the wind is apparent within only a few weeks as a slowly growing change in layer thickness (Fig. 46, lower) that continues for a few hundred or a few thousand days, depending upon location. The sense and the magnitude of the change is predicted well by the thickness tendency due to the divergence of Ekman transport alone (no geostrophic flows, yet) (Eqn. 12),

$$\frac{\partial h_{Ek}}{\partial t} \;=\; -\nabla\cdot(h\mathbf{V_{Ek}}) \;=\; -\frac{1}{\rho_o}\nabla\times(\frac{\tau}{f}),$$

and in the special case considered here that τ is $\tau^x(y)$ only, then

$$\frac{\partial h_{Ek}}{\partial t} \;=\; \frac{1}{\rho_o}\frac{\partial}{\partial y}\left(\frac{\tau^x}{f}\right) \;=\; \frac{1}{\rho_o f}\left(\frac{\partial \tau^x}{\partial y} \;-\; \frac{\beta}{f}\tau^x\right), \tag{51}$$

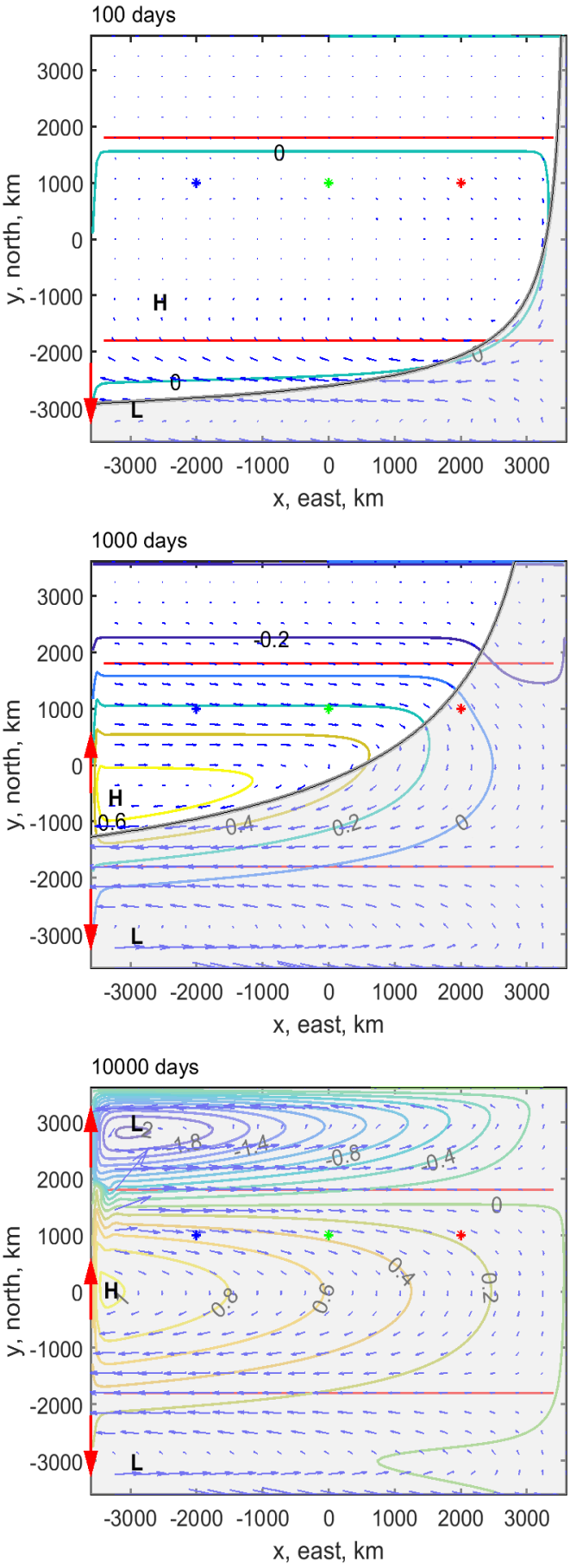

Figure 20: Three snapshots from the basic case, wind-driven experiment computed by the 1l-rg model and sampled at, from top to bottom, 100, 1000 and 10,000 days after the wind stress was switched on. The last time appears to be in a quasi-steady state throughout the interior of the basin. The thin red horizontal lines are the axis of the westerly and easterly wind stress (Fig. 16). The contours are of the inferred SSH anomaly in units of the Sverdrup geostrophic slope (Fig. 22) at basin center times the basin width, $2L$, about 0.4 m in this case. The field of small blue arrows are the current, though with the comparatively very large currents within the wbc omitted (shown in Sec. 3.3.2). The largest currents shown here are approx. 0.3 m sec^{-1}. The sense of the wbc is indicated by the red arrows on the west edge of the model domain. The blue, green and red dots along $y = 1000$ km mark the positions sampled in Fig. (23). The gray shading extends westward from the eastern boundary at the y-dependent speed of a long, baroclinic Rossby wave, $-\beta R_d^2$, and was sketched on top of the solution. Notice that the unshaded region to the north and west of the wave front (in the top two panels) shows mostly zonal currents, said to be the Stage 2 response. The shaded region to the south and east of the wave front is in Stage 3, Sverdrup flow. An animation of these data is threegyres.mp4 included in aCt-videos.zip??

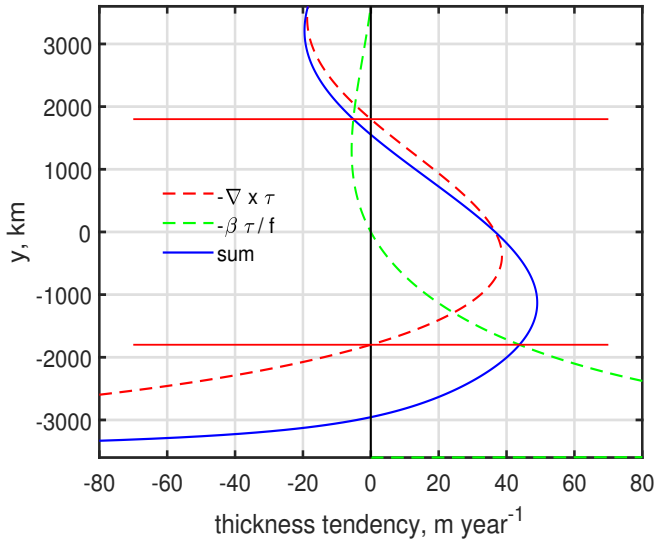

Figure 21: The divergence of the Ekman transport, Eqn. (51) (blue line), given the wind stress field Eqn. (35). Divergence of Ekman transport causes thickness tendency, which is a very significant aspect of the wind forcing on the ocean. At higher latitudes the divergence is due mainly to the curl of the wind stress $(\partial\tau^x/\partial y)/(\rho_o f)$ (dashed red line). At lower latitudes, the beta-induced divergence of the meridional Ekman transport $-\beta\tau^x/(\rho_o f^2)$ (dashed green line) is appreciable.

which varies with y only. This has terms proportional to the wind stress curl and to β times the meridional component of the Ekman transport. Both terms are important, with the beta term being especially important at lower latitudes on account of the factor $1/f^2$. (Fig. 21).

At the site sampled in Fig. (19), $y = 1000$ km on the north side of the subtropical gyre, the Ekman transport is convergent, and the rate of change in layer thickness is positive, and about 12 m year^{-1}. At the same distance from the gyre center but to the south side where the wind stress curl is the same but f considerably smaller, the thickness tendency is 45 m year^{-1}. The interface is pushed downwards by the converging Ekman transport, often called 'Ekman pumping'. When converted to SSH perturbation via the reduced gravity approximation, the equivalent SSH change is about 0.1 m per 500 days, Fig. (22), at the gyre center. This raised SSH indicates a growing high pressure that characterizes the subtropical gyre. Over the tropical and subpolar regions, the sense of the Ekman divergence is reversed and hence the layer thickness is decreased, and the interface is raised, 'Ekman suction'. The resulting SSH and surface pressure anomaly is then a low, that will characterize the steady subpolar and tropical gyres.

Because the wind stress field is assumed here to vary with y only, the Ekman pumping (or suction) also varies with y only (is independent of x) Fig. (22). Because the wind stress is constant once the wind stress is switched on, the Ekman pumping-induced thickness tendency given by Eqn. (51), is constant in time. The period during which the actual thickness rate of change is constant is said to be the Stage 2 of the transient response. Judging from Fig. (22), the duration of Stage 2 depends very much upon location: at $(x,\ y)\ =\ (0,\ 0)$ the thickness rate of change is constant for about 1000 days, and then becomes very small as Stage 3 Sverdrup flow begins to develop at that site (more on this in the next section). At the same y but closer to the eastern boundary, say $x = 2000$ km, the Stage 2 steady Ekman pumping goes on for only about 500 days.

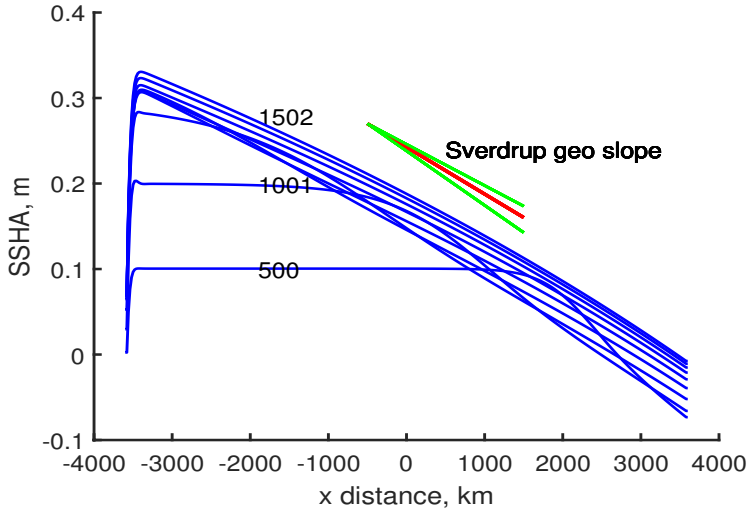

Figure 22: A sequence of sea surface height sections, $\eta(x)$, sampled at 500 day intervals up to 5000 days along $y = 0$, the center of the subtropical gyre. These were computed from the layer thickness via the reduced gravity approximation, Eqn. (44). The Stage 2 response is a steady rise of the sea surface, approx. 0.1 m per 500 days at this y, with no zonal tilt ($\eta(x)$ looks to be flat in this section during Stage 2). Stage 3 begins when the sea surface slopes down to the east and becomes quasi-steady; at $x = 2000$ km (eastern side of the basin) this starts at about 500 days, and at $x = -2000$ km (western side of the basin) the same thing starts much later, at about 1400 days. At this latitude, $\tau^x = 0$, and the meridional Ekman transport vanishes. Thus the quasi-steady meridional current over the interior region, $x \geq -3400$ km, is geostrophic and may be characterized by the zonal slope of the sea surface. The geostrophic slope expected from the Sverdrup relation Eqn. (1) for this y and given an average layer thickness, $h = 580$ m, is the red line that tilts down to the east. The flanking green lines are the sea surface slope for $h = 500$ and $h = 660$ m, which are found at the eastern and western ends of the section where the slope is slightly less and slightly greater than the average. This is a small but noticeable finite amplitude effect.

In this experiment — conducted in a closed basin and with a wind stress field that is independent of x — it is very compelling that the duration of Stage 2 is greater with greater distance from the eastern boundary. However, this need not be the case if the important zonal length scale comes from the wind field rather than the distance to the eastern boundary (an experiment discussed in Sec. 7.3).

5.2.2 Zonal geostrophic currents accompany the changing mass field

The change in layer thickness causes a pressure anomaly in the surface layer that develops very slowly compared to f, and so is accompanied by slowly growing, nearly geostrophic zonal currents,

$$\frac{\partial u_{S2}}{\partial t} = -\frac{g'}{\rho_o f}\frac{\partial^2}{\partial y^2}\left(\frac{\tau^x}{f}\right), \tag{52}$$

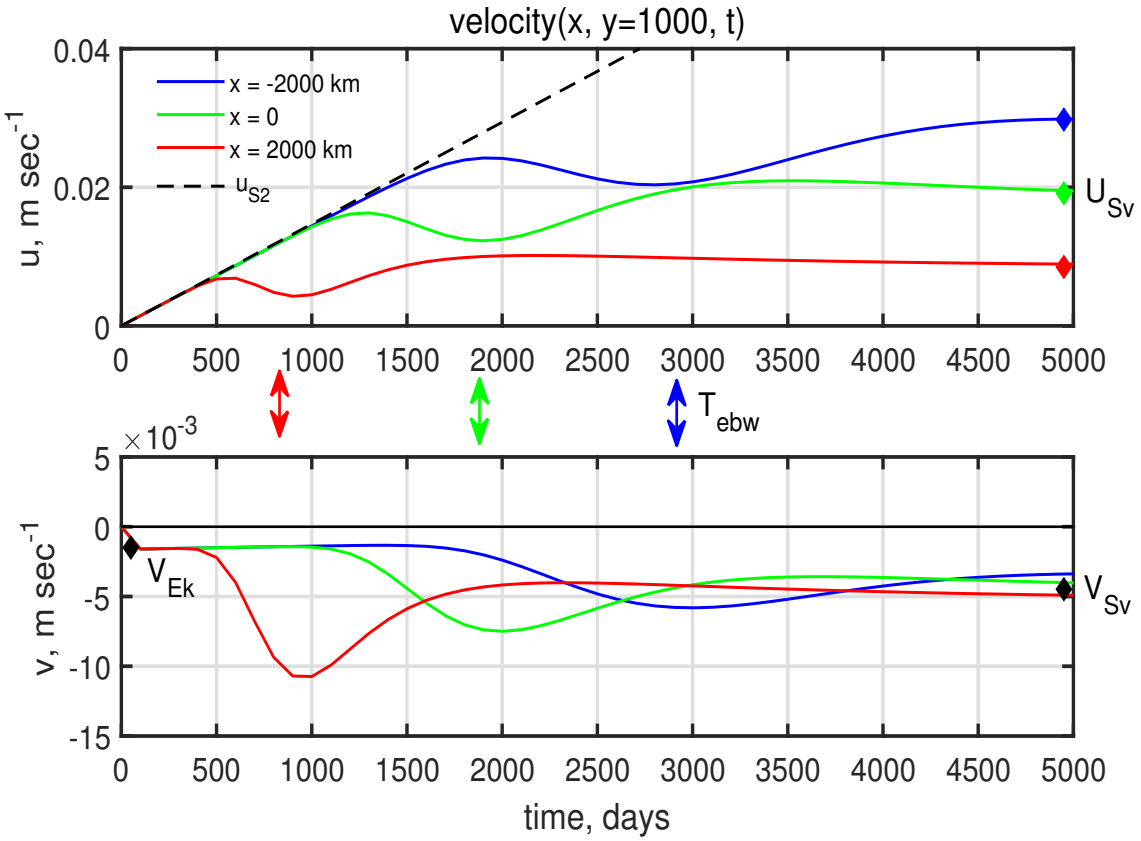

Figure 23: Zonal and meridional current components sampled in time along the northern side of the subtropical gyre, $y = 1000$ km, at three sites: $x = 2000$ km (red line), $x = 0$ (green line), and $x = -2000$ (blue line), which are nearest to farthest from the eastern boundary. The sampling time interval in this figure, 100 days, misses the inertial motions generated at start up (Sec. 4.1). **(upper)**. Zonal or east current component. The dashed black line is the estimate by Eqn. (53) of the zonal geostrophic current produced by Ekman pumping at this y and is the same at all x. The actual current follows this very closely for a few hundred or a few thousand days, depending upon distance from the eastern boundary. The red, green and blue double arrows denote the time, T_{ebw}, when a long Rossby wave starting on the eastern boundary at $t = 0$ is expected to arrive at the corresponding x. At around $t = T_{ebw}$, the zonal current shows a low frequency oscillation and then settles into a quasi-steady state consistent with the expected Sverdrup flow, marked by the colored diamonds on the right margin. Notice that the steady state zonal current increases approximately linearly with distance from the eastern boundary. **(lower)** Meridional or north current component. For short times, $t \leq T_{ebw}$, the meridional current is Ekman flow, Eq. (10), which is the same at these sites and noted by the black diamond near the left margin. The transition from Ekman flow to Sverdrup flow occurs around the time T_{ebw}. The expected Sverdrup flow at this y and for a nominal h is noted by the black diamond at right.

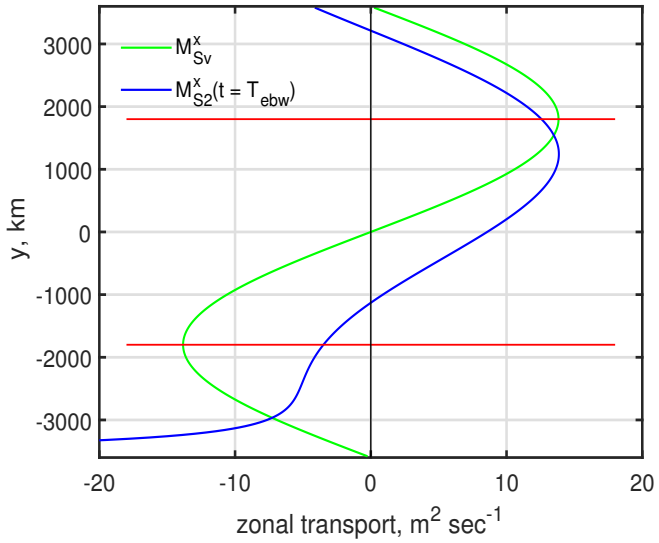

Figure 24: The zonal transport (per unit width) that accompanies the Sverdrup relation (green line that we will come to in Sec. 3.3) and the Stage 2 zonal current evaluated at $t = T_{ebw}$ (blue line) discussed in Sec. 4.1.3. At higher latitudes these currents are somewhat similar, but they are quite different at lower latitudes. The initial zonal currents in the interior closely match the Stage 2 profile (blue line) while the steady state zonal currents follow the Sverdrup profile (green line).

where the subscript $S2$ denotes that this is relevant to Stage 2 only. Because the stress is constant once switched on,

$$u_{S2}(y,t) \;=\; -\frac{g'}{\rho_o f}\frac{\partial^2}{\partial y^2}\left(\frac{\tau^x}{f}\right)t, \tag{53}$$

where t is the time elapsed since the start. In this experiment, the Stage 2 geostrophic current is purely zonal, since the Ekman pumping varies with y only, and it is independent of x, as is the wind stress. This is bound to fail on or very near the equator, where the Ekman balance is not appropriate, and also near a meridional (north-south) boundary, which has far reaching effects discussed below. It is also entirely baroclinic, there being no free surface and no barotropic pressure anomaly possible in the 1l-rg model.

The Stage 2 geostrophic zonal current (53) evaluated at $y = 1000$ km is sketched onto Fig. (23, upper) as a dashed black line. This gives a very good account of the actual zonal currents in the interior of the basin for a period of time — within the central subtropical gyre, (Fig. 23, the green line was sampled at $x = 0$) Eqn. (53) is valid for about 1000 days, just as noted before in the discussion of the Stage 2 layer thickness. The duration of Stage 2 depends upon both the latitude, being greater at higher latitudes, and greater also with increasing distance from the eastern boundary (the red, green and blue lines of Fig. (23) are at the same y, but increasing distance from the eastern boundary). An explicit estimate of the duration of Stage 2 will follow from considering the onset of the Stage 3 (Sverdrup) response in the next section.

The Stage 2 zonal geostrophic current given by (53) is proportional to $1/f^2$, and, all else equal, is considerably larger at lower latitudes than at higher latitudes (Fig. 24). Most of this essay emphasizes the meridional Sverdrup flow and western boundary currents, since these transport sea water properties equatorward and poleward (subtropical gyre) and so are generally of greater significance for Earth's climate. However, this locally wind-forced, zonal current is a robust signal in the transient response of this model, and is also prominent in the response of the tropical ocean to an annually-varying wind (O3 of Sec. 1.1.3 and Sec. 6.1).

5.3 Stage 3: Blocking at the boundaries and the onset of meridional Sverdrup flow

Because the present experiment is set within a finite basin having meridional boundaries, the x-independence of the Stage 2 zonal geostrophic currents can not go on forever. The zonal flow that approaches a meridional boundary is blocked, and must turn either north or south. Meridional boundaries thus have the effect of breaking the zonal symmetry that characterizes the Stage 2 response. As this 'blocking effect' of meridional boundaries becomes important, the overall pattern of the layer thickness anomaly and geostrophic currents begins to resemble a closed, gyre-like circulation, e.g., within the eastern part of the subtropical gyre, $x > 2000$ km, this is evident by about 500 days (Fig. 49).[16]

The blocking effect of the eastern meridional boundary — a zonal tilt of SSH and thus a change from purely zonal to at least partly meridional flow — spreads westwards into the interior of the basin. At $y = 0$, equivalent to 30^o N, this spreading is at a slow but steady rate of about 3 km per day (Fig. 49), which is roughly the westward propagation speed of mesoscale eddies at that latitude (Part 3). There are two fairly persuasive reasons to identify this westward 'spreading' of eastern boundary blocking as the westward propagation of a long, divergent Rossby wave reviewed in Sec 1.4. First, the balance of potential vorticity is consistent with long Rossby wave motions. The (low frequency) β-effect begins immediately with the meridional component of the current. Because the horizontal scale of the currents is the scale of the wind stress and very much larger than the radius of deformation, the β-effect produces mainly a change in layer thickness rather than a change of relative vorticity (Part 3, Section 2.4). In fact, the relative vorticity remains very, very small, i.e., $\nabla \times \mathbf{u} \ll f$ (this is not true near the *western* boundary, however). Thus the potential vorticity balance in the vicinity of the spreading eastern boundary blocking is linear and divergent, Eqn. (2), in common with long (baroclinic) Rossby waves. The motion evolves very slowly and is very nearly geostrophic, and so the first order wave/advection equation (18) is expected to be valid and predicts westward propagation at the baroclinic long Rossby wave speed (Eqn. 17). To test this, (Eqn. 17) has been used to define a gray-shaded mask that extends westward from the eastern boundary by

$$X \; = \; C_{longRo}\, t \; = \; -\beta \frac{C^2}{f^2}\, t, \tag{54}$$

Fig. (49).[17] The baroclinic long Rossby wave speed varies strongly with latitude; the gravity wave speed C is somewhat reduced at higher latitudes due to reduced stratification, but much more important at this early stage is the $1/f^2$ dependence, which indicates much larger C_{longRo} at lower latitudes. Notice that

[16] Imagine that the meridional boundaries are removed, and that the no-flow boundary condition on those boundaries is replaced by a symmetric or reentrant condition that $u(x = -L) = u(x = L)$, and the same for other variables. The domain would then be an east-west oriented channel, as more or less actually occurs in the Antarctic Circumpolar region. In a channel domain, the zonally-oriented thickness anomalies and geostrophic currents of the Stage 2 response would grow until the currents either became unstable and began to spread vertically and horizontally, or, drag on the current reached an equilibrium with the wind stress.

[17] The equatorial limit $f \to 0$ is handled by assuming that the westward wave speed can be no faster than the fastest, westward propagating equatorial Rossby wave, $-2C/3 \approx -2$ m sec^{-1}. See Part 3, Sec. 3 for a little more on equatorial wave dynamics.

the disruption of the Stage 2, zonal geostrophic flow is indeed closely coincident with the expectations of (54) at all latitudes (though with the near-equator aside, Fig. 49). Given this line of evidence, the westward spreading of the boundary blocking effect will be referred to as an 'eastern boundary Rossby wave', or 'ebw', despite that the profile $h(x,t)$ looks nothing like an elementary wave (Fig. 22).

The end of the Stage 2 local response to Ekman pumping and the start of the Stage 3 non-local or basin scale response may then be estimated by

$$Stage\ 2\ \rightarrow\ Stage\ 3: \quad t\ =\ T_{ebw}, \tag{55}$$

where

$$\boxed{T_{ebw}\ =\ -\frac{(L-x)}{C_{longRo}}} \tag{56}$$

with $(L-x)$ the distance from the eastern boundary. Thus T_{ebw} is $T_{ebw}(x,y)$ since C_{longRo} varies with y. Subsequent to T_{ebw}, the volume transport has a significant meridional component that approximates Sverdrup balance, Eqn. (1), Figs. (22) and (23), lower.

Judging from Fig. (23), the flow does not switch instantaneously from purely zonal to Sverdrupian at $t = T_{ebw}$. Rather, the eastern boundary wave has a very gradual leading edge, Fig. (22), and a close Sverdrup balance requires as much as $2*T_{ebw}$, which can be another few hundred or even a thousand days, depending upon latitude and distance from the eastern boundary. The key point is that the time required for the eastern boundary (blocking) effect to reach a given point in the interior is proportional to T_{ebw}, and thus is strongly dependent upon latitude and distance from the eastern boundary. In this important respect, the meridional flow of low latitude oceans exhibits a comparatively fast response to changing wind stress. The latitudinal-dependence of the baroclinic long Rossby wave speed Eqn. (17) is thus a very prominent, qualitative feature of the developing gyre circulation in this experiment, and often in the real ocean (Part 3, Sec. 2.6). (see Sec. 10.2, 5)[18]

5.4 Stage 4: Inter-gyre exchange, and basin-wide steady state

The three gyres come into steady state at quite different times, as described above, and clearly the laggard is the subpolar gyre. Even after 10 years, most of the subpolar region is still in Stage 2 and continuing to lose volume from the upper ocean since $\nabla\times\tau > 0$ (Ekman suction). The decrease of layer thickness within the subpolar gyre is quite pronounced, with h eventually reaching a minimum of about 100 m just

[18] Given that we are for now working with a single layer, baroclinic only model, there is only one long Rossby wave speed given by Eqn. (54). In the more complex model three layer model of Sec. 8 there will be other Rossby wave speeds, a very fast barotropic wave, and a slower, second mode, baroclinic wave that is associated with a sinuous motion of the thermocline (see Appendix to Sec. 3). The present baroclinic wave corresponds to the first baroclinic mode, and in-phase motion across the thermocline. If a model can represent only one wave mode, then this is the one to mimic.

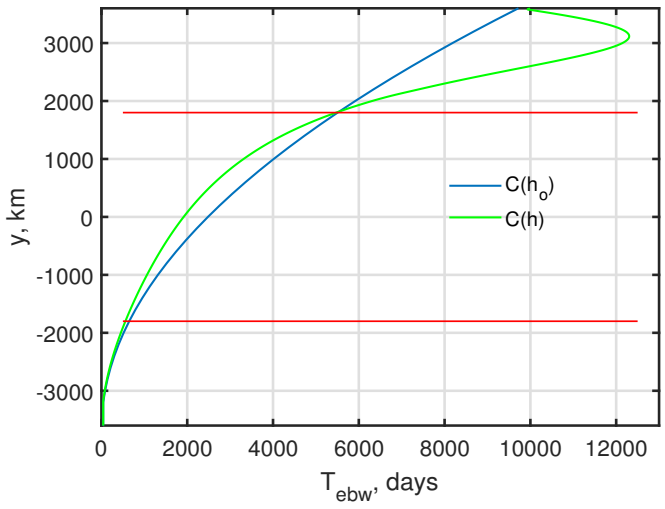

Figure 25: Transit time from the eastern boundary to the western boundary at the baroclinic, first mode, long Rossby wave speed. The blue line assumes the nominal layer thickness $ho = 500$ m for evaluating the baroclinic gravity wave speed, while the green line uses the actual, steady, zonal average thickness, which is somewhat different, especially in the western part of the subpolar gyre where $h \approx 100$ m. The expected transit times for the gyre centers are: tropical gyre, 350 days; subtropical gyre, 2500 (2000) days; subpolar gyre, 7500 (12000) days.

offshore of the western boundary current (Fig. 49, bottom). The basin-wide volume of the single layer of this model is conserved (there being no mechanism to convert abyssal water to upper ocean water, for example) and so the fluid that is expelled from the subpolar gyre is absorbed into the subtropics and tropics where the layers continue to slowly thicken more or less uniformly over the basin, long after the current in these gyres has reached a near steady state. A literal steady state of the subtropics, i.e., constant h and constant $\mathbf{v}$, here dubbed Stage 4, requires that the entire basin, subpolar region included, must be swept by an eastern boundary Rossby wave. Thus a basin-wide steady state requires an elapsed time

$$Stage\ 4: \quad t = max(T_{ebw}) = \frac{2L(f_o + \beta L)^2}{\beta C^2},$$

where *max* is evaluated over the basin as a whole. Given a nominal value of the gravity wave speed, $C = 3$ m sec^{-1}, then $max(T_{ebw}) \approx 9200$ days. In fact, the numerical solution indicates a somewhat longer time, closer to 12,000 days, mainly because the gravity wave speed is significantly reduced within the subpolar gyre (Fig. 25) due to the greatly reduced layer thickness in especially the western part of the gyre (Fig. 49, lower panel). (see Sec. 10.2, 4) This is one of several finite amplitude effects associated with large thickness changes away from the (arbitrary) initial condition of uniform upper ocean thickness.

Time out for a pop quiz. Suppose you were asked — How long does it take to establish steady Sverdrup flow in a mid-latitude basin? If all that you knew was the solution above, then you might reply,

Oh, several thousand days ... the eastern boundary wave is so slow ... yada, yada, yada.

Well, yes, but be warned that this response is incomplete, unless you make clear that it recognizes the *baroclinic* response only, while omitting the possible barotropic response. In practice, baroclinic is often implicit, since the baroclinic response is observable in historical (and modern) field data, and is most important for transport processes, e.g., meridional heat transport. But as will be seen in Sec. 8, a *barotropic* response, including Sverdrup flow, occurs much, much faster than seen here, and is then very

slowly supplanted by the baroclinic response described above. So, if the question is posed exactly as above, then a better (because more complete) response is

Just a couple of weeks ..... the barotropic waves are so fast, you know .....

5.5 Western boundary currents

At the same time that the interior of the basin is developing very slow and broadly distributed zonal and meridional (Sverdrup) currents, something quite different transpires near the western boundary. In the subtropical gyre, the flow near the western boundary is northward and very fast, up to 1 m sec^{-1}, within a narrow O(100 km) western boundary current (wbc). This western boundary current is a crucial part of the basin-scale flow, accounting for volume, energy and vorticity balance for the basin overall.

The Stage 2 response includes zonal currents that impinge on the western boundary just as much as occurs on the eastern boundary. The result is necessarily meridional currents along the western boundary that are subject to a low frequency beta effect. Propagation of this western boundary blocking into the interior by wave propagation requires an *eastward* group velocity. You may recall from Part 3, Sec. 2.3, that short baroclinic Rossby waves have an eastward group velocity, but the maximum eastward group velocity of these waves is very, very slow, only a few hundred meters per day, which is just a few percent of the western group velocity of long waves, C_{longRo}. Moreover, eastward group velocity obtains only for short waves, $kR_d \leq -1$ and $k \leq 0$. Such short waves are just barely resolved in the present numerical solution, and so it is not surprising there is no evidence of eastward spreading or propagation. Instead, the meridional currents along the western boundary appear to be effectively trapped onto the boundary on a width of 50 - 100 km (Fig. 30), which is roughly the local radius of deformation (discussed below in the Appendix).

The volume transport of a wbc is estimated by

$$N_{wb} \; = \; \int_{-L}^{-L+L_{wb}} v \; h dx,$$

where L_{wb} = 150 km, by inspection (or several times R_d). The steady state wbc of the subtropical gyre has a volume transport of about 28 Sv, and northward, which is opposite the Sverdrup volume transport of the interior. The western boundary currents of the tropical and subpolar gyres are southward, and opposite the Sverdrup transport in those regions.

The immediate cause of a western boundary current is zonal inflow: in the subtropical gyre, there is an inflow to the wbc at latitudes $0 \; > \; y \; > \; -L/4$, and an outflow at latitudes $L/4 \; > y \; > \; 0$. During the first one thousand days of the experiment, the zonal current near the wbc is mainly the Stage 2 geostrophic flow discussed in the previous subsection. As time runs, the inflow is better described as the

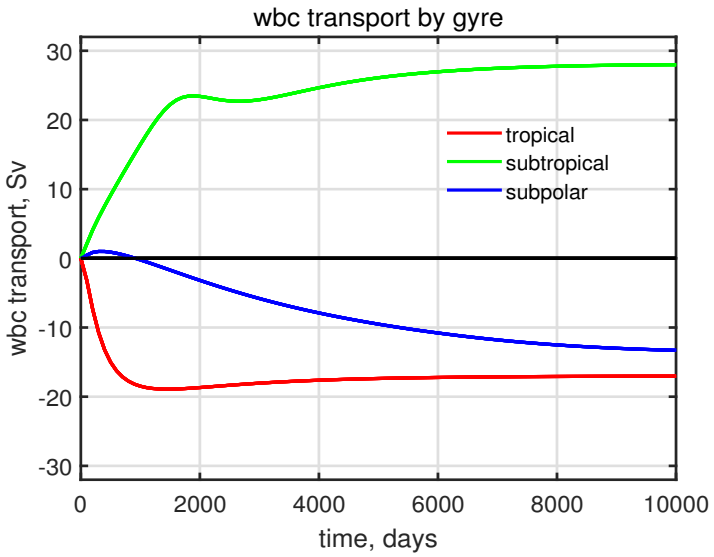

Figure 26: Meridional volume transport N_{wb} within the western boundary currents of the three gyres. These were sampled at the north-south center of the gyres. Notice that the wbc of the tropical gyre reaches a steady state within about 700 days after the start of the experiment, while the wbc of the subpolar gyre requires much longer, roughly 12,000 days.

Sverdrup zonal flow. From this we can infer that the time scale for development of a wbc is proportional to the time scale of U_{S2} and thus proportional to $1/f^2$, i.e., much faster at lower latitudes (Fig. 30, cf upper and lower panels). The subtropical wbc begins to appear within a few hundred days after the start of the experiment, and reaches its full, steady state amplitude in about 2000 days. This is roughly the same time scale on which the subtropical gyre interior reaches steady state Sverdrup flow, and comparable to the transit time of the eastern boundary Rossby wave. Two things to note: the arrival of the eastern boundary Rossby wave on the western boundary is *not* the dramatic event that seems to be implied, and, the coincidence in time does not imply that the eastern boundary Rossby wave is the cause of the western boundary current except in a very indirect way. The arrival of the eastern boundary wave implies that the interior region to the east and equatorward (subtropical gyre) is close to being in steady state with regards to meridional transport and the Sverdrup relation, and that is what really counts. The same attends the volume transports of the wbc in the other gyres: — wbc steady state requires about 1000 days in the tropical gyre, and about 10,000 - 12,000 days in the subpolar gyre (Fig. 26), a factor of roughly ten.

There is a very strong hint in the discussion above that a wbc is just a mirror of (compensates for) the Sverdrup flow of the interior. To test this in detail, we can evaluate the mass balance over a control volume that is the entire southern half of the basin, the light green shading of Fig. (27) having an area A. The areally integrated continuity equation appropriate to this control volume is

$$A\frac{dh_{avg}}{dt} = \oint h\mathbf{V}\cdot\mathbf{n}ds$$

since our shallow water model has no source term, i.e., no mechanism to convert upper layer water to abyssal water, for example. Thus the areal-average thickness of the layer within the control volume can change only if there is a net volume flux across the horizontal sides of the control volume. The line integral may be divided into pieces that represent the flow across specific sides of the control volume,

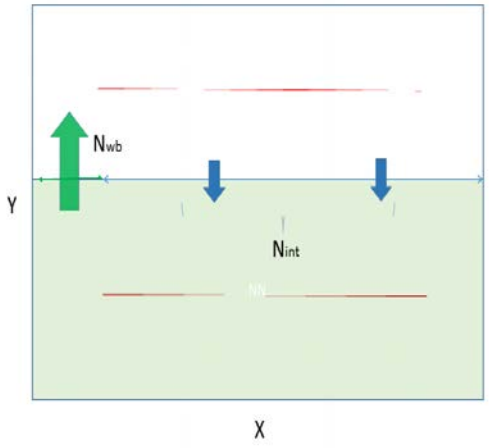

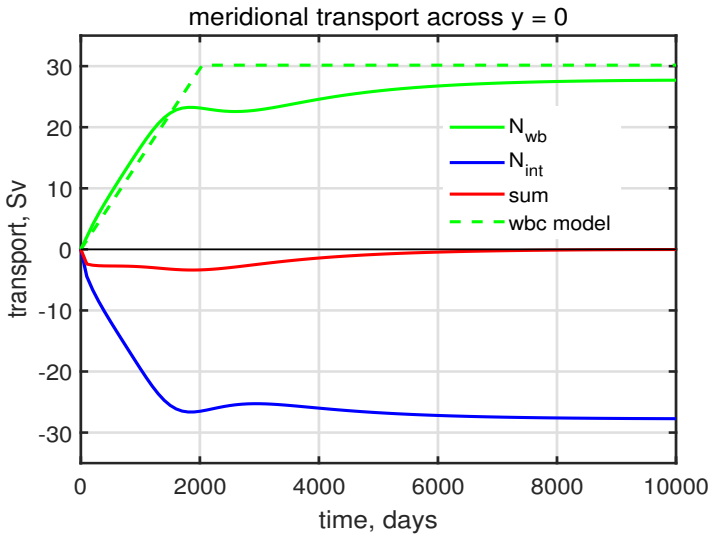

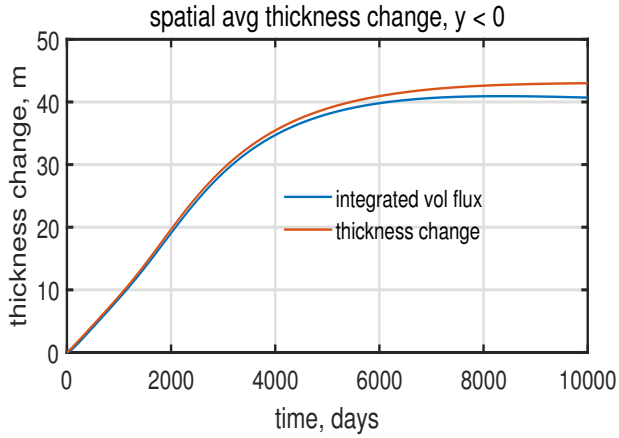

Figure 27: **(upper)** A control volume (light green area A) defined over the southern half of the basin. The volume transport through $y = 0$ is evaluated over a western boundary region, N_{wb}, and the interior, N_{Sv}. **(middle)** The volume transports through $y = 0$ (green and blue lines) and their sum (red line). The dashed green line is a model of wbc transport, Eqns. (62) and (63) discussed in the Appendix to this section. **(lower)** The time-integrated net volume flux into the control volume (blue line) and the observed thickness change over the control volume (red line), about 40 m. Given the adiabatic continuity equation (39), these should be exactly equal aside from numerical errors.

e.g., in this case

$$N_{int} \;=\; \int_{-L+L_{wb}}^{L} v\,h\,dx,$$

is the volume transport across $y = 0$ in the interior of the basin (no need to identify this as Sverdrup flow), and the volume flux of the comparatively very narrow and intense northward flowing western boundary current (Fig. 30) is N_{wb}, already noted. The integrated mass balance (continuity equation) then reads

$$A\frac{dh_{avg}}{dt} \;=\; N_{int} \;+N_{wb}.$$

Either of the volume flux terms is considerably larger than the storage term, but they do not sum to zero: during the first several thousand days of the experiment there is a small but significant net meridional transport across $y = 0$, $N_{Sv} + N_{wb}$, (the red line of Fig. 27, middle). The subtropical gyre is a region of increased layer thickness, about 40 m on areal average, and thus elevated SSH and higher pressure. Indeed, the subtropical gyre is characterized by this high pressure, as noted above. The volume of fluid required to thicken the layer in the region south of $y = 0$ is provided by (must be provided by) the basin-wide meridional volume flux across $y = 0$ (Fig. 27, lower). As the region to the south of $y = 0$ reaches a steady state and $\partial h/\partial t = 0$, which requires a little more than 5000 days, the net volume flux across $y = 0$ also vanishes. This is somewhat longer than the time required to reach a steady state within the subtropical gyre interior at this latitude.

Remarks on the real Gulf Stream. This picture of a simple, direct compensation between interior and wbc transport is valid in a wind-driven circulation experiment set within an enclosed basin. However, the real Gulf Stream has a considerably more complex relationship with the interior. There is no doubt a significant wind-driven component to the Gulf Stream transport of this sort, but there is more. The global overturning circulation noted several times in this essay includes about 15 Sv of upper ocean flow to the north and occurring within the wbc, and a comparable return flow of very cold water to the south within dense bottom currents. Thus the real, baroclinic Gulf Stream (above about 1500 m, say) has a magnitude about half again greater than the Sverdrup transport of the subtropical gyre. A second process, eddy generation via instability of the Gulf Stream, produces fairly narrow, recirculating flows on either side of the Gulf Stream (near Cape Hatteras) that are mainly barotropic. The amplitude of the associated currents is not large compared to the surface flow, but because this flow is depth-independent, carries a very large transport. If only the northeastward flow is considered (and the compensating southwestward flow on the flanks omitted), then the estimated Gulf Stream transport can be very large, exceeding 100 Sv. These barotropic recirculating flows may not contribute to meridional heat flux, say, but they surely do make fraught the estimation of the wind-driven component of the real Gulf Stream.

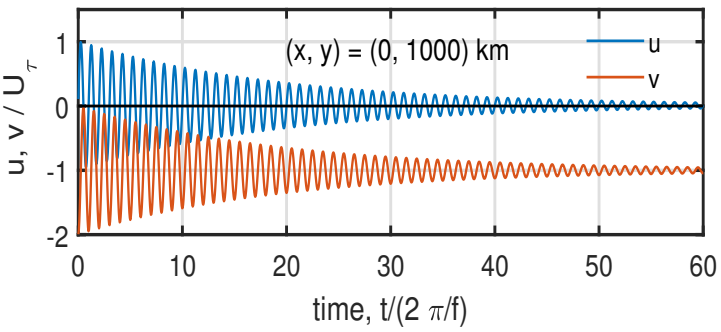

Figure 28: The solution for local, damped wind-driven motion, Eqn. (60) that may be compared to the full model solution, Fig. (19). There is no layer thickness shown here since in this local model there is no velocity divergence, and hence $h = h_o$ and constant. For that reason there is also no linear trend in the zonal component.

5.6 Appendix to Sec. 4

5.6.1 A local model of wind-driven inertial and Ekman motions

The dominant motions in the first several weeks after the wind is switched on are inertial motions and Ekman currents (Fig. 19). These are essentially local phenomenon that may be modelled by the linearized subset of Eqn. (40) in which all the terms involving horizontal spatial derivatives are omitted,

$$\frac{\partial h}{\partial t} = 0, \tag{57}$$

$$\frac{\partial u}{\partial t} = fv - ru + \frac{\tau^x}{\rho_o h}, \tag{58}$$

$$\frac{\partial v}{\partial t} = -fu - rv.$$

You may notice that these equations are exactly the form used to model the motion of a dense parcel released onto a slope (Part 1, Sec. 5), though here the external force is a wind stress rather than a buoyancy force. These equations are local in the sense that they apply to what amounts to a single parcel, or since the equations are linear, a single position, and that does not interact in any way with its surroundings, i.e., no pressure gradient and no advection.

Given an initial condition that is a state of rest,

$$u(t=0) = 0 \text{ and } v(t=0) = 0,$$

the solution for the so-called Stage 1 velocity is, in dimensional form,

$$\begin{pmatrix} u \\ v \end{pmatrix} = \frac{\tau^x}{\rho_o f h}\left(\frac{1}{1+(r/f)^2}\right)\begin{pmatrix} r/f + \exp(-rt)(\sin(ft) + (r/f)\cos(ft)) \\ -1 - \exp(-rt)(\cos(ft) - (r/f)\sin(ft)) \end{pmatrix}, \tag{59}$$

In non-dimensional form the same solution is

$$\begin{pmatrix} u \\ v \end{pmatrix}/U_\tau = \left(\frac{1}{1+E^2}\right)\begin{pmatrix} E + \exp(-E\gamma)(\sin(\gamma) + E\cos(\gamma)) \\ -1 - \exp(-E\gamma)(\cos(\gamma) - E\sin(\gamma)) \end{pmatrix}, \tag{60}$$

where

$$\gamma = tf$$

is time scaled by the rotation time, $1/f$,

$$E = r/f \tag{61}$$

is the Ekman number, and the velocity scale

$$U_\tau = \tau^x/(\rho_o f h)$$

repeats Eqn. (48). The velocity of the local model (60) is the sum of a time-dependent inertial oscillation and a time-independent Ekman flow (Fig. 28).

Inertial oscillations are a clockwise rotation of the velocity at a rate f; at 30 N, the frequency is the Earth's rotation rate, 7.292×10^{-5} sec^{-1}, and the period is approximately one day.[19] At the site sampled in Figs. (46) and (28) $(x,\ y) = (0, 1000)$ km, equivalent to about 41 ^{o}N, the inertial period is about 17 hours and the wind stress is about $\tau^x = 0.008$ N m $^{-2}$. The amplitude of the inertial oscillation at this site is thus $U_\tau \approx 0.002$ m sec^{-1}, which is unrealistically small because of the excessively thick wind-driven layer, $h = 500$ m. If the amplitude of inertial oscillations played an important part in the low frequency response (they do not), then this would be a serious shortcoming of a single layer shallow water model that was configured to have a reasonable baroclinic wave speed. The inertial oscillation of (60) decay with time as $\exp(-Eft)$, e-folding in 15 days due to Stokes drag.

The inertial oscillations computed by the full shallow water model Fig. (19) differ from the solution of the local model (60) in that the frequency of rotation is a few percent greater than f (very hard to see this in the present figures) and the amplitude decay is somewhat faster than is given by the frictional e-folding alone. These two features plus the very small but nevertheless significant oscillation of the layer thickness (Fig. 19, lower) indicate that what look like inertial oscillations in the numerical model solution are better described as very long wavelength, near-inertial gravity waves. The longer term (several weeks) evolution of the inertia-gravity waves is significantly influenced by the variable f of this shallow water model, which leads to propagation towards the equator.

One of the subthemes of this essay is the latitudinal dependence of the ocean response and circulation. With respect to the steady circulation, the natural demarcation of latitude is by gyre, i.e., supolar gyre, subtropical gyre. At this very early stage there are no gyres, and so to investigate how the response varies with latitude it is sufficient to pick two sites, the easterly and westerly wind maxima, roughly 15 N and 45 N, and consider the zonal, u velocity component only (Fig. 29). The data are shown in two formats; in dimensional form (Fig. 29, left column) and in nondimensional form (right column) in which the speed is normalized with $U_\tau = \tau/(\rho_o f h)$ and time with the local inertial period, IP = $2\pi/f$. The dimensional format doesn't require any explanation (which is a good thing) but neither does it give

[19] The inertial period is less than a day by the fraction $\approx 1/365$. Can you recall from Part 1 why the inertial period at 30 N is less than a day, and why that value?

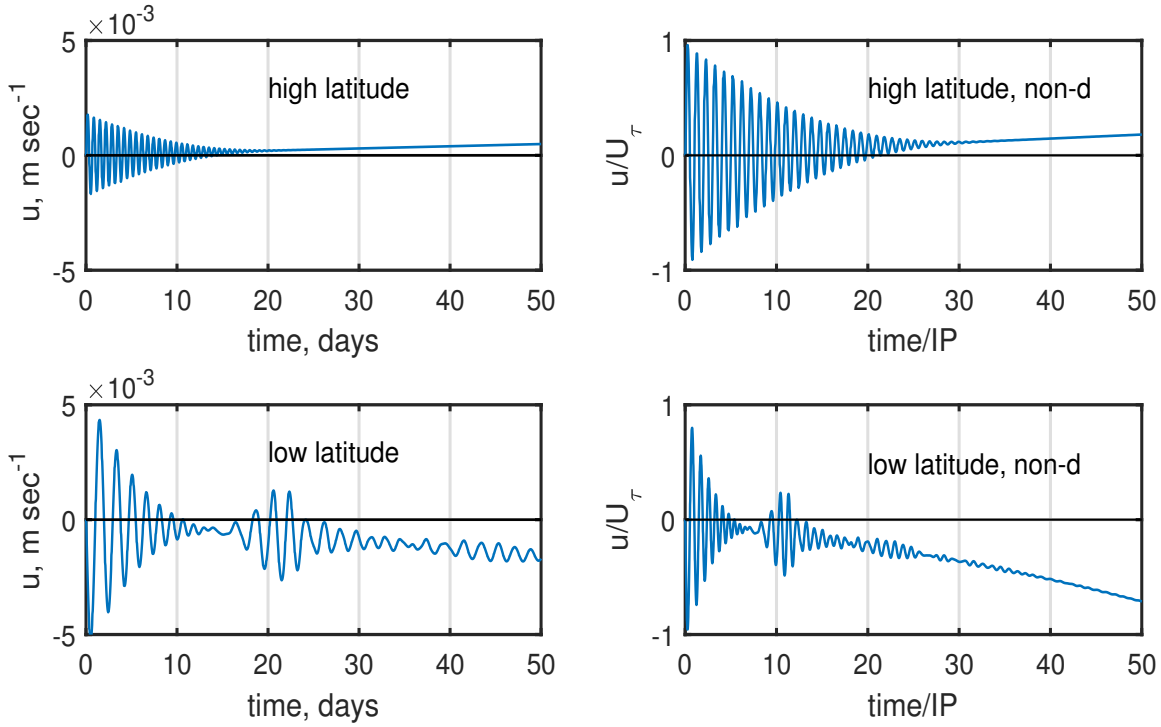

Figure 29: The zonal or u component of velocity sampled at two sites, a comparatively high latitude site on the axis of the westerly winds, **(upper row)** and a low latitude site, the axis of the easterly winds **(lower row)** . The data are plotted in dimensional format **(left column)** and in a non-dimensional format **(right column)**. The former emphasizes the significant differences in the response due to the differing latitude, while the latter makes clear that the sites have two things in common; the amplitude of near-inertial motion goes as U_τ and the period of the oscillation is approximately the local inertial period.

anything more than a qualitative hint at parameter dependence, i.e., it is clear that the amplitude of inertial motion and the period of the inertial motion is greater at lower latitude.

Given the non-dimensional format, it is evident that the amplitude is ≈ 1 at both sites, evidence that the amplitude does indeed vary with f and τ as U_τ implies it should. Moreover, the period of the oscillation is very close to 1 IP at both sites and thus the period of the high frequency oscillation is $\propto 1/f$. Neither of these results is the least bit surprising given the solution Eqn. (60), but could have made these inferences even without an explicit solution given the appropriate nondimensional scaling. The latter may be found by dimensional analysis and then verified with numerical experiments, a procedure that is generally far more accessible than is an explicit solution. If the main goal of a modeling study is to explore and expose parameter dependence rather than simulation of an observed case, then the non-dimensional format will often have real merit. That is certainly a part of the goal here, and so a nondimensional format (units) will be used when it adds value.

5.6.2 Simple models of a western boundary current

Transport in a transient wbc. A very simple estimate of the time-dependent western boundary transport can be constructed on the basis that the wbc transport will be opposite and equal to the meridional Sverdrup transport to the east of the eastern boundary Rossby wave, i.e., as if

$$N_{int} \; + \; N_{wb} \; = \; 0.$$

and now $N_{int} = N_{Sv}$. While the eastern boundary wave is in transit across the basin,

$$0 \; < \; t \; < \; T_{ebw}(x=-L,y); \quad N_{wb} \; = \; -\frac{\nabla\times\tau}{\rho_o\beta}\, C_{longRo}\, t \; = \; -N_{Sv} \tag{62}$$

The wind stress curl and the long Rossby wave speed are evaluated at the y of the wbc observation, in Fig. (26), the center of the subtropical gyre, $y = 0$. After the wave arrives on the western boundary, the western boundary transport is assumed to exactly compensate the steady state Sverdrup transport across the basin interior and so for longer times,

$$t \; > T_{ebw}; \quad N_{wb} \; = \; constant \; = \; -\frac{\nabla\times\tau}{\rho_o\beta}\, 2L. \tag{63}$$

This estimate (62) and (63) is shown as the green dotted line of Fig. (27) middle, and is a plausible first description of the actual (numerical) boundary current transport, though far from perfect. There are two ways that this model and this estimate are inconsistent in detail with the numerical solution: the transition from Stage 2 purely zonal, local flow to Stage 3 Sverdrup flow is not instantaneous as Eqn. (62) assumes, and, the northward wbc transport does not return all of the southward Sverdrup transport during the first several thousand days of the experiment when some fluid is stored at the rate of several Sv within the thickening layer south of $y = 0$. These fairly significant details aside, what is most striking and robust is that a wbc develops much faster in the tropical gyre, within very roughly 1000 days, than it does in the subpolar gyre, where the time scale is closer to 10,000 days (Fig. 26). This very large difference in the rise time of the wbc in these gyres is a consequence of the $1/f^2$ dependence of the Stage 2, locally wind-forced geostrophic current, Eqn. (53), and of the long Rossby wave transit time, Eqn. (56).

Western boundary current width. The water that makes up the western boundary current of the subtropcial gyre flows into the boundary current from the eastern side. This inflow begins with the start of the Stage 2 zonal current, and continues into the steady state. Assuming that the inflowing water conserves potential vorticity and that the across stream momentum balance is geostrophic, leads to an estimate of the boundary current profile and width. (See Stommel (1966) [1], Ch. 8, who has an interesting discussion of this applied to the actual Gulf Stream.) The relative vorticity is approximated well by the x variation of the north component of the current, and hence the potential vorticity inside and just outside of the western boundary current are

$$\frac{f+\frac{\partial v}{\partial x}}{h} \; = \; \frac{f}{h_0}, \tag{64}$$

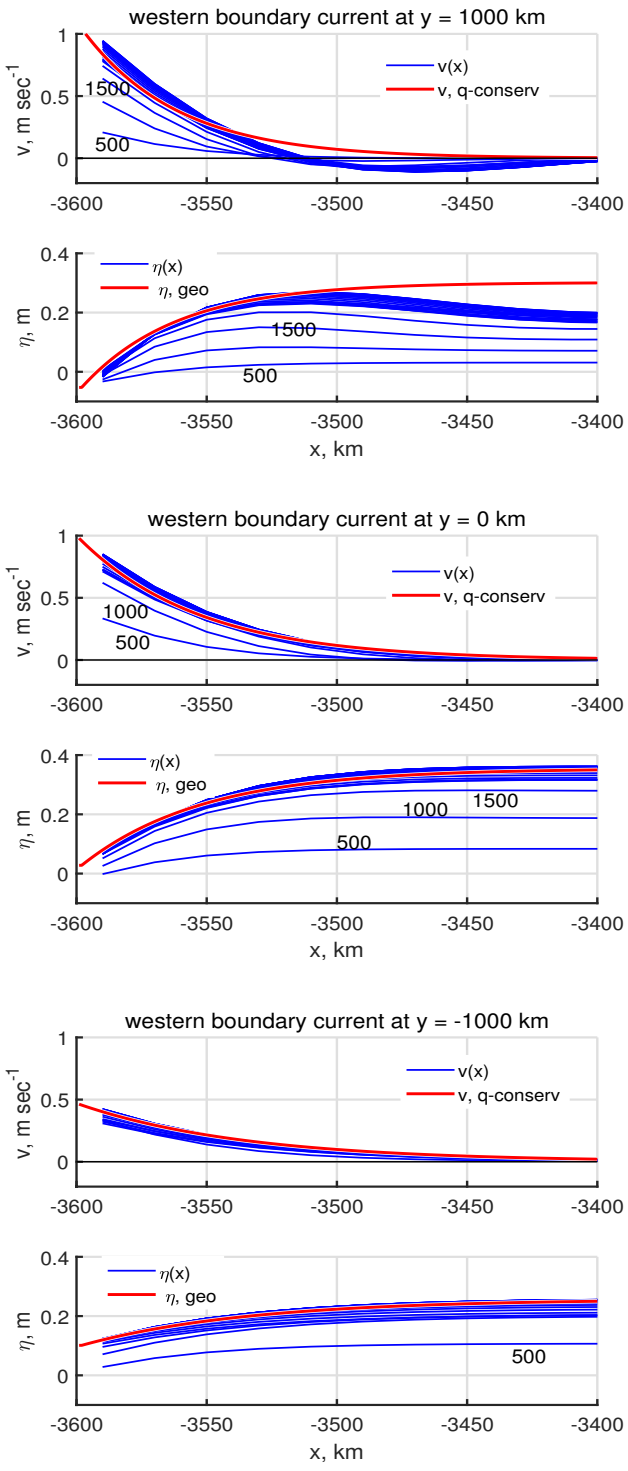

Figure 30: Zonal profiles of the north velocity and the SSH anomaly within 200 km of the western boundary at three sites within the developing subtropical gyre: **(upper)** $y = 1000$ km, on the north side of the subtropical gyre, **(middle)**, $y = 0$, the center of the subtropical gyre, and **(lower)** $y = -1000$ km, the south side of the subtropical gyre. Profiles are shown as the blue lines at 500 day intervals. The north velocity expected for a q-conserving inflow is shown as the red line, an exponential with the x scale being the radius of deformation, at $y = 1000$ km, $R_d = 36$ km; at $y = 0$, $R_d = 45$ km, and at $y = -1000$ km, $R_d = 64$ km (discussed in Sec. 3.2). The corresponding SSH anomaly profiles are computed from the respective q-conserving velocity using geostrophy (also plotted as a red line). Notice that currents and stratification at the more southerly site (lower panels) reach steady state in about 500 days, while the higher latitude site (upper panels) requires about 2000 days.

where h_0 is the thickness just outside the boundary current. If we evaluate this at $y = 0$, $h_0 \approx 600$ m. The momentum balance is very nearly geostrophic,

$$fv \;=\; g' \frac{\partial h}{\partial x},$$

which may be combined with (64) to form a single equation for the boundary current velocity,

$$\frac{\partial^2 v}{\partial x^2} \;= \frac{f^2}{g' h_0} v. \tag{65}$$

This has exponential solutions

$$v(x) \;=\; V_0 \exp\left(\pm((x+L)/R_d\right), \tag{66}$$

where $R_d \;=\; \sqrt{g'h}/f$ is the familiar radius of deformation. Suitable boundary conditions are that $v \to 0$ as $x+L$ becomes large, which selects the minus sign in the exponential. For the central latitude of the subtropical gyre, $y = 0$ of Fig. (27), $V_0 = 1.0$ m sec^{-1}. The solution for $v(x)$ is then complete, and the corresponding geostrophic thickness, represented here by the SSH anomaly η, may then be easily computed as well (Fig. 27, red lines). These make quite good representations of the actual velocity and thickness (or η), which suggests that the width of the western boundary current is approximated well by the radius of deformation, the natural length scale of the shallow water model. That is a neat and satisfying result that will be cited repeatedly in the description of the circulation. However, closer inspection and thought suggests that there may be more to this than the simple, local inflow model takes account of. First, this simple model doesn't work as well along the northern side of the subtropical gyre, $y = 1000$ km (upper panel of Fig. 30) where the boundary layer current appears to have a reversal offshore that is not captured by the monotonic profile (66). In one respect that is not all bad, since that region is characterized by *outlfow* from the wbc into the interior, not an inflow. So, there is evidently more to the wbc dynamics than just (65). Second, the water that makes up the wbc at $y = 0$, say, came mostly from lower latitudes, not from a local inflow. If the wbc current was q conserving along stream, then the q at that latitude should be lower than the local q. Later it will be clear that frictional effects should be significant in the western boundary current, and friction acts to increase q along the path of the current. Friction implies a length scale that, for the r used here, is the same order as R_d (Sec. 4.2.2). It appears that while Eqn. (65) works very well in a numerical sense, local inflow and q conservation are not a complete explanation.

6 The (almost) steady circulation

The currents and stratification in the interior of the basin eventually reach an instantaneous steady state, $\partial(\,)/\partial t \;=\; 0$. However, there is one region where the flow never becomes even approximately steady, the confluence of the western boundary currents of the subtropical and subpolar gyres at around $y = 1800$ km. There the colliding western boundary currents meander and produce intense, mesoscale eddies of both

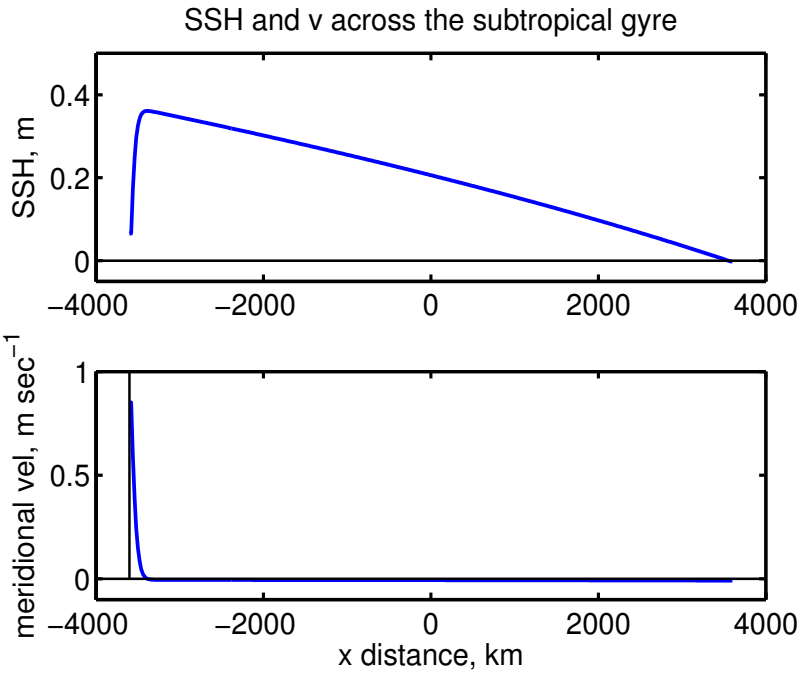

Figure 31: **(upper)** A zonal section of SSH across the center of the subtropical gyre, $y = 0$, computed from layer thickness anomaly via the reduced gravity approximation. The basin-scale variation of SSH is much like that seen in the North Atlantic (Fig. 1); a very narrow western boundary current and a broad interior with almost uniform slope down to the east. Notice, though, that the amplitude of the SSH high in this model solution is considerably less than is observed in the real North Atlantic subpolar gyre (about which more in Sec. 7). **(lower)** The meridional velocity along the section above. The velocity is very nearly geostrophic and is northward and very fast in a thin western boundary current, up to about 1 m sec^{-1}. The interior, meridional velocity is southward and very slow, a little less than 0.01 m sec^{-1}.

signs. The eddies remain close to the western boundary, and do not appear to affect the interior region. The confluence region does become steady in the statistical sense that the eddy amplitude, size and frequency are no longer changing after about 10,000 days. 'Steady' in reference to the basin-wide circulation, is really a shorthand for steady excepting the wbc confluence region.

One straightforward way to characterize the basin-wide, steady circulation is to simply make a cut of SSH anomaly and northward velocity through the center of the subtropical gyre Fig. (31), which may be compared to Fig. (1). There is a comparatively very narrow western boundary region, e-folding on the radius of deformation and so the full width is O(100 km), within which SSH slopes up to the east and the current is northward and fast, up to 1 m sec^{-1}. Over the much broader interior region — the rest of the basin — there is a quasi-linear decrease of SSH all the way to the eastern boundary (Fig. 31). Given the zonally uniform wind stress curl of the model winds, this nearly constant slope of SSH would be expected for a linear Sverdrup interior for which $\delta h \ll H_o$. This is the shallow water model-equivalent of the east-west asymmetry of the observed wind-driven ocean circulation noted as O2 in Sec. 1.1.

6.1 A streamfunction depiction of the circulation

A second and very useful way to characterize the basin-wide steady circulation is to construct a map of the streamfunction. When the solution is in steady state, $\partial h/\partial t = 0$, the volume transport, $\mathbf{M} = H\mathbf{V}$, is nondivergent, $\nabla\cdot\mathbf{M} = 0$. In that case the vector field $\mathbf{M}(x,y)$ may be represented by a scalar field, the streamfunction, $\Psi(x,y)$, without loss of information. The streamfunction is related to the east and north components of $\mathbf{M}$ by

$$\frac{\partial \Psi}{\partial y} = HU \quad \text{and} \quad \frac{\partial \Psi}{\partial x} = -HV, \tag{67}$$

or in a vector form,

$$\mathbf{M} = -\mathbf{k}\times\nabla\Psi$$

where the upper case H and U,V are the steady state thickness and velocity components. The sign convention of (67) is arbitrary, and is reversed in some applications. The streamfunction may be computed from the vector field by integrating either of (67). Here we integrate the HV term westward, starting from the eastern boundary,

$$\Psi(x,y) = \Psi(L,y) \; - \; \int_L^x H(x,y)V(x,y)dx. \tag{68}$$

The dimensions (units) of this streamfunction is volume transport, $\mathrm{m}^3\ \mathrm{sec}^{-1}$. The volume transport of major ocean currents is in the range 1 - 150 $\times 10^6\ \mathrm{m}^3\ \mathrm{sec}^{-1}$ and often reported in a non-SI but widely used and accepted unit, 'Sverdrups', with 1 Sv = $10^6\ \mathrm{m}^3\ \mathrm{sec}^{-1}$. The normal component of the velocity vanishes on all of the side walls, and hence $\Psi(L,y) = constant$, that may as well be taken to be zero. It would be equally valid to perform an integration of HU in the y direction. The resulting streamfunction lines (Fig. 32, left) are everywhere parallel to $\mathbf{M}$, and hence the streamfunction makes an intuitive presentation of the direction of the underlying vector field. With this choice of sign, lower values of Ψ are to the right of the vectors (which is opposite the geostrophic relationship for SSH). The density of streamfunction lines is proportional to the magnitude of $\mathbf{M}$ and notice that $\partial\Psi/\partial x$ is very large in thin western boundary regions where the wbc current is correspondingly very large compared to the currents in the interior of the basin.

Sverdrup transport may also be represented by a streamfunction (Fig. 32, right), here computed from Eqns. (1) and (68) and integrating westward from the eastern boundary,

$$\Psi_{Sv}(x,y) = \Psi_{Sv}(L,y) \; + \; \frac{1}{\rho_o\beta}\int_L^x \nabla\times\tau(x,y)dx. \tag{69}$$

The starting value is taken to be $\Psi_{Sv}(L,y) = 0$ for all y, which ensures that there is no normal flow through the eastern boundary. Since only one integration is needed to compute Ψ_{Sv}, no additional boundary data may be applied and so the Sverdrup streamfunction can not satisfy a no normal flow condition through any of the other boundaries. In this case the stress curl $\nabla\times\tau(x,y) = -\partial\tau^x/\partial y$ and independent of x and hence the streamfunction is

$$\Psi_{Sv}(x,y) = \; -\frac{(L-x)}{\rho_o\beta}\frac{\partial\tau^x}{\partial y}. \tag{70}$$

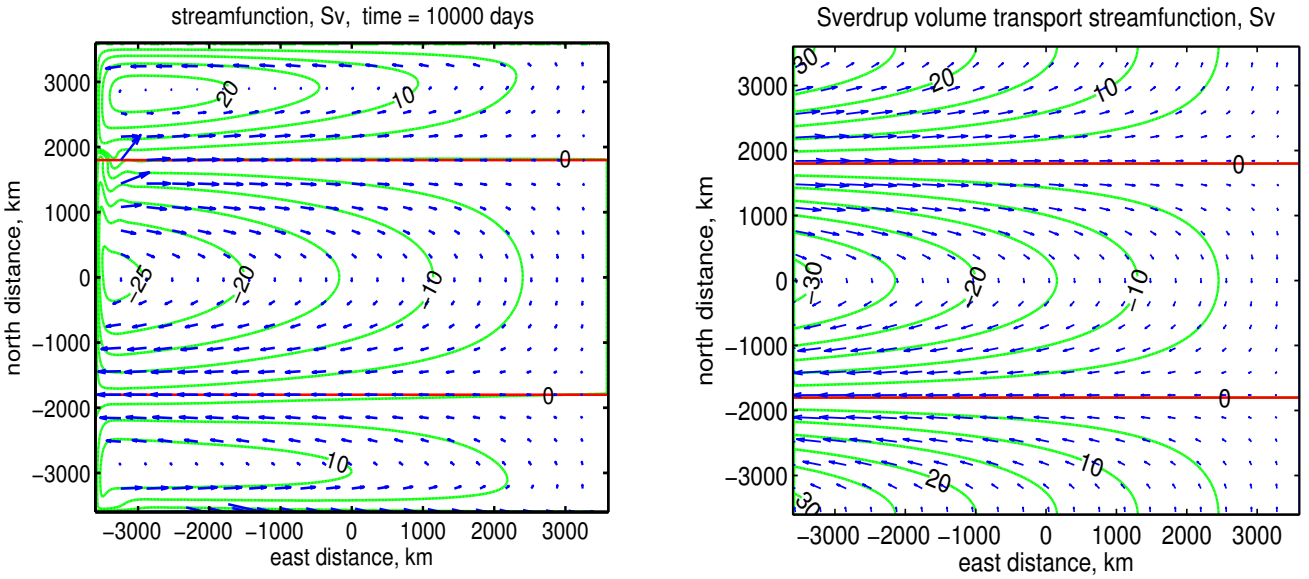

Figure 32: **(left)** The volume transport streamfunction (green lines) computed from the steady state numerical solution by integrating Eqn. (68) starting from the eastern boundary. Labeled in Sverdrups, 10^6 m^3 sec^{-1}. The blue vectors are the volume transport per unit width, **M**, and are parallel to lines of constant streamfunction. The very large **M** vectors in the western boundary regions are omitted here but shown in a later Fig. 14. The red horizontal lines are the axes of the westerly and easterly winds, and also approximate gyre boundaries. **(right)** The Sverdrup volume transport streamfunction (green lines) computed from the wind stress of the numerical experiment (Fig. 16) and Eqn. (69) and starting from the eastern boundary. In the numerical model-computed streamfunction field at left, $\Psi = 0$ is found on all of the boundaries, indicating no normal flow through the boundaries, as should hold exactly. The Sverdrup streamfunction at right can not satisfy a zero normal flow condition on more than one boundary, here chosen to be the eastern boundary.

The zonal component of mass transport is then

$$HU = \frac{\partial}{\partial y}\Psi_{Sv}(x,y) = \; -\frac{(L-x)}{\rho_o \beta}\frac{\partial^2 \tau^x}{\partial y^2}, \tag{71}$$

and the meridional component is Sverdrup transport,

$$HV = -\frac{\partial}{\partial x}\Psi_{Sv}(x,y) = \; -\frac{1}{\rho_o \beta}\frac{\partial \tau^x}{\partial y}, \tag{72}$$

as expected.

A comparison of the two streamfunction fields (Fig. 32) is one way to see where Sverdrup balance is valid in the numerical solution. The steady circulation in this experiment consist of three gyres within which the meridional flow has the sign of the wind stress curl, e.g., equatorward in the subtropical gyre where $\nabla \times \tau < 0$, and so qualitatively consistent with the Sverdrup relation Eqn. (1). Each of these gyres is very strongly compressed onto the western side of the basin in the sense that the largest SSH and thus

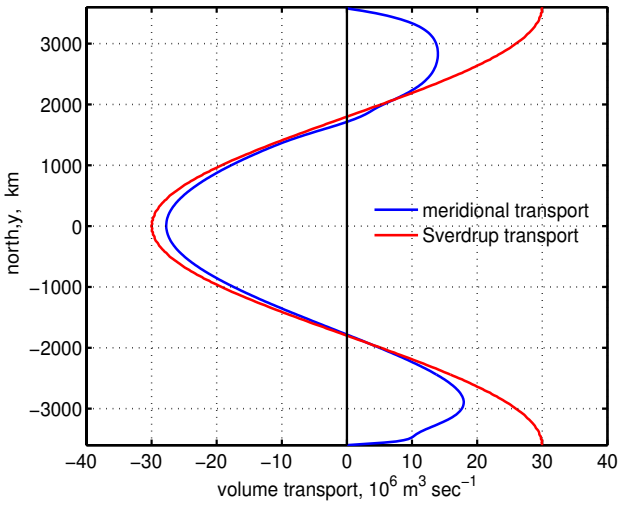

Figure 33: The north-south variation of the zonally-integrated meridional transport computed from the steady model solution (blue line) and computed via the ideal Sverdrup transport relation, Eqn. (1) (red line). The integration extends from the eastern boundary to just outside of the western boundary current. Notice that the actual (numerical) meridional transport vanishes on the zonal boundaries at $y = \pm 3600$ km due to a no normal flow boundary condition. This is something that the Sverdrup relation (red line) can take no account of. The north-south extent of the affected zonal boundary region is 500 - 1000 km, which is a significant part of the tropical and subpolar gyres.

the largest pressure anomaly is found about a hundred kilometers offshore of the western boundary. (see Sec. 10.2, #6)

Another and more quantitative way is to evaluate the interior meridional transport for all y, Fig (33). The Sverdrup relation gives a fairly accurate account of the meridional transport over the interior of most of the subtropical gyre, and to a much lesser degree, the subpolar and tropical gyres. The Sverdrup relation is clearly not valid within a western boundary region, nor is it valid within roughly 500 - 1000 km of the northern and southern zonal boundary regions. In these zonal boundary regions the Sverdrup relation indicates significant meridional flow which does not happen in the numerical model solution. What is perhaps surprising is how broad the affected zonal boundary regions are (more on this in Sec. 6.2.3). One consequence of such broad zonal boundary regions is that the transport of the western boundary currents of the tropical and the subpolar gyres is somewhat less than is the transport of the subtropical gyre, which (in this model) is not similarly affected by a zonal boundary (Fig. 26).

6.2 Dynamics of the steady circulation: the balance of potential vorticity

The dynamics of the circulation may be described most fruitfully in terms of the balance of potential vorticity, Eqn. (42), here expanded and multiplied by H,

$$\begin{aligned} \beta VH &= \frac{1}{\rho_o}\nabla\times\tau - rh_o\nabla\times\mathbf{V} + HOT, \\ beta &= curl\ tau + curl\ drag + higher\ order\ terms. \end{aligned} \tag{73}$$

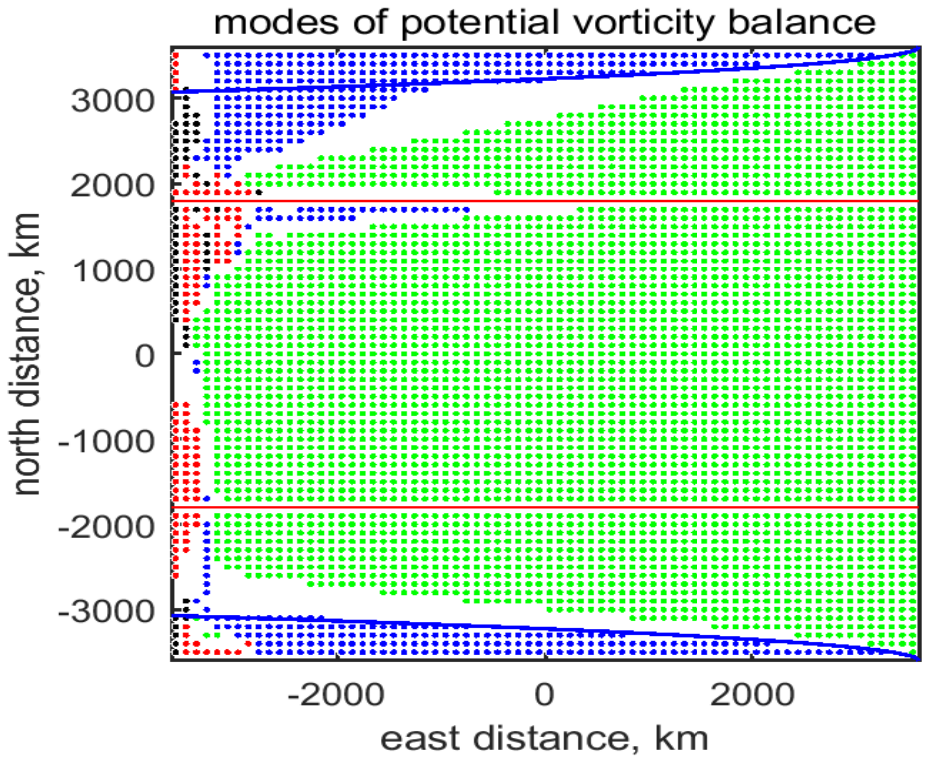

Figure 34: The steady potential vorticity balance characterized by the distribution of the modes (approximate two term balances) of Eqn. (73). Horizontal red lines are the gyre (wind stress curl) boundaries as before. A **green dot** indicates that the Sverdrup mode, $beta = curltau$, accounts for more than 90% of the variance of the steady potential vorticity balance at that point. This (approximate) Sverdrup balance holds over about 75% of the basin. A **black dot**, shows where $beta = drag$ is the dominant mode, mainly near the western boundary. A **blue dot** indicates the mode $0 = curltau + drag$ found near the northern and southern zonal boundaries . A **red dot** indicates that the HOT, the collection of nonlinear terms, was larger than two of the linear terms. If there is **no colored dot**, then there is no dominant mode, and the balance of potential vorticity is shared among at least three of the terms of Eqn. (73). The blue lines near the northern and southern zonal boundaries are a simple, linear estimate of zonal boundary region width that is discussed in Sec. 5.2.3.

The higher order terms are the collected nonlinear terms involving the advection of potential vorticity and the gradient of layer thickness;

$$HOT = -H\mathbf{V}\cdot\nabla\xi \; + \; h_o HQ\mathbf{V}\cdot\nabla H \; - \; \frac{1}{\rho_o h}\tau\times\nabla H \; + \; \frac{rh_o}{H}\mathbf{V}\times\nabla H.$$

In general, the steady potential vorticity balance includes a contribution from all of these terms, including the HOT. However, in this solution the nonlinear HOT terms are important only in special places (marked with red dots in Fig. 34) where large currents are combined with large horizontal gradients, e.g., the confluence of the subtropical and subpolar western boundary currents near $(x,y) = (-L, L/2) = (-3600, 1800)$ km.

6.2.1 Sverdrup interior

Aside from these important but spatially limited regions, the steady potential vorticity balance can be characterized by the regional distribution of two term balances or modes among the linear terms of Eqn. (73), Fig. (34). One of these, the Sverdrup mode,

$$\begin{aligned} \beta VH &= \frac{\nabla\times\tau}{\rho_o}, \\ beta &= curltau, \end{aligned} \tag{74}$$

accounts for at least 90% of the variance of the potential vorticity balance over most of the interior region of the basin (the green dots of Fig. 34), especially within the subtropical gyre, and which is often and appropriately called the Sverdrup interior.

Eqn. (42) describes the potential vorticity balance at a fixed point. Consider a site in the subtropical gyre interior where the wind stress curl is negative, which by itself would cause Q to decrease with time. A steady state will occur if the meridional flow advects higher Q water from the north at the same rate (opposite sign) of the stress curl tendency. Since the potential vorticity in the interior is approximated well by the planetary vorticity, $Q \approx f/h_o$ (with h_o a constant), then this occurs by the advection of planetary vorticity, $V\partial f/\partial y$, as if f was a fluid property. For this steady, Sverdrup balance to exist throughout the interior of the basin, there must be some mechanism that serves to recharge the higher latitudes (within the subtropical gyre) with high Q water, or specifically, with water having $Q \approx f/h_o$. What is the source of this high Q water? The western boundary current, described next. (see Sec. 10.2, 7)

6.2.2 Western boundary currents

The Sverdrup balance certainly does not hold within the western boundary currents (Figs. 31 and 32), where the meridional current is counter to the Sverdrup flow. The beta effect on a fast-flowing wbc current is in any case far larger than can be balanced by the curl of the wind stress (as occurs in the Sverdrup interior), and so in this model the steady vorticity balance within a wbc is mainly between the beta effect and the curl of the friction, 'drag',

$$\begin{aligned} \beta VH &\approx -\, rh_o\nabla\times\mathbf{V}, \\ beta &\qquad\quad drag. \end{aligned} \tag{75}$$

For example, the western boundary current of the subtropical gyre has very large negative relative vorticity (Fig. 30) , and a correspondingly large, positive, curl of the friction, or 'drag'. This drag largely balances the negative vorticity tendency of the beta effect, allowing a steady state within the subtropical wbc. Regions where this frictional balance holds in the sense described above are denoted by the black dots in Fig. (34), and are very near the western boundary in all three gyres.

An Ekman number equivalent for the vorticity balance,

$$E_Q \;=\; \frac{drag}{beta} \;=\; \frac{r\nabla\times\mathbf{V}}{\beta V}, \tag{76}$$

ignoring signs and taking $H = h_o$. The usual Ekman number is the ratio of frictional force to Coriolis force, but in this case it is the curl of the friction divided by (compared to) the beta effect (see Sec. 10.2, #11). To evaluate E_Q it is helpful to use a streamfunction representation of the velocity and its curl,

$$V \;\approx\; \frac{\Psi}{L_{wb}},$$

where L_{wb} is the east-west width of the wbc, which for now we will treat as an unknown. Within the narrow western boundary current, the horizontal scale in the x direction (normal to the boundary) is much less than the scale in the y direction and hence the curl of the velocity (the Laplacian of the streamfunction) is approximately

$$\nabla\times\mathbf{V} \;=\; \nabla^2\Psi \;\approx\; \frac{\partial^2\Psi}{\partial x^2} \;\approx\; \frac{\Psi}{L_{wb}^2}.$$

Using these estimates in (76) gives

$$E_Q \;=\; \frac{r}{\beta L_{wb}}. \tag{77}$$

If the balance is indeed Eqn. (75), then it should also be the case that $E_Q \approx 1$ and readily solve for the purely frictional wbc width, $L_{wb} \;=\; L_{fric}$ to find

$$L_{fric} \;=\; \frac{r}{\beta}. \tag{78}$$

Notice that this L_{fric} does not depend upon f, and so should be the same along the entire western boundary. Neither does it depend upon stratification and so should obtain even for a fully barotropic wbc. There will be an opportunity to check that with a three-layer model in Sec. 8.

For the present values of r and β this $L_{fric} \approx 50$ km, which is numerically about the same as the (subtropical) first mode, baroclinic radius of deformation (Sec. 4.7). Said a little differently, for the present r, the Q balance of a wbc having a width equal to the radius of deformation is significantly frictional. Recall that in this experiment, the value $r \;=\;$ 1/15 days, was chosen in an *ad hoc* manner, the minimum r (least viscous) that permitted a near steady state solution. This is a partial rationalization of this choice. However, there is no independent means for identifying an appropriate value of r (that I know of), and no reason to assert that the physical process of dissipation by or in a wbc is well-represented by linear drag. Given all of this, we have to be very chary about interpreting this solution as if it were a realistic model of an actual wbc.

The shallow water model solution is worth understanding on its own, however, and at a minimum it is essential to know what happens when r is changed; say that r is doubled to 1/7.5 days. This makes the

solution somewhat more viscous. The pattern of the Sverdrup interior is nearly unchanged, and the amplitude of the Sverdrup transport is reduced only very slightly, a few percent. The Sverdrup interior is thus not much affected by the choice of r. The wbc becomes somewhat thicker, as (78) indicates it should. Since the wbc transport is reduced and the wbc width increased, the wbc speed is reduced considerably, by about 30%. In that event the flow is steady throughout the model domain. More interesting is the solution when r is reduced to half the present value, to $r = 1/30$ days. The volume transport in the interior is then a few percent greater and so is a slightly better match to the ideal Sverdrup transport. But again the overall pattern of the interior circulation is indistinguishable from the nominal experiment. The width of the subtropical wbc is slightly narrower, though not nearly as much as the purely frictional boundary layer width (78) suggests, and so it appears that $L_{wb} = R_d$ is a lower limit that obtains for smallish friction. The wbc current speed is slightly greater, by about 10%, and so the inertia of the wbc is also greater. The nonlinear terms of the q balance are enhanced, and the colliding western boundary currents at the subpolar/subtropical gyre confluence (on the western boundary at about $y = 1800$ km; the largest red dot region of Fig. 34) are considerably more vigorous than in the nominal experiment (Fig. 49, lower). This kind of unstable, eddying flow is an important and very interesting characteristic of nearly all strong ocean currents that are not constrained by topography. However, this aspect of boundary current dynamics is sensitively dependent upon details of the ocean bottom topography and the vertical structure of currents, among others, and so is outside the scope of this essay (see Sec. 10.2, Problems 9 and 11).

6.2.3 Zonal boundary regions

There are extensive regions adjacent to the zonal boundaries (northern and southern boundaries) where the ideal Sverdrup balance does not hold, as evident in the qualitative mismatch of Sverdrup transport with the actual transport within about 500 to 1000 km of the zonal boundaries (Figs. 32 and 33). As noted at the outset, the Sverdrup balance *per se* is unable to satisfy the boundary condition that the meridional current must vanish on the zonal boundaries, and so if there is wind stress curl on these boundaries (as there is here, Fig. 16) then the Sverdrup balance will necessarily fail; something else must happen. Very near the zonal boundaries there is no meridional velocity and thus no β effect. The steady, linear potential vorticity balance in this model must reduce to the steady, linear, forced, damped mode,

$$\begin{aligned} 0 &= \frac{1}{\rho_o}\nabla\times\tau - rh_o\nabla\times\mathbf{V} \\ &= curltau + drag, \end{aligned} \tag{79}$$

indicated by blue dots in Fig. (34).

Like the wbc, this boundary region is also highly anisotropic (typical of all boundary layers), but in this case the meridional, north-south scale is much less than the zonal, east-west scale and hence

$\nabla^2\Psi \approx \frac{\partial^2\Psi}{\partial y^2}$. The balance (79) may then be written via the streamfunction as

$$0 \;\approx\; \frac{1}{\rho_o}\nabla\times\tau \;+\; r\frac{\partial^2\Psi}{\partial y^2}.$$

The curl of the drag has to be large enough to balance the wind stress curl in the zonal boundary region, and the question is what zonal boundary layer width, L_{zb}, is required to achieve this? Estimating $\partial(\,)/\partial y \approx 1/L_{zb}$ and $\partial^2(\,)/\partial y^2 \approx 1/L_{zb}^2$, then

$$0 \;=\; \frac{1}{\rho_o}\nabla\times\tau \;-\; \frac{r\,\Psi}{L_{zb}^2}.$$

It is not obvious what Ψ should be, but as a first guess, let's try the Sverdrup streamfunction, Eqn. (69), even though the Sverdrup Ψ can not be correct right on the boundary. Given a tentative estimate $\Psi = (L-x)\nabla\times\tau/\rho_o\beta$, where $L-x$ is the distance from the eastern boundary (positive), the boundary layer width is easily found to be

$$L_{zb} \;=\; \sqrt{\frac{r\;(L-x)}{\beta}}. \tag{80}$$

This is sketched onto Fig. (34 as blue lines near the southern and northern zonal boundaries. At the midpoint of a zonal boundary, $x = 0$, $L_{zb} \approx 400$ km, which is a reasonable estimate of the half-width of the zonal boundary region evident in Figs. (34) and (33). Notice that the region significantly affected by the zonal boundary dynamics (the width of which is defined by the no dot transition region between the blue and green regions) is about twice this width.

The width of this boundary layer estimate decreases toward the east, which is qualitatively consistent with the distribution of modal balances, i.e., a narrower blue region toward the east. An eastward decrease of L_{zb} arises because, while the vorticity needed to achieve the balance $0 = curltau + drag$ on the zonal boundary is uniform along the boundary (recall that *curltau* is here taken to be uniform in x, which is generally not true over the real oceans, Fig. 3) and hence the zonal current, which is qualitatively the zonal component implicit in the Sverdrup relation, decreases eastward. As a consequence, the north-south horizontal scale over which the current varies must also decrease eastward in order to have the necessary relative vorticity and thus curl of the frictional drag sufficient to balance the curl of the wind stress.

Like the western boundary layer, the width of the zonal boundary regions is expected to be independent of f and thus should be the same along the southern and northern zonal boundaries since the imposed wind stress is the same on those boundaries (Sec. 3.2). However, judging from the east-west distribution of q-balance modes found in the numerical model solution (Fig. 34), the zonal boundary layer is in fact markedly wider in the western-most third of the sub-polar zonal boundary region. The reason for this discrepancy is mainly that the subpolar gyre of this numerical experiment has a significantly reduced layer thickness compared to the initial thickness, h is as little as 100 m in the western subpolar gyre, and hence there is considerably greater drag than is accounted for by the linear equation (79) that presumed $H = h_o = 500$ m. A straightforward experimental test of this hypothesis

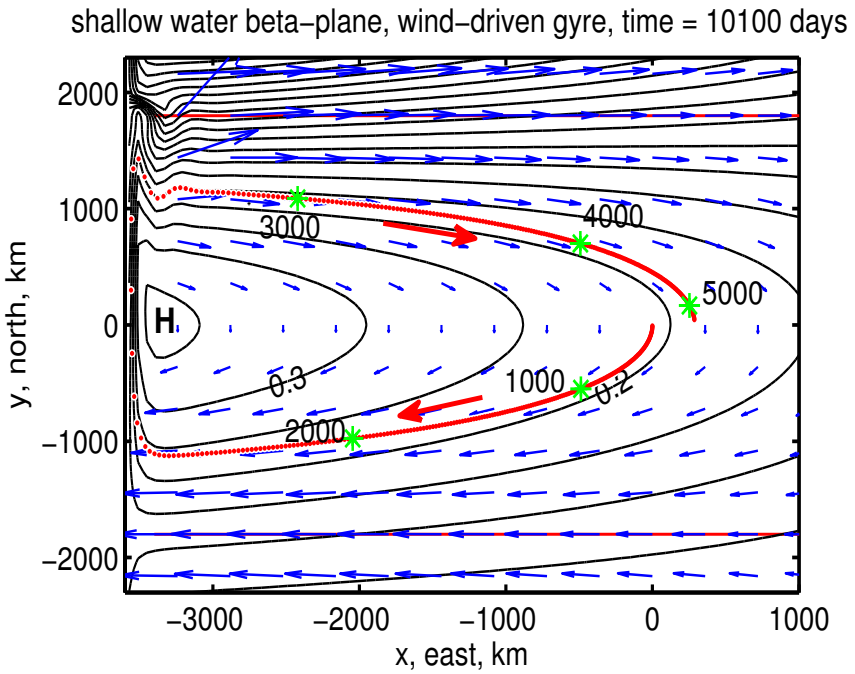

Figure 35: The (almost) steady subtropical gyre, shown by contours of SSH anomaly and a field of velocity vectors. A parcel trajectory that was started at $(x,\ y) = (0,\ 0)$ and followed for 5,500 days is the red line. The green asterisks along the trajectory are at 1000 day intervals. The parcel entered the western boundary current at about 2,600 days after starting, and it exited the western boundary current about 200 days later. The parcel returned close to its starting position. Notice that the trajectory is almost parallel to isolines of SSH, but not exactly so.

follows from setting the imposed wind stress small enough — $\tau_o = 0.01$ N m^{-2} suffices — that the dynamics are linear in the respect that $H \approx h_o$ throughout the model domain. In that case the comparison between the numerical and the estimated boundary layer width (80) is quite good at all longitudes outside of the wbc. Thus the linear estimate of zonal boundary layer width (80) is valid for a linear problem, and it is straightforward to understand the sense and the approximate magnitude of the finite amplitude effects that occur when there are large spatial variations in layer thickness, as do occur in this numerical solution.

6.3 Appendix to Sec. 6: A (Lagrangian) trip around the subtropical gyre

In the previous section, the analysis considered the currents, vorticity, etc., as observed at fixed locations, a point of view often dubbed 'Eulerian'. This is the natural starting point, since the shallow water equations and their numerical implementation are Eulerian. However, our intuition for classical mechanics has roots in a parcel-following, or 'Lagrangian' description, since the m and the a of $F = ma$ are the mass and acceleration of a specific chunk of material, and not the fluid properties observed at a point in space (the Eulerian view). This section will take this kind of parcel-following view on a complete trip around the gyre. Besides connecting a little better with our intuition for mechanics, this

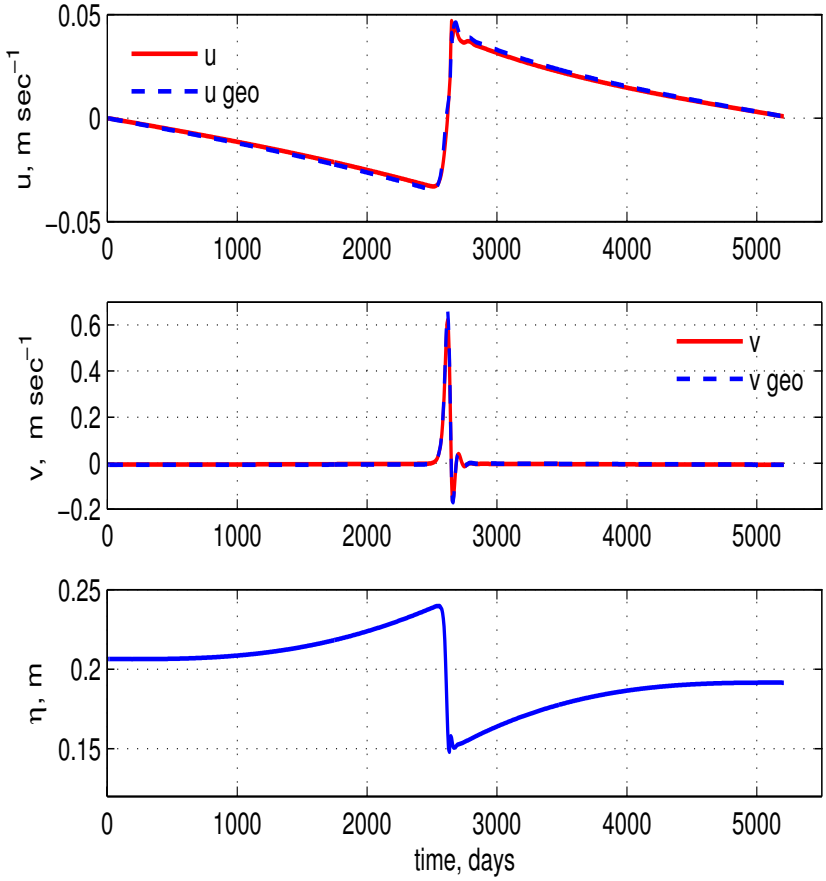

Figure 36: Velocity components along the trajectory of Fig. (35). **(upper)** East velocity (red line) and the geostrophic velocity estimated from the layer thickness (dashed blue line). **(middle)** North component of velocity. Note the very large change in the scale compared to the east component above. The actual velocity and the geostrophic velocity are close enough that the lines are difficult to distinguish. **(lower)** The SSH anomaly along the trajectory. While within the interior region, the parcel slowly climbs the SSH high of the subtropical gyre. While in the wbc, it descends comparatively very rapidly.

also gives a holistic view of the circulation in that it helps to show that the western boundary current is an essential component of a steady circulation.

A Lagrangian description starts with the solution for parcel trajectories, $X(t;(X_o,Y_o)), Y(t;(X_o,Y_o))$ by integrating the velocity along the path of a specific parcel,

$$X(t) \;=\; \int_0^t U(x,y)dt \;+\; X_o, \qquad \text{and,} \qquad Y(t) = \int_0^t V(x,y)dt \;+\; Y_o, \tag{81}$$

where (X_o,Y_o) is the initial position and the $t=0$ here is the time this integration starts (not the starting time of the numerical integration as in Sec. 3). The key thing is that the (x,y) dependence of the velocity field is continually updated as the integration proceeds, i.e., the $(x,\ y)$ in the integrand is set $\;=\;(X,\ Y)$ at each time step. Since the velocity field is available only at the 20 km resolution of the numerical model, the evaluation of velocity at an arbitrary parcel position requires an interpolation of the discrete model data, which is bound to incur some error, much like the finite difference evaluation of a derivative.

The initial position may be chosen anywhere in the model domain; the trajectory shown in red in Fig. (35) was started in the center, $(X_o,\ Y_o)\ =\ (0,\ 0)$. The initial position is, in effect, the tag on the parcel

that happened to be there at the time t_o. Not surprisingly, different initial positions result in different trajectories. In this circulation, small initial position differences yield only rather small trajectory differences (some examples to follow). A flow having this property may be described as 'laminar'.[20]

A complete trip around the subtropical gyre from this starting position $(X_o,\ Y_o) = (0,\ 0)$ requires a little more than 5000 days and extends over about 11,000 km. If the circulation was exactly steady (it isn't quite), and if the integration method used to construct the trajectory was without error (it can not be), then the parcel would return to its starting point. However, this parcel didn't quite make it (Fig. 35). Nevertheless, the interesting changes in parcel properties along the track are considerably larger than the starting point/ending point mismatch, and so the semi-quantitative inferences from this trajectory are valid.

Assuming that the fluid is not at rest, then there is no Lagrangian steady state comparable to the steady state of an Eulerian frame. Rather, fluid parcels continuously change position and generally all other properties with time. To find the potential vorticity of the parcel, we can either evaluate the (presumably known) $q(x,y)$ field at the parcel position, or, integrate the q conservation equation along the trajectory.

6.3.1 Momentum balance and energy exchanges

The relationship of parcel motion to the local slope of the SSH anomaly (the pressure or geopotential anomaly) is closely analogous to the motion of a dense parcel on a slope studied in Part 1. Differences in detail include that the slope changes quite a lot along the trajectory, especially near the western boundary, and, there is an additional external force, the wind stress, which is essential for compensating the slow but inexorable effects of friction.

During the first several hundred days, the parcel moved very slowly toward the south, which is consistent with the meridional Sverdrup flow at the starting latitude. Eventually, the parcel turned toward the southwest (Fig. 36) and began to pick up some speed. The trajectory was roughly parallel to the SSH lines with higher SSH to the right. Thus the parcel motion was, to a first approximation, geostrophic.

An important but small departure from strict geostrophy is that the parcel had a rather small, systematic component of motion across the SSH lines. While the parcel was in the interior, it slowly climbed up the SSH high of the subtropical gyre. The damping effect of friction alone would cause the parcel to descend the local SSH slope, though at a very small angle consistent with the small Ekman number, E is O(0.01). The small component of motion toward higher SSH is a consequence of the wind

[20] If instead the sensitivity to initial position was large, then the flow would be characterized as chaotic or turbulent. Most large scale fluid flows, and including the real ocean circulation, are turbulent in this sense.

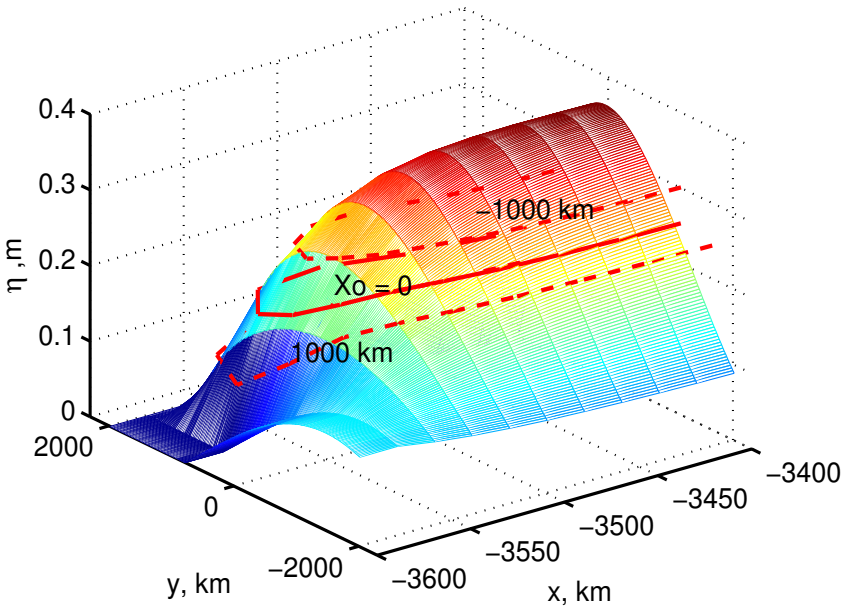

Figure 37: Three trajectories superimposed on the SSH anomaly, η, of the western side of the subtropical gyre. The trajectories differ in their starting points, X_o, that is noted. The solid red trajectory has $X_o = 0$ and is shown also in Fig. (35). Notice that the x scale is greatly expanded compared to the y scale so that the very large zonal slope of SSH within the wbc and its relationship to these trajectories is apparent.

stress. From an energy perspective, the positive wind work experienced by the parcel when it was in the interior was stored as gravitational potential energy.

After several thousand days, the parcel began to approach the western boundary, where the SSH topography was by comparison, very steep, about two orders of magnitude greater than in the interior. As the parcel neared the western boundary it accelerated to the north, reaching speeds of O(1 m sec^{-1}), or about two orders of magnitude greater than the speeds that characterize the slow, Sverdrup flow of the interior. The parcel motion never showed any significant inertial motion, and the momentum balance remained almost geostrophic (Fig. 36, middle). This implies that the acceleration associated with the steep wbc topography was slowly-varying compared to the rotation time, $1/f$. The kinetic energy associated with this rapid northward flow came from the potential energy that was released as the parcel descended about 0.1 m while within the western boundary current (Fig. 36, lower). There was also some energy loss to friction. After about 200 days, the parcel left the western boundary current and entered the slow eastward flow along the north side of the subtropical gyre. While moving eastward, it slowly climbed back up the high SSH of the subtropical gyre and returned fairly close to its starting value of SSH anomaly.

6.3.2 Potential vorticity balance along a trajectory

Potential vorticity conservation provides another way to think of the Sverdrup relation. Given that the field of q is presumed to be steady at fixed locations, $\partial q/\partial t = 0$, then the q of the moving parcel is just

the q at its present position (this sounds both profound and trivial at the same, but be sure to understand this before going on). Moreover, the spatial variation of potential vorticity is due mainly to the spatial variation of f, at least in the subtropical gyre interior, where the circulation is very slow. The parcel was subject to the overlying wind stress, whose curl was negative, and thus would tend to reduce the q of the parcel (Fig. 38, upper). Since the q of the parcel had to be consistent with the q of the presumed steady field, the parcel must move southward toward lower q, given that the q field is dominated by the meridional variation of f. Said a little differently, the southward motion of the parcel must be just sufficient to keep the q of the parcel consistent with the steady field of potential vorticity, $(\nabla \times v + f)/h$. In the subtropical gyre, the spatial variation of q is due mainly to the latitudinal variation of f, and hence the Sverdrup relation. This is a rigorous argument for the Sverdrup relation, given the assumptions of a steady, linear q balance. However, it feels awfully thin as an explanation for existence of the circulation in the first place. And, you might add, so does the usual (Eulerian) Sverdrup relation.

It is a fair surmise that a parcel can not be subject solely to a negative wind stress curl, or else the basin-wide average of q would surely decrease with time, which is not consistent with the steady state of the Eulerian circulation. It must be the case that parcels occasionally experience a process that increases q — a (relatively) quick pass through the western boundary current where there is a very strong, positive curl of the drag. This positive drag curl resets the parcel's q to a value that is consistent with the interior q (Fig. 38) where it reenters the Sverdrup interior. Thus the western boundary current is a crucial part of the gyre-scale circulation with respect to potential vorticity.

7 Experiments with other wind fields and basin configurations

The idealized wind field and square basin considered up to now are an appropriate model configuration for this introduction to wind-driven circulation, but these choices make the solution specific (special) in ways that may not be obvious. This section will consider briefly three other, equally idealized wind fields and/or basin configurations that will help reveal several important aspects of the wind-driven circulation.

7.1 Annually-varying winds and the baroclinic circulation

The experiment described in Secs. 5 and 6 assumed that the wind field was steady, once switched on, and had an amplitude modeled loosely on the long-term, observed mean. On the other hand, almost everyone with experience living in a coastal region will attest that the wind over the ocean is very seldom steady for more than a few hours or at most a few days. Wind varies on a wide range of time scales, including with the changing seasons, and in some regions it varies quite a lot; the annual variation of the westerlies over the northern North Atlantic is roughly $\pm 50\%$ of the annual mean, with the highest winds and wind

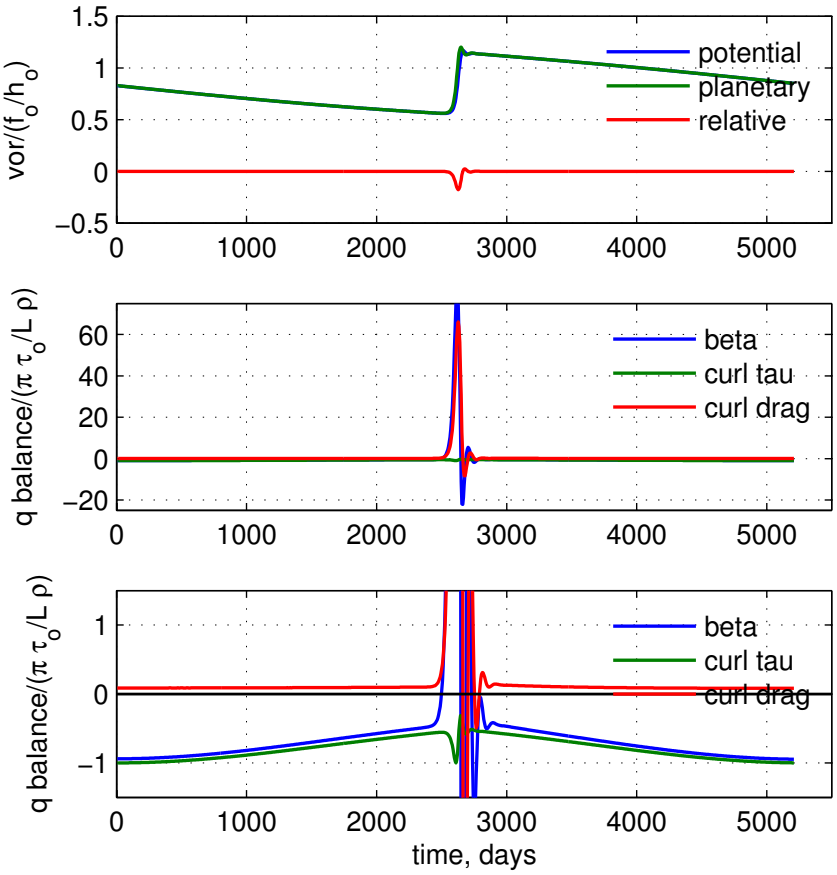

Figure 38: Potential vorticity along the trajectory of Fig. (35). **(upper)** The full potential vorticity (blue line), the planetary vorticity (green line) and the relative vorticity (red line). These are normalized by f_o/h_o. Notice that the relative vorticity is very small except when the parcel is within the western boundary current where it has a maximum magnitude of -1/4 (normalized). **(middle)** Leading terms in the potential vorticity balance, Eqn. (73). These data are normalized by a nominal wind stress curl, 8×10^{-8} m sec^{-2}. When plotted at this scale, about all that can be told is that the beta term is approximately balanced by the drag curl term while the parcel is within the western boundary current. **(lower)** Same data as above, but with a clipped ordinate that reveals the interior balance between the beta term and wind stress curl.

stress curl during winter, Figs. (8) and (9). The annual variation of easterly wind magnitude is somewhat less, though the annual migration of the Inter-Tropical Convergence Zone (furthest north in summer) produces a large annual variation in the local wind stress curl over the tropical North Atlantic.[5] Meridional winds show an especially marked annual variation that also contributes significantly to the annual variation of stress curl. Given this large amplitude annual variation of the wind, not to mention the day-to-day variation with the weather, one might argue that the time-mean wind scarcely exists, outside of climatologies.

Given that the rise time of the basin-wide circulation in the subtropics is O(1000 days), it is a reasonable guess that the annual cycle of the ocean circulation will be small but let's find out by calculating the solution for an idealized, annually-varying wind stress,

$$\tau^x(x,y,t) = (0.1 + 0.05 \sin(2\pi\, t/365)) \sin(\pi y/L),$$

where t is the time in days. Note that this wind stress amplitude varies quite a lot, between 0.05 and 0.15 Pa. This annually-varying wind was applied from the start of an integration that was continued past 10,000 days. The solution never comes to a steady state, but the annual cycle in the ocean circulation

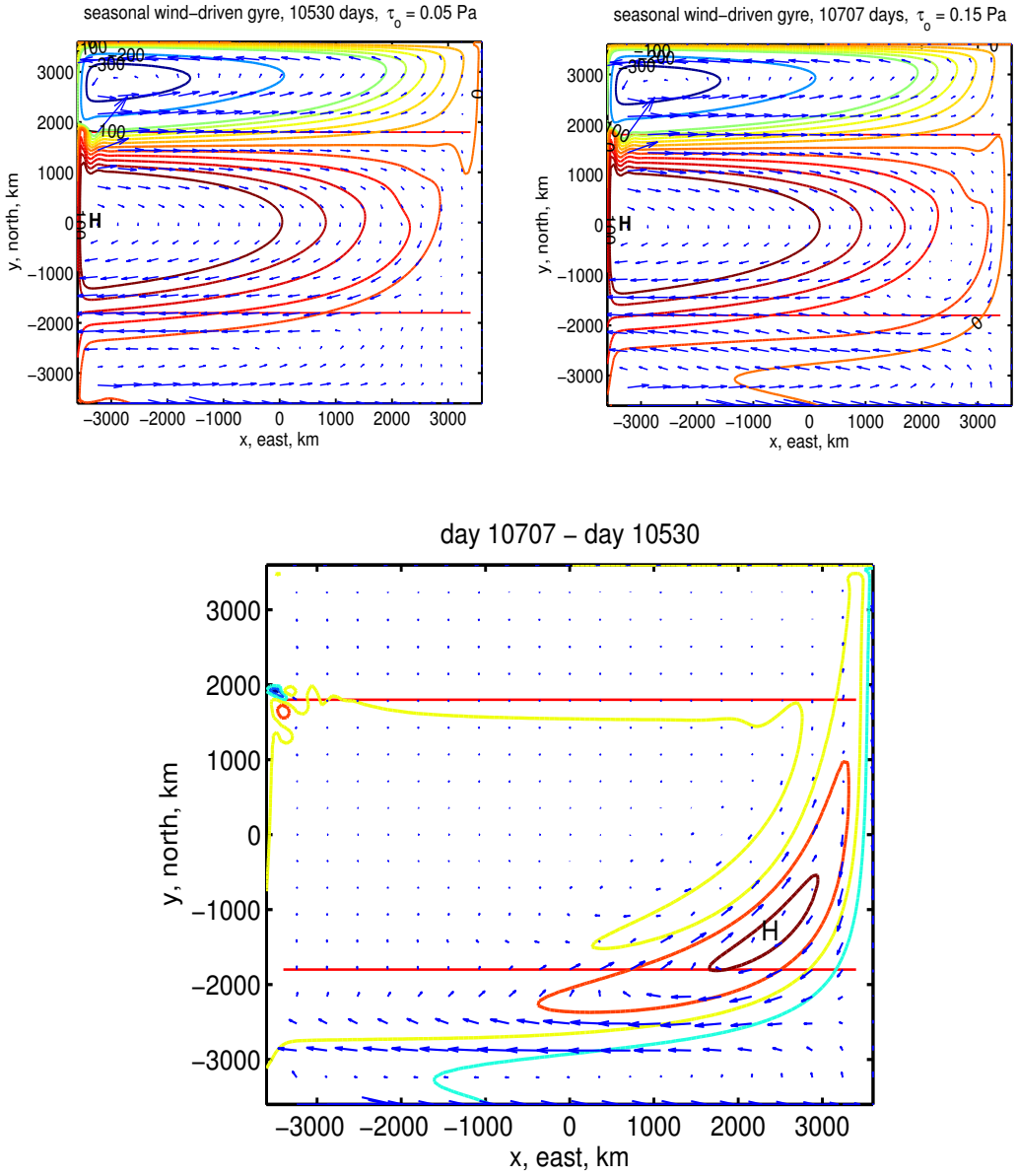

Figure 39: **(upper)** Two snapshots of the circulation taken 180 days apart and near a minimum (left) and maximum (right) of the tropical circulation. The latter occurs about one month after the maximum of the annually-varying wind stress amplitude. An animation of these data is available from https://www2.whoi.edu/staff/jprice/seasonal-gyres **(lower)** The difference of the two snapshots, showing the pattern of the annual cycle. Notice the small, intense eddies near the western boundary at about $y = 1800$ km, the confluence of the subpolar and subtropical western boundary currents. This kind of time-dependent eddy variability arises from an instability of the ocean currents, and so is present even with a steady wind stress.

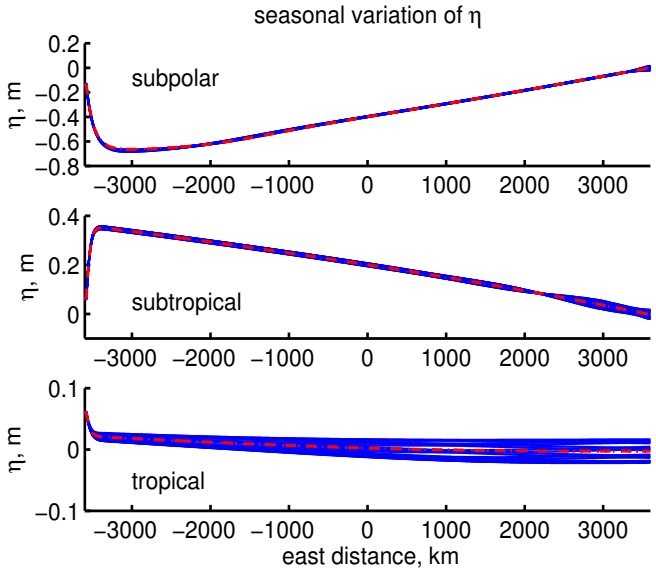

Figure 40: Zonal profiles of SSH, $\eta(x)$, from the annually-varying winds experiment. These profiles were taken through the centers of the three gyres noted. The blue lines were taken at 40 day intervals after time = 10,000 days when the solution appeared to be in a statistically steady state. The single red dashed line is a slice through the base case solution having steady winds, and notice that it goes through the center of the envelope of blue lines. Notice too that the η scale differs considerably between the three panels, consistent with the considerably larger η in the subpolar gyre.

becomes stationary in the sense that it repeats from one year to the next and so the startup transient has been minimized by 10,000 days.

Snapshots of the resulting circulation at times that are near the minimum and maximum response in the tropical gyre are in Fig. (39), and a series of slices through the center of the gyres shows the (inferred) η (Fig. 40). The $\eta(x)$ from the steady wind experiment (red dashed line) runs through the center of the envelope of the time-varying $\eta(x,t)$, indicating that the dynamics are effectively linear, i.e., the time-mean of the solution computed with an oscillating wind stress is very nearly the same as the solution computed with the time-mean of the wind stress. The first result of this experiment is that if the steady or long time-mean of the ocean circulation was the only thing of interest, then we would not have to be concerned with resolving explicitly the annual variation of the wind; the long term (yearly or more) time-mean of the wind stress would evidently suffice, at least for this model.

A second important result of this experiment is that the amplitude of the annual variation in the ocean varies greatly with latitude. Specifically, the tropical gyre responds much more vigorously to the annually-changing wind than does either the subtropical or especially the subpolar gyre. This is consistent with the basic start up experiment, which showed a much faster rise of the tropical gyre vs. the subpolar gyre. The amplitude of the annual variation in the ocean depends very much upon the variable of interest. For example, the zonal current sampled on the north side of the middle of the tropical gyre (Fig. 41, solid red line) varies by $\pm 50\%$ in this experiment, or the same as the wind stress. The explanation for this vigorous low-latitude response appears to be as simple and direct as the $\propto 1/f^2$ dependence of the local, wind-induced (Stage 2) geostrophic current, Eqn. (53). The observed annual variation of zonal currents in the tropics is likely of this sort.[5] There is also an annual period eastern boundary wave that has an appreciable amplitude in the lower subtropics. This wave penetrates only about one wavelength into the interior.

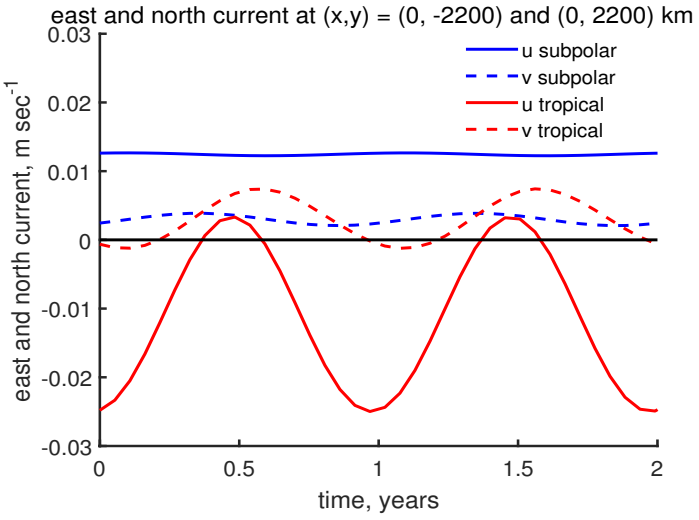

Figure 41: East and north component of the current from the annually-varying wind experiment. The current was sampled at two sites, on the south side of the subpolar gyre $(x, y) = (0, 2200)$ km (solid and dashed blue lines), and on the north side of the tropical gyre at $(x, y) = (0, -2200)$ km (solid and dashed red lines). The current at the subpolar site is almost constant in time despite a significant annual variation of the wind stress. The current at the tropical site oscillates by about $\pm 50\%$ around a mean, which is very close to the steady state current found in the steady wind stress experiment of Sec. 3.

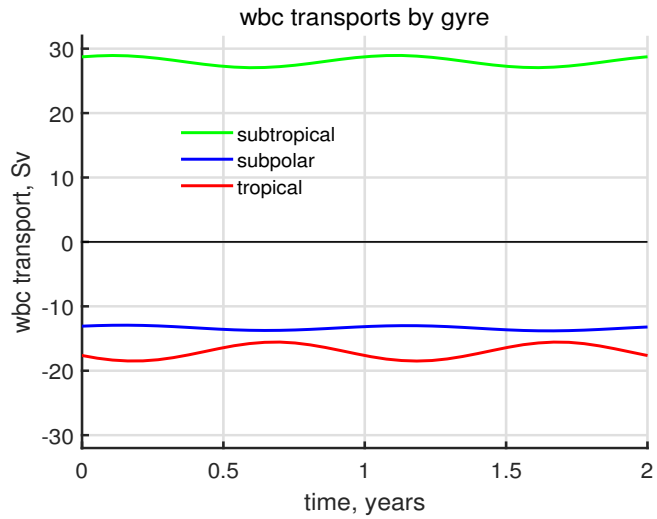

Figure 42: Transports of the western boundary current in each of the gyres from the annually-varying wind experiment. Colors are as in Fig. (26). Notice that the annual variation of the wbc transport in the tropical gyre (red line) is modest when compared to the very large annual variation of especially the zonal current in the interior of that gyre, cf. the red, solid line of Fig. (41).

Wbc transport is one measure of the gyre circulation: in the subpolar gyre, the wbc transport varies by about ± 0.3 Sv, in the subtropical gyre by about ± 0.7 Sv, and in the tropical gyre, by about ± 1.2 Sv or only about $\pm 8\%$ (Fig. 42). The latter is much less than the response of zonal currents in the tropics, just noted. The western boundary current transport is a bulk property of a gyre, and responds on the time scale of the basin-wide meridional (Sverdrup) flow, $2L/C_{longRo}$, Eqn. (56). The long Rossby wave speed is $\propto 1/f^2$ and much faster within the tropical gyre, but nevertheless, the rise time of the wbc transport of the tropical gyre is many hundreds of days (Fig. 26) and fairly long compared to the time scale of the annually-varying wind, a few months. The response time of the subtropical and subpolar gyres is much longer still, a thousand to many thousands of days, and hence the wbc transport of higher latitude gyres varies even less in response to annually-varying wind.

7.2 A wind stress field with no curl

The discussion of wind stress has emphasized importance of the curl of the wind stress curl, rather than the stress itself. And yet, the Ekman transport depends only upon the stress, and the Stage 2 response includes a term proportional to the β-induced divergence of the Ekman transport, and thus the stress itself. This raises the question, can there be a steady circulation driven by wind stress alone, that is, by a stress field with no curl?

This suggests an experiment in which a spatially uniform stress is imposed over the ocean basin. To avoid troublesome instances of vanishing layer thickness near boundaries, the stress is made very small, 0.01 N m^{-2}. The amplitude of the resulting currents and layer thickness are also very small, but not too troublesome if the goal is to find the structure of the response, rather than its amplitude.

If the spatially uniform stress is eastward, say, then the Ekman transport is southward throughout the basin, and divergent, Eqn. (51). For short times, $t \leq 1000$ days, this produces a thinning of the active layer (low pressure) that is most pronounced at lower latitudes, while also causing a pileup of water near the equatorial boundary where there is a growing high pressure. The resulting zonal current near the equatorial boundary is thus eastward, and there is a weaker, more distributed westward flow at higher latitudes, evident at $y >$ -2000 km in Fig. (43) (upper and middle).

These zonal currents are necessarily turned into the meridional direction along the eastern boundary, and the result is to initiate a long Rossby wave-like front that propagates westward across the basin. This eastern boundary Rossby wave signals the adjustment toward a steady state, and not too long after the Rossby wave passage the stratification (layer thickness) and flow are indeed quasi-steady. The steady state sea surface (inferred from the layer thickness) slopes up toward the east so that a zonal pressure gradient opposes the wind stress. Most notably, the current in the adjusted steady state vanishes. The bottom line is that absent a curl of the wind stress, there is a vanishing meridional flow in the interior. This is, of course, consistent with expectations of the Sverdrup relation. Given a closed basin, neither can there be a steady zonal flow. (see Sec. 10.2, #12)

7.3 Meridional winds over a basin without sidewalls (a channel)

One last experiment: consider a basin with dimensions as before, but now replace the no normal flow boundary condition on the eastern and western boundaries with a reentrant boundary condition, i.e., for the zonal velocity,

$$u(x = -L) \; = \; u(x = L),$$

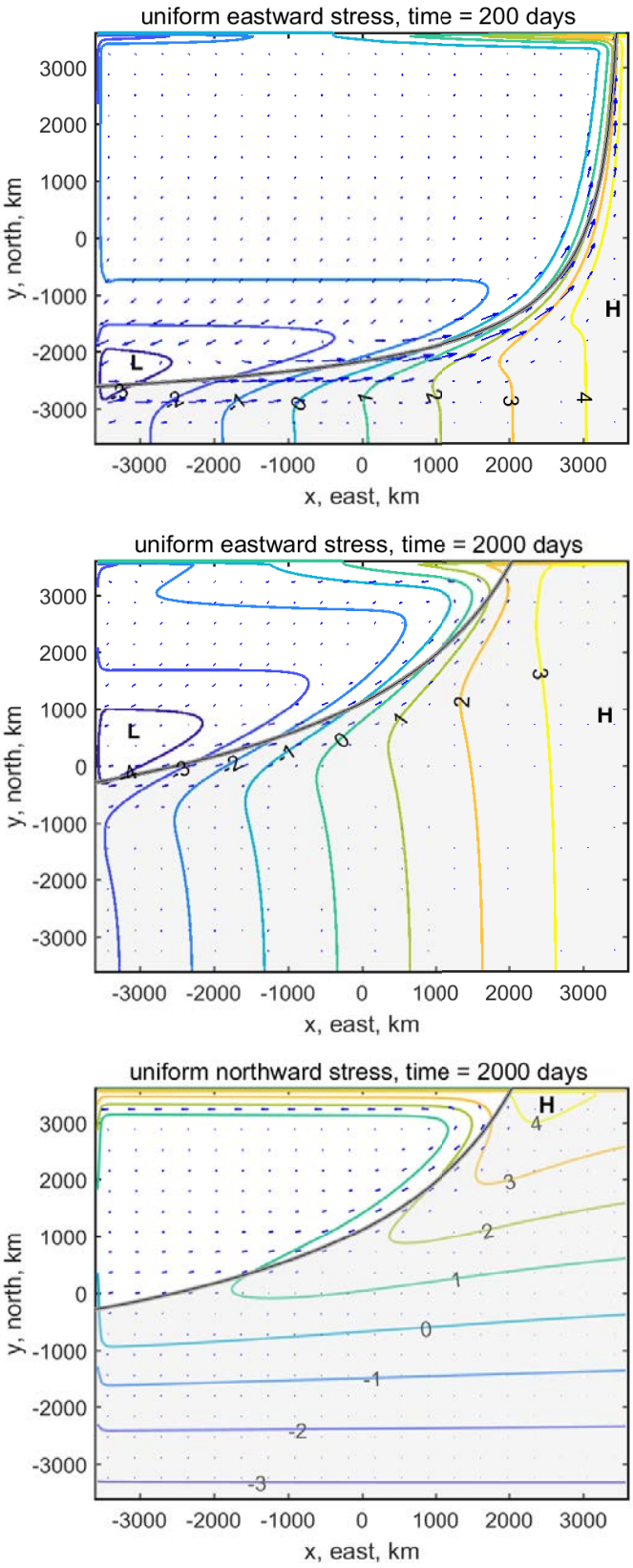

Figure 43: **(upper)** and **(middle)**Two snapshots from a wind-driven experiment in which the wind stress was spatially uniform and eastward at a very small value, 0.01 N m^{-2}. The times were 200 and 2000 days after the stress was switched on. The contours are of the anomaly of layer thickness, in meters. The blue arrows are the current, though with the comparatively very large currents within boundary currents omitted. The gray shading extends westward from the eastern boundary at the y-dependent speed of a long Rossby wave. **(lower)** A snapshot at 2000 days from an experiment in which the wind stress was spatially uniform and northward.

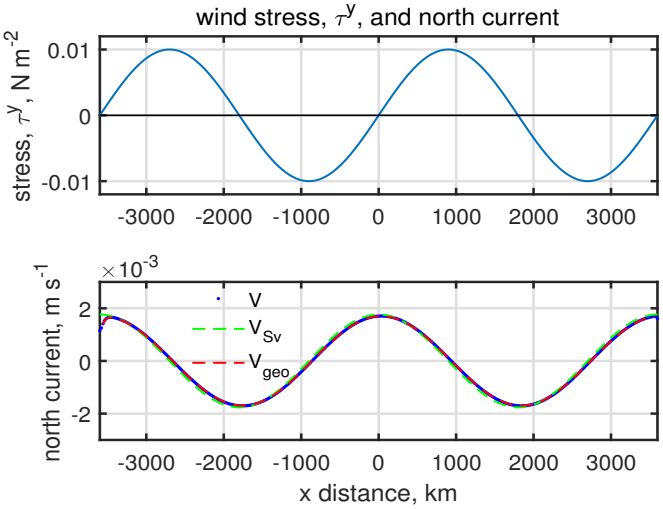

Figure 44: **(upper)** The x profile of the northward wind stress field applied in the channel experiment. The stress was independent of y. **(lower)** The north component of current across $y = 0$ at time = 10,000 days (blue dotted line) along with the expected Sverdrup current (green dashed line) and the meridional, geostrophic current estimated from the thickness field (red dashed line). These are almost identical, and hence the steady meridional flow in this experiment is both geostrophic and Sverdrup, there being no meridional Ekman flow.

as if the basin was a channel that wrapped all the way around a cylinder. Similar boundary conditions are applied to h and v. The wind stress is presumed to be in the *meridional* direction. To be consistent with the channel configuration and the reentrant boundary conditions,

$$\tau^y(x) \;=\; \tau_0 \sin(2\pi x/L), \tag{82}$$

(Fig. 44, upper) so that $\tau^y(-L) \;=\; \tau^y(L)$ and independent of y. The stress amplitude is made very small, $\tau_o = 0.01$ N m^{-2}, to avoid vanishing layer thickness in boundary currents. Meridional winds certainly do occur over the oceans, especially near boundaries (Fig. 5), but a basin-wide, meridional wind stress field of this sort is found in approximate form only in the Arabian Sea (Part 5). This idealized wind stress field helps to make an important point regarding the role of an eastern boundary vis-á-vis the Sverdrup relation. Given the boundary condition (82) the zonal length scale of the stress field will be written

$$L^x_\tau \;= L/2\pi,$$

to distinguish from the distance to the eastern boundary that plays such a prominent role in the closed basin cases considered to now.

The Ekman transport that accompanies this meridional wind stress is zonal, and is divergent. The resulting Stage 2 thickness anomaly grows linearly with time as

$$h_{S2} \;=\; \frac{\tau_o}{\rho_o f L^x_\tau} \cos(2\pi x/L)\; t,$$

and forms alternate highs and lows, Fig. (45). The Stage 2 meridional geostrophic current is

$$v_{S2} \;=\; \frac{\tau_o g'}{\rho_o f^2 L^{x2}_\tau} \sin(2\pi x/L)\; t \tag{83}$$

where f is $f(y)$, and so v_{S2} is much bigger at lower latitudes (smaller y) as we have seen before. Like the Stage 2 response of the closed basin cases, this steadily accelerating current persists for only a finite time, hundreds or thousands of days depending upon y, after which it is supplanted by a nearly steady Sverdrup balance,

$$v_{Sv} = \frac{\tau_o}{\rho_o L_\tau^x \beta H} \cos(2\pi x/L).$$

In this experiment, where there is no eastern boundary, the near-steady Sverdrup balance develops first at low latitude, and then spreads northward. At a given y, the adjustment occurs in the time required for a long Rossby wave to propagate westward over the distance L_τ^x, the length scale of the wind stress. The northward extent of the adjusted region is then estimated by

$$L_\tau^x = \frac{\beta C^2}{f^2} t, \tag{84}$$

where f is $f(y)$. Using the beta-plane representation of $f(y)$ and solving for the northward extent of the adjusted region, Y, gives

$$Y = \sqrt{\frac{C^2}{\beta L_\tau^x}}\ t^{1/2}, \tag{85}$$

which is used to define the gray shading of Fig. (45). This makes a plausible estimate of the y that separates the Stage 2 response to the north from the quasi-steady Sverdrup regime to the south. Since L_τ^x is proportional to the basin scale, and so this one case is not completely convincing. The test is that when the east-west scale of the wind stress is made smaller, say $L_\tau^x = L/4\pi$ and thus $\tau^y(x) \propto \sin(4\pi x/L)$, while holding the basin width L constant, the adjustment to Sverdrup balance at a given y occurs in half the time seen in this case.

This experiment shows that the relevant east-west scale for adjustment to Sverdrup balance is the smaller of the zonal scales that is imposed on the meridional flow. In the case of a closed basin with zonal winds that are independent of x, that scale is the distance to the eastern boundary. In the present experiment, this zonal scale comes from the wind field itself. This is an important result used in Part 5 to rationalize the very rapid response of the Arabian Sea to monsoon winds.

8 Barotropic and baroclinic circulation of the three layer, free surface model, 3l-fs

In this section we will take a look at the same experiment — same winds and basin — but solved with the more capable three layer model described in Sec. 4.6.2 and dubbed 3l-fs. Compared with the single layer, reduced gravity model, this new model has a somewhat thinner surface layer that absorbs the wind stress,

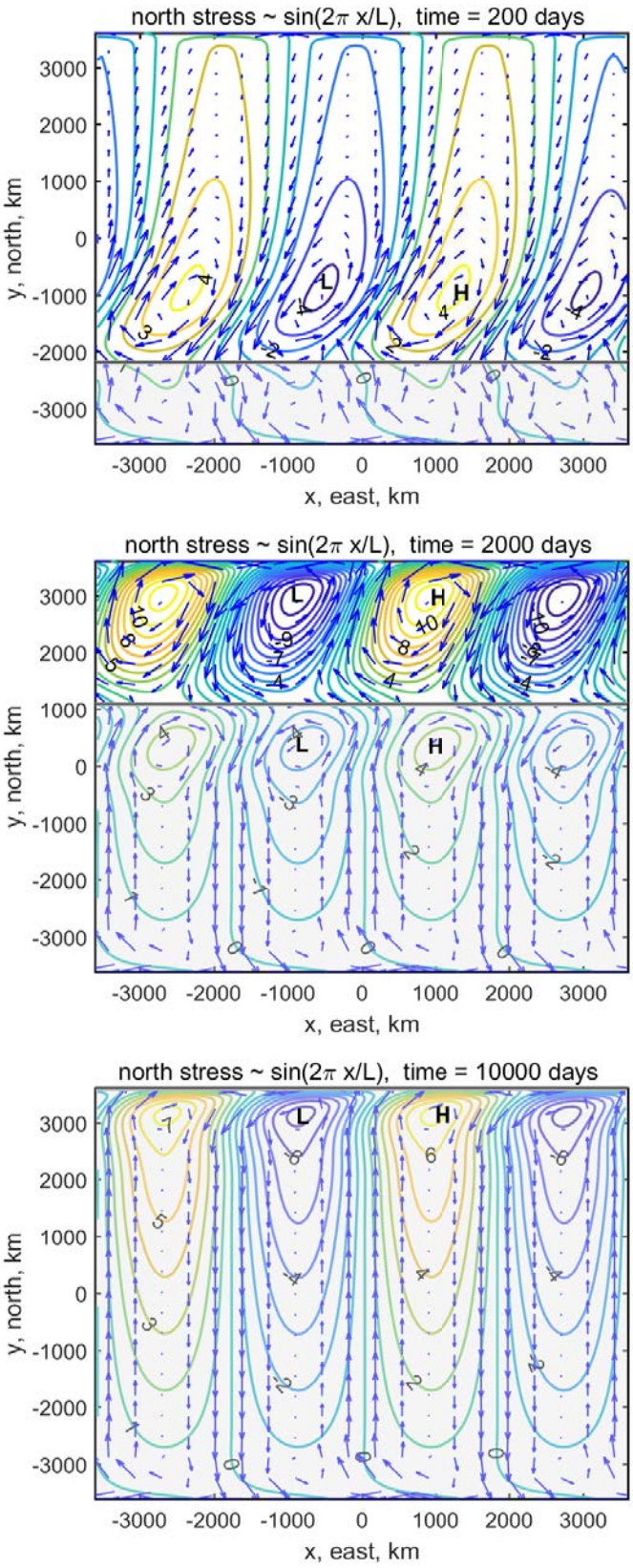

Figure 45: Snapshots from a wind-driven experiment in which the basin is a channel, and the wind stress was northward and x-dependent (Fig. 44, upper). The stress was set to a very small value, 0.01 N m^{-2}. Times were 200, 1000 and 10000 days (upper, middle, lower) after the stress was switched on. The contours are the anomaly of layer thickness in meters and the blue arrows are the current, though with boundary currents omitted. The gray shading extends northward from the southern boundary to a distance Y determined by the time, the y-dependent long Rossby wave speed and the zonal scale of the wind, L_τ, via Eqn. (85). Poleward of Y the flow is in Stage 2. Notice that there is clear evidence of westward propagation in especially the southern part of this region. Equatorward of Y the flow is adjusted to a near steady state Sverdrup balance (Fig. 44, lower). At a given y, the progression from Stage 2 to Sverdrup flow occurs at the same time across the entire channel (independent of x).

a thermocline layer, and a thick, active abyssal layer. It solves for a free sea surface and so the pressure anomaly is computed from the mass field in a completely straightforward way (Sec. 4) with no appeal to the reduced gravity approximation.

The baroclinic phenomena of the reduced gravity model are contained within the three layer model, let $h_2 \to 0$, and $h_3 \to \infty$, though with somewhat different amplitudes. The important point is that everything that was learned from the reduced gravity model makes a useful contribution towards understanding the more comprehensive (and also more interesting) results described next. The solution of the 3l-fs model contains additional phenomenon, and especially barotropic phenomena, that are different in amplitude and time scale from the purely baroclinic phenomenon of 1l-rg, but are not truly different in kind.

The new solution is certainly more voluminous in the sense that $u = u(x,y,z,t)$ in place of $u = u(x,y,t)$. Though the z dimensionality is still strongly truncated, it is nevertheless challenging to display the full solution in a manuscript. To start, the emphasize will be one 'latitude', $y = -1000$ km, which is on the south side of the subtropical gyre. At this latitude there is both an appreciable wind stress, $\tau^x = -0.075$ Pa toward the west, and a significant stress curl, $\nabla \times \tau = -5.8 \times 10^{-8}$ Pa m^{-1}, which implies clockwise turning. The data from this latitude are shown in three forms. 1) At the basin center 'longitude', $(x,y) = (0,-1000)$ km, the current east and north components for each layer are shown for the first 30 days in Fig. (46). 2) The meridional component of the transport at the same site but for short, medium and long times is in Fig. (47). 3) The meridional volume transport across the interior of the basin is in Fig. (48).

8.1 Inertial motion and Ekman transport in the surface layer

For short times, a few tens of days, the surface layer current and transport is familiar from the reduced gravity model, or for that matter, a purely local model, viz., near-inertial currents in both components, and Ekman transport in the meridional component, (the surface layer is represented by the red lines of Figs. (46) - (48). At the site sampled in these figures, $y = -1000$ km, the wind stress is westward, hence the Ekman transport is positive (northward) and has the magnitude expected for the wind stress at this site. This Ekman transport occurs throughout the model domain, though of course with varying amplitude and sign depending upon the local wind stress (just as in Sec. 4.1).

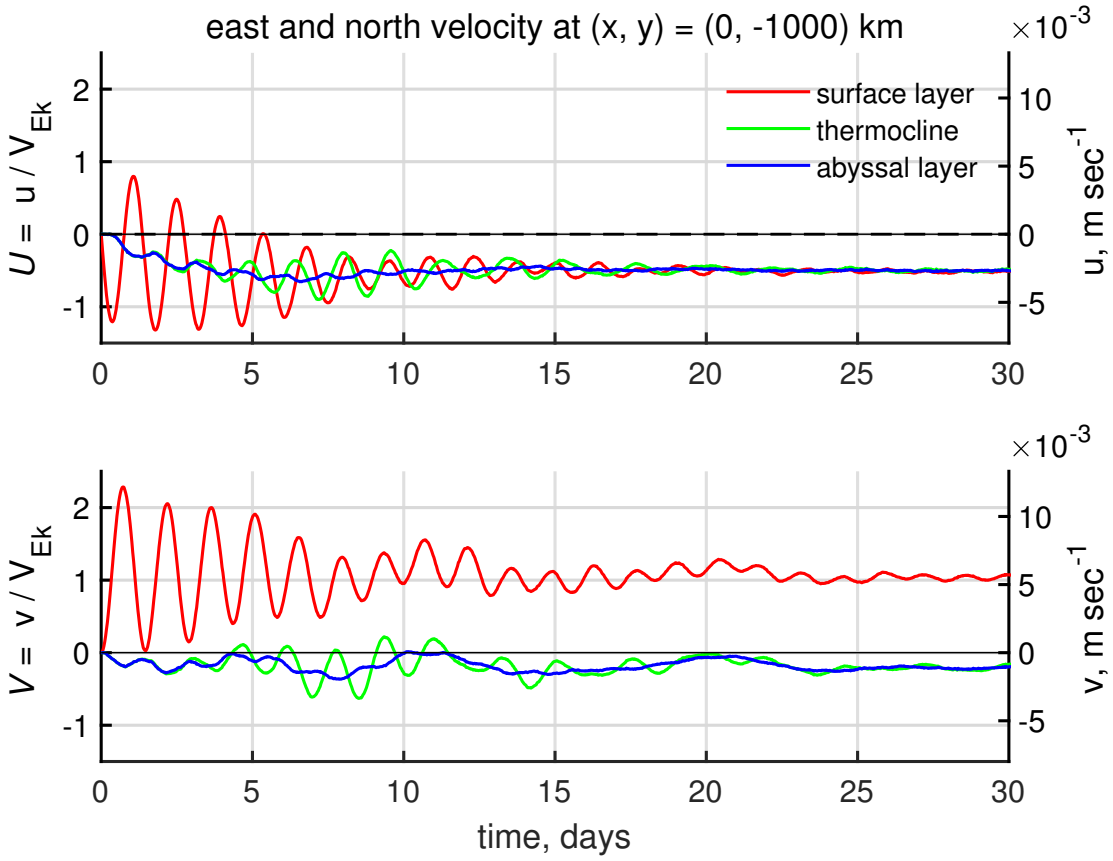

Figure 46: The short time evolution of the east and north components of the current computed by the three-layer model and sampled on the southern side of the subtropical gyre, $(x,y) = (0,-1000)$ km. Currents are normalized by the Ekman velocity scale, Eqn. (48), evaluated at this location, $V_{Ek} = 5 \times 10^{-3}$ m sec^{-1}. **(upper)** East currents in each of the the three layers; surface layer currents are in red, etc. The high frequency oscillations seen here are near-inertial motion. The time-mean of u is associated with barotropic Sverdrup flow discussed in the main text. **(lower)** North currents. The time mean dimensional current is about 5×10^{-3} m sec^{-1} and the non-dimensional value is about 1. This is as expected if the surface layer current is mainly Ekman flow. Layers 2 and 3 are unaffected by the direct wind stress, but nevertheless evidence a small, southerly barotropic Sverdrup flow that is modulated by barotropic Rossby waves having a period of about five days. The barotropic (depth independent) motions are much more prominent in the transport, bext figure.

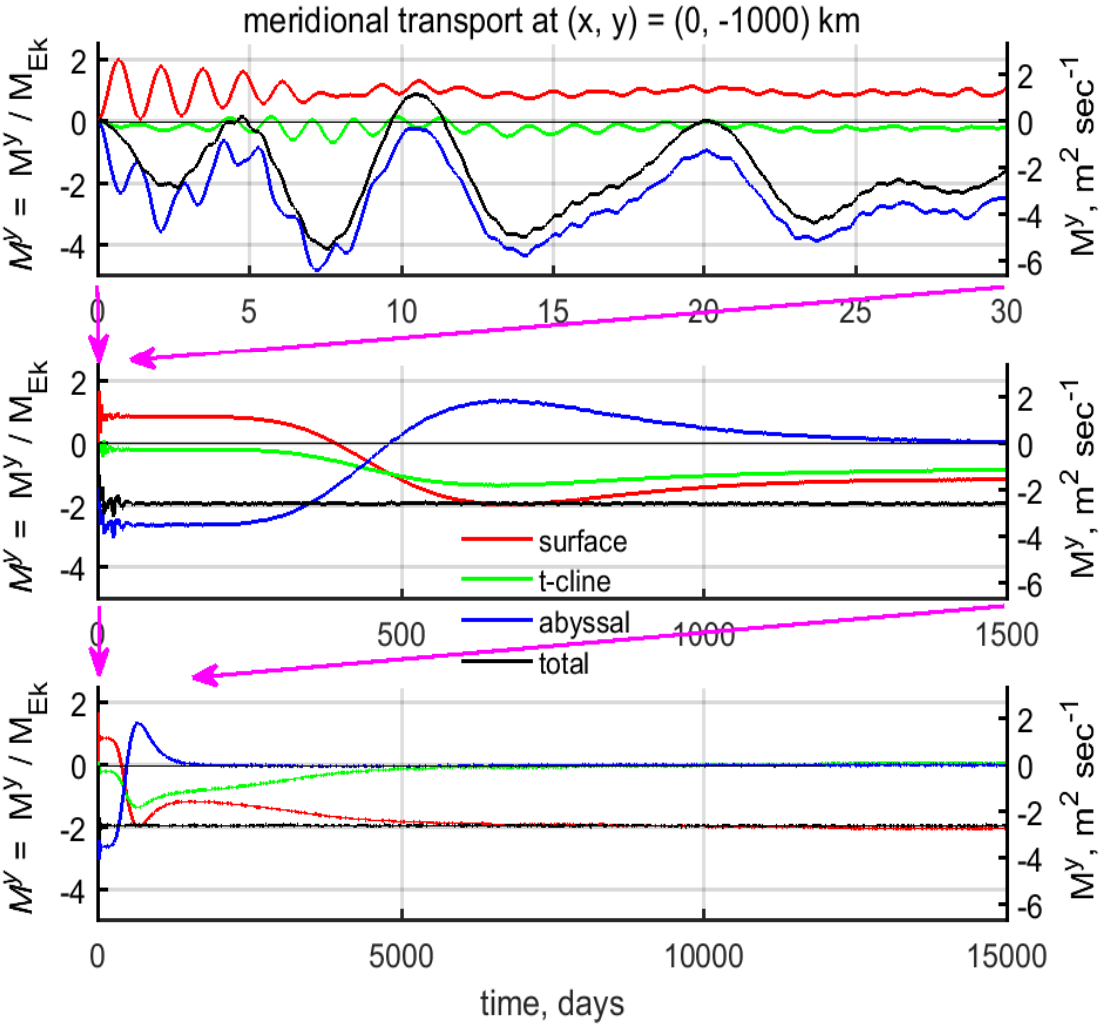

Figure 47: The meridional component of the transport at $(x, y) = (0, -1000)$ km. The data are shown on three time scales, **(upper)** 0 - 30 days, **(middle)** 0 - 1500 days, and **(lower)** 0 - 15000 days. Dimensional scale is shown at right, and nondimensional scale is at left. In this figure the transport is normalized with the expected Ekman transport magnitude at this y, $M_{Ek} \approx 1$ m^2 sec^{-1}. The surface layer transport (red line) is mainly Ekman transport and is northward. The total transport (all three layers) is the black line, which notice, has a very large contribution from the abyssal layer at short times, and is southward.

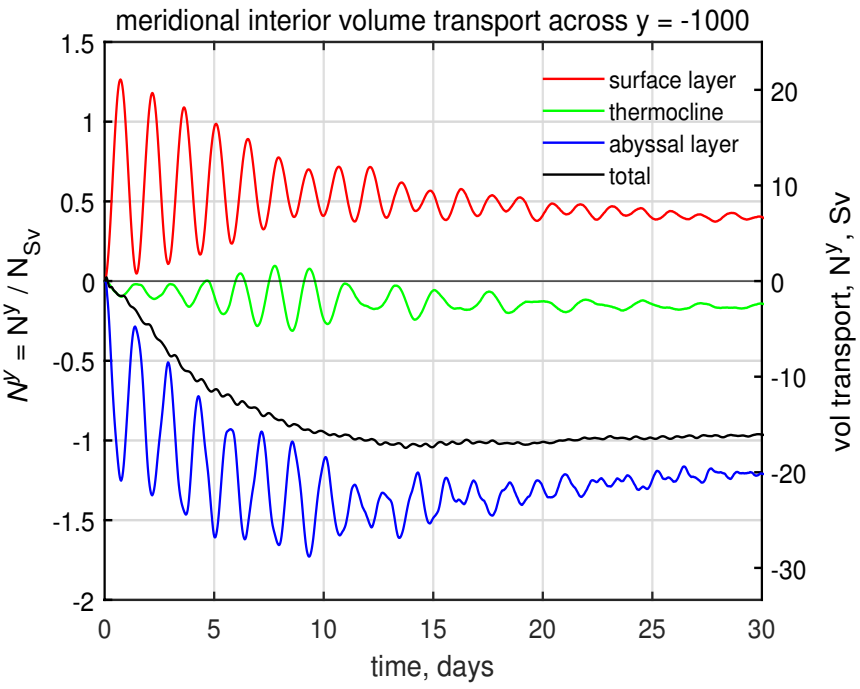

Figure 48: Meridional volume transport in the basin interior across y = -1000 km. The transport has been integrated from the eastern boundary to within 200 km of the western boundary. The volume transport within the surface layer (red line) is mainly Ekman transport and is northward as in the previous figure. The volume transport in the thermocline and abyssal layers is shown by green and blue lines; the sum over the three layers (the full water column) is the total volume transport shown as the black line. The dimensional scale is at right, and a nondimensional scale based upon the expected Sverdrup transport magnitude at this y, $N_{Sv} = 17$ Sv, is at left. Notice that the total transport appears to be quasi-steady from day 10 onward, and is -1 in these nondimensional units. Hence, the total transport is consistent with Sverdrup transport at this y.

8.2 Transient, barotropic flows

Over the region of negative stress curl that becomes the subtropical gyre, the Ekman transport is convergent. If that was all that was relevant, this Ekman convergence would thicken the surface layer at a rate of about 3 cm per day. In the context of a reduced gravity model, this produces a slowly growing baroclinic pressure gradient, and consequently a slowly increasing baroclinic, geostrophic current. By slowly is meant that it takes hundreds of days for this purely baroclinic process to produce an appreciable pressure gradient. The presence of an active (or free) sea surface and an active abyssal layer in the present model gives a much quicker barotropic response. A thickening of the surface layer by a few centimeters will tend to cause a positive displacement of the sea surface by a few centimeters/2. A displacement of the Layer 2 interface by this amount is hardly noticeable, but a displacement of the sea surface by a few centimeters is quite significant insofar as it produces a significant pressure gradient and thus flow within the thick abyssal layer. The resulting abyssal and thermocline layer currents are small amplitude, but the associated transport (current times thickness) is large since the abyssal layer is very thick, (Fig. 47). For short times, a few weeks or even just a few days (Fig. (48, upper) the meridional transport at the observation site $(x,y) = (0,-1000)$ km shows a time mean to the south, and a pronounced oscillation having a period of about five days. These oscillations are associated with short, barotropic Rossby waves, which like higher frequency inertial oscillations, are an unintended byproduct

of the impulsive start of the wind stress.

8.3 Basin scale circulation; barotropic Sverdrup flow

The convergence of Ekman transport in the middle of the model domain leads to a small positive SSH anomaly and thus a high pressure, Figs. (49) and (50). On day 1, SSH was a fairly symmetric mound with an amplitude of about 1 cm, centered in the model domain, and accompanied by geostrophic currents that flowed clockwise around the high pressure. These currents were subject to the beta-effect, divergence where the flow was southerly and convergent where it was northerly. The result is that the growing SSH anomaly had a tendency for a beta-induced westward translation, just as we have seen in mesoscale eddies, for example. A key difference is the rate, O(1000 km day^{-1}), which is much, much faster than westward translation of baroclinic mesoscale eddies and baroclinic Rossby waves. This speed is in the range of long, barotropic Rossby waves. By day 3, the positive η_1 hump was compressed up against the western boundary, and by day 10 the slope over the interior of the subtropics was an almost uniform tilt down from west to east. The plan view of the SSH shows cyclonic gyres in the tropics and subpolar regions and an anti-cyclonic gyre that fills the subtropics. Thus within the first ten days of the experiment, the ocean circulation develops as three gyres that in many respects — save for their depth-independence and small amplitude — are a foretelling of the baroclinic circulation that will follow in the next several years of this integration, and that characterized the purely baroclinic circulation of the 1l-rg model.

If the barotropic flow in the interior is consistent with the Sverdrup relation, then the barotropic meridional velocity is

$$V_{Sv-btr} = \frac{1}{\rho_o H \beta} \nabla \times \tau.$$

Along $y = 0$, the center of the subtropical gyre, the expected Sverdrup flow has a dimensional amplitude $V_{Sv-btr} = 1.0 \times 10^{-3}$ m sec^{-1}. In the gyre center $y = 0$, the wind stress and Ekman flow vanish, and so this V_{Sv-btr} is nearly geostrophic. The sea surface slope is thus expected to be

$$\frac{\partial \eta_{Sv-btr}}{\partial x} = \frac{f}{g} V_{Sv-btr} = \frac{f}{\rho_o g H \beta} \nabla \times \tau. \tag{86}$$

If this holds across the entire basin, then the SSH amplitude across the basin is just

$$\eta_{Sv-btr} = 2L \frac{\partial \eta_{Sv-btr}}{\partial x} = \frac{2fL}{\rho_o g H \beta} \nabla \times \tau. \tag{87}$$

For the present experiment at $y = 0$, $\eta_{Sv-btr} \approx 0.06$ m. These estimates are very close to the slope and SSH amplitude found in the numerical experiment, Fig. (50), but are much, much less than the amplitude found in the western subtropical North Atlantic, which is about 1 m east-to-west, Fig. 1. At this time the volume transport within the subtropics was very close to that expected from the Sverdrup relation (Fig. 51, left), and of the expected sense in the tropics and subpolar regions. As we saw before with the

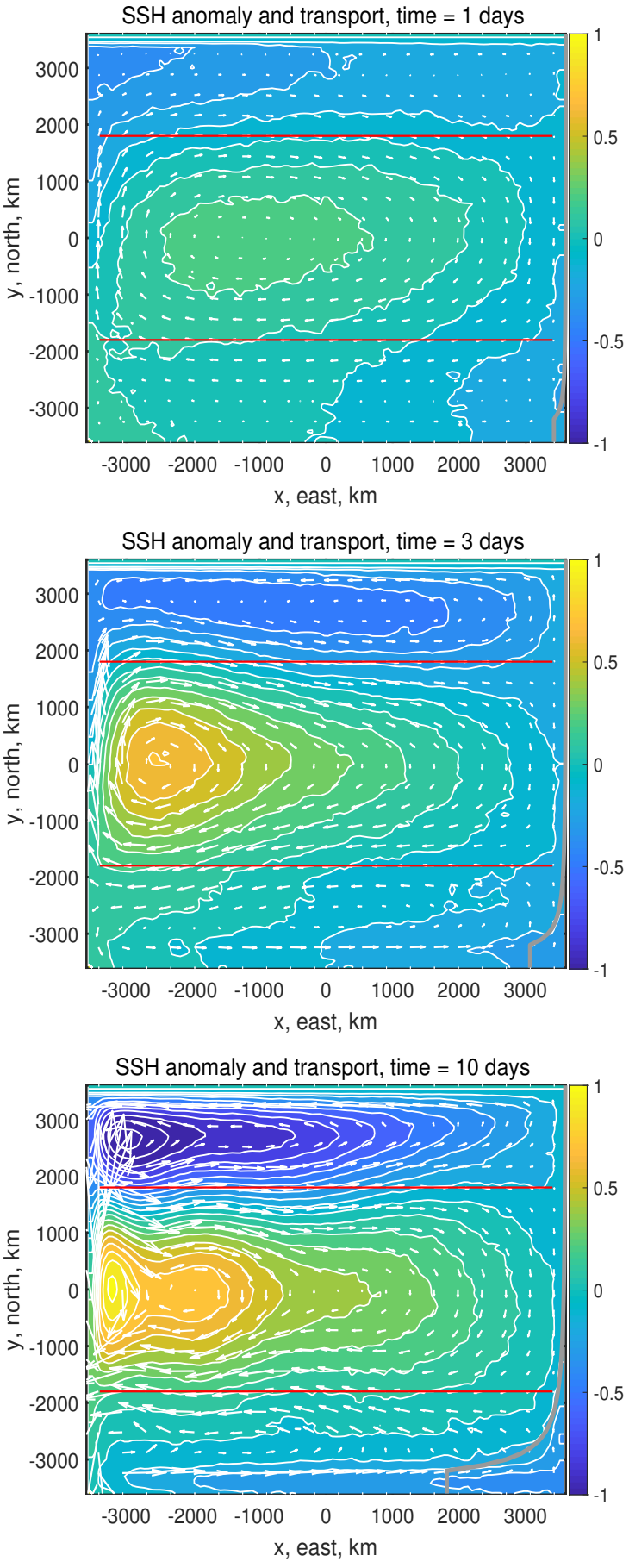

Figure 49: Three snapshots of SSH anomaly from a wind-driven, three-layer experiment at 1 day, 3 days and 10 days (top to bottom) after wind stress was switched on. The thin red horizontal lines are the axis of the westerly and easterly wind stress (Fig. 16). The small white arrows are the transport, though with the comparatively very large transports within the wbc omitted. The contours and colors are the SSH anomaly normalized with the barotropic Sverdrup SSH scale, Eqn. (87), evaluated at 30^o N $\eta_{Sv-btr} = 0.06m$. The largest positive SSH anomaly at day 10 is (dimensional units) $\eta \approx 0.06$ m in the western central subtropical gyre, and the greatest negative value is ≈ -0.09 m in the western subpolar gyre. The basin scale pattern evident here, *viz*, three highly asymmetric gyres, persists with minor changes for hundreds of days.

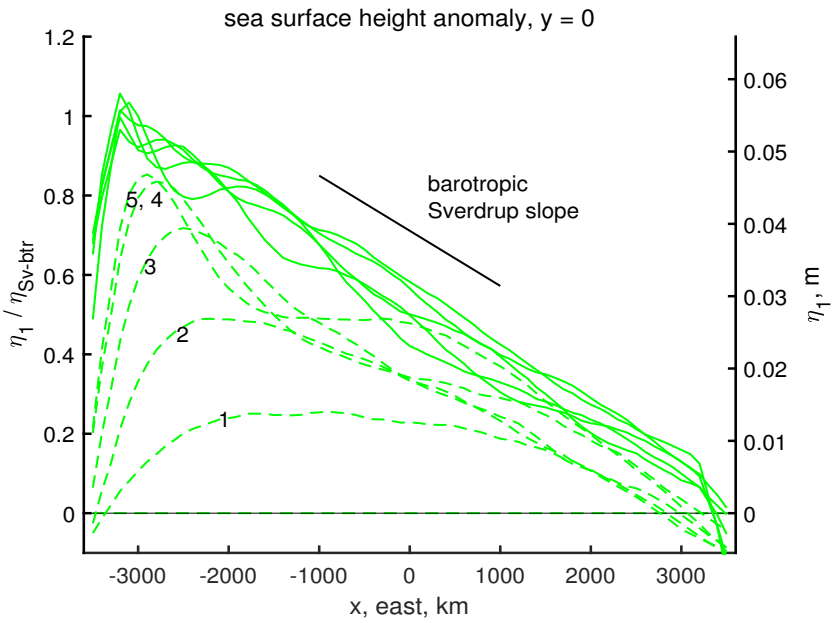

Figure 50: Successive across-basin profiles of SSH anomaly along $y = 0$. The first five days are the dashed green lines at 1 day intervals, and the next 25 days are solid green lines at 5 day intervals. The amplitude is scaled with the barotropic scale, Eqn. (86) which, for the parameters of this experiment, $\eta_{Sv-btr} = 0.05$ m. Note that on day 1 the SSH was a fairly symmetric mound. By day 3 this mound had shifted noticeably to the west, implying very rapid westward propagation, O(1000 km day^{-1}). After only about a week, the SSH slope over the interior region was close to the slope expected for a barotropic Sverdrup flow in geostrophic balance.

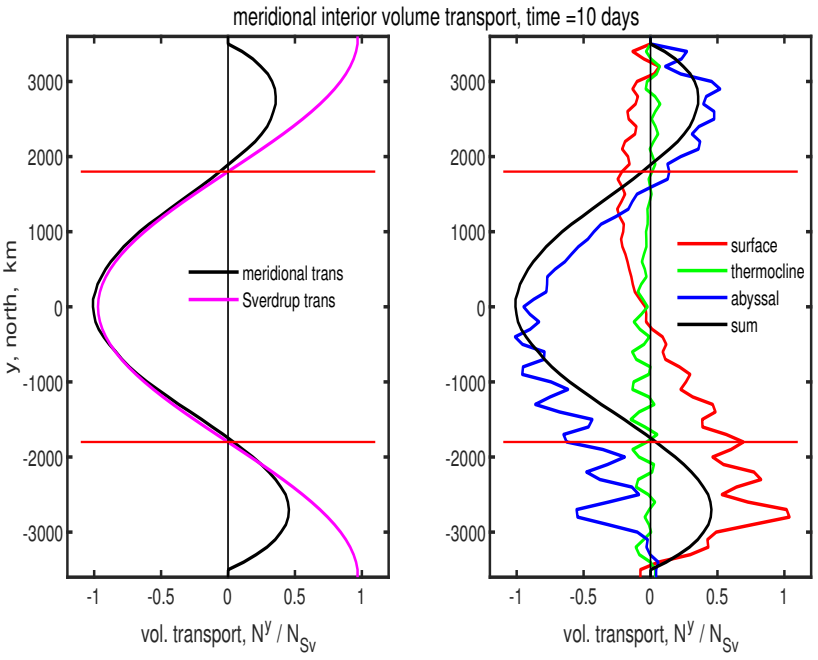

Figure 51: Meridional volume transport across the interior portion of the basin for all y and at time = 10 days. **(left)** Total transport (black line) and the expected Sverdrup transport (magenta). These are very similar over the subtropical gyre, but differ considerably near the northern and southern boundaries where the actual meridional transport must vanish. **(right)** Meridional transport in each of the layers of the three layer model, and summed to give the total transport, the black line, which is the same as at left.

reduced gravity model, there is a rather wide region adjacent to the northern and southern boundaries within which the meridional transport goes to zero as it must to satisfy the no normal flow condition on the solid boundaries. At this short time, the Sverdrup transport occurred throughout the water column, and in fact was mainly in the abyssal layer, Fig. (51, right).

8.4 Baroclinic adjustment to a surface intensified, steady state

After the first week, the SSH slope over the interior appeared to be quasi-steady. However, there was also evidence that SSH was continuing to evolve, albeit slowly. Sea level was rising very slowly over the entire subtropics, and, there was a region of much steeper SSH slope developing close to the eastern boundary and spreading slowly westward. This was the start of a baroclinic adjustment toward a surface-intensified, steady state.

The currents at $(x,y) = (0,-1000)$ km continued to evolve, albeit very slowly compared to the very rapid onset of the barotropic state. The abyssal layer transport, which early on made up most of the total Sverdrup transport, began to weaken at about 400 days, and then oscillated once and settled to nearly zero at about 1400 days, Fig. (47, middle). The total transport remained consistent with Sverdrup transport, but thereafter, the Sverdrup transport was contained within the thermocline and surface layers. At about 1500 days, the thermocline layer transport started a slow decrease and then nearly vanished by about 7000 days, Fig. (47, lower). Thereafter, the Sverdrup transport was contained almost entirely within the surface layer. These times, very roughly 1000 days and 5000 days, are very broadly consistent with the expected transit time of the first and second baroclinic modes from the eastern boundary to the basin center, about 700 days and 2700 days for the first and second baroclinic modes at this y which is equivalent to about latitude = 22^o . Consistent with this, and perhaps more convincing of a modal description is that the change of the current profile over time looks a lot like the first and second baroclinic modes (Fig. 53), e.g., from 1500 days to 7000 days the change in the current is consistent with the arrival of a second mode (the abyssal layer remains at rest, while the thermocline and surface layers accelerate in opposite directions). If you look closely you can see that the change in the current profile is not exactly like a second mode in that the decrease of the thermocline layer is greater in amplitude than the is the evident increase of the surface layer. The size of the change is inversely proportional to the layer thicknesses, which at this time had changed quite a lot from the initial values; the surface layer was considerably thicker and the thermocline significantly thinner than in the initial state, Fig. (54).

The total transport — Sverdrup transport — is unchanged as these baroclinic waves pass by, but the distribution of the transport becomes increasingly surface intensified. In the final, steady state, the Sverdrup transport occurs entirely within the surface layer. At one level this is not surprising, as the surface layer absorbs all of the wind stress and stress curl. Thus, only the surface layer can sustain a steady meridional flow in the presence of a beta effect. The deeper layers can be set into motion during the transient stage of the response, since they are subject to pressure gradients, and hence can sustain geostrophic motion. They are also subject to being compressed and stretched, Fig. (55), and so can display some of the consequences of potential vorticity conservation, i.e., there can be a q-conserving flow in the deep and thermocline layers so long as they are being stretched. However, this can not continue into a steady state in which stretching (time changing thickness) vanishes.

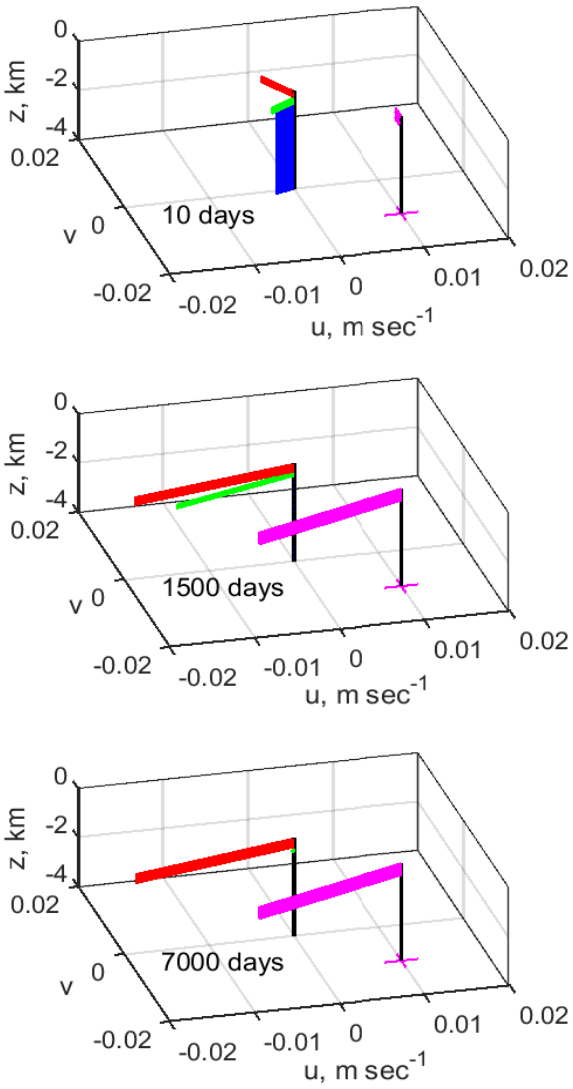

Figure 52: Model-computed current profiles from the site $(x,y) = (0,-1000)$ km, shown at three times, **(top)** to **(bottom)**, 10 days, 1500 days and 7000 days. The three-color profile is from the three-layer model, and red, green and blue are the surface layer, thermocline and abyssal layers, respectively. The magenta only profile (offset from center) is from the single layer model. The view is towards the north-northeast. An abyssal layer flow is appreciable only at 10 days in the former. The three-layer profile goes from being barotropic with a small Ekman flow in the surface layer at 10 days, to entirely surface trapped at 7000 days. At this site the flow in the steady Sverdrup regime at 7000 days is somewhat stronger in the zonal direction than in the meridional direction, cf. Fig. (56). Notice that the current in the single layer model is quite similar to the three-layer profile, except at 10 days.

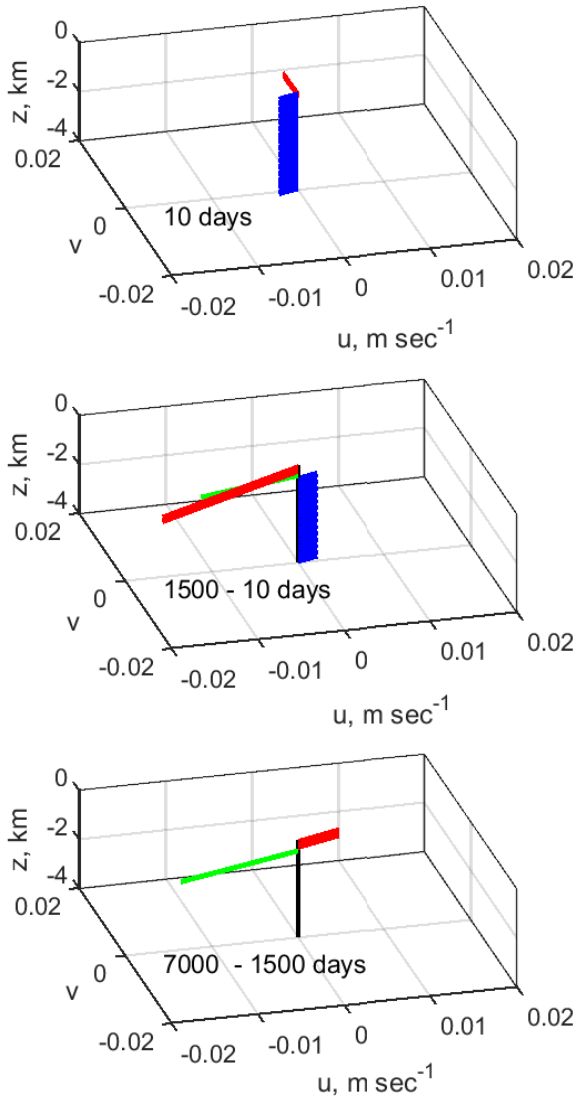

Figure 53: Current difference profiles from the site $(x,y) = (0,-1000)$ km, shown at three times, **(top)** to **(bottom)**, 10 days, 1500 days and 7000 days, as in the previous figure. In the top panel, the red arrows are mainly Ekman flow, and blue vectors are the abyssal layer, the depth-independent barotropic flow at 10 days. The middle panel is the velocity difference, 1500 days - 10 days. Notice that this velocity difference is qualitatively much like the first baroclinic mode; upper and middle layers are in roughly the same direction and opposite the abyssal layer. (Fig. 18). The bottom panel is the velocity difference 7500 days - 1500 days. There is only a very small current in the abyssal layer, while the surface and thermocline currents are in approximately opposite directions, much like the second baroclinic mode.

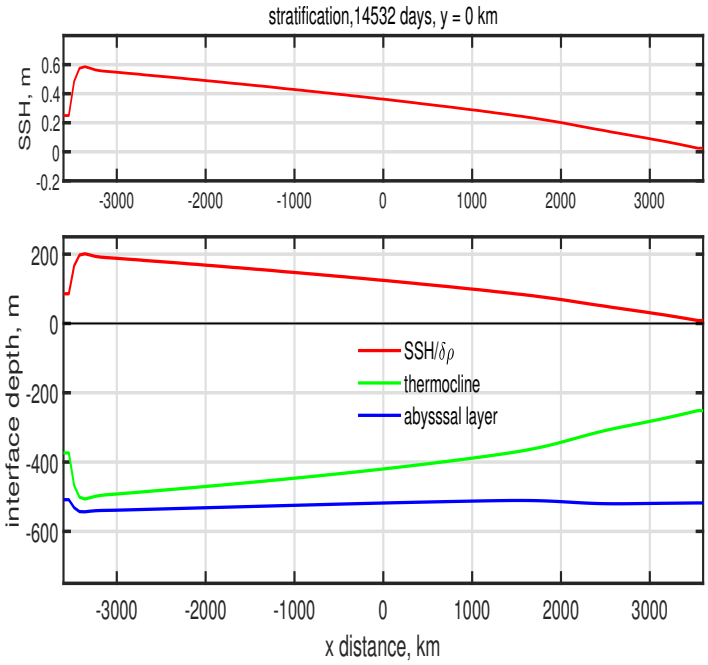

Figure 54: The SSH (upper panel, red line) and the interface between layers across the basin at y = -1000 km (red, green and blue; lower panel). Notice that the interface between the abyssal and thermocline layers (blue line) is essentially flat; there is almost no flow in the abyssal layer or the thermocline at this time. Also, note that the surface layer thickens markedly to the west and is generally much thicker than it was in the initial condition (250 m). The thermocline is generally much thinner.

9 Summary and closing remarks

9.1 O1: Upper ocean gyres seen in SSH are correlated with the wind stress curl

The large scale pattern of SSH anomaly, Figs. (1) and (4), correlates well visually with the large scale distribution of wind stress curl: SSH highs (the five subtropical gyres) are found beneath regions of negative stress curl, and SSH lows (the two subpolar gyres) are beneath positive stress curl. There is a simple mechanism behind this correlation, insofar as wind stress curl is approximately proportional to the divergence of the wind-driven Ekman transport (and negative stress curl yields a convergence of Ekman transport and thus a high of SSH and a thick upper ocean layer). This is the Stage 2 local response to wind and windstress curl discussed in Sec. 4.2. Model results suggest that a steady state, which is presumably what we see in the long-term mean of Fig. 1, follows from an adjustment to Sverdrup flow, in which the correlation is between meridional flow and wind stress curl.

9.2 O2: Upper ocean gyres are markedly asymmetric east to west

Sverdrup flow over most of the interior of a basin. The basin-scale, horizontal structure of the wind-driven ocean circulation, including western intensification and several of the qualitative differences between tropical, subtropical and subpolar gyres, have a plausible analog in solutions of the shallow

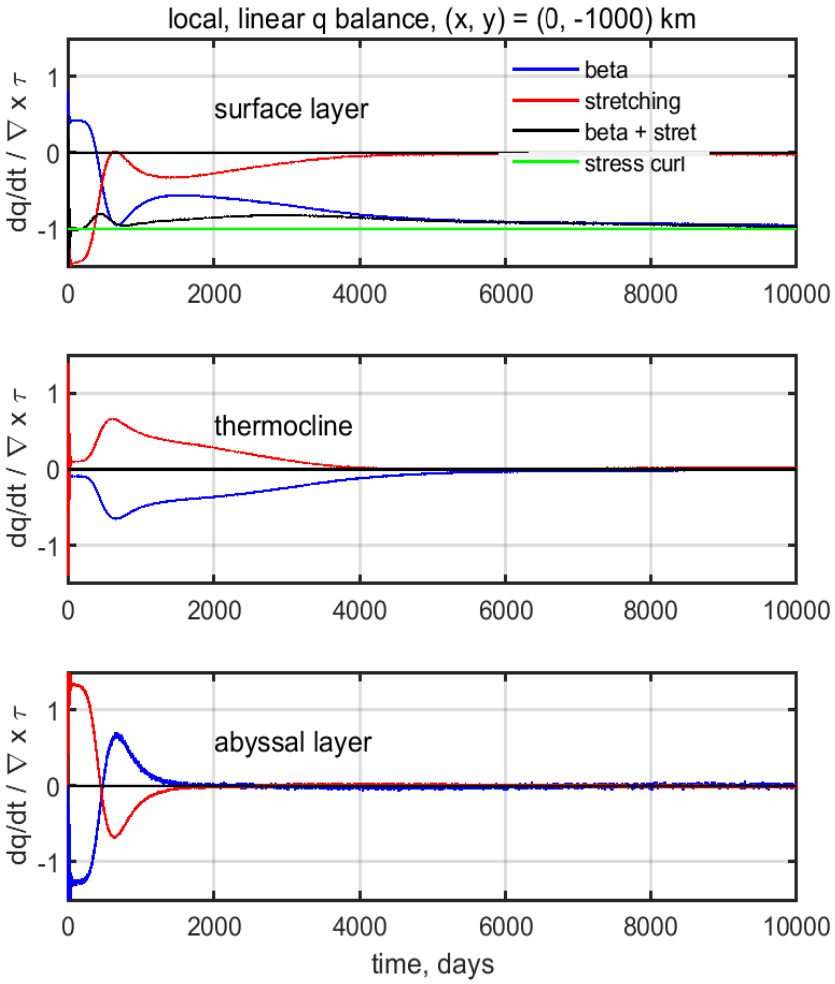

Figure 55: The linear balance of potential vorticity in, top to bottom, the surface layer, the thermocline and the abyssal layer.

water model. Over the subtropical North Atlantic, where the wind stress curl is negative, the interior meridional flow is southward as expected from the Sverdrup relation. Over the tropical and subpolar regions, the stress curl is positive and the meridional flow is northward, also as expected from the Sverdrup relation. This general result — that the Sverdrup relation provides a plausible and useful explanation of the major wind-driven gyres — has been accepted since at least the 1940s, and has been tested and validated quantitatively in modern, field data-based studies[10].

The Sverdrup relation is expected to be valid provided that the dominant processes of the potential vorticity balance are just two: the beta effect acting upon a very slow and thus linear meridional current, in balance with the curl (torque) of the wind stress. In practice, this holds in the majority of interior regions that are well away from zonal or meridional boundaries (hundreds of kilometers).

Departures from Sverdrup flow in zonal and meridional boundary regions. In a steady circulation, the meridional Sverdrup transport across every zonal, cross-basin section must be returned in

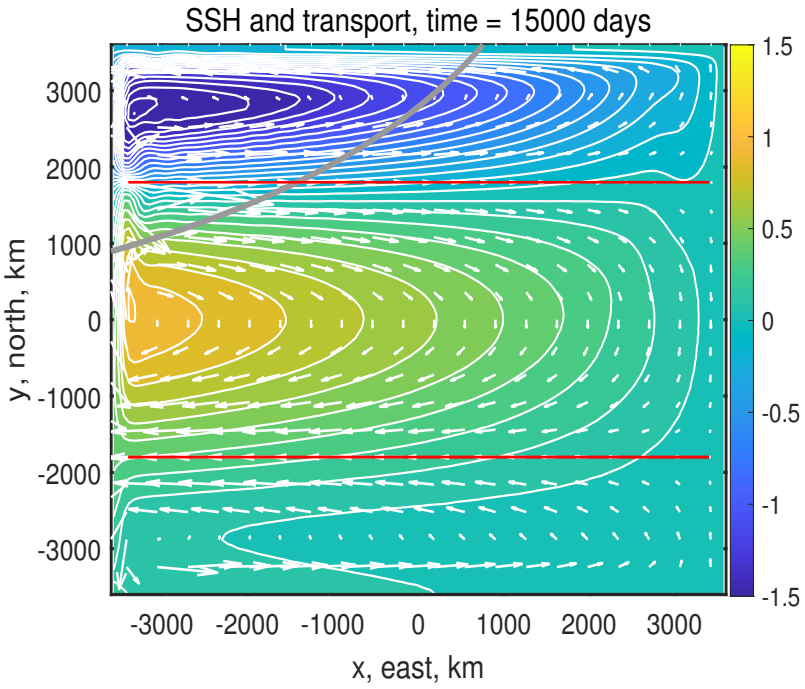

Figure 56: SSH anomaly from the three layer model experiment at time 15000 days. The thin red horizontal lines are the axis of the westerly and easterly wind stress (Fig. 16). The small white arrows are the transport, though with the comparatively very large transports within the wbc omitted. The SSH anomaly is nondimensionalized by the baroclinic scale, $\eta = 0.9$ m. The parabola at upper left is the second baroclinic eastern boundary wave, which notice, has still not swept the entire basin.

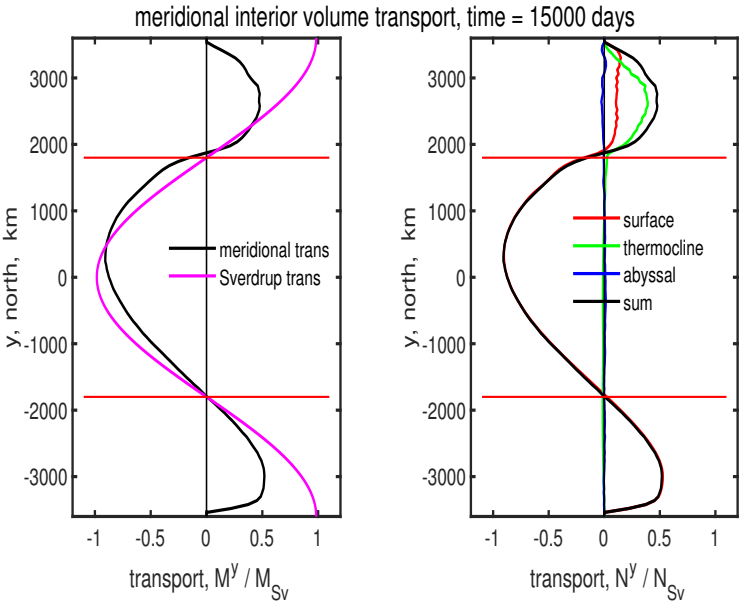

Figure 57: Meridional volume transport across the interior portion of the basin for all y and at time = 15000 days. **(left)** Total transport (black line) and the expected Sverdrup transport (magenta). These are similar over the subtropical gyre, but differ considerably near the northern and southern boundaries where the actual meridional transport must vanish. **(right)** Meridional transport in each of the layers of the three layer model, and summed to give the total transport, the black line, which is the same as at left. Notice that the total transport is mainly in the surface layer except in the subpolar gyre where there is still considerable transport in the thermocline, cf. Fig. (56).

the opposite direction by some other process. In the shallow water model and in the real ocean, this return flow occurs in a comparatively narrow and thus very intense western boundary current (wbc). The wbc is northward in the subtropical gyre where the Sverdrup transport is southward, and reversed in the subpolar and tropical gyres. The width of the western boundary region is observed to be very narrow, O(100 km). In the simple shallow water model used here, the width of the wbc is the baroclinic radius of deformation. The inviscid, linear Sverdrup interior fills the rest of the basin, 7000 km, and hence the westward intensification (east-west asymmetry) of the major ocean gyres is very pronounced, about 7000/100 in a North Atlantic-size basin.

The meridional flow must vanish on zonal boundaries. In the present model, the zonal boundary dynamics includes a significant contribution from linear friction, which is dubious as a model of dissipation in the real ocean. The width (north-south extent) of the affected zonal boundary region is rather wide, O(1000 km) and thus the meridional flow in the northern half of the subpolar region is less than would be expected from a Sverdrup balance and goes to zero on the boundary (which is expected, of course).

9.3 O3: Subtropical and subpolar gyres are quasi-steady while tropical circulation shows significant seasonal variation

Startup time of the baroclinic circulation. A wind-driven, start-up experiment in the 1l-rg (one layer, reduced gravity) model shows that the baroclinic circulation at a given point in the interior of a large ocean basin reaches an approximate, steady, Sverdrup flow some time after the passage of what amounts to a long, baroclinic Rossby wave starting from the eastern boundary. The long Rossby wave speed, $\beta C^2/f^2$, which has a strong dependence upon latitude, is thus a crucial parameter in the time-dependent response of a wind-driven gyre. For a North Atlantic-sized basin, the elapsed time required to reach full steady state is about thirty years at a subpolar latitude, about five years in the subtropics, and much less, about a year, in the tropics.

Annually-varying winds. This marked latitudinal variation in the rise time of the baroclinic wind-driven circulation is relevant to understanding the observed response to an annually-varying wind stress. Model experiments that assumed a $\pm 50\%$ annual period variation of the wind stress find that the subpolar circulation varies almost not at all, the subtropical gyre varies only a little, while some aspects of the tropical circulation vary quite a lot. The transport of the tropical wbc varies by only about $\pm 10\%$, but the zonal flow in the eastern half of the tropical gyre varies by $\pm 50\%$. This latter variation is mainly a local a response to the annually-varying stress curl, and partly a Sverdrup flow. Thus a seasonally varying wind stress that will have almost no effect on the subpolar or subtropical circulation (interior or wbc) and yet will produce a fairly pronounced response of especially the zonal, open ocean SSH and currents within the eastern tropical ocean.

Barotropic circulation. This essay emphasizes the baroclinic circulation because that is what we can see in the kinds of observations that are most widely available — SSH from satellites and upper ocean density from a variety of *in situ* methods, e.g., Figs. (1) and (2). As well, baroclinic circulation contributes the majority of meridional heat transport by the oceans. However, we shouldn't dismiss out of hand the possibility and importance of a barotropic circulation (which is inaccessible to the 1l-rg model). To get a sense of the barotropic circulation requires a model with a free (moving) sea surface and that supports very fast barotropic waves (here, 3l-fs). Now let's ask the question — how long does it take to establish a quasi-steady Sverdrup regime after the onset of a wind field? The answer is about one week, if we acknowledge the barotropic response. The currents associated with the barotropic response are distributed throughout the water column, and hence the upper ocean current is very small. Similarly, the SSH signature is about 10% of that observed.

9.4 O4: The Sverdrup flow of the subtropical gyre is somewhat surface intensified

The vertical profile of the geostrophic current that makes up the Sverdrup transport of the North Atlantic subtropical gyre was observed to have a depth scale of about 300 - 600 m, with shallower values to the eastern side of the basin (Sec. 2.4). It is probably not coincidental that this is closely comparable to the thickness (depth) of the main thermocline. The zonal tilt of the main thermocline provides the thermal wind that leads to the somewhat surface intensified Sverdrup flow. A multi-layer model (Sec. 8) that was initialized with a plausible main thermocline thickness will develop Sverdrup flow within a surface layer that has about that same thickness and zonal tilt. That seems promising at first, but contains two difficulties. First, the approximate depth scale of the thermocline was initial data for the model, and so not truly predicted. Second, the Ekman layer and the Sverdrup layer of the present three-layer model are *per force* the surface layer of the model, and considerably thicker than is the actual Ekman layer of the ocean (400 m vs 100 m). A fully predictive model of the Ekman and Sverdrup layers will have to recognize vertical mixing associated with surface layer processes (wind mixing and air-sea heat flux, among others) in order to have a realistic Ekman layer thickness. As well, baroclinic instability will likely help redistribute horizontal momentum in the vertical, and increase the effective thickness of the Sverdrup layer well beyond that of the Ekman layer.[21]

[21] To follow up on this requires a depth-dependent model and some means to specify the depth of the Ekman layer, d_{Ek}. These are outside the present scope, but note that a landmark advance on the theory of wind-driven circulation was developed along this line by Jim Luyten, Joe Pedlosky and Hank Stommel, 'The ventilated thermocline', J. Phys. Oceanogr., Feb. 1983.

10 Supplemental material

10.1 Links to models and updated manuscripts

The code used to solve the wind-drive circulation problems discussed here is very similar to that used in the Parts 2 and 3 treatments of geostrophic adjustment and eddy propagation. However, the data required to specify the configuration of the wind-driven experiments is sufficiently different that a dedicated program was written:

gyre.for is a Fortran code that solves the shallow water equations for the wind-driven circulation in an enclosed ocean basin. A variety of wind stress forms and time histories may be specified. The numerical methods are not highly sophisticated or complex, and the code should be fairly amenable to modification. The longest integrations shown here will run in a few hours on a fairly capable, PC workstation. Output goes to a Matlab.mat file which may be read by a Matlab script,

gyre_plot.m makes several kinds of diagnostic plots from the data generated above.

These codes may be downloaded from https://www2.whoi.edu/staff/jprice/aCt-codes

10.2 Homework problems

1. At 30^o N, $f = \Omega$, and the inertial period is $2\pi/\Omega = 23$ hrs, 56 min, or less than a day by $\approx 1/365$ days. Can you explain where this small difference with a day comes from?

2. Starting with Eqns. (8) and (7), eliminate v to derive the corresponding governing equation for h. Is it significant that this wave equation is first order vs. the more common second order equation, e.g., shallow water gravity waves? What is the consequence of the beta effect in the case that the zonal gradient of thickness is positive? Is it relevant that the momentum balance Eqn. (8) is geostrophic?

3. Can you relate the observed summer to winter change in SSH over the subtropical gyre (Fig. 10) to the change in steric height (change in upper ocean density)?

4. The steady solution Fig. (49) includes three gyres, tropical, subtropical and subpolar. Contrast the model-computed tropical and subpolar gyres with respect to the magnitude of their currents, layer thickness anomaly, and transports. Compare the solution Fig. (49, lower) with the observed SSH of Fig. (2). Why does the tropical gyre (or region) have a comparatively small SSH anomaly? The

subpolar and tropical gyres have roughly comparable anti-clockwise circulations, and yet the wind over the subpolar gyres is westerly, and the wind over the tropical gyre is easterly. But haven't we been saying all along that these gyres are wind-driven?

5. Explain the signs and the comparative magnitudes of the current components of Fig. (23). Notice that the Sverdrup meridional flow at the three sites is not identical. Why is there a small but systematic difference?

6. The overall pattern of SSH (Fig. 6, lower) and of the transport streamfunction (Fig. 11, left) are similar but not identical. Why is there a difference?

7. The potential vorticity derivation of the Sverdrup relation in Sec. 5.1 omitted some important details. 1) Can you show that the drag term in the q-balance equation for the interior is proportional to the Ekman number times L_{Earth}/L_{tau}, where L_{tau} is the horizontal scale of the wind stress field. 2) Given speed and space scales of the interior (Sverdrup) flow, show that the relative vorticity of the Sverdrup flow is indeed very, very small compared to planetary vorticity, f, and so to an excellent approximation the potential vorticity in the interior is given by $q \approx f/h$. 3) The advective term of Eqn.(42) may be approximated as Eqn. (18) because the geostrophic flow does not advect layer thickness. What evidence can you find in the steady solution, Fig. (49), that supports this (highly plausible) assertion?

8. The real ocean thermocline is continuously stratified in the vertical, and so the best one layer baroclinic model representation of the thermocline will likely have to compromise on something. The values used here, H =500 m, and $\delta\rho = 2$ kg m^{-3} are round numbers that give an appropriate gravity wave speed. What thickness slope is consistent with the Rossby wave view of the subtropical gyre developed in Sec. 4.4, and where is that slope found in the water column of Fig. (1)?

9. Assuming that the boundary current will have a maximum current adjacent to the boundary (and so a single sign of relative vorticity), show that the mode $beta = drag$ can obtain also for the case of an equatorward western boundary current as occurs in the tropical and subpolar gyres. Can you envision this balance for an eastern boundary current of either sign?

10. In the discussion of the Stage 3 transient response we noted that the change in the current from Stage 2 zonal flow to meridional Sverdrup flow occurs at a time that is proportional to the transit time of a long Rossby wave starting from the eastern boundary. This suggests an interesting derivation of the Sverdrup relation (albeit for a slightly special wind field) that makes especially clear the crucial role of the eastern boundary in a problem in which there is no other imposed zonal scale. Assume that the wind stress is purely zonal, and is switched on at $t = 0$ and then held constant, as in the base case. The Stage 2 zonal flow u_{S2} then grows linearly with time until the arrival of the eastern boundary wave. How does the then extant zonal flow compare with Sverdrup zonal flow? In general, the $u_{S2}(x,y)$ current is not the same as the steady state Sverdrup zonal flow, since the former depends upon $\partial^2(\tau/f)/\partial y^2$ and not $f^{-1}\partial^2\tau/\partial y^2$ as does the Sverdrup zonal current (and see Figs. 21 and 24). To remedy this, suppose that the y scale of the wind stress field is

much less than R_E. This will result from setting $n = 6$ in the wind stress Eqn. (35), and thus $\tau^x(y) \propto \sin(6\pi y/L)$. Can you show that the zonal transport at $t = T_{ebw}$ is then approximated well by

$$hu_{S2}(t = T_{ebw}) \approx -\frac{(L-x)}{\rho_o \beta}\frac{\partial^2 \tau^x}{\partial y^2} = \frac{\partial \Psi_{Sv}}{\partial y},$$

where the last step used Eqn. (71). Why does the zonal transport increases in magnitude in proportion to distance from the eastern boundary, $L - x$?

11. Can you show that the vorticity balance form of the Ekman number appropriate to a western boundary current, Eqn. (76), is related to the usual, momentum balance form $E = r/f$, by

$$E_Q = E\frac{L_\tau}{R_d}.$$

12. Assume a steady, wind-driven circulation. What would you expect to follow if the wind stress suddenly vanished? Check your intuition against https://www2.whoi.edu/staff/jprice//wind-off Now Imagine an experiment in which the wind stress is spatially uniform over the entire basin, and northward. What would you expect for Stage 2 and Stage 3? (Major hint: consider the stress curl.) What is the steady response? Once you have formed your answer, take a look at the circulation computed from such an experiment shown in Fig. (43, lower).

Index

adiabatic, 42

balanced current, 29
barotopic response, 93
barotropic and baroclinic, 46
beta effect, 28
beta plane, 28

coastal upwelling, 23
Coriolis force, 27

depth of no motion, 11

eastern boundary
    blocking, 57
    Rossby wave, 57, 58
Ekman current and transport, 50
Ekman layer thickness, 50
Ekman pumping and suction, 53
energy balance, 81

f-plane, 27

gyres
    exchange between , 58
    relationship to westerly wind , 22
    seven gyres worldwide, 21

inertial force, 27
inertial motion, 49

Lagrangian perspective, 80
layer thickness changes, 59
layered model
    single layer, 1l-rg, 43
    three layer, 3l-fs , 44

meridional winds, 90

normal modes, 45

potential vorticity, 43
    steady balance, 74

reanalysis, 11
Rossby wave
    arrested, 33
    baroclinic wave speed, 31
    barotropic long wave, 46
    dependence upon f, 58

seasonality
    tropical ocean, 13
shallow water model equations, 42
steady state, 48
Stokes drag, 42
streamfunction, 71
surface intensified, 100
Sverdrup flow
    depth scale, 12
Sverdrup relation
    q balance, 75
    range of validity, 18
    transport, 7
Sverdrup transport
    baroclinic, 37
    barotropic, 37
    streamfunction, 71

thermal wind, 11
thermocline, 9, 43

upper ocean, 12

vertical velocity, 35

wave/advection equation, 30
western boundary current, 75
    width, 76
western intensification, 8
westward propagation, 30
wind stress, 7, 40
    acceleration, 40
    seasonality, 84
wind stress field, 7

zonal boundary region, 77
    q balance, 77
    width, 78

a Coriolis tutorial, Part 5:

on the seasonally-varying circulation of the Arabian Sea

James F. Price

Woods Hole Oceanographic Institution,
Woods Hole, Massachusetts, 02543
https://www2.whoi.edu/staff/jprice/ jprice@whoi.edu

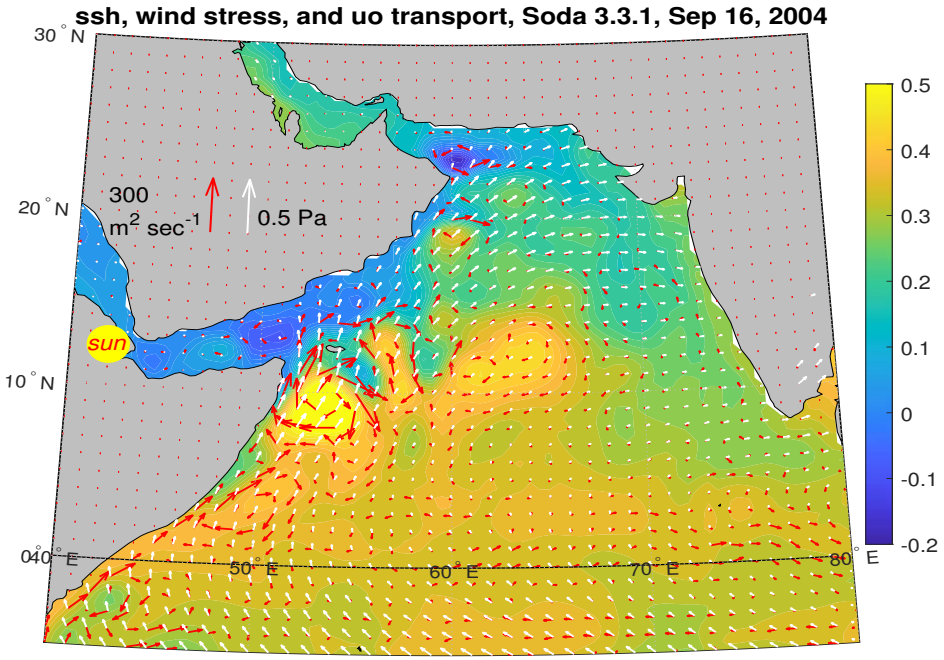

Figure 1: A snapshot from an animation of winds and ocean circulation of the Arabian Sea https://www2.whoi.edu/staff/jprice/AS-winds/ These data are from the Soda 3.3.1 reanalysis discussed below. The background is Soda-computed sea surface height, with a color bar at right in meters. The white vector field is wind stress from satellite scatterometry, with a scale vector at left. The red vectors are upper ocean transport, with a scale at left. The animation runs from January 2004 to January 2005. This frame is from mid-September 2004 and shows a typical summer circulation — a high over the central and western Arabian Sea, that is significantly perturbed by large eddies. The yellow disk that slides up and down the left side of the frame indicates the sun's declination. This figure and the accompanying animation will probably be overwhelming on first sight. An implicit goal of this essay is that you be able to interpret and anticipate much of what you see here.

Contents

1 Seasonal variability of the Arabian Sea **3**
- 1.1 The plan/summary . . . 3
  - 1.1.1 A description of the winds and the ocean circulation phenomena of the Arabian Sea 3
  - 1.1.2 Explaining the link between the wind and the summer circulation . . . 6
- 1.2 About this essay . . . 6

2 Data sources: SODA and AVISO **7**
- 2.1 SODA ssh compared with AVISO observed ssh . . . 10
- 2.2 Transport and volume transport . . . 11

3 South Asia Monsoon winds reverse with the seasons **13**
- 3.1 Summer winds, the Southwest Monsoon . . . 13
- 3.2 Winter winds, the Northeast Monsoon . . . 14

4 Arabian Sea circulation varies strongly with the seasons **15**
- 4.1 Summertime ssh and circulation . . . 15
- 4.2 The Great Whirl and lesser eddies . . . 19
- 4.3 Wintertime ssh and circulation; remote forcing from the Bay of Bengal . . . 22

5 Sverdrup transport is correlated with the summertime, meridional transport **23**
- 5.1 Regional, seasonal Sverdrup transport . . . 24
- 5.2 Monthly-varying transport across western boundary and interior regions . . . 26
- 5.3 Sverdrup and meridional transport are highly correlated at annual and semi-annual frequencies . . . 29
- 5.4 Summary of the description . . . 34

6 Experiments with western-biased, jet-like winds show a very fast adjustment **35**
- 6.1 Baroclinic Sverdrup flow . . . 36
- 6.2 Summary, why the Sverdrup relation is relevent . . . 38

7 Appendix: Finite amplitude effects — is that a great whirl? **38**
- 7.1 Froude, Ekman and Rossby numbers . . . 38
- 7.2 Speculation on an eddy formation process . . . 40

8 Concluding remarks **41**

9 Problems **43**

Index **44**

1 Seasonal variability of the Arabian Sea

The North Indian Ocean (NIO) is the only major ocean that did not appear in the list of basin-scale, time-mean gyres compiled as Table 1 of Part 4, since its annual mean circulation is not representative of an observable state. The NIO offers something different, and for our purpose, something better — a *seasonally-varying* circulation that is mainly a response to seasonally-reversing winds. Winter and summer circulation patterns are qualitatively different (Fig. 2) and largely repeatable from year to year. The summer circulation is especially interesting as it is the outstanding example of a significant, wind-driven circulation that is generated anew each year.

The object here is to offer a concise description of some of the remarkable phenomena that make up the Arabian Sea circulation, Fig. (3), both winter and summer. The specific goal is to explain as simply as possible (but not simpler) the link between the wind and the vigorous, summertime circulation.[1]

1.1 The plan/summary

1.1.1 A description of the winds and the ocean circulation phenomena of the Arabian Sea

The data sources that make this study possible are reviewed briefly in Sec. 2, and the all-important South Asia Monsoon winds are introduced in Sec. 3. The monsoon winds are different in almost every respect from the midlatitude winds of the North Atlantic; there is modest northeast wind over most of the Arabian Sea during the winter, and then very strong southwest winds develop during the summer. This seasonality has a profound effect upon the physical oceanography of the Arabian Sea, which is introduced in Sec. 4. The summertime circulation includes a compact anticyclonic gyre in the interior of the basin, and a poleward western boundary current, the Somali Current, which has meridional transport of about 30 Sv. There are several large anticyclonic eddies that recur in most summers, including the very strong Great Whirl. The wintertime circulation has by comparison a modest amplitude, meridional transport of roughly 10 Sv, and shows a significant influence of remote forcing coming from the Bay of Bengal.

[1] An excellent entree to descriptive oceanography of this region is the text by Talley, L., G. Pickard, W. Emery and J. Swift, 2011, Descriptive Physical Oceanography, Elsevier, ISBN:9780750645522. Some of the pioneering estimates of circulation amplitude and time-dependence are reported by Düing, W. and H. Szekielda (1970) Monsoonal response in the western Indian Ocean, J. Geophys. Res., 76, 4181-4187. An insightful and accessible research paper that anticipates much of what is found here is by Bruce, J. G., 1983, The wind field in the western Indian Ocean and the related ocean circulation. Mon. Wea. Rev., 111, 1442 - 1452. Also very useful is Shetye, S.R., Gouveia, A.D. and Shenoi, S.S.C., 1994, Circulation and water masses of the Arabian Sea. Proc. Indian Acad. Sci. (Earth Planet Sci.) 103, 107 - 123. https://doi.org/10.1007/BF02839532. A comprehensive and authoritative research review of the entire Indian Ocean is by Schott, F. A. and J. P. McCreary Jr., 2001, The monsoon circulation of the Indian Ocean, Prog. in Oceanogr., 51, 1 - 123.

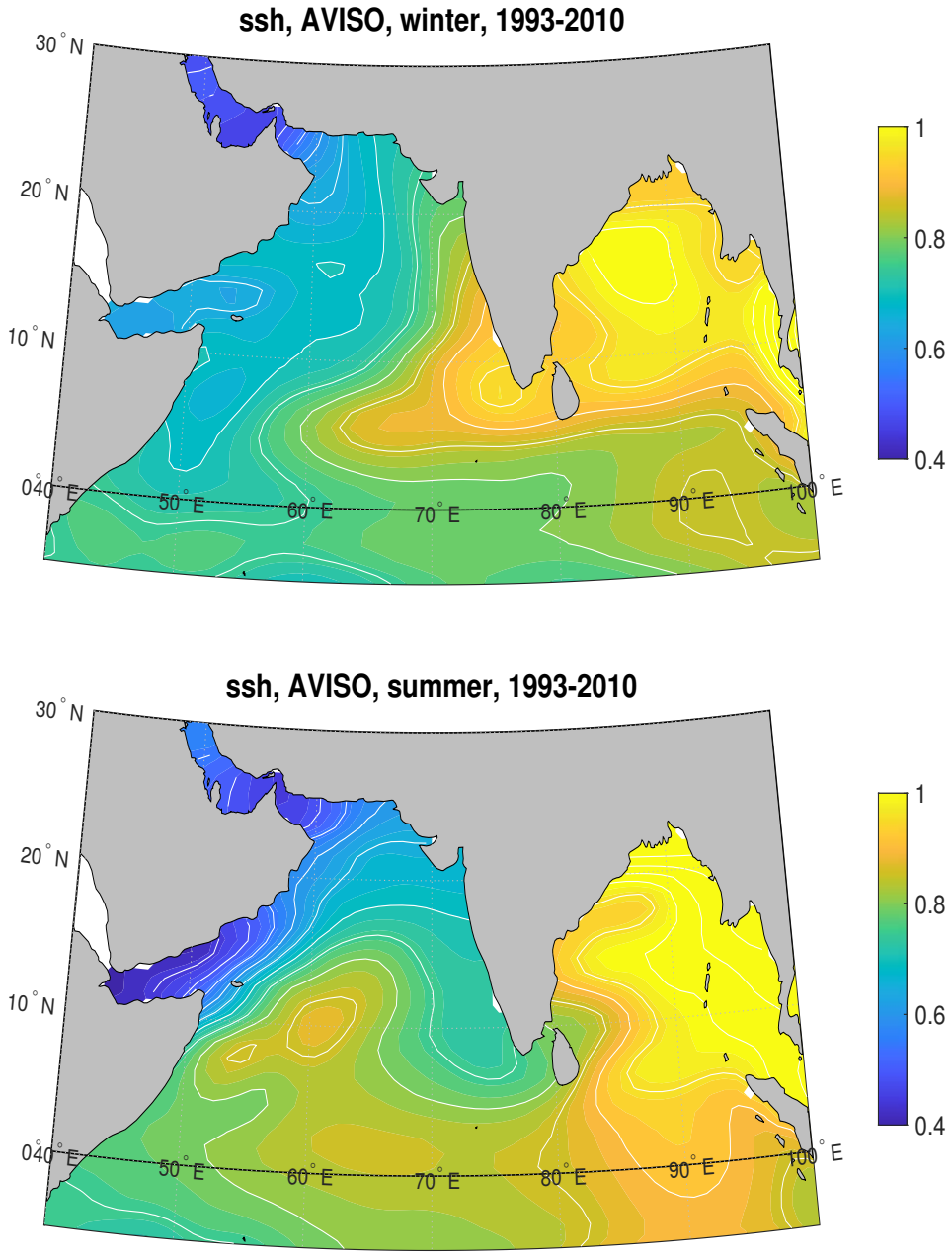

Figure 2: Seasonal averages of sea surface height observed by satellite altimetry and analyzed and archived by the AVISO project (https://www.aviso.altimetry.fr). These data are from the already smoothed (one degree, monthly) AVISO Level 4 analysis that was then composite averaged over winters **(upper)** and summers **(lower)** of almost two decades, 1993-2010. The colorbar at right is in meters. In the winter, high ssh emanates from the Bay of Bengal and spreads northward along the west coast of India and westward across the Arabian Sea along about 6 N latitude. The resulting 6 N ridge is said to be the result of remote forcing from the Bay of Bengal. In the summer, there is a compact high of ssh in the central basin of the Arabian Sea, centered on 10 N, 62 E. This summertime ssh high and the associated circulation are consistent with local and basinwide wind forcing.

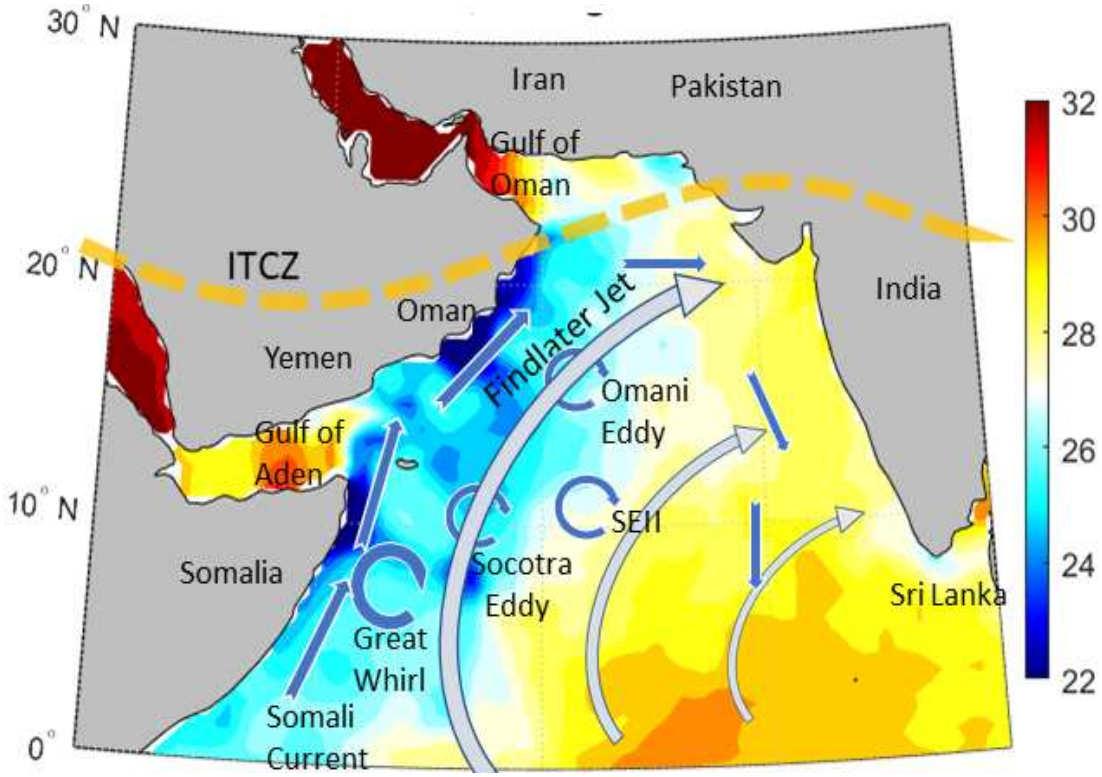

Figure 3: A schematic of the Arabian Sea during the summer, showing a number of the features discussed here. The background is the actual observed SST from mid August, 2021, with a color scale in degrees C at right. Meteorology includes the low pressure trough of the Intertropical Convergence Zone (ITCZ, heavy yellow dashed line), which in summer is near the northern edge of the Arabian Sea, and the Findlater Jet (the clockwise turning gray vector), which is a significant local maximum of the Southwest Monsoon winds. Notable oceanographic features include very cool SST in the coastal upwelling regions offshore of Somalia and Oman, a northward flowing western boundary current called the Somali Current, a large and intense anticyclone offshore of Somalia called the Great Whirl, and a somewhat weaker but still significant anticyclone called the Socotra Eddy. Two other anticyclones that appear in many years are also noted, SEII, a neighbor of the Socotra Eddy, and the Omani Eddy to the north. During boreal winter, the ITCZ is displaced well to the south of the equator, and the winds over the Arabian Sea are then reversed and weakened considerably compared to the summer winds depicted here — these oceanographic features soon disappear.

1.1.2 Explaining the link between the wind and the summer circulation

The scope then narrows to address where, when and why there is meridional flow into the Arabian Sea across 10 N latitude. Despite the complication of eddies and remote forcing, the Sverdrup relation is found to give a good account of the meridional transport during the summer, when the winds and the transport are largest, but not during the winter, Sec. 5. Even a partial success is somewhat surprising — why is the time-independent Sverdrup relation relevant to this seasonally-varying circulation? The explanation offered here comes in two steps. First is the recognition that the circulation, measured by the western boundary current, responds very quickly to the onset of Southwest Monsoon winds,[1] within only a few weeks, Sec. 5.3, and thus the circulation is not far from steady state with respect to a seasonally-varying wind. This rapid response of the Arabian Sea may be compared to the western boundary current of a typical mid-latitude basin, which requires about five years to reach nearly full speed (estimated from the baroclinic model results of Sec. 5.3, Part 4). The ratio of response times of the Arabian Sea vs. a mid-latitude gyre is thus about two orders of magnitude. The second step is to offer a simple (as possible, but not too simple) explanation of this very large difference. Useful guidance comes from start-up experiments that include a jet-like windfield, Sec. 6. The most important factor appears to be the low latitude of the Arabian Sea and the $1/f^2$ dependence of locally-wind forced geostrophic currents (Sec. 5.2, Part 4).[2] A second important factor comes from the western-biased and jet-like form of the Southwest Monsoon wind field, which imposes a zonal length scale that is much less than the width of the basin. The fast response of the model Arabian Sea is consistent with small amplitude (linear) dynamics. Finite amplitude (nonlinear) effects appear to be very important in the formation of an intense, mesoscale anticyclone that has some properties in common with the Great Whirl discused briefly in Sec. 7. The final section, 8, points out several of the more important limitations of this study.

1.2 About this essay

The tenor of this discussion is academic and pedagogic insofar as the aim is enhanced understanding for its own sake. Like Parts 1 - 4, it has been written for students who are beginning a study of geophysical fluid dynamics. It is meant to be somewhat self-contained, but draws upon many of the concepts and results of Parts 3 and 4.

The topic is one of great societal interest. The climate and the weather of the South Asia monsoon affect the lives of everyone living around the Indian Ocean, roughly a third of the world's population.

[2]This very important latitudinal dependence was discussed by Lighthill, M. J. (1969) Dynamic response of the Indian Ocean to onset of the southwest monsoon, Phil Trans. Roy. Soc. of London, Vol. 265, No. 1159, 45-92. Lighthill's paper is a landmark, written before the advent of remote sensing and the widespread use of numerical modelling; do not be discouraged if you find it a difficult read. An early, interesting numerical modelling study of the monsoon response was by Hurlbert, H. E., and J. D. Thompson (1976) A numerical model of the Somali Current, J. Phys. Oceanogr., 6, 646-664. A very wide-ranging and thorough modeling study is by McCreary, J. P., P. K. Kundu and R. L. Molinari (1993) A numerical investigation of dynamics, thermodynamics and mixed-layer processes in the Indian Ocean, Prog. Oceanog., 31, 181-224. More recent is an in-depth study by Wang, H., J. L. McClean, L. D. Talley and S. Yeager (2018) Seasonal cycle and annual reversal of the Somali Current in an eddy-resolving global ocean model, J. Geophys. Res-Oceans, 123, 6562-6580.

The timing and the amplitude of the Southwest Monsoon onset is especially important; alongshore, upwelling favorable winds induce an ocean bloom along the coasts of Somalia and Oman that supports a major fishery (the very cool SST along the western boundary of Fig. 3). The flow of relatively moist maritime air onto the Indian subcontinent ends a wintertime drought, and is the vital source of fresh water to the subcontinent. Improved understanding of the ocean and atmosphere that could lead to better forecasting of these phenomena is the prime motive for ongoing, innovative research in this region.[3]

Acknowledgments. Financial support during the preparation of these essays was provided by the Academic Programs Office of the Woods Hole Oceanographic Institution. Additional salary support has been provided by the U.S. Office of Naval Research. My thanks to Kenneth Brink, Viviane Menezes, Robert Todd and Alex Kinsella of the Woods Hole Oceanographic Institution and to Amit Tandon of University of Massachusetts at Dartmouth for their valuable comments on a draft of this essay. Administrative support was provided by Woods Hole Oceanographic Administration.

These essays and associated materials may be cited by the MIT OpenCourseWare address: Price, James F., 12.808 Supplemental Material, Topics in Fluid Dynamics: Dimensional Analysis, a Coriolis tutorial, and Lagrangian and Eulerian Representations (Spring 2022), https://ocw.mit.edu/courses/res-12-001-topics-in-fluid-dynamics-spring-2022 (date accessed). License: Creative Commons, CC BY-NC-SA. For rights and obligations under this license see https://creativecommons.org/licenses/

Author's note. You may notice that this essay differs from the previous four parts of a Corolis tutorial in that it reads more like a research report than an introductory-level textbook; there is a greater emphasis on attribution than is necessary in a textbook, and you may detect a sense of discovery. This stems mainly from the topic being a new one for me; I was learning along the way, as I hope you will too.

This study is dedicated to Dr. Walter O. Düing, RSMAS, University of Miami, whose enthusiasm for observational oceanography and for the Arabian Sea has been a lasting inspiration.

2 Data sources: SODA and AVISO

This description of Arabian Sea winds and currents is built with three kinds of data from three sources.

[3]Centurioni, L.R. et al. (2017) Northern Arabian Sea Circulation-Autonomous Research (NASCar): A research initiative based on autonomous sensors. Oceanography 30(2):7487, https://doi.org/?10.5670/oceanog.2017.224, and Todd, R. E. (2020). Equatorial circulation in the western Indian Ocean during onset of the 2018 summer monsoon and links to the Bay of Bengal. Geophysical Research Letters, 47, e2020GL087215. https://doi.org/10.1029/2020GL087215. The surface layer response to wind-forcing and the resulting impacts upon bio-relevant properties are examined by Lee, C. M., B. H. Jones, K. H. Brink and A. S. Fischer (2000), The upper-ocean response to monsoonal forcing in the Arabian Sea: seasonal and spatial variability, Deep Sea Res, Part II, 47(7), 1177-1226. An up to date and comprehensive presentation of ongoing research is by Phillips, H. E. and colleagues (2021), Progress in understanding Indian Ocean circulation, variability, air-sea exchange and impacts on biogeochemistry, Ocean Science Discussions, EGU, https://doi.org/10.5194/os-2021-1.

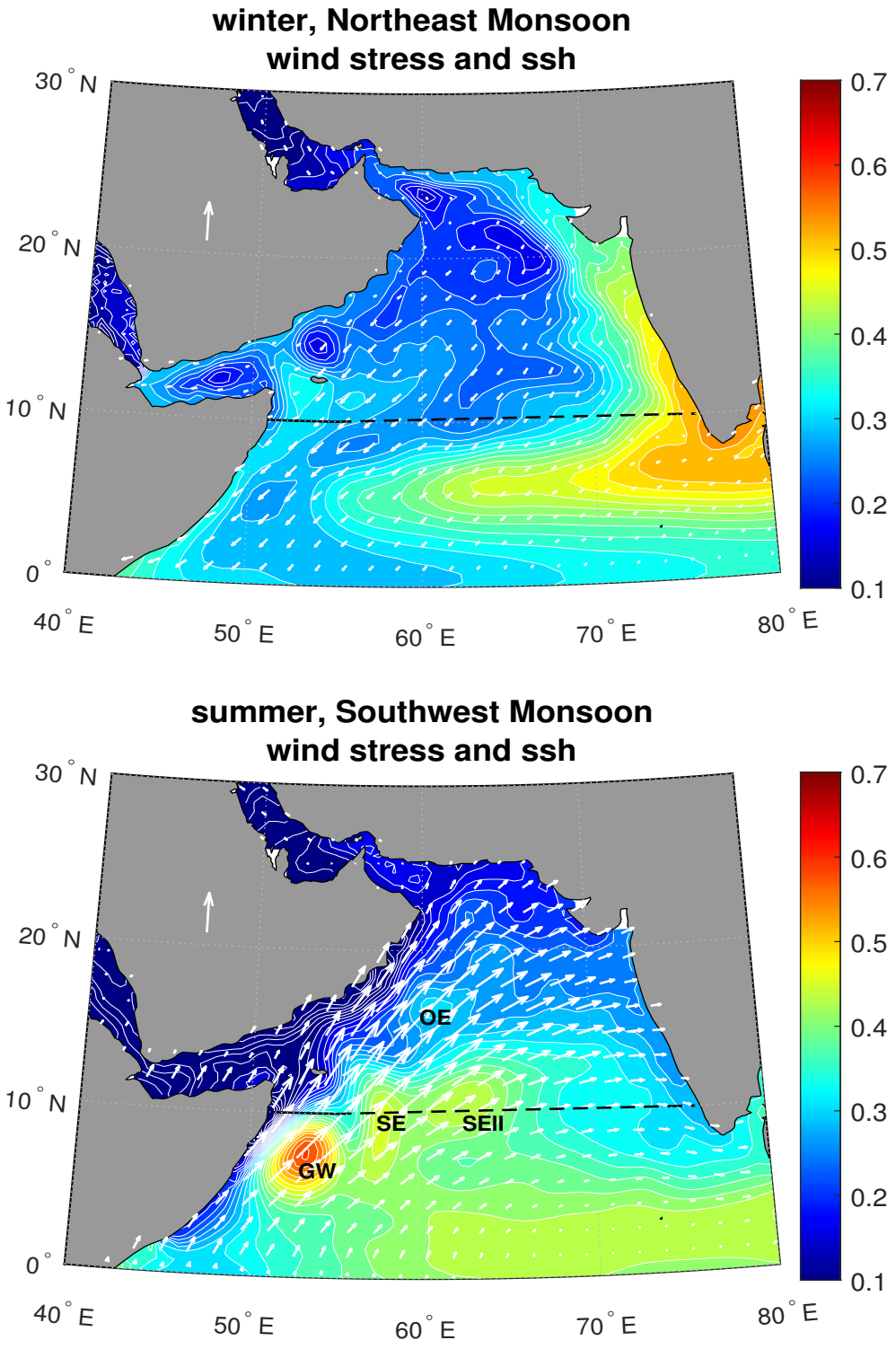

Figure 4: Winter **(upper)** and summer **(lower)** over the Arabian Sea. The white vectors are wind stress from scatterometry reported by SODA 3.3.1; the isolated vector over the Arabian peninsula has an amplitude of 0.3 Pa. The colored background is ssh computed by the SODA 3.3.1 surface reanalysis. The colorbar at right is in meters. The seasons were composite-averaged over two decades starting in 1990. The black solid and dashed line along 10 N is the open boundary of an Arabian Sea control volume defined in Sec. 4. In the upper panel, notice the ridge of high ssh (yellow and orange) that extends westward from the southern tip of India during winter, and in the lower panel, the intense, almost circular high (red bullseye) at about the same latitude during the summer, the Great Whirl, GW. Three other eddies are also noted in summer, SE, SEII and OE, and discussed below.

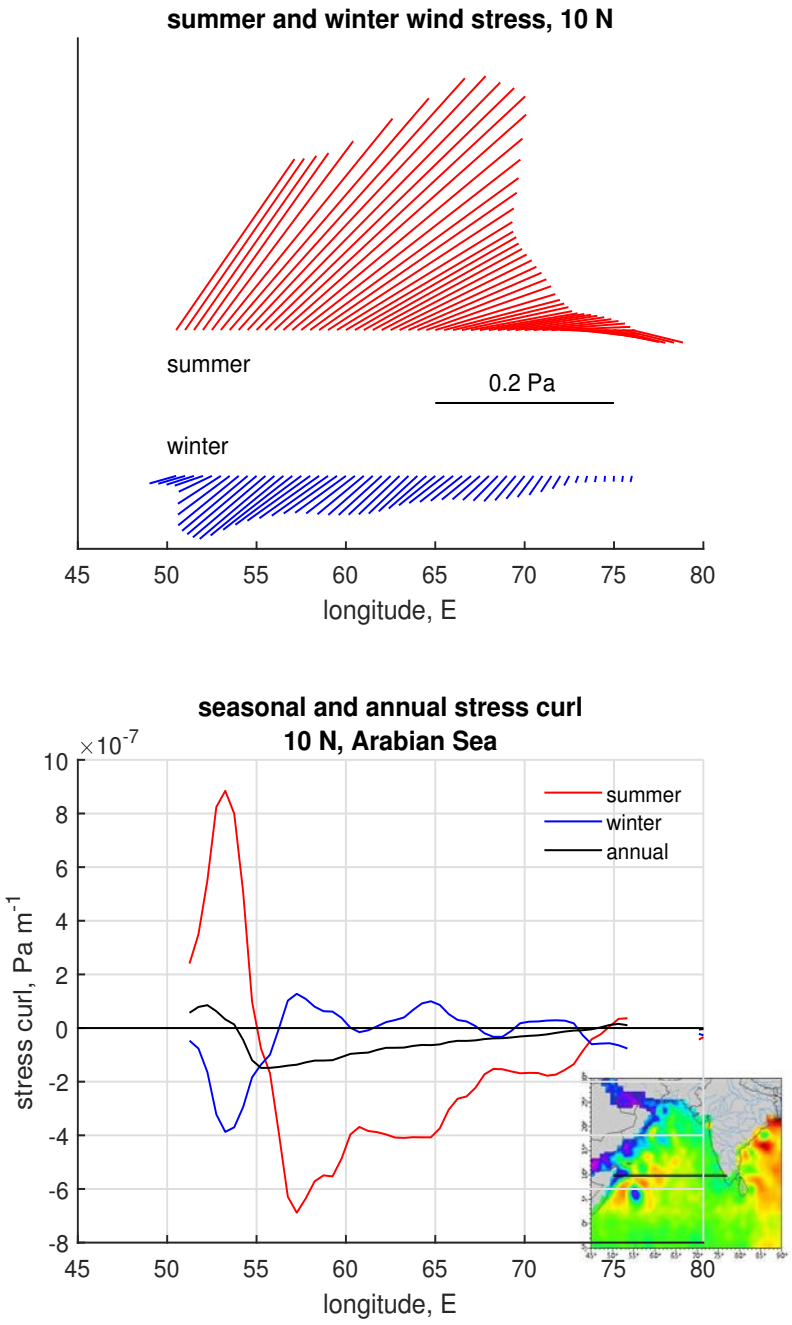

Figure 5: **(upper)** Wind stress along 10 N from the SODA 3.3.1 reanalysis of sea surface properties. North is up, and the magnitude may be compared to the black line segment labeled 0.2 Pa. The maximum of wind stress is at about 55 E in both summer and winter; the summer maximum is known as the Findlater Jet. **(lower)** Wind stress curl along 10 N by seasons and on annual average. Wind stress curl changes sign across the jet axis.

- **Wind stress from satellite scatterometery**, as reported by the SODA 3.3.1 surface reanalysis[4].[4] Wind stress is regarded as external and given. These are the data of Fig. (4).

- **Sea surface height from satellite altimetry** that has been analyzed and archived by the AVISO project, especially the smoothed and averaged (one degree, monthly) Level 4 analysis (Fig. 2) prepared for climate model intercomparisons.[5] This data set is a synthesis of the measurements made by five altimetric satellites and referenced to a geoid. It is highly reliable, however the smoothing does suppress some smaller scale, O(200 km), variability that shows up well in other, less smoothed data sets.

- **Ocean currents and sea surface height computed by the SODA 2.2.4 reanalysis.** These data are the solution of a comprehensive Ocean GCM that was continually updated and made to be consistent with a wide range of oceanic and atmospheric observations including scatterometry-derived wind stress, satellite-derived SST, and many types of *in situ* temperature and salinity observations, but not ocean currents or ssh.[6] The SODA data are served at 1/2 degree intervals in latitude and longitude and at depths from very near the surface where the sampling interval is 10 m, all the way down to the sea floor at almost 5 km depth where the depth interval is a few hundred meters. Monthly-averaged velocity is available from the two decade period beginning 1990. The huge appeal of these reanalysis data (compared with actual, obtainable ocean field observations) is that they are fully four-dimensional, e.g., the meridional velocity component v is $v(x,y,z,t)$ at tens of millions of discrete points and over almost the entire ocean. From the SODA data archive it is possible to estimate of volume transport, heat transport, etc., that are generally not resolved well by ocean observations standing alone. To describe *where* and *when* there is ocean circulation we need only make an intelligible presentation of these invaluable data; to explain *why* there is ocean circulation, we will work toward an understanding of the link between currents and the wind. This will involve models.

2.1 SODA ssh compared with AVISO observed ssh

It is outside the scope here to attempt a thorough ground-truthing of SODA data (see Carton et al., 1988[4]), but a consistency check is highly desirable, and can be made against AVISO observed sea surface height since it was not incorporated within the reanalysis process. A comparison of the SODA-computed ssh (Fig. 4) with the AVISO-analyzed, smoothed ssh (Fig. 2) suggests that large scale features (several hundreds of kilometers or greater) are in common between these two independent realizations. This is a

[4]Carton, J. A., G. A. Chepurin and L. Chen, 2018. SODA3: A new ocean climate reanalysis. *J. Clim.*, Vol. 31, 6967-6983.

[5]Details and the data itself are at https://doi.org/10.5067/DYNTO-1D1M1

[6]The reason for omitting satellite altimeter-derived ssh is interesting and relevant. Even a rather small error in ssh that is imposed upon an OGCM will cause large errors in deep ocean currents and thus in the total transport. However, if the altimetric data are averaged long enough in space and time to suppress random noise, then it will likely be at the expense of genuine mesoscale variability. There are presently two versions of AVISO ssh that are served on the ERDDAP web page and that illustrate this tradeoff between resolution and reliability; a high resolution version (quarter degree spatial resolution and 5 day temporal sampling) and a lower resolution version (one degree spatial and monthly temporal) that was used to make Fig. (2).

positive consistency check on the SODA ssh and the SODA reanalysis generally. There are some significant smaller scale features that are suppressed in the smoothed AVISO L4 analysis, but more on this below.

2.2 Transport and volume transport

Ocean circulation will be represented mainly by the transport, $\mathbf{M}$, [m^2 sec^{-1}], a two component vector field,

$$ {}^{x}M(x,\ y,\ t) \ = \ \int_{-b}^{0} u(x,y,z,t)\ dz, \qquad \text{and} \qquad {}^{y}M(x,\ y,\ t) \ = \ \int_{-b}^{0} v(x,y,z,t)\ dz. $$

(A more descriptive but tedious name for this is volume transport per unit width.) If, as here, the vertical integral is over the full water column, then this will be called the total transport, or sometimes just transport. Alternatively, if the vertical integral is over the shallowest 400 m only,

$$ {}^{y}_{uo}M(x,\ y,\ t) \ = \ \int_{-400}^{0} v(x,y,z,t)\ dz, $$

then the result is said to be the upper ocean transport.

The three-dimensional $\mathbf{M}(x,y,t)$ can be displayed via an animation.[7] More often, the transport will be time averaged or space averaged in one of several ways; a simple time average over the full record length, 1990 - 2010, T,

$$ {}^{y}M(x,\ y)^{ann} \ = \ \frac{1}{T}\int_{1990}^{2010} {}^{y}M(x,\ y,\ t)\ dt, $$

and called the annual average, or a composite average over a given season, all of the winters (November, December and January) of 1990 - 2010, ${}^{y}M(x,y)^{win}$, or all of the summers (June, July, August), ${}^{y}M(x,y)^{sum}$, Fig. (6), upper and lower. On each instance of integrating (or averaging) there is a gain in simplicity made by eliminating unwanted and inessential details. Of course, what is inessential may not be obvious, and will certainly depend upon the context.

Two kinds of current profiles. The distinction between total transport and upper ocean transport can be a valuable diagnostic that will be used here on several occasions.

- **Equivalent barotropic:** In the case of a steady, wind-driven Sverdrup flow, the total transport is mainly within the upper ocean. Deeper flow, while it may be very weak, is in the same direction (Sec. 8.4, Part 4, and the Sverdrup flow of the North Atlantic subtropical gyre). The current profile is thus unidirectional and surface-intensified, sometimes referred to as 'equivalent barotropic' flow. In that event, the total transport and the upper ocean transport will be similar in magnitude and direction.

[7] https://www2.whoi.edu/staff/jprice/as-transport/ which omits the wind and ssh of Fig. (1). The eddy variability is very large, and will leave you wondering if a concise and simple description of the circulation is possible. The eddy variability of the upper ocean transport (upper 400 m) is a little less so: https://www2.whoi.edu/staff/jprice/as-uotransport/

- **Baroclinic wave:** The flow in a baroclinic wave is surface-intensified and bidirectional (Sec. 4.7, Part 4). The upper ocean transport may be substantial, but compensated by a transport of equal magnitude and opposite direction in the deep ocean so that the total transport vanishes. [8]

Estimating volume transport via a pseudo-streamfunction

The amplitude of a circulation is often best represented by the volume transport, $\mathbf{M} \times width$ [m^3 sec^{-1}], or via a (pseudo-)streamfunction,

$$\Psi(x)^{ann} \; = \; -\int_{India}^{x} {}^{y}M(x,\, y_o)^{\,ann}\, dx, \tag{1}$$

where y_o is the constant latitude equivalent. In the cases considered here, the starting point of the integration is the west coast of India where $\Psi = 0$, and integration proceeds westward (the usual convention for ocean circulation studies). The ${}^{y}M$ may be time-averaged over the record length or a composite average over a specific season, e.g., all of the summers to give $\Psi(x)^{sum}$. Alternatively, if the transport is summed over the upper 400 m only, then the notation for the winter composite average is

$${}_{uo}\Psi(x,t)^{win} \; = \; \int_{Somalia}^{x} {}^{y}_{uo}M(x,\, y_o)^{win}\, dx. \tag{2}$$

These Ψs are said to be pseudo-streamfunctions because the vector field ${}_{uo}\mathbf{M}(x,y,t)$ is not strictly incompressible and so in general, ${}^{x}M \neq \partial\Psi/\partial y$. Nevertheless, the Ψs are well-defined and meaningful when taken on their own.

Local, basinwide, and remote wind forcing.

The relationship between wind forcing and the ocean circulation at a given point may be characterized as one or several of

- **Local:** The Sverdrup relation is local in that the meridional transport at a point is attributable to the wind stress curl at that point, and nothing more. Ekman transport is also local.
- **Basinwide:** A classical western boundary current is a basinwide, wind-driven phenomenon, insofar as its amplitude will depend upon the wind stress curl over the full span of the basin to the east (and not just the local stress curl). When applied to the Arabian Sea in Sec. 6, the basin width will be replaced by the scale of the wind stress, but the fundamental idea holds. Some authors refer to this as a 'nonlocal' relationship, and others refer to it as 'remote'. Either usage is sensible, but here remote will be reserved for something that is both very distant and only incidentally connected to the basin winds.

[8] Any given current profile is likely to be a superposition of these two archetypes. A case can be made for investigating two shallower vertical integration intervals. A surface layer O(50 m) thick, would be weighted much more towards Ekman transport. The sea surface, or shallowest possible level, is of greatest practical importance and is also the most readily observed (Beal et al., 2010[14]). The intent here is to be concise, and given that the main interest is the wind-driven, dynamic response, two depth intervals of transport is enough.

- **Remote:** An anomaly of ssh that originates within an adjoining basin may propagate to the observation site with no immediate connection to local or basinwide winds. In this case the adjoining basin is the Bay of Bengal, and wind forcing by the South Asia Monsoon appears to set the annual periodicity and the phase of the process. Nevertheless, this will be termed remote forcing, rather than remote wind forcing, since the most salient feature is the waveguide and propagation mechanism within the Arabian Sea.

3 South Asia Monsoon winds reverse with the seasons

The winds over the Arabian Sea are a part of the South Asia Monsoon system. An important feature of the surface wind field is the Intertropical Convergence Zone (ITCZ), which marks the ascending branch of the Hadley Cell. The ITCZ is a low pressure trough that encircles the globe, and is the convergence of the northeast and southeast trade winds. ITCZ weather is characterized by persistent cloud cover and often heavy precipitation. The ITCZ is generally not far from the thermal equator and so follows the sun's annual march, though with a lag of one to two months and with very large zonal perturbations caused by longitudinal variation of land/sea distribution.[9] Associated with the ITCZ's annual migration, the winds over the Arabian Sea have a pronounced seasonal variation in both amplitude and direction and this in turn causes a marked seasonal variation of the Arabian Sea circulation.

3.1 Summer winds, the Southwest Monsoon

During boreal (northern hemisphere) summer, the land mass of South Asia warms well beyond the SST of the NIO, and the ITCZ migrates northward, as far as 20 N by June or July (Fig. 3). The southeast trade winds coming from the southern hemisphere are almost due north crossing the equator, and are deflected farther clockwise by the Coriolis force over the Arabian Sea. The winds to the south of the ITCZ are predominantly southwesterly (from the southwest, Figs. 3 - 5), and the summer season is often called the Southwest Monsoon. The ITCZ is somewhat localized in the meridional direction compared with the broad expanse of the high pressure (descending) side of the Hadley cell (the Mascarene or South Indian Ocean high in boreal summer), and so the passage or the arrival of the ITCZ is somewhat event-like, taking a couple of weeks, typically. In early summer, when the ITCZ is moving northward, the change in wind and weather associated with the ITCZ's northward passage is especially noteworthy and is termed the Southwest Monsoon onset. The north-south translation of the ITCZ is not smoothly sinusoidal and not well-defined by a single value, but nevertheless it will be useful later to have at least a rough idea of the translation rate, $V_{itcz} \approx$ 23 deg of latitude in 3 months $\approx$ 0.4 m sec^{-1}.

[9] Gadgil, S. (2003) The Indian monsoon and its variability, Ann. Rev. of Earth Planet. Sci., 31:429-467. doi: 10.1146/annurev.earth.31.100901.141251

By midsummer, when the ITCZ is established over the northern Arabian Sea and Northern India and Pakistan, the Southwest Monsoon has some of the character of a large scale land-sea breeze — a thermally direct circulation driven by the large temperature difference between the comparatively cool Arabian Sea and the very warm land mass of the Indian subcontinent.[10] Strong southwest winds with stress up to 0.5 Pa prevail over most of the basin. The Southwest Monsoon winds have a local maximum about 400 km offshore known as the Findlater Jet.[11] Along 10 N, the jet axis is typically near 55 E. This jet structure of the wind field gives the wind stress curl two signs over the Arabian Sea: there is negative stress curl over most of the central Arabian Sea, up to -6 $\times 10^{-7}$ Pa m^{-1} (Fig. 5), with largest values on the western side of the basin, there is a sign reversal on the axis of the Findlater Jet, and very large, positive stress curl, up to 8 $\times 10^{-7}$ Pa m^{-1}, within a few hundred kilometers adjacent to the western coast.[12] As discussed in Secs. 4 and 5, the somewhat intricate horizontal structure of the Southwest Monsoon wind stress curl makes a clear imprint onto the summertime, meridional volume transport. By comparison, the correlation between wind stress curl and meridional transport is much less clear during the wintertime, Northeast Monsoon season.

3.2 Winter winds, the Northeast Monsoon

During the boreal winter, the land mass of South and Central Asia is much cooler than the SST of the Indian Ocean and the ITCZ is at about 8 S over the South Indian Ocean. The descending branch of the Hadley cell over Central Asia (Mongolian/Siberian High) sets up a flow of dry continental air from northeast to southwest over the Arabian Sea (Fig. 4 upper), and ultimately into the low pressure trough of the ITCZ. This is called the Northeast Monsoon. The associated wind stress over the open Arabian Sea is

[10] The sun's annual march across the sky is the essential cause of seasonality, including the South Asia monsoon and the annual migration of the ITCZ, and yet the timing and the rate of the ITCZ passage and monsoon wind reversals do not exhibit the kind of smoothly sinusoidal, astronomical regularity that this implies. Rather, the ITCZ moves quickly between winter and summer modes, spending comparatively little time over the equator. As well, the ITCZ is embedded within the irregular hemispheric-scale weather associated with a meandering jet stream, the El Nino/Southern oscillation, and Madden-Julian oscillations, among others, with the result being considerable year-to-year variation in the rate and amplitude of the Southwest Monsoon onset. For much more on the ITCZ, see the review by Schneider, T., T. Bischoff and G.H. Haug (2014), Migrations and dynamics of the intertropical convergence zone, Nature, 513, 45-53, and an excellent web site, https://climate-dynamics.org/why-does-the-itcz-shift-and-how/

[11] The Findlater Jet has a maximum at an altitude of only about 1.5 km above sea level, and so is steered by the mountainous topography of East Africa and Madagascar. It is often likened to an oceanic western boundary current. One of the pioneering papers on this phenomenon is highly recommended, Findlater, J. (1969), A major low-level air current near the Indian Ocean during the northern summer. Q J Royal Met. Soc., 95, 362-380.

[12] Other estimates of wind stress and wind stress curl may be found in Schott and McCreary (2001)[1] and by Halpern, D., M. H. Freilich, and R. A. Weller, (1998), Arabian Sea surface winds and ocean transports determined from ERS-1 scatterometer. J. Geophys. Res., 103, 7799-7805.

moderate, about 0.1 Pa, and varies spatially from northwest to southeast. The strongest northeast winds are on the western side of the basin; along 10 N, the maximum is typically about 400 km offshore (Fig. 5). The curl of the wind stress is positive over most of the Arabian Sea and modest amplitude, about 0.5×10^{-7} Pa m^{-1}, and large and negative, up to -3×10^{-7} Pa m^{-1}, over a several hundred kilometer wide region adjacent to the western boundary.

4 Arabian Sea circulation varies strongly with the seasons

The most compelling aspect of NIO and Arabian Sea oceanography is the marked seasonality of the winds and the ocean circulation. But not everything changes with the seasons. The relative high of ssh within the comparatively fresh Bay of Bengal and the relative low ssh within the salty Persian Gulf and Gulf of Aden persist year-round (Fig. 2). These essentially thermohaline properties owe to regional climate: high river runoff and high precipitation over Southeast Asia, and strong evaporation in excess of precipitation over Southwest Asia.

4.1 Summertime ssh and circulation

The major feature of the ensemble-averaged, summertime ssh is a compact, high pressure anticyclonic gyre centered on about 10 N, 60 E (Fig. 2, lower). The ssh amplitude is modest, about 0.4 m, (Fig. 7, upper) but significant at this tropical latitude. In the smoothed AVISO ssh, this high appears to be a more or less single feature. There is a hint of a Great Whirl at 8 N, 52 E, which is a very vigorous feature of the real ocean. In the less heavily smoothed SODA ssh (Fig. 4, lower), this anticyclonic gyre appears to be a collection of three anticyclonic eddies, GW, SE and SEII, about which more in Sec. 4.2.

The most dramatic and most remarked-upon aspect of the summertime Arabian Sea circulation (Fig. 4) is a strong, upper ocean flow to the northeast along the coast of Somalia and Oman, the Somali Current (east of Oman, this is also called the East Arabian Current). This western boundary current appears in early summer, usually within a few weeks after the onset of the Southwest Monsoon winds. The timing depends upon the location along the western boundary, and varies from year to year, as does the onset of the Southwest Monsoon wind. In situ observations[1] show that the fully-developed, Southwest Monsoon Somali Current has a near-surface speed that can exceed 2 m sec^{-1}, a depth (e-folding) of about 300 m, (Fig. 8), and a volume transport of roughly 30 Sv, (though with some estimates considerably higher). The summertime Somali Current is thus comparable in speed and volume transport to several of the semi-permanent western boundary currents of Table 1.

To make a quantitative estimate of the Arabian Sea circulation it will be helpful to define a control volume that has a simple but interesting configuration: all of the Arabian Sea north of 10 N latitude, and extending from the sea surface to the sea floor, Fig. (4). This bounding southern latitude is arbitrary, but has the advantage that it intersects land on both ends, and is more or less midway between the Great Whirl and the island of Socotra. As noted above, 10 N does cut through the Socotra Eddy and SEII,

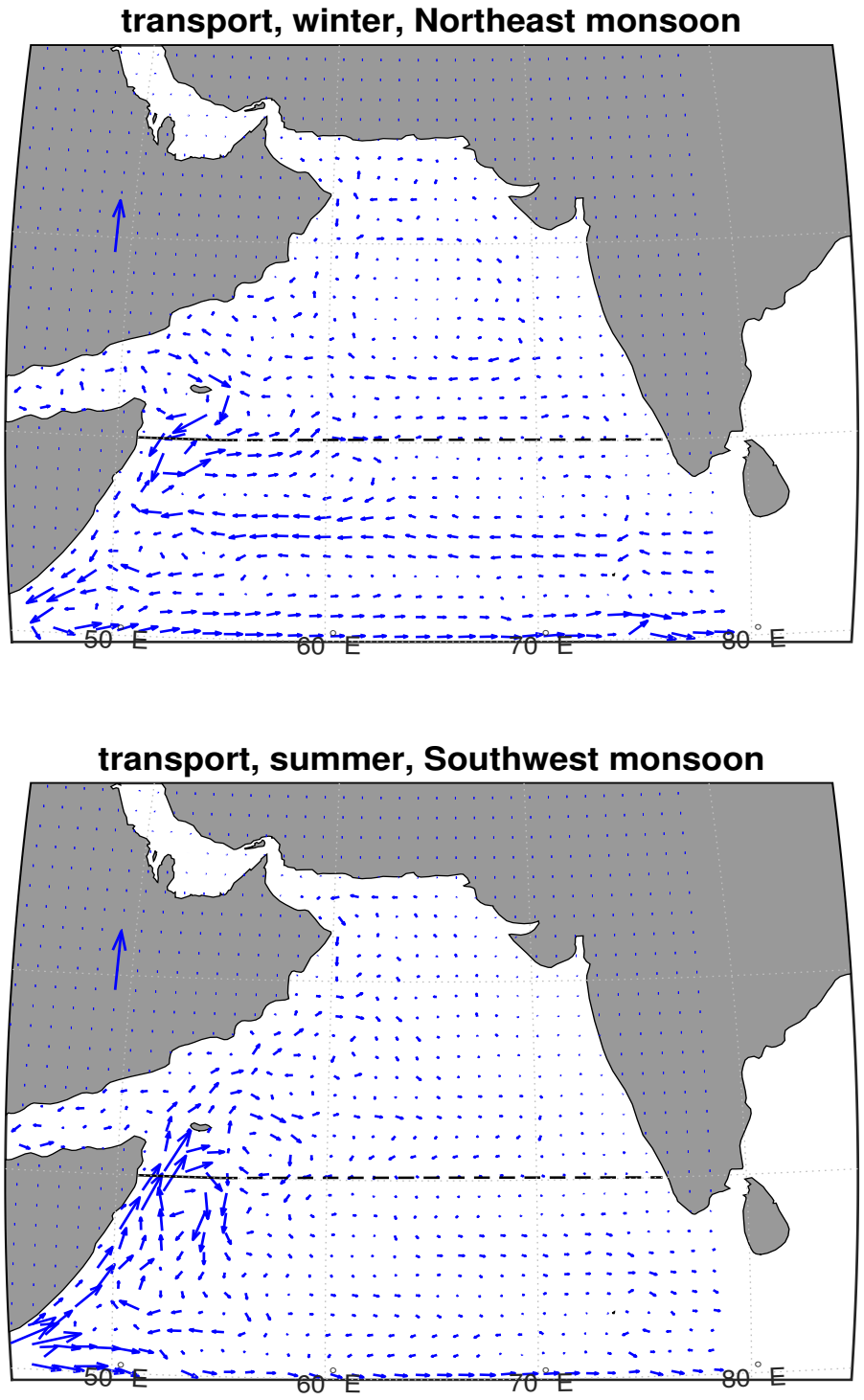

Figure 6: Transport (volume transport per unit width) computed from SODA reanalysis ocean currents integrated over the full water column and then composite averaged over the **(upper)** winter, $\mathbf{M}(x,y)^{win}$, and over the **(lower)** summer, $\mathbf{M}(x,y)^{sum}$, 1990 - 2010. The isolated vector over the Arabian peninsula has an amplitude of 250 m^2 sec^{-1}. The black line along 10 N is the open, southern boundary of a control volume used to evaluate meridional volume transport discussed in Sec. 5. The pronounced seasonality of the Somali Current is clearly evident here, as are the summertime Great Whirl centered on 8 N, 53 E, and the Socotra Eddy at about 11 N, 57 E, cf. Fig. (4), lower.

which are evident in several of the analyses. There are two mediterranean basins on the western and northern side of the Arabian Sea (Red Sea/Gulf of Aden and Persian Gulf/Gulf of Oman, Fig. 3) that inject distinctive, warm and saline water masses into the thermocline, but not a substantial volume flux. Hence the western, northern and eastern boundaries of this Arabian Sea control volume are effectively impermeable (no normal flow) coastlines, while the southern boundary along 10 N is completely open. To define the Arabian Sea circulation we will first seek to describe *where* and *when* there is meridional flow across the 10 N boundary in Secs. (4) and (5), and then seek to explain *why* there is meridional flow in Sec. (6).

The integration (1) that evaluates the streamfunction can be continued all the way from India to the western boundary on the coast of Somalia to give just one number, the net volume transport across 10 N. The streamfunction returns very close to its presumed starting value, 0, at the western boundary (Fig. 7, lower). This is to be expected on a physical basis, assuming that there is no significant secular trend of sea level, i.e., that the volume of sea water within the control volume is effectively constant. The inference is that the sampling in depth and longitude of the SODA ocean currents gives a reasonably well-resolved volume transport across the 10 N section.

The annual mean streamfunction (the black line of Fig. 7, upper) shows a modest flow to the south over most of the basin, reaching a maximum of about 5 - 10 Sv, and a fairly narrow flow to the north near the western boundary. More interesting is the seasonality of the transport, here defined over the summertime Southwest Monsoon period, the composite average over June, July and August (the red line of Fig. 7) and a wintertime Northeast Monsoon, the composite average over December, January and February (the blue line). These are dramatically different, as the maps of seasonally-averaged transport and ssh imply they should be, cf. Fig. (6).

The summertime streamfunction indicates southward transport over the interior, 75 E to 55 E, with a maximum of about 30 Sv to the south. The upper ocean transport is just slightly less, indicating that the vertical structure is approximately equivalent barotropic, and implying wind-driven flow. Farther west, the streamfunction goes rapidly to zero on the western boundary, indicating a northward volume transport of the same magnitude within a fairly narrow western boundary region. The narrow width of this northward flow implies a rapid current — the Southwest Monsoon season Somali Current, which is readily apparent in the transport map of Fig. (4), lower. The summertime ssh profile across 10 N thus displays a pattern like that of the North Atlantic subtropical gyre, a fairly narrow region of large positive slope on the west side of the basin associated with the rapid, north-eastward flowing Somali Current, and a more gradual negative slope over the basin interior suggesting southward geostrophic flow in the upper ocean (Fig. 7, lower). The corresponding ssh amplitude is about 40 cm, noted above. The interior, southward flow of the Southwest Monsoon season isn't usually considered to be part of a named current, but as shown below, it has a magnitude consistent with the overlying negative wind stress curl and the Sverdrup relation.

The upshot is that the Somali Current appears to be the western boundary current of a basin-scale, anti-cyclonic gyre that is well-established for a few months during the summer Southwest Monsoon season, but not during the winter, Sec. 4.3.

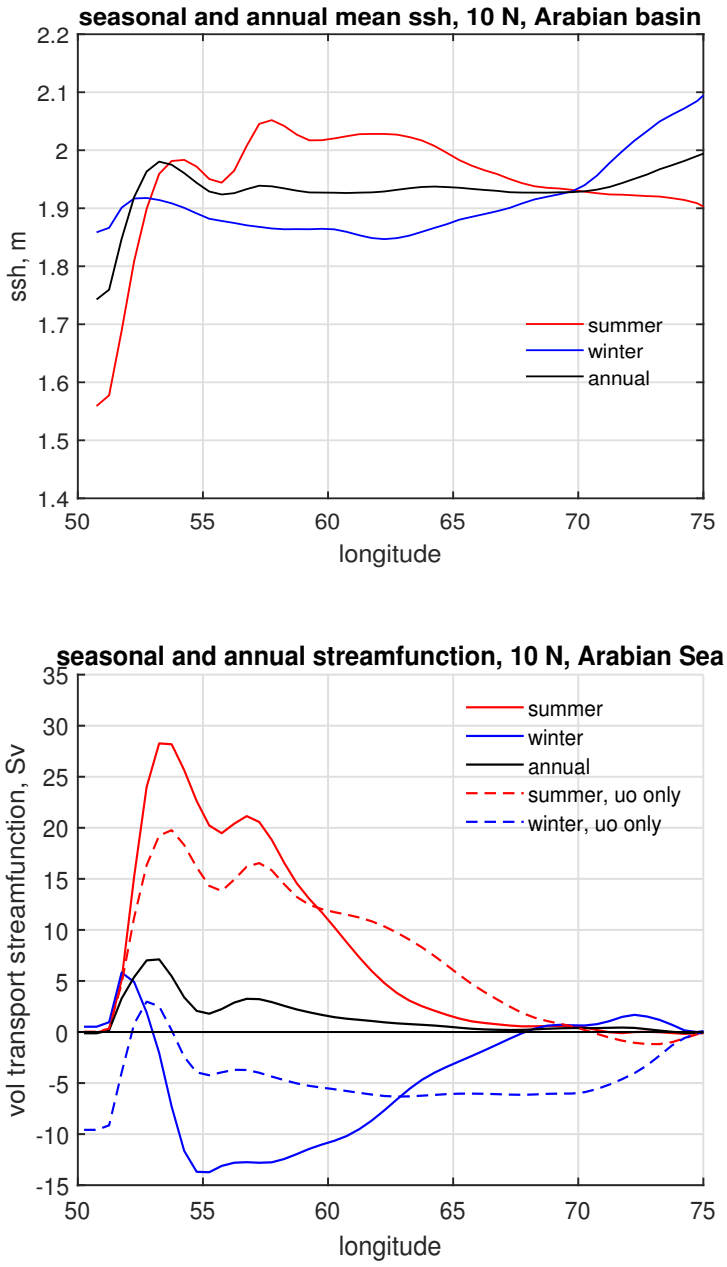

Figure 7: **(upper)** Sea surface height along 10 N in the Arabian Sea for annual mean (black) and for composite-average summer and winter (red and blue). These were computed over about 20 years of satellite altimetry complied by the AVISO project. **(lower)** Transport streamfunction computed from seasonal mean meridional velocity from twenty years of SODA reanalysis. Seasons are coded by color. The integration started on the eastern side of the basin and continued to the coast on the western side. Thus the streamfunction starts at zero and should return to zero if the net transport vanishes, which it nearly does. The dashed lines are the volume transport within the upper 400 m only. These need not return to zero on the western side of the basin. Notice the small bump in the summer streamfunction near 57 E, and also in ssh. This appears to be the composite-average signature of the Socotra Eddy.

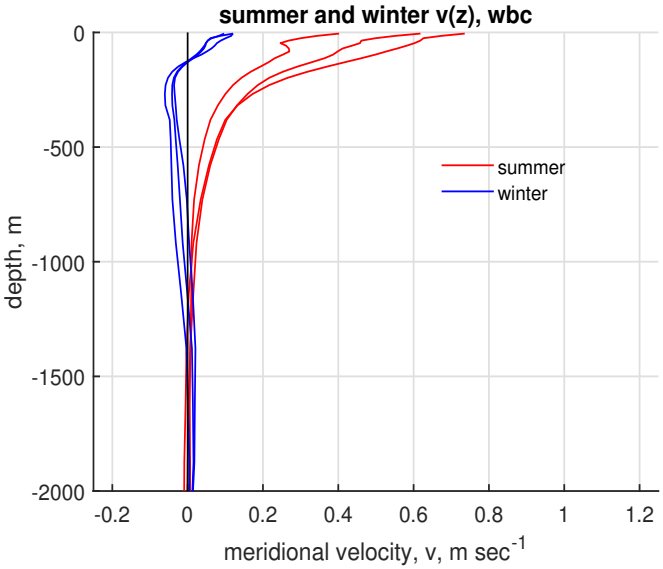

Figure 8: Profiles of the monthly mean of meridional velocity within the western boundary current on 10 N from SODA reanalysis data. Notice that the surface current in the western boundary region is northward during the summer and the winter and hence the surface current at this site does not reverse with the seasons. The volume transport does reverse, though is comparatively weak in the winter.

4.2 The Great Whirl and lesser eddies

During the summertime Southwest Monsoon season, an ensemble average of transport will show a northeastward-flowing Somali Current along the coast of Somalia and Oman up to about 20 N (Fig. 6, lower). This gives the impression that a summertime Somali Current is present instantaneously along almost the entire western boundary, and that a parcel released along the coast of Somalia would travel quickly and smoothly along a continuous trajectory all the way to the northern Arabian Sea, as if in a laminar flow. Probably not; direct evidence from drifter trajectories[13] and from monthly maps of transport[7] is that the Somali Current is frequently disrupted by large amplitude eddies and meanders. Indeed, the Arabian Sea is as eddy-rich and chaotic as any mid-latitude basin, and moreover, some of the eddies are large and intense.

An especially impressive eddy is the high pressure anticyclone that appears regularly in summertime near 8 N, 53 E (Figs. 4, lower, and 6, lower). This feature was recognized long ago and dubbed, fittingly, the Great Whirl.[14] In most years the Great Whirl forms in late spring when and where the 6 N ridge intersects the western boundary of the Arabian Sea and forms a small, pinched off, anticyclonic loop.

[13] A comprehensive, modern, data-based analysis of the annual variation of the near-surface circulation is by Beal, L. M., V. Hormann, R. Lumpkin and G. R. Foltz, 2013, Journal of Physical Oceanography, The response of the surface circulation of the Arabian Sea to monsoonal forcing. 43, 2008 - 2022. For North Indian Ocean eddies see Trott, C. B., Subrahmanyam, B., Chaigneau, A., and Roman-Stork, H. L. (2019). Eddy-induced temperature and salinity variability in the Arabian Sea. Geophysical Research Letters, 46, 2734 2742. https://doi.org/10.1029/2018GL081605.

[14] Excellent discussions of the Great Whirl are by Beal, L. M., and Donohue, K. A. (2013). The Great Whirl: Observations of its seasonal development and interannual variability. Journal of Geophysical Research: Oceans, 118, 1 13. https://doi.org/10.1029/2012JC008198, and by Melzer, B. A., Jensen, T. G., and Rydbeck, A. V. (2019). Evolution of the Great Whirl using an altimetry-based eddy tracking algorithm. Geophysical Research Letters, 46, 43784385. https://doi.org/10.1029/2018GL081781

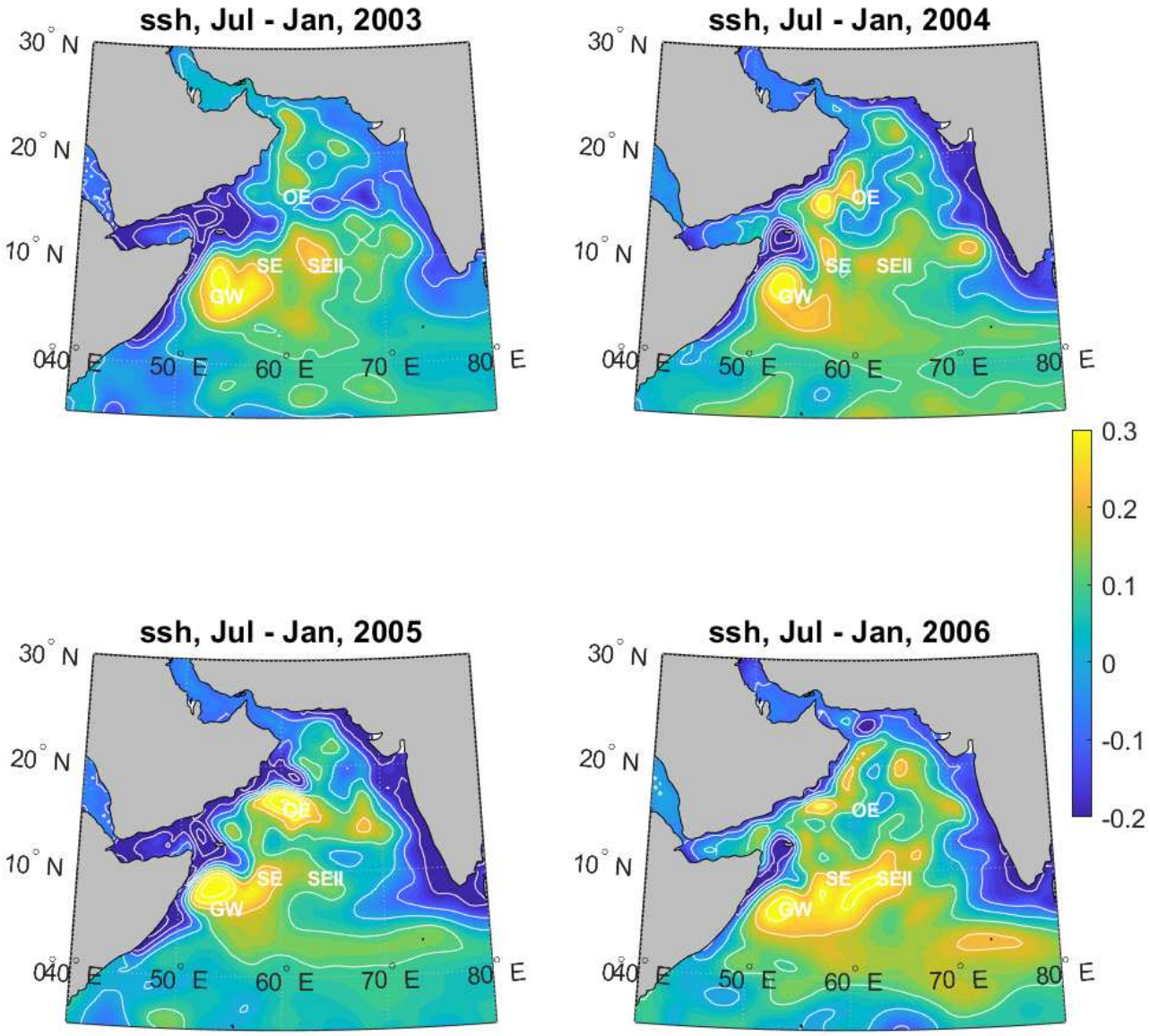

Figure 9: Snapshots of ssh in July - ssh in January, for four successive years, 2003 - 2007. The anticyclonic gyre is a roughly 1500 x 1500 km relative high centered on about 9 N, 62 E. Notice that the northern half of the gyre is very lumpy; you could argue that the gyre is nothing more than a small handful of anti-cyclonic eddies. The largest and most regular of these is the Great Whirl, GW, usually at about 8 N, 53 E. Three other eddies that are apparent in the ensemble mean ssh are the Socotra Eddy, SE, its neighbor, SEII, and the Omani Eddy, OE. The GW and SE are widely recognized in the literature; SEII and OE are not.

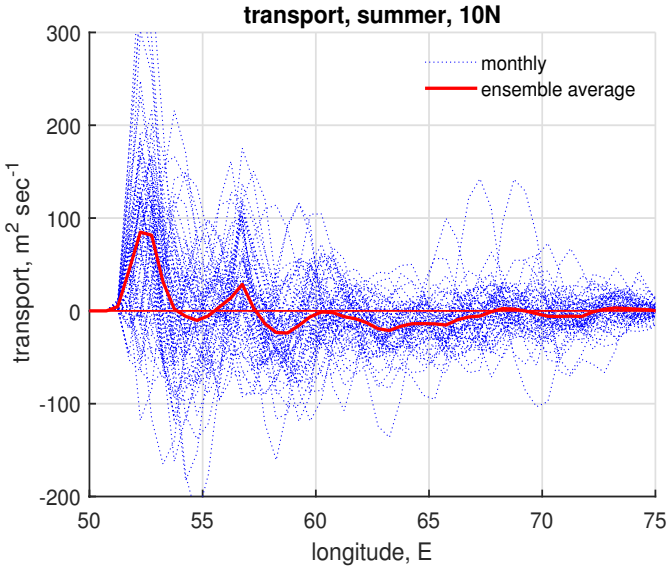

Figure 10: Meridional transport across 10 N for each summer month between 1990 and 2010 (60 samples). The thicker red line is the summer ensemble average. The month-to-month variability is very large, and any one transport estimate might look nothing like the ensemble mean.

The amplitude increases rapidly, apparently in response to the Southwest Monsoon winds, and by midsummer the Great Whirl has a diameter of about 300-400 km, which is about three times the baroclinic radius of deformation, and an azimuthal transport that is comparable to that of the Somali Current. It is noteworthy that the initial formation of the Great Whirl appears to be a matter of remote forcing by internal, mesoscale ocean dynamics, mainly, rather than the local and basin-wide wind stress curl/Sverdrup transport relationship that will be emphasized in most of what follows. The Great Whirl disappears not long after the Southwest Monsoon winds die out in the fall.

The Great Whirl remains mostly to the south of the 10 N section that will be of particular interest here (the dashed black line of Fig. (4), discussed next). However, there is another high pressure, anticyclone, the Socotra Eddy (SE), that is squarely in our sights. The Socotra Eddy is typically centered near 11 N, 57 E, and is comparable in size to the Great Whirl, but about half or a third as intense, judging from its ssh signature in Fig. (4). The Great Whirl and the Socotra Eddy are widely recognized as significant features of the Arabian Sea. Putting names on still other eddies would seem to be (and might actually be) a frivolous and unproductive endeavor, but, there is evidence in the summer ensemble mean ssh (Fig. 4) of two additional anticyclones that are fairly prominent in many years, and that will be mentioned again later (and evident also in the hydrographic data studied by Bruce[1]). One of these is an eastern neighbor of the Socotra Eddy, centered on about 12 N, 61 E. This eddy appears to be similar overall to the Socotra Eddy, though usually not as strong or as symmetric, and so SEII seems appropriate (Fig. 9). The fourth eddy is an anticyclone centered on about 18 N and 61 E, the northern edge of the gyre and just offshore of Oman; Omani Eddy, or OE seems appropriate. This eddy is coincident with a local maximum of negative wind stress curl that is noted below.

All of these eddies are seasonal, appearing in summer and disappearing in winter. Given this clear-cut seasonality, it appears that these eddies are wind-driven, though perhaps only indirectly via

instability of the gyre. At least GW and SE can be simulated by a fairly simple (one layer, reduced gravity) model provided with realistic basin geometry and realistic, seasonally varying winds.[15] These features are referred to as 'eddies' solely because of their sub-basin horizontal scale and roughly circular planform. However, a good case can be made for calling them 'gyres' insofar as they appear to be wind-driven and deterministic in that they repeat from year to year, though of course with some variation. Collectively, these eddies make up a significant fraction of the basin-scale anti-cyclonic gyre (a subjective judgment) and so the distinction between gyre and eddy is significantly blurred in the Arabian Sea.[16]

4.3 Wintertime ssh and circulation; remote forcing from the Bay of Bengal

During winter, the ssh over the central and western Arabian Sea is almost featureless, at least in the smoothed and averaged AVISO ssh of Fig. (2), upper. There is a weak, relative low, only about 5 - 10 cm, compared to the western boundary region, which is not inconsistent with the weak, mostly positive stress curl of the wintertime, Northeast monsoon. There is somewhat higher ssh evident in the eastern and southern part of the Arabian Sea, roughly 30 cm compared to the center. This high ssh appears to have an origin in the relatively fresh Bay of Bengal, where sea level is on average about 40 cm higher than in the saltier Arabian Sea. The Bay of Bengal is also subject to the South Asia Monsoon. During the Southwest Monsoon winds of summer, the ssh near the southern tip of India and Sri Lanka is somewhat lower than over most of the Bay of Bengal (Fig. 2, lower). During the winter, when the wind comes from the northeast, the characteristic high ssh of the Bay of Bengal fills in all the way south to Sri Lanka, and then appears to spread around the southern tip of India and Sri Lanka beginning in early winter (the orange and yellow wedge of high ssh on the southeastern side of the Arabian Sea in Fig. 4, upper and Fig. 2, upper). High ssh then spreads into the Arabian Sea along two axes: northward along the eastern coastal boundary (west coast of India) as a coastal Kelvin wave, and westward in a several hundred kilometer wide ridge that is centered on roughly 6 N latitude. Beginning in early to mid-winter, the 6 N ridge begins to extend (propagate) westward at about the speed expected of a low mode, baroclinic Rossby wave, a few 10s of km per day at this latitude, and thus crosses the Arabian Sea basin in O(100 days).[17]

The slope of ssh over the wintertime Arabian Sea is dominated by the coastal high and the 6 N ridge, but notice that there is little obvious, corresponding signature within the field of the total transport, cf. Fig. (6, upper). To detect the ocean current signature of the 6 N ridge, and specifically the meridional current, it is helpful to evaluate the pseudo-streamfunctions along 6 N latitude, $\Psi(x,t)^{win}$ (the solid blue line of Fig. 11, lower) and the upper-ocean version, ${}_{uo}\Psi(x,t)^{win}$ (the dashed blue line). These are just like Eqns.

[15] Luther, M. E., and J. J. O'Brien (1985) A model of the seasonal circulation in the Arabian Sea forced by observed winds. Prog. Oceanogr., 14, 353-385, and recently by Wang et al. (2018)[2].

[16] Compare this with the North Atlantic subtropical gyre of Figs. 1 - 3. Given sufficient temporal averaging on hydrographic data, several decades, North Atlantic mesoscale eddies largely disappear leaving behind a smoothly varying, large-scale, time-mean subtropical gyre.

[17] This description is merely what can be seen in the ssh field. For a much more complete treatment see Yu, L., J. J. OBrien and J. Yang (1991) On the remote forcing of the circulation in the Bay of Bengal, J. Geophys. Res. Oceans, 96, C11, 449-454 and Shankar, D., and S. H. Shetye (1997) On the dynamics of Lakshadweep high and low in the southeastern Arabian Sea. J. Geophys. Res-Oceans, 102, C6, 12,551 - 12,562. More recent is Wang et al., (2018)[2].

(1) and (2) except for the latitude. The ${}_{uo}\Psi(x)^{win}$ shows a significant signal of northward, meridional, upper ocean transport between about 55 E and 70 E (also in Fig. 1 and the animation linked there), coincident with the western leading edge of the 6 N ridge, cf., the ssh of Fig. (11), upper. The amplitude of the northward volume transport is about 12 Sv. There is little or no sign of this in the total transport. This is additional evidence, along with the westward propagation rate, that the remote forcing that comes from the Bay of Bengal (the 6 N ridge) may be characterized as a free, baroclinic Rossby wave.

Within the western third of the basin (west of 60 E) the streamfunctions along 6 N and 10 N reveal a different pattern. The total transport and the upper ocean transport are in the same direction and have comparable magnitudes. This suggests a mainly wind-driven flow very near the western boundary having a magnitude of about 10 Sv, and which is also referred to as the Somali Current. There is a comparable northward flow a few hundred kilometers offshore. The wintertime Somali Current is quite variable in time and space (Fig. 6, upper) and even on ensemble average, there is little suggestion of a continuous western boundary current. The wintertime ssh has a similar character, i.e., small amplitude and somewhat indistinct pattern on the basin scale. The Arabian Sea circulation doesn't so much 'reverse' with the seasons, which implies symmetry in the winter and summer amplitudes, but rather it 'varies' seasonally, and by quite a lot.

5 Sverdrup transport is correlated with the summertime, meridional transport

You may have noticed that there is at least a qualitative consistency between the mainly negative wind stress curl over the basin interior during summer, and the Sverdrup expectation of an anticyclonic gyre and poleward western boundary current during summer (noted by Bruce, 1983[1]). That suggests that it might be fruitful to evaluate the Sverdrup relation quantitatively, and define where and when it succeeds (summer), and just as important, where and when it fails (winter). To do this, take the wind stress curl used to make Fig. (5) and evaluate the Sverdrup streamfunction,

$$S(x)^{ann} = \frac{-1}{\rho\beta}\int_{India}^{x} \overline{\nabla\times\tau(x,y_o,t)}^{\,ann}\, dx, \tag{3}$$

where the time average can be the annual mean (the black line of Fig. 12) or over a given season (red and blue lines) and y_o is 10 N equivalent. The Sverdrup streamfunction predicts rather weak and indistinct transport on annual mean and during winter (signs are reversed between these two). There is significant meridional Sverdrup transport during the summer, approx. 27 Sv southward over the interior, i.e., east of about 55 E. This may be compared to the meridional transport streamfunction, (Fig. 7), which indicates about 30 Sv southward during the summer over the basin interior. From this first look, it appears that the time-independent Sverdrup relation gives a fairly good account of the amplitude of the summer, Southwest Monsoon season, meridional transport found in the interior of the Arabian Sea at 10 N (and, it should be noted, within the SODA reanalysis). This does not hold during the wintertime Northeast Monsoon, when the Sverdrup estimate has the correct sign, but considerably smaller magnitude compared to the actual meridional transport.

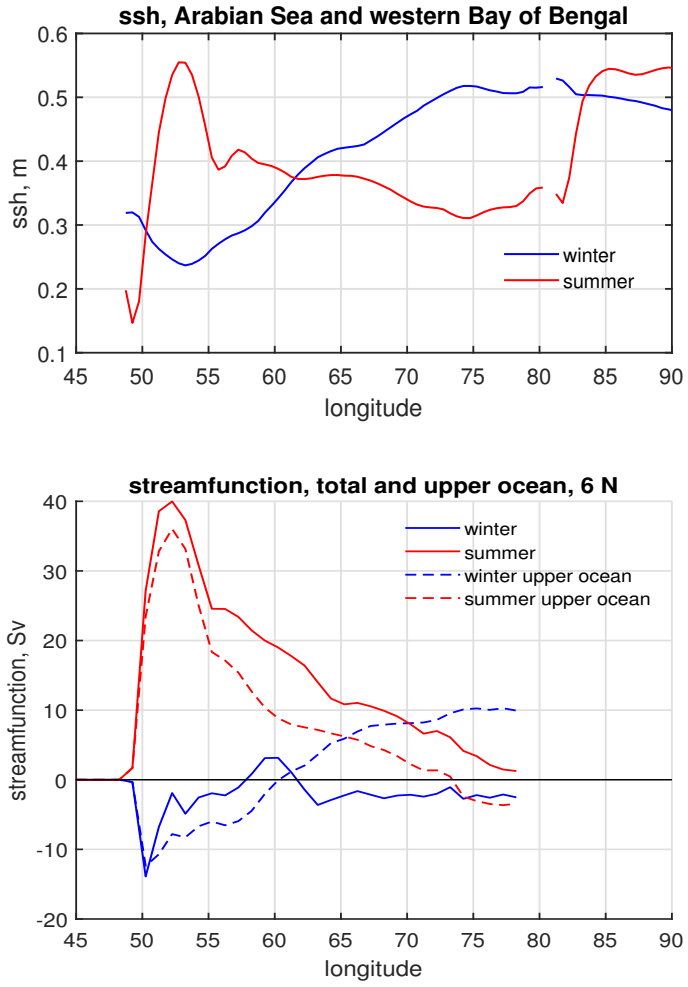

Figure 11: A zonal section along 6 N. **(upper)** The ssh along 6 N from the coast of Somalia to the western Bay of Bengal. Summer composite average (red) and winter (blue). The small gap at about 81 E is the southern tip of Sri Lanka. These are composite averages over 20 years. **(lower)** The composite-averaged streamfunctions $\Psi(x,t)$ and ${}_{uo}\Psi(x,t)$ Eqn. (2) evaluated along 6 N. **(lower)** The total transport and upper ocean transport are fairly similar during the summer (compare the red solid and red dashed lines) suggesting equivalent barotropic flow. They are quite different during winter (blue solid and dashed lines), especially in the eastern half of the basin. The northward upper ocean transport is coincident with the positive ssh slope on the western side of the 6 N ridge, cf. the blue line of the upper panel.

5.1 Regional, seasonal Sverdrup transport

There is nothing special about 10 N insofar as the Sverdrup relation is concerned, and so it should be just as appropriate to compare the Sverdrup transport $S(x,y)$ to the meridional transport ${}^{y}M(x,y)$ throughout the Arabian Sea — Figs. (14) and (13) are for winter and summer. The Sverdrup transport is mapped even at locations immediately adjacent to a zonal boundary, as in the narrow and shallow Gulf of Aden, where a significant meridional transport is not expected or observed.

Wintertime. It has already noted that the wintertime meridional transport and Sverdrup transport are not consistent along 10 N, and this presentation is no different; ${}^{y}M(x,y)^{win}$ and $S(x,y)^{win}$ display fairly small scale, and generally low amplitude features that are evidently not correlated.

Summertime. With some allowance for the obvious, unphysical features in the S^{sum} field noted above,

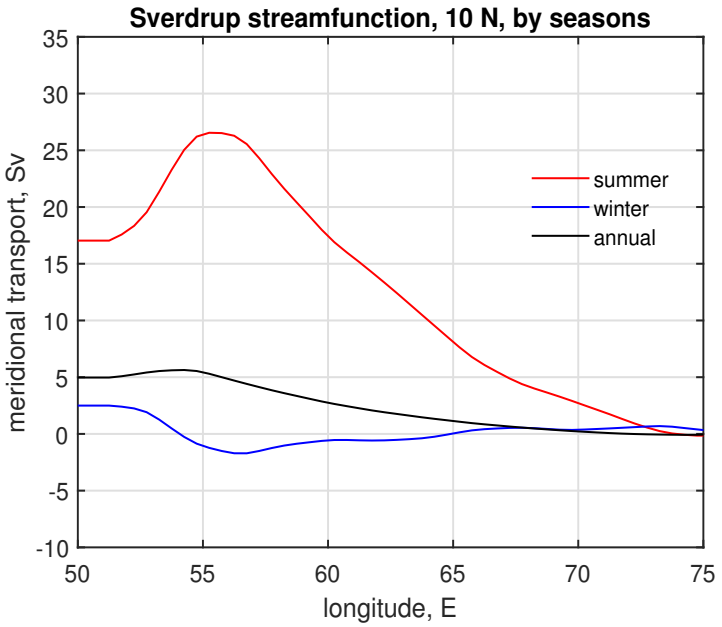

Figure 12: The Sverdrup transport streamfunction computed from the annual and seasonal mean wind stress curl Fig. (5) via Eqn. (3). Seasons are coded by color. The integration started on the eastern side of the basin and continued to the coast on the western side. Thus the streamfunction starts at zero, but as we noted in Sec. 6, Part 4, the Sverdrup streamfunction need not and in this case does not return to zero on the opposite coast. The summertime Sverdrup streamfunction (red line) compares reasonably well with the streamfunction computed from meridional velocity, the red line of Fig. (7), in the region east between about 56 E and the coast of India, i.e., the interior, but not in the western boundary region. During the winter, Sverdrup streamfunction (the blue line) does not compare well with the streamfunction computed from meridional velocity, cf. the blue line of Fig. (7).

the basin-scale distributions of ${}^{y}M(x,y)^{sum}$ and $S(x,y)^{sum}$ are fairly consistent in showing three broad regions based upon the sign of ${}^{y}M^{sum}$.

- Eastern boundary region. Within a few hundred kilometers of the eastern side of the basin (west coast of India) there is fairly low amplitude, mostly positive (northward) ${}^{y}M^{sum}$, as well as mostly positive S^{sum} of comparable, small magnitude. This is a region where one would expect significant influence of remote forcing from the Bay of Bengal,[1], and all that will be added here is that local wind forcing in the Sverdrup sense might be of some importance as well.

- Central basin. Over the central region of the Arabian Sea, the transport ${}^{y}M^{sum}$ is negative (southward) Fig. (13) associated with the eastern side of the Findlater Jet noted in the discussion of the wind field. Larger values are found towards the western side of the basin (but not directly adjacent to the western boundary, discussed below). There is roughly comparable negative S throughout the central part of the basin, and including the occurrence of larger values in the

western third of the basin, so that there is a fairly convincing correlation of S^{sum} with ${}^{y}M^{sum}$ on the basin scale. This correlation would be expected if the Sverdrup relation was relevant.

There appears to be a correlation of stress curl and meridional transport within the central basin on somewhat shorter scales, O(300) km. One interesting feature is the local maximum of stress curl and transport at the northern end of the gyre, roughly 18 N, 62 E, which is the site of the so-called Omani Eddy (Fig. 3). In fact, it is no great exaggeration to say that the Omani Eddy *is* most of the gyre at this latitude. There are also more or less coincident maxima at 11 N, 63 E, the Socotra Eddy, and at 13 N, 70 E, the site of the SEII eddy. This visual correlation suggests that these eddies may be, in part, a result of the local wind stress curl.[18]

- Western boundary region. The region immediately adjacent to the western boundary is important and interesting. The ${}^{y}M^{sum}$ field is strongly positive (northward) close to the western boundary, with an amplitude up to 200 m^2 sec^{-1} (cf. Fig. 13, lower) in some places, and well beyond the color range of the figure. This is, of course, the region of the summertime Somali Current and so very large ${}^{y}M^{sum}$ is expected. The Sverdrup transport also has very large positive values in a nearly coincident region along the coast. The values of the Sverdrup transport are, however, considerably less than the meridional transport, the maximum values are roughly $S^{sum} \approx 50$ m^2 sec^{-1}. If, as suggested earlier, the summertime Somali Current can be seen as a western boundary current that returns the interior, southward Sverdrup transport back to the north, then the western boundary transport need not have any relation to the local Sverdrup transport, as occurs in the central basin. Or said a little differently, the western boundary region is more likely to have a basinwide relationship to the wind stress curl over the basin to the east, and only an incidental correlation to the local wind stress curl.

  In most western boundary currents, the local wind stress curl is a good deal smaller than the leading terms of the vorticity balance of the current, and so is negligible in the local dynamics of the western boundary current. However, the wind stress curl over the Somali Current is large enough, roughly 20% of βv, that it may be significant. The sense is that the positive wind stress curl will act to amplify the northward-going Somali Current that is expected from basin-wide volume conservation alone.

5.2 Monthly-varying transport across western boundary and interior regions

The SODA data are archived at monthly intervals, which should in principle allow a more finely resolved temporal view of the meridional transport across 10 N. However, some kind of spatial averaging is going to be required to suppress eddy variability. Here this is done by integrating over two segments of the 10 N boundary, a western boundary region (the solid line along 10 N in Fig. 4) extending from the Somali

[18] This is intriguing but far from definitive. The correlation is clear enough within the SODA reanalysis, but it isn't known (to me) that the small scale variability of the stress field and these two eddies are features of the real Southwest Monsoon wind and the Arabian Sea in the same way that the Findlater Jet and the Great Whirl undoubtedly are.

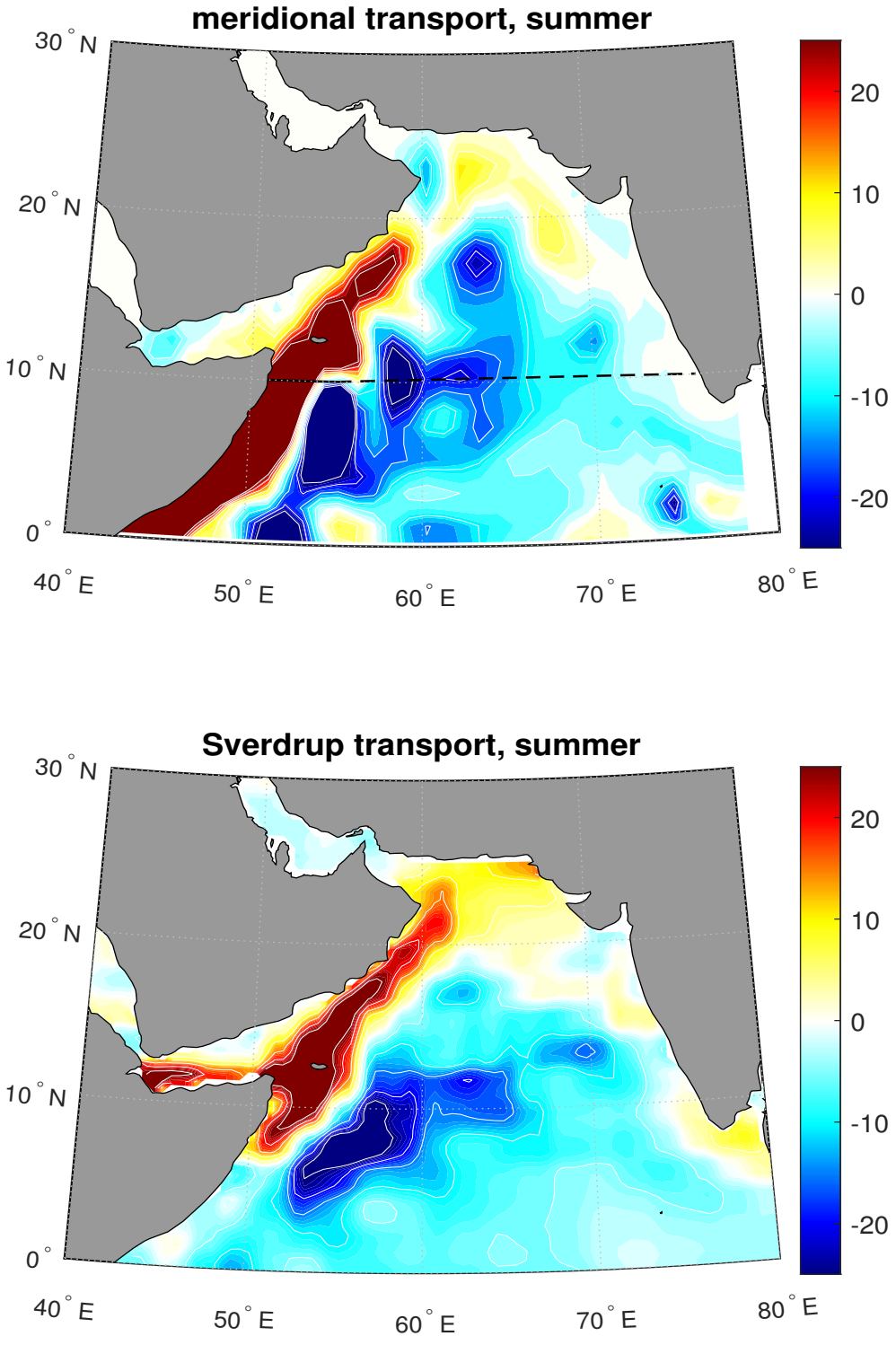

Figure 13: **(upper)** Meridional transport composite-averaged over the summer, ${}^{y}M(x,y)^{sum}$. The colorbar at right is in units m^2 sec^{-1}. The dark red region adjacent to the western boundary has some very high values, up to 200 m^2 sec^{-1}, that saturates the colorbar scale. **(lower)** Sverdrup transport, $S(x,y)^{sum}$, also composite-averaged over the summer. This figure requires considerable interpretation attempted in the main text.

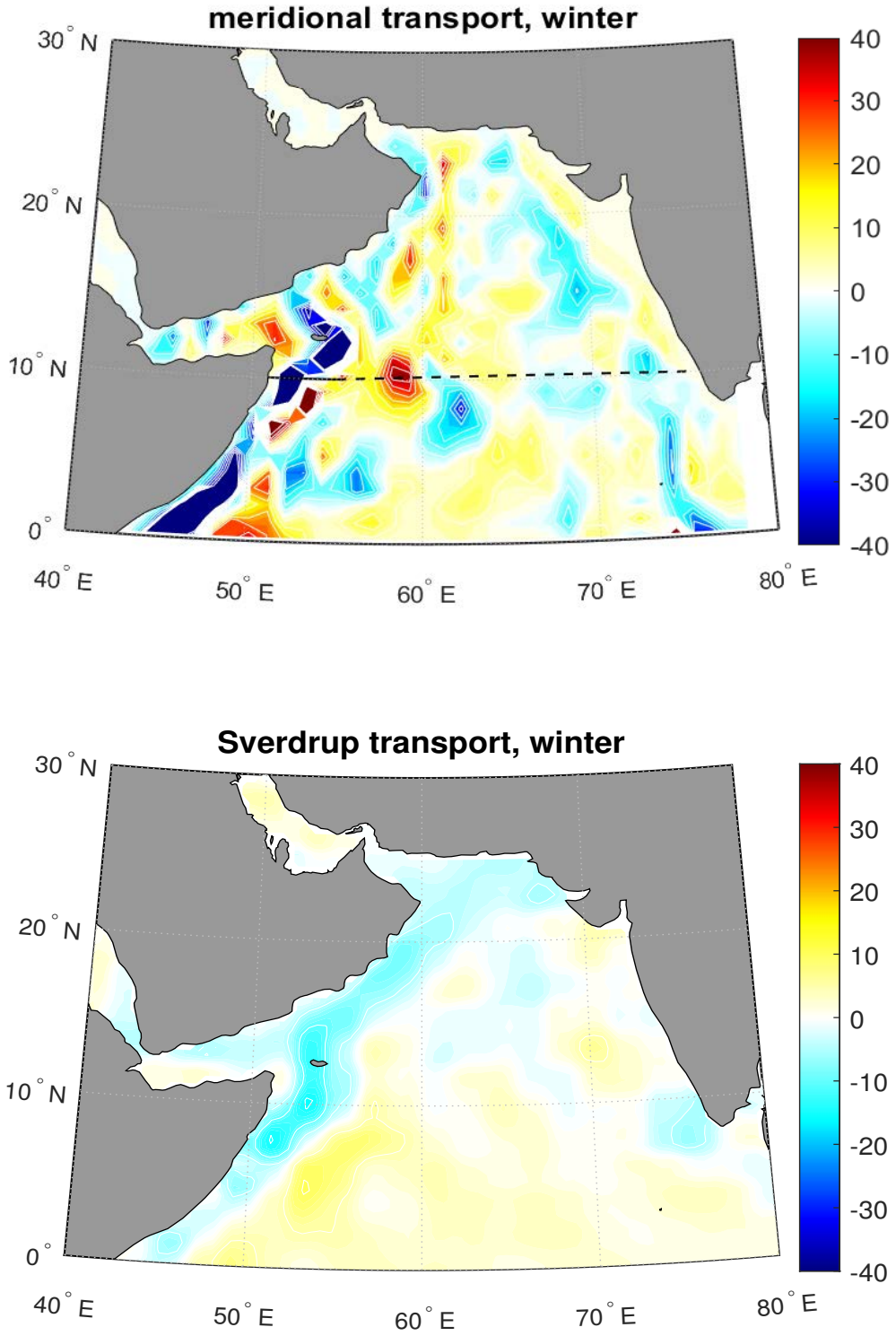

Figure 14: **(upper)** Meridional transport, ${}^{y}M(x,y)^{\,win}$, composite averaged over the winter. The colorbar at right is in units $\mathrm{m}^2\ \mathrm{sec}^{-1}$. The dark blue regions adjacent to the western boundary have high values, up to 50 $\mathrm{m}^2\ \mathrm{sec}^{-1}$, that saturate the colorbar. **(lower)** Sverdrup transport, $S(x,y)^{\,win}$, composite averaged over the winter. The generally favorable comparison of $S^{\,sum}$ with ${}^{y}M^{\,sum}$ that obtains in summer is not evident here.

coast to 55 E,

$$N(t)_{wbc} \;=\; \int_{Somalia}^{55E} {}^{y}M(x,\, y_o,\, t)\, dx,$$

and an interior region from 55 E to the coast of India (the dashed line along 10 N),

$$N(t)_{int} \;=\; \int_{55E}^{India} {}^{y}M(x,\, y_o,\, t)\, dx$$

and y_o is 10 N. This has introduced a parameter, the eastern extent of the western boundary region, 55 E, which is the Findlater Jet axis in summer (Fig. 5) and thus the longitude of zero stress curl (on average). The intent is that this N_{wbc} will represent the Somali Current, rather than the Great Whirl or the Socotra Eddy, say, but this simple-minded criterion is no guarantee of that.[19]

5.3 Sverdrup and meridional transport are highly correlated at annual and semi-annual frequencies

The monthly, meridional volume transport through these two regions shows a somewhat ragged but quite pronounced annual cycle, Fig. (15). The interior region has a southward going (negative) peak in summer, typically about 30 Sv, while the wbc region (Somali Current) has a closely comparable northward (positive) peak at the same time. The winter peak in transport is considerably smaller, about 10 Sv. It is notable that the interior transport and the wbc transport are almost exact complements, $N_{wbc} \approx -N_{int}$ whose sum, the net transport through 10 N, (the black line) is very small, $N_{wbc} + N_{int} \approx 0$, in the sense that $N_{wbc} + N_{int} \ll N_{int}$, as it should be. The same thing held for the long-term mean streamfunction, and here it is evident that conservation of volume holds also month by month. Thus the monthly transport can be represented equally well by the interior component, $N(t)_{int}$, which is unnamed and unremarked upon, or by the wbc component, $N(t)_{wbc}$, which is the justly famous Somali Current, or so intended. We will most often choose the former, given its possible connection to the Sverdrup relation.

Does the time-independent Sverdrup relation give a useful estimate of the monthly-averaged transport? On the face of it this seems unlikely, but is readily testable; evaluate $S(t)_{int}$ along the 10 N interior segment at monthly intervals,

$$S(t)_{int} \;=\; \frac{-1}{\rho\beta} \int_{India}^{55E} \nabla \times \tau(x, y_o, t)\, dx, \tag{4}$$

and compare with the corresponding meridional transport, $N(t)_{int}$ from the SODA meridional velocity. There is an obvious visual correlation between N_{int} and S_{int} (Fig. 16, upper). The auto spectra indicate

[19] You might suppose that defining and then estimating the transport of a western boundary current like the Somali Current or the Gulf Stream would be straightforward. However, in practice, there are often large, geostrophic eddies on the flank of what looks to be the main current, and so not easily distinguished from the main current, which will in any case meander significantly unless constrained by topography. The result is that the estimated transport will likely be dependent upon the criteria used to discriminate the current from the surroundings, see e.g., Heiderich, J., and Todd, R. E. (2020). Along-Stream Evolution of Gulf Stream Volume Transport, Journal of Physical Oceanography, 50(8), 2251-2270. Retrieved Sep 24, 2021, from https://journals.ametsoc.org/view/journals/phoc/50/8/jpoD190303.xml

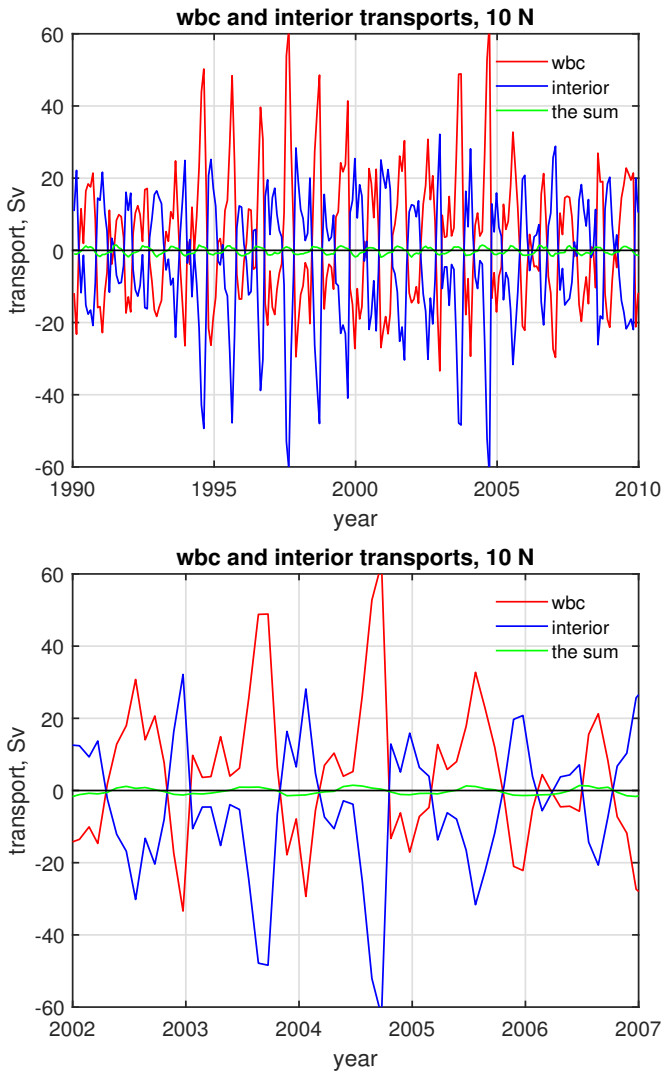

Figure 15: Volume transports across 10 N evaluated over the interior, $N(t)_{int}$ (the red line) and over the western boundary region, $N(t)_{wbc}$ (blue line). The **(upper)** panel is over two decades, 1990 - 2010, and the **(lower)** panel is a subset, 2002 - 2007. These data are from the monthly-averaged and sampled SODA 2.2.4 reanalysis and so have a somewhat spiky, unphysical appearance. Notable features are the large amplitude seasonal variation, roughly $\pm$ 30 Sv in summer, and that N_{wbc} and N_{int} are almost exact complements; their sum (the green line) is much smaller than either piece separately.

that S_{int} is a little smaller than N_{int}, roughly consistent with the the ratio of the two streamfunctions (cf., Figs. 7 and 12). The corresponding statistical measures, lagged correlation and coherence of the cross-spectra, bear out the visual impression of high correlation (Fig. 17). The maximum of the lagged correlation is approx. 0.8. The asymmetry suggests a small phase difference, with the volume transport lagging the Sverdrup transport by about two weeks. The cross-spectral coherence (frequency domain analysis) is similar; the coherence ≥ 0.9 at the annual frequency and the phase difference at the annual frequency is very small (Fig. 17, center). These results indicate that the monthly-varying meridional transport, either over the Arabian Sea interior or the western boundary current/Somali Current, can, with considerable confidence, be estimated by the monthly-varying wind stress curl via the time-independent Sverdrup relation applied in a straightforward way.[20]

To be sure, the scatter diagram of Fig. (16), lower, gives pause to this last claim, as some monthly

[20]Something to note: the monthly winds are (auto-)correlated in time and especially within a season. A similarly high correlation would not hold if the monthly wind varied randomly.

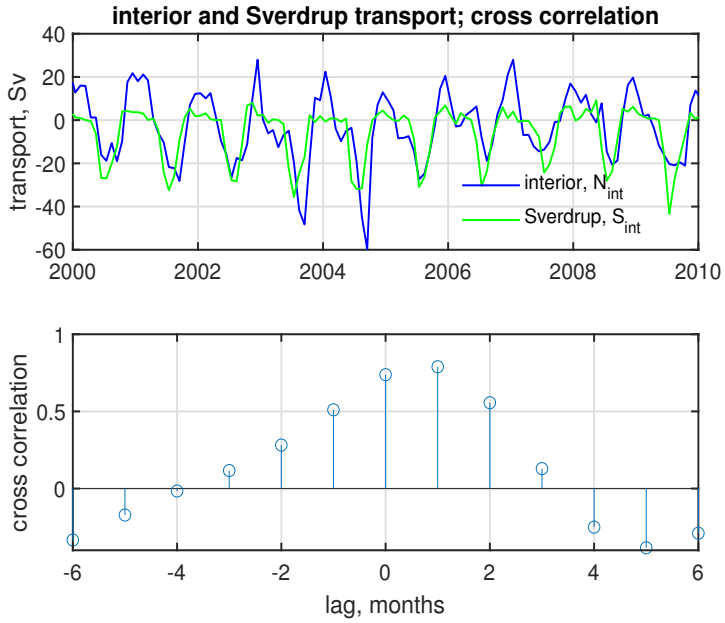

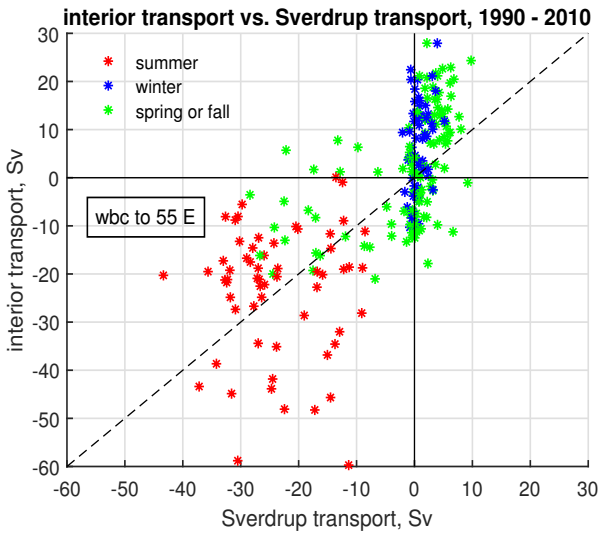

Figure 16: **(top)** Meridional volume transports across the 10 N interior boundary as computed from SODA meridional velocity, $N(t)_{int}$, (blue line) and as estimated from stress curl and the Sverdrup relation, S_{int}, (green line). **(middle)** Lagged cross-correlation between $N(t)_{int}$ and $S(t)_{int}$. The small asymmetry indicates that N_{int} lags S_{int} by about two to three weeks. **(lower)** Scattergram of monthly N_{int} and S_{int} with season color-coded. The S_{int} gives some account of the year-to-year variation in the amplitude of the summertime, Southwest Monsoon season transport (red markers), though with considerable scatter about the 1-to-1 line. The same can not be said of the wintertime, Northeast Monsoon transport (blue markers) when the actual transport systematically exceeds the Sverdrup transport. Notice the very large asymmetry in the distribution of data overall, a reflection of the summer to winter difference in volume transport magnitude.

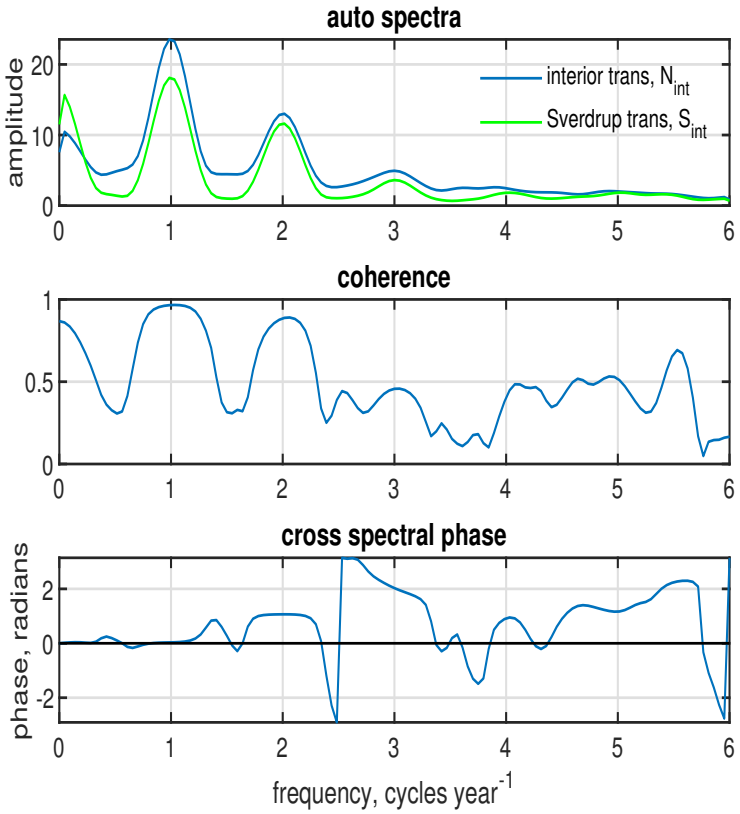

Figure 17: Frequency domain analysis of meridional transport across the 10 N interior from SODA reanalysis and Sverdrup transport for the two decade period 1990 - 2010. **(top)** Auto spectrum of $N(t)_{int}$ and $S(t)_{int}$ showing significant peaks at 1 cycle per year, and a secondary peak at 2 cycles year^{-1}. These peaks are broadened considerably by averaging over six frequency bands which is required to estimate coherence; these peaks are quite narrow when estimated via a periodogram. **(middle)** Coherence between $N(t)_{int}$ and $S(t)_{int}$, which is high at the annual and semi-annual frequencies. **(lower)** Phase; at the annual frequency, the phase is not distinguishable from zero.

estimates are far from the one-to-one line. Some of this is due to eddy variability, which is quite strong anywhere near the western boundary, e.g., the Great Whirl and especially the Socotra Eddy, which is usually near 10 N but is not stationary in space or time. The eddy contribution to this transport estimate might presumably be suppressed somewhat by choosing a wider western boundary region, say the Somali coast to 58 E, and thus including almost the entire Socotra Eddy within the western boundary segment, and leaving less of it within the interior. With that change, the maximum lagged correlation goes up to 0.9, and the scatter diagram for summer tightens up considerably (Fig. 18). There is no significant change for the winter estimates. The first definition for the western boundary region made here, 55 E, the Findlater Jet axis, was plausible *a priori*, and so will be retained pending a better means for discriminating the Somali Current from eddy variability.[19]

The auto spectra and the coherence reveal a second significant peak at 2 cycles per year, the semi-annual frequency. This is not immediately apparent to the eye in the monthly time series, but after a second or third look you may notice some higher frequency (than annual) variability that is most apparent in winter, when the transport is smaller. A semi-annual variation of wind stress is quite prominent along the equator, where the sun goes directly overhead twice a year (March on the way north, September on the way south), and evidently this semi-annual variability reaches to at least 10 N (in the SODA reanalysis). The coherence is high also at this semi-annual frequency, and the phase lag is about 0.5 radians, with the sign indicating that the semi-annual meridional transport lags the semi-annual Sverdrup transport by several weeks to a month.

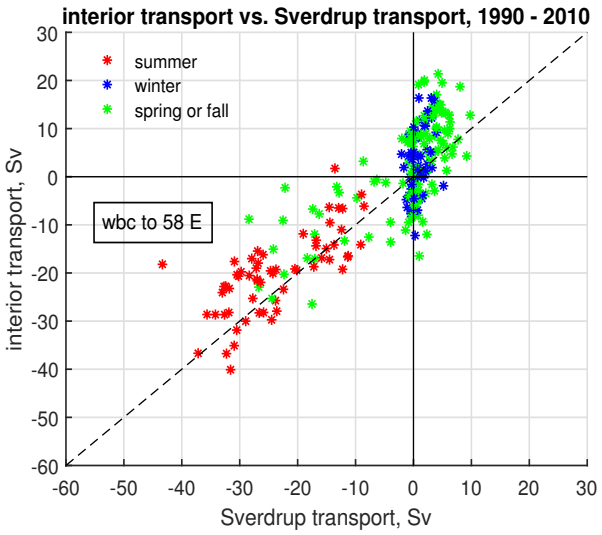

Figure 18: Scattergram of monthly N_{int} and S_{int} with season color-coded. This is exactly Fig. (16) with the exception that the eastern edge of the western boundary region was extended three degrees east to 58 E.

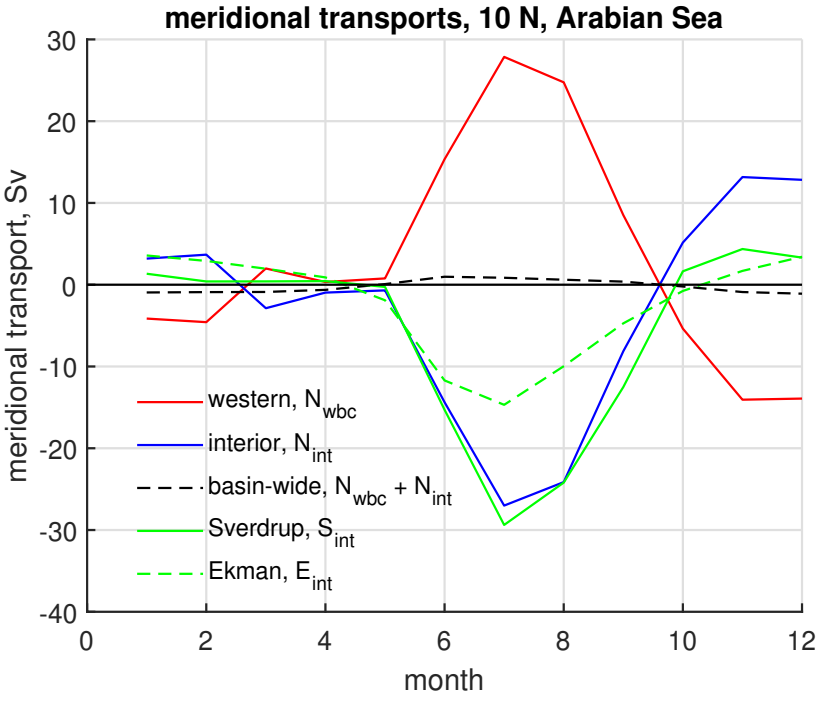

Figure 19: A composite average annual cycle of meridional volume transports across 10 N in the Arabian Sea computed over 2002 through 2006. Transport is evaluated over a western boundary region, N_{wbc} (solid red line), and over the interior, all the rest of the basin to the east, N_{int} (solid blue line). The dashed black line is their sum, $N_{wbc} + N_{int}$, which should be very small compared to either the wbc or interior transports as in the previous figure. The green line is the composite average Sverdrup transport by month, S_{int}, estimated from wind stress curl along the interior segment of the 10 N boundary. The Sverdrup transport has very similar magnitude and phase to the interior transport during the summer months of the Southwest Monsoon, but not so during the winter, when it is considerably less than the interior transport.

5.4 Summary of the description

The wind-driven circulation of the Arabian Sea has been framed in very specific (and one could say narrow) terms, *viz.,— where, when* and *why* is there meridional transport across 10 N?

Where. Meridional transport is strongest within a western boundary region several hundred kilometers wide (Figs. 6 and 19) that includes the summertime Somali Current. A closely compensating meridional transport occurs over the interior of the basin. The summertime circulation of the Arabian Sea is thus not unlike the time-mean circulation of the North Atlantic subtropical gyre. One difference in detail is that the interior transport is considerably stronger toward the western side of the basin, as is the wind stress curl. This appears to be a significant aspect of the time-dependent response discussed further in the next section, Swec. 10.6.2.

When. The meridional transport (and the flow generally) shows a very striking seasonal variation. The western boundary region includes a northward Somali Current in summer, having a magnitude of roughly 20 - 40 Sv. On average over several decades the maximum summertime transport is about 30 Sv. This northward flow is usually established within a few weeks of the onset of the Southwest Monsoon winds at 10 N. There is a considerably weaker and less well organized southward flow in the western boundary region during the winter, about 10 Sv.

Why. The results to here demonstrate that the Sverdrup relation plus wind stress curl give a fairly good account of the seasonal, and even the monthly, meridional transport across interior and western boundary regions of 10 N in the Arabian Sea. This is at least slightly surprising, and before concluding that the Sverdrup relation explains the meridional transport, it is necessary to explain why the Sverdrup relation is relevant, i.e., why the Sverdrup relation should make a plausible estimate of the summertime meridional transport.[21]

The Sverdrup relation predicts amplitude. So far as time goes, the Sverdrup relation taken literally indicates that the meridional transport should track the stress curl instantaneously. Clearly this can not be true, which is perhaps the reason that the Sverdrup relation has been somewhat overlooked in this context. However, the Arabian Sea circulation responds quickly enough — within a few weeks — that the Sverdrup relation makes a fairly good approximation of the link between the seasonally-varying (and even the monthly-varying) winds and circulation. As noted in the introduction, the same response time for a mid-latitude basin is roughly 1500 days (Sec. 5.4, Part 4), or two orders of magnitude greater. This suggests a slightly sharper question: why this very large difference between the Arabian Sea and the subtropical North Atlantic?

The experiments and results of Sec. 6, Part 4 show that an important parameter in the adjustment of

[21] Suppose that the issues surrounding time-dependence can be put aside. Would the Sverdrup relation then make a good explanation of the transport? Another example: suppose that a current is known to be geostrophic balance. Would geostrophy make a good explanation of the currents? I would say no, not if that is all that is on offer. To make a good explanation requires an explanation of why geostrophy should hold in the case at hand (to be sure, these circumstances are so common that geostrophy is often taken for granted), and better, explain how the pressure field came to be established. Here the task is to explain why Sverdrup should hold, given the significant time-dependence of the phenomenon.

a typical midlatitude basin to steady, baroclinic Sverdrup flow will in many cases be the east-to-west basin transit time for a first mode baroclinic, long Rossby wave having a phase and group speed $C_{Ro} = \beta R_d^2$. Applied to the Arabian Sea ($L_{basin} = 2500$ km) this gives an estimate

$$T_{basin} \; = \; \frac{L_{basin}}{\beta {R_d}^2} \; = \; L_{basin} \frac{f^2}{\beta C^2} \; \approx \; 100 \;\; \text{days.} \tag{5}$$

This basin transit time is appropriate when the wind stress field is independent of x, and the basin width, L_{basin}, is the relevant, zonal, external length scale. The ratio of this T_{basin} evaluated at 10 N Arabian Sea vs T_{basin} at 30 N in the subtropical North Atlantic is about 0.05, or a factor of about 20. Thus, latitudinal dependence and the reduced basin width of the Arabian Sea go a long way towards explaining the very large difference in response times. However, such a large extrapolation is not entiely convincing, and in any event (5) comes up short of the factor O(10^2) that characterizes the ratio of Arabian Sea and subtropical gyre response times.

6 Experiments with western-biased, jet-like winds show a very fast adjustment

It is helpful to consider briefly two additional numerical experiments that are configured as a highly idealized Arabian Sea basin driven by a jet-like wind field. These experiments will reveal another factor of roughly 5 that favors a fast response of the Arabian Sea. The basin is taken to be rectangular, 4000 km north-south extent, centered on the equator, and 2500 km east-west. A three-layer stratification, including a free sea surface, is as before, though with a slightly thinner (shallower) thermocline that gives a slightly reduced baroclinic fist mode gravity wave speed, C = 2.6 m sec^{-1} and a baroclinic radius of deformation $R_d \approx 100$ at 10 N latitude.

An important difference vis-a-vis a typical mid-latitude basin arises from the Southwest Monsoon wind stress field. As noted in Sec. 3.1, the summertime Arabian Sea wind stress is mainly the Findlater Jet, which is as much meridional as it is zonal, and is present over the western side of the basin (Sec. 3). To model this, the wind stress field will be taken as meridional only, and given a jet-like, hyperbolic secant profile that is independent of y,

$$\tau_y(x,t) = \tau_o(t) sech((x - x_o)/L_{jet}), \tag{6}$$

the red line of Fig. (20), right. The jet axis is set on x_o = -850 km, which is 400 km from the western boundary, and the jet width $L_{jet} = 300$ km. The issue here is time-dependence, not amplitude, and so in this first experiment the wind stress amplitude is taken to be a nominal $\tau_o = 0.1$ Pa. In order to minimize inertial motions and short Rossby waves, the wind stress amplitude was ramped up from zero to τ_o in the first 20 days of the experiment and thereafter held constant. The most important result from these experiments will be apparent in this small amplitude (linear) case. However, finite amplitude (nonlinear) effects are in some respects very interesting and will be investigated in a second experiment (Sec. 7) having a more realistic wind stress amplitude, $\tau_o = 0.5$ Pa.

A plan view of the solution at 30 days after startup and time series of the transport in each layer are in Figs. (20) and (21). The dominant feature of the circulation is an anticyclonic gyre that is mainly in the western half of the basin. This gyre is elongated north to south compared with the real Arabian Sea gyre, no doubt because the model wind jet does not turn clockwise over the basin, as does the real, terrain-following Findlater Jet (Fig. 3). It is notable that the volume transport almost keeps pace with the wind stress (cf. the black and cyan lines of Fig. 21) lagging by less than a week on average. In Sec. 8, Part 4 it was noted that a barotropic, quasi-steady Sverdrup response sets up very quickly, within a week or two even within a large, mid-latitude basin. In that light, the (almost) quasi-steady barotropic response of a relatively small, low latitude basin is not at all surprising — it should happen, and is part of the reason why the Sverdrup relation gives fairly good estimates of the monthly transport in the Arabian Sea.

6.1 Baroclinic Sverdrup flow

However, a fast barotropic response can not be the whole story; the Somali Current would hardly be noticed if it was strictly barotropic. Rather, the Somali current is significantly surface-intensified, i.e., it is baroclinic and equivalent barotropic, Fig. (8), right, and see, e.g., Düing and Szekielda (1970)[1], which the Sverdrup relation by itself does not explain. The experiments of the previous sections provide some additional guidance.

Sverdrup transport is the sum of geostrophic and Ekman transports (Sec. 3.1, Part 4),

$$S_{int} \;=\; G_{int} \;+\; E_{int}\,,$$

where the

$$E(t)_{int} \;=\; \frac{1}{\rho f}\int_{India}^{55E} \tau_x(x,y_o,t)\;dx$$

can be readily evaluated. During the summertime Southwest Monsoon, the Ekman transport is estimated to be about a third or even up to a half of the Sverdrup transport, Fig. (19). Ekman transport sets up very quickly, essentially in phase with the wind stress, and is strongly surface-intensified, being confined to the shallowest 50 - 100 m, at most. Hence, the Ekman transport can account for a significant part of the surface-intensified Sverdrup flow in the interior. Of course, this applies to the SODA reanalysis (and the real Arabian Sea) where there is a zonal component of the wind stress, but not to the new model solution where the winds are meridional only and hence there is no meridional Ekman transport.

Within the western boundary region of the model solution, the upper layer transport (upper 250 m) lags the stress curl by only about one to two weeks (estimated by inspection of the red and magenta lines of Fig. 21), and after only about three weeks, most of the Sverdrup transport is found within the surface layer. This is considerably faster than would be expected from the usual, baroclinic basin transit time, Eqn. (5). The wind field over the Arabian Sea, and specifically the Findlater Jet, is likely to be an important factor insofar as the most important zonal length scale in this experiment comes from the wind field, L_{jet}, as in the experiments of Sec. 7.3, Part 4, rather than the basin width, as assumed in Eqn. (5) and which is appropriate when the wind is purely zonal and varies only in the meridional direction. The

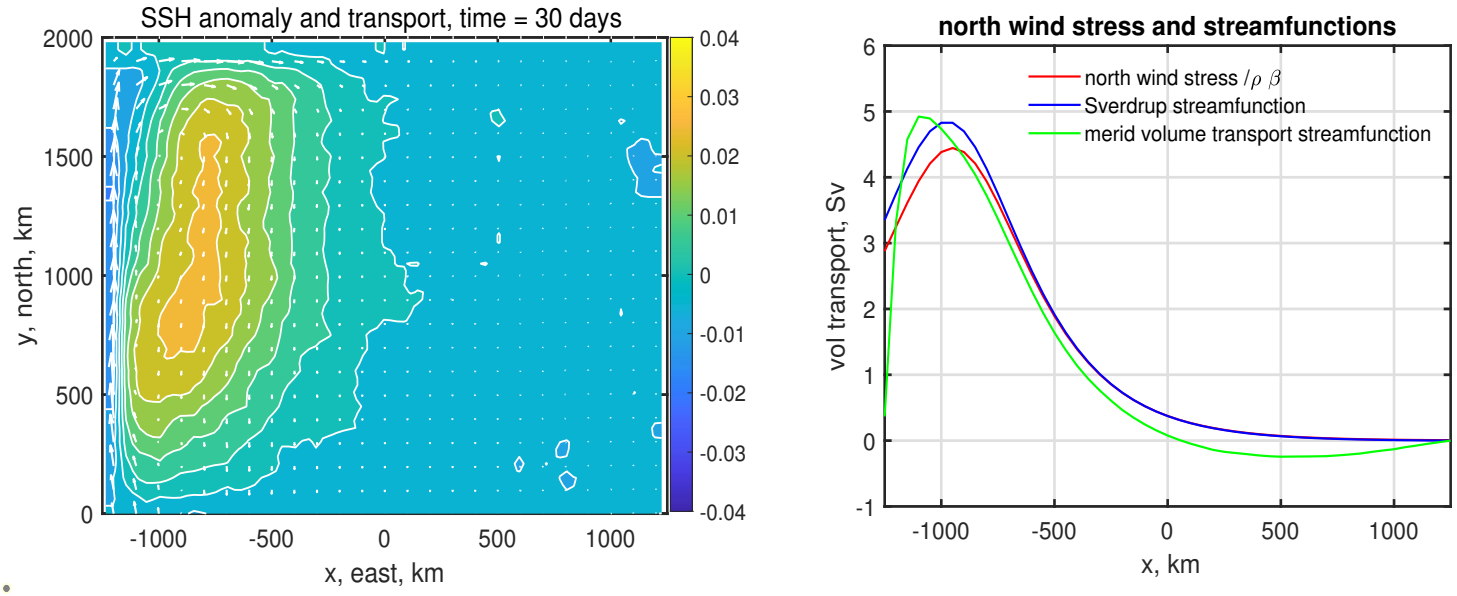

Figure 20: **(left)** A plan view of the northern half of the Arabian Sea model domain at 30 days after the start of the small amplitude experiment ($\tau_o = 0.1$ Pa). The background color depicts the ssh anomaly (scale at right is in meters), and the vectors are volume transport. The pattern of ssh includes a maximum that is almost coincident with the wind stress jet axis, and the transport occurs in a nearly geostrophic flow that is more or less along the flanks of the ridge, though compressed somewhat onto the western boundary. **(right)** Wind stress and volume transport streamfunctions for the small amplitude experiment (note the small values of transport). The wind stress zonal profile is the red line (scaled here with $\rho\beta$) and the corresponding Sverdrup streamfunction is blue. The meridional transport streamfunction $\Psi(x)$ sampled 30 days after the start is in green. A question for you: Can you explain why the scaled wind stress and the Sverdrup streamfunction are (almost) identical?

response time estimated with $L_{jet} = 300$ km is, from Eqn. (5),

$$T_{jet} = \frac{L_{jet}}{\beta R_d^2} \approx 15 \text{ days}, \tag{7}$$

and which is O(10^{-2}) compared to the basin transit time of the North Atlantic subtropical basin. One way to think of this is to note that the entire Arabian Sea basin does not contribute equally to the Sverdrup transport (as it will in a basin driven by the shear between the eastward and westward global wind belts) simply because the wind stress curl is by far strongest within a few hundreds of kilometers of the western boundary.[22]

[22]There is another way to think about this adjustment to steady Sverdrup flow that you may find more physical. First, compute(estimate) the wind-forced Ekman pumping, and then the corresponding geostrophic current, which will be meridional and time-dependent. This has previously been dubbed the Stage 2, locally-forced current. Suppose that a steady state will be achieved when the beta effect acting upon this current is just sufficient to cancel the Ekman pumping. Ignoring spatial phase(!) and assuming a hard start-up of the wind stress, the time this takes is just (7). If L_{jet} is the relevant horizontal scale, and if geostrophy and beta are of leading importance, then (7) seems inevitable.

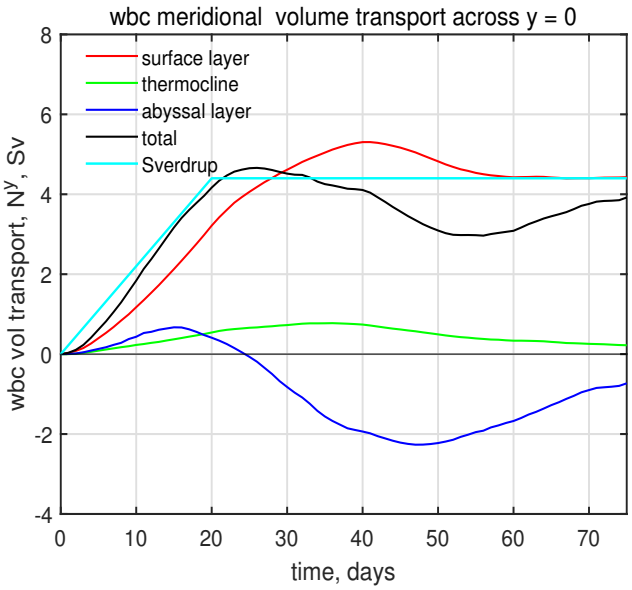

Figure 21: Time series of the meridional transport within the western boundary region at the equivalent of 10 N and in the small amplitude experiment. The Sverdrup transport, which is proportional to the time-dependent wind stress divided by $\rho\beta$, is the cyan line, and the volume transport over the full water column is the black line. Notice that the volume transport almost keeps pace with the Sverdrup transport. The volume transport within each of the three model layers are the colored lines. The surface layer transport (red line) lags the Sverdrup transport by only about one to two weeks.

6.2 Summary, why the Sverdrup relation is relevent

This simple experiment indicates that a baroclinically adjusted, surface-intensified Sverdrup flow may be expected within the western Arabian Sea within only a few weeks of the onset of (Findlater) jet-like Southwest Monsoon winds. This very fast response (compared to a mid-latitude ocean basin) is due mainly to the low latitude of the basin, Eqn. (5), and enhanced significantly by the western-biased and jet-like structure of the Southwest Monsoon wind field. These lead to an estimate of the baroclinic response time, Eqn. (7), of about two weeks, which is consistent with the idealized model solution, Fig. (21),and the SODA reanalysis soliution.

7 Appendix: Finite amplitude effects — is that a great whirl?

The nearly linear solution described above misses an interesting finite amplitude effect that arises in a second experiment in which the wind stress amplitude is set to a more realistic value, $\tau_o = 0.5$ Pa. The meridional velocity within the surface layer of the western boundary current then becomes very large within a few tens of days, exceeding 2 m sec^{-1}, which is not inconsistent with the largest observed speeds observed within the summertime, Somali Current (Düing and Szekielda, 1970[1]).

7.1 Froude, Ekman and Rossby numbers

A rough idea of the likelihood of finite amplitude effects can be gleaned from estimates of several nondimensional numbers that may be formed given values of the current, $U = 2$ m sec^{-1}, the Coriolis

parameter (at 10 N) $f = 2.5 \times 10^{-f}$ sec^{-1}, $\beta = 2.3 \times 10^{-11}$ sec^{-1} m^{-1}, the wind stress, $\tau_o = 0.5$ Pa, the gravity wave phase speed, $C = 2.6$ m sec^{-1}, an along stream length scale, $L = 1000$ km (by inspection of Fig. (20), left), and an eddy length scale, $L_{eddy} = 200$ km (same comment). These may be combined into more or less familiar ratios,

- wind stress Ekman number, $\frac{U^2}{L} / \frac{\tau_o}{\rho_0 h1} \approx 0.8$,
- Froude number, $U/C \approx 0.7$,
- eddy Rossby number, $\frac{U^2/L_{eddy}}{fU} = U/fL_{eddy} \approx 1.2$.

From the first of these it is evident that the inertia of the current $\propto U^2/L$ is appreciable compared to the wind stress (the Ekman number is O(1)) and to the possible baroclinic pressure gradient (the Froude number is also O(1)).[23] As a consequence of the large currents, there are substantial finite amplitude (nonlinear) effects, by horizontal advection and by large changes in layer thickness.[24]

Despite the large currents and thickness gradients of this second experiment, there is more in common with the the small amplitude solutions than might have been expected, cf. Figs (20) and (21) with Figs. (22) and (23). The amplitude of the circulation in the new experiment is about 5 times that of the former, consistent with the ratio of the wind stresses and so the circulation amplitude is quasi-linear in τ_o. The rise time (response time) of particular interest here also appears to be about the same as in the small amplitude experiment, and so the response time is also is a linear phenomenon (i.e., is independent of τ_o). Notice, though, that there are quite large oscillations in the transport, and most notably an initial, positive overshoot by about 50%.

The most obvious difference made by finite amplitude effects is the appearance of a comparatively small, roughly 300 km diameter, anti-cyclonic eddy that on day 30 is at about $(x,\ y) = (-1000,\ 700)$ km. This eddy is adjacent to the western boundary current, not the basin boundary, and it is somewhat to the south of and almost separated from the main gyre. This eddy begins to form at about day 15, and then strengthens as it moves very slowly toward the north. By day 30 it has an azimuthal transport of about 15 Sv, which is comparable to the western boundary current. Depending upon just where this eddy sits with respect to the presumed eastern edge of the western boundary region, it can thus have a substantial impact

[23] An excellent article discussing the many forms and interpretations of a Froude number is available online at https://en.wikipedia.org/wiki/Froude_number

[24] Large indeed: in the northwestern corner of the model domain the surface layer thickness goes to almost zero at about 60 days after the start of the experiment, and of course that immediately sets off a figurative 'KaBoom' in the numerical integration. This is a shortcoming of the present numerical model and its layered representation of the momentum and continuity equations. The cure is twofold. First, utilization of a gridded finite difference representation in the vertical so that division by a material layer thickness is not needed. Second, a representation of upper ocean vertical mixing which will help keep the Ekman layer at a reasonable thickness even in the presence of very large and sustained wind stress and upwelling. Both of these are an integral part of the Regional Ocean Modeling System (ROMS), which is thus much better suited to a detailed simulation of the Somali Current than is the present, elementary layered model. For more on ROMS, see https://en.wikipedia.org/wiki/Regional_Ocean_Modeling_System (you may have to type this into your browser).

upon the estimated western boundary current transport, and just the complementary effect on the interior meridional transport, Sec. 5.2.

7.2 Speculation on an eddy formation process

An eddy formation process might be characterized in any of several ways, e.g., by a momentum, vorticity or energy balance, but here the discussion emphasizes phenomenology, i.e., what can be seen in this solution and in the SODA solution (Fig. 1). Hurlbert and Thompson (1980)[1] emphasized that the Somali Current is an inertial western boundary current in the sense that it has the potential to overshoot the region where it is generated by and be in approximate balance with a wind stress and stress curl. The best-known example of such an inertial boundary current is provided by the the western boundary current of a multi-gyre circulation of the sort considered in Sec. 5.5, Part 4. The northward-going subtropical western boundary current will have enough inertia to cross the wind stress curl-defined gyre boundary and intrude a significant distance into the adjacent subpolar gyre where it will be far out of balance with the prevailing wind stress curl. Potential vorticity conservation will tend to bring the intruding current back into its home gyre, likely triggering a Rossby wave, and/or, the intruding current may form a cutoff ring or eddy. It is speculated that something similar could occur in space and time in the Arabian Sea. The qualitative evidence for this in the SODA solution is that during early summer, the western boundary current (Somali Current) forms first at lower latitudes, where the Southwest Monsoon onset occurs first, and extends for few hundreds of kilometers northward along the coast. The current then detaches from the western boundary and rolls up into a fairly large (300 km diameter), anticyclonic eddy. This typically happens several times during early summer, eventually forming something like a Great Whirl in the reanalysis solution. In the present experiment, in which the wind field is fixed in space but time-dependent, the adjustment to Sverdrup flow occurs first at lowest latitude, and progresses northward as discussed in Sec. 7.3, Part 4. From Eqn. (87), the y-dependent rate of the northward progression evaluated at $y_o = 1000$ km is

$$V_{Sv} = \frac{C^2}{2\beta L_\tau y_o} = 0.7 \text{ m sec}^{-1}.$$

This is comparable to but a little less than the northward current speed within the western boundary current (which is, of course time-dependent). Thus the northward flowing western boundary current could outrun the adjustment to Sverdrup flow. A variant on this is that a sufficiently fast western boundary current may also outrun the northward translation of the ITCZ, $V_{itcz} \approx 0.4$ m sec^{-1} (Sec. 3.2), and thus the Southwest Monsoon onset (this is not relevant in the present numerical experiment in which the wind is switched on over the entire model domain at once). These ratios of northward speeds may be written as Froude numbers,

- Sverdrup adjustment Froude number, $F_{Sv} = U/V_{Sv} \approx 3$,
- ITCZ translation Froude number, $F_{itcz} = U/V_{itcz} \approx 5$,

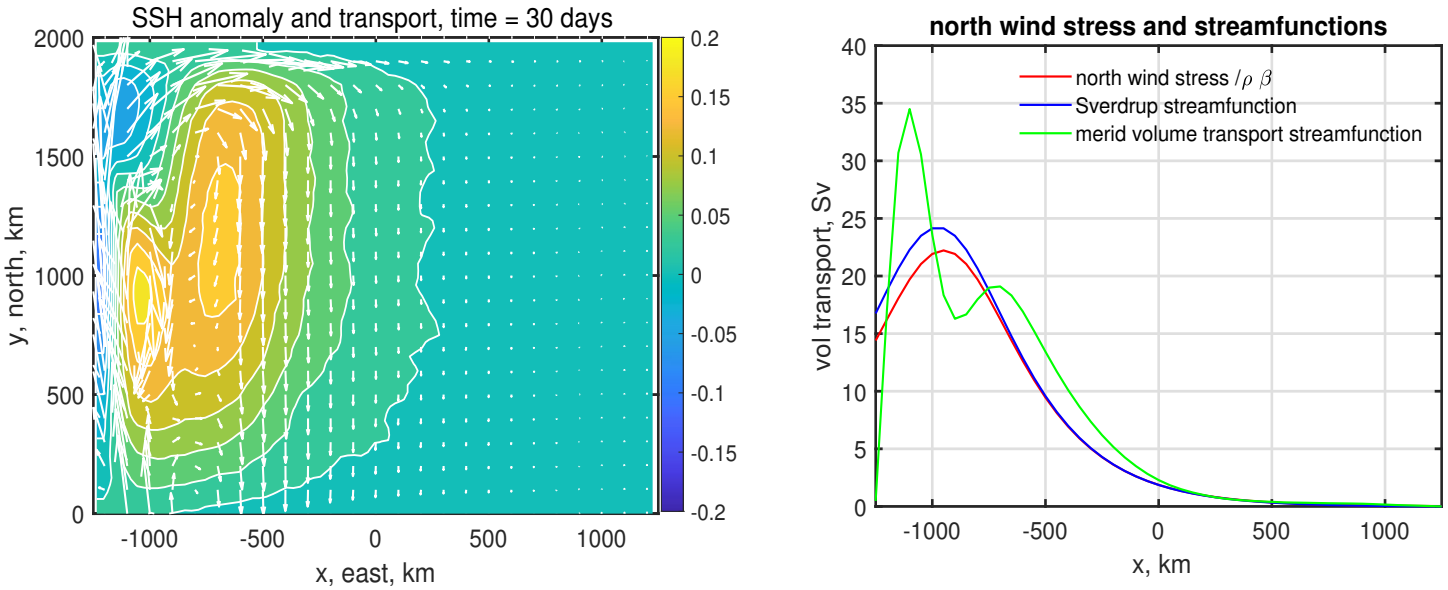

Figure 22: **(left)** A plan view of the Arabian Sea model domain, 30 days after the start of the large amplitude experiment ($\tau_o = 0.5$ Pa). The background color depicts the ssh anomaly (scale at right is in meters), and the vectors are volume transport. Compare this with the small amplitude (linear) solution of the two previous figures. **(right)** Wind stress and volume transport streamfunctions. The wind stress zonal profile is the red line (scaled here with $\rho\beta$) and the corresponding Sverdrup streamfunction is blue. The meridional transport streamfunction $\Psi(x)$ sampled 30 days after the start is in green. Note that the amplitude here is about five times that of the small amplitude experiment, Fig. (21), right, and that there is a large mismatch between Sverdrup and actual meridional transport near the western boundary.

though they do not scale the magnitude of terms in a momentum balance in the way that the conventional Froude number does.

It is fair to say that this eddy is the great whirl (n.b., l/c) of the present model, but could it be an analogue of the real Great Whirl of the Arabian Sea? It has several properties in common with the Great Whirl — approximate size, amplitude comparable to the central gyre, location compared to central gyre, and movement. However, the genesis process is not in common. Beal et al. (2013)[14] and references therein, as well as the data displayed in the animation of Fig. (1), make a compelling case that the real Great Whirl begins in the spring when the 6 N ridge intersects the western boundary, a process not included in this simulation. In most years this occurs weeks before the Southwest Monsoon onset. Thereafter the Great Whirl strengthens alongside the wind-driven Somali Current, which could be in common with the present eddy formation.

8 Concluding remarks

The plan for this essay was to provide a concise description of the seasonally-varying circulation of the Arabian Sea (summarized in Sec. 5.4 and not repeated here), and the specific goal was to construct an explanation of the link between the winds and the circulation that would entail the observed, rapid

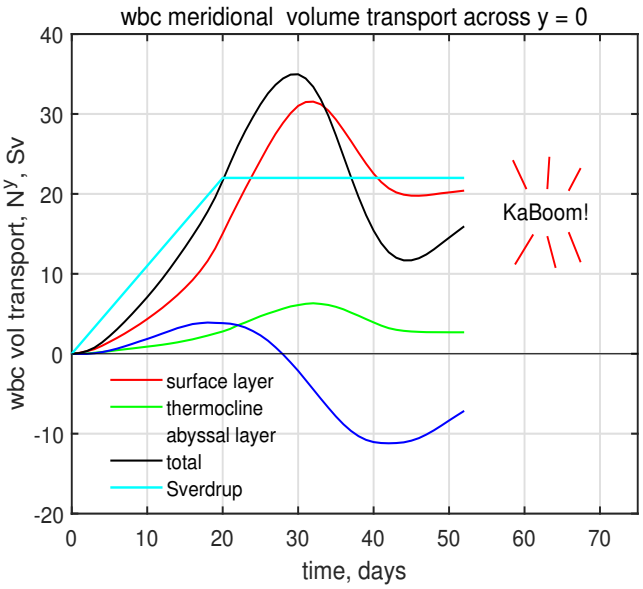

Figure 23: Time series of the meridional transport within the western boundary region of the large amplitude experiment, cf. the small amplitude experiment of Fig. (20). An untoward event at about 60 days is discussed in the main text and footnote 24.

response to the monsoon winds. The intent was that the explanation should be as simple as possible, but not simpler.[25]

It is very seldom that we will have the opportunity to adjudicate simplicity among a collection of otherwise suitable explanations, but we do have the freedom to choose a new problem and to define a question that might lead to a useful, simple explanation. The key in this case was a narrow focus on the meridional transport into and out of an Arabian Sea control volume that was open along one latitude, 10 N. And then, the time-dependent transport across 10 N was represented by just two components, an interior piece, $N(t)_{int}$, and the complementary western boundary piece, $N(t)_{wbc}$. Since

$$N(t)_{wbc} \approx -N(t)_{int}, \tag{8}$$

this reduced the spatially complex circulation of the Arabian Sea to one variable, the meridional transport integrated over the interior of the basin, a span of about 2000 kilometers. It was found that

$$N(t)_{int} \approx S(t)_{int}, \tag{9}$$

with S the Sverdrup transport evaluated on monthly wind stress curl (Sec. 5.3). It was argued that the Sverdrup relation may be regarded as an explanation of the link between the wind and the Arabian Sea

[25] This famous aphorism has been distilled from rather more emphatic advice offered by Albert Einstein, "It can scarcely be denied that the supreme goal of all theory is to make the irreducible basic elements as simple and as few as possible without having to surrender the adequate representation of a single datum of experience." A. Einstein, On the Method of Theoretical Physics, The Herbert Spencer Lecture, Oxford, England, June 10, 1933. Einstein was a keen student of physics generally, including fluid mechanics, and wrote his PhD thesis on the variation of viscosity with the molecular size of a solute. His aim was to support the then tenuous molecular hypothesis. Einstein later developed an insightful theory on erosion and sediment deposition in meandering river flows by analogy with the centripetal motion of tea leaves suspended in the bottom boundary layer of a swirling cup of tea, https://www.ias.ac.in/article/fulltext/reso/005/03/0105-0108 (you may have to type this into your browser). No one of Einstein's generation could have been a witness to the eddy variability and complexity of the ocean circulation in the way that we are today thanks to satellite observations. Here's an entirely hypothetical question for you: If Einstein had seen the animation of Arabian Sea circulation, Fig. (1), would he have insisted that a theory of the Arabian Sea must represent every single datum of that experience?

circulation because of the very fast response of baroclinic Sverdrup flow, which follows from the low latitude of the Arabian Sea and the jet-like form of the Southwest Monsoon wind field (Sec. 6.2).

There is no doubt that Eqn.(9) is simple, but does it explain enough? A two component representation of the circulation Eqn. (8) is a very low resolution view of a spatially and temporally complex flow field, and it is fair to ask: Has the Arabian Sea circulation been made too simple? The opening remarks suggested one possible criterion for judging the utility of the annual mean circulation, *viz.*, does it represent an observable state of the circulation? The answer in the case of the Arabian Sea is a fairly clear 'no', which motivated a look at the seasonal circulation. So now let's suppose that the seasonal mean is known — but does that look like an observable state of the circulation? The data in Fig. (10) allow an informal test, and a generous assessment might be 'just barely', but you can decide for yourself.

What is clear is that there is much more to learn about the Arabian Sea circulation than is contained within this brief and limited introduction. The best result is that it might spark your curiosity and a desire to make your own contribution.

9 Problems

(1) Using the animation of the data of Fig. (1), consider the following. The ITCZ is not sketched onto the frames, and it isn't readily apparent as a shear line or divergence maximum in the stress field. However, the associated wind reversals, especially the onset of the Southwest Monsoon, are clearly evident. Pick a latitude along the western boundary: How long after the passage of the sun does the wind reversal occur? Does this vary with latitude? Is there anything special about the near-equatorial region? Is there any obvious temporal variation in the wind field aside from the marked seasonal variation?

(2) During the discussion of the streamfunctions of Fig. (7), it was noted that the streamfunction should go back to near zero on the western boundary, presuming only that the net volume transport through the 10 N section is small compared to the regional volume transport. We also noted that the ssh (geostrophic) slope has the sign of the meridional transport, and is generally large where the transport is large. However, the ssh does not return to its starting value going from east to west across the basin; the interior slope is smaller by a factor of two or three than is needed to accomplish this. Any thoughts on why that might be the case? A second question: How are the annual mean and the seasonal mean streamfunctions related?

(3) Using the animation linked in Fig. (1): When are the first signs of the Great Whirl? When does it reach a maximum amplitude? How quickly does the Great Whirl expire after the wind reversal in the fall? How about the Socotra Eddy? Can you discern a relationship between these eddies (don't forget SEII) and the somewhat larger anti-cyclonic gyre identified with the interior Sverdrup flow? Which develops first, the gyre or the eddies?

(4) Questions regarding remote forcing seen in the animation https://www2.whoi.edu/staff/jprice/NIO-ssh/. Do you see any evidence that the western basin of the NIO (the Arabian Sea) can have a significant impact upon the eastern basin (the Bay of Bengal), or is remote

forcing one way only, i.e., westward only? Is there evidence of remote forcing from the equator?

(5) How does the western boundary region mismatch of meridional transport and Sverdrup transport seen in Fig. (13) show up in the Sverdrup streamfunction? What sets the western boundary value of the Sverdrup streamfunction?

(6) The net transport through 10 N (the black line of Fig. 15) has an amplitude of roughly 1 Sv, and oscillates with an annual period. Could this possibly be a genuine signal of ssh variation over the control volume (as opposed to a sampling issue with the velocity)? The surface area of the control volume is about 2.5×10^6 km^2.

Index

control volume, 17

East Arabian Current, 15

Findlater Jet, 14

Great Whirl, 21

ITCZ, 13

monsoon, 13
    Northeast, 15
    Southwest, 13

Omani Eddy, 22

SEII, 22
Socotra Eddy, 21
Somali Current, 15

MIT OpenCourseWare
https://ocw.mit.edu/

RES.12-001 Topics in Fluid Dynamics
Fall 2024

For information about citing these materials or our Terms of Use, visit: https://ocw.mit.edu/terms.